**12th Biennial SGA Meeting**
12–15 AUGUST 2013, UPPSALA, SWEDEN

# Mineral deposit research for a high-tech world

SOCIETY for GEOLOGY APPLIED to MINERAL DEPOSITS

# Proceedings

## VOLUME 1

**12th Biennial SGA Meeting**
12–15 AUGUST 2013, UPPSALA, SWEDEN

# Mineral deposit research
# for a high-tech world

# Proceedings

## Volume 1

Edited by
Erik Jonsson et al.

The 12th Biennial Meeting was organised by the Geological Survey of Sweden with assistance from Uppsala University, Stockholm University, the Geological surveys of Finland and Norway, Luleå University of Technology and the Swedish Museum of Natural History.

A digital version of these volumes is available from the SGA website at www.e-sga.org

Cover photograph: View of the Aitik open pit copper mine in the very north of Sweden. Mining operations started in 1968 and the current mining depth is 430 m. The open pit is c. 3 km long and 1.1 km wide. The production in 2012 was 34,3 million tonnes of ore containing 67 100 tonnes of copper, 51 700 tonnes of silver and 1,9 tonnes of gold. Photo: Olof Martinsson, Luleå University of Technology.

**VOLUME 1**

## New advances in geochemical exploration ............... **395**

**Alistair J R White, Raymond E Smith, Patrick Nadoll & Monica LeGras**

## PREFACE

Sweden has a long history of mining and metal production, stretching back more than a thousand years. Because of the direct use for, and economic interest in mineral deposits, they also became an early focal point of the burgeoning natural sciences. During the past decades, there has been an accelerating increase in exploration in the Fennoscandian shield, and the number of exploration permits in Sweden during the last ten years has reached record levels. With this background, it is very fitting to host the twelfth of the biennial meetings of the Society for Geology Applied to Mineral deposits (SGA) here in Uppsala, located in the eastern part of Sweden's oldest and most classical ore province, Bergslagen. Mining commenced in this area at least before the 13th century and is still on-going, as exemplified by e.g. Boliden's base-metal and silver mines at Garpenberg.

Beside metals, that have been fundamental to society for centuries, the recent global increase in demand for rare or "critical" metals has resulted in expanding interest in both exploration and research related to such metals and their deposits. Because of this, and the increase in public and political awareness of these matters, we find the theme of this SGA meeting, Mineral deposit research for a high-tech world, to be relevant and timely.

We hope this meeting will offer all interested a broad and interesting array of science related to mineral deposits, as indicated by the variety of topics covered by the 25 different scientific sessions. The present volumes, containing some 450 extended abstracts, capture the state of the art in mineral deposit research over the world. We are particularly pleased to see a very strong student attendance to the meeting, comprising 180 of the registered participants. This should give us all high hopes for the future of our science.

The Geological Survey of Sweden is proud to host the 12th SGA Biennial Meeting in Uppsala, Sweden. We are thankful to the academic organisations and institutes supporting and helping us to organise this meeting: Uppsala university, Stockholm university, Luleå university of technology, the Geological surveys of Finland and Norway, and the Swedish Museum of Natural History. We are also very grateful to our sponsors, who have supported this meeting: Boliden AB (main sponsor), LKAB, Agnico-Eagle Mines Limited and Mawson Resources Ltd. The support and scientific sponsorship from IMA-COM, CODMUR/IAGOD, IGCP/SIDA and SEG to specific sessions is gratefully acknowledged.

In closing, we also want to express our sincere thanks to all others who have made this meeting possible and worked hard for it – the local organising committee, the scientific committee, the excursion organisers and leaders, all administrative, technical and editorial staff, student volunteers and last, but very far from least, all convenors and co-editors of these volumes, who have invested tremendous efforts and a lot of patience to ensure the success and quality of their respective scientific sessions and abstracts.

**Erik Jonsson**
Chair of the scientific committee

**Per Klingbjer**
Chair of the local organising committee

## EDITORS

(in alphabetical order)

**Mehraj Aghazadeh**
Department of Geology, University
of Payame Noor, Iran

**Rodney Allen**
Boliden Mineral AB and Luleå University
of Technology, Sweden

**Thomas Angerer**
Centre for Exploration Targeting, University
of Western Australia, Australia

**Tobias Bauer**
Division of Geosciences and Environmental
Engineering, Luleå University of Technology,
Sweden

**Georges Beaudoin**
Département de Géologie et de Genie
Géologique, Université Laval, Canada

**Rognvald Boyd**
Geological Survey of Norway, Norway

**John Carranza**
School of Earth and Environmental Sciences,
James Cook University, Australia

**Zhaoshan Chang**
Centre of Excellence in Ore Deposit Studies
(CODES), University of Tasmania, Australia,
and Economic Geology Research Unit
(EGRU), School of Earth and Environmental
Sciences, James Cook University, Australia

**Michel Cuney**
CREGU and UMR CNRS-UL
Georessources, France

**Paul Duuring**
Centre for Exploration Targeting (CET),
University of Western Australia, Australia

**Pasi Eilu**
Geological Survey of Finland, Finland

**Håvard Gautneb**
Geological Survey of Norway, Norway

**Richard Goldfarb**
United States Geological Survey, USA

**Steffen Hagemann**
Centre for Exploration Targeting (CET),
University of Western Australia, Australia

**Jeffrey Hedenquist**
Department of Earth Sciences,
University of Ottawa, Canada

**Richard Herrington**
Department of Mineralogy, Natural History
Museum, London, England

**Karin Högdahl**
Department of Earth Sciences,
Uppsala University

**Zengqian Hou**
Institute of Geology, Chinese Academy of
Geological Science, Beijing 100037, China

**Robert Hough**
Commonwealth Scientific and Industrial
Research Organisation (CSIRO), Australia

**Nils Jansson**
Boliden Mineral AB, Sweden

**Erik Jonsson**
Geological Survey of Sweden, and
Department of Earth Sciences,
Uppsala University

**Christopher Juhlin**
Department of Earth Sciences,
Geophysics, Uppsala University

**Kalin Kouzmanov**
Earth and Environmental Sciences,
University of Geneva, Switzerland

**Yann Lahaye**
Geological survey of Finland, Finland

**Raimo Lahtinen**
Geological survey of Finland, Finland

**Pertti Lamberg**
Department of Civil Environmental and
Natural Resources Engineering, Luleå
University of Technology, Sweden

**Ross Large**
Centre of Excellence in Ore Deposit Studies
(CODES), University of Tasmania, Australia

**Laura Lauri**
Geological Survey of Finland, Finland

**David Leach**
Centre for Exploration Targeting (CET),
University of Western Australia, Australia

**Michael Lesher**
Mineral Exploration Research Centre,
Department of Earth Science, Laurentian
University, Canada

**Wolfgang Maier**
Department of Geology, University
of Oulu, Finland

**Alireza Malehmir**
Department of Earth Sciences,
Geophysics, Uppsala University

**Karel Miskovsky**
Department of Civil, Environmental and
Natural Resources Engineering, Luleå
University of Technology, Sweden

**Ferenc Molnár**
Geological Survey of Finland, Finland

**George Morris**
Geological Survey of Sweden, Sweden

**Axel Müller**
Geological Survey of Norway, Norway

**Vesa Nykänen**
Geological Survey of Finland, Finland

**Hugh O'Brien**
Geological Survey of Finland, Finland

**Jan Pašava**
Czech Geological Survey, Czech Republic

**Gervais Perron**
Mira Geoscience, Canada

**Iain Pitcairn**
Department of Geological Sciences,
Stockholm University

**Richard Přikryl**
Institute of Geochemistry, Mineralogy and
Mineral Resources, Charles University in
Prague, Czech Republic

**Jeremy Richards**
Department of Earth & Atmospheric
Sciences, University of Alberta, Canada

**Brian Rusk**
School of Earth and Environmental Sciences,
James Cook University, Australia

**Pertti Sarala**
Geological Survey of Finland, Finland

**Peter Sorjonen-Ward**
Geological Survey of Finland, Finland

**Krister Sundblad**
Department of Geography and Geology,
University of Turku, Finland

**Hans Thunehed**
GeoVista AB, Sweden

**Fernando Tornos**
Centro de Astrobiología, Spain

**Thomas Wagner**
Department of Geosciences and Geography,
University of Helsinki, Finland

**Yasushi Watanabe**
National Institute of Advanced Industrial
Science and Technology (AIST), Japan

**Roberto Xavier**
Institute of Geosciences, University
of Campinas, Brazil

**Federica Zaccarini**
Department of Applied Geological
Sciences and Geophysics, University
of Leoben, Austria

## LOCAL ORGANISING COMMITTEE

**Per Klingbjer (chairman)**
Geological Survey of Sweden

**Katarina Nilsson**
Geological Survey of Sweden

**Raimo Lahtinen**
Geological Survey of Finland

**Alireza Malehmir**
Uppsala University

**Kjell Billström**
Swedish Museum of Natural History

**Rodney Allen**
Boliden Mineral AB

**Erik Jonsson**
Geological Survey of Sweden

**Magnus Ripa**
Geological Survey of Sweden

**Rognvald Boyd**
Geological Survey of Norway

**Iain Pitcairn**
Stockholm University

**Peter Hedin**
Uppsala University

**Karin Högdahl**
Uppsala University

**Pär Weihed**
Luleå University of Technology

## SCIENTIFIC COMMITTEE

**Erik Jonsson (chairman)**
Geological Survey of Sweden

**Iain Pitcairn**
Stockholm University

**Rodney Allen**
Boliden Mineral AB

**Axel Müller**
Geological Survey of Norway

**Jan Pašava**
Czech Geological Survey

**Thomas Wagner**
University of Helsinki

**Christopher Juhlin**
Uppsala University

**Jochen Kolb**
Geological Survey of Denmark
and Greenland

**Wolfgang Maier**
University of Oulu

**Gilles Bellefleur**
Geological Survey of Canada

**Kirsti Loukola-Ruskeeniemi**
Geological Survey of Finland

**Björn Schouenborg**
Swedish Cement and Concrete
Research Institute

**Henrik Stendal**
Greenland Bureau of Minerals and
Petroleum

**Pasi Eilu**
Geological Survey of Finland

**Holly Stein**
Colorado State University

**Raimo Lahtinen**
Geological Survey of Finland



Falu copper mine, Bergslagen, Sweden. Photo: Katarina Persson Nilsson.

# Plenary lectures

# The moral case for mining – is it a question the industry can answer?

Michael Harris
*Technical Director, Business Development, Rio Tinto plc, London*
*Department of Earth Science & Engineering, Imperial College London*

**Abstract.** The mining industry operates in an environment increasingly demanding of its products. However, establishing the moral case for taking natural resources from one area to benefit another with most of the profits leaving the host country is becoming increasingly difficult. The same is true of the often irreparable change to delicate ecosystems from mining - why should plants, animals and peoples suffer, often die, in one place to benefit development in another while dominantly enriching distant investors?
Most modern mining companies try to operate in an environmental- and community-friendly way but with varying degrees of success. Mining companies answer to shareholders and are regulated by governments; they make common use of tax havens and fiercely resist increased taxation or any hint of "resource nationalism".
Large segments of the industry are suffering from self-inflicted over-investment during the post-GFC euphoria. Increasing demand for most commodities appears likely to continue but the industry will at some point return to a more expansive mood although reserves of most commodities are being easily replaced with peak metal not on the horizon.
Mining companies and universities should lead society in establishing an honest debate on the morality of mining in the context of the forecast demand for its products.

**Keywords.** Morality in mining

## 1 The questions to be asked

Establishing the moral case for taking natural resources from one part of the world to benefit another with most of the profits leaving the host country is becoming increasingly difficult. The same can be said about the often irreparable change to delicate ecosystems through mining - why should plants, animals and peoples suffer, often die, in one place to benefit development in another while dominantly enriching distant investors?

The following questions are suggested as a basis to consider society's moral stance on mining:

- *Who owns the earth's resources and who is empowered to licence their depletion?*

- *Who should benefit from the depletion of irreplaceable natural resources?*

- *Given an acceptance that the global "poor" are aspiring to standards equivalent to those of the global "rich" – who has the moral right to deny them the supply of the mineral resources required to meet that?*

- *Should the world agree that all of its population should share equally in prosperity, who will decide on how and where delicate ecosystems will disappear to supply this demand?*

- *Is the global mining industry sufficiently engaged in these moral questions or too absorbed in short term profits?*

- *Is society being active enough in this debate?*

## 2 Some background

In trying to judge whether disturbance of the earth's surface and consumption of its mineral resources at ever accelerating scales is justified, society must understand what is required from the mining industry to meet the demand for its products and to consider the moral questions listed above. Even though many economists are sceptical that the current cycle of higher commodity prices is sustainable in the long term, there is sufficient evidence of escalating demand for there to be sustained market pressure on the mining industry for dramatic increases in production.

To meet the forecast demand for commodities, mining companies are struggling with escalating operating and capital costs from price inflation and governments are increasingly demanding that companies share the proceeds of mining with them. Recent examples include agreeing a 34 per cent share in the Oyu Tolgoi project for the Mongolian government, a 35 per cent share in the Simandou iron ore project for the Guinean government and Australia's debate on the Mineral Resource Rent Tax.

These pressures have led to increased competition for access to the most profitable orebodies creating a market favouring miners with the skills demanded by society as compensation for the changes inflicted on ecology, water resources and communities.

## 3 Some suggestions

### 3.1 Sustainable development
An answer to how mining companies can compensate for the value they take out is the often quoted "sustainable development" approach. In its purest form, this means a company creating benefits to society and nature that can continue (i.e., be sustainable) without prolonged support from the company for long periods both during mining and afterwards.

This includes delivering benefits that compensate for

the loss of what is destroyed in the mining process. Effective rehabilitation of mined areas is now an advanced practice and a key element of project planning which can add sustainable value for communities both during and following the extraction of mineral resources. This can be through creative rehabilitation which replaces natural habitats but also establishing new business opportunities for local communities.

An example exists at the Richards Bay heavy mineral sands mine in South Africa. Richards Bay Minerals replants two thirds of its mined areas with casuarina to be used for charcoal production and rehabilitates the other third of mined dunes by re-planting indigenous forest from seeds collected from the area before mining starts or grown locally. This results in rehabilitated dunes and restored ecosystems which are home to indigenous species plus sustainable cash crops for use by the local community.

There are other examples but care must be taken to distinguish between programmes aimed at delivering sustainable solutions from those that give "gifts" as compensation even if these are hospitals, schools, etc. The latter are important but only part of the moral answer.

### 3.2 Environmental & community

By its very nature, mining is destructive to existing ecosystems. Increasingly, investors and governments are demanding that respect for the environment be central to a company's approach to sustainable development.

Most modern, responsible mining companies attempt to minimise, mitigate and remediate harmful effects of their operations on the environment. An essential first step is an accurate assessment of habitats before exploration commences.

At the Simandou iron ore project in eastern Guinea, Rio Tinto formed a partnership with Conservation International to carry out surveys of flora and fauna at the very initial exploration stages of the project. It also contracted respected third parties to document the communities around Simandou before plans to access the project for exploration were agreed.

These data will stand as records for Rio Tinto and its advisors to work with the Guinean authorities, the local communities and international agencies to develop plans benefitting from common baselines when considering future development for Simandou.

Many modern mining companies have been leaders in implementing long term programmes of social development. For these to be successful, they must build on a solid knowledge of what existed before they arrived and how the community wishes to develop.

Successful miners have always known and stressed that relationships with their neighbours is one of the most important factors to guaranteeing a successful operation. Effective community relations are as necessary for business success as the effective management of operations. Understanding the social, environmental and economic implications of mining activities so that the support will result in long term sustainable improvements to living standards now forms a fundamental part of mine planning. Governments and society should demand this and the industry should accept it. To be competitive, mining companies will increasingly seek orebodies amenable to low carbon extraction, product distribution and utilisation. They will have to develop technologies that reduce emissions throughout the mining process from extraction to final product. However there must be a balance between punitive legislation and achieving development goals. Effective and price competitive carbon capture technology remains one of the most important technical improvements in front of mining.

Society must also demand that miners improve utilisation rates in the extractive process. It will become increasingly unacceptable for companies to use inefficient processing technologies, the consequences of which are that even further areas of the earth have to be disturbed. Investing in innovative new recovery technologies that maximise extraction rates and hence minimise wastage of earth resources will prove to be a crucial differentiators between miners in the future.

## 4 The increasing impact of mining projects on national economies

The increased cost and size of many mining projects, especially if they require large scale infrastructure, has changed their impact on national economies from their traditional marginal positions to now being comparable with oil projects. Large mining projects are capable of transforming national economies, with the ensuing potential for wealth creation. They are also capable of introducing the deleterious effects associated with the oil sector during the latter part of the twentieth century, known as "Dutch disease" or unbalancing stable societies as a result of a sudden uncontrolled in-rush of revenue, out of proportion with the capabilities to invest it.

The potential for positively affecting the economies of underdeveloped countries is especially acute where mining projects include construction of large scale infrastructure such as railways and ports. Sharing the benefits of new rail, road and port facilities is becoming an increasingly important way that large mining projects can introduce sustainable benefits beyond direct taxation. Electrification and improvements to water infrastructure fall into the same category. It is hoped that the trans-Guinean railway and the first deep water port to be built on the Guinean coast by Rio Tinto's Simandou iron ore project may provide benchmarks for this.

Mining companies cannot dictate to sovereign governments how they spend income from mining. Many countries do not have the skills or experience to ensure that proper systems of care are in place nor that such high rates of income arriving so quickly are properly safeguarded and used in the best interests of the country. Mining companies should work closely with international agencies and routinely publish reports on these activities to support this. Although some of this comes as a result of stock market regulations or industry bodies such as the Extractive Industry Transparency Initiative, it is increasingly being driven by mining companies themselves as a direct result of pressure by

investors and NGOs. This reflects recognition of the fundamental importance of establishing "a moral case for mining".

## 5 Economic contributions from mining companies

It is now widely accepted that mining operations can and should provide strong bases for economic growth. However, the true value of their contributions is not always appreciated. To do so, it is important to separate the direct from the indirect effects of investments:

*Direct economic contributions: the value added by paying wages, employee benefits, taxes and royalties and returns on capital along with payments made to suppliers.*

*True economic contributions: includes the indirect effects of spending wages, governments distributing tax and royalty revenues, and neighbouring communities using the infrastructure developed from mining operations and significantly raise the impact of a mining investment.*

In 2011 Rio Tinto made $66.6 billion in direct economic contributions. Of this, 35% was made at local/regional levels and a further 45% at a national level. This included 72% of wages and employee benefits paid to local residents, 76% of taxes and royalties charged by local and regional governments and 62% of all purchases supplied at the local and regional levels. These payments do not include the multiplier effect of the indirect effects that these payments will have on local economies and how they will affect people far beyond those receiving the direct payments mentioned above.

Ensuring these indirect effects are as beneficial and sustainable as possible, is an area that mining companies recognise as part of earning their right to mine. However, this is not typically a core skill and they often need help with implementing best practices.

## Conclusions

- Global demand for the major industrial commodities has doubled roughly every 20 years for the last century and is likely to continue doing so.

- Global reserves and resources for most commodities are replaced as fast as they are mined. Peak metal is not on the horizon.

- Miners can achieve competitive advantages if they improve how they distribute the benefits from the deposits they mine and go beyond merely paying taxes and royalties.

- The industry has a similar need to address how it cares for the environment if it is to keep its licence to operate from society.

- Resource quality is an important criterion for a major mining company like Rio Tinto. "Low-carbon" ore bodies will become increasingly important as we move towards a carbon-constrained world.

- To be competitive, mining companies will increasingly develop technologies that reduce emissions throughout the process from extraction to carbon capture. However there must be a balance between punitive legislation and achieving development goals. Improved mineral extraction technology to reduce the wastage of natural resources is also essential.

- Society must engage in the debate on how to apportion natural resources and the level of environmental and social change it is willing to tolerate to enjoy the benefits from their extraction.

## Acknowledgements

## Reference

Rio Tinto Annual Report, 2012, 2011.

# Challenges for heavy rare earth production: lessons from Japan

**Yasushi Watanabe**
*Geological Survey of Japan, AIST, Higashi 1-1-1, Tsukuba, Japan*

**Abstract.** Heavy rare earth elements (HREE) have been produced from ion-adsorption type deposits in southern China. Despite extremely low REE grades (0.2-0.05wt.%) of the deposits, the exploitation of REE from this deposit type is very competitive because of the easiness of REE extraction. For the purpose of producing heavy REE outside China, a variety of sources are examined. They are 1) ion adsorption deposits outside China, 2) HREE-rich carbonatites, 3) alkaline rock complexes, 4) sediment-hosted phosphates associated with uranium mineralization, 5) xenotime associated with tin granites, and 6) submarine mud. This presentation reviews the geological, mineralogical and geochemical characteristics of these deposit types and discusses the challenges for heavy rare earth production from hard rocks.

.

**Keywords.** Heavy rare earth elements, carbonatite, apatite, xenotime, alkaline rock

## 1 Introduction

The heavy rare earth elements (Gd to Lu) (HREE) (Henderson, 1996), in which often Y is included, are used to produce permanent magnets, phosphors, condensers, zirconia stabilizers, etc. Among them, dysprosium (Dy) is indispensable to improve heat resistance of the NdFeB magnets, which are applied in modern high-tech materials such as the driving motors of hybrid vehicles, factory automation machinery, home electronics and wind turbines (Minowa, 2008). HREE have been mostly produced from ion-adsorption type deposits in southern China, except for a very limited amount of production from xenotime in placer deposits.

Although China has been the main producer of REE in the world, due to the restriction of the production and export of HREE by the Chinese government, many countries have had difficulty in the supply of HREE. In particular, Japan, the second largest REE magnet producer after China, has been concerned about a stable supply of HREE to maintain its domestic REE applied high-tech industries.

On the other hand, this Chinese policy has resulted in the worldwide HREE exploration activities recently (Figure 1). These activities mainly focus on the REE mineralization in hard rocks rather than ion-adsorption type mineralization, probably because the formation of ion-adsorption deposits requires several specific conditions. This paper reviews representative HREE mineral deposit types and their challenges for the development of the deposits.

## 2 Review of the HREE deposits

### 2.1 Ion adsorption deposits

Ion-adsorption type mineralization is formed in the following geological and climatic environments; 1) presence of HREE enriched host rocks (mostly ilmenite-series granite), 2) tropical to semi tropical climate to form a thick saprolite unit, and 3) presence of soluble HREE minerals (carbonates, mostly secondary) in the host rocks. This type of mineralization is found not only in southern China, but also in neighboring countries such as Vietnam (Machida, 2008) and Thailand (Sanematsu et al, 2013). Exploration is conducted for this type of the mineralization related to syenite in Madagascar and Malawi as well.
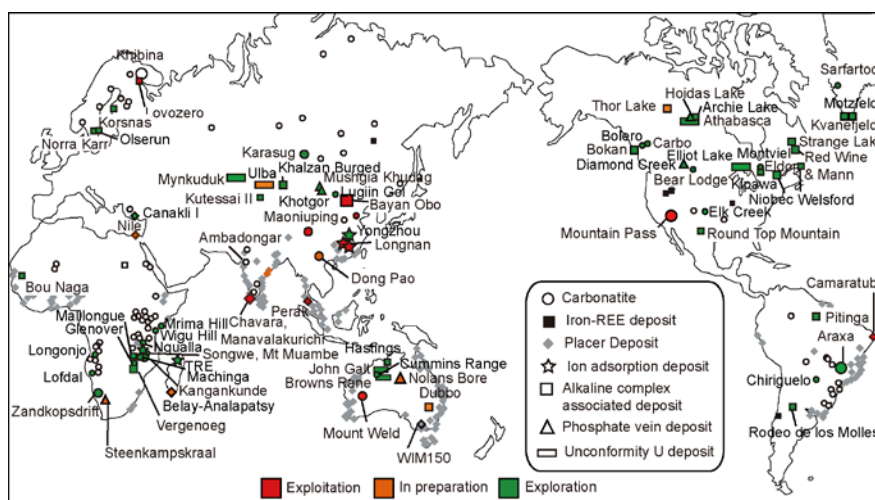


**Figure 1.** Distribution of major REE exploration and exploitation projects in the world.

## 2.2 Carbonatite deposits

High-grade carbonatite deposits are generally enriched in LREE because of enrichment of bastnasite due to magmatic fractionation. However, some carbonatites (e.g. Glenover and Zandkopsdrift in South Africa) are relatively enriched in HREE hosted in phosphate minerals, although REE grades are lower than LREE-enriched ones. The Yen Phu deposit in northern Vietnam and Lofdal deposit in Namibia are the most HREE-enriched examples. The Yen Phu deposit consists of two lensoidal orebodies; 260m x 160m x 60m (thickness) and 70m x 20-50m x 13m (thickness) in size in sericite-quartz schist (Machida, 2008). The orebodies occur in the weathered and hydrothermaly altered zone above a dolomitic carbonatite intrusion and include xenotime and samarskite as ore minerals with abundant iron oxides.

## 2.3 Deposits associated with alkaline rock complexes

This type of the mineralization is explored worldwide. Advanced stage projects are known in Canada (Nechalacho, Strange Lake, Kipawa), USA (Bokan Mountain), Greenland (Kvanefjeld), Scandinavia (Norra Kaar), Australia (Dubbo) and Mongolia (Khaldzan Burgei). These deposits are associated with peralkaline syenite (Nechalacho, Kipawa, Kvanefjeld, Norra Kaar, Dubbo) or fractionated granites (Strange Lake, Bokan Mountain, Khaldzan Burgei) in the complexes. The orebodies are variable in form; cumulate units (Kvanefjeld), dissemination (Kvanefjeld, Kipawa, Dubbo, Khaldzan Burgei), pegmatite (Strange Lake), and vein (Bokan Mountain). Some of the deposits (Strange Lake, Kvanefjeld, Nechalacho) have extremely large reserves, although ore grades are generally low (2-0.5wt.%). Ore mineralogy is quite variable and complex in each deposit, including unconventional zirconium silicates (zircon at Nechalacho and Dubbo, eudialyite at Kipawa, Kvanefjeld and Norra Kaar, elpidite at Khaldzan Burgei).

## 2.4 Sediment-hosted phosphate deposits associated with uranium mineralization

Unconformity related and/or sediment-hosted uranium mineralization is occasionally associated with sediment-hosted xenotime mineralization. Representative examples are found in Canada (Douglass River) and Australia (Hastings, Brown Range). Despite relatively small proven reserves of these deposit so far, ore mineralogy (xenotime) is simple and REE is heavily enriched in HREE. REE is being recovered from phosphate minerals in the tailing of uranium mine in Kazakhstan.

## 2.5 Xenotime mineralization associated with Sn granites

Xenotime mineralization is associated with Sn granites, and xenotime was recovered from heavy placer sands in Australia and Malaysia. Now it is recovered as a byproduct of cassiterite in tin mines in Malaysia. Xenotime is also recovered or planned to recover from Sn tailing materials (Amang) in Malaysia, Indonesia and Brazil.

## 2.6 Heavy rare earth mineralization in submarine ferruginous mud

It is confirmed that submarine mud in a large part of the Pacific Ocean contains a few thousands ppm of REE with a high proportion of HREE (Kato et al., 2011). Similar mineralization has been confirmed off Minami Torishima Island recently (Press Release by University of Tokyo, 2013). In Minami Torishima area, several thousands ppm of REE are detected in a couple of meter thick mud about 3m below the sea floor. This HREE-bearing mud is ferruginous and HREE are mainly included in apatite (Kon et al., 2013).

## 3 Challenges for HREE production

Although more than five years have been passed since many REE exploration project started, no project has started HREE production except the SARECO project in Kazakhstan, which plans to produce 1500t rare earth oxides in 2013. Many challenges exist before the exploitation of HREE from hard-rock deposits to compete with low-cost HREE production from the ion adsorption deposits in China.

In the exploration stage, high grade ores are preferred, but mineralogy is also a key. Weathering may upgrade the ores, especially in the case of carbonatites, but secondary minerals formed in the weathered condition are fine in size and refractory in general, resulting in difficulty in making high-grade mineral concentrates and HREE extraction.

Major target minerals for HREE recovery in the hard-rock deposits are carbonate [synchysite-(Y)], phosphate (xenotime, apatite) and zirconium-silicate minerals (zircon, eudialyite, mosandrite, gittinsite, elipdite), in addition to Nb oxide minerals (fergusonite, samarskite, euxenite, etc.). Simple mineralogy is preferred to conduct simple mineral dressing and processing, although HREE deposits associated with alkaline rocks are generally complex in mineralogy. Ore minerals that contain high amounts of REE are preferred because high-grade mineral concentrates can be produced. The ore minerals listed above are new for REE extraction except carbonates and xenotime, it is required to establish economically feasible beneficiation and REE extraction methods.

At last, the ores may be radioactive because of concentration of thorium and uranium. If the ores are highly radioactive, treatment of radioactivity is indispensable.

## 4 Epilogue

There is a common perspective that the demand of REE, in particular, HREE will steadily increase in future. However, recent efforts to reduce the amounts of REE used in the products or during polishing, or to replace REE with other materials have been successful in Japan. Dysprosium content in NdFeB magnet has decreased 1/3 compared to the content five years ago, and now the production of Dy free magnet is explored. Recycling of REE is also popular, and REE-containing scraps generated during the production of finished goods are completely recycled. As the result, the demand of REE in Japan has significantly decreased in the last five years (Figure 2). In conclusion, the real competition in the production of HREE is not among the mining companies or countries but against the rapid innovation of high technology.
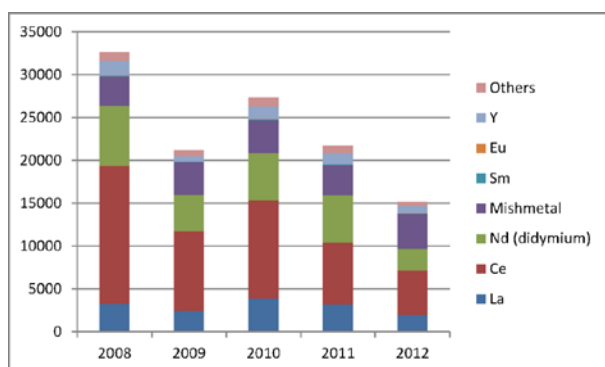


**Figure 2.** Demand of rare earths (shown as oxide t) in Japan (Rare Metal News, 2013).

## References

Henderson P (1996) The rare earth elements: introduction and review. In AP Jones et al. eds., Rare earth minerals Chemistry, origin and ore deposits, The Mineralogical Society Series 7: 1-19

Kato Y, Fujimoto K, Nakamura K, Takaya Y, Kitamura K, Ohta J, Toda R, Nakashima T and Iwamori H (2011) Deep-sea mud in the Pacific Ocean as a potential resource for rare-earth elements. Nature Geoscience 4: 535-539

Kon, Y, Hoshino M, Sanematsu K, Okamoto N, Yano N, Tanaka M and Takagi T (2013) Mineralogical and geochemical characteristics of apatite in the REE-bearing deep sea mud off Minami Torishima. Abstracts of Annual Meeting of the Society of Resource Geology (in Japanese)

Machida S (2008) Rare earth resource exploration in Lao Cai district, Vietnam. Kinzokushigen Report, 7, JOGMEC: 19-138 (in Japanese)

Minowa T (2008) Rare earth magnets: Conservation of energy and the environment. Resource Geology 58: 414-422

Rare Metal News (2013) Rare Metal News No. 2570

Sanematsu K, Kon Y, Imai A, Watanabe K and Watanabe Y (2013) Geochemical and mineralogical characteristics of ion-adsorption type REE mineralization in Phuket, Thailand. Mineralium Deposita 48: 437-451

University of Tokyo (2013) Press Release Discovery and distribution of mud containing very high concentrations of rare earth elements and yttrium around Minami-Torishima Island (Minami-Torishima Survey Cruise) http://www.jamstec.go.jp/e/about/press_release/20130321/

U.S. Department of Energy (2010) Critical Materials Strategy. U.S. Department of Energy: 165p

S 1:
# Sustainability in mining and exploration: the role of geosciences

Convenors:
Jeremy Richards & Rognvald Boyd

# Critical metals: scarcity, security of supply and solutions

Gus Gunn
*British Geological Survey, Environmental Science Centre, Nicker Hill, Keyworth, Nottingham, NG12 5GG, UK*

**Abstract.**
Rapid increases in world population, the spread of prosperity across the globe and the demands of new technology have led to a revival of concerns about the availability of secure and adequate supplies of raw materials needed by society. Although physical exhaustion is unlikely, we need to know which 'critical' materials we should really be concerned about so that we can act now to develop strategies to mitigate the effects of supply disruption. There have been several recent attempts to identify critical metals, but it is not surprising that, with no consensus on the methodology and the criteria to be used, a variety of results have been produced. In fact, there can never be a single or correct list of critical metals that is universally applicable and that will not change over time. We need detailed analysis of the life-cycle of individual metals to identify specific problems and develop appropriate solutions. Geological research has a fundamental role to play in helping us to locate new deposits of the critical metals.

**Critical metals, mineral scarcity, criticality assessment, security of supply**

## 1 Metal scarcity?

Minerals are essential for economic development, for the functioning of society and for maintaining our quality of life. Everything we have or use is ultimately derived from the Earth, produced either by agricultural activities or by the extraction of minerals from the crust.

Consumption of most metals has increased steadily since World War II and demand is expected to continue to grow in response to the burgeoning global population and the spread of prosperity across the world. New technologies such as those required for modern communication and computing and to produce clean energy also require considerable quantities of many metals. For some metals, especially those used in high-tech applications, the rate of use has increased particularly strongly in recent decades with more than 80% of the total global cumulative production of PGM, REE, indium and gallium having taken place since 1980 (Hagelüken et al., 2012). We are also using a greater variety of metals than ever before. In the 1980s manufactured products were made from a relatively small number of metals, perhaps fewer than 20 in all. Today, however, modern technology and the continuing quest for improved performance have led to designers employing the majority of elements in the periodic table. For example, electronic microchips now use about 60 metals.

In the light of these trends there is increasing global concern over the long-term availability of secure and adequate supplies of the minerals and metals needed by society. It has therefore become important to ask if we can continue to meet the increased demand and whether our resources will ultimately be exhausted. Similar questions concerning the adequacy of natural resources to support the needs of economic growth and the spread of prosperity have been asked for centuries. More recently the Club of Rome, a think tank based in Europe, raised the possibility that mineral exhaustion would, by the middle of the 21st century, cause the collapse of the prevailing high standards of living, especially in the developed world (Meadows et al., 1972). Among the scenarios analysed the Club of Rome reported that only 550 billion barrels of oil reserves remained and that they would run out by 1990. In fact, the world consumed 600 billion barrels of oil between 1970 and 1990, and at the end of 2011 there were estimated to be more than 1650 billion barrels of proven reserves (recoverable at current prices under current conditions) (BP, 2012).

In recent years there has been renewed debate about the long-term availability of adequate and secure supplies of minerals. There is concern that the level and effectiveness of mineral exploration are inadequate to replenish reserves and that changes in the economic, political or environmental climate could severely restrict access to undeveloped deposits in particular countries.

Much of the recent discussion has focussed on the adequacy of reserves to meet future demand rather than on the political and economic barriers. Several authors have concluded that mineral scarcity and, ultimately, depletion are unavoidable (Ragnarsdóttir, 2008; Cohen, 2007). Some have made alarmist forecasts which suggest that for some minerals and metals depletion may occur over relatively short timescales of a few decades or even years. However, these predictions are based on 'static lifetimes', derived from existing known resources or reserves divided by current or projected future demand (Cohen, 2007; Gilbert, 2009; Sverdrup, 2009). These forecasts fail to recognise that resources and reserves are neither well known nor fixed. Reserves are economic entities that depend on scientific knowledge of minerals and on the price of the target metal or mineral. As our scientific understanding has improved reserves have continually been replenished through new discoveries, and by improved mining and processing technology. Furthermore, market mechanisms help to overcome supply shortages - if prices rise, then reserves will extend to include lower grade ore; if prices fall then they will contract to include only higher grade material.

Crowson (2011) showed that, despite escalating production, reserve levels have actually grown over time and outpaced production. For example, global copper reserves in the early 1930s were reported to be about 100 million tonnes, thought at the time to be sufficient for

about 80 years. However, in 2010 the USGS reported copper reserves of 540 million tonnes (USGS, 2010) and, in 2011 the estimate was again revised upwards to 630 million tonnes, an increase of more than 16 per cent in a single year (USGS, 2011). Similar trends can be seen in the global reserve levels for several minor metals, including, for example, tungsten and the rare earth elements (REE). It is clear, therefore, that reserve estimates, and the static lifetimes calculated from them, are unreliable indicators of the long-term availability of metals.

The petroleum industry's debate about 'peak oil' has also been extended to non-fuel minerals (Hubbert, 1956). Various authors have advocated 'peak metals' as a tool for understanding future trends in the production of metals (Bardi and Pagani, 2007; Giurco et al., 2010). However, the application of the peak concept to metals production is seriously flawed and fails to address the real causes of variations in production and consumption in the mineral markets (Crowson, 2011; Ericsson and Söderholm, 2012). Records from the last 200 years show that metal prices are cyclical, with intermittent peaks and troughs closely linked to economic cycles. Declining production is generally driven by falling demand rather than by declining resources or lack of resource discovery. At times of increasing scarcity the price of minerals will increase, which, in turn, will stimulate increased substitution and recycling and will encourage investments in new capacity, more exploration and improved technology. It is concluded therefore that peak concept is not valid for modelling non-fuel mineral resource depletion and it cannot provide a reliable guide to future metal production trends.

## 2 Security of supply - criticality

In the last decade the term 'critical' has been applied to those metals that might cease to be available in adequate quantities to meet the demands of technology. Governments and businesses worldwide are trying to identify which materials they should be worried about and their level of dependence on unreliable supplies of these materials. Of greatest concern are those of growing economic importance that might be particularly susceptible to long-term scarcity, regardless of the reason. We would like to be able to identify those materials in advance so that we can mitigate the associated risks and thus enhance security of supply in the longer term.

Numerous factors influence the availability of non-renewable resources and make the assessment of criticality highly complex. Various geological parameters, such as crustal abundance and the nature and distribution of deposits, are fundamental controls. However, a wide range of economic, technological, environmental, geopolitical and social factors may also constrain mineral supply. Consequently the analysis can never be perfect: the results will inevitably vary over time and can never be universally applied or equally valuable to all users.

It is important to point out that criticality is a matter of degree, a position on a sliding scale and not a binary choice. It is not the position of a switch, such that a metal is either critical or non-critical, but rather a position on a dial where any position above a certain level could arbitrarily be designated as the dividing line between critical or not. Another major complexity concerns the metric itself: what is the dial measuring? Because criticality is dependent on a broad range of factors various multi-dimensional methodologies have been used for its assessment leading to considerable diversity of results.

### 2.1 Criticality assessment

Several recent studies in the EU, USA, Japan, UK and elsewhere have attempted to identify the most 'critical' metals and minerals. Given that there is no consensus on the metrics of criticality, and that the assessments have been conducted at various organisational levels (company, national and international) and over different time frames, it is hardly surprising that the results have been inconsistent and sometimes contradictory. Most studies have evaluated a wide range of materials and have tended to prescribe a range of generic measures for the mitigation of supply risk. Recommended mitigation strategies generally focus on diversification of the supply base, improved resource efficiency and recycling, and increased substitution. However, in reality, each metal is different and there are no universal solutions. Detailed analysis of the life-cycle of each is required in order to identify particular problem areas and to develop appropriate solutions.

Buijs and Sievers (2012) reviewed criticality assessments from the USA and EU carried out in the 1970s and 1980s. Although similar approaches to those of today were used, the critical minerals identified in the earlier assessments differ from those now classified as critical, thus highlighting that such studies provide only a 'snapshot' of a dynamic system and have little predictive value. However, the causes and solutions proposed at that time are similar to those of today. Then, as now, it was concluded that, although geological scarcity was highly unlikely, the main supply risks were import dependence, the concentration of production in a small number of politically unstable countries and increased resource nationalism. The measures proposed to alleviate future supply shortages included stockpiling of raw materials, establishment of long-term supply contracts and exploitation of indigenous resources.

The first recent attempt to demonstrate the concept of metal criticality and suggest metrics that might be employed to assess it was that of the US National Research Council (2008) which proposed that criticality was a two-parameter variable, one parameter being supply risk and the other the impact of supply disruption. Further, each of those parameters in turn was based on the aggregation of a number of contributory metrics: geological availability, political factors, technological capacity and other factors for supply risk; and substitutability, importance of end-use applications and other factors for impact of supply restriction.

A second important evaluation was undertaken to identify those metals and minerals critical to the EU economy (European Commission, 2010). The EC working group retained the two-axis concept, with

supply risk being one of the parameters, but defined the second axis on the basis of the potential economic impact of supply disruption on European industry. Supply risk was further defined as the aggregate of three parameters: the political stability of the producing countries, the potential to substitute the metal being evaluated, and the extent to which the metals are recycled.

These and several other criticality assessments were reviewed by Erdmann and Graedel (2011) and Buijs and Sievers (2012). They found that the great differences in methodology, in the sets of metals reviewed, and in the selection criteria utilised, combine to make the distinction between critical and non-critical metals too complex to be easily resolved. It is clear that, although this topic is generating a high level of interest from governments and businesses throughout the world, the methodology is immature and the results are not necessarily helpful to all parties whose ultimate aim is to secure future supplies of minerals.

Particular aspects of the published assessments that have been criticised include: the lack of predictive power; the tendency to overstate the potential economic impacts of supply disruption; the failure to discriminate between short- and long-term problems; the failure to take account of the differences in the markets of individual commodities; and the focus on raw materials while neglecting other parts of the life cycle.

The lack of suitable high quality data is another serious issue which can impact on the results of the criticality assessment. For example, some data required for the analysis is not available for individual members of element groups such as the platinum-group metals and REE. Similarly, for many minor metals trade data is not available in adequate detail on individual metals, ores, concentrates and intermediate products to allow definition of global import and export patterns.

Given the inherent complexities and the data shortcomings it is inevitable that the results of criticality assessments are fraught with uncertainty. They may suggest that certain materials are at risk when, in fact, market forces may be able to solve the problems in the short or medium term. They may also produce false negatives whereby supplies of some materials are incorrectly identified as secure. However, as these limitations have come to be appreciated and while interest in criticality remains at a high level, so there have been continual refinements of the methodology, adapting it for particular purposes, different organisational levels and over different timescales.

To date the most advanced generic approach for the determination of criticality is that developed at Yale University which aims to help corporate, national and global stakeholders conduct risk evaluation and to inform resource utilisation and strategic decision-making (Graedel et al., 2012). This method involves three dimensions: Supply Risk, Environmental Implications and Vulnerability to Supply Restriction. It uses a combination of data and expert judgement, the latter especially important for speciality metals used in high-tech application for which little data are available. It is designed to be flexible so that indicators can be selected and weighted according to user preference.

## 2.2 Improving criticality assessment

While it is clear that no single criticality assessment is universally applicable, shortlists of critical raw materials have an important role to play in warning decision makers in government and industry about current issues of concern and possible impacts on security of supply in the short term. Development of a longer term predictive capacity is the ultimate goal of such assessments, but there are many challenges to address before this can be achieved. Key requirements include the necessity to analyse individual metals and underlying issues in more detail, to acquire better data and to analyse trends and patterns of future demand.

A revised list of critical raw materials for the EU is scheduled for publication by the end of 2013. Projections for both supply and demand, particularly taking into account the more widespread adoption of emerging technologies, will be developed in order to enhance the predictive value of the analysis. However, projecting future supply and demand is very challenging and the results will inevitably be subject to high levels of uncertainty. For some applications, such as in batteries for electric vehicles and in thin-film photovoltaic materials for solar power, there is considerable uncertainty over which of a number of alternative technologies will prevail in the future and consequently about the requirements for particular materials (US Department of Energy, 2011). In general the inclusion of projections in criticality assessment will be a step forward because it will reduce reliance on the future validity of indicators compiled from historic and current data. However, projections inevitably represent a present view of future market states and, though useful for orientation, cannot be relied upon to provide accurate assessments of future demand.

There is a requirement to improve the availability and quality of data used in criticality assessments, especially where markets are small and lack transparency, as is the case for many minor metals. In order to develop more rigorous and dynamic assessments of future availability more detailed analysis of all supply and demand issues for individual commodities will be required in the future. Broad criticality assessments will remain useful to provide early warning of potential supply issues, but focused studies are likely to be more useful to particular stakeholder groups.

## 3 Characteristics of critical metals

Many of the metals designated as 'critical' share certain common features. For most the West is heavily dependent on imported supplies, mainly derived from a few countries in which reserves and production are concentrated. The global markets for critical metals are generally small, measured in hundreds or thousands of tonnes. They are dominated by a small number of companies and are characterised by high levels of price volatility. For most of them in many of their applications they are not readily substituted and recycling rates are very low, commonly less than 1% (UNEP, 2011). For many our knowledge base is limited and we have little

information on the processes that concentrate them in the crust, how to explore for them, how to extract them from their ores and how to handle, recycle and dispose of them safely.

Another characteristic is that many rare or critical metals are not mined on their own, rather they are by-products of the mining of the ores of the more abundant and widely used metals, such as aluminium, copper, lead and zinc. They are present as trace constituents in the ores of the host metals and, under favourable economic conditions, they can be produced from ores, concentrates and slags of the major metal. For example, indium and germanium are chiefly by-products from zinc production, while tellurium is mainly derived from copper mining. However, the low concentration of the by-product metal in the host ores means that there is little economic incentive to increase production at times of shortage. For example, only about 25–30% of the 1000 tonnes of indium that is potentially available globally each year from mining indium-rich zinc ores is actually recovered. The rest ends up in wastes because it is not economic to install the additional indium extraction capacity at zinc refineries or because the efficiency of the indium recovery is poor (Mikolajczak and Harrower, 2012).

## 4   Solutions – the role of geology

Ignorance of economic geology is a significant contributory factor to the broad divergence of criticality assessment methods, results and derived solutions that have been proposed in recent years. If the consequences of critical metal supply constraints are to be minimised we need to develop strategies now that will ensure we have adequate reserves available in the future.

For metals which are used in large quantities, such as iron, aluminium and copper, we have always succeeded in finding, extracting and processing adequate quantities of these metals and economic development has not been constrained by metal scarcity. However, for many of the rare metals, especially those that have been brought into wide use relatively recently, information on their occurrence, concentration and the quantities that might be available for exploitation is generally very limited. We need research and innovation on all parts of the life-cycle of these metals, from exploration and mining, through mineral processing and manufacture, to reuse, recycling and disposal. Without these we will not be able to secure adequate supplies of these metals or ensure that we manage their resources in a sustainable manner.

Economic geologists have a fundamental role to play in identifying resources of these metals. We need to understand the processes responsible for mobilising and concentrating rare metals in the crust and thus to develop improved models for the formation of deposits enriched in these metals. This will facilitate the identification of additional resources and the recognition of new ore types and deposit classes to provide the additional metals we need. Using this knowledge we can develop new and improved exploration technologies to allow us to locate additional deposits. We will need to re-evaluate terranes previously explored for other metals and assess 'new' terranes hitherto regarded as unprospective or which

have previously been inaccessible for political or other reasons. We will also need to expand our search to new frontiers, such as the polar regions and the seafloor.

## Acknowledgements

## References

Bardi, U, Pagani, M (2007) 'Peak Minerals' posted by Vernon C. in The Oil Drum: Europe. http://www.theoildrum.com/node/3086

BP (2012) BP Statistical Review of World Energy 2012

Buijs, B, Sievers, H (2012) Critical thinking about critical minerals: assessing risks related to resource security. Briefing paper within the Polinares FP7 project

Cohen, D (2007) Earth's natural wealth: an audit. New Scientist, 23 May, 34–41

Crowson, PCF (2011) Mineral reserves and future minerals availability. Mineral Economics, 24, 1–6

Erdmann, L, Graedel, TE (2011) The criticality of non-fuel minerals: A review of major approaches and analyses, Environmental Science & Technology 45, 7620-7630

Ericsson, M, Söderholm, P (2012).Mineral depletion and peak production. Polinares, Working Paper No. 7, September 2010

European Commission (2010) Critical Raw Materials for the EU. Report of the ad-hoc working group on defining critical raw materials

Gilbert, N (2009) The disappearing nutrient. Nature, 461, 716–718

Giurco, D, Prior, T, Mudd, G, Mason, L, Behrisch, J (2010) Peak minerals in Australia: A review of changing impacts and benefits. Prepared for CSIRO Minerals Down Under Flagship, by the Institute of Sustainable Futures (University of Technology, Sydney) and Department of Civil Engineering (Monash University)

Graedel, TE, Barr, R, Chandler, C et al. (2012) Methodology of metal criticality, Environmental Science & Technology, 46, 1063–1070

Hagelüken, C, Drielsmann, R, Ven den Broeck, K (2012) Availability of metals and materials. In: Precious Materials Handbook (Hanau-Wolfgang, Germany: Umicore AG Co. KG.)

Hubbert, M.K (1956). Nuclear energy and the fossil fuels. Presentation at the Spring Meeting of the Southern District, American Petroleum Institute, San Antonio, Texas, March 1956.

Meadows, DH, Meadows, DL, Randers J, Berhens, WW (1972) The Limits to Growth. (New York: Universe Books)

Mikolajczak, C, Harrower, M (2012) Indium Sources and Applications. Minor Metals Conference, February 2012

Ragnarsdóttir, KV (2008) Rare metals getting rarer. Nature Geoscience, 1, 720–721

Sverdrup, H, Koca, D, Robert, KH (2009) Towards a world of limits: The issue of human resource follies. Goldschmidt Conference Abstracts 2009

UNEP (2011) Recycling Rates of Metals - A status report, A report of the Working Group on the Global Metal Flows to the International Resource Panel

U.S. Department of Energy, (2011) Critical Materials Strategy, Washington, DC

USGS (2010) Mineral Commodity Summaries 2010: Copper

USGS (2011) Mineral Commodity Summaries 2011: Copper

U.S. National Research Council (2008) Minerals, Critical Minerals, and the U.S. Economy, Washington, DC: National Academy Press

# Mineral resource management and society: perspectives from Norway

Rognvald Boyd, Rolv Dahl, Eyolf Erichsen & Peer-Richard Neeb
*Geological Survey of Norway*

**Abstract.** Public focus on the mineral potential of Norway and on the importance of responsible management of its mineral resources has increased dramatically within the last five years. This encompasses both the positive impact of the mining industry within Norway and the role it plays in meeting national and international demand for its products. The key roles of the geoscience community and the mining industry have included intensive communication with decision makers and with the public. The government has presented a national mineral strategy which includes further emphasis on "best practice" in relation to the sustainability of the industry. The industry already has many elements which are directed towards sustainability at different levels of its markets.

**Keywords: Mineral resources, Norway, strategy**

## 1. Mineral and mineral-based industries in Norway

Primary production from the mining industry in Norway had a production value of NOK 12,400 million in 2011 (38 % construction materials, 23.5 % industrial minerals, 19.5 % metallic ores, 7.5 % natural stone and 11.5 % coal) (Neeb, 2012). 60 % of the production (in terms of value) was exported. Major products include Ti minerals, olivine, ground calcium carbonate, high-purity quartz and hard-rock aggregate.

Imports of mineral raw materials to Norway in 2011 had a value of over NOK 30,000 million (50 % from Canada alone, 10 % from Brazil) (Statistics Norway, 2013a): these imports, along with domestically produced ore and minerals and, not least, hydroelectric power, form the basis for Norway's metallurgical industry, the largest producer (in 2010) of aluminium, ferroalloys, nickel and manganese in W. Europe (British Geological Survey, 2012). The mineral processing and metallurgical industries had a combined production value of NOK 82,000 million with exports exceeding NOK 60,000 million (Statistics Norway, 2013b).

Approximately 1 million t of metallic waste is recycled annually in Norway (Statistics Norway, 2013c): the latest figure available for turnover for the companies involved is reported as > NOK 4,000 million in 2007 (Norsk Returmetallforening, 2013).

A national database for resources of construction materials (sand, gravel and hard-rock aggregate), developed in cooperation with industry and local and regional governmental authorities, has existed since 1982. National coverage was achieved in 1995 and a complete revision in 2013. The database covers the surface dimensions, tonnage and quality of the deposits and includes a classification of the deposits into those of national, regional and local importance. Among its main applications are securing the deposits for current or future exploitation in planning processes and rational exploitation in relation to transport and the quality requirements of different market segments. It also provides key information on consumption patterns, demonstrating that crushed rock has replaced the use of natural sand and gravel in certain markets, due to a combination of quality criteria and the exhaustion of available deposits of the latter. Production of hard-rock aggregate increased by circa 66 % from 2005 to 2011: this increase is partly due to export demand.

The databases for industrial mineral and metallic deposits have been primarily directed towards users in industry and the geosciences. They have included information on the geology, tonnage and grade/quality (where available) for over 4,000 metal deposits and over 1,500 industrial mineral deposits and comprehensive listings of source documentation. The national database for natural stone follows a similar pattern. All the above-mentioned databases are accessible on-line at www.ngu.no. Within the coming two years, data on deposits defined as of national importance, will be upgraded to include information on the surface extent or projections of the deposits as a basis for securing their status in planning processes at all levels.

Deposits of national importance are defined as:

- Deposits which are in production and which are important in meeting market demand in Norway or abroad and which are important sources of employment, directly or indirectly.
- Deposits for which the documented tonnage and quality indicate the potential for future production
- Provinces in which there are clear indications of deposits with a tonnage and quality with the potential for future production.

Deposits of commodities which are critical for Norwegian industry will be given priority.

The Norwegian Petroleum Directorate publishes annual estimates of the "in situ" value of the hydrocarbon resources on the continental shelf. A recent step, aimed at heightened public consciousness of the value of Norway's mineral resources on land has been to calculate the theoretical "in situ" value of the mineral deposits of

national importance. Provisional results are a total of NOK 2,528 billion (thousand million), of which 467 billion for sand, gravel and hard-rock aggregate, 250 billion for natural stone, 400 billion for industrial minerals, 23 billion for coal (on Svalbard) and 1,388 billion for metal deposits. The calculations use current price levels and, for certain commodities, the improbable postulate of a stable market 100 years ahead. It is clear that prediction of the development of future markets for certain industrial minerals is challenging, even on a scale of a few decades. In other respects the calculations are conservative: they do not include prognoses for the value of many weakly quantified deposits, nor the value of very large industrial mineral deposits which could potentially meet dramatic increases in demand relative to current markets over periods much greater than 100 years.

## 2. Public focus and government policy

Public and commercial interest in Norway's mineral potential has, in the last five years, reached a level not seen since the 1970s. Developments in metal markets, the political implications of access to key mineral resources and debate for/against several new mining projects have heightened this interest. Industry, the Geological Survey and other bodies, ably supported by sections of the media, have attempted to raise awareness of the critical role played by mineral resources in our daily lives – at all levels from construction materials for roads to the Rare Earth Elements in our flat screens and cell phones, and in "green" technology in general. At several political levels attention has focused on the opportunities offered by Norway's mineral potential, with numerous mineral deposits close to deep-water ports, both in general but also in relation to a future, several decades hence, in which the hydrocarbon industry will have a declining importance in relation to employment and the economy in general.

Government policy in relation to the mineral sector has included several elements. A new Mining Act, introduced in January 2010 allows companies or individuals to claim single blocks of land for prospecting for metals up to an area of 10 km$^2$ at fees which are at a low level for the first three years. The extent of areas being claimed has increase dramatically in the last three years, including extensive areas held by international companies.

The Ministry of Trade and Industry of Norway (NHD) stated, on 17$^{th}$ October 2012, in relation to its work on a national mineral strategy: "*The government wishes to ensure that the international mining industry views Norway as an attractive country for the mineral industry, to show that the country is positive to investment and industrial development, and that it offers predictability for investors. At the same time,*

*mining companies are expected to have proactive attitudes to environmental issues and to social responsibility, and should have the ambition to play a constructive role in the long-term development of the communities in which they operate.*" It is anticipated that the mineral strategy will be released in the first quarter of 2013.

NHD is supporting the Geological Survey of Norway (NGU) with additional funding to improve coverage of basic geological data in the three northernmost counties of Norway, allocating NOK 25 million/year for the period 2011 - 2014. Much of the funding is devoted to coverage of airborne magnetic, electromagnetic and radiometric data. Results are made public, free of charge, when the data are finally processed. A similar programme for the southern part of Norway commenced in 2013 and is scheduled to extend to 2018.

## 3. Levels of sustainability

The phrase "think globally, act locally" is commonly applied to defend local and national environmental regulations and concerns for protection of the environment at local levels, and as a contribution to national and international environmental goals. In many countries in Europe these genuine concerns are applied in opposition to the extractive industries – with scant thought for the probability that the "not in my back yard" approach will simply drive parts of the industry to establish or increase production in other countries, in many of which the freedom to oppose such developments and their regulation in terms of environmental impact or employment conditions is severely limited, if existent at all. This places an even greater responsibility on the industry to focus on socially and environmentally sustainable approaches. "Think globally, act locally" can thus also be applied to the responsibility developed countries have in relation to, as far as possible, utilizing their resources for the benefit of their own societies and for the relevant markets: many developed societies insist on "best practice" conditions for approval of mining projects, ensuring that environmental impacts are at a minimum and that social and economic impacts are positive.

The establishment of national mineral strategies can be considered as an example of "thinking globally and acting locally". Finland's mineral strategy (Ministry of Employment and the Economy, Finland, 2010) includes an introductory statement which could serve well in many contexts: "*Efficiently managed and sustainable utilisation of our mineral resources secures the long-term supply of raw materials at a national level, while creating the preconditions for stable regional development far into the future. Expertise in the minerals sector also enables Finland to effectively promote responsible and sustainable management of*

*mineral resources within a global environment, as well as generating opportunities for new international business activities."* In many cases these strategies provide a framework for an integrated approach covering the whole value chain from exploration, via production to closure and environmental restoration, including responsible management of waste rock and emissions and focus on recycling and substitution. Mineral strategies are also being prepared for Sweden and Norway (see above).

The dramatic development of China's economy in the period since 2000 and the consequent increase in its demand for mineral resources have changed global metal and mineral markets in ways which were not widely envisaged previously. China's development gives some indications as to the implications of a similar pattern of development in other countries or regions which lack infrastructure or have large populations which have a right to aspire to a better future. In parallel, and linked to these trends, there have been dramatic developments in demand for special metals for use in high-technology applications in the electronic industry and in various types of "green" technology. These developments, increased demand in general and in relation to specific metals and minerals, as well as "politicization" of access to metals and minerals have been important reasons for the development of the European Union Raw Materials Initiative and for increased attention to critical metals/minerals and mineral strategies in general, in many countries.

Former Prime Minister of Norway, Gro Harlem Brundtland, defined sustainable development in 1997 as: "Development that meets the needs of the present without compromising the ability of future generations to meet their own needs" (United Nations, 1997). The degree to which mining can approach sustainability depends on the balance between future patterns of demand, extraction, recycling and substitution and on perceptions related to its social and environmental acceptability: it also depends on the collective skills of geologists, mining engineers and metallurgists in finding, mining and processing new and perhaps unconventional deposits. Energy consumption and responsible management of waste are key elements. The shale gas "revolution" in the United States illustrates the way in which development of a new type of energy source can rapidly change perspectives on the energy supply crisis. Use of gas hydrates as an energy source could have a similar or even greater impact on energy supply in the future (Smith, 2009). Scott (2012) demonstrates the potential of seafloor massive sulphides, ferromanganese nodules and other types of deep-ocean mineral resource as a supplement to resources on land. There is reason to believe that technological advances will provide commercially and environmentally viable solutions for utilization of these resources (Nautilus Minerals, 2012) and

that their potential could change perspectives on metal supply in a manner similar to the impact of new energy sources.

At a different level the EU Raw Materials Initiative, including its focus on improved, systematic knowledge of the region's mineral resources and on research into all elements of the value chain, including recycling, substitution and environmental aspects, is a major step towards achieving a greater degree of sustainability in relation to the demand for mineral resources in Europe. Progress towards many of the goals of the Initiative is greatly facilitated by the prioritization of the knowledge base, of mineral-related research and the establishment of national mineral strategies as exemplified by Finland. Sweden and Norway have many of the same elements in place or under development.

Norway was one of the first countries in Europe to establish a national database for sand, gravel and hard-rock aggregate, a tool which is used to achieve rational supply for long-term needs at local and regional levels within Norway. The database is increasingly important in relation to meeting European demand for hard-rock aggregate, a commodity of which Norway has exceedingly large resources, in coastal locations. The country also has resources of a number of industrial mineral commodities and certain metals which can meet at least a very large part of European demand, and for some, of global demand in an environmentally acceptable manner. Further along the value chain, Norway makes an important contribution to the environmental sustainability of the industry, in utilising renewable energy to power one of the most important metallurgical industries in Europe.

## 4. Conclusion

A sound knowledge base for all types of mineral resource is a prerequisite for national mineral strategies of the type found in the Nordic countries (and others). Both form the basis for achieving a greater degree of sustainability in relation to the mineral industry and for contributing, to the extent that resource availability permits, to demand for its products in our own societies and regions. There is reason to believe that long-term demand can be met by a combination of new discoveries and increased emphasis on recycling and substitution, combined with a "best practice" approach at all stages of the value chain. These aims must build on public understanding of the importance of mineral raw materials in our daily lives and on a constructive relationship between the public and the industry.

## Acknowledgements

## References

British Geological Survey, 2012: European Mineral Statistics 2006-10, Keyworth, 366 p.

Ministry of Employment and the Economy, Finland, 2010: Finland's Mineral Strategy. http://www.mineraalistrategia.fi/etusivu/fi_FI/etusivu/_files/84608401427464240/default/FinlandsMineralsStrategy.pdf

Nautilus Minerals, 2012: Mineral resources estimate, Solwara Project, Bismarck Sea, PNG. http://www.nautilusminerals.com/i/pdf/SL01-NSG-DEV-RPT-7020-001_Rev_1_Golder_Resource_Report.pdf

Neeb, P.-R., 2012; Mineralressurser i Norge 2011. Geological Survey of Norway, 50 p.

Norsk Returmetallforening, 2013: http://www.norskreturmetall.no/

Scott, S., 2012: Mining the oceans, Mining Magazine, November 28. http://www.miningmagazine.com/management-in-action/mining-the-oceans?SQ_DESIGN_NAME=print_friendly

Smith, T. 2009: Gas Hydrates-Not So Unconventional. GeoExpro 6. http://www.geoexpro.com/article/Gas_Hydrates_Not_So_Unconventional/b9d997f9.aspx

Statistics Norway, 2013a: External trade by country with commodity groups. Two-digit ITC. 2009-2011 http://www.ssb.no/uhaar_en/tab-22-en.html :

Statistics Norway, 2013b: Exports by sections and divisions of the SITC. http://www.ssb.no/muh/mu2011/tab09-01.shtml

Statistics Norway, 2013c: Waste accounts for Norway. Final figures 1995 to 2011. http://www.ssb.no/english/subjects/01/05/40/avfregno_en/

United Nations, 1997: Report of the World Commission on Environment and Development: Our Common Future. http://www.un-documents.net/ocf-02.htm 300 p.

# Sustainability in the minerals industry – supporting and training the next generation of geoscientists

Alan Goode
*Director Data Metallogenica, AMIRA International, Melbourne, Australia*

## 1 Introduction

The minerals industry, supported by associated geological surveys and professional societies, has invested over A\$4 million (30 million krona) to date through AMIRA International to build *Data Metallogenica* as a web-based not-for-profit global encyclopedia of ore deposits.

While the unique core of DM comprises high-quality photographs of over 70,000 representative samples of ore, alteration, host rocks and regolith from thousands of deposits of all styles from around the world, supporting technical data is presently being added for other information such as descriptions, photos, maps and sections (Figures 1, 2). The first compilation list of all Australian geoscience theses was also added to DM as part of its information resource, together with about 70 full theses on deposits from around the world (Figure 3).



**Figure 1.** The distribution of gold, copper, zinc and nickel deposits in DM in 2012
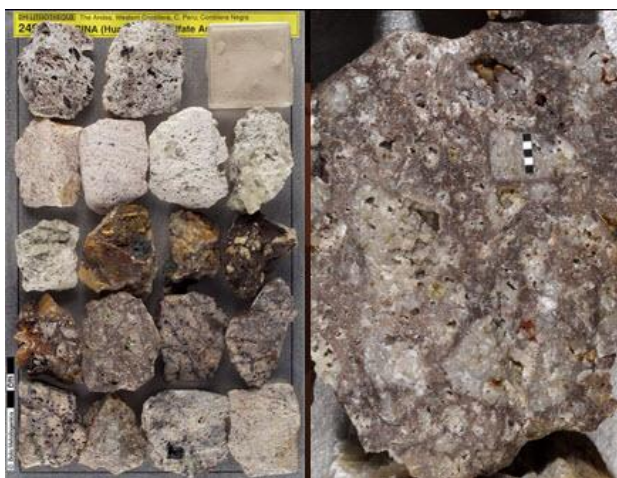


**Figure 2.** An example of sample photos in DM

New samples also continue to be added to DM (eg those recently collected by Peter Laznicka from deposits in Iran, Armenia, Turkey, Peru, Colombia, Vietnam and China). DM has also recently acquired a significant set of samples collected by the late Rod Kirkham from many parts of the world. The physical collection is owned by AMIRA International on behalf of the minerals industry, and is stored by the South Australian Government at the DMITRE Core Library in Adelaide.



**Figure 3.** Distribution of full text theses in DM in 2012

The Foundation Sponsors who supported the initial projects in difficult times from 1999-2004 included over 100 major and minor mining and exploration companies, government organisations and professional/learned societies from around the world. Apart from being used for training and reference in many organisations and by individuals, DM is now also being used as an educational resource in about 50 universities worldwide. In 2011, with little advertising, the website (www.datametallogenica.com) attracted over 760,000 hits with a significant quantity of data downloaded by subscribers. These usage figures surprised some senior managers in companies who did not realise the value their younger staff gained from accessing the world's deposits via "virtual" web visits at any time.

## 2 AMIRA P1040 – Building the Global Encyclopaedia of Ore Deposits

DM has been self-funding as a community project since 2004 but the greatly increasing backlog of data plus the increasing need to provide this material for training and reference has lead to the need for a new AMIRA International project, P1040 (Building the Global Encyclopaedia of Ore Deposits). The three-year collaborative project began in June 2012 with 50 sponsors and aims to make major advances in data addition and in key educational aspects for the ultimate benefit of all working in the global mining industry – for reference, training and education, as well as acting as an

important data repository for fragile and transient information of value to the industry. While initially focusing on geoscience, the website will extend to cover all technical aspects of mining. It is also intended to develop DM into a wiki to allow all to contribute information if they wish.

Apart from annual sponsor review meetings, the project is also assisted by a senior industry Advisory Panel composed of Dan Wood (ex-Newcrest), Doug Kirwin (ex-Ivanhoe), John Hammond (Newmont), David Wallace (MMG) and Dugi Wilson (Xstrata).

An early aim of P1040 has been to develop a new website which will increase the searchability of DM as a data repository and reference as well as providing better training for young geoscientists in industry and in universities. While this website is still being developed, an early promising aspect for training is the potential to provide DM in many languages (including all European and Scandinavian languages, Arabic, Hindi, Swahili, Chinese and Russian) which will allow its use in training and reference to be maximised around the world.

Apart from the sample photos, associated spectral mineralogy and summary descriptions, other search categories for deposits will include geology, geophysics, geochemistry, drilling, core photographs, petrography, regolith, remote sensing, selected bibliographies, detailed technical reports, theses, discovery histories, mine construction, mining, mineral processing, environmental, mine closure and historical data.

Web users can also access global overviews of commodities and deposit types by world experts. This will be extended in P1040, and regional context overviews will also be added for key mineralised areas (eg Athabascan Basin, Yilgarn Block, Fennoscandian Shield etc).

Other aspects of P1040 include the financial support to be provided to SEG Student Chapters going on field visits to major ore deposits. In return for this support, students provide reports and photos on those deposits which are then permanently lodged in DM. Previous trials of this approach with Eötvös Loránd University (who went to Bulgaria) and the University of Tasmania (who visited China, South Africa and Botswana) were very successful for all involved (Figure 4).

Students are also supported in P1040 by providing paid technical assistance to prominent individuals to allow them to preserve their often valuable but potentially fragile photos of early mines and deposits (early recipients are Emeritus Professors Spencer Titley, USA and Antonio Arribas Snr, Spain).

One of the sponsor benefits is to provide free "permanent" access to DM in universities and geological surveys in developing countries, building on previous support (Figure 5). This is a win/win for all, in that universities in these regions will have access to

better technical resources and ultimately better graduates (potential employees) will result. This also applies to universities in developed countries and of course this will achieve one of the key objectives of DM in assisting training the next generation of geoscientists. DM also provides potential lifetime usage of the resource for young graduates, building on the knowledge and experience of current and past geoscientists.



**Figure 4.** Example of an SEG Student Chapter report in DM



**Figure 5.** Distribution of universities with access to DM, including those in developing countries (courtesy of sponsors)

## Acknowledgements

# Successful mineral exploration using multispectral remote sensing data – ASTER Geoscience Map of Australia

**Carsten Laukamp, Tom Cudahy, Mike Caccetta**
*Western Australian Centre of Excellence for 3D Mineral Mapping, Minerals Down Under Flagship, CSIRO Earth Science and Resource Engineering*

**Matilda Thomas**
*Geoscience Australia*

**Dorothy Close**
*Northern Territory Geological Survey*

**Rudy Lennartz**
*Kentor Gold*

**Abstract.** Mineral maps, derived from multispectral remote sensing data, have been successfully applied for mineral exploration in the Jervois area of the eastern Arunta Region (Northern Territory, Australia). Muscovite, chlorite and biotite, associated with known polymetallic hydrothermal ore deposits, were targeted using the AlOH and MgOH/C Group maps of the continental Australian ASTER Geoscience Products developed by CSIRO's Centre of Excellence for 3D Mineral Mapping and supported by Australian state geological surveys and Geoscience Australia. The spatial distribution of these indicator minerals indicates mafic rocks of the Attutra Metagabbro as a potential source of mineralising fluids for known mineral occurrences. Furthermore, new Au occurrences have been found along the potential fluid pathways, in areas that were not regarded as prospective before. Our study shows that regional scale, moderate resolution remote sensing data sets can be used to discover not only hydrothermal alteration patterns but also new previously unknown mineral occurrences in greenfields environments, when applied in combination with a mineral systems model. We propose that multispectral data can improve exploration targeting and save resources at the same time.

Keywords: ASTER, exploration, mineral mapping

## 1 Introduction

Mineral exploration at the start of the 21st century still leaves a large footprint, with vast amounts of drill cores sank in barren ground. The discovery rate for gold in Australia for example has been declining since the 90's, with gold resources mainly being extended at existing deposits (Huleatt and Jaques 2005). Both observations question the usually applied exploration technologies - or at least the approach during their application - and highlight the need for improving greenfields (and brownfields) exploration.

Multi- and hyperspectral remote sensing technologies have been used for mineral exploration over the last three decades, but the acceptance of this technology is not as high as for conventional exploration methods, such as geophysics. Amongst the reasons for this may be the perceived ambiguities when interpreting visible and infrared reflectance spectroscopic data or the sheer mistrust in a technology that claims to provide mineral mapping from space. Furthermore, the increasing belief that all near surface showings have been discovered and that new deposits will only be detected undercover via drilling, are not improving the stakes for a technology that is, in geological terms, a pure surface detection method.

However, our paper shows that the strengths of spectroscopic remote sensing lie in the fact that it is a non-invasive, remote sensing method that can cover large areas with minimal resources. Our application of the world's first, publically available (ftp://ftp.csiro.au/arrc/Australian_ASTER_Geoscience_Map/), continental scale mineral maps, derived from multispectral remote sensing data (Cudahy 2012), for mineral exploration shows that there remains significant potential for new discoveries on the Earth's surface and that we can considerably decrease our impact on the environment and our exploration budget when combining currently available remote sensing methods with a mineral system based approach.

The eastern Arunta Region was chosen as a case study area, with focus on the Jervois area (Figure 1) and Bonya Hills ENE of Alice Springs. The eastern Arunta Region is mainly a greenfields environment, prospective for polymetallic hydrothermal ore deposits, such as iron-oxide copper-gold deposits (Hoatson et al. 2005). Trends of known Cu-Au mineralisation were investigated in respect to the shortwave infrared active mineralogy of host rocks and/or associated alteration minerals, as well as their location compared to possible sources of mineralising fluids.

## 2 Multispectral remote sensing

The Advanced Spaceborne Thermal Emission and Reflection Radiometer (ASTER) is a multispectral remote sensing system that captures 14 bands across the electromagnetic spectrum, namely in the visible-near (VNIR), shortwave (SWIR) and thermal (TIR) infrared (Yamaguchi et al. 1999). ASTER data have been successfully applied for mineral exploration, for example by mapping infrared functional mineral

assemblages that are typical for hydrothermal alteration associated with ore deposits (e.g. argillic alteration, Mars and Rowan 2010; Witt et al. 2013).

The Australian ASTER Mineral Maps used ASTER L1B data converted to apparent surface reflectance (Cudahy, 2012) to create a suite of continental scale mineral abundance and composition maps, which have a spatial resolution of 30m/pixel for the VNIR/SWIR derived images. For example, the AlOH Group Content image maps the relative abundance of Al-clays (i.e. kaolin group, Al-smectites, white micas), whereas the MgOH/C Group Content image reveals hydrated Mg and/or Fe-silicates (e.g. chlorite, amphibole, biotite) as well as carbonates. The MgOH/C Group Composition image can be used to infer the composition of carbonates, ranging from calcite through dolomite to magnesite, based on the position of the $CO_3$ absorption band in carbonates, which shifts with increasing Mg/Ca ratio to shorter wavelengths. However, the same mineral map can also indicate, which one of the hydrated Mg and/or Fe-bearing silicates is dominant, depending on the relative depth and position of diagnostic absorption features, representing the combinations bands of hydroxyl-related vibrations. The carbonate and hydroxyl related absorption features can't be easily separated with the ASTER SWIR data, requiring a basic geological understanding of the study area necessary for successful interpretation.

# 3 Application in the eastern Arunta Region

## 3.1 Regional Geology and the Jervois Range

The eastern Arunta Region comprises greenschist to granulite facies metamorphic rocks of the Palaeo-proterozoic Aileron Province and the Neoproterozoic to Palaeozoic Irindina Province, which are overlain by Neoproterozoic to early Cambrian sedimentary rocks of the Georgina Basin to the north (Collins and Shaw 1995). Palaeoproterozoic metamorphic rocks within the Aileron Province have protolith ages typically in the range 1850-1780 Ma, and are intruded by numerous generations of mafic and felsic rocks (Scrimgeour in press).

The Jervois Range is located about 280 km ENE of Alice Springs. Cu-Au-Ag mineralisation in the Jervois area east of the main Jervois Range is hosted by the Palaeoproterozoic Bonya Schist featuring quartz-chlorite (biotite) ± muscovite ± cordierite ± garnet ± magnetite (Figure 1). Further major bedrock types are rhyolite, granite gneiss, amphibolite and cordierite biotite schists. The bedrock is covered by Quaternary scree, soil and alluvium forming often an only thin veneer (Freeman 1986).

## 3.2 Exploration potential

For the Arunta Region, Hoatson et al. (2005) pointed out the potential for structurally controlled, polymetallic hydrothermal deposits that are associated with mafic and ultramafic intrusions, such as the Attutra Metagabbro or the Riddock Amphibolite. The Bonya Schist, hosting known Cu-Au deposits east of the Jervois Range, were intruded by the Attutra Metagabbro (1786.4 ± 4.2 Ma, Figure 1a), which has anomalous concentrations of V, Cu, Pd, Pt and Au (Hoatson et al. 2005). The Riddock Amphibolite shows quartz-carbonate-tourmaline veins with elevated Au and Cu values, associated with chlorite-hematite alteration. Recent studies have highlighted the potential for iron-oxide copper-gold mineralisation in the eastern Arunta Region (Whelan et al. 2012).

In the Jervois mineral field, known deposits occur along isoclinal folded, subvertical greenschist facies rocks that are folded around a subvertical axis in the south. Mineral exploration focussed on this mineralised trend (Figure 1) until 2012, with Bellbird and Marshall being two of the major Cu-Au-Ag deposits and Cox's Find one of the prospects in this area (Figure 1). Rocks of higher metamorphic grade to the east and south of this trend were regarded as relatively non-prospective.

## 3.3 Results

Even though Cu-Au mineralisation in the eastern Arunta Region has been known since the last century, little is known about the source, fluid pathways and the conditions that lead to the formation of this mineral system. However, the hitherto observed alteration mineralogy could provide a key towards the understanding of this mineral system and the comparison with regional mineral distribution patterns may help regional greenfields exploration. From the described mineral assemblage of the host rocks, only the SWIR active muscovite, chlorite and biotite are considered for this exercise.

The AlOH Group Content image (Figure 1b) shows increased values in sediments of the Georgina Basin in the northwest and, in patches, along the mineralised trend, including known deposits, such as Bellbird and Marshall. In the Bonya Schist, this signal can be related to the high abundance of muscovite, one of the major minerals in the host rocks.

The MgOH/C Group Content image (Figure 1c) highlights a significant abundance of carbonates or Mg and/or Fe-bearing silicates in two major zones to the southeast and east of the known mineralised trend. Taking the MgOH/C Group Composition map (Figure 1d) into account, this could be interpreted as enhanced chlorite and/or biotite alteration, as previous field work did not report carbonates with the metamorphic rocks. Low to intermediate values in the Georgina Basin, however, could reflect abundant carbonates in the sedimentary successions.

It should also be noted that the AlOH Group Content image roughly shows the extent of outcropping Bonya Schist, different to the published geological map. The high chlorite and/or biotite abundance though is located in two distinct zones that cannot be followed along strike of the Bonya Schist. This suggests localised hydrothermal alteration in two zones along the mineralised trend, increasing the prospectivity of the lower grade metamorphic schists in these zones. Both zones are spatially close, but not in direct contact with past mining operations.
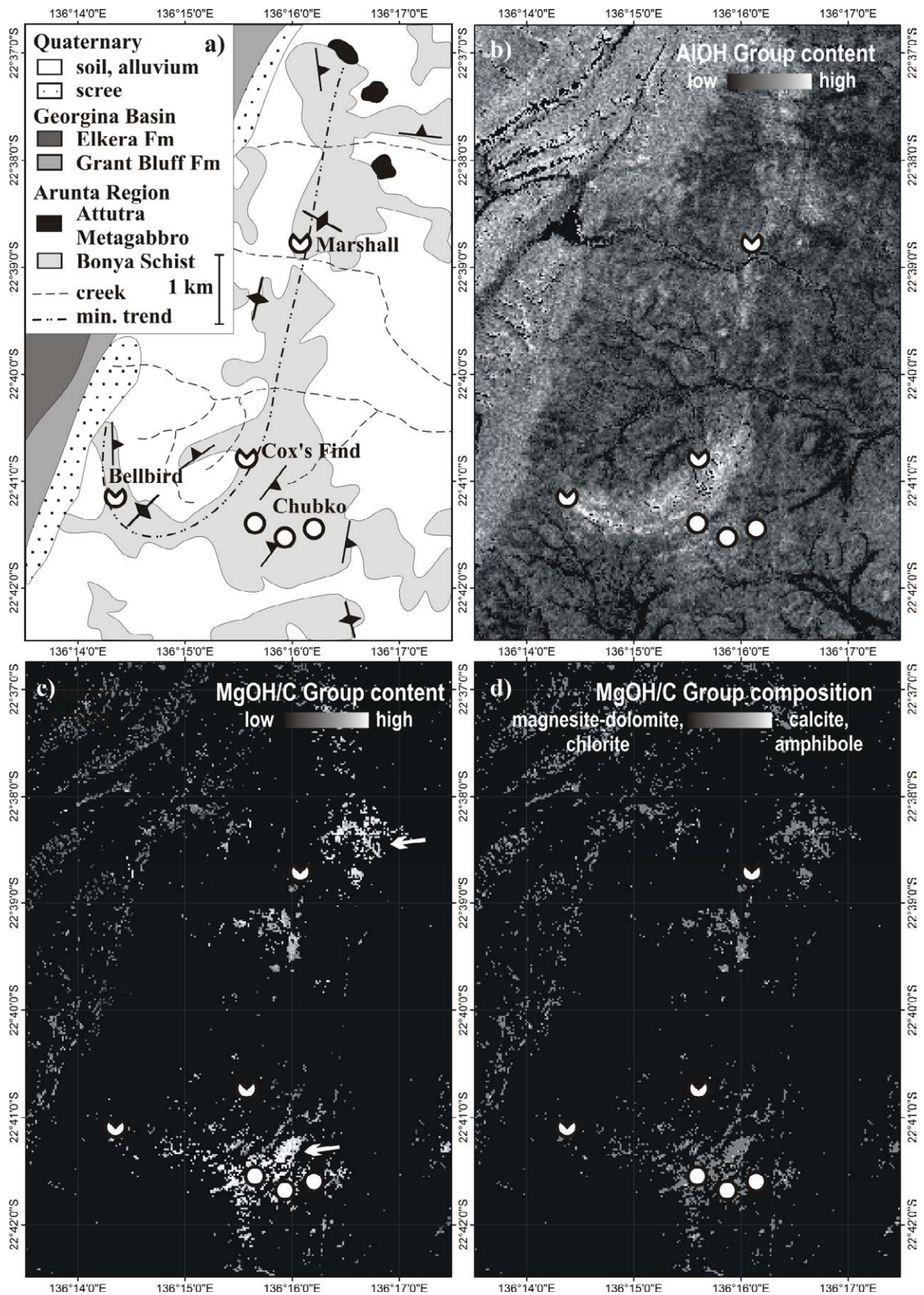
**Figure 1.** Simplified geology and mineral maps of the Jervois mineral field area: a) Geological map (modified after Freeman, 1986), b) AlOH Group Content, c) MgOH/C Group Content, d) MgOH/C Group Composition.

The northern chlorite/biotite zone in the higher metamorphic schists neighbours outcrops of the Attutra Metagabbro, which contains anomalous Cu, Au and PGE values and was suggested as a possible source for polymetallic mineralisation in the greater Jervois area (Hoatson et al. 2005). The northern chlorite/biotite zone is located between the mafic rocks and known mineralisation (e.g. Marshall), and could be the result of hydrothermal alteration along pathways of mineralising fluids, making it a prospective area itself. It is reasonable to assume that the Attutra Metagabbro also occurs, concealed or unmapped, to the southeast of the southern chlorite/bitotite zone. This zone could represent a pathway for mineralising fluids important for deposits such as Bellbird. Further to the east of Jervois, mafic rocks are mapped by the AlOH Group Content image, suggesting potassic alteration in these possible source rocks.

Based on this geological model of the mineral system and the careful selection of described mineral maps derived from ASTER data, the Chubko Prospect was discovered in 2012 by Kentor Gold Ltd. Mineralisation at Chubko is hosted by lensed quartz veins, showing up to 50 - 56 g/t Au associated with elevated Bi and As. This opens up the higher metamorphic schists to the south and east of the known mineralised trend for exploration for quartz-lode hosted Au deposits.

## 3.4 Regional application

The geology of the Bonya Hills area to the west of Jervois is similar to the Jervois field, comprising Bonya Schist intruded by mafic rocks with similarities to the Attutra Metagabbro (Hoatson et al. 2005). The AlOH and MgOH/C Group mineral maps show similar muscovite and chlorite/biotite distribution patterns, leading to additional areas prospective for Cu-Au mineralisation hosted by low grade metamorphic Bonya Schist or Au mineralisation in higher grade metamorphic equivalents. In fact, historical data show a number of polymetallic prospects (Freeman 1986) in the very same area of the Bonya Hills, supporting the applied mineral systems model.

## 4 Conclusions

New Au occurrences have been found in the Jervois area of the eastern Arunta Region (Northern Territory, Australia) using mineral maps derived from ASTER data. The successful application of the multispectral remote sensing data in this greenfields environment can be attributed to the study of the distribution of known polymetallic deposits, the associated mineral assemblages and the consideration of a larger scale mineralising system. To date, it is not clear which deposit type the new Au showings can be assigned to, other than associated with quartz lodes. However, the mapped distribution of indicator minerals (i.e. muscovite, chlorite/biotite) points to Proterozoic mafic/ultramafic rocks as one possible source for mineralising fluids, and suggests that the newly

identified Au occurrences are located along potential fluid pathways to known polymetallic deposits.

## Acknowledgements

## References

Collins WJ, Shaw RD (1995) Geochronological constraints on orogenic events in the Arunta Inlier: a review. Prec Res 71:315-346

Cudahy T (2012) Satellite ASTER Geoscience Product Notes for Australia. CSIRO report EP30071244, 26 pages

Freeman MJ (1986) Huckitta, Northern Territory 1:250,000 Geological Map Series SF53-11. North Territ Geol Surv, NT, Australia, 58 pages

Hoatson DM, Sun S, Claoue-Long JC (2005) Proterozoic mafic-ultramafic intrusions in the Arunta Region, central Australia Part 1: Geological setting and mineral potential. Prec Res 142:93-133

Huleatt MB, Jaques AL (2005) Australian gold exploration 1976 - 2003. Res Pol 30:29-37

Mars JC, Rowan LC (2010) Spectral assessment of new aster swir surface reflectance data products for spectroscopic mapping of rocks and minerals. Rem Sens Env 114:2011-2025

Whelan JA, Webb G, Close DF, Kositcin N, Bodorkos S and Maas R (2012) New copper-gold discoveries in the eastern Arunta Region: Implications for Cu-Au mineralisation in the Arunta, in 'Annual Geoscience Exploration Seminar (AGES) 2012. Record of Abstracts.' Northern Territory Geological Survey, Record 2012-002

Witt WK, Hagemann SG, Ojala J, Laukamp C, Vennemann T, Nykanen V (2013) Targeting gold mineralisation at regional- to lode-scales, pataz gold field, northern Peru. Austr J Earth Sci 60:

Scrimgeour IR(in press) Aileron Province: in Ahmad M and Munson T (editors) 'Geology and Mineral Resources of the Northern Territory' Northern Territory Geological Survey, Darwin

Yamaguchi Y, Fujisada H, Kudoh M (1999) ASTER instrument characterization and operation scenario. Adv Space Res 23:1415-1424

# Sustainable development and the Minerals Industry 25 years on

Jeremy P. Richards

*Dept. Earth and Atmospheric Sciences, University of Alberta, Edmonton, Alberta, Canada, T6G 2E3*

**Abstract.** Progress in the understanding and application of sustainable development principles in the mining industry are discussed, relative to the classic definition of this concept in the 1987 Brundtland Commission Report. The industry has responded relatively well in terms of environmental impacts, but is struggling to deal with the social aspects of the concept, in part because few industry employees, who are mostly scientists and engineers, are familiar with or trained to deal with these issues.

**Keywords.** Sustainable Development, mining, exploration, metals, equality

## 1 Evolution of the concept of sustainable development

The concept of "sustainable development" means different things to different people, especially when shortened to "sustainability". These phrases are widely and excessively used today to describe objects, lifestyles, businesses, and governments that have arguably reduced environmental impacts, are financially sound, or are long-lived. These definitions have little to do with one of the most widely accepted definitions of sustainable development, which is to "**meet the needs of the present without compromising the ability of future generations to meet their own needs**" (from the Brundtland Commission Report, United Nations, 1987, p. 43) (e.g., Kuhlman and Farrington, 2010).

As has been pointed out by numerous commentators, mining of non-renewable resources is an inherently *un*-sustainable activity, if it is considered in isolation from of its wider role in society. Mineral exploration is even less "sustainable", because most exploration work leads to no discovery but simply consumes capital and disturbs (admittedly to a relatively minor degree) the environment and local communities. And yet many exploration and mining companies tout their "sustainability" credentials in annual reports and websites. Is this simply "greenwashing", as many environmentalists argue (e.g., Whitmore, 2006), or does it serve a useful purpose?

## 2 The contribution of mining to broad societal sustainable development objectives

Mining creates economic and material goods for society, without which modern lifestyles and industry could not function. The metals and other commodities produced by mining underpin every aspect of life, from electricity generation and transmission, to roads, buildings, furniture, and machines. Mining also creates wealth, by converting worthless material in the ground into useful raw materials that can be sold at a net profit.

However, mining also has major costs, some of which are visible and accounted for (e.g., costs of mine construction, and fuel and power for mining), but others of which are invisible and commonly not paid for by current mine owners or society (e.g., the long-term environmental and opportunity costs of land disturbance and waste disposal, water usage and contamination, and atmospheric emissions of pollutants; e.g., Corson, 2002).

So how can mining fit within the sustainable development paradigm? The Brundtland Commission's definition of sustainable development does not say that there can be no development (e.g., mining), and accepts that the simple act of living on this planet affects the environment and one's neighbours to some degree. The challenge for mining is to minimize and remediate its environmental impact, while aiming to provide net benefits to all affected members of society, both now and in the future (Richards, 2005).

The benefits to wider society of having an affordable supply of raw materials is clear, and with the globalization of commodity trading, this could be argued to positively affect a large proportion of the planet's inhabitants.

However, the benefits of wealth creation are much less equally distributed. A mining company operating in the capitalist world must aim to maximize profits for its shareholders, otherwise shareholders will not invest in the industry, no mining will occur, and greater society will see no benefits. However, in most countries a share of the income from mining is collected by governments, who represent the "owners" of natural resources (the ultimate owners being the people who live in the country or province). And this is where problems and arguments arise.

Firstly, what is a reasonable share of the income from mining that a government can expect to collect, and how should that share be calculated (e.g., Otto et al., 2006)? Is it a share of net profits, or a share of the value of the commodity mined? In general, companies prefer a profit-based royalty, because that protects them during down-cycles in commodity prices (i.e., if a mine is not making a profit because prices are low, then it will not have to pay royalties). However, many companies are adept at minimizing their booked profits, and thereby minimizing the royalties paid to governments, even when prices are high. Consequently, governments would do better to apply a royalty based on gross revenue from mineral extraction (commonly called a net smelter return, which represents the money gained from the sale of a commodity). Few governments levy such royalties,

however, because they view themselves as being in competition for investment with other jurisdictions, who might offer a more generous profits-based royalty structure (Otto, 2006). Thus, the financial benefits returned to governments and the people they represent are commonly much lower than they should be.

A present-day example is the province of Alberta, Canada, where the government is running deficit budgets despite high global oil prices, in large part because of a generous profits-based royalty system from which almost half the operating companies are exempt (because they are still paying off initial investment costs with any revenue they generate, and thus can show no net profit). The companies themselves, however, are growing rapidly and creating considerable wealth for shareholders.

The next problem that arises is how resource revenues collected by the government should be spent? This is potentially where the revenue from non-renewable resource extraction can be used to further sustainable development objectives (e.g., ICMM, 2009), but more commonly governments end up using this money to balance current operating budgets and to pay for delivery of social programs. A better use of these revenues is investment in various forms of human capital, such as investment in education and health-care capacity and expertise (as distinct from paying current salaries of teachers and doctors), investment in new technologies that increase energy use efficiency or reduce environmental impacts, or investment in durable infrastructure that improves quality of life and societal efficiency. This type of investment is referred to as converting mineral wealth into human capital, and is consistent with long-term sustainable development goals.

However, this still leaves the negative impacts on the environment and affected communities unaccounted for. In the past, these impacts were largely ignored, and environmental degradation from mining activities, including abandoned mines, was extensive (e.g., Mackasey, 2000; Smith and Underwood, 2000). Local communities were commonly simply forced to leave their land with minimal or no compensation for lost property and livelihoods. Today, largely due to pressure from activist groups and instant exposure of transgressions on the internet (Porritt, 2002), mining companies are much more careful about the visible impacts of mining and the treatment of affected communities, especially indigenous communities. But while engineering solutions to environmental problems can be as elaborate and effective as costs will allow, the industry is still far behind social norms in dealing with impacted communities, partly because this concern has only risen in priority in recent years (e.g., Joyce and MacFarlane, 2001; Handelsman et al., 2003; Handelsman, 2005; Thomson and Joyce, 2006; Solomon et al., 2008; Himley, 2010).

A watershed event might have been the forced closure of the Bougainville copper mine on Bougainville Island, Papua New Guinea, in 1989, ostensibly on political (secessionist) grounds. But behind the secessionist revolt was anger at the treatment of local people over the decades since the mine had opened in 1972. At that time, landowners were compensated with one-off cash payments that were quickly spent, but there was little continuing compensation. And yet the mine not only stayed in place but grew. When the mine lease was due to be renegotiated, the company, which recognized the problems, was keen to negotiate new, perhaps more favourable terms (for landowners). However, the national government (which was a major beneficiary of the mine's revenues) delayed opening discussions. In the end, the Bougainville islanders and took matters into their own hands, and a highly profitable mine with many years of ore left in the ground was closed with some loss of life (Connell, 1991; Hilson, 2006). Clearly this was a major economic loss to the company, affecting its profitability and therefore shareholders' interests; these issues therefore rose in priority in the boardroom.

Many other examples of lost mining opportunities due to social opposition have occurred since then (e.g., the Esquel deposit in Argentina (BSR, 2003), and the Tambo Grande deposit in Perú), but industry is beginning to take such issues more seriously at early stages, before the trust and goodwill of communities are lost.

Other issues that are moving quickly to the top of the agenda are equality, both within the mining industry itself and in its dealing with community members, and the concept of "free, prior and informed consent" (MacKay, 2004). Inequality is particularly evident in exploration and mining employment, where the vast majority of employees are male (Lahiri-Dutt, 2011), but it also manifests itself in dealings with community members, where males are most commonly the spokespeople and therefore the decision-makers (Campbell, 2006).

"Free, prior and informed consent" requires that communities potentially affected by mining should be fully informed about planned activities before being asked freely whether they agree to it or not. Withholding of consent should mean that a project cannot go ahead; it is therefore imperative that companies work closely with communities if they wish to obtain their permission to continue working.

An important development has been the internet resource e3Plus (www.pdac.ca/e3plus), developed by the Prospectors and Developers Association of Canada, which provides a set of principles, guidelines, and practical advice on a wide range of environmental and social issues that exploration companies should address when planning and conducting their work. However, this is a voluntary program, and some countries have opted to legislate such principles, elevating them from guidelines to mandated actions.

## 3 A way forward

Enlightened mining and exploration companies work with local communities from day one to ensure that their work is compatible with the aspirations of community members (e.g., Veiga et al., 2001; Togolo et al., 2001), and with the aim of improving their quality of life both during and after mining activities have ceased

(Fernandez, 2000). We now talk about creating "sustainable communities" that can survive and prosper long after the mine has run its course (e.g., IFC, 2000; Laurence, 2001; Sherlock et al., 2003; Walker and Jourdan, 2003; Meech et al., 2006). A major aspect of this "sustainability", especially for indigenous communities, is provision of education and training, so that local people can participate directly in the new economy generated by mining activities, and diversify into new economic activities that are not be dependent on the mine.

Mining engineers also talk about "planning for closure" when developing a mine. It is much easier and cheaper to close down and remediate a mine if this step has been planned from the outset. For example, old workings can be backfilled with proximally stacked waste, and mine tailings impoundments can be sealed off and stabilized more effectively if they were originally sited and designed with that objective in mind.

Progressive mine planning can even anticipate long-term net benefits from closed and properly remediated mining operations, perhaps as wilderness areas or parks.

However, we are still a long way from where this is the normal expectation, and part of the blame for that is to be found in the way we educate scientists and engineers separately from the social sciences, such that there is minimal understanding between these two essential disciplines (e.g., Emery and Southern, 2000).

## Acknowledgements

## References

BSR (Business for Social Responsibility), 2003, Minera El Desquite Report Esquel, Argentina: San Francisco, CA, Business for Social Responsibility, 29 p.

Campbell, B., 2006, Good governance, security and mining in Africa: Minerals and Energy - Raw Materials Report, v. 21, p. 31–44.

Connell, J., 1991, Compensation and conflict: The Bougainville copper mine, Papua New Guinea, *in* Connell, J., and Howitt, R., eds., Mining and indigenous peoples in Australasia: Sydney University Press, Sydney, Australia, p. 55–75.

Corson, W.H., 2002, Recognizing hidden environmental and social costs and reducing ecological and societal damage through tax, price, and subsidy reform: The Environmentalist, v. 22, p. 67–82.

Emery, A.C., and Southern, P., 2000, Education needs for environmental miners: Mining Environmental Management, January 2000, p. 8–9.

Fernandez, W., 2000, From marginalization to sharing the project benefits, *in* Cernea, M.M., and McDowell, C., eds., Risks and reconstruction: Experiences of resettlers and refugees: Washington, D.C., World Bank, p. 205–225.

Handelsman, S.D., Scoble, M., and Veiga, M., 2003, Human rights and the minerals industry: challenges for geoscientists: Exploration and Mining Geology, v.12, p. 5–20.

Handelsman, S.D., 2005, Human rights: commitment or lip service?: Mining Environmental Management, December 2005, p. 2.

Hilson, C.J., 2006, Mining and civil conflict: revisiting grievance at Bougainville: Minerals & Energy, v. 21, p. 23–35.

Himley, M., 2010, Global mining and the uneasy neoliberalization of sustainable development: Sustainability, v. 2, p. 3270–3290.

ICMM (International Council on Mining and Metals), 2009, The Challenge of Mineral Wealth: Using resource endowments to foster sustainable development. Minerals Taxation Regimes, A review of issues and challenges in their design and application: Analysis and observations: ICMM, London, 80 p.

IFC (International Finance Corporation), 2000, Investing in people: Sustaining communities through improved business practice: International Finance Corporation, Washington, DC, 76 p.

Joyce, S.A., and MacFarlane, M., 2001, Social impact assessment in the mining industry: Current situation and future directions: International Institute for Environment and Development, and World Business Council for Sustainable Development, Report No. 46, 28 p.

Kuhlman, T., and Farrington, J., 2010, What is Sustainability?: Sustainability, v. 2, p. 3436–3448.

Lahiri-Dutt, K., 2011, Gendering the field: Towards sustainable livelihoods for mining communities: Canberra, The Australian National University E Press, 230 p.

Laurence, D., 2006, Optimisation of the mine closure process: Journal of Cleaner Production, v. 14, p. 285–298.

Mackasey, W.O., 2000, Abandoned mines in Canada: Report prepared for MiningWatch Canada, 11 p. Available at: http://www.miningwatch.ca/publications/abandoned-mines-canada

MacKay, F., 2004, Indigenous People's Right to Free, Prior and Informed Consent and the World Bank's Extractive Industries Review: Sustainable Development Law and Policy, v. 4, p. 43–65.

Meech, J.A., McPhie, M., Clausen, K., Simpson, Y., Lang, B., Campbell, E., Johnstone, S., and Condon, P., 2006, Transformation of a derelict mine site into a sustainable community: the Britannia project: Journal of Cleaner Production, v. 14, p. 349–365.

Otto, J.M., 2006, The competitive position of countries seeking exploration and development investment: Society of Economic Geologists, Special Publication 12, p. 109–125.

Otto, J.M., Andrews, C., Cawood, F., Doggett, M., Guj, P., Stermole, F., Stermole, J., and Tilton, J., 2006, Mining Royalties: Washington, D.C., World Bank, 296 p.

Porritt, J., 2002, From the fringe to the mainstream: The evolution of environmental and social issues in private sector projects, *in* The environmental and social challenges of private sector projects: IFC's experience: Washington, DC, International Finance Corporation, p. 75–84.

Richards, J.P., 2005, The role of minerals in sustainable human development, *in* Marker, B.R., Petterson, M.G., McEvoy, F., and Stephenson, M.H., eds., Sustainable Minerals Operations in the Developing World: Geological Society, London, Special Publication 250, p. 25–34.

Sherlock, R.L., Scott, D.J., and MacKay, G., 2003, Bringing sustainability to the people of Nunavut: Geotimes, December 2003, p. 18–20.

Smith, F.W., and Underwood, B., 2000, Mine closure: the environmental challenge: Transactions of the Institution of Mining and Metallurgy, Section A, v. 109, p. A202–A209.

Solomon, F., Katz, E., and Lovel, R., 2008, Social dimensions of mining: Research, policy and practice challenges for the minerals industry in Australia: Resources Policy, v. 33, p. 142–149.

Thomson, I., and Joyce, S., 2006, Changing mineral exploration industry approaches to sustainability: Society of Economic Geologists, Special Publication 12, p. 61–70.

Togolo, M., Rae, M., and Omundsen, T., 2001, Meeting society's expectations through stakeholder engagement: Mining Environmental Management, March 2001, p. 10–11.

United Nations, 1987, Our common future, Report of the World Commission on Environment and Development (the

Brundtland Commission): Oxford, Oxford University Press, 383 p.

Veiga, M.M., Scoble, M., and McAllister, M.L., 2001, Mining with communities: Natural Resources Forum, v. 25, p. 191–202.

Walker, M., and Jourdan, P., 2003, Resource-based sustainable development: an alternative approach to industrialization in South Africa: Minerals and Energy, v. 18, p. 25–43.

Whitmore, A., 2006, The emperors new clothes: Sustainable mining? Journal of Cleaner Production, v. 14, p. 309–314.

# Theory of metallogenic systems: principles and applications to mineral exploration

Zhai Yusheng, Deng Jun, Wang Jianping, Peng Runmin, Liu Zhenjiang
*State Key Laboratory of Geological Processes and Mineral Resources, China University of Geosciences, Beijing, China*

**Abstract:** The theory of metallogenic systems combines systematic thinking and historical thinking. There are four principles in the theory of metallogenic systems: ①Major types of metallogenic system are classified by tectono-dynamic system; ②Coupling of many factors and criticality- transition is basic ore-forming mechanism; ③ Ore deposit series and anomaly series constitute the mineralization network; ④The evolutionary process of a single ore deposit includes its formation, transformation and -preservation. The holistic, spatial, temporal and historical analysis of a metallogenic system can provide guiding information for regional mineral exploration.

**Key words:** metallogenic systems, mineral exploration, holistic analysis, spatial analysis, temporal analysis, historical analysis

## Introduction

Mineral resources are important materials for the existence and development of the human society. But they are being consumed at an increasing rate to support modern lifestyle and to cater for the increasing demands from developing counties. How to supply adequate mineral resources for sustainable development of the world economy becomes a focus in the field of prospecting and mining. Since the beginning of 21st century, mining industry has been facing many environmental problems. At the same time, mineral deposits become more and more difficult to be found because most of outcropped deposits near the surface have been discovered. In order to find concealed ore deposit, indiscernible ore deposit and new types of ore deposit, there is an urgent need for new ore-forming theory and new technology. Metallogenic system may be one of the effective ways to successful exploration.

## 1 Definition of a Metallogenic System

A metallogenic system, often developed within a certain geological temporal–spatial realm, is defined as a natural system with ore-forming functions. It consists of geological factors controlling ore-formation and preservation, and ore-forming processes and its products ——ore deposit series and anomaly series (Zhai 1999). The study of metallogenic systems is a systematic approach and a global trend in metallogeny research. One of the main aspects in the study of metallogenic systems is to stress integration of time, space, material and movement during the study of regional metallogeny. It is an effective way to understand ore-forming dynamic mechanism and to probe into the regularities of ore formation and distribution.

The significance of metallogenic system study lies in the following aspects: (1) to promote the development of metallogeny and benefit the mutual amalgamation between ore deposit geology and other disciplines of geosciences; (2) to build strategic view and integrated thought in ore prediction and prospecting in order to accelerate regional mineral exploration and mineral resource potential assessment; and (3) to provide scientific base for evaluation of environmental quality and environmental protection by studying the behavior of noxious contents in metallogenic systems.

## 2 Principles of Metallogenic Systems

The theory of metallogenic systems is a new concept of studying mineral deposit. It is not equal to a mineral deposit, and mineral deposit is just a small part of a metallogenic system. Metallogenic system consists of ore-forming environment, ore-control factors, ore-forming processes, ore-forming products, and post-ore modification and preservation (Fig. 1). Based on systematic and historical view, the following aspects are emphasized in the study of metallogenic system.

### 2.1 Types of Metallogenic Systems

Different tectonic environments produce different types of mineral deposits. So metallogenic system can be divided into the following seven basic types based on their forming tectono-dynamics: □extensional structural metallogenic system (e.g. rift metallogenic system); □compressional structural metallogenic system (e.g. orogenic metallogenic system); □strike-s1ip structural system (e.g. macroscopic slip fault metallogenic system); □uplift structural metallogenic system (e.g. granite dome metallogenic system); □subsidence structural metallogenic system (e.g. sedimentary basin metallogenic system）；□ macroscopic ductile shear structural metallogenic system (e.g. ductile shear zone go1d metallogenic system); and □impact structural metallogenic system (e.g. meteor-impact magmatic-1iquation metallogenic system such as the Sudbury Ni-Cu-$\Sigma$Pt deposit).

### 2.2 Ore-forming dynamics

The study on mineral deposit geology for decades shows that multi-factor coupling and critical transformation are the main contents of ore-forming dynamics (Zhai et al. 2011). The basic ore-forming mechanisms can be summarized as : ①multi-factor-coupling ore formation (ore-source, fluid, thermal field, stress field, geochemical factor, geophysical factor etc.) and ②critical-

transformation ore formation (such as temperature-
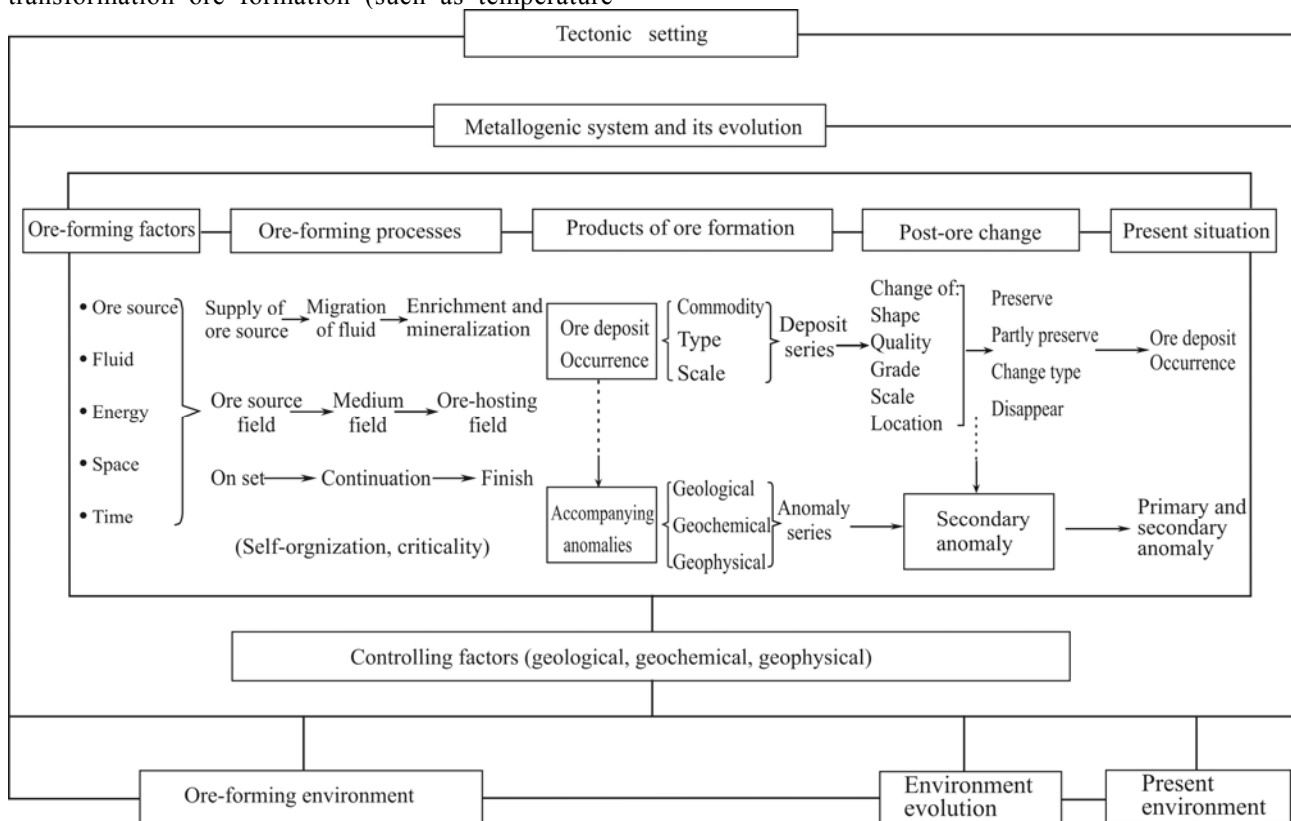
Figure 1 Metallogenic system and its evolution

pressure transformation, lithofacies transformation, structural-stress-field transformation, main physical-chemical-parameter transformation, especially their catastrophic transformation). The coupling of these two basic mechanisms is the basic condition for the formation of large mineral deposits.

In the process of mineralization, transition of tectonic and dynamic regime may play a fundamental role in controlling the critical transition and forms of mineralization parameters. Local transition under a certain tectonic setting is a common ore source-transportation-enrichment structure (e.g. local extension under compressional tectonic setting, local closing in an extensional basin). The coupling transition of many ore-forming parameters induced by the tectonic dynamic transition is one of the most important mechanisms of formations of large-size ore deposit.

## 2.3 Mineralization network

Ore deposit series and anomaly series constitute the mineralization network (Zhai et al. 2003). Products of ore-forming processes contain not only mineral deposits and occurrences but also different kinds of geo-anomalies (geological, geophysical, and geochemical). Both series are closely related under the same geological processes, and are called "mineralization network". The mineralization network usually has larger space than the mineral deposit itself.

The study of metallogenic systems begins with mineralization network. The main scopes include: ① development degree of different types of ore deposits; ②spatial relationship of different types of ore deposits; ③temporal relationship of different of types ore deposits; ④genetic relationship of different types of ore deposits; ⑤transformation of different types of ore deposits. The above highlights are the common scopes for ore deposit geology and mineral prediction, and therefore, systematic and thorough study on them is significant both in theory and in practice.

## 2.4 The whole story of an ore deposit

With the development of ore deposit research, it has been realized that much more attention has been paid to the study of the genesis and forming environment of ore deposits. But the forming environment may not be the same as the current location of an ore deposit. For example, podiform chromite deposits in the ophiolite suite are mostly formed in the oceanic ridge, while we often locate them in collisional orogenic belts. The preservation of ore deposit is quite different in various tectonic setting. So it is important to understand full processes of formation, modification and preservation of ore deposits, especially in mineral exploration (Zhai et al. 2000).

Ore-forming processes can be generalized as: "ore-source supply→migration of ore-bearing fluids →

concentration of ore-forming substance → localization of ore deposits". With the evolution of ore-forming environments in geological history, most deposits are subject to change. Some deposits are destroyed; some are preserved or partly preserved, while some others could be transformed into another type of deposits by post-ore geo-processes. Consequently, it is important to study the post-ore modification and preservation of ores for both mineral deposit geology research and mineral exploration.

# 3 Metallogenic System analysis for mineral exploration

## 3.1 Holistic analysis of Metallogenic System: from known to unknown

Because of strong mineralization, diversity and complexity of ore-forming materials, and ore-controlling factors, many types of ore deposits may occur in a regional metallogenic system. For example, there may occur skarn type, porphyry type, lode type, breccia pipe type, and hot spring type ore deposits in an extensively distributed hydrothermal metallogenic system that is related to sialic igneous rocks. They were formed in the same geological metallogenic event. Being a member in the ore deposit series, each had occupied certain tempo-spatial position and had special material components and structures. When one or more ore deposit types were discovered in a region, it can be inferred whether there were ore deposits of other types according to metallogenic theory, especially the theory of metallogenic system. For instance, if a skarn type ore deposit has been discovered in a region, then it can be inferred that there may occur veinlet-disseminated type ore deposits or lode type ore deposits in the same region. If the method was properly applied, good results can be obtained in discovering new-type ore deposits from known to unknown.

## 3.2 Spatial analysis of Metallogenic System: searching the depth

Regional mineralization network, including minerali-zation zonation, was the main form of the spatial structure of a metallogenic system (Zhai et al. 1999). Vertical zoning refers to vertical changes in material components, textures and mineralization types of the ore deposit. Lots of exploring data indicated that vertical zoning was very clear in an extensively distributed hydrothermal metallogenic system. Such examples in China include the zoning model of the volcano-subvolcanic hydrothermal metallogenic system of the Yinshan–Tongchang ore field in Jiangxi province (Huang 1992), and the Zijinshan type mineralization zoning in the hydrothermal metallogenic system in the southern

Fujian province (Zhai et al. 1996). Examples abroad include the zoning model in the porphyry metallogenic system in the west part of Canada (Maclntyre, 1995).

Vertical mineralization zoning was significant both for exploration in the deep part of known ore deposits and for discovering new-type ore deposits. The discovery of concealed Dongguashan large copper ore deposits in the Shizishan ore field in Tongling area, Anhui province, was a successful example. "Multi-layer controlling" is an important characteristic in a metallogenic system in the region. Margins of the igneous rock bodies are usually the favored mineralizion areas. In addition, the mineralization locations also include the bottom of the Triassic (the Datuanshan ore deposit), the bottom of the Dalong Group of Permian (the Laoyaling ore deposit), and the Huanglong–Chuanshan Group of Carboniferous (e.g. the Tongguanshan ore deposit). According to this characteristic, the No. 321 Geological Team of the Anhui Geology and Mineral Resource Bureau discovered 50 meters thick copper ore bodies in the depth of 880 meters through drilling in the Shizishan ore field. After detailed exploration, the Dongguashan ore deposit with 1.41 million metric tons of copper was confirmed, resulting in a great breakthrough in deep ore prospecting (Editing committee of the Anhui Volume of the Discovering History of Ore Deposits in China, 1996).

## 3.3 Temporal analysis of Metallogenic System: finding out missing nodes of the ore forming chain

In a large-scale metallogenic event, the nature of ore-forming fluids and ore-controlling factors changed in the different steps of the ore-forming processes. Ore deposit types changed accordingly, and all the ore deposits may constitute an integrated metallogenic series (metallogenic chains). It can be used to find out missing nodes (i.e., new-type(s) of ore deposits) which are not discovered, by studying the known nodes (known ore deposit type). There were many examples in a metallogenic system formed in the magmatic evolution.

In an Fe (P, V, Ni, Co) metallogenic system related to the evolution of diorite-gabroids in the northern Hebei ore belt, the Taihangshan ore belt and the middle and lower reaches of the Yangtze River ore belt, there often developed metallogenic series containing late magmatic differentiation type →pegmatic type and ore-magma type (injection type) → ore-magma–hydrothermal transitional type → hydrothermal type （Zhai et al. 1992）. The Cu and Au metallogenic system in the area along the Yangtze River, Anhui province, also showed mineralization type changing with time (Tang et al. 1998). Stratabound skarn type, ore-magma injection type, pegmatic type and contact skarn-type ore deposits were formed in the early stage of the system. Then porphyry

type, hydrothermal type and sedimentary–transformed type ore deposits followed. The latest was hydrothermal lode type ore deposits only.

According to the analysis of temporal evolution of the metallogenic system, successiveness and relative pedigree of different metallogenic systems at different times in the same region can be studied. The pedigree map of a metallogenic system can serve as guidance to find the undiscovered deposit.

### 3.4 Historical analysis of Metallogenic System: correct evaluation of a mineral deposit

The formation of ore deposits is a result of complex geological processes. Most ore deposits are subjected to change and reworking in various forms and degrees after their formation. The main scopes of post-ore change research are: ① the controlling parameters; ② the reworking process; ③ the product of post-ore modification; ④ the different modification track of various ore deposit types; ⑤ore deposit modifications in different geological environment and periods; ⑥ the conditions for ore deposit preservation. It is important to establish the post-ore change models of certain ore deposit types, studying not only the single ore deposit but also the ore deposit series in certain metallogenic belt. When both the forming processes and the preserving processes are clear, a historical judgment of a mineral deposit can be obtained, positioning us to answer with confidence questions such as "Is an ore deposit at present the same as past, or was it much bigger than it is?"

### Conclusion

Metallogenic system is a systematic approach and a global trend in ore deposit geology research. It emphasizes the study of ore-forming environment, ore-controlling factors, ore-forming processes, the production of ore-forming process——ore deposit series and anomaly series and preserving condition, and evolution of ore deposits. Holistic, spatial, temporal and historical analysis of a metallogenic system is instructive to mineral exploration. Its guidance to mineral exploration becomes more and more important in sustainable development of the society.

### References

Editing Committee of the Anhui Volume of the Discovering History of Ore Deposits in China (1996) Anhui Volume of the Discovering History of Ore Deposits in China. Beijing: Geological Publishing House, 83-86.

Huang SQ (1992) Genetic Model of Vocano-porphyry Copper Multi-metallic Ore Deposits in the Northeastern Jiangxi. In "Synopsis of Academic Interchange Meeting on Important Science and Technology Achievements of the 7th five-year-program" (edited by China Association of Geology). Beijing: Science and Technonogy Publishing House, 484-489.

MacIntyre DG (1995) Sedex sedimentary exhalative deposit, ore deposits, tectonics and metallogeny in the Canadian Cordillera. Ministry of Energy, Mines and Petroleum Resources, British Columbia, Queen's Printer for British Columbia, Victoria, 5-20.

Tang YC, Wu YC, Chu GZ (1998) Geology of Copper–gold Polymetallic Deposits along the Yangtze River in Anhui Province. Beijing: Geological Publishing House, 281-296.

Zhai YS (1999) On the Meallogenic System. Earth Science Frontiers, 6(1): 13-28.

Zhai YS, Deng J, Li XB, et al. (1999) Regional metallogeny. Beijing: Geological Publishing House, 154-171.

Zhai YS, Deng J, Peng RM (2000) Research Contents and Methods For Post-ore Changes, Modifications and Preservation. Earth Science—Journal of China University of Geosciences, 24(4):340-345.

Zhai YS, Lin XD, Yao SZ (1992) Metallogenic Regularities of Fe, Cu and Au in the Middle and Lower Reaches of the Yangtze River. Beijing: Geological Publishing House, 227-230.

Zhai YS, Yao SZ, Cui B (1996) Research on Metallogenic Series. Wuhan: China University of Geosciences Publishing House, 84-88.

Zhai YS,Wang JP, Deng J, et al. (2003) Metallogenic System and Mineralization Network. Mineral Deposits, 21(2):106-112.

Zhai YS, Deng J, Peng RM, et al. (2011) Theory of metallogenic system. Beijing: Geological Publishing House, 1-320.

S 2.1:
# 3D-modelling of ore deposits

Convenors:
Alireza Malehmir, Tobias Bauer & Gervais Perron

# 3D modelling for mineral exploration: confronting the challenges of hard rock settings by optimal extraction and use of geological constraints

**Ernst Schetselaar, Eric de Kemp, Mike Hillier**
*Geological Survey of Canada, 615 Booth Street, Ottawa, Ontario, Canada K1A 0E9 ernst.schetselaar@nrcan.gc.ca*

**Gervais Perron**
*Mira Geoscience #309 – 310 Victoria Avenue Westmount, H3Z 2M9 Montreal, Quebec, Canada*

**Abstract.** 3D modelling in hard rock settings is challenging due to post-ore tectono-metamorphic processes and the structural complexity and heterogeneity of ore-hosting crystalline basement rocks. This paper discusses avenues towards confronting the challenges from the perspective of optimally using geologic constraints.

**Keywords.** 3D modelling, ore deposits, drill hole data, common earth model, structural anisotropy

## 1 Introduction

3D geologic modelling (or geomodelling) has evolved from the application of computer-aided design (CAD) software since the 1980's into a matured Earth science discipline that covers geomatics, geophysics and geology. The petroleum industry has been its main driver, where application development in 3D and 4D hydrocarbon exploration and reservoir modelling have been at the forefront in terms of innovation and quantitative rigour. With the increasing global demand for mineral resources in the last decade, there is increasing interest in applying 3D geologic modelling to ore deposits. The hard rock geological setting in which most ore deposits are hosted, combined with the much lower expenditures on subsurface data acquisition have a significant impact on the accuracy and validity of 3D modelling results. In this paper we focus on the limiting geological factors of ore deposit 3D modelling, compare them with those in hydrocarbon reservoir modelling and discuss working procedures and methodologies to confront the hard rock-specific challenges.

## 2 The Challenges of 3D Geologic Modelling in Hard Rock Settings

Regardless of geological setting, the uncertainty associated with 3D geologic modelling is generally much higher than the uncertainty associated with 2D geological mapping, simply because of the fact that the subsurface structure is rarely directly accessible to observation or only where it intersects drill holes. As a result, the subsurface structure needs to be inferred between the available observations (hard or direct geological constraints) using to variable degree available geophysical measurements (soft or indirect geological constraints). With the exception of present-day epigenetic mineralization, ore deposits were generally buried at greater crustal depths and have been affected by long-lived post ore formation histories. Hence, the setting in which most ore deposits are preserved is structurally far more complex, as it evolved under polyphase deformation, metamorphic and magmatic processes that partly obliterated the original geometry of source, migration path and trap of the ore system and the topological relationships between them. In comparison to the sedimentary basin setting of hydrocarbon reservoirs, this renders the subsurface interpretation of hard rock settings exceedingly more difficult. More specifically, given the available types of geoscience data, the following two challenges apply:

**Challenge 1: the indirect relationship between host rock descriptions and ore system components**
Drill core geological observations and descriptions serving as 'hard' 3D modelling constraints in ore deposit settings often encode multiple themes, including terms to describe igneous or sedimentary processes of formation (igneous or sedimentary, i.e. basalt, tuff), metamorphism (i.e. schist, gneiss), deformation (i.e. mylonite, cataclasite) and alteration (i.e. albitite, chloritite). This multi-thematic encoding renders the association of host rock descriptions with ore system components ambiguous and commodity-dependent. In the extreme case of a high-grade metamorphic setting, the modelled rock units could all have been classified using metamorphic descriptors that only have indirect bearing on the characterization of a stratiform mineral deposit and its alteration envelope. Geological formations and primary structures of a hydrocarbon reservoir, on the other hand, are usually readily interpreted in terms of its components (i.e. porous sandstone = reservoir rock, halite = cap rock, bituminous shale = source rock).

**Challenge 2: the structurally complex and heterogeneous ore-hosting medium**
Post-ore magmatism, metamorphism and deformation commonly increase the structural complexity of ore deposit settings that may have resulted in physical property contrasts that obliterated those associated with the formation of the ore deposit itself. These processes have folded, faulted, recrystallised or intruded primary igneous or stratigraphic layering, including the ore horizon (Forbes et al. 2008). Where laterally continuous seismic reflectors, in combination with sequence stratigraphy, permit mapping the strata and structures throughout a hydrocarbon reservoir, seismic imaging in

hard rock settings is challenging as a result of seismic wave scattering in a structurally complex and heterogeneous medium with relatively low impedance contrasts (L'Heureux et al. 2005; Salisbury and Snyder, 2007) yielding, as a result, far less laterally-continuous seismic markers. Consequently, there is much more reliance on the integration of geologic and multi-source geophysical datasets in ore deposit settings, all having a complementary contribution to mapping particular aspects of the ore-hosting geological structure. Using each type of data constraint individually, the attitude and type of structure can only be established at particular subsurface locations that are favourable to the surveying technique being employed. This makes the correlation of subsurface markers difficult, particularly in ore deposit settings dominated by rapid lateral variations in volcanic and sedimentary lithofacies. The notion for the need for dedicated integration of geological and geophysical data is in line with the concept of the common earth model (CEM) that is a quantitative model of the earth consistent with all available data, testable by drilling and subject to editing and refinement with the acquisition of new data (McGaughey, 2006). Although the acronym was originally tossed by the oil industry where is has become standard practice in asset management (Garrett et al. 1997) the need for it, is actually more pressing in mineral exploration.

The 3-D Imaging and Earth Modelling Section of the Geological Survey of Canada is, in addition to research on seismic and magneto-telluric deep crustal imaging, focusing on research that strives at finding solutions to the aforementioned 3D modelling challenges and cooperates with industry partners, such as Mira Geoscience, in application development. The following sections provide comprehensive summaries of achievements and ongoing developments.

## 3  Optimizing the extraction of drill hole constraints and hole-to-hole correlation

Standardized use of terminology in extracting suitable 3D modelling constraints from drill log descriptions is a minimum requirement for confronting challenge 1. Drill hole database management in our mine camp to regional scale 3D modelling projects is based on importing recent and legacy drill hole logging reports in a relational database structure in $3^{rd}$ normal form (Codd, 1970). Populating the drill hole database involves parsing out protolith, tectono-metamorphic fabric and alteration themes from drill logs encoded by industry (Fig. 1). Hierarchical classification systems are defined for each of these themes that enable multi-thematic visualization of drill log data on several levels of generalization. This semantic generalization may effectively eliminate discrepancies at the most detailed level(s) that are due to classification errors and classification preferences of individual geologists. An example of the benefits of drill hole database normalization is shown in Fig. 2 where the 3D visualization of alteration minerals in combination with geochemical data analysis aids reconstructing parts of the ore-fluid migration paths (hydrothermal vents)
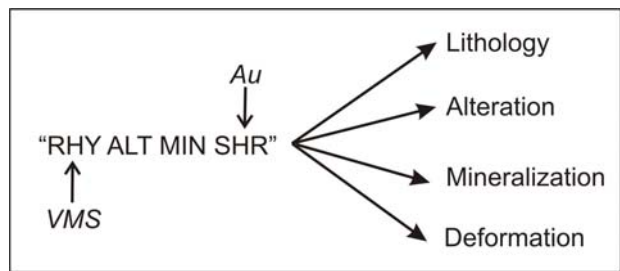


**Figure 1.** Parsing of lithology, alteration, mineralization and fault rock themes from legacy drill codes. Note that each theme may have relevance to a particular commodity (VMS, gold)
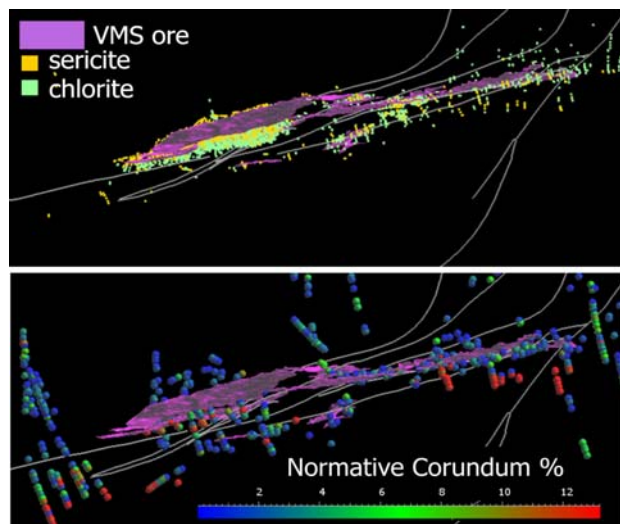


**Figure 2.** 3D visualization of alteration minerals from drill hole observations (top) and normative mineral percentages (corundum) from lithogeochemistry (bottom) allow reconstructing ore fluid migration paths in a deformed and metamorphosed VMS ore system, Flin Flon, Manitoba, Canada

associated with the formation of VMS deposits that were affected by polyphase deformation and metamorphism.

Standardized and unambiguous geologic knowledge representation of drill hole data is even more important for confronting challenge 2. The objective here is to seek drill hole categorizations that enhance layer-parallel continuity and permit tracing geological formations into the subsurface. In addition, to systematically encoding and generalizing drill core lithofacies, which may enhance the ability to recognize strata-parallel trends in dense 3D drill hole datasets, this goal can be accomplished by encoding drill logs into lithostratigraphic units. These are in effect abstracted containers of grouped lithofacies, hence are at least equal, but usually of much greater dimension, particularly in settings with rapid lateral lithofacies variations, such as those hosting volcanic massive sulphide (VMS) and sedimentary exhalative (SEDEX) deposits. The lithostratigraphic approach has been implemented in building a camp scale 3D model of the Flin Flon VMS deposits (Schetselaar et al. 2010, Fig. 3). A selected set of 62 drill holes were re-logged providing laterally-persistent constraints for modelling 3D lithostratigraphic surfaces throughout the mine camp. The lithostratigraphic information was acquired in producing a 1 : 10,0000 scale geological map of the mine camp providing a wealth of lithostratigraphic
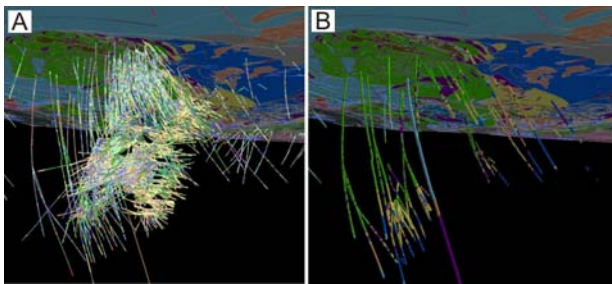
**Figure 3.** A) Legacy lithology encoding mine camp drill holes; B) subset of re-logged lithostratigraphic reference holes harmonized with geological map legend, Flin Flon Canada
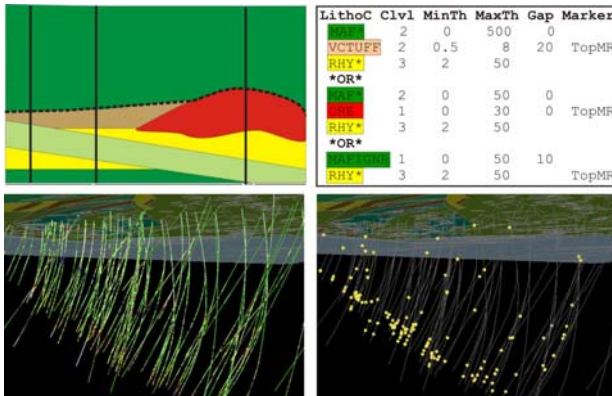


**Figure 4.** Automated extraction of lithostratigraphic marker 'TopMR' using 'genecoding' drill hole query algorithm: lithofacies configuration (upper left) search pattern with specification of class level (Clvl) minimum and maximum thickness (MinTh, MaxTh) thickness wildcard interval (Gap) to bypass intrusion and marker (upper right) drill holes subjected to query (lower left) and query results (lower right)

information that enabled to reconcile lithofacies mapped in outcrop to their recognizable equivalents in drill core. Hence this approach can provide significant dividends in establishing laterally-persistent subsurface markers, particularly when geological maps of the mine camp are available. Mapping lithofacies in outcrop or mine workings has the obvious benefit in providing better spatial context in establishing the diagnostic and unique lithofacies associations that define the lithostratigraphic column or legend. In summary, for 3D modelling the subsurface geological structure, it is advised to use lithostratigraphic instead of lithofacies constraints and reconcile them with lithostratigraphic units of a geological map where possible.

Computer-assisted pattern recognition provides an alternative data mining approach for establishing laterally-persistent markers. A 'gene coding' drill hole query algorithm was developed (Schetselaar and Lemieux, 2012) that extracts lithostratigraphic contacts by searching for diagnostic sequences in lithofacies variations, recurrent in adjacent drill holes. Wildcard '*' gap intervals in the query pattern can be used to search across unconformable, intrusive and tectonic contacts. Multiple search patterns can be combined in a single query to account for lateral lithofacies variations (Fig 4). The 'gene-coding' query algorithm supplements geological interpretation when analysing large drill hole databases and markers need to be extracted in a systematic and time-efficient manner.

# 4 Using structural orientation data as secondary constraints

The importance of confronting challenge 2 by using structural orientation data has been widely recognized (Lajaunie et al. 1997; de Kemp, 2000; Caumon et al. 2009). The general idea is that by including strike/dip measurements, a reasonable prediction of the 3D geometry of a geological surface can be made even in areas where no primary geological or geophysical constraints are available. This is because in areas with a harmonic conformable layering or strata, strike/dip elements will tend to honour the attitude of the geological structure at nearby structural levels. Higher-order tectonic surfaces can be modelled, as well, by honouring structural vector fields defined by $S_{0+n}$ orientation data (i.e. cleavage, foliation or gneissosity). The structural orientation data are sampled on the geological surface of interest itself, below or above it. Although they are mostly collected in outcrops, strike/dip measurements are increasingly being acquired in drill holes or can be indirectly derived from intersected horizons in nearby drill holes or by measuring the attitude of prominent reflectors in 3D seismic cubes.

With the same objective as mapping geological structures by using manually-drafted 2D form lines, 3D structural form lines can be constructed by interpolating the direction cosines of strike/dip or lineation data. A structural vector field interpolation algorithm (SFI, Hillier et al. *in press*) was developed for this purposes that constructs 3D form lines by connecting interpolated unit vectors. Similar to anisotropy characterization of fabric shape analysis and stereographic projection (Woodcock, 1977) the vector interpolation employs a weighting scheme derived from eigen analysis of a 3 X 3 matrix A constructed from the sums of cross products of the direction cosines $(l_i, m_i, n_i)$ of the pole to the $i^{th}$ strike/dip measurement (Fara and Scheidegger, 1963; Watson, 1965):

$$A = \begin{pmatrix} \sum l_i^2 & \sum l_i m_i & \sum l_i n_i \\ \sum m_i l_i & \sum m_i^2 & \sum m_i n_i \\ \sum n_i l_i & \sum n_i m_i & \sum n_i^2 \end{pmatrix}$$

The smallest eigenvector $v_3$ of the three eigenvectors $(v_1, v_2, v_3)$ defines the plunge vector (i.e. pole to the best-fit girdle) in the user-defined neighbourhood provided that the data do not form an axially symmetric cluster, which can be tested by verifying that (Woodcock, 1977):

$$\frac{\ln(E_2/E_3)}{\ln(E_1/E_2)} < 1$$

where E1, E2, E3 are the eigenvalues corresponding to the eigenvectors. The anisotropic inverse distance weighting scheme is based on the following transformation matrix T:

$$T = V^T S V$$

Where V is the eigenvector matrix, $V^T$ its transpose and

S the scaling matrix defined as:

$$S = \begin{bmatrix} 1 & 0 & 0 \\ 0 & \sqrt{E_2/E_1} & 0 \\ 0 & 0 & \sqrt{E_3/E_1} \end{bmatrix}$$

Local estimates of the plunge vector assure plunge-normal structural form line reconstruction with unidirectional propagation of form lines across fold and fan structures. The method is advantageous for modelling the anisotropy of geologic structures from sparsely distributed data and has shown to be effective in reconstructing the 3D geometry of regional-scale fold structures (Fig 5). The vector interpolation has also been used to mapping orientation data on a grid to constrain 3D potential field inversions (Davis et al. 2012.)

Orientation data also provide gradient constraints in implicit geologic surface modelling (Lajaunie et al. 1997). We are currently developing methods for implicit surface modelling based on Hermite-Birkoff radial basis function (RBF) interpolation that incorporates strike/dip measurements as gradient constraints and includes anisotropy characterization. One of the main advantages of this approach is that complex folding geometries sampled in the structural orientation data are honoured so that the surface can be extended into areas where contact constraints are not available (Fig 6).
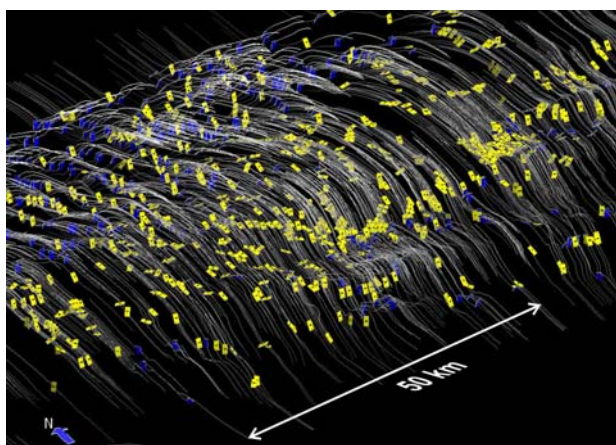


**Figure 5.** Plunge-orthogonal 3D structural form lines modelled from bedding elements of folded contact between supracrustal rocks (quartzite, psammite) overlying orthogneiss Baffin Island, Canada)
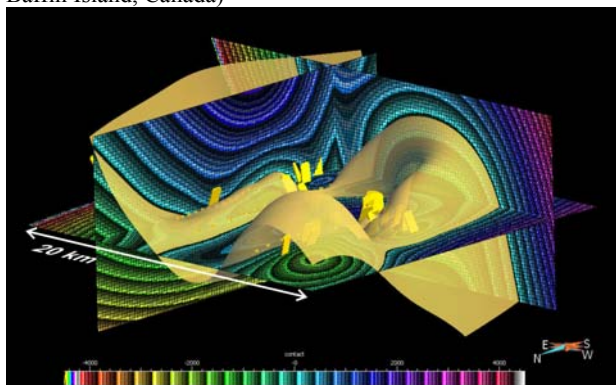


**Figure 6.** Implicit surface model of folded contact between supracrustal rocks overlying orthogneiss basement using strike/dip and contact constraints in Hermite-Birkhoff radial basis function interpolation (Baffin Island, Canada).

## Conclusions

Geological constraints are indispensible for building 3D models of ore deposits, without, any detected subsurface feature is a guesstimate that cannot be uniquely interpreted in ore system and host rock components. Geological data should be unambiguously encoded to assure meaningful categorizations that are relevant to the modelling objectives. The onus is on those developing CEM methods that exploit the complementary value of geological and multiple geophysical constraints and use geochemical and physical property models in establishing their mutual relationships.

## References

Caumon G, Collon-Drouaillet P, Carlier de Veslud C, Viseur S, Sausse J (2009) Surface-based 3D modeling of geological structures. Math Geosci 41:927-945

Codd EF (1970) A relational model of data for large shared data banks. In: Communications of the ACM 13:377–387.

Davis K, Oldenburg, DW, Hillier M (2012) Incorporating geologic structure into the inversion of magnetic data. ASEG Extended Abstracts 2012, 1-4, doi:10.1071/ASEG2012ab174.

de Kemp EA (2000) 3-D visualization of structural field data: Examples from the Archean Caopatina Formation, Abitibi greenstone belt, Québec, Canada. Computers and Geosciences 26(5):509-530

Forbes, CJ, Betts, PG, Giles, D, Weinberg R (2008) Reinterpretation of the tectonic context of high-temperature metamorphism in the Broken Hill Block, NSW and implications on the Paleo- to Mesoproterozoic evolution. Precambiran Res 166(4):338-349

Fara HD, Scheidegger AE (1963) An eigenvalue method for the statistical evaluation of fault plane solutions of earthquakes. Seismol. Soc. America, Bull. 53:811-816

Garrett S, Griebach S, Johnson D, Jones D, Lo M, Orr W, Sword C (1997) Earth model synthesis: First Break 15:13-20

Hillier M, de Kemp E, Schetselaar E (in press) 3D form line construction by Structural Field Interpolation (SFI) of geologic strike and dip observations. Journal of Structural Geology

Lajaunie C, Courrioux G, Manuel L (1997) Foliation fields and 3D cartography in geology: principles of a method based on potential interpolation. Mathematical Geology 29:571-584

L'Heurex E, Milkereit B, Adam E (2005) 3D seismic exploration for mineral deposits in hardrock environments. CSEG Recorder, November 2005:36-39

McGaughey WJ (2006) The common earth model: a revolution in mineral exploration data integration. In: Harris (ed.) GIS for the Earth Sciences Geological Association of Canada, special publication 44:567-576

Salisbury M, Snyder D (2007) Application of seismic methods to mineral exploration. In: Goodfellow, W.D. (ed) Mineral Deposits of Canada: A Synthesis of Major Deposit-Types, District Metallogeny, the Evolution of Geological Provinces, and Exploration Methods: Geological Association of Canada, Mineral Deposits Division, Special Publication 5, p 971-982

Schetselaar E, Pehrsson S, Devine C, Lafrance B, White D, Malinowski, M (in press) 3D Geologic Modeling in the Flin Flon Mining District, Trans-Hudson Orogen, Canada: Evidence for Polyphase Imbrication of the Flin Flon - 777-Callinan Volcanogenic Massive Sulfide (VMS) Ore System Economic Geology

Schetselaar E, Lemieux D (2011) A drill hole query algorithm for extracting lithostratigraphic contacts in support of 3D geologic modelling in crystalline basement. Computer and Geosciences 44:146-155

Watson GS (1966) The statistics of orientation data. Journal of Geology 74:786-797

Woodcock NH (1977) Specification of fabric shapes using an eigenvalue method. Geol Soc Am Bull 88:1231-1236

# 3D seismic interpretation and forward modeling – an approach to providing reliable results from 2D seismic data

Omid Ahmadi, Peter Hedin, Alireza Malehmir, Christopher Juhlin
*Department of Earth Sciences, Uppsala University, Sweden*

**Abstract:** Accurate 3D interpretations is challenging when only 2D seismic reflection data are available. This can be compensated for by using additional data. Here we present two case studies where 2D seismic reflection data have been used in combination with geological/geophysical data to create and verify 3D interpretations of specific structures targeted for scientific deep drilling and mining. In the first case, a surface geological map and high resolution 2D seismic reflection data were used to create a 3D lithological model of the subsurface structures in an area around a scientific deep drilling site. This model was also compared to results from constrained 3D inverse modeling of gravity data. In the second case, seismic forward ray-trace modeling was used to delineate a massive sulfide ore body by using high resolution 2D seismic reflection data. By comparison of the generated synthetic data with the real data, it was found that the top of the ore body was detected.

**Keywords:** Reflection seismics, 3D interpretation, inverse gravity modeling, seismic forward modeling

## 1  Introduction

In geosciences, and especially resource prospecting, an understanding of the 3D geometry of subsurface structures is essential and often the desired goal of geophysical surveying. Different geological and geophysical methods provide a multitude of information about the subsurface that, when combined with other information, may resolve the different lithologies and structures beneath the surface. Full 3D seismic acquisition, however, is expensive, time consuming and very problematic in rough terrain. Here we present two case studies: (1) combining bedrock geology and 2D seismic profiling to create a 3D model of sub-surface structures in the cover nappes of the Scandinavian Caledonides in preparation for scientific deep drilling; and (2) using 3D forward modeling to provide information for more accurate interpretation of 2D seismic data in exploration of a massive sulfide deposit in central Sweden. Furthermore, in the first case, potential field modeling was an important tool in verifying some of the key features in the 3D interpretation.

## 2  3D Seismic Interpretation

The scientific deep drilling project COSC (Collisional Orogeny in the Scandinavian Caledonides) was designed to study major tectonic features and key questions regarding orogenic processes and, in particular, the emplacement of hot allochthons (Gee et al., 2010). Two fully cored boreholes of about 2.5 km each at carefully



Köli Nappe Complex (phyllites and metagreywackes; ophiolite at base)

Seve Nappe Complex (amphibolites, metadolerites, psammitic and pelitic gneisses)

Särv & Offerdal Nappes (Neoproterozoic metasandstones; with dolerites in Särv)

Jämtlandian Nappes (Cambro-Silurian quartzites, shales, turbidites)

Midproterozoic felsic volcanites

Décollement zone (sole thrust underlain mainly by Cambrian alum shales)

Proterozoic basement (granites)

CCT acquisition line, 1988-92

COSC acquisition lines, 2010

**Figure 1.** (a) Bedrock geological map projected to a digital elevation model; (b) reflection seismic sections with picked horizons separating major tectonic units; (c) the resulting structural and lithological 3D interpretations; (d) the 3D interpretation in a view cut from south-west. COSC-1 is the first drill site of the COSC project.

selected locations are planned in west central Sweden, with the first, COSC-1, scheduled for drilling in 2014. More than 40 km of high resolution 2D reflection seismic data were acquired in 2010 for locating the most suitable drill site and for helping to plan the drilling (Hedin et al., 2012). The seismic sections revealed a highly reflective subsurface and, when combined with an older regional profile (Juhojuntti et al., 2001) and knowledge of the bedrock geology and physical rock properties, allowed interpretation in 2D and identification of the first drill site location.

A deep drilling project of this scale requires a good 3D geological understanding of the environment to be drilled. To create a 3D interpretation around the drill site, the migrated and depth converted seismic sections and bedrock geology were imported into 3D modeling software. As a first step, boundaries separating major tectonic units were traced in the surface geology and projected to a digital elevation model (Fig. 1a). Horizons were then picked on the seismic sections along major reflections that separate these tectonic units according to the 2D interpretations (Fig. 1b). Finally, surfaces roughly tracing the boundaries between adjacent units were created by extending picked horizons laterally (with their extension and thickness as indicated by surface geology) and linking them with the boundaries in the surface geology (Fig. 1c). This 3D interpretation was kept as simple as possible, despite the complex reflectivity observed in several places (Hedin et al., 2013), yet it gives a better understanding of the large scale, thrust emplaced structures of the Caledonian cover.

To test the consistency of this interpretation, 3D inverse modeling, constrained by the seismic data, was performed on residual Bouguer gravity data covering the area around the drill site. Two key points for validation of the inversion was the 3D geometry of the central high density Seve Nappe Complex (one of the main targets of the COSC project) and whether this is separated from an assumed high density basement by low density material. Iterative inversion of a cubical model with cells assigned density contrasts from a background of 2700 kg m$^{-3}$, containing rough volumetric shapes (from digitized surface geology and seismics), reproduced the residual gravity field within an error misfit of 0.2 mgal. The calculated response from the 3D inversion model satisfies the observed residual gravity data very well with only minor differences. The majority of these discrepancies are likely due to the forced geometry of the initial model (Hedin et al., 2013). In the produced 3D inverse model (Fig. 2a), the central high density unit corresponding to the Seve Nappe Complex stands out clearly, apparently being at its thickest just west of the drill site and becoming more shallow both towards North and South. The 3D geometry of this high density unit is converging on the shape of the Seve Nappe Complex in the 3D interpretation (Fig. 1) which is highlighted in Figure 2b, where the latter has been imported into the inverse gravity model. It is also seen in Figure 2 that, to generate an accurate response from the model, low density material is required beneath this unit. It is not, however, possible to resolve the thickness of this layer, hence neither can the depth to the basement be resolved (Hedin et al., 2013).
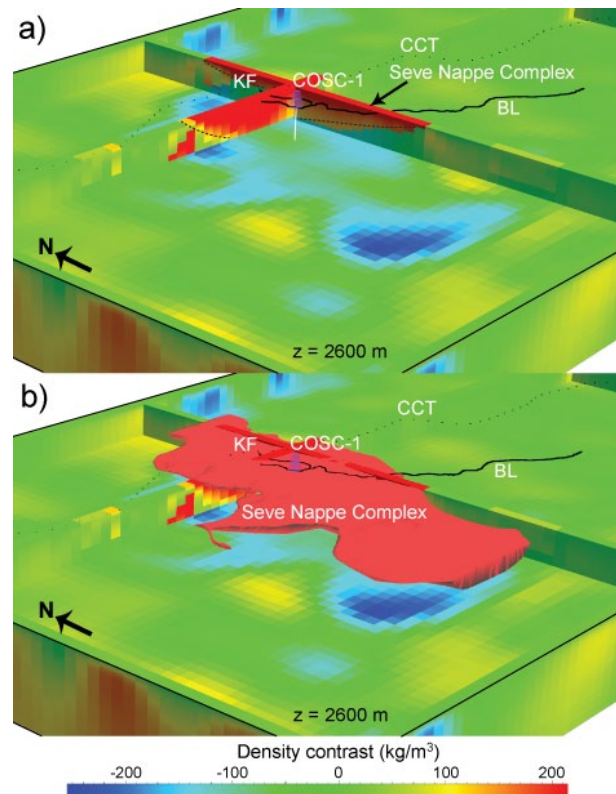


**Figure 2.** (a) Constrained 3D inverse density model; (b) 3D view illustrating the close fit between the interpreted and modelled high density Seve Nappe Complex and underlying low-density material. COSC-1 is the first drill hole of the COSC project and abbreviations are: KF – Kallsjön-Fröå Profile (2010), BL – Byxtjärn-Liten profile (2010), CCT – Central Caledonian Transect (1988-92).

## 3  3D Seismic Forward Modeling

By constructing a 3D model based on geological interpretations and geophysical and/or geological measurements in 3D modeling software, it is possible to generate a seismic response which should be similar to stacked sections resulting from the processing of real seismic data. This approach is called forward modeling and this method can help validate geological interpretations and strengthen their reliability. This is very challenging when dealing with 3D geometries and all associated problems. As shown in previous work (Malehmir et al., 2010; White and Malinowski, 2012), out-of-the-plane reflectors can generate a significant seismic response and therefore it is important to perform 3D forward modeling. This provides a good understanding of the delineation of the geological horizons in the subsurface. Drilling locations should be recommended based on 3D interpretations, especially when only 2D seismic data is available (White and Malinowski, 2012). Seismic forward modeling can be done by ray-tracing approaches or using wave equations (acoustic or elastic waveform modeling). Forward modeling based on the wave equation is generally more robust than the ray-tracing approach, but computation is time consuming and therefore expensive. The Born approximation method is another robust method which could be used to model the seismic response of
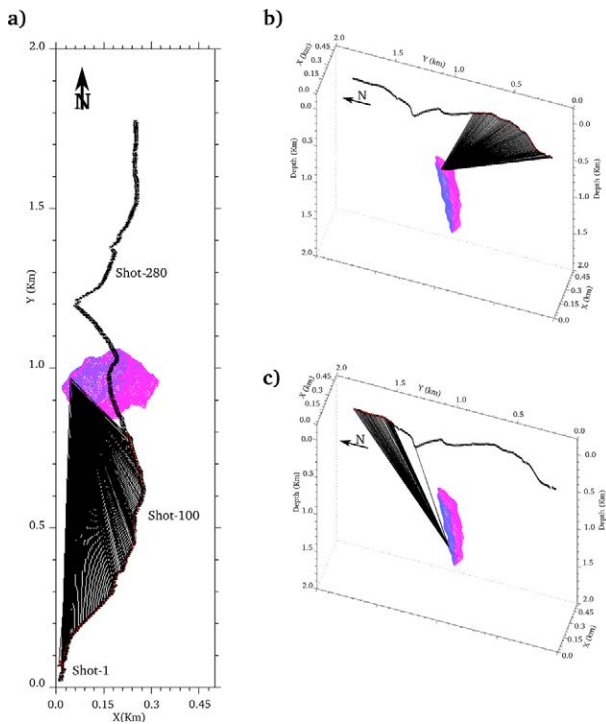
**Figure 3.** The ore body model. (a) top view of the ore body model and plotted P-wave rays for the first shot. (b) and (c) show the ore body (bird view from the south-west) and the plotted P-wave rays for the shots 100 and 280, respectively.

inclusions, but it is most accurate if the impedance contrast is small (Bohlen et al., 2003). On the other hand, ray-trace modeling provides us with rays which hit the target and are reflecting back to the receivers. This can be useful to determine where to expect a seismic signal from the target in the real data (Ahmadi and Juhlin, 2013; Ahmadi et al., 2013; White and Malinowski, 2012).

Forward modeling based on ray-tracing consists of the following steps: (1) building the geological model;

(2) smoothing the model structure (necessary because ray-tracing is sensitive to the shape of the surfaces); (3) introducing the geological model and seismic survey geometry to the ray-trace modeling software; (4) defining petrophysical parameters for the model and its surroundings; (5) running the ray-tracing program; and (6) generating synthetic data. The resulting generated synthetic data may then be compared with the real seismic data.

Here we show an example from a high resolution 2D seismic profile which was acquired at Garpenberg, central Sweden, in 2011. The main aim of the study was to image a massive sulfide ore body which is hosted in the bedrock of the area (Ahmadi et al., 2013). Figure 3a shows the top view of a 3D model of the targeted ore body, based on coordinates provided by Boliden Mineral AB, and the 2D seismic reflection profile. As our focus was only on the response from the ore body which is located partially under the seismic profile, all other sources of reflectivity were neglected. Table 1 shows the petrophysical parameters that were introduced to the modeling program. We assumed two media in the model, the ore body and host rock. A velocity for the ore body was calculated by taking the average of the slowness of those minerals assumed to be the main composition of the deposit. We used a density of 3.5 $g/cm^3$ for the ore body and 2.7 $g/cm^3$ for the host rock, interpreted to be limestone based on geological information. It is interesting to see the reflections off the top of the ore body emanate from an out-of-the-plane reflection zone (Fig. 3a). This should be taken into account in the interpretation and when suggesting drilling location(s). Furthermore, it shows that we cannot always trust 2D seismic data when we are dealing with complex 3D geology. Figures 3b and 3c show how plotted rays reflect back from the ore body for the two selected shots (100 and 280) of the profile, respectively. Generating synthetic data now allows an interpreter to fairly easily
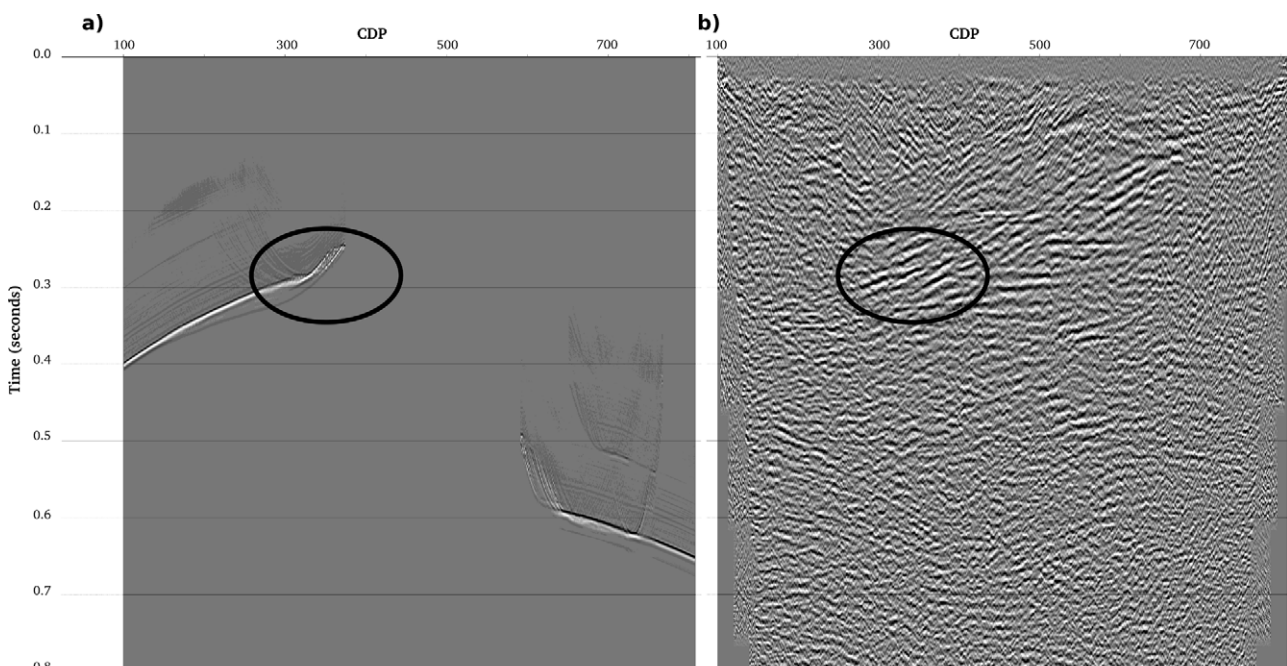


**Figure 4.** DMO corrected stacked sections of (a) synthetic and (b) real seismic data. The ellipse highlights the similar reflection group in both sections.

**Table 1.** Physical rock parameters used to define the ore body model (based on Salisbury et al. (2003), Sheriff and Gerald (1995) and information from Boliden Mineral AB).

| Mineral | Density (g/cm$^3$) | $V_P$ (km/s) | $V_S$ (Km/s) | Poisson's ratio |
|---|---|---|---|---|
| **Ore Body** | | | | |
| Sphalerite | - | 5.44 | 2.8 | 0.32 |
| Galena | - | 3.69 | 2.11 | 0.26 |
| Pyrite | - | 7.99 | 4.94 | 0.19 |
| Pyrrhotite | - | 4.6 | 2.73 | 0.23 |
| Chalcopyrite | - | 5.12 | 2.49 | 0.35 |
| Average | 3.5 | 4.84 | 2.66 | 0.28 |
| **Host Rock** | | | | |
| Meta-Limestone | 2.7 | 5.5 | - | 0.25 |

compare with the real data to see where to expect a signal from the true target. In Figure 4a, showing the synthetic DMO stacked section, a south dipping reflector is distinguishable from 0.25 s to 0.4 s. In the real DMO corrected stacked section (Fig. 4b) this part of the section is populated by a group of reflections marked by the ellipse. These reflections appear at the same time as the synthetic reflection, but do not continue down to 0.4 s. This is probably due to the complexity of the real geological structures which are not introduced into the smooth model, or the low CDP fold in the southern part of the profile (Ahmadi et al., 2013). Further north of the seismic profile, another reflection from 0.6 s to 0.65 appears on the synthetic data. No sign of this reflection, which is the result of reflections off the base of the ore structure, is seen in the real data (Figs. 4a and 4b). Ahmadi and Juhlin (2013) have explained this as due to decreasing CDP fold to the north of the profile.

This study shows how forward modeling can be valuable for mineral exploration as it provides more confidence for interpretations produced from other data. However, more advanced forward modeling using a 3D wave equation approach should add additional constraints on the interpretations.

## Conclusions

Understanding the 3D geometry of subsurface structures is of great importance in geophysical exploration, such as resource prospecting, yet acquisition of full 3D geophysical surveys are costly, time consuming and difficult. We have here shown two ways in which 2D reflection seismic data can be used for 3D interpretations and verification of the interpretations based upon them. Firstly, combining seismic data with bedrock geology allows the creation of a simple 3D interpretation of the major structures which can be verified with other geophysical data, in our case gravity. Secondly, seismic forward modeling based on ray-tracing is a good way of fast constructing synthetic data which indicate where reflections from targeted units should be expected in the processed seismic sections. This latter approach takes into account out-of-the-plane reflections in 2D seismic sections and can help define the location of drilling targets more accurately. Thus, 2D reflection seismic data combined with other available geological/geophysical data, can be used in several ways to produce better 3D interpretations, giving better control of, for example, specific drilling targets.

## References

Ahmadi O, Juhlin C (2013) Seismic Forward Modeling of a Poly-metallic Massive sulfide Deposit at Garpenberg, Central Sweden. 75th EAGE Conference. London, accepted extended abstract

Ahmadi O, Juhlin C, Malehmir A (2013) High-resolution 2D seismic imaging and forward modeling of a ploy-metallic massive sulfide at Garpenberg, central Sweden. Geophysics, submitted manuscript

Bohlen T, Muller C, Milkereit B (2003) Elastic Seismic-Wave Scattering from Massive Sulfide Orebodies: On the Role of Composition and Shape. In: D. W. Eaton, B. Milkereit, M. H. Salisbury (eds) Hard rock Seismic Exploration, Geophysical Developments No.10, Society of Exploration Geophysicists, pp 70-89

Gee DG, Juhlin C, Pascal C, Robinson P (2010) Collisional Orogeny in the Scandinavian Caledonides (COSC). GFF 132(1): 29-44, doi: 10.1080/11035891003759188

Hedin P, Juhlin C, Gee DG (2012) Seismic Imaging of the Scandinavian Caledonides to define ICDP drilling sites. Tectonophysics 554-557:30-41, doi: 10.1016/j.tecto.2012.05.026

Hedin P, Malehmir A, Juhlin C, Gee DG, Dyrelius D (2013) 3D interpretation and potential field modelling in the vicinity of the proposed COSC-1 drill site, central Swedish Caledonides. The Geological Society, London, Special publications, submitted manuscript

Juhojuntti N, Juhlin C, Dyrelius D (2001) Crustal reflectivity underneath the Central Scandinavian Caledonides. Tectonophysics 334, 191-210, doi: 10.1016/S0040-1951(00)00292-4

Malehmir A, Bellefleur G, Müller C (2010) 3D diffraction and mode converted scattering signatures of base-metal deposits, Bathurst Mining Camp. First Break 28:41-45

Salisbury MH, Milkereit B, Ascough G, Adair R, Matthews L, Schmitt DR, Mwenifumbo J, Eaton DW, Jianjun W. (2000) Physical properties and seismic imaging of massive sulfides. Geophysics 65:1882-1889, doi: 10.1190/1.1444872

Sheriff RE, Geldart LP (1995) Exploration seismology. Cambridge University Press, Cambridge

White D, Malinowski M (2012) Interpretation of 2D seismic profiles in complex geological terrains: Examples from the Flin Flon mining camp, Canada. Geophysics 77:WC37-WC46, doi: 10.1190/GEO2011-0478.1

# Using 3D/4D modelling tools in exploration for porphyry and manto-polymetallic potential areas in Eastern Chalkidiki peninsula, N. Greece

**Arvanitidis N.D., Michael C.**
*Institute of Geology and Mineral Exploration (IGME), Greece*

**Christidis C.**
*National and Kapodistrian University of Athens, Greece*

**Weihed P.**
*Luleå University of Technology, Luleå, Sweden*

**Gaál G.**
*Geological Survey of Finland, P.O.Box 96, 02151 Espoo, Finland*

**Royer J.J.**
*Université de Lorraine, CNRS, Nancy, France*

**Perantonis G., Bakalis V., Ballas D.**
*Hellas Gold S.A., Greece*

**Abstract.** The challenge of mineral exploration is to approach new exploration targets. 3D and 4D modelling are the new exploration tools that can help the mineral explorers to visualise, interpolate and interpret geological data are a critical time- and money-saving method.

In NE Greece, where most of the potential resources and feasible deposits are hosted, polymetallic-gold mineralizations occur in a wide range of genetic types comprising magmatic, hypothermal/ mesothermal manto-type, orogenic, epithermal and supergene mineralization types.

The genetic link between porphyry copper and large polymetallic manto style sulphide deposits can be incorporated into regional exploration strategies in a complex metamorphic terrain of schists, gneisses and marbles of Palaeozoic age, whereas the epithermal type deposits were emplaced within a broad volcanic belt of Oligocene-Miocene age, which developed first in Bulgaria and then moved south through northern Greece to the region of Thrace.

Local, semi-regional and regional scales of 3D models and a semi-regional 4D model were applied on the porphyry and manto-polymetallic deposit types of Eastern Chalkidiki, to achieve new metallogenetic interpretations and exploration perspectives in Greece.

**Keywords.** Mineral belt, 3D/4D modelling, manto-polymetallic deposits, exploration tool, potential areas.

## 1 Introduction

Greece's geology favors a potent and dynamic use of mineral resources. Among the Non-Energy Metallic Minerals commodities, base and precious metals, in particular zinc, lead, copper gold, and silver are becoming an increasingly important and rapidly growing target of the mining industry. In NE Greece, where most of the potential resources and feasible deposits are hosted, polymetallic-gold mineralizations occur in a wide range of genetic types. The mineralization potential is consisted of magmatic porphyry copper type deposits, hypothermal/ mesothermal manto-type polymetallic sulphides and epithermal gold systems (Arvanitidis 2010).

The Eastern Chalkidiki peninsula in northern Greece with polymetallic replacement deposits (Olympias, Madem Lakkos, Mavres Petres) and porphyry copper deposit (Skouries) is the study area (Fig. 1).



**Figure 1.** The study area of Eastern Chalkidiki peninsula.

The following geomodels have been constructed:
- 3D geomodels at deposit scale in Olympias, Mavres Petres, Skouries.
- 3D geomodels at semi-regional scale at North-Eastern Chalkidiki peninsula (Arvanitidis et al. 2012) and
- regional scale model of the Hellenic-Balkan belt.

## 2 Geology of Eastern Chalkidiki peninsula (Serbomacedonian zone)

The Serbomacedonian zone is a complex metamorphic terrain of schists, gneisses and marbles that are often mineralized and intruded by Variscan granitic rocks. It trends NW, is some 500 km long, and is host to numerous deposits, including Olympias and Stratoni manto-type polymetallic deposits, and Skouries and Pontokerasia, porphyry copper in Greece, Sasa and

Zletovo Pb – Zn deposits, and Bucim porphyry copper in the Former Yugoslav Republic of Macedonia, as well as the Lece polymetallic deposit in Serbia – Montenegro.

The Serbomacedonian zone consists of two major lithostratigraphic units of Paleozoic age, known as the Kerdylia and Vertiskos formations. The Olympias, Madem Lakkos and Mavres Petres belong geotectonically to the Kerdylia formation whereas the Skouries porphyry copper-gold deposit to the Vertiskos one.

The Serbomacedonian zone incorporated into Kerdylia and Vertiskos formations (Fig. 2).
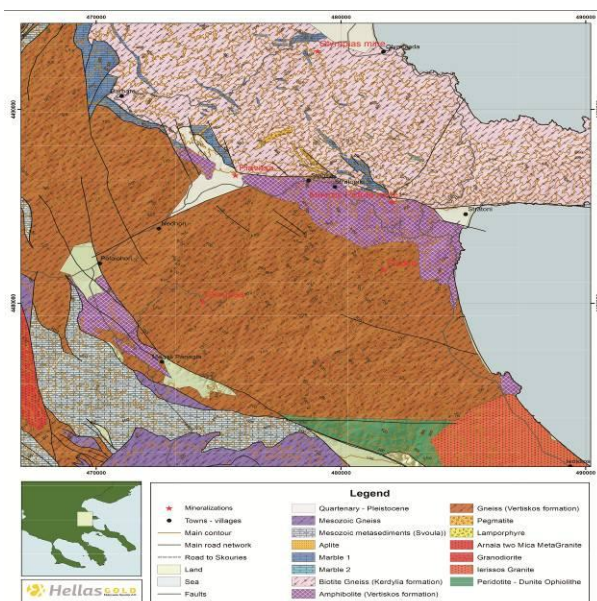


**Figure 2.** Geological map of Eastern Chalkidiki peninsula.

The contact between the Kerdyllia and Vertiskos formations is partly gradational, but largely deformed and displaced by the major Stratoni-Varvara fault zone.

## 3. Building of 3D models

Local, semi-regional and regional scales of 3D/4D models were applied in most of the above mentioned deposit types and areas achieving new metallogenic interpretations and exploration perspectives in relation to the geology, the structural setting, the stratigraphy, the tectonic evolution, the ore bodies geometry, the alteration zones, the ore grades distribution and the genetic links between the spatially related porphyry and manto systems, based on airborne geophysics, along with further interpretations for across border regional exploration and prospecting potential.

Information and data used for 3D modelling, included:
- Aeromagnetic data.
- Semi-regional strategic geochemical survey.
- Geological and structural data.
- Geological cross sections
- Soil geochemical data.
- Ground geophysical survey.
- Down-hole surveys and drill hole logs providing information on

- Wallrock lithology and geochemistry
- Alteration zones
- Ore metals distribution (drill hole mineralization intersections)
- Structural data

### 3.1 Olympias manto-type polymetallic deposit (deposit scale model)

The Olympias deposit is a polymetallic (Pb, Zn, Ag, Au) massive sulphide replacement ore body hosted by Kerdylia marbles. The mineralization is emplaced in deep-seated fault zones and their intersections with marble beds giving place to replacement and formation of lateral stratabound mantos, very often deposited at the contact zone between marbles and overlying gneisses (Kalogeropoulos et al., 1989; Arvanitidis N., 1993).

Two main deposits have been identified, the West and East deposits.

The 3D model created shows the structure of the deposit and the fault-controlled setting of the ore-bodies, as well as the stratabound replacement mantos on behalf and inside the marbles (Fig. 3). A deeper-seated extension of the west ore body is indicated and makes a potential target to further underground surveys and exploration drilling.
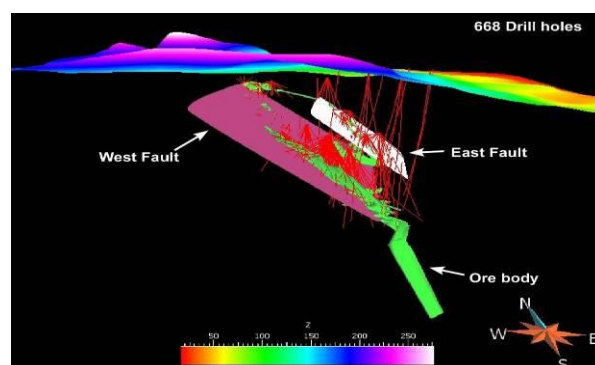


**Figure 3:** 3D visualization of the Olympias ore deposit.

### 3.2 Madem Lakkos and Mavres Petres polymetallic replacement deposits (deposit scale model)

Madem Lakkos and Mavres Petres are, like Olympias massive, stratabound lead-zinc-silver carbonate replacement deposits hosted by Kerdylia formation marbles and developed, when spatially (in time and space) intersected by cross-cutting fault zones. The geological setting comprises also the major Stratoni-Varvara thrust fault bringing tectonically in contact Kerdylia marble interbedded, biotite gneiss and Vertiskos amphibolite.

The Mavres Petres ore body was 3D modelled (Fig. 5), with respect to intersecting fault zones (Figs. 4, 5), the overall geological setting and the compositional distribution of metal grades.

Setting up the complete 3D geological model of the Mavres Petres ore deposit all available data and sources of information were compared and integrated (Fig. 5).
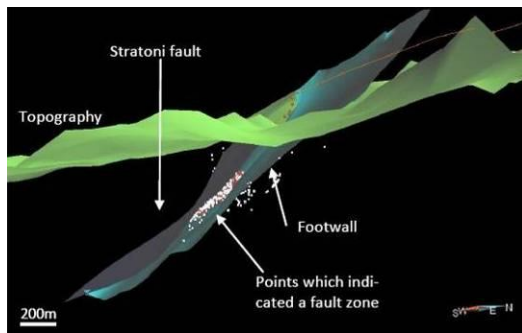
**Figure 4:** The Stratoni-Varvara fault depth extension and cross-cutting fault structures indicated by white dots corresponding to observations and descriptions of mylonite, breccia and kaolin zones in the drillcores available.

During the creation of the model, a considerable amount of knowledge concerning the mineralization area and the ore body was specifically updated; some new N-S striking and cross-cutting fault structures were interpreted, but further investigations are required to determine their metallogenetic relationship to any of the mineralization processes (Penet 2010).
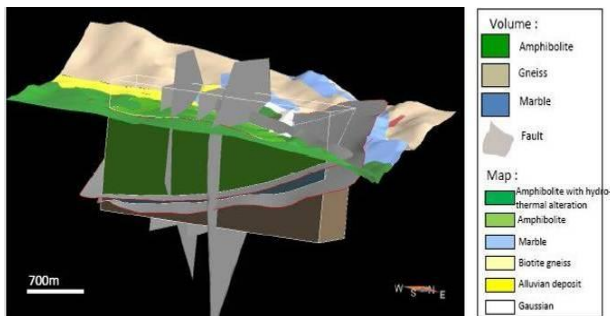


**Figure 5:** Final 3D model of the Mavres Petres mining area.

The in situ reserve estimation of the Mavres Petres ore has provided a mining oriented 3D model which makes a useful tool for improving the knowledge of the area.

### 3.3 Skouries porphyry copper-gold deposit (deposit scale model)

The Skouries ore deposit is part of the NW trending Serbomacedonian porphyry copper belt extending through FYROM to Serbia and Romania. The Skouries porphyry intrusion consists of a series of rhyodacitic, dioritic to andesitic dykes and stocks emplaced into Vertiskos amphibolitic basement rocks in association with ultrabasic lithologies. It forms a pipe-like, mineralized subvolcanic body (Frei 1995). The deposit is characterized by more or less concentric potassic, propylitic, phyllic and argillic alteration zones, affecting mostly the host schists (Frei R 1995; Kalogeropoulos et al 1991).

Based on existing data and the work carried out by Penet (2010), it was possible to identify and map the major brittle deformation features, in terms of faults and related fracture zones, and using digital interpretations of the topography to better model and locate the main lineaments controlling and defining the porphyry intrusive corridor (Fig. 6). Three mainly NE striking

directions of faulting were identified (Fig. 6).

The Skouries 3D models are becoming efficient explorations tools to target and locate new potential porphyry copper – gold mineralizations in the area.
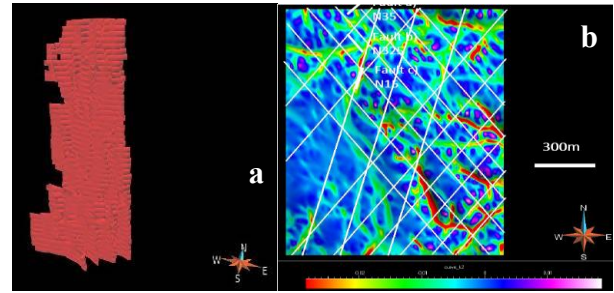


**Figure 6:** a. Skouries orebody. b. Three main faulting directions of N35°E, N 35°W and N15°E were identified.

### 3.4 Semi-regional 3D modelling of North-Eastern Chalkidiki

The local deposit scale 3D models were integrated and co-interpreted along with the regional scale geological knowledge to provide semi-regional 3D modelling of the metallogenetic evolution. For the region of North-Eastern Chalkidiki peninsula the previously presented deposit scale 3D models were evaluated along with regional scale data on: i) Geological setting, ii) Structural characteristics, iii) Geophysical measurements

The creation of the 3D geological map was further elaborated by fifteen geological sections across the area, for better understand the 3rd dimension.

By integrating structural, geological and the geophysical data it was possible to 3D model the intrusive bodies and the basement rocks of the area considering also the perspective of the crossborder geotectonic zones e.g. Carpathian-Balkan belt. In this respect, figure 7 shows the semi-regional geological setting of Vertiskos and Kedyllia formations, composing the Paleozoic Serbomacedonian zone, in tectonic contact with Mesozoic Circum Rhodope Belt.
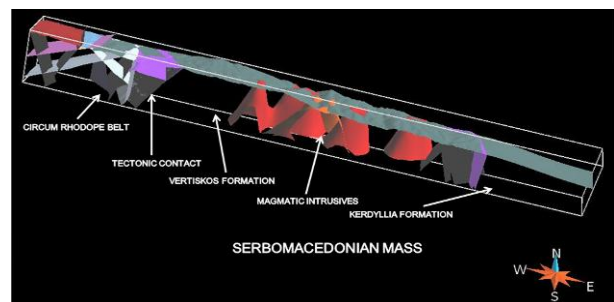


**Figure 7:** 3D geological cross section through the Serbomace-donian mass.

### 4. Conceptual 4D modelling in polymetallic manto and porphyry type systems of Eastern Chalkidiki peninsula

The geological information used to analyze the geological history in order to create the 4D model of Eastern Chalkidiki peninsula included: Geochronology

of formations, main deformation process and orientation/dip analysis, geological evolution of Kerdyllia and Vertiskos formation, and hydrothermal alteration, fluid inclusion, stable isotopes studies.
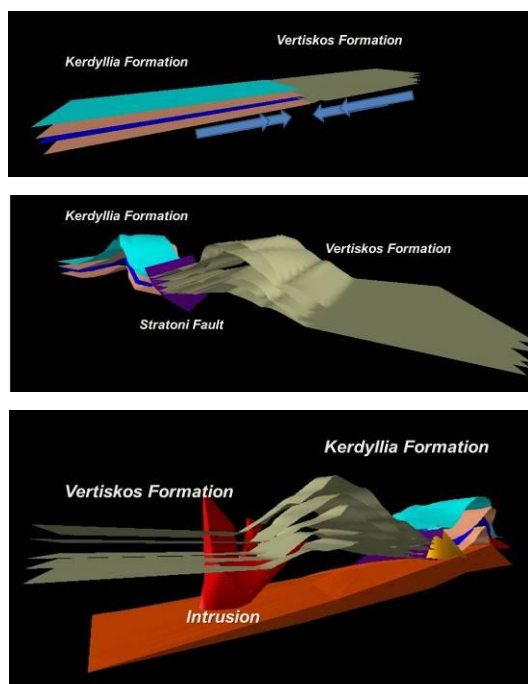


**Figure 8:** Screenshots from the 4d model that depicts the main stages of the development of polymetallic replacement deposits.

4D models were incorporated into local exploration as they proved to be significance to identify new potential mineralization targets.

## Summary and conclusions

In the study areas, the 3D models not only contribute to ore feasibility evaluation but also enable better understanding of the mineralizing processes.

The Mavres Petres mine 3D modelling revealed a series of parallel faults, vertical to the main Stratoni-Varvara fault, and established a reliable tool for exploration of new ore potential areas at depth and along the westward extension of the main fault structure, in the area of Piavitsa.

In the semi-regional scale 3D modelling of NE Chalkidiki peninsula, the interaction between faults and magmatic intrusions was very much obvious. In addition the geological sections across the area indicated the types of mineralization processes taken place.

The 3D models are very useful tools for improving the knowledge of the ore deposition and conduct an efficient and successful mineral exploration for locating deep-seated mineralizations. Given the multi-disciplinarity of the existing data and the advanced IT capabilities it is realistic to further develop 3D into 4D models when the time parameter is combined and added. This will secure even more and make the exploration efficiency more sustainable to determine additional potential areas and discover new exploitable deposits with the same or different resource characteristics.

The research leading to these results has received

## References

Arvanitidis N (1993) Regional ore geologic studies setting controls and distribution of Metallic ore deposit types in the Serbo-Macedonian and Western Rhodope zone. I.G.M.E. technical report

Arvanitidis N (2010) New metallogenetic concepts and sustainability perspectives for non-energy metallic minerals in Greece. 12th International Congress Of The Geological Society Of Greece Bulletin Of The Geological Society Of Greece Volume XLIII. No 5. 2010

Arvanitidis ND, Michael C, Perantonis G, Bakalis V, Ballas D, Christidis C (2012) Using 3D/4D modelling tools in exploration of gold-polymetallic potential areas in Greece. 7th EUREGEO- Bologna 2012

Frei R (1992) Isotope (Pb. Rb - Sr. S. O. C, U- Pb) geochemical investigation on Tertiary intrusive and related mineralizations in the Serbomacedonian Pb-Zn. Sb+Cu-Mo metallogenetic province in N. Greece - Ph D Thesis. Swiss Federal Institute of Technology (ETH) Zurich, Switzerland. 231 pp

Kalogeropoulos SI, Economou GS, Gerouki F, Karamanou E, Kougoulis C, Perlikos P (1991) The mineralogy and geochemistry of the Stratoni granodiorite and its metallogenic significance - Geological Society of Greece. Bulletin, v. 25. P. 225 – 243

Kalogeropoulos SI, Kilias SP, Bitzios DC (1989) Genesis of the Olympias Carbonate-hosted Pb-Zn(Au.Ag) Sulfide ore deposit, eastern Chalkidiki Peninsula, northern Greece - Econ. Geol vS4 pp 1210-1234

Penet A (2010) 3D Geomodeling of the Mavres Petres (Pb-Zn-Ag) and Skouries (Cu-Au) minera-lizations, Stratoni (Greece). MSc thesis in INPL-NNancy

# Using 3D/4D modelling tools in exploration for epithermal gold potential areas in Eastern Rhodope zone (Western Thrace, NE Greece)

**Arvanitidis N.D., Michael C.**
*Institute of Geology and Mineral Exploration (IGME), Greece*

**Christidis C.**
*National and Kapodistrian University of Athens, Greece*

**Weihed P.**
*Luleå University of Technology, Luleå, Sweden*

**Gaál G.**
*Geological Survey of Finland, P.O.Box 96, 02151 Espoo, Finland*

**Royer J.J.**
*Université de Lorraine, CNRS, Nancy, France*

**Perantonis G., Bakalis V., Ballas D.**
*Hellas Gold S.A., Greece*

**Abstract.** 3D/4D modelling tools are gaining ground day to day as advanced exploration technologies in mineral industry. The ability to visualise, interpolate and interpret geological data is a critical time- and money-saving method for mineral explorers. The models can contribute to better understand the geological evolution of mineralizing and ore-forming processes. These models can be key inputs for generating predictive models at different scales.

In NE Greece, where most of the potential resources and feasible deposits are hosted, polymetallic-gold mineralizations occur in a wide range of genetic types comprising magmatic, hypothermal/ mesothermal manto-type, orogenic, epithermal and supergene mineralization types.

The epithermal deposits were emplaced within a broad volcanic belt of Oligocene-Miocene age, which developed first in Bulgaria and then moved south through northern Greece to the region of Thrace.

Deposit, semi-regional, regional scales 3D models and 4D model were produced to achieve new metallogenetic interpretations and exploration perspectives in Greece.

**Keywords.** 3D/4D modelling, epithermal gold deposits, exploration tool, gold potential areas.

## 1  Introduction

Greece's geology favors a potent and dynamic use of mineral resources. Among the Non-Energy In NE Greece, where most of the potential resources and feasible deposits are hosted, polymetallic-gold mineralizations occur in a wide range of genetic types.

The most prospect area for epithermal gold deposits (Perama and Aghios Demetrios deposits) in Greece is the region of western Thrace (Fig. 1):

For the exploration of epithermal gold potential areas the following geomodels have been constructed:

- 3D geomodels at deposit scale (Perama Hill and Aghios Demetrios).

- 3D geomodel at semi-regional scale across Petrota Tertiary graben and Sappes – Kirki Tertiary basin.

- Regional scale model of Rhodope zone and

- Conceptual 4D model for the metallogenic evolution of epithermal Au deposits in the Tertiary basins of Western Thrace.



| Neogene - Quaternary | Middle Eocene | Paleozoic |
|---|---|---|
| Sedimentary deposits | Basal conglomerates and molasse | Metamorphic basement |
| **Oligocene** | **Lower - Upper Cretaceous** | Faults. |
| Volcanic rocks | Circum-Rhodope zone-Drimou-Melia unit. Flysch and diabase | Overthrust. |
| Plutonic rocks | **Upper Triassic-Upper Jurassic** | |
| **Upper Eocene - Lower Oligocene** | Circum-Rhodope zone-Makri unit a.Basic rocks (gabbro-diorites) | |
| Flysch and volcanosedimentary series | b. Phyllite series | |

Geological sketch map of Western Thrace. (P. Papadopoulos,modified by C. Michael).

**Figure 1:** The study area of the Western Thrace region.

## 2  Epithermal gold deposits in Thrace

The epithermal gold deposits in the Thrace region are related to the post-collisional extension during late Eocene-Oligocene, forming structurally controlled rift-basins along the southern and eastern margins of the Rhodope zone. These Tertiary basins are characterized by deposition of Early Eocene sediments (molasses, limestones) followed up by late-Eocene – early-Oligocene volcanosedimentary series with calc-alkaline

to shoshonitic volcanic activities (Innocenti et al. 1984). The Saint Demetrios and Perama deposits are related to a volcanic arc of Oligocene age.

This arc extends across the Greek-Bulgarian border hosting epithermal gold systems of high exploration and exploitation potential.

## 3. Building of 3D models

Local, semi-regional and regional scales of 3D/4D models were constructed for most of the above mentioned deposits achieving new metallogenic interpretations and exploration perspectives in relation to the geology, the structural setting, the stratigraphy, the tectonic evolution, the ore bodies geometry, the alteration zones and the ore grades distribution along with further interpretations for across border regional exploration potential.

For the construction of the 3d model were used:
- Aeromagnetic data
- Semi-regional strategic geochemical survey
- Available surface geological and structural data
- Geological cross sections
- Soil geochemical data
- Ground geophysical survey
- Down-hole surveys and drilholes logs providing information on:
    - Wall rock litholoqy and geochemistry
    - Alteration zones
    - Ore metals distribution (drill hole mineralization intersections)
    - Structural data

### 3.1 Perama Hill epithermal gold deposit (deposit scale model)

The Perama Hill epithermal gold deposit is located in the eastern part of Petrota graben consisting of subaqueous pyroxene andesitic flows, debris-flows and hyaloclastites, resting on the turbiditic series (Lescuyer et al. 2003). The Perama sandstones which host the gold mineralization are coeval with subaerial felsic eruption in the western part of the graben (pyroclastic flows, accretionary lapilli tuff, quartz porphyry domes and dacite flow; Lescuyer et al. 2003).

The metamorphic basement close to the deposit is part of the Circum Rhodope zone (Mesozoic age) and consists of greenschists and calcschists.
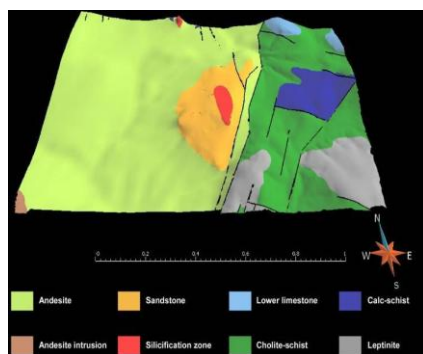


**Figure 2:** 3D local geology of the Perama.

It is obvious from the 3D modelling applications that:

- The mineralizing hydrothermal system was structurally controlled (Fig. 3)
- The rift-fault between the Mesozoic basement and the Petrota graben was possibly the conduit for mineralizing hydrothermal fluids (Fig. 3)
- The sandstones were favouring fluids migration and deposition of gold.
- The deposit is characterized by a vertical pattern of metal distribution zones. The main part of the base metals sulphide mineralization is hosted by volcanic breccias and tuffs at depth.
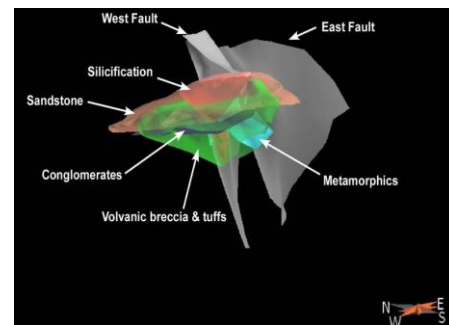


**Figure 3:** Major faults at the contact of the Tertiary basin and metamorphic basement rocks (Perama Hill deposit).

### 3.2 Aghios Demetrios epithermal gold deposit (deposit scale model)

The geological setting comprises strongly altered agglomerate andesitic tuffs, lavas and volcanic breccias. According to the paragenetic distribution of the mineral assemblages four main and two overlapping alteration zones are distinguished in the area (Michael 1988, 1993, 1995, 2005).

Main alteration zones
- Silicification zone (hydrothermal eruption vent breccias) (Fig. 4)
- Advanced argillic zone (subzones of alunite, diaspore, argillic alteration and pyrophyllite)
- Propylitic alteration
- Potassic alteration (southern part of the Tertiary basin)

The hydrothermal eruption vents breccias make favourable structural setting for the gold mineralization at Aghios Demetrios deposit. Younger in age north-eastern faults has caused displacement of the wall rocks (Michael 1993; Bridges et al., 1998; Border et al., 1999; Andrew and Constantinides 2001).

Based on the 3D modelling approach of the two epithermal deposits the following can be concluded:
- The ore forms a flat lying body trending NW and dipping N-NE (Fig. 5)
- The N-NE part of the area is of a high potential for gold exploration
- The ore body is approximately 550 m long and 100-160 m wide (Fig. 5)
- A NE trending fault zone intersects and separates the ore body (Figs. 4, 5). This fault zone has also caused displacement of the wall rock alteration zones.
- Gold mineralization is mainly associated with hydrothermal eruption vent breccias (Fig. 4).
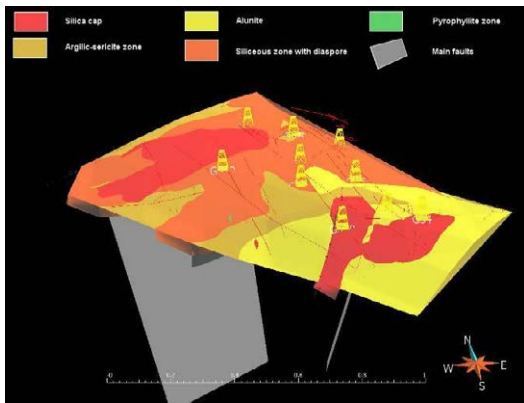
**Figure 4:** Hydrothermal alteration zones and main faults of the Aghios Demetrios epithermal gold deposit.
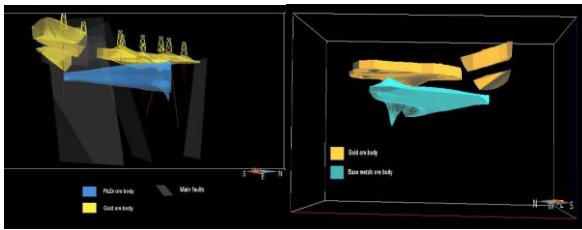


**Figure 5:** Structural setting of the Aghios Demetrios gold and base metal ore bodies.

- Base metals mineralization is developed at deeper levels (Fig. 5).
- The deposit is characterized by vertical zonal pattern of the ore metals and alteration zones distribution (Fig. 5).
- The advanced argillic zone is widespread (Alunite, diaspore, kaolinite, pyrophyllite; Fig. 4).
- The mineralizing hydrothermal system was structurally controlled related with deep structures.

### 3.3 Semi-regional 3D modelling across Thracian epithermal gold deposits

A geological reconstruction of the area in semi-regional scale has been created using cross sections (Fig. 6), aeromagnetic data, rift basin structures (Fig. 7) and the 3D models developed at deposit scale. Fifteen geological cross sections were set up across the Petrota and Sappes-Kirki Tertiary basins (Fig. 6).
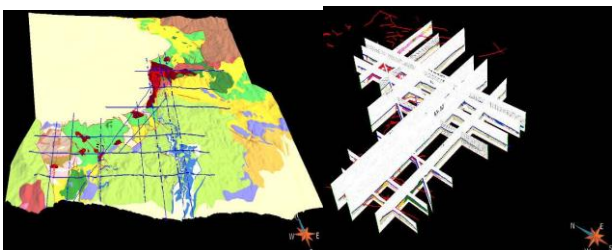


**Figure 6:** 3D geological map and geological sections across the epithermal gold deposits areas in Thrace.

The geological reconstruction of the Petrota graben and Sappen-Kirki Tertiary basin shows that the NNE and NS (deep structures forming the rift graben) seems to have been the conduit for hydrothermal fluids and fissure vent systems.



**Figure 7:** Rift-basins structures of Petrota graben and Sappes-Kirki Tertiary basin.

### 3.4 Regional 3D model of Rhodope zone

Using 3D models, metallogenetic data and mineral districts in Rhodope zone from the both sides area of Greece and Bulgaria, it can be outlined a perspective province for epithermal gold and copper-molybdenum deposits (Fig. 8).

The epithermal gold deposits in both sides developed at contact (graben structures) between Tertiary rocks and metamorphic basement.

The hydrothermal breccia is the favorite site for gold deposition. Gold mineralization is mainly connected with hydrothermal eruption vent breccias and fissure vent systems.
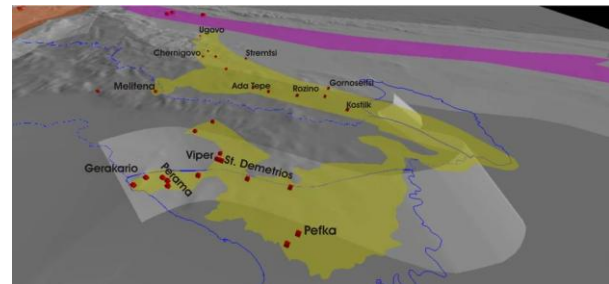


**Figure 8:** 3D model that depicts the epithermal perspective province in Rhodope zone.

The lithologically favorite sites for epithermal gold deposition are tuffs, breccias, volcanics of intermediate composition, sedimentary rocks, shoshonitic rocks, acid volcanic and metamorphic rocks

The high-sulphidation and low-sulphidation epithermal gold systems in Greece and Bulgaria respectively are potential for new discoveries.

The Cu-Mo occurrences and the potassium hydrothermal alteration that found in many areas, indicate that the porphyry copper type of mineralization is also a perspective target.

It is suggested that the hydrothermal system is created by intrusions basing on spatial relationship between granitoids and epithermal systems. Sulfur isotopes results indicate that the fluids were predominantly magmatic (values ~0‰).

### 4. Conceptual 4D model of epithermal Au deposits in Tertiary basins of Western Thrace

For the construction of the 4D model of epithermal

metallogenetic evolution in western Thrace have been used: i) Geological evolution throughout the Rhodope zone, ii) Main deformation process, iii) Geochronology of the formations, iv) Magmatic activity (volcanic and emplacement of granitoids and shallow porphyry intrusives), v) Hydrothermal alteration study, vi) Fluid inclusion study and vii) Stable isotopes geochemistry.
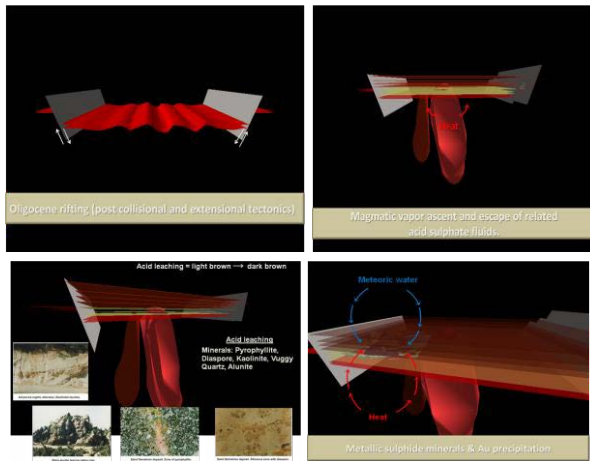


**Figure 9:** Screenshots from the 4d model that depicts the main stages of the development of epithermal gold system.

Acid sulphate fluids escaped from the magmatic source (granitoid intrusives and porphyry stocks; Fig. 9) causing acid leaching, creation of silica supersaturation solutions and precipitation of massive chalcedonic silica (impermeable horizon) at the base of water table. Convecting fluids have trapped beneath the impermeable horizon and a hot overpressured aquifer is formed. The increased pressure was led to a hydrothermal explosion with a formation of hydrothermal breccias and precipitation of gold and base metals (Michael 2005).

The hydrothermal breccia is favorite site for gold deposition. Gold mineralization is mainly connected with hydrothermal eruption vent breccias and fissure vent systems.

The 4D models proofed to be very useful tools for improving the knowledge of the ore deposition and conduct a successful mineral exploration in order to determine new potential areas.

## Summary and conclusions

The use of a 3D geomodel method has an increasingly important role in integrating and analyzing geoscientific information to make it easier to present and understand, and to develop more efficient exploration tools.

In the Greek study areas, the 3D models not only contributes to ore feasibility evaluation, which is a key factor in mining industry, but also enables better understanding of the mineralizing processes that led to the ore formation, and to assist the exploration of new deposits as well as the expansion of known.

In general the 3D model of Aghios Demetrios provides the geometry and orientation of the ore body, the pattern metals distribution zones, the role of later faults in displacing the ore body and the reserves verification of the deposit. In the Perama Hill epithermal gold deposit, the 3D model shows the development of

mineralization zones, as well as the structural and lithological control of ore deposition.

A geological reconstruction of the epithermal deposits in Thrace region, at semi-regional scale, shows that N-NE (Perama Hill) and N-S (Aghios Demetrios) trending structures seems to have been the conduit of hydrothermal fluids and the fissure vent systems. These faults correspond to deep structures forming the rift/graben Tertiary basins.

## References

Andrew S, Constantinides D (2001) The Sappes gold project-Bulletin of the Geological Society of Greece, 34 (3): 1073–1080. Proceedings of the 9th International Congress, Athens, September 2001

Arvanitidis N (1993) Regional ore geologic studies setting controls and distribution of Metallic ore deposit types in the Serbo-Macedonian and Western Rhodope zone. I.G.M.E. technical report

Arvanitidis N (2010) New metallogenetic concepts and sustainability perspectives for non-energy metallic minerals in Greece. 12th International Congress Of The Geological Society Of Greece Bulletin Of The Geological Society Of Greece Volume XLIII. No 5. 2010

Border AJM, Constantinides DC, Michael C (1999) Discovery and evaluation of the Sappes gold deposits, North-eastern Greece. In: New generation Gold Mines 99. Conference proceedings, 22-23 November, Perth, Western Australia

Bridges PS, Gordon MJ, Michael C, Abatzioglou M (1998) Gold mineralization at Sappes, northern Greece. Europe's Major gold Deposits, Irish Association for Econ. Geol., Abstract volume, IAEG, c/o Geological Survey of Ireland. 95-107

Dinter DA, Royden L (1993) Late Cenozoic extension in northeastern Greece: Strimon valley detachment and Rhodope metamorphic core complex. Geology 21, 45-48

Innocenti F, Kolios N, Manneti P, Mazzuoli R, Peccerillo A, Rita F, Villari L (1984) The geology and geodynamic significance of Tertiary orogenic volcanism in Northeastern Greece. Bull. Volcnol., 47-1, 25-37

Lescuyer JL, Bailly L, Cassard D, Lips A, Piantone P, Mc Alister M (2003) Sediment - hosted gold in south - eastern Europe : the epithermal deposit of Perama, Thrace, Greece. Mineral Exploration and Sustainable Development et al. (eds)

Michael C (1988) Epithermal gold mineralization at Konos area, Rhodope county, Xanthi. IGME (In Greek), p.1-23

Michael C (1993) Geology and Geochemistry of the epithermal gold deposit in Konos area. Xanthi. IGME. 1-75 (In Greek)

Michael C (1995) Conceptual model of Konos epithermal system. Geol. Soc. Greece, sp. Publ. 4/2

Michael C (2005) Mineralogical and Geochemical characteristics of Sappes epithermal system in western Thrace (Northern Greece). Comptes rendus de I'Academie Bulgare des Sciences, vol. 58, N6. Geologie, cites metalliferes

Michael C, Perdikatsis V, Dimou E, Marantos I (1995) Hydrothermal alteration and ore deposition in epithermal precious metal deposit of Agios Demetrios, Konos area, Northern Greece. Geol. Soc. Greece, sp. Publ., 4/2

# A regional scale 3D-model of the Skellefte mining district, northern Sweden

**Tobias E. Bauer, Saman Tavakoli, Pär Weihed**
*Division of Geosciences and Environmental Engineering, Luleå University of Technology, SE-971 87 Luleå, Sweden*

**Pietari Skyttä**
*Department of Geosciences and Geography, University of Helsinki, FI-00014 Helsinki, Finland*

**Tobias Hermansson, Rodney Allen**
*The Boliden Group, SE-936 81 Boliden, Sweden*

**Mahdieh Dehghannejad, María A. García Juanatey, Christopher Juhlin**
*Department of Earth Sciences, Uppsala University, SE-75236 Uppsala, Sweden*

**Abstract.** Three dimensional geological modelling was carried out in the Palaeoproterozoic Skellefte district in northern Sweden. Modelled volumes range from regional to semi-regional to deposit scale. A multidisciplinary approach combined both geological studies, such as structural and facies analysis and geochronology with geophysical techniques, such as reflection seismic, magnetotelluric, electrical, potential field, and petrophysical studies. Resulting data was interpreted and visualised as 3D-surfaces and bodies in gOcad. Additionally, modelling uncertainties showing the origin and handling of data were assigned and presented as a colour-coded model. The resulting model reveals a framework of major high-strain zones, key lithological contacts and the setting of deformed VMS deposits in the Skellefte district. The 3D-model of the Skellefte district can act as a background for exploration activities in the region.

**Keywords:** 3D-modelling, VMS deposit, Skellefte district, Palaeoproterozoic

## 1 Introduction

The Palaeoproterozoic Skellefte mining district is one of the most important mining districts in Europe hosting 79 volcanogenic massive sulphide (VMS) and several orogenic gold deposits and prospects (Allen et al. 1996; Kathol and Weihed 2005). Currently five active mines are producing Zn, Cu, Pb, As and Au. As most of the near-surface deposits have been discovered, ore deposits at greater depths need to be found. Therefore, 3D-geometry of geological structures and their evolution through time (4D-modelling) need to be constrained.

The project aimed at developing robust 3-dimensional models of the upper 4 km of the Earth's crust in the Skellefte District. Modelling incorporated both geological and geophysical investigations and was carried out in three different scales: deposit-, semi-regional-, and regional-scale (Fig. 1). Based on these data a 3-dimensional multi-scale model was constructed using the gOcad software platform (Paradigm) allowing to visualize geological features from the detailed deposit-scale models of 21 VMS deposits to a regional-scale structural model. The combination of geological and geophysical data reveals the crustal architecture of the Skellefte District and the structural setting of

associated mineral deposits. In addition to the 3D-model, a 4-dimensional model schematically illustrates the geological evolution of the Skellefte District (Skyttä 2012).

## 2 Regional geological framework

The bedrock of the Skellefte district comprises 1.95 – 1.86 Ga Palaeoproterozoic volcanic arc rocks and associated intrusive rocks (Allen et al. 1996; Kathol end Weihed 2005). The main unit is the c. 1.9 Ga Skellefte Group, comprising mainly felsic, meta-volcanic rocks. The VMS deposits are located in the uppermost part of Skellefte Group stratigraphy at the transition to the overlying Vargfors Group which is characterised by meta-sedimentary rocks (Fig. 1; Kathol and Weihed 2005). The dominant intrusive rocks are represented by calc-alkaline, multiple phase intrusions of the Jörn intrusive complex (1,89 – 1,86 Ga; Bejgarn et al. 2012 and references therein). The rocks were deformed and metamorphosed during the Svecokarelian Orogeny at 1.90 – 1.80 Ga (Weihed et al. 2002). Structures in the Skellefte district are characterised by a distinct pattern of WNW-ESE and NNE-SSW-striking faults. Allen et al (1996), Allen (2005 unpublished company report), Coller (2008 unpublished company report) and Bauer et al (2011) have showed that these faults have a syn-extensional origin and have been reactivated during subsequent compressional events.

## 3 Geological and geophysical in-data

Regional and semi-regional scale field mapping and associated structural analysis were tested and validated by 2D-forward modelling with MOVE by Midland Valley Exploration Ltd. (Bauer et al. 2011). Combined with sedimentary facies analysis by Bauer (2012) and structural analysis with geochronological studies by Skyttä et al. (2012) a structural conceptual model was developed. This conceptual model was tested and validated by observation of the sparse drill-cores. For the deposit scale models abundant near-mine drill core data, level plans and cross-sections were available (Boliden Mineral AB). For regional scale modelling,
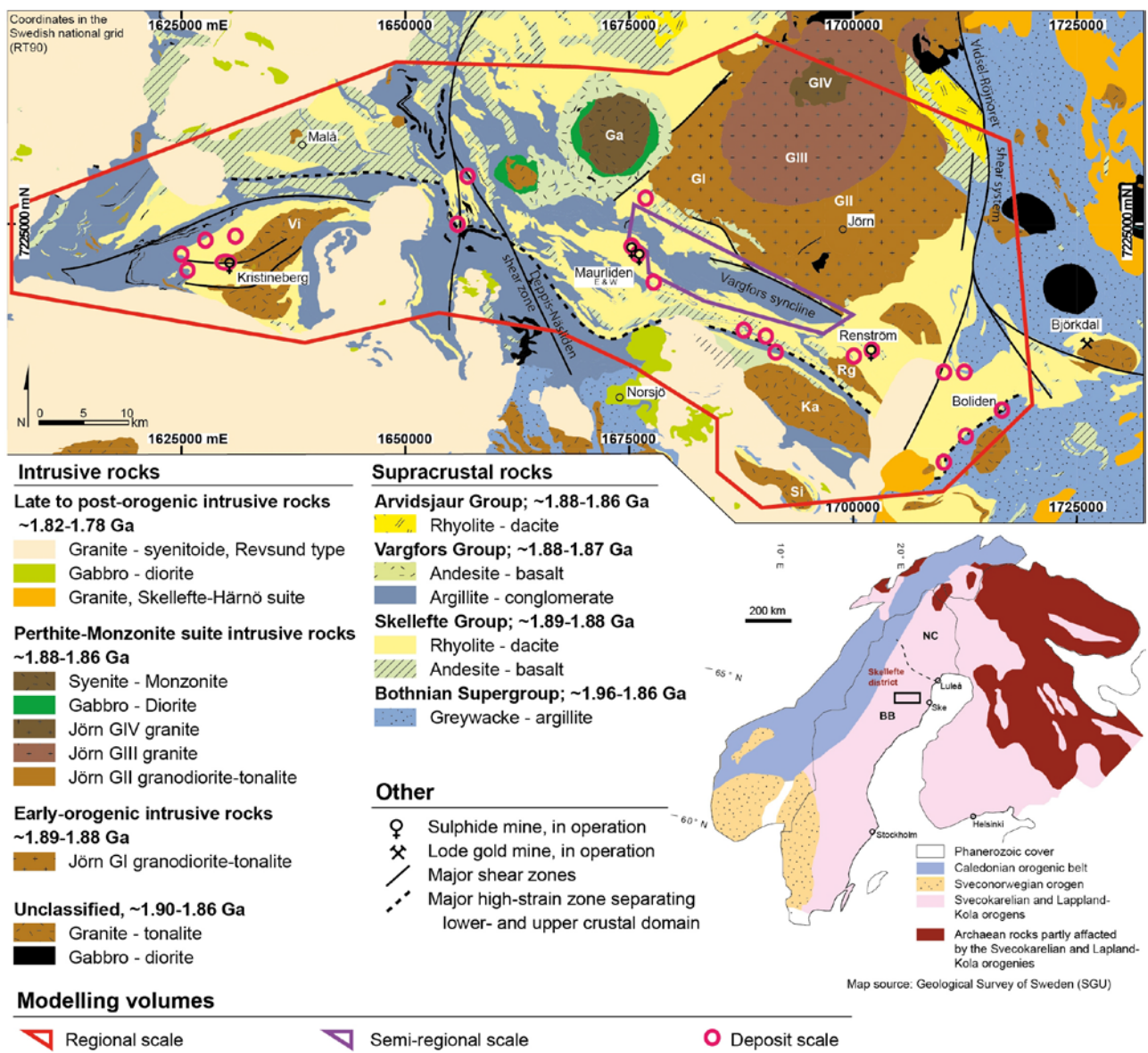
**Figure 1.** Inset map: Generalized Fennoscandian Shield geology. Geological domains: BB = Bothnian Basin; NC= Norrbotten Craton. The dashed line marks the boundary between the rocks with Archaean and Proterozoic Nd-signatures (Mellqvist et al., 1999). Geology drawn after Koistinen et al. (2001). Main map: Geological overview of the Skellefte district, as loosely defined by the occurrence of the Skellefte Group metavolcanic rocks, and their immediate vicinity. Intrusions: Vi = Viterliden, Ga = Gallejaur, Rg = Rengård, Ka = Karsträsk, Si = Sikträsk, GI, GII, GIII, GIV = Jörn type intrusions, phases I-IV. Geology after Kathol et al. (2005) and Bergman Weihed (2001).

142 km of seismic reflection lines along six profiles in the Kristineberg area, the central Skellefte district, and northwest of the district provided a framework for identifying major shear zones and lithological contacts (Malehmir et al. 2006, 2007, 2009a, 2009b; Dehghannejad et al. 2010, 2012a, 2012b; Ehsan et al. 2012). Additionally, 120 broadband magnetotelluric sites along six profiles and a 3D grid were recorded (Garcia Juanatey et al. 2012; Hübert et al. in review).

Geophysical semi-regional scale modelling in the central Skellefte district utilized electrical, potential field and petrophysical data (Tavakoli et al. 2012a, 2012b; Skyttä et al. 2012).

## 4  Modelling methodology

Several models were built at three different scales, whereas special emphasis was put at the regional scale model in this work. Three dimensional modelling was mainly carried out in gOcad (Paradigm) using the SPARSE plug-in (Mira Geoscience). To simplify modelling workflows, the regional scale modelling volume was split up into several semi-regional scale sub-projects. For each sub-projects available data was imported in form of maps and cross-sections into gOcad. Drill holes were visualised as lines with attached lithological information. Structural measurements were visualised as disks and lineation vectors with real 3D orientation. Furthermore, strike and dip values of

geological contacts were interpolated along the map traces of the corresponding contacts. Based on these results, structures and lithological contacts were modelled in three dimensions as surfaces (Fig. 2). VMS deposits were either available as 3D-models from the Boliden Group exploration department or modelled from digital and paper level plans and cross-sections.

## 5 Uncertainties

Modelling uncertainties were assigned for the final 3D-model of the Skellefte district in order to visualise the bases on which 3D-surfaces and bodies were constructed.

The resulting uncertainty model shows the distribution of primary data, interpolation of structural data, interpretation of geophysical data as well as areas without sufficient data. In order to visualise the modelling uncertainties, uncertainty values from 1 to 4 for the relevant regions on the 3D-objects have been assigned and colour-coded (Fig. 2). The assigned uncertainty values represent: 1) observed in field, mine or drill-core; 2) interpreted from geophysical data;

3) Interpreted from structural data or extrapolated from geophysical data, and 4) inferred / unknown.

## 6 Description of the model

The current 3D-model shows a series of parallel, regional-scale, south-dipping faults which are cross cut by a set of north-dipping ones (Fig. 2). In the central Skellefte district a set of sub-vertical faults approximately perpendicular to the previously named ones are presented. The geometry of the ore bodies, which are mainly adjacent to the faults, generally reflect the deformation features of the associated faults. The lower-strain domains between the major faults are characterized by either semi-regional scale syn- and anticlines with inclined or doubly-plunging fold axes, for example the Vargfors basin, or uniformly-dipping strata sub-parallel to the faults. In general, significantly more domains with gently-dipping bedding have been recognized which allows for enhanced stratigraphical correlations in the future. Several intrusive suits are represented by irregular bodies and coloured according to their age.
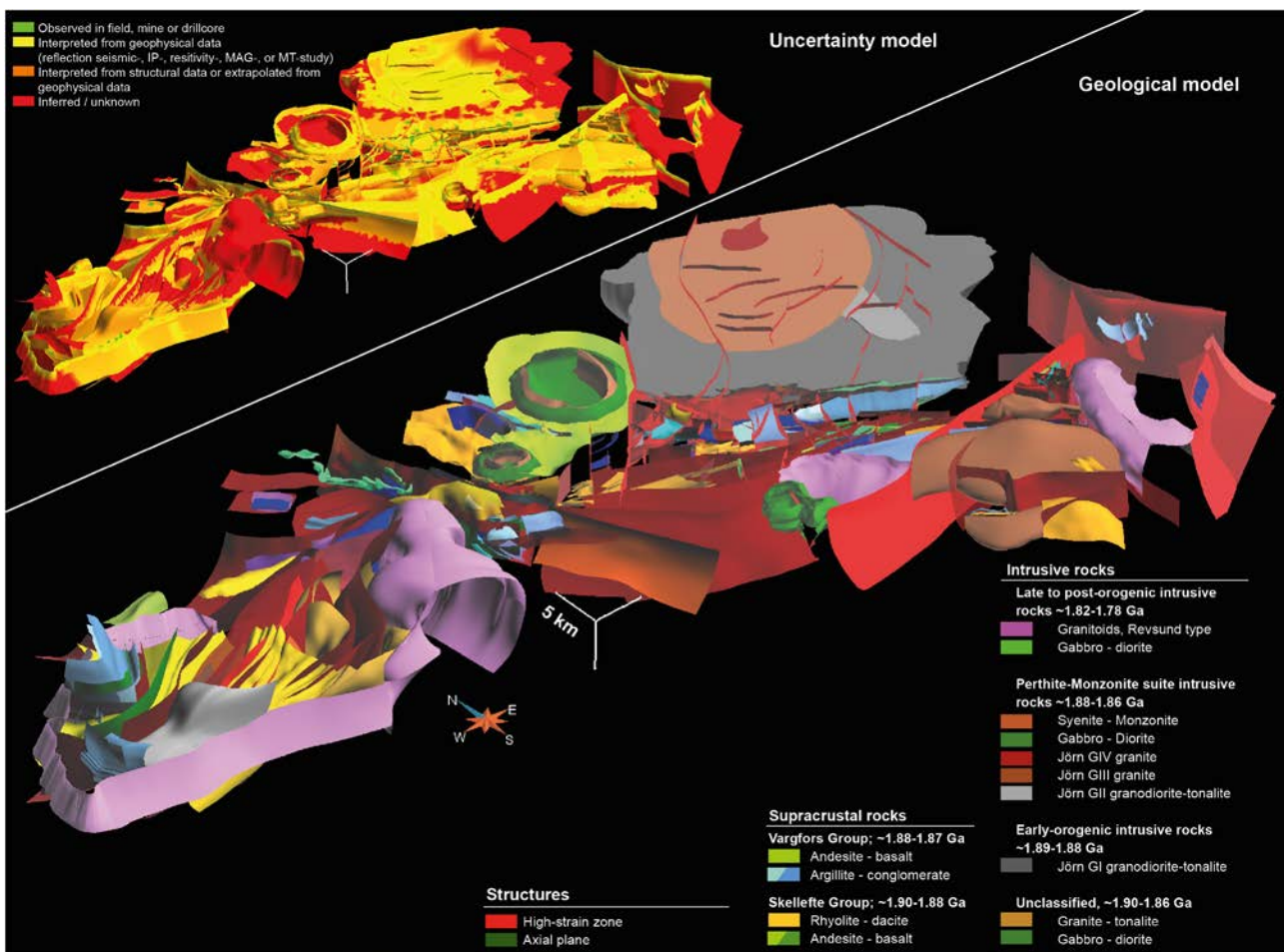


**Figure 2.** Screenshot from gOcad showing the regional scale, geological 3D-model and the uncertainty model of the ore-bearing Skellefte district.

## Acknowledgements

## References

Allen RL, Weihed P, Svenson S-Å (1996) Setting of Zn-Cu-Au-Ag massive sulphide deposits in the evolution and facies architecture of a 1.9 Ga marine volcanic arc, Skellefte district, Sweden. Economic Geology 91:1022

Bauer TE, Skyttä P, Allen RL, Weihed P (2011) Syn-extensional faulting controlling structural inversion – Insights from the Palaeoproterozoic Vargfors syncline, Skellefte mining district, Sweden. Precambrian Research 191:166-183

Bauer TE, Skyttä P, Allen RL, Weihed P (2012) Fault-controlled sedimentation in a progressively opening extensional basin: the Palaeoproterozoic Vargfors basin, Skellefte mining district, Sweden. International Journal of Earth Sciences, DOI 10.1007/s00531-012-0808-x

Bejgarn T, Söderlund U, Weihed P, Årebäck H, Ernst R (2012) Palaeoproterozoic porphyry Cu–Au, intrusion-hosted Au and ultramafic Cu–Ni deposits in the Fennoscandian Shield: Temporal constraints using U–Pb geochronology. Lithos, doi:10.1016/j.lithos.2012.06.015

Bergman S, Kübler L, Martinsson O (2001) Description of regional geological and geophysical maps of northern Norrbotten County (East of the Caledonian Orogen), vol. Ba 56. Sveriges geologiska undersökning, p. 110

Bergman S, Billström K, Persson P-O, Skiöld T, Evins P (2006) U-Pb age for repated Palaeoproterozoic metamorphism and deformation near the Pajala shear zone in the northern Fennoscandian shield. GFF 128: 7–20

Bergman Weihed J (2001) Palaeoproterozoic deformation zones in the Skellefte and the Arvidsjaur areas, northern Sweden. In: Weihed P (ed) Economic Geology Research 1. Sveriges Geologiska Undersökning C 833: 46–68

Dehghannejad M, Juhlin C, Malehmir A, Skyttä P, Weihed P (2010) Reflection seismic imaging of the upper crust in the Kristineberg mining area, northern Sweden. Journal of Applied Geophysics 71:125-136

Dehghannejad M, Malehmir A, Juhlin C, Skyttä P (2012a) 3D constraints and finite-difference modeling of massive sulfide deposits: The Kristineberg seismic lines revisited, northern Sweden. Accepted for publication in Geophysics

Dehghannejad M, Bauer TE, Malehmir A, Juhlin C, Weihed P (2012b) Crustal geometry of the central Skellefte district, northern Sweden – constraints from reflection seismic investigations. Tectonophysics 524–525:87-99

Ehsan SA, Malehmir A, Dehghannejad M (2012) Re-processing and interpretation of 2D seismic data from the Kristineberg mining area, northern Sweden. Journal of Applied Geophysics 80: 43-55

García Juanatey MA, Hübert J, Tryggvason A, Pedersen LB (2012) Imaging the Kristineberg mining area with two perpendicular magnetotelluric profiles in the Skellefte Ore Distric, northern Sweden. Accepted for publication in Geophysical prospecting

Hübert J, García Juanatey M A, Malehmir A, Tryggvason A, Pedersen LB (2012) Upper crustal resistivity structure of the Kristineberg area, Skellefte district, northern Sweden with 3D magnetotellurics. In review at Geophysical journal international

Kathol B, Weihed P (2005) Description of regional geological and geophysical maps of the Skellefte district and surrounding areas. Geological Survey of Sweden SGU, Uppsala

Kathol B, Weihed P, Antal Lundin I, Bark G, Bergman Weihed J, Bergström U, Billström K, Björk L, Claesson L, Daniels J, Eliasson T, Frumerie M, Kero L, Kumpulainen RA, Lundström H, Lundström I, Mellqvist C, Petersson J, Skiöld T, Sträng T, Stølen L-K, Söderman J, Triumf C-A, Wikström A, Wikström T, Årebäck H (2005) Regional geological and geophysical maps of the Skellefte District and surrounding areas. Bedrock map. Sveriges geologiska undersökning Ba 57:1

Koistinen T, Stephens MB, Bogatchev V, Nordgulen Ø, Wennerström M, Korhonen J (2001) Geological map of the Fennoscandian Shield, scale 1:2 000 000. Geological Surveys of Finland, Norway and Sweden and the North-West Department of Natural Resources of Russia

Malehmir A, Tryggvason A, Juhlin C, Rodriguez-Tablante J, Weihed P (2006) Seismic imaging and potential field modeling to delineate structures hosting VHMS deposits in the Skellefte Ore District, northern Sweden. Tectonophysics 426: 319−334

Malehmir A, Tryggvason A, Lickorish H, Weihed P (2007) Regional structural profiles in the western part of the Palaeoproterozoic Skellefte ore district, northern Sweden. Precambrian Research 159: 1−18

Malehmir A, Thunehed H, Tryggvason A (2009a) The Paleoproterozoic Kristineberg mining area, northern Sweden: Results from integrated 3D geophysical and geologic modeling, and implications for targeting ore deposits. Geophysics 74: B9−B22

Malehmir A, Schmelzbach C, Bongajum E, Bellefleur G, Juhlin C, Tryggvason A (2009b) 3D constraints on a possible deep >2.5 km massive sulphide mineralization from 2D crooked-line seismic reflection data in the Kristineberg mining area, northern Sweden. Tectonophysics 479: 223−240

Mellqvist C, Öhlander B, Skiöld T, Wikström A (1999) The Archaean-Proterozoic Palaeoboundary in the Luleå area, northern Sweden: Field and isotope geochemical evidence for a sharp terrane boundary. Precambrian Research 96:225-243

Skyttä P (2012) Crustal evolution of an ore district illustrated – 4D-animation from the Skellefte district, Sweden. Computers and Geosciences 48: 157-161

Skyttä P, Bauer TE, Tavakoli S, Hermansson T, Andersson J, Weihed P (2012) Pre-1.87 Ga development of crustal domains overprinted by 1.87 Ga transpression in the Palaeoproterozoic Skellefte district, Sweden. Precambrian Res 206–207:109-136

Tavakoli S, Elming S-Å, Thunehed H (2012a) 3D Modelling of the Central Skellefte district, Northern Sweden; an Integrated Model based on the electrical, potential field and petrophysical data. Journal of Applied Geophysics 82: 84-100

Tavakoli S, Bauer T, Elming S-Å, Thunehed H, Weihed P (2012b) Regional-scale geometry of the central Skellefte district, northern Sweden - results from potential field modelling along three previously acquired seismic profiles. Journal of Applied Geophysics 85: 43–58

Weihed P, Billström K, Persson P-O, Bergman Weihed J (2002) Relationship between 1. 90–1.85 Ga accretionary processes and 1. 82–1.80 Ga oblique subduction at the Karelian craton margin, Fennoscandian Shield. GFF 124:163-180

# 3D geochemical modelling of hydrothermal alteration related to 1.89 Ga VHMS-type deposits, Kristineberg area, Skellefte District, Sweden

Riia M. Chmielowski[1], Nils Jansson[2], Mac Fjellerad Persson[2], Pia Fagerström[2], Pär Weihed[1]
[1]Luleå University of Technology
[2]Boliden Mineral AB

**Abstract.** A 3D geochemical model of the Kristineberg area of the Skellefte District, Sweden, is currently under construction, utilizing data from more than 1600 regionally distributed whole-rock lithogeochemical samples. The model will improve our understanding of the formation the VHMS deposits in this area. The model is built by mapping geochemical variations in 3D, and using this as a basis for modelling hydrothermal alteration in the unsampled portions of the rock column. A better understanding of the geometry, intensity, vectors of transport, and zonation of the hydrothermal zones in 3D will aid deep exploration for massive sulphide deposits in the Kristineberg area, and may potentially lead to new discoveries.

**Keywords.** 3D geochemical model, Skellefte district, VHMS, hydrothermal alteration, mass balance, fluid flow

## 1 Introduction:

The Palaeoproterozoic Skellefte mining district, northern Sweden (Figure 1), is one of the most important mining regions in Europe, containing more than 85 pyritic Zn-Cu-Au-Ag massive sulphide deposits (Kathol and Weihed 2005). Despite a long history of mining, exploration, and research, it is only in recent years that the detailed, regional 3D structure of the district is starting to be understood. This understanding has come about due to the construction of advanced 3D geological models (produced under the banners of the VINNOVA project "4D modelling of the Skellefte District" and the PROMINE project) developed in collaboration between geologist and geophysicists from Boliden Mineral AB, Luleå University of Technology, and Uppsala University.

However, these models have focused on regional structure and tectonic evolution, while the geometry, size and distribution of the hydrothermal alteration zones associated with the mineral deposits have not yet been studied in 3D. The goal of this research project is to develop a 3D geochemical model for one the most important areas in the district; the Kristineberg area, which hosts the currently mined 26.5 Mt Kristineberg volcanic-hosted massive sulphide (VHMS) deposit (Fig. 1).

This study is the first to apply a 3D approach to the lithogeochemistry of a significant mining area in Sweden. Indeed, very little has been done worldwide in interpreting hydrothermal alteration systems in VHMS districts in 3D, primarily due to a lack of high quality geochemical whole-rock analyses obtained from sufficient drill holes to provide good regional cover.

The project is undertaken in collaboration between Luleå University of Technology and Boliden Mineral AB. It aims at better understanding the regional 3D geometry, size and zonation of the hydrothermal system, which envelopes metamorphosed and deformed VHMS deposits. It furthermore aims at understanding the chemical changes involved in hydrothermal alteration, the intensities thereof, the path and flow directions of mineralizing hydrothermal fluids, and the mass changes in whole rock composition resulting from hydrothermal alteration. The project carries on from previous two dimensional (surface maps, cross-sections) studies, which addressed the chemical changes in the rock units caused by the hydrothermal alteration related to mineralization in the Kristineberg area (e.g. Barrett et al. 2005; Schlatter 2007; Bachmann 2010).

In addition to improving our understanding of ore formation in the Skellefte district, the model will directly assist exploration in the Kristineberg area. The methodology and approach can furthermore be applied to other mature mining districts around the world.

## 2 Geological background

The Kristineberg area covers around 120 km$^2$ (Figure 1). The main unit outcropping in this region is the Skellefte Group, a thick sequence of Proterozoic (1.9 Ga) greenschist to amphiboilite facies felsic- to intermediate submarine metavolcanic rocks (Figure 1). These are overlain by the dominantly metasedimentary Vargfors Group, which contains metamorphosed, fine-grained turbiditic sedimentary rocks, graphitic phyllites, conglomerates and mafic-intermediate volcanics (Weihed 2010). These units are interpreted to have formed via accretionary processes in a volcanic arc setting. Massive sulphide deposits occur both within the Skellefte Group and close to the contact with the Vargfors group (Fig. 1)

All of the samples analysed for this project come from low-medium grade metamorphosed volcanic and volcano-sedimentary units within the Skellefte Group; these samples have also undergone variable degrees of hydrothermal alteration related to mineralization.
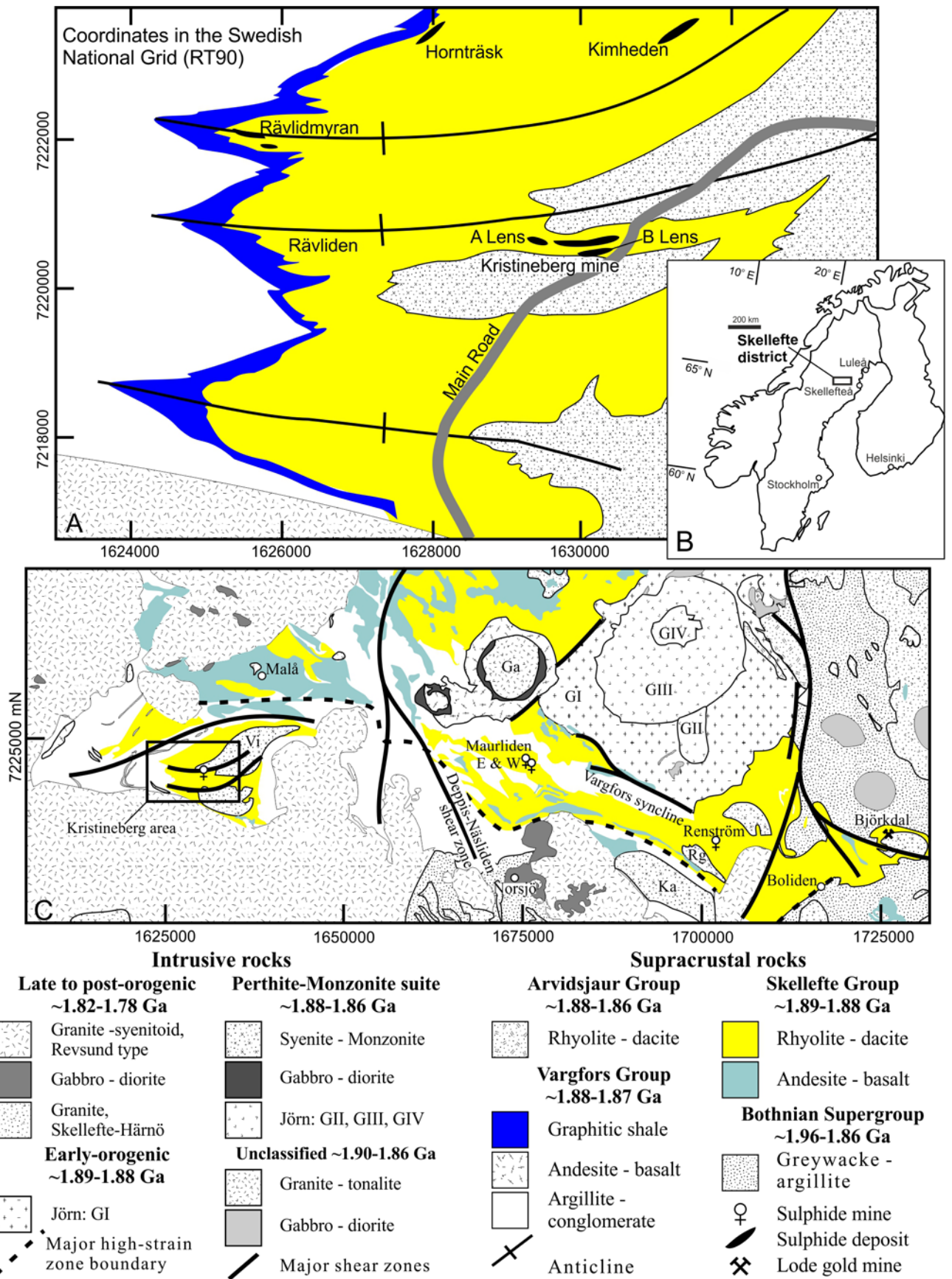
**Figure 1. A:** General geology of the Kristineberg area, Skellefte district, Sweden (modified after Barrett et al, 2005). **B:** Location of the Skellefte District within Scandinavia. **C:** General geology of the Skellefte district. Intrusions: Vi = Viterliden, Ga = Gallejaur, Rg = Rengård, Ka = Karsträsk, GI, GII, GIII, GIV = Jörn type intrusions, phases I-IV. Geology after Kathol et al. (2005) and Bergman Weihed (2001).

## 3 Processing lithogeochemical data

The Kristineberg area has been chosen, in part, based on the availability of a pre-existing data set (containing 1569 lithogeochemical analyses from 82 drill holes) and numerous additional drill holes in the area from which to select additional samples. As of January 2013 an additional 167 new lithogeochemical samples have been collected and analysed from 10 drill holes in the Kristineberg area specifically for this project and additional sampling is in progress.

Lithogeochemical analysis has been conducted in several labs, but primarily by ACME in Vancouver, Canada, using fusion ICP-AES for major and certain trace elements, fusion ICP-MS for REE and other trace elements, and an aqua regia digestion for the metals.

In addition to the whole-rock lithogeochemical analysis, over 100 representative samples have also been chosen for petrographic analysis in thin section. Most samples exhibit intense alteration; the most common alteration minerals include sericite, chlorite, pyrite, and potassium feldspar, all of which are accompanied by Na-depletion (Figure 2).

The samples are grouped using ratios of immobile element ratios to help differentiate between different pre-alteration rock types (MacLean and Barrett 1993). Once the protoliths have been determined it is possible to identify the "least altered" examples of each group. Despite the pervasive intense hydrothermal overprint in this region there are sufficient "least altered" samples available to provide the requisite baseline for mass balance calculations (MacLean 1990). It is these mass balance calculations which provide the framework for the model.
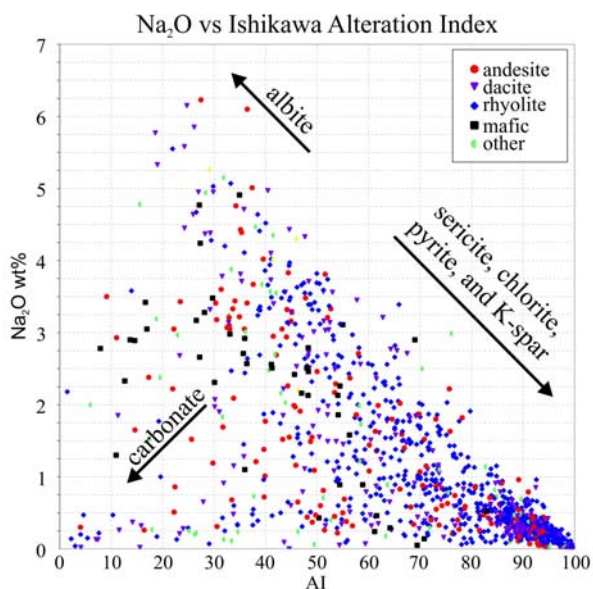
## 4 Preliminary results: Building a 3D model

The 3D model is developed using the LeapfrogGeo modelling software, which permits a 3D display of geochemical data using polyharmonic Radial Basis Functions (Carr et al. 2001) to create smooth surfaces from scattered data points, such as isolated samples collected from drill holes. As a result of this technique, the program also facilitates the interpolation of likely concentrations of elements between the existing data points, which is necessary for building a 3D model.

The geochemical data will be bounded and constrained using the 3D structural model generated for this region (Bauer et al. 2011; Skyttä 2012), in order to ensure that the interpreted geometries of the alteration zones are plausible. In addition results from the petrographic analysis of selected thin sections will permit linking the 3D geochemical model to specific alteration mineral assemblage zones.

The first step in building the model involves simple viewing of the geochemical data in 3D. Figure 3 shows the locations of the sample analyses with colours indicating the rock type, and the size of the spot is determined by the Alteration Index (Ishikawa et al. 1976). This region is heavily altered, and more than 90% of the samples have an AI greater than 40. However, Figure 3 clearly shows that the most intense alteration is concentrated along certain drill holes, which are located near the mine itself. The few isolated samples on the centre left of the figure which also display high AI values (94 to 96) are indicative of a region which should be targeted for additional sample acquisition in order to build a more accurate model.
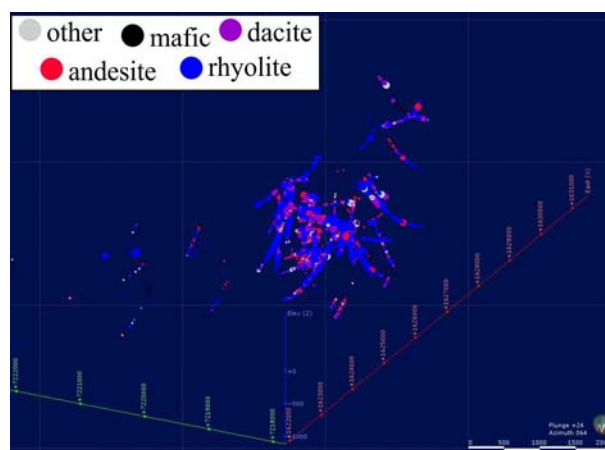


**Figure 3.** 3D view from LeapfrogGeo. The size of the sample spots is based on the Ishikawa Alteration Index, not the size of the sample itself. There are 10 size ranges, each containing 10% of the samples. The upper limit of the AI for each range is (rounded to): 40.5, 54.2, 69.0, 81.0,89.1, 92.2, 94.0, 95.4, 96.4, 100.0

The second step in building the model is to interpolate likely values between known data points. Figure 4 shows a rough interpolation based on AI values (Ishikawa et al. 1976). Further model development will result in smoother models which are based upon a variety of possible indices for alteration and which show vectors to mass gains and losses of various elements.



**Figure 2.** Comparison of the Alteration Index (Ishikawa et al. 1976) with the $Na_2O$ content of the samples. AI = [100 ($K_2O$ + MgO)]/($K_2O$ + MgO + $Na_2O$ + CaO) Note that, in general, the more intense the alteration the more depleted the sample is in $Na_2O$.
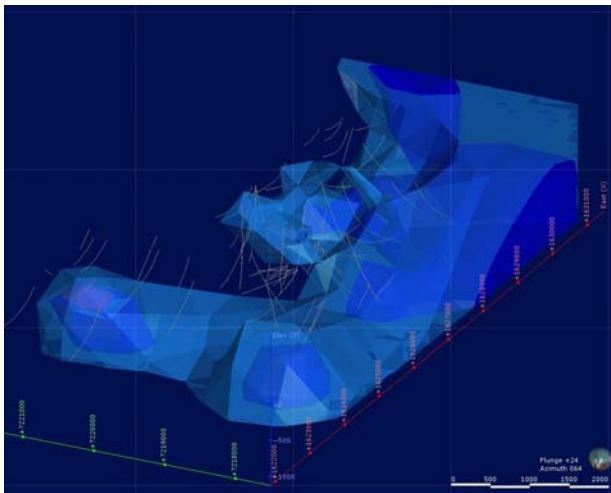
**Figure 4.** 3D view from LeapfrogGeo showing shells of the regions with interpolated similar AI values. Shown are the shells with upper limits (rounded to): 89.1, 92.2, 94.0, 95.4, 96.4, and 100.

## Conclusions

One of the main advantages for constructing 3D volumes instead of 2D cross sections is the ability to define volume gains and losses to the full hydrothermal systems. When conducted in 3D, mass-balancing may be used to constrain key features pertinent to ore genetic models, such as net gains or losses of elements within the entire hydrothermal system as well as the source of metals in the deposits. A better understanding of mass changes and better differentiation between the different types of intensely altered samples is furthermore necessary for vectoring towards mineralization in the Kristineberg area, where intensely altered rocks are found several 100 m away from the deposits.

## Acknowledgements

## References

Bachmann K (2010) Chemostratigraphy and alteration in the area of the Kristineberg VHMS deposit, Skellefte district, Sweden. Technicshe Universität Bergakademie Freiberg,

Barrett TJ, MacLean WH, Årebäck H (2005) The Palaeoproterozoic Kristineberg VMS deposit, Skellefte district, northern Sweden. Part II: Chemostratigraphy and alteration. Mineralium Deposita 40 (4):368-395

Bauer TE, Skyttä P, Allen RL, Weihed P (2011) Syn-extensional faulting controlling structural inversion – Insights from the Palaeoproterozoic Vargfors syncline, Skellefte mining district, Sweden. Precambrian Research 191:166-183

Bergman Weihed J (2001) Palaeoproterozoic deformation zones in the Skellefte and the Arvidsjaur areas, northern Sweden. In: Weihed P (ed) Weihed P (ed) Economic Geology Research 1. Sveriges Geologiska Undersökning C 833. pp 46-68

Carr JC, Beatson RK, Cherrie JB, Mitchell TJ, Fright WR, McCallum JE, Evans TR Reconstruction and Representation of 3D Objects with Radial Basis Functions. In: SIGGRAPH Computer Graphics Proceedings, 2001.

Ishikawa Y, Sawaguchi T, Iwaya S, Horiuchi M (1976) Delineation of prospecting targets for Kuroko deposits based on modes of volcanism of underlying dacite and alteration halos. Mining Geology 26:105-117

Kathol B, Weihed P (2005) Description of regional geological and geophysical maps of the Skellefte District and surrounding areas. Geological Survey of Sweden,

Kathol B, Weihed P, Antal Lundin I, Bark G, Bergman W, J., Bergström U, Billström K, Björk L, Claesson L, Daniels J, Eliasson T, Frumerie M, Kero L, Kumpulainen RA, Lundström H, Lundström I, Mellqvist C, Petersson J, Skiöld T, Sträng T, Stølen L-K, Söderman J, Triumf C-A, Wikström A, Wikström T, Årebäck H (2005) Regional geological and geophysical maps of the Skellefte District and surrounding areas. Sveriges geologiska undersökning Ba 57:1.

MacLean W, Barrett T (1993) Lithogeochemical techniques using immobile elements. Journal of Geochemical Exploration 48:109-133

MacLean WH (1990) Mass change calculations in altered rock series. Mineralium Deposita 25 (1):44-49

Schlatter DM (2007) Volcanic Stratigraphy and Hydrothermal Alteration of the Petiknäs South Zn-Pb-Cu-Au-Ag Volcanic-hosted Massive Sulfide Deposit, Sweden. Luleå University of Technology, Luleå

Skyttä P (2012) Crustal evolution of an ore district illustrated – 4D-animation from the Skellefte district, Sweden. Computers &amp; Geosciences 48 (0):157-161. doi:10.1016/j.cageo.2012.05.029

Weihed P (2010) Palaeoproterozoic mineralized volcanic arc systems and tectonic evolution of the Fennoscandian shield: Skellefte District Sweden. GFF 132 (1):83-91

# 3D modelling of epithermal Au-Ag mineralisation at Golden Cross, Hauraki Goldfield, New Zealand

**A.B. Christie**
*GNS Science, P O Box 30-368, Lower Hutt. t.christie@gns.cri.nz*

**R. Carver**
*GCXplore Pty Ltd, 67 Chelmsford Road, Mt Lawley, WA 6050, Australia. richard.carver@gcxplore.com*

**Abstract.** Legacy geological and geochemical data have been compiled to enable 3D modelling of the epithermal mineralisation at the former Golden Cross Au-Ag mine in the Hauraki Goldfield and Coromandel Volcanic Zone, New Zealand. Preliminary analyses of drill hole assay data shows that Au (n = 74,115) and Ag (n = 74,566) exhibit good correlation (r = 0.70). The Au/Ag ratio has a mean of 0.25. As (n = 9797) and Sb (n = 9649) have a good correlation (r = 0.69), but are poorly correlated with Au and Ag. Cu (n=2873), Pb (n=2866) and Zn (n=2869) are present in low concentrations. Au and Ag concentrations and Au:Ag ratios peak in a depth range of RL 125-200 defining a main Au-Ag depth zone. As and Sb concentrations peak above and below this main Au-Ag depth zone

**Keywords.** Golden Cross, epithermal, gold, silver, 3D, database, geological modelling

## 1 Introduction

Golden Cross is a volcanic-hosted epithermal gold-silver quartz vein deposit located in the southern part of the Hauraki Goldfield and Coromandel Volcanic Zone, about 8 km northwest of the world-class Martha Au-Ag deposit in Waihi. Golden Cross was mined in two periods; between 1895 and 1920, and between 1991 and 1998, with a total production of approximately 23,504 kg of Au and 73,134 kg of Ag (Christie et al. 2007).

Exploration from the late 1970s is documented in reports submitted to the Government agency New Zealand Petroleum & Minerals (NZP&M). The only digital data amongst these submissions were drill hole data for approximately 507 holes drilled from surface, another 139 holes drilled from surface in the open pit, 640 holes drilled from underground, and an additional 145 geotechnical holes. These data consist of collar location, down hole surveys, lithology codes and assays (McOnie 1999). All other exploration data were in only hard copy form at the commencement of our project. GNS Science has compiled much of the available hard copy data in digital form and constructed a 3D model to assist research on the deposit. This paper describes progress of our project, which to date includes development of a 3D geological block model and preliminary analysis of the assay data.

## 2 Geological setting

The Golden Cross veins occur in Miocene Coromandel Group andesite and dacite (Fig. 1). Early underground mining worked the northeast-striking Golden Cross No.

1 reef, whereas mining between 1991 and 1998 was on the Empire section, which lies along strike and to the north of the old workings (Mauk and Purvis 2006; Begbie et al. 2007). In the Empire section, an upper stockwork zone was mined from an open pit (Empire stockwork), and deeper veins (Empire vein zone) were mined underground (Fig. 1).
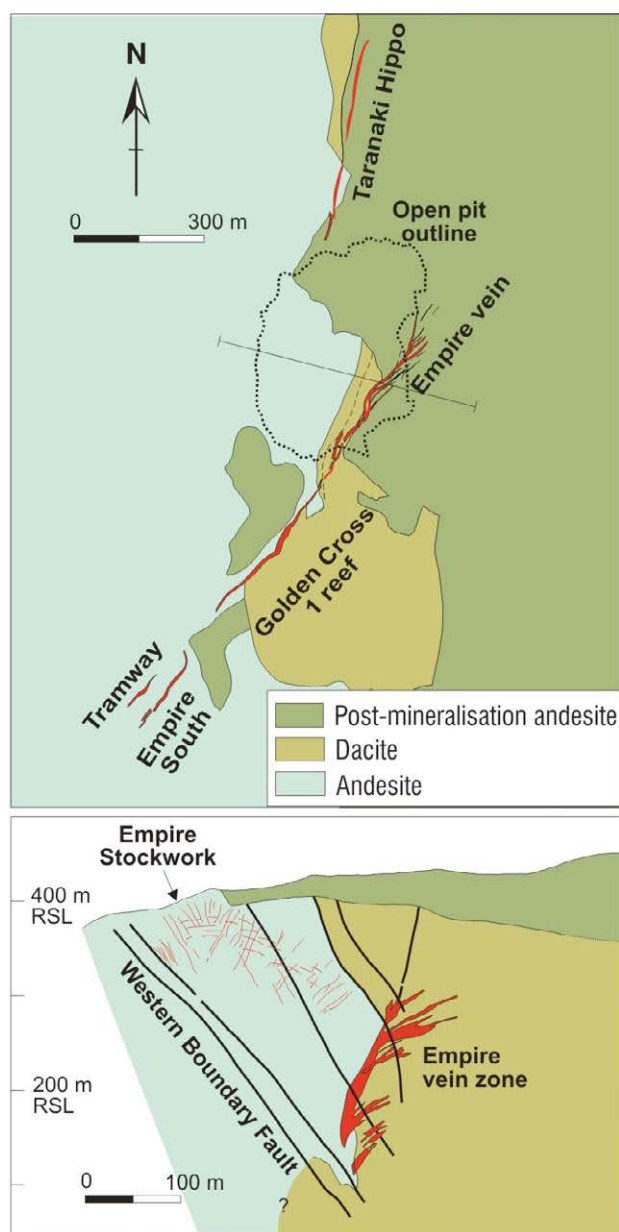


**Figure 1.** Geological map and cross section of Golden Cross (modified after Christie et al. 2007).

## 3 Assembly of the database and 3D model

The available digital drill hole data were loaded in a Leapfrog 3D database (Fig. 2). Additionally we scanned 10 hand drafted large scale level plans and 22 cross sections, and oriented these in the Leapfrog 3D database. Faults, geological units, and the trend of the Empire vein zone were digitised from each cross section. Surfaces for eight major faults, geological unit contacts, and the Empire vein zone were extrapolated between the sections using the level plans as additional guides. This enabled the development of a block geological model (Fig. 3; Christie et al. 2011).
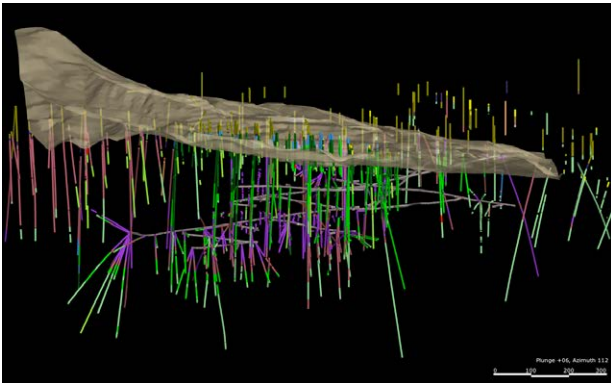


**Figure 2.** Perspective view of drill holes showing colour coded lithology, underground mine workings and topography with the completed open pit.
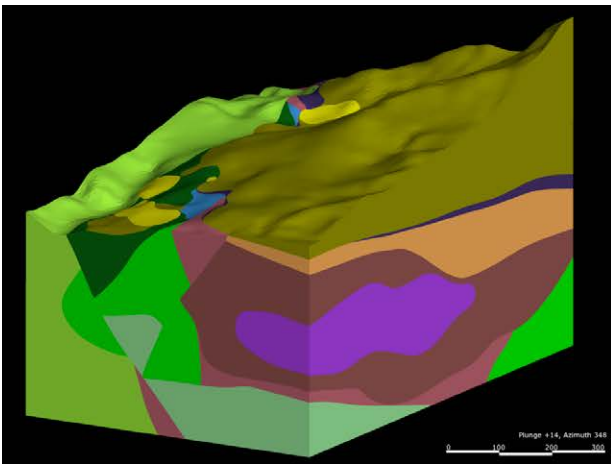


**Figure 3.** Perspective view of the 3D geological block model. See Christie et al. (2011) for legend, details of construction, a digital version and source digital data.

## 5 Drill hole assays

The total number of samples is large, with >74,000 analyses of Au and Ag, >9000 analyses of As and Sb, >2600 analyses of Cu, Pb and Zn, and between 130 and 750 analyses of Ba, Bi, Cd, Hg, Mo, Ni, Se and Tl. Some elements have a significant proportion of their analyses below their detection limits, e.g. approximately 25% of Au, Ag and Ni assays, 40% of Hg and Tl, 50% of Bi, Cd and Se and all Te analyses.

Histograms for Au and Ag exhibit bimodal distributions with low concentration populations probably resulting from variations in detection limits in different batches of assays (Fig. 4). For As and Sb, the histograms are not bimodal, but there is likely to be a second population in the low (background) side of the distribution (Fig. 4).
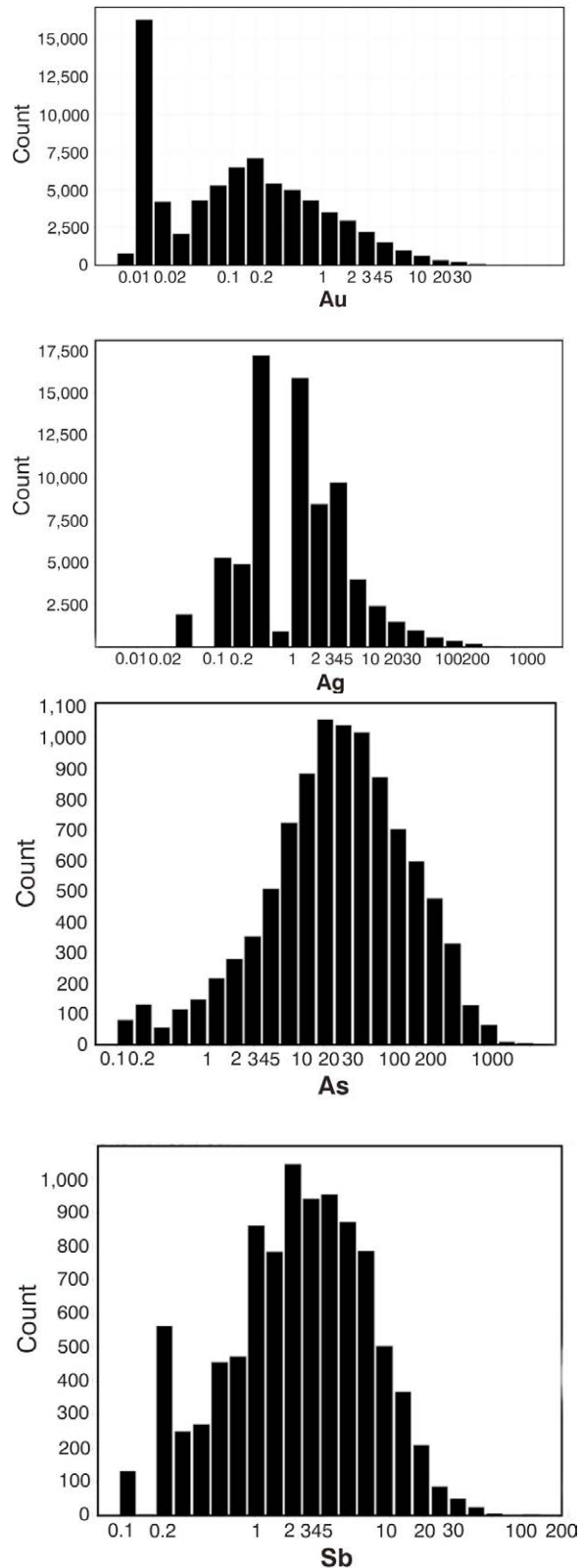


**Figure 4.** Histograms of Au, Ag, As and Sb analyses (ppm) for samples of drill core

Correlation coefficients between specific elements are listed in Table 1. There is good correlation between Au and Ag and between As and Sb, but much weaker correlations between Sb and Au or Ag, and even lower correlation between As and Au or Ag.

Table 1 Correlation between Au, Ag, As and Sb.

| Element a | Element b | Correlation coefficient |
|---|---|---|
| Au | Ag | 0.70 |
| As | Sb | 0.69 |
| Sb | Ag | 0.23 |
| Sb | Au | 0.14 |
| As | Ag | 0.11 |
| As | Au | 0.09 |

The histogram of Au/Ag ratios shown in Fig. 5 exhibits a single population with a mean of 0.25. Graphical analysis shows that at Au grades above 5 ppm there are two clusters; one with a Au/Ag ratio of about 0.2 and another smaller cluster with a Au/Ag ratio of about 1.
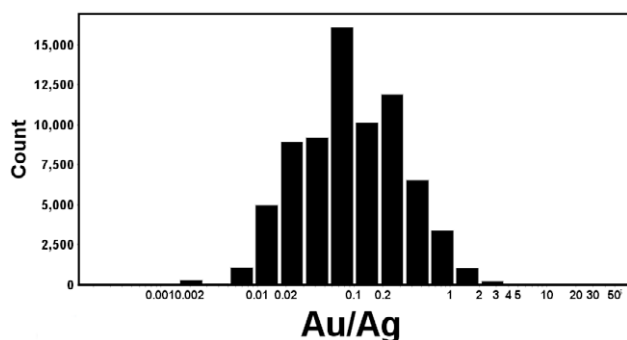


Figure 5. Histogram of Au/Ag ratios.

In terms of spatial distribution, a plot of Au concentration versus depth (Fig. 6) shows that there is a distinct peak in Au concentrations defining a main Au-Ag depth zone between RL 125 and RL 200, with high values extending to RL 250 (note that the current hilly ground surface is between approximately RL375 and RL425 and there has been at least 40 m of erosion since mineralisation; see Fig. 15 of Christie et al. 2007). This is also partly reflected by Ag concentrations (not shown). The Au:Ag ratio is highest in this zone, and generally follows the gold concentration (Fig. 6).
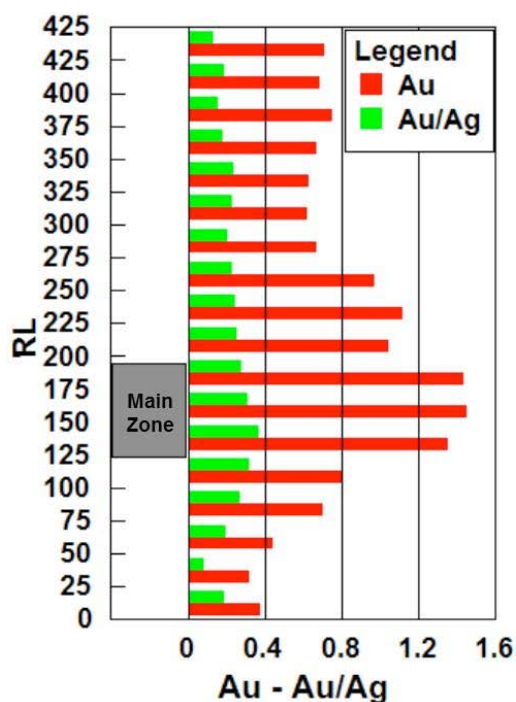


Figure 6. Variation of Au (ppm) and Au:Ag ratio (Au/Ag) with depth (RL) for values of >0.25 ppm Au. The values represent medians for each 25 m depth interval.

Similar depth analyses of As and Sb show that the concentrations of these elements peak above and below the main Au-Ag depth zone. Copper, Pb and Zn are in relatively low concentrations throughout the depth range, consistent with previous interpretations that Golden Cross represents a shallow epithermal system with a depth range c. 100-400 m below the paleo water table (see Fig. 15 of Christie et al. 2007).

# 6 Conclusions and future work

Work to date has focussed on developing the 3D geological model and a preliminary assessment of the assay data. This shows that:

- Au and Ag exhibit strong correlation, as would be expected in this epithermal style of mineralisation;
- Au and Ag concentrations and Au:Ag ratios peak in a depth range of RL 125 and 200 defining a main Au-Ag depth zone;
- As and Sb have a high correlation, but are poorly correlated with Au and Ag;
- As and Sb concentrations peak above and below the main Au-Ag depth zone; and
- Cu, Pb and Zn are present in low concentrations.

In addition to further analysis of the assay data, future work will also include compiling research data such as hydrothermal alteration mineralogy, fluid inclusion Th and salinity, and stable isotope data in the Leapfrog database for spatial analysis.

## Acknowledgements

## References

Begbie MJ, Spörli KB, Mauk JL (2007) Structural evolution of the Golden Cross epithermal Au-Ag deposit, New Zealand. Economic Geology 102: 873-892

Christie AB, Simpson MP, Brathwaite RL, Mauk JL, Simmons SF (2007) Epithermal Au-Ag and related deposits of the Hauraki Goldfield, Coromandel Volcanic Zone, New Zealand. Economic Geology 102: 785-816

Christie AB, Thomas J, McOnie A, Carver R (2011) 3D Modelling and geochemistry of epithermal Au-Ag mineralisation at Golden Cross based on legacy mining and exploration data, GNS Science Report 2011/06. 35 p

Mauk JL, Purvis A (2006) The Golden Cross epithermal Au-Ag deposit, Hauraki Goldfield. Australasian Institute of Mining and Metallurgy Monograph 25: 151-156

McOnie A (1999) Golden Cross mine: cross sections showing locations, skeletonised drill holes and summary drill logs 1-169, 201-257 – drill hole data included: Coeur Gold NZ Ltd. Ministry of Business, Employment and Innovation, Wellington, unpublished open-file mineral report MR3714

# A new storage approach for 3D Modeling

**Paul Gabriel, Jan Gietzel**
*GiGa infosystems GbR*

**Le Hai Ha, Prof. Helmut Schaeben**
*TU Bergakademie Freiberg*

**Abstract.** In a spatial data infrastructure an uncomplicated but secured access to the data is tremendous. A webportal can help to overcome the limitations that emerge from the use of highly sophisticated and platform dependent software packages. Latest internet technologies allow to port applications from the desktop to the web browsers. Using WebGL technology makes it possible to visualize 3D geomodels in real time and lets the user interact with the model. Combining this approach with a check in and check out system makes a distributed editing of the data possible.

Using "Geosciences in Space and Time" (GST) it is possible to check out the demanded region for edits. Thus several people can work simultaneously on the same model. By working on parts of the object the institutions are enabled to manage huge models like countrywide subsurface geology. Likewise 2D map services the seamless 3D models can be requested tile based in several spatial resolutions. Instead of using the common approach of a fixed tiling a large area GST stores a seamless model in a data base providing a history management.

**Keywords:** Data management, team work, presentation.

## 1 Introduction

When tremendous and excessive resource models are created more people and different teams become involved. This may also include the usages of different software for structural modelling, predictive modelling and ground water modelling to mention just a few applications.

The integration of different people demands the usage of a generic storage system (Görne 2003; Pouliot 2009).

Within the context of the EU Project ProMine the TU Bergakademie Freiberg has developed a data model and prototypical software which enables its users to profit from a centralized data store in 3D modelling. Since October 2011 the new founded company GiGa infosystems turned the prototype in a full-featured software.

The core benefits of the software alongside of the example of the modelling process of an ore deposit will be shown with the focus on how the software will support the modeller's daily work.

## 2 Geosciences in Space and Time – GST

Based on the long term discussion with geologists we found some specific problems which are addressed by almost all of them. Thus we started working on a data model which is capable of overcoming many issues that are faced by every days work.

Such issues are for example the handling of large datasets which occur either during creation of either wider areas on a country scale or models of reservoirs with a decent spatial resolution. Such models involve a group of modellers working at on different parts of the models at the same time. Mostly these modellers are based in different location. With the common file based approach a collaboration becomes very unhandy.

The involvement of several modellers usually brings up a heterogeneous software pool. Much time is therefore spent on conversion processes.

Using the approaches supplied by e.g. a database management system like multiuser access, multi version concurrency control (MVCC), high availability makes it possible to design a system, which can overcome the pitfalls of a file based storage approach. Additionally more features can support the modeller when handling high-resolution models and letting these models being accessed by others.

The software based on the data model of the ProMine project is called Geosciences in Space and Time or GST. It enables the user to combine geoscientific 3D modelling and store it in a centralized database independently from the modelling software. With its components GST aims towards a Spatial Data Infrastructure (SDI) for 3D Models. It also allows querying a model of an ore deposit e.g. for the areas with the highest degree of a certain mineralization. That is not the only reason why geological surveys in Europe are using GST.

Through the central data store many users can access the data simultaneously. This means that not just colleagues from one particular institution but also colleagues from other institutions can be involved in order to comment or even contribute to the models.

### 2.1 General Architecture

In order to keep the data within the companies and institutes that produce and work with them our software used a basic 3 tier architecture. The first layer stores all the data and manages the models. It can be either
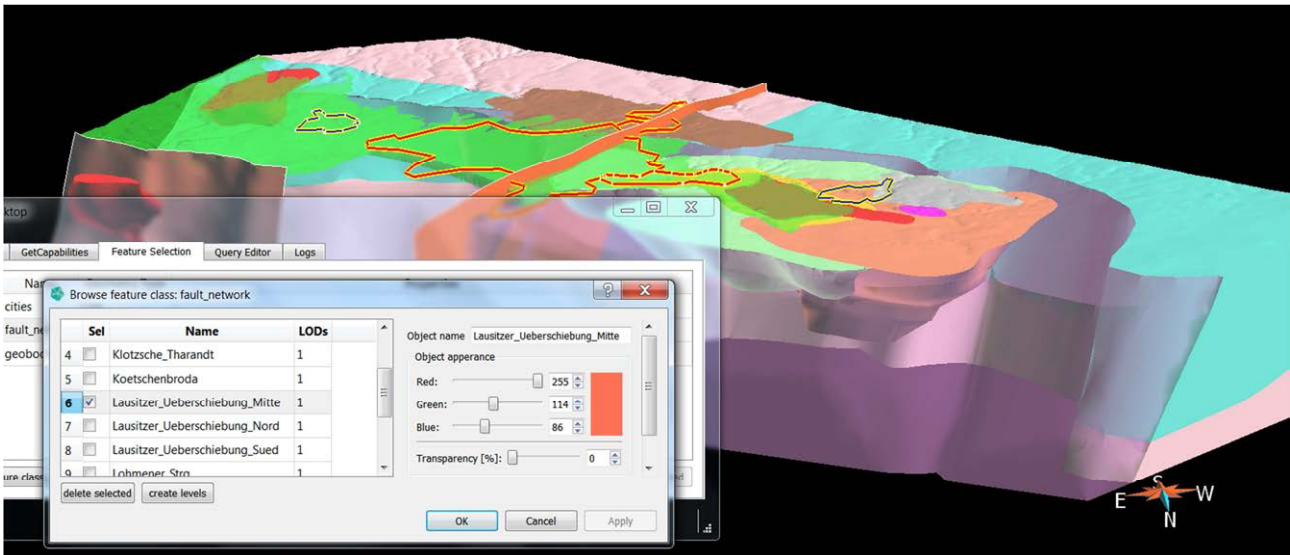
**Figure 1.** Direct integration of the GST Client in the 3D environment let's a team work on deposit models simultaneously.

accessed directly or via a web service. Thus it is secured that only people who are allowed are able to view data and edit data. This is done with second layer. The third layer is able to present the model or just parts of it to others. This presentation layer can be implemented either in a modelling environment such as gOcad, Petrel or Move or a simple web browser can be used to display the data.

## 2.2 Compatibility

Many of the ore deposits today do not stop at particular borders of countries. Thus the compatibility between several coordinate reference systems (CRS) has to be ensured by the modelling environment. Usually these steps are getting done manually and consume a lot of time which might be better used to understand the overall model. A central data stored keeps track of the used CRS and transforms the data on-the-fly into the needed systems.

Another time crucial process when working with several software is the compatibility amongst them. To get a complex geologic structural model into a groundwater simulation software might take days or even weeks. This process can be automated in such way that the underlying data is transformed in to a more generic approach and can be outputted in the right format on the users request.

## 2.3 Seamless Tiles

While modelling large areas or small areas with a high spatial resolution you might reach the physical boundaries of your workstation in terms of memory or graphic power. Sometimes you need to work with several modellers at the same time on different parts of the model.

Using the common approach of a file based storage

many of these things can achieved by splitting the work area in several parts and synchronising every steps manually.

Technologies like databases are capable of letting different users work on partial data at the same model but they lack the ability to handle 3D models coming from geology and they lack the ability to handle complex data structures which mainly occur within such 3D models.

Thus a GST combines the advantages of a database and overcomes the disadvantages that arise from a file based storage. The systems can check out areas or whole models, letting the users work in parallel. They can update the model and the system takes care, that the model keeps consistent. This makes the daily modelling process easier and faster.

## 2.4 History Management

In order to be able to track changes within a multi user environment version management systems like Subversion or Git have been developed. These systems store each change within a new version. Thus it is possible to revert changes to a specific version if they are not applicable or include errors.

Such approaches are useful for 3D modelling as well. So the users can see the changes of their models over the time and may also conclude new knowledge from the creation process of the model.
This includes a storage of the users and timestamps as well as the storage of the new version without duplicating the data in order to avoid redundancy.

## 2.5 Presentation

Another essential point when creating ore deposit models is the inclusion of third party opinions. Todays modelling software is hardly capable of providing an
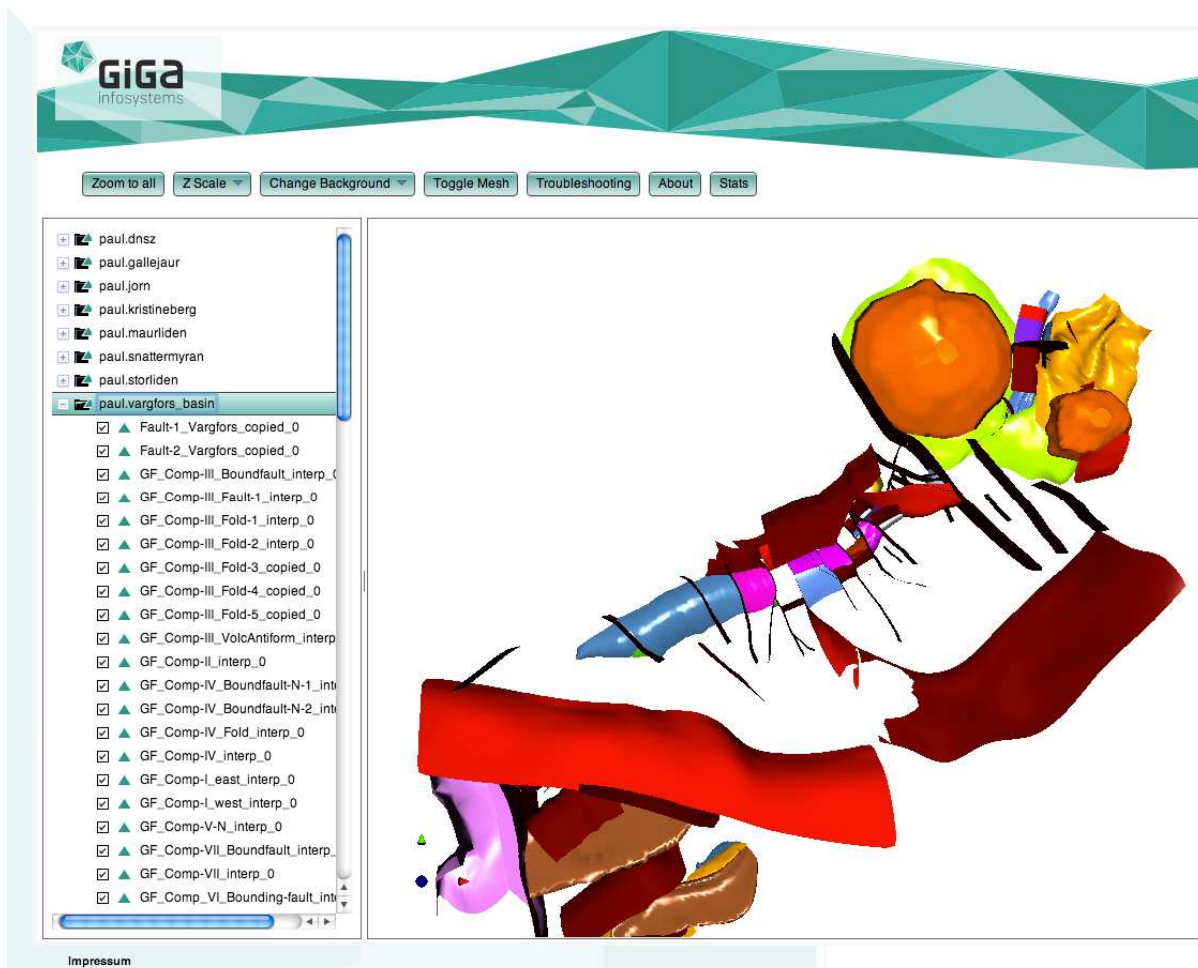
**Figure 2.** Display of parts (Vargfors basin, Gallejaur and Jorn) of the Skellefte district in web application (data courtesy of LTU Sweden).

easy to use and yet compatible presentation layer.

On the other hand new technologies like WebGL allow everyone with a modern web browser to see and use 3D models out of the box.

We have developed a new state of the art geomodel viewer which allows people who are not directly involved in a particular company or software to view the geological model at the current state. Thus they are able to take part in the reviewing process and contribute to the discussion.

## Acknowledgements

## References

Görne S, Krentz O, Horna F, Block C, Hübschmann M (2003) 3D-Modellierung mit Gocad auf dem Weg zur routinemäßigen Anwendung im LfUG. 57. Berg- und Hüttenmännischer Tag. http://www.umwelt.sachsen.de/umwelt/download/geologie/57BHT.pdf [Online, 2013.02.22]

Pouliot J, Badard T, Desgagné E, Bédard K, Thomas V (2009) Development of a Web Geological Feature Server (WGFS) for sharing and querying of 3D objects. Developments in 3d geo-information sciences

# 3D modelling for VMS exploration in the Pyhäsalmi district, Central Finland

**Marcello Imaña**
*Scandic Peruana Minerals, FIN-86800, Pyhäsalmi, Finland*

**Suvi Heinonen**
*Institute of Seismology, University of Helsinki, FIN-00014, Helsinki, Finland*

**Timo Mäki, Tuulia Häkkinen**
*Pyhäsalmi Mine Oy, FIN-86801, Pyhäsalmi, Finland*

**Jouni Luukas**
*Geological Survey of Finland, FI-70211, Kuopio, Finland*

**Abstract.** A multidisciplinary 3D modelling project carried out in the highly metamorphosed Pyhäsalmi base metal district in Central Finland has helped to characterize, predict and visualise the three dimensional continuation of sulphide rich volcanic units "ore horizons" in the immediate six kilometres of the Pyhäsalmi VMS deposit. The results show that exploration data such as borehole lithogeochemistry, surface mapping, and deep penetrating geophysical surveys can be combined efficiently using a three dimensional GIS platform in order to generate 3D models that facilitate the exploration of deeply buried massive sulphide orebodies. In the uppermost kilometre, 3D models are based on detailed geological information obtained from exploration drilling and surface mapping, whereas deeper portions of the models are based mostly on geophysical observations (reflection seismic and magnetotellurics). The models were tested by deep exploration boreholes, which confirmed that the steeply dipping altered stratigraphy in the area is confined to late vertical shear structures; and that several distinct ore horizons occur within a significant portion of the volcanic stratigraphy that remains intact and unexposed under sill shape synvolcanic intrusions.

**Keywords**: 3D modelling, reflection seismics, VMS exploration

## 1 Introduction

The 1.93 – 1.92 Ga metavolcanic rocks of the Vihanti - Pyhäsalmi district are located on the north east edge of the Svecofennian domain, within few kilometres of the boundary with the Archaean Karelian craton to the East. The area is known to contain two large Zn and Zn-Cu VMS deposits, few smaller mines and several unexploited base metal deposits and occurrences (Eilu et al. 2012). Currently, only the Pyhäsalmi Zn-Cu mine is active, with mining operations taken place up to a depth of 1450 meters below surface.

Traditionally, exploration in the Pyhäsalmi district has been constrained by the depth penetration of conventional geophysical techniques and was focused along major vertical faults associated with the Oulujärvi shear system. In 2007, a collaborative research project (HIRE, High Resolution Reflection Seismics for ore exploration, directed by the Geological Survey of Finland, started with the aim to understand the crustal configuration of the Vihanti – Mullikkoräme base metal district. Seismic reflectors were identified and interpreted to represent possible shear zones or continuations of the volcanic stratigraphy under thick layers of barren granitoids (Kukkonen et al. 2011, unpublished company report). The contrasting nature of the bimodal volcanic succession in the Pyhäsalmi arc (Lahtinen 1994; Weihed et al. 2005) has enabled comprehensive interpretation of seismic data. This, in addition to detailed borehole petrophysical information has allowed characterization of the geophysical response of key lithological contacts around the mine (Heinonen et al. 2012)

This project aims to produce 3D models of areas of economic interest to enhance exploration around the mines and predict areas of additional exploration potential in the district. The models are constrained by geochemical and geophysical data, and their geometry adapts to the structural evolution of the area.

## 2 District geology and semi-regional 3D model

The semi-regional model of the Pyhäsalmi zone covers an area of 20 km x 35 km in the vicinity of the Archaean - Proterozoic boundary in Central Finland. Structurally the area lies in the southwestern end of the Oulujärvi shear zone (Kärki et al. 1993). The main lithological units in the study area are 1.93 – 1.92 Ga bimodal metavolcanic rocks (Fig. 1) and related tonalitic subvolcanic intrusions which form domal fold structures. A major part of VMS style of mineralization in the district is situated in this sequence. A slightly younger intermediate to felsic volcanic rocks with minor calc silicate – dolomite interlayers (Vihanti group) are deposited on the top of Pyhäsalmi type rocks. Structurally these rocks are in the synformal basins inside the domal structures. During the later geological evolution voluminous Svecofennian intrusive rocks (1.89 – 1.87 Ga) were intruded into the volcanic sequences. The Pyhäsalmi orebody was tectonically transposed and overturned in the vicinity of reactivated faults related to the Oulujärvi shear system (Fig. 1)
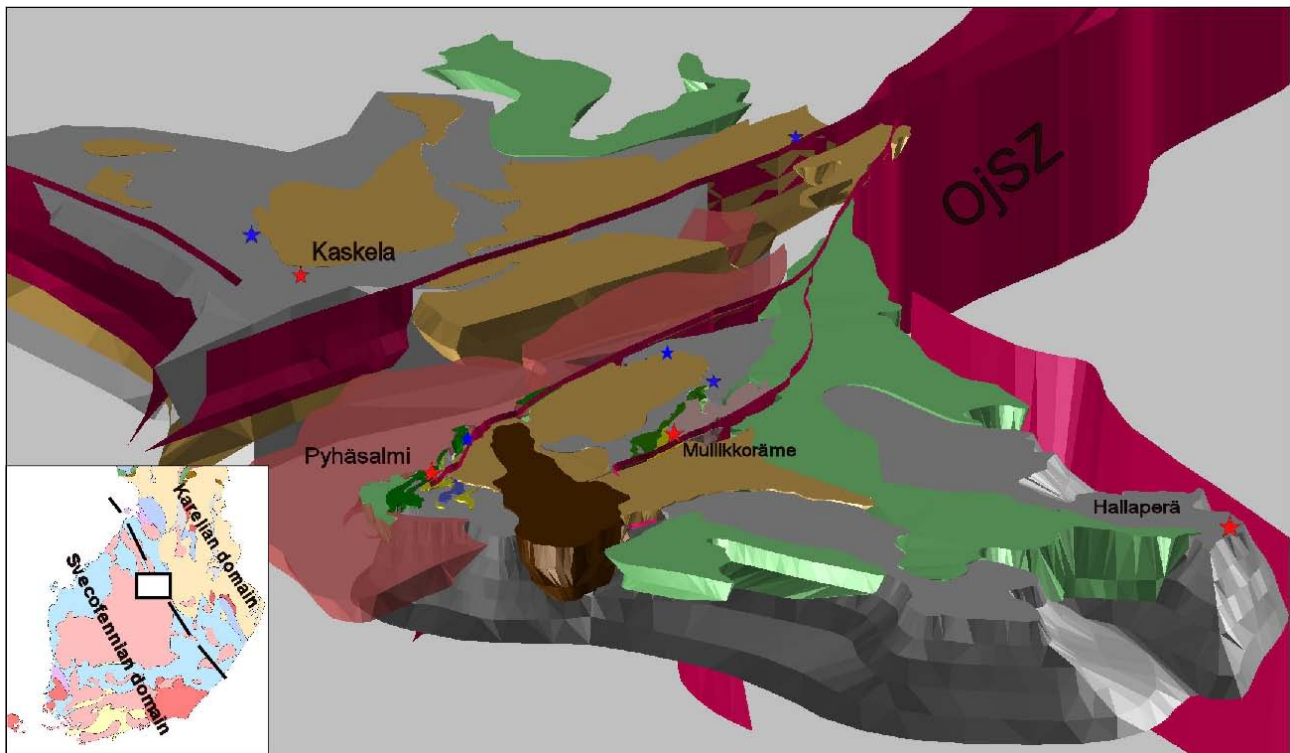
**Figure 1.** Semi-regional 3D model of the Pyhäsalmi-Mullikkoräme district. Massive sulphide deposits (red stars) and smaller base metal occurrences (blue stars) are spatially associated to subvertical shear zones of the Oulujärvi fault system. Vihanti Group (pale green), felsic subvolcanic intrusions (pale brown), felsic volcanic rocks (grey), predominantly mafic bimodal volcanic (dark green) and late granites and diorites in pink and brown respectively. Caption view looking toward North.

## 3 Methodology

The 3D models were based on the combined application of multidisciplinary techniques that include geophysics, lithogeochemistry and structural geology which were visualised in a three dimensional geological modelling software (gOcad).

### 3.1 Lithogeochemistry

Whole rock samples were obtained systematically from selected drillcore and analysed by mass spectrometry methods following fusion of the rock powder and dissolution of the bead in nitric acid. Immobile element techniques (Barrett and MacLean 1999) were applied to treat the data, to identify the volcanic protolith of altered rocks and establish the chemostratigraphic framework. 3D downhole plots of chemostratigraphic units were used for modelling of the main ore horizons and marker lithological contacts in the district.

### 3.2 Reflection seismics and Magnetotellurics

The Pyhäsalmi-Mullikkoräme reflection seismic survey consist of 14 interconnected profiles with a total length of 95 kilometers. The survey provided high resolution seismic images exceeding 5km depth. Seismic data was acquired using the network of existing roads resulting in crooked line geometry. The observed rock properties derived from drillhole logging show that massive

sulphide ore is a strong reflector in contact with any lithology typical for the area. However, the main cause of reflections in the area is a contact between mafic and felsic volcanic rocks.

Not only the physical rock properties but also the size and orientation of the geological structure influence its reflectivity. Multiphase deformation history of the Pyhäsalmi deposit is demonstrated in the seismic profiles as complex reflectivity patterns lacking continuous reflections. Seismic reflection data acquired from surface struggles to image subvertical structures typical for the shallow parts of alteration zones associated with shear structures. Typically, altered volcanic strata and faults are subvertical near surface and become gently dipping at depth. Gently dipping strata are visible in the seismic section and typically comprise shallowly dipping portions of bimodal volcanic sequences and sub-horizontal fold hinges (Fig. 2), while vertical fold flanks and shear zones are interpreted indirectly by recognizing abrupt truncations in the reflectivity characteristics. Major faults are interpreted from the non-reflective zones dividing the seismic profiles into areas with different reflection dips, while minor faults cause minor dislocation of the reflections.

In the Pyhäsalmi deposit, alteration zones with variable amounts of pyrite typically give low resistivities (600-800 $\Omega$-m), with massive sulphides in the range of 10-100 $\Omega$-m. (Hattula and Rekola 1997). In order to test the continuation of the ore horizons at depth, 79 kilometres of Titan-24 DC/IP and MT surveys distributed in 23 survey lines were used to delineate deep MT resistivity low targets associated to deep seismic

reflectors. Two dimensional inversions of the Titan data were compared to the seismic anomalies and several new exploration targets were delineated, one of them was tested and resulted in a discovery of a new ore horizon near the mine, the Arttu zone.
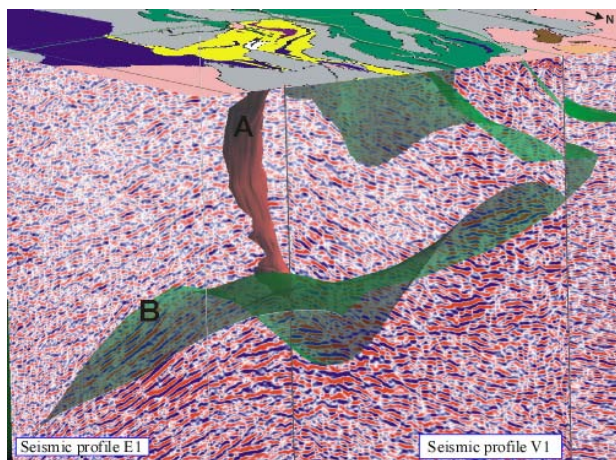


**Figure 2.** Reflective patterns associated with volcanic host rocks of the Pyhäsalmi VMS deposit. A) VMS deposit, B) contact surface between felsic volcanic rocks and highly reflective bimodal volcanic sequence.

## 3.3 Structural geology

Direct structural measurements (foliations, layering, folds and faults) were obtained from oriented drillcore using the EasyMark system and plot them in gOcad.

Figure 3 shows four important steps on the modelling process. Location of selected Rhyolite X volcanic protolith (Fig. 3a). Foliations measurements are treated by calculating average dip and dip directions from similar structures every 50-100 meters down the hole (Fig. 3b). Fold patterns were constructed using Sparse module for gOcad by Mira Geosciences (Fig. 3c). Finally, the ore horizon can be modelled to a continuous solid by combining geochemical information according to folding patterns (Fig. 3d).
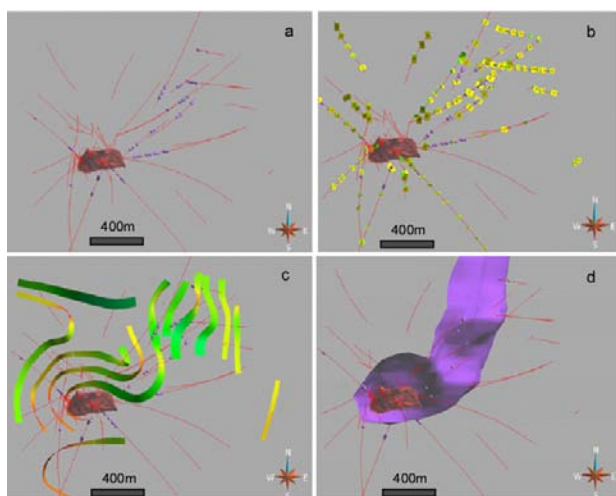


**Figure 3.** Steps for constructing a 3D model in Pyhäsalmi mine site. a) drillhole traces showing the intersection of Rhyolite X horizon, b) downhole plots of average foliation

markers, c) constructed fold patterns d) 3D model of the Rhyolite X unit (violet), folded around massive sulphide orebody (dark red).

## 4 Results

The initial results of the 3D modelling project were tested during ongoing near mine exploration activities conducted around the Pyhäsalmi and Mullikkoräme deposits (e.g. Le Vaillant 2010; Miettinen 2011). New data obtained from deep exploration drilling confirmed and validated our models allowing the prospective horizons to be extended and correlated into new deeper areas between the two VMS deposits (Fig. 4).

Contrary to the traditional assumption that all structures are near vertical in the district (Kousmanen et al. 1998), the new interpretation shows that a significant portion of the prospective volcanic stratigraphy have had little deformation and lies dipping gently under a series of subvolcanic units interpreted as sill complexes (Lahtinen 1994).

Three ore horizons have been characterized in terms of their volcanic protolith and magmatic affinities, style of mineralization and stratigraphic position. These horizons are associated to three different volcanic cycles: a) The main Pyhäsalmi horizon (Rhyolite B-transitional), b) The Arttu horizon (Rhyolite X-tholeiitic) and c) Calc-silicate bearing rhyolites of the Pellonpää Formation (Rhyolite D-calc-alkaline) which is similar to mineralized felsic volcanic rocks of the Vihanti area.

## Acknowledgements
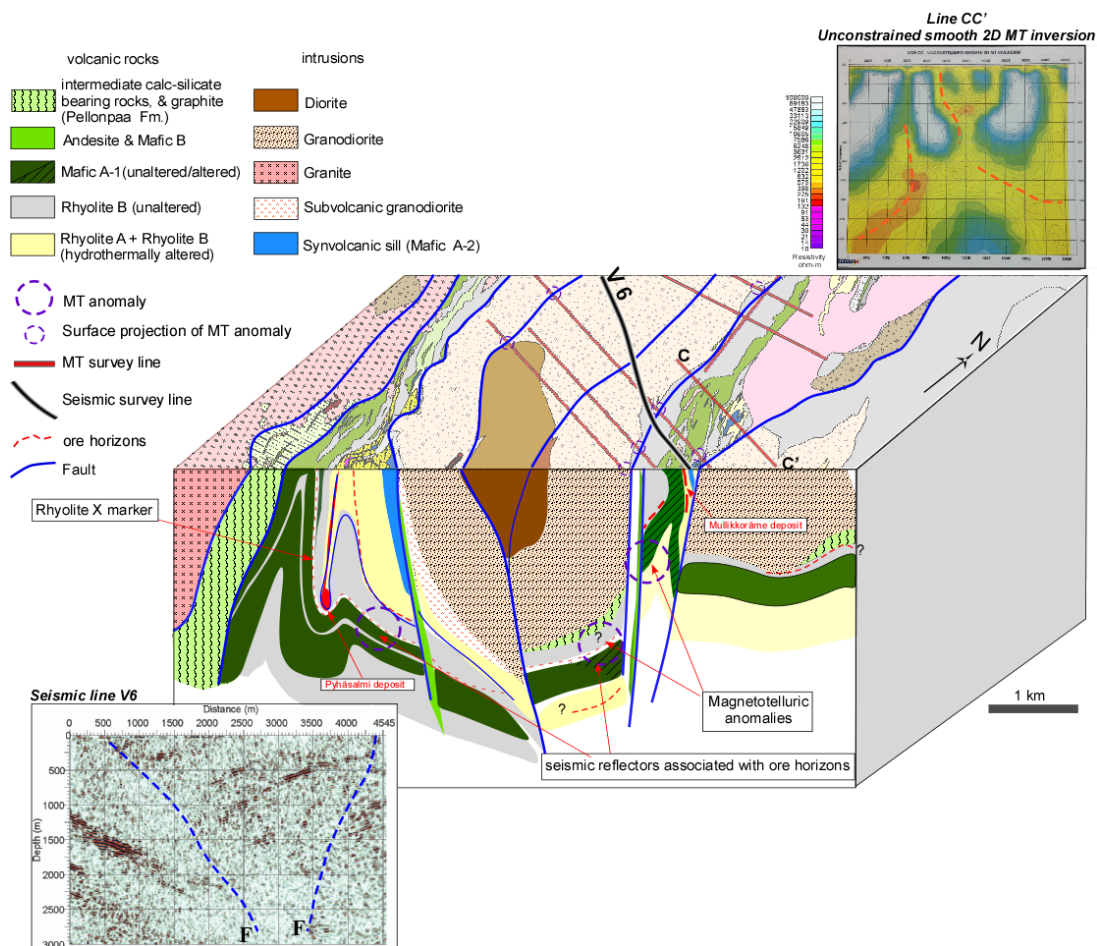
**Figure 4**. 3D geological interpretation representing the VMS exploration potential in the Pyhäsalmi district

# References

Barrett TJ, MacLean WH, (1999) Volcanic sequences, lithogeochemistry and hydrothermal alteration in some bimodal volcanic-associated massive sulphide systems: Reviews in Economic Geology 8:101 − 131

Eilu P, Ahtola T, Äikäs O, Halkoaho T, Heikura P, Hulkki H, Iljina M, Juopperi H, Karinen T, Kärkkäinen N, Konnunaho J, Kontinen A, Kontoniemi O, Korkiakoski E, Korsakova M, Kuivasaari T, Kyläkoski M, Makkonen H, Niiranen T, Nikander J, Nykänen V, Perdahl JA, Pohjolainen E, Räsänen J, Sorjonen-Ward P, Tiainen M, Tontti M, Torppa A, Västi K (2012) In: Eilu P (ed) Mineral deposits and Metallogeny of Fennoscandia, GSF special paper 53:207 − 352

Hattula A, Rekola T, (1997) The power and role of geophysics applied to regional and site-specific mineral exploration and mine grade control in Outokumpu Base Metals Oy. In: Gubins AG (ed) Proceedings of mineral exploration 97: Fourth Decennial International Conference on Mineral Exploration, p.617 − 630

Heinonen S, Imaña M, Snyder D, Kukkonen I, Heikkinen P (2012) Seismic reflection profiling of the Pyhäsalmi VMS deposit: A complementary approach to the deep base metal exploration in Finland. Geophysics 77: WC15 − WC23

Kärki A, Laajoki K, Luukas J (1993) Major Palaeoproterozoic shear zones of the central Fennoscandian Shield. Precambriam Research 64:207 − 223

Kousmanen V, Arkimaa H, Gaál G, Huhtala T, Koistinen E, Lindqvist E, Murtoniemi S, Nikander J, Ruskeeniemi K, Salonen V-P, Suppala I, Talvitie J, Tenhola M, Tiainen M, Ward P (1988) Exploration target selection by integration of geodata using statistical and image processing techniques: an example from Central Finland. In: Gaál G (ed) Report of Investigation 80. Geological Survey of Finland, p.157

Kukkonen I, Heikkinen P, Heinonen S, Laitinen J, Luukas J (2011) HIRE Seismic Reflection Survey in the Mullikkoräme Zn-Cu exploration area, Central Finland. Geological Survey of Finland, Report Q 31/2011.

Lahtinen R (1994) Crustal evolution of the Svecofennian and Karelian domains during 2.1 − 1.79 Ga, with special emphasis on the geochemistry and origin of 1.93 − 1.91 Ga gneissic tonalities and associated supracrustal rocks in the Rautalampi area, Central Finland. Geological Survey of Finland, Bulletin 378: 1 − 128

Le Vaillant M (2010) Geological-Geophysical 3D modelling of the Mullikkoräme VMS deposit, Finland. MSc. Theses, Luleå University of Technology, p. 65

Miettinen E (2011) Detailed geology of the level -1275, Pyhäsalmi mine, central Finland and genetic implications of rock inclusions within the ore. University of Helsinki

Weihed P, Arndt N, Billström C, Duchesne JC, Eilu P, Martinsson O, Papunen H, Lahtinen R (2005) Precambrian geodynamics and ore formation: the Fennoscandian Shield. Ore Geology Reviews: Vol. 27:273 − 322

# Integrated 3D interpretation of geological, geophysical and petrophysical data— A case study from a gabbro intrusion in Boden, Sweden

Jochen Kamm[1], Ildikó Antal Lundin[2], Mehrdad Bastani[2] & Martiya Sadeghi[2]
[1]Uppsala University, Dept. of Earth Sciences, Villavägen 16, SE-752 36 Uppsala, Sweden
[2]Geological Survey of Sweden, Box 670, SE-751 28 Uppsala, Sweden

**Abstract.** Gabbro intrusions may host Cu-Ni and PGE mineralization and modeling their geometry in 3D is crucial for planning mineral exploration. In this work we present the results of individual 3D inversions of gravity and magnetic field data collected over a gabbro intrusion in the Boden area, Sweden. The main aim is to integrate the geophysical model with the geological information to make a 3D geological model of the intrusion. During several field campaigns, rock samples for the determination of the density and the magnetic properties have been collected from outcrops within the study area. Individual 3D inversions of gravity and magnetic field data show that the final models become more realistic when the upper and lower bounds of the density contrast and susceptibility are set to the bounds dictated by the petrophysical data. The models of the intrusion also show fairly similar geometrical extents with high density and high susceptibility features and a maximum depth extent of ca. 4 km. The lateral extent fits reasonably well with the geological field observations.

**Keywords: Magnetic, gravity, inversion, 3D model, Boden**

## 1 Introduction

With the recent advancement in geophysical data acquisition systems and computing power, 3D modeling and interpretation of geophysical data has attracted a lot of attention and has played an important role in geological mapping and mineral exploration (Li and Oldenburg, 1996; Li and Oldenburg, 1998; Malehmir et al., 2009). Geophysical methods are cost-effective, non-invasive and can provide considerable coverage in a reasonably short amount of time. Different geophysical measurements can be utilized to determine the geometry and physical properties of targets of interest.

For larger surveys, usually structural interpretations are used that are based on for example Euler deconvolution (e.g., Thompson 1982). Although these methods give us information about the sources of the potential field, they do not provide information in terms of a 3D earth model of the physical properties. Therefore, making a full 3D inversion is an important step in quantitative interpretation - particularly at the deposit scale (Čuma et al. 2012). Gabbro intrusions may host Cu, Ni and PGE mineralization and usually have distinct geophysical signatures that give rise to well-isolated positive gravity anomalies because of their high density. They also have a high magnetic susceptibility and appear as strong magnetic anomalies. A combination of gravity and magnetic data may produce useful images of the shape and depth of the causative body.

The Geological Survey of Sweden (SGU) carries out geophysical measurements to obtain information about the physical properties of the bedrock. Measurements of the magnetic field, gamma radiation and electromagnetic fields are carried out regularly from aircraft. The data are collected with 200 m line separation, 16 - 40 m point distance and with a nominal altitude of 30 - 60 m. Gravity data is collected on the ground and SGU attempts to not exceed a distance of 1.5 km between the measuring points. SGU also collects bedrock samples since the 1960s for measurements of the petrophysical properties. Density, magnetic susceptibility and natural remanent magnetization are measured.

The Gunnarsträsk gabbro is clearly seen on the magnetic anomaly map (Figure 1B) as a round, high magnetic anomaly of about 4000 nT. Complementary gravity measurements were carried out during 2011 (Aaro, 2011) to achieve better resolution on the positive gravity anomaly caused by the gabbro. It is well defined (Figure 1A) and corresponds very well with the magnetic anomaly. The size of the gravity high is about 13 mGal.

Forward modeling of gabbro intrusions in northern Sweden was done earlier by Henkel (1981) and interpretive techniques were discussed by Ponce et al. (2003). In this study we present the results from 3D inversion of gravity and magnetic data collected over a 1.9 Ga gabbro, with the aim to understand its geometry in 3D. In SGU's database, there are 40 petrophysical samples from the Gunnarsträsk gabbro and 64 samples from the surrounding bedrock. Petrophysical analyses were done earlier by Arkko, 1986. Such data are used to constrain the inversion.

## 2 Geological setting of the study area

The study area is located in the northern part of Sweden, ca. 30 km Northwest from the town of Boden. The bedrock consists of the palaeoproterozoic rocks, including metasupracrustal and plutonic units. The majority of bedrock was formed in two distinct phases during the Svekokarelian Orogen, the first one during 2.44 - 1.96 Ga and the second one at 1.96-1.75 Ga (Sadeghi et al, in press).

The oldest bedrock in the area contains sedimentary quartzite and gneiss, which belong to the Råneå group. The volcanic rocks most commonly have compositions ranging from andesite to rhyolite (Perdahl, 1995) and were formed in a continental marginal arc setting during the Svekokarelian orogeny.

The intrusive rocks between Luleå and Jokkmokk and specifically in the Boden area were described by Mellqvist et al. (1999) and, during an ongoing bedrock

mapping at SGU, by Kathol et al. (2012), respectively. The bedrock consists mainly of Svecofennian plutonic rocks of ca. 1.91 - 1.87 Ga and 1.8 Ga. The early intrusive rocks are represented by the Haparanda Suite (aged between 1.91 – 1.87 Ga) ranging from gabbro to granodiorite, calc-alkaline. They are medium to coarse-grained and moderately to intensely deformed. There is another early intrusive rock of similar age, the so-called Perthite Monzonite Suite (Bergman et al., 2001). Generally, the suite consists of quartz monzonite granite, with an alkaline trend. The main magmatic event can probably be set at 1.97-1.88 Ga, with the emplacement of the composite monzonite-syenitic-granitic intrusions.

The younger intrusive rocks in the area consist of two type of granitoids, the so-called Lina and Edefors suites. The Lina suite is composed of granite and pegmatite. It is slightly prealuminous, with low Zr content and high Mg/Fe+Mg content. It has been produced by remobilization of continental crust with a small input of juvenile material (Mellqvist et al., 1999). On the other hand, the Edefors suite consists of gabbro, syenite and granite, with an alkali rich-trend, distinctly meta–aluminous, and high Zr content and lower Y, REE, Ta, Nb and Mg/Mg+Fe , and were produced by mixing mantle derived magma and continental material.
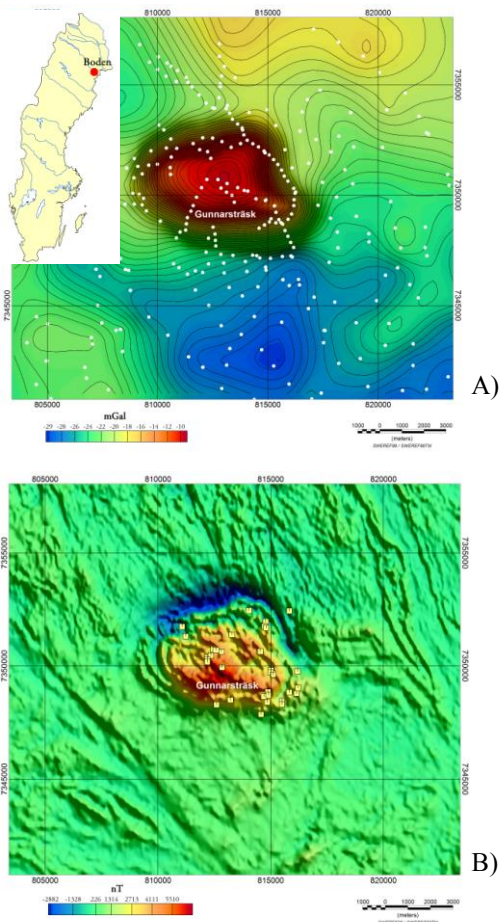


**Figure 1.** A) Bouguer gravity map. Measurement points in white. B) Magnetic anomaly map. The site location is on the left. Petrophysical sampling locations in yellow.

# 3  3D inversion

The 3D inverse modeling relies on a cell-based model parametrization. For the anomalies due to prism-shaped bodies, analytical expressions exist (Blakely, 1996). Since both gravity data and (approximately) magnetic data are linear in their respective physical parameters (i.e., density and susceptibility) anomalies of multiple cells can be superimposed to simulate measurements over any three-dimensional structure.

The inversion is accomplished by minimizing an objective functional via an iterative gradient descent technique (non-linear conjugate gradients, see for example Zhdanov, 2002). The functional is a combined measure of the data misfit and a regularization term. The latter is required because the inverse problem is ill-posed. This means that without it, we can find infinitely many gradient directions that decrease the data misfit, most of which leading to models that do not agree with geological intuition. This is because potential field data are (1) non-unique (infinitely many solutions can satisfy a data set) and (2) have extremely unbalanced sensitivity towards model cells in different geometrical relation to the measurements.

For these reasons we choose a regularization that does not only stabilize the solution but also balances the sensitivity. By choosing the square root of the diagonal Hessian matrix as a weighted damping term, we make sure that data and regularization have approximately the same influence on the direction of the model update vector that is taken within each iteration.

In the inversion, formation and storage of the full Jacobian matrix is avoided through the use of the conjugate gradient scheme, making it possible to process very large models and data sets with low memory requirements. Only forward modeling is required, which for both gravity and magnetics can be performed by shifting a translationally invariant data kernel to each measurement position.

In order to maintain upper and lower limits on the model parameters, we use a non-linear transform that maps the bounded domain to an unbounded parameter space. While the problem is linear in the physical model parameters, it is non-linear in the transformed space.

## 3.1  Gravity results

The model (Figure 2A) was obtained by limiting the range of the density contrast from -100 to 700 kg/m$^3$. The individual measurements have been interpolated on a regular dense grid. The original data (not gridded) were fitted within the confidence limits of 0.5 mGal. The estimated gravity data are shown in Figure 2B. We observe that the high density anomaly in the model does not reach the surface. This is due to the weighting term, which allows too little variation near the surface. The model shows a density contrast range from about -100 kg/m$^3$ (background in the south east), to 220 kg/m$^3$. Disregarding the uppermost layer, the model is sensible regarding geological understanding.

At depth, the gabbro intrusion seems to reach until about 4 km. More investigation on the reliability of this result is necessary.
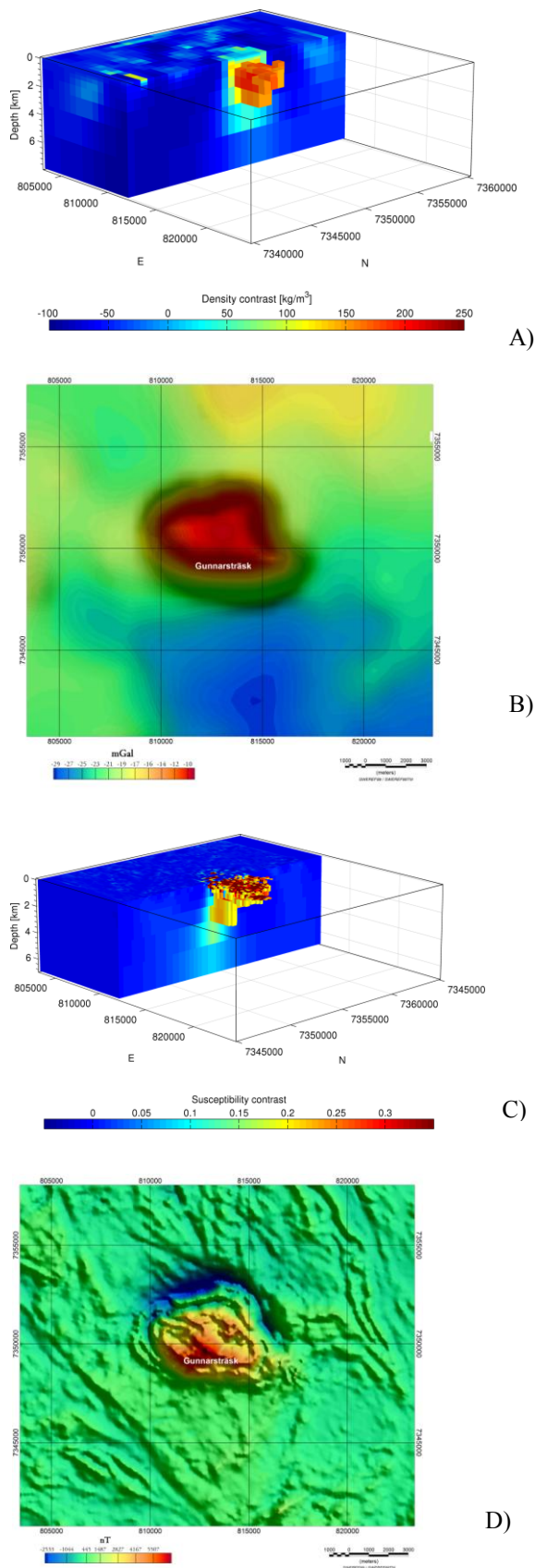
**Figure 2.** A) Density contrast model from gravity inversion. B) Predicted gravity data. C) Susceptibility contrast model from magnetic inversion. D) Predicted magnetic field data.

## 3.2 Magnetic results

The magnetic model is displayed in Figure 2C. The susceptibility range was set from -0.02 to 1. No interpolation was necessary, as the magnetic data is already very densely sampled.

In Figure 2D we present the estimated magnetic field data which are in good accord with the observed data shown in Figure 1B. The data were fitted within the confidence limits of 25 nT. Contrary to the effect of too much damping in gravity in the shallow part, we obtained very strong high-frequency near-surface structures. This is the only place where the model exceeds the color scale shown in the figures, but locally it does so very much (up to 0.9). This indicates that the damping is not strong enough near the surface.

The gabbro exhibits a decrease in susceptibility from the surface downwards. It is to be expected that the actual values at depth are underestimated, while they may be overestimated at very shallow levels. Therefore, the interpretation should at this point remain geometric. The model looks geometrically sensible, when the uppermost 100 m are discarded. Then, it also matches partially with the gravity result. We observe a slight shift to the south for the deeper part of the model. Like the gravity results, the reliability of the model requires assessment.

It is observed that our weighting helps in obtaining useful models at depths greater than 150 m. Above that, we have to conclude that our approximation of the Hessian matrix is too much of a simplification. The discrepancies between the two results are expected to be ameliorated by performing a joint inversion of both data sets. Geological a priori information other than parameter bounds have not yet been incorporated.

## 5 Conclusions

Integrated geological and geophysical studies provide valuable information to characterize mafic intrusions such as gabbro intrusions. Geophysical measurements such as gravity and magnetic field data are helpful in determining the shape of intrusions. In the case of the Gunnarsträsk gabbro, both the magnetic and the gravity anomalies show the same anomaly pattern at the surface, a round structure with 5-7 km in diameter.

To estimate the depth and the 3D shape of the gabbro, 3D inverse modeling based on a cell-based model parametrization has been used. So far, individual inversions of gravity and magnetic field data were carried out, and both data sets can be explained very well with our models. Both results indicate that the gabbro intrusion extends to about 4 km depth. More investigation on the reliability of this result is necessary. The model is geometrically credible if the near-surface part is ignored. There, both models disagree because of our particular choice of regularization.

We plan to study the sensitivity of each data set to the variation of the depth to the bottom of causative body to check the validity of the inversion models using the petrophysical data. A joint inversion with an appropriate coupling of the models is indicated to further improve

the sensibility of our results. A priori information, like geological boundaries at the surface and outcrop information should be included in the inverse modeling process as well.

## References

Aaro S, Johansson P, Jönberger J (2012) SGUs tyngdkraftsundersökningar - bakgrund, syfte och Gunnarsträskgabbron. Sveriges geologiska undersökning, SGU-rapport 2012:2, 29 p

Arkko V, (1986) The Nordkalott project - Geophysical aspects of large mafic intrusions in northern Sweden. Geological Survey of Sweden BRAP 86401, 80 p

Bergman S, Kübler L, & Martinsson O (2001) Description of regional geological and geophysical maps of northern Norrbotten county. Sveriges geologiska undersökning, Ba 56. 110 p

Blakely RJ, (1996) Potential Theory in Gravity & Magnetic Applications. Cambridge University Press

Čuma M, Wilson GA, Zhdanov MS (2012) Large-scale 3D inversion of potential field data. Geophysical Prospecting, 60 1186-1199, doi: 10.1111/j.1365-2478.2011.01052.x

Henkel H, (1981) Stora gabbrointrusioner i norra Sverige, kompletterad version. Sveriges geologiska undersökning BRAP 81408 65 p

Kathol B, Sadeghi M, Triumf CA, Larsson D (2012) Bedrock mapping Jäkkvikk-Boden. In: Berggrudsgeologiska undersökning. Sammanfattning av pågående verksamhet 2011. Sveriges geologiska undersökning. SGU-Rapport 2012:5 41p

Li Y, Oldenburg DW (1996) 3D inversion of magnetic data. Geophysics, 61:394-408

Li Y, Oldenburg DW (1998) 3D inversion of gravity data. Geophysics 63:109-119

Malehmir A, Thunehed H, and Tryggvason A, (2009) The Palaeoproterozoic Kristineberg mining area, northern Sweden: Results from integrated 3D geophysical and geologic modeling, and implications for targeting ore deposits. Geophysics, 74, B9-B22.

Mellqvist C (1999) Sequential injections of mafic magma into a crystallizing magma chamber – a case study from the Luleå area, northern Sweden. Geologiska Föreningens i Stockholm Förhandlingar 121:43–48

Perdahl J-A (1995) Svecofennian volcanism in northernmost Sweden. Doctoral thesis, Luleå University of Technology

Ponce DA, Hildenbrand TG, Jachens RC (2003) Gravity and magnetic expression of the San Leandro gabbro with implications for the geometry and evolution of the Hayward Fault zone, northern California. Bulletin of the Seismological Society of America 93:1-13

Sadeghi M, Morris GA, Carranza EJM, Ladenberger A, Andersson, M (2012) Rare earth element distribution and mineralization in Sweden: An application of principal component analysis to FOREGS soil geochemistry. Journal of geochemical exploration, in press, special issue on Rare Earth elements

Thompson DT (1982) EULDPH: A new technique for making computer assisted depth estimates from magnetic data. Geophysics 47: 31–37, doi: 10.1190/1.1441278

Zhdanov MS. (2002) Geophysical inverse and regularization problems, first ed.: Elsevier Science B. V.

# 3D modelling of the ore body structural complexities: KDC East Gold Mine, South Africa

**Musa M.S. Manzi**
*University of the Witwatersrand Johannesburg, SOUTH AFRICA*

**Kim A.A. Hein**
*University of the Witwatersrand Johannesburg, SOUTH AFRICA*

**Raymond J. Durrheim**
*University of the Witwatersrand Johannesburg, SOUTH AFRICA*

**Abstract.** Complex faults and dykes can sub-divide ore-bearing reefs (or ore bodies) into compartments, which may not be ideal for deep underground mining. The Ventersdorp Contact Reef (VCR) at the Kloof-Driefontein Complex (KDC) East Gold Mine is crosscut by a complex arrangement of faults and dykes. These faults and dykes include; (1) multi-fault segments that bound discrete VCR blocks; (2) multiple bifurcations from a single plane to form a branched fault array and; (3) faults that crosscut and offset older faults, or fault systems. This paper presents the VCR ore body model at KDC East Gold Mine as derived from 3D seismic reflection data, faults and dykes mapped in excavations, as well as intersections of the VCR from both surface and underground exploration boreholes. To ensure robust VCR ore body modelling we used Non-Uniform Rational B-Splines (NURBS) and biharmonic based techniques to handle and incorporate complex structural architectures, which are not easy to model through conventional techniques.

**Keywords.** KDC East Gold Mine, VCR ore body, compartmentalization, structural modelling, 3D seismics

## 1 Introduction

The geologically complex Witwatersrand Basin of South Africa is the largest gold depository in the history of mining. Gold mining in the goldfields takes place at depths ranging from 500 to 4500 m below surface. There are about 20 or more gold ore bodies (quartz pebble conglomerates) that have been mined, or are currently in production. The Ventersdorp Contact Reef (VCR~1.5 m in thickness) in particular, is one of the richest ore bodies in the basin. The orebody is too thin to be directly imaged by the seismic method. However, it coincides with a major acoustic impedance contrast between relatively high–velocity/dense metabasalts of the Klipriviersberg Group and underlying low-velocity/dense quartzite units of the Central Rand Group that produces a strong seismic reflector. In this paper we present a state-of-the-art model of the VCR ore body for the Kloof-Driefontein Complex (KDC) East Gold Mine (Fig. 1), as developed from new modelling techniques.

At KDC East Gold Mine, the VCR lies at 1.0 to 4.2 km depth and presents 97% of the reserve portfolio of Sibanye Gold (a subsidiary of Gold Field Ltd). With the VCR becoming increasing difficult to mine at greater depths, the technical challenge for mining engineers is to design new techniques to optimize the remaining ore reserves. Understanding the complex geometric attributes of faults (i.e., fault dip, dip direction, spacing, throw, and heave) and dykes that crosscut the VCR ore body is critical for its quantitative modelling. Improved seismic interpretations and structural modelling techniques enhance our ability to effectively 'see' faults with throws beyond seismic resolution limits, and model complex distribution of faults and dykes.
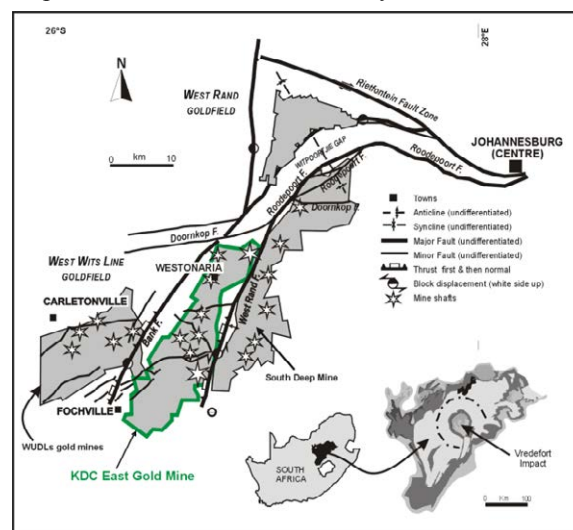


**Figure 1.** Location map of the KDC East Gold Mine of the Witwatersrand Basin. Modified after Dankert and Hein (2010).

## 2 3D seismic and structural complexities

The modelling of the VCR began with the 3D seismic imaging of the VCR horizon, and faults and dykes that crosscut it (Figs. 2a, b and c). The 3D seismic data for the KDC East Gold Mine, which was acquired in 2003, is characterized by a seismic wavelet with the dominant peak frequency of 65 Hz and an interval velocity of 6500 m/s (Manzi et al, 2012a). Thus, faults with throws of less than a quarter of the seismic dominant wavelength (~25 m in this case) are difficult to detect through conventional interpretation. Furthermore, subsequent to seismic data migration, faults and dykes with spacing much less than the seismic dominant wavelength (~100 m in this case) may also not be resolvable.

After picking the VCR horizon data points in 2D seismic sections, the noise introduced during picking was smoothed using post-fault interpolation smoothing operators such as the bi-harmonic smoothing algorithm developed by Halenbrook (2001). This algorithm is used

in seismic interpretation to detect subseismic faults, to filter-out the isolated horizon noise, and to separate gross structural configurations (long wavelength) from faults and dykes (short wavelength) (Fig. 2c). It also tends to maximize the resolution for the identification and location of faults, eliminate errors resulting from false complex geometries created by conventional picking around faults, and thus minimizes unrealistic fault-horizon geometries (Fig. 2c). The advantage of applying this algorithm post-fault projection is that filtering only occurs within the horizon rather than across the faults. However, care must be taken not to filter out the faults and dykes, since the bi-harmonic smoothing algorithm is capable of filtering-out noise in addition to real faults and dykes, which can significantly affect the fault geometry.
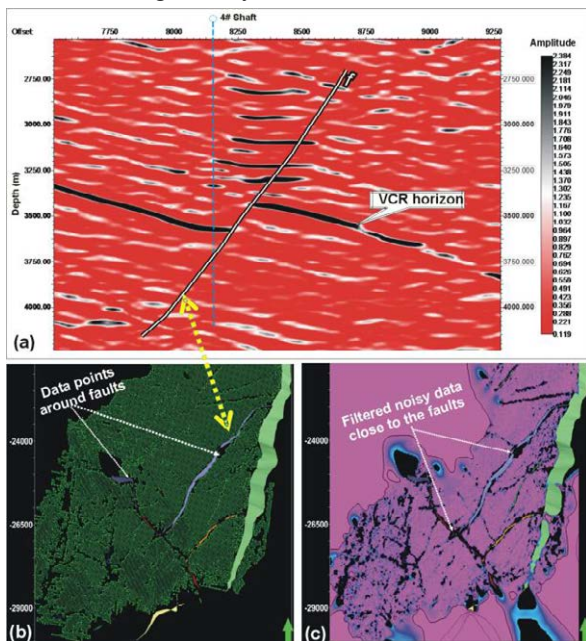


**Figure 2.** (a) Seismic section (amplitude display) showing a strong reflective VCR horizon. (b) Picked seismic horizon data points and fault polygons. (c) Smoothed horizon-fault projection by bi-harmonic smoothing algorithm.

## 3  3D fault-horizon projection modelling

The VCR ore body at the Kloof Gold mine is characterized by a series of complex normal faults. The geometric complexities that present challenges in the generation of the VCR ore body modelling include; (1) multi-fault segments that bound discrete VCR blocks; (2) multiple bifurcations from a single fault plane to form a branched fault array and; (3) faults that crosscut and offset older faults or fault systems. The newly developed modelling and interpolation technique 'Non-Uniform Rational B-Splines (which is implemented in Petrel software packages) is capable of modelling complex faulted ore bodies and provides flexibility in designing and modelling different geometries (Rock Deformation Research, 2004; Piegl and Tiller, 1997). Conventional modelling techniques only model the faults with linear interpolation between fault pillars, i.e., they restrict fault-pillars (Fig. 3a, b) in moving along specific degrees and planes. This often creates horizon geometries that are

jagged. NURBS, in contrast, is a tetrahedral volume modelling technique, i.e., it allows multi degrees of movement through fault pillars during interpolation.

To avoid unrealistic VCR ore body modelling, the fault pillars (derived from seismics) were modified to give tight correlation with the seismically defined VCR horizon (Figs. 3c, d). The data was then gridded (using Kriging gridding algorithm), and the faults were re-modelled using NURBS repeatedly until the stable VCR ore body geometry was achieved (Fig. 4a, b and c).
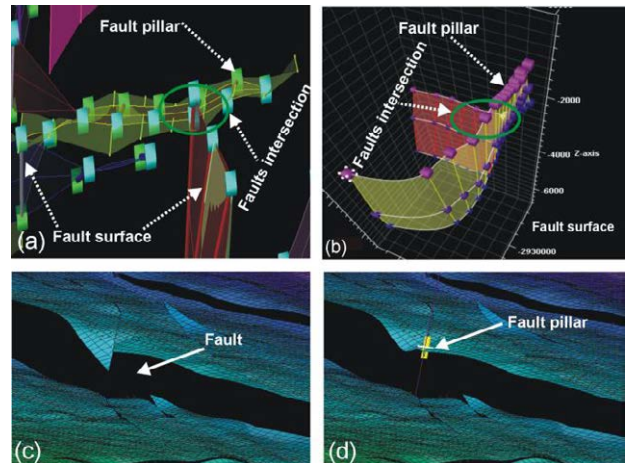


**Figure 3.** (a) Modelled fault surfaces and fault pillars (changed dip of faults from vertical) using NURBS. (b) Modelled fault surfaces showing fault intersections. (c) Horizon modelling around the fault zones. (d) Projection of fault pillars into horizon breaks (faults).
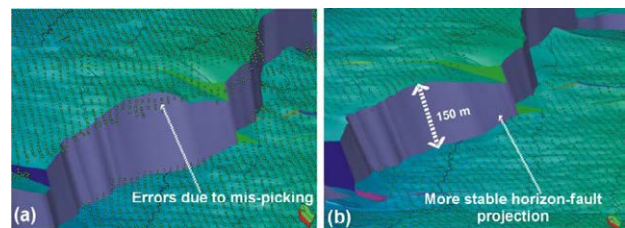


**Figure 4.** (a) Seismic horizon data points overlap across the fault throw, the dip of the fault is thus in error. (b) Horizon is projected in a sensible manner to the fault. (c) Re-modelled faults and horizon, showing the stable throw variations.

## 4  3D edge detection attributes

Generally, fault sticks that were picked manually on seismic sections did not exactly correspond to VCR horizon breaks in 3D environments (Fig. 5a). The fault-

horizon projection was therefore enhanced using edge detection attribute analysis. The application of this technique ultimately allowed for tieing of uncorrelated fault sticks to their appropriate positions (Fig. 5b). The edge-detection algorithm is the combination of dip and azimuth variations, normalized to the local noise surface, which overcomes the difference in detectability between the dip and dip azimuth attributes. This technique also improves the lateral resolution of the fault traces, which aids in characterizing fault continuity and connectivity, and thus minimizes unrealistic 3D fault-horizon geometries (Manzi et al., 2012b).

Some of the interpretation techniques are sensitive to the fault trend, so care was taken to ensure that trend is correctly modelled. When a VCR horizon on either side of a fault was significantly offset near the fault boundary, the application of the attributes allowed for the projection of one fault onto another (Fig. 5b), allowing gaps between a branching fault and its stem fault to be closed.
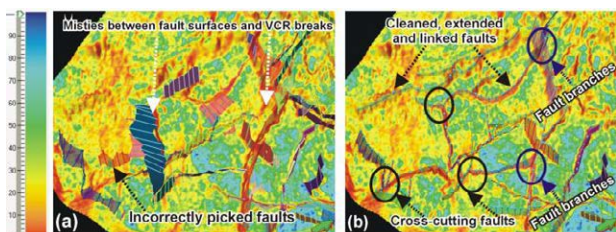


**Figure 5.** (a) Picked fault surfaces show no correlation with the VCR horizon breaks (faults) derived from edge attributes. (b) Re-modelled faults showing cleaned, extended and linked fault surfaces.

## 5 Ore body compartment sizes

Faults and dykes can severely compartmentalize ore bodies in the KDC East Gold Mine. The spacing between faults/dykes or 'fault spacing' is one of the major parameters that define whether or not VCR ore body blocks are accessible for mining, thus compartment sizes were incorporated into the fault-horizon model. Arguably, the larger the compartment, the more accessible the ore, provided that the gold grade is suitable for recovery, and the cost and risk of ore recovery is acceptable.

The compartment maps derived from seismic and underground mapping data are presented in Fig. 6a and Fig. 6b, respectively. The results show that seismically-imaged faults subdivide the VCR ore body into compartment sizes ranging from 150 to 500 m. However, structural maps from the stoped-out areas resolve compartment sizes ≤ 50 (which is equivalent to 2 bins of the seismic survey). It follows that seismics fail to detect fault-bounded compartments falling below the seismic dominant wavelength (124 m). This means that it is inaccurate to use a 3D geological model based only on seismic data as the final geological model. Rather, it is prudent to incorporate other models based on datasets, such as underground mine maps and exploration boreholes, to arrive at a robust ore body model. Quality geological mapping data, in particular, is extremely useful when attempting to model faults and dykes that fall below seismic resolution limit.

Finally, the ore body model which incorporated the seismic data, and complex fault-dyke architectures extracted from seismic and underground mapping, was transferred into mine software packages for future mine planning and design (Fig. 7a, b).
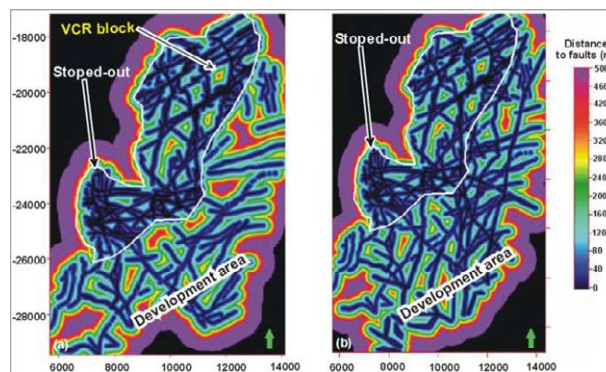


**Figure 6.** (a) Compartment size maps derived from seismically defined faults; (b) Compartment size maps derived from the integration of seismically defined faults and underground mapped faults and dykes.
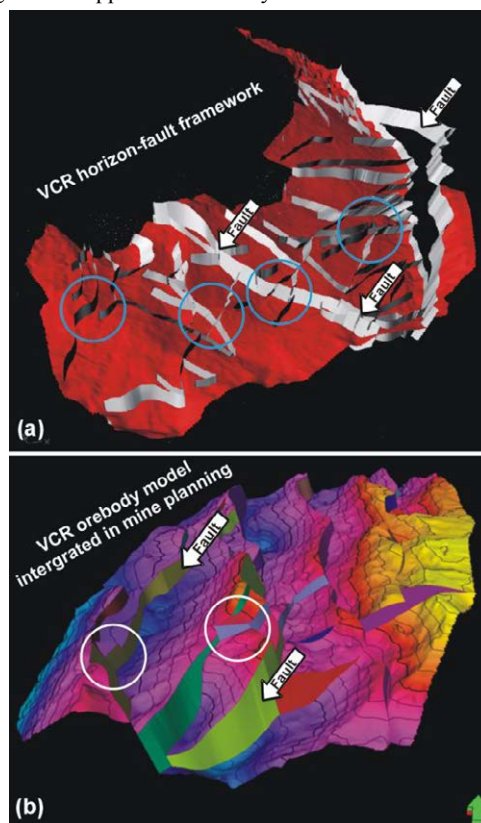


**Figure 7.** (a) Seismically defined fault-horizon projection. (b) Integration of the 3D structural ore body model into mine software packages (e.g. AutoCAD).

## 6 Conclusion

We have presented a geologically reasonably 3D ore body model of the KDC East Gold Mine, as derived from 3D seismics, exploration holes and underground mapping information. The newly developed modelling techniques were used to manage complex structural architectures that are impossible to model using traditional modelling tools. Moreover, we used unique horizon-based edge attribute analysis (post fault-horizon

projection) to incorporate subseismic structural complexity in the model. This model has been factored into future mine development strategies for better placement of shafts and improved life-of-mine planning; i.e., the high degree of structural resolution afforded by these modelling techniques will guide future exploration drilling activities and enable the layout of tunnels and stopes to be optimized.

## Acknowledgements

## References

Dankert, B.T., and K.A.A. Hein, 2010. Evaluating the structural character and tectonic history of the Witwatersrand Basin: Precambrian Research, 177, 1-22.

Halenbrook, B.T., 2001. Mesh deformation using the biharmonic operator. International Journal for Numerical Methods in Engineering 2, 1-30.

Manzi, M., Durrheim, R.J., Hein, K.A.A., King, N., 2012a. 3D edge detection seismic attributes used to map potential conduits for water and methane in deep gold mines in the Witwatersrand Basin, South Africa. Geophysics 77(5), WC133–WC147.

Manzi, M.S.D., Gibson, M.A.S., Hein, K.A.A., King, N., Durrheim, R.J., 2012b. Application of 3D seismic techniques in evaluation of ore resources in theWestWits Line goldfield and portions of the West Rand goldfield, South Africa. Geophysics 77(5), WC163–WC171.

Piegl, L., Tiller W., 1997. The NURBS Book, 2nd Edition, Springer, 646 p.

Rock Deformation Research, 2004, Structural and seismic appraisal of the Kloof and surrounding area: Report 9350 (unpublished), 1–37.

# Enhancing copper predictions at the base of Zechstein with 4D modelling

**P. Mejía, J.J. Royer**
*Université de Lorraine, Georessources (UMR 7359)—ENSG, Vandoeuvre-Lès-Nancy, France*
*Email: mejia@gocad.org*

**J. Hartsch**
*G.E.O.S. Ingenieurgesellschaft mbH, Freiberg, Germany*

**P. Hielscher**
*Institut für Geophysik und Geoinformatik—TU Bergakademie, Freiberg, Germany*

**Abstract.** $3D$ restoration can help to better understand the history of geological formations, to identify fossil mineralizing fluid pathways, to establish the physical and chemical processes involved in ore formations and to predict the locations of potential economic mineral resources. In the case of sediment-hosted ore deposits, the unfolding and unfaulting techniques allow to visualize the impact of tectonic events during the mineralization stages and their role in the final ore-distribution. We applied a $3D$ restoration procedure on the German and Polish Kupferschiefer, pointing out the role played by the Late Cretaceous—Early Paleocene uplifting which affected Central Europe. On both sides of the Fore-Sudetic block, the fluids trapped beneath the Zechstein formations reached over-pressurized conditions due to the inverse up-lift phase, provoking the hydro-fracturing and the re-opening of previous discontinuities. This set of hydro-fractures was necessary in the Cu re-mobilization and later during its precipitation as enriched Cu (Cu-Fe) sulfides. A hydro-fracturing index accounting for the stress and the geomechanical constraints in the ore-series was estimated and seems to correlate with the presence of Cu-sulfides within the Kupferschiefer.

**Keywords.** Restoration, sediment-hosted ore-deposits, hydro-fracturing, Late Cretaceous—Early Paleocene uplifting.

## 1 Introduction

Significant advances have occurred these last decades in $3D$ structural restoration. In the oil industry, $4D$ structural modelling is key to identify favourable target mother rock formations, to reconstitute fluids migration (Moretti et al. 2007) and to predict faults and fracturing in the rock mass (Mace et al. 2005). Less developed in mineral prospecting, $4D$ modelling has been applied in similar contexts. Accounting for geometric or geomechanical constrains, $3D$ reconstruction tools allow better understanding and evaluating the several geo-variables related to the mineralization processes including the paleo-pressures, paleo-temperatures, paleo-strains and strengths evolution. In the Kupferschiefer case, the fractures often control the concentration of metals as sulfides filling the open spaces (Blundell et al. 2003; Gouin 2008; Jowett et al. 1987), letting the re-mobilization of metals and the Cu enrichment on the primary sulfides (Wagner et al. 2010). To simulate the overburden and fluid pressures necessaries to create the mineralizing fractures, we have restored sequentially the $3D$ models of the Fore-Sudetic Monocline in Poland and the North-Sudetic Trough in Poland and Germany (Fig. 1), taking into account the main tectonic episodes in the ore-evolution.
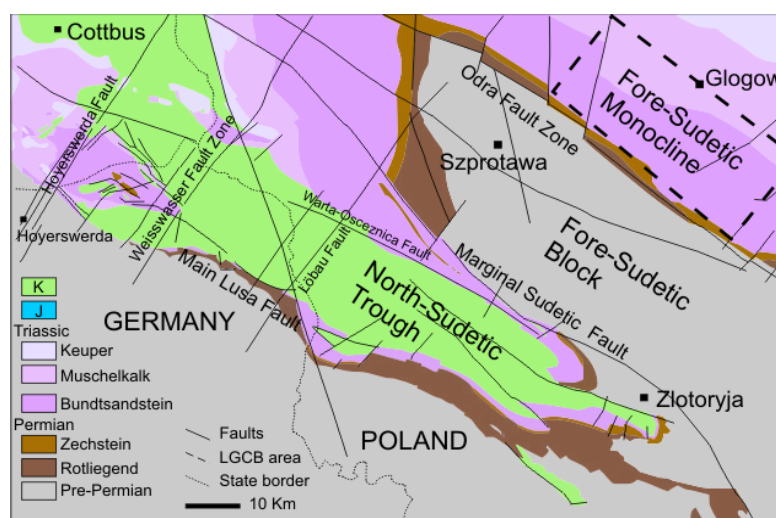


**Figure 1.** Study area with main rock units (without Cenozoic) and fault systems. The Legnica-Głogów Copper Belt Area (LGCB), located within the Fore-Sudetic Monocline, is the $4^{th}$ world Cu mined source and $1^{st}$ in Ag at present time (KGHM Polska Miedź S.A. 2012).
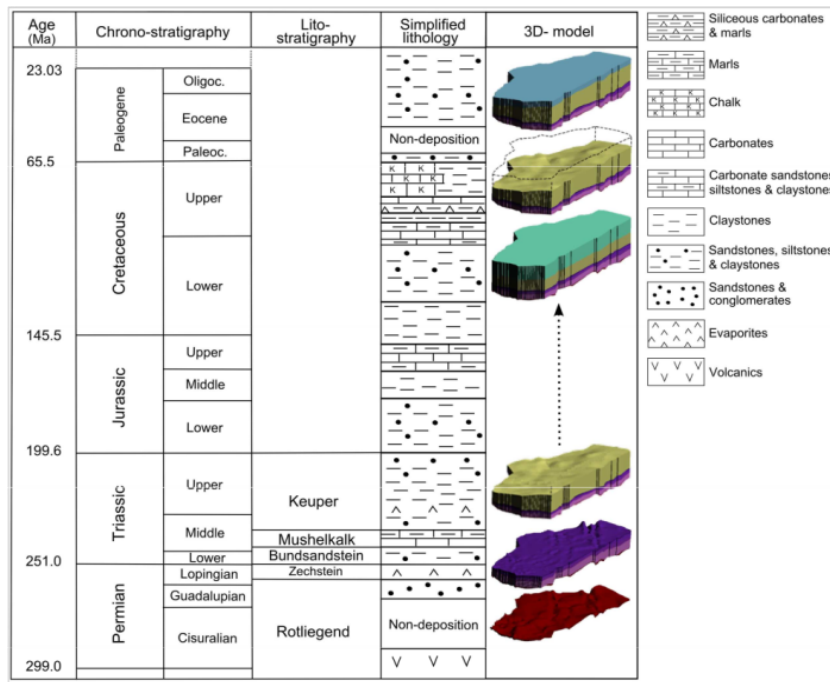
**Figure 2.** Sequential restoring in the LGCB. The most important erosion event in this region corresponds to the uplifting at Late Cretaceous—Early Paleocene time.

The results show two subsidence episodes as sources for fluid overpressure: at Late Permian—Early Triassic and at Late Jurassic—Early Cretaceous, respectively. These ages are in agreement with some isotopic dating (Bechtel et al. 1999; Michalik 1997) and paleo-magnetic dating (Symons et al. 2011) achieved in the ore-series. However, the Late Cretaceous—Early Paleocene uplifting, which occurred in this part of Europe (Mazur et al. 2005; Resak et al. 2008), is thought to be the major event which had structured the present ore-distribution in the Fore-Sudetic area (Fig. 2). We established a hydro-fracturing index (HF) accounting for the tensile strengths in the ore-series, the overpressure of the trapped fluids beneath the Zechstein layers and the overload pressure during the uplifting time. Positive (HF) values correspond to the zones with high probability for developing fractures at the base of the Zechstein during the tectonic inversion and correlate to the areas containing Cu (Cu-Fe) sulfides (Fig. 3).

## 2 Methodology

The restoration procedure applied on the North-Sudetic Trough and the Fore-Sudetic Monocline regions removes the tectonic deformations from Cenozoic to Upper Permian rock layers, accounting for the compaction effects due to the weight of the upper series. We chose the flexural slip method to flattening the deformed and eroded layers using the Kine3D® suite of Gocad®. Thickness of eroded series, paleo-reliefs, and presence of basins were estimated from the literature and by comparing eroded and non-eroded levels of similar series when possible. The analysis of the organic matter contained in the Kupferschiefer (Gouin 2008; Resak et al. 2008; Stephenson et al. 2003) allow estimating the layer depths before the erosion times. The

HF was calculated considering the pore and overburden pressures below the Zechstein before and after the uplifting event, and the tensile strengths in the ore-series obtained from geotechnical studies in Polish copper mines (Pytel 2003).
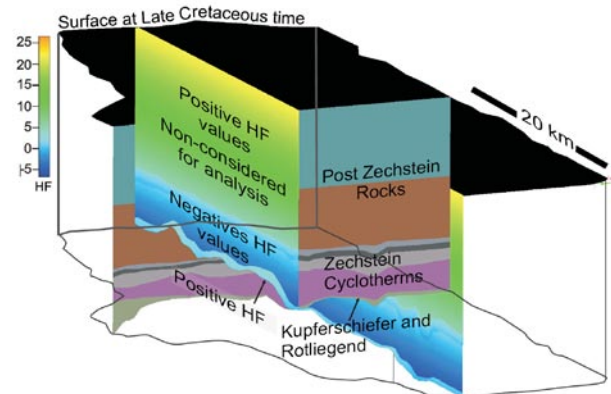


**Figure 3.** Pseudo-stratigraphic grid representing the LGCB 3D model at Late Cretaceous—Early Paleocene. The high HF index points out possible hydro-fracturing zones favourable to re-circulation fluids and precipitations of Cu-sulfides, located under the sealing Zechstein formation (vertical exaggeration × 5) (Mejia and Royer 2012).

## 3 Discussion

During a tectonic inversion and uplifting, the overlying layers are removed by erosion. The pore pressures state changes due to the variations in the vertical and horizontal stress components. Hence, two situations may occur: (i) a normal de-watering if the fluids can escape from the rocks or, on the contrary, (ii) an over-pressure in the fluid trapped in the rock mass produces hydraulic

fracturing, if the rock tensile strengths and the overburden pressure are appropriated (Cosgrove 1995; Cosgrove 2001; Sibson 2003). This last process has been invoked to explain the metal remobilization at the base of Zechstein. The very low porosity rocks of the Zechstein formation (evaporites mainly) isolate the lower hydrogeologic system from the overlaying post-Zechstein rocks. Fluids in these lower layers are maintained at high pressures during the uplifting, whereas the overburden pressure reduces over the time. The open spaces, caused by the over-pressured fluids in the layers with relative low tensile strengths, drove the re-circulation of fluids bearing Cu and other base and precious metals. In this closed model, the Cu is remobilized along convective cells beneath the evaporite series. The Cu solubility is controlled by the hematite contained in the Rote Fäule, differing of the open circulation system proposed by Brown (2011) in which the Cu solubility is controlled by the meteoric water. In our closed and convective circulation model, it is assumed the pre-existence of Cu (Cu-Fe) sulfides and the Rote Fäule as necessary conditions for the later replacement/enrichment of secondary Cu sulfides due the uplifting. An alternative paleo-magnetic age of $53\pm3$ Ma found in the ore Kupferschiefer at the Sangerhausen location in Germany (Symons et al. 2011) may corresponds to this Cu re-mobilisation/enrichment event.

## 4  Conclusions

This study shows that the *4D* structural modelling is useful and can be applied in explorations surveys as tool to better understand the genesis and evolution of sediment-hosted ore deposits. The restoration tools provide effective structural attributes (as the hydro-fracturing index) that can help to better know the current distribution of metals in the study area. In this particular case, it is possible to define exploration targets at the base of Zechstein from the correlation between copper contents and the HF index in the Fore-Sudetic Monocline and the North-Sudetic Trough regions.

## Acknowledgements

## References

Bechtel A, Elliott WC, Wampler JM, Oszczepalski S (1999) Clay mineralogy, crystallinity, and K-Ar ages of illites within the Polish Zechstein Basin; implications for the age of Kupferschiefer mineralization. Economic Geology 94:261 – 272. doi: 10.2113/gsecongeo.94.2.261

Blundell DJ, Karnkowski PH, Alderton DHM, et al. (2003) Copper mineralization of the Polish Kupferschiefer: a proposed basement fault-fracture system of fluid flow. Economic Geology 98:1487 –1495

Brown AC (2011) Adding geochemical rigor to the general basin-scale genetic model for sediment-hosted stratiform copper mineralization. 11th SGA Biennial Meeting. Antofagasta, Chile

Cosgrove JW (1995) The expression of hydraulic fracturing in rocks and sediments. Ameen, M.S. (ed.) Fractography: fracture topography as a tool in fracture mechanics and stress analysis, Geological Society Special Publication No. 92. pp 187–196

Cosgrove JW (2001) Hydraulic Fracturing During the Formation and Deformation of a Basin: A Factor in the Dewatering of Low-Permeability Sediments. AAPG Bulletin 85:737 –748. doi: 10.1306/8626C997-173B-11D7-8645000102C1865D

Gouin J (2008) Mode de genèse et valorisation des minerais de type black shales : cas du Kupferschiefer (Pologne) et des schistes noirs de Talvivaara (Finlande). Ph.D. Thesis Report., Université d'Orléans

Jowett EC, Pearce GW, Rydzewski A (1987) A Mid-Triassic Paleomagnetic Age of the Kupferschiefer Mineralization in Poland, Based on a Revised Apparent Polar Wander Path for Europe and Russia. J Geophys Res 92:581–598. doi: 10.1029/JB092iB01p00581

KGHM Polska Miedź S.A. (2012) Report on the Mining Assets of KGHM Polska Miedz S.A. located within the Legnica-Glogów Copper Belt Area. 45

Mace L, Muron P, Mallet J-L (2005) Integration of fracture data into 3d geomechanical modeling to enhance fractured reservoirs characterization. SPE Annual Technical Conference and Exhibition

Mazur S, Scheck-Wenderoth M, Krzywiec P (2005) Different modes of the Late Cretaceous–Early Tertiary inversion in the North German and Polish basins. International Journal of Earth Sciences 94:782–798. doi: 10.1007/s00531-005-0016-z

Mejia P, Royer J-J (2012) Explicit Surface Restoring-Decompacting Procedure to Estimate the Hydraulic Fracturing: Case of the Kupferschiefer in the Lubin Region, Poland. 32nd Gocad-Meeting. Nancy, France

Michalik M (1997) Chlorine containing illites, copper chlorides and other chloride bearing minerals in the Fore-Sudetic copper deposit (Poland). Mineral deposits, research and exploration— where do they meet 543–546

Moretti I, Delos V, Letouzey J, et al. (2007) The Use of Surface Restoration in Foothills Exploration: Theory and Application to the Sub-Andean Zone of Bolivia. In: Lacombe O, Roure F, Lavé J, Vergés J (eds) Thrust Belts and Foreland Basins. Springer Berlin Heidelberg, pp 149–162

Pytel W (2003) Rock mass-mine workings interaction model for Polish copper mine conditions. Int Journal of Rock Mechanics and Mining Sciences 40:497–526

Resak M, Narkiewicz M, Littke R (2008) New basin modelling results from the Polish part of the Central European Basin system: implications for the Late Cretaceous–Early Paleogene structural inversion. International Journal of Earth Sciences 97:955–972. doi: 10.1007/s00531-007-0246-3

Sibson RH (2003) Brittle-failure controls on maximum sustainable overpressure in different tectonic regimes. AAPG Bulletin 87:901 –908. doi: 10.1306/01290300181

Stephenson RA, Narkiewicz M, Dadlez R, et al. (2003) Tectonic subsidence modelling of the Polish Basin in the light of new data on crustal structure and magnitude of inversion. Sedimentary Geology 156:59–70. doi: 10.1016/S0037-0738(02)00282-8

Symons D, Kawasaki K, Walther S, Borg G (2011) Paleomagnetism of the Cu–Zn–Pb-bearing Kupferschiefer black shale (Upper Permian) at Sangerhausen, Germany. Mineralium Deposita 46:137–152. doi: 10.1007/s00126-010-0319-2

Wagner T, Okrusch M, Weyer S, et al. (2010) The role of the Kupferschiefer in the formation of hydrothermal base metal mineralization in the Spessart ore district, Germany: insight from detailed sulfur isotope studies. Mineralium Deposita 45:217–239. doi: 10.1007/s00126-009-0270-2

# Visualization of mineralization and alteration zones in Biely Vrch Au-porphyry deposit by MapInfo Discover 3D

**Jana Michňová, Peter Koděra,**
*Department of Geology of Mineral Deposits, Faculty of Natural Sciences, Comenius University, Mlynská dolina - G, 842 15 Bratislava, Slovakia,*
*michnova@fns.uniba.sk*

**Peter Pauditš**
*State Geological Institute of Dionýz Štúr, Department of Engineering Geology, Mlynská Dolina 1, 817 84 Bratislava, Slovakia*

**Abstract.** The purpose of our study was to visualize various mineralization zones, especially the zone with high grade ore mineralization and alteration zones of the Biely Vrch Au-porphyry deposit, based on subsurface data. 3D block models were made for main element of ore mineralization using Ordinary Kriging method with variogram modelling. Grades of ore elements vary with changes of geological properties. Analysed subsurface data were compared with threshold block models and isosurface models of element grade distributions. Preliminary results show concentration of Au and Cu grades in the central part of the system and Mo, Zn and Pb grades distribution at the margins of the central zone. Zones with advanced argillic alteration with typical Bi and Te anomalies access the outer part of this zone. Zones with pyritization and pyrhotitization at the edge of the porphyry bodies are poorly mineralized.

**Keywords.** Au porphyries, geochemistry modelling, 3D GIS modelling, mineralization zones, Detva-Biely Vrch deposit

## 1 Introduction

The Biely Vrch deposit is the only Au-porphyry system with economically exploitable accumulation of gold in the Western Carpathians. Mineralization was discovered recently by EMED Mining Ltd. (Bakos et al. 2011).

The deposit is situated in the central zone of the Javorie stratovolcano. A parental intrusion of diorite to andesite porphyry is emplaced into andesitic volcanic rocks (Fig. 1).

Rocks hosting the deposit are affected by extensive alteration, dominated by intermediate argillic type of alteration. It variably overprints earlier high-T K-silicate and Ca-Na silicate alteration in deeper levels of the system. Propylitic alteration dominates the outer zone of the system. Ledges of advanced argillic alteration correspond to the youngest stage of alteration (Koděra et al. 2010).

Au mineralization occurs in the vicinity of quartz veinlets and exploration drilling confirmed its presence still in about 750 m depth. K-metasomatic alteration situated in the central part of the porphyry intrusion is probably the primary source of gold (Bakos et al. 2011). High grade Au occurs in the vicinity of quartz veinlets, in altered rocks with clays, chlorite and K-feldspar, sometimes attached to sulphides or Fe-Ti minerals (Koděra et al. 2010).
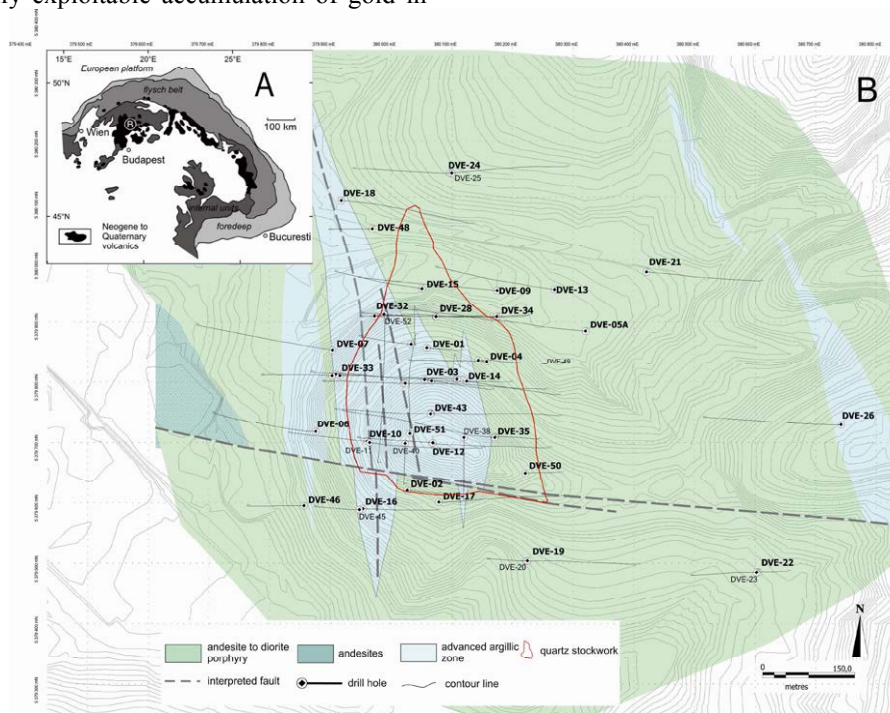


**Figure 1.** A) Localization of the Biely Vrch deposit in Western Carphatians, B) Schematic geological map of the Biely Vrch deposit with drill holes plan (modified from Hanes et al. 2010)

## 2 Data preparation and block modeling

### 2.1 Datasets

The database with drill hole collar, survey, assay and lithological data have been provided by EMED Mining Ltd. The database contains detailed documentation of 52 drill holes with length ranges from 65 to 782 m. Drilling extends approximately 700 m N-S and 900 m E-W, limiting off the mineral resource in both directions. Drill holes are spaced between 50 to 100 m and sampled at 1 or 2 meters and the total database contains information about 14,482 pieces of drill core samples. The database provides information about the location of drill holes, their depth and orientation, lithology, mineralogy and geochemistry (AAS, ICP analysis of 36 chemical elements). Mineralogy data and alteration data are estimated in % and are documented on a macroscopic scale in estimating intensity from 0 to 5. EMED supplied raw drill hole data in PostgreSQL format and surface topography data in GIS Grass software format. The database was imported to MapInfo Discover 3D. Top cut statistics such as extreme values, minimum, maximum, mean, standard deviation and coefficient of variation were determined.

### 2.2 Visualization and interpretation of drill hole attributes

Drill hole attributes were displayed in 2D space using MapInfo Discover. The distribution of data according to logical grouping of studied correlations was visualized by logs. Overall, for each drill hole 5 types of profiles were made that characterize and visualize various aspects of the deposit: 1. geological parameters (lithology, texture, structure and fragmentation), 2. mineralization and associated metals (silicification, quartz, Au, Ag, Cu, Mo, Pb, Zn, Cd, Bi, Ba), 3. different types of alterations apart from advanced argillitization (argillite, illite, epidote, kaolinite, biotite, sericite, chlorite, K, Na, Ca, Mg, Mn), 4. advanced argilitization (Al, P, Ti, Sr, Sc, La, Ga, Ni, Co, Cr, V), 5. oxidized zone of the deposit and distribution of potentially hazardous elements (oxidation, limonite, pyrite, pyrhotite, magnetite, hematite, Fe, S, As, Sb). Data exceeding the selected range in the profiles (extreme values) was coloured in red. 2D vertical slices with several associated boreholes show correlation of elements grades in the form of histograms and line graphs.

### 2.3 3D modelling of mineralized and altered zones

Interpolation between 3D objects to create smooth gridded surfaces and 3D block modelling (3D gridding) were done using Discover 3D. 3D block models were used to produce vertical and horizontal slices at required depth levels. "Chair clipping" view was created to visualize 3D distribution within the investigated area. Threshold attribute values have been used to create the isosurfaces or threshold block models. Discretised voxel models, where a series of unique attributes, e.g. rock or alteration codes, have been used to create the block model coloured using an appropriate colour legend.

An element grade distribution block model was generated via ordinary kriging method. Ordinary kriging was developed by Matheron (1971) in the early sixties and plays a special role because it is compatible with a stationary model, only involves a variogram and it is the form of kriging used most in resource exploration (Chile´s and Delfiner 1999). Ordinary kriging estimates based on moving average of the variable of the interest satisfying different dispersion forms of data (Goovaerts 1997). The gold mineralization at Biely Vrch deposit spatially overlaps with quartz veinlet system and zones of brecciation however, in local scale gold grades can be low even if veinlets or brecciation are present. Mineralisation is not identified with a specific lithology or alteration type or oxidation state. Therefore, estimation of domains was modeled based only on metal grade, with definition of cut-off grade and top cut grade values. For example, in resource calculation EMED defined a cut-off grade of 0.3 g/t for Au based on visual inspection of the drill hole sample grades and grade distribution (Chapman 2009). Cut-off grades for elements were defined by examining sample histograms, log histograms, probability plots and by examining spatial location of extreme values. Top cut values were examined by statistical plots. Using top cutting we have reset all values above a certain threshold value to the threshold value. Block size selection and spherical sample search parameters were selected. Directional variogram was modelled for three principal directions. Modelled variograms were comprised of structure-nested spherical models. After the voxel model generation, validation of the block model by statistical comparison of composite grades versus block grades, inspection of the block model in plan and section and visual comparison of block grades to drill data were done.

Components of the block model were then exported for use with other models, such as isosurfaces above a certain threshold of element grade and threshold block models. Using combination of all types of visualization we have tried to visualize mineralization and alteration zones in the Biely Vrch deposit. Results of 3D element grade distribution show that mineralized zones with increased Au grades are accompanied by increased Cu and Pb grades within the central part of the porphyry system with advance argillic alteration (Figs. 2 and 3). These anomalies coincide with zones of quartz veinlets with associated silicification. The central zone contains at its margins several times lower concentrations of Au, Cu, Pb and Zn (Fig. 4).
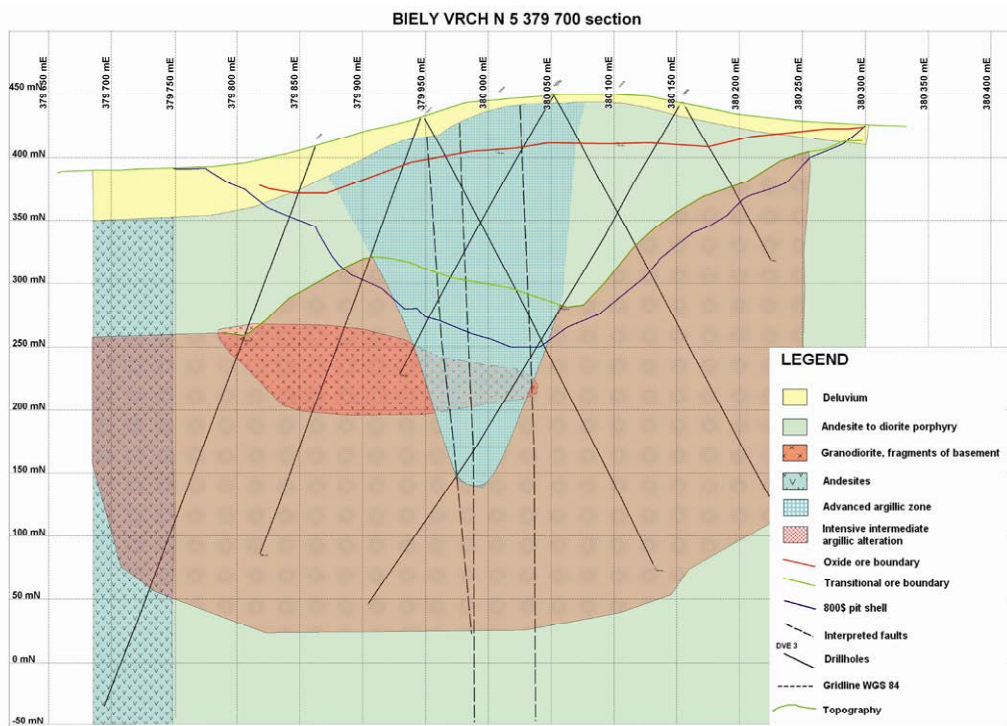
**Figure 2.** Schematic cross section of the Biely Vrch deposit with major alteration patterns (provided by EMED Mining Ltd.)
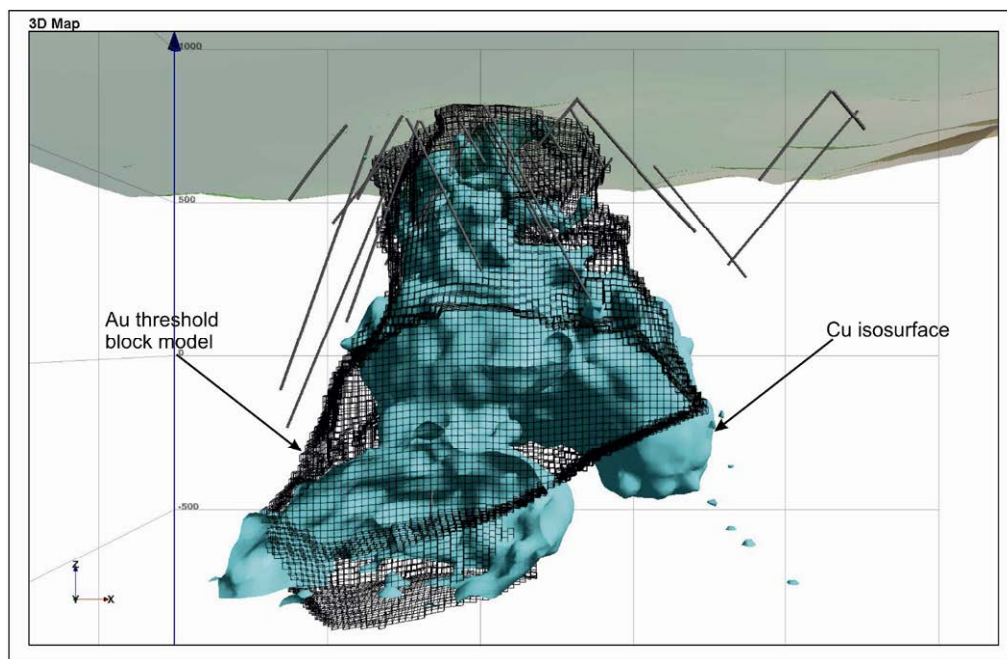


**Figure 3.** Wireframed threshold block model of Au grade above cut-off value 0.3 ppm and isosurface of Cu upper quartile grade 146 ppm.

Pb and Zn concentrations decrease toward depth and trend of Mo distribution is oriented to southwest. Increased content of Mo up to 10 ppm (Fig. 4) and anomalies of Bi and Te are also typical for zones of advanced argillic alteration. Zones of pervasive pyritization and pyrhotitization at the edges of porphyry bodies are poor in metals.
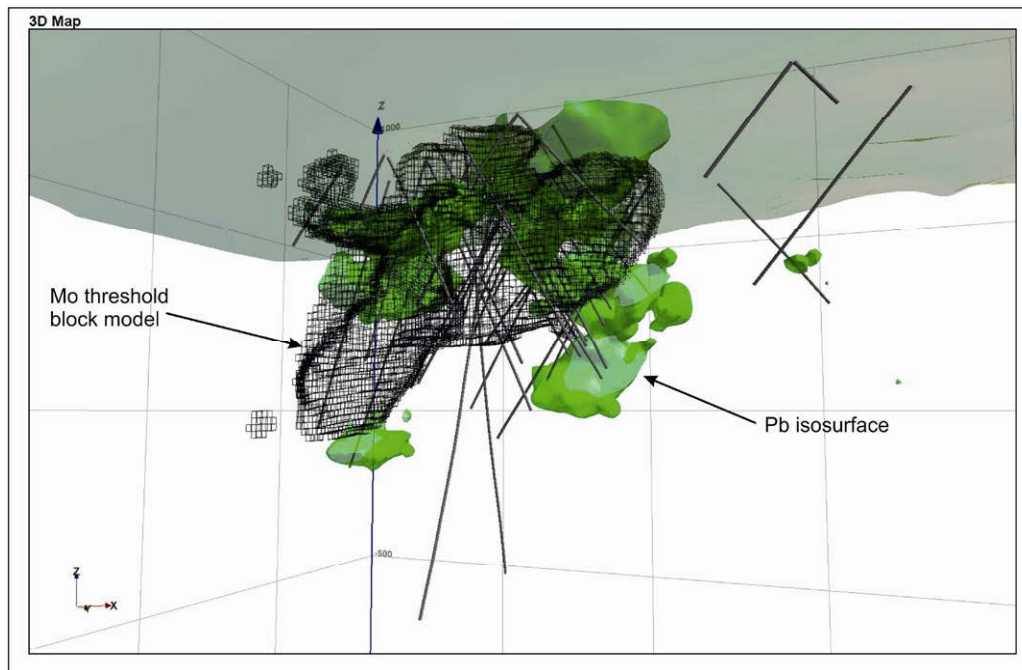
**Figure 4.** Wireframed threshold block model of Mo grade above upper quartile value 20 ppm and isosurface of Pb upper quartile grade 145 ppm.

## 2.4  Conclusions

3D visualization of the element grade distribution and modelling of alteration and mineralized zones are still under development, so this contribution contains only preliminary results. Dataset will be supplemented by data from detailed mineralogical and petrological study. 3D models of alteration and geology based on macroscopic drill hole logging will be upgraded to accurate detail models. The main task of our modelling is to create a complete model of the Biely Vrch Au-porphyry system, including detail definition of the alteration boundaries and possible correlation with distribution of ores. Modelling will be also used for visualization of areas with potential utilization as secondary raw clay materials and zones with potentially hazardous elements e.g. sulphides and other hazardous components.

## Acknowledgements

## References

Bakos F, Koděra P, Jánošík M (2011) Geochemistry of Au-porphyry mineralisations in the Central Slovakia Neogene Volcanic Field, in practice (in Slovak). Abstracts of the conference Geochémia 2011, Bratislava: 16-18

Goovaerts P (1997) Geostatistics for natural resources evaluation. Oxford University Press, New York: 496

Hanes R, Bakos F, Fuchs P, Žitňan P, Konečný V (2010) Exploration results of Au porphyry mineralization in the Javorie stratovolcano. Mineralia Slovaca 42 (1): 15-32

Chapman E (2009) EMED Biely vrch porphyry gold resource estimation, Slovakia, Resource Estimate. Intermal report EMED Slovakia, Snowden, Vancouver: 69

Chile´s J P, Delfiner P (1999) Geostatistics: Modeling spatial uncertainty. Ciley, New York: 695

Koděra P, Lexa J, Biroň A (2010) Gold mineralization and associated alteration zones of the Biely Vrch Au-porphyry deposit, Slovakia. Mineralia Slovaca 42 (1): 33-56

Matheron G (1971) The Theory of Regionalized Variables and Its Applications. Ecole des Mines, Fontainebleau, France.

# 3-D ore body modeling of vein-hosted Co-Ni-Cu-Au-mineralization in the Siegerland district, Rhenish Massif, NW Germany

Meike Peters, André Hellmann, Franz Michael Meyer
*Institute of Mineralogy and Economic Geology, RWTH Aachen University, Aachen, Germany*

**Abstract.**

The Siegerland district in the Rhenish fold- and thrust-belt hosts diverse hydrothermal vein-type mineral deposits of which five different syn- to late-orogenic mineralization types have been recognized. The most important structural feature in the region is the Siegen main reverse fault which shows a splay into three major faults. Mineralized ore veins are located in the hanging wall of the southern branch of the Siegen main reverse fault. The mineralization is structurally controlled and hosted by reactivated siderite-quartz veins and reverse faults. In this study, we focus on early $D_2$-Co-Ni-Cu-Au-ore bearing siderite-quartz lodes of the abandoned Alte Buntekuh mine which we have portrayed in 3-D and structurally analysed utilizing AutoCAD and Datamine Studio software. Modeling of the ore bodies was carried out in two steps: Structural features were digitized in AutoCAD. Linking of point and string data and the intersection of the DTM, fault- and ore body-wireframes were done with Datamine Studio. Our 3-D ore body model combines historical, geological, structural, and mineralogical information that facilitates new insights into the genetic evolution and structural control of Co-Ni-Cu-Au-mineralization. The model forms the basis for further evaluation of the ore potential with respect to possible ore body extensions in hitherto non-explored depths.

**Keywords.** Siegerland mining district**,** Co-Ni-Cu-Au-mineralization, ore body modeling, structural analysis.

## 1 Introduction

The Siegerland district is located in the fold- and thrust-belt of the Rhenish Massif from which is known for a diversity of syn- to late orogenic mineralization styles. The geology of the region is complex due to regional metamorphic overprint accompanied by intense structural deformation. Peak-metamorphism and deformation occurred at 312-316±10 Ma (Ahrendt et al. 1978) at PT-conditions of 280-320°C and 0.7-1.4 kbar (Hein 1993). In addition to $D_1$-syn-orogenic siderite-quartz mineralization, at least four additional syn-to late-orogenic mineralization stages are identified, comprising Co-Ni-Cu-Au, Pb-Zn-Cu, Sb-Au, and hematite-digenite-bornite ores (Table 1, Hellmann et al. 2012).

In this study, we investigated the structural setting of Co-Ni-Cu-Au-mineralization that belongs to the early $D_2$-mineralization stage, utilizing AutoCAD 2013 and Datamine Studio3 software. The main aim was to, firstly, develop a 3-D ore body model of the abandoned Alte Buntekuh mine and, secondly, to use this model for the analysis of the genetic evolution and structural control of the mineralization.

The former consolidated Alte Buntekuh mining license had a size of 381,035 $m^2$ (Kreutz 1922). Mining of iron ore started in the 17th century. Soon after the discovery of cobalt ore in 1790, the mine became one of the major Co-producers of the Siegerland district. The mine was shut down several times due to decreasing demands for Co used in the manufacturing of smaltite and declining commodity prices. Co-mining ceased in 1856 on account of the increasing importance of artificial ultramarine (Franz 1925). Artisanal mining proceeded discontinuously until 1903 (Kreutz 1922).

Fourteen different ore vein segments are known from the Alte Buntekuh area (i.e. Franz 1925). The main lode, a 6 m wide reactivated siderite-quartz vein, is the most prominent mineralized structure, trending NE-SW and dipping steeply to the NW. The Grenze vein represents a cobalt-mineralization bearing quartz lode that dips to the SE, oppositely to the main lode and parallel to the major reverse faults. A copper bearing vein, the Kupfer vein, is steeply dipping to the NW and runs subparallel to the main lode.

## 2 Geology

The Rhenish Massif is part of the Rhenohercynian zone of the mid European Variscan Orogen. Deposition of sedimentary and volcano-sedimentary units mainly occurred in a passive continental margin setting from Gedinnian to Upper Carboniferous. Due to a NW-SE directed compression during the Variscan Orogeny, the general structural trend is NE-SW (Franke 1989).

The rock-sequences within the Siegerland district consist of thick sediment-layers of the Lower-, Middle- and Upper Siegen (Lower Devonian). Marginal zones show rocks of Emsian ages (Middle Devonian). Sediments of the lower Siegen beds, which are dominated by shales, are the host rocks of the Alte Buntekuh ore veins.

Within the Siegerland district, the Siegen main reverse fault and associated parallel faults are the most significant structural features. The reverse fault is more than 140 km long and shows an offset into three, NE-divergent paths.

The ore veins of the Alte Buntekuh mine are located in the hanging wall of the southern branch of the Siegen main reverse fault. In the Siegerland district, different mineralization styles (cf. Table 1) are related to three main deformation stages, $D_1$ to $D_3$ (Hellmann et al. 2012). During $D_1$, a N-S and E-W trending diagonal shear vein system formed, hosting siderite-quartz mineralization, which was reactivated during $D_2$. Deformation stages $D_2$ (late) and $D_3$ are characterized by E-W trending vein systems and fault fill veins. (Oblique) reverse faults, kink-bands and strike slip faults are recognized. In general, veins showing an original orientation of N-S dip to the west. E-W-trending veins are characterized by a dip direction to the south.

The reactivated siderite-quartz veins of the first stage as well as reverse faults host the Co-Ni-Cu-Au-mineralization of the Alte Buntekuh mine. The main ore lodes show a predominant dip direction to the NW. In contrast, the majority of faults dip to the SE. Dip angles vary (mostly) between 35° to 70°.

**Table 1. Structures, veins and mineralization styles of the different deformation stages within the Siegerland district (Hellmann et al. 2012)**

| Deforma-tion stage | Structures | Veins | Minerali-zation |
|---|---|---|---|
| $D_1$ | NE-SW trending folds, $F_1$, $S_1$, reverse faults | diagonal-shear vein systems hosting E-W and N-S trending fault fill veins | siderite-quartz |
| $D_2$ (early) | $F_2$-folds, $S_2$, reverse faults, minor thrusts | reactivation of diagonal-shear vein systems, fault fill veins, NW-SE trending veins | Co-Ni-Cu-Au |
| $D_2$ (late) | $S_2$, reverse faults | E-W trending vein systems, fault fill veins | Pb-Zn-Cu |
| $D_3$ | $F_3$-folds, $S_3$, kink-bands, oblique reverse faults, strike slip faults | E-W and NW-SE trending veins, fault fill veins | Sb-Au |
| | | E-W and NW-SE trending veins | hematite-digenite-bornite |

## 3 Methods

Basic data was taken from historical mine level plans, geological maps and topographical maps. The three main levels are the Adler level (213.419 m), the Grenze level (238.269 m) and the Alte Buntekuh level (260.019 m) (cf. Figure 1). In total, 31 faults and 49 ore vein segments have been modeled.
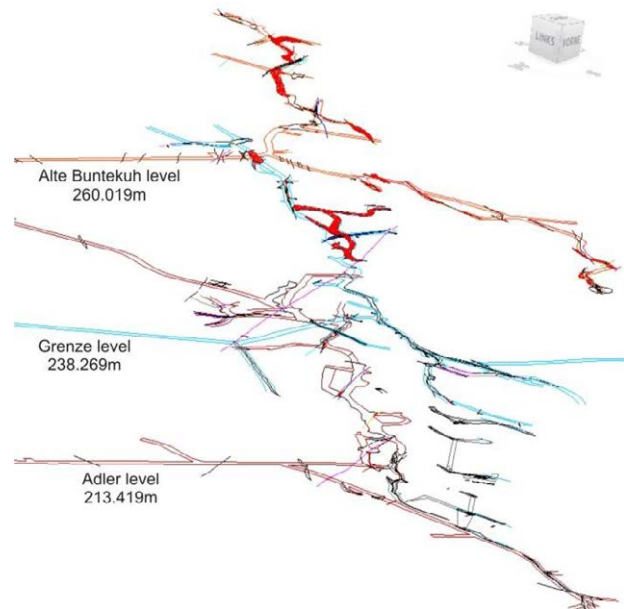


**Fig. 1**. Area of investigation (AutoCAD) showing the three main levels of the mine (red = Alte Buntekuh level, blue = Grenze level, brown = Adler level)

### 3.1 AutoCAD

At first, mine level plans were imported in raster-format into AutoCAD 2013. The plans were subsequently scaled, rotated to the appropriate northing and were moved to the WGS84 coordinate system (UTM). Special attention was given to the superimposition of the structural features and infrastructures shown on the mine level plans.

To simplify the subsequent export to Datamine, topography isolines, faults, ore body outlines and adit-floor lines were digitized on separate layers, respectively.

Correlations of structures within the different depth levels were made, beginning with the faults (2-D-polylines). Regarding large faults like the western or eastern main reverse faults, the correlation was obvious because fault segments are identified within all three levels. For smaller faults, mostly a single structure within one layer was indicated within the maps. The structural features were projected down- and upwards with the aid of dip directions and dips recorded on the mine level plans. Intersectional features of structures were honoured during the modeling process. Closed polylines were generated from parallel fault lines.

Ore body outlines (2-D-polylines) were correlated and edited subsequently. However, geometrical variations within the different depth levels rendered a

direct correlation difficult. A duplication of ore vein segments was made for modeling purpose, where no spatial information of the ore body position could be gathered. Additional spatial information was taken from historical literature (Franz 1925). Numerous cross-cuttings of distinct ore bodies were observed.

Further modeling was done with Datamine Studio.

## 3.2  Datamine Studio3

In Datamine Studio, at first the Digital Terrain Model as well as fault and ore body outlines were imported as .dxf files and loaded subsequently. For orientation purposes, the Adler, Grenze and Alte Buntekuh adits were also imported and loaded into the Datamine project.

Each structural feature was modeled on a separate wireframe, using the before imported point and string data. The advantage of separate wireframes is the possibility to intersect and inspect the structures individually. To obtain flat plains of the modeled structures, tag strings were created before linking the faults and ore bodies. Thereby, tag strings connect the different sub-levels of structural features. Subsequent linking caused fewer errors due to these strings. Faults were modeled as 2-D plane structures, ore bodies as 3-D bodies, showing varying geometries. Concerning the ore bodies, the upper- and lowermost limitation was closed.

Opposite dip directions of faults and ore bodies as well as geometrical variations caused cross-cuttings of two or several structural features. Therefore, intersections of these structures were made which generated two new wireframes, including the upper und lower part of the dissected object, respectively.
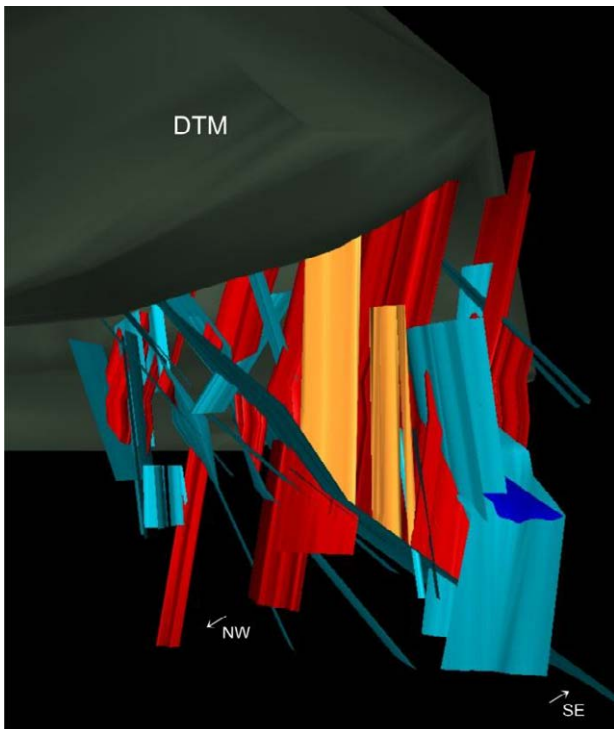


**Figure 2.** Datamine Studio image showing the major part of the 3-D ore body model including the DTM, siderite-quartz veins (red), dipping to the NW; faults (turquoise); copper-vein (orange); quartz-siderite vein (blue), highly enriched in Co

After the first modeling phase it became obvious, that several faults were too short to be intersected properly with the respective ore body. In AutoCAD, these structures were adapted, referring to historical maps and, subsequently, modeled again in Datamine.

As the data base mostly relies on historical data, several assumptions had to be made for modeling. Faults, only marked within one level, have been projected to quite short distances (10-20 m). Values for dip directions and dips were estimated from geological knowledge and personal observations. For ore bodies, a subdivision of dips and according dip directions into four different parts was made. Three parts thereof show a NW dip direction and a dip angle of 70°-80°. The intermediate segment between 236 m and 246 m is dipping steeply (85°) to the SE.

## 4  Discussion and Results

The majority of faults strike parallel to the Co-ore shoots (ENE-WSW). Fault-pole point maxima of a stereo net plot indicate dip directions and dips of 156/44° and 136/78°, and less frequent 135/59°. They represent oblique reverse faults, locally known as Western Main and Eastern Main Faults as well as smaller-scale sub-parallel faults. In addition, a number of smaller vein-bounding faults are randomly orientated. Particularly, in the northern part of the Alte Buntekuh level (260 m a.s.l.) short segments of steeply dipping (almost vertical) faults are developed. Formation of major faults is closely related to the first-order Siegen main reverse fault which is the most important structural feature within the Siegerland district. The fault shows a splay into three major faults, trending NE to ENE (Fenchel et al. 1985). According to Fenchel et al. (1985), dip angles vary between 50° to 70° with a dip direction to the SE. Dip angles and dip directions of the majority of faults in our model are in accordance with the orientation of the Siegen main reverse fault. Thus, these SE-dipping faults are interpreted as (smaller/second-order) branches of the first-order Siegen main reverse fault. Structural data on historical mine level plans also point to the presence of the larger SE-dipping faults.

The 3-D ore body model (Figure 2) shows that the earlier siderite-quartz veins (red), dipping steeply to the NW, are cross-cut and segmented by oppositely dipping oblique reverse faults. Several ore body segments are rotated and displaced, showing a plunge direction to the SW. The ore bodies are bounded by the reverse faults.

The Grenze vein, a cobalt-quartz vein, is exceptional compared to the other ore veins in that it dips to the SE (about 130°), in the opposite direction to the Alte Buntekuh main load. According to the 3-D ore body model, the Grenze vein is displaced by the Western Main Fault. The vein segment in the hanging wall of the Western Main Fault is displaced to the NW. Geological field observations show pinching and swelling of the vein width in the fault zone, indicating a formation of both structures during the same deformation stage.

It can be seen from the 3-D ore body model that the Grenze vein and several ore body segments of the main lode merge below the deepest mine level, the Adler adit.

Further high grade cobalt mineralization is expected to occur in this intersection zone below the deepest mine level.

Furthermore, hook-like, folded vein arrays, highly enriched in cobalt mineralization, can be interpreted from the model. The most significant one is the Bogentrum in the south-western part of the Alte Buntekuh mine (cf. Figure 1 between the Adler and Grenze level). Contrary to the plunge of $F_1$-folds, these hook-like vein arrays show a fold-axis plunge of 45° to 65° to the SW and W. The hooks are the result of movement between two oblique reverse faults, leading to oblique extension parallel to the fold axis.

Historical mine information terminates at a depth of about 213 m, i.e. the level of the Adler adit. However, our 3-D ore body model predicts the continuation of the ore veins to much greater depths. This leads to the conclusion that the depth extension of the mineralized zone is much larger than previously known. Especially the ore bodies of the second NE-vein segment which at their upper parts are enclosed by the Western and Eastern Main faults may represent potential target areas for further exploration. In addition, the angle between the Eastern and Western Main Fault opens to depth which could indicate an increase in the length of the enclosed ore bodies.

Our 3-D model combines historical mining information with new geological and mineralogical data and provides new insights into the structural evolution of Co-Ni-Cu-Au-mineralization. It can be used to evaluate further mineral potential of the area. The 3-D ore body model is also vital for resource calculation and the design of a brown-fields drilling program.

## Acknowledgements

## References

Ahrendt H. Hunziker J.C. Weber K. 1978. Age and degree of metamorphism and time of Nappe emplacement along the Southern Margin of the Damara Orogen/ Namibia (SWAfrica). *Geol. Rdsch.*, 67, *2*: 719-742

Fenchel W. & Lusznat M. 1985. Tektonik. In: Fenchel et al. 1985. Die Sideriterzgänge im Siegerland-Wied-Distrikt: Geologische Übersicht:. *Geologisches Jahrbuch, Reihe D*, 77: 43-63

Franke W. 1989. The mid-European segment of the Variscides: tectonostratigraphic units, terrane boundaries and plate tectonic evolution. *Geological Society, London, Special Publications 2000*, 179: 35-61

Franz M. 1925. Beschreibung der Bergwerke Alte Buntekuh, Auguste und Hermannsburg bei Niederschelden im Bergrevier Siegen. Printed by W. Vorländer

Hein U.F. 1993. Synmetamorphic Variscan siderite mineralization of the Rhenish Massif, Central Europe. *Mineralogical Magazine 57*: 451-476

Hellmann A. Wagner T. Meyer F.M. 2012. Structural setting of syn- to late orogenic Variscan hydrothermal mineralization, Siegerland district, Rhenish Massif (European Variscides, NW Germany). *Conference Proceedings Geologica Belgica*

# 3 & 4D geomodeling applied to mineral exploration

J.J. Royer, P. Mejia, G. Caumon, & P. Collon-Drouaillet
*Université de Lorraine-ENSG, CNRS-Georessources, Vandoeuvre-Lès-Nancy, France - Email: royer@gocad.org*

**Abstract.** 3 & 4D geomodeling is a computer method to construct the geometry and the deformation history of geological formations. Developed as an exploration tool in oil and gas, it begins to be applied nowadays in mineral exploration. After summarizing the basic notions, concepts, and methodology of 3&4D geomodeling, we describe its application to mineral resources assessment and to the modeling of ore deposits. A 3&4D GeoModeling case study of Kupferschiefers, Foresuedic Belt (Poland, Germany), achieved during the EU FP7 ProMine research project, illustrates the methodology. Perspectives and recommendations on applying 3&4D geomodeling in mineral resources appraisal are given in conclusion.

**Keywords.** Resource modeling, CAD, GOCAD, restoration, mineral resources, ore deposits, Kupferschiefer, ProMine.

## 1  Introduction

3 & 4D geomodeling is used as an exploration tool to better understand mineral resources appraisal, both at the mining exploitation and exploration stages. Several packages are available for processing datasets acquired during mining exploration and exploitation such as GIS and geomodelers (Bonham-Carter, 1994; Mallet, 2002). Among them, the most used are: the 3D Geomodeler (Geomodeler, 2012) from BRGM and Intrepid, GOCAD/SKUA from Paradigm (2012) for geological applications, GOCAD Mining Suite from Mira Geoscience (2013) for mining, MicroMine (2012), Move3D from MidlandValley (2012), Surfer (2012), Petrel from Schlumberger (2009), Surpac and GEMS from Geovia (2013), a subsidiary of Dassault System, and Vulcan (Vulcan, 2012) from Maptek. Only one or few specific modeling applications are treated by the above software; none of them can encompass all tasks required in an integrated mining study (i.e. structural geology, geobody modeling, restoration, geophysical inversion & interpretation, geochemical analysis, resource & reserves estimation, mine planning, design and risk and environmental impact mitigation). Such a general-purpose modeling framework is nonetheless relevant as observed by McGaughey (2006), Caumon et al. (2009) and Caumon (2010). Basic geo-modeling notions and concepts do not depend on the software package used, although some aspects are more or less exposed to the user depending on the software package and its underlying technology. After a short presentation of geomodeling to beginners, we will present examples obtained on the GOCAD software platform during the EU FP7 ProMine research project on several European belts, including Fennoscandinavia (Finland, Sweden), Hellenic (Greece), Iberian Pyrite Belt (Spain, Portugal) and Fore-Sudetic monocline (Poland).
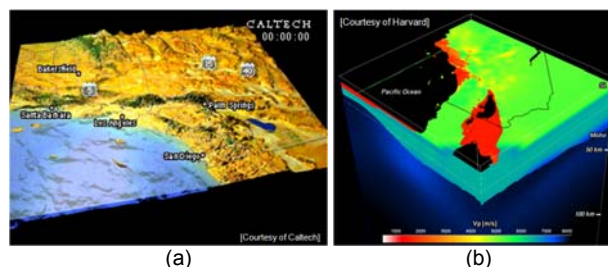


**Figure 1.** Earthquake simulation (a) and velocity model (b) in the Los Angeles basin. GOCAD was used to build the crust and upper mantle velocity model for predicting seismic risk (From Tape et al, 2009 and Plesch et al, 2009).
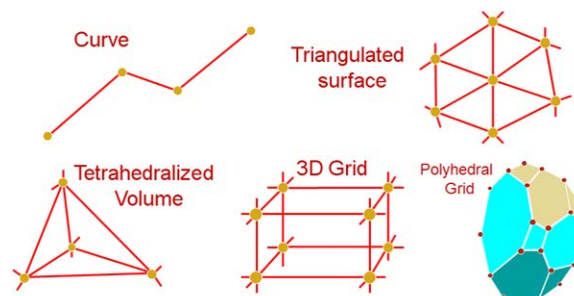


**Figure 2.** Basic elements used to build discrete geo-objects. The topology is the set of connections or links between nodes.

## 2  Introducing 3D GeoModeling

Geomodeling, a term coined in the 90's to name computer techniques used to build 3D models (Mallet, 2002) have been extensively used in the geosciences (Fig. 1). The different basic notions involved in geomodeling will be explained in the following.

### 2.1  Geometrical Elements (micro-topology)

The basic simple elements used in geomodeling are:
- *Point*: location defined by coordinates X, Y, Z.
- *Curve*: points linked together by segments, may content several components (i.e. contours map).
- *Triangle*: three linked points; a set of adjacent triangles form a triangulated surface (TSurf), which may have several connected components (e.g., one per fault block in the case of lithological contact).
- *Tetrahedron*: four points linked together delineate an elementary volume called a *Tetrahedron*; a set of tetrahedra form an unstructured grid delimitating a volume. Such tetrahedral meshes are a classical support in the finite element method.
- *Rectangular prism* (or Voxel): a cube may be deformed so as to form an elementary hexahedron cell; when the cells are all identical (same sizes) and adjacent together, they delimitate a regular Cartesian Grid. Prisms may also be deformed to fit curvilinear stratigraphic formations (SGrid).
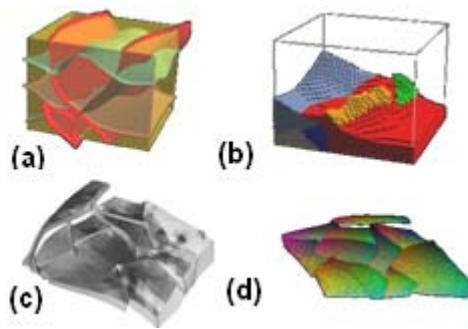
**Figure 3.** From left to right: Surface models; Regular rectangular grid model (sugar box or Voxet); regular deformed cells (SGrid or stratigraphic grids); tetrahedral cells.

- *Polyhedral cell*: irregular cells whose juxtaposition forms unstructured grids.

## 2.2 Notion of Topology

Topology relates to the *connections* and *relative layout* between objects. It refers to object properties that are preserved under continuous transformations (including stretching, shearing and bending, but not *tearing*). For instance during a tectonic episode, the topology remains constant if the number of faults and faults connectivity remains constant in this model (i.e. the number of fault blocks in the horizon does not change).

## 2.3 Notion of Properties

Geomodeling needs to process categorical (rock types, alteration types) and quantitative properties (grade, thickness, etc…). In discrete models, properties or attributes are stored at the node location (Fig. 2) or at the center of cells.

## 2.3 Notion of Regions

In geomodeling, the concept of region is very useful to consider object's subsets for processing and querying tasks. In quantitative geology, regions are often represented by an indicator formalism, whereby a point or cell belongs to a region if its indicator value is equal to 1 and outside the region if the indicator is equal to 0. Regions may be defined according to various criteria which can be geometric (above, nearby a surface), defined using a property (grade greater than a cut-off), or using a categorical property (rock type). The BGS, British Geological Survey, the Geological Survey of Denmark and at the Canadian Geological Survey are using triangulated surfaces and regular grids as well as regions to represent and query 3D geological structures.

## 3 Introducing the 4D Modeling

Structural restoration has developed rapidly during these last two decades. It has been used to identify favorable target mother and host rock formations, to reconstitute fluid migration in oil and gas surveys and to predict faults and fracturing in the rock mass (Novoa et al., 2000; Sanders et al., 2004).
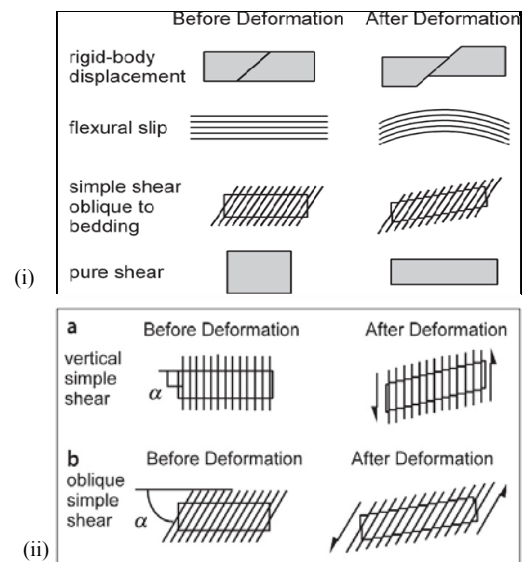


**Figure 4.** (i) Various basics restoration kinematic models; (ii) Simple shear oblique to bedding a) Vertical simple shear; b) Oblique simple shear (after Groshong, 2006).

## 3.1 Restorable and non-restorable models

A *restorable* model can be unfolded and deformed perfectly to its original pre-deformation geometry. Its geometry is internally and topologically consistent. A non-restorable structure cannot be flattened according to classical rock deformation principles and therefore is geologically questionable (Dahlstrom, 1969).

Chamberlin (1910) was a pioneer in performing a restoration of geological cross sections using the surface conservation principle (keeping areas constant).

Later, this concept has been expanded to constant volumes by Dahlstrom (1969). Several elementary deformation style models (kinematics models) are usually investigated including: rigid-body displacement, flexural slip, simple shear and pure shear (Fig. 4):

- *Block rigid* deformation, the simplest one, restores the un-deformed shape by translations and rotations of elementary blocks until they fit together;
- *Flexural slip* involves slip along bedding planes or along foliation surfaces keeping constant the individual strata thickness (unless otherwise specified) and the resultant folds being parallel. It preserves in a vertical plane the area of the structures to be restored, their lengths and thicknesses (Moretti, 2008).
- *Simple shear* is produced by slip on closely spaced parallel planes with no parallel or perpendicular to the slip planes length or thickness changes. *Simple shear* parallel to bedding is equivalent to flexural slip. *Simple shear* that is oblique to bedding causes bed length and bed thickness changes. Simple shear method preserves distances in the shear direction, but length and thickness are not necessarily kept constant, consequently the area is not preserved.
- *Pure shear* is an area-constant shape change for which the shortening in one direction is exactly balanced by orthogonal extension (Groshong, 2006).
- *Flexural slip* and the simple shear are available in the restoration module know as KINE3D-2 of the geomodeler GOCAD® (Moretti, 2008).

Block rigid deformations, simple and pure shearing, and geomechanical modeling are implemented both in 3DMove (Midland Valley, 2012) and GOCAD®.

### 3.2 Discussion and Perspectives

4D modeling have been proved to be helpful applied in many exploration situations in oil and gas exploration, but is still in its early beginning when applied to mineral exploration. Nevertheless, 3&4D approaches provide significant improvements in better understanding the geological background of the mineralization zones. There is a growing interest in many parts of the world, including Europe, regarding the 4D modeling and its importance for the future availability of mineral resources. Challenges for future research in the 3&4D geomodeling area are: (i) a geological 3D model is never complete; it is changing all the times with the acquisition of new data and new ideas, and automatic procedures would be helpful in up-dating geomodels when new data are acquired; (ii) current 3&4D software enables performing 4D geological structures modeling, although, in case of more than two deformation phases, or intrusive ore body, 4D modeling remains very difficult, especially in igneous complex contexts.

## 4 The Fore-Sudetic belt, Poland

The Poland Kupferschiefer, a sediment-hosted polymetallic (Cu, Ag, Au, PGE) deposit, is one of the most important sources of silver and copper in the world, and may be a future provider for Europe in some critical strategic commodities (Re, PGE). The Kupferschiefer ore combines several geological singularities like the existence of organic matter, overlaying by thick evaporitic rocks and a placement near basement/cover unconformity.

Several studies (see Hartsch (2013) for a review) indicate that the Kupferschiefer deposit in Central Europe is the result of two or more superimposed mineralization events mainly during Permian and the inversion of the basin at Alpine times.

A 3D geomodel based on regional interpreted vertical geological cross-sections, more than 280 wells and two contour lines maps of the bottom of Zechstein from the KGHM database, has been built on the Lubin area. Then, a sequential geologic restoration-decompaction from the Upper Permian to Cenozoic was conducted using flexural slip assumptions in the Lubin-Sieroszowice district of Poland using the 3&4D restoration methodology described in §3 (Fig. 5). The restoration of the whole sedimentary pile provides indication on the pressure history of trapped fluids. It allows better understanding the hydraulic fracturing stage within the base of Zechstein shales, which occurred during an inversion phase at the Late Cretaceous-Early Paleocene time (Fig. 5).

A hydro-fracturing index is then calculated from the estimated overpressures during this uplifting, and seems to correlate with the copper content distribution in the ore-series. These results are in agreement with an Early Paleocene dating in the Germany part of the Kupfer-schiefer ore, which perhaps represents the last mineralizing stages (Fig. 6).
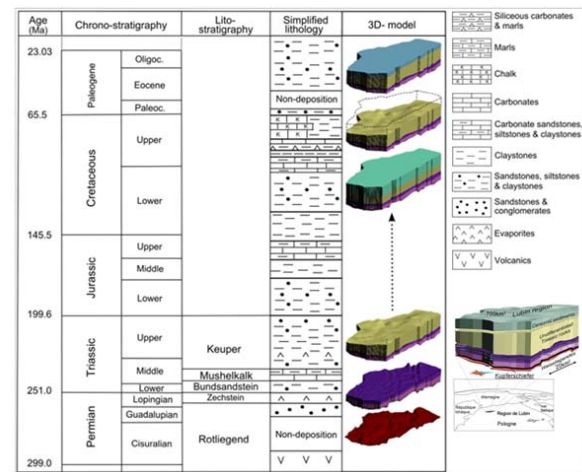


**Figure 5.** Reconstitution of the Kupferschiefer - Forsudetic basin/Poland evolution through the geological times (After Mejia and Royer, 2012b)
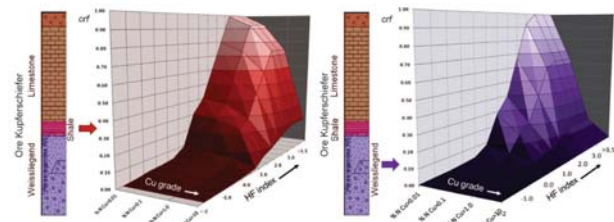


**Figure 6.** Correlation between the copper content and hydro-fracturing index (HF). Cu content rises abruptly for HF >0.

This Late Cretaceous uplifting yields the conditions for hydrothermal recirculation of mineralizing brines explaining the location of Cu (Cu-Fe) sulfides ores in the area. The restoring-decompacting procedure allows reconstituting the burial, deformation and natural hydro-fracturing history of the Foresudetic basin (Mejia and Royer, 2012).

## 5 Discussions and Conclusions

Various case-studies related to mineral exploration or/and mining using different 3&4D geomodeling tech-nologies have been investigated during the ProMine project. They demonstrate that new geomodeling methods, tools and ore potential mapping are now commonly used in subsurface and structural geology interpretations. 3&4D geomodeling technologies contribute in improving knowledge and understanding of the mineralization zones. In ore exploration, they provide new ideas and methods for helping in making new discoveries. Since now half a decade, there has been a growing interest regarding the 4D modeling as a tool for investigating future availability of minerals in Europe. Beside this ideal picture, work ahead remains to explain stakeholders the benefit of these new technologies, to make them fully accepted by the mining industry and to further improve geomodeling technology applied to mineral resources. Firstly, improvements can be made on the technological point of view:

• Most of 3D models in mining exploration are based on the surface data and very few drill holes. a geomodel reflects the present knowledge at the moment the model is built. Building such a model

calls for hypotheses and significant uncertainty may therefore exist in terms of concepts. Of course, 3D models are never complete as they evolve as soon as new data are acquired. It is therefore primordial to retrieve 3D models including metadata describing location of available data, quality of data and assumed hypotheses.

- Models evolve through time, it is therefore important to benefit of simple procedures and technologies making data model updating as simple as possible. Present workflows are more or less linear making up-dating complicated and time consuming, especially in 4D. More research is needed in this field.
- Data quality and uncertainty are important issues in geomodeling. Advanced visualization techniques must be investigated (colors, textures, sounds, animation, see Viard et al. (2011)).
- Mineral resource exploration handles data coming from different sources such as drilling, sampling in galleries, chemical analyses, etc… or indirect measurements or modeling such as from geophysics. These data are heterogeneous and specific methods are needed to integrate them on the same platform.

Secondly, improvements must be made in the European infrastructures related to deep mineral resource exploration in order to benefit from new technologies. A hand to hand cooperation between mining companies, software providers, public research institutes and geological surveys was made possible during the ProMine project. It has been a catalysis place where good talents from different areas and disciplines worked closely together as a team with common interests and not as isolated units. However, this move must be strongly sustained and encouraged in the coming years.

## 6 Conclusions

Geomodeling is a technology of choice to integrate subsurface information into a consistent quantitative interpretation. The development of time-varying models additionally opens new perspectives to better understand mineral deposits and define exploration targets. It is too early (and may be confidential because of economic interests issues) for clearly identifying 3&4D modeling success stories of the ProMine project which has lead to a major mineral resources discovery. Nonetheless, we are convinced that some indirect discoveries or advances would be made soon, confirming the add-on value of geomodeling to mineral exploration. Publication of discoveries of mineral extensions based on 3D models would benefit the whole mining community.

## Acknowledgements

## References

Bonham-Carter G. F (1994) - *Geographic Information Systems for Geoscientists: Modelling with GIS*. Computer Methods in the Geosciences. Pergamon Press, New York, 414p.

Chamberlin R.T. (1910) - The Appalachian folds of central Pennsylvania. *Journal of Geology*. 18, 228-251

Caumon G., Collon-Drouaillet P., Le Carlier de Veslud C., Viseur S., Sausse J. (2009) - Surface-Based 3D Modeling of Geological Structures. *Mathematical Geosciences*, **41**(8), 927-945.

Caumon. G (2010) - Towards stochastic time-varying geological modelling: *Mathematical Geosciences* **42**(5), 555-569

Dahlstrom C.D.A. (1969) - Balanced cross sections. Canadian *Journal of Earth Sciences*, **6**, 743–757

Geomodeler (2012) - Intrepid vendor of 3D geomodeller. URL http://www.geomodeller.com

Geovia (2013) – Virtual planet. http://www.3ds.com/products/geovia/

Groshong R. (2006) - *3-D Structural Geology: A Practical Guide to Quantitative Surface and Subsurface Map Interpretation.* Springer, Heidelberg. 400p

Hartsch J. (2013) - Copper Mineralisation at the Zechstein Basis in the North-Sudetic Trough and Geological Model – An Introduction. Springer, (in Press), 23p.

Mallet J.-L. (2002) - *Geomodeling. Applied Geostatistics.* Oxford University Press, New York, NY, 624 p.

McGaughey J. (2006) - The Common Earth Model: A Revolution in Mineral Exploration Data Integration. In: J. Harriss (Ed), GIS for the Earth Sciences, SP 44: 567-576, Geological Association of Canada, St John, NL, Canada.

Mejia P. and Royer J.J. (2012) - Explicit Surface Restoring-Decompacting Proccedure to Estimate the Hydraulic Fracturing: Case of the Kupferschiefer in the Lubin Region, Poland. 32th Gocad Meeting, Nancy, France, September, 19p.

MicroMine's consulting (2012) - http://www.micromine.com/

Midland Valley (2012) – Vendor of 3D Move. http://www.mve.com/software/move

Mirageoscience (2013) – Modeling the Earth. http://www.mirageoscience.com/

Moretti I. (2008) Working in complex areas: New restoration workflow based on quality control, 2D and 3D restorations. *Marine and Petroleum Geology*. **25**, 205–218

Novoa E., Suppe J. and Shaw J.H. (2000) Inclined-Shear Restoration of Growth Folds. *AAPG Bulletin,* **84**(6), 787–804

Paradigm (2012). Vendor of the Gocad suite. URL http://www.pdgm.com/

Plesch, A., C. Tape, J. H. Shaw, and members of the USR working group, 2009, CVM-H 6.0: *Inversion integration, the San Joaquin Valley and other advances in the community velocity model*, in 2009 Southern California Earthquake Center Annual Meeting, Proceedings and Abstracts, 19, 260-261

Sanders C., Bonora M., Richards D., Kozlowski E. Sylwan, and Cohen M., 2004, Kinematic structural restorations and discrete fracture modeling of a thrust trap: a case study from the Tarija Basin, Argentina. *Marine and Petroleum Geology*, **21**(7), 845-855

Schlumberger (2009) - Vendor of Petrel and Eclipse. URL http://www.slb.com/content/services/software/index.asp

Surfer 9 (2012) - Grapher, Didger, Mapviewer and Strater, Voxler http://www.ssg-surfer.com/

Tape, C., Q. Liu, A. Maggi, and J. Tromp, (2009) - Adjoint tomography of the southern California crust, *Science*, 325, 988-992

Viard T., Caumon G. and Levy B. (2011) - Adjacent versus coincident representations of geospatial uncertainty: Which promote better decisions? *Computers and Geosciences*, **37**(4), 511-520

Vulcan (2012) – Maptek vendor of Vulcan. URL: http://www.maptek.com/products/vulcan/

# Advances in 3D geological modelling of the Leon sediment hosted stratabound copper/silver deposit, NW Argentina

**Hector Santiago S Sanchez Rioja**
*Department of Geology, University of Buenos Aires. Argentina*

**Diana Irene Mutti**
*Department of Geology, University of Buenos Aires. Argentina*

**Abstract.** In recent years, a great number of mineral resource evaluations and estimations have been carried out on Argentinian project sites. The Leon Project is defined as a Cu and Ag stratabound type deposit and is one of the most-studied projects in northwest Argentina in terms of geological-economic studies. However, some aspects related to origin and control of mineralisation are controversial. This paper aims to point out the important advances we have achieved in 3D geological modelling, not only in the estimation of mineral resources, but also in providing tools which can help us reach a better knowledge of the controls of mineralisation and metalogenetic aspects of the deposit.

**Keywords.** Stratabound deposit, 3D Geological Modelling, Leon, Argentina.

## 1   Indroduction

Leon (formerly named Juramento), is one of the most important sediment hosted, stratabound copper/silver deposit in Argentina. It is located about 60km southeast of Salta City, NW Argentina (Fig 1). Alexander Mining (2006) established a JORC Code copper resource statement for Leon Project (El Cobre and El Plomo deposits) of 6.43Mt@0.64%copper and 17.9g/t silver for contained metal of 41,100t copper and 3.7Moz silver.

The Project has been classified by previous work as a sediment hosted, stratabound copper/silver deposit, with similar characteristics to world-class deposits like the copperbelt of central Africa and Kupferschiefer in central Europe (Espisúa y Amengual 1983; Wormald 1998; Peral and Wormald 1999; Gorustovich et al. 1999; Durieux and Brown 2007).

The generally accepted model for the genesis of the deposit involves the leaching and transport of metals from red bed sediments or interlayered basalts by basin brines. Brine migrates through permeable formations and structural conduits to trap sites and reducing environments, where copper is precipitated.

Leon has been explored by different mining companies, Pecomrio (1979-1980), Paramount (1994-1997) and recently Alexander Gold. This last company carried out a more detailed drilling campaign, totalising 17, 200 m of diamond core from 216 holes. The first results of the analysis of this information allow one to question the interpretations about the controls of mineralisation and the process linking to the genesis of the deposit where the role of the structure was underestimated.

The objective of this contribution is to highlight the relevance of 3D geological modelling in the determination of controls of mineralisation and the analysis of metalogenetic aspects of the Leon deposit. This study will provide powerful tools for the exploration and research of potential ore bodies within the project area.
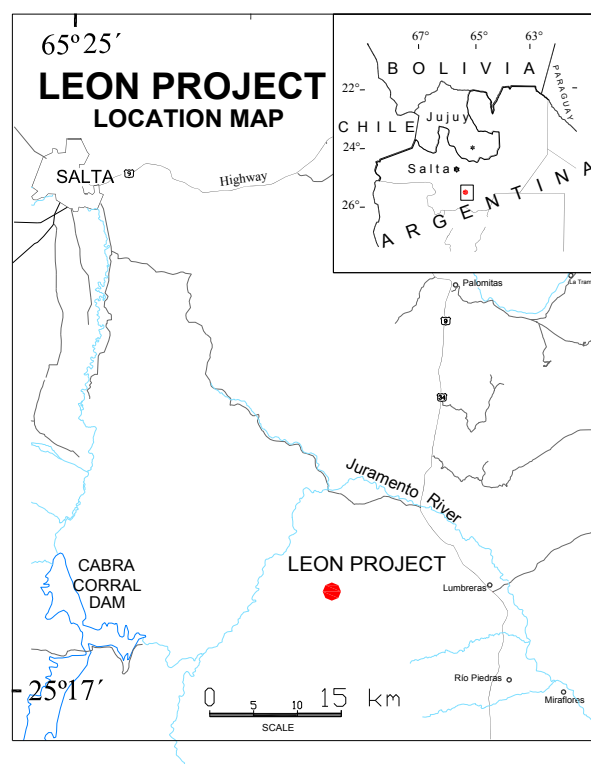


**Figure 1.** Location of Leon Project.

## 2   Geology Description

### 2.1 Regional geology

Leon deposit is located on Sub Andean Ranges, which comprises sub-parallel ranges of N/S trending in Northwest Argentina. These ranges are part of an active

thin-skinned fold and thrust belt and represent the easternmost expression of the Central Andes.

The Leon Project lies close to the eastern border of the major Upper Cretaceous to Eocene Salta Basin. During its development, the basin was filled by the Cretaceous Pirgua Sub-group sediments, which attained a thickness of over 3 km in the vicinity of the Project area. The Pirgua sub group comprises a sequence of red continental mudstones, sandstones and conglomerates with local rift-related alkaline basaltic rocks. The overlying Cretaceous Balbuena Sub-group contains the Lecho, Yacoraite and Tunal Formations that comprise basinal and terrestrial sedimentary rocks, which are succeeded by the Eocene Santa Barbara Sub-groups.

## 2.2 Geology of the deposit and mineralisation

The deposit comprises two north trending sub-parallel zones, hosted by the Lecho sandstone and the Yacoraite limestone and siltstone and is in the shape of a horseshoe, open to the northwest. The terms referring to the eastern and western zones are El Plomo and El Cobre respectively. El Plomo zone is truncated in the south by a fault, beyond which the Yacoraite Formation swings to the southwest along El Pelado ridge. The geology of the deposit is shown in Figure 2.
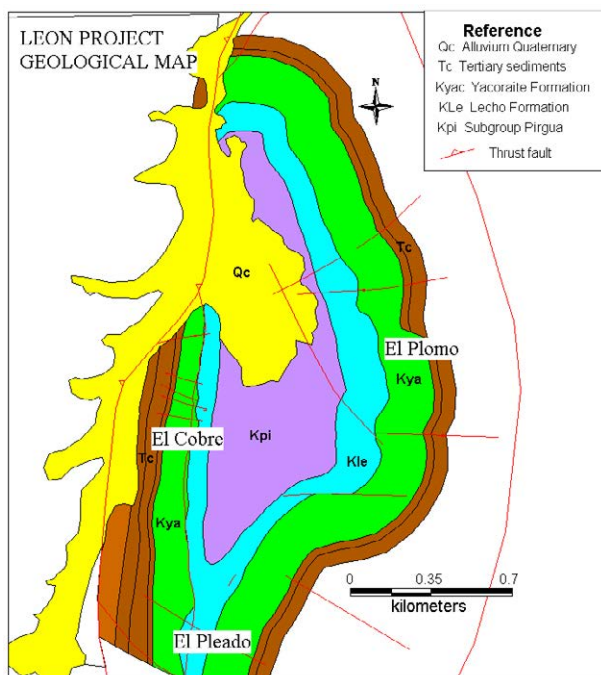


**Figure 2.** Geological map of Leon project.

Limestones of the Yacoraite Formation are the most resistant rocks and generally occupy the crests of the ridges. The rocks are extensively brecciated, especially on Cerro El Cobre. Less resistant Lecho and Pirgua Formations crop out on the ridge flanks and in the intervening valley. El Cobre and El Plomo zones converge to the north as the El Plomo ridge trends west.

The geometry of El Cobre, El Plomo and El Pelado

zones, together with outcrop and bedding data, suggest an original anticlinal fold closure to the north and possibly south of the deposit. Subsequent faulting and thrusting have disrupted the fold, resulting in the present geometry.

El Cobre Zone appears to be the most highly deformed sector of the deposit. Closely spaced transverse faults are visible on aerial photos in El Cobre Zone. These faults dislocate the deposit but do not apparently affect overall continuity of the mineralised zone.

The primary mineralisation generally occurs as veinlets and fine dissemination in the limestone dominated Lower Yacoraite and consists of bornite, tenantite, tetraedrite, chalcopyrite, chalcosine, galena, sphalerite and pyrite.

Supergene oxide predominantly comprises malachite and azurite, digenite (blue chalcosite) and covellite, iron and manganese oxides and complex, fine grained mixtures of oxides containing Cu, Fe, Mn, Pb, Zn, As and Sb. Secondary lead and zinc carbonates also occur in the oxide zone.

## 3  3D Geological Modelling

The 3D geological modelling of the Leon deposit was undertaken using information from the drilling campaign provided by Alexander Gold. The building of the 3D Model was carried out using Datamine Studio 3 (Exploration & Mining Software).

### 3.1    Data and Metodology

The work has been divided in three phases: 1) Modelling of lithological and alteration variations in the host- rocks 2) Modelling of structural features that controlled El Plomo mineralisation  3) Modelling of mineralogical zones (delineation of oxide, transition and sulphide zones).

The geological data used in this work includes: geological logs, digital geological map, a set of five thousand geochemical data from drill core samples, Digital Terrain Models (DTM) and geological field descriptions.

The methodology for lithological modelling was based on geochemical correlations from quantitative and qualitative analysis of chemical elements. This study was supported by geological descriptions of geological logs.

### 3.2    3D Lithological Modelling

Given the geological-structural complexity of the deposit, the work was divided into 4 regions:  EC Zone (El Cobre hill), EP_A Zone (El Plomo North Zone), EP_B (El Plomo Center) y EP _C Zone (El Plomo

South).

Analyses of geological field data and drill core data showed that the highest proportions of copper and silver were found in the zones of greatest structural complexity. This is the case of the EC and EP_B zones.
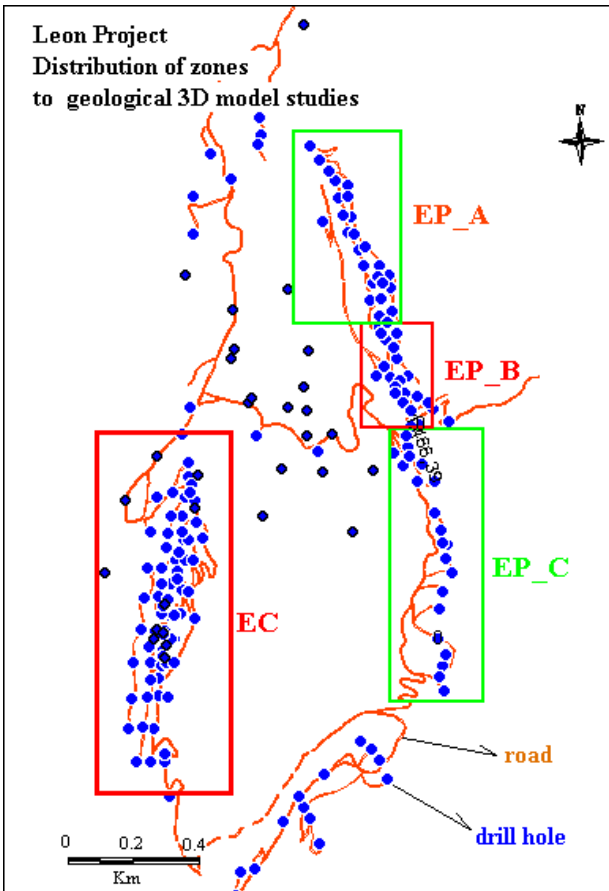


**Figure 3.** Leon Project: geological zones according to the structural complexity. The area in red indicates the zone with more deformation.

The work of lithological modelling began in the EP_A Zone and EP_C Zone. These only slightly deformed regions have therefore shown a good correlation between the lithological units. The copper and silver grade is low in these areas.

After the building of 3D solids of these lithological units, statistics analysis of copper and silver was made on each lithological unit. The results obtained were similar in all cases analyzed.

Inspection of cross sections from drill core data has enabled us to verify that the grade of copper bears little correlation to lithological units. In the part of the EP_A Zone near the EP_B Zone, a northwest fault associated to tectonic breccia that seems to have genetic relationship with the formation of the deposit was detected. Other post-mineralisation faults that produce displacements of the ore body were also identified; however, no detailed study has been carried out on the link between this structures and the mineralisation process (Figure 4).
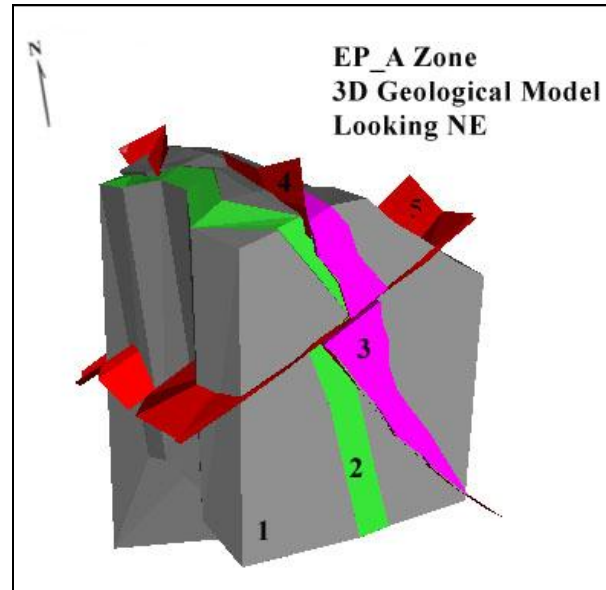


**Figure 4.** 3D Geological Model EP_A Zone looking NE. **1**: Yacoraite Formation; **2**: Marked bed; **3**: Mineralized envelope (> 0.6%Cu); **4**: Syn-mineralisation fault; **5**: Post-mineralisation fault.

## 4 Discussion

Leon deposit has broadly similar characteristics to red-bed associated copper deposits elsewhere (central Europe, central Africa) where the lithological and chemical characteristics were important in the processes linking source rocks-brine generation-fluid transport-trap sites and seals leading to mineral deposition.

At the project scale, the preliminary results of the 3D geological modelling have allowed to highlight the relevant control of structure in locating copper and silver mineralisation.

The strong link between geological-structural complexity zones and the main mineralised zone suggests an important structural control on processes that lead to mineral deposits in a discordant lens or pocket. This aspect has been frequently neglected in previous works.

The characterization of the geological variables through 3D geological modelling will allow a better knowledge of the control on mineralisation and will give powerful tools together with other techniques to understand the genesis of the deposit.

## Acknowledgements

# References

Alexander Mining (2006) Annual Report and Accounts, Alexander Mining.http://www.alexandermining.com/files/reports/Alexander_Mining_Annual_Report_2006.pdf

Espisúa E, Amengual R (1983) Juramento, un depósito estratoligado de cobre, plata y plomo, provincia de Salta, República Argentina. Facultad de Ciencias Exactas, Físicas y Naturales – Universidad Nacional de San Juan. Congreso Nacional de Geología Económica, San Juan. Actas 2: 71-90

Durieux CG, Brown AC (2007) Geological Context, Mineralization, and Timing of the Juramento Sediment-Hosted Stratiform Copper-Silver Deposit, Salta District, Northwestern Argentina. Miner Deposita 42(8): 879-899

Gorustovich SA, Marquillas RA, Matthews S, Sabino I, Salfity JA (1999) Depósitos estratoligados de Cu-U (Ag, Pb, Zn) en el sur de la cuenca del Grupo Salta (Cretácico-Paleógeno) norte argentino. Decimocuarto Congreso Geológico Argentino, Salta. Actas 2: 398-401

Peral MA, Wormald PJ (1999) Mineralización cuprífera del área Juramento, Salta. In: Zappettini E (ed.) Recursos Minerales de la República Argentina. Instituto de Geología y Recursos Minerales, Segemar. Anales 35, pp 951-957

Wormald PJ (1998) The Juramento stratabound copper-silver deposit. Séptima Reunión Argentina de Sedimentología, Salta. Actas de resúmenes: 46-50

# Integrated 3D mineral systems maps for iron oxide copper gold (IOCG) Deposits, Eastern Gawler Craton, South Australia

Simon van der Wielen, Adrian Fabris, John Keeling, Alan Mauger, Georgina Gordon, Tim Keeping, Phillip Heath, Gary Reed, Laz Katona, Martin Fairclough, Steven Hill
*The Geological Survey of South Australia, Department of Manufacturing, Innovation, Trade, Resources and Energy.*

David Giles
*The University of Adelaide, Deep Exploration Technologies Cooperative Research Centre.*

Scott Halley
*Mineral Mapping Propriety Limited*

**Abstract.** The eastern Gawler Craton hosts the giant Olympic Dam iron oxide copper gold (IOCG) deposit as well as other large IOCG deposits (i.e. Prominent Hill and Carrapateena). The region is covered by a thick sequence of Mesoproterozoic to Cenozoic sedimentary and volcanic rocks making the region difficult to explore using conventional methods. The project utilises high quality geoscientific datasets that have been systematically acquired by the Geological Survey of South Australia over the eastern Gawler Craton. Modern IOCG mineral system models are combined with the latest three dimensional geological mapping and data integration techniques to produce 3D mineral system maps. These maps provide a powerful new predictive tool to explore for IOCG-style mineralisation undercover.

**Keywords.** IOCG mineral systems, 3D modelling, data integration, geophysics, geochemistry, spectroscopy, HyLogger™, gOcad™, Gawler Craton.

## 1 Introduction

The Gawler IOCG belt is located along the eastern margin of the Gawler Craton and covering approximately 126,500 km$^2$ (Fig. 1). The belt hosts the giant Olympic Dam deposit, several large deposits and numerous prospects. Despite the proven mineral endowment the region remains largely under explored due to a thick sequence of Mesoproterozoic to Cenozoic sedimentary and volcanic rocks. This makes exploration using conventional methods costly and restrictive.

To assist IOCG exploration within the Gawler Craton a collaborative research project has been set up between the Geological Survey of South Australia (GSSA), University of Adelaide and the Deep Exploration Technologies Cooperative Research Centre. The project uses mineral system concepts (Wyborn et al. 1994) along with the latest data integration techniques to produce integrated IOCG mineral system maps from the vast trove of open file geoscientific data that has been systematically acquired by the GSSA.

## 2 IOCG Mineral System Model

There is still conjecture over processes of IOCG mineral system formation. It is generally regarded, however, that multiple fluids and metal sources play an important role in the formation of economic mineralisation (Williams et al. 2010).
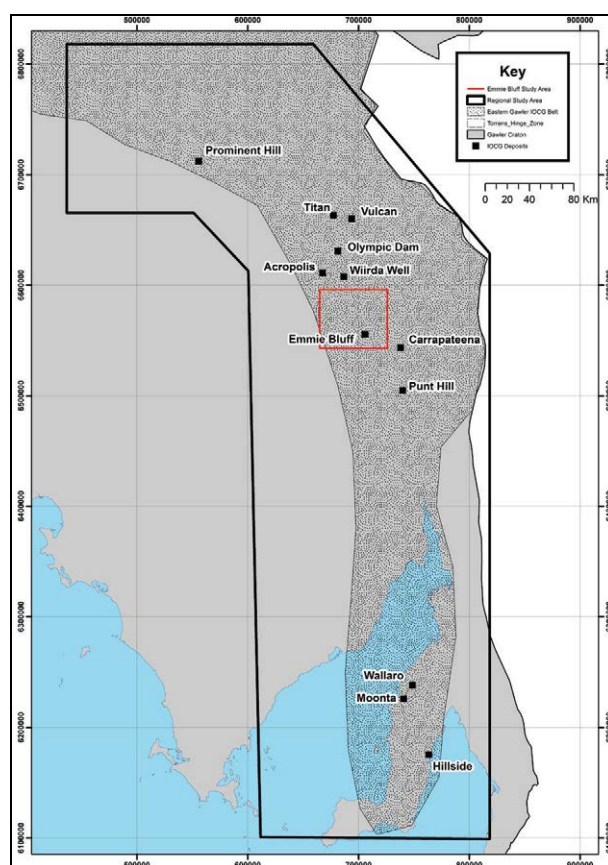


**Figure 1.** A locality map showing an outline of Gawler Craton, eastern Gawler IOCG belt and IOCG deposits in relation to the regional and Emmie Bluff study areas.

The following features are important in the formation of IOCG mineral systems within the Gawler Craton:
1. Melting of metasomatised mantle resulted in the emplacement of mafic intrusions along the eastern margin of the Gawler Craton. This also provided a source of metals and ligands and an energy source to drive hydrothermal fluids (Hayward and Skirrow 2010).
2. Meteoric water percolated through a rift package

containing thick sequence of evaporates producing dense oxide saline brine. The brine stripped out metals from the underlying rocks forming the characteristic distal Na-Ca alteration (e.g. albitisation) that is widespread in the belt (Bastrokov et al. 2007).

3. The mechanism for metal deposition for IOCG systems within the Gawler Craton is still unclear and may vary between deposits. The consensus is that metal deposition will occur at a change in redox conditions, either by fluid mixing or fluid wall rock interaction (Williams et al. 2010). Temperature, pH and ligand activity may play an important role in particular deposits (Bastrokov et al. 2007).

IOCG mineral systems have a characteristic pattern of zoned alteration that extends significant distances from the deposit (Fig. 2). K-feldspar-sericite forms the distal alteration assemblage and becomes progressively more intense towards the centre of the system. The deepest parts of the system have magnetite-biotite alteration assemblage. Higher in the system magnetite-chlorite alteration assemblage becomes dominate followed by hematite-sericite alteration that forms at the highest levels of the system (Fig. 2). Chemical modelling by Bastrokov et al. (2007) has shown that high grade copper and gold mineralisation tends to occur in regions where hematite has replaced earlier magnetite alteration.
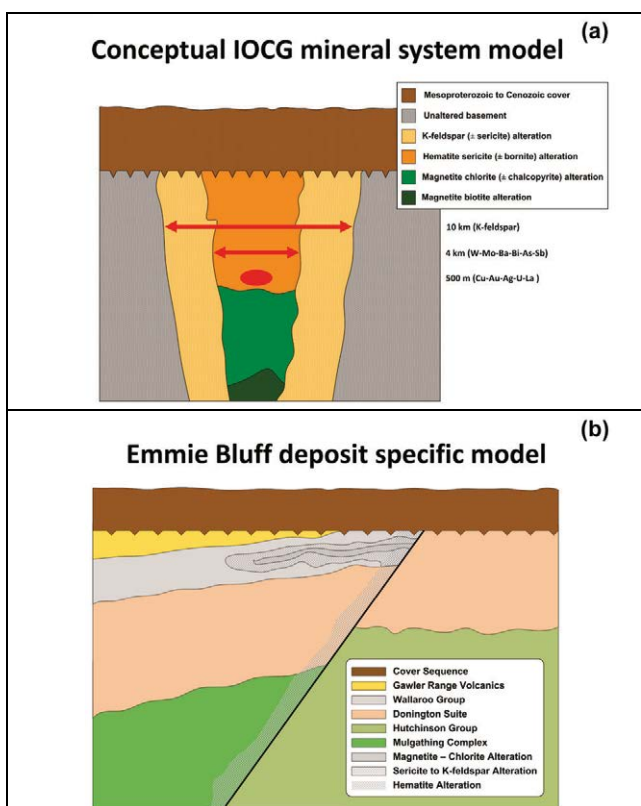


**Figure 2.** A conceptual mineral system model for granite hosted IOCG deposits (a); and an alteration model for Emmie Bluff IOCG deposit.

# 3 Workflow

A workflow to map IOCG mineral systems in 3D has been developed:
1. Construction of a 3D geological map. This is used as a container to integrate geophysics, geochemistry and spectral data, and to query and visualise results.
2. Mapping hematite and magnetite in 3D using potential field inversions.
3. Mapping chlorite, sericite, K-feldspar, albite in 3D with geochemistry and spectral data.

# 4 Construction of 3D geological map

Three dimensional geological surfaces were built in gOcad™ using solid geology, drill hole stratigraphic markers, and seismic data (Fig. 3a). The geological surfaces were converted into geological block model (Fig. 3b) so that other proprieties such as geochemistry, spectral, potential field and petrophysical data can be integrated with geology, queried and visualised.
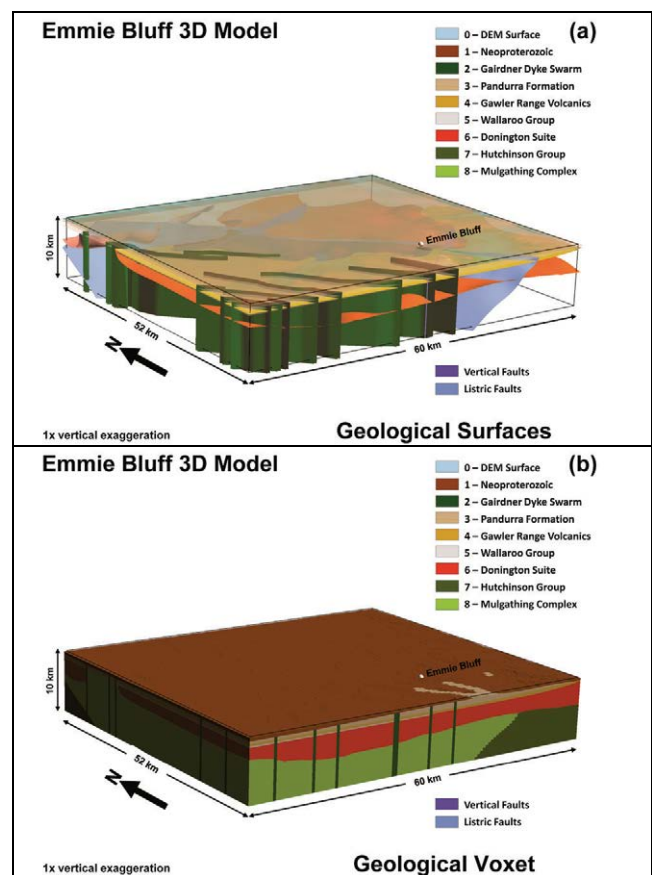


**Figure 3.** The Emmie Bluff 3D geological map showing geological surfaces and major faults (a); and Emmie Bluff 3D geological voxet (b).

# 5 Mapping the distribution of magnetite and hematite with potential field inversions

In simplest terms alteration changes the mineral composition of the host rock. These changes in mineral composition in turn modify the physical and/or chemical properties of a rock. For example, hematite alteration

will increase the iron content of a rock and increase the density. Where the physical properties of the un-altered host lithology and the alteration minerals are known, it may be possible to predict the type and amount of alteration present by measuring the petrophysical properties of a rock.

Using the principles outlined above Chopping and van der Wielen (2009) developed a technique using potential field inversions in conjunction with petrophysical data and a geological block model to map oxide and sulphide minerals in 3D. This technique was used to map out the distribution of magnetite and hematite alteration associated with IOCG mineral systems in 3D (Fig. 4).
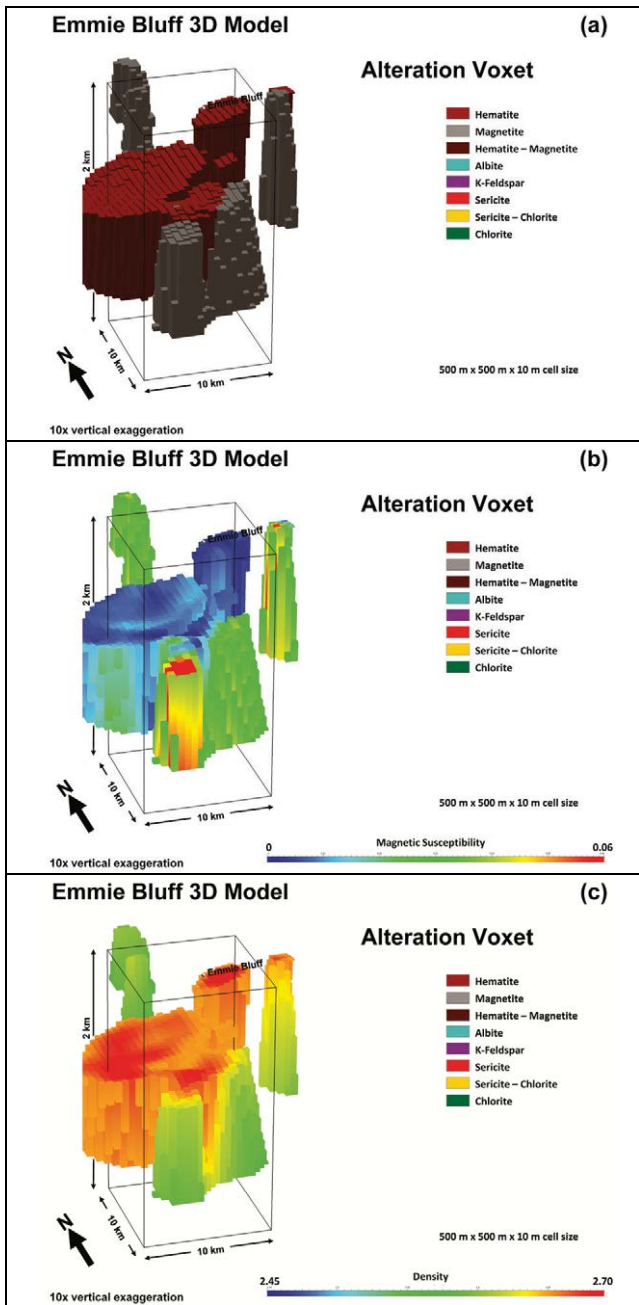


**Figure 4.** The Emmie Bluff 3D model showing mapped distribution of hematite and magnetite that was derived from potential field inversions (a); magnetic susceptibility inversion values draped onto the alteration shell (b); and density inversion values draped onto the alteration shell (c).

## 6 Mapping the distribution of sericite, albite, K-feldspar and chlorite alteration using geochemistry and HyLogger™ data

The GSSA is custodian of exploration drill core that has become public domain in South Australia. Drill holes that have intercepted basement within eastern Gawler IOCG province are being systematically scanned with a visible to thermal infra-red wavelength spectrometer HyLogger™ and basement intercepts are sampled every 10 metres and analysed for a suite of 66 elements (Fabris et al. 2012).
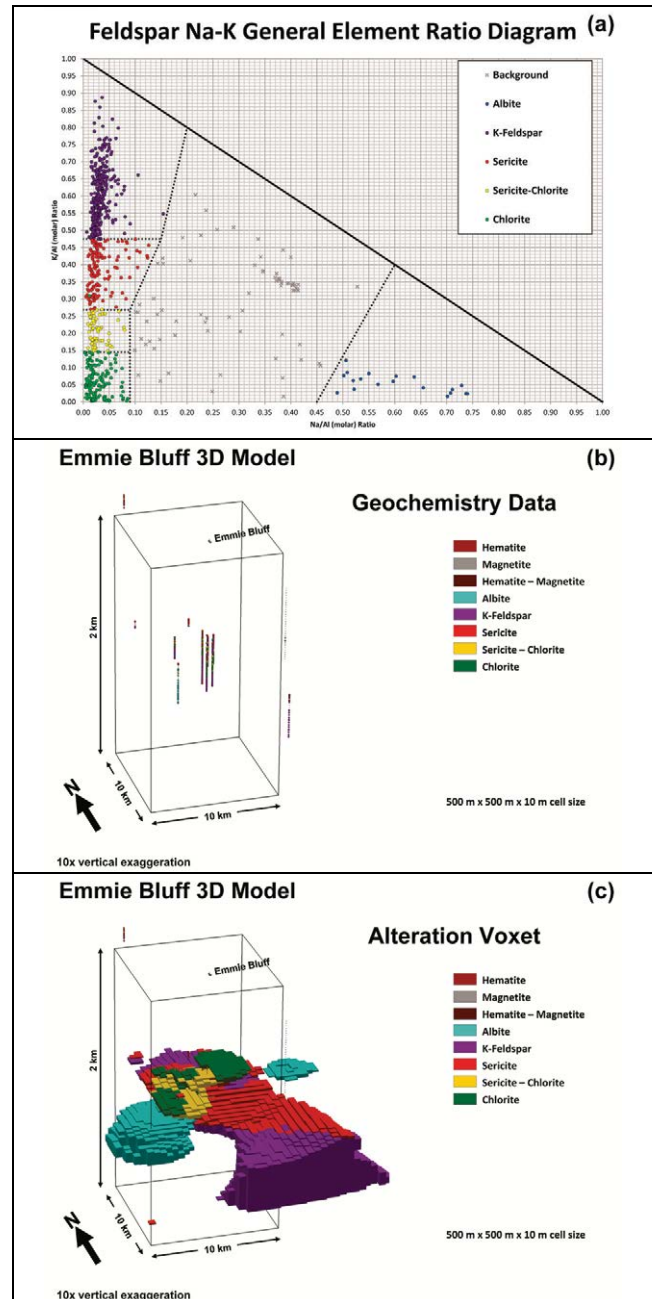


**Figure 5.** Geochemistry data for Emmie Bluff region displayed on a feldspar Na-K general element diagram (a); geochemical samples displayed in 3D and characterised using the feldspar Na-K general element diagram (b); a 3D model of alteration derived from gridded geochemistry data (c).

As with potential field data, geochemistry can be used to predict the amount and type of alteration present. Drill core geochemistry can be plotted on a feldspar Na-K general element ratio diagram to discriminate sodium and potassium alteration from un-altered host lithology (Fig. 5a). Albitisation will increase the Na/Al ratio when compared to an un-altered host lithology whereas chlorite, sericite and K-feldspar alteration will decrease Na/Al ratio (Fig. 5a). Chlorite, sericite and K-feldspar alteration can be distinguished from each other by variation of the K/Al ratio (e.g. chlorite low K/Al ratio, sericite moderate K/Al ratio and K-feldspar alteration high K/Al ratio). This can be taken a step further and gridded geochemical data can be classified and plotted in 3D space (Fig. 5).



**Figure 6.** HyLogger™ data displayed in 3D and coloured by wavelength of the AlOH absorption feature (a); a 3D model of sericite and sericite-chlorite alteration derived from gridded geochem data (b); wavelength of the a AlOH absorption feature draped onto the sericite alteration shell (c).

Sericite alteration is made up of fine-grain white mica, usually muscovite ($K_2Al_4(Si_6Al_2)O_{20}(OH)_4$) or phengite ($K_2(Al,Mg,Fe)_4(Si_{6+x},Al_{2-x})O_{20}(OH)_4$). Muscovite and phengite are indistinguishable in hand specimen but can be readily identified with HyLogger™. Muscovite has an AlOH absorption minimum at wavelength ~2,206 nm whereas phengite has an absorption minimum at longer wavelengths (e.g. 2,218 nm).

Variation in sericite mineral composition can be used as a proxy for fluid chemistry. Assuming the temperature is the same muscovite will form under acidic conditions whereas phengite will form under neutral conditions. This is important as metals will likely to be precipitated at sites where there is a change in fluid chemistry. By plotting the wavelength of the AlOH absorption minimum (Fig. 6) it is possible to directly map the spatial distribution of muscovite (e.g. green and blue regions in Fig. 6c) and phengite (e.g. orange and red regions in Fig. 6c) and identify likely regions where chemical conditions favoured metal deposition.

## Acknowledgements

## References

Bastrokov EN, Skirrow RG, Davidson GJ (2007) Fluid Evolution and Origins of Iron Oxide Cu-Au Prospects in the Olympic Dam District, Gawler Craton, South Australia. Economic Geology 102:1415-1440

Chopping R, van der Wielen SE, (2009) Querying potential field inversions for signatures of chemical alteration: an example from Cobar, NSW. ASEG Extended Abstracts 2009, pp 1-8

Fabris A, van der Wielen SE, Mauger A, Halley S, Keeping T, Keeling J (2012) Geochemical trends in IOCG alteration – new data from the Gawler Craton. In: Baker T (eds) Unlocking SA's mineral wealth, technical forum, 2 May 2012, extended abstracts, pp 7-8

Hayward N, Skirrow RG (2010) Geodynamic Setting and Controls on Iron Oxide Cu-Au (±U) Ore in the Gawler Craton, South Australia. In: Porter TM (eds) Hydrothermal Iron Oxide Copper-Gold & Related Deposits: A Global Perspective, PGC Publishing, Adelaide, 3:105-131

Williams PJ, Kendrick MA, Xavier RP, (2010), Sources of ore fluid components in IOCG deposits. In: Porter TM, (eds) Hydrothermal Iron Oxide Copper-Gold and Related Deposits: A Global Perspective, PGC Publishing, Adelaide, 3:107-116

Wyborn LAI, Heinrich CA, Jaques AL (1994) Australian Proterozoic Mineral Systems: Essential Ingredients and Mappable Criteria. The AusIMM Annual Conference, pp 109-115
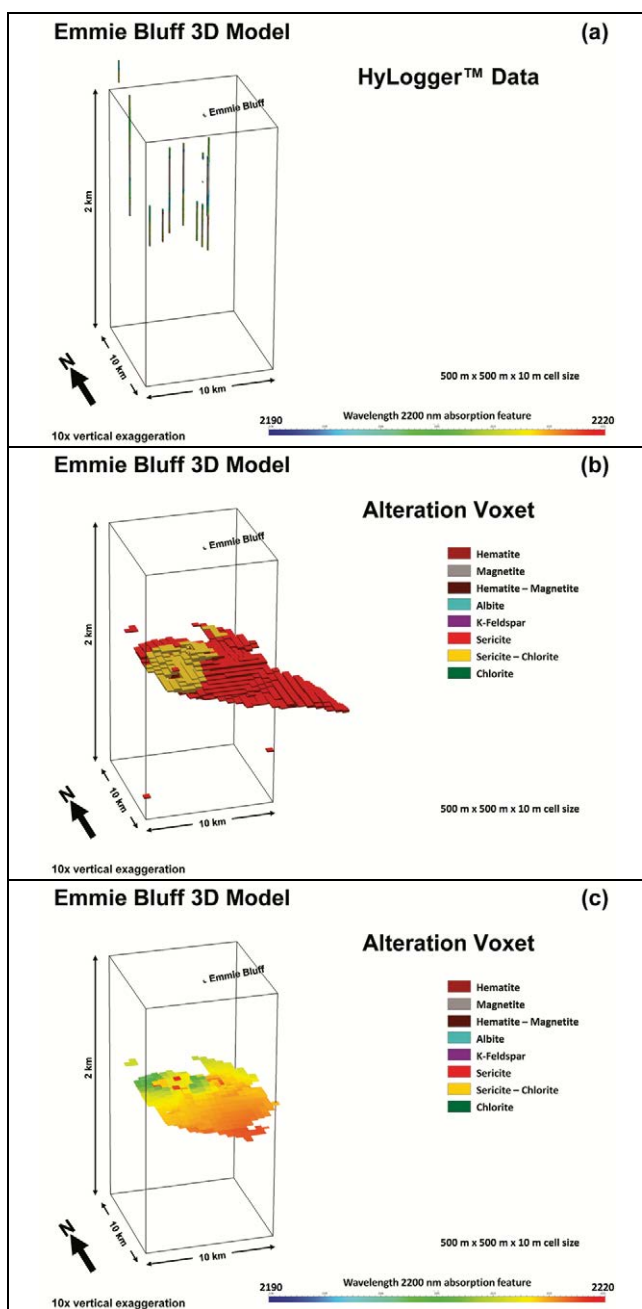
# 3D implicit geological modelling of a gold deposit from a structural geologist's point of view

**Stefan A. Vollgger, Alexander R. Cruden**
*School of Geosciences, Monash University, Australia*

**E. Jun Cowan**
*Orefind Pty Ltd, Australia*

**Abstract.** Tectonic processes and the resulting deformation of Earth's crust are known to control and influence the location as well as shape of ore bodies. Furthermore, ore body geometries and associated spatial relationships provide fundamental clues to the genesis of ore deposits. Therefore, it is important to establish consistent 3D geological models to visualise and analyse ore delineation in order to understand the controls on mineralisation processes. Implicit modelling generates objective 3D geological models directly from drill-hole data. Instead of manual linkage of hand-digitised 2D cross-sections, mathematical interpolation functions are used to generate 3D isosurfaces. These surfaces can represent ore grade shells, lithological boundaries or structural trends. The 3D implicit model can be used to define ore body geometries, grade continuity direction(s) and spatial relationships between mineralisation, lithological boundaries and major structures, helping to explain the structural evolution of ore deposits. Working hypotheses based on these geometrical analyses are subsequently validated in the field. Our case study at AngloGold Ashanti's Navachab gold mine (Namibia) shows that high grade mineralisation trends obtained from a 3D implicit model can be directly linked to field observations, suggesting a structural control on gold mineralisation during the growth and lockup stages in the formation of a nearby regional scale dome.

**Keywords.** Implicit modelling, folding, orogenic gold, Navachab

## 1 Introduction

The world-class orogenic gold deposits in the Yilgarn Craton (Hodkiewicz et al. 2005) and the famous vein-hosted gold deposits of central Victoria (Cox et al. 1991) are well known examples of structurally controlled gold mineralisation. These and many more deposit types, such as iron ore and V(H)MS, have shown to be generated and/or influenced by tectonic forces, resulting in deformation manifested at regional to deposit scales as ductile and brittle features such as folds, faults and shear zones. Consequently it follows that the shape, orientation and spatial distribution of ore bodies and their host rocks provide important information on the role that deformation plays in controlling mineralisation. Therefore, the visualisation and precise positioning of mineralisation, lithological boundaries and geological structures of an ore deposit are fundamental.

## 2 Three dimensional geological modelling

Modern computational tools allow us to process vast geological datasets and assist in generating 3D geological models. Two major modelling methodologies are employed, termed explicit and implicit modelling.

The traditional explicit modelling technique is the currently accepted industry standard (Cowan et al. 2011), and it is therefore used in most 3D geological modelling software packages. It is mainly based on the manual definition of boundaries by digitisation. Explicit modelling therefore follows a traditional approach by producing a digital version of former hand-drawn cross sections and linking them to form 3D bodies. Its basic concept emerged out of computer aided design applications (CAD) and is, strictly speaking, not suitable for modelling in data-rich and geometrically complex geological environments. Indeed, the explicit approach regularly forces the model creator to manually adapt and simplify the model to overcome technical problems (such as invalid triangulations) and to keep within a practical and financially feasible timeframe. Additionally, explicit modelling cannot incorporate structural field measurements (e.g., foliation, bedding) directly into a 3D geological model; such data have to be processed and analysed separately, and are therefore disconnected from the model. A further major shortcoming is the inability to make simple updates and changes when additional or new data becomes available. Changes have to be applied manually to all files "downstream" to achieve a coherent geological model again. In summary, explicit geological modelling is a subjective, time-intensive and non-repeatable process in which geological interpretation is inherited from the outset; hence its use for the purposes of structural interpretation must be viewed with caution.

Conversely, implicit modelling (Cowan et al. 2003) is capable of generating internally consistent 3D geological models directly from drillhole and outcrop data without manual digitisation. Implicit modelling allows the construction of 3D (iso-) surfaces and solids that are defined by a single mathematical volume function (implicit function), which is calculated by spatial interpolation of numerical (e.g., assay) and non-numerical (e.g., lithology) data. These attributes make the processes of implicit modelling repeatable and they minimise model bias, making it suitable for use in the structural analysis of ore bodies.

## 3 Active folding and mineralisation

In compressional tectonic settings, active folding (buckling) is a prevalent and important deformation mechanism. Buckling initiates when layers of different competence (e.g. sedimentary packages) are shortened parallel to layering (e.g., Fossen 2010).

In fold-related settings mineralisation, commonly classified as pre-, syn- or post-deformational based on structural relationships, petrographical analysis and/or geochemical evidence, can be linked to the four main stages of active folding in systems characterised by pure shear: (1) initial homogeneous shortening, (2) nucleation of a buckling instability, (3) amplification of buckle-folds and (4) lockup (Schmalholz 2012). Depending on the stage of folding during which mineralisation occurs, geometrically distinct high grade ore zones can form at different preferred sites with respect to a fold.

The nucleation of folds is mainly determined by initial heterogeneities, which may play a role in the development and preservation of certain types of mineral deposits. For example, in the case of V(H)MS deposits, heterogeneities that have the potential to control fold nucleation include the mound shape of primarily accumulated massive sulfides, associated faults or the relative incompetence of massive sulfides themselves.

During the fold amplification stage, the highest shear strain is reached along the inflection lines of folds. Maximum layer-parallel displacements due to flexural shear/flexural flow are confined to these areas, potentially forming low-pressure zones of maximum dilation, thereby generating suitable traps for ore bearing fluids.

When considering regional-scale folding, the significant uplift generated by the fold growth will result in elevated thermal gradients, increased weathering and reduced confining pressures. The latter can encourage hydraulic fracturing to produce veins (Cox and Etheridge 1987), which are important for emplacement of vein-hosted mineralisation.

## 4 Case study Navachab (Namibia)

The Navachab open pit gold mine (owned by AngloGold Ashanti Ltd.) is situated 5km southwest of Karibib, Namibia, within Neoproterozoic amphibolite facies metasediments of the Pan-African Damara Orogen. Mineralisation occurs in two main styles: 1) early bedding-parallel massive sulfide bodies (ore shoots) mainly consisting of pyrrhotite, quartz, calc-silicate minerals and carbonate, and 2) bedding-parallel as well as highly discordant sets of quartz-sulfide veins, mostly comprising quartz and pyrrhotite with minor pyrite and chalcopyrite. Crosscutting mafic and felsic dykes postdate gold mineralisation. Several diorite and leucogranite intrusions are located within 5km of the Navachab deposit, but there is no direct connection between the mineralised system and any major intrusive body (Steven et al. 2011). The most likely source of the mineralising fluids are mid-crustal fluids in equilibrium with Damaran metapelites that underwent prograde metamorphism under amphibolite to granulite facies

conditions (Wulff et al. 2010). Recent structural studies by Kisters (2005) indicate that veining occurred during folding, pointing to an origin consistent with orogenic gold deposits.

### 4.1 Implicit 3D modelling

Data for implicit 3D modelling was extracted from Navachab's existing drillhole database. The collar, survey, geology and assay tables were imported into the software package Leapfrog Mining (version 2.4) to compute an initial implicit 3D model based exclusively on drillhole data.

First, an implicit 3D lithological model was generated. Lithology and unit codes were grouped into formations and used to compute formation boundaries. No manual digitisation, which could introduce a bias in the model, was carried out. An isotropic interpolation (= no preferred orientation) was chosen to keep the modelling results as objective as possible. In order to constrain the 3D model to the volume where drillhole information was available, a "visualisation buffer" with a radius of 60m (adjusted to the drillhole spacing) was generated along every drillhole trace (Fig. 1). The resulting lithological model revealed a generally NE bedding trend of the NW dipping metasedimentary units. Bedding steepens and its strike changes slightly at depth. Analysis of the main gold-hosting marble unit (Okawayo Fm) shows that its true thickness varies both laterally and vertically.
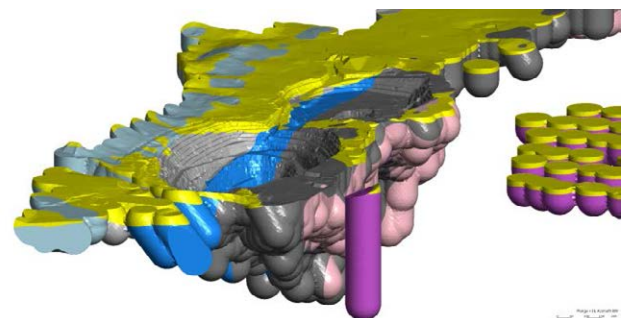


**Figure 1.** Implicit 3D lithological model of the Navachab deposit with a 60m visualisation buffer along each drillhole

For the computation of ore grade shells (implicit 3D assay model), approximately 197,000 assay samples were reduced to about 90,000 data points by converting them into 4m composites. This was done to reduce computational time and to ensure that all samples represent an equal volume. The histogram of ore grades from the 4m gold composites reveals a positively skewed distribution, which is common for gold assay distributions, but a problem when modelling grade values with an interpolant that uses a weighted sum of the data (as in Leapfrog Mining). A nonlinear logarithmic transformation reduces this effect. In the next step, isotropically (= no imposed trend) interpolated 3D ore grade shells were computed for cut-off grades representing low and high-grade mineralisation. Analysis of the 3D grade shells allowed us to identify distinct trends and geometries of gold mineralisation.

Additionally, an implicit 3D bedding trend model based

on bedding measurements extracted from regional geological maps and additional field measurements was generated to investigate the spatial location of the mineralisation within a regional context.

## 4.2 Field observations compared with implicit 3D modelling results

The initial 3D implicit model allowed us to identify key areas for fieldwork in the Navachab Main Pit. Surface mapping revealed that one type of gold mineralisation is hosted in stacked, folded quartz-sulfide veins that vary in thickness and form shallowly dipping packages of higher vein frequency. The mean principal vein orientation calculated from field measurements resembles the orientation of the implicitly modelled, shallowly dipping high grade mineralisation within the Lower Schist (Fig. 2). Depending on host rock rheology (silicified biotite schist versus marble), the auriferous vein packages are tightly to openly folded and crosscut subvertical bedding at a high angle (Fig. 2). The latter suggests that veining occurred when bedding was already rotated to subvertical attitudes, pointing towards emplacement during the final lockup stage of regional scale folding.

The lateral extent of the quartz-sulfide veins is restricted and is most probably controlled by changes in host rock lithology; this is also supported by the implicit 3D model, and suggests that gold mineralisation is preferentially hosted at the contacts between and within certain geological formations.
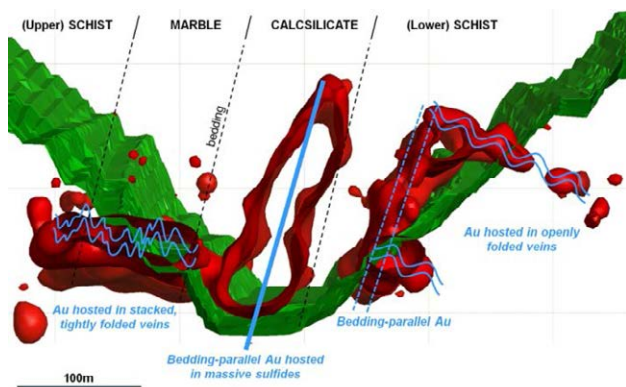


**Figure 2.** Vertical WNW-ESE slice through the central part of the Navachab Main Pit (pit face green) and the isotropically interpolated high-grade ore zones (grade shells in red). Schematic annotations of mineralisation trends observed in the field are indicated in blue.

Sub-vertical (bedding-parallel) quartz and quartz-sulfide veins were also mapped in the Lower Schist of the Navachab Main Pit. Their unfavourable orientation parallel to the pit face has limited their recognition in the field, but they have been identified in drill cores from sub-horizontal dewatering holes (Deltenre 2012). The geometry and orientation of the computed high-grade ore shell within the Lower Schist also suggests the existence of bedding-parallel gold mineralisation (Fig. 2).

Ambiguous and mutually crosscutting relationships between the bedding-parallel and the discordant vein systems are consistent with contemporaneous emplacement during the late stages of regional fold growth and lockup. The highly discordant vein set is oriented sub-parallel to the horizontal principal compressive stress $\sigma1$ expected for the regional folding event. In contrast, bedding-parallel veins are oriented perpendicular to $\sigma1$ and were most probably generated under high fluid pressure conditions, being emplaced along planes of strong mechanical anisotropy such as bedding. This might explain their limited abundance and lower thickness due to their unfavourable orientation with respect to the main stress field. Additionally, bedding-parallel veins observed in drillcore from the Upper Schist are boudinaged, which is consistent with the bulk strain regime that folded the discordant vein set during late stage fold lockup.

Mapping of the auriferous massive sulfide lenses was not possible because of limited exposure and ongoing mining activities. Nevertheless, we were able to improve understanding of their occurrence based on available data. Bedding measurements extracted from regional geological maps and collected in the field were used to compute a regional implicit 3D bedding trend model. The data suggests a spatial relationship between a first order domal structure (Karibib dome) and the auriferous massive sulfide lenses (ore shoots). The ore shoots were emplaced near the inflection line of the regional dome's steep NW limb, where shear strain reached peak values during fold amplification. This is in agreement with the model proposed by Kisters (2005) that interprets the massive sulfide lenses as dilational jogs that opened during flexural flow along bedding parallel slip planes during the amplification of the Karibib Dome.

## 5 Conclusion

Our case study at Navachab shows that implicit modelling in combination with selective structural fieldwork is a powerful technique to identify and evaluate structural controls on deposit and regional scales, thereby improving the understanding of the relationship between mineralisation and deformation.

## Acknowledgements

## References

Cowan EJ, Beatson RK, Ross HJ, et al. (2003) Practical Implicit Geological Modelling. Fifth International Mining Geology Conference Proceedings. AusIMM Publication Series 8:89–99

Cowan EJ, Spragg KJ, Everitt MR (2011) Wireframe-Free Geological Modelling - An Oxymoron or a Value Proposition? Eighth International Mining Geology Conference,

Queenstown, New Zealand

Cox S, Etheridge M (1987) The role of fluids in syntectonic mass transport, and the localization of metamorphic vein-type ore deposits. Ore Geology Reviews 2:65–86

Cox S, Wall V, Etheridge M (1991) Deformational and metamorphic processes in the formation of mesothermal vein-hosted gold deposits - examples from the Lachlan Fold Belt in central Victoria. Ore Geology Reviews 6:391–423

Deltenre A (2012) Understanding the different auriferous quartz vein orientations in the footwall of Navachab Gold Mine, Namibia. Master thesis, Camborne School of Mines

Fossen H (2010) Structural Geology. Cambridge University Press

Hodkiewicz PF, Weinberg RF, Gardoll SJ, Groves DI (2005) Complexity gradients in the Yilgarn Craton: Fundamental controls on crustal-scale fluid flow and the formation of world-class orogenic-gold deposits. Australian Journal of Earth Sciences 52:831–841

Kisters AFM (2005) Controls of gold-quartz vein formation during regional folding in amphibolite-facies, marble-dominated metasediments of the Navachab Gold Mine in the Pan-African Damara Belt, Namibia. South African Journal of Geology 108:365–380

Schmalholz SM (2012) Folding. ETH Zürich. http://www.files.ethz.ch/structuralgeology/JPB/files/English/7folding.pdf. Accessed 12 September 2012

Steven N, Wulff K, Bell G, Hill J, Sales M (2011) The increasing importance of Neoproterozoic (Pan-African) gold deposits in Africa and South America. 11th Biennial SGA Conference - Let's Talk Ore Deposits, Antofagasta, Chile

Wulff K, Dziggel A, Kolb J, Vennemann T, Öttcher ME, Meyer FM (2010) Origin of Mineralizing Fluids of the Sediment-Hosted Navachab Gold Mine, Namibia: Constraints from Stable (O, H, C, S) Isotopes. Economic Geology 105:285–302

## S 2.2
# New advances in geophysical mineral exploration

Convenors:
Christopher Juhlin & Hans Thunehed

# Advances in geophysical technologies for the exploration and safe mining of deep gold ore bodies in the Witwatersrand basin, South Africa

**Raymond J Durrheim**
*CSIR Centre for Mining Innovation & University of the Witwatersrand, Johannesburg, South Africa*

**Declan Vogt**
*CSIR Centre for Mining Innovation, Johannesburg, South Africa*

**Musa Manzi**
*University of the Witwatersrand, Johannesburg, South Africa*

**Abstract.** Gold is currently mined at depths reaching 4 km in the Witwatersrand basin of South Africa. Geophysical techniques have been used to explore for new resources, and to design and operate mines efficiently and safely. We report on recent advances in technologies for 3D reflection seismics, borehole radar, and rock mass monitoring.

**Keywords.** Witwatersrand basin, reflection seismology, borehole radar, mining-induced seismicity

## 1 Introduction

The Witwatersrand basin (Fig. 1) hosts the world's largest known gold ore body. Since its discovery near present-day Johannesburg in 1886, the quartz pebble conglomerates (locally known as "reefs") have produced more than 50,000 tonnes of gold, about one-third of the gold ever mined.

The reefs are generally only a few decimetres to metres thick and relatively low grade, yet are continuous for many kilometres along strike and dip. Over the last century, mining has progressed to ever increasing depths. Several mines are now approaching 4 kilometres below surface. Production peaked in the 1970s at 1000 tonnes/p.a. but has since declined to 200 tonnes/p.a. However, substantial resources remain that could become profitable to mine, depending on technological advances and increases in the gold price.

## 2 Exploration of the Witwatersrand Basin

### 2.1 Geology

A succession of volcano-sedimentary basins developed on the Kaapvaal craton during Archean and Paleoproterozoic times. The predominantly volcanic Dominion Group lies on granite-greenstone basement. It is overlain by the Witwatersrand Supergroup, with ferruginous shales prominent in the (lower) West Rand Group, while gold-bearing conglomerates are found in the quartzites of the Central Rand Group. The massive lavas and quartzites of the Ventersdorp Supergroup lie above the Witwatersrand Supergroup. A very important ore body, known as the Ventersdorp Contact Reef, lies at its base. The Ventersdorp Supergroup is overlain by the relatively thin and laterally extensive Black Reef Formation, which marks the base of the Transvaal

Supergroup, a succession of dolomites, shales, quartzites and lavas. Finally, much of the southern half the basin is covered by sandstones and shales of the Phanerozoic Karoo Supergroup.
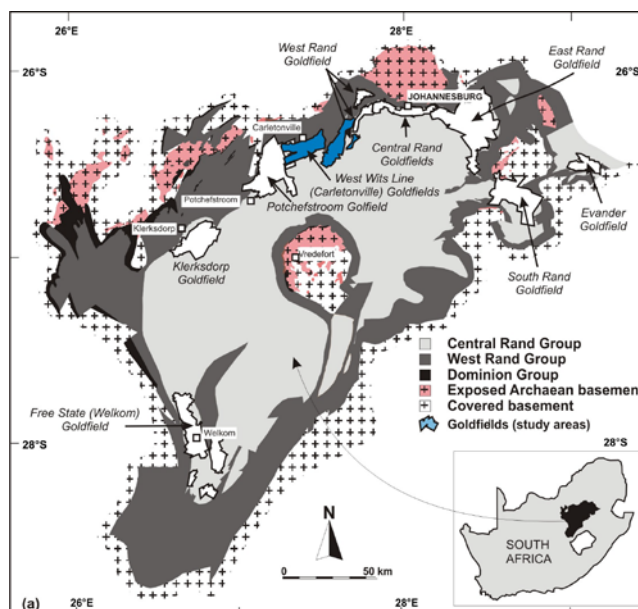


**Figure 1.** Witwatersrand basin with younger strata removed.

The origin of the gold continues to be debated (e.g. Muntean et al., 2005). The concentration of the heavy metal in conglomerates formed on the margin of a sedimentary basin is regarded by many to be evidence for the placer origin of the gold. However, while some gold has been found in the greenstone belts exposed in the ancient granite-gneiss terrains that were the source of the Witwatersrand sediments, it is difficult to account for the sheer size of the gold resource. The gold grains are very fine and visible gold is rarely seen, but microscope studies reveal that the gold has been hydrothermally mobilized, leading some researchers to proposed post-depositional introduction of the gold by mineralized fluids circulating through the permeable conglomerate horizons. It is proposed that the heat that drove the hydrothermal circulation (and possibly the gold) was supplied by magmatic events such as the eruption of the Ventersdorp lavas or the intrusion of the Bushveld Complex.

## 2.2 Geophysical exploration

The Main Reef and other reefs that crop out on the flanks of the Johannesburg dome were traced along the northern rim of the Witwatersrand basin for tens of kilometres. Beyond the Johannesburg dome these strata are concealed by Transvaal and Karoo Supergroup rocks. In the 1930s and 1940s the magnetic and gravity methods proved to be very effective in tracing the magnetite-rich horizons in the relatively dense shales of the West Rand Group, which lie a predictable distance below the reefs, and the Far West Rand and Free State gold fields were discovered. However, these methods lack the resolution required to explore the deeper and structurally complex parts of the basin effectively.

A new era of exploration began in the 1980s when the reflection seismic method, widely used to explore for hydrocarbons in soft rocks, was adapted to the hard rock environment (Malehmir et al., 2012). Vertical Seismic Profiles were first shot to establish that reflections could be reliably obtained (Fig. 2). Within a decade, a network of 2D reflection seismic profiles covered the basin and areas where extensions to the basin were thought to exist. No major new gold fields were discovered, although several "brownfields" prospects were identified.
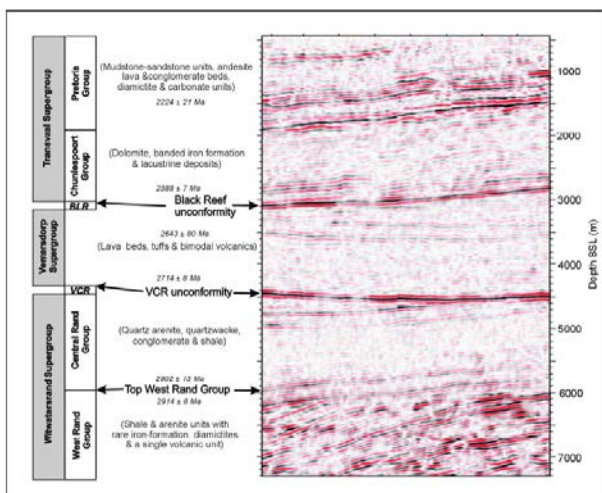


**Figure 2.** Seismic stratigraphy of the Witwatersrand basin with younger strata removed (after Dankert and Hein, 2010).

# 3 Challenges of deep mining

## 3.1 Planning

A detailed knowledge of the structure and grade of the ore body is required to reduce the financial and technical risks of deep mining operations. The first 3D reflection seismic survey was conducted in South Africa in 1987 on the South Deep prospect. Since then, 3D reflection seismic surveys have become an essential part of any feasibility study (e.g. Pretorius, 2003). Recent advances in signal processing, such as attribute analysis, have made it attractive to reprocess data acquired a decade ago. Faults with throws as small as 10 meters can be imaged.

Four surveys acquired between 1988and 2003

(Fig. 3) covering the West and Far West Rand gold fields were reprocessed and merged to produce a data cube with a surface projection of approx. 640 km$^2$, and interpreted by Manzi et al. (2012a, 2012b, in press).The seismic data were integrated with geological mapping in underground workings and a deep drilling programme, and used to map the down-dip extension of the ore bodies, and potential resources in structurally complex areas that could be accessed from existing shafts (Fig. 4).
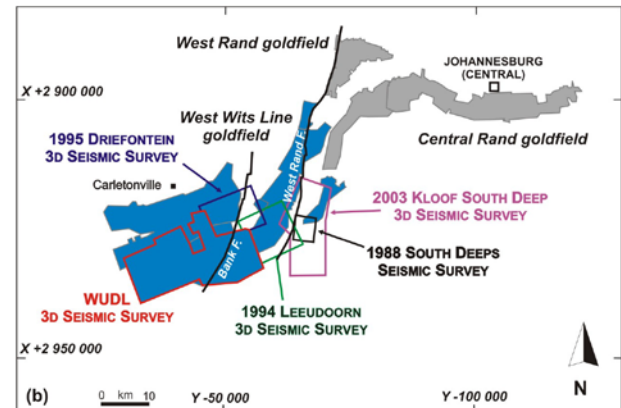


**Figure 3.** Witwatersrand basin with younger strata removed.
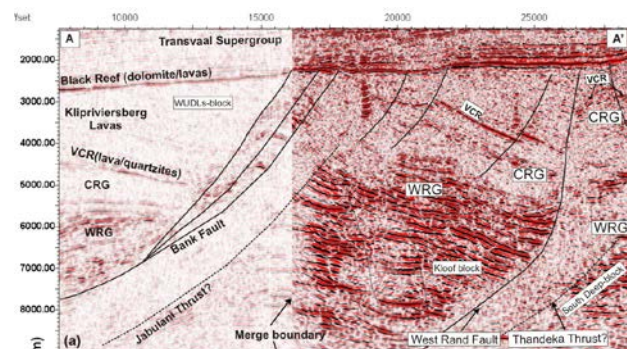


**Figure 4.** Seismic section (amplitude display) across the West Rand and Bank faults

## 3.2 In-mine geophysics

A fault with a throw as small as two meters is a significant obstacle to thin reef mining, hampering production and presenting a hazard. Current technology cannot image faults with small throws from the surface. As part of the DeepMine Collaborative Research Programme (Durrheim, 2007), in-mine geophysical techniques were developed to image the ore body ahead of mining. Both electromagnetic and seismic techniques were investigated, and borehole radar proved to be the most practical.

Boreholes drilled from mine workings to map the ore body (structure and grade) and detect water and flammable gases are used to deploy the radar transmitters and receivers. In the resistive quartzite environment, reflections from a suitable target (such as the lava hangingwall of the Ventersdorp Contact Reef) may be obtained from a range of 80 metres.

In Fig. 5, radar data from a number of boreholes has been combined to image the topography of a 150 m × 250 m section of Ventersdorp Contact Reef.
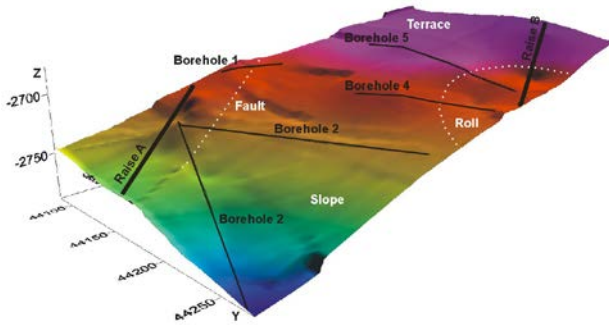
**Figure 5**. 3D model of the Ventersdorp Contact Reef using radargrams from five boreholes as well as a priori information. A roll and fault that will affect mining are visible. Two facies types are visible on the reef: the terrace, which is usually gold bearing, and the slope which is usually barren, Two obstacles to mining are also present: a fault and a roll. (Du Pisani and Vogt, 2004).

## .3  Rockbursts

Rockbursts (mining-related seismic events that cause damage to mine workings) pose a significant human and financial risk to deep level mining (Durrheim, 2010).All rockburst-prone mines in South Africa are equipped with mine-wide seismic systems that continuously monitor the response of the rock mass to mining, and the seismic hazard is assessed daily at least.

Seismic events cannot be predicted with current technology and knowledge. However, working places canbe protected to some degree by rockburst-resistant support elements and structures. The risk can further be reduced by reducing the exposure of workers in hazardous areas. Technology for remote control and automation is currently being developed. Furthermore, seismic energy release can be controlled, to some extent, by (i) appropriate regional support systems (e.g. pillars, backfill), and (ii) by identifying seismogenic areas and structures ahead of mining and adjusting the mining geometryand sequence accordingly. Reflection seismic techniques to identify faults have been described above, and pillars are often designed to "bracket" these structures.

An investigation of the mining-induced seismicity is currently being carried out in three deep South African gold mines (Durrheim et al., 2012). The 5-year Japanese-South African collaborative project entitled "Observational studies to mitigate seismic risks in mines" commenced in August 2010. Faults at Cooke #4, Moab-Khotsong and Driefontein gold mines considered likely to become seismically active during mining activity were indentified. About 70 boreholes totalling more than 2 km in length were drilled to locate fault zones accurately and to deploy sensors. Acoustic emission sensors, geophones, accelerometers, strain- and tilt meters, and controlled seismic sources have been installed to monitor the deformation of the rock mass, the accumulation of damage during the earthquake preparation phase, and changes in stress produced by the propagation of the rupture front (Fig. 5 and Fig. 6).

The suite of sensors has greater sensitivity and dynamic range than those typically used in civil or mining engineering applications, making it possible to record very small changes in stress and strain as well as violent rock mass deformation associated with large seismic events. These data sets will be integrated with measurements of stope closure, strong ground motion in stopes, seismic data recorded by the mine-wide network, and stress modelling. Ten surface seismic stations have been deployed in the Far West Rand to complement the sub-surface close-monitoring data.
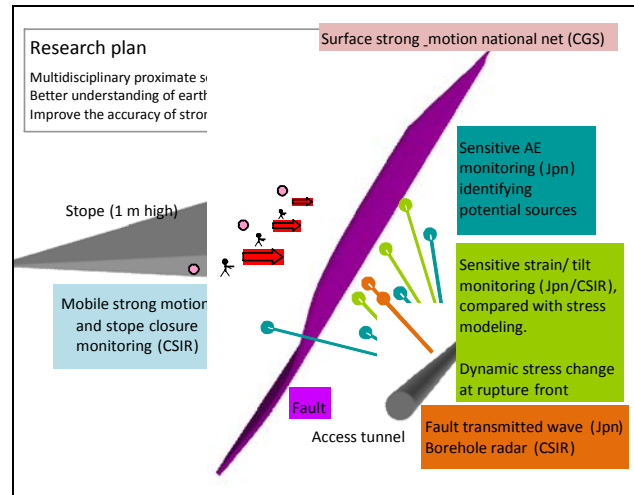


**Figure 5.** Schematic illustration of the research design for the project "Observational study in South African mines to mitigate seismic risks". Jpn: Japanese researchers, CSIR: Council for Scientific and Industrial Research, South Africa, CGS: Council for GeoScience, South Africa
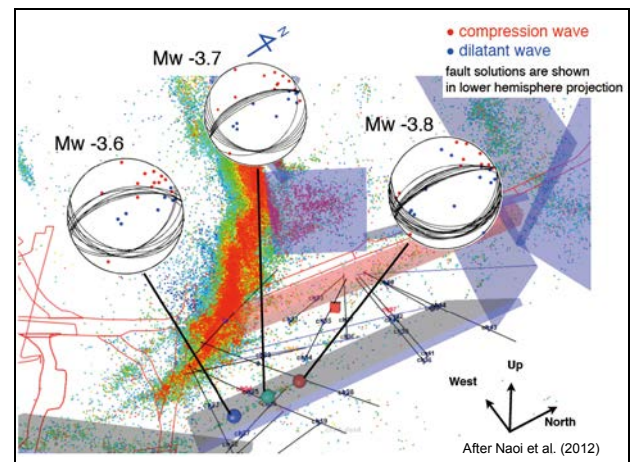


**Figure 6.** Seismic response of the rock mass to mining at Cooke No. 4 Shaft, West Rand (after Naoi et al., 2012). The dense cloud of seismic events delineate the mining front.

## 4  Conclusions

The world's deepest mines are found in the Witwatersrand basin of South Africa. Mapping and mining the laterally extensive but thin gold-bearing conglomerate horizons at depths exceeding 4 km presents significant technological challenges. Advances in geophysical techniques such as reflection seismology, borehole radar, and seismic monitoring of the dynamic response of the rock mass to mining have contributed to profitability and safety.

## Acknowledgements

Many researchers and practitioners have contributed to the work described in this paper. In particular we acknowledge the contributions of Mr Thabang Kgarume (CSIR), Mr Nick King (South Deep Mine, Gold Fields Ltd), Professor Masao Nakatani (Tokyo University), Professor Kim Hein (Witwatersrand University), Dr Alexander Milev (CSIR), Professor Hiroshi Ogasawara (Ritsumeikan University), Dr Michael van Schoor (CSIR), and Professor Yasou Yabe (Tohoku University).

## References

Dankert, B.T., and Hein, K.A.A., 2010. Evaluating the structural character and tectonic history of the Witwatersrand Basin: Precambrian Research, 177, 1-22.

Du Pisani P., and Vogt, D., 2004. Borehole radar delineation of the Ventersdorp Contact Reef in three dimensions, in Exploration Geophysics 35, 319-323.

Durrheim, R.J., 2007. The DeepMine and FutureMine Research Programmes - Knowledge and Technology for Deep Gold Mining in South Africa, Chapter 15 in Challenges in Deep and High Stress Mining, Y Potvin, J Hadjigeorgiou and D Stacey (editors), Australian Centre for Geomechanics, ISBN 978-0-9804185-1-4, pp. 131-141.

Durrheim, R.J., 2010. Mitigating the rockburst risk in the deep hard rock South African mines: 100 years of research, in Extracting the Science: a century of mining research, J. Brune (ed), Society for Mining, Metallurgy, and Exploration, Inc., pp. 156–171.

Durrheim, R.J., Ogasawara, H., Nakatani, M., Yabe, Y., Kawakata, H., Naoi, M., Ward, A.K., Murphy, S.K. Wienand, J., Lenegan, P., Milev, A.M., Murakami, O., Yoshimitsu, N., Kgarume, T., Cichowicz, A., and the SATREPS research group, 2012. Establishment of SATREPS experimental sites in South African gold mines to monitor phenomena associated with earthquake nucleation and rupture. Proc. Sixth Int. Seminar on Deep and High Stress Mining, Y Potvin (ed), Australian Centre for Geomechanics, ISBN 978-0-9806154-8-7, pp. 173-187.

Malehmir, A., Durrheim, R., Bellefleur, G., Urosevic, M., Juhlin, C., White, D., 2012. Seismic methods in mineral exploration and mine planning: a general overview of past and present case histories and a look into the future. Geophysics 77(5), WC173–WC190.

Manzi, M., Durrheim, R.J., Hein, K.A.A., King, N., 2012a. 3D edge detection seismic attributes used to map potential conduits for water and methane in deep gold mines in the Witwatersrand Basin, South Africa. Geophysics 77(5), WC133–WC147.

Manzi, M.S.D., Gibson, M.A.S., Hein, K.A.A., King, N., and Durrheim, R.J., 2012b. Application of 3D seismic techniques in evaluation of ore resources in the West Wits Line goldfield and portions of the West Rand goldfield, South Africa. Geophysics 77(5), WC163–WC171.

Manzi, M.S.D., Hein, K.A.A., King, N., and Durrheim, R.J., Neoarchean tectonic history of the Witwatersrand Basin and Ventersdorp Supergroup: New constraints from high-resolution 3D seismic reflection data. Tectonophysics, in press.

Muntean, J.L., Frimmel, H.E., Phillips, N., Law, J., Myers, R., 2005. Controversies on the origin of world-class gold deposits, part II: Witwatersrand gold deposits. Soc.1005 Econ. Geol. Newsl. 60, 7–19.

Naoi, M., Nakatani, M., Phillip, J., Horiuchi, S., Otsuki, K., Kgarume, T., Morema, G., Khambule, S., Masekale, T., Miyakawa, K., Watanabe, A., Moriya, H., Murakami, O., Yabe, Y., Kawakata, H., Yoshimitsu, N., and Ogasawara, H., 2012. AE Measurements at 1 km depth in a deep South African gold mine and their activities related to two M0 earthquakes. Abstracts, Jpn. Geoscience Union Meeting, SSS28-07.

Pretorius, C.C., Muller, M.R., Larroque, M., Wilkins, C., 2003. A review of 16 years ofhard rock seismics on the Kaapvaal Craton. In: Milkereit, B., Eaton, D., Salisbury, M. (Eds.), Hardrock Seismic Exploration. SEG, Tulsa, Oklahoma, pp. 247–268.

# Field considerations in the acquisition of surface to borehole interferometric seismic data

Sharon Deemer, Charles Hurich
*Earth Sciences Dept., Memorial University, St. John's, NL, A1B3X5*
*e-mail: sdeemer@mun.ca*

**Abstract.** Effective field parameters for recording surface-borehole seismic data for interferometric processing requires that the surface sources are located over an offset range which will produce stationary phase arrivals for creation of virtual sources. Ray-based analyses for a limited surface source aperture show that the relative dip between the borehole and target determines which part of the target will be imaged and which virtual sources will have valid stationary phase arrivals. When the borehole and target are both vertical the near surface part of the target will be imaged and stationary phase arrivals will occur on shallow virtual sources. When the borehole dips toward the target, the target is imaged down to the intersection point except for the very shallowest part of the target. All the virtual sources could have stationary phase arrivals. When the target dips toward a vertical borehole a large part of the near surface target may not be imaged but all virtual sources should have stationary phase arrivals. Proper stationary phase representation is seen in the unstacked correlation gather to be limited to depth ranges similar to the depth of the virtual source.

**Keywords.** Interferometry, Borehole Seismology, Seismic Acquisition

## 1 Introduction

Seismic imaging of ore deposits in crystalline rocks is often a difficult problem due to complicated shapes and suboptimal orientations. For example, steeply dipping ore bodies are very hard to image if sources and receivers are located on the earth's surface. This necessitates other recording arrangements such as locating receivers in boreholes where appropriate to record sources on the surface. The redatuming of vertical seismic profiles (VSP) to the borehole via interferometric processing (Bakulin and Calvert, 2006; Hornby and Yu, 2007, Schuster, 2009) produces a geometry which allows the geophysicist to create a common midpoint (CMP) stack with its familiar cross section view (recording surface subparallel to target). Recording data for interferometric processing requires us to record specific source-receiver geometries that will ensure that we have energy travelling through the virtual sources that result from redatuming and on to receivers (stationary phase arrivals, Snieder, 2004). The success of interferometric techniques also relies on sufficient source and receiver sampling for noise suppression (Mehta, 2008). Recognizing the practical limitations which prevent the fulfillment of ideal criteria, several investigations have been made to determine how much flexibility there is in acquiring seismic data under nonideal, but more realistic, conditions (Mehta 2008, Draganov 2006, Brand 2013).

If boreholes of favourable orientation exist in the vicinity of an ore body there is an opportunity to record seismic data in the borehole to gain a more detailed image of the ore body. Using interferometric processing to redatum surface sources to virtual source locations in the borehole coincident with receiver locations requires locating the surface shots effectively. The following discussion presents a variety of geometries between borehole and target orientations and illustrates the different requirements necessary to image properly in each case or the inherent practical limitations in each case. The basic scenario is sources located on the earth's surface and receivers in the borehole with an orebody shaped like a dike and oriented at a steep angle to the earth's surface. The dip between the borehole and target orebody is varied.

## 2 Optimizing Field Parameters in Surface to Borehole Interferometry

The following demonstrations illustrate how the wavefield coverage is affected by the dip of the borehole where the recording string is located and the dip of the target. The parameters are taken from a field example recorded by Memorial University in 2010. In each case, the separation between the borehole and target at the surface is 175 m and the surface sources are located from the borehole to a maximum distance of 230 m. There were 150 receivers spaced at 2 m and the interferometric virtual sources coincided with the receiver locations. The dip of the target or borehole in each case was 55 degrees with a converging geometry so that the borehole and target dip towards each other. In the dipping cases, the receiver string is long enough to go past the intersection point so only the receivers above the intersection point have valid information for interferometric processing.

For the following discussion straight ray tracing is used to locate the stationary phase surface source locations for three different configurations of vertical and steeply dipping borehole and target. Scatter diagrams are also shown to summarize the surface sources which can contribute stationary phase arrivals to the range of possible virtual sources in each geometry.

### 2.1 Starting Model: Vertical Borehole and Target

In the case in which the borehole and target are both

vertical (Figure 1a) the upper part of the target is imaged down to the midpoint of the receiver string for a virtual source near the surface. For deeper virtual sources, reflections result from midpoints deeper on the target from the far offset surface sources only and the shallow part of the target does not get imaged. The scatter plot in Figure 2a shows that virtual sources that contain stationary phase arrivals are limited to less than about 130 m depth with the surface source location restriction in our model. A more desirable maximum surface source offset of 500 m would provide greater coverage of shallower reflection points on the target. For example, a virtual source at 100 m depth would have reflection points over 135-210 m instead of ~175-210 m obtained with the shorter offset limitation.

## 2.2   Dipping Borehole Intersects Vertical Target

When the borehole dips towards the target (Figure 1b) stationary phase events occur deeper in the borehole for the near surface virtual source. For this particular geometry, the target is sampled completely from the surface to the intersection point between the target and borehole. For virtual sources located deeper in the borehole a broader area is imaged on the target for each virtual source than in the previous case where borehole and target were both vertical. Every virtual source has stationary phase arrivals over the full range of surface source locations although the optimal locations become more widely spaced with deeper virtual sources. Figure 2b summarizes the surface source locations for each virtual source and shows that there is more opportunity for recording stationary phase arrivals than in the case of the vertical borehole and target.

If the maximum surface source offset is increased from 230 m to 500 m there is only a very marginal improvement in coverage of the target. At a virtual source depth of 50 m the shallowest reflection point will be about 50m instead of 70 m and the change is similar for other virtual sources deeper in the borehole.

## 2.3 Vertical Borehole Intersected by Dipping Target

When the borehole is vertical and the target dips towards the borehole (Figure 1c) there is a problem imaging the upper part of the target. On near surface virtual sources only surface sources near the borehole contribute stationary phase arrivals. For virtual sources below halfway down the borehole surface sources along the full extent of surface locations are needed although the area imaged on the target is increasingly narrower and nearer the intersection point with the borehole.

A significant increase in coverage of the target can be achieved with upgoing waves when the maximum surface source coverage is increased from 230 m to 500m. The near surface portion of the target continues to be unimaged however.

## 2.4 Upgoing Wave Geometry

One interesting observation from these simple diagrams is the presence of arrivals above the virtual source location in the third case which doesn't happen in the first two examples. This illustrates a potential filtering option whereby known nonstationary arrivals may be excluded from further processing in the construction of the CMP profile from the virtual sources. As long as the geometry clearly is vertical borehole and target to dipping borehole with vertical target there would be no arrivals on receivers above the virtual source which would have stationary phase arrivals. These traces show up in virtual sources with a signed offset opposite of channels below the virtual source and so are easy to identify and exclude. In the case of the dipping target there are valid stationary phase arrivals in the virtual sources so it would be important not to exclude channels without careful analysis. It is also important to remember that if the orebody has major geometrical complexities there could be significant upgoing energy locally that shouldn't be muted.

## 2.5 Synthetic   Model:   Dipping   Borehole Intersects Vertical Target

Unstacked synthetic virtual source correlation gathers in Figure 3 illustrate which channels record the stationary signal. The model geometry is scenario b in Figure 1. Stationary signal appears in the unstacked gathers as flat segments which will sum constructively. Virtual source 1, which is located at the top of the borehole, has stationary events on near surface channels (Figure 3a) because even though the surface sources are changing significantly in distance from the borehole they all have travel paths close to the stationary ray for recordings on channel 1. This geometry produces a similar effect on deeper virtual sources which record the best stationary signal on successively deeper channels.

## 3   Summary

Seismic imaging of complicated targets which are common in many mining scenarios can be approached using   surface-borehole   recording   geometries. Redatuming the survey to the borehole through interferometric processing can be particularly beneficial but there are complications resulting from the geometry which must be accounted for. The limited range of surface source locations imposed by practical constraints results in not all channels of all virtual sources having stationary signal which can produce misleading data. The examples presented here show that recording on a borehole dipping towards a vertical target will be more favourable in terms of achieving stationary phase geometries than the cases where borehole and target are both vertical or where the target dips towards a vertical borehole. In the most favourable geometry the range of channels   with   the   best   stationary   coverage   was correlated   with   the   virtual   source   position   in   the borehole.

## Acknowledgements

## References

Bakulin A, Calvert R (2006) The virtual source method: Theory and case study: Geophysics, 71: SI139-SI150

Brand E, Hurich C, Deemer S (2013) Geometrical considerations in the acquisition of borehole interferometric data for imaging near-vertical features: design of field experiments, Geophysics, in press.

Claerbout JF (1968) Synthesis of a layered medium from its acoustic transmission response: Geophysics, 33:264-269

Draganov D, Wapenaar K, Thorbekke J (2006) Seismic interferometry: Reconstructing the earth's reflection response, Geophysics, 71:S161-S170

Hornby B, Yu J (2007) Interferometric imaging of a salt flank using walkaway VSP data. The Leading Edge, 26:760-763

Mehta K, Snieder R, Calvert R, Sheiman J (2008) Acquisition geometry requirements for generating virtual-source data: The Leading Edge, 27:620-629

Schuster GT (2009) Seismic Interferometry: Cambridge Press.

Snieder R (2004) Extracting the Green's function from the correlation of coda waves: A derivation based on stationary phase, PhysRevE.69.046610. doi: 10.1103
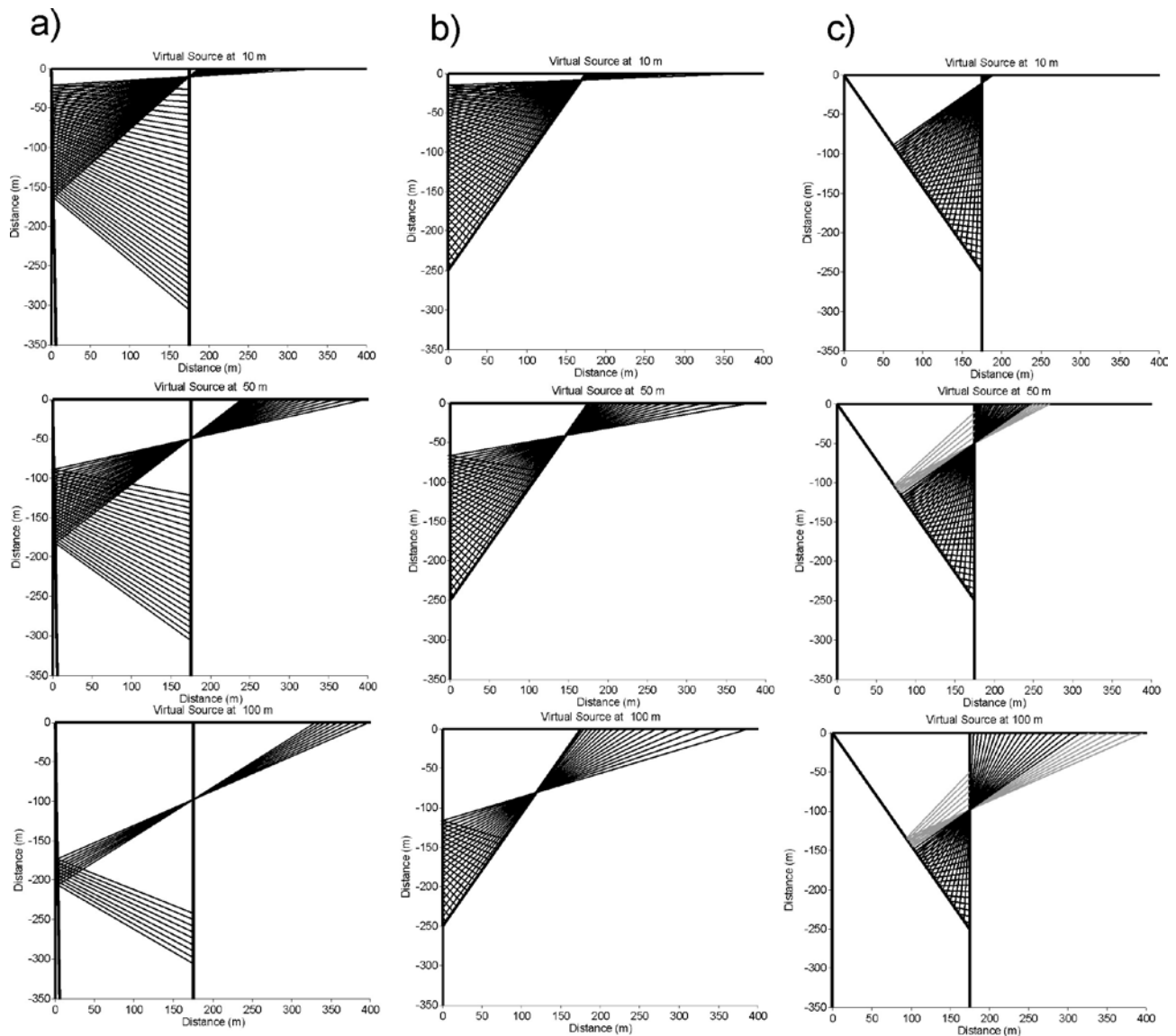
**Figure 1.** The effect of target and borehole dip on location of stationary phase ray paths. a) Target and borehole are both vertical. b) Target is vertical and borehole is dipping. c) target is dipping and borehole is vertical.
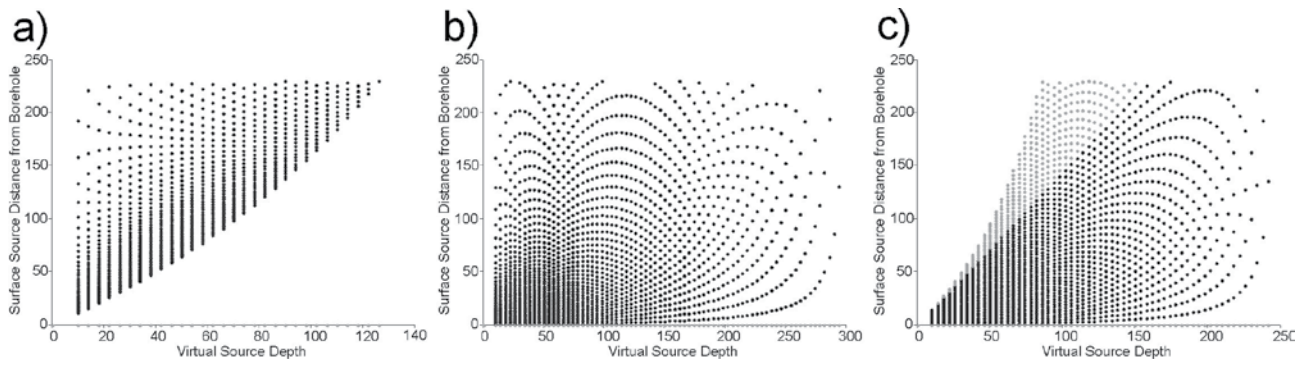
**Figure 2.** Scatter plots illustrating the surface source locations of stationary phase arrivals for virtual source locations along theborehole. a) Vertical borehole and target. b) Dipping borehole with vertical target. c) Vertical borehole with dipping target.
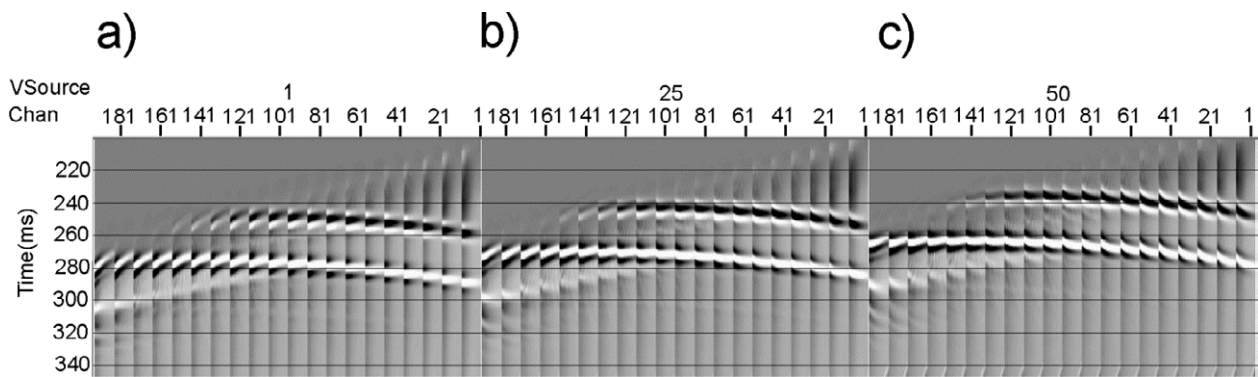


**Figure 3.** Selected channels for synthetic virtual source correlation gathers at a) the top of the borehole (VSource=1), b) 50 m depth (VSource=25) and c) 100 m depth (VSource=50). Channel 1 is at the top of the borehole.

# Reflection seismic imaging in the Skellefte ore district, northern Sweden

**Mahdieh Dehghannejad, Christopher Juhlin, Alireza Malehmir, Maria A. Garcia Juanatey**
*Department of Earth Sciences, Uppsala University, SE-75236 Uppsala, Sweden*

**Pietari Skyttä,**
*Department of Geosciences and Geography, University of Helsinki, FI-00014 Helsinki, Finland*

**Tobias E. Bauer, Pär Weihed**
*Division of Geosciences and Environmental Engineering, Luleå University of Technology, SE-971 87 Luleå, Sweden*

**Abstract.** The Skellefte ore district is one of the major mining districts in Sweden and is well known for its volcanogenic massive sulphide and gold deposits. Mineral exploration in the area is important and has been the reason to conduct various studies e.g., reflection seismic surveys, detailed field geological mapping, magnetotelluric measurements, and potential field modeling with the aim of understanding the relationship between the ore bearing volcanic and volcano-sedimentary formations and their surrounding intrusive rocks. Following a pilot project in the western part of the area, the Kristineberg mining area, a 3D/4D-modeling of mineral belts project was launched to improve the initial 3D model in the area and to provide more information in the shallow parts, but also to develop the model in the central parts of the district. Results from seismic reflection data were used as a backbone of the 3D geological modelling in the district and helped us to obtain a better understanding of the overall structures and their relationship with major mineralization zones.

**Keywords.** Skellefte district, 3D modelling, reflection seismic

## 1 Introduction

The Skellefte mining district covers an area of 120 by 30 km in northern Sweden (Figure 1) and is one the most important mining districts in the country, producing Zn, Cu, Pb, As and Au from volcanogenic massive sulphide and orogenic gold deposits (Allen et al. 1996; Kathol and Weihed 2005). Today, mineral exploration in the district is aimed at locating deposits at deeper levels e.g., down to 2000 m. To be successful in exploration, a better understanding of geological structures and the evolution of the area is necessary. Since 2003, the area has been the subject of several geological and geophysical studies with the aim of understanding the contact relationships between the ore bearing volcanic and volcano-sedimentary formations and the surrounding intrusive rocks (Tryggvason et al. 2006; Malehmir et al. 2006, 2007, 2009a, 2009b; Hübert et al. 2009, 2013; Skyttä et al. 2009, 2010, 2011, 2012; Dehghannejad et al. 2010, 2012a, 2012b; Bauer et al. 2011, 2012; Ehsan et al. 2012; Garcia et al. 2013).

Reflection seismic methods have proven to be effective together with other geophysics in imaging structures and lithological contacts in the western part of the area, the Kristineberg mining area (Tryggvason et al. 2006; Malehmir et al. 2007, 2009a, 2009b). Based on the earlier investigations, a 3D/4D-modeling project was launched in 2008. The project aims at understanding both the structure of the Earth's crust down to a few kilometers depth, and the relationship between the structure and the mineral deposits occurring in the area (Dehghannejad et al. 2010, 2012a, 2012b; Bauer et al. 2011, 2012; Ehsan et al. 2012; Skyttä et al. 2012).

Therefore, more than 100 km of new reflection seismic data with varying resolution and research objectives were acquired in the western and central parts of the district during 2008-2010. Geological observations (Skyttä et al. 2010 and 2011), magnetotelluric data (Hübert et al. 2013; Garcia et al. 2013), as well as potential field and deep IP measurements (Tavakoli et al. 2012a, 2012b), accompanied the reflection seismic data to facilitate their interpretations. Integration of these data with mine observations allowed an improved geologic model of the Kristineberg mining area and the construction of a 3D geologic model of the central Skellefte district. Here we present results from the reflection seismic study, which was used as a backbone of the model for the area.

## 2 Results from the seismic reflection data

### 2.1 Kristineberg mining area

Since 2003, four reflection seismic profiles with a total length of approximately 70 km have been acquired in the Kristineberg mining area (Figure 1). First, Profiles 1 and 5 were acquired with the aim of providing information about major geological structures down to 12 km in the crust (Tryggvason et al. 2006; Ehsan et al. 2012). Later, Profile 2 and the HR profile were acquired with the aim of providing higher resolution images of near-surface geological structures near the Kristineberg mine (Dehghannejad et al. 2010). Dynamite as a source was used for Profiles 1 and 5 and an impact source (Cosma and Enescu 2001) was used for Profile 2 and the HR (a higher resolution profile than Profile 2) profile to
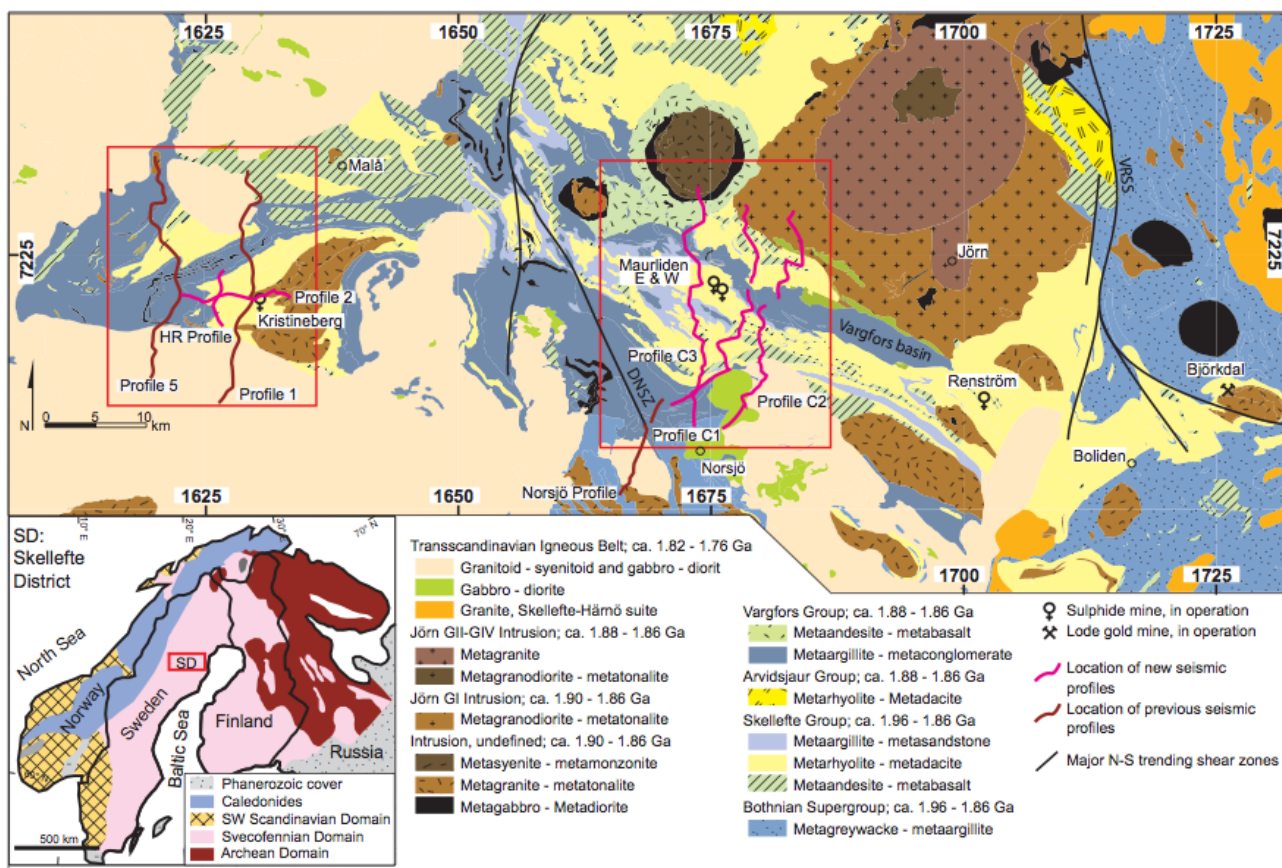
**Figure 1.** Simplified geological map of the Skellefte district with location of the previous and new seismic reflection profiles. Geological map is modified after Kathol and Weihed (2005). Seismic data in the Kristineberg mining area and central Skellefte district are the focus of this article.

generate the seismic signal. Data processing was carried out following a series of conventional processing steps used in the hard rock environment (for details about processing steps see Tryggvason et al. 2006 and Dehghannejad et al. 2010).

The quality of the data is good and we could image clear reflections, some of which reach the surface and allow correlation with surface geology and recent field geological mapping. Some of the reflections correlate well with known location of faults or high-strain zones and some appear to occur within a zone where the Kristineberg ore bodies are situated. Although, it is not clear if these reflections are generated from mineralization zones, a reflective package extending down to about 2.25 km can be suitable target for future deep exploration in the area. Numerical modelling results recently carried out using available geological and petrophysical knowledge support that some of the reflections could be generated from massive sulphide bodies (Dehghannejad et al. 2012b). Nevertheless, a 3D seismic survey is required to accurately locate these reflections and provide targets for drilling.

Figure 2 shows 3D views from the acquired seismic profiles (i.e., Profiles 1, 2 and HR) and the correlation of seismic events from one profile to another and also the relationship with ore horizons in the area. It also shows a 3D visualization of the seismic reflections interpreted along the HR profile, the most important geological

surfaces, and the ore lenses of the Kristineberg deposit. Structurally, the reflective zones (Figure 2b) are cut by steeply south-dipping high-strain zones which locally steepen the dip of reflections. Similar to the reflective zones, the ore lenses have also been affected by deformation along the high-strain zones.

## 2.2 Central Skellefte district

During 2009-2010, three sub-parallel, ~ N-S trending reflection seismic profiles were acquired (Profiles C1, C2 and C3, Figure 1) to constrain a 3D geological model of the central Skellefte district (Dehghannejad et al. 2012a). Each profile is about 30 km long and approximately 3 to 7 km apart from each other. The profiles were placed perpendicular to the main structural trend of the district. To compare the results, we used the same recording system as we used in the Kristineberg mining area in 2008.

These seismic profiles resulted in imaging several steeply dipping reflections, many of which correlate with surface geological observations. The majority of the reflections that extend to the surface were correlated with geological features either observed in the field or interpreted from the aeromagnetic map of the study area. Main reflections correlate well with major faults and shear-zones and/or represent lithological contacts
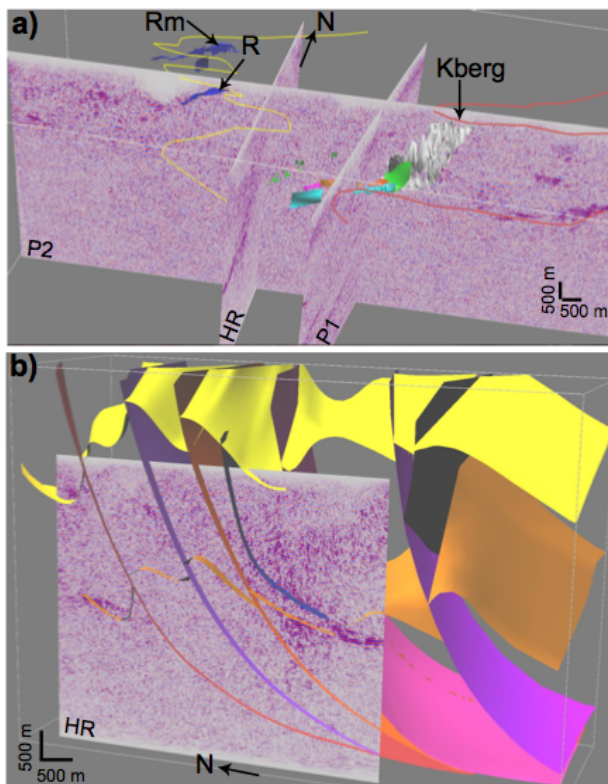
**Figure 2.** a) 3D visualization of the seismic data along profiles 1, 2 and HR with the known mineralized bodies, showing correlation of the reflections with the orebodies in the area. Yellow and brownish lines mark the top contacts of the Skellefte Group metavolcanic rocks and Viterliden intrusion, respectively.  R=Rävliden,  Rm=Rävlidmyran, Kberg=Kristinberg ore bodies (marked by white, green, orange, light blue, and pink colors). b) Interpreted 3D structure of the Kristineberg area showing relationships between the seismic data, ore deposits, major faults, and lithostratigraphical units, view toward east-northeast. Yellow surfaces=the top of the Skellefte Group volcanic rocks, Orange surfaces=the inferred top contact of the Viterliden intrusion, the steeply dipping blue-purpled surfaces=known and inferred faults. Modified from Dehghannejad et al. (2012b).

(Dehghannejad et al. 2012a). 3D views of the seismic profiles in the central Skellefte district and their 3D interpretation are shown in Figure 3.

## 3  Conclusions

The new seismic results in the Kristineberg area confirmed some of the previous interpretations, but also provided additional and local-scale constraints on the subsurface geology. High-resolution data along the HR profile proved to be successful in imaging potentially reflections associated with mineralization zones, although this needs further support.

Results from the three new seismic profiles in the central Skellefte district show a relatively different seismic character compared with those of the Kristineberg mining area, but also have helped us to understand the geological structures and significance of major shear zones in the creation of the sedimentary basins in the central Skellefte district.
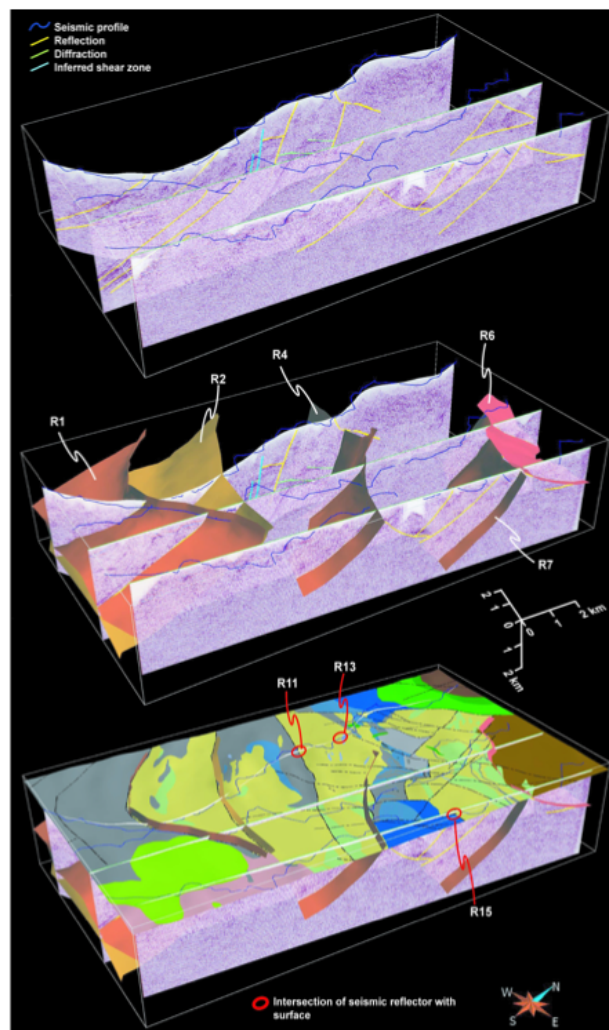


**Figure 3.** 3D views of the seismic profiles in the central Skellefte district, showing correlation between the imaged reflectors and surface geology. Modified from Dehghannejad et al. (2012a).

## References

Allen RL, Weihed P, Svenson S-Å (1996) Setting of Zn-Cu-Au-Ag massive sulphide deposits in the evolution and facies architecture of a 1.9 Ga marine volcanic arc, Skellefte district, Sweden. Economic Geology 91:1022

Bauer TE, Skyttä P, Allen RL, Weihed P (2011) Syn-extensional faulting controlling structural inversion − Insights from the Palaeoproterozoic Vargfors basin, Skellefte mining district, Sweden. Precambrian research 191:166−183

Bauer TE, Skyttä P, Allen RL, Weihed P (2012) Fault-controlled sedimentation in a progressively opening extensional basin: the Palaeoproterozoic Vargfors basin, Skellefte mining district, Sweden. International Journal of Earth Sciences, DOI 10.1007/s00531-012-0808-x

Cosma C, Enescu N (2001) Characterization of fractured rock in

the vicinity of tunnels by the swept impact seismic technique. International Journal of Rock Mechanics and Mining Sciences 38: 815−821

Dehghannejad M, Bauer T, Malehmir A, Juhlin C, and Weihed P (2012a) Crustal geometry of the central Skellefte district, northern Sweden-constraints from reflection seismic investigations. Tectonophysics 524−525: 87−99

Dehghannejad M, Juhlin C, Malehmir A, Skyttä P, Weihed P (2010) Reflection seismic imaging of the upper crust in the Kristineberg mining area, northern Sweden. Journal of Applied Geophysics 71: 125−136

Dehghannejad M, Malehmir A, Juhlin C, and Skyttä P (2012b) 3D constraints and finite-difference modeling of massive sulfide deposits: The Kristineberg seismic lines revisited, northern Sweden. Geophysics 77(5): WC69−WC79

Ehsan SA, Malehmir A, Dehghannejad M (2012) Re-processing and interpretation of 2D seismic data from the Kristineberg mining area, northern Sweden. Journal of Applied Geophysics 80: 43−55

Garcia Juanatey MA, Hübert J, Tryggvason A, Pedersen LB (2013) Imaging the Kristineberg mining area with two perpendicular magnetotelluric profiles in the Skellefte Ore District, northern Sweden. Geophysical Prospecting 61: 200−219

Hübert J, Garcia M, Malehmir A, Tryggvason A, and Pedersen L.B, (2013) Upper crustal resistivity structure of the Kristineberg area, Skellefte district, northern Sweden, revealed by 3D magnetotellurics. *Geophysical Journal International (GJI)* 192: 500-513

Hübert J, Malehmir A, Smirnow M, Tryggvason A, Pedersen LB (2009). MT measurements in the western part of the Paleoproterozoic Skellefte Ore District, Northern Sweden: A contribution to an integrated geophysical study. Tectonophysics 475: 493−502

Kathol B, Weihed P (2005) Description of regional geological and geophysical maps of the Skellefte district and surrounding areas. Geological Survey of Sweden SGU, Uppsala

Malehmir A, Schmelzbach C, Bongajum E, Bellefleur G, Juhlin C, and Tryggvason A (2009a) 3D constraints on a possible deep >2.5 km massive sulphide mineralization from 2D crooked-line seismic reflection data in the Kristineberg mining area, northern Sweden. Tectonophysics 479: 223−240

Malehmir A, Thunehed H, and Tryggvason A (2009b) The Paleoproterozoic Kristineberg mining area, northern Sweden: Results from integrated 3D geophysical and geologic modeling, and implications for targeting ore deposits. Geophysics 74: B9−B22

Malehmir A, Tryggvason A, Juhlin C, Rodriguez-Tablante J, Weihed P (2006) Seismic imaging and potential field modeling to delineate structures hosting VHMS deposits in the Skellefte Ore District, northern Sweden. Tectonophysics 426: 319−334

Malehmir A, Tryggvason A, Lickorish H, Weihed P (2007) Regional structural profiles in the western part of the Palaeoproterozoic Skellefte ore district, northern Sweden. Precamberian Research 159: 1−18

Skyttä P, Bauer TE, Tavakoli S, Hermansson T, Andersson J, Weihed P (2012) Pre-1.87 Ga development of crustal domains overprinted by 1.87 Ga transpression in the Palaeoproterozoic Skellefte district, Sweden. Precambrian Research 206−207: 109−136

Skyttä P, Hermansson T, Bauer TE (2009) Three Dimensional Structure of the VMS-hosting Palaeoproterozoic Kristineberg Area, Northern Sweden. Proceedings of the 10th biennial SGA meeting, Townsville, Australia, 909−911

Skyttä P, Hermansson T, Andersson J, Weihed P (2011) New zircon data supporting models of short-lived igneous activity at 1.89 Ga in the western Skellefte District, central Fennoscandian Shield. Solid Earth 2: 205–217

Skyttä P, Hermansson T, Elming S.-Å, Bauer TE (2010) Magnetic fabrics as constraints on the kinematic history of a pre-tectonic granitoid intrusion, Kristineberg, northern Sweden. Journal of Structural Geology 32: 1125–1136

Tavakoli S, Elming S-Å, Thunehed H (2012a) 3D Modelling of the Central Skellefte district, Northern Sweden; an Integrated Model based on the electrical, potential field and petrophysical data. Journal of Applied Geophysics 82: 84−100

Tavakoli S, Elming S-Å, Thunehed H, Weihed P (2012b) Regional-scale geometry of the central Skellefte district, northern Sweden- results from potential field modelling along three previously acquired seismic profiles. Journal of Applied Geophysics 85:43−58

Tryggvason A, Malehmir A, Rodriguez-Tablante J, Juhlin C (2006) Reflection seismic Investigations in the Western Part of the Paleoproterozoic VHMS- Bearing Skellefte District, Northern Sweden. Economic Geology 101: 1039−1054

# Testing the use of FDEM EM34 for disseminated chromite prospecting in Trás-os-Montes, Portugal

**Elsa C. Ramalho**
*LNEG (Laboratório Nacional de Energia e Geologia), Mineral Resources and Geophysics Unit, Apartado 7586, 2721-866 Alfragide, Portugal*

**Daniel P. S. de Oliveira**
*LNEG (Laboratório Nacional de Energia e Geologia), Mineral Resources and Geophysics Unit, Apartado 7586, 2721-866 Alfragide, Portugal and CREMINER (Centro de Recursos Minerais, Mineralogia e Cristalografia), Edifício C6, piso 3, 1749-016 Lisboa, Portugal*

**Helena M.C.V. Santana**
*LNEG (Laboratório Nacional de Energia e Geologia), Mineral Resources and Geophysics Unit, Apartado 7586, 2721-866 Alfragide, Portugal and DGEG (Direcção Geral de Energia e Geologia), Av. 5 de Outubro, nº 87, 1069-039 Lisboa*

**Abstract.** The use of geophysics electromagnetics Geonics EM34 applied to disseminated chromite prospecting is not common. Other methods, such as magnetics, induced polarisation or gravimetry are used instead. This work refers to some tests made in Trás-os-Montes, Northern Portugal, regarding the use of frequency domain electromagnetics using the device Geonics EM43 for chromite prospecting, in areas where soil geochemistry data were also available. Several electromagnetic profiles were made and data were inverted so that potential conductivity contrasts between mineralised metadunite formations and metaperidotites, shape of the mineralised bodies, dimensions and depth could be visualised. Inverted resistivity data were correlated with surface geology, borehole logs information and soil geochemistry. In this paper, results for the selected area of Sardoal are presented.

**Keywords. Geophysics, electromagnetic methods, chromite.**

## 1 Introduction

The application of geophysical methods to disseminated chromites prospecting is usually based on magnetic, induced polarisation and especially gravimetric methods (Frashieri et al. 1995; Frashieri 2006). Although the use of frequency domain electromagnetic (FDEM) methods, namely the Geonics EM34, in chromite prospecting is not common, tests were conducted in some selected areas, in Trás-os-Montes, NE Portugal. Results were correlated with soil geochemistry conducted in the same places by Pires (1998). This test was justified not only by the easy-to-use characteristics of the equipment to conduct preliminary surveys, but also by the fact that modelling may give interesting information about the way chromite mineralisation develops at depth, since the method reaches small investigation depths. In this paper, results for the selected study area of Sardoal are presented.

## 2 Local geology

The most promising spots in the Sardoal area are located in a metadunite unit or other metaperidotites with chromite mineralisation, with intense serpentinisation (Fig. 1). The metadunites and metaperidotites are characterised as fine to very fine-grained and by being dark in handspecimens with the presence of abundant, rounded to subrounded disseminated chromite grains with sizes ranging from 0.1 to 2 mm (Fig. 2), which make observation of chromite very difficult.
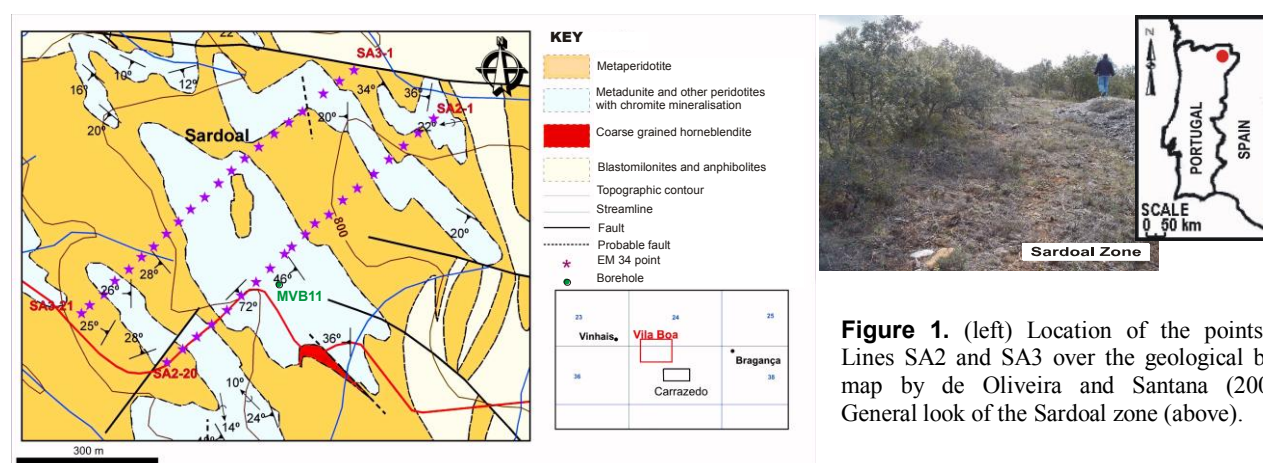


**Figure 1.** (left) Location of the points in Lines SA2 and SA3 over the geological base map by de Oliveira and Santana (2007). General look of the Sardoal zone (above).

This mineralised unit occurs inside a metaperidotite unit, whose appearance varies considerably, generally with fine to medium size, where all the ultrabasic lithologies not containing mineralisation were included in the same unit, namely the metaperidotites, metadunites and amphibolites (from 1cm to several centimetres of thickness).

## 3 Geophysical data acquisition and processing

The chromite grains produced as a result of serpentinisation processes are frequently altered to ferrichromite and magnetite, and, in some cases, are covered by magnetite membranes crystallised as finely disseminated grains due to the intense dynamic processes or due to the presence of secondary magnetite, in the serpentinised dunites (Frashieri et al. 1995). It is also the magnetite, acting as a good conductor when it appears as single crystals (Reynolds 1997), that gives higher conductivities to the serpentinised metadunites (Telford et al. 1990). Its contrast with conductivities of the adjacent metaperidotite formations may be detected with appropriate methods, such as magnetics, induced polarisation or gravimetry.

Since the metadunite serpentinisation gives them low resistivity that Frashieri et al. (1995) refer as varying between 100 and 650 ohm.m), they contrast electrically with non-serpentinised dunites (whose electrical resistivity, according to the same authors varies between 2200 and 7000 ohm.m), and therefore may eventually respond positively to this method.

This method was applied to several zones in the Trás-os-Montes area, Northern Portugal, where soil geochemistry analysis were conducted and also where a few boreholes were drilled.

In this paper the results for the Sardoal zone are presented. In this zone, two FDEM lines with the Geonics EM34 device headed perpendicularly to the main axis of the metadunitic structures (Fig. 1) were conducted. Data acquisition took place every 40 m with cables of 10 and 20 m (6.4 and 1.6 kHz, respectively). FDEM data processing was carried out with the software EM34-2D, developed by Monteiro Santos (2004), where the bi-dimensional model used in the inversion process consists of a number of blocks, where their distribution and size depend on the locations and spacings number between the coils used in data acquisition. The use of the cumulative response to calculate the model response in each point means that the interaction between the blocks that form the model is not being considered (Monteiro Santos 2004). The model has the objective of obtaining an inverse 2D model and to distinguish between layers with different conductivity producing layers (showing significant contrasts between serpentinised metadunites and metaperidotites) and highlighting their different alteration degrees. The obtained errors were 2.3 and 3.1 % to the Lines SA2 and SA3, respectively.

## 4 Borehole data

The analysis of the MVB11 borehole (Fig. 1, left), reaching 50 m depth in the Sardoal area (de Oliveira et al., 2008), near Line SA3 allowed interpreting and correlating electrical resistivity modelled values and observed lithology. The borehole was drilled in an area that simultaneously shows resistivity modelled values that may be attributed to serpentinised dunites and where soil Cr and Pt concentration values give good prospects in depth. The borehole lithology shows that the existence of disseminated chromite is constant along the borehole, with Pt concentrations varying from <2 to 10 ppb. However, serpentinisation processes only occur at 10 m and from 17 to 34 m (with intense serpentinisation between 17 to 30 m).



**Figure 2.** Metadunite with disseminated chromite and microfractures filled with serpentine (de Oliveira et al., 2008).

## 5 Discussion

The analysis of modelled electrical conductivities and resistivities from both Sardoal FDEM lines (Figs. 3 and 4), allowed inferring that the investigation depth of the method in seems to be higher in some areas than the depth of the formations where, according with Frashieri et al. (2006), can occur serpentinised dunites, which seems to be in average about 20 m deep.

Inverse modelling confirms the existence of resistivities ranging from 100 to 650 ohm.m in zones where old chromite exploitations are registered. This is the case of points SA2-4 and SA2-5 in Line SA2 that may indeed be related with the presence of disseminated chromite. However, from the observation of MVB11 borehole log and the geological mapping these doesn't seem to exist a systematic correlation between the metadunitic zones and the electrical resistivity models and resistivity ranges defined by Frashieri et al. (1995).
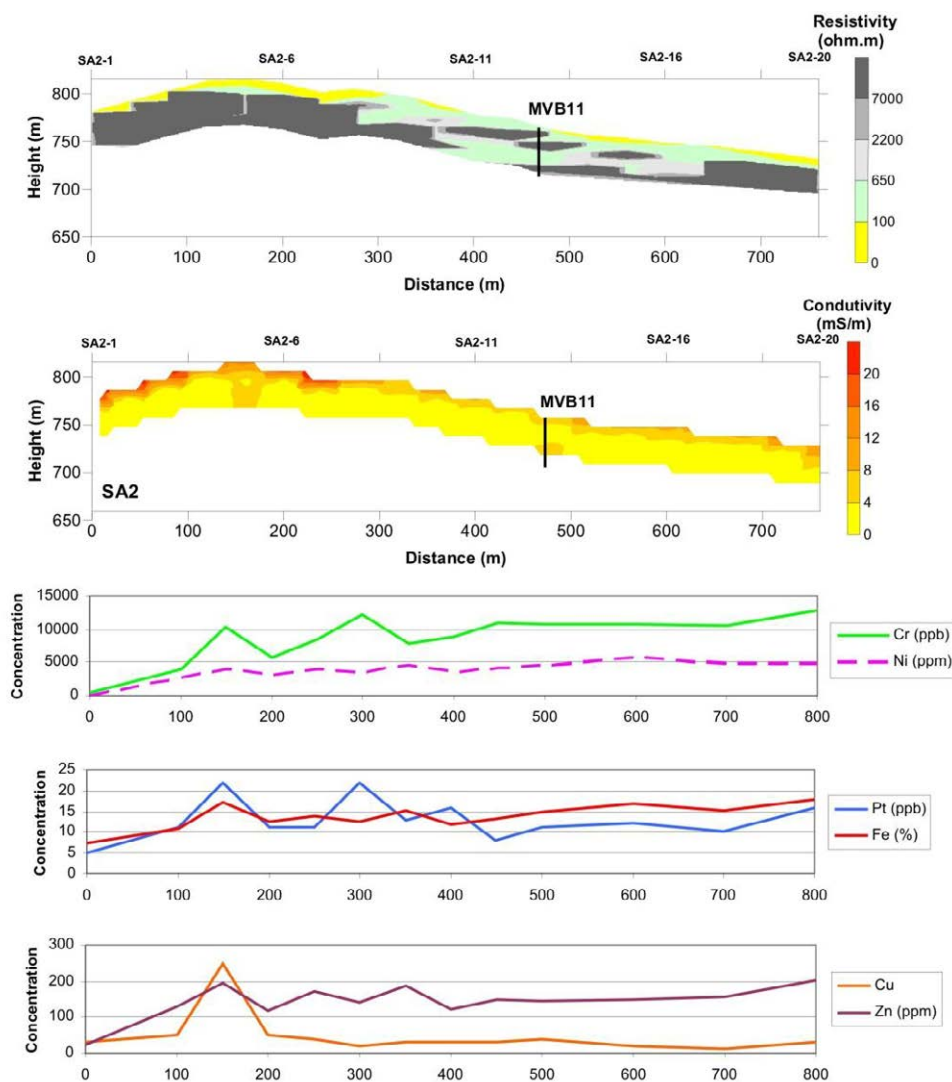
**Figure 3.** Correlation between the inverse electrical conductivity and resistivity models and the concentrations of some elements determined on Line 0 from the Pires (1998) report, corresponding to the Line SA2. The vertical borehole MVB11, whose location is presented in Fig. 1, is also shown.

On the other hand, the metadunitic spot located in the NE studied area shows lower resistivity values than those that were found in the inverted electromagnetic profiles, larger than the mapped metadunitic spot. These lower conductivity values seem to have continuity, since they were mapped in both profiles. For instance, the Line SA2, where the mapped dunitic spot between points SA2-10 to SA2-16 is slightly smaller than the outcropping electrical resistivity values ranging from 100 to 650 ohm.m. These values, however, vary in depth, creating a body where Cr and Pt concentrations have some peaks in those zones. Between points SA2-5 and SA2-8 the lower resistivity may not correspond to serpentinised metadunites, since they are located in metaperidotite outcrops.

In Line SA3, the correspondence between the metadunite outcrops and the lower resistivity values near the surface is much more correlated than in Line SA2. However, these lower electrical resistivities are not reflected in higher surface concentrations of Cr, Fe and Pt. It must be highlighted that in this profile, the lowest resistivities that correspond to the large metadunitic central spot are not continuous. The average depth of 20

m of the electrical resistivities affects zones topographically lower, whose resistivity is affected by the existence of crossing streamlines and with a shallower saturated zone, which may also affect the results obtained by the method.

Line SA2 was conducted in a zone where the Pt concentration registered by Pires (1998) ranged from 5 to 25 ppb and with Cr values varying from 6660 and 16300 ppm. Line SA3 was conducted in a zone where Pt concentration is between 2.5 and 11 ppb, lower than the average values of Line SA2 (Pires 1998). Regarding Cr, concentration values vary from 7730 to 17100 ppm. In general, for Line SA2, the best correlation between shallow low resistivity values and elements analysed by Pires (1998) seems to correspond to higher contents of Pt. However, for Line SA3, this correlation doesn't work in the same way.

# 6 Summary

Based on works conducted by Frashieri (1995) and Frashieri et al. (2006), and keeping in mind the results of

the inverse resistivity models, the FDEM Geonics EM34 is a method that may be considered as an interesting and easy-to-use method to obtain some preliminary information about the development in depth of the disseminated chromite mineralised structures. In the tested Sardoal zone, there seems to be a relation among the electrical resistivity inverse model and soil geochemistry, borehole lithology and chemical analysis related with some elements, whose presence could explain the resistivity variation values. Although there is a strong correlation between the identification of

serpentinisation processes and the modelled electrical resistivities attributed to these processes, the relation between shallow modelled resistivity values with mapped geology is not clear and in some areas they do not seem so correspond. Nevertheless, it is important to use other methods whose applicability has proved to obtain more consistent results with this objective, such as magnetic and gravimetric prospecting.
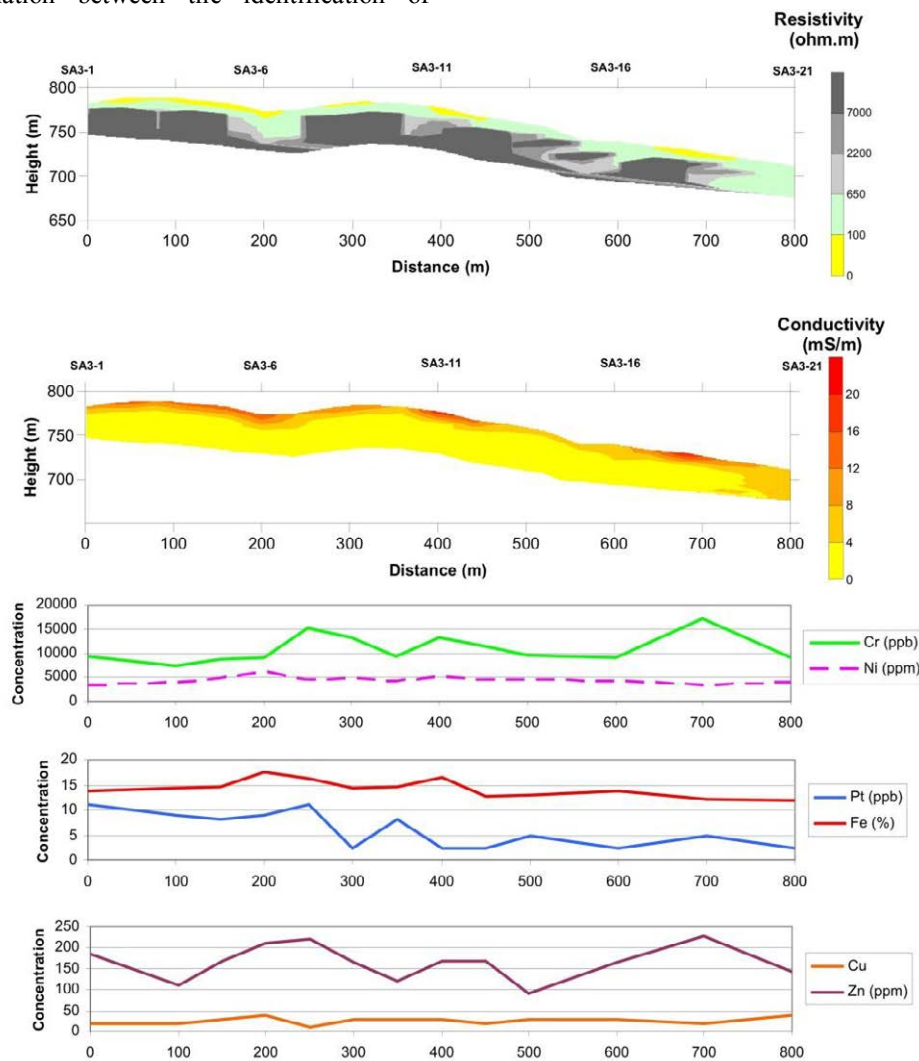


**Figure 4.** Correlation between the inverse electrical conductivity and resistivity models and the concentrations of some elements determined by Pires (1998) in his Line 200, corresponding to the Line SA3.

# References

de Oliveira DP and Santana HM (2007). Geological mapping of 30 km² of the Bragança Massif in the Carrazedo-Alimonde-Conlelas. Vila Boa de Ousilhão area (NE Portugal): A guide to further chromite exploration and other possible associated PGE's. INETI internal report, 57p.

de Oliveira DP, Santana HM and Ramalho EC (2008). Campanha de Sondagens no Maciço de Bragança para prospecção de Platinídeos. INETI internal report, 46p.+annexes

Frasheri A (2006). Outlook on the application of geophysical methods in exploration for copper and chrome ores in Albania. Polytechnic University of Tirana.

Frasheri A, Lubonja L and Alikaj P (1995). On the application of geophysics for copper and chrome ores in Albania. Geophysical Prospecting, v.43, pp.743-757.

Pires M (1998). Relatório anual 1998. Relatório interno do Instituto Geológico e Mineiro, Refª #2829 and #2836.

Reynolds JM (1997). *An Introduction to Applied and Environmental Geophysics*, West Sussex, John Wiley & Sons.

Monteiro Santos FM (2004). 1-D laterally constrained inversion of EM34 profiling data. Journal of Applied Geophysics. v.56, pp.123-134.

Telford WM, Geldart LP and Sheriff RE (1990). *Applied Geophysics*, Cambridge University Press, 770p.

# Seismic techniques for ore deposit delineation and resource evaluation

C. Hurich*, S. Deemer, B. Reid, O. Onabiyi, P. Zheglova & C. Farquharson
*Earth Sciences Department, Memorial University, St. John's, NL, Canada. (churich@mun.ca)*

**Abstract.** Seismic techniques have significant potential for providing data that are critical for deposit delineation and resource evaluation. Developing and emerging seismic technologies include; combined surface and borehole imaging and surface to borehole and borehole to borehole tomography. Combined surface and borehole imaging using seismic interferometry to redatum surface sources into the borehole helps mitigate imaging bias inherent in surface seismic data and allows imaging of structures with dips ranging from horizontal to vertical. Tomography that combines the flexibility of unstructured meshes with appropriate choices of seismic arrivals provides convenient links between the geophysical data and mesh based geologic models. This paper demonstrates the potential of these techniques through examples using both synthetic and real seismic data.

**Keywords. Seismic imaging, seismic interferometry, tomography, deposit delineation, resource evaluation**

## 1 Introduction

There is significant interest in applying seismic techniques for delineation and evaluation of hard rock minerals deposits because of the inherent high resolution of seismic techniques compared to more traditional geophysical methods. In particular, the number of traditional two- and three-dimensional surface surveys is increasing. These surveys predominantly provide structural information that can be used to infer the controls on and trends of mineralization. In addition these data allow for fault mapping and occasionally direct detection of ore deposits.

Seismic data also have the potential to play a significant role in detailed deposit delineation, resource evaluation and mine planning. An array of seismic techniques that take advantage of both surface and borehole sources and receivers are undergoing continuing development and are starting to demonstrate their value for deposit evaluation and resource estimation.

In this paper we discuss and demonstrate the potential and limitations of combined surface and borehole imaging using seismic interferometry, surface to borehole tomography and borehole to borehole tomography. These techniques are part of a growing group of seismic techniques that should join our geophysical toolbox in the near future.

## 2 Combined surface and borehole imaging

The response of seismic reflection techniques is biased by the orientation of the source and receiver arrays. For instance, surface seismic surveys that employ CMP stacking are inherently biased against steep dips by the array response of the stack. Ore deposits commonly are geologically complex with dips of any orientation with respect to the surface. Combined surface and borehole imaging offers a larger range of illumination angles than conventional surface techniques which partially mitigates imaging bias and allows imaging of wider range of geologic dips.

Combined imaging is implemented by collocating a 2-D common midpoint (CMP) surface survey and a walk-away vertical seismic profile (VSP). The VSP data are redatumed to the borehole receiver locations using a form of seismic interferometry (Sneider, 2004, Bakulin and Calvert, 2006; Draganov et al. 2006, Hornby and Yu, 2007, Schuster, 2009). Redatuming results in a virtual seismic profile with sources and receivers in the borehole. The virtual seismic profile can then be processed as a standard CMP profile. Combination of the surface and borehole profiles effectively results in illumination of the subsurface from both above and the side which allows imaging of a broad range of dips.

### 2.1 Examples: Seismic interferometry and combined surface-borehole imaging

Figure 1 illustrates a synthetic example of the use of seismic interferometry to convert walk-away VSP data into a virtual seismic profile and the method's effectiveness for imaging steep dips. The geologic model (Figure 1a) represents a deformed dike with an average dip of 70° and thickness varying between 30 and 60 m. The synthetic VSP data were acquired using an acoustic finite difference solution because the receivers in our field experiments comprise hydrophone cables in water filled boreholes. In this example we model a vertical borehole with a 4 m receiver spacing over the entire depth of the borehole (300 receivers) and 180 surface shots with an 8 m spacing and a maximum offset of 1440 m from the borehole.

Figure 1b shows a time migration of the virtual CMP profile in the borehole created through the interferometry process. The method successfully images many of the details of the dike and in particular the steeply dipping components that would not have been imaged in a surface profile. The quality of the image decreases near the top of the dike where the conditions for interferometry are not satisfied ((Mehta 2008, Brand 2013).

The large number of source locations used in this demonstration model would likely be difficult and expensive to attain under ordinary field conditions in a minerals exploration setting. However, additional work with the data demonstrates that decimation of the source data by 10 (180 to 18 shots) results in minor degradation of the final image. A walk-away VSP with 18 shot points is a potentially viable field acquisition scenario as

will be demonstrated in the following examples of field data.

## 2.2 Field examples

Two field experiments were carried out as a collaborative project of Memorial University and Vale at Vale's Voisey's Bay mine site in northern Labrador, Canada. The Voisey's Bay sites host extensive nickel-copper-cobalt mineralization associated with a magmatic event that is locally characterized by intrusion of sulphide-bearing troctolitic magma. Massive sulphide concentrations are associated with both the large troctolite bodies and the system of dikes that fed the troctolite bodies. Within the feeder system, massive sulphides are concentrated at kinks in the feeder dikes making the mapping of the generally steeply dipping dikes, and particularly the kinks in the dikes an important exploration objective.
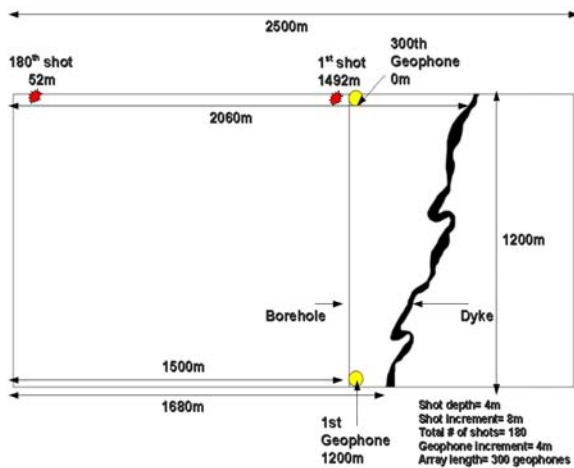


**Figure 1a.** Geologic model used to generate the walk-away VSP data used to derive the synthetic seismogram shown in Figure 1b.
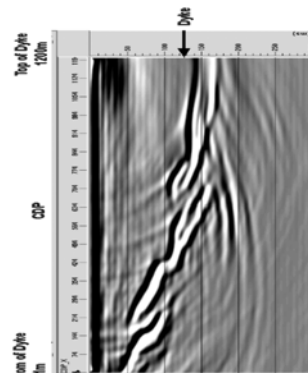


**Figure 1b.** Synthetic seismic image of the dike generated by using seismic interferometry to redatum the walk-away VSP data into the borehole.

The experiments were carried out in the Reid Brook zone of the Voisey's Bay deposit with the objective of imaging the mineralized troctolite dike that intrudes the gneissic country rock and dips at 50-90°. The detailed geometry of the dike is relatively complex with segments of variable dip. The thickness of the dike varies from 20 to 60 m in the area of the experiments. Physical properties data indicate an average reflection coefficient between the troctolite and the gneisses. However, the contrast between the gneiss and troctolites is only moderately higher than that between the felsic and mafic components of the gneisses (±0.05).

The first example (Figure 2) (Hurich and Deemer, 2013) is a situation in which the dike dips at about 60° and intersects the near vertical borehole. The field experiment consisted of a walk-away VSP and a surface seismic profile that is centered on the borehole used for the VSP. The receivers for the VSP comprised a 60 m hydrophone cable with 2 m hydrophone spacing. The borehole was surveyed over the depth range of 750 m to 272 m so the VSP was constructed from eight passes over the source locations, raising the hydrophone cable for each pass to provide continuous two m sampling over the surveyed depth range. The source was a swept impact source mounted on a medium-sized excavator. The source spacing was 20 m with five sweeps of the source at each shot point for a total of 20 shot points and maximum offset from the borehole of 400 m. The walk-away experiment resulted in 20 individual VSP panels each of which record the full depth range of the borehole array.

Interferometric processing of the VSP data resulted in 240 borehole referenced virtual shot gathers with a 2 m shot spacing. The resulting virtual shots were processed using a standard CMP processing flow resulting in a borehole based CMP profile with fold varying from 1 at the ends of the profile to 236 in the middle of the profile and imaged using post-stack Kirchhoff depth migration.

The surface data were acquired using a fixed receiver spread of 150 stations with a 10 m geophone spacing and shot spacing of 20 m. The data were acquired by shooting through the entire spread. This acquisition geometry resulted in a 5 m CMP spacing. Processing of the surface data followed a standard processing sequence resulting in CMP fold varying between eight at the ends of the spread to 69 in the center of the spread. The data were imaged with a post-stack Krichhoff depth migration.

Figure 2 shows the two seismic profiles. In both profiles, the reflection wave field is complex with event coherence limited to 100-200 m, a response that is typical of polydeformed gneissic sequences. Correlation with lithologic and televiewer logs indicate that the reflections predominantly originate from fluctuations between the mafic and felsic components of the gneiss. However, despite the limited length of the surface profile, the data were quite successful in imaging the target dike in the (300-650 m range) where the dip of the dike shallows to about 45 degrees. The virtual source profile clearly images the lower portion of the dike. However, the geometry of the experiment (dipping target and near-vertical borehole), does not allow imaging of the upper portion of the dike. This is because the stationary phase ray paths required for interferometric processing do not occur.

The second field example tested the case of a near-vertical target and dipping borehole. This geometry is more favourable than the first example with respect to imaging the near-surface. Figure 3 shows the results of this experiment. The lower and upper parts of the dike

are well imaged but the middle portion that is more geometrically complex is only partially imaged. In addition, some of the reflected energy in the middle portion is interpreted as coming from out of the plane of the profile due to the 3-D geometry of the dike. Based on the geometry of the dike, this experiment would have benefited from a collocated surface profile but the topography restricted the access of the seismic source.
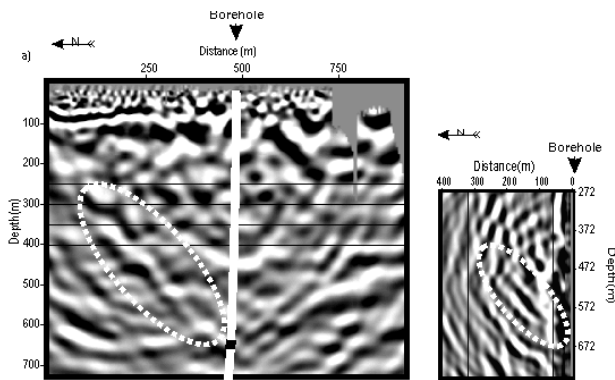


**Figure 2.** Results of collated surface and VSP experiments. This experiment tested the case of a dipping target and near-vertical borehole. The left panel shows the surface data and the right panel the virtual source data. In both case the target dike is highlighted.
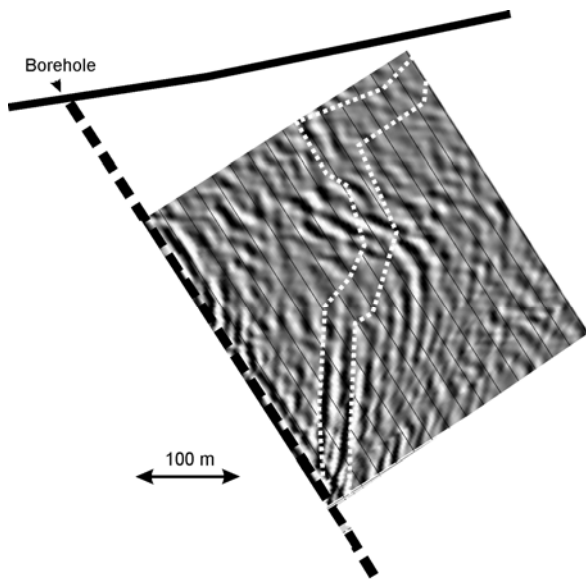


**Figure 3.** Results of experiment testing the case of a dipping borehole and near-vertical target. The outline of the dike inferred from boreholes is shown in the dashed line.

## 3 Tomography

Mineral deposits characterized by significant velocity contrasts with respect to their host rocks are good candidates for seismic tomography. The resolution of tomography is dependent on a number of parameters but key among them is the frequency content of the data. The frequencies available in surface to borehole seismic data used for interferometric processing or surface to borehole tomography are expected to be higher than surface data due to the one- versus two-way travel

through the near-surface zone and decreased scattering associated with shorter travel paths. The higher frequency content offers the opportunity for deposit delineation using the same walk-away VSP data used to derive virtual seismic profiles.

Figure 4 shows a synthetic example that illustrates the potential benefits of surface to borehole tomography. The geologic model is based on borehole data from the Eastern Deeps zone of the Voisey's Bay deposit. The massive sulphide ores in the Eastern Deeps zone occur at the base of a large troctolite body at 500 m depth. In this case, surface sources are recorded in four boreholes and first arrival times inverted resulting in a minimum structure tomogram that effectively localizes the massive sulphide body. The example illustrates that surface to borehole tomography has the potential to test large areas of the subsurface in support of exploration and deposit delineation.
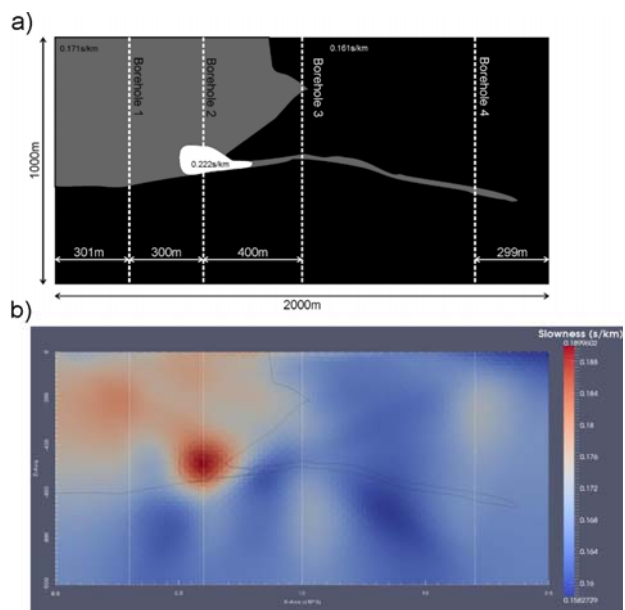


**Figure 4.** a) Geologic model of the Eastern Deeps zone of the Voisey's Bay massive sulphide deposit derived from borehole data. b) Tomogram derived from minimum structure inversion of the first arrivals from four boreholes that demonstrates clear localization of the massive sulphides at 500 m.

Borehole to borehole tomography offers significantly higher resolution than surface data because of the availability of frequencies in the range of one to three KHz. The resolution available with these high frequencies holds potential for high resolution deposit delineation and for building resource evaluation models. Resource evaluation models generally require identification of distinct rock bodies with specific properties. This requirement demands approaches to inversion that generate sharp boundaries as compared to the gradational boundaries resulting from typical minimum structure inversion. Figure 5 shows a comparison between tomograms generated using minimum structure inversion and a level sets-based inversion. The tomograms were generated from borehole to borehole seismic data collected in the Reid Brook zone of the Voisey's Bay deposit. The level sets approach (Zheglova et al., 2013) requires knowledge of

the velocity of the ore bodies and the host rocks but in turn generates sharp boundaries that are directly compatible with wire-frame style geologic modelling software. Using both types of inversion in conjunction, the minimum structure tomogram (together with borehole sonic logs) provides the velocity constraints and a starting velocity model for the level sets inversion which provides the distinct bodies required for resource evaluation.
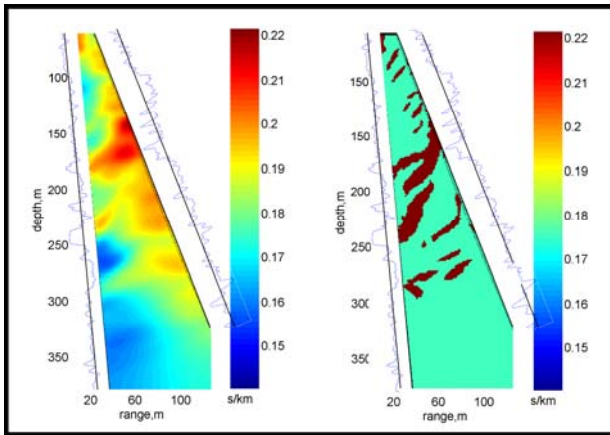


**Figure 5.** Comparison between borehole to borehole tomograms derived from minimum structure (left panel) and levels sets (right panel) inversion styles.

## 4 Summary

Seismic interferometry and tomography in conjunction with surface seismic data are representative of a variety of seismic techniques presently available or under development that have significant potential to make valuable additions to the geophysical tool box for minerals exploration. In particular, seismic techniques have unexploited potential for deposit delineation and resource evaluation. It is our contention that the minerals industry needs to take a long, hard look at these technologies as minerals exploration moves to deeper and covered terrains.

### Acknowledgements

### References

Bakulin A, Calvert R (2006) The virtual source method: Theory and case study: Geophysics, 71: SI139-SI150

Brand E, Hurich C, Deemer S (2013 in press) Geometrical considerations in the acquisition of borehole interferometric data for imaging near-vertical features: design of field experiments, Geophysics.

Draganov D, Wapenaar K, Thorbekke J (2006) Seismic interferometry: Reconstructing the earth's reflection response, Geophysics, 71:S161-S170.

Hornby B, Yu J (2007) Interferometric imaging of a salt flank using walkaway VSP data. The Leading Edge, 26:760-763.

Hurich, C. and Deemer., S., (2013 in press) Combined surface and borehole seismic imaging in a hard rock terrain: a field test of seismic interferometry, Geophysics.

Mehta K, Snieder R, Calvert R, Sheiman J (2008) Acquisition geometry requirements for generating virtual-source data: The Leading Edge, 27:620-629

Schuster GT (2009) Seismic Interferometry: Cambridge Press.

Snieder R (2004) Extracting the Green's function from the correlation of coda waves: A derivation based on stationary phase, PhysRevE.69.046610. doi: 10.1103.

Zheglova, P., Farquharson, C. G., and Hurich, C.A. (2013) 2-D reconstruction of boundaries with level set inversion of travel times, Geophysical Journal International, v. 192:688-698.

# Magnetotelluric measurements in the Skellefte ore district, northern Sweden

**María A. García Juanatey, Juliane Hübert, Ari Tryggvason, Christopher Juhlin, Laust B. Pedersen, Mahdieh Dehghannejad**
*Department of Earth Sciences, Uppsala University, SE-752 36 Uppsala, Sweden*

**Tobias E. Bauer, Pär Weihed**
*Division of Geosciences and Environmental Engineering, Luleå University of Technology, SE-971 87 Luleå, Sweden*

**Pietari Skyttä**
*Department of Geosciences and Geography, University of Helsinki, FI-000 14 Helsinki, Finland*

**Abstract.** Broadband magnetotelluric (MT) data were acquired as part of the VINNOVA project "4D modelling of the Skellefte District" in one of the most important mining districts in Sweden. The project aims were to provide a better understanding of the local and regional processes that took place in the district, and in that way provide a framework for new exploration strategies to target deeper deposits. The MT data consist of about 100 stations along profiles that follow seismic reflection surveys. The dimensionality and quality of the data were carefully analysed and 2D and 3D inversions were carried out. The resulting models exhibit extreme resistivity values with several highly resistive and conductive features. With the help of geological observations, borehole data and the results from seismic reflection lines, it was possible to interpret the resistivity structures present in the models in geological terms. The most interesting outcomes are conductors that correspond with hydrothermally altered, ore-bearing volcanic rocks, and their relationship with faults inferred from the surface geology and co-located seismic surveys. These faults probably acted as conduits for the ore-forming hydrothermal fluids.

**Keywords.** Skellefte district, Vinnova 4D modelling, magnetotellurics.

## 1 Introduction

The Skellefte District is one of the richest metallogenic mining areas in Sweden. The main deposits consist of volcanic-hosted massive sulphides (VHMS) rich in zinc, copper, lead, gold and silver, that have been explored and mined for more than a century (Allen et al., 1996; Weihed et al., 2002). Considering that technological advancements allow deeper mining, and that today new discoveries occur less often, new efforts have been directed at locating targets at greater depths. Thus, current exploration strategies need to be adjusted, and a better understanding of regional scale structures is necessary. Following this direction the project VINNOVA "4D modelling of the Skellefte District" was launched. Its main purpose was to unravel the regional structures and tectonic setting of the Skellefte district by constructing a 3D geological model and its evolution over time. To pursue these goals, new geophysical and geological data were acquired at different scales concentrating in two key localities of the district (Bauer et al., 2009, 2010, 2011; Skyttä et al., 2009). Among the newly acquired geophysical data,

approximately 100 magnetotelluric (MT) stations were installed along seismic reflection profiles. Since the depth of penetration of the MT data is within a couple of hundred meters to several kilometres depth, and since it provides a better depth resolution than potential field methods, it complements nicely the seismic reflection data.

## 2 MT data

MT is an electromagnetic method in which the data are normally analysed in the frequency domain. It uses natural electromagnetic fields to explore the electrical resistivity distribution of the subsurface. The Skellefte District has been previously investigated with MT in a coarse manner by Rasmussen et al. (1987). The data acquired within the VINNOVA project aimed a more detailed study of the top 10 km of the crust. The stations were installed in the Kristineberg mining area to the west, and around the Maurliden deposits in the central part of the district (see Figure 1). The data acquisition was carried out in four different field campaigns between 2007 and 2010, and have been partially presented by Hübert et al. (2009); García Juanatey et al. (2011); Hübert et al. (2013).

Most of the sites were placed along 2D profiles with the exception of a few stations that were located to complete a 3D grid in the Kristineberg area. The spacing between the sites varies from 0.5 to 2 km along the profiles, and can be as wide as 4 km when in the 3D grid. The instrumentation consisted of non-polarizable Pb/PbCl electrodes from Uppsala University (Sweden), induction coils MFS05/MFS06 (Metronix, Germany) and LEMI120 (Ukraine), and Earth Data PR 6-24 data loggers. The measurements were undertaken with a 1000 Hz sampling rate for two hours, and 20 Hz sampling for almost a day.

The time series processing was carried out with the algorithm MTU2000 (Smirnov, 2003) and yielded stable transfer functions in the frequency range of 150 Hz – 200 s. The data quality is in general good, although the sites located in the vicinity of the Kristineberg mine and the Vargfors power plant in the central part of the district are affected by noise.

Dimensionality analyses of the data have shown that the subsurface resistivity structures do not have a single preferred geoelectrical strike direction. Particularly in the Kristineberg mining area, there is a clear change of
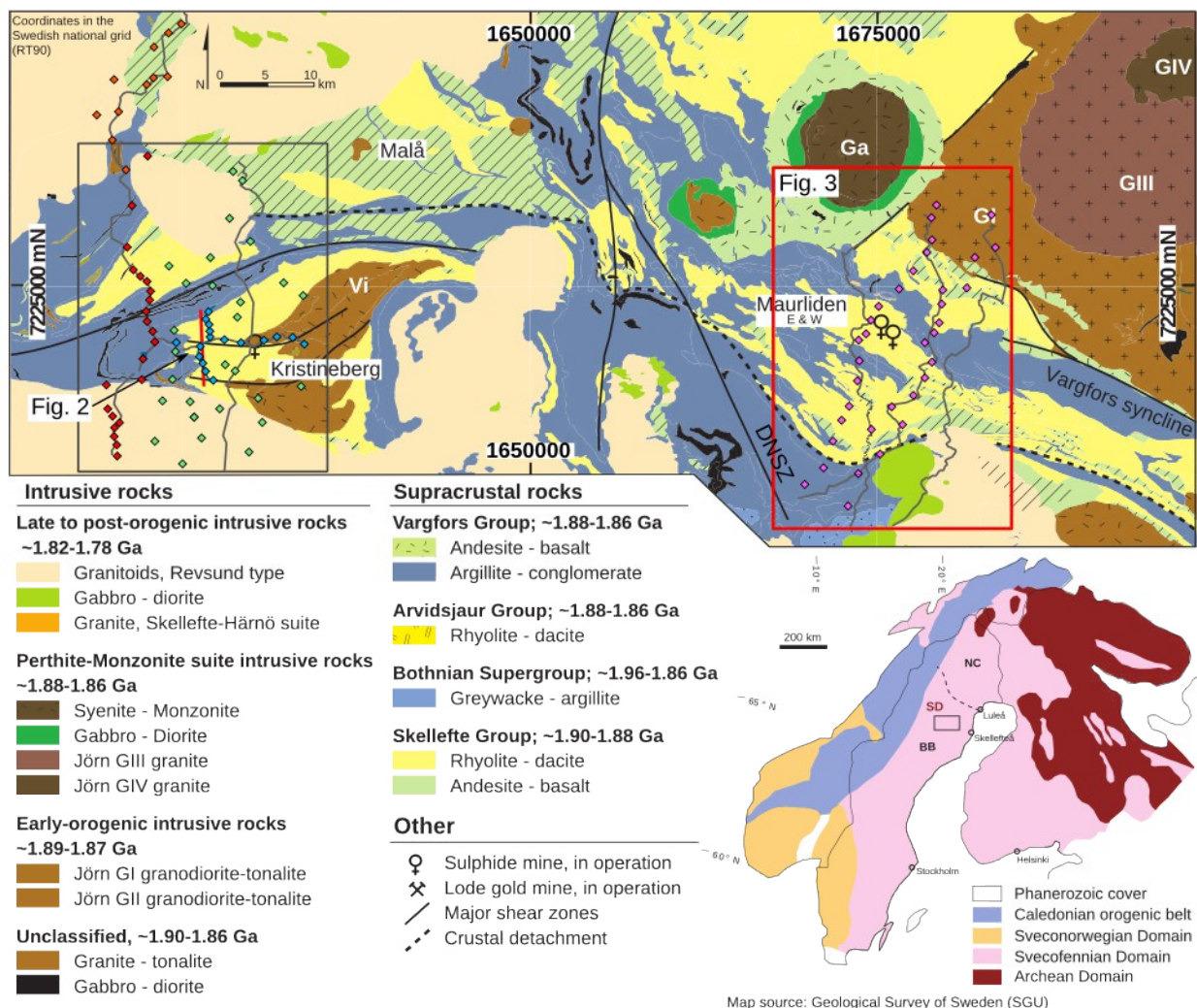
**Figure 1.** Geological map of the western and central Skellefte district with the location of the MT sites (diamonds), different colours indicate different field campaigns. The rectangles denote the areas where 3D MT inversions were computed. The position of the seismic reflection lines are in grey for reference (Tryggvason et al. 2006, Dehghannejad et al. 2010, 2012). Modified after Kathol and Weihed (2005), Geological Survey of Sweden (SGU). Inset: Generalized geology of the Fennoscandian shield. Geological domains: BB: Bothnian Basin, NC: Norrbotten Craton, SD: Skellefte District (shown above). The dashed line represents the boundary between rocks with Proterozoic and Archaean Nd-signatures (Mellqvist et al. 1999). Modified after Weihed et al. (2002).

preferred strike with depth, indicating the presence of at least two different geological regimes.

## 3 Inverse modelling

Considering that 3D MT inversion is not yet a well established procedure, as a first approach, all the MT data was inverted in 2D along profiles to obtain resistivity models of the subsurface. The algorithm used was REBOCC (Siripunvaraporn & Egbert, 2000) modified to invert for the determinant of the impedance tensor (Pedersen & Engels, 2005), as it has been shown that the inversion of the determinant is less influenced by 3D effects than that of the single modes. Whenever possible, reflections from co-located seismic reflection lines were introduced in the MT inversions as a priori information. In some cases this produced resistivity models with better data fit. Figure 2 shows one of such models with the migrated seismic stack on top for reference.

Taking into account that the resistivity structures in the Skellefte District have a complex geometry, and that

2D assumptions might not hold, additional 3D inversions of the data were performed and compared with the standard 2D results to better determine the location of conductive bodies. Figure 1 shows the two areas in the district where the 3D inversions were performed.

In general, both 2D and 3D models show resistivity values spanning up to five orders of magnitude. Even though there is a great variation of values, the resulting models do not exhibit clear resistivity boundaries due to the nature of the inversion process. The only sharp boundaries present are those provided by the constraints introduced from the seismic reflection surveys and accepted by the MT data (see Figure 1).

## 4 Interpretation

Geological observations at the surface and in the mines, together with lithological information from boreholes, provided the base for the interpretation of shallow features in the models. At deeper levels (> 1km) the interpretation can only be supported by seismic reflection surveys and regional geological models.
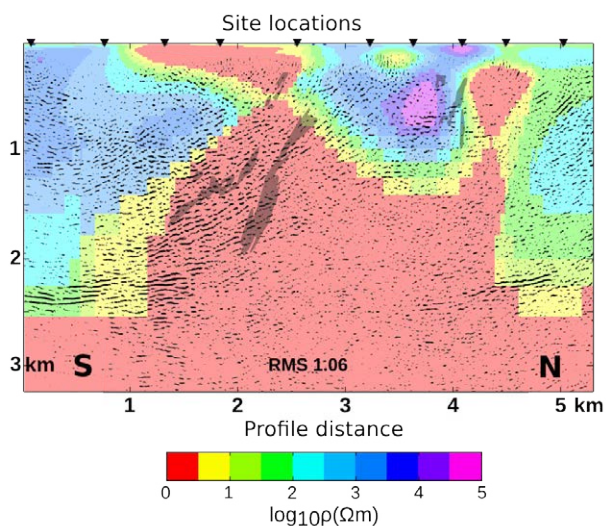
**Figure 2.** 2D resistivity model along the high resolution North-South profile in the Kristineberg mining area (García Juanatey et al. 2013), see Figure 1 for profile location. The migrated stack section of the co-located seismic reflection profile (Dehghannejad et al. 2010) is shown in black on top of the resistivity model. The shadowed areas are the projection of the Kristineberg ore bodies (kindly provided by New Boliden). Note that sharp boundaries in the resistivity model were achieved by introducing the seismic reflections as a priori information in the MT inversion.

In both surveyed localities, resistive bodies are located at shallow depths and associated, by comparison with the surface geology, to late-orogenic intrusions (Revsund granites) and unaltered volcanic rocks of the Skellefte Group. Very shallow high conductivities are most likely related to graphitic black slates in the meta-sedimentary rocks of the Vargfors Group.

In the Kristineberg mining area,  it was possible to relate intermediate depth conductors (1-3 km depth) to hydrothermally altered volcanic rocks containing the ore deposits of the Kristineberg mine. Further to the east, in the central part of the district, conductors are found to be associated to faults interpreted from seismic reflection and surface geology (see Figure 3). Thus, considering that faults might have acted as conduits for the transport of hydrothermal fluids (Allen et al., 1996; Bauer et al., 2012), it is very likely that these conductors are depicting fluids or alteration zones along the faults.

However, it would be expected that the low resistivities extend to the surface where hydrothermal alteration has been observed in the field. This is not the case as DC resitivity measurements around the Maurliden deposits (Tavakoli et al., 2012) produced models with resistivities of 1 kΩm or higher down to 430 m depth. Thus, either (i) the conductive fluids are only present at greater depths, (ii) the resistivity of the alteration zones is being affected by depth dependent conditions (e.g. oxidizing environment at shallower depths), or, (iii) the low resistivities are caused by graphitic black slates from the Vargfors group (as observed in Kristineberg at shallow depths) and their relationship with the observed seismic reflections is rather unclear.

Summarising, the main findings of the MT data
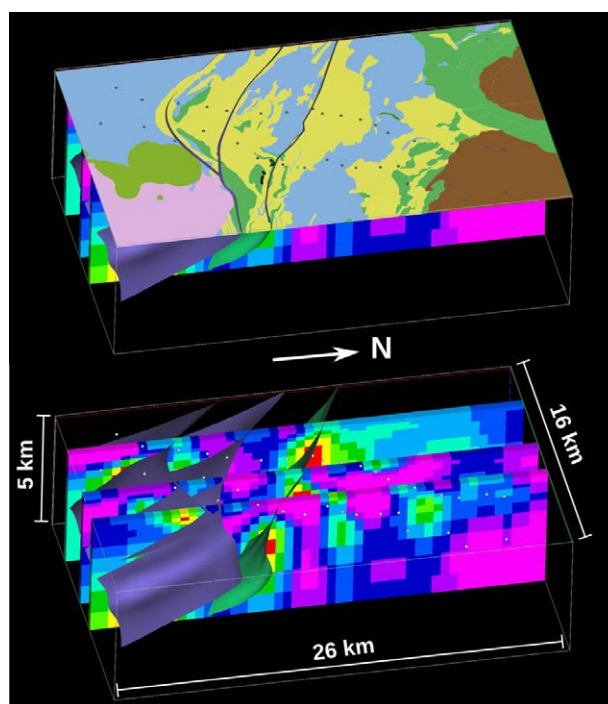


**Figure 3.** 3D view of three slices of the 3D resistivity model in the central part of the district (see Figure 1 for location). The shown surfaces are modelled faults from surface geology and seismic reflection lines (Dehghannejad et al. 2012). The resistivity colour scale is as in Figure 2. Observe the relationship between intermediate depth conductors and the fault surfaces.

analysis in the district include: (1) conductive hydrothermally altered zones within the otherwise resistive rocks of the ore-bearing volcanic units, (2) the depth extension of early and late-orogenic intrusions as depicted by features with high resistivity, and (3) several prominent conductive shear zones in the central part of the district.

## 5 Conclusions

Although the application of the MT method is challenged by the complex geological setting and extreme resistivity contrasts, a careful processing and analysis of the data made it possible to render robust images of the deep subsurface resistivity. By combining the results from the MT with the findings of seismic reflection surveys and geological observations, our understanding of the geological structure of the Skellefte District was greatly improved. Moreover, even though at more than 1 km depth the MT method lacks the resolution to image anomalies solely associated to ore bodies, it can successfully image the alteration zones containing them, implying that the method might be a valuable tool for deep exploration.

## Acknowledgements

# References

Allen R, Weihed P, Svenson S (1996) Setting of Zn-Cu-Au-Ag massive sulfide deposits in the evolution and facies architecture of a 1.9 Ga marine volcanic arc, Skellefte district, Sweden. Economic Geology and the Bulletin of the Society of Economic Geologists 91: 1022–1053

Bauer T, Skyttä P, Allen R, Weihed P (2009) 3-D modelling of the Central Skellefte District, Sweden. In Smart science for exploration and mining: Proceedings of the 10th biennial SGA meeting, Townsville, Australia. pp. 394–396

Bauer T, Skyttä P, Allen R, Weihed P (2012) Fault-controlled sedimentation in a progressively opening rift basin: the Palaeoproterozoic Vargfors basin, Skellefte mining district, Sweden. International Journal of Earth Sciences. doi:10.1007/s00531-012-0808-x

Bauer T, Skyttä P, Dehghannejad M, Tavakoli S, Weihed P (2011) Geological Multi-Scale Modelling as a Tool for Modern Ore Exploration in the Skellefte Mining District, Sweden. In Proceedings of the IAMG conference, Salzburg. p. 759

Bauer T, Tavakoli S, Dehghannejad M, García Juanatey MA, Weihed P (2010) 4-dimensional geological modelling of the Skellefte district, Sweden. In The international archives of the photogrammetry, remote sensing and spatial information sciences, vol. XXXVIII. pp. 93–96

Dehghannejad M, Bauer TE, Malehmir A, Juhlin C, Weihed P (2012) Crustal geometry of the central Skellefte district, northern Sweden - constraints from reflection seismic investigations. Tectonophysics 524: 87–99

Dehghannejad M, Juhlin C, Malehmir A, Skyttä P, Weihed P (2010) Reflection seismic imaging of the upper crust in the Kristineberg mining area, northern Sweden. Journal of Applied Geophysics 71: 125 – 136

García Juanatey M, Hübert J, Juhlin C, Malehmir A, Tryggvason A (2011) Integrated MagnetoTelluric and seismic reflection study: Skellefte Ore District, northern Sweden. SEG Technical Program Expanded Abstracts 30: 1247–1251

Hübert J, García Juanatey MA, Malehmir A, Tryggvason A, Pedersen LB (2013) The upper crustal 3-D resistivity structure of the Kristineberg area, Skellefte district, northern Sweden revealed by magnetotelluric data. Geophysical Journal International 192: 500–513

Hübert J, Malehmir A, Smirnov M, Tryggvason A, Pedersen LB (2009) MT measurements in the western part of the Paleoproterozoic Skellefte Ore District, Northern Sweden: A contribution to an integrated geophysical study. Tectonophysics 475: 493 – 502

Kathol B, Weihed P (2005) Description of regional geological and geophysical maps of the Skellefte District and surrounding areas. SGU Uppsala

Mellqvist C, Öhlander B, Skiöld T, Wikström A (1999) The Archaean-Proterozoic Palaeoboundary in the Luleå area, northern Sweden: field and isotope geochemical evidence for a sharp terrane boundary. Precambrian Research 96: 225 – 243

Pedersen L, Engels M (2005) Routine 2D inversion of magnetotelluric data using the determinant of the impedance tensor. Geophysics 70: G33–G41

Rasmussen T, Roberts R, Pedersen L (1987) Magnetotellurics along the Fennoscandian Long-Range profile. Geophysical Journal of the Royal Astronomical Society 89: 799-820

Siripunvaraporn W, Egbert G (2000) An efficient data-subspace inversion method for 2-D magnetotelluric data. Geophysics 65: 791–803

Skyttä P, Hermansson T, Bauer TE (2009) Three Dimensional Structure of the VMS-hosting Palaeoproterozoic Kristineberg Area, Northern Sweden. In Smart science for exploration and mining: Proceedings of the 10th biennial SGA meeting, Townsville, Australia. pp. 909–910

Smirnov M (2003) Magnetotelluric data processing with a robust statistical procedure having a high breakdown point. Geophysical Journal International 152: 1–7

Tavakoli S, Elming S-Å, Thunehed H (2012) Geophysical modelling of the central Skellefte district, Northern Sweden; an integrated model based on the electrical, potential field and petrophysical data. Applied Geophysics 82: 84-100

Tryggvason A, Malehmir A, Rodriguez-Tablante J, Juhlin C, Weihed P (2006) Reflection seismic investigations in the western part of the paleoproterozoic VHMS-bearing Skellefte district, northern Sweden. Economic Geology 101: 1039–1054

Weihed P, Billstrom K, Persson P, Weihed J (2002) Relationship between 1.90-1.85 Ga accretionary processes and 1.82-1.80 Ga oblique subduction at the Karelian craton margin, Fennoscandian Shield. Journal of the Geological Society of Sweden 124: 163–180

# Application of remote sensing techniques in exploration for VMS deposits, Matchless Belt, Namibia

**Fred Kamona**
*University of Namibia*

**Moses Angombe**
*Geological Survey of Namibia*

**Abstract.** Remote sensing techniques Remote sensing techniques in conjunction with field geological mapping are proving to be very useful in determining exploration targets in partially covered terrains of the Matchless Belt in Namibia which is known to contain volcanogenic massive sulphide (VMS) deposits in certain places along the belt. The application of advanced spaceborne thermal emission reflectance radiometer (ASTER) data in combination with magnetic and electro-magnetic data is particularly useful in determining geological features associated with exploration targets both on surface and at depth. Initial surveys undertaken at two of the currently operating mines on the 350 km long Matchless Belt, namely Matchless and Otjihase Cu-Au mines, show some exciting results which are useful in identifying exploration targets associated with VMS deposits, including the discrimination of mafic units from metapelites as well as the characterisation of alteration zones related to mineralization.

**Keywords:** Remote sensing, VMS deposits, Matchless, Otjihase

## 1 Introduction

The combination of remotely sensed data with conventional geological field mapping techniques is recommended during exploration campaigns for VMS type deposits along the Matchless Belt of Namibia since it is more economic and less time consuming compared to conventional field geological surveys in extensive exploration areas with limited exposure of geological outcrops.

Some of the benefits of combing geophysical and geological techniques in exploration surveys at an early stage of the exploration programme include: (i) the rapid identification of geological features associated with mineralisation (e.g. different lithological units, alteration zones, structures and gossans), (ii) the rapid identification of exploration targets for further detailed studies based on the associated geological features, (iii) the identification and location of suitable drill sites as well as the optimal estimation of the length of drillholes below the surface.

Based on the composition of the amphibolites and dykes at some localities, the Matchless Belt has been interpreted as originally representing a mid-oceanic ridge between the Congo and Kalahari Cratons (Miller, 2008). The exact length of the Matchless Belt is not well constrained due to a cover of Kalahari sands towards the eastern extension of the Damara Belt in Botswana, but it is known to be at least 350 km long in Namibia (Fig. 1). The volcanic activity associated with the formation of

the original Matchless tholeiitic basalts probably contributed to the formation of a number of pyritic Cu-Au ores which include Matchless, Gorob, Hope and Otjihase (Adamson and Teichmann 1986, Killick 2000). The massive sulphide mineralization is associated with a magnetite-bearing quartzite which is interpreted as a possible metamorphosed equivalent of chert-rich exhalites typical of VMS deposits (e.g. Killick, 2000).
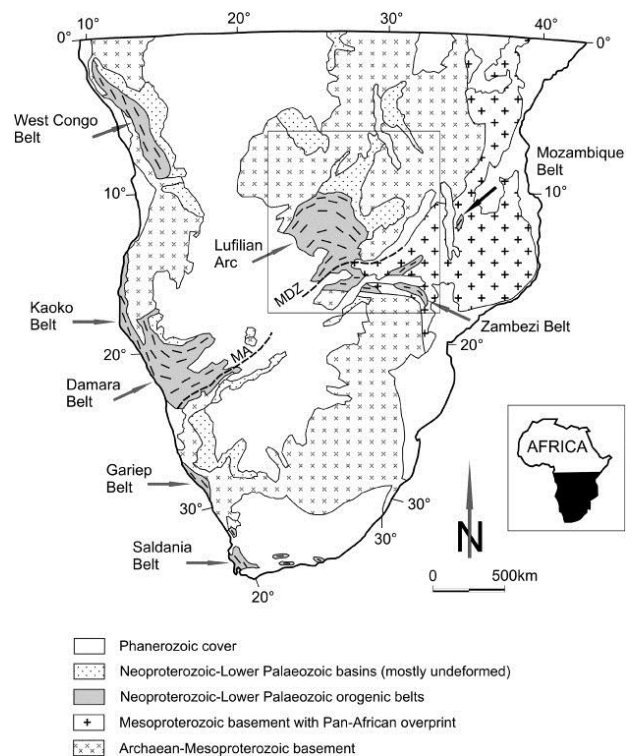


**Figure 1.** Location map of the Damara Belt and the Matchless Amphibolite (MA) in southern Africa (after Kampunzu et al. 2009).

## 2 The Matchless Mine

The New Matchless Mine is located on a mafic amphibolite-metagabbro unit with associated magnetite quartzite and mica schist 550m south of the main Matchless Member and about 1.9 km southwest of the defunct Old Matchless Mine (Fig. 2, M1). The local geology at the Mine consists mainly of mica schist (the Kuiseb Formation) with north-east trending mafic amphibolite and metagabbro (Matchless Member). The Matchless Amphibolite member consists of hornblende, plagioclase, tremolite, epidote and minor quartz, whereas the Kuiseb Formation is dominated by schists

with biotite, muscovite and quartz. The sulphide orebody occurs as massive ore with associated stringer and vein type mineralization within sericite-quartz schist and mica schist with associated magnetite quartzite and amphibolite in the hanging wall (Weatherly, 2012, unpublished report).
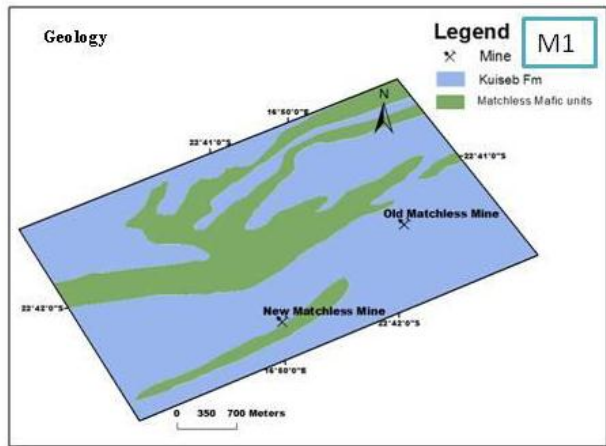


**Figure 2.** Generalised geology and location map of the Old Matchless Mine and the New Matchless Mine in relation to the Matchless mafic units and the Kuiseb Formation.

Application of ASTER data at the Matchless Mine showed that the different lithological units and alteration zones associated with massive sulphide mineralisation could be discriminated on the basis of bands and ratios RGB (1, 3, 13), RGB (2/1, 4/2, 6/8) and RGB (5/4, 4/5, 6/8) as shown in Figs. 3, 4 and 5. RGB (1, 3, 13) is good for discriminating between the mafic amphibolite-metagabbro units, which appear blue, and the mica schists, which are yellowish green in colour (Fig. 3, M2). The intense blue colour is related to the predominance of amphibole minerals (hornblende and tremolite) in the amphibolite as confirmed by X-ray diffraction (XRD) analysis of samples from the Old Matchless Mine. In contrast, the yellowish green colour of the schist is attributed to the combined effect of amphibole (hornblende), phyllosilicates (biotite, chlorite, talc) and quartz.
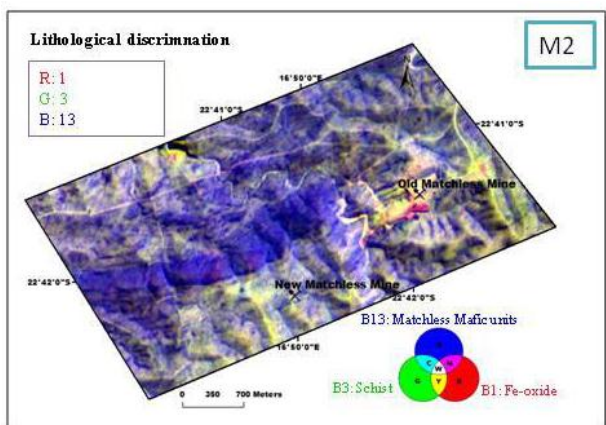


**Figure 3.** ASTER image (RGB: 1, 3, 13) of the Matchless Mine area, discriminating between the blue mafic units (and the mica schists (yellowish-green) of the Kuiseb Formation.

Using ASTER ratios RGB (2/1, 4/2, 6/8) the distinction between the mafic and metapelitic units is not as distinct as with bands RGB (1, 3, 13), but the occurrence of Fe-oxide and hydroxide alteration zones in the schist is more pronounced by numerous patches of red colour (Fig.4, M3), especially near the Old Matchless Mine as well as in the New Matchless Mine area, in both the footwall and hanging wall zones. The altered Fe-oxide and hydroxide zones are attributed to the presence of goethite-limonite and chlorite which formed mainly from the alteration of magnetite and biotite, respectively.
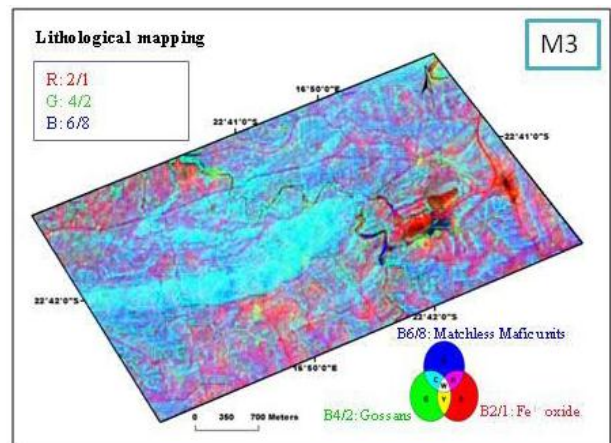


**Figure 4.** ASTER image (RGB: 2/1, 4/2, 6/8) of the Matchless Mine area, discriminating between the mafic units (cyan) and the red alteration zones within the mica schists of the Kuiseb Formation.

Figure 5, M4 was produced on the basis of ASTER ratios RGB (5/4, 4/5, 6/8) and clearly characterizes the epidote-chlorite zones (magenta) of the main Matchless Member, whereas the mineralized zones are associated with green phyllic alterations due to the presence of sericite and talc. In addition, a prominent red zone is well developed at the Old Matchless Mine due to the occurrence of an old tailings dam in that area.
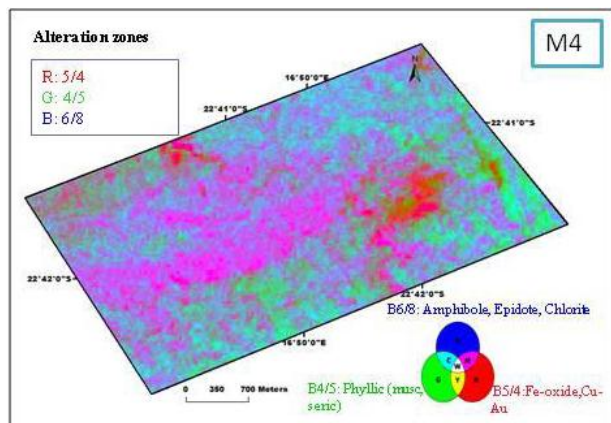


**Figure 5.** ASTER image (RGB: 5/4, 4/5, 6/8) of the Matchless Mine area, discriminating between the mafic units (magenta) and the green phyllic alteration zones within the mica schists of the Kuiseb Formation with patches of red Fe-oxide zones.

## 2.1 Otjihase Mine

The geology of the Otjihase Mine area (Fig. 6, O1) is composed mainly of quartz-mica schist (Kuiseb Formation) with mafic units (amphibolite and serpentinite) and magnetite quartzite. The serpentinites occur in the north-east, whereas magnetite quartzite units with associated gossans are situated in the centre of the mine area with a general NE-SW strike orientation. The massive sulphide ores occur close to the Matchless Member amphibolite within quartz-mica-garnet schist of the Kuiseb Formation as four sub-parallel, spatula-shaped mineralized shoots, separated by more than 100 m of quartz-mica schist country rocks (Unpublished Mine Report, 1989).
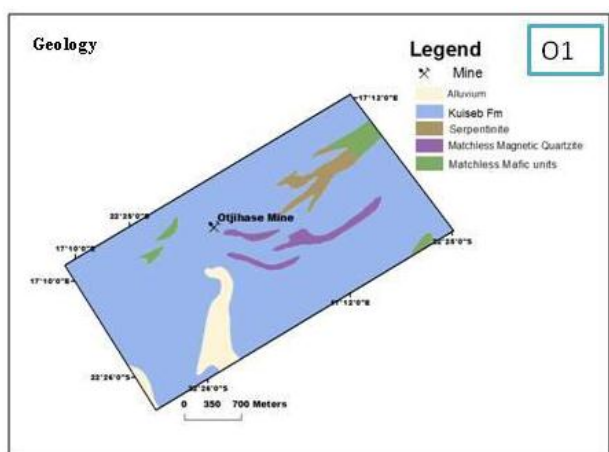
**Figure 6.** Generalised geology and location map of the Otjihase Mine in relation to the Matchless mafic units, magnetite quartzite and serpentinite in metapelites of the Kuiseb Formation.

In Figure 6, O2 a lithological discrimination using RGB: 4/7, 4/3, (2/3*4/3) was applied to the ASTER scene of the area. The red colour was assigned to the schist, the magnetite quartzite was assigned a green colour and the blue colour indicates units that have experienced intense weathering and oxidation, including the tailings dam, the processing plant and the old mine pit area. In addition, both the schist and magnetite quartzite have also been affected by weathering, resulting in the cyan and magenta colours for magnetite quartzite and schist, respectively. North-south oriented structural trends, probably related to late rift faults, are also clearly visible on this image as in the following two images (Figs. 8 and 9).

Using ASTER ratios RGB (2/1, 4/2, 6/8) the oxidation zones around the tailings dam, the processing plant and the old mine pit area are clearly discriminated (Fig. 8, O3). This is attributed to the development of Fe-oxides and hydroxides in these areas. In addition, the mica schists of the Kuiseb Formation show cyan colours with patches of magenta due to the presence of goethite-limonite and chlorite which formed through the oxidation Fe-bearing minerals such as magnetite and biotite.
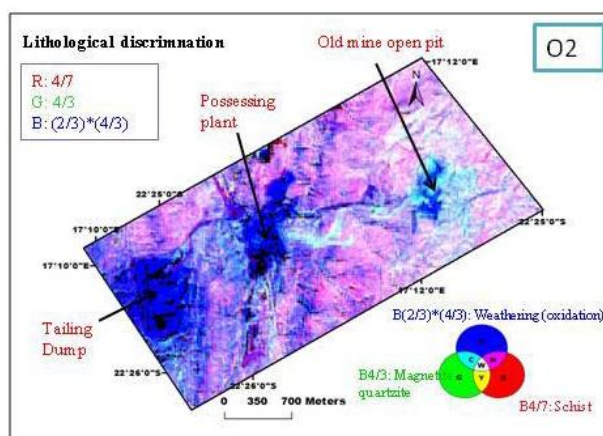
**Figure 7.** ASTER image (RGB: 4/7, 4/3, 2/3*4/3) of the Otjihase Mine area, showing mostly magenta coloured mica schists of the Kuiseb Formation with blue patches of secondary oxidation at the tailings dump, the processing plant, the old open pit mine and the local stream.
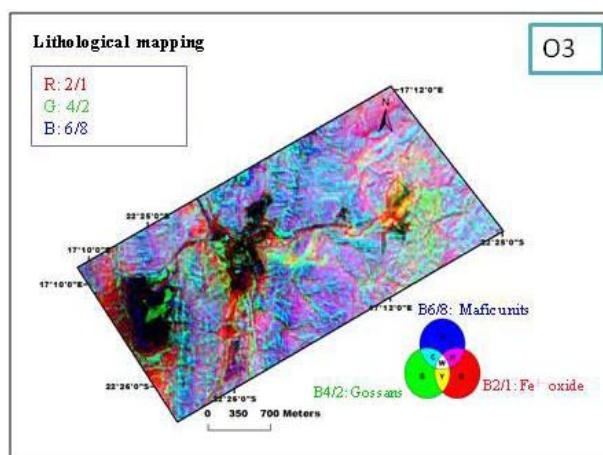
**Figure 8.** ASTER image (RGB: 2/1, 4/2, 6/8) of the Otjihase Mine area, showing red Fe-oxide alteration zones around the tailings dump, the processing plant areas (dark) and the local stream. The mica schists of the Kuiseb Formation are characterised by cyan colours with patches of magenta due to oxidation.

Figure 9, O4 was produced on the basis of ASTER ratios RGB (5/4, 4/5, 6/8) and clearly discriminates between the epidote-chlorite alteration zones (magenta) and the green phyllic alterations due to the presence of sericite and talc in the quartz-mica schists of the Kuiseb Formation. In addition, prominent red alteration zones are well developed at the tailings dump, the processing plant and the old open pit mine area as observed in the previous images at Otjihase.
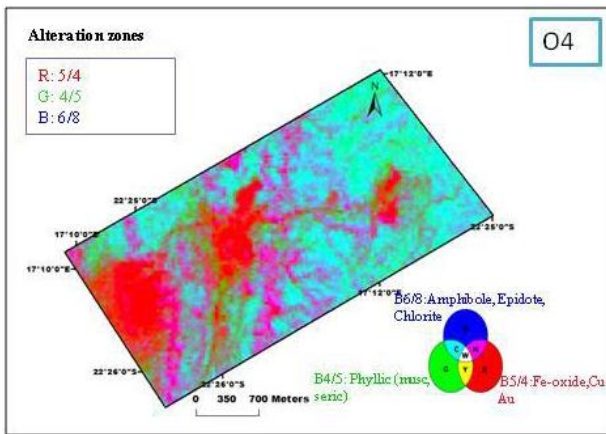
**Figure 9.** ASTER image (RGB: 5/4, 4/5, 6/8) of the Otjihase Mine area, discriminating between epidote-chlorite (magenta) and phyllic (green) alteration zones within the mica schists of the Kuiseb Formation with patches of red Fe-oxide zones associated with the tailings dump, the processing plant and the old mine pit areas.

## 3 Discussion

The application of remotely sensed data based on processed ASTER images clearly discriminate between mafic and metapelitic units which dominate the geology along the Matchless Belt with its associated VMS type massive sulphide mineralisation. In addition, it is also possible to characterize different alteration zones such as those due to Fe-oxidation, epidote-chlorite alteration and phyllic alteration, especially in the Matchless Mine area. However, in the Otjihase mine area, the occurrence of particularly the tailings dump and the processing plant masks most of the signatures from the lithological units. Nevertheless, mineral alteration zones within the mica schist of the Kuiseb Formation are still recognisable.

Lithologically, exploration targets for VMS deposits along the Matchless Belt are clearly associated with magnetite quartzites occurring together talc-sericite schists and mafic units within the Kuiseb Formation. Good exploration guides include well developed red coloured Fe-oxide and hydroxide alteration zones linked to the sulphide mineralisation in the host schists and associated magnetite quartzite, as observed near the Old Matchless Mine and in the New Matchless Mine area.

## Acknowledgements

## References

1.  Adamson, RG, Teichmann, RFH (1986) The Matchless cupreous pyrite deposit, South West Africa/Namibia. In: Anhaeusser, C.R. and Maske, S. (Eds.), Mineral Deposits of southern Africa, Geol. Soc. S. Afr., v. II, 1755-1760 pp.

2.  Breitkopf, JH and Maiden, KJ (1988) Tectonic setting of the Matchless Belt pyritic copper deposits, Namibia. Economic Geology, 83, 710-723.

3.  Kampunzu, AB, Cailteux, JLH, Kamona, AF, Intiomale, MM, & Melcher, F (2009) Sediment-hosted Zn–Pb–Cu deposits in the Central African Copperbelt. Ore Geology Reviews, 35, 263 – 297.

4.  Killick, AM (2000) The Matchless Belt and associated sulphide mineral deposits, Damara Orogen, Namibia. Communs. Geol. Surv. Namibia, v. 12, pp. 73-80.

5.  Miller, R McG (2008) The geology of Namibia. Geological Survey of Namibia, Ministry of Mines & Energy, Windhoek, pp. 1-1 – 28-13.

# Integrating geological constraints into 3D geophysical inversions using unstructured meshes

Peter G. Lelièvre, Colin G. Farquharson & Cassandra J. Tycholiz
*Memorial University, Department of Earth Sciences, St. John's, Newfoundland, Canada*

**Abstract.** The non-uniqueness of the underdetermined geophysical inverse problem requires that any available geological information be incorporated to constrain the problem and obtain geologically interpretable solutions. Such information commonly includes petrophysical and structural measurements. It can also involve 3D geological Earth models, e.g. ore deposit models commonly created during delineation drilling. Such models typically comprise wireframe surfaces that represent geological contacts between different rock units. Wireframe surfaces, comprising tessellated triangular facets, are sufficiently flexible to allow efficient representation of arbitrarily complicated geological structures. These surfaces can be honoured exactly within fully unstructured 3D volumetric tetrahedral meshes. This contrasts with standard rectilinear meshes, on which complicated geological structures are often difficult or impossible to represent adequately without computationally infeasible refinement. By working directly with unstructured discretizations of the subsurface in our geophysical inversion methods, we are able to seamlessly combine geological and geophysical data to push the limits of the geophysical data resolution and produce higher accuracy common Earth models.

**Keywords.** Geophysical inversion, constrained inversion, unstructured meshes, common Earth model.

## 1 Geological and Geophysical Models

3D geological ore deposit models are commonly created during delineation drilling. Geological structures may be known at points from down-hole intersections and outcrop mapping. The contacts can be interpolated between boreholes and extrapolated outwards to produce a 3D geological model. Contacts may also be interpreted from seismic sections. Rudimentary geological models are important for visualization purposes during exploration and delineation stages. More sophisticated models can be used to calculate volumes of ore reserves and other information ultimately important for mine planning. The accuracy of these models is crucial when used to determine if a deposit is economic.

These 3D Earth models typically comprise wireframe surfaces that represent the geological contacts between different rock units. An example is shown in Figure 1. Wireframe surfaces (tessellated surfaces comprising connecting triangles) are appropriate for representing geological contacts as they are sufficiently general and flexible that they can be made to represent arbitrarily complicated geological structures (e.g. contacts between rock units) and topography.
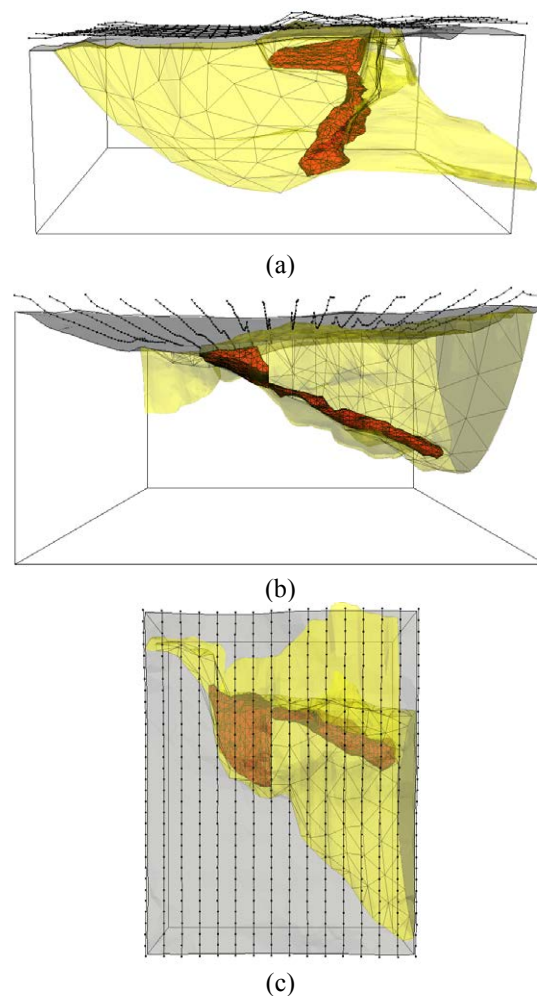


**Figure 1.** Perspective views of a 3D geological model from the Voisey's Bay deposit. The views are from the east in (a), the south in (b) and overhead in (c). The surface of the sulphide unit is red with triangular surface facets indicated by black lines. The troctolite surface is transparent yellow without facets indicated. An approximate troctolite surface used in constrained inversions is shown as a grey wireframe. The topography surface is transparent grey and the boundary of a modelling volume is drawn with black lines. The locations of gravity observations are indicated by black dots with flight lines drawn in black.

In contrast, most current 3D geophysical modeling is performed on rectilinear meshes because they simplify the development of numerical methods. Algorithms can be made more computationally efficient by exploiting the underlying mesh structure. However, it can be impossible to adequately model complicated geology using rectilinear meshes, which produce pixellated representations of the Earth no matter how fine the discretization. Such a mesh is always incompatible with geological models comprising wireframe surfaces.

To address this incompatibility, we are using unstructured tetrahedral meshes to specify 3D geophysical Earth models. Unstructured meshes can be used to discretize the volumes between general wireframe surfaces while honouring exactly those surfaces within the volumetric discretization. It is therefore possible to have geological and geophysical models that are, in essence, the same Earth model.

## 2 The Voisey's Bay Deposit

The Voisey's Bay nickel-copper-cobalt deposit, located on the northeast coast of Labrador, is considered to be one of the most significant mineral discoveries made in Canada in the past few decades. An extensive drilling campaign has provided an extensive collection of core samples. Detailed geological models have been built from this information.

Figure 1 shows a geological model from the Eastern Deeps region of the Voisey's Bay site. We have simplified the geology slightly for illustrative purposes. The model contains three tessellated wireframe surfaces that delineate the topography and a sulphide unit hosted within a troctolite unit. The sulphide unit consists of two parts: a smaller tabular body closer to the surface and a deeper elongated dipping extension.

## 3 Discretizing the Earth on Rectilinear and Unstructured Meshes

It can be difficult to represent complicated geology on rectilinear meshes and some intermediary process is always required to convert from a geological model to a geophysical model, or the reverse. As an example, take the geology in Figure 1. In Figure 2, a rectilinear mesh has been chosen and its cells segregated according to the known contacts between the main rock units. The rectilinear mesh has $55 \times 82 \times 31 = 139,810$ cells, a reasonably fine discretization, but "stair casing" of the contacts and topography is still evident. These inaccuracies in the geophysical model discretization lead directly to errors in forward modelling and constrained inversion results. Finer discretization is possible, but computation times and memory requirements quickly become inconvenient or unfeasible.

The power of unstructured meshes is that they provide the ability to intelligently mesh the subsurface for modelling purposes. They can capture fine-scale structure without considerably increasing memory requirements by placing smaller tetrahedral cells where required and larger cells elsewhere. The generation of quality unstructured meshes is a topic of ongoing research in the computer science community. Interested readers can find more information in Owen (1998). We do not intend to make any form of endorsement for a particular package but we currently make use of TetGen (Si 2008) to generate 3D tetrahedral meshes.

TetGen generates tetrahedral meshes from piecewise polygonal complexes (PPCs). A PPC comprises

interconnected planar polygonal facets. The meshing algorithm subdivides those facets into triangles, which become the faces of the tetrahedra in the subsequent volumetric mesh. In an exploration application, a PPC would contain the boundary of the modeling volume, the topography surface, any subsurface geological contacts that are known a priori, and any further facets required to separate the modeling volume into different watertight regions. The meshing algorithm discretizes the volume between the tessellated surfaces while maintaining those surfaces exactly. As such, geological and geophysical models can share the same modelling mesh; they can be the same model, with no intermediary process required to convert from one to the other.

For TetGen and other meshing packages there are many possible options that allow the user to control the characteristics of the final mesh. This provides a suite of flexible options for generating volumetric tetrahedral meshes from the wireframe surfaces in a 3D geological model.



(a)



(b)
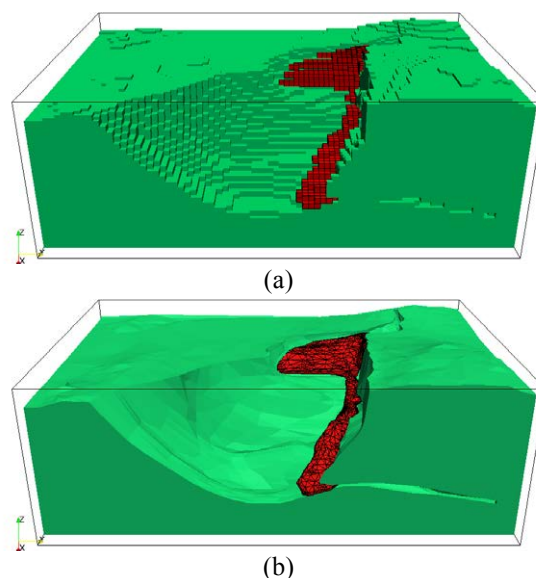
**Figure 2.** Discretization of the Voisey's Bay model on a rectilinear mesh (a) and unstructured tetrahedral mesh (b). The view is from the east. The troctolite unit has been removed to aid visualization of the troctolite/gneiss and troctolite/sulphide contacts. The gneiss unit is shown in green and the sulphide unit in red. The edges of the sulphide unit are drawn with black lines.

## 4 Geophysical Modelling on Unstructured Meshes

Although unstructured meshes provide utilitarian advantages over structured rectilinear meshes, there are some significant challenges involved in using unstructured meshes for the purposes of geophysical forward and inverse modeling. We can no longer benefit from the same numerical advantages presented by rectilinear meshes. Despite these challenges, we have developed forward modeling methods on unstructured tetrahedral meshes for gravity (Jahandari and Farquharson 2011), magnetic, seismic (Lelièvre et al. 2011a, 2011b), DC/IP, and EM data (Ansari and

Farquharson 2011).

A major challenge involved in inversion on unstructured meshes is designing the regularization required to obtain smooth models and for incorporating geological information. Some authors (e.g. Günther et al. 2006) have performed inversions on unstructured meshes with simple smoothness regularization. We have developed more flexible and functional regularization methods that allow us to specify preferred orientation directions and aspect ratios and thereby encourage the recovery of different types of model features.

## 5  Constrained Inversion Example

Here we apply our inversion methods to a 3D example based on the Voisey's Bay deposit, taking the model in Figure 1 as our ground truth. The sulphides and troctolite have densities of 1.65 g/cc and 0.09 g/cc respectively, relative to the background gneiss. Survey data is not available to us at the time of writing; as such, we model synthetic gravity gradiometry data at 512 locations (16 flight lines with 32 points along each line) at an elevation of 80 m above the topography surface. We add a small amount of random Gaussian noise (standard deviation equal to 3.0 eotvos) before inverting all tensor components at once. The zz-component of the gradiometry data with noise added is plotted in Figure 3(a). In Figure 3(b) we plot that same data but with the response of the troctolite and shallow sulphide body removed: the remaining response from the deeper sulphide extension is barely evident and is considerably masked by the added noise.

Our inversion volume is 2600 m by 3300 m by 1425 m (easting by northing by depth) and has topography ranging over 223 m. We begin with an unconstrained inversion. We use TetGen to discretize the inversion volume, specifying a maximum tetrahedron area constraint of 200,000 m$^3$. The resulting mesh has 100,755 cells of relatively constant volume across the modelling volume. We apply distance weighting as described in Li and Oldenburg (2000) and across-face smoothing as by Günther et al. (2006). The recovered model in Figure 4(a) only recovers the shallower part of the sulphide and extends that body too deep with only a small dip indicated. The predicted zz-component data and data residuals for this inversion are plotted in Figure 3(c) and 3(d). The predicted data and residuals were similar for all components and for all other inversions presented here (as such, we do not show all plots).

For our second inversion, we assume that a 3D wireframe model of the troctolite unit has been created from surface and down-hole observations. For this purpose, we do not use the surface from the true model but, instead, generate it independently from sparse information. The constraining troctolite surface is indicated in Figure 1: comparing to the true surface, it is clear that the constraining surface only captures the larger scale features of the troctolite. We use TetGen to discretize the inversion volume, now using a maximum tetrahedron volume constraint of 30,000 m$^3$ inside the constraining surface and no such volume constraint outside. The resulting mesh has 102,312 cells of

relatively constant volume inside the constraining surface but larger towards the boundaries. Had we meshed the entire volume with a maximum cell volume of 30,000 m$^3$ there would have been 655,884 cells, over 6 times as many, demonstrating one of the advantages of using flexible unstructured meshes: the potential for a significant reduction in problem size while still allowing complicated geometries to be honoured exactly. We apply distance weighting and include bound constraints on [-0.02,0.02] and [0.07,∞) g/cc outside and inside the constraining surface respectively. The recovered model is in Figure 4(b).



(a)            (b)

(c)            (d)
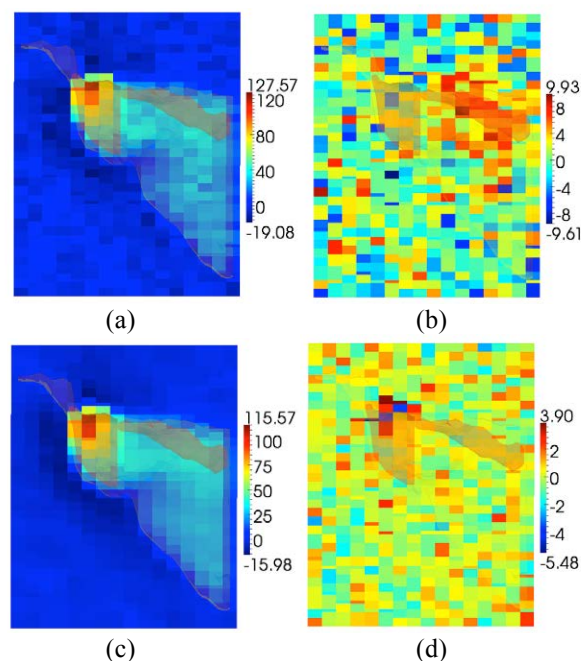
**Figure 3.** Maps (north up the page) of the zz-component gravity tensor data (eotvos) and inversion residuals normalized by noise uncertainties (unitless) for the 3D inversion example: (a) shows the data with noise added; (b) shows the noisy data with the response of the troctolite and shallow sulphide body removed; (c) shows the predicted data for the unconstrained inversion; (d) shows the normalized predicted data residuals for the unconstrained inversion (for the recovered model in Figure 4(a)). The locations of the sulphide and troctolite surfaces are indicated by transparent red and yellow overlays respectively.

This second inversion better recovers the shallower part of the sulphide and clearly indicates a possible extension at depth, dipping to the east. The exploration question here is how far the body may extend to depth. To attempt to answer this question we perform two more constrained inversions as before, however we now specify preferred orientation directions. We rotate the coordinate system, following a similar approach to Lelièvre and Oldenburg (2009), so that one of the smoothness axes is directed along the approximate trend of the extension as indicated by our second recovered model. We first set smoothness weights to encourage the recovery of an elongated depth extension. We then set the weights to encourage the recovery of a shortened extension, with the least possible elongation. The recovered models are in Figure 4(c) and 4(d). The fact that the latter inversion, Figure 4(d), still recovers the

extension indicates that at least part of it is required by the data, giving us further evidence that the extension is a real subsurface feature. The inversion with an encouraged extension, Figure 4(c), indicates that the body could go further, i.e. there is nothing in the data to suggest that the body doesn't extend further.
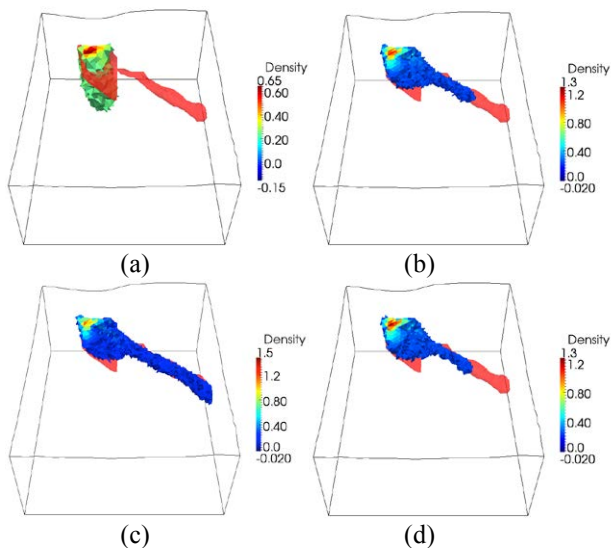


**Figure 4.** A perspective view, overhead from the south, of the recovered models for the Voisey's Bay inversion example. The unconstrained result is in (a), the bound-constrained result in (b), the elongated result in (c), and the shortened result in (d). All images show the sulphide surface in transparent red and 0.23 g/cc density isosurfaces for the recovered models. Colour bars indicate the density range of the recovered models in g/cc.

## 6 Conclusion

Geophysical inversion provides the means to unite geophysical survey data with the geological information contained in ore deposit models. Incorporation of geological information into inversions is always an iterative process. One begins with the geologists' best guess about the Earth (i.e. the geological model) and the models recovered from geophysical inversion may indicate that the geological model should be changed slightly prior to the next iteration of the procedure. In this way, geological and geophysical data can be combined through inversion and we can move towards the creation of a common Earth model consistent with all data available.

Unstructured tetrahedral meshes can honour geological contacts, can represent fine-scale structure, and yet are efficient discretizations of the modeling domain when compared to the less flexible yet commonly used rectilinear mesh alternative. Hence, working on unstructured meshes provides advantages when one wishes to incorporate prior information associated with structurally complicated subsurface geometries, which may be difficult or impossible to represent adequately on rectilinear meshes.

There are some significant challenges involved in working with unstructured meshes for the purposes of geophysical forward and inverse modeling. We are developing computational methods and utility tools to meet these challenges. By working directly with unstructured discretizations of the subsurface in our geophysical modelling methods, we are able to seamlessly combine geological and geophysical data within the framework of common Earth models. This strategy enables effective constrained inversion methods that can push the limits of the geophysical data resolution and produce higher accuracy Earth models.

## References

Ansari S, Farquharson CG (2011) 3D finite-element simulation of electromagnetic data for inductive and galvanic components. 81st SEG Annu Int Meet Expand Abstr. doi:10.1190/1.3628189

Günther T, Rücker C, Spitzer K (2006) Three-dimensional modelling and inversion of dc resistivity data incorporating topography - II Inversion. Geophys J Int 166:506-517.

Jahandari H, Farquharson CG (2011) Forward modelling of gravity data for unstructured grids using the finite-volume method. 81st SEG Annu Int Meet Expand Abstr. doi:10.1190/1.3628213

Lelièvre PG, Oldenburg DW (2009) A comprehensive study of including structural orientation information in geophysical inversions. Geophys J Int 178:623-637.

Lelièvre PG, Farquharson CG, Hurich CA (2011a) Computing first-arrival seismic traveltimes on unstructured 3D tetrahedral grids using the Fast Marching Method. Geophys J Int 184:885-896.

Lelièvre PG, Farquharson CG, Hurich CA (2011b) Inversion of first-arrival seismic traveltimes without rays, implemented on unstructured grids. Geophys J Int 185: 749-763.

Li Y, Oldenburg DW (2000) Joint inversion of surface and three-component borehole magnetic data. Geophys 65:540-552.

Owen SJ (1998) A survey of unstructured mesh generation technology. 7th Int Meshing Roundtable, Sandia National Lab 239-267.

Si H (2008) Three dimensional boundary conforming Delaunay mesh generation. Dissertation, Technische Universität Berlin.

# Application of multispectral remote sensing for gold exploration targeting in Wadi Halfa district, North Africa

**Liangming Liu, Wei Yao, Yaozu Qin**
*Computational Geosciences Research Centre, Central South University, Changsha 410083, China*

**Xinqun Fu**
*Fu Mining Company, Soba Ind. Area, Khartoum, Republic of Sudan*

**Abstract.** The Wadi Halfa terrane, located in the transition between the Sahara metacraton and Araban-Nubian shield, is a very promising, but poor understood, gold district. The main gold deposits are of vein-type and closely associated with iron-oxide and hydroxyl alteration. We use multispectral remote sensing data, ETM+ (Enhanced Thematic Mapper Plus) and ASTER (Advanced Spaceborne Thermal Emission and Reflection Radimeter), to extract gold-related alteration information and to facilitate selecting of exploration targets. The checking results have demonstrated that the methods are effective .

**Keywords.** multispectral remote sensing, alteration map, selection of exploration targets, Wadi Halfa gold district

## 1 Introduction

The Wadi Halfa terrane, located in east to the Sahara desert and south to the Aswam Dam, is the most west part of the unique Nubia gold province. The ancient Egyptian word "nbu" means "gold". The gold mining in this province can date back to the Predynastic time (about 3500 BC), and plentiful gold wealth from this region must have made great contribution to the prosperity of the Ancient Egypt (Klemm et al. 2001, Klemm & Klemm 2013). Geological investigation and exploration in this region are still very poor. Lack of documented geological information has become the major obstacle for selecting the gold exploration targets in this region. The advancement of the multispectral remote sensing has provided an effective technique for selecting exploration targets in such well outcropped and poor understood region (Meer et al. 2012). In this paper, we present our research about applying ETM+ and ASTER data to facilitate selecting of exploration targets by extracting gold-related alteration information in the Wadi Half district.

## 2 Geology Setting

The Wadi Halfa terrane is tectonically located in the transition between the Sahara metacraton and Araban-Nubian shield (Fig.1). The most important orogeny is subduction leading to collision at about 700 Ma ago, accompanied by post-orogenic rifting at about 650Ma. Thereafter the crust has been stable in the region (Stern et al. 1994, Shang et al. 2010).
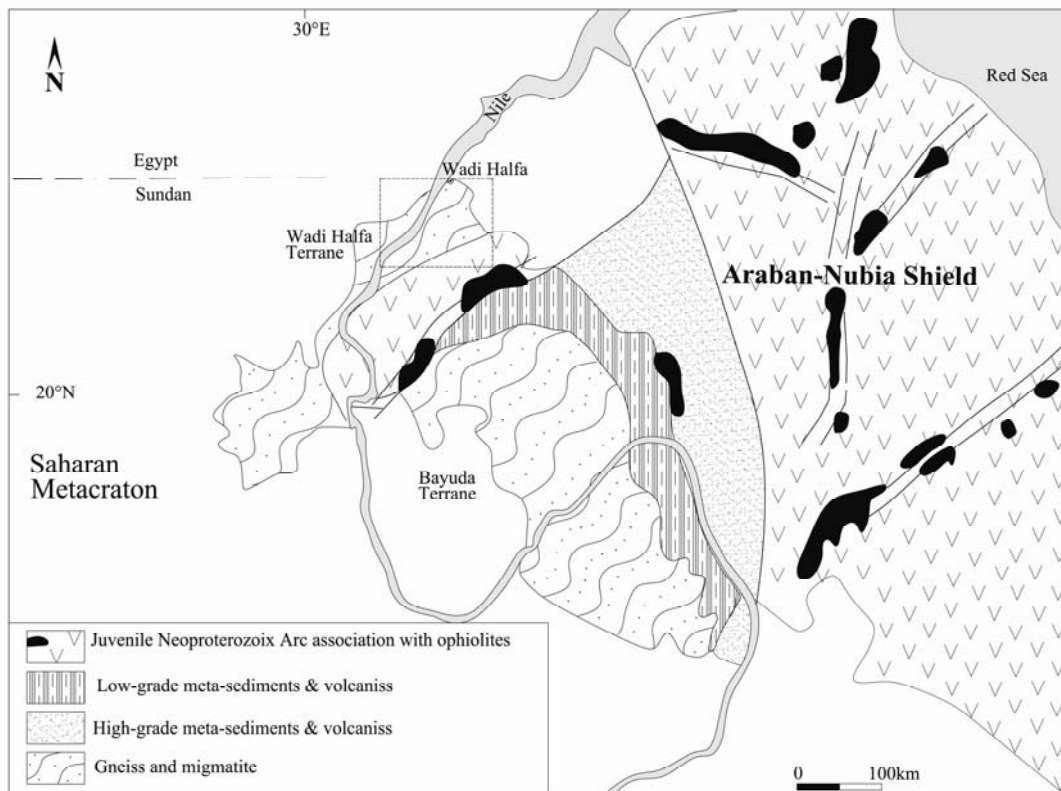


**Figure 1. Tectonic Location of the Wadi Halfa terrane, modified after Bailo et al (2003)**

The major rocks exposed in the district are Proterozoic metamorphics consisting of three groups: (1) gneises, (2) predominately metamorphic mafic volcanic and (3) meta-sediments and metamorphic predominately felsic volcanic (Fig.1). The magmatic intrusions extensive in the district consist of three major groups: (1) granodiorite and diorite, (2) granite and (3) gabbro. The gabbro and the granodiorie and diorite are generally thought as syn-orogenic, and some granites, especially with high alkali contents, are thought as post-orogenic. The structures in the Wadi Halfa district are very complex. The foliation and bed trends indicate complex folds with various axis directions and styles. The faults and shear zones with various trending are scattered in the whole district, that include NEE- and NE-trending, NNE-trending and NNW-trending. The NEE- and NE-trending faults and shear zones are the predominately channel structures that control the gold mineralization in the district.

## 3  Gold Mineralization

Although gold prospects and gold-mining relics are spread extensively over the whole district, the gold mineralization is very poor understood, for lack of research and exploration. The gold deposits discovered in this district can be classified into three main types: (1) gold-bearing volcanic-hosted massive sulfide deposit, such as Hay Sub; (2) gold-bearing quartz vein and associated altered rocks in deformed metamorphic, such as Duweishat and Umm Fahm; (3) placer gold deposit, mostly of modern gold-bearing alluvial and eluvial sediments. The major gold deposits and prospects outcropped in the field are gold-bearing quartz veins.

## 4  ETM+ and ASTER Data and Extraction of Gold-related Alteration Information

The ETM+ and ASTER are important commercial multispectral satellite imagery data. They cover same range of the electromagnetic spectrum that is from visible infrared (VNIR), shortwave infrared (SWIR) to thermal infrared (SWIR). But the ASTER has 11 bands in SWIR and TIR range, and the ETM+ only has 3 SWIR and TIR channels. Generally the spectral characteristics of the earth surface materials is closely associated with their composition, the channelled multispectral data of ETM+ and ASTER are applied successfully to extract alteration information for mineral exploration. Because the ASTER has more and finer the SWIR and TIR channels than the ETM+, the ASTER is more effective to detect the hydrothermal alteration mineral s than the ETM+.
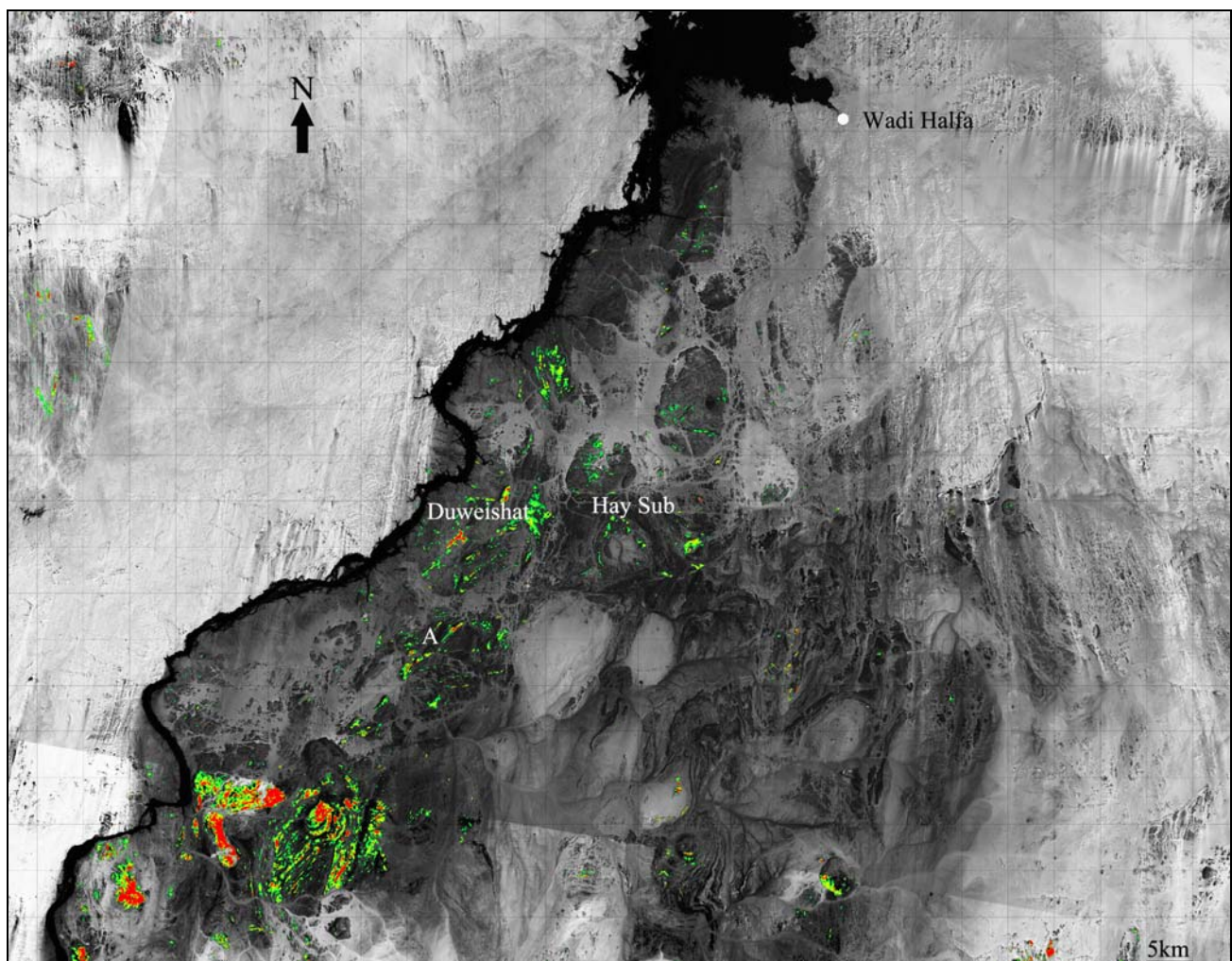


**Figure 2. Fe-alteration extracted from the ETM+ data, the red, yellow and green indicate strong, middle and weak alteration respectively**

The alteration information is general extracted via computation of false colour composite, bands radio and PCA (Principal Component Analysis). The bands 1, 3, 4 and 5 of ETM data are usually selected to extract iron-oxide alteration information by PCA (Loughlin, 1991). PC4 is used to map Fe-oxide alteration (Fig.2), because of its moderate magnitude and opposite sign of eigenvectors loadings in bands 1 and 3 (Table1).

**Table1    Eigenvector matrix of PCA**

|     | ETM1 | ETM3 | ETM4 | ETM5 |
|-----|---------|---------|---------|---------|
| PC1 | 0.13755 | 0.55318 | 0.47437 | 0.67085 |
| PC2 | -0.2314 | -0.61332 | -0.23353 | 0.71824 |
| PC3 | -0.90411 | 0.03455 | 0.40561 | -0.12993 |
| PC4 | 0.33184 | -0.56283 | 0.74560 | -0.13118 |

For gold mineralization in the Nubia region, the average spectra for the altered mineralized and non-mineralized rocks show the same lower reflectance in ASTER bands 5, 6, 7 and 8 and slight to moderate reflectance in band 9 than the ASTER band 4, while in the visible portion of the spectrum only the ASTER band 2 of the altered mineralized rocks has a higher spectral reflectance than those of the unaltered and altered non-mineralized zones. The reflectance of the average spectra of the unaltered rocks appears the same as those of the altered mineralized and non-mineralized rocks except for its highest reflectance in band 9 (Gabr et al. 2010). So the false colour image composited by bands ratio 4/8, 4/2, and 8/9 in RGB respectively can highlight the mineralized zones (Fig. 3). In the Fig.3, the gold-related alteration zones are whitish colour inside the pink zones. The pink colour represents the mineralized surface weathering.

The Fe-oxide alteration map from ETM+ presents very interesting and useful results. Over the existing gold mining areas, such as Hay Sub and Duweishat, the result shows obviously alteration. And a lot of intensive alteration zones where no economic gold deposits have been discovered before should be the promising target areas for the next exploration (Fig.2). The ASTER alteration map not only demonstrates the conclusion of the ETM+, but also focuses the promising target areas more precisely (Fig. 3).
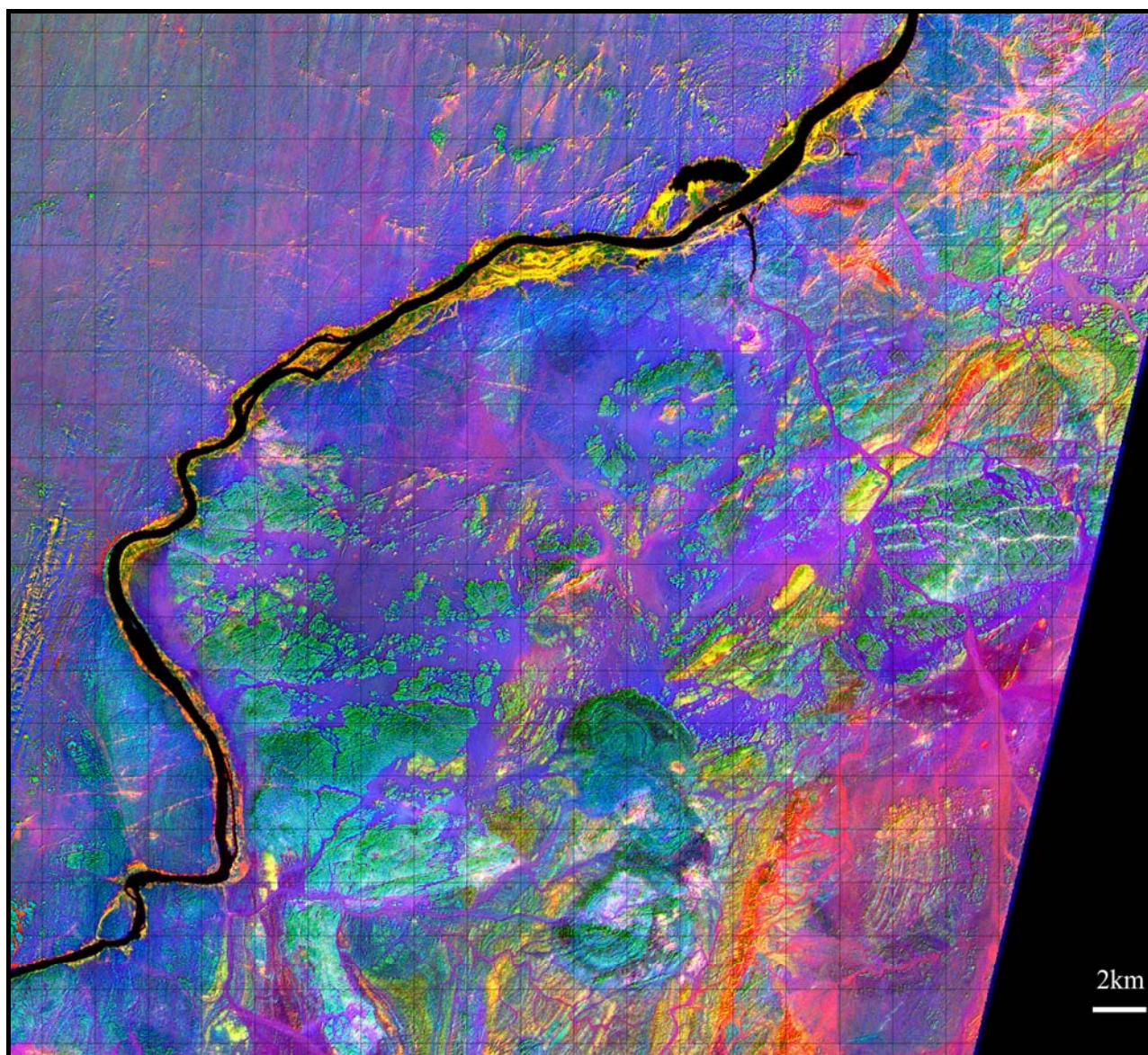


**Figure 3. Bands ratio composite image of ASTER, show the gold –related alteration as white in pink area**

## 5 Checking Results and Conclusion

By field detail investigation and sampling in some promising target areas indicated by the alteration information from the ETM+ and ASTER data (Figs. 2 & 3), we have found several vein-type gold deposits and related modern placer gold in these areas. The gold mineralization outcrops are definitely discovered in the white in pink areas in Fig.3. The discovered gold mineralization outcrops show relative intensive Fe-oxide alteration and silicification (Fig.4). It is demonstrated that the alteration information extracted from the ETM+ and ASTER data is effective for selecting gold exploration targets in the Wadi Halfa district.



**Figure 4. Gold-bearing alteration zone in the promising target area A (see Fig.2 for location), show intensive Fe-oxide alteration and silicification, with 23 ppm Au in the quartz vein and silificated rocks**

## References

Bailo T, Schandelmeier H, Franz G, Sun CH, Stern RJ (2003) Plutonic and metamorphic rocks from the Keraf Suture (NE Sudan): a galimpse of Neoproterozoic tectonic evolution on the NE margin of W. Gondwana. Precambrain Research 123: 67-80.

Dabr S, Ghulam A, Kusky T (2010) Detecting areas of high-potential gold mineralization using ASTER data. Ore Geology Reviews 38: 59-69.

Klemm D, Klemm R, Murr A (2001) Gold of the Pharaohs–6000 years of gold mining in Egypt and Nubia. African Earth Sciences 33: 643–659

Klemm R, Klemm D (2013) Gold and Gold Mining in Ancient Egypt and Nubia. Springer, Heidelberg, pp649

Meer FD, Werf HM, Ruitenbeek FJA, Hecker CA, Bakker WH, Noomen MF, Meijde M, Carranza EJM, Smeth JB, Woldai T (2012) Multi- and hyperspectral geological remote sensing: a Review. International Journal of Applied Earth Observation and Geoinformation 14: 112-128.

Loughlin WP (1991) Principal component analysis for alteration mapping. Photogrammetric Engineering and Remote Sensing 57: 1163-1169

Shang CK, Morteani G, Stair M, Taubald H (2010) Neoproterozoic continental growth prior to Gondwana assembly: Constraints from zircon-titanite geochronology, geochemistry and petrography of ring complex granitoids, Sudan. Lithos 118: 61-81

Stern RJ, Kröner A, Bender R Reischmann T (1994) Precambrian basement around Wadi Halfa, Sudan: A new perspective on the evolution of the East Saharan Craton. Geologische Rundschau 83: 564-577.

# Reflection seismic imaging and petrophysical investigation of the Dannemora iron ore bodies, central Sweden

Alireza Malehmir, Emil Lundberg, Peter Dahlin, Christopher Juhlin, Håkan Sjöström & Karin Högdahl
*Uppsala University, Department of Earth Sciences, SE 75236, Uppsala, Sweden*

**Abstract.** Bergslagen is a major mineralized region in south-central Sweden. In 2010, two reflection seismic profiles each about 25 km long were acquired in the northeastern part of the region to check its overall crustal structures. One of the seismic lines crosses the Dannemora iron oxide deposit where tighter shot and receiver spacing was used and additional shots off the acquisition line were generated. Results suggest a series of strong reflections associated with iron oxide mineralization. This interpretation is constrained by ultrasonic velocity measurements on a series of rock and iron ore samples, cross-dip analysis, prestack time/depth migration, and swath 3D imaging, as well as by other available geophysical and geological observations. To further support the interpretation, we carried out a simple exploding reflector modelling based on the available geometry of the iron ore bodies. This, for example, shows the importance of the additional shots but also enhanced the understanding of the expected signal from the ore bodies. A series of major poly-phase deformation zones is also imaged by the seismic data.

**Keywords.** Dannemora iron ore, reflection seismics, petrophysics, modelling

## 1 Introduction

The Bergslagen region in south-central Sweden is one of three major ore producing areas in Sweden. With more than 1000 years of continuous mining and more than 6000 known mineralization (including mines and prospects), the region is historically considered the most prosperous ore district in the country (Allen et al. 1996; Stephens et al. 2009). The Bergslagen region contains a diverse range of mineral deposits including banded iron formation (BIF), manganiferous skarn and carbonate-hosted iron ore, rare earth elements (REE) deposits, tungsten (W) skarn deposits, apatite-bearing iron deposits including Mn-rich iron ores, and volcanic-hosted massive sulphide (VHMS) deposits. Currently, four deposits are mined: Garpenberg, Zinkgruvan, Dannemora and Lovisa. Several others are in different stages of the start-up process of mining. Of these, Dannemora is iron mine, and the others are base-metal mines. Dannemora mine (see Dahlin et al. 2012) and areas close to the mine are the main focus of this study.

In 2010, we acquired two reflection seismic profiles each about 25 km long in the area in the northeastern part of the Bergslagen region (Malehmir et al. 2011). The main purpose of the seismic survey was to image crustal structures in the area and especially those associated with major deformation zones. One of the seismic lines (Profile 2), however, was designed to cross the Dannemora deposit (Figure 1). To provide high-resolution image of subsurface structures at/near the mine and potentially from iron ore bodies, we acquired seismic data across the mine using 10 m shot and receiver spacing. Based on *a priori* information from the mineralization dip direction, additional shots were also fired in the western side of the mine in order to provide better illumination at depth (Figure 1).

In this study, we present seismic data at the Dannemora deposit, petrophysical measurements conducted on a series of samples from the iron ore and its hostrock and seismic modelling of the iron ore bodies. Our main objectives are (i) to evaluate the potential of reflection seismic methods for iron ore exploration by imaging existing iron ore bodies and potentially providing new targets for future deep exploration, (ii) to measure physical properties (here P- and S-wave velocities) of iron ore samples and their host rock in the Dannemora and (iii) to obtain a better understanding about the origin of a deep (800-2200 m) reflector that is imaged in the continuation of the main Dannemora ore bodies.

## 2 Reflection seismic survey

Based on our previous experience from reflection seismic surveys that aimed at imaging the upper few km of crust in the northeastern Bergslagen region and on present knowledge of geological structures, we used a receiver spacing of 20 m and a shot spacing of 40 m for the acquisition of the reflection seismic data. We used an asymmetric split-spread geometry using 360 active channels (with a 100 channel arm in the expected up-dip direction). Two nearly perpendicular seismic reflection profiles, each about 25 km long, were acquired. A mechanical hammer (VIBSIST) was used to generate seismic signal. Profile 1 starts ~5 km south of the Forsmark site; it crosses a series of complex deformation zones, and continues to the south nearly 9 km southeast of the Dannemora iron mine. Profile 2 starts nearly 10 km east of the Dannemora mine and continues westward an additional 15 km to a large granitic intrusion (Figure 1). The profile crosses a major deformation zone east of the Dannemora mine.

The receiver spacing across the Dannemora deposit was reduced to 10 m to potentially provide a higher-resolution image of the iron mineralization at this

location. Shot spacing was reduced to 10 m over the mine and partly to the west of the mine. To potentially provide additional information about the 3D geometry of geological structures, a series of additional shot points west of the mine (in the down-dip direction) was activated perpendicular to the actual profile (Figure 1). The additional shot points (about 50 shots) were used in constraining the 3D geometry of the structures at Dannemora and the iron ore bodies. In total, nearly 1350 shots were fired along both profiles. Seismic data processing followed a conventional prestack DMO and poststack migration algorithm with focus on key processing steps often crucial for data acquired in crystalline environment. Advanced processing methods such as cross-dip analysis, swath 3D processing and prestack depth and time migration were also carried out to provide improved images of structures. Further details about the seismic survey and processing results can be found in Malehmir et al. (2011).
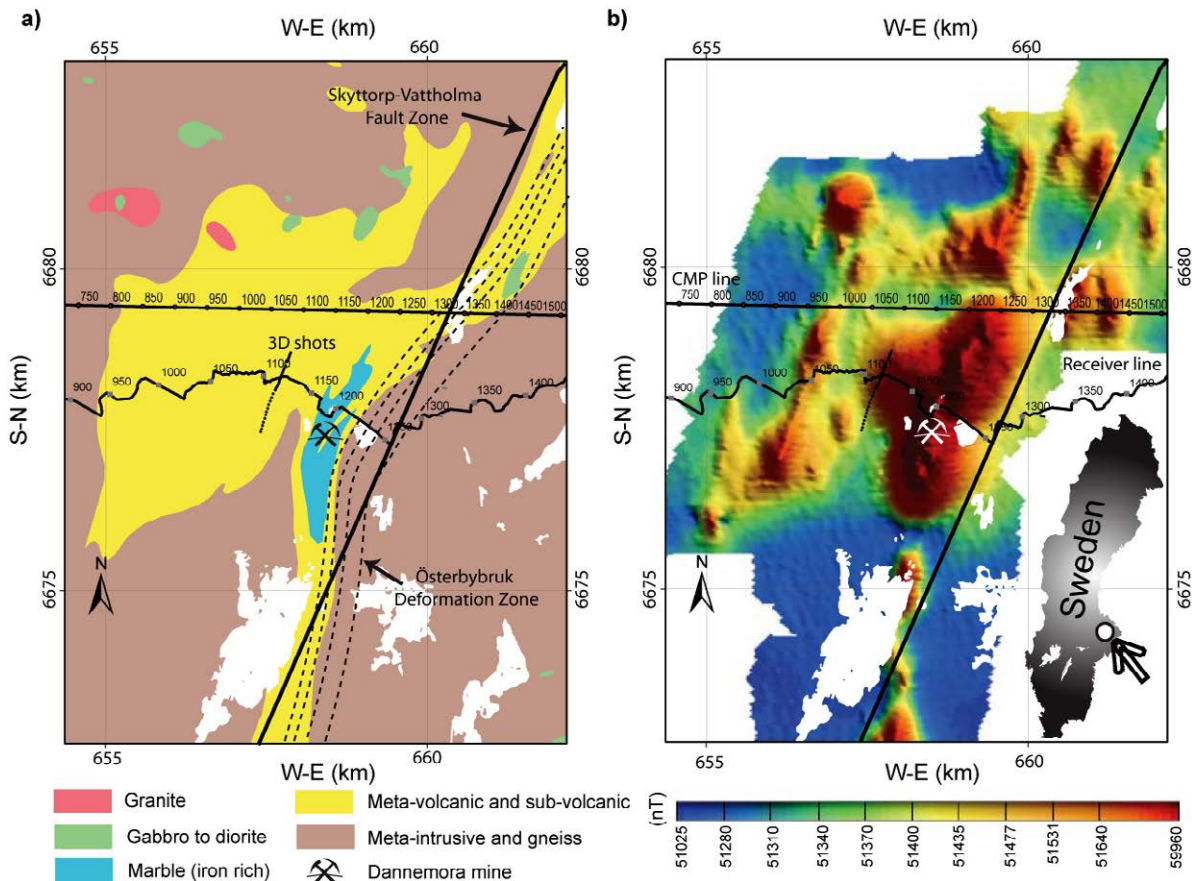


**Figure 1.** (a) Geological map (Geological Survey of Sweden) of the Dannemora mining area and (b) corresponding high-resolution helicopter total field aeromagnetic map (Dannemora Mineral AB), showing that a strong northeast-southwest directed magnetic signature is produced by the main iron ore bodies. The magnetic high about 500 m west of the main iron ore bodies is associated with the Diamant 2 iron ore. Black crooked-line shows a portion of the seismic Profile 2 (the focus of this study) and how it crosses the mine. Additional shots, about 50, were generated in the western side of the mine to provide better illumination at depth.

## 3 Petrophysical measurements

In a larger sampling and petrophysical campaign, more than 50 rock samples from about 25 different types of rocks and mineral deposits from three regions of Sweden were collected. The samples were chosen based on their importance for future deep mineral exploration and their proximity to the existing seismic profiles (e.g., Dehghannejad et al. 2010; Malehmir et al. 2011). About 25 samples are from the Dannemora mining area.

Using both P- and S-wave transducers (0.5 MHz central frequency), we measured ultrasonic wave velocities of our samples at both atmospheric and at elevated confining pressure of up to 65 MPa (equivalent to a maximum depth of 3 km). Although higher pressures up to 200 MPa would be required to fully close any existing cracks, we chose a maximum

pressure of 65 MPa because the equipment used did not allow higher pressures; moreover, higher pressures than this are not expected to be present at depths of 2–3 km. These depths (exploration depths) are the focus of our study.

Figure 2 shows measurement results for both P- and S-wave velocities plotted against densities of the samples. As evident from the figure, iron ore samples (magnetite with more than 30% Fe) from the Dannemora deposit show the highest contrast against almost all the lithologies used in the measurements. In fact, the samples show the highest even among most massive sulphide samples collected in Sweden. This implies that iron mineralization should, with this characteristic and composition, be easily detectable if that they meet the necessary requirements (e.g., size and shape) for their imaging. We later show that one of the

known iron ore bodies in the area correlate well with a high-amplitude anomaly in our seismic image further proving that this significant contrast exist between the

iron mineralization and their host rock. Further details about the petrophysical measurements can be found in Malehmir et al. (2013).
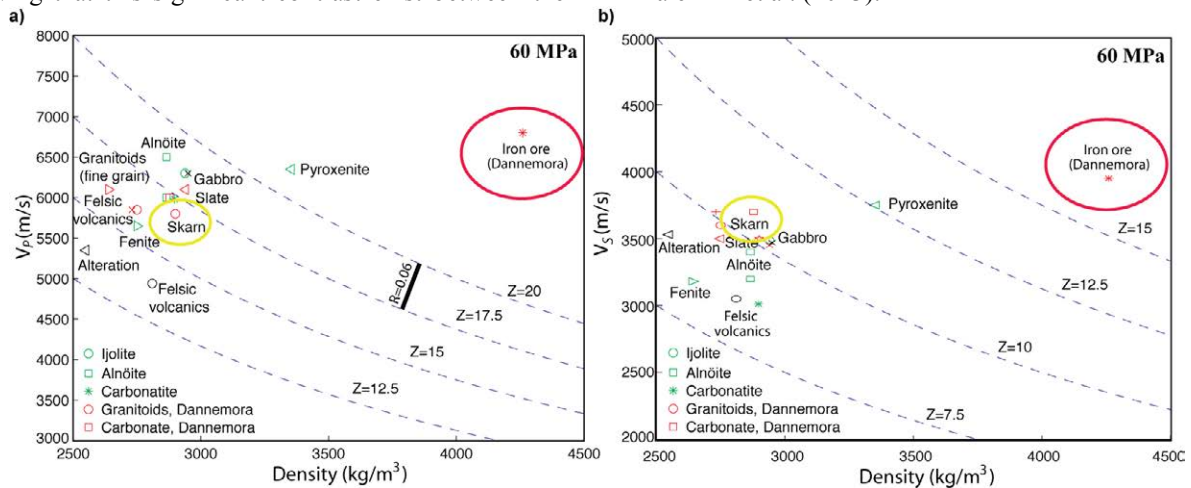


**Figure 2.** (a) P- and (b) S-wave velocity measurements on a series of Swedish crystalline rocks and the Dannemora iron ore samples at a confining pressure of 60 MPa. Results indicate that the iron ore samples should be strongly reflective if they have a proper size and geometry for 2D reflection seismic surveying. Iron ores in the Dannemora area are often hosted by marble and skarn type rocks.

## 4 Seismic results and modelling

Based on geological data, the main ore body terminates at 800-900 m depth where the mineralization has been cross cut by a late intrusion (Dahlin et al. 2012). However, this is only indicated by a few drill-cores and a seismic study would therefore yield a better understanding of the geology at depth. Seismic imaging near the Dannemora mine proved to be difficult due to various reasons but the most important one is the ability to acquire high-fold data in this highly populated and noisy area. Initial processing results allowed imaging general structures in the area but careful processing and imaging strategies were required to image reflections from the iron ore bodies in the site. The seismic line is extremely crooked (Figure 1) across the mine and this makes any 2D seismic imaging a challenge. Figure 3 shows an example shot recorded almost on the top of one of the ore bodies (see Figure 1) with a clear steeply dipping reflection (R1) generated at the location of the Dannemora open pit.
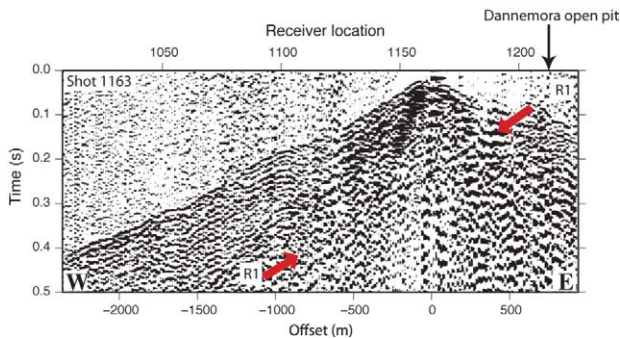


**Figure 3.** An example shot gather recorded almost on the top of the iron ore bodies showing a steeply dipping reflection (R1) at the location of the Dannemora abandoned open pit.

To properly account for the crookedness of the line and turn that into an advantage, we performed swath 3D imaging and processing in this area. It helped not only

imaging strong reflections at the very shallow depths but also allowed to obtain information about the strike of the reflections. The additional shots in the western side of the mine were crucial in imaging some of these reflections and recommended to be done if possible for this type of survey. Figure 4 shows 3D visualization of the Dannemora ore bodies (some already mined some are being mined) with a 2D representation of the seismic results. Diamant 2 ore body correlates well with a strong reflection in the west of the main ore bodies at about 400-500 m depth. A steeply dipping reflection extending from 700 m to about 2.5 km depth is imaged in the continuation of the main ore bodies. This is an interesting feature in the seismic data and of great interest for future investigations.
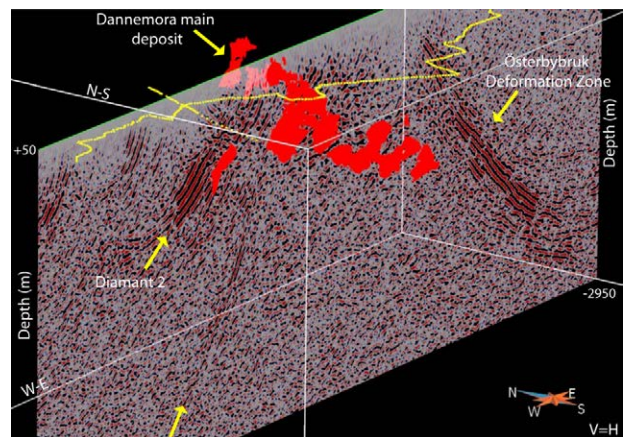


**Figure 4.** 3D visualization of seismic data with the known locations of the iron ore bodies showing a good correlation between a strong westward dipping reflection and the Diamant 2 and a set of south dipping reflections and the deformation zone. The origin of a steeply dipping reflection in the continuation of the main iron ore bodies is unknown.

### 4.1 Exploding reflector modelling

To better understand the potential imaging of the known

ore bodies in our seismic profile, we performed an exploding reflector modelling (White and Malinowski, 2012) based on the geometry of the ore bodies constrained by drilling. Using these geometries as input to the modelling, we output three normals to each triangulated surface of the body itself and simply projected them onto the Earth's surface along a specified acquisition line to check where potential signals can be observed. This was carried out for the geometry of known ore bodies (Figure 5a), those that are already mined (Figure 5b; assuming nothing left), and those that are currently being mined (Figure 5c). For example, the modelling work demonstrates why the acquisition of the additional shots in the western side of the mine is helpful in not only increasing the seismic fold but also better target illumination. The modelling further supports that the steeply dipping reflection imaged in the continuation of the main ore bodies does not belong to the known ore bodies and must be a separate feature since it appears at around CDPs 800-900, although this is expected due to the steep nature of the reflection.
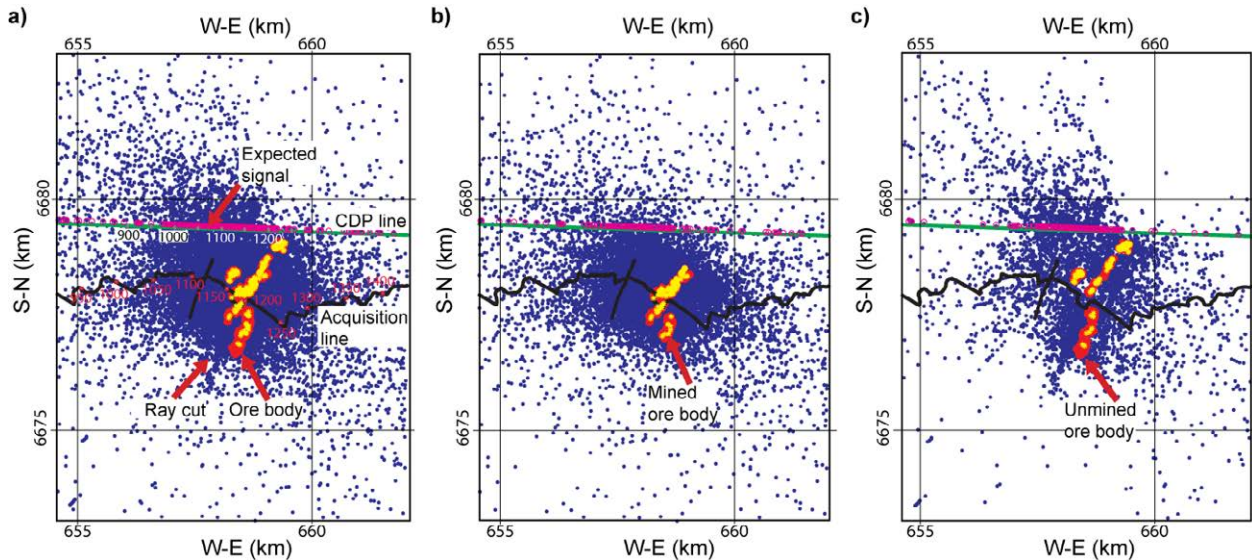


**Figure 5.** Exploding reflector modelling results based on the known geometry of (a) all iron ore bodies (b) mined ore bodies and (c) unmined ore bodies. Blue dots represent expected locations of the signal from the known ore bodies. As evident, to illuminate these ore bodies, a northwest-southeast directed 2D line is best suited. Any future 3D survey could also benefit this direction as an optimum survey direction. Scattering pattern of the rays is due to the undulated surfaces of the ore bodies.

## 5 Conclusions

The reflection seismic experiment in the Dannemora mining area, although challenged by the crookedness of the line and low signal-to-noise ratio at the mine site, proved the potential of the method for direct targeting of iron ore bodies. Exploding reflector modelling based on the geometry of the known ore bodies demonstrated how the additional shots off from the acquisition line could be helpful in providing improved image of the subsurface structures. Future underground seismic studies can most likely provide a better understanding about the geometry and origin of the deep reflector especially when the Diamant 2 mining tunnels are accessible.

## References

Allen RL, Lundström I, Ripa M, Simenov A, Christofferson H (1996) Facies analysis of a 1.9 Ga, Continental margin, back-arc, felsic caldera province with diverse Zn-Pb-Ag-(Cu-Au) sulfide and Fe oxide deposits, region, Sweden. Economic Geology 91: 979–1008.

Dahlin P, Allen R, Sjöström H (2012) Palaeoproterozoic metavolcanic and metasedimentary succession hosting the Dannemora iron ore deposits, Bergslagen region, Sweden. GFF 134: 71–85.

Dehghannejad M, Juhlin C, Malehmir A, Skyttä P, Weihed P (2010) Reflection seismic imaging of the upper crust in the Kristineberg mining area, northern Sweden. Journal of Applied Geophysics 71: 125–136.

Malehmir A, Andersson M, Lebedev M, Urosevic M, Mikhaltsevitch V (2013) Experimental estimation of velocities and anisotropy of a series of Swedish crystalline rocks and ores. Geophysical Prospecting 61: 153–167.

Malehmir A, Dahlin P, Lundberg E, Juhlin C, Sjöström H, Högdahl K (2011) Reflection seismic investigations in the Dannemora area, central Sweden: insights into the geometry of poly-phase deformation zones and magnetite-skarn deposits. Journal of Geophysical Research 116: B11307.

Stephens MB, Ripa M, Lundström I, Persson L, Bergman T, Ahl M, Wahlgren C-H, Persson P-O, Wickström L (2009) Synthesis of the bedrock geology in the region, Fennoscandian Shield, south-central Sweden. Geological Survey of Sweden, report Ba 58, ISBN 978-91-7158-883-8.

White D, Malinowski M (2012) Interpretation of 2D seismic profiles in complex geological terrains: Examples from the Flin Flon mining camp, Canada. Geophysics 77: WC37–WC46.

# Petrophysical laboratory measurements of two ore formations in Southern Finland

Satu Mertanen, Fredrik Karell, Heikki Säävuori & Meri-Liisa Airo
*Geological Survey of Finland, South Finland Unit, 02151 Espoo, Finland, satu.mertanen@gtk.fi*

**Abstract.** Petrophysical, rock magnetic and anisotropy of magnetic susceptibility (AMS) measurements have been carried out on orogenic gold deposit in Uunimäki and on porphyry type Cu-Au deposit in Kedonojankulma in the Paleoproterozoic Häme belt of Southern Finland. The main aim of laboratory studies has been to identify and characterize possible alteration processes that might be reflected in the physical properties of rocks. In the Uunimäki gabbroic occurrence the highest magnetization values correlate with strong IP anomalies, and the magnetization is carried by monoclinic pyrrhotite with high Curie temperature. In the more weakly magnetized rocks the magnetization resides dominantly in magnetite.

In the Kedonojankulma quartz-plagioclase porphyrite occurrence, the induced and remanent magnetizations are slightly higher in the altered auriferous shear zone than in the less altered host rock. In the altered zone the only magnetic mineral is monoclinic pyrrhotite with high Curie temperature, while in the host rock the main magnetic mineral is magnetite.

Based on AMS data, the magnetic foliation planes follow the general foliation structures in both formations, although the degree of anisotropy varies considerably.

**Keywords.** Petrophysics, AMS, gold, Paleoproterozoic, Finland

## 1 Introduction

Petrophysical laboratory measurements of mineralized samples and ores have been carried out on two locations in the Paleoproterozoic Häme belt of Southern Finland (Fig. 1). The study areas were selected utilizing airborne geophysical data, the petrophysical measurements being made in order to aid geological interpretation of the data. Detailed investigations were made at outcrop scale to delineate differences between ore and host rocks, with the main aim of identifying and characterizing possible alteration processes that might be reflected in the physical properties of rocks. The studies also included magnetic fabric investigations (AMS).

## 2 Geological background

The bedrock of southern Finland was formed during the Svecofennian orogeny at 1.9–1.8 Ga, involving several collisional and metamorphic stages that produced different types of ore formations. Both studied formations occur in the Häme belt where the age of magmatic activity is in general 1.88 Ga (Saalman et al. 2009), and the last active orogenic evolution took place at ca. 1.79 Ga (Lahtinen et al. 2005). The study objects comprise the Uunimäki orogenic gold deposit hosted by gabbro and uralite porphyry gabbroic rocks, and Kedonojankulma porphyry type Cu-Au deposit hosted by subvolcanic quartz-plagioclase porphyritic phase of a tonalitic intrusion (Tiainen et al. 2012). The mineralizations occur in strongly altered and sheared zones.

## 3 Sampling and methods

In the Uunimäki gold deposit oriented drill core samples were taken from 10 outcrops transecting a strong IP anomaly (Fig 2). In addition, measurements were carried out on three borehole cores and results were correlated with geochemical data. At Kedonojankulma porphyry type Cu-Au deposit samples were taken from two locations; from Rusakkokallio and Passi (Fig. 8). At Rusakkokallio the sampling comprised two separate
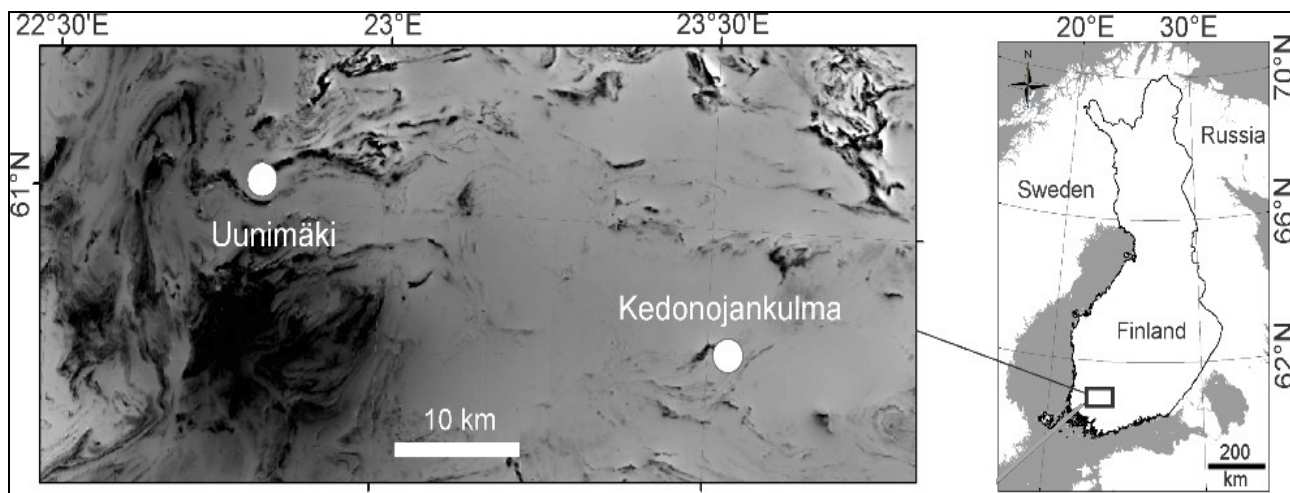
**Figure 1.** Aeromagnetic map of the Häme belt showing the study locations.

outcrops of quartz-plagioclase porphyrite with varying degrees of alteration, and one profile trough unsheared quartz-plagioclase porphyrite to a sheared and altered auriferous zone. At Passi, samples were taken from a tonalite outcrop and from an outcrop containing the contact between quartz-feldspar porphyrite and tonalite.

In the laboratory, samples were prepared to standard cylinders (hight 2.5 cm, diameter 2.1 cm). The principal petrophysical parameters measured were magnetic susceptibility (applied field intensity of 130 A/m), conductivity and density. Alternating field and thermal demagnetizations, coupled with measurements by RF SQUID magnetometer were applied to part of the samples for remanent magnetization studies. Anisotropy of magnetic susceptibility (AMS) measurements were conducted with KLY-3S kappabridge (applied field intensity of 300 A/m). Determinations of magnetic mineralogy comprised thermomagnetic analyses and three component IRM measurements (see Mertanen and Karell 2011).

## 4 Results

### 2.1 Uunimäki orogenic gold deposit

The Uunimäki gabbroic occurrence (Fig. 2) is characteristically weakly magnetized (both susceptibility
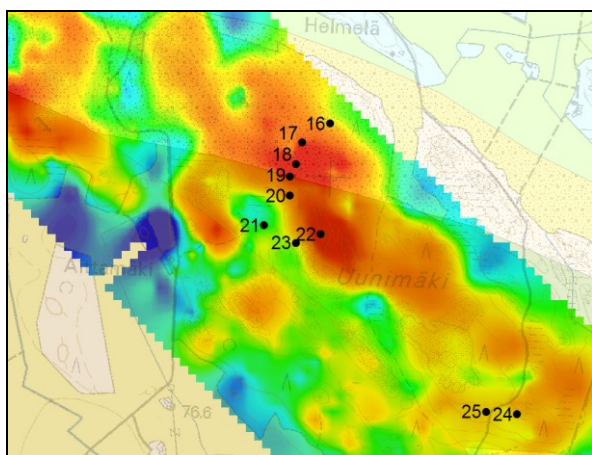


**Figure 2.** IP anomaly map of Uunimäki deposit showing the sampling sites.
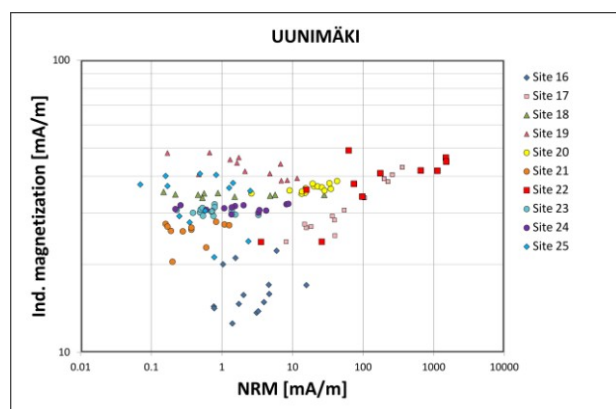


**Figure 3.** Induced magnetization versus remanent magnetization (NRM) of the samples from Uunimäki.

and remanence), the highest magnetization values and conductivities correlating with strong IP anomalies (Fig. 3). The rocks among the highest IP anomaly carry monoclinic subordinate pyrrhotite with exceptionally high Curie temperature of ca. 350-370°C (Fig. 4), which
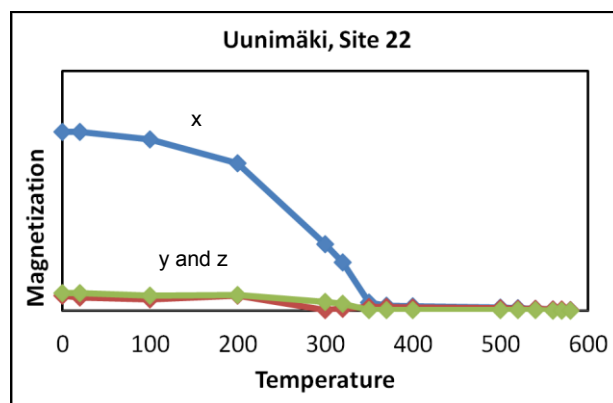


**Figure 4.** Three component IRM measurement of a sample from Uunimäki site 22 showing the Curie temperature of 370°C in the soft x (blue) component demonstrating disordered pyrrhotite as the only magnetic mineral in the sample.

is believed to be due to partially disordered vacancy distribution (Gendler et al., 1997). These rocks are probably most altered, seen as alteration of magnetite to pyrrhotite. The lowest magnetization values are found among weak IP anomalies, where the magnetization is carried by magnetite, in addition to small amounts of pure monoclinic pyrrhotite with typical Curie temperature of 320°C (Fig. 5). Remanent magnetization
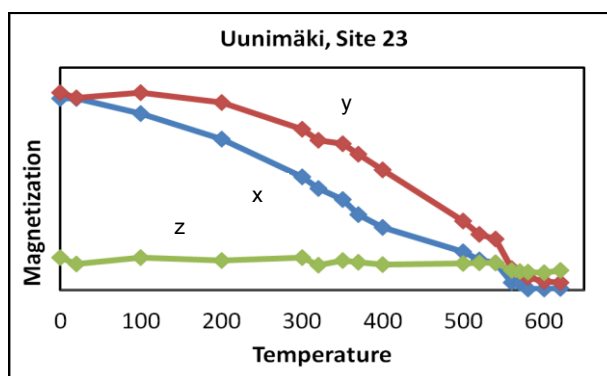


**Figure 5.** Three component IRM measurement of a sample from Uunimäki site 23. The sample carries magnetite (Curie temperature of 580°C) and minor of pyrrhotite (320°C) in the soft x (blue) intermediate y (red) and hard z (green) fractions.

directions between sites are generally highly scattered. However, at one site the uralite porphyritic gabbro with the highest conductivity and magnetization values (site 22, Figs. 2 and 3) carries a stable Svecofennian age (e.g. Mertanen and Pesonen 2012) remanence direction (Fig. 6) which may be due to young magmatic pulse post-dating deformation, or due to better preservation of the site from later tectonic processes.

Preliminary AMS directional data within Uunimäki are characterized by NW-SE striking, almost vertically
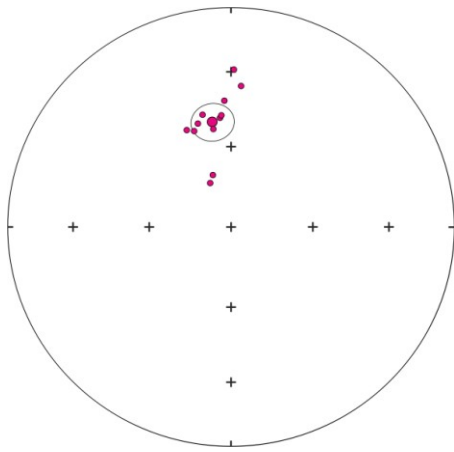
**Figure 6.** Remanent magnetization directions of samples from Uunimäki site 22. The mean direction (with α95 confidence cone) corresponds to Svecofennian age (ca. 1.8 Ga) remanence direction.

dipping magnetic foliations and predominantly vertically plunging magnetic lineations (Fig. 7). The anisotropy degree is generally low, 2-5%, but in the northern part the anisotropy degree increases up to 13%. The shapes of the AMS ellipsoids are both oblate and prolate.
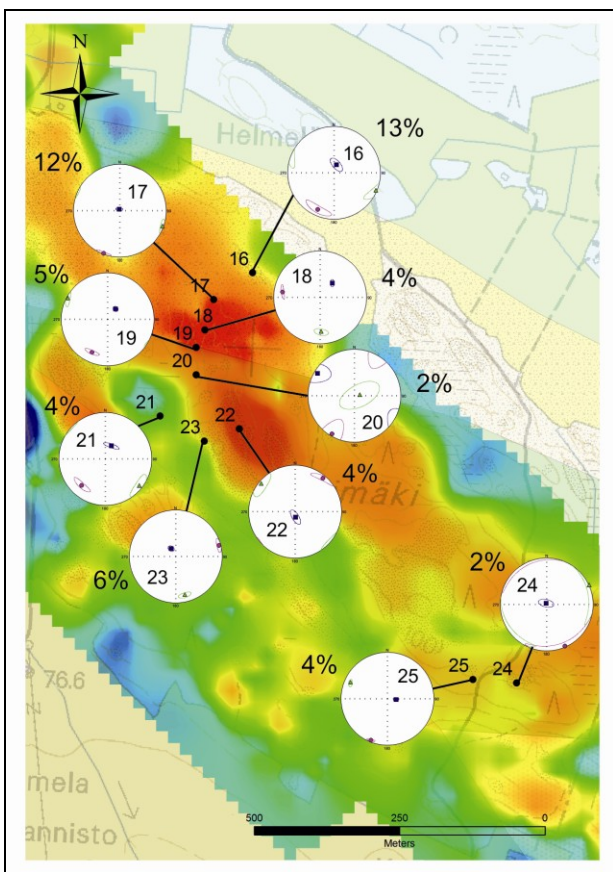


**Figure 7.** AMS data from Uunimäki.

Geochemical correlations of the three borehole cores show that the occurrence of gold is only weakly correlated with other heavy metals. From petrophysical parameters gold is best correlated with inductive conductivity, consistent with the occurrence of pyrrhotite.

## 2.2 Kedonojankulma porphyry type Cu-Au deposit

The quartz-plagioclase porphyrites at site Rusakkokallio in the Kedonojankulma deposit (Fig. 8) are typically weakly magnetized (Fig. 9). The magnetization values
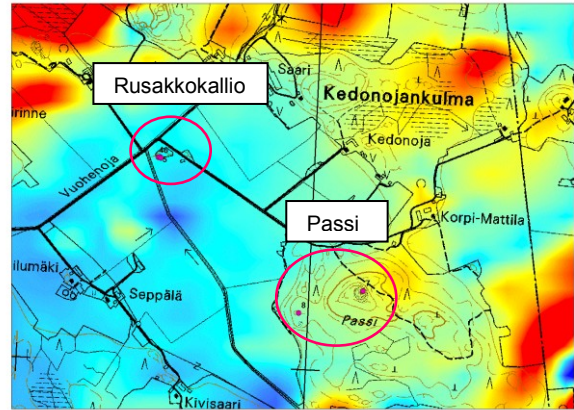


**Figure 8.** Aeromagnetic anomaly map of Kedonojankulma deposit showing the sampling sites of Rusakkokallio (sites 4-6) and Passi (sites 7 and 8).

increase slightly within the auriferous hydrothermal shear zone, the Q values being highest within the shear zone, which indicates the dominance of remanent magnetization over induced magnetization. In the Passi outcrops the susceptibilities of quartz-plagioclase porphyrites are in general higher than in Rusakkokallio, while the highest magnetizations occur in magnetite bearing tonalite, consistent with the aeromagnetic data.
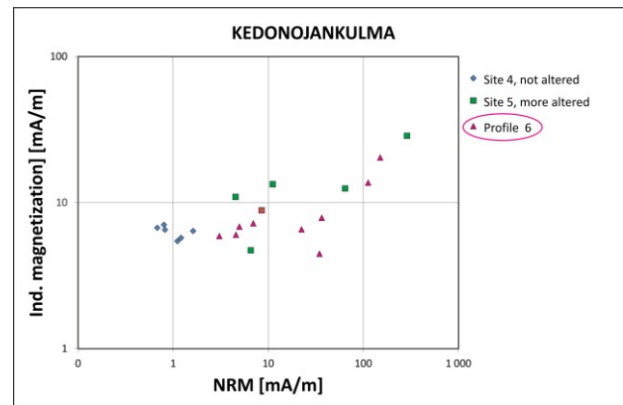


**Figure 9.** Induced magnetization versus remanent magnetization of the samples from site Rusakkokallio in Kedonojankulma deposit.

In the Rusakkokallio sites the typical magnetic mineral is monoclinic pyrrhotite, but like at Uunimäki deposit, there are two types of it. A disordered pyrrhotite with high Curie temperature of ca. 370°C occurs within the most altered part of the shear zone (Fig. 10) while in the unsheared rock, the main magnetic mineral is magnetite that occurs together with monoclinic pyrrhotite with Curie temperatures of 320°C and/or 370°C.

The magnetic foliations in Rusakkokallio strike
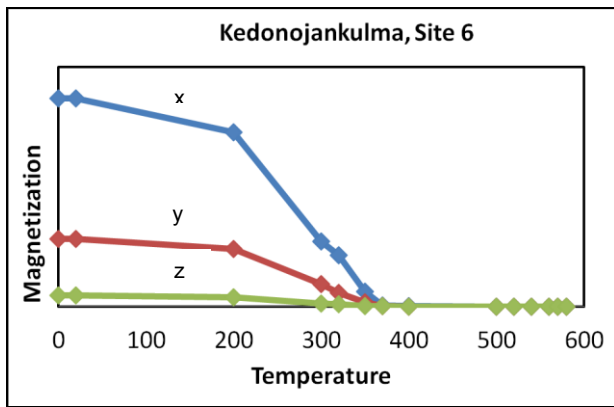
**Figure 10.** Three component IRM measurement of a sample from the altered auriferous shear zone of quartz-plagioclase porphyrite in site 6 of Rusakkokallio in Kedonojankulma. The sample carries only pyrrhotite (350°C) in the soft x (blue) intermediate y (red) and hard z (green) fractions.

almost vertically along the general trend of shearing, and magnetic lineations plunge moderately to SW (Fig. 11). In Passi the magnetic foliations dip steeply to SE and the magnetic lineations plunge moderately to S-SE. The shapes of AMS ellipsoids are predominantly oblate. The Rusakkokallio samples have slightly lower anisotropy degrees than the samples in Passi. In particular the least altered samples in Rusakkokallio are characterized by low magnetic susceptibilities and low anisotropy degrees.
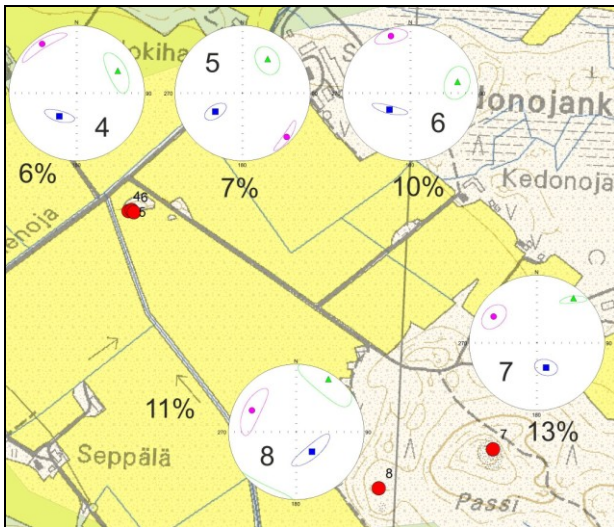


**Figure 11.** AMS data from Kedonojankulma showing higher anisotropy (%) in the Passi tonalite (sites 7 and 8) than in the Rusakkokallio quartz-plagioclase porphyrite (sites 4-6).

## 4  Conclusions

In the Uunimäki gabbroic occurrence the highest magnetization values and conductivities correlate with strong IP anomalies, though the formation is in general weakly magnetized. Rock magnetic analyses show that in the samples of highest magnetization, which are believed to represent the most altered part of the deposit, the only magnetic mineral is monoclinic pyrrhotite with exceptionally high Curie temperature of 350-370°C. The

less altered areas show dominance of magnetite with minor amounts of pyrrhotite. At one site with the highest magnetization values, the remanent magnetization has retained its original Svecofennian age direction, while at other sites the remanences are scattered due to deformation. AMS directions are characterized by NW-SE striking, approximately vertically dipping magnetic foliations and vertically plunging magnetic lineations.

In the Kedonojankulma quartz-plagioclase porphyrite occurrence, the induced and remanent magnetizations are slightly higher in the altered auriferous shear zone than in the less altered host rock. In the altered zone the only magnetic mineral is monoclinic pyrrhotite with high Curie temperature of ca. 370°C, while in the host rocks the main magnetic mineral is magnetite. Based on AMS data the least altered quartz-plagioclase porphyrite in Rusakkokallio also has the smallest degree of anisotropy.

## Acknowledgements

## References

Gendler TS, Krasnov SG, Pechersky DM, Stepanova TV, Tsel'movich VA, Sharonova ZV, Sholpo LE, Khaliulina EA (1997) Magnetomineralogical characteristics of ores from the Middle Valley oceanic sulfide deposit, Ocean Drilling Program Leg 139, Juan de Fuca Ridge. Izvestiya, Physics of the Solid Earth 33:89-112.

Lahtinen R, Korja A, Nironen M (2005) Paleoproterozoic tectonic evolution. In: Precambrian geology of Finland: key to the evolution of the Fennoscandian Shield. Developments in Precambrian geology 14. Amsterdam, Elsevier 481-531.

Mertanen S, Karell, F (2011) Rock magnetic investigations constraining relative timing for gold deposits in Finland. Bull Geol Soc Finland 83:75-84.

Mertanen S, Pesonen, LJ (2012) Paleo-Mesoproterozoic Assamblages of Continents: Paleomagnetic Evidence for Near Equatorial Supercontinents. In: Haapala I (ed), From the Earth's Core to Outer Space. Lecture Notes in Earth System Sciences 137, Springer-Verlag Berlin Heidelberg 11-35.

Saalmann K, Mänttäri I, Ruffet G, Whitehouse MJ (2009) Age and tectonic framework of structurally controlled Palaeo-proterozoic gold mineralization in the Häme belt of southern Finland. Prec Res 174:53-77.

Tiainen M, Kärkkäinen N, Koistinen E, Lohva J, Sipilä P, Huhta P (2012) Discovery of the Kedonojankulma Cu-Au occurrence, hosted by a Svecofennian porphyritic granitoid in Southern Finland. In: Gold in Southern Finland: results of GTK studies 1998-2011. Geol Surv Finland, Spec Pap 52:73-90.

# Seismic imaging of shallow sediment-hosted massive sulphide deposits

**Laura Quigley***
*Department of Earth Science, University of Toronto, ON, Canada*
*quigley@es.utoronto.ca*

**Bernd Milkereit**
*University of Toronto, ON, Canada*

**Abstract**. In this study synthetic seismic data is used to investigate the challenges associated with imaging shallow sediment-hosted massive sulphide deposits. Comprehensive drilling, logging and core analysis in sediment-hosted mineralized zones provided the means to compile petrophysical information required for the seismic experiment. Using the petrophysical data obtained from logged boreholes, 2D rock physics models were constructed for two different sediment-hosted Zn-Pb deposits. The logged borehole data was obtained from regions of shale-hosted and carbonate-hosted mineralization. Synthetic seismic data for the rock physics models was generated in an effort to better understand their seismic wavefield responses. The first model is a shale-hosted Zn-Pb deposit overlain by barite and the second model is a very shallow (175m) lens shaped Zn-Pb orebody hosted in a carbonate layer. Both models presented unique processing challenges due to the shallow, finite nature of the targets. Interference of the target reflections with the source generated noise is the primary problem encountered in the seismic data from both models. Seismic modeling of the full elastic wavefield was accomplished using a finite difference code (Bohlen 2002) which is a numerical approach to solving the wave equation for a given medium.

**Keywords:** massive sulphide deposits, seismic modeling, elastic properties

## 1 Seismic Imaging of a Large Shallow SEDEX Deposit

Using Matlab, a petrophysical database from logged borehole data and a geological cross section, a 2D rock physics model of a shale-hosted Zn-Pb±Ba deposit was constructed (Fig. 1) to study its seismic wavefield response. Using a finite difference elastic wavefield code (Bohlen, 2002) realistic seismic data was simulated using the rock physics model as input. The model represents a geological setting typical of sedimentary exhalative (SEDEX) deposits, which are major sources of zinc and lead. Elastic wavefield modeling required that p-and s-wave velocities (Vp, and Vs) and density values were known for each lithology within the model. A comprehensive petrophysical data base was compiled from logged borehole data.

The boreholes were located in close proximity to a SEDEX deposit and allowed us to obtain average values for the elastic properties of the lithologies in our model. The borehole data consisted of p-wave (Vp) and density (ρ) measurements for over 200000 shale values,
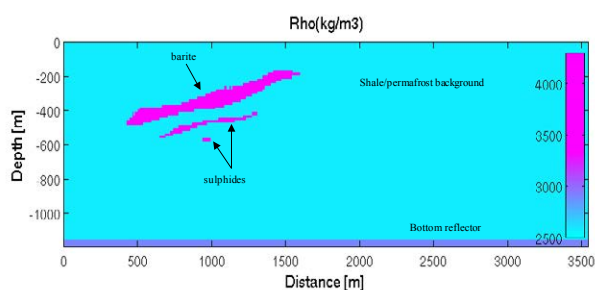


**Figure 1:** A density display of the SEDEX rock physics model including two sulphide orebodies and barite in a shale background (Quigley et al., 2012).

close to 70 sulphide values, and more than 1300 barite values. Figure 2 shows a portion of a logged borehole that intersected both barite and sulphide. A median filter was applied to smooth velocity and density data for this borehole. S-wave velocities (Vs) were not measured and therefore they were calculated using measured Vp and
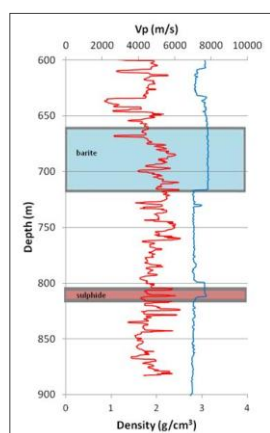


**Figure 2:** A Logged borehole displaying filtered p-wave velocity (left) and density (right) versus depth for depths 600-900m. Areas were sulphide and barite are intersected are highlighted.

Poisson's ratio values (υ) that are consistent with geophysical literature. The following formula was used to calculate Vs for our model lithologies (Brocher, 2005).

$$Vs = Vp * \sqrt{((2v - 1)/2(v - 1))}$$

Figure 3 shows a summary of the p-wave velocities obtained from all logged boreholes for each lithology in our model. An average value for all petrophyics data, Vp, Vs and ρ, was calculated for each litholgy. The seismic modeling experiment consisted of nine shot points spaced at 400m increments along the surface of our model from x=100m to x=3300m. The receiver spread included 725 geophones spaced 4m apart and positioned along the surface from x=100 to x=3000m. The choice of receiver spacing resulted from previous tests that were conducted to determine the maximum allowable spacing such that spatial aliasing of the surface wave was avoided. Using a seismic source (Ricker wavelet) centered at a frequency of 75Hz, a maximum receiver spacing of 4-5m was needed to avoid spatial aliasing of surface waves.
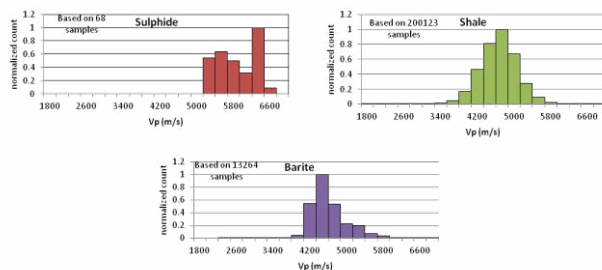


**Figure 3**: Histograms showing the distribution of logged borehole data for shale, barite and sulphides

The synthetic seismic data from our SEDEX model is characterized by high amplitude surface wave energy and a weak high velocity direct wave (Fig. 4). One of the main challenges when processing the shallow reflection seismic data is attenuating source generated noise (direct and surface waves) in close proximity with the reflections from the sulphide target. Using an f-k filter is an effective way to attenuate the surface and direct waves, however this requires a dense receiver spacing. As an alternative to using an f-k filter using an optimum
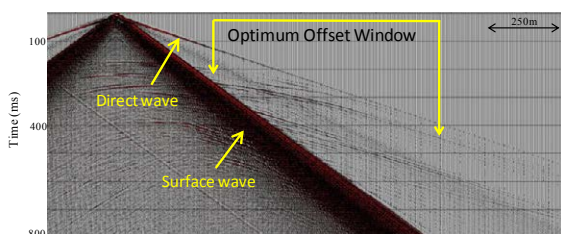


**Figure 4:** A synthetic seismogram showing an offset window between 600-2000m where the reflected energy from our target sulphide at 500m depth, is unaffected by source generated noise.

offset window (Hunter et al., 1984), such that source generated noise is avoided by keeping only data the falls within an optimum offset window and muting the source

generated noise. The optimum offset window is defined as the region where the target reflections are unaffected by source generated noise (Fig. 4). The optimum offset window is dependent on the target depth and rock velocities. For the sulphide orebody at ~500m in our model, an optimum offset window of 600-2000m seemed to be the region where the reflections from the target are isolated from the surface and direct waves (Fig. 4). Figure 5a shows a migrated section of the synthetic seismic data, for all offsets, for the SEDEX model (Fig. 1). Processing the seismic data involved using an f-k filter to attenuate surface and direct waves. The data was stacked using a constant velocity of 4600m/s which is close to the background velocity. A post-stack f-k migration was the final processing step.
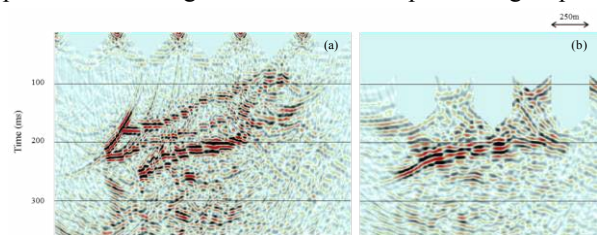


**Figure 5:** (a) A Migrated section of seismic data from our SEDEX model (Figure 1) for all offsets and (b) a migrated section with offsets 600-2000m, which targeted the orebody at 400m depth.

Figure 5b is the same migrated section as in Figure 5a, however windowed to keep only the data for offsets 600-2000m. Using only these offsets, an image of the sulphide orebody at ~500m depth, was obtained. This example shows that, if need be, an optimum offset window approach may be applicable to recover an image of a given orebody. The optimum offset processing procedure is an alternative to conventional processing and may prove useful when f-k filtering is not conducive to attenuate surface wave energy.

## 2 Imaging a Small Very Shallow Carbonate-Hosted Zn-Pb Deposit

The second rock physics model consisted of a shallow (175m) Zn-Pb lens shaped orebody within a 75m thick carbonate layer in a background limestone (Fig. 6). This is a typical geological setting for an MVT or Irish-type deposit. The acoustic impedance of the sulphide body is higher than that of the carbonate layer however these values are not represented in the final migrated section when using conventional processing procedures. Figure 7 shows a very weak (low amplitude) reflection for the orebody. The data shows that using conventional processing may not be effective in imaging a small orebody with these dimensions (40x100m) in this geological setting. The seismic source used for the modeling study was a Ricker wavelet with a center

frequency of 75Hz. The surface source array consisted of nineteen shot points that were spaced 100m apart from x=100 to x=1900m. The receiver spread consisted of 450 receivers spaced 4m apart on the surface from x=100 to x=1900.
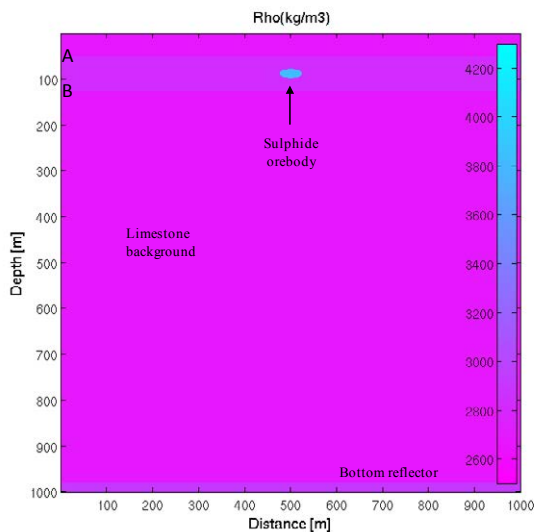


**Figure 6:** A density display of the carbonate-hosted Zn-Pb deposit model. A and B mark the top and bottom of the carbonate layer respectively.

The weak sulphide reflection that is apparent in our synthetic data migration (Fig. 7) may be a best case scenario. Future work involves investigation of alternative data analysis procedures for indentifying such an orebody. If any trends are present, such as an increase in Vs/Vp ratios in the vicinity of the orebody, then it may be useful to look at multicomponent seismograms to locate the orebody.
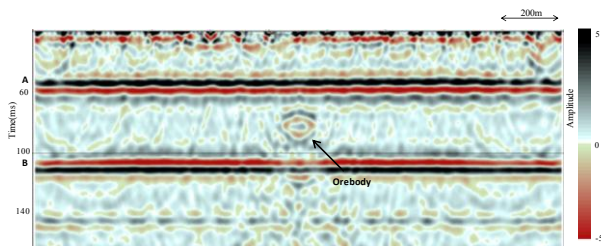


**Figure 7:** Migration of the carbonate-hosted Zn-Pb deposit model. Reflections from the top and bottom of the carbonate layer are labelled A and B respectively

## 3 Conclusions

Seismic imaging of shallow sediment-hosted massive sulphides seems to be promising, for larger deposits, such as the SEDEX model that has a lateral dimension of 400m, provided source generated noise can be attenuated or avoided. However, conventional processing sequences that are typically used in oil and gas exploration to image laterally continuous, deeper

interfaces need to be modified for small shallow targets such as the orebody in the carbonate hosted model. The high density driven impedance of Zn-Pb sulphides makes reflection seismic images a promising exploration method. The main issue for high resolution reflection seismic surveys involve the interference of source generated noise with the shallow reflection events. F-k filtering of the noise can be useful and has implications for seismic survey design requiring a maximum trace spacing of 4-5m. For the SEDEX model the seismic data showed that using an optimum offset window which avoids the source generated noise was also successful in recovering an image of the target. Additionally, to image targets that are smaller, such as the carbonate-hosted deposit, using a source frequency center at 75Hz was required to resolve the 40m thick orebody. The seismograms from this model are characterized by weak, low amplitude orebody reflections despite the high acoustic impedance contrast between the ore and the carbonates. Attenuating the source generated noise is imperative to recovering an image of such small targets. In addition if the target is not detected using conventional processing techniques, alternative methods should be considered. The next stage of this research involves, for the carbonate-hosted small shallow target, comparing the horizontal and vertical component seismogram responses to see if this is a viable way to detect the orebody.

## Acknowledgements

## References

Bohlen, T. (2002). "Parallel 3-D viscoelastic finite difference seismic modelling", Computers and Geosciences 28, pp.887-899.

Brocher, T.M (2005). "Empirical Relations Between Elastic Wavespeeds and Densities in the Earths Crust", Bulletin of the Seismological Society of America 95(6), pp.2081-2092

Hunter, J.A., Pullan, S.E., Burns, R.A., Gagne, R.M., Good, R.L. (1984). "Shallow seismic reflection mapping of the overburden-bedrock interface with the engineering seismograph-Some simple techniques", Geophysics 49 (8), pp.1381-1385

Quigley, L., Bongajum, E., Milkereit, B. (2012)" A seismic survey in a permafrost environment: challenges in imaging sediment hosted massive sulphide Zn-Pb deposits" 82nd Annual International Meeting, SEG, Expanded Abstracts, pp.1-5.

Salisbury, M.H., Harvey, C.W., Matthews, L. (2003), " The Acoustic properties of Ores and Host Rocks in Hardrock Terranes" in W. Eaton, B. Milkereit, and M. H. Salisbury, eds., Hardrock seismic exploration: SEG, pp.9-19

# Mapping potential mineral targets using integration of geophysical and geochemical data at Nietverdiend mafic layered intrusion, the Bushveld Complex, South Africa

A. Tessema, P. Nyabeze & E. Chirenje
*Council for Geoscience, Geophysics Unit, Pretoria 0001, Private Bag X112, South Africa, Email: atessema@geoscience.org.za, pnyabeze@geoscience.org.za and echirenje@geoscience.org.za*

## Abstract

Integration of magnetic, radiometric and geochemical data covering the Nietverdiend layered mafic rocks, located in the North West Province of South Africa was carried out. The study area is situated in the far-westward extension of the Western Limb of the Bushveld Complex (BC). The main aim of integration of geophysical and geochemical data is to assess mineral potential targets, with special emphasis on exploration of magmatic sulphide deposits (Cu-Ni-PGEs), similar to those found elsewhere in the main Bushveld Complex. Data integration was carried out using principal component analysis.

The results show that the transition from high-to-moderate magnetic values coincides with similar patterns of Cr and Ni geochemical signatures (moderate-to-high), but low Cu content. The strong spatial correlation between moderate magnetic values and Cr and Ni content points to a certain stratigraphic horizon within the mafic and ultramafic rocks of the Nietverdiend layered intrusion. The moderately elevated Ni content in the lower part of the stratigraphic horizon may indicate possible basal-contact style of Ni-Cu-PGEs mineralization, where the occurrence of ultramafic Ni-Cu-PGEs hosting rock is in contact with the floor rocks, similar to that of the Platreef in the Northern Lobe of the BC. Detailed geochemical sampling and analysis combined with sulphur and oxygen isotopes studies may provide comprehensive understanding of the style of mineralization in the area.

**Keywords:** Soil sampling, Targets, Bushveld Complex, Mafic-ultramafic and Geochemical signature.

## 1. Introduction

The Bushveld Complex (BC) is a 2.05 Ga old (Walraven *et al.*, 1990) layered suite intruded into the sedimentary and volcanic rocks of the Transvaal Supergroup and is the largest layered igneous intrusion known on Earth. It is located in the northern part of the Kaapvaal craton of South Africa (Figure 1). The Complex covers an area of ~65 000 km$^2$ and has a thickness of 7-9 km. Rock types within the layered mafic intrusion range between dunite and pyroxenite to anorthosite and pure oxide layers (Eales & Cawthorn, 1996). The BC hosts 80% of the world's resources of PGEs as well as abundant reserves of chromium and vanadium (Walraven *et al.*, 1990). There are five limbs that constitute the BC, *viz.* the Eastern and Western Limbs, Northern Lobe, the far Western Limb and the fifth is the Bethal Limb which is the southward extension of the Eastern Limb (Figure 1). The Bethal Limb is concealed below younger sedimentary cover and its surface expression can only be viewed from gravity and magnetic map of the area.

The BC is well recognized for PGEs, chromium, vanadium, nickel, copper, cobalt among other economically useful mineral resources. Most of the mining operations are mainly focussed at the three ore bodies, *viz.* Merensky reef and UG2 chromitite seams that are located in the Western and Eastern limbs, while the Platreef is situated in the Northern lobe of the BC. However, detailed geological, geophysical and geochemical exploration may enable targeting similar ore bodies elsewhere within the Bushveld Complex. The present study is therefore aimed at mapping potential Ni-Cu-PGEs and associated mineral resources that are possibly hosted by the far-westward extension of the BC (Figure 1). It is peripheral to the main Bushveld Complex and underlain by floor rocks of the Transvaal Supergroup. In the present study, several data including high-resolution aeromagnetic, gamma-ray spectrometry, soil geochemical and geological data were used in order to assess the mineral resource potential.

The mafic-ultramafic layered rocks underlying the area of interest comprised of dunite, harzburgite, pyroxenite and bronzite (Figure 2), which are typical rock assemblages equated to the Lower Zone observed elsewhere in the BC. In order to investigate the Ni-Cu-PGEs resource potential of the area, high resolution airborne geophysical surveys were carried out at a flight line spacing of 200 m and terrain clearance of 120 m. This was supplemented by a grid-based soil geochemical sampling at a spacing of 1 km. The soil samples were analysed for Cu, Ni, Cr, Co, TiO$_2$, vanadium (V) and other elements. In addition, the geophysical data were processed and integrated with other dataset.
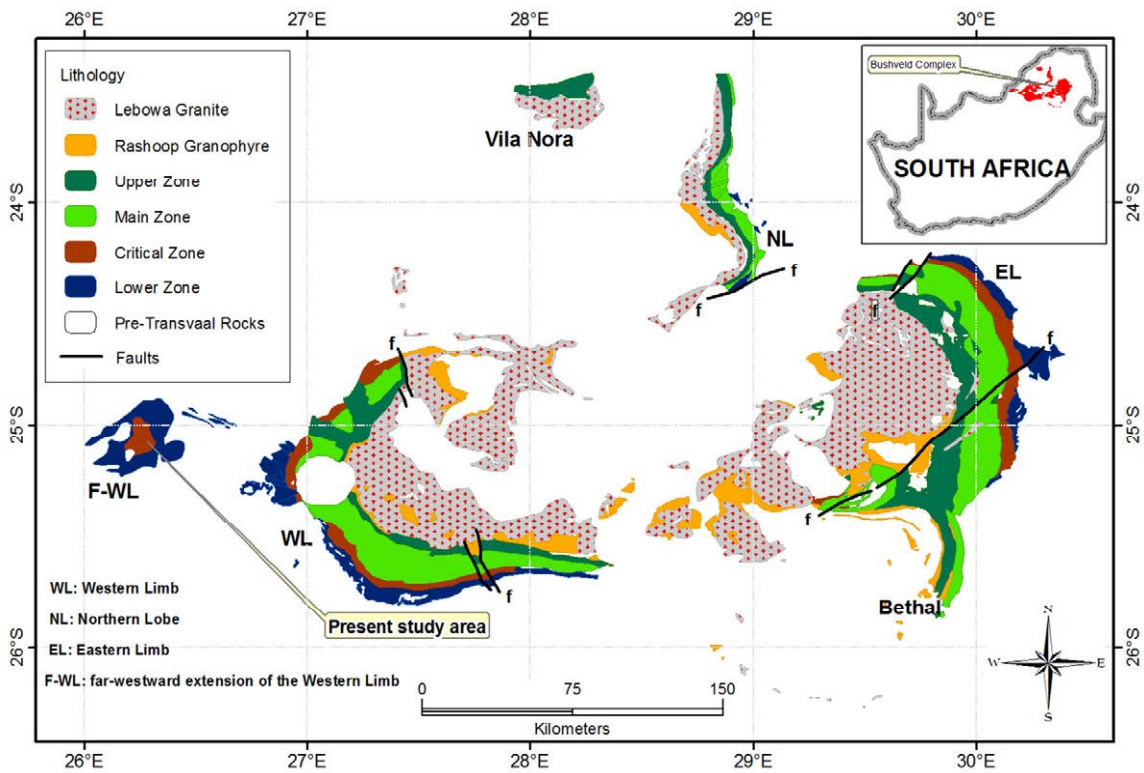
Figure 1: Schematic geological location map of the Bushveld Complex, South Africa showing the five limbs and the associated lithological domains.
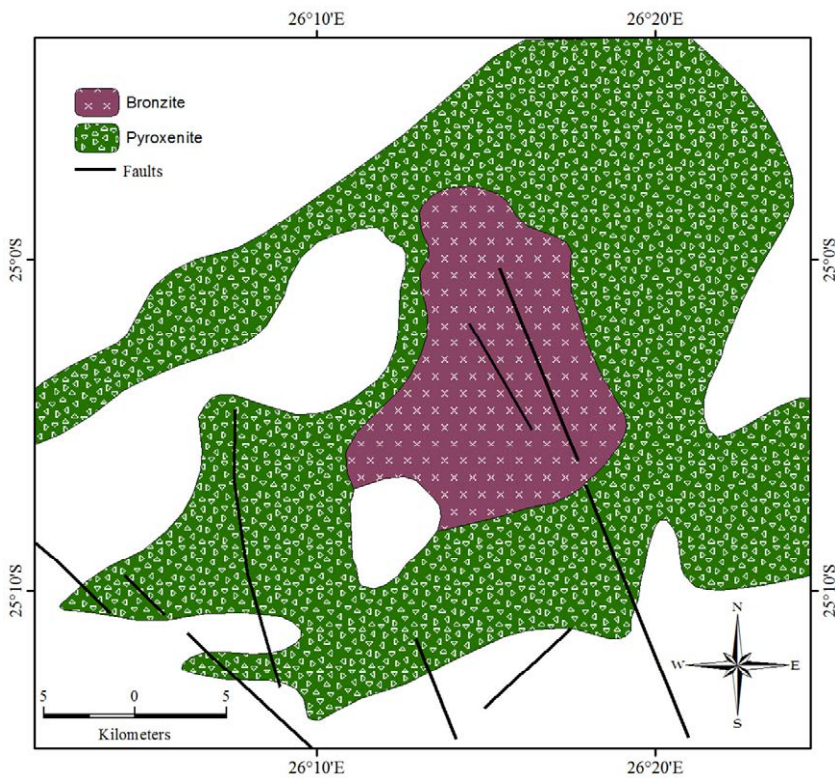


Figure 2: Simplified geological map of the study area.

## 1.2 Methodology and Results

Principal component analysis was applied to 7 thematic layers (Ni, Cu, Co, Cr, V, aeromagnetic and gamma-ray spectrometry). Based on this approach, five possible targets were identified (Figure 5). The targets are shown with a decreasing order of probability of occurrence of sulphide bearing bodies. Target 1 stretches over an area of ~200 sq.km and corresponds to high Cr, Ni and Co geochemical signatures, and moderately high magnetic values (Figures 3 and 4). This target lies between two E-W striking basic dykes and bounded in the east by N-S trending major fault zone (*conf*. Figures 3 and 5). Target 2 is located at the intersection between the NW-SE orientated faults and the E-W striking dykes, and corresponds to moderate Ni and Cu values. The point at which the fault displaces dykes can be interpreted as an important area of focus for exploration of Ni-Cu sulphide deposit. Targets 3 and 4 coincide with elevated Ni-Co values which may be potential target for PGEs and Ni-Co sulphide deposit. In addition, in Target 3, elevated Cu values correspond well with high Ni and Co, and can be attributed to sulphide mineralization within the mafic-ultramafic layered rocks of the far-westward extension of the Bushveld Complex.

## 3. Discussion of Results and Conclusion

The mafic rocks of the Bushveld Complex consist of significant amounts of Ni, Co, Cr, V and Cu, which are mainly associated with PGEs (Wilson, 1998 and Cawthorn, 1999). In the Nietverdiend area, potential targets for these minerals coincide with the transition from moderate-to-high Cr-Ni content that represent the geochemical signatures of the Lower Zone that are dominantly exposed in the area (Figures 2 and 4). The moderately elevated Ni content in the basal rocks of the layered intrusion may be interpreted as contact-type Ni, Cu, PGEs mineralization where the occurrence of ultramafic Ni-Cu-PGEs hosting rock is in contact with the floor rocks similar to that of the Platreef in the Northern Lobe of the BC.
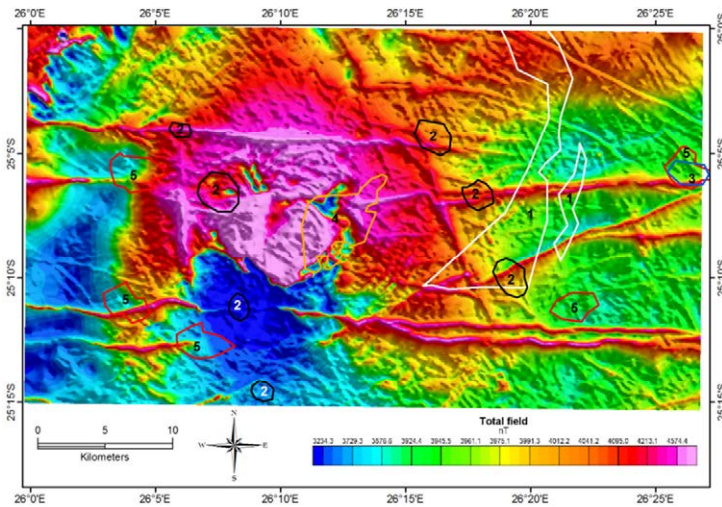


Figure 3: Total magnetic intensity map of the area.
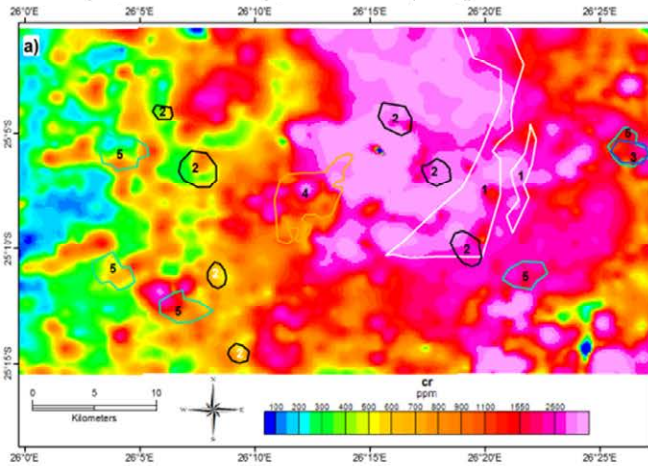


Figure 4a: Distribution of Cr in the study area. The five potential targets discussed in the text are shown using irregular polygons.
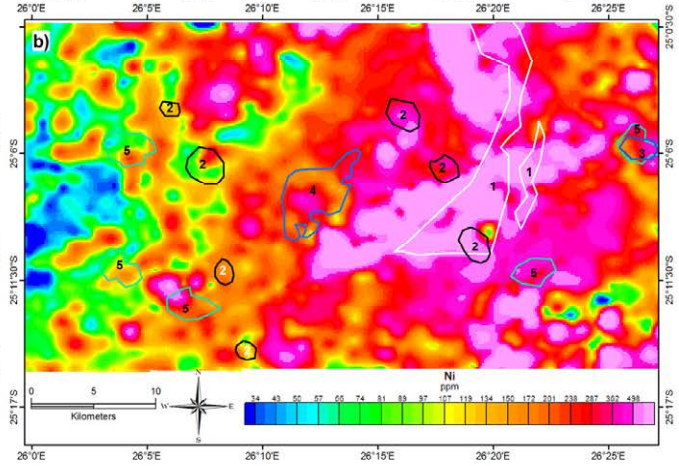
Figure 4b: Distribution of Ni in the study area.
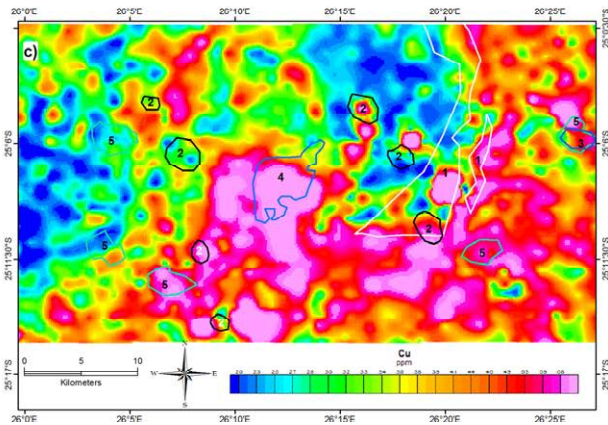
Figure 4c: Distribution of Cu in the study area.

The airborne magnetic data revealed the presence of three discrete phases of dyke swarms that intruded into the host rocks. The E-W striking dyke swarms (Figures 3 and 5) are the oldest, and were subjected to faulting and the zone of fracture concentration may be associated with Ni-Cu sulphide mineralization, which is similar to the Vlakfontein faulted dykes that are potential targets for Ni-Cu sulphide deposits. The displacement of the dykes during faulting possibly accompanied by orthomagmatic Ni-Cu-PGEs deposit.

In summary, the present data integration approach is very effective in delineating potential targets that may host Ni-Cu-PGEs. However, it is suggested that more detailed geochemical sampling and analysis through the stratigraphic sequence of the mafic rocks can be recommended to provide a comprehensive understanding of the style of mineralization. In addition, sulphur, oxygen and strontium isotopes studies may provide additional information about the processes of sulphide mineralization in the area.

## Acknowledgement

Figure 5: Map showing potential targets derived from integration of geophysical and geochemical data.

## References

Cawthorn, RG (1999), The platinum platinum and palladium resources of the Bushveld Complex. South African Journal of Science, 95:481-489.

Eales , H.V. & Cawthorn, R.G. (1996). The Bushveld Complex. In Cawthorn, R.G. (Editor.) Layered Intrusions. *Elsevier Science*, 181-229
.

Walraven, F., Armstrong, R.A. & Kruger, F.J. (1990). A chronostratigraphic framework for the north-central Kaapvaal craton, the Bushveld Complex and Vredefort Structure, Tectonophysics, 171:23-48

Wilson, MGDC (1998). A brief overview of the economic geology of South Africa (MGDC Wilson and CR Anaeuser, eds): Hand Book, 16:1-4.

S 2.3:
# New analytical methods and applications in mineral deposit studies

Convenors:
Hugh O´Brien & Yann Lahaye

# Integration of laser ablation-ICPMS with automated SEM for in situ geochronology and geochemistry of mineral deposits

**Paul Sylvester & Kate Souders**
*Department of Earth Sciences, Memorial University, St. John's NL A1B 3X5 Canada*

**Abstract.** Laser ablation – ICPMS analyses of age, elemental, and isotopic composition of minerals in ore deposits is enhanced by targeting grains for analysis in the context of quantitative mineralogical data provided by an automated scanning electron microscope (SEM) such as a Mineral Liberation Analyser (MLA). Magmatic and metamorphic domains in zircon and other accessory minerals can be targeted for in situ analysis of U-Pb age in a more systematic and rigorous fashion. Appropriate locations for in situ analysis of chemical compositions of minerals intergrown in complex textures can be identified more readily. Automated searches for rare minerals of interest such as precious metal minerals in massive sulphides and heavy minerals (tourmaline, rutile, etc.) in sediments can reveal grains sufficiently large for LA-ICPMS analysis, including in situ isotope measurements using multi-collector devices.

**Keywords.** Laser Ablation ICPMS, Automated SEM, Mineral Liberation Analyser, In Situ Analysis, Isotopes

## 1 Background

Geochronology and trace element/isotope geochemistry of mineral deposits are increasingly studied using in situ analyses of minerals rather than bulk analyses of whole rocks. Mineral analyses linked to textural relationships may preserve a detailed record of ore-forming events or processes that are homogenized or obscured at the whole rock scale. Studies of complexly intergrown minerals in ore systems are often critical to understanding the origins and pathways of metal-bearing magmas and fluids, and alteration histories.

Laser ablation – inductively coupled plasma mass spectrometry (LA-ICPMS) has become the most widely used method for in situ analysis of mineral age and trace element/isotopic composition, largely because of its versatility and low cost compared to competing in situ technologies (Sylvester 2008). A limitation to effective use of the technique however is the selection of mineral grains for analysis that exhibit both representative and unusual textures relevant to particular investigations. Mineral characterization by automated scanning electron microscopy (SEM) provides exactly the information required. Several automated SEM instruments have been developed over the past several decades including the Mineral Liberation Analyser (MLA), which has become the most popular system available commercially (Fandrich et al. 2007).

Here we show how in situ mineral analyses by LA-ICPMS can be integrated with the MLA to provide robust investigations of the age and geochemistry of mineral deposits, including high precision isotope measurements.

## 2 Instrumentation and Methods

### 2.1 Laser Ablation-ICPMS

LA-ICPMS (Fig. 1) was invented in the 1980s and introduced into geoscience laboratories in the 1990s. Ablated aerosols from a mineral surface are carried from a sample cell in a stream of carrier gas (typically helium) via a transfer tube to the ICP source of a mass spectrometer for atomization and ionization and detection of gas blank and laser ablation signal intensities. Quantification is commonly performed by external calibration against standard reference materials. For isotope ratio measurements, mass discrimination corrections are typically made by normalization of the measured ratio to an invariant isotope ratio of the same element (see chapters in Sylvester 2008 for a review).
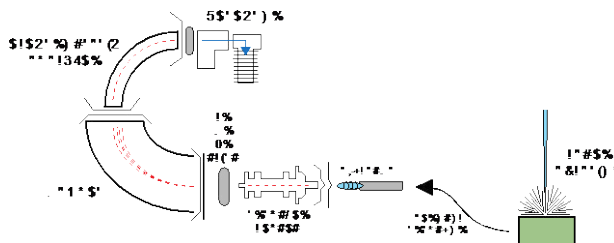


**Figure 1.** Schematic diagram of a laser ablation – sector field ICPMS instrument equipped with a single detector (Thermo Scientific ELEMENT XR).

Initial applications of LA-ICPMS in the geosciences were concerned largely with in situ elemental analyses of minerals (Jackson et al. 1992) including precious metal geochemistry (Sylvester and Eggins 1997). Over the past decade, the technique has been increasingly used for in situ U-Pb accessory mineral geochronology and high-precision isotopic determinations (see Košler 2012 for a review), the latter requiring simultaneous measurements of the ablation aerosol using multiple collector arrays.

Recent trends in the technique include the use of femtosecond laser ablation to reduce elemental fractionation and the need for matrix-matched calibration standards for some applications (Poitrasson et al. 2003); elemental and isotopic mapping of minerals and other materials by digital stitching of parallel ablation transects (Woodhead et al. 2007); and simultaneous analysis of zircon for U-Pb age, trace elements and/or Hf isotope composition by splitting the ablation aerosol

from one laser ablation system between two ICP instruments (Yuan et al. 2008).

## 2.2 Automated mineralogy (MLA)

The MLA instrument was developed at the Julius Kruttschnitt Mineral Research Centre (Australia) in the mid-1990s (Gu 2003), became available commercially in 2000, and is now marketed by FEI Company. The SEM of the MLA is equipped with two energy dispersive X-ray (EDX) spectrometers, and computer software that automates microscope operation and data acquisition for automated mineralogy. Various quantitative data sets including modal mineralogy, porosity, grain size and shape, mineral associations and digital textural maps are collected on polished surfaces of thin or thick (slab) sections or epoxy mounts of grain separates (Sylvester 2012).

MLA measurements are based on backscattered electron (BSE) image analysis for determining grain boundaries and locations for x-ray spectral acquisition, and classification of the characteristic X-ray spectra of mineral species by comparison to a library of reference spectra (Fig. 2). An EDX analysis is either made at a single point in the center of the grains in the segmented image, or the entire particle is mapped in detail using a grid of EDX analyses in order to define the minerals present and their proportions.
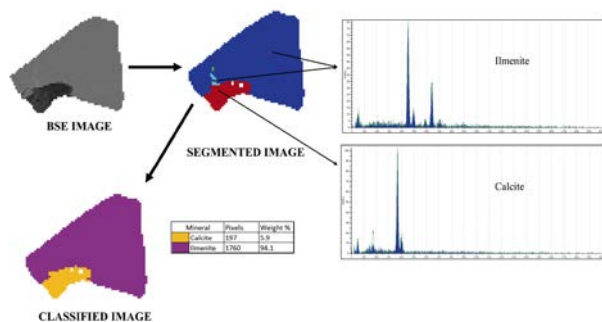


**Figure 2.** Schematic illustration of MLA measurement and discrimination of the distribution of ilmenite and calcite grains in a composite particle.

## 2.3 Integration of techniques

The MLA software produces false colour mineral maps of polished sections or grain mounts (Fig. 3). Coordinates of particular grains of interest in the section or mount can be translated easily from the MLA stage to the LA-ICPMS stage using reference images and a spreadsheet-based calculation. The precision of stepper motors on the stages of modern LA systems is sufficient for relocation of specific grains of interest to within tens of microns of the MLA coordinates. This allows the user to enter in a series of points for LA-ICPMS analysis in short order and merely adjust them for errors in the stage translation, before carrying out manual or automated LA-ICPMS runs. Rare grains can be located readily using this approach. Grains exhibiting complex intergrowth or replacement textures that preserve critical information about the ages or compositions of ore-forming events can be targeted for LA-ICPMS analyses

effectively. For instance, elemental changes associated with supergene alteration of magnetite and hematite in iron ore can be determined by targeted LA-ICPMS analyses using the MLA mineral map shown in Figure 3.
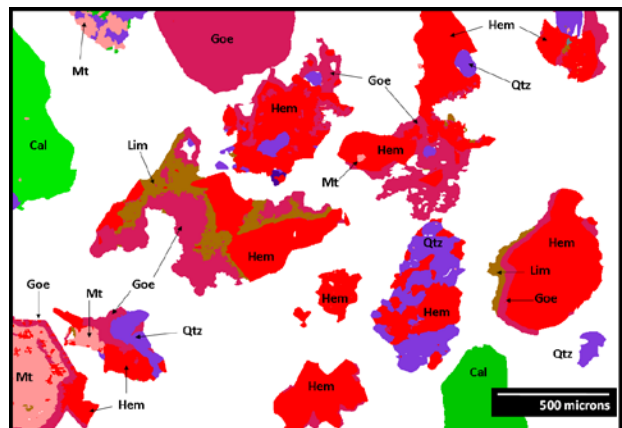


**Figure 3.** False colour MLA map of part of a grain mount, showing complex textural relationships between minerals in an iron ore sample. Mt=magnetite, Hem=hematite, Goe=goethite, Lim=limonite, Qtz=quartz, and Cal=calcite.

Grains of a particular mineral can be compared using an MLA "line-up", which arranges them in order of decreasing size (Fig. 4). This display is commonly used for U-Pb geochronology where grains of zircon, baddeleyite, monazite, rutile or apatite are of interest. The sizes, shapes and inclusion population of the grains may be compared so that the measured U-Pb ages maybe understood in petrographic context. For instance, LA-ICPMS U-Pb ages for magmatic grains forming euhedral, bipyramidal zircon crystals may be older than the ages measured from more irregular-shaped, inclusion-rich, hydrothermal zircon grains.
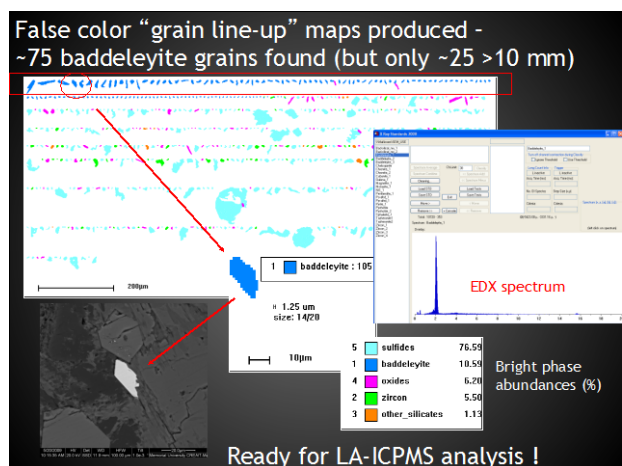


**Figure 4.** Line-up of baddeleyite grains identified by MLA in a polished thin section of a mafic dyke. Grains are arranged in order of decreasing size, with baddeleyite grains in the successive rows being tiny attachments to larger grains of other minerals. The MLA software allows the user to display a large image of any grain in the line-up, providing a detailed map of its mineral components, as is shown for a monomineralic baddeleyite grain in the centre of the figure. The corresponding BSE image of the highlighted baddeleyite is shown at the lower left. The EDX spectrum of baddeleyite used by the MLA to identify the mineral is shown at the right.

## 3 Applications

A variety of in situ applications are now routinely carried out using the combination of LA-ICPMS and MLA techniques. There include (1) U-Pb accessory mineral geochronology; (2) Lu-Hf isotope geochemistry of zircon and baddeleyite; (3) Common Pb isotope geochemistry of feldspar, tourmaline and sulphides; (4) Geochemistry of sulphides and precious metal minerals; and (5) Trace element geochemistry of magnetite and hematite.

One of the more exciting applications involves in situ Pb isotope analyses in uranium-, thorium- and lead-poor minerals such as feldspar, tourmaline (Fig. 5) and sulphides using multiple ion counting devices (Souders and Sylvester 2010). In situ lead isotope analyses of these minerals in ore deposits by laser ablation – multicollector (MC) – ICPMS can provide information about the sources of magmas and fluids that formed and modified them.

Tourmaline, in particular, is currently of much interest, given that it occurs in hydrothermal systems in seafloor, sedimentary, magmatic, and metamorphic environments, and is highly resistant to later physical and chemical overprinting (Slack and Trumbull 2011). Where micro-textures of tourmaline are well documented by MLA techniques, in situ lead isotope analysis of grains or domains of the mineral can be used to reconstruct ore-forming events that might not be preserved in less resistant phases.
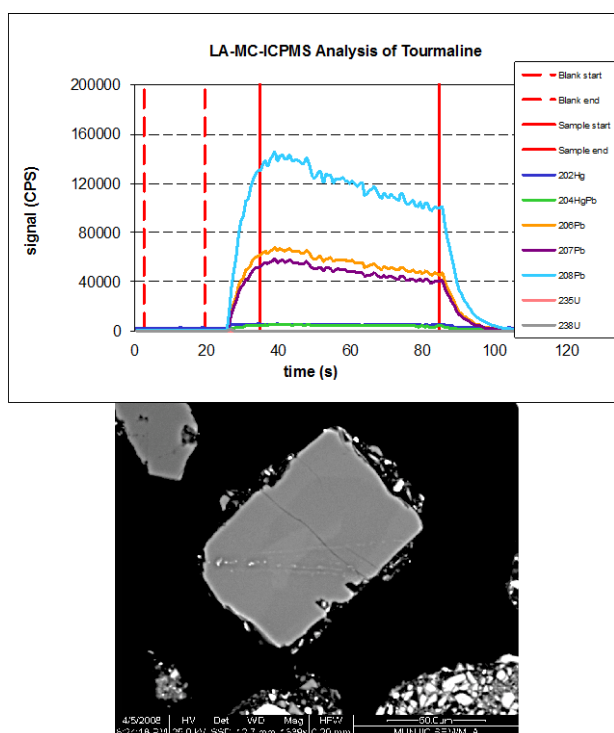


**Figure 5.** LA – multicollector (MC) – ICPMS analysis of tourmaline. (Bottom) Backscattered electron image of a tourmaline grain identified using MLA techniques. (Top) Time resolved LA-MC-ICPMS spectrum of Pb and U isotopes for a spot analysis of the grain. Hg isotopes contributed by the carrier gas must be measured in order to correct for the isobaric interference on Pb at $m/z = 204$. LA parameters: 5J/cm$^2$ energy density; 10Hz repetition rate; 59-um spot size.

## References

Fandrich R, Gu Y, Burrows D, Moeller K (2007) Modern SEM-based mineral liberation analysis. International Journal Mineral Processing 84:310–320

Gu Y (2003) Automated scanning electron microscopy based mineral liberation analysis. An introduction to JKMRC/FEI Mineral Liberation Analyser. Journal Minerals & Materials Characterization & Engineering 2:33–41

Jackson SE, Longerich HP, Dunning GR, Fryer BJ (1992) The application of laser-ablation microprobe-inductively coupled plasma-mass spectrometry LAM-ICP-MS to in-situ trace element determinations in minerals. Canadian Mineralogist 30:1049–1064

Košler J (2012) U-Pb geochronology and Hf isotope geochemistry of detrital zircon in sedimentary systems. In: Sylvester P (ed) Quantitative Mineralogy and Microanalysis of Sediments and Sedimentary Rocks, Mineralogical Association of Canada Short Course Series 42, pp. 185–202

Poitrasson F, Mao X, Mao SS, Freydier R, Russo RE (2003) Comparison of ultraviolet femtosecond and nanosecond laser ablation inductively coupled plasma mass spectrometry analysis in glass, monazite, and zircon. Analytical Chemistry 75:6184–6190

Slack JF, Trumbull RB (2011) Tourmaline as a recorder of ore-forming processes. ELEMENTS 7:321–326

Souders AK, Sylvester PJ (2010) Accuracy and precision of non-matrix-matched calibration for lead isotope ratio measurements of lead-poor minerals by LA-MC-ICPMS. Journal of Analytical Atomic Spectrometry 25:975–988

Sylvester PJ, Eggins SM (1997) Analysis of Re, Au, Pd, Pt and Rh in NIST glass certified reference materials and natural basalt glasses by laser ablation ICP-MS. Geostandards Newsletter 21:215–229

Sylvester PJ (ed.) (2008) Laser ablation ICP-MS in the Earth Sciences: Current practices and outstanding issues. Mineralogical Association of Canada Short Course 40, 348 pp

Sylvester PJ (2012) Use of the Mineral Liberation Analyser (MLA) for mineralogical studies of sediments and sedimentary rocks. In: Sylvester P (ed) Quantitative Mineralogy and Microanalysis of Sediments and Sedimentary Rocks, Mineralogical Association of Canada Short Course Series 42, pp. 1–16

Woodhead JD, Hellstrom J, Hergt JM, Greig A, Maas R (2007) Isotopic and elemental imaging of geological materials by laser ablation inductively coupled plasma-mass spectrometry. Geostandards and Geoanalytical Research 31:331–343

Yuan H, Gao S, Dai MN, Zong CL, Günther D, Fontaine GH, Liu XM, Diwu CR (2008), Simultaneous determinations of U-Pb age, Hf isotopes and trace element compositions of zircon by excimer laser-ablation quadrupole and multiple-collector ICP-MS. Chemical Geology 247:100–118

# In situ determination of trace elements in magmatic sulphides and oxides: implications for petrogenesis, exploration and exploitation

Sarah-Jane Barnes, Sarah A. S. Dare, Philippe Pagé & Dany Savard
*Sciences de la Terre, Université du Québec à Chicoutimi, Chicoutimi G7H 2B1, Canada.*

**Abstract.** A combination of technical and economic developments over the past 15 years have made sophisticated tools such as CT-scanners and LA-ICP-MS more readily available than previously. The information from these offer the opportunity to better understand the petrogenesis of ore deposits and hopefully in turn this will lead to better exploration for and exploitation of the deposits. In our laboratory (LabMaTer) we document the textures, carry out image analysis and whole rock analyses before lasering the minerals of interest. This allows us to perform a mass balance so as to fully understand which mineral controls each element. We have focussed our attention on magmatic ores, in particular; Platinum-group elements (PGE), Ni, Cu, Cr, Fe, V, Ti and P deposits. Results on the oxide deposits indicate that both chromite and magnetite could be used in provenance studies. In addition the details of the trace element patterns may be used to indicate the fertility of an area. Studies of the sulphide, arsenide and platinum-group minerals of Ni-PGE deposits can be used to unravel the complex history involved in the formation of PGE deposits.

**Keywords.** Laser ablation, chromite, magnetite, platinum-group elements, pyrrhotite, pentlandite, chalcopyrite, pyrite, arsenides.

## 1 Introduction.

There has been a small revolution in analytical techniques in the past 15 years and these are now being applied to exploration for, and exploitation of, ore deposits. There has been such a large increase in computer power and the ability to miniaturize that micro-XRF apparatus and computer tomography (CT) scanners have been reduced both in price and size sufficiently for them to become commonly available. This allows sophisticated image and textural studies to be widely applied, for example the modal amount of each mineral phase can be calculated (Fig. 1).
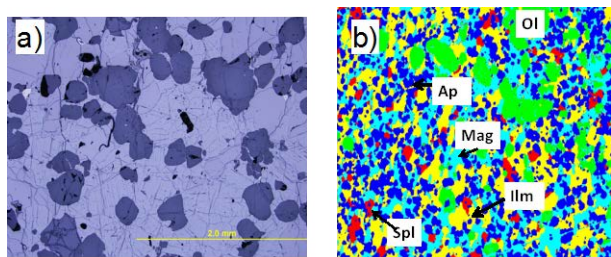


**Figure 1.** Comparison of photomicrograph of oxide-apatite ore (a) with micro-XRF map (b) for Mg (to map olivine), Ca (to map apatite), Fe (to map magnetite,) Ti (to map ilmenite) and Al (to map spinel) (Martin-Tanguay, 2012).

Furthermore ICP-MS and laser ablation equipment is now commonly available permitting the accurate determination of trace elements at the ppm to ppb level both in whole rock and in situ. The in situ determinations can even be used to map the distribution of the elements at the ppb level (Fig. 2).

At LabMaTer ([www.uqac.ca/labmater/index.html](www.uqac.ca/labmater/index.html)) we specialize in characterizing ore deposits, and in particular magmatic deposits. Our general approach involves first understanding and quantifying the textures we observe using petrography, micro-XRF maps, SEM images and CT scans. We carry out whole rock analysis and then determine the trace element content of the minerals using laser ablation ICP-MS (LA-ICP-MS). The results are combined to produce a mass balance for each element which allows us to determine which mineral controls which element. The textural studies help us to understand when the mineral formed. Combining the mass balance and textual studies allows us to better understand which process was the most important in controlling a particular element.
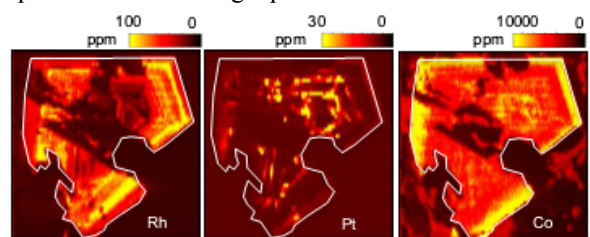


**Figure 2.** Maps of Rh, Pt and Co distribution in pyrite from the Aguablanca Ni deposit showing oscillatory zoning (Piña et al. accepted).

## 2 Oxides.

The trace element concentrations in chromite and Fe-oxides can be used in exploration to indicate the fertility of the area. For example studies of the Ru content in chromites from komatiites have been used to indicate whether a sulphide liquid has segregated from the magma (Locmelis et al. 2011; Méric et al., 2013). Dare et al. (this volume) have also found the depletion of Ti, Sc and Mn in magnetite indicating ilmenite has crystallized before magnetite, favouring the formation of a Ti deposit.

Oxides are resistant during weathering and metamorphism thus it has been suggested that their composition can be used in provenance studies (e.g. Dupuis and Beaudoin, 2011). Laser ablation analysis offers a wide choice of elements for these types of studies and we have found that chromites from different environments show distinct trace element patterns (Fig.

3; Pagé et al. 2011; Pagé et al. this volume).
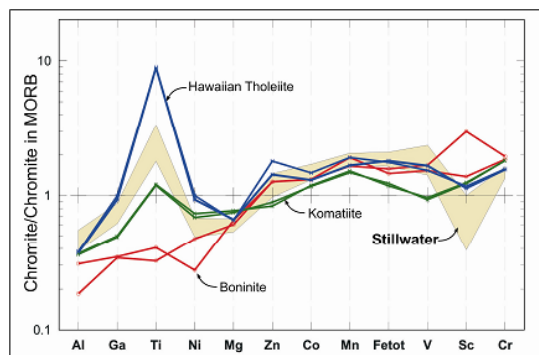


**Figure 3.** MORB normalized trace element patterns for chromites showing that chromites from different environments have different patterns (Pagé et al., 2011)

Work is in progress on Fe-oxides (Fig. 4), and it is clear that magnetites from different environments also have distinctive trace element patterns (Dare et al. this volume).
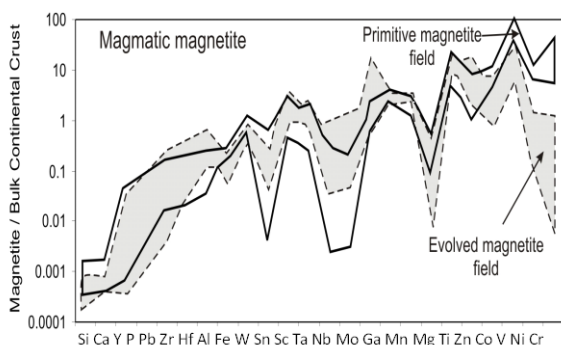


**Figure 4.** Trace element concentrations in magnetites from layered intrusions normalized to average crust and plotted in order of compatibility into magnetite. The patterns change as the magma evolves. The primitive pattern is more suitable for a V deposit and the evolved for a P deposit (Dare et al., this volume).

## 3 Platinum-Group Element Deposits

Magmatic nickel and platinum-group element (PGE) deposits form by collection of the metals from a magma into sulphide droplets. As evidence of this we can see natural examples of sulfide droplets both on the hand specimen and microscopic scale (Fig. 5). Using the laser to determine the metal contents in both the glass and sulphide MORB droplet the partition coefficients for most of the metals have been estimated (Fig. 6).

If the metals were collected by a sulphide liquid then they could be present in the sulphide minerals. In the case of rapidly cooled droplets, such as those found at the sub-volcanic Noril'sk nickel deposits, this seems to be true. A mass balance for Ni, Cu and PGE found that most of the PGE and Re are in pyrrhotite and pentlandite (Fig. 7). Interestingly most of the Pt is not in the sulphide minerals (Fig. 7). It is found in small Pt-minerals associated with the sulphide minerals.
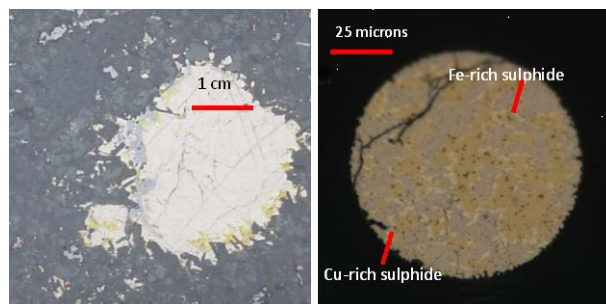


**Figure 5.** Sulphide droplets from; a) the Voisey's Bay nickel deposit, and b) MORB (Patten et al., 2012).
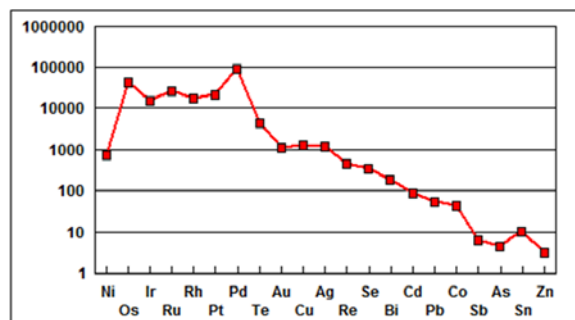


**Figure 6.** Empirical partition coefficients based on MORB glass and sulphide droplets (Patten et al., 2012) illustrating that the PGE and Te have partition coefficients at least an order of magnitude greater than Ni, Cu, Au and Ag. The partitioning decreases from Re through to Zn.
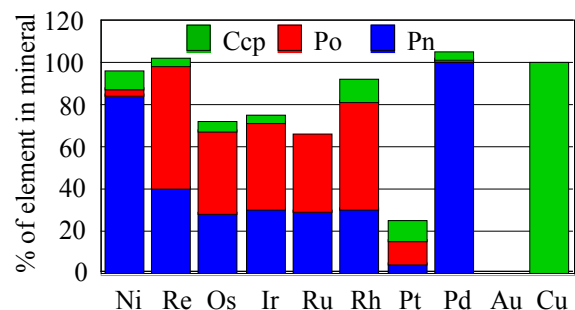


**Figure 7.** Mass balance for PGE, Ni and Cu in Noril'sk sulphide droplets (Barnes et al., 2006).

In contrast to the rapidly cooled Noril'sk deposit, in deposits from more slowly cooled intrusions (e.g. the JM reef, the Merensky reef, the Main sulphide reef, Lac des Iles, Sudbury and Aguablanca) only 30 to 70 % of the Os, Ir, Ru, Rh and Pd are present in pyrrhotite and pentlandite (Fig. 8). (Barnes et al., 2008; Dare et al., 2011; Djon and Barnes, 2012; Godel et al, 2007; Pina et al., 2012). Furthermore even less of the Pt is present in sulphides than at Noril'sk. Both the Pt and other PGE occur as platinum-group minerals (PGM) associated with the sulphides as illustrated in a CT scan of the Merensky Reef (Fig. 9). These minerals could have formed by a number of processes: a) exsolution from the sulphide minerals, b) crystallization from the sulphide liquid; c) crystallization from a semi-metal liquid.
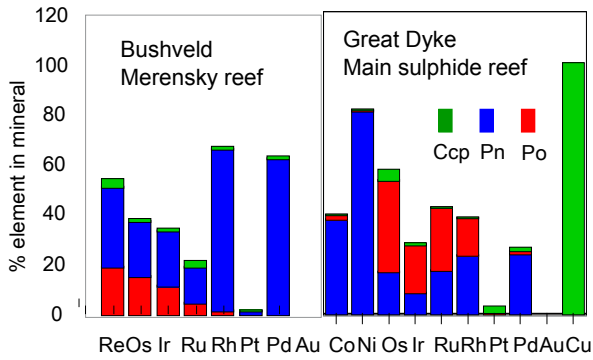
**Figure 8.** Examples of mass balances for PGE from the Merensky reef of the Bushveld Complex and the Main sulphide reef of the Great Dyke (Barnes et al., 2008).
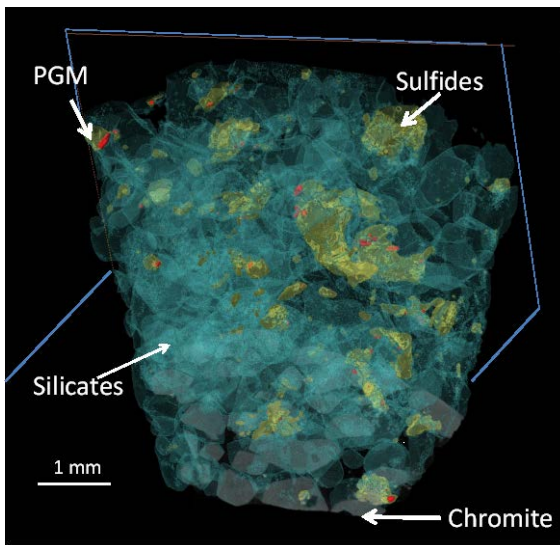


**Figure 9.** CT scan of the Merensky Reef showing Pt minerals in red, sulphide minerals in yellow and silicate minerals in blue (Godel et al., 2010). Note the association of Pt-minerals with the sulphides.

At high temperature the sulphide minerals present are (FeNi)-sulphide monosulphide solid solution (MSS) and (FeCu)-sulphide intermediate solid solution (ISS). As they cool MSS exsolves forming pyrrhotite, pentlandite, +/-pyrite and ISS exsolves to form chalcopyrite +/- cubanite. During exsolution PGE and semi-metals that originally fitted into the MSS or ISS structure may be excluded from the lower temperature sulphide and a PGM forms (Fig. 10).

However not all PGM form by exsolution. Some appear to crystallize from the sulphide liquid. When a sulphide liquid crystallizes; Re, Os, Ir, Ru and Rh partition into the MSS and are present in its exsolution products (pyrrhotite and pentlandite). The remaining liquid becomes Cu-rich and eventually crystallizes ISS. Platinum and Pd and many semi-metals tend to concentrate in this Cu-rich liquid. Some sulphide droplets show this zonation (Fig. 11) as do many magmatic Ni-Cu ore bodies (Fig. 11).
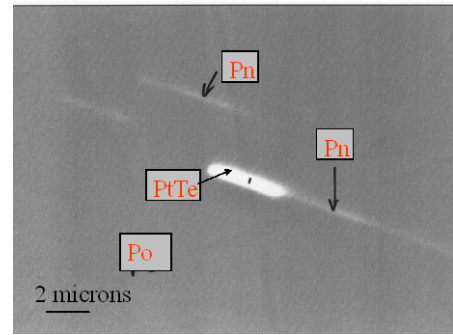


**Figure 10.** SEM photo of PGM formed along pentlandite exsolutions in pyrrhotite. Main sulphide reef of the Great Dyke (Barnes et al., 2008).
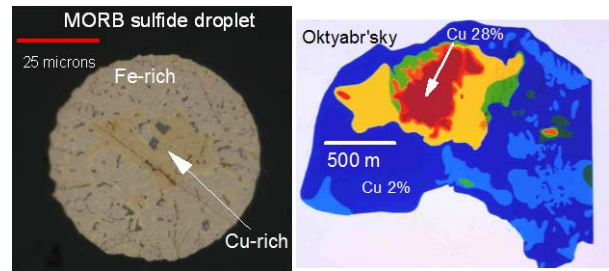


**Figure 11.** Compositional zoning resulting from fractional crystallization of a sulphide liquid can be observed on the micron scale in MORB droplets (Patten et al., 2012) to the km scale in ore bodies e.g. Oktyabr'sky (modified after Togashin, 1994)

The main sulphide found in the Cu-rich ores is chalcopyrite and this does not contain PGE (e.g. Figs. 6 and 9). The Pd and Pt concentrate in last dregs of liquid and crystallize as semi-metal rich PGM between the sulphide minerals (Fig. 12).
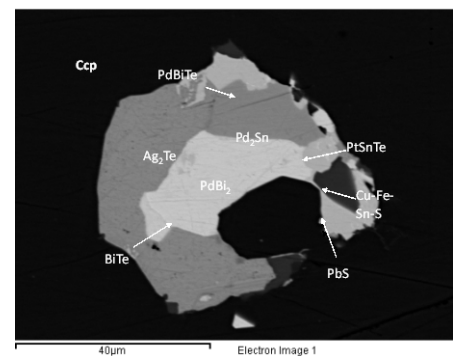


**Figure 12.** Composite PGM in Cu-rich ores from the McCreedy East Mine, Sudbury. It believed to represent the product of extreme fractionation of a sulphide liquid (Dare et al., accepted).

These composite PGM may crystallize at fairly low temperatures (400-600 °C) and thus (provided there is some permeability) they could be mobile either during late cooling of an intrusion or during metamorphism. The mobile semi-metal-PGE liquid could explain ore deposits such as the High Grade Zone of Lac des Iles (Fig. 13) where the mineralization takes the form of Pd bismuth-tellurides, antinomides and arsenides (Barnes and Gomwe, 2011; Djon and Barnes, 2012),
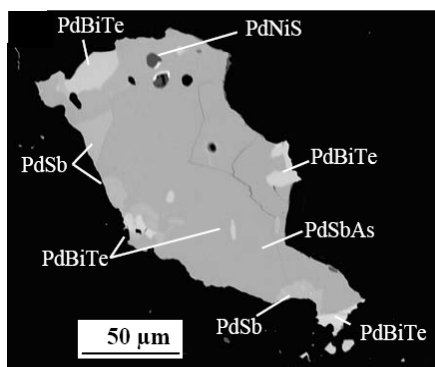
**Figure 13.** SEM photo of composite PGM in silicates from the High Grade Zone of the Lac des Iles Pd-deposit (Barnes and Gomwe, 2011). This type of PGM may represent a PGE rich semi-metal liquid that has migrated away from the sulphides.

Finally many PGE appear to have a strong affinity with arsenic (Fig. 14). If sufficient As is present it is possible that an arsenide liquid may segregate from the sulphide liquid, or that arsenide minerals may crystallize from the sulphide liquid. The arsenide minerals are generally enriched in PGE relative to the sulphide minerals (Dare et al., 2010; Godel et al., 2012; Piña et al., accepted).
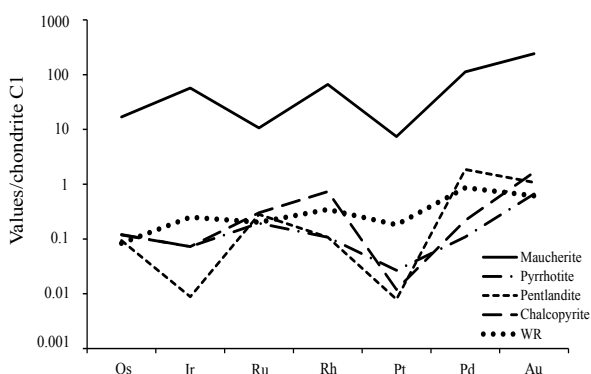


**Figure 14.** PGE concentrations in sulphide and arsenide minerals of Beni Bousera showing that Ni-Co arsenide (maucherite) preferentially concentrates the PGE and Au (Piña et al., accepted).

## Acknowledgements

## References

Barnes S-J, Gomwe TS (2011) Pd deposits of the Lac des Iles Complex, Northwestern Ontairo. In: Li. C, Ripley EM (eds) Reviews in Economic Geology, vol 17. Society of Economic Geologists,pp. 351-370

Barnes S-J, Cox RA, Zientek ML (2006) Platinum-group element, Gold, Silver and Base Metal distribution in compositionally zoned sulfide droplets from the Medvezky Creek Mine, Noril'sk, Russia. Contributions to Mineralogy and Petrology. 152:187-200

Barnes S-J, Prichard HM, Cox RA, Fisher PC, Godel B (2008) The location of the chalcophile and siderophile elements in platinum-group element ore deposits (a textural, microbeam and whole rock geochemical study): Implications for the formation of the deposits. Chemical Geology 248:295-317

Dare SAS, Barnes S-J, Prichard HM, Fisher PC (2010) The timing and formation of platinum-group minerals from the Creighton Ni-Cu-Platinum-group element sulfide deposit, Sudbury, Canada: Early crystallization of PGE-Rich sulfarsenides. Economic Geology 105:1071-1096

Dare SAS, Barnes S-J, Prichard HM, Fisher PC (2011) Chalcophile and platinum-group element concentrations in sulfide minerals from the McCreedy East deposit, Sudbury, Canada, and the origin of PGE in pyrite. Mineralium Deposita 46:381-407

Dare SAS, Barnes S-J, Prichard HM, Fisher PC (accepted) Mineralogy and geochemistry of Cu-rich Ores from the McCreedy East Ni-Cu-PGE deposit (Sudbury, Canada): Implications for the behaviour of PGE and chalcophile elements at the end of crystallization of a sulfide liquid. Economic Geology

Djon MLN, Barnes SJ (2012) Changes in sulfides and platinum-group minerals with the degree of alteration in the Roby, Twilight, and High Grade Zones of the Lac des Iles Complex, Ontario, Canada. Mineralium Deposita 47:1-22

Dupuis C, Beaudoin G (2011) Discriminant diagrams for iron oxide trace element fingerprinting of mineral deposit types. Canada. Mineralium Deposita 46:319-335

Godel B, Barnes S-J, Maier WD (2007) Platinum-group elements in sulphide minerals, platinum-group minerals, and the whole rocks of the Merensky Reef (Bushveld Complex, South Africa): Implication for the Formation of the Reef. Journal of Petrology 48:1569-1604

Godel B, Barnes SJ, Barnes S-J., Maier WD (2010) Platinum ore in three dimensions: Insights from high-resolution X-ray computed tomography. Geology 38:1127-1130

Godel B, González-Álvarez I, Barnes SJ, Parker P, Day J (2012) Sulfides and Sulfarsenides from the Rosie Nickel Prospect, Duketon Greenstone Belt, Western Australia. Economic Geology 107:275-294

Locmelis M, Pearson NJ, Barnes SJ, Fiorentini ML (2011) Ruthenium in komatiitic chromite. Geochimica et Cosmochimica Acta 75:3645-3661

Martin-Tanguay, B. (2012) Pétrographie et caractérisation des oxydes de Fe-Ti a Saint-Charles de Bourget (Québec). Projet fin d études. Université du Québec a Chicoutimi, 58p

Méric' J, Pagé P, Barnes S-J, Houlé M.G. (2013) Trace element and PGE content of chromites from komatiites in the Alexo area (Abitibi, Ontario) and implication for exploration : a LA-ICP-MS study. GAC-MAC Winnipeg. Abstract vol

Page P, Barnes SJ, Zientek ML (2011) Formation and evolution of the chromitites of the Stillwater Complex: a trace element study. In: Barra F, Reich M, Campos E, Tornos F (eds) Let's Talk Ore Deposits, 11'th SGA, Antofagasta, pp 676-678

Patten C, Barnes S-J, Mathez EA (2012) Textural variations in MORB sulfide droplets due to differences in crystallization history. Canadian Mineralogist 50:675-692

Piña R, Gervilla F, Barnes S-J, Ortega L, Lunar R (2012) Distribution of platinum-group and chalcophile elements in the Aguablanca Ni–Cu sulfide deposit (SW Spain): Evidence from a LA-ICP-MS study. Chemical Geology 302:61-75

Piña R, Gervilla F, Barnes S-J, Ortega L, Lunar R (accepted) Partition coefficients of platinum-group and chalcophile elements between arsenide and sulfide phases as determined in the Beni Bousera Cr-Ni mineralization (North Morocco) Economic Geology

Torgashin AS (1994) Geology of the massive and copper ores of the western part of the Oktyabr'sky deposit. In: Lightfoot PC, Naldrett AJ (eds) Proceedings of the Sudbury Noril'sk Symposium, vol 5. Ontario Geological Survey, Toronto, pp 231-241

# Spatial geochemistry to characterize heterogeneity and inimal analytical mass in reference materials

**L.P. Bédard, A. Néron**
*Sciences de la Terre, Université du Québec à Chicoutimi, Chicoutimi, QC, G7H 2B1 Canada. PBedard@uqac.ca*

**Abstract.** Reference materials are critical components of a good analytical procedure. Two tendencies have been observed in analysis of geological materials over the past years: 1) smaller analytical masses and 2) development of microbeam techniques. Both tendencies are more demanding on reference material quality. Regarding the decrease of the analytical mass, representativeness of sample has to be reconsidered especially in the case of mineral deposit studies (Au, PGE, REE, etc.) where large heterogeneities and nugget effects are prevalent. Microbeam techniques need reference materials that are homogenous at the μm scale. Assessing and characterizing small size heterogeneities should be addressed. Geochemical mapping of sulphide- or chromite-rich reference material has been used to develop spatial geochemistry. Simple mathematical tools have been developed to calculate uncertainty associated with analytical mass and quantify heterogeneity to compare samples to be used for laser ablation. Spatial geochemistry gives access to the size and proximity of heterogeneities and defines minimal analytical sample mass.

**Keywords:** Reference materials, sulphide, chromite, analysis, heterogeneity.

## 1  Small analytical mass

Recent models of analytical instruments such as ICP-MS and elemental carbon sulphur analyser nowadays use smaller sample mass for many reasons such as better detection limits, detector saturation, limitations by high levels of dissolved salts, etc. Many elements of interest to those who study mineral deposits have an erratic behaviour expressed as nugget effect. As sample mass becomes smaller the sampling uncertainty becomes more important (Gy 1998; Moore 1979; Pitard 1993). Trace elements that are also major constituents of some mineral phases such as rare earth elements (REE) in bastnasite and monazite, Au in native gold, and platinum group elements (PGE) in platinum group minerals are those which pose the most difficulties. The inclusion or exclusion of a grain of mineral rich in the trace element of interest in the analytical sub-sample creates large concentration differences between analysed sub-samples. For example, Savard et al. (2010) in their study of PGE reference materials (RM), found that techniques using small sample mass, such as isotope dilution, created larger differences between samples than techniques using large sample mass such as NiS fire assay. Typically the minimal representative mass is determined using smaller and smaller analytical mass until the uncertainties become larger than a set limit. Can we do better?

Microbeam techniques such as laser ablation inductively coupled mass spectrometry (LA-ICP-MS) determine concentration on a minute volume of sample, typically with a beam diameter of $20 - 80$ μm and a depth of a few hundreds of μm or less, which represent sample mass at the ng level. Although LA-ICP-MS uses very small analytical masses, finding reference materials that are homogeneous at the μm scale makes the problem more critical. The main technique used to assess heterogeneity is to do a set of determinations in different areas of the reference material (Bédard 1996; Jochum et al. 2005; Norman et al. 1996; among others) and compute an average and a standard deviation. No information is available on size, magnitude and distribution of heterogeneities. Some groups made important forays into heterogeneity distribution (Eggins and Shelley 2002; Molloy and Sieber 2008) but further progress is required. Nowadays different beam size in different areas of the reference material are used to compute average and standard deviation taking into account only location of measurement within the sample (Jochum et al. 2011; Wilson et al. 2002). The addition of spatial information (size and distribution of heterogeneities) will improve the knowledge of reference materials and their usefulness.

## 2  Spatial geochemistry

Simple mathematical tools named SPATIAL GEOCHEMISTRY have been developed to study heterogeneity in geological samples. It has been developed from micro-XRF (EDAX Eagle III) mapping of sulphide- or chromite-rich geological reference materials. Ore samples are notorious for heterogeneity problems and nugget effects. Chemical maps from about 10 000 contiguous determinations with a beam of 50 μm are used to produce two diagrams. The first diagram uses analysed area (increasing multiple beam footprints) as a function of standard deviation (Fig. 1). These diagrams give a relative standard deviation associated with a number of beam footprints that can be converted to a sampled volume convertible into mass. Beam footprints are aggregated using contiguous beam shots to ensure that heterogeneity distribution is taken into account. Such diagrams can be interpreted in similar fashion as geostatistical variograms with sill, range and nugget. A small program has been written to automate the calculation.
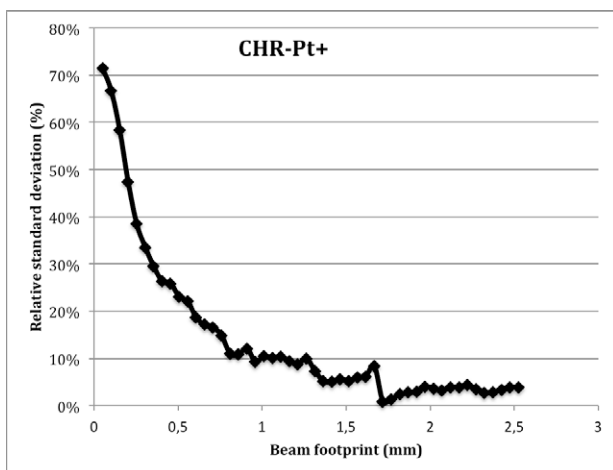
**Figure 1.** Beam footprint as function of relative standard deviation showing uncertainty diminishing as a function of sample size.

In order to characterize distribution, size and magnitude of heterogeneities, another simple mathematical tool has been developed: the proximity number. The number is computed by assigning a value of "1" to all pixels that have a concentration higher or lower than average plus or minus one standard deviation and "0" to values within average plus or minus one standard deviation. A second function adds together neighbouring "1" in order to enhance the effect on proximal values. A graph of proximity number as a function of average +/- x standard deviations presents in a single view: size, magnitude and spatial distribution of heterogeneities (Fig. 2).
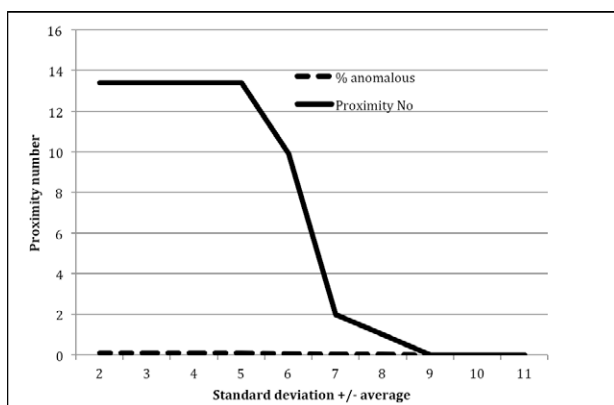


**Figure 2.** Proximity number as a function of average +/- x standard deviations for a model chemical map of a single small heterogeneity shown in Figure 3.
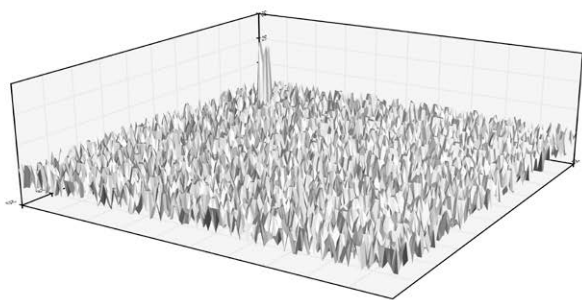


**Figure 3.** Model chemical map showing the topography of a single small heterogeneity analysed in Fig. 2 with proximity number function.

A model chemical map of a single small heterogeneity (Fig. 3) has been analysed in a proximity number diagram (Fig. 2). The solid line (proximity number) shows a magnitude of about 5 standard deviations + average and a size of a few pixels wide (proximity number approximately 13) decreasing rapidly to zero. The dashed line (% anomalous) is below 1 indicating that there are very few heterogeneities (only one in fact). The response of the proximity number diagram is concordant with a single small heterogeneity (Fig. 3). The diagram has been shown to represent adequately different chemical topography. Proximity number interpretation can be easily self-taught with a few examples.

## 3 Characterisation of heterogeneity for microbeam techniques

In order to validate the SPATIAL GEOCHEMISTRY tools, chemical maps of sulphide- or chromite-rich RM have been tested. Reference Materials CHR-Bkg, CHR-Pt+, MASS-1, MASS-3, WMS-1 and WMS-1a have been prepared as pressed pellets and mapped with a micro-XRF over a surface of about 25 mm$^2$ (~10 000 determinations). CHR-Bkg and CHR-Pt+ RM are known to have heterogeneity issues and large nugget effects (Potts et al. 1992). WMS-1 and WMS-1a have a smaller degree of heterogeneities. These RM heterogeneities show clearly in proximity number diagrams. SPATIAL GEOCHEMISTRY analysis of MASS-1 and MASS-3 samples indicates they are the least heterogeneous RM among those studied. CHR-Bkg and CHR-Pt+ show small and large heterogeneities of low magnitude although they have small-size high-magnitude heterogeneities in Ti and S. WMS-1a is a resampling of WMS-1 but it shows some differences: WMS-1 shows small to medium-size high-magnitude heterogeneities in Si while WMS-1a shows Ti heterogeneities.

## 4 Defining a minimal analytical mass

Using the same micro-XRF maps of RM, minimum analytical mass graphs, such as Fig. 1, have been computed for many elements (Ca, Co, Cu, Cr, Fe, Ni, Pb, S, Si and Ti). Overall, it has been determined that analytical masses have to be large for Cu and Ti in CHR-Bkg (more than 20 beam footprints for a relative standard deviation (RSD) of 5 % or less). CHR-Pt+ needs large analytical masses for Ca, Cu, Pb, S and Ti. MASS-1 and MASS-3 samples can be used with very low mass except for Co in MASS-1 and Cu in MASS-3. WMS-1 sample shows a RSD below 5 % with large masses required for Ni and Si while WMS-1a requires a large sample mass for Ca, Cu, Ni and Ti to have a low

RSD. For elements that are prone to nugget effects such as Au and PGE, a different approach was used because the number of pixels showing anomalies was too low for SPATIAL GEOCHEMISTRY analysis and most pixels were below detection limits. Each anomalous PGE or Au pixel was remapped with the micro-XRF at a different scale to ensure that it was a real heterogeneity (nugget). Using element concentrations, maximum numbers of nuggets have been computed assuming all gold or PGE are in nuggets. This gives a maximum limit to the number of nuggets to be found and a validation of the model. CHR-Pt+ has the highest number of nuggets (calculated and observed with the micro-XRF) as expected (Potts et al. 1992). CHR-Bkg contains some nuggets although it has low precious metal concentrations. MASS-1 and MASS-3 have no nuggets (despite the high concentrations of precious metals) as expected from a chemical precipitate (Wilson et al. 2002). WMS-1 has a few nuggets of Pd while WMS-1a has no nuggets suggesting it was better prepared and that an adequate sample preparation procedure (pulverisation and homogenisation) can diminish the number of nuggets. Using number of nuggets and precious metals concentrations, minimal analytical masses for each RM have been computed.

## 5  Conclusion

The use of a technique, such as SPATIAL GEOCHEMISTRY, offers new insight into reference materials and analytical chemistry of geological materials. Not only average elemental concentrations and standard deviations are available from samples but also spatial distribution and proximity of heterogeneities. Knowing that heterogeneities are grouped in a RM will suggest a different calibration strategy for microbeam techniques. Being able to define a minimum analytical mass is important especially for ore samples as many have nuggets creating heterogeneities. It will also help determine mass of sample (beam size) to use with microbeam techniques for pulverised RM samples.

## Acknowledgements

## References

Bédard LP (1996) Reevaluation of the homogeneity of REE, Th and U in geochemical reference zircon 61.308B. Geostds Newslet 20: 289-293

Eggins SM, Shelley MG (2002) Compostional Heterogeneity in NIST SRM 610-617. Geostds Newslet 26: 269-286

Jochum KP, Weis U, Stoll B, Kuzmin D, Yang Q, Raczek I, Jacob DE, Stracke A, Birbaum K, Frick DA, Günther D, Enzweiler J (2011) Determination of Reference Values for NIST SRM 610--617 Glasses Following ISO Guidelines. Geostds Geoanal Res 35: 397-429

Gy P (1998) Sampling for analytical purpose. Wiley, New York

Jochum KP, Willbold M, Raczek I, Stoll B, Herwig K (2005) Chemical characterisation of the USGS reference glasses GSA-1G, GSC-1G, GSD-1G, GSE-1G, BCR-2G, BHVO-2G and BIR-1G using EPMA, ID-TIMS, ID-ICP-MS and LA-ICP-MS Geostds Geoanal Res 29, 285-302

Molloy JL, Sieber JR (2008) Classification of microheterogeneity in solid samples using microXRF. Analytical and Bioanal Chem 392: 995-1001

Moore F (1979) Some statistical calculation concerning the determination of trace constituants. Geostds Newlet 3: 105-108

Norman MD, Pearson NJ, Sharma A, Griffin WL (1996) Quantitative analysis of trace elements in geological materials by laser ablation ICPMS: Instrumental operating conditions and calibration values of NIST glasses. Geostds Newslet 20: 247-261

Pitard F (1993) Pierre Gy's sampling theory and sampling practice: heterogeneity, sampling correctness, and statistical process control. CRC Press, Boca Raton, USA

Potts PJ (1987) A handbook of silicate rock analysis. Blackie Academic professional, London

Potts PJ, Gowing CJB, Govindaraju K (1992) Preparation, homogeneity, evaluation and cooperative study of 2 new chromitite reference samples CHR-Pt+ AND CHR-Bkg. Geostds Newslet 16: 81-108

Savard D, Barnes S-J, Meisel TC (2010) Comparison between Nickel-Sulfur Fire Assay Te Co-precipitation and Isotope Dilution with High-Pressure Asher Acid Digestion for the Determination of Platinum-Group Elements, Rhenium and Gold. Geostds Geoanal Res 34: 281-291

Wilson SA, Ridley WI, Koenig AE (2002) Development of sulfide calibration standards for the laser ablation inductively-coupled plasma mass spectrometry technique. Jour Anal At Spect 17: 406-409

# Test of a user defined calibration in a portable XRF for lithogeochemistry applications

Federico Cernuschi; Mark T. Ford; Darrick Boschmann; John H. Dilles
*College of Earth, Ocean and Atmospheric Sciences, Oregon State University, Corvallis, Oregon, USA, cernuscf@geo.oregonstate.edu*

Richard M. Conrey
*Peter Hooper Geoanalytical Lab, School of the Environment, Washington State University, USA*

**Abstract.** Lithogeochemistry is a commonly used tool in mineral exploration for mapping and correlating rocks. Portable X-ray fluorescence spectrometers (pXRF) have the potential to be used for lithogeochemical purposes. However, many of the commercially available devices only provide pre-set calibrations that are suitable for restricted uses, where the analysis do not have to be compared with commercially available chemical analysis or data gathered with pXRFs of different brands.

We produced and tested two calibrations (basalts and rhyolites) using rock samples and influence coefficient calibrations, using a Bruker Tracer IV XRF spectrometer and SPECTRA EDX software. Calibrations and tests were performed using rock powders previously analysed by XRF and ICP-MS at Washington State University. We were able to reproduce concentrations for a wide range of analytes including K, Ca, Ti, Mn, Fe, Cr, Ni, Cu, Sr, Y, Zr and Nb in powdered basaltic samples, and for Si, Ti, Al, Fe, Mn, Ca, K, Rb, Sr, Y, Nb, Zr, Zn and Pb in powdered rhyolitic samples. Most of the errors of the replicated analysis vary between 5% and 10%. Portable XRF analysis properly calibrated for similar compositions and matrix to the unknowns can be reliably used to measure a selected set of elements.

**Keywords:** Portable XRF, lithogeochemistry, influence coefficient calibration, analytical tools, field analysis

## 1 Introduction

Lithogeochemical methods are commonly used in mineral exploration to aid the mapping and correlation of rocks from grassroots exploration to mine site. Portable XRFs (pXRFs) have been used in several applications in the last few years, and can be helpful tools in lithogeochemistry applications (*e.g.* Boschmann 2012). However, most of the commercially available devices provide pre-set calibrations that are only suitable for narrowly defined uses.

Current pre-set calibrations produce results that are not comparable between different pXRF brands (see Goodale *et al.,* 2011) or against commercially available XRF, ICP-OES or ICP-MS analysis. Some user defined pXRF calibrations rely on multivariate statistical analysis (MVA) to correct intensities of one element based on other elements that are supposed to be proxies. As pointed out by Conrey *et al.* (2012), in many cases no physical reasons support these corrections, inducing error in the analysis.

We produced and tested two calibrations for a Bruker Tracer IV XRF spectrometer, one for basaltic rock powders and one for rhyolitic rock powders. The calibration procedure followed the method described by Conrey *et al.* (2012) using influence coefficient calibrations (ICC) in Bruker's SPECTRA EDX software. ICC calibrations (empirical or calculated) are traditionally used in bench top XRFs to compensate element peak intensities from the interference produced by the presence of other elements in the sample.

The calibrations were then tested by re-analyzing rock powders already analysed by conventional bench top XRF and ICP-MS at Washington State University.

## 2 Methods

### 2.1 Calibrations

Eighteen basaltic powders and fourteen rhyolitic powders were analysed with a Bruker Tracer IV to produce two calibrations, one for the analysis of basaltic rocks and one for rhyolitic rocks.

The samples were selected to cover a broad range of compositions in each of the groups, especially in trace elements and metals. Both the samples used to make and to test the calibration were either powders previously analysed at WSU by WDXRF and ICP-MS (Johnson *et al.,* 1999; Knaack *et al.,* 1994) and selected from the Oregon State University collection, or USGS standards.

Analyses were performed on uniformly ground powders placed in sample cups with XRF film bottoms. No filters were used in the pXRF, which used a Rh filament operated at 45keV and a 240 second dwell for each sample.

The data were independently treated for each composition and the calibration was done using SPECTRA EDX software following the procedure described by Conrey *et al.* (2012). The measured peaks were manually selected at full width at half maximum (FWHM) and minimizing inter-element peak overlap. The calibration calculations were done in SPECTRA EDX using influence coefficient calibrations (Figure 1).

Al, Ca, Fe, K, Mn, P, Si, Ti, Cr, Cu, Nb, Ni, Rb, Sr, V, Y and Zr for basaltic samples and Al, Ca, Fe, K, Mn, Si, Ti, Ba, Nb, Pb, Rb, Sr, Y, Zn and Zr for the rhyolitic samples produced resolvable individual peaks in the X-ray spectra and were selected for the calibration.
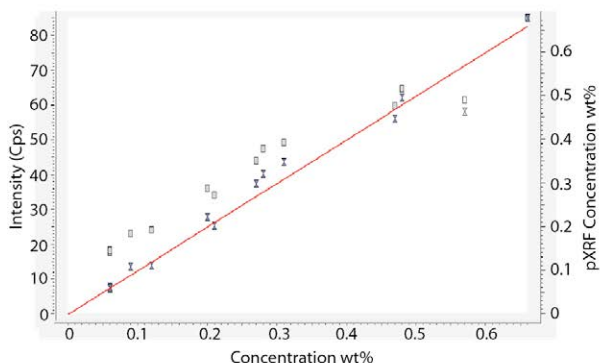
**Figure 1.** Example of a calibration for $TiO_2$ using basaltic rock powders in SPECTRA EDX. Open squares are the original data and closed symbols are corrected values using ICC.

## 2.2 Testing of the calibrations

Basaltic rock powders (n = 22) and rhyolitic powders (n = 28) previously analysed at WSU (see above), were re-analysed with the pXRF and the results calibrated with the previously produced calibration in SPECTRA EDX according to their composition (*i.e.* basaltic or rhyolitic).

## 3 Results

The measured concentration for each element in the pXRF were plotted against the WSU (XRF/ICP-MS) concentrations, and compared to a 1:1 line to evaluate how well the original values were reproduced.

Results for rhyolitic rock powders are presented in Figure 2 and results for basaltic rock powders in Figure 3.
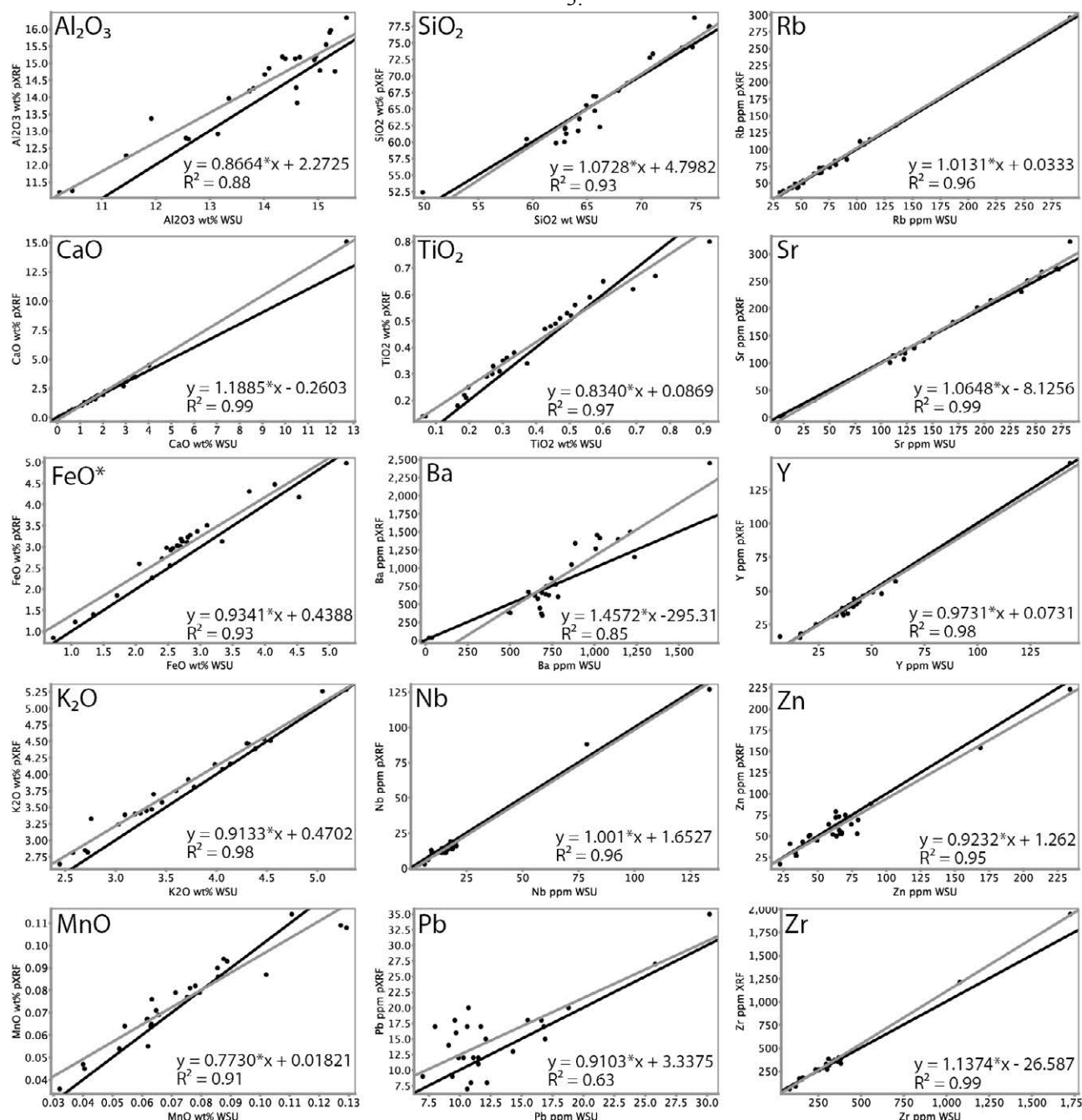


**Figure 2.** Comparison of pXRF data from this study versus WDXRF or ICP-MS for rhyolitic powders. Black lines are 1:1 and grey lines are the regression to fit the data.
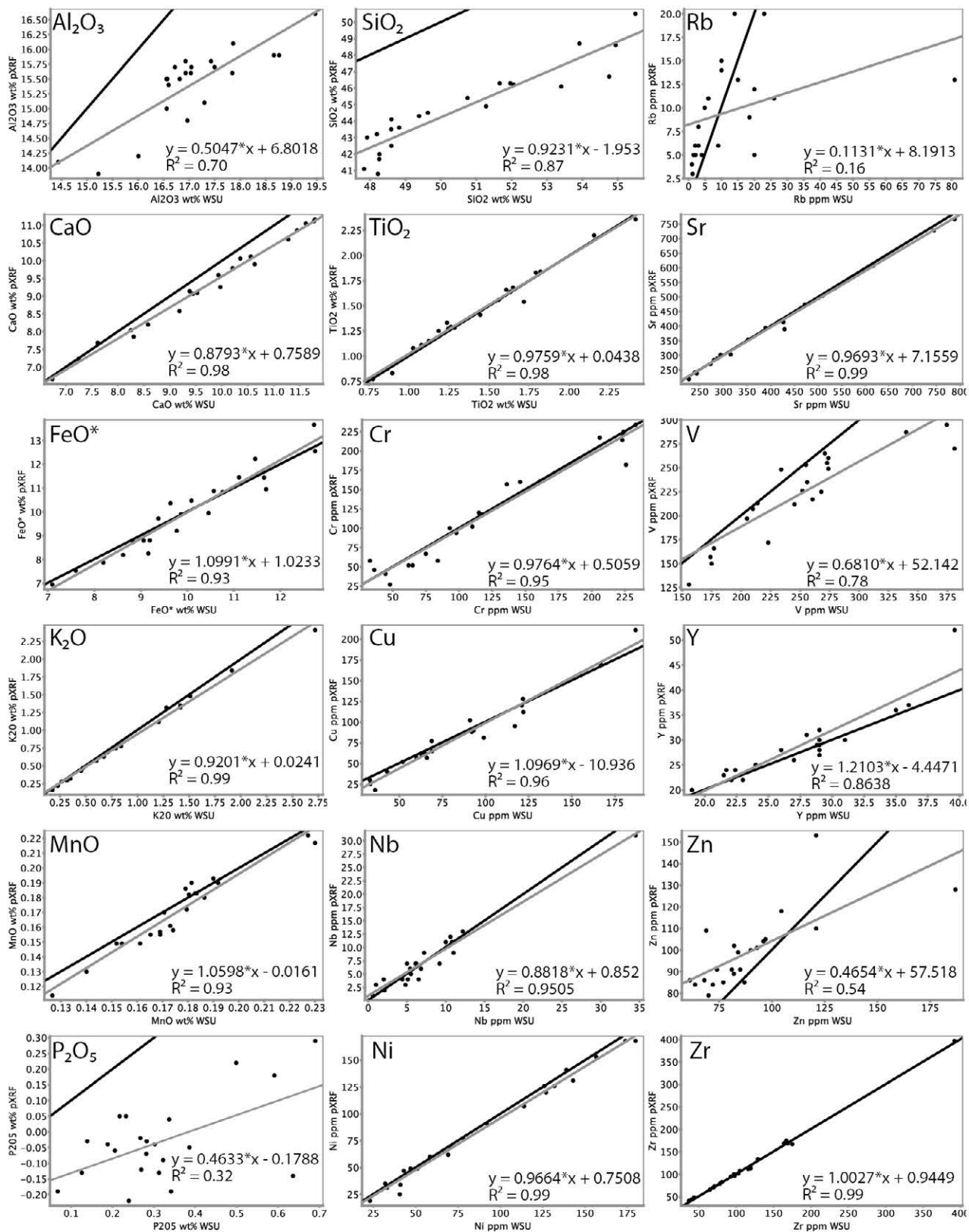
**Figure 3.** Comparison of pXRF data from this study versus WDXRF or ICP-MS for basaltic powders. Black lines are 1:1 and the grey lines are the regression to fit the data.

Average lower limits of detection (LLD) and average error % for each element are summarized in Table 1. LLD were calculated projecting the background level below the element peak from contiguous areas in the spectra, to estimate the smallest possible measurable peak. The calculated concentrations at this background levels were averaged for each element in each calibration. The LLD are reported as the average concentration at background + 3 standard deviations. The error % was calculated using:

Error % = {([*measured*]-[*standard*])/[*standard*]}*100

[*measured*] is the measured concentration of an element using the pXRF and [*standard*] is the measured concentration for the same element using the bench-top XRF at WSU. Error % are reported as averages for each element/calibration.

## 3 Discussion and conclusions

$K_2O$, CaO, $TiO_2$, MnO, FeO*, Cr, Ni, Cu, Sr, Y, Zr and Nb all fit close to 1:1 line for basaltic rock powders. The same was observed for SiO2, $TiO_2$, $Al_2O_3$, FeO*, MnO, CaO, $K_2O$, Rb, Sr, Y, Nb, Zr, Zn and Pb in the rhyolitic powdered samples. This indicates that the original bench top analyses were accurately reproduced with the pXRF for these elements.

Al, Si, P, Rb and Zn in basaltic powders were not accurately reproduced using this method, at least for these rock compositions and compositional ranges.

Table 1 - Average lower limit of detection and error %

| Element | Basalts | | Rhyolites | |
| --- | --- | --- | --- | --- |
| | Average LLD (bkg+ 3stdv) | Avg. Error % | Average LLD (bkg+ 3stdv) | Avg. Error % |
| **Al2O3** | n.a. | | 0.22 wt % | 4.4% |
| **CaO** | 0.03 wt % | 4.2% | 0.01 wt % | 6.0% |
| **FeO*** | 0.01 wt % | 3.9% | 0.01 wt % | 12.5% |
| **K20** | 0.04 wt % | 5.3% | 0.04 wt % | 4.8% |
| **MnO** | 0.01 wt % | 4.4% | 0.01 wt % | 8.5% |
| **P205** | n.a. | | n.d. | |
| **SiO2** | n.a. | | 0.09 wt % | 2.0% |
| **TiO2** | 0.03 wt % | 3.0% | 0.02 wt % | 19.6% |
| **Ba** | n.d. | | 191.4 ppm | 23.7% |
| **Cr** | 11.4 ppm | 14.2% | n.d. | |
| **Cu** | 5.9 ppm | 10.1% | n.d. | |
| **Nb** | 3.1 ppm | 31.2% | 3.4 ppm | 17.7% |
| **Ni** | 6.0 ppm | 7.4% | n.d. | |
| **Pb** | n.d. | | 3.9 ppm | 30.4% |
| **Rb** | n.a. | | 3.8 ppm | 5.2% |
| **Sr** | 3.4 ppm | 1.9% | 3.9 ppm | 6.3% |
| **V** | 13.6 ppm | 10.8% | n.d. | |
| **Y** | 2.9 ppm | 6.2% | 3.9 ppm | 10.7% |
| **Zn** | n.a. | | 4.2 ppm | 16.1% |
| **Zr** | 4.5 ppm | 3.5% | 4.6 ppm | 9.9% |

Key: n.d.: no data, n.a.: not accurately reproduced, LLD: lower limit of detection, bkg: background, stdv: standard deviation, avg.: average

Lead in rhyolites has a good correlation at concentrations over ~12 ppm. Silica in the basalts does not plot close to the 1:1 line, but the analysis regression line presents almost the same slope of a 1:1 line. If ~5 wt% SiO2 is added to the pXRF results, the WSU analyses can be matched. This might be due to an error in the calibration for that element. Al and P in the basalts do not have good correlations, P probably because of its low concentrations.

With both basaltic and rhyolitic rock compositions, the relatively immobile elements (*e.g.* Nb, Zr, Ti and Y), which are often resistant to hydrothermal alteration, are measured with high precision, enabling the use of pXRFs for lithogeochemistry in mineral exploration. Other elements, commonly more mobile, such as Sr, Rb, Si, K are confidently measured and can also aid lithogeochemistry applications in fresh or slightly altered rocks.

Portable XRF analysis on samples of a similar matrix calibrated using influence coefficient calibrations for compositions similar to the unknowns can be reliably used to accurately measure a selected set of elements over a wide range of composition.

## References

Boschmann, D (2012) Structural and Volcanic Evolution of the Glass Buttes Area, High Lava Plains, Oregon [Masters Thesis]. Oregon State University, 100 p.
Conrey R M, Wolff J A, Seyfarth A, Vanhoose A, Goodman Elgar A, Betterncourt N, Boschmann D, and Werling K (2012) Portable XRF Calibration Using Influence Coefficients. 8th International Conference on the Analysis of Geological and Environmental Materials, 67. Buzios, Rio de janeiro, Brazil.
Goodale N, Bailey D G, Jones G T, Prescott C, Scholz E, Stagliano E, and Lewis C (2011) pXRF: a Study of Inter-instrument Performance. Journal of Archaeological Science.
Johnson, D M, Hooper P R, and Conrey R M (1999) XRF Analysis of Rocks and Minerals for Major and Trace Elements on a Single Low Dilution Li-tetraborate Fused Bead. Advances in X-ray Analysis 41: 843–867.
Knaack C, Cornelius S B, and Hooper P R (1994) Trace element analyses of rocks and minerals by ICP-MS: Washington State University, open file report, http://www.sees.wsu.edu/Geolab/note/icpms.html,

# Morphology and compositional features of pyrite in the Martinovo and Chiprovtsi deposits, northwestern Bulgaria

**Dimitrina A. Dimitrova, Tzvetoslav H. Iliev**
*Geological Institute, Bulgarian Academy of Sciences, Sofia, Bulgaria*

**Vassilka G. Mladenova**
*Sofia University "St. Kliment Ohridski", Sofia, Bulgaria*

**Abstract.** Pyrite is formed in all mineral assemblages described in the Martinovo and Chiprovtsi deposits. It is observed as euhedral, cubic to cubic-octahedral, coarse- to fine-grained crystals and spherulitic aggregates. Pyrite associates with molybdenite and scheelite in the retrograde skarn assemblage; with arsenopyrite and löllingite in the later postskarn assemblage; with galena, sphalerite, chalcopyrite, tennantite-tetrahedrite and Ag-Sb sulfosalts in the polymetallic assemblage and with chalcopyrite, tetrahedrite-tennantite, galena and cinnabar in the low temperature assemblage. In all assemblages pyrite is enriched in As. Arsenic contents vary in a wide range - from <0.10 wt. % up to 4.78 wt. %. Pyrite from the retrograde skarn assemblage show enrichment in Ti, Co, Zr, Y, La, Ce, Dy, Yb, Th, U, Bi and Pb. Gold has concentrations between 0.90 and 1.93 ppm. Pyrite from the polymetallic assemblage is enriched in Cu, Zn, Ag, Pb, As and Sb. Spherulitic pyrite is enriched in Co, Ni, Zn, Se, Ag, Sb, Pb, Tl and Hg. Chemical composition of pyrite of different mineral assemblages from the Martinovo and Chiprovtsi deposit reflect the gradual change of the elemental composition of the ore-forming fluids in the area.

**Keywords.** Pyrite, trace elements, LA-ICP-MS, Martinovo and Chiprovtsi deposits

## 1 Introduction

Pyrite is the most widespread sulfide mineral in many types of ore deposits. It is also an important concentrator of precious metals such as Au and Ag, as well as the main source of other rare metals such as Tl. Pyrite usually also contains certain amounts of Cu, As and Sb. Minor and trace elements in pyrite occur as discrete mineral inclusions or are structurally bonded. Although pyrite forms in quite different environments, its trace element composition indicates the mineral forming conditions and composition of the fluids.

The Martinovo iron skarn deposit is unique in Bulgaria, although it resources were estimated as small. It was mined during the $80^s$ and $90^s$ of the last century with production of 94.3 t at 0.12% Mo (Milev et al. 1996).

Chiprovtsi is one of the largest lead-silver deposits in northwestern Bulgaria. The mine has been closed since 1999 after producing 4.79 Mt at 1.84% Pb since 1951 (Milev et al. 1996). Mining activities started on the fluorite bodies in the eastern part of the deposit in 2009.

## 2 Geological Setting

The Martinovo iron skarn and Chiprovtsi lead-silver replacement deposits are hosted in low-grade metamorphic rocks (marbles and schists) of the Diabase Phyllitoid Complex (DFC) (Precambrian - Early Ordovician age, Carrigan et al. 2003, Fig. 1). The formation of the Martinovo deposit is related to the intrusion of the Sveti Nikola granite (313.8 ± 3.5 Ma, Late Carboniferous age, Carrigan et al. 2005) into the DFC rocks. The exoskarn zone, developed in the siderite and calcite marbles, is divided into 3 subzones (Tarassova and Tarassov 1988): pyroxene, garnet-pyroxene and garnet subzone. The economically important magnetite ore is related to the outer garnet zone. The origin of magnetite is considered as a result mainly of the thermometamorphic alteration of siderite (Dragov 1992). The skarns can be classified as Mo-W according to the abundant molybdenite-scheelite mineralization associated with the garnet (grossular-andradite) – pyroxene skarns (Einaudi et al. 1981; Einaudi and Burt 1982; Meinert 1992). A rare accessory mineral observed and typical for this type of skarns is uraninite.

The formation of the main Pb-Ag metasomatic mineralization of the Chiprovtsi deposit is considered to be of Carboniferous age (Amov et al. 1981) and it is stratabound within thick siderite and calcite marble layers in the metamorphic series. The genesis of the deposit remains uncertain and it has been classified as being both granite intrusion-related and stratabound telethermal types of mineral deposits (Atanassov and Pavlov 1983; Dragov et al. 1991).

## 3 Materials and Methods

Polished sections were made from representative samples from the Martinovo and Chiprovtsi deposit and were studied by reflected light microscopy.
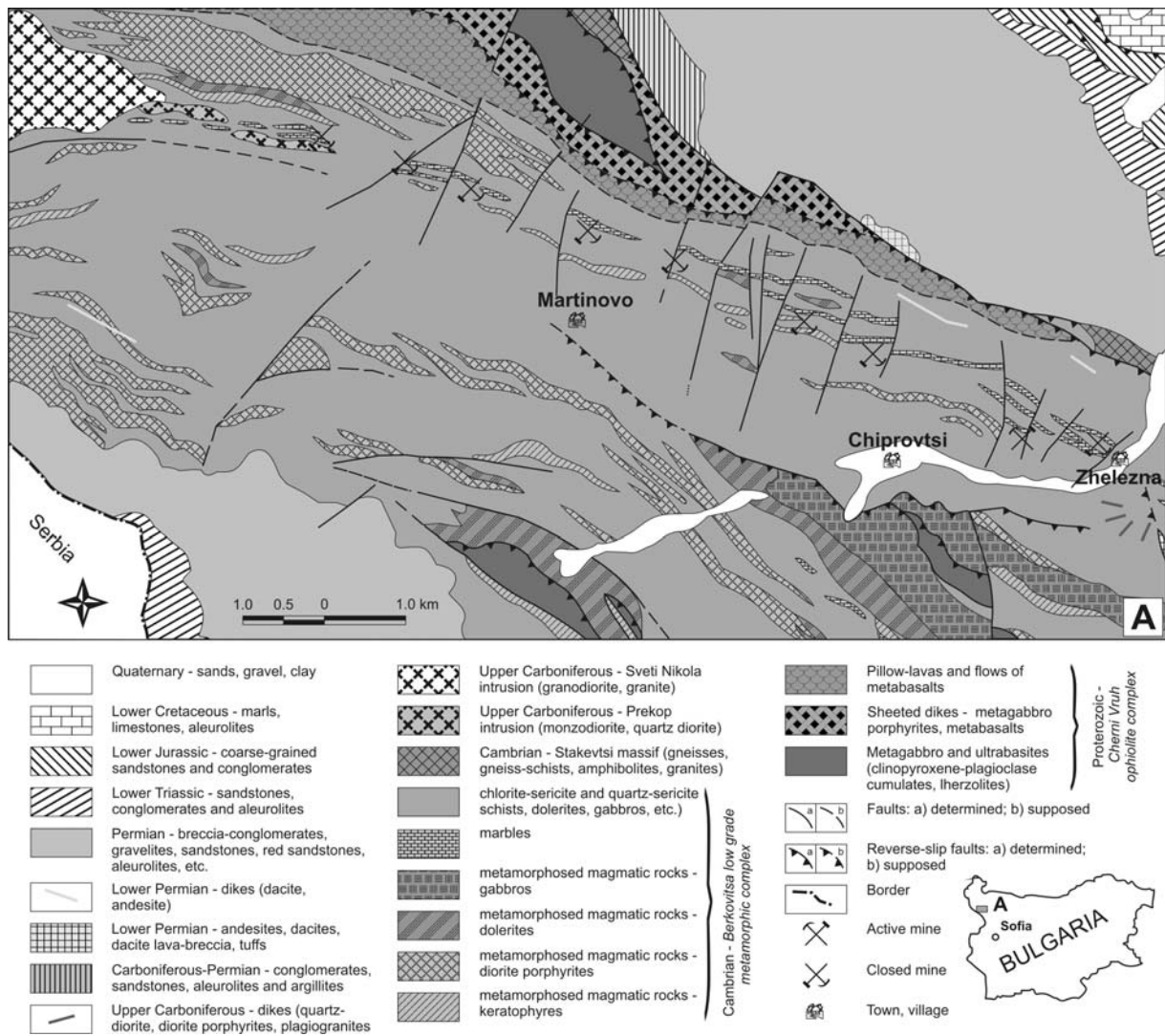
**Figure 1.** Geological map of the Martinovo and Chiprovtsi deposits, modified after Angelov et al. 2008

Trace element concentrations in pyrite were measured by laser ablation inductively coupled plasma mass spectrometry (LA-ICP-MS) on polished sections at the Geological Institute (Bulgarian Academy of Sciences), Sofia, Bulgaria. The analyses were made using the PerkinElmer ELAN DRC-e ICP-MS equipped with a New Wave UP193-FX excimer laser ablation system. NIST SRM 610 glass was used as external standard. The laser system was operated at constant 10 Hz pulse rate; laser energy density was 1.80-2.60 J/cm$^2$ on the sample using a 50 μm spot size. The following isotopes were monitored: $^{49}$Ti, $^{51}$V, $^{53}$Cr, $^{55}$Mn, $^{57}$Fe, $^{59}$Co, $^{62}$Ni, $^{65}$Cu, $^{66}$Zn, $^{71}$Ga, $^{73}$Ge, $^{75}$As, $^{77}$Se, $^{89}$Y, $^{94}$Zr, $^{97}$Mo, $^{106}$Pd, $^{107}$Ag, $^{111}$Cd, $^{115}$In, $^{120}$Sn, $^{121}$Sb, $^{126}$Te, $^{181}$Ta, $^{182}$W, $^{185}$Re, $^{195}$Pt, $^{197}$Au, $^{202}$Hg, $^{205}$Tl, $^{208}$Pb, $^{209}$Bi, $^{232}$Th, $^{238}$U and REE. Isotope masses to be measured have been chosen so that isobaric and known polyatomic interferences to be avoided (May and Wiedmeyer 1998). Data reduction was done using SILLS ver. 1.1.0 software (Guillong et al. 2008) and Fe as internal standard. Iron contents in pyrite were measured by JEOL Superprobe 733 electron microscope equipped with an ORTEC energy-dispersive system at the Geological Institute, BAS.

## 4 Pyrite Morphology and Mineral Assemblages

Pyrite is one of the main ore minerals in the Martinovo and Chiprovtsi deposits and occurs in almost all mineral assemblages. Early pyrite, found in the Martinovo deposit, occurs with molybdenite, scheelite, rutile, titanite, garnet, epidote, actinolite, chlorite, quartz, apatite and uraninite in the retrograde skarn assemblage (Fig. 2A). It is observed as euhedral, cubic to cubic-octahedral crystals, sometimes intimately intergrown with molybdenite and scheelite. Pyrite is also formed together with arsenopyrite and löllingite in the later postskarn assemblage, exhibiting euhedral cubic or coarse- to medium-grained morphology and is intensively fractured (Fig 2C).

In the main polymetallic assemblage, described in the Chiprovtsi deposit, which some authors consider being part of the whole mineralization process in the area, pyrite is observed as fractured intergrown coarse- to fine-grained crystals, enclosed by later galena, sphalerite, chalcopyrite, tetrahedrite-tennantite and Ag-Sb sulfosalts (polybasite-pearceite, stephanite, pyrargyrite). In the eastern parts of the Chiprovtsi

deposit, where the low temperature assemblages occur, pyrite is also observed as colloform, spherulitic aggregates, associated mainly with chalcopyrite, tetrahedrite-tennantite, galena and cinnabar (Fig. 2D). In this assemblage pyrite also occurs as tiny euhedral crystals included in quartz crystals, formed almost simultaneously with spherulitic pyrite and cinnabar.

## 5 Chemical Composition of Pyrite

Chemical composition of pyrite was determined by electron microprobe analysis (major and some minor elements) and by LA-ICP-MS (trace elements). In spite of the expected minor and trace elements that are usually incorporated in pyrite (Cu, Zn, As, Sb, Ni, Co, Ag, Au, etc.), the REE, U and Th were also monitored. This was done in order to distinguish the presence of other minerals, such as zircon, rutile, apatite, uraninite as inclusions. Pyrite usually contains other minerals as inclusions, which cannot be predicted and avoided when choosing spots for LA-ICP-MS analysis. The presence of such inclusions can be discarded in the time resolved spectrum of the analysis. These data allow us to establish attributes of pyrite from different assemblages in the Martinovo and Chiprovtsi deposits in regards to its trace element composition.
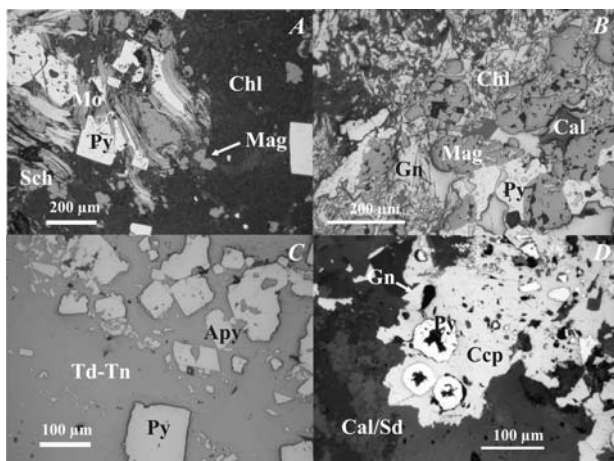


**Figure 2.** Photomicrographs: A) Pyrite crystals (Py) intergrown with molybdenite (Mo) and scheelite (Sch), magnetite (Mag) in chlorite; B) pyrite crystals intergrown with magnetite in galena (Gn) and chlorite (Chl); C) Pyrite and arsenopyrite (Apy) in tetrahedrite-tennantite (Td-Tn); D) Pyrite spherulites in chalcopyrite (Ccp), replacing calcite/siderite (Cal/Sd)

In general, pyrite in all assemblages is enriched in As. Arsenic contents vary in wide range from <0.10 wt. % in small euhedral pyrites enclosed in quartz crystals, up to 4.78 wt. % in spherulitic pyrite. Mostly, As content is between 0.70 wt. % up to 1.60 wt. %. Antimony is also enriched in pyrite but at much lower rates - its maximum values reach 1.48 wt. %. It is noteworthy that Sb is detected in pyrites from the Chiprovtsi deposit denoting the first major difference between pyrites from the Martinovo and Chiprovtsi deposits. This reflects change of the chemical composition of later

hydrothermal fluids from which the minerals in the polymetallic assemblage precipitated.

Major differences in chemistry of pyrites from different assemblages were detected in trace element compositions, determined by LA-ICP-MS. Pyrite from the retrograde skarn assemblage show enrichment (in ppm) in Ti (191-1863), Co (34-305), Zr (7.92-96.97), Y (0.60-7.81), La (0.12-2.23), Ce (0.17-5.21), Dy (0.24-1.19), Yb (0.60-7.81), Th (0.35-1.44), U (1.68-21.42), Bi (15.26-107.7) and Pb (25-1254). These concentrations do not reflect inclusions of other minerals such as zircon, apatite, uraninite in pyrite, because the measured isotopes show uniform intensities throughout the time resolved spectra acquisitions. This suggests that these elements are incorporated structurally in pyrite, probably occupying defects or substituting for $Fe^{2+}$. Cobalt and Ti are known impurities substituting for Fe in pyrite, but the other elements are not typical. The presence of these elements can be explained by an enrichment of the hydrothermal fluids in Zr, Y, La, Ce, HREE (Dy, Tb), U, Th. This is understandable because pyrite from the retrograde skarn assemblage is associated with skarn minerals such as garnet, titanite, chlorite, and accessory minerals such as apatite and uraninite. These minerals are typical for W-Mo skarns related to granite post-collisional intrusions. Gold was also detected in this pyrite, having concentrations between 0.90 and 1.93 ppm. Unlike the previous mentioned elements, Au show single peak intensities in the time resolved spectra, which suggest that it exists as tiny inclusions (3-5 μm). Larger gold grains (10-15 μm) were observed in pyrrhotite and chalcopyrite together with Bi minerals in the late postskarn mineralization (pyrite-arsenopyrite and pyrrhotite-chalcopyrite assemblages).

Pyrite from the postskarn assemblage has similar compositions to pyrite in the skarn assemblage but the concentrations of Zr, Y, La, Ce, Dy, Yb, Th, U and Bi are significantly lower, which suggest a change of the hydrothermal fluid composition. In contrast, antimony is enriched up to 60 ppm.

Chemical composition of pyrite from the polymetallic assemblage of the Chiprovtsi deposit is evolved in comparison to the earlier pyrites. The concentrations of As and Sb are considerably higher and reach 9000 ppm and 1200 ppm, respectively. Trace element signatures are also distinct. High concentrations of Cu, Zn, Pb, Ag are typical and correspond to the mineral association represented by galena, sphalerite, tetrahedrite-tennantite, Ag-Sb sulsosalts. Concentrations of Au in this pyrite are low.

The trace element concentration trend evolves further in pyrite from the spherulitic pyrite assemblages, reflecting the specifics of the low temperature hydrothermal fluid. SEM-BSE (back scattered electron) images and EPMA analyses of spherulitic pyrite revealed a distinct microscale zoning in As distribution in the spherulite aggregate, along the axis of elongation of the needle-like crystals. Arsenic contents vary between 0.74 and 4.78 wt. %, while Sb is < 0.10 up to 2.43 wt. %.

LA-ICP-MS analysis of spots in different zones revealed fluctuations in distribution of other trace and minor elements such as Sb, Tl, Cu, Co, Ni, Ag, Pb and

Hg. Although, Hg could not be quantified due to its absence in the external standard, it was clearly observed with sufficient intensities in the time resolved spectra. All these data suggest fluctuations in the chemical composition of the hydrothermal fluid, as a result of sudden supersaturation in these elements, present in the fluid most likely in the form of complex ions.

Similar Au concentrations in the range 0.19-2.39 ppm were determined in all samples from the low temperature assemblage. The measured concentrations of the following minor and trace elements were (in ppm): Ti (9.94-19.14), Cr (2.45-15.76), Mn (6.91-9.98), Co (0.10-1180), Ni (1.77-3361.15), Cu (12.44-1686), Zn (4.94-1316), Ge (not detectable - 6.68), Se (3.83-19.12), Ag (146.34-6853), Sb (725->1000), Pb (17.46-9281), Tl (12-3319) and Te (0.89-2.01). Vanadium, Cd, In, Sn, Ga, Mo and Bi were not detected.

Concentration fluctuations for some metals (Pb, Cu, Co, Zn, Ag) are significant and probably related to inclusions of galena, chalcopyrite or tetrahedrite. However, Tl and Hg most likely occur as substitutes for Fe, showing stable high intensities in the time resolved spectra.

Depletion or enrichment of some of the components in the fluid, especially As and Sb, causes distinct chemical zonation of the aggregates. The rapid crystallization from the supersaturated hydrothermal fluid facilitates the incorporation of gold as micro- to nano-sized particles (<1-2 μm) on the growth surfaces, as well as other elements substituting for Fe and S in the crystal structure of the spherulitic pyrite.


# 6 Conclusions

Apparent relation between pyrite morphology and chemical composition in different assemblages cannot be established, except for the spherulitic pyrite, in which supersaturation of hydrothermal fluids has produced rapid crystal growth and incorporation of an abundance of trace elements into the structure.

Trace element compositions of pyrite show the specifics of the hydrothermal fluids from which the mineral crystallizes. Having the ability to sequester a wide range of elements from the hydrothermal fluid, pyrite can give genetic implications about ore-forming hydrothermal fluids unlike other ore minerals (galena, sphalerite, chalcopyrite), which concentrate fewer trace elements.

In this study, the chemical composition of pyrite of different mineral assemblages from the Martinovo and Chiprovtsi deposit reflect gradual changes of the elemental composition of the ore-forming fluids. This supports the idea that both deposits are related and represent the mineralization process in the area, temporally and spatially associated with the intrusion of the Sveti Nikola granite into the low grade metamorphic rocks of DPC.

## References

Angelov V, Antonov M, Gerdzhikov S, Aydanlyiski G, Petrov P, Kisselinov H (2008) Geological map of Bulgaria M 1:50000, Map sheet "Chiprovtsi"

Amov B, Arnaudov V, Pavlova M, Dragov P, Baldjieva Ts, Evstatieva S (1981) Lead isotope data on the Paleozoic granitoids and ore mineralizations from the Western Balkan Mountains and the Tran district (West Bulgaria). I. Isotopic ratios and geochronology. Geologica Balc 11:3-26

Atanassov V, Pavlov I (1983) Notes about mineralogy and paragenetic zoning of minerals deposits in Chiprovtsi ore region. Ann Ecol Sup Min Geol 28:159-178 (in Bulgarian)

Carrigan CW, Mukasa SB, Haydoutov I, Kolcheva K (2003) Ion microprobe U-Pb zircon ages of pre-Alpine rocks in the Balkan, Sredna Gora and Rhodope Terranes of Bulgaria: Constraints on Neoproterozoic and Variscan tectonic evolution. J Czech Geol Soc 48:32-33

Carrigan CW, Mukasa SB, Haydoutov I, Kolcheva K (2005) Age of Variscan magmatism from the Balkan sector of the orogen, Central Bulgaria. Lithos 82:125-147

Dragov P (1992) Ore-Forming Processes in the Chiprovtsi Ore Zone. DSc Thesis. Sofia 179p (in Bulgarian)

Dragov P, Galiy SA, Zhukov FI (1991) Carbon, oxygen and sulphur isotopes in minerals from the Chiprovtsi ore zone. Rev Bulg Geol Soc 52:50-61 (in Bulgarian)

Einaudi MT, Meinert LD, Newberry RJ (1981) Skarn deposits. Econ Geol 75:317-391

Einaudi MT, Burt DM (1982) Introduction - terminology, classification, and composition of skarn deposits. Econ Geol 77:745-754

Guillong M, Meier DL, Allan MM, Heinrich CA, Yardley BWD (2008) Appendix A6: SILLS: A MATLAB-based program for the reduction of laser ablation ICP-MS data of homogeneous materials and inclusions, In: Sylvester P (ed.), Laser Ablation ICP–MS in the Earth Sciences: Current Practices and Outstanding Issues. Mineralogical Association of Canada Short Course 40: pp328–333

Haydoutov I (1991) Origin and Evolution of the Precambrian Balkan-Carpathian Ophiolite Segment. Sofia, BAS Press, 179p (in Bulgarian)

May TW, Wiedmeyer RH (1998) A table of polyatomic interferences. At Spectrosc, 19:150-155

Meinert, L. D. 1992. Skarns and skarn deposits. Geosci Canada 19:145-162

Milev V, Stanev V, Ivanov V (1996) The Extracted Ores in Bulgaria during 1878-1995 - Statistical Reference Book. Sofia, Zemya 93, 196p (in Bulgarian)

Tarassova E, Tarassov M (1988) Horizontal zonality and mineral composition of skarns in the Martinovo deposit. Geochem Mineral Petrol, 24:68-76 (in Bulgarian)

# Some patterns of formation of gold-sulphide deposits, West Kalba, east Kazakhstan

Olga Frolova, Anastassiya Miroshnikova, Katerina Petrich
*East Kazakh State Technical University, Ust-Kamenogorsk, Kazakhstan*

**Abstract.** The process of generating gold-bearing pyrites and arsenopyrites in the ores of gold-sulphide deposits in West Kalba is discussed. Studies of petrophysical and geochemical features show that these minerals are formed as a result of transformation of syngenetic globular iron sulphides that are localised in black-shale deposits of West Kalba. According to geochemical studies it has been established that the content of silver and gold increases with the transformation of the sulphides.

**Keywords.** Metallogenic belt, gold-sulphide deposits, gold-containing minerals, gold-bearing arsenopyrite, gold-bearing pyrite.

## 1 Introduction

Some formation specifics of gold-sulphide mineralization in the West Kalba Metallogenic Belt (WKMB) in Eastern Kazakhstan were identified based on the analysis of geophysical survey information.

Interpretation of the geophysical fields, confirmed by geological observations and separate deep holes confirmed formation of gold-sulphide deposits above intrusions. Stratification depth of the intrusions roof varies from several meters to 3.5 km.

According to the results of seismic reflection survey (Bortsov, 1981) ore-controlling faults, containing the gold-sulphide mineralization, reach the roof of these intrusions. They are confirmed by drilling in the upper parts of the cross-section at the depths of 1000-1500 m.

## 2 Zoning of gold-sulphide mineralization of the WKMB

Zoning of WKMB gold mineralization (Bortsov et al. 2004) was examined using the physical properties of samples and measurements of physicochemical properties of ore minerals.

Geochemical zoning is determined in the direction from the intrusion roof towards the paleosurface. Rare-metal mineralization is localized in the intrusion roof and in the adjacent areas (Jubileiny Oktabr' deposit). Intersections of rare-metal-bearing veins with gold-bearing veins, as well as intersections of gold-bearing quartz veins with rare-metal tin-bearing veins were noted at the distance of 600m from the intrusion roof. This confirms simultaneous formation of rare-metal and gold-bearing veins (Mynchunkur deposit). Further away from the intrusion roof, gold mineralization is localized within fault zones (Suzdal, Kuludzhun and Bakyrchik deposits). As a result, rare-metal deposits, localized in the lower part of the fault zone that reach the intrusions roof, and the gold mineralization limited to the upper part of the fault zones, form a single ore chute. (Fig. 1).

Formation of deposits with different mineral specialization is accompanied by a certain zoning of thermoelectric properties of the basic sulphides: pyrite and arsenopyrite. These sulphides are semiconductors and their semiconductor properties are determined by the composition and concentration of the impurity elements. (Shui, 1979). Zoning of semi-conduction type is especially clearly manifested in arsenopyrites. The arsenopyrites localized in the lower layer of the ore chute in rare-metal deposits and occurrences are characterized by p-type conduction only, which is caused by the presence of such impurity elements as tungsten, tin and other rare-metals. Arsenopyrites with p-type and n-type conduction are found at the Mynchunkur deposit. Moreover, the arsenopyrites with n-type conduction bear gold mineralization. Gold-bearing arsenopyrites with exclusively n-type conduction are noted in the upper part of the ore chute at the Bakyrchik deposit (Bortsov and Sulakvelidze 2002).
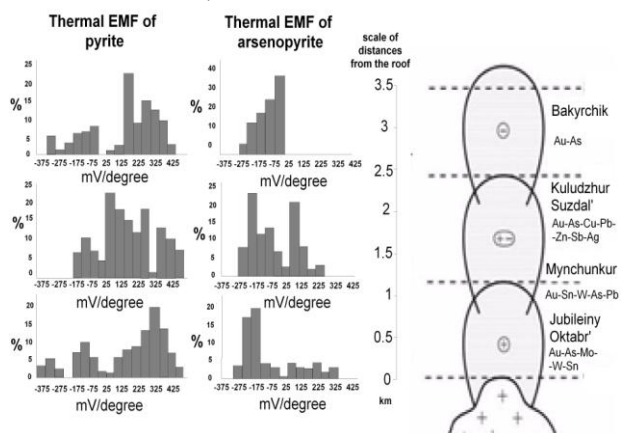


**Figure 1.** Scheme of conduction type of pyrite and arsenopyrite in gold-sulphide deposits of the West Kalba metallogenic zone

## 3 Petro-physical characteristics

Most researchers studying the Kalba gold sulphide mineralization associated it with the black shale strata. This also includes terrigenous formations of the WKMB black shale strata (Bakyrchik, Suzdal, and Kuludzhun deposits).

The studies of the petro-physical features of the black-shale sequence that host gold-sulphide mineralization in the West Kalba Belt show that this sequence plays the most important role in the formation of gold-sulphide mineralisation.

Rocks that comprise the black-shale strata are differentiated according to their electrochemical

properties. Siltstones, silty sandstones, sandstones, containing carbon-bearing minerals of the shungite group are characterized by oxidation reduction potential of 5-15 mV; rocks, containing carbonaceous matter – by the natural electrical potential of 10 to 600-700 mV.

In bulk they form natural galvanic cells with which natural electrical anomalies are connected. It has been established that these natural electrical cells formed in the WKMB black-shale strata and influenced the localization of gold mineralization (Mokievskiy et al. 1956). Study of the three-dimensional structure of such electric fields indicates that the mineralisation is localised in the transitional areas from positive values of an electric field to negative.

In general, black-shale strata are a single electrochemical formation and are detected as regional anomalies of the natural electrical field.

The possibility of formation of gold-sulphide deposits at the expense of gold mobilization from the black-shale strata was repeatedly emphasized (Narseev, 2001). It was also stated that noble metals are present in the black-shale strata as non-autonomous phases in sulphides (pyrite, arsenopyrite) and carbon-bearing minerals of the shungite group (Marchenko, 2008).

Analyses of mineral composition of ores show that the main gold-bearing minerals (pyrites and arsenopyrites) were formed as a result of transformation of globular syngenetic iron sulphides during the genesis of the black-shale sequences. The following stages were identified:

1. Formation of syngenetic iron sulphides of globular shape, in the range of 20-150 microns in size (Fig. 2a). Carbon-bearing minerals with ring shapes are often present in these sulphides.

2. Formation of cubic or dodecahedral grains from the globular iron sulphide grain accumulations (Fig. 2b).

3. Growth of crystal faces in cubical or dodecahedral forms (Fig. 2c).

4. Growth of gold-bearing pyrites of cubical or dodecahedral grains. In some of these, traces of original iron sulphide globules remain.

Gold-bearing arsenopyrite grains are formed following the same sequence.
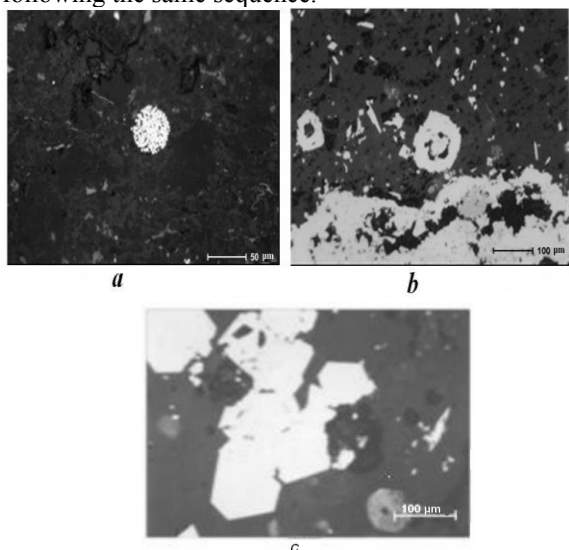


**Figure 2.** Transformation of syngenetic globular iron sulphides by recrystallization into faceted forms

Figure 3 shows histograms characterizing contents of impurity elements in globular iron sulphides and in the products of their transformation during metamorphism of the black-shale strata.
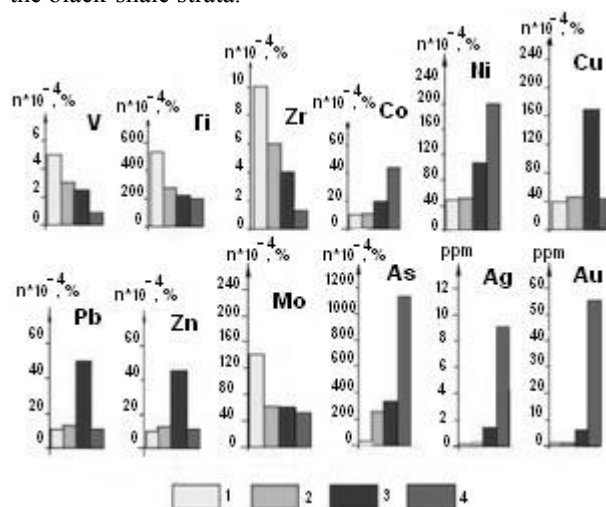


**Figure 3.** Characteristics of impurity elements in progressively recrystallized iron sulphides
1 – globular iron sulphides; 2 – accumulations of round, cubical and dodecahedral globular iron sulphides; 3 – formation of faces and cubical and dodecahedral accumulations; 4 – gold-bearing pyrites.

Lithophile elements undergo subtraction in globular disulphides and in gold-bearing pyrite grains. Their content decreases as follows: Zr from 10 to 1.5%, V from 5 to 1%, and Ti from 500 to 200%.

Analysis of chalcophile elements showed the following regularity: highest content of Zn, Pb and Cu is observed in pyrite containing fragments of globules and in pyrrhotite. The lowest content of these elements is found in gold-bearing pyrite. Highest content of As, Ag, Au is observed in gold-bearing pyrite. It should be noted these elements are present in concentrations of less than 0.01 g/t at the primary stages of formation of globular Fe sulphides.

The content of siderophile elements of Co and Ni increases from 10 to 40% in the primary stage (globular pyrite) and from 45 to 200% in the final stage (gold-bearing pyrites) of pyrite formation. This implies that these elements were cyclically introduced from intrusive hydrothermal solutions. In case of Mo inverse mechanism took place, i.e. drastic element subtraction.

Rare metals (Zr, V, Mo, Ti) are present in large quantities at the primary stages of the pyrite formation; that confirms their transfer by the residual rare-metal hydrothermal solutions.

Analysis of histogram shows a continuity of geochemical specialisation of the products of transformation of syngenetic iron sulphides from globular forms to gold-bearing pyrites. It confirms the formation of gold-bearing minerals as a result of transformation of syngenetic iron sulphides.

## 4 Summary

Based on the results of this study, the genesis of gold-sulphides deposits in the West Kalba can be represented

as follows:

1. During the formation of intrusions of the West Kalba intrusion belt, residual rare-metal (Zr, V, Mo, Ti) hydrothermal fluids were generated.

2. Movement of the hydrothermal fluids to the paleosurface took place along the faults originating in the roof of intrusions, and is accompanied by mobilization of elements, including gold derived from the black-shale strata.

3. The source of gold and other elements are carbonaceous fine-grained sandstones, siltstones and clay-stones. Most likely the bulk of gold was extracted from the superficial phases of the carbon-bearing minerals (Marchenko, 2008).

4. During the migration of hydrothermal fluids to the paleosurface along the faults and reaching the roof of intrusions, the rare-metal paragenesis was replaced by the gold ore. At 0.5-0.6 km distance from the roof, gold and rare-metal (tin) mineralization are equally developed, at more than 1.5-2 km gold mineralization is dominant (Fig. 1)

6. Formation of gold-bearing minerals (pyrites, arsenopyrites) is connected with the transformation of syngenetic globular iron sulphides, concentrated in the black-shale strata.

## References

Bortsov VD (1981) Integration of geophysical methods in the study of ore-hosting structures (example of mineral deposits of Kalba). PhD thesis. Ust-Kamenogorsk, pp.34

Bortsov VD, Rafailovich MS, Titov DV (2004) Zonation of gold mineralisation in the Western Kalba (East Kazakhstan). Geology and subsurface protection 3-12:20-26

Bortsov VD and Sulakvelidze NV (2002) Electro-physical characteristics of ore minerals of gold-sulphide deposits. Vniitsvetmet Bulletin 1: 59-62

Marchenko LG (2008) About forms and association of noble metals with rare and dispersed metals in "black-shale" type of deposits of Kazakhstan. Bulletin of the National Academy of Science, Geology series 6:49-69

Mokievskiy VA, Stulov NN, Tsigelman IS (1956) About mineral formation in natural electric field. Bulletin of Mineralogical Society 2:39-48

Narseev VA, Gostev YV, Zakharov AV (2001) Bakyrchik: geology, geochemistry and mineralization. Moscow CSRGEI. pp.174

Shui RT (1979) Semi-conducting ore minerals. Nedra Leningrad. pp. 288

*All references are in Russian*

# The application of high-resolution X-ray computed tomography to ore deposits

Bélinda Godel, Stephen J. Barnes
*CSIRO Earth Science and Resource Engineering, Australian Resources Research Centre, Kensington, Western-Australia*

**Abstract.** High-resolution X-ray computed tomography (HRXCT) is a powerful and non-destructive technique allowing, at the sample scale, the acquisition of 3D mineral distribution data. These 3D data can be processed and analysed to provide direct 3D measurements of rock textures (e.g crystal size and distributions, degree of interconnectivity, abundances, shapes, textural relationship, intergrowth characteristics, and mineral orientation) at the sample scale, with resolution down to 0.7 µm. When HRXCT is incorporated into routine ore characterization of natural or synthetic ore materials, it provides a better understanding of ore mineralogy, ore-forming processes and geometallurgy.

**Keywords.** 3D mineralogy, sulfides, gold, nickel, platinum-group elements

## 1 Introduction

High-resolution X-ray computed tomography (HRXCT) is a non-destructive technique that allows the exploration of the 3 dimensional (3D) distributions of minerals and pore spaces in natural rock or synthetic samples up to several centimetres across. Over the past 10 years, HRXCT has been used in a range of fields of geosciences including notably paleontology (Balanoff et al. 2010), volcanology (Baker et al. 2012 and references therein), igneous petrology (Godel et al. 2013), petroleum engineering (Akin and Kovscek 2003) and meteoritics (Hezel et al. in press). High-resolution X-ray computed tomography has been applied to various ore types including gold deposits (Kyle and Ketcham 2003; Kyle et al. 2008), platinum-group element deposits (Godel in press; Godel etl. in press; Godel et al. 2010; Holwell et al. 2012), magmatic Ni-Cu sulfide deposits (Godel et al. 2012; Barnes et al. 2008; Barnes et al. 2011a; Barnes et al. 2011b; Godel in press) and iron ore (Fonteneau et al. in press)

Recent technological developments allow the 3D characterization of samples at a resolution down to 0.7 µm. The data generated not only provide striking 3D images, but can also be used to provide in-situ quantitative 3D mineralogical and textural measurements, inaccessible by any other methods. The development of dedicated workflow, algorithm and softwares to process the HRXCT data is opening new doors for the quantitative 3D characterization of ores at the sample scale. The combination of HRXCT, quantitative 3D image analysis and in-situ geochemistry provides an improved understanding of ore mineralogy, ore forming processes and parameters required for mineral or metallurgical processing.

## 2 Principle and methodologies

### 2.1 Data acquisition

Typically, a micro-focus X-ray beam source illuminates the sample as it rotates by increment around 360°. The range of X-ray energies used allows the X-rays to be transmitted through complex and dense materials including ore samples. At each increment, a sensitive X-ray detector collects radiographs (referred to as projections) of the sample. These projections are then used to reconstruct either a set of consecutive 2D greyscale images (referred to as slice) or a 3D volume of the attenuation of X-rays through the sample. The attenuation of the X-rays mainly depends on the average atomic number, the density of the material and the spectral characteristics of the X-ray source.

The samples presented in this contribution were scanned using a XRADIA XRM 500 high-resolution 3D X-ray microscope system installed at the Australian Resources Research Centre (Kensington, Western Australia). This system has the ability to generate multi-scale imaging of a given sample (up to 3.5 cm across) at a voxel size down to ~0.3 µm.

### 2.1 Data processing and 3D quantitative analysis

After reconstruction, the dataset represents a regular volumetric grid where each voxel has a unique greyscale value, function of the attenuation of the X-ray at that location. Dedicated image processing procedures (Fig. 1) allow the 3D visualization and the extraction of quantitative 3D textural parameters required for the characterization of the samples (Godel, in press).

## 3 Examples of applications

High-resolution X-ray computed tomography and quantitative 3D image analysis can be applied to a range of geological materials to provide an improve understanding of ore mineralogy, textures and ore-forming processes, which had not been recognised previously using 2D techniques.

This contribution will present examples of applications of these 3D techniques to magmatic ore deposits hosted within mafic-ultramafic intrusions and komatiite flows including (Fig. 2):

- The 3D distribution and textural characteristics of rare phases (e.g. platinum-group minerals) in ore samples
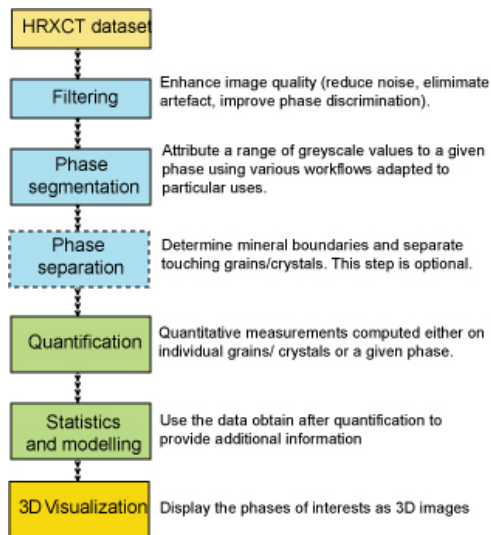
**Figure 1.** Typical workflow for typical HRXCT data processing and 3D quantitative analysis.

- The 3D distribution, size, morphology and degree of connectivity of base-metal sulfides to quantify their textures and assess constraint on sulfide topology.
- The direct calculation of sulfide mineral abundances and metal tenors at the sample scale to assess heterogeneities within and between samples.
- The determination of mineral orientation in 3D and to evaluate the relative timing of mineral growth and deformation.
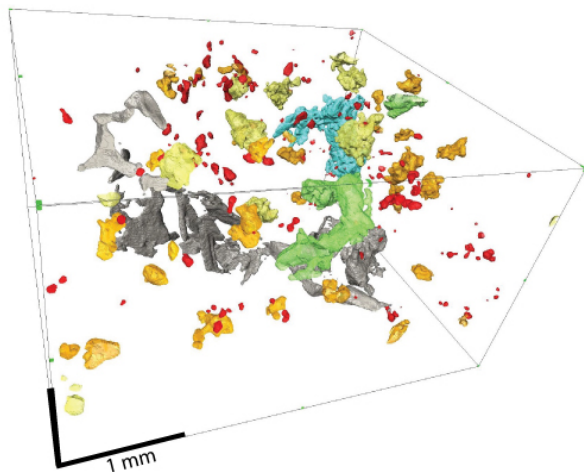


**Figure 2.** Example of 3D visualization of poikilitic chromite (grey) and magmatic base-metal sulfides (color scale corresponding to particle size) in adcumulate from komatiite hosted Ni-sulfide deposit (Mount Keith, Western Australia). It should be noted that a volume of interest has been selected with a larger sample to facilitate the display.

## 3 Conclusions

High-resolution X-ray computed tomography is a powerful technique that allows the acquisition of 3D dataset allowing the 3D visualization and quantification of rock texture in 3D. When HRXCT is combined with dedicated workflows and softwares and supplemented with in-situ mineralogical and mineralogical investigations, it provides 3D dataset which are almost impossible to collect using conventional 2D techniques. Over the past few years, HRXCT has been incorporated into routine ore characterization of samples from various deposit types. The 3D results obtained allow a better understanding of ore mineralogy and processes and a better constraint of parameters required for geometallurgy. Hence, the application of HRXCT benefits both academic studies and mineral industry applications

## Acknowledgements

## References

Akin S, Kovscek AR (2003) Computed tomography in petroleum engineering research In: Mees F, Swennen R, Van Geet M, Jacobs P (eds) Application to X-ray Computed Tomography in the Geosciences. Geological Society, London, pp 23-38

Baker DR, Mancini L, Polacci M, Higgins MD, Gualda GAR, Hill RJ, Rivers ML (2012) An introduction to the application of X-ray microtomography to the three-dimensional study of igneous rocks. Lithos 148:262-276

Balanoff AM, Bever GS, Ikejiri T (2010) The Braincase of Apatosaurus (Dinosauria: Sauropoda) Based on Computed Tomography of a New Specimen with Comments on Variation and Evolution in Sauropod Neuroanatomy. American Museum Novitates 3677:1-32

Barnes SJ, Fiorentini ML, Austin P, Gessner K, Hough RM, Squelch AP (2008) Three-dimensional morphology of magmatic sulfides sheds light on ore formation and sulfide melt migration. Geology 36:655-658. doi: 10.1130/g24779a.1

Barnes SJ, Godel B, Locmelis M, Fiorentini ML, Ryan CG (2011a) Extremely Ni-rich Fe-Ni sulfide assemblages in komatiitic dunite at Betheno, Western Australia: results from synchrotron X-ray fluorescence mapping. Australian Journal of Earth Sciences 58:691-709

Barnes SJ, Osborne G, Cook D, Barnes L, Maier WD, Godel B (2011b) The Santa Rita Nickel Sulfide Deposit in the Fazenda Mirabela Intrusion, Bahia, Brazil: geology, sulfide geochemistry and genesis. Economic Geology 106:1083-1110.

Fonteneau L, Godel B, Ramanaidou E (in press) Application of high-resolution X-Ray computed tomography to iron ore geometallurgy. Iron Ore 2013:Paper 41

Godel B, Barnes SJ, Barnes S-J, Maier WD (2010) Platinum ore in 3D: Insights from high-resolution X-ray computed tomography. Geology 38:1127-1130

Godel B, Gonzalez-Alvarez I, Barnes SJ, Barnes S-J, Parker P, Day J (2012) Sulfides and sulfarsenides from the Rosie Nickel Prospect, Duketon Greenstone Belt, Western Australia. Economic Geology 107:275-294

Godel B, Barnes SJ, Austin P, Gürer DM, Fiorentini ML (2013) Chromite in komatiites: 3D morphologies and sizes with implications for crystallization mechanisms. Contribution to Mineralogy and Petrology 165:173-189. doi: http://dx.doi.org/10.1007/s00410-012-0804-y

Godel B (in press) High resolution X-ray computed tomography and its application to ore deposits: case studies from Ni-Cu-PGE deposits. Economic Geology

Godel B , Barnes SJ, Barnes S-J (in press) Deposition mechanisms of magmatic sulfide liquids: evidence from high-resolution X-

ray computed tomography and trace element chemistry of komatiite-hosted diseeminated sulfides. Journal of Petrology.

Hezel DC, Elangovan P, Viehmann S, Howard L, Abel RL, Armstrong R (in press) Visualisation and quantification of CV chondrite petrography using micro-tomography. Geochimica et Cosmochimica Acta:http://dx.doi.org/10.1016/j.gca.2012.1003.1015,.

Holwell D, Abraham-James T, Keays R, Boyce A (2012) The nature and genesis of marginal Cu–PGE–Au sulphide mineralisation in Paleogene Macrodykes of the Kangerlussuaq region, East Greenland. Mineralium Deposita 47:3-21. doi: 10.1007/s00126-010-0325-4

Kyle JR, Ketcham RA (2003) In situ distribution of gold in ores using high-resolution X-ray computed tomography. Economic Geology 98:1697-1701. doi: 10.2113/98.8.1697

Kyle RJ, Mote AS, ketcham RA (2008) High resolution X-ray computed tomography studies of the Grasberg porphyry Cu-Au ores, Papua, Indonesia. Mineralium Deposita 43:519-532

# Trace element analysis of wolframite by LA-ICP-MS

Simon Goldmann, Hans-Eike Gäbler, Frank Melcher
*Federal Institute for Geosciences and Natural Resources (BGR), Stilleweg 2, 30655 Hannover, Germany*

**Abstract.** The trace element composition of wolframite in ore concentrates from various tungsten deposits worldwide was analysed using LA-ICP-MS. A large number of trace elements at different concentration levels are common in wolframite: Nb, Mg, Zn, Y, Ta, Ti, Sc, Sn, Co, Mo, In, Hf, Zr, V, U, Th, Pb, and REE. Chondrite-normalised REE patterns show that HREE are enriched compared to LREE and have negative Eu anomalies. The trace element distribution and REE patterns of wolframite are characteristic for a particular deposit, although the trace elements vary within a deposit.

**Keywords.** wolframite, trace elements, LA-ICP-MS, fingerprinting

## 1 Introduction

Wolframite $(Fe,Mn)WO_4$ and scheelite $CaWO_4$ are the most important tungsten ore minerals. The former represents a solid solution series between the ferberite $(FeWO_4)$ and hübnerite $(MnWO_4)$ endmembers. Tungsten features unique properties and its major applications are in cutting tools, production of high speed steel and as filaments in light bulbs, but also in military equipment.

Tungsten is enriched by fractional crystallization in residual melts and is subsequently concentrated in hydrothermal fluids forming a range of deposit types (e.g., greisen, hydrothermal veins, skarn, and porphyry deposits) which are generally related to evolved felsic magmatism. Various parameters and processes (e.g., magma composition, composition and evolution of the fluid, chemistry of the host rocks, alteration) control the trace element composition of wolframite during the formation of the different tungsten deposits.

Most previous studies report major element compositions of wolframite only with just a few of these dealing with a small number of trace elements in wolframite by either electron microprobe analysis (Tindle and Webb 1989; Belkasmi et al. 2000; Ferenc and Uher 2007; Barkov et al. 2008; Neiva 2008) or atomic absorption spectroscopy (Mignardi et al. 1998). In this study, the trace element compositions of wolframite were analysed by LA-ICP-MS covering a larger number of elements. The trace element distribution and chondrite-normalised REE patterns are variable between different tungsten deposits worldwide. This variability in the trace element composition and in normalised REE patterns can be used to discriminate individual deposits and forms the basis for the 'Analytical Fingerprint' (Melcher et al. 2008).

## 2 Materials & Methods

### 2.1 Samples

Ore concentrate samples (59 samples in total) from 33 different tungsten deposits worldwide were analysed by LA-ICP-MS. Polished sections were prepared from these concentrates to generate a uniformly flat, scratch-free, and highly reflective surface. Concentrates are the preferred sample material for our purpose because they provide a sufficient number of individual target grains to record the variability in the chemical composition of wolframite from a single deposit.

### 2.2 Instrumental

As a first step, the mineralogical composition of the ore concentrates is determined by automated scanning electron microscopy (Gu 2003) to identify adequate target grains for in-situ analysis by LA-ICP-MS. About 50 individual mineral grains per concentrate are analysed for their major, minor and trace element composition using a Thermo Scientific ELEMENT-XR high resolution sector field inductively coupled plasma mass spectrometer coupled to a New Wave UP193-FX laser ablation system with an ATLEX-300-SI excimer laser.

The following isotopes have been analysed: $^{69}Ga$, $^{75}As$, $^{89}Y$, $^{95}Mo$, $^{107}Ag$, $^{111}Cd$, $^{115}In$, $^{118}Sn$, $^{121}Sb$, $^{137}Ba$, $^{139}La$, $^{140}Ce$, $^{141}Pr$, $^{146}Nd$, $^{147}Sm$, $^{153}Eu$, $^{157}Gd$, $^{159}Tb$, $^{163}Dy$, $^{165}Ho$, $^{166}Er$, $^{169}Tm$, $^{172}Yb$, $^{175}Lu$, $^{177}Hf$, $^{201}Hg$, $^{204}Pb$, $^{205}Tl$, $^{206}Pb$, $^{207}Pb$, $^{208}Pb$, $^{209}Bi$, $^{238}U$ in low resolution (LR) and $^{12}C$, $^{24}Mg$, $^{27}Al$, $^{29}Si$, $^{31}P$, $^{32}S$, $^{44}Ca$, $^{45}Sc$, $^{47}Ti$, $^{51}V$, $^{52}Cr$, $^{55}Mn$, $^{56}Fe$, $^{59}Co$, $^{60}Ni$, $^{63}Cu$, $^{66}Zn$, $^{88}Sr$, $^{90}Zr$, $^{93}Nb$, $^{181}Ta$, $^{182}W$, $^{232}Th$ in medium resolution (MR). For all elements both secondary electron multiplier (SEM) and Faraday detector are used depending on the count rate.

At each sampling point, eight passes of $50 \times 130$ μm lines are ablated at 10 Hz with a speed of 5 μm/s. The laser energy is fixed to 2.6 mJ for ablation of wolframite and 3.2 mJ for the ablation of the reference material NIST 610. Prior to every analysis a pre-ablation scan is run to remove any contamination from the sample surface (one pass, $75 \times 155$ μm, 10 Hz, 15 μm/s). The wash out time after every ablation process takes 80 s. Data acquisition by the mass spectrometer takes 358 s and during the first 140 s the background signal is analysed. The mass spectrometer performs 25 passes over the whole mass range in LR and MR.

An external calibration using a non-matrix matched reference material with internal standardization has been applied. The glass NIST SRM 610 is used as reference material (Pearce et al. 1997) and was measured repeatedly during a sequence. Tungsten was used as

internal standard calculated from the known stoichiometry of wolframite. The concentrations for each element are calculated using the equation given by Longerich et al. (1996). Detection limits are calculated for each element on the basis of three times the standard deviation of the background measurement. Data reduction was done by an in-house software tool implemented in JAVA using the libraries JFreeChart, commons Math and POI (Gäbler et al. 2011).

## 3    Results & Discussion

About 50 individual grains per ore concentrate are analysed in order to obtain a representative estimate of the variability in trace element composition of wolframite within a single deposit (Fig. 1). The wolframite group minerals form a solid solution series with major element compositions varying between the Fe-rich and Mn-rich endmembers. Common trace elements in wolframite are Nb, Mg, Zn, Y, Ta, Ti, Sc, Sn, and HREE with contents of up to 1000 ppm or even higher, whereas Co, Mo, In, Hf, Zr, V, U, Th, Pb, and LREE usually are in the range of up to 100 ppm. Some elements are predominantly below the detection limit (Ga, As, Ag, Cd, Sb, Tl, Bi, Ni, Cu, Sr, Ba, and Cr). As a rule, relatively small cations with ionic radii of less than 0.9 Å are preferentially substituted for Fe and Mn in wolframite (Hazen et al. 1985; Macavei and Schulz 1993; Kuzmin and Purans 2001).
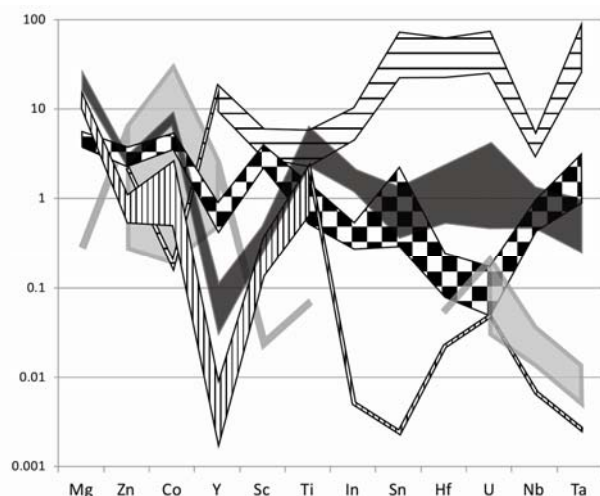


**Figure 1.** Variation in the trace element composition of wolframite from selected deposits (black: Mount Carbine, Australia; horizontal lines: Ranong, Thailand; light grey: Nyakabingo, Rwanda; chessboard: Bishasha, Democratic Republic of the Congo; vertical lines: Khovd Gol, Mongolia) normalised to the median of all wolframite analyses. The variability within a deposit is indicated by the 25th (lower line of the contour) and 75th percentile (upper line of the contour) of the data. Percentile data below the detection limit are omitted. A single line represents 75th percentile data only.

In general, the incorporation of particular trace elements into wolframite seems to be dependent on the Mn/Fe ratio. High field strength elements correlate positively with Mn, whereas elements with low valency show positive correlation with Fe. For example, this is documented in the trace element compositions of

hübnerite from Ranong compared with ferberite from Khovd Gol (Fig. 1). The trace elements show variable concentration levels within a deposit. However, the distribution of trace elements or even certain element concentrations are distinctive for a particular deposit.

The REE distribution generally shows inclined chondrite-normalized patterns enriched in HREE with a distinct negative Eu anomaly (Fig. 2). The HREE are preferentially incorporated into the wolframite structure as they exhibit smaller ionic radii compared to the LREE. The REE patterns also appear to be controlled by the Mn/Fe ratio, as Mn-rich wolframite contains higher total REE concentrations compared to Fe-rich wolframite (Fig. 2).
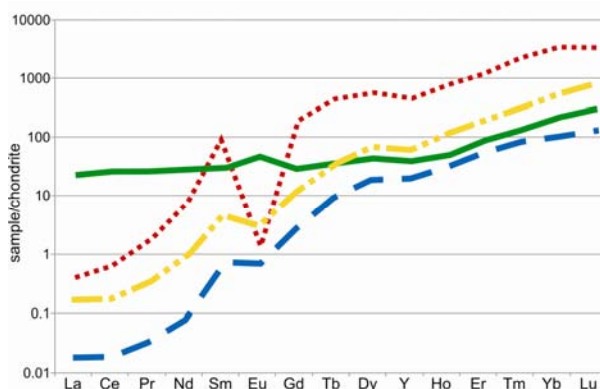


**Figure 2.** Typical chondrite-normalised REE patterns for wolframite ranging from Fe-rich to Mn-rich compositions; blue (dashed line): ferberite, yellow (dot-dashed line): wolframite, red (dotted line): hübnerite, green (solid line): reinite.

A special case is observed in the trace element composition of reinite which represents a pseudomorph of ferberite after scheelite. In comparison with primary wolframite group minerals, reinite (e.g., Nyakabingo in Fig. 1) shows very distinctive concentrations in Ca, Sr, Pb, and Ba, but very low Sn, Zr, Hf, In, Ti, Sc, Nb, Ta, and Mg contents. The REE distribution of reinite also differs significantly and displays flatter chondrite-normalized patterns with weak positive Eu anomalies and higher LREE concentrations compared with primary wolframite (Fig. 2). The distinctive trace element composition and normalised REE patterns of reinite are caused by pseudomorphism and were inherited from precursor scheelite, because cations with ionic radii larger than 0.9 Å (like Ca, Sr, Pb, Ba, and LREE) are favourably incorporated into the scheelite structure (Hazen et al. 1985; Macavei and Schulz 1993; Kuzmin and Purans 2001).

## 4  Conclusions

A broad spectrum of trace elements can be measured in wolframite using LA-ICP-MS analysis. The chemical composition and chondrite-normalised REE patterns of wolframite can be used to discriminate various ore deposit types as well as different ore provinces or even mining sites. This site specific variability of trace element concentrations in wolframite forms the basis of the possibility to develop a geochemical fingerprint for wolframite-bearing ore concentrates.

## References

Barkov AY, Martin RF, Shi L, LeBarge W, Fedortchouk Y (2008) Oscillatory zoning in stanniferous hematite and associated W- and Bi-rich minerals from Canadian Creek, Yukon, Canada. Can Mineral 46: 59-72

Belkasmi M, Cuney M, Pollard PJ, Bastoul A (2000) Chemistry of the Ta-Nb-Sn-W oxide minerals from the Yichun rare metal granite (SE China): genetic implications and comparison with Moroccan and French Hercynian examples. Mineral Mag 64: 507-523

Ferenc Š, Uher P (2007) Magnesian wolframite from hydrothermal quartz veins in the Rochovce granite exocontact, Ochtiná, Western Carpathians, Slovakia. Neues Jb Miner Abh 183: 165-172

Gäbler H-E, Melcher F, Graupner T, Bahr A, Sitnikova MA, Henjes-Kunst F, Oberthür T, Brätz H, Gerdes A (2011) Speeding up the analytical workflow for Coltan fingerprinting by an integrated Mineral Liberation Analysis/LA-ICP-MS approach. Geostand Geoanal Res 35: 431-448

Gu Y (2003) Automated scanning electron microscope based mineral liberation analysis; an introduction to JKMRC/FEI Mineral Liberation Analyzer. Journal of Minerals and Materials Characterization and Engineering 2: 33-41

Hazen RM, Finger LW, Mariathasan JWE (1985) High-pressure crystal chemistry of scheelite-type tungstates and molybdates. J Phys Chem Solids 46: 253-263

Kuzmin A, Purans J (2001) Local atomic and electronic structure of tungsten ions in $AWO_4$ crystals of scheelite and wolframite types. Radiat Meas 33: 583-586

Longerich HP, Jackson SE, Günther D (1996) Laser ablation inductively coupled plasma mass spectrometric transient signal data acquisition and analyte concentration calculation. J Anal Atom Spectrom 11: 899-904

Macavei J, Schulz H (1993) The crystal structure of wolframite type tungstates at high pressure. Z Kristallogr 207: 193-208

Melcher F, Sitnikova MA, Graupner T, Martin N, Oberthür T, Henjes-Kunst F, Gäbler H-E, Gerdes A, Brätz H, Davis DW, Dewaele S (2008) Fingerprinting of conflict minerals: columbite-tantalite ("coltan") ores. SGA News 23: 1-13

Mignardi S, Ferrini V, Masi U, Nabais LC, de Sousa Bernardo M (1998) Significance of the major- and trace-element contents of wolframite from the deposits of Panasqueira and Vale de Gatas, Portugal. In: Hagni RD (ed) Proceedings of the Ninth Quadrennial IAGOD Symposium, Beijing, China, August 12-18, 1994. Schweizerbart, Stuttgart, 475-484

Neiva AMR (2008) Geochemistry of cassiterite and wolframite from tin and tungsten quartz veins in Portugal. Ore Geol Rev 33: 221-238

Pearce NJG, Perkins WT, Westgate JA, Gorton MP, Jackson SE, Neal CR, Chenery SP (1997) A compilation of new and published major and trace element data for NIST SRM 610 and NIST SRM 612 glass reference materials. Geostandards Newslett 21: 115-144

Tindle AG, Webb PC (1989) Niobian wolframite from Glen Gairn in the Eastern highlands of Scotland: A microprobe investigation. Geochim Cosmochim Acta 53: 1921-1935

# aFieldWork – handheld application for offline recording of geological localities and visualization of geodata

Martin Hansen, Bo Møller Stensgaard, Thomas F. Kokfelt & Tomas Næraa
*Geological Survey of Denmark and Greenland (GEUS), Øster Voldgade 10, DK-1350 Copenhagen, Denmark*

**Abstract.** GEUS has for several years successfully used a handheld digital device with a software system for digital data capturing during fieldwork in remote areas in Greenland. In the last years, as it has become increasingly difficult to replace these devices, and as new faster alternative platforms have been commercially available, it was by end 2011 decided at GEUS to develop an Android based application (App) to replace the existing system.

The application developed for 2012 fieldwork was designed to register localities with information on earth materials, samples, structural measurements (measured by internal censors or a compass) and photographs. Data entry is mainly made through selection lists and data are stored in a SQLite database. The use of a relational database makes it easy to move the data to central databases after returning from fieldwork.

During 2012 fieldwork in Greenland the App was tested on four different Android devices ranging in size from 3.56" to 7". Based on the field experience it was decided to focus on devices ranging from 5.3" to 7" as they have sufficiently large screens, yet still fit in a pocket. In 2013 the system is being extended with new functionality and offline map access.

**Keywords.** Fieldwork, digital data collection, handheld devices, rock sampling, mapping, locality description

## 1 Background

The Geological Survey of Denmark and Greenland (GEUS) has since 2008 used handheld devices for collecting field data in a digital format through a modified version of the 'Ganfield' software system that was first developed by the Geological Survey of Canada (Buller 2005). The 'Ganfield' system utilized ESRI ArcPAD software for data collection and visualization and was developed to run on handheld personal digital assistant devices that were linked up with an external GPS device via Bluetooth® connection (Schlatter et al. 2010). As PDA's are going out of production and as improved functionalities and new features in the software system are desirable it was decided to develop an Android based application (App) and to test this on a range of different devices during the 2012 fieldwork in Greenland.

The main objectives with the system are to provide field geologists working out of small field camps in harsh and remote areas, such as in Greenland, with a quick and efficient way of (1) recording information on a geological locality in a digital format and (2) visualizing existing digital geodata on maps in the field, (3) enabling and securing a consistent way of reporting data (i.e. consistent descriptions and classification schemes for geological features such as rocks, structures etc.), and (4) allowing for the data to be quickly and efficiently transferred into the central databases and GIS environments once out of the field.

Before it was decided to develop an in-house software system, other available software products were examined. However, many of the existing devices and software systems that are directed towards geological fieldwork run on larger, more power consuming and more expensive devices such as rough-use tablets. Also it was found that for many of these software systems the primary focus was on mapping purposes and lacked the functionalities and ability to do efficient and quick registration of information on localities (general descriptions of localities, description and classifications of rocks, descriptions of photos, sampling, etc.).

The handheld device and the App should allow the users to collect the same data as the old system (see Schlatter et al. 2010 for a description) but with improved functionalities and a more user-friendly interface. The main requisites for the handheld device and the application were:

- Device has to be relatively robust, lightweight, small and easy handled with an internal GPS system and camera. The devices have to be easily replaceable and relatively cheap. They must be independent of mobile networks and work offline
- Low power consumptions; must be able to recharge using solar panels, hand-driven, or mobile gasoline-driven power generator
- Internal backup of the device (onto SD card) as well as facility to easily backup onto laptop or PC during fieldwork
- App must ensure that data are stored well-structured and in a format that makes them easy to import into other GIS environments
- New captured data as well as existing geodata and maps (topographical data, geological maps, geochemistry, geophysics, etc.) should be visualized and easily imported into the App
- The system should allow both data collection and visualization of data in the field and editing of data in the field camp
- A simple intuitive user interface easy to use in the field under difficult field conditions

It was decided to develop an App for the Android platform. This decision was based on the wide variety of relatively cheap Android devices available in many different sizes (including several toughened versions), the Java development language running on a Window

platform which is the main development platform at GEUS, and the possibility to store data on a removable secure digital memory card (SD Card) that can easily be used from a laptop or PC in the field camp.

## 2 The aFieldWork App

The App was designed to be simple to use and to require as little typing as possible. This was done to make registering as easy and efficient as possible and to make data as structured and consistent as possible. The App is database driven. Although some of the data entry is compulsory and entered via either fixed predefined selection lists as scrollable drop-down lists, other information is optional and consists of both selection lists and free-text entries. The mandatory entry points and the predefinition of selection lists also force the field geologists to describe and classify localities and geological features in a uniform and consistent way.

The first version of the App is intended as a prototype sufficient for collecting information's about localities, earth materials, samples, structures and photographs, rather than a fully functional version. Further development and refinement of the system is based on the experience gathered from testing in the field.

## 3 Data entry

All data entries are geo-referenced via coordinates taken from an internal GPS in the Android device together with information about its accuracy. The sample number (e.g. for a rock sample) is according to GEUS's sample numbering system, a docket book system, where each user is allocated a slot of sample numbers (six digit number, each slot consisting of 99 sample numbers).

Functionalities for a manual text entry may be prompted by the user when relevant (e.g. for longer descriptions of localities, earth materials or samples) E.g., the data entry point, or menu, for samples will first appear when the user selects the 'sample button'. This is to avoid that unnecessary information and menus interfere with a smooth and efficient data entry. The selection lists are in many cases designed so that the most frequently used entries are listed first.

### 3.1 Localities

A locality is created by tapping the 'New Locality' button on the start-up screen of the aFieldWork App (Figure 1). The user is then prompted for a description of the locality (not mandatory). User can see the co-ordinates (as decimal degree, degree decimal minutes and as UTM), their accuracy and time of creation. The locality is automatically provided with a locality id which consists of the year, the initials of the geologist and the number of the locality e.g. 12tfk003 for tfk's third location in 2012.

From the locality screen it is possibly to add free text notes about the locality itself and what has been seen since the last locality. At the locality screen it is possible to press buttons to open the entry points for 'Earth Materials', 'Samples', 'Structure' and 'Photos'.
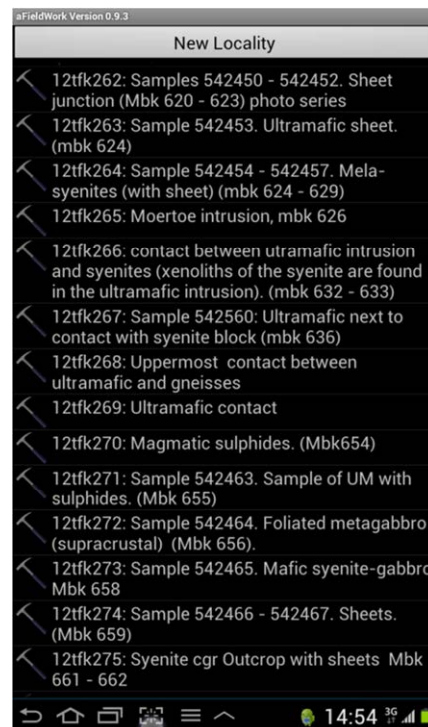


**Figure 1.** The App's main screen showing a list of the localities described.

### 3.2 Earth Materials

The entry point 'Earth Materials' refer to information on the rocks at the locality. This information is entered by selecting a predefined 'Rock Class' list (e.g. metamorphic, plutonic, sedimentary, etc.) (Figure 2). After the 'Rock Class' is selected, it is possible to select a 'Rock type' (e.g. gneiss, migmatite, schists) matching the selected rock class. When a rock type is selected it becomes possible to select a 'Rock Name'. In this way the long list of rock names can be narrowed down to a few items with a few taps on the screen. The classification of the earth materials (the rocks) is done according to internationally agreed classifications schemes for rocks (e.g. according to classifications schemes suggested by the International Union of Geological Sciences IUGS). It is possible to omit designating a rock name to an earth material in case it is uncertain.

As part of the rock description it is possible (optional) to enter information about rock colour, metamorphic grade, mineralogy (as common-, alterations- and ore minerals), alteration and fossils. This information is mostly also entered via predefined selection lists.

### 3.2 Samples

The entry point 'Sample' enables the user to number and register information on a rock sample.

The rock samples must be connected to an 'Earth Material' entry and cannot be saved without such an entry. The 'Earth Material' entry can either be an existing one or one that is created when the 'Sample' entry point is selected. This is done to minimize interaction with the

system. The sample is automatically assigned a sample number (one larger than the previous sample).

A sample type, a sample purpose can be selected from dropdown lists and a free text description can be entered.
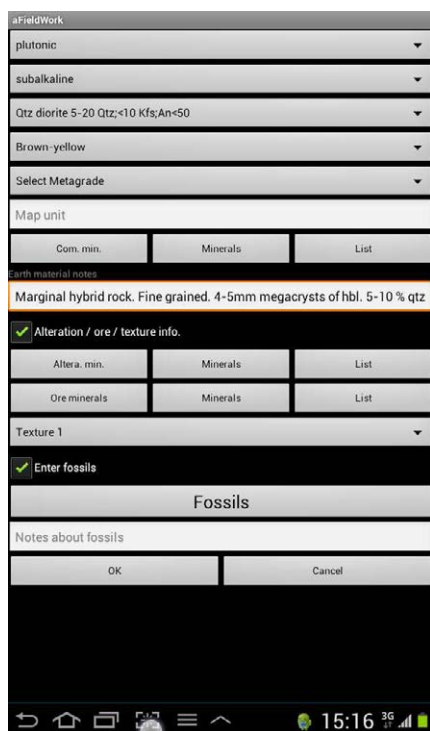


**Figure 2.** The Earth Material data entry screen.

### 3.2 Structural measurements

The entry point 'Structure' enables the user to number and register information on a structural measurement. Like rock samples, structural measurements must be connected to an earth material.

Structural class (linear or planar), type (e.g. fault, shear zone for a planar class) and detail (e.g. generation for a foliation) can be selected from selection lists as dropdown lists. Measurements made by a handheld compass can be entered as numbers using a keyboard or by two sliding bars. It is also possible to use the devices internal compass but its accuracy has not been well tested.

### 3.2 Photos

Photos can be taken using the internal camera, in which case there is no need for data entry besides an optional free text description to the photo. If an external camera is used, the user must enter the first and last number of the photos taken on the locality. The first number is by default the highest number given but can be overruled in case other photos has been taken between two localities. Also for photos taken by an external camera is it possible to provide a free text description to the photo.

### 4 Behind the screen

All data are stored in a SQLite database. SQLite is the internal database system of most small digital devices

and even though it is capable of running on many small devices it is a rather advanced database system supporting foreign keys, triggers and (with an extension) for spatial data. The database backend makes it much easier to ensure good data quality and makes transfer of the data to central databases much easier. As the predefined selection lists are based on the database queries it is quite easy to extend the system or to configure it to suit the geology of specific field expeditions.

Part of the application is based on open source projects. The database handling part is based on the Android SQLite Manger (http://sourceforge.net/projects/asqlitemanager/) and the map part will probably be based on Mapsforge (http://code.google.com/p/mapsforge/) or OSMDroid (http://code.google.com/p/osmdroid/) libraries. Both are capable of displaying off-line maps.

### 5 Testing in the field

The system has been tested during field work on four different devices (Figure 3). The devices were selected based on their size only as the system has few demands for the hardware.
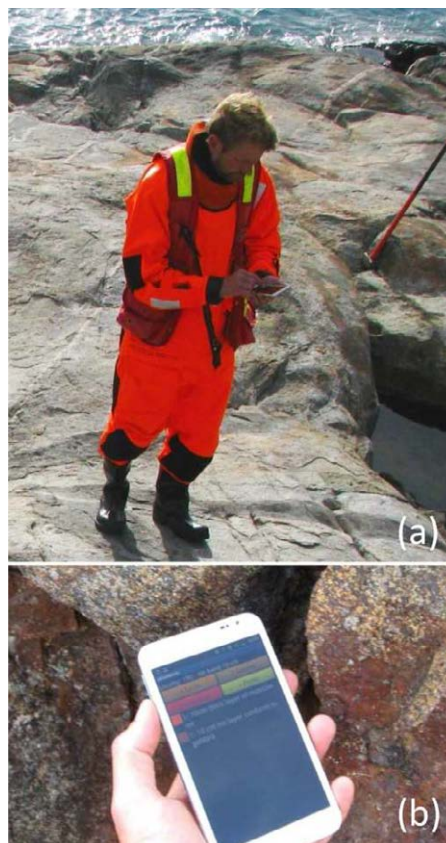


**Figure 3.** Testing of the system in the field in Greenland. (a) Data entry at outcrop. (b) The Samsung Galaxy Note (5.3").

The devices tested were (with screens sizes):

- Samsung Galaxy X Cover (3.56")
- Samsung Galaxy Note (5.3")
- Samsung Galaxy Tab 7 (7")

The devices were used throughout the field season under all weather conditions. It was concluded that the optimal size of the devices was 5" to 7". These devices could fit in a pocket on the jacket and still have a fair screen size.

## 6 Future development

It has been decided to extend the system. The version to be used in the field by GEUS in 2013 will be extended with the following functionality:

- A optimised user interface; including a uniform colour code system for the different entry points allowing the user to quickly navigate and access information
- User defined mineral templates / list of recently used minerals
- Use of the device's internal camera with support of drawing tools for annotating/drawing on top of photos
- Easy export of data to ArcGIS for data analysis and planning of fieldwork in field camp
- Use of air pressure sensors to improve altitude determinations
- Sorting of the locality list (e.g. group by day or by distance to present location)
- New information fields will be added, e.g., the user should have the option to register the type of locality, e.g. geological locality, field camp, ruins, emergency pick-up site, etc.
- Future versions of the App will also enable the user to take other kind of samples, e.g. stream sediment samples, and attribute information associated with that kind of sample.

Of high priority is a map interface on the device. The map must be off-line based and stored on the internal SD Card in the digital device. On the map interface the user should be able to:

- Show current position on a geological / topographical map
- Show the localities for this and earlier seasons and see / edit the locality description by tapping on it on the screen
- Show the paths taken during the expedition
- Show point data information (e.g. earlier rock samples with geochemistry)
- Show geo-referenced raster images (e.g. images of geophysical, geochemical and remote sensing data)

It is planned to save pre-made maps as tiles or at one of the open source off-line formats and to store routes, localities, contour lines (and, if possible also geological maps) as spatial data in a SQLite database with a SpatiaLite extension (http://code.google.com/p/spatialite-android/). This will allow the user, to some extent, to configure the map static pre-made maps by changing the contour line equidistance and decide which other point line themes to display. It might even be possible to bring a geological map stored as spatial data, allowing the geologist to query the spatial attributes and for example find localities situated in a specific geological setting.

In the future it will be possible to develop and add new modules and functionalities to the aFieldWork App, e.g., modules for collection of petrophysical data could be developed. Also the front end and back end tools for getting data and maps into the aFieldWork App and extracting data from the App, e.g., as a report of the field data captured during fieldwork will be developed further.

## 7 Conclusions

Compared to the previous PDA based system, data entry is much easier with the new Android system, and the design is made simpler and more intuitive. The presence of a real database system and look-up tables on the devices makes it possible to ensure data integrity. It also makes it easier to move data to central databases after fieldwork. The SQLite databases are binary compatible between different platforms so a SQLite database generated on an Android device can simply be moved to a Windows computer and used from this without any conversions.

The Android system is highly configurable and the large open source community makes a lot of free frameworks available.

The difference between devices with different operating systems must not be underestimated. Even though smartphones and tablets of different brands are considered equal, the difference in operating the different systems (Android, iOS and Windows 8 Mobile), can make it difficult for a user accustomed to one system to effectively operate another type without practice.

GEUS has successfully used small digital handheld devices and software for capturing data and observations on localities, earth materials, samples, etc. in remote parts of Greenland for more than five years. With the development of the new aFieldWork App GEUS consolidates this tradition further.

### Acknowledgements

### References

Buller G (2005) A conceptual approach to the development of digital geological field data collection. Open File report US Geological Survey, no. 2005-1428, 91-96

Schlatter DM, Buller, G, Larsen, U, Stensgaard, BM (2010) Digital field data capture: the Geological Survey of Denmark and Greenland experiences in Greenland. The Association of Applied Geochemistry, Explore, 147, 2-14

# Applications of LA-ICP-MS element mapping in mineral deposit research and exploration

**Simon E. Jackson**
*Geological Survey of Canada, Ottawa, ON, K1A 0E8, Canada*

**Benoit Dube**
*Geological Survey of Canada, 490 De la Couronne Street, Québec City, QC, G1K 9A9, Canada,*

**John Chapman**
*Geological Survey of Canada, 1500 - 605 Robson Street, Vancouver, BC, V6B 5J3, Canada*

**Jian-Feng Gao**
*Geological Survey of Canada, Ottawa, ON, K1A 0E8, Canada*

**Abstract.** Element mapping of geological samples by LA-ICP-MS is growing rapidly because it elegantly presents detailed information on the behaviour and paragenesis of trace elements during mineral crystallisation and precipitation processes. More often than not, it reveals complex paragenetic histories in hydrothermal minerals, which are not otherwise evident. In igneous minerals, element maps allow visualisation of the chemical evolution of the magmatic system, including changes in oxidation state.

Here, we summarise new techniques for generating *quantitative element concentration maps* of geological samples of mixed mineralogy by LA-ICP-MS. Sampling is performed as lines of edge-to-edge square spots with interspersed cleaning shots to remove surface contamination, providing spot size-limited spatial resolution. Calibration is performed by external standardisation and internal normalisation to 100% total element abundance, allowing generation of quantitative, high resolution (down to <10 μm), trace element concentration maps (down to low ppb) without any prior knowledge of mineral chemistries.

The power of the technique is illustrated using applications to testing the gold content of nodular pyrite as a potential source for orogenic gold deposits in volcano-sedimentary terrains, determining complex hydrothermal paragenesis in a porphyry gold deposit, and in measuring and applying zircon $Ce^{4+}/Ce^{3+}$ ratios as a proxy for magma oxidation state in exploration for porphyry copper deposits.

**Keywords.** Element mapping, LA-ICP-MS, mineral exploration

## 1 Introduction

With the development of sophisticated data processing software (e.g., Iolite; Hellstrom et al. 2008), 2-D element mapping by LA-ICP-MS has become routinely possible (Hellstrom et al. 2008; Woodhead et al. 2008). In the geosciences, there has been particularly strong interest in mapping element distributions in ore samples because it elegantly presents information on the behaviour and paragenesis of ore and other elements during mineral crystallisation and precipitation processes. This is especially important for trace elements that commonly do not form mineral phases in hydrothermal and magmatic ore systems.

The conventional procedure for producing element maps of petrographic samples by LA-ICP-MS is to acquire time-resolved signal intensity data during multiple, parallel, continuous line-ablations across a selected area of the section. The data are then deconvoluted and digitally combined to generate elemental signal intensity maps. There are, however, several shortcomings of this approach: (1) it results in degraded spatial resolution (i.e., resolution that is greater than the spot size) because new ablation aerosol is continuously mixing with previously ablated material; (2) spatial resolution in the X and Y directions are different, which must be accounted for during data processing; (3) it does not allow appropriate handling of surface contaminants (smearing of softer minerals during polishing and condensation of ablation products), which can be the source of very large signal artefacts, especially when samples containing low hardness sulfide phases are mapped. This contamination can result in erroneous signal enhancements of several orders of magnitude; (4) signal intensity maps are subject to substantial biases related to differing ablation efficiency of the minerals, particularly where transparent and opaque minerals coexist in the area mapped.

In this study, we present techniques for element mapping of geological samples of mixed mineralogy that eliminate the problems of surface contamination and aerosol mixing, resulting in true spot-size-limited spatial resolution. Furthermore, the techniques produce quantitative element concentration maps with no requirement for prior knowledge of the concentration of elements in the mineral grains. We then illustrate the power of this technique using three case studies: (1) locating a potential source of gold in the Musselwhite orogenic gold deposit (Ontario, Canada), which has implications for exploration for sediment-hosted and orogenic gold deposits in sedimentary terrains; (2) unravelling the complex hydrothermal paragenesis of the Colosseum intrusion-related ("porphyry") gold deposit, California; (3) explaining anomalous results encountered in applying zircon $Ce^{4+}/Ce^{3+}$ ratios as a proxy for host magma oxidation state and associated fertility for generating hydrothermal copper deposits in the Canadian cordillera of the Yukon.

## 2 Methodology

Ablation sampling was performed using a Photon

Machines Analyte.193 laser ablation sampler coupled to an Agilent 7700x quadrupole ICP-MS. The sampling protocol was to ablate lines of individual (7 to 17 µm) square spots ("line of spots" sampling - LOS), aligned edge to edge, on 7 to 17 µm line spacing. Each LOS commenced with a 30 second data acquisition with the laser off to measure instrument background. This was followed by analysis of a line of up to >100 separate spots. Each spot analysis (40 or 60 laser pulses at 20 or 30 Hz laser repetition rate) was preceded with 3-5 laser pulses, followed by 1.5 s of flushing, to rid the sample surface of contamination from mineral smearing and condensed ablation products, and allow this material to be flushed out of the sample cell. Analyses of GSE-1D or GSE-1G (USGS basaltic reference materials; Jochum and Stoll 2008) were interspersed in the LOS ablations of the sample at the rate of two per sixteen sample lines.

Signal intensity vs. time data files for each LOS were processed in three stages using in-house, automated spreadsheet software: (1) the signals for each spot ablation were detected using peak-recognition algorithms and integrated into a single reading for each element; (2) net background-corrected signal intensity data were converted to concentrations on a spot by spot basis by calibration against bracketing analyses of USGS GSD-1G or GSE 1G, and internal normalization to 100% total element abundance (Halicz and Günther 2004). This method is uniquely suited to analysis of multi-mineral samples since it requires no prior knowledge of the concentration of elements in the mineral grains and it effectively deals with instances where two or more mineral phases are ablated simultaneously (grain boundaries, inclusions). It does, however, require that all elements present in the sample at percent level concentrations are measured or can be calculated (e.g., C, O); (3) the concentration data for each LOS were combined and converted to concentration maps by assigning colours using one of three user-selectable colour scales (linear, logarithmic or percentile).

# 3 Applications

## 3.1 Auriferous nodular pyrite at the Musselwhite gold deposit, NW Ontario

The Musselwhite gold deposit is located within the North Caribou Greenstone Belt of NW Ontario. The stratigraphy in the immediate mine vicinity is dominated by mafic volcanics, banded-iron formation, felsic volcanics, siliciclastic sediments (Biczok et al. 2012) and local argillaceous units bearing diagenetic pyrite nodules ranging in size up to > 1 cm in diameter. All units in the immediate mine area have been metamorphosed at amphibolite facies. Mineralization is concentrated in hinges of tightly folded banded-iron formation and along highly-strained fold limbs, and is characterized by abundant pyrrhotite, quartz flooding, garnet and, rarely, visible gold (e.g. Biczok et al. 2012).

Large et al. (2011) have recently proposed a two-stage model for generation of some orogenic gold deposits: (1) gold and arsenic are introduced early into black shale and turbidite basins and are concentrated into early diagenetic arsenian pyrite; (2) during diagenesis and early metamorphism, the diagenetic pyrite is recrystallized to form coarser grained pyrite. Under higher grade metamorphism (lower greenschist facies and above) arsenian pyrite is converted to pyrrhotite. These processes release Au, As, S and other elements, which are concentrated by hydrothermal processes in structural sites, such as shear zones and fold hinges, within or above the black shale sequence.
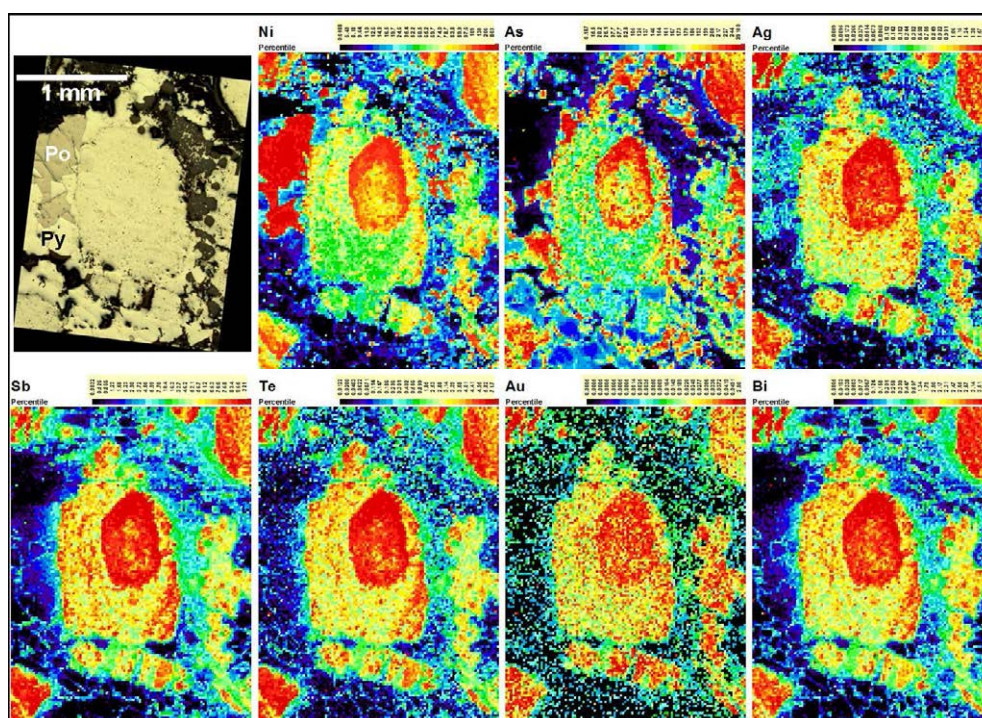


**Figure 1.** Element maps for a pyrite nodule from the vicinity of the Musselwhite mine. Note the high concentrations of Au and other trace elements in the nodule compared to recrystallised pyrite and pyrrhotite. Scales are in ppm.

LA-ICP-MS element mapping was conducted on a nodule and recrystallised framboidal pyrite from the Musselwhite area. As shown in Figure 1, element maps reveal significant metal enrichment in diagenetic pyrite nodules from a semi-massive pyrite zone, while surrounding recrystallised pyrite and pyrrhotite are barren of most elements, including gold. Gold concentrations in the zoned nodule achieve values of up to > 600 ppb. Large et al. (2011) proposed that invisible gold contents of greater than 250 ppb in diagenetic pyrite are indicative of source rocks with the potential to produce economic gold deposits. Our preliminary results need to be supported by more data before being conclusive but illustrate the potential of LA-ICP-MS mineral mapping.

### 3.2 Mineral paragenesis at the Colosseum porphyry gold deposit, California

The new methodologies have been tested on several samples of gold ore from the Colosseum gold deposit, Clark Mountains, California. This deposit is hosted within a 102 Ma rhyolite breccia pipe complex intruded into Precambrian granite gneisses. In detail, the complex consists of two small mineralised rhyolite and rhyolite breccia pipes (north and south), each approximately 150 m x 100 m and extending to over 500 m deep, connected by a rhyolite dyke. Open pit mines operated in both pipes between 1988 and 1992. The larger and higher grade deposit was centred on a breccia in the south pipe, which is thought to be the product of explosive hydrothermal fluid movements through the rhyolite and rhyolite breccia. This pipe is composed of fragments of Precambrian gneiss and younger sedimentary rock (shale and dolomite) in a matrix of rock flour, cemented by siderite and minor sericite and quartz. In this pipe, two stages of pyrite deposition are evident petrographically - an early,

coarse grained, fractured, subhedral to euhedral pyrite and later, fine-grained pyrite and intergrown base metal sulfides (largely Ccp, Sp and minor Gn, Apy and Ttr-Tnt) and gold. The matrix generally consists of siderite ± sericite. Visible gold is paragenetically late and occurs with late fine pyrite and in fracture fillings ± base metal sulfides in early pyrite.

The Colosseum element maps (Fig. 2) reveal a much more complex paragenesis than is apparent from petrographic examination, and highlight the chemical complexity common in hydrothermal systems. At least four chemically distinct stages of pyrite deposition were identified. Coarse-grained, early pyrite includes: (1) early euhedral cores of arsenian pyrite with high Ni, low Sb (Cu, Ag), and variable Au and Te in antithetic spatial relationships, showing that, while co-precipitated, they are spatially decoupled; (2) a later, low Ni-As-Sb-Au (Cu, Ag), high Te pyrite; (3) late low As-Te-Au, high Ni-Sb (Cu, Ag). Subsequently, (4) late fine-grained pyrite, enriched in Ni-As-Sb-Te-Au (Co, Cu, Zn, Ag, Pb), was deposited.

Element maps of the Colosseum ores provide an extraordinary amount of paragenetic information that could not realistically be gleaned from petrographic examination or even multiple single spot analyses alone. Element maps of this sort have wide-ranging implications, including: (1) ore processing: element mapping provides important information on the sites of the economic and deleterious elements in the ore minerals for optimising of ore processing methods; (2) metal isotope studies: as gold is monoisotopic, the isotope ratios of commonly associated elements (e.g., Ag, Sb, Te) are being considered as proxies for Au. Evident from the Colosseum element maps, however, is that these elements are not necessarily closely cogenetic with Au. Thus, their isotopic compositions may not be directly applicable to the study of hydrothermal processes that generate and localise gold deposits.
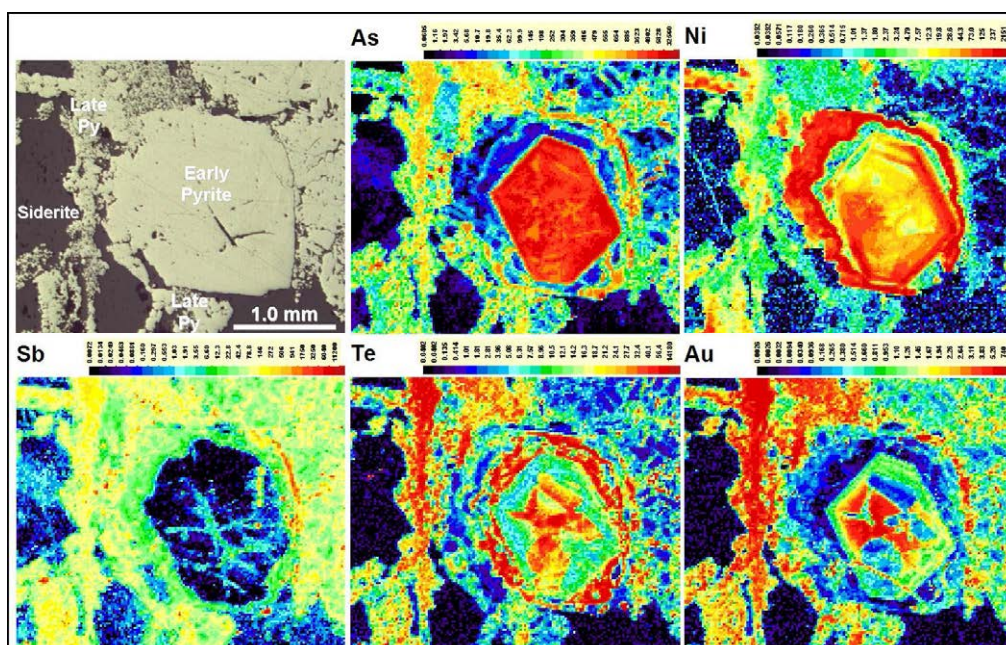


**Figure 2.** Element maps for gold ore from the Colosseum south pipe hydrothermal breccia deposit. Scales are in ppm.

### 3.3 Interpreting anomalous Ce⁴⁺/Ce³⁺ ratios in zircon, a proxy for magma fertility for porphyry copper generation

Ballard et al. (2002) demonstrated that LA-ICP-MS analyses of zircon for REE, Hf, Th and U can be used to calculate the $Ce^{4+}/Ce^{3+}$ ratio in the zircon, and that this is a robust proxy for magmatic oxygen fugacity. High $Ce^{4+}/Ce^{3+}$ ratios in zircon indicate crystallization from more oxidized magmas and values > 300 are associated with Cu-mineralized porphyry systems in the Chuquicamata-El Abra porphyry copper belt of northern Chile. This association is generally attributed to the fact that oxidised magmas do not crystallize an early sulfide phase that strips the melt of its metals. Metals are thus retained in the melt and remain available to partition into an exsolved magmatic hydrothermal fluid. Thus zircon chemistry may be used as a vector to more prospective intrusive phases in porphyritic igneous systems.

LA-ICP-MS spot analyses targeting the terminations of zircons from Cretaceous intrusive rocks in the vicinity of the major Casino porphyry Cu (Mo-Au) deposit, Yukon territory, confirm a $Ce^{4+}/Ce^{3+}$ value of about 300 as the threshold that distinguishes barren intrusive rocks from those hosting the Casino deposit (Chapman and Jackson 2012). However, zircons from sampled Jurassic intrusions in the Yukon often show very high $Ce^{4+}/Ce^{3+}$ ratios (>1,000), even for apparently barren plutons. To investigate this, we have developed procedures for high resolution (7 µm) mapping of $Ce^{4+}/Ce^{3+}$ ratios in individual zircons.
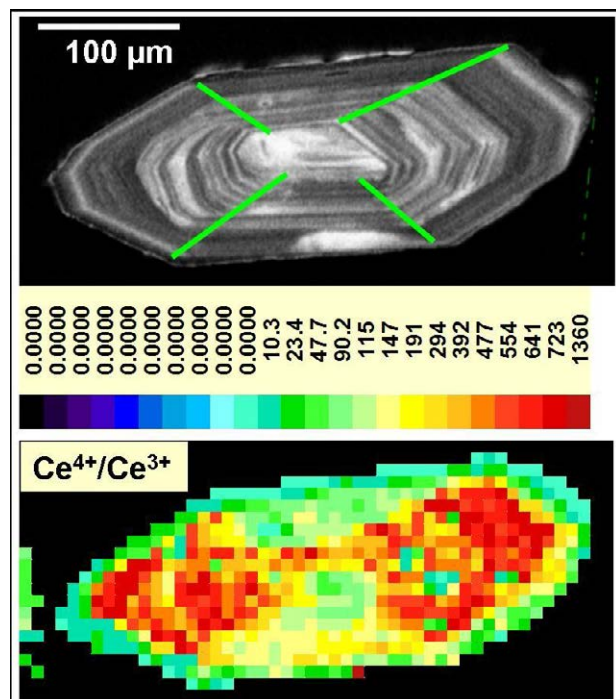


**Figure 3.** $Ce^{4+}/Ce^{3+}$ map of a Yukon Jurassic zircon showing control of sector zoning on REE distributions and resulting calculated $Ce^{4+}/Ce^{3+}$ ratios.

The Jurassic zircons studied frequently show sector zoning. Moreover, REE and $Ce^{4+}/Ce^{3+}$ maps clearly reveal that REE substitution in zircon is strongly controlled by the sector zoning such that the pyramidal

sectors of these zircons have very high calculated $Ce^{4+}/Ce^{3+}$ ratios compared to the prismatic sectors (Fig. 3). If unrecognised, this can lead to significant biases in calculated $Ce^{4+}/Ce^{3+}$ ratios for single spot analyses. In light of this, we consider that element mapping is a critical component of a robust analytical strategy for applying LA-ICP-MS zircon chemistry to exploration for porphyry Cu deposits.

## 3 Conclusions

In this work, we have demonstrated that quantitative element concentration mapping by LA-ICP-MS is routinely possible and has immense potential for unravelling complex paragenetic histories of ore forming systems. It can also be applied in mineral exploration for sediment-hosted and orogenic gold deposits in sedimentary terrain and is an essential component of a robust analytical strategy for applying LA-ICP-MS to fingerprinting potentially fertile intrusions for porphyry Cu generation using zircon $Ce^{4+}/Ce^{3+}$ ratios.

## Acknowledgements

## References

Ballard JR, Palin JM, Campbell IH (2002) Relative oxidation states of magmas inferred from Ce(IV)/Ce(III) in zircon: application to porphyry copper deposits of northern Chile. Contrib Mineral Petrol 144:347–364

Biczok J, Hollings P, Klipfel P, Heaman L, Maas R, Hamilton, M, Kamo S, Friedman R (2012). Precamb Res 192-195:209-230.

Chapman J, Jackson S, Ryan J (2012) Anomalous zircon $Ce^{4+}/Ce^{3+}$ ratios from early Jurassic plutons in Yukon: implications for porphyry exploration. Min Mag 76:1562

Halicz L, Günther D (2004) Quantitative analysis of silicates using LA-ICP-MS with liquid calibration. J Anal Atom Spectrom 19:1539-1545

Hellstrom J, Paton C, Woodhead J, Hergt J, (2008) Iolite: Software for spatially resolved LA–(QUAD and MC)–ICP–MS Analysis. Mineral Assoc Canada Short Course Series 40:343-348

Jochum K-P, Stoll B (2008) Mineral Assoc Canada Short Course Series, 40-147

Large RR, Bull SW, Maslennikov VV (2011) A Carbonaceous sedimentary source-rock model for Carlin-type and orogenic gold deposits. Econ Geol 106:331-358

Woodhead J, Hellstrom J, Paton C, Hergt J, Greig A, and Maas R (2008) A guide to depth profiling and imaging applications of LA–ICP–MS. Mineral Assoc Canada Short Course Series 40:135-145

# New precise timing constraints for Keketuohai pegmatite No. 3 vein, Altaid orogen, northwest China

**Feng Liu & Qiang Li**
*MRL Key Laboratory of Metallogeny and Mineral Assessment, Institute of Mineral Resources, Chinese Academy of Geological Sciences, Beijing, China, 10037*
**Zhixin Zhang**
*Xinjiang Research Center for Mineral Resources, Xinjiang Institute of Ecology and Geography Chinese Academy of Sciences, Urumqi , Xinjiang China, 830011*

**Abstract** No.3 pegmatite vein in Keketuohai has been famous for magmatic differentiation study. However, there are still more conflicting opinions about its geochronology. We have collected 6 molybdenites from the marginal zone of No.3 vein, whose geological features indicate hydrothermal metasomatism and implied that the molybdenite formed during the marginal zone formation. Our chronological result from 6 molybdenites indicates a Re-Os isochron age of 208.8 ± 2.4 Ma (MSWD = 0.89), which is consistent with the model age of 209.9 ± 1.3 Ma (MSWD = 0.69), implying that our result can represent the time of molybdenite depositing from the fluid. Taking into account the previous geochronological results, we suggest that formation of No.3 vein began at 209 Ma, namely the late middle-Triassic.

**Keywords**: No.3 pegmatite vein, Molybdenite, Re-Os dating, Keketuohai, China

## 1 Introduction

Hundreds of thousands of pegmatite veins were formed during the Altay orogen in northwest China. It is worldwide known that the Keketuohai pegmatite No.3 vein is the most typical pegmatite characterized by a superlarge scale composite rare metal-bearing deposit. Many researchers have persistently worked on it. Presently, the model of crystallization and differentiation from the original granitic magma has been accepted by most researchers (Zou et al., 1975, 2006; Wang et al., 1993; Chen et al., 1999; Zhu et al., 2006). However, the age of mineralization is still a matter of debate. For example, Zou et al. (2006) proposed that the No. 3 vein had formed from Carboniferous to Cretaceous, sustaining more than 200 Ma. Zhu et al. (2006) concluded that the No. 3 vein began crystallizing around 218 Ma, whereas Wang et al. (2002) and Chen et al. (1999) insisted that it formed during the Cretaceous. Our work constrains more precisely the age of formation of this vein, by Re-Os dating of molybdenite.

## 2 Geological background

Keketuohai No.3 rare metal-bearing pegmatite vein is situated in Paleozoic Kanas-Keketuohai magmatic-arc, the middle North Altay, an active belt at the continental edge of the Sinerian block (Fig.1a, b). The vein occurs in the southern outer-contact zone of the Aral granite, distributied in the southwest limits of the Keketuohai pegmatite field. The country rocks of the region have been strongly metamorphosed, mainly forming Sinian–Early Paleozoic gneisses and schists. Granitic rocks are widely distributed in the region, with intrusive bodies representing periods from the Caledonian to the Indosinian–Yanshanian. There is also a small amount of metamorphosed basic rock of Caledonian age. The No.3 vein intruded into an early Devonian gabbro (U-Pb zircon age of 408 Ma by SHRIMP, Wang et al., 2006) with
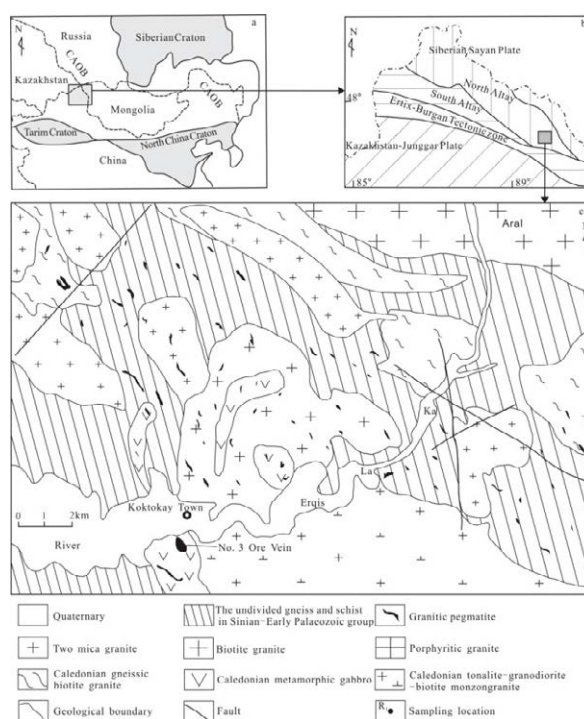
**Figure 1.** Geological tectonic map (after He et al., 2004) and simplified geological map of Keketuohai pegmatite field (after Zou et al., 2006)

sharp contacts (Fig.1c). Spatially, it is shaped like a kupola, consisting of an upper vertical pipe and a slightly tilted vein at the bottom. Based on mineralogical assemblages, the vertical pipe can be divided into nine internal zones, forming a perfect homocentric ring from outside to the center of the kupola (Zou et al., 2006).

## 3 Sample description

Six molybdenites were sampled at the contact between the vertical pipe and its wallrock, which represents the outer zone of No.3 vein. Three coarse (3

to 5 mm) molybdenites (M1, M2, M3) , coexisting with hydrogarnet, hornblende and tourmaline, were sampled from the inner contact. Three other fine grained (less than 1 mm) molybdenites (M4, M5, M6) were collected from a fine grained vein in pegmatite.

## 4 Isotopic ages

Molybdenite analyses were carried out in the Re–Os Isotope Geochronological Laboratory of the National Research Center for Geoanalysis, Beijing, China. Molybdenite dating involved pretreatment of the samples and isotope mass spectrometry measurements (Du et al., 1994, 2001, 2004). The isotope ratios of Re and Os were measured using a TJA PQ ExCell ICP–MS. Finally, the Re–Os isotopic data were processed using the software developed by Ludwig (1999), and the isochron age was then obtained. The decay constant used in the calculations was $\lambda(^{187}Re) = 1.66 \times 10^{-11}a^{-1}$ (Smoliar et al., 1996).

The analytical Re-Os isotopic data and related model ages of six molybdenites are listed in table 1.

**Table 1.** The result of Re-Os isotopic composition of molybdenite in the margin zone of No.3 vein

|     | Re ppm | Os ppb | $^{187}$Re ppm | $^{187}$Os ppb | Model age （Ma） |
| --- | --- | --- | --- | --- | --- |
| M1 | 517±5 | 0.95±0.39 | 325.1±3.1 | 1134±13 | 209±3 |
| M2 | 530±5 | 0.15±0.17 | 333±2.8 | 1170±11 | 210.6±3 |
| M3 | 552±8 | 0.34±0.90 | 346.6±4.8 | 1202±11 | 207.8±4 |
| M4 | 166±2 | 0.46±0.64 | 104±1.1 | 368±3.7 | 212.2±3 |
| M5 | 174±1 | 0.15±0.65 | 109.4±0.9 | 382±3.3 | 209.5±3 |
| M6 | 433±4 | 0.14±0.61 | 272.1±2.4 | 952±10.5 | 209.7±3 |

Their model ages vary from 207.8 ± 3.8 Ma to 212.2 ± 3.5 Ma, yielding an average weighted age of 209.9 ± 1.3 Ma (MSWD = 0.69, Fig.2). This model age is consistent with the isochron age of 208.8 ± 2.4 Ma (MSWD = 0.89, Fig.3), implying that isotopic decoupling of Re-Os within molybdenites can be neglected (Du et al., 2007). The age of 209 Ma or 210 Ma can represent the time of molybdenite depositing from the hydrothermal fluid.



Mean=209.9±1.3Ma(0.64%)95%conf.
Wtd by data-point errors only
MSWD=0.69,probability=0.63
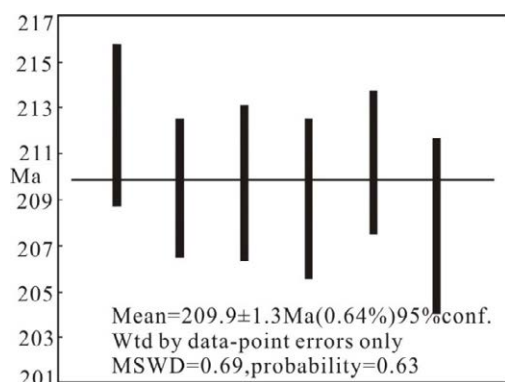
**Figure 2.** Plot of the Re-Os weighted age of molybdenite



Age=208.8±2.4Ma
Initial $^{187}$Os ng/g=3.2±6.4
MSWD=0.89
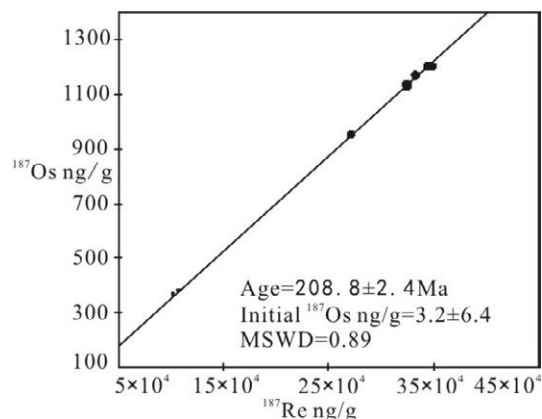
**Figure 3.** Plot of the Re-Os isochron age of molybdenite

## 5 Discussion and conclusion

Previously published ages related to No.3 vein by K-Ar, Rb-Sr and Ar-Ar dating indicates a range of crystallization ages. However, they don't show the feature of orderly crystallization from the outside to the center of the kupola. There are also obvious ages differences for a single zone, using the same or different dating technique. The ages differences between the outside and the inside zone from Zou et al. (1986) by K-Ar dating is more than 200 Ma. According to previous studies, multiple periods of strong tectonic activities took place in the Altay orogenic belt. During the formation of the pegmatite, hydrothermal activity is also very intense. So timing contraints using K-Ar or Ar-Ar dating technique may cause obvious ages differences. Rb-Sr isotope, in complicated granitic pegmatite, can generate a wide range of ages (Clark, 1982). Based on a detailed study, using Rb-Sr isotopic data which Zhu et al. (2006) obtained from No.3 vein, Zhong et al. (2011) have discovered that the Rb-Sr isotopic system is really disturbed or open.

We found that there are complications concerning the zircon ages from the No. 3 vein obtained by SHRIMP and LA-MC-ICP-MS techniques. The first complication is that the U content in zircon is generally high, the second is that most zircons were altered in varying degrees and the last is related to the metamictization, developed in many zircons, caused by the radioactive decay of U and Th (Zhong et al., 2011). Each factor makes the interpretation of the analytical data very complex. Wang et al. (2007) obtained U-Pb data from the 1th , 5th and 7th zone by SHRIMP and obtained the corresponding ages of 220 ± 9 Ma, 198 ± 7Ma and 213 ± 6 Ma, which does not display the feature of orderly crystallization toward the center of the structure. We have recently tried to date the zircon using our LA-MC-ICP-MS , but we were not successful.

After the formation of the molybdenite, it is very difficult to destroy and reset the Re-Os isotopic system (Stein et al., 1998). Re-Os age of molybdenite is often used to constrain metallogenic age. Geologically, the molybdenites we have collected were formed during the

intrusion of No.3 vein inside metamorphosed gabbro, as a result of hydrothermal metasomatism with the wallrock. Its crystallization is nearly simultaneous with the formation of the marginal zone of the vein. We have obtained an isochron age of 208.9 Ma and an average weighted model age of 209.9 Ma for six molybdenites. They are very close to the age of the 3[A] vein near to No.3 vein (208 Ma, Ren et al., 2012). So we can infer that the formation of No.3 vein began around 209 Ma or 210 Ma, which correspond to the late middle-Triassic, middle Indosinian.

## Acknowledgements

## References

Clark G S (1982) Rubidium-Strontium isotope systematic of complex granitic pegmatites. In Cerny P ed. Granitic pegmatites in science and industry. Winnipey, 347-371

Chen F W, Li H Q, Wang D H (1999) New isochronological evidence of lithogeny and metallogenesis during Yanshanian in Altay orogen, China. Science Bulletin, 44(11): 1142-1148 (in Chinese)

Du A D, He H M, Yin N W (1994) A Study on the Rhenium-Osmium geochronometry of molybdenites. Acta Geologica Sinica, 68(4): 339-347 (in Chinese with English abstract)

Du A D, Zhao D M, Wang S X, Sun D Z, Liu D Y (2001) Precise Re-Os Dating for Molybdenite by ID-NTIMS with Carius Tube Sample Preparation. Rock and Mineral Analysis, 20(4): 247-252 (in Chinese with English abstract)

Du A D, Wu S Q, Sun D Z, Wang S X, Qu W J, Ricard M H S, John M and Dmitry M (2004) Preparation and Certification of Re-Os Dating Reference Materials: Molybdenite HLP and JDC[J]. Geostandard and Geoanalytical Research, 28 (1): 41-52

Du A D, Qu W J, Wang D H, Li H M, Feng C Y, Liu H, Ren J, Zeng F G (2007) Subgrain-size decoupling of Re and [187]Os within molybdenite. Mineral deposits, 26(5): 572-580 (in Chinese with abstract)

He G Q, Cheng S D, Xu X, Li J Y, Hao J (2004) An introduction to the explanatory text of the map of tectonics in Xinjiang and its neighbouring areas. Beijing: Geological Publishing House, 1-65 (in Chinese with English abstract)

Ludwig K (1999) Isoplot/Ex, version 2.0: a geochronogical toolkit for Microsoft Excel. Geochronology Center

Ren B Q, Zhang H, Tang Y, Lv Z H (2012) LA-ICPMS U-Pb Zircon Geochronology of the Altai Pegmatites and Its Geological Significance. Acta Mineralogica Sinica, 31(3): 587-596 (in Chinese with abstract)

Smoliar M I, Walker R J and Morgan J W (1996) Re-Os ages of group IIA, IIIA, IVA and VIB iron meteorites. Science 271, 1099-1102

Stein J, Sundblad K, Markey R J, Morgan M J (1998) Re - Os ages for Archahaean molybdenite and pyrite Kuittila-Kivisuo, Finland, and Proterozoic molybdenite, Lithuania: Testing the chronometer in a metamorphic and metasomatic setting. Mineralium Depisita, 33: 329-345

Wang S Z, Kang X, Wang Y L (1993) Granitic pegmatite deposits in Altaid, China. Mineral Deposits, 12(S): 135-146 (in Chinese with English abstract)

Wang D H, Chen Y C, Xu Z G, Li T D, Fu X J (2002) Mineragenetic series and regularity of mineralization in the Altai metallogenetic Province, China. Beijing: Atomic Press, 1-493 (in Chinese)

Wang T, Hong D W, Jahn B M, Tong Y, Wang Y B, Han B F and Wang X X (2006) Timing, petrogenesis, and setting of Paleozoic synorogenic intrusions from the Altai Mountains, Northwest China: implications for the tectonic evolution of an accretionary orogen. The Journal of Geology, 114: 735-751

Wang T, Tong Y, Bor-ming J (2007) SHRIMP U-Pb Zircon geochronology of the Altai No.3Pegmatite,NW China, and its implications for the origin and tectonic setting of the pegmatite. Ore geology review, 32: 325-336

Zhu Y F, Zeng Y S, Gu L B (2006) Geochemistry of the rare metal-bearing pegmatite No. 3 vein and related granites in the Keketuohai region, Altay Mountains, northwest China. Journal of Asian Earth Sciences, 27: 61-77

Zou T R, Xu J G (1975) On the origin and classification of granite pegmatite. Geochemica, (3): 161-173 (in Chinese)

Zou T R, Zhang X A, Jia FY, Wang R C, Cao H Z, Wu B Q (1986) The origin of No.3 pegmatite in Altayshan, Xinjiang. Mineral Deposits, 5(4): 34-48 (in Chinese with English abstract)

Zou T R, Li Q C (2006) Rare metal and REE deposits in Xinjiang, China. Beijing: Geological Publishing House, 34-51 (in Chinese)

Zhong L, Wang Z H, Liu Y L (2011) The geochronology research status of Altai pegmatite, NW China: the confusion of the conventional dating methods used in granitic pegmatite. Xinjiang Geology, 29(4): 412-415 (in Chinese with English abstract)

# S/Se ratios study of Xiaorequanzi copper, zinc (selenium) deposit in East Tianshan, Xinjiang, China

MinLiu, Cheng Wenming, Zhang Zuoheng
*MLR Key Laboratory Metallogeny and Mineral Assessment, Institute of Mineral Resources, CAGS, Beijing 100037, China*

**Abstract.** The Xiaorequanzi deposit is a medium to large size copper, zinc (selenium) deposit, which was discovered in 1993 and has a good economic prospect. Selenium-rich sulfides generally exist in this deposit. There are differences in the selenium contents of different sulfides from the ore bodies and the host rocks. Among sulfides, arsenopyrite contains the lowest selenium concentration. Comprehensive research has shown that there is more than one kind of mineralized environment responsible for the formation of sulfides in the deposit. This deposit is connected to an endogenous magma.

**Keywords.** S/Se ratio, sulfide, Xiaorequanzi

## 1 General geology

The Xiaorequanzi deposit is a medium to large size copper, zinc (selenium) deposit discovered in 1993 and has a good economic prospect. It is located in the Harlik-Dananhy arc, where the Tarim and Junggar plates collide, within a former volcanogenic-dominated sedimentary basin that is now exposed on the northeastern edge of the middle Tianshan uplift. This exposed series of littoral to neritic facies from the Lower Carboniferous Xiaorequanzi Formation comprises mainly black-mottled tuffaceous sandstones, epiclastic sediments and volcaniclastic rocks along with bimodal intrusives and subvolcanic porphyries. The copper and zinc ore grade of the deposit is generally high, and is correlated with other metals and semi-metals such as gold, silver and selenium.

## 2 S/Se ratio study

A total of 241 different sulfides have been analysed by electronic microprobe, and the result shows that sulfides from the Xiaorequanzicopper-zinc deposit are generally selenium-rich. The average selenium content of the sulfides is 0.045%, the average S/Se ratio is 829. The selenium content of copper concentrate is 0.028%, with a S/Se ratio of 1099 and a Cu/Se ratio of 680. Taking pyrite as an example, the average Se content in this deposit is 0.054%, which is 1080~270 times higher than is generally seen in pyrite of sedimentary origin (0.5ppm~2ppm), and 27 times higher than in pyrite associated with endogenous magma. The selenium content of the deposit is high enough to be at an economic level. According to preliminary calculations, the deposit hosts 813 tons of Se (calculation based on 552.6 thousand tons of copper and a Cu/Se ratio of 680), which makes it a large selenium deposit. Therefore, Se should be extracted together with Cu, during the mining process.

According to microscopic identification and electron microprobe analysis, selenium in the Xiaorequanzi deposit has two main occurrences: 1. An independently mineral, and 2. in its isomorphic sulfide form. During the course of this research, Clausthalite, a lead selenide mineral was identified for the first time from this deposit. It's chemical formula is Pb(Se, S), which is the result of S replacement by Se in galena, and represents an end member of the isomorphic series between galena PbS and clausthalite PbSe (Liu et al. 1987, Wang et al. 1987). Clausthalite is mainly located on the rims of chalcopyrite, sphalerite and pyrite grains. It generally occurs with a euhedral-hypidiomorphic granular texture, and a grain size around 50~100μm. Clausthalite has been found in both deposit No.1 and No.3. The average selenium contents are respectively 10.37% and 7.44%, and their relative average Se/S ratios are 0.83 and 1.35.

The average selenium concentration in chalcopyrite, sphalerite, covellite and pyrite are 0.048%, 0.041%, 0.034% and 0.054%, with respective S/Se ratios of 717, 803, 831 and 976. Arsenopyrite has the lowest selenium concentration, less than 0.001% on average. The overall average selenium concentration of deposit No.1 is 0.076%, which is significantly higher than that of deposit No.3(0.013%). In deposit No.1, the average selenium concentration of the main sulfides, such as chalcopyrite, sphalerite and pyrite, are respectively 0.084%, 0.069% and 0.09%; and the corresponding average S/Se ratios are 413, 481 and 590. As for deposit No.3, the average selenium concentration in chalcopyrite, sphalerite and pyrite are 0.011%, 0.013% and 0.018%; and the corresponding average S/Se ratios are 984, 2615 and 2864. These data indicate that deposit No.1 and deposit No.3 formed in different mineralization environments. The mineralization temperature in deposit No.1 may be higher than in deposit No.3. In host rocks of the deposit, average selenium contents of sulfides in tuffaceous clastic rocks and chlorite rocks (including chloritized tuffaceous mudstone) are 0.056% and 0.047%, and the corresponding average S/Se ratios are 635 and 804. In the quartz vein, sulfide's selenium content is on average 0.018%, with a S/Se ratio of 2102. These data indicate that the average selenium content of sulfide in the quartz vein is lower than that in tuffaceous clastic rocks and chlorite rocks. The average S/Se ratio of the former is higher relative to the latter as well. The formation temperature of sulfide in quartz vein should be lower than in the tuffaceous clastic rocks and chlorite rocks.

## 3. Discussion

Clausthalite and selenium-bearing galena, both occur in the Xiaorequanzi copper-zinc(selenium) deposit. The $\delta^{34}S_{SV-CDT}$ value of pyrite, chalcopyrite and sphalerite ranges from 3.1‰ to 13.4‰. This indicates that the sulfur from the deposit comes from various sources, that the deposit was formed in a variety of environments and experienced several episodes of mineralization. The average selenium contents of chalcopyrite, sphalerite and pyrite in deposit No.1 are all higher than that in deposit No.3. This indicates that the mineralized environments as well as the mineralization temperature were different. The quartz vein is younger, and the mineralization temperature of formation of the sulfide in the quartz vein should be lower than in the tuffaceous clastic rocks and the chlorite rock environments. The high concentration of Se in pyrite, by comparison to concentrations observed in endogenous and sedimentary occurrences indicates that the mineralization temperature in this deposit is high and connected to magmatic activity.

## References
LiuYingjun, Cao Liming  Li Zhaolin, Wang Henian, Chu Qingtong, Zhang Jingrong. (1987)  Element Geochemistry. Geological Publishing House, Beijing, pp. 1-548 (in Chinese)

Wang Pu, Pan Zhaolu ,  Weng Lingbao. (1987) Systematic mineralogy. Geological Publishing House, Beijing, pp. 1-522 (in Chinese)

# TIN-based 3D morphological analysis method for geological interfaces and its application

Xiancheng Mao[1], Jin Chen[1], Hao Deng1, Weifang Mao[2]
[1] MOE Key Laboratory of Metallogenic Prediction of Non-ferrous Metals, School of Geosciences and Info-Physics, Central South University, China
[2] Huazhong University of Science and Technology, China

**Abstract.** For analysis of the spatial relationship between mineralization spatial distribution and geological interface shapes, this paper proposes a three-dimensional morphological analysis method for any curved surface based on TIN model by using the theories of 3D TIN model, spatial interpolation, distance field and spatial analysis. The models and algorithms implemented include (1) calculation of the general geometric parameters (slope, angle, etc.) of geological surfaces, (2) extraction of hierarchical morphology trend and morphology undulance of the surface, and (3) quantitative simulation of various ore-controlling geological factors, which are represented by ore-controlling geological fields. Finally, a case study is presented to demonstrate the effectiveness of the proposed method, in which the 3D morphological analysis is applied to the ore-controlling geological interfaces of the Dingjiashan lead-zinc deposit in Fujian Province, China.

**Keywords.** geological interface, three-dimensional morphological analysis, Triangulated Irregular Network

## 1 Introduction

A macroscopical geological interface (Hu et al. 2005) is the boundary surface or discontinuity surface of a geological body, which is also called a planar geological body (Yuan 2005; Deng 2008), and can be simulated by a surface. In nature, the metallogenic phenomena occurring at geological interfaces are ubiquitous. Mineral resources often preferentially occur at geological interfaces in various forms. When using the geological interface ore-controlling principle for prediction, the key is to accurately identify and position the geological interfaces, study their properties and understand their ore-controlling function, while integrating other metallogeny theories for further analysis (Zhang et al. 2009). Therefore, quantitative extraction and analysis of the mathematical characteristics, such as the 3D geometric shape of a geological interface, by using spatial analysis method have great significance for discovering favorable metallogenic information.

At present, the modeling of a geological interface is mainly built by using a TIN (Triangulated Irregular Network) model (Peng 2002; Zhang 2005). TIN models can triangulate scattered points without repeating in space, and make a continuous but nonoverlapping triangulated irregular network with some rule (such as

the Delaunay rule) , so as to simulate the surface of a 3D body. Such a model can eliminate redundant data in visualization, has a fixed structure and is easy for processing. In addition to representing the spatial positions of elements, it also represents the topological relationships among triangles, while keeping the original measured data, and having the advantages of representing the discontinuities at the geological interface (Lu et al. 2007; Zhu et al. 2008). Therefore, the TIN model can take account of surface features well, which accurately represents the undulating changes in surface, while avoiding the redundant data of flat areas.

To fulfil the need of morphological analysis for geological interfaces, combining with the 3D TIN model, spatial interpolation, distance field and spatial analysis theories, this paper proposes a three-dimensional morphological analysis method for any surface based on TIN. The framework includes calculation of geometric parameters (slope, angle, etc.) for the surface, and extraction of morphology trend and undulance of the curved surface. Taking Dingjiashan lead-zinc deposit in Fujian, China as a research region, we exploit the morphological analysis to geological interfaces, and build the raster models of ore-controlling geological factors, and implement the quantification and visualization of ore-controlling geological factors, which lays the foundations for construction of the stereoscopic quantitative metallogenic prediction model.

## 2 3D Morphological Analysis Algorithm

### 2.1 Slope calculation

Slope is a basic attribute of the geological interface. Based on the TIN model of a geological interface, the slope calculation of a given point at the interface means calculating the slope of the corresponding triangle of the point in the TIN model. The computational formulas are as follows:

If an arbitrary triangle $\triangle ABC$ ($A(x_1, y_1, z_1)$, $B(x_2, y_2, z_2)$, $C(x_3, y_3, z_3)$) is on TIN model, then its plane equation is $z = a_0 + a_1 x + a_2 y$. Because the slopes are equal everywhere on the plane, so the slope of the triangle is computed by equation (1), and the plane equation of the triangle is equation (2).

$$\alpha = \arccos \frac{1}{\sqrt{a_1^2 + a_2^2 + 1}} \tag{1}$$

$$\begin{vmatrix} x - x_1 & y - y_1 & z - z_1 \\ x_2 - x_1 & y_2 - y_1 & z_2 - z_1 \\ x_3 - x_1 & y_3 - y_1 & z_3 - z_1 \end{vmatrix} = 0 \tag{2}$$

Then $a_1$ and $a_2$ are:

$$a_1 = \frac{(y_2-y_1)\times(z_3-z_1)-(y_3-y_1)\times(z_2-z_1)}{(x_3-x_1)\times(y_2-y_1)-(x_2-x_1)\times(y_3-y_1)},$$

$$a_2 = \frac{(x_3-x_1)\times(z_2-z_1)-(x_2-x_1)\times(z_3-z_1)}{(x_3-x_1)\times(y_2-y_1)-(x_2-x_1)\times(y_3-y_1)} \qquad (3)$$

Finally, $a_1$ and $a_2$ are substituted in formula (1) to obtain α, namely the slope corresponding to each triangle. The procedure for the slope extraction algorithm is as follows:

Step1: Initialization.

Step2: Search for a triangle.

Step3: Obtain the plane equation for the triangle.

Step4: Calculate the plane equation coefficients $a_1$ and $a_2$ using equation (3) through solving the simultaneous equations.

Step5: According to equation (1), calculate the slope α of triangle.

Step6: Save the slope value. The label ID for the nearest triangle to a voxel is obtained through the distance field algorithm in geological space. And then the slope of triangle is assigned to the voxel.

## 2.2 Dihedral angle calculation

In the TIN model, the dihedral angle of two surfaces at a point of their intersecting curve is the dihedral angle between the two triangles which both pass through the point. For the TIN model, however, computation of the triangles which pass through the intersection curve is time-consuming. Therefore, this paper presents an efficient method to extract the dihedral angle between two surfaces, which rasterizes the surfaces first, then obtains the voxels corresponding to the intersection curve, and finally calculates the angle between the two surfaces. The procedure for the dihedral angle parameter extraction algorithm is as follows:

Step1: Initialization. The three vertices of a triangle are projected on the XY plane, such that the projected triangle $\triangle ABC$ is obtained.

Step2: Create the voxel indices.

Step3: Obtain the minimum bounding rectangle of the triangle.

Step4: Calculate the planar grids which pass through the three sides of the triangle by using the Liang-Barsky algorithm (Foley 1996) in computer graphics .

Step5: Compute the grid index $(i_x, i_y)$ inside $\triangle ABC$ using the scan line algorithm.

Step6: Repeat above steps to obtain internal grid indices in the XZ plane and YZ plane respectively, and then obtain intersections of the grid indices for the three projected planes. Finally compute the indices of the voxels which pass through the $\triangle ABC$, and record the triangle ID.

Step7: Generate a block model by computing all the triangles on the surface.

Step8: Perform the intersection for geological interface voxels. Firstly, calculate the index value of the coincident voxel in the block model, and then record the ID of the triangle which passes through the coincident voxel.

Step9: Calculate the dihedral angle between the two triangles which both pass through the same voxel. But when the voxel corresponding to the intersection can also corresponds to a vertex of a triangle, there would be many triangles passing through the voxel. In this case, calculate the dihedral angle between every two triangles and take the average as the result.

Step10: Calculate the angle between geological interfaces: first the two normals $V_1(x_1, y_1, z_1)$ and $V_2(x_2, y_2, z_2)$ which are constrained to be upward for the two triangles is calculated, and then the angle α of the normals is the dihedral angle between the two triangles, which is calculated as,

$$\alpha = \arccos\frac{x_1\times x_2 + y_1\times y_2 + z_1\times z_3}{\sqrt{x_1^2+y_1^2+z_1^2}\sqrt{x_2^2+y_2^2+z_2^2}}, \qquad (4)$$

Step11: Save the resulting dihedral angles. So the voxel set corresponding to the intersection of two surfaces is obtained, in which the dihedral angles are also contained. To extend the dihedral angle information to an entire geological space, for an arbitrary cubic cell in the geological space, its dihedral angle information is obtained by calculating the nearest distance cell in the voxel set. Here the dihedral angle of the corresponding nearest voxel is the dihedral angle information of the cell we wish to obtain.

## 2.3 Analysis of morphological trends and undulance

*1) Morphological trend*

The spatial trend shape of a geological object reflects the main geological characteristic of the object, by ignoring the local undulance. The local shape of an object can be described by the undulance in an object's surface. Trend-residual analysis method can simulate geometric morphology, and analyze spatial distribution and spatial structure for objects with a high degree of continuity and small undulance.

According to the traditional trend morphological analysis method for a curved surface, based on the TIN model, this paper uses the inverse distance squared method to analyze the trend shape of a surface. The inverse distance squared method is a weighted average interpolation method, whose basic principle is that the information between assumed sample points is related. So the information of an estimated point comes from the surrounding known points. The known points have different distances to the estimated point, so they have different effects to the estimated point. Here the influence of a known point on the estimated point is inversely proportional to the square of the distance between the estimated point and known point.

The trend morphological analysis method for surfaces is actually to replace the original elevation $z$ value of the estimated point by interpolated $z$ values of the sample points around the estimated point within a certain distance, and so as to generate the trend surface with the new interpolated $z$ values. The specific process is as follows:

Step1: Initialization.

Step2: Define a range for window analysis, that is, specify a search distance $d$, which is the 2D distance of two points on the XY plane. The sample point can participate in interpolation only if its distance to the estimated point is less than $d$.

Step3: Window analysis. Use the inverse distance squared method to calculate the new $z$ values of an estimated point:

$$z = \frac{\sum_{i=1}^{n} \frac{z_i}{d_i^2}}{\sum_{i=1}^{n} \frac{1}{d_i^2}} \qquad (5)$$

Step4: Moving window calculation for each vertex in the TIN model.

Step5: Rebuild the TIN model of the trend surface. Use the new interpolated $z$ values to build a new TIN model and so generate the trend surface.

*2) Morphological undulance*

The morphological undulance of a geological object can be described by the wave-like undulance on the surface. Such wave-like undulance can be expressed through the deviation of trend surface from its original surface. In this paper, the degree of deviation is also called amplitude, which reflects the bending of a surface and the degree of change of the undulance.

To model the morphological undulance, the previously described trend morphological analysis can be utilized. It decomposes the observation values of elevation $z$ into two components. One is the reconstructed surface of the trend of observation values, namely trend surface $T(x, y)$. Another one is the variation of the observation, regarded as signal, i.e. the residual surface $R(x, y)$: $z(x, y) = T(x, y) + R(x, y)$. So the residual surface is $R(x, y) = z(x, y) - T(x, y)$.

For a point $z(x_0, y_0)$ on the surface, the local morphology undulance at the point can be described with the corresponding absolute value of $R(x, y)$:

$$R(x_0, y_0) \begin{cases} > 0, \text{convex} \\ = 0, \text{smooth} \\ < 0, \text{concave} \end{cases} \qquad (6)$$

The procedure for the morphology undulance analysis algorithm is as follows:

Step1: Initialization.

Step2: Search for the corresponding points.

Step3: Calculate the residual value.

Step4: Reconstruct the remainder surface.

The hierarchical extraction of morphology undulance can be implemented through the above method by changing $d$ values.

The residual surface reflects the fluctuation changes of a curved surface with the amplitude in space. The amplitude of any point on the surface can be quantitatively described by the difference value between the $z$ value of the original surface and that of the trend surface at the 2D $(x, y)$ coordinate of the point. The calculation process is as follows:

If an arbitrary triangle $\triangle ABC$ ($A(x_1, y_1, z_1)$, $B(x_2, y_2, z_2)$, $C(x_3, y_3, z_3)$) is on the TIN model of the geological interface, and an arbitrary point $M(x, y, z)$ is on the plane of the triangle ABC, then the plane equation is the same as equation (2), and the $z$ value is:

$$z = \frac{b}{a} + z_1 . \qquad (7)$$

where $a = (x_2 - x_1) * (y_3 - y_1) - (y_2 - y_1) * (x_3 - x_1)$, and $b = (z_2 - z_1) * (y_3 - y_1) * (x - x_3) + (y - y_1) * (x_2 - x_1) * (z_3 - z_1) - (x - x_1) * (y_2 - y_1) * (z_3 - z_1) - (y - y_1) * (z_2 - z_1) * (x_3 - x_1)$.

Note that equation (7) fails when the triangle $\triangle ABC$ is perpendicular to XY plane. In this case, the $z$ value is set as the half of the minimum and maximum $z$ value of the triangle, that is:

$$z = \frac{z_{max} + z_{min}}{2} . \qquad (8)$$

## 3 Application

In order to demonstrate the feasibility and practicality of the above three-dimensional morphological analysis method，we have developed a system by using VC++ 6.0 platform integrated with the Microsoft Access database software under the Windows environment. To test the effectiveness of the three-dimensional morphological analysis method for surfaces by using the system, a set of real geological data of the main ore-controlling geological interface from the Dingjiashan lead-zinc deposit in Fujian of China is used in our application. Firstly we constructed the 3D TIN models and the raster models of the geological interfaces with the 3D Geological Modeling software Datamine. And then by using the proposed three-dimensional morphological extraction method, the stratum interfaces and the uncomformity surface were analyzed. Secondly, the parameters of the slope and angle were calculated, and the morphological trend and the morphological undulance of the uncomformity surface were extracted. Finally, mineralization space raster models were constructed to represent the ore-controlling geological factor fields.

With the three-dimensional morphological analysis system, the slope factor $g$U of the uncomformity surface is acquired. Its raster model is given as Figure 1a. Figure 1b illustrates the dihedral angle factor $a$U_S between the uncomformity surface and the stratum interfaces. The undulance factors of the uncomformity surface were extracted, aiming at revealing the ore-controlling influence of the uncomformity surface mophology on the geological space surrounding the uncomformity surface. The extracted factors, $wa$U and $wb$U, are illustrated in Figure 1c-d, which denote the 1st-level and 2nd-level undulance of the uncomformity surface respectively.

## 4 Conclusion

This paper has proposed a three-dimensional morphological analysis method for TIN modeled surfaces, in which spatial interpolation, distance field and spatial analysis theories are integrated. The proposed method effectively and efficiently achieves computation of the geometric parameters, such as slope and angle of a

curved surface, as well as extraction of the morphological trend and the morphological undulance of geological surfaces, and so enables quantitative extraction of ore-controlling geological factors in 3D geological space.

By applying the morphological analysis method to the Dingjiashan lead-zinc deposit in Fujian Province of China, the morphology of the geological interfaces such as the uncomformity surface and stratum interfaces were analysed. A resulting series of correlative geological morphological factors related to lead-zinc mineralization were extracted. Thus the geological phenomenon are able to be quantitatively described, which plays an important role in metallogenic prediction.
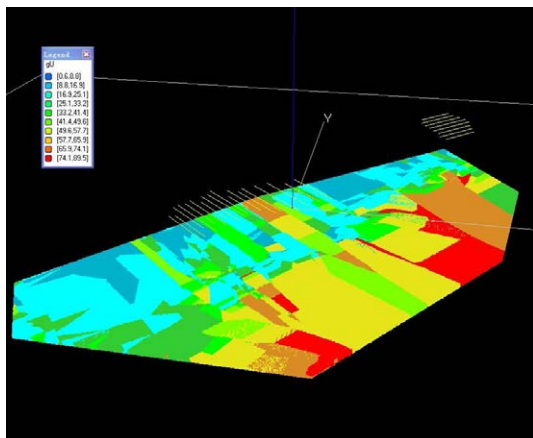


(a) Uncomformity surface slope factor (*g*U)
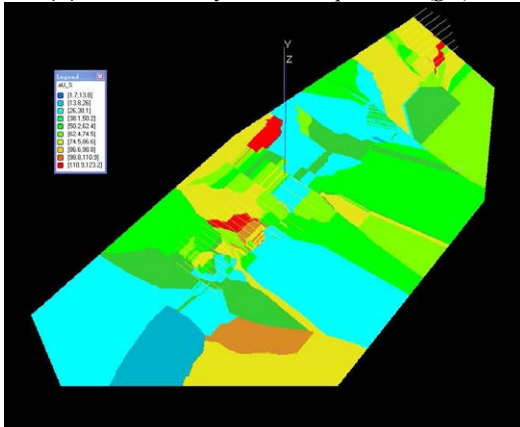


(b) Angle factor (*a*U_S) between the uncomformity surface and the geological interfaces
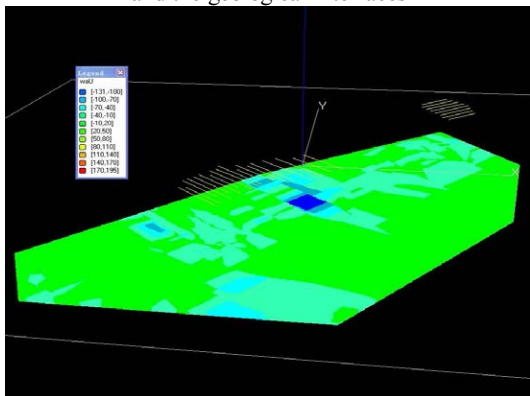


(c) 1st-level morphological undulance (*wa*U)
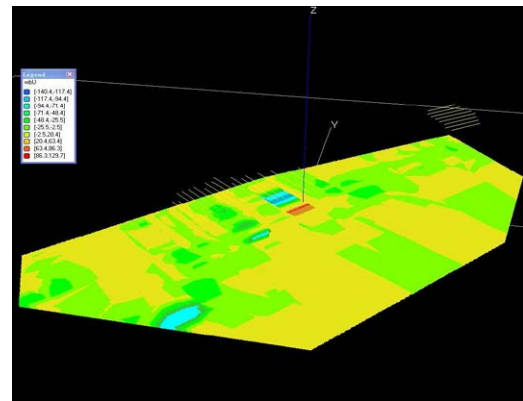


(d) 2nd-level morphological undulance (*wb*U)

**Figure 1.** The raster models (from -150m to -200m elevation) of the uncomformity surface morphological factors.

## Acknowledgements

## References

Deng H (2008). Study on 3d geological modeling and spatial analysis for prediction of buried ore bodies. Thesis of Central South University, China (In Chinese)

Foley DJ (1996). Computer graphics: principles and practice. Addison-Wesley Professional: pp 117

Hu M, Xu B, Cao X, Zhang K (2005). Control significance of geological surface for Pb-Zn ore deposits in guizhong depression. Earth Science-Journal of China University of Geoscience 30: 353-357

Lu L, Guo H (2007). Visualization of a digital elevation model. Data Science Journal 6: 481-484

Peng Y (2002). Studying on three-dimension visualization and real-time rendering of terrain. Thesis of Southwest Jiaotong University, China (In Chinese)

Yuan B (2005). Research on 3d grid geological modeling and spatial analysis method. Thesis of Xi'an University of Science and Technology, China (In Chinese)

Zhang H (2005). Research on three dimensional modeling of complicated geological interfaces. Thesis of Xi'an University of Science and Technology, China (In Chinese)

Zhang S, Lu X, Deng G, Zhou X (2009). Ore-controlling mechanism of geological interface and the key of application. Geological Science and Technology Information 28: 51-56

Zhu Q, Zhang Y, Li F (2008). Three-dimensional TIN algorithm for digital terrain modeling. Geo-spatial Information Science 6: 79-85

# Geology and exploration model of the world-class Bakyrchik gold deposit, East Kazakhstan

**Indira Mataibayeva, Olga Frolova, Anastassiya Miroshnikova**
*East Kazakh State Technical University, Ust-Kamenogorsk, Kazakhstan*

**Mikhail Rafailovich**
*YugGeo, Almaty, Kazakhstan*

**Abstract.** Geology of the Bakyrchik type of gold deposits in carbonaceous terrigenous rocks is described, including model of axial zoning of ore and primary geochemical halos. An exploration model for this deposit is also proposed.

**Keywords.** Geology, Bakyrchik deposit, exploration model, gold, Kazakhstan.

## 1 Introduction

The Bakyrchik geological and economic type of gold deposits is the most important category of ore closely related to mineralized carbonaceous terrigenous rocks. The reference world-class giant Bakyrchik deposit is located in the West Kalba metallogenic zone formed in the Late Paleozoic as a linear suture between the Kazakhstan and Altay-Mongolian paleocontinents.

## 2 Geology and metallogeny

The NW-trending West Kalba lithotectonic zone adjoins the Kalba-Naryn rare-metal belt in the northeast. The Shar-Gornostaevka ophiolitic suture plunging beneath the gold-bearing Kalba is its southwestern boundary (Fig. 1).

At the level of the upper mantle, a swell-like doming of the asthenosphere with the upper edge at a depth of 65 km as opposed to 130 km in the adjacent structural areas corresponds to the West Kalba zone. The epicenter of this doming fits the Miyaly Uplift – a complexly differentiated paleovolcanic arc clearly expressed in gravity field, seismic and electric sections (Lyubetsky, 2008). The contrasting increase in thickness of granulitic-basic layer and the reduction of granitic-metamorphic layer are typical. In regional gravity field data, the West Kalba is manifested as a zone of high gradients dividing positive and negative anomalies pertaining to neighboring metallogenic zones.

The nearly latitudinal shear zones and faults that break the region into a series of stepwise blocks play a special role in localization of the gold-sulfide deposits. These shear zones and faults are elements of the trans-regional Kyzylovo-Serebryansk Lineament traced by V.N. Lyubetsky in geophysical fields from the Gorny Altay to the Shyngyz Range. The Bakyrchik ore district and the reference Bakyrchik deposit within it are related to the latitudinal Kyzylovo Shear Zone.

The Kyzylovo Shear Zone, gently dipping to the north, cuts the Carboniferous carbonaceous terrigenous

complex that is characterized by elevated magnetization, owing to the enrichment in pyrrhotite.
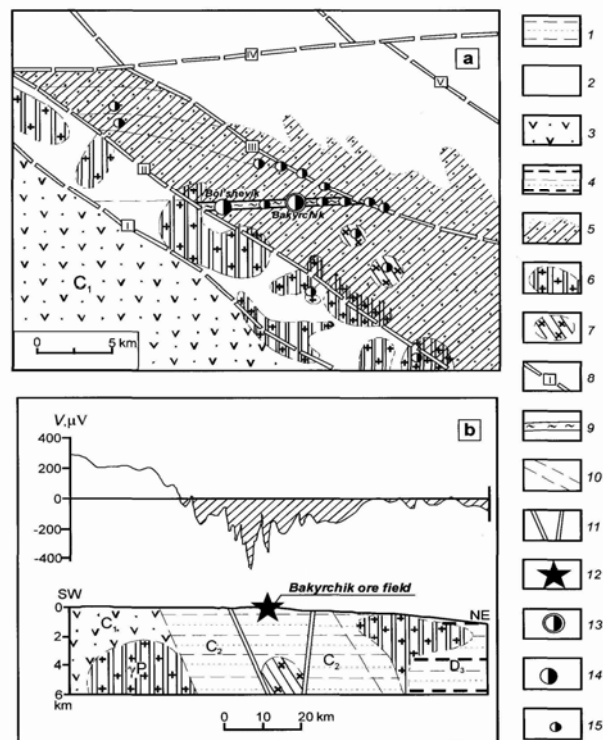


**Figure 1.** The Bakyrchik gold district in East Kazakhstan: (a) geological scheme and (b) curve of redox potential and geological section across the ore district, (*after Narseev and Bortsov, 2001*)

(1) Middle Carboniferous carbonaceous terrigenous complex; (2) Lower and Middle Carboniferous carbonaceous terrigenous complexes, unspecified; (3) Lower Carboniferous volcanic-terrigenous complex of the Shar (Charsk) Zone; (4) Upper Devonian black shale, siltstone, and sandstone of the Takyr Formation; (5) fields of carbonaceous terrigenous rocks with elevated magnetization (250-500-10 5 CGSM and higher); (6, 7) buried granitic plutons: (6) Permian Kalba Complex and (7) Late Carboniferous Kunush Complex; (5) master faults (numerals in boxes): I, Shar (Igorevka); II, West Kalba; III, Northwestern; IV, Miyaly; V, Seismic; (9) Kyzylovo Shear Zone; (10) other faults; (11) faults inferred from seismic data; (12-15) gold deposits and ore fields: (12) Bakyrchik ore field, (13) giant Bakyrchik deposit; (14) large Bolshevik deposit, (15) small Bakyrchik-type deposits.

The most important ore-controlling structural elements – thrust-fault sutures with angular bends of their surfaces, tectonic lenses, cataclastic zones, cleavage, mylonitization, boudinage, intraformational detachments, and diamictite units. According to Bortsov and Mizernaya, the Kyzylovo Shear Zone is

characterized by negative anomalies of natural polarization reaching -100 to -300 mV against the background values of 0 to -50 mV in barren sequences (data of SP geophysical exploration method). The zones of carbonic metasomatisn and superimposed sulfidation in thermal fields of intrusions pertaining to the Kunush Complex are additionally noted by anomalies of induced polarization in intensity of 5-10% (Mizernaya, 2001).

The Bakyrchik deposit is hosted in carbonaceous terrigenous rocks (siltstone, sandstone, gravelstone, conglomerate) containing pyrite-pyrrhotite, ferrous carbonate (siderite, ankerite), and phosphate mineralization. Tectonic and gravity diamictites are typical. These coarse clastic, unsorted, and non-stratified complexes of rocks with sandstone, siltstone, and shale fragments cemented by coaly and clayey material are reservoir rocks and geochemical barriers controlling the formation and localization of gold mineralization (Narseev et al., 2001). Diagenetic alteration and early metamorphism correspond to the zeolite facies. The carbonaceous matter belongs to the kerite-anthraxolite-shungite-graphite-bitumoid series. Dispersed carbon, plant remnants, spore and pollen complexes are contained in the productive unit. The Bakyrchik deposit is characterized by chains of 2D-ordered carbonic matter, hexagonal graphite polycrystals, fine tabular crystalline aggregates of shungite, montmorillonite films, and colloform silica. Linear carbon polymer (carbine) occurs occasionally. A significant percentage of gold at the Bakyrchik deposit is concentrated in carbonaceous matter. Electron microscope examination shows that the finest grains of native gold are contained in shungite (Marchenko, 2007). In bitumoids of the alcohol-benzene fraction, gold is linked to carbonyl-carboxyl hydrocarbons. Other Au-bearing organometallic compounds are suggested. The quantity of gold contained in carbon-bearing compounds can attain 10-30% of its total amount in ore (Marchenko, 2007).

The relationships of carbonaceous terrigenous and volcanic rocks are of special interest. Andesitic and trachyandesitic subvolcanic intrusions, including interformational sills; lava flows and tuffaceous interlayers of the same composition; dacitic tuffs and tuffites; and silicic volcanic rocks are known in the Bakyrchik formation. These not easily identified rocks are distinct indicators of formation conditions of the host sequence and specific elements of the pre-ore stage. Intermediate volcanic rocks of elevated alkalinity: andesitic, trachyandesitic, and trachytic lavas, tuffs, tuffites, tuffstones, tuffaceous siltstones, and other pyroclastic rocks are predominant (Zenkova, 1975). Submarine volcanic eruptions are coeval with terrigenous sedimentation. Breccias consisting of fragments of volcanic rocks (50-70%) cemented by coaly and clayey material and transformed into quartz-sericite aggregate are typical. The fragments are enriched in acicular arsenopyrite. Tuffaceous siltstone and silty claystone also contain arsenopyrite grains. Pyrite commonly concentrates in chemogenic-terrigenous cherty-clayey, calcareous clayey, and clayey-calcareous-phosphate rocks. The rhythmic pulsatory mechanism of sedimentation and volcanic activity controlled the variable distribution of organic matter, carbonates, silica,

sulfides, and trace elements (Au, As, Fe, P, Ni, B, Cl, etc.) in rocks of the Bakyrchik Formation. The Middle Carboniferous terrigenous rocks of this formation and volcanics incorporated therein can be correlated with the coeval carbonaceous terrigenous and volcanic rocks (sandstone, siltstone, volcanogenic sandstone, tuffaceous siltstone, and tuffaceous breccia) of the Karashakh Formation in Uzbekistan, which hosts the giant gold-sulfide orebody at the Kokpatas deposit. The intrusive rocks at the Bakyrchik deposit comprise minor stocks and dikes of the Late Carboniferous Qunush diorite-granodiorite-plagiogranite complex. The granitoid magma chamber occurs at a depth of 3.0-3.5 km, whereas dikes are localized above within the ore-bearing thrust-fault zone. The Au-PGE-bearing "carbonic fluidisite" inferred to be explosive in origin is noteable (Marchenko, 2007).

A model of vertical axial zoning of ore and primary geochemical halos at the Bakyrchik deposit is as follows: V, Ni, Co, Cr – Sn, Zr, Cu, Mo, W – As, Au – Zn, Pb, Ag – Sr, Ba – Sb, Hg (Novozhilov and Gavrilov, 1999). The ordering of elements in pyrite and arsenopyrite (from deep to shallow): Sn, Bi, As – Cu, Ni, Co, Mo – Zn, Pb – Ag, Sb, Hg is consistent with this series. The Cu contents in pyrite and arsenopyrite are 0.8-1.0% at middle and deep levels and 0.1-0.3% in the near-surface zone (Fig. 2). Pyrite and arsenopyrite from the upper level are enriched in Sb (up to 1%) and Hg (up to a few ppm).
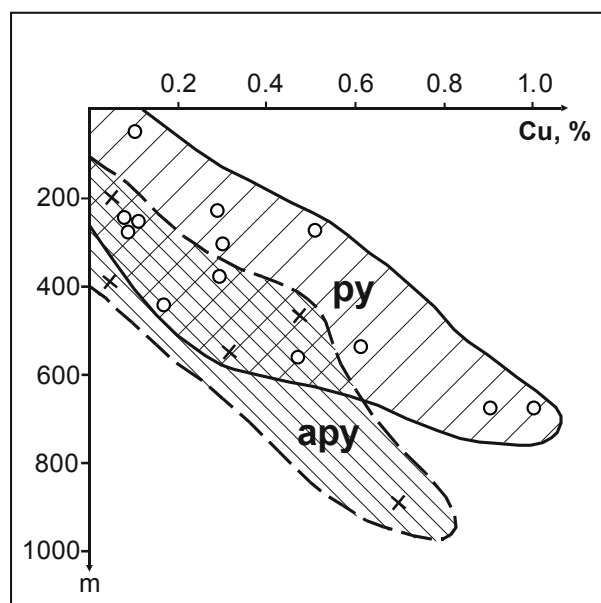


**Figure 2.** Cu content in pyrite (py) and arsenopyrite (apy) at depths of 0-1000m at the Bakyrchik deposit *(after Rafailovich, 2011)*

The ore from the Bakyrchik deposit is important as a source of PGM. The Pt and Os contents in sulfidized silty sandstones attain a few gpt (stripping voltammetry analysis). High PGM concentrations are characteristic of stringer-disseminated pyrite-arsenopyrite ore (gpt): 5.71 Pt, 2.8 Os, 3.2 Ir and 0.27 Pt. Platinum accumulates in gravity and flotation concentrates (first gpt). Further studies of reproducibility of PGM contents and the an in-depth study of their speciation are necessary (Rafailovich, 2008).

## 3 Summary

The significance of the Bakyrchik deposit as a type example of ore hosted in carbonaceous terrigenous sequences and as a model of a giant deposit with a long and complex evolution can scarcely be exaggerated. The reference chronological events in its history were (1) near-shore marine and deltaic sedimentation with formation of vast fields of the source carbonaceous terrigenous formation; (2) metamorphism, fold-and-nappe and ductile deformation, localization of shear zones and screens, rejuvenation and concentration of primary ore; (3) fluid and magmatic activity and metasomatism as a result of collision and accretion. The distinct multistage evolution, several mineralisation sources, stepwise concentration of gold, contrasting zoning, and location in a relatively restricted geological volume are the defining characteristics of the Bakyrchik deposit.

## References

Lyubetsky VN (2008) Deep structure and geodynamics of the belt hosting super-large deposits. Geosciences of Kazakhstan, pp 22-33

Marchenko LG (2007) Model of noble metal deposits with mineralization finely dispersed in black shales. Geology and protection of subsoil 1:33-41

Mizernaya MA (2001) Shungites of the West Kalba: formation localization and criteria of forecasting. PhD thesis Ust-Kamenogorsk, pp 30

Narseev VA, Gostev YV, Zakharov AV (2001) Bakyrchik: geology, geochemistry and mineralization. Moscow CSRGEI, pp 174

Novozhilov YI, Gavrilov AM (1999) Gold-sulfide deposits hosted in carbonaceous terrigenous sequences. Moscow, p 175

Rafailovich MS (2008) PGE in subsurface of Kazakhstan: systematics of deposits, mineral species, and resources. Geology and protection of subsoil 4: 9-19

Rafailovich MS (2011) Large gold deposits in black shales: formation mechanisms and similarities. Luxe Media Group, Almaty, 272 pages

Zenkova VI (1975) Formation of rocks and ores at the Bakyrchik gold deposit. Geology, geochemistry, and mineralogy of the gold districts and deposits of Kazakhstan. Almaty, pp 104-113

*All references are in Russian*

# Re-Os ages for sulphides from the (gold-)polymetallic deposits in the eastern metamorphic cover of the Karkonosze Massif (SW Poland)

**Stanisław Z. Mikulski**
*Polish Geological Institute – National Research Institute, Rakowiecka St. 4, 00-975 Warszawa, Poland*

**Holly J. Stein**
*AIRIE Program, Department of Geosciences, Colorado State University, Fort Collins, CO 80523-1482 USA and CEED Centre of Excellence, University of Oslo, Norway*

**Abstract.** Several sulphide samples (molybdenites, Co-arsenopyrites, arsenopyrite and pyrrhotite) from 3 different polymetallic deposits located in the eastern metamorphic cover of the Karkonosze Massif were subject of Re-Os studies. Molybdenites from the Kowary Fe-U deposit yield Re-Os ages of 312 ± 1 Ma, whereas the one molybdenite sample from the Miedzianka Cu deposit gives 305 ± 15 Ma. Most of other studied sulphides have low Os contents and are impacted by Os contributions from procedural blanks. None are low level highly radiogenic (LLHR) sulphides except for one – massive arsenopyrite from the Czarnów As-Au deposit which has a high $^{187}Re/^{188}Os$ ratio of 18,415 and an associated $^{187}Os/^{188}Os$ of 97.0. No matter what reasonable initial $^{187}Os/^{188}Os$ we assume for the age calculation, it has an age in the range of 315-309 Ma. The crystallization of molybdenites and massive arsenopyrite is related to post-magmatic pneumatolitic/hydrothermal processes associated with the younger medium- and fine-grained Karkonosze granitoids which are dated at ca. 317-310 Ma. The youngest determined molybdenite age, from the Miedzianka Cu deposit (213 ± 1 Ma), indicates molybdenite deposition during tectonic activity in the Intra-Sudetic fault zone on the southern margin of the Zechstein basin in the Upper Permian.

**Keywords.** molybdenite, arsenopyrite, Re-Os, Sudetes, Bohemian Massif

## 1 Introduction

The Re-Os method has been successfully applied to molybdenite and also applied to other sulphides with much lower concentrations of Re and Os, but with very high Re/Os ratios. Such sulphides are referred to as LLHR (low level highly radiogenic), as their Os isotopic composition mimics molybdenite (Stein et al. 2000). LLHR sulphides are samples whose $^{187}Os$ dominates the total Os. They are common in some hydrothermal environments, and may be particularly common in small crustally-derived deposits (Stein et al. 2001). Analysis of samples with extremely low-level Os contents may be dominated by Os contributions from procedural blanks (Markey et al. 2003). Subtraction of blank contributions in such cases may result in significant adjustments to the $^{187}Os/^{188}Os$ ratio, with a commensurate increase in the uncertainties of both the isotopic composition and the concentration of Os in the samples.



**Figure 1.** Location of polymetallic deposits studied by Re-Os sulphide dating

## 2 Geological setting

Small (gold-)polymetallic deposits are located in the eastern metamorphic cover of the Variscan Karkonosze granitoid massif in the Sudetic Block (Fig. 1). This area constitutes the NE margin of the Bohemian Massif and forms the eastern elongation of the Saxothuringian zone of the central European Variscides. In the eastern

metamorphic cover of the Karkonosze massif three lithostratigraphic units (Kowary-Czarnów, Leszczyniec and Przybkowice) of Lower Paleozoic age were distinguished based on geochemical and tectonic analysis (Kozdrój, 2003). They are in tectonic contact and have different rock compositions and metamorphic grades from greenschist facies (south) to amphibolite facies (north). The metamorphism occurred during Famennian to Tournaisian (ca. 375-345 Ma) based on Ar-Ar on micas (Marheine et al. 2002).

The rocks are strongly folded and crossed by several faults; they generally strike NE-SW with dips of 65-75° SE. These units originated in distant geotectonic environments, which were juxtaposed into a prism of nappes during the Variscan orogeny (Kozdrój, 2003). In the final stages of the Variscan orogeny post-kinematic granitoids of the Karkonosze massif (KM) and numerous syn-plutonic (composite) mafic dykes, pegmatites and quartz veins with ore mineralization were emplaced. The KM is classified as a post-collisional intrusion of *S*-type and *I*-type granites (e.g. Mikulski 2007). SHRIMP data for Karkonosze granitoids provide Carboniferous ages from ca. 325 to 300 Ma (e.g. Machowiak, Armstrong 2007; Kusiak et al. 2009; Kryza et al. 2012). Re-Os data for molybdenites from the KM provide ages from 326 ± 1 to 310 ± 1 Ma (Mikulski and Stein, 2011). Molybdenite formation reflects two main periods of post-magmatic pneumatolitic/hydrothermal activities in the Carboniferous.

## 2 Sulphide mineralization and Re-Os results

### 2.1 The Miedzianka Cu deposit

In the northern part of the Rudawy Janowickie Mountains in Miedzianka-Ciechanowice, rich polymetallic sulphide mineralization is dominated by copper ores. Ore mineralization appears within numerous small quartz veins which cut Lower Paleozoic volcanic-metasedimentary rocks representing several lithotectonic units (e.g. Teisseyre, 1968; Kozdrój, 2003). These rocks were metamorphosed first to amphibolite grade and carry a retrograde greenschist facies overprint. Four main vein systems dominated by W-E and NW-SE strike directions are distinguished. Veins are steeply dipping (70-80°) to the N or S-SE. They have variable thickness (5-30 cm; maximum 3 m) and strike length (up to 200 m), and depth (100-120 m). The main ore mineral is chalcopyrite. Chalcocite, bornite, covellite, malachite,

tetrahedrite, arsenopyrite, sphalerite, galena, pyrite, pyrrhotite, uraninite, nasturane and numerous rare minerals such as argentite or proustite may also be present (Zimnoch, 1978). Among the gangue minerals quartz and associated chlorite, hornblende, diopside, epidote, barite and calcite dominate.

We analyzed two sulphide samples: a molybdenite and a Co-bearing arsenopyrite. Molybdenite is rare in this deposit. However, it may occur in quartz veins as aggregates up to a several cm in size. Our molybdenite sample forms tiny blades (<0.5 mm) which constitute an aggregate (up to 5 cm long) intergrowth with quartz. This gangue quartz may also contain K-feldspar and fine-grained pyrite. The MDT-998 analysis shows a low concentration of Re and $^{187}$Os, ca. 0.225 ppm and 0.5042 ppb, respectively (Table 1). This molybdenite yields a Re-Os age of 213 ± 1 Ma. The larger uncertainty for the 305 Ma Re-Os age of MDT-991 sample is the result of over spiking.

**Table 1.** Re-Os data for molybdenite from the Miedzianka (1-2) and Kowary (3-4) deposits

| (Sample) | Re, ppm | $^{187}$Os, ppb | Age, Ma |
|---|---|---|---|
| 1. MDT-991 | 0.22 (1) | 0.7025 (3) | 305 ± 15 |
| 2. MDT-998 | 0.225 (1) | 0.5042 (2) | 213 ± 1 |
| 3. MDID-685 | 22.42 (2) | 73.48 (6) | 312 ± 1 |
| 4. MDT-997a | 2.9700 (9) | 9.718 (4) | 312 ± 1 |

Footnotes to Table 1:

(1) Assumed initial $^{187}$Os/$^{188}$Os for age calculation = 0.2 ± 0.1

(2) 2σ ages include all analytical and $^{187}$Re decay constant errors

(3) Decay constant used for $^{187}$Re is 1.666 x 10$^{-11}$yr$^{-1}$ (Smoliar et al. 1996) and age calculated using $^{187}$Os = $^{187}$Re (e$^{\lambda t}$ − 1)

(4) Blanks are: Re = 0.72 ± 0.01 pg, total Os = 0.730 ± 0.002 pg, $^{187}$Os/$^{188}$Os = 0.257 ± 0.001

The sample of cobaltiferous arsenopyrite represents disseminated semi-massive crystalline aggregates of coarse-grained euhedral crystals in strongly altered amphibolitic rocks. Co-arsenopyrite has a constant cobaltium admixture up to 0.7 wt%. Additionally it may contains tiny inclusions of electrum and other ore minerals. Co-arsenopyrite is cataclased and locally overprinted by younger generations of base metal sulphides. Because Co-arsenopyrite contains low Re and extremely low Os concentrations (1.3-1.7 ppt) (Table 2), knowledge of blank correction and blank uncertainty is crucial. In this case, blank constitutes 30-50% of the

total Os and hence these data should be treated with caution. Ratios of $^{187}$Re to $^{188}$Os are low (283 for LL-517 and 465 for LL-487) showing that Co-arsenopyrite from Miedzianka is not LLHR (Stein et al. 2000).

## 2.2. The Kowary Fe-U-polymetallic deposit

Two molybdenites (MDID-685 and MDT-997a) were collected from the dump at the abandoned Kowary Fe and U mine, located in the southern part of the eastern metamorphic cover of KM (Fig. 1). Molybdenite occurs along fractures in calc-silicate (skarn-like) rocks as curved blades and aggregates up to 3 cm in diameter. Molybdenite is commonly associated with fine- and medium-grained euhedral arsenopyrite which forms irregular aggregates up to a few cm in size. In addition, chalcopyrite and pyrrhotite may occur. Arsenopyrite may contain inclusions of galena and rarely of Bi minerals. Molybdenite and arsenopyrite are accompanied by gangue quartz and carbonates which infill fractures in these skarn-like rocks. Analyzed molybdenites have Re concentrations of 22 and 3 ppm (Table 1). Both molybdenites provided a Re-Os age of 312 ± 1 Ma.

## 2.3. The Czarnów Au-As-polymetallic deposit

At the Czarnów deposit, a steeply dipping quartz-ore lode/vein (~ 80°SE) is hosted by Lower Paleozoic mica schists, calc-silicate rocks, amphibolites, and gneisses, which are in close contact on the western margin with the KM (Fig. 1). The vein is several meters thick and about 500 m long and has a SW-NE direction of strike. The ore mineralization is composed mostly of arsenopyrite and pyrrhotite that form lens-like bodies within the main quartz vein or semi-massive impregnations that form lense-like bodies in the country rocks. Gold ore is also associated with polymetallic sulphides (pyrite, galena, sphalerite, stibnite, and others), magnetite or cassiterite. Native gold is also found together with electrum, and Bi-, and Ag-minerals as fine inclusions (up to 20 μm in size) and occurs as micro-veinlets within sulphides (Mikulski, 2010). Arsenopyrite occurs in two forms: massive and coarse-grained euhedral crystals in quartz or country rocks. As a rule, massive arsenopyrite is intergrown with patches of fine-grained pyrrhotite, pyrite and chalcopyrite (up to 1.5cm).

For Re-Os studies, three sulphide samples were selected: massive arsenopyrite, Co-bearing arsenopyrite and massive pyrrhotite. For arsenopyrite sample LL-580, Re concentration is well determined at 3.356 ppb. This is an extreme LLHR sample with $^{187}$Re/$^{188}$Os of 18,415 and

an associated $^{187}$Os/$^{188}$Os of 97.0. No matter what reasonable initial $^{187}$Os/$^{188}$Os we assume for the age calculation, we still have an age in the range of 315-309 Ma. The data in Table 2 show a Re-Os age of 315 for an initial $^{187}$Os/$^{188}$Os of 0.2 (our default ratio).

Although the Czarnów pyrrhotite (LL-579) has a similar Os concentration, this pyrrhotite is dominated by common Os (80%) and a model age cannot be calculated without good knowledge of the initial Os ratio. The Re concentration is somewhat higher than Co-rich arsenopyrites, but Os concentrations are low (Table 2).

**Table 2.** Re-Os data for sulphides from the E-metamorphic cover of the Karkonosze massif; 1–2 - Miedzianka Cu deposit; 3–5 - Czarnów Au-As deposit

| (Sample) | Re, ppb | Os, ppb | Model Age, Ma |
|---|---|---|---|
| 1. LL-487; co-asp | 0.1013(8) | 0.00126(1) | not LLHR |
| 2. LL-517; co-asp | 0.0778(3) | 0.00167(2) | not LLHR |
| 3. LL-580, asp | 3.356(6) | 0.012(12) | ca. 315 |
| 4. LL-579; po | 0.327(4) | 0.01102(5) | not LLHR |
| 5. LL-516; co-asp | 0.0579(3) | 0.00430(2) | not LLHR |

Footnotes to Table 2:

(1) Assumed initial $^{187}$Os/$^{188}$Os for age calculation = 0.2

(2) Absolute uncertainties at 1σ for last digit indicated

(3) Sample-spike equilibrium through Carius tube dissolution using single $^{185}$Re and $^{190}$Os spikes; ratios measured by NTIMS

(4) Blanks are: Re = 16.3 ± 0.03 pg, total Os = 0.285 ± 0.001 pg, $^{187}$Os/$^{188}$Os = 0.216 ± 0.001

(5) Abbreviation: co-asp – cobaltiferous arsenopyrite; asp – arsenopyrite; po – pyrrhotite

## 3 Discussion

Re-Os ages for two molybdenites samples from the Kowary Fe-U deposit yield identical ages of 312 ± 1 Ma. This age is comparable with Re-Os ages of molybdenites from the Szklarska Poręba (315 ± 1 Ma) and Michałowice (310 ± 1 Ma) granite quarries on the Karkonosze massif (Mikulski and Stein, 2011). We suggested that precipitation of the studied sulphides reflect post-magmatic pneumatolitic/hydrothermal processes associated directly with emplacement of medium-, and fine-grained granites dated at ca. 315 Ma (e.g. Marheine et al. 2002).

Only one of the five studied sulphides provided a very high $^{187}$Re/$^{188}$Os ratio (>18,000) that can be used to calculate a model age. Ages calculated using a range of

initial Os ratios show that the Re-Os age for this LLHR massive arsenopyrite is almost certainly between 315 and 309 Ma. This result agrees with our earlier published Co-rich arsenopyrite isochron age from the Radzimowice Au-As-Cu (317 ± 17 Ma, with poorly constrained initial $^{187}Os/^{188}Os$ of about 0.42), our LLHR Co-rich arsenopyrite from Klecza (316.6 ± 0.4 Ma; Mikulski et al. 2005a,b), and our 312 ± 1 Ma Kowary Re-Os age for molybdenite. Also, our collective results agree well with U-Pb zircon age (ca. 315 Ma) of equigranular granite from the Karkonosze Massif (Kusiak et al. 2009).

The genesis of the discussed deposits were the result of multiple hydrothermal activity surrounding Upper Carboniferous post-kinematic granitoids intrusions of the KM and later remobilization in the regional shear zones (e.g. Mochnacka 1982; Mikulski 2010). The circulation of hydrothermal fluids facilitated by intensive fracturing lasted relatively long. A reported age for younger galena from the Czarnów lode gave a common Pb model age of 250 to 210 Ma (Legierski 1973). This time range correspond to our youngest molybdenite from the Miedzianka deposit that yields a Re-Os age of 213 ± 1 Ma. It reflects a period of hydrothermal fluid ingress associated with renewed tectonic activity along the regional Intra-Sudetic Fault Zone in the southern part of the Permian-Triassic Zechstein basin.

## Acknowledgements

## References

Kusiak MA, Dunkley DJ, Słaby E, Martin H, Budzyń B (2009) Sensitive high-resolution ion-microprobe analysis of zircon reequilibrated by late magmatic fluids in a hybridized pluton. Geology 37:1063-1066

Kozdrój W (2003) Ewolucja geotektoniczna krystaliniku wschodnich Karkonoszy. In: Ciężkowski A, Wojewoda J, Żelaźniewicz A (eds) Sudety Zachodnie od wendu do czwartorzędu. WIND, Wrocław. pp 67-80.

Legierski J (1975) Model age and isotopic composition of ore leads of the Bohemian Massif. Czes Miner Geol 18/1:1-23

Machowiak K, Armstrong R (2007) SHRIMP U-Pb zircon age from the Karkonosze granite. Mineralogia Polonica Special Papers 31:193-196

Markey R, Hannah JL, Morgan JW, Stein HJ (2003) A double spike for osmium analysis of highly radiogenic samples. Chemical Geology 200:395-406

Marheine D, Kachlik V, Maluski H, Patocka F, Zelazniewicz A (2002) The Ar-Ar ages from the West Sudetes (NE Bohemian Massif): constraints on the Variscan polyphase tectonothermal development. In: Winchester JA, Pharaoh TC, Verniers J (eds) Palaeozoic Amalgamation of Central Europe Special Publications 201 Geological Society, London, pp 133–155.

Kryza R, Crowley QG, Larionov A, Pin C, Oberc-Dziedzic T, Mochnacka K (2012) Chemical abrasion applied to SHRIMP zircon geochronology: an example from the Variscan Karkonosze Granite (Sudetes), SW Poland). Gondwana Res. 21:757-767

Mikulski SZ (2007) Metal ore potential of the parent magma of granite – the Karkonosze massif example. In: Kozlowski A, Wiszniewska J (eds) Granitoids in Poland. AM Monograph no. 1, 2007 pp 123-145

Mikulski SZ, Markey RJ, Stein HJ (2005a) The first Re-Os ages of auriferous sulphides from European Variscides. Geochim et Cosmochim Acta 69(10S), A572

Mikulski SZ, Markey RJ, Stein HJ (2005b) Re-Os ages for auriferous sulphides from the gold deposits in the Kaczawa Mountains (SW Poland). In: Mao J, Bierlein FP (eds) Mineral Deposit Research: Meeting the Global Challenge. pp 793-796 Springer

Mikulski SZ, Stein HJ (2007) Re-Os age for molybdenite from the Western Sudetes, SW Poland. In: Kozlowski A, Wiszniewska J (eds) Granitoids in Poland. AM Monograph no. 1, 2007 pp 203-216

Mikulski SZ, Stein HJ (2011) Re-Os ages for molybdenites from the Variscan Karkonosze massif and its eastern metamorphic cover (SW Poland) In: Barra F, Reich M, Campos E, Tornos F, (eds) Let's Talk Ore Deposits Proceedings of the Eleventh Biennial SGA Meeting 26-29th September 2011 Antofagasta, Chile Volume I. Ediciones Universidad Catolica del Norte, Antofagasta, pp 130-133

Mikulski SZ, Stein HJ (2012) Wiek molibdenitów w Polsce w świetle badań izotopowych Re-Os [The age of molybdenites in Poland in the light of Re-Os isotopic studies]. Biuletyn Państwowego Instytutu Geologicznego 452:199-216 [in Polish with English Sumary]

Mochnacka K (1982) Mineralizacja polimetaliczna wschodniej osłony metamorficznej granitu Karkonoszy i jej związek z geologicznym rozwojem regionu. Biuletyn Instytutu Geologicznego 341:273-289

Smoliar MI, Walker RJ, Morgan JW (1996) Re-Os ages of group II1, IIIA, IVA and IVB iron meteorites. Science 271:117-133

Stein HJ, Markey RJ, Morgan JW, Hannah JL, Scherstén A (2001) The remarkable Re-Os chronometer in molybdenite: how and why it works. Terra Nova 13:479-486

Stein HJ, Morgan JW, Scheresten A (2000) Re-Os of low level highly radiogenic (LLHR) sulfides: The Harnas gold deposit, southwest Sweden, records continental-scale tectonic events. Econ Geol 95:1657-1671

Teisseyre J (1968) Budowa geologiczna wschodniej części okrywy granitu Karkonoszy w okolicy Miedzianki (Sudety). Geologia Sudetica 4:482-541

Zimnoch E (1978) Mineralizacja kruszcowa złoża Miedzianka w Sudetach. Biuletyn Instytutu Geologicznego 308:91-122

# Geochemical and mineralogical characteristics of the giant Bakyrchik gold deposit, East Kazakhstan

Anastassiya Miroshnikova, Olga Frolova, Indira Mataibayeva
*East Kazakh State Technical University, Ust-Kamenogorsk, Kazakhstan*

Mikhail Rafailovich
*YugGeo, Almaty, Kazakhstan*

**Abstract.** Presented here are complex metasomatic, mineralogical, and geochemical characteristics of the giant Bakyrchik gold deposit (East Kazakhstan) hosted in carbonaceous terrigenous rocks. Possibilities for an increase in gold resources of the Bakyrchik ore district are also discussed.

**Keywords.** Bakyrchik deposit, metasomatic zoning, geochemical specialization.

## 1 Introduction

The Bakyrchik deposit is hosted in carbonaceous terrigenous rocks (siltstone, sandstone, gravelstone, conglomerate) containing pyrite-pyrrhotite, ferrous carbonate (siderite, ankerite), and phosphate mineralization. The Bakyrchik gold deposit is potentially economic and a type example of ore closely related to mineralized carbonaceous terrigenous rocks (Marchenko, 2007).

## 2 Geochemical and mineralogical characteristics

Systematic metasomatic, mineralogical, and geochemical zoning at different scales is the basis for the prospecting model and ore estimation of the Bakyrchik deposit.

Carbonaceous sericite rocks, kaolinite-hydromica, quartz-sericite, sericite-phlogopite-carbonate, chlorite-albite, and other metasomatic rocks occur at the deposit (Marchenko, 2007; Rafailovich, 2009). Carbonaceous sericite rock is the leading type of hydrothermal alteration. The total carbon content varies from 0.3 to 26.5% in the host terrigenous rocks and 2.5-6.0% in ore zones. Carbon occurs as carbonates (oxidized species) and as kerite, anthraxolite, shungite, graphite, and bitumoids (reduced species).

Metasomatic carbonate bodies consisting of dolomite, ankerite, and breunnerite are often sulfidized. Kerite-anthraxolite-shungite, graphite, and bitumoids occur throughout the ore-bearing sequence. Chloroformic bitumoid dominates in the orebodies, and alcohol-benzene bitumoid is prevalent in geochemical haloes.

The metasomatic zoning of the Bakyrchik deposit is as follows. The carbonaceous-kaolinite-hydromica metasomatic rocks occur at the upper levels; carbonaceous sericite rocks occur throughout with a maximum in the middle zone; sericite-phlogopite-

carbonate assemblage with apatite and tourmaline occupies the lower levels. Breunnerite, ankerite, dolomite, quartz, native gold, chalcopyrite, and scheelite also occur at the deeper levels. Albite and albite-chlorite alteration (10-20%) is developed in the upper ore and supraore zones, spreading along fracture zones for many hundreds of meters. Thin chlorite-albite veinlets combined with supraore haloes of carbonaceous matter act as indicators of hidden ore mineralization (Fig.1).
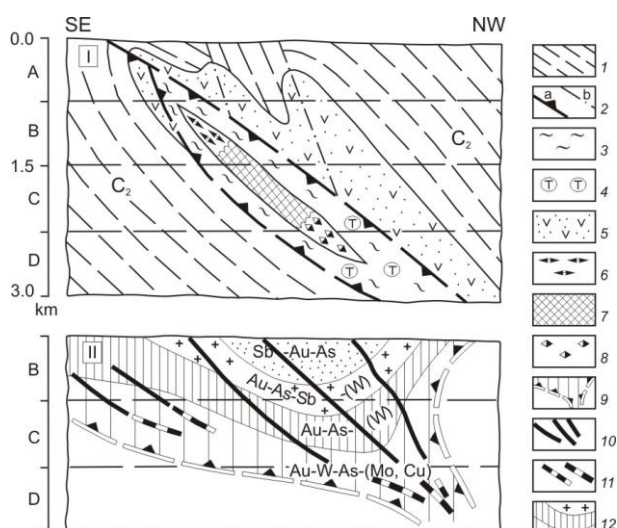


**Figure 1.** Model of metasomatic (I) and geochemical (II) zoning of the Bakyrchik deposit (*after M. Rafailovich, 2011*)
1-carbon-terrigenous rock; 2-faults and fractures: a-thrust faults, b-fault fissures; 3-sericitization; 4-tourmalinization; 5-clinochlore-albite alteration; 6-8-hydrothermal alterations in-line of main metalliferous deposits: 6-carbon-kaolinite-hydromica, 7-carbon-sericite, 8-sericite-phlogopite-carbonaceous; 9-contour of ore zone in longitudinal section; 10-11 - axial line of metalliferous deposits: 10 - confirmed, 11- proposed; 12-geochemical zone; A-D-reference zones

Five ore mineral assemblages are distinguished: (1) early melnikovite-pyrite-pyrrhotite-marcasite with nickeline and pentlandite; (2-4) productive (2) gold-pyrite-arsenopyrite with cubanite and gersdorfite, (3) gold-quartz-polymetallic with fahlore, chalcopyrite, galena, and sphalerite; (4) gold-quartz-carbonate-scheelite-chalcopyrite with breunnerite, dolomite, aikinite, and free gold; and (5) late quartz-carbonate-stibnite-tetrahedrite with marcasite and fine redeposited gold.

The gold-pyrite-arsenopyrite assemblage appears ubiquitous; melnikovite-pyrite-pyrrhotite-marcasite and gold-quartz-carbonate-scheelite-chalcopyrite assemblages are noted at great depth; gold-quartz-

polymetallic and quartz-carbonate-stibnite-tetrahedrite assemblages occur at the middle and upper levels.

The leading role (>90%) in the total gold budget belongs to the stringer-disseminated gold-pyrite-arsenopyrite assemblage (1.5-22.0% pyrite and 3-15% arsenopyrite).

At the upper levels pyrite prevails over arsenopyrite (3.5 : 1); at the middle and lower levels pyrite is of subordinate abundance (1 : 3) (Fig. 2). Fe disulfide forms aggregates, globules, cubic, pentagonal dodecahedral, and cubic octahedral crystals. In the middle zone crystals of complex habits {210}, {210} + {100}, and {100} + {111} are predominant, whereas crystals of cubic habit dominate in the upper and lower zones.
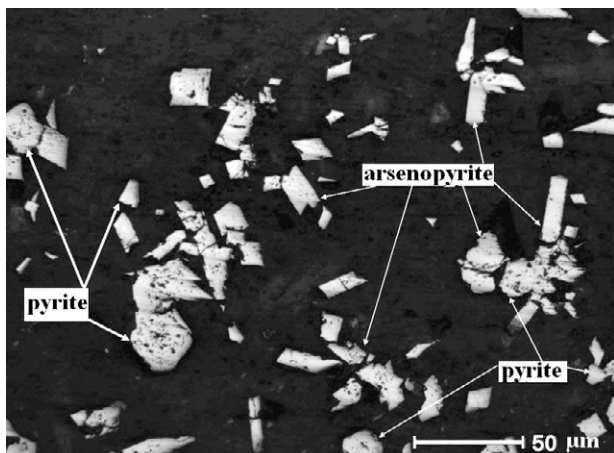


**Figure 2.** Pyrite-arsenopyrite mineralization.

Pyrite contains inclusions of native gold, arsenopyrite, chalcopyrite, galena, and tennantite-tetrahedrite. Acicular, prismatic, and columnar crystals are characteristic of arsenopyrite. Pyrite and arsenopyrite contain Au (tens and rarely hundreds ppm in pyrite and hundreds ppm in arsenopyrite as per ICP-MS analyses). Native gold occurs as films, droplike grains, spherules, amoeba-like and lumpy grains, dendrites and veinlets (Fig. 3). Microscopic and submicroscopic (< 10 um) dusty and amoeba-like gold inclusions in pyrite and arsenopyrite are predominant.
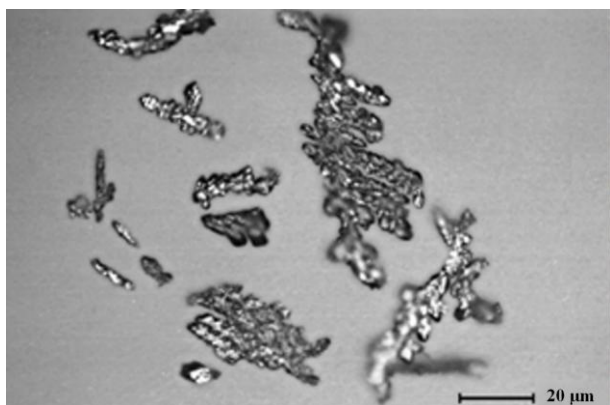


**Figure 3.** Native gold has the form of dendrites.

Gold in microfractures of sulfides in association with tennantite-tetrahedrite, sphalerite, galena, chalcopyrite, quartz, and carbonate, as well as gold in quartz-sericite-carbonate rocks rimming pyrite and arsenopyrite grains, are of subordinate abundance. Free lumpy gold grains in quartz-polymetallic and quartz-carbonate-scheelite-chalcopyrite assemblages are sporadic, as well as minute redeposited gold associated with late quartz, stibnite, and tetrahedrite. The fineness of minute gold in sulfides at the upper level is 760‰, whereas free gold at the middle and lower levels exhibit a fineness of 960‰.

The mineral distribution is characterised by telescoping and redeposition features. The zonal series of epigenetic Fe-As sulfides and other minerals have been established within a depth interval from 1200-1500 m to the surface and are as follows: pyrrhotite, arsenopyrite, pyrite – pyrite, arsenopyrite – pyrite, nickeline, gersdorffite – chalcopyrite, scheelite, aikinite, molybdenite – chalcopyrite, sphalerite – tennantite, galena – stibnite, tetrahedrite, and native antimony.

The Bakyrchik deposit is highly enriched in Au, As, Sb, Ag, Cu, Pb, Zn, Mo, W, Sn, Bi, Co, Ni, V, P, PGE, etc. The widespread elemental association and mineral assemblages (in parentheses) are: upper ore and supraore Au-Sb-As (quartz-carbonate-stibnite-tetrahedrite), middle ore Cu-Pb-Zn (chalcopyrite-sphalerite-galena-tennantite-tetrahedrite), middle and lower ore As-Ni-Co (combined pyrite-pyrrhotite-marcasite and pyrite-arsenopyrite) with ubiquitous Au-As (Au-pyrite-arsenopyrite) throughout. The Au content in geochemical haloes is 0.01-1.0 gpt and a few gpt to 20-25 gpt in orebodies (average of the deposit is 9.4 gpt). The As contents are 0.005-0.6 and 0.7-1.4%, respectively. Uniform direct correlations are characteristic of the following element pairs: Au-As, As-Sb, Cu-As, Cu-W, Cu-Co, and Co-Ni.

The orebodies in the Bakyrchik ore field are bundle-like with 3D concentric zoning. According to the geochemical data, the following zones are distinguished in the vertical plane: upper Sb-Au-As, first intermediate Au-As-Sb (with W), second intermediate Au-As (with W), and the lower Au-W-As-Cu-Mo in the lower root zone (Rafailovich, 2009). Two kinds of geochemical zonal patterns are distinguished: centrifugal vertical (vector is oriented updip of the ore bunch) and centripetal horizontal (from flanks to center).

The Main orebody in the axial part of the cluster is characterized by maximum geochemical heterogeneity and strongest contrasts in zoning. In contrast, the small flanking orebodies (e.g., Intermediate, Glubokii Log) are simpler in elemental composition and have lesser zoning.

## 3 Summary

A cutoff grade of 3.0 gpt Au, which has existed for many years, is today probably overestimated, especially in the light of impressive progress in processing of low-grade ores. The transition to a cutoff of 1.0-1.5 gpt, like at the Muruntau, Sukhoi Log, Kumtor and other giant deposits, will double gold resources and thus increase capitalization of the mine. Such a transition will allow transformation of the Kyzylovo Zone into a single giant

orebody no less than 4-5 km in extent and with a vertical range of ore mineralization reaching 2.5-3.0 km depth (Narseev et al. 2001). The enormous mass of ore and its complex composition (Au, shungite, probably PGM) reinforce the attractiveness of the Bakyrchik-type mineralization.

## References

Marchenko LG (2007) Model of noble metal deposits with mineralization finely dispersed in black shales. Geology and protection of subsoil 1:33-41

Narseev VA, Gostev YV, Zakharov AV (2001) Bakyrchik: geology, geochemistry and mineralization. Moscow CSRGEI. pp.174

Rafailovich MS (2009) The giant Bakyrchik gold deposit: geology, and perspectives for development. Mining journal of Kazakhstan 4:2-7

Rafailovich MS (2011) Large gold deposits in black shales: formation mechanisms and similarities. Luxe Media Group, Almaty, 272 pp

*All references are in Russian*

# Intra-cratonic architecture and the localisation of mineral systems

**David Mole, Marco Fiorentini, Nicolas Thebaud, Campbell McCuaig**
*Centre for Exploration Targeting, University of Western Australia, Stirling Hwy, Crawley 6009, Perth, Western Australia*

**Kevin Cassidy**
*Bare Rock Geological Services, PO BOX 1633, Fremantle WA 6160, Australia*

**Chris Kirkland, Sandra Romano, Michael Doublier**
*Geological Survey of Western Australia, 100 Plain Street, East Perth 6004, Western Australia*

**Elena Belousova**
*Centre for Geochemical Evolution and Metallogeny of Continents, Macquarie University, Macquarie, NSW2109, Australia*

**Steve Barnes**
*CSIRO Earth Science & Resource Engineering, 26 Dick Perry Ave, Kensington 6151, Western Australia*

**Abstract.** The generation and evolution of the Earth's continental crust modified the composition of the mantle and provided a stable, buoyant reservoir capable of capturing mantle material and ultimately preserving ore deposits. In addition, major cratonic margins within the continental crust represent a first-order control on camp-scale mineralisation. As a result, constraining the evolution and architecture of the crust and lithosphere is fundamental in understanding the large-scale localisation of multiple mineral systems. Here we show that the variable spatial development of the Archean crust of the Yilgarn Craton, Western Australia, controlled the localisation of gold, iron and nickel systems. The age and source characteristics of Archean lithosphere, which change in space and time, are recorded by the varying Sm-Nd and Lu-Hf isotope ratios of crustal rocks. These spatial and temporal variations in isotopic character document the evolution of the intra-cratonic architecture through time, and in doing so map transient lithospheric discontinuities where gold, nickel and iron mineral systems may have formed at specific times. This work shows that intra-cratonic architecture can be effectively imaged and used to identify prospective regions within a craton.

**Keywords.** Lithospheric architecture, gold, nickel, iron, Sm-Nd, craton-margin, Yilgarn, Archean.

## 1 Introduction

The spatial occurrence of Precambrian cratons within the continental crust and their margins with younger terranes are a major control on the location of world-class mineral camps and deposits worldwide (Begg et al., 2009; Begg et al., 2010). However, there is clearly potential for large-scale mineralisation *within* cratonic blocks as demonstrated by large nickel, gold, base metal and iron deposits found within many Archean cratons. The host rocks for these deposits were formed before, during or shortly after craton amalgamation, but before cratonisation itself. As a result, the distribution of mineral deposits, specifically gold, nickel and iron, corresponds to the margins of pre-existing lithospheric blocks or terranes that make up the craton. This study presents the isotopic mapping of the Yilgarn Craton of Western Australia. As one of the most intensely mineralised terranes on Earth, this Archean craton is an ideal natural laboratory in which to study the large-scale expression of mineral systems. The isotopic techniques identify discreet crustal blocks and associated intra-cratonic paleo-sutures and craton margins. These sites are potential exploration targets.

## 2 Method

This method uses Sm-Nd and Lu-Hf isotopes of crustal granitoid and felsic volcanic rocks to map the spatial and temporal variation in lithospheric age and source. The Sm-Nd method is a whole-rock technique. As a result, the extent of temporal analysis is limited by the magmatic age of the crustal rock itself. Conversely, the Lu-Hf method is an in-situ technique on zircons (Griffin et al., 2004). As a result, it allows the investigation of crustal architecture up to 3.1 Ga using inherited zircons. The Lu-Hf data are divided by U-Pb age into timeslices which image the changing source and age of the crust, subsequently documenting the evolution of the cratonic architecture through time.

## 3 Localisation of mineral systems by intra-cratonic architecture

The intra-cratonic architecture mapped by the Sm-Nd (Figure 1) and Lu-Hf (Figure 2) methods demonstrates the empirical spatial relationship between crustal evolution and mineral systems.

### 3.1 Gold

Gold deposits of the Yilgarn Craton cluster along large-scale fault systems and/or terrane boundaries internal to, and on the margins of, juvenile crustal domains. Gold camps in the Murchison Domain and Eastern Goldfields Superterrane (Figure 1) show this correlation well. In the Murchison, gold deposits are localised along major structures in the juvenile 'failed rift' crustal domain (Ivanic et al., 2010). These structures parallel the orientation of the juvenile domain, suggesting they are related.
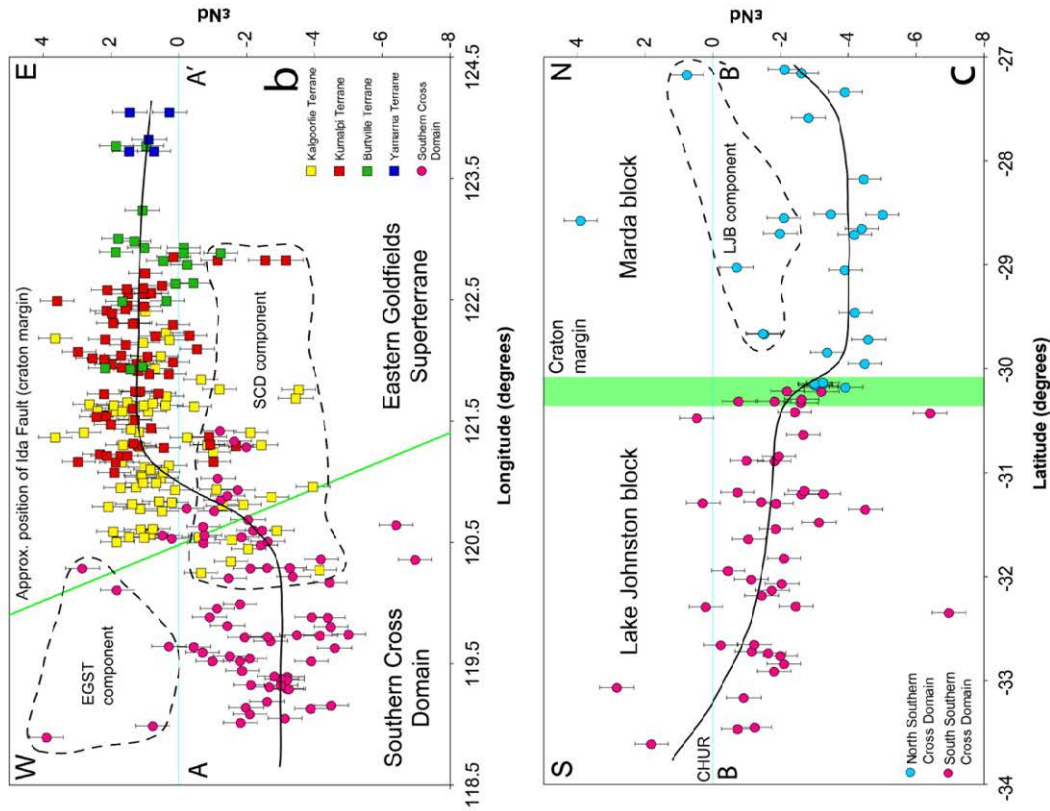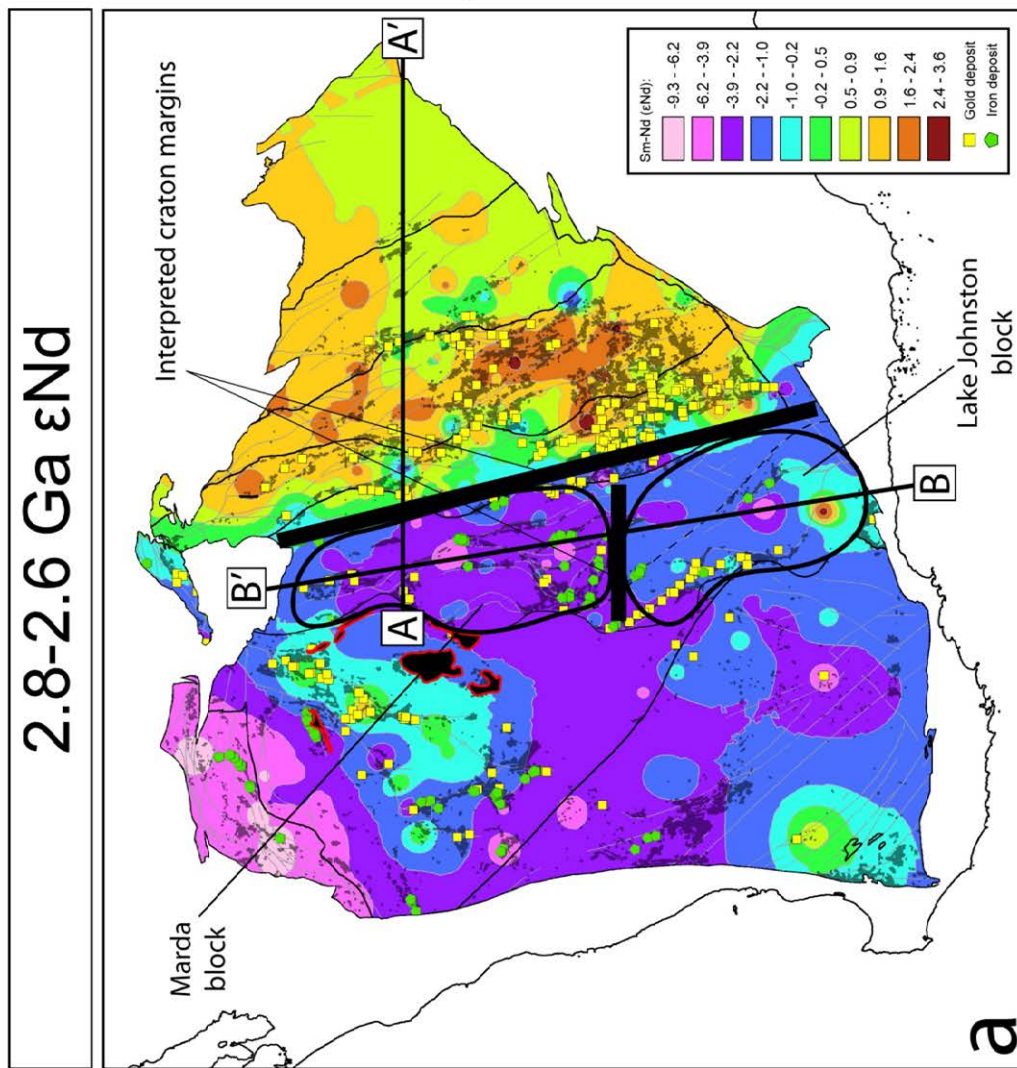
**Figure 1.** This diagram illustrates how the spatial use of Sm-Nd can highlight the position and extent of craton margins within an area: (a) εNd contour map (geometric interval; 2.8-2.6 Ga) showing the position of inferred craton margins (thick black bars), the delineation of different crustal blocks (i.e. the Marda and Lake Johnston blocks of the Southern Cross Domain), and the orientation of isotopic cross sections through regions of crust shown by (b) and (c). The cross section lines are not typical in that they do not only represent isotopic data along that line but also areas adjacent to the line, in order to constrain the full N-S or E-W variation in Sm-Nd isotopic values between different terranes/domains; (b) diagram of an E-W isotopic section (A-A') from the Yamarna Terrane in the east to the Southern Cross Domain in the west, as shown by (a); and (c) diagram of a N-S isotopic section (B-B') through the Southern Cross Domain. Both these sections highlight and constrain craton margins identified in the maps.
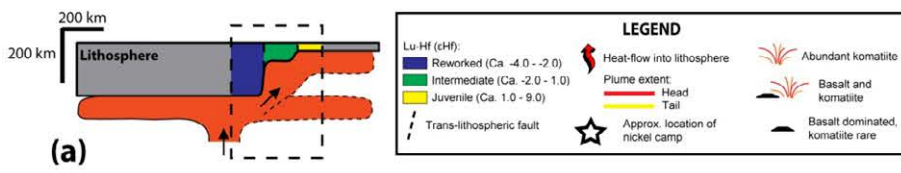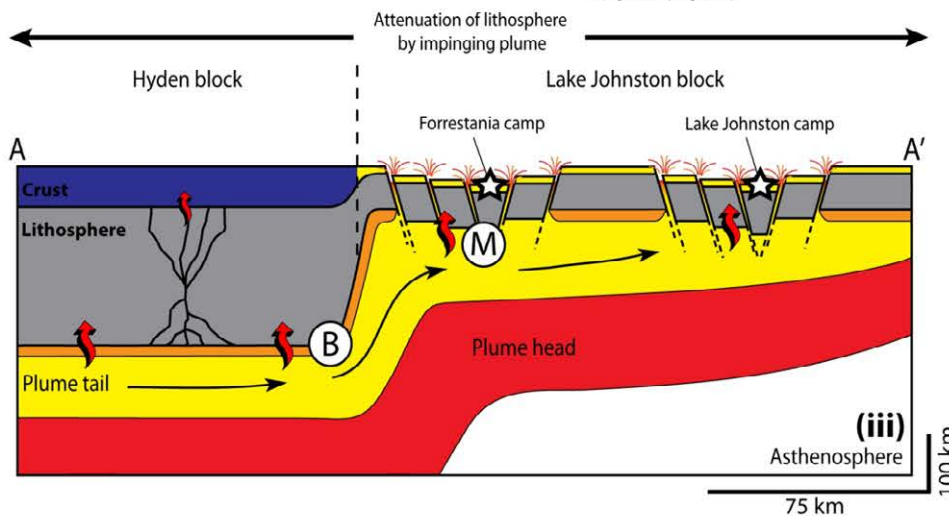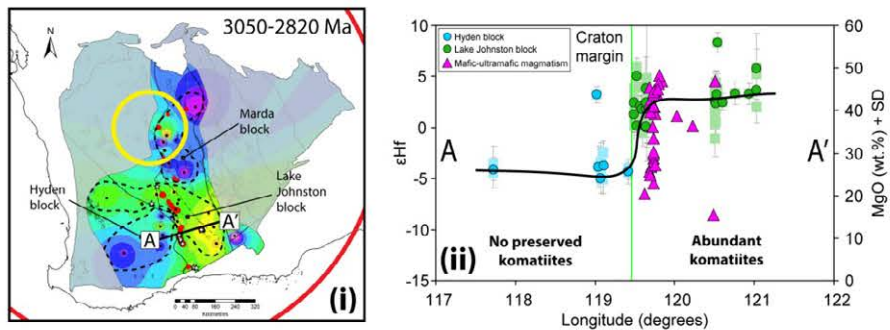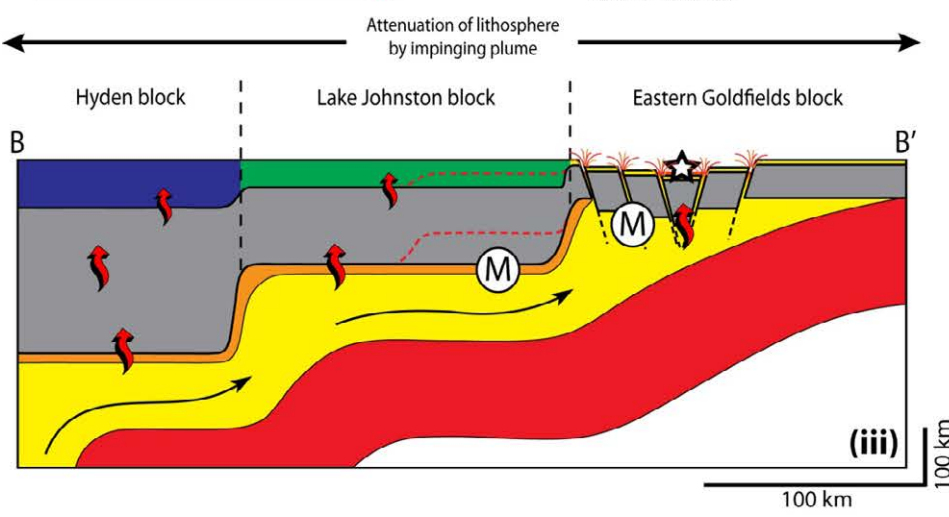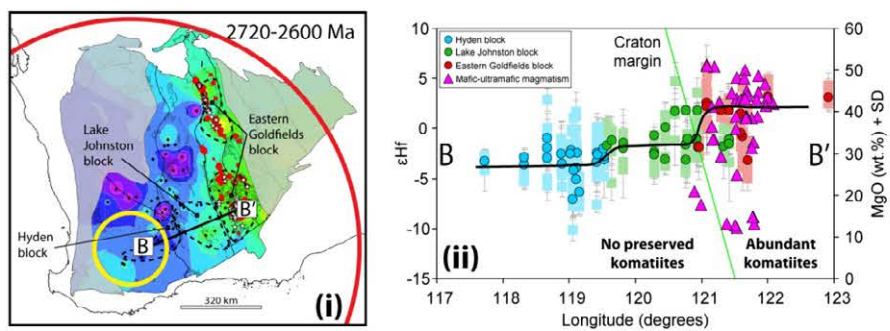
**Figure 2.** Isotopic cross-sections and interpreted lithospheric architecture during the emplacement of komatiites in the Yilgarn Craton. (a) Schematic lithospheric cross-section. Diagrams (b) and (c) show the interpreted lithospheric setting of the ca. 2.9 Ga komatiites in the southern Youanmi Terrane and the ca. 2.7 Ga komatiites in the Eastern Goldfields (Kalgoorlie Terrane), respectively. Each diagram has three parts: (i) εHf map showing the isotopic architecture at the time of plume emplacement; (ii) isotopic cross sections documenting the changing crustal source from east to west together with the occurrence of ultramafic-mafic magmatism; and (iii) interpreted lithospheric architecture. Approximate values for developed Archean lithosphere were ca. 250-150 km taken from Begg et al. (2009). The approximate scale of the plume head (ca. 1600 km), tail (200-100 km) and thickness (150-100 km) were taken from Campbell *et al.* (1989). These values are proxies based on modern analogues and experiments.

In the Eastern Goldfields Superterrane, gold is primarily concentrated in the Kalgoorlie Terrane, adjacent to the more reworked Youanmi Terrane. Here, gold deposits are clustered along major structures/terrane boundaries within a juvenile domain. The exception to this correlation is the Southern Cross gold deposits, which are localised along a major structure, but within a more reworked crustal domain (Figure 1). However, Figure 2bi shows that this area was juvenile at ca. 2.9 Ga and proximal to an isotopic boundary, suggesting that pre-existing, historic crustal architecture potentially has a significant control on later gold mineralisation. The gold camp at Southern Cross suggests that while juvenile crust is preferable, major structures and pre-existing architecture may be more important controls on the formation of major gold systems.

## 3.1 BIF-hosted Iron

Iron deposits of the Yilgarn Craton are similar to gold in that they are localised along major structures (see Murchison and Marda areas in Figure 1). However, iron systems cluster in the older, more reworked crustal domains. This is particularly apparent in the Marda area of the central Yilgarn, which hosts the Windarling BIF-hosted iron deposits. The iron deposits of the Murchison form on the more reworked margin of the 'failed rift'. These areas demonstrate that iron systems can occur on the margin, and internal to, older more reworked crustal domains. These relationships correlate with the current understanding of the formation of banded iron formations. The most extensive, thick sequences would have formed in a relatively shallow, continental platform setting, characterised by tectonic stability. The older, more reworked crust would have been more rheologically robust, buoyant and resistive to tectonic stresses and major magmatic events, providing a long-lived stable environment for the formation of thick BIF sequences.

Further to this, the current understanding of BIF upgrade to iron ore (Evans et al., 2012), suggests that passive margins are the ideal tectonic environment for the creation of the required fluids and temperatures. The deposits in the Murchison domain particularly reflect a potential passive margin setting, as they are located in an older reworked domain at the boundary with a more juvenile area. This isotopic setting may represent a passive margin which developed post-rifting or on the failure of rifting.

## 3.3 Komatiite-hosted nickel

There are two komatiite events in the Yilgarn Craton that host nickel sulphides: the 2.9 Ga komatiites of the southern Youanmi Terrane (Figure 2b); and the 2.7 Ga komatiites of the Kalgoorlie Terrane (Figure 2c). In order to image the cratonic architecture from 2.9 to 2.7 Ga, Lu-Hf isotopes were used from magmatic and inherited zircons. These data were sub-divided by U-Pb age and plotted as time-slice contour maps. The results of this mapping indicate that high-MgO mineralised komatiites were consistently emplaced within juvenile domains, at the margin with more reworked crustal

blocks. For example, at 2.9 Ga in the southern Youanmi Terrane (Figure 2b) the high-MgO mineralised komatiites of the Forrestania and Ravensthorpe belts occur in the juvenile 'Lake Johnston block', at the margin with the more reworked 'Hyden block' (Figure 2b). The mineralised komatiites of the Lake Johnston greenstone belt occur along a major crustal discontinuity within the juvenile 'Lake Johnston block'.

The localisation of komatiite magmatism on the juvenile side of an isotopic margin is mirrored at 2.72-2.6 Ga in the Eastern Goldfields (Figure 2c), and is due to the physical control of lithospheric architecture on an impinging plume (see Figure 2). The more reworked blocks are inferred to be thicker crust/lithosphere and the juxtaposition of these against thinner, more juvenile blocks creates an architecture which channels the plume into the craton margin. This allows komatiites to be erupted with minimal interaction with the crust, and hence the magmas are hotter, more primitive, and have higher flux than in evolved areas (i.e. Marda). These properties are essential for the formation of komatiite-hosted nickel sulphide deposits.

## 4 Summary

This study has demonstrated that Sm-Nd and Lu-Hf isotopes can be used to map intra-cratonic architecture and its evolution through time. Further to this, it has shown the Yilgarn Craton is composed on a number of crustal domains whose evolution through time affects the localisation of gold, iron and nickel mineral systems.

## Acknowledgements

## References

Begg GC, Griffin WL, Natapov LM, O'Reilly SY, Grand SP, O'Neill CJ, Hronsky JMA, Djomani YP, Swain CJ, Deen T, Bowden P (2009) The lithospheric architecture of Africa: Seismic tomography mantle petrology and tectonic evolution. Geosphere 5: 23–50.

Begg GC, Hronsky JMA, Arndt NT, Griffin WL, O'Reilly SY, Hayward N (2010) Lithospheric, cratonic and geodynamic setting of Ni-Cu-PGE sulfide deposits. Econ Geol 105: 1057–1070.

Campbell IH, Griffiths RW, Hill RI (1989) Melting in an Archaean mantle plume: heads it's basalts tails it's komatiites. Nature 339: 697–699.

Evans KA, McCuaig TC, Leach D, Angerer T, Hagemann SG (2012) Banded iron formation to iron ore: A record of the evolution of Earth environments? Geology 41/2: 99–102.

Griffin WL, Belousova EA, Shee SR, Pearson NJ, O'Reilly SY (2004) Archean crustal evolution in the northern Yilgarn Craton: U-Pb and Hf-isotope evidence from detrital zircons. Precambrian Res 131: 231–282.

Ivanic TJ, Wingate MTD, Kirkland CL, Van Kranendonk MJ, Wyche S (2010) Age and significance of voluminous mafic-ultramafic magmatic events in the Murchison Domain, Yilgarn Craton. Aust J Earth Sci 57: 597–614.

# Crust-mantle interaction and genesis of the Kidston gold-rich breccia pipe deposit in north-east Australia: U–Pb, Hf and Os isotope evidence

Valeria Murgulov, William L. Griffin, Suzanne Y. O'Reilly
*Australian Research Council Centre of Excellence for Core to Crust Fluid Systems/GEMOC, Department of Earth and Planetary Sciences, Macquarie University, Sydney, NSW 2109, Australia*

**Abstract.** Hf model ages yielded by rutile grains in a lower-crustal granulite xenolith provide evidence for intrusion of basaltic magmas into and below the lower crust around 420 Ma and 1,570 Ma. A host rock to the Kidston gold-rich deposit in the north-eastern Australian craton, the Oak River Granodiorite (U–Pb crystallisation age of 418 ± 2 Ma), formed by remelting of the heterogeneous ca. 1,550 Ma crust (initial $^{176}$Hf/$^{177}$Hf from 0.28228 to 0.28167) that may have been produced by mixing of mantle-derived magmas with the melting products of 1,935 Ma to 3,260 Ma crustal rocks. The Kidston gold-rich Median Dyke (336 ± 4 Ma) is contemporaneous with the Lochaber Granite (338 ± 3 Ma) within a spatially associated magmatic complex. However, the less radiogenic Hf-isotope compositions of zircons in the Median Dyke (0.28234 to 0.28211) than in the Lochaber Granite (0.28253 to 0.28234) suggest mixing between Lochaber Granite magmas and magmas derived by remelting of the Oak River Granodiorite. The Os model age of a sulfide grain in a mantle-derived lherzolite xenolith records a metasomatic event in the lithospheric mantle around 350 Ma related to back-arc extension; however, no juvenile mantle input was required to produce the Median Dyke magmas.

**Keywords.** Crust-mantle interaction, zircon and rutile Hf isotopes, sulfide Os isotopes, Kidston deposit, north-east Australia

## 1 Introduction

To improve our understanding of the genesis of mineral deposits associated with magmatic complexes requires knowledge of crust-mantle interaction through geologic time. The potential to investigate the coupling of crust and lithospheric mantle beneath the north-eastern edge of the Australian craton (Murgulov et al. 2011; 2012) has only recently become available, owing to the development and application of micro-analytical techniques for isotope geochemistry and geochronology. In particular, the integration of *in situ* U–Pb and Lu–Hf analyses of zircon grains recovered from volcanic and plutonic rocks and *in situ* Lu–Hf analysis of rutile grains in lower-crustal xenoliths with *in situ* Re–Os analysis of sulfide grains in mantle-derived xenoliths offers insights into both crust and mantle. Combined *in situ* U–Pb dating and Hf-isotope information on zircon can resolve magma-generation processes and is an effective tool for investigating crustal evolution (e.g., Murgulov et al. 2007). The Re–Os in sulfide chronometer (e.g., Alard et al. 2002) and the Lu–Hf in rutile chronometer (e.g., Choukroun et al. 2005) have been used to constrain timing of modification of the lithospheric mantle by

asthenosphere-derived metasomatic fluids and silicate melts.

In this study, zircon grains recovered from the Oak River Granodiorite (a host rock to the Kidston gold-rich breccia pipe deposit; Baker and Andrew 1991), the gold-rich Median Dyke (coeval with brecciation and mineralisation within the Kidston deposit) and the intrusive rocks (the Black Cap Diorite and Lochaber Granite) within the spatially associated Lochaber Ring Dyke Complex (LRDC) were analysed by *in situ* Laser Ablation (LA)-ICPMS techniques to provide U–Pb crystallisation ages and by LA-Multi Collector (MC)-ICPMS to derive Hf-isotopic compositions. Hf-isotope ratios of rutile grains in a lower-crustal granulite xenolith from the McBride lava-field Province (90 km north-east of the Kidston deposit) and Os-isotope ratios of sulfide grains in mantle-derived lherzolite xenoliths from the Chudleigh lava-field Province (90 km south-east of the Kidston deposit) were measured *in situ* by LA-MC-ICPMS to determine the timing of magmatic events in the lower crust and metasomatic events in the lithospheric mantle, respectively.

An overlap in *in situ* data will imply a close temporal linkage between events in the upper and lower crust domains and lithospheric mantle beneath the north-eastern edge of the Australian craton. The coincidence of the events will provide a more effective way to evaluate the relative contributions of crustal and juvenile mantle sources to the Kidston gold-rich deposit, its host rock and the spatially associated LRDC (Murgulov et al. 2009), and hence to re-assess their genetic relationships.

## 2 Geological Context And Samples

The north-eastern edge of the Australian craton represents a unique geological setting ideal for investigation of temporal correlation of events recorded in the lithospheric mantle and overlying crust during Proterozoic time and before the Carboniferous gold-mineralisation at Kidston. This part of the craton is the remnant margin of the Australian continent after Neoproterozoic break-up of the Rodinia supercontinent (e.g., Cawood 2005). Several distinct periods of orogenesis along the margin commenced in the Cambrian and continued through to the Mesozoic. Rifting and associated seafloor spreading was accompanied by the formation of extensive intraplate flood-basalt fields in the Cenozoic. The major episodes of granitoid production in the craton were coincident with magmatic-arc development at 1585–1545 Ma and

back-arc extension at 430–420 Ma and 345–300 Ma (e.g., Black and McCulloch 1990; Murgulov et al. 2007).

The Kidston gold-rich breccia pipe is a subvolcanic breccia-hosted porphyry deposit (Baker and Andrew 1991). The typical size range of zircon grains in the sample of the Median Dyke, a quartz-feldspar porphyritic rhyolite, is from 50–150 μm. Most zircon grains in the sample of the Lochaber Granite, which is the dominant unit within the LRDC, are 50–250 μm long. The original texture in these samples is overprinted by phyllic and sericitic alteration. Zircons in the Black Cap Diorite, which is the most mafic intrusive unit within the LRDC, have lengths in the range 100–250 μm. Most zircons in these rocks have anhedral grain shapes. The Oak River Granodiorite zircons are 100 μm to 200 μm long and in some core/rim relationships were observed. Many zircons in all rock samples show late to post-magmatic recrystallisation that has completely overprinted the primary oscillatory zoning; metamict structures were observed in some grains. The inclusions in zircons are most likely silicate, oxide and/or sulfide phases, but these have not been analysed.

Cenozoic basalts of the McBride and Chudleigh lava-field Provinces carry abundant lower-crustal granulite and mantle-derived lherzolite xenoliths (Murgulov et al. 2011; 2012). Rutile is a rare accessory mineral phase in lower-crustal xenoliths and was found in a garnet-rich granulite sample from the McBride Province (Murgulov et al. 2012). It is composed of kelyphitised garnet, plagioclase, quartz and rutile, and has partially equilibrated igneous microstructure. Most rutiles are 250 μm to 1,500 μm long and 350 μm to 1,000 μm wide, and have up to 150 ppm Hf. Sulfide is an accessory mineral phase in mantle-derived xenoliths and controls Re–Os systematics of lithospheric peridotites (e.g., Alard et al. 2002). In this study, sulfides were found in four lherzolite xenolith samples from the Chudleigh Province. The samples are composed of olivine, orthopyroxene, clinopyroxene and spinel, and have porphyroclastic microstructures (Murgulov et al. 2011). In these samples, enclosed sulfides usually occur within silicate minerals (rarely in spinel), whereas interstitial sulfides occur on grain boundaries, which are sometimes filled with glass. Most sulfides are interstitial and range from 20 μm to 120 μm in length, and are either Ni-rich or Ni-poor mono sulfide solid solution.

## 3 Analytical Methods And Data Presentation

Back-scattered electron (BSE)–cathodoluminescence (CL) images and Zr, Y and Hf analyses of zircon grains in polished mounts were acquired using the CAMECA SX50 electron microprobe (method described in Murgulov et al. 2007; 2009). The same instrument and operating conditions were used to image and analyse rutile grains in polished thick sections (Murgulov et al. 2012). Sulfide grains in polished thick sections were imaged for compositional maps and analysed for Cu, Fe, Ni, Co, S, Si, K and O using the CAMECA SX100 electron microprobe. The operating conditions during analyses are given by Murgulov et al. (2011).

A New Wave Research 213 nm UV laser-ablation microprobe coupled to a HP4500 ICPMS and supported by the GLITTER software package for data reduction was used to carry out the *in situ* U–Pb dating of zircons. The instrumentation and protocols are described by Murgulov et al. (2009). The crystallisation age for each sample is given by the error-weighted mean of the $^{206}Pb/^{238}U$ ages and $^{207}Pb/^{206}Pb$ ages of the selected grains at the 95% confidence level.

$^{176}Hf/^{177}Hf$ ratios in zircon grains were measured using a New Wave Research UP193 laser-ablation microprobe (incorporating a Lambda Physik Optek Excimer) attached to a Nu Plasma multi-collector ICPMS. The operating conditions during analysis, standards used for calibration, limits of detections and data reduction procedure are described in detail by Murgulov et al. (2009). Initial $^{176}Hf/^{177}Hf$ values and Depleted-Mantle model age ($T_{DM}$) were calculated using the Söderlund et al. (2004) $^{176}Lu$ decay constant ($1.867 \times 10^{-11}$ $y^{-1}$) and the present-day values of a depleted mantle ($^{176}Hf/^{177}Hf=0.283251$ and $^{176}Lu/^{177}Hf= 0.0384$). A more realistic "crustal" model age ($T_{DM}^{C}$) was calculated by assuming that the source rocks of the magma had the composition of the average continental crust ($^{176}Lu/^{177}Hf=0.015$).

$^{176}Hf/^{177}Hf$ ratios in rutile grains were measured *in situ* in polished thick sections and blocks using a New Wave Research LUV213 laser-ablation microprobe attached to a Nu Plasma multi-collector ICPMS. The operating conditions during analysis, standards used for calibration, limits of detections and data reduction procedure are described in detail by Murgulov et al. (2012). Initial $^{176}Hf/^{177}Hf$ values and rutile Hf model age ($T_{DM}$) were calculated using the same decay constant and the present-day values of a depleted mantle as those used in calculations of values for zircons. The reported rutile Hf model age represents the error-weighted mean of the $T_{DM}$ ages.

Most Re-Os data on sulfide grains in polished thick sections and blocks were collected with a New Wave Research UP213 laser microprobe attached to a Nu Plasma multi-collector ICPMS; some analyses were done using a Merchantek LUV266 nm laser. The description of instrumentation, analytical and calibration methods are given by Murgulov et al. (2011). The $T_{RD}$ "Re-depletion age" assumes that all Re was removed from the residue by the melt, and that any Re present has been added recently. The sulfide Os model ages ($T_{RD}$) were calculated using $^{187}Os/^{188}Os=0.1275$ and $^{187}Re/^{188}Os=0.40186$ for the present-day values of a chondritic mantle (Walker and Morgan 1989).

## 4 Results

In the sample of the Oak River Granodiorite, data for the Palaeozoic zircon grains and rims that were characterised by Pb loss and/or contained uncorrected common Pb were rejected. The Proterozoic zircon cores that have been reset were also rejected. The Oak River Granodiorite has 1,551 ± 6 Ma (n=9 and MSWD=0.66) old zircon cores overgrown by 418 ± 2 Ma (n=14 and

MSWD=0.98) rims; the latter is accepted as the crystallisation age of the sample. The data for zircons from the LRDC rocks and the Median Dyke that required common−Pb correction > 12.57% and/or were characterised by Pb loss were rejected. The Black Cap Diorite and Lochaber Granite have U–Pb crystallisation age of 351 ± 1 Ma (n=39 and MSWD=0.90) and 338 ± 3 Ma (n=9 and MSWD=0.74), respectively. The crystallisation age for the gold-rich Median Dyke (336 ± 4 Ma; n=5 and MSWD=1.15) overlaps that for the Lochaber Granite. However, the Median Dyke zircons have less radiogenic Hf-isotope compositions (0.28234 to 0.28211; $\epsilon_{Hf}$ from -8.1 to -16.0) than those from the Lochaber Granite (0.28253 to 0.28234; $\epsilon_{Hf}$ from -1.3 to -7.8) and the Black Cap Diorite (0.28256 to 0.28234; $\epsilon_{Hf}$ from 0.2 to -7.4), but within the range defined by zircon grains and rims from the Oak River Granodiorite (0.28228 to 0.28167; $\epsilon_{Hf}$ from -8.3 to -29.5), as shown in Figure 1. The Median Dyke zircons yielded older crustal model ages (1,860 Ma to 2,360 Ma) than those in the Black Cap Diorite (1,345 Ma to 1,830 Ma) and the Lochaber Granite (1,430 Ma to 1,845 Ma), but mostly younger crustal model ages than those yielded by the Palaeozoic zircon grains and rims in the Oak River Granodiorite (1,935 Ma to 3,260 Ma).
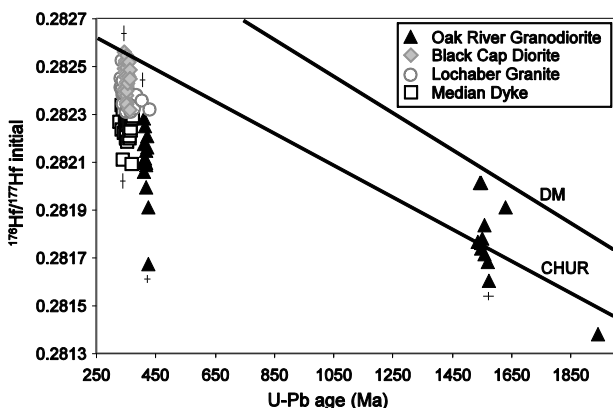


**Figure 1.** Initial $^{176}$Hf/$^{177}$Hf *vs.* U–Pb age plot for all samples showing the spread of initial $^{176}$Hf/$^{177}$Hf relative to CHUR and Depleted Mantle (DM) evolution lines. 2σ average error crosses for each sample, the Palaeozoic zircon grains and rims and the Proterozoic zircon grains and cores in the Oak River Granodiorite, are shown.

Modelling of rutile Hf-isotope data yielded seven unrealistic $\epsilon_{Hf}$ and/or 2σ values, which were rejected. A relatively wide range of initial $^{176}$Hf/$^{177}$Hf values at t=420 Ma (0.28295 to 0.28206 corresponding to $\epsilon_{Hf}$ from 15.5 to -16.1, based on twenty-one analyses) is defined by nineteen rutile grains in a lower-crustal granulite xenolith from the McBride Province. The rutile Hf model ages were calculated at 420 ± 190 Ma (n=1), 880 ± 100 Ma (n=1), 1,000 ± 40 Ma (n=2), 1,110 ± 30 Ma (n=6), 1,330 ± 160 Ma (n=3) and 1,570 ± 50 Ma (n=8).

About half of the analysed sulfide grains in four lherzolite xenolith samples from the Chudleigh Province yielded sub-chondritic $^{187}$Os/$^{188}$Os (0.1130–0.1252) and $^{187}$Re/$^{188}$Os (0.0214–0.1961). There is no correlation between the sulfide Os model ages (T$_{RD}$) and the occurrence of sulfides (interstitial or enclosed) and their

composition. The *in situ* Re–Os data for single grains of sulfides provide evidence for the presence of several sulfide populations: 350 ± 100 Ma (n=1); 810 ± 150 Ma (n=2); 1,230 ± 190 Ma (n=2); and 1,820 ± 290 Ma (n=1).

## 5 Discussion

The number of *in situ* analyses of Re–Os systematics in sulfides is not statistically significant enough to place a firm constraint on the timing of metasomatic events in the lithospheric mantle. Nevertheless, the data still provide insights into the evolution of the lithospheric mantle beneath the north-eastern edge of the Australian craton, and can be correlated to magmatic events in the overlying crust. The sub-chondritic $^{187}$Os/$^{188}$Os and $^{187}$Re/$^{188}$Os values yielded by sulfide grains suggest that subsequent metasomatic processes have not affected the isotopic composition of these sulfides and their Os model ages. Metasomatism of the lithospheric mantle most likely involved infiltration of asthenosphere-derived metasomatic fluids and silicate melts during lithospheric thinning and rifting around 1,820 Ma, 810 Ma and 350 Ma, and during suturing around 1,230 Ma beneath the Chudleigh Province, and by inference beneath the craton. The overlap between the sulfide Os model age around 1,820 Ma and the well-defined U–Pb ages for detrital zircons (Murgulov et al. 2007) and crustal model ages yielded by zircons in the Median Dyke, LRDC rocks and Oak River Granodiorite suggests coincidence of a metasomatic event in the lithospheric mantle and minor granitoid production in the overlying crust. A metasomatic event around 350 Ma, related to asthenospheric mantle upwelling, lithosphere rifting and back-arc extension, is recorded in the lithospheric mantle beneath the craton; however, no juvenile mantle input was required to produce the magmas of the gold-rich Median Dyke and the LRDC rocks (Fig. 1).

The overlap between rutile Hf model ages and the well-defined U–Pb ages for detrital zircons suggest that the rutile grains have not been affected by retrograde metamorphism and alteration. Intrusion of basaltic magmas into and below the lower crust around 1,570 Ma and 420 Ma coincide with two major episodes of granitoid magmatism in the overlying crust (Black and McCulloch 1990; Murgulov et al. 2007). The Oak River Granodiorite contains inherited ca. 1,550 Ma zircon cores and is interpreted to have formed by remelting of the heterogeneous Mesoproterozoic crust that may have been produced by mixing of mantle-derived magmas with the melting products of Palaeoproterozoic to Archaean crustal rocks, probably coincident with magmatic-arc development. No juvenile mantle input was required to produce the Oak River Granodiorite magmas, although intrusion of basaltic magmas into and below the lower crust may have provided heat for crustal melting. The overlap in Hf-isotope compositions of rutiles and zircons (Fig. 2) suggests that intrusion of basaltic magmas in the lower crust during mantle upwelling and back-arc extension around 420 Ma could have contributed magmas of more radiogenic Hf-isotope signature to the granitoid magmas. However, this is not required; modelling of the zircon data simply suggests

remelting of the heterogeneous ca. 1,550 Ma crust. The events recorded in the lower crust around 1,330–1,000 Ma and 880 Ma and in the lithospheric mantle around 1,230 Ma and 810 Ma are not obviously associated with known episodes of granitoid magmatism, but do correspond to the time of the Rodinia amalgamation and break-up (Cawood 2005).

The Hf-isotope data for zircons in the Median Dyke, Lochaber Granite and Black Cap Diorite rule out fractional crystallisation relationship between the Kidston gold-rich deposit and the LRDC (Murgulov et al. 2009). The less radiogenic Hf-isotope composition of zircons in the gold-rich Median Dyke and the presence of inherited Siluro-Devonian zircons (Fig. 1) suggest that the Median Dyke may have been produced by mixing between Lochaber Granite magmas and magmas derived by remelting of the Oak River Granodiorite, which was itself derived from Proterozoic crust.
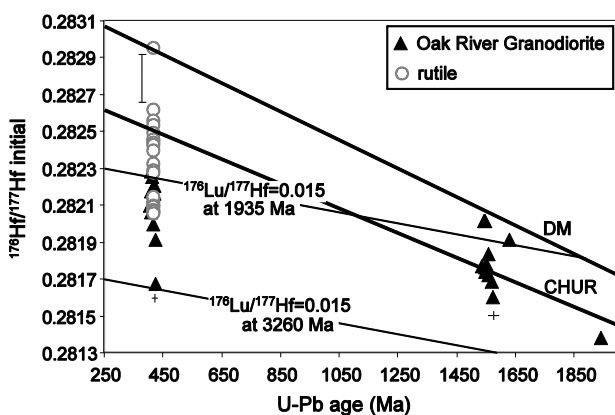


**Figure 2.** Plot of initial $^{176}Hf/^{177}Hf$ vs. U–Pb age showing the spread of initial $^{176}Hf/^{177}Hf$ relative to CHUR and Depleted Mantle (DM) evolution lines and relationship between the rutile data ($2\sigma$ average error bar shown for initial $^{176}Hf/^{177}Hf$ values) and the zircon data for the Oak River Granodiorite ($2\sigma$ average error crosses shown).

## 6  Conclusions

This study has shown that an overlap in *in situ* data imply a close temporal linkage between events in the upper and lower crust domains and lithospheric mantle beneath the north-eastern edge of the Australian craton. It has provided a more effective way to evaluate crust-mantle interaction during the formation of the Kidston gold-rich breccia pipe deposit, its host rock and the spatially and temporally associated LRDC, and established a re-assessment of their genetic relationships.

The metasomatic episode in the lithospheric mantle around 1,820 Ma (recorded by a sulfide Os model age) coincides with a minor episode of granitoid production in the upper crust (recorded by crustal model ages); such episodes were probably initiated by mantle upwelling and lithospheric rifting. The rutile Hf model ages imply that intrusion of basaltic magmas into and below the lower crust around 1,570 Ma provided heat for remelting and supplied magmas with juvenile mantle isotope signatures to the upper crust. Similar magmas provided enough heat to cause melting in the lower crust around

420 Ma, but have not contributed magmas with juvenile mantle isotope signatures to the upper crust. The metasomatic events in the lithospheric mantle around 1,230 Ma and 810 Ma and intrusion of basaltic magmas into and below the lower crust around 1,330–1,000 Ma and 880 Ma correspond to the time of the Rodinia amalgamation and break-up.

Although a metasomatic event around 350 Ma is recorded in the lithospheric mantle beneath the craton, no juvenile mantle input was required to produce the magmas of the Median Dyke in the Kidston gold-rich deposit and the LRDC rocks. The Median Dyke magmas were produced by mixing the Lochaber Granite magmas with material from the Oak River Granodiorite, and hence reflect the multi-stage reworking of the Proterozoic crust in a back-arc continental setting.

## References

Alard O, Griffin WL, Pearson NJ, Lorand J-P, O'Reilly SY (2002) New insights into the Re–Os systematic of sub-continental lithospheric mantle from in situ analysis of sulfides. Earth Planet Sci Lett 203: 651–663

Baker EM, Andrew AS (1991) Geologic, fluid inclusion, and stable isotope studies of the gold-bearing breccia pipe at Kidston, Queensland, Australia. Econ Geol 86: 810–830

Black LP, McCulloch MT (1990) Isotopic evidence for the dependence of recurrent felsic magmatism on new crust formation; an example from the Georgetown region of north-eastern Australia. Geochim Cosmochim Acta 54: 183–196

Cawood PA (2005) Terra Australis Orogen: Rodinia breakup and development of the Pacific and Iapetus margins of Gondwana during the Neoproterozoic and Palaeozoic. Earth Sci Rev 69: 249–279

Choukroun M, O'Reilly SY, Griffin WL, Pearson NJ, Dawson JB (2005) Hf isotopes of MARID (mica-amphibole-rutile-ilmenite-diopside) rutile trace metasomatic processes in the lithospheric mantle. Geology 33: 45-48

Murgulov V, Griffin WL, O'Reilly SY (2012) Temporal correlation of magmatic-tectonic events in the lower and upper crust in north-east Australia. IJES 101: 1091–1109

Murgulov V, Griffin WL, O'Reilly SY (2011) Lithospheric mantle evolution beneath northeast Australia. Lithos 125: 405–422

Murgulov V, Griffin WL, O'Reilly SY (2009) Temporal and genetic relationships between the gold-bearing breccia pipe at Kidston and the Lochaber Ring Dyke Complex, North Queensland, Australia: insights from in situ U–Pb and Hf-isotope analysis of zircon. Mineral Petrol 95: 17–45

Murgulov V, Beyer E, Griffin WL, O'Reilly SY, Walters SG, Stephens D (2007) Crustal evolution in the Georgetown Inlier, North Queensland, Australia: a detrital zircon grain study. Chem Geol 245: 198–218

Söderlund U, Patchett PJ, Vervoort JD, Isachsen CE (2004) The $^{176}Lu$ decay constant determined by Lu–Hf and U–Pb isotope systematics of Precambrian mafic intrusions. Earth Planet Sci Lett 219: 311–324

Walker RJ, Morgan JW (1989) Rhenium-Osmium systematics of carbonaceous chondrites. Science 243: 519–522

# Quantitative morphogenetic analyses – effective method of prospecting and economical estimation of diamond deposits

T.V. Posukhova, V.K. Garanin
*Department of Mineralogy, M.V. Lomonosov Moscow State University, Moscow, Russia*

**Abstract.** The methods of morphogenetic study of kimberlite indicator minerals (KIM) with case study of the northern part of the East European platform are described. The techniques of selection of morphologic and genetic groups of garnets, pyroxenes, Cr-spinels and ilmenite are discussed. The basis of a technique is performed with several programs: the program of the quantitative analysis of the back scattering electron images (BEI), quantitative microprobe analysis of phases; identification of phases on the basis of the database and statistical analysis, which was developed by the authors earlier (Garanin et al., 1984). The types of the KIM from kimberlites of the Arkhangelsk diamondiferous province and surrounding regions are characterized.

**Keywords.** Diamond deposit, prospecting works, SEM images, kimberlites

## 1. Introduction

Exploration and evaluation of the industrial potential of new diamond-bearing regions is still an actual problem for Applied Mineralogy. Large-scale exploration for diamond deposits has allowed the collection of a large amount of information about the modification of the shape and composition of kimberlitic indicator minerals (KIM) during the forming of dispersion halos and placers. Stages of KIM morphology modification during weathering of kimberlites and the transportation and deposition of KIMs in continental and marine environments were studied and the basic form of surface corrosion and mechanical abrasion were determined and stages of deep morphogenesis of the KIM were described and the basic features that allow estimation of distance and the conditions of transport in scattering KIM haloes were established (Afanasiev et al. 2001).

However, during the exploration for diamond deposits in the Arkhangelsk province some factors that greatly complicate the mineralogical studies were identified:

- relatively low content of the KIM in these kimberlites and the predominance of chromites;
- good preservation of the crater facies and insignificant erosian of the pipes;
- substantial thickness of overlying Paleozoic and Cenozoic cover rocks;
- significant role of glacial ice in transport and redeposition of material and a weak dynamic activity of modern streams.

The best solution of these problems is the improvement of the prospecting techniques available and consequently the morphogenetic method was created at the Diamond Deposits Laboratory of the Lomonosov Moscow State University. The new technique of evaluation of diamond potential of the prospecting regions is based on the study of morphology and chemical composition of garnets, ilmenite, chromites and other minerals accompanying diamonds in kimberlites.

## 2 Division of indicator minerals into morphogenetic groups and the prospecting works

Over the course of several years, we have studied the KIM from kimberlites and individual exploration sites in the northern part of the East European Platform and surrounding territories. To assess the history of migration of the KIMs, we conducted a full analysis of the mineralogical features of these grains. Several hundred samples from kimberlites, from the overlying Paleozoic rocks and from different Quaternary sediments were studied.

The method includes sampling and selection of mono-mineral fractions of garnets, chromites and ilmenite and analysis of their morphological features and chemical compositions. The conditions of preservation of diamonds and accompanying minerals during transport from the source rock determine features of their morphology and internal structure. Different factors changing the surface of minerals (corrosion and mechanical abrasion) and features of their chemical composition are taken into account.

The method also employed the use of several computer programs: the programs for quantitative analysis of the optical and SEM images and programs for the statistical analysis of the micro-beam data. Comprehensive studies of KIM are conducted in several stages:

- identification and description of the different morphological types of KIM on the basis of optical and electron microscopy;
- separation of genetic groups of garnets, ilmenite and chromites on the base of the features of their composition and physical properties;
- statistical analysis of materials, typification and localization of diamond-bearing rocks;
- evaluation of primary sources of diamonds.

The first stage begins with the optical study of KIM. We divide them into groups according to simplified morphological schemes (Kudryavtseva et al. 2005). The scheme provides for the division of KIM into a small number of groups according to the main characteristics (Fig.1):
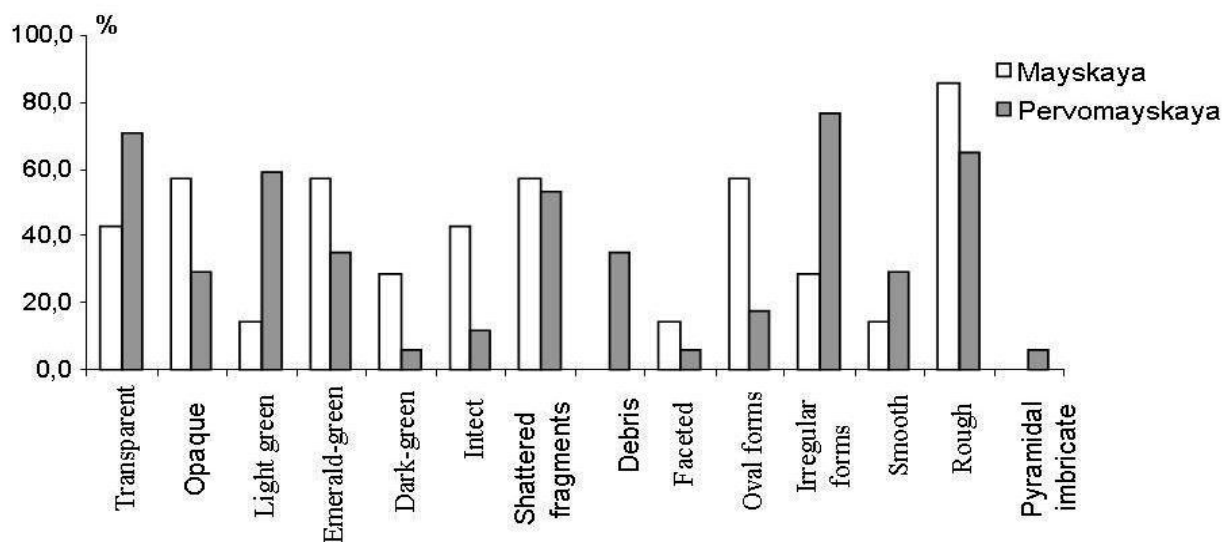
**Figure 1.** Distribution of different morphological types of pyroxenes in the Mayskaya pipe (Verkhotinskoe field) and Pervomayskaya pipe (Zolotitskoe field), Arkhangelsk diamondiferous province

size, optical properties (color, transparency), morphology (degree of splitting, shape, surface texture), specific internal structure. Preliminary separation of the KIM into different morphological groups may be already done on the basis of the following first results.

The second stage involves the study of minerals in the SEM and quantitative processing of the images. Quantitative assessment of topographic detail in micrographs allows us to estimate the degree of roundness of the grains.

Contours of the particle are represented in polar coordinates as a function of the radius R of the central angle. The resulting function is expanded in a Fourier series in the formula:

$$R_\theta = R_0 - \sum_{n=1}^{\infty} (A_n\cos\theta + B_n\sin\theta)$$

$R_0$ - the average radius of the projection of grain;

$A_n$, $B_n$ - Fourier amplitudes (coefficients of trigonometric functions);

$n$ - number of harmonic series.

Then, by setting n, we can describe any shape of the grains with any accuracy.

Influence of scale image and the grain size can be excluded when calculating the mean-square values of the amplitudes, normalized by the average particle radius:

$$P_n = 1/R_0 \ [(A_n^2 + B_n^2)/2]^{1/2}$$

RMS values of amplitude of the first ten harmonics are a quantitative measure of the shape of particles (the deviation of the projection of grain from a circle). RMS values of amplitudes of the second and third dozens of harmonics - is the value of the irregularities which determine the nature of the surface (micro-relief).

The proposed method uses a measure of the degree of preservation of a grain to identify the presence of specific forms of dissolution and abrasion on the basis of their images in the SEM (Fig. 2).

The third stage involves electron microbeam analysis of the KIM and their spectroscopic study. These results are statistically processed and compared with a database using cluster and discriminate analysis programs. The application of this scheme allows to subdivision of the KIM at studied target of the Arkhangelsk province into genetic groups based on their composition and typomorphic properties.
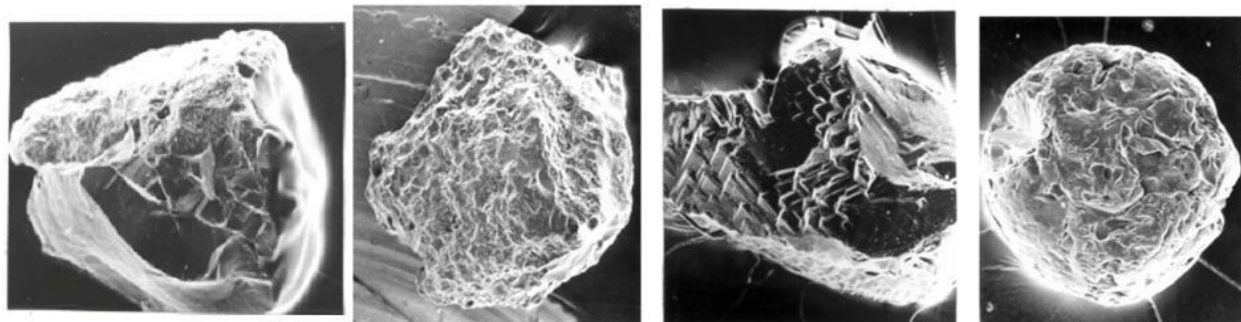


**Figure 2.** Different morphogenetic groups of garnets from the Arkhangelsk kimberlites

The *first group* consists of crustal material that is introduced to the kimberlitic pipes, secondary halos and placers from the host rocks. These include pink and yellow-orange round-oval grains of manganese garnets with a shiny smooth surface and a specific "facet" sculpture that is characteristic for supergene processes. High-Ti and high-Fe octahedra chromites with exsolution lamellae also included.

The *second group* includes grains, which are characteristic of the upper horizons of pipes exposed to weathering and for tuffaceous sedimentary rocks or placers. They are characterized by a fine-brushed surface, the nature of which is caused by the presence of numerous small cavities formed during corrosive dissolution. Supergene changes are manifested in the formation of secondary rims on the surface of the grains and in formation of special physical properties.

The *third group* is typical to the kimberlitic mantle parageneses. There are red, purple and orange garnets and oval grains of ilmenite and chromites. Surface sculpturing of such grains is due to interaction with kimberlitic melts (kelyphitic rims) or the process of cracking (conchoidal cleavage) during formation of pipes. Their chemical compositions and spectroscopic characteristics confirmed the similarity to the minerals from mantle xenoliths belonging to different mineral assemblages and vary in different pipes and fields. This fact is the basis to link of exploration halos.

The fourth group includes grains of garnets and clinopyroxenes with pyramidal imbricate surface sculpture and chromites with triangular-layered micro-relief. Such relief can be formed in the process of dissolution and as a result of regeneration of cleavage surfaces during metasomatic and diagenetic processes.

The fifth group consists of grains with high mechanical abrasion. They have undergone repeated redeposition, long-range transport, coastal and marine processing and cannot be traced to their original source.

Quantitative relationships between the groups naturally vary in the vertical section of bodies and in different types of kimberlites and placers.

Based on the described technique a database of the morphology and chemical composition of indicator minerals of diamond was assembled for six prospecting regions of the Arkhangelsk diamondiferous province. Morphological features help determine conditions during accumulation of minerals in the studied area. Grains having an average degree of wear have been transported from the source arelatively short distance and show no sings of litoral abrasion – they came directly from their native sources. These grains have been found among the garnets from the Belorechensky, Zolotitskoy, Dolmatovskaya and Pioneersky exploration areas and among the ilmenite from the Pioneersky area. Grains that have a strong degree of mechanical abrasion due to the sea-littoral conditions and have consequently lost the link to their sources include some garnets from the Emetskaya and Pinegskaya areas, as well as some ilmenites from the Belorechenskaya, Zolotitskaya and Dolmatovskaya areas.

Features of KIM in secondary halos around the kimberlites of the Arkhangelsk Province indicate three main types of reservoirs: alluvial and deltaic facies of the Urzuga Formation in the Zolotitskoe field; in sedimentation Paleozoic sea basin with a hot arid climate in the Tovskaya area; and the Later-Vise reservoir on the river Padun which were formed during oxidation weathering.

A study of the chemical composition of garnets and ilmenite from these sites allows identification of the chemical-genetic groups of grains, which have no analogues among the known primary deposits of the Arkhangelsk province (Fig. 3). The discovery of garnets and ilmenites of such compositions indicates the presence of unknown primary sources that are targets for further exploration.
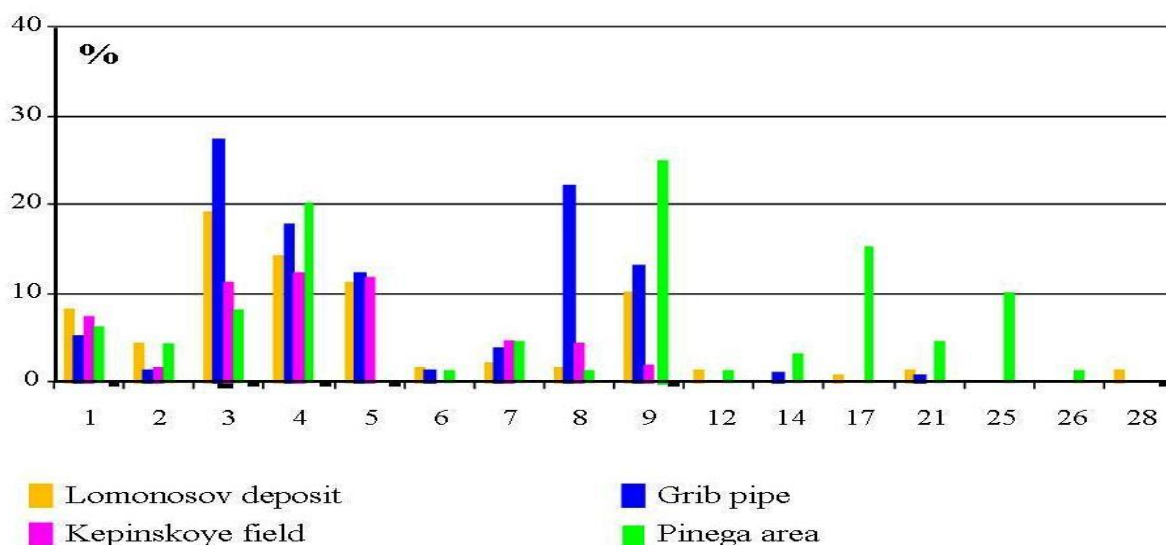


**Figure 3.** The distribution of chemical-genetic groups of garnets (1-28) in kimberlites and searching areas of the Arkhangelsk province

### 3. Division of indicator minerals into morphogenetic groups **and economical estimation of diamond deposits**

Morphological and genetic analysis can also improve the accuracy of the evaluation of the diamond-bearing potential of kimberlites. Mineralogists usually use characteristics of the chemical composition of the KIM for this purpose. In the proposed method we establish diamondiferous potential of the kimberlitic areas by using morphological analysis of the garnet, chromites and ilmenite.

The method takes into account the conditions of preservation of diamonds and associated minerals during transporting from the mantle source to the surface in the kimberlitic magma. Changes in mineral surface characteristics (corrosive relief) and peculiarities of the internal structure of the grains indicate unfavorable conditions of preservation of diamonds in kimberlites and hence low diamond grades.

The method involves the analysis of several features of the morphology and internal structures of the KIM grains (Table 1):

- the degree of corrosion on the surface of the grains;
- the presence (absence) of a needle micro-inclusions of the ore minerals in garnets;
- the presence (absence) of the lattice structures of the exsolution lamellae in ore minerals (chromites, ilmenite).

A kimberlitic area can be inferred to be diamond-bearing on the following conditions (Table 1):

- if gross corrosive forms of relief with cavities over 30 micrometers deep on the surface of 70% of grains of ilmenite, chromites and pyropes are absent;
- if the presence of needle inclusions of the ore minerals in less than 15% of the grains of garnets;
- if lattice structures occur in less than 5% of the octahedral chromites;
- if the lamellar micro-inclusions occur in less than 10% of the ilmenites.

**Table 1.** Comparative characteristic of the morphological features of KIM in diamond-bearing and barren pipes

| Degree of diamond potential | Features of the internal structure | | | Corrosive form |
|---|---|---|---|---|
| | Ilmenite | Garnets (pyropes) | Chromites | |
| | the presence of lamellar micro-inclusions in ferromagnetic grains | the presence of needle inclusions of ore minerals | the presence of lattice structures in the octahedral crystals | |
| High | < 10% | < 15% | < 5% | Absent |
| Low | > 10% | > 15% | > 5% | Common |

In addition, another new technique of evaluation of diamond potential of kimberlites, based on study of chemical composition of microphenocryst (less than 100 mkm) oxides from kimberlite groundmass, has been developed (Bovkun et al., 1998). The technique is based on the correlations between compositions of such oxides and kimberlite diamond potential. The conditions of high contents of diamond are the following:

- the presence of high-Cr-picrocromites of the cluster group 1 with >53.0 wt.% $Cr_2O_3$, < 3.5 wt.% $TiO_2$ and 9.0-14.0 wt.% MgO;

- the absence or afleust low content ( < 25% in random statisticaly reliable grains selection) of titanomagnetites and other Ti-mineral-phases (ilmenites, rutiles, perovskite, titanite).

### Acknowledgements

### References

Afanasiev VP, Zinchuk NN, Pokhilenko NP (2001) Morphology and morphogenesis of kimberlite indicator minerals. "Geo" Pub. SO RAN, "Manuscript Pub.", Novosibirsk

Bovkun AV, Garanin VK, Kudriavtseva GP, Possukhova TV (1998) Chemical-genetic classification of microcrystalline oxides from kimberlite groundmass and new system of diamondiferous prospecting. In: Ext. abstracts of the 7 Int. Kimb. conf. Cape Town, pp 91–93

Kudriavtseva GP, Posukhova TV, Verdjak VV, Verichev EM, Garanin VK, Golovin NN, Zuev VM (2005) Atlas. Morphogenesis of diamond and satellite minerals in kimberlites and associated rocks of the Arkhangelsk Province. Polyarny Krug, Moscow

# The structure of nodular chromite from the Troodos ophiolite, Cyprus, revealed using high-resolution X-ray computed tomography and EBSD

**Hazel M. Pritchard**
*School of Earth and Ocean Sciences, Cardiff University, Cardiff, CF 10 3AT, Wales, UK*

**Stephen J. Barnes, Belinda Godel, Angela Halfpenny**
*CSIRO Earth Science and Resource Engineering, ARRC, 26 Dick Perry Avenue, Kensington, WA, 6151, Australia*

**Chris Neary**
*School of Earth and Ocean Sciences, Cardiff University, Cardiff, CF10 3AT, Wales, UK*

**Abstract.** Nodular chromite characterises ophiolitic podiform chromitite but there has been much debate about how it forms. Nodular chromite from the Troodos ophiolite in Cyprus contains skeletal crystals enclosed within the centre of the nodules. 3D imaging and electron backscatter diffraction have shown that the essentially undeformed skeletal crystals are single crystals that are surrounded by a rim of chromite. This rim is composed of a patchwork of chromite grains that are truncated on the outer edge of the rim. Thus the skeletal crystals formed first in a tranquil environment from a magma supersaturated in Cr and silicates were trapped between the crystal blades of the skeletal crystals as they grew. These skeletal crystals were then engulfed by a crystallisation event which formed a silicate-poor rim of chromite grains that were subjected to corrosion or erosion probably in a turbulent environment. At contact points where nodules impinge on each other the grains of chromite are deformed.

**Keywords** Chromite, nodules, skeletal crystals

## 1 Introduction

Nodular and orbicular chromites are common in ophiolite complexes and have been described by many authors (e.g. Rynearson and Smith 1940; Thayer 1964; Brown 1980; Ahmed 1982; Paktunc 1989; Zhou 2001; Huang et al. 2004; Xu et al. 2011). Nodules generally range from 2-30 mm in size, usually have smooth outer surfaces but may be either mostly composed of chromite or contain silicates in their cores. They are commonly associated with euhedral chromite grains, as first noticed by Thayer (1964), although corners may be rounded. Nodules generally occur together and may touch each other. Occasionally the nodules have skeletal or dendritic chromite in their cores (Greenbaum 1977, Huang et al. 2004). The chromite nodules studied here are those described by Greenbaum (1977) from the Troodos ophiolite in Cyprus, from a locality on Mt Olympus, just south of Kokkinorotsos which is the largest chrome mine in this ophiolite. Greenbaum concluded that the skeletal crystals in the centres of these chromite nodules formed from supersaturation and /or supercooling of a water-rich magma.

However there have been many mechanisms suggested for the growth of nodular chromite. The main ideas include:

(1) Growth from suspended aggregates accumulating concentrically in fast flowing magma (Huang et al. 2004) with aggregation, and coalescence or clustering of free-formed chromite grains prior to settling (Ahmed 1982; Lorand and Ceuleneer, 1989) and snowballing in a turbulent flow (Dickey 1975).

(2) Separation of chromite from silicate magma by its attachment to a water-rich collector fluid that envelopes the chromite forming spherical aggregates (Matveev and Ballhus 2002).

(3) Formation in turbulent picritic magma flow accompanied by a water-rich fluid (Moghadam et al. 2009).

(4) Solidification of globules from a (hypothetical) chromite-rich immiscible liquid (Pavlov 1977).

(5) Association with silica-rich droplets arising from wall-rock reaction causing chromite crystallisation around the droplet and their 'collapse' to form chromite nodules (Zhou et al. 2001).

Nodules have been reported to lack chemical zoning (Greenbaum 1977; Ahmed 1982). Other researchers report chemical differences towards the rim including Cr decrease and Ti increase (Leblanc and Ceuleneer 1992). However there is no agreement on how these nodules form or even whether the nodules crystallised from the smooth bounding ellipsoidal surface inwards towards the core or grew from the centre outwards.

## 2 Methods

Two 25 mm diameter cores were drilled within the dendritic nodular chromite (Figs. 1 and 2). These cores were scanned using the XRADIA XRM 500 high-resolution 3D X-ray microscope system installed at the Australian Resources Research Centre (ARRC, Kensington, Western Australia). The data generated were processed and analysed using AvizoFire and CSIRO-developed codes following methods described in Godel (in press). One core was subsequently cut and polished down to a particular area where a skeletal crystal-cored nodule had been observed in the 3D scan. This area was selected for electron backscatter diffraction (EBSD) analysis. Full crystallographic orientation data were obtained from automatically indexed Kikuchi diffraction

patterns collected on a Zeiss Ultraplus FEG SEM at the CSIRO facilities, Kensington, WA. The SEM was operated using an accelerating voltage of 20kV, a 120µm aperture, in high current mode which produced a beam current of 12.1nA. The EBSD data were collected using the Bruker Quantax Espirit 1.9 software, using an EBSP resolution of 200x150, a 11.5ms exposure time and a step size of between 5.12µm (determined by the size of the smallest grain of interest). If the pattern quality was poor then the software was unable to find the correct crystallographic solution and the point was not indexed. Non-indexed points are common in areas of poor surface quality, on grain boundaries, cracks and where the surface is contaminated.

## 3 Results

In 2D the samples consist of groups of nodules enclosing skeletal crystals that are locally in contact with each other and are all surrounded by serpentinised olivine. Skeletal crystals are also present between the nodules especially on the edge of the groups of nodules (Figs. 1 and 2). Away from the nodules skeletal crystals occur sporadically within the dunite.



**Figure 1.** Skeletal crystals located between and on the edge of a group of chromite nodules.
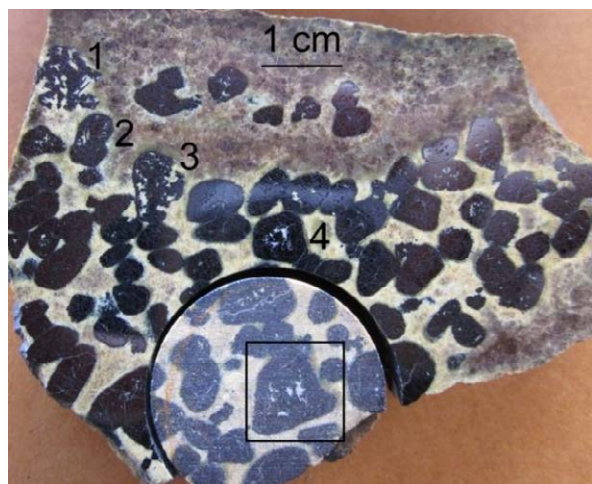


**Figure 2.** A group of chromite nodules (black) in serpentine with skeletal crystals showing stages of chromite rim development, from the edge to the centre of the group of nodules (1) no rim, (2) a thin rim, (3) a partial rim and (4) a thick rim. The nodule chosen for EBSD analysis is surrounded by a square.

At the edge of the group of nodules, skeletal crystals are sometimes partially surrounded by a thin or semi-complete rim of chromite (Fig. 2), suggesting that the skeletal crystals formed first and then the outer rim of chromite formed around them.

The high-resolution X-ray computed tomography gives 3D insights into the structure of the nodules and their core skeletal crystals allowing sections of a sample to be examined in different planes at right-angles (Fig 3). The nodule selected for detailed studies is elongate and shows a herring bone skeletal texture in the sections parallel to the long axis and a double Y shape in the orthogonal section (Fig. 4). The skeletal crystals are coated with the chromite rim draping around the skeletal crystals and mimicking the shape of the outer surfaces of the skeletal crystals (Figs. 2-4). The 3D images of the nodules containing skeletal crystals show that the skeletal crystals form "cages" visible in a 3D perspective view (Fig. 5).
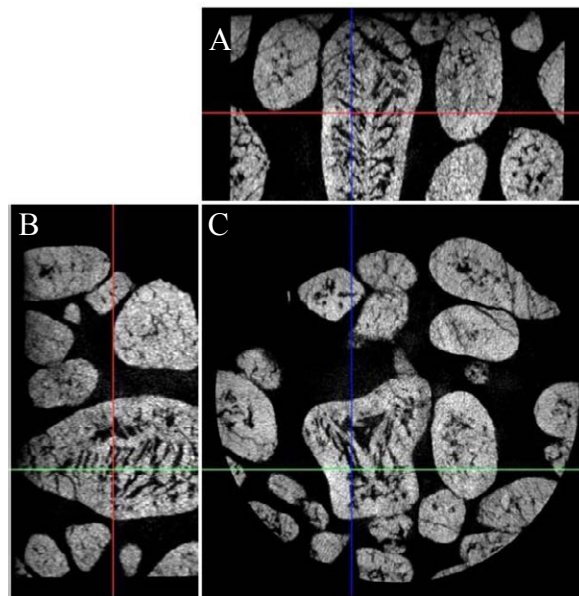


**Figure 3.** Two slices (A and B) across the elongate axis and a section at right-angles (C) across the nodule surrounded by a box (Fig 2). For scale see Fig. 2.
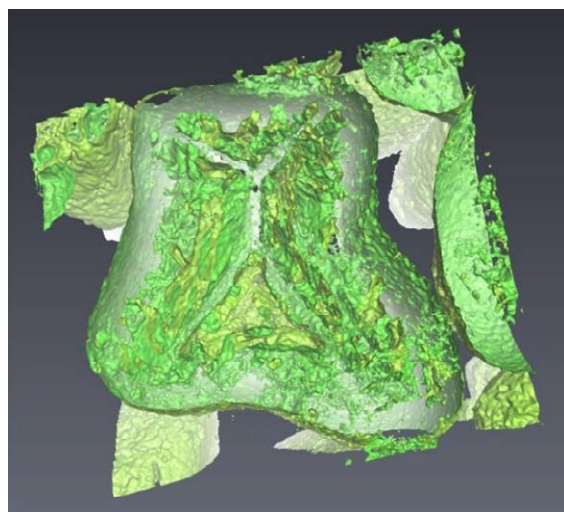


**Figure 4.** 3D image of the chromite nodule with the edge of chromite outlined to show the edge of the chromite rim and the skeletal crystal structure in cross section (C) (Fig. 3).
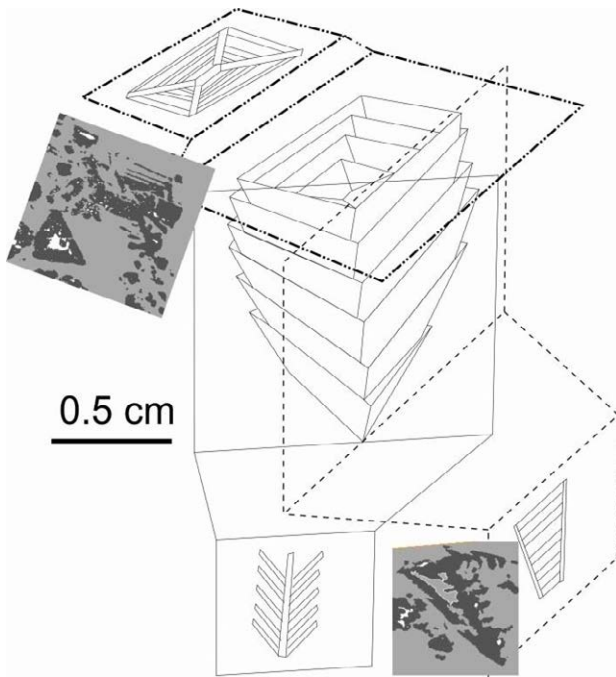
**Figure 5.** Sketch of a skeletal crystal in 3D showing the "cage" structure with three cross sections observed in 2D. Grey images are parts of slices taken across the skeletal crystals analysed using high-resolution X-ray computed tomography.
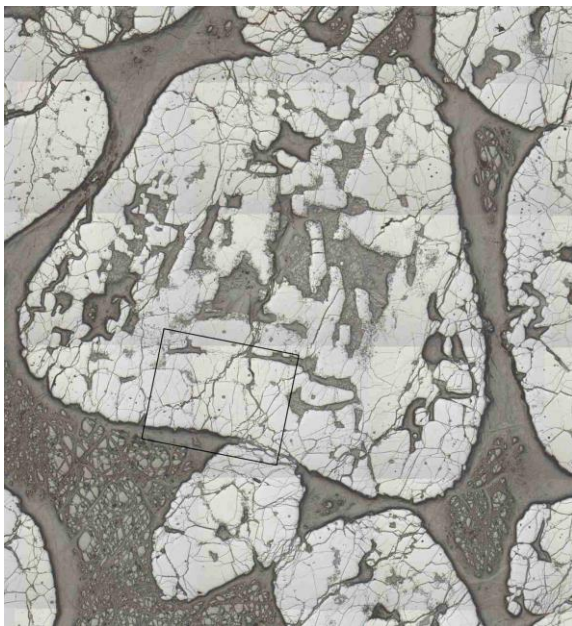


**Figure 6.** Reflected light image of the nodular chromite containing a core skeletal crystal as shown in Figs 2-4. The square box shows area imaged using EBSD.

The sample chosen for EBSD analysis consists of a part of a nodule containing a skeletal crystal (Figs. 2, 4 and 6). This and other images show that the whole of the skeletal crystal forms a single crystal with clinochlore, clinopyroxene and serpentine occupying the spaces between the skeletal crystal blades. The skeletal crystal is surrounded by a rim composed of polycrystalline chromite grain aggregate (Fig. 7).
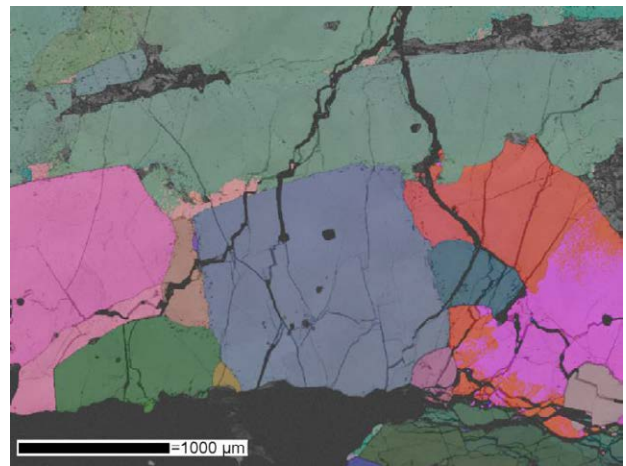


**Figure 7.** EBSD image, with a branch of the skeletal crystal at the top and the rim of the nodule, composed of grains, below. The silicate is shown in black and the nodule is impinging on another nodule in the bottom right hand corner.

Chromite grains on the smooth (but in detail crenulated) edge of the rims are truncated. The skeletal crystal is essentially undeformed as are most of the chromite grains in the rim (Fig. 8). Deformation occurs where the chromite grains have been impacted by another nodule (Fig. 9).
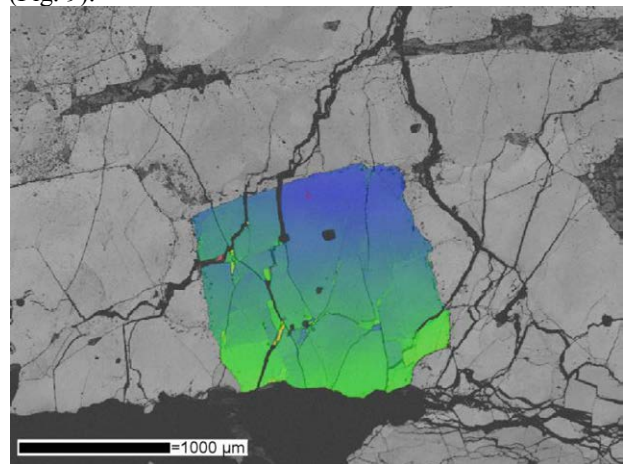


**Figure 8.** EBSD image showing a lack of variation in crystallographic orientation for a grain of chromite in the rim.
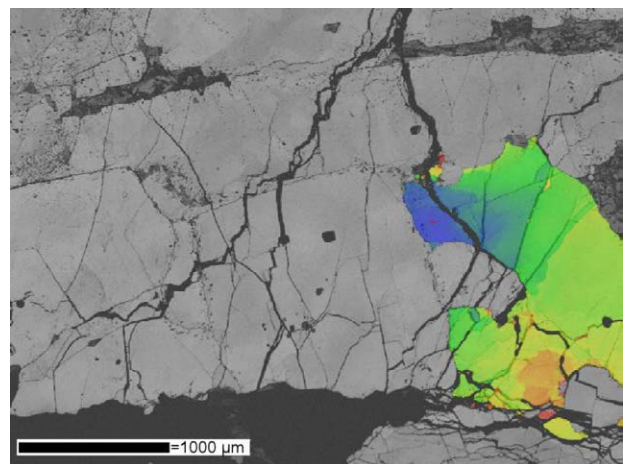


**Figure 9.** EBSD image showing greater changes in orientation (up to 10º) (indicated by a greater colour range of red to blue) in the rim chromite grain at the point in contact with an adjacent chromite nodule, compared to the adjacent grain (where the colour range is only blue-green) (Fig 8).

## 3 Interpretation

Skeletal chromite crystals have been reported previously from magmatic environments and interpreted as the result of rapid crystal growth from chromite-supersaturated magma (Godel et al. 2013). The evidence presented here implies that these skeletal crystals from the Troodos ophiolite formed first and were then coated with equant chromite to form nodules, indicating that the nodules grew from the centre outwards. The skeletal crystals are likely to have grown rapidly along preferred fast-growing crystallographic planes in a regime of chromite supersaturation, giving blades of chromite that form a cage-like network in 3D. Then, as the degree of supersaturation decreased, the rate of chromite nucleation increased relative to the rate of growth, and multiple individual grains formed around the skeletal crystals. These coalesced to produce a rim that retains the overall geometric outline of the skeletal crystal. This accounts for the crystal-like morphology of the entire polycrystalline nodule. Truncation of the grains on the edge of the rim suggests that the nodules were subsequently either partially dissolved, accounting for the small scale smooth outline and the apparent truncation of individual grains revealed by the EBSD images. Turbulence in the magma may also have contributed to mechanical abrasion of the nodules. The nodules then underwent compaction and were weakly deformed at impingement points during this process. This suggests an order of crystallisation that is not likely to have occurred by collection of chromite in any kind of spherical droplet, but which records sequential crystallisation of a suspended crystal aggregate under varying degrees of chromite saturation. The progression from skeletal crystals in the core to equant polycrystalline rim to subsequent resorption records a growth sequence influenced by changing chemical and dynamic environments. This study has shown how these particular nodules grew. Similar processes may account for formation of the more common types of nodular chromite, frequently described from ophiolite complexes, which do not contain skeletal crystals in their cores.

## Acknowledgements

## References

Ahmed Z (1982) Porphyritic-nodular, nodular, and orbicular chrome ores from the Sakhakot-Qila complex, Pakistan, and their chemical variations. Mineral Mag 45:167-178

Brown M (1980) Textural and geochemical evidence for the origin of' some chromite deposits in the Oman ophiolite. In: Panayiotou A (ed) Ophiolites. Proc Int Ophiolite Symp pp. 714-721

Dickey JS Jr (1975) A hypothesis of origin for podiform chromite deposits. Geochim Cosmochim Acta 39:1061-1074

Godel B (in press) High-resolution X-ray computed tomography and its application to ore deposits: case studies from Ni-Cu-PGE deposits. Economic Geology

Godel B, Barnes SJ, Gurer D, Austin P, Fiorentini ML 2013. Chromite in komatiites: 3D morphologies with implications for crystallization mechanisms. Contributions to Mineralogy and Petrology, v. 165, 173-189

Greenbaum D (1977) The Chromitiferous rocks of the Troodos ophiolite, Cyprus. Econ Geol 72:1175-1194

Huang X, Li J, Kusky TM, Chen Z, (2004) Microstructures of the Zunhua 2.50 Ga podiform chromite, North China Craton and implications for the deformation and rheology of the archaean oceanic lithospheric mantle. In: Kusky TM (ed) Precambrian ophiolites and related rocks, Developments in Precambrian geology, Ch 10, v13, (K C Condie series ed) pp 321-337

Leblanc M, Ceuleneer G (1992) Chromite crystallization in a multicellular magma flow:Evidence from a chromitite dike in the Oman ophiolite. Lithos 27:231-257

Lorand JP, Ceuleneer G (1989) Silicate and base-metal sulphide inclusions in chromites from the Maqsad area (Oman ophiolite, Gulf of Oman): A model for entrapment. Lithos 22: 173-190

Matveev S, Ballhaus C (2002) Role of water in the origin of podiform chromitite deposits. EPSL 203:235–243

Moghadam HS, Rahgoshay M, Forouzesh V (2009) Geocheomical investigation of nodular chromites in the Forumad ophiolite, NE of Iran. Iranian Jl Sci and Tech, Trans A. 33:103-108

Paktunc AD (1990) Origin of podiform chromite deposits by multistage melting, melt segregation and magma mixing in the upper mantle. Ore Geol Rev 5:211-222

Pavlov NV, Grigoryeva I, Tsepin AI (1977) Chromite nodules as an indicator of liquation of a magmatic melt. Int Geol Rev 19:43-56.

Rynearson GA, Smith CT (1940) Chromite deposits in the Seiad Quadrangle Siskiyou county, California. Strategic Minerals Investigations, Bulletin 922-J:281-306

Thayer TP (1964) Principal features and origin podiform chromite deposits, and some observations on the Guleman-Soridag district. Turkey. Econ Geol 59:1497-1524

Xu X, Yang J, Ba D, Guo G, Robinson PT, Li J (2011) Petrogenesis of the Kangjinla peridotite in the Luobusa ophiolite, southern Tibet. J Asian Earth Sci 42:553-568

Zhou M-F, Malpas J, Robinson PT, Sun M, Li J-W (2001) Crystallisation of podiform chromites from silicate magmas and the formation of nodular textures. Res Geol 51: 1-6

# U-Pb baddeleyite geochronology by laser ablation multi-collector ICPMS using multi-ion counting

A. Kate Souders & Paul J. Sylvester
*Department of Earth Sciences, Memorial University, St. John's, NL, Canada A1B 3X5 (kate.souders@mun.ca, psylvester@mun.ca)*

**Abstract.** Baddeleyite is a common U-bearing accessory mineral found in many mafic rocks including those associated with many ore deposits. An in-situ U-Pb LA-MC-ICPMS method to date baddeleyite is presented. The method allows for the simultaneous measurement of $^{202}$Hg, $^{204}$Pb, $^{206}$Pb, $^{207}$Pb, $^{208}$Pb, $^{235}$U, $^{238}$U isotopes in Channeltron ion counters. Standard-sample-standard bracketing using FC-4b baddeleyite as the external standard is used to correct for instrumental mass bias. A slow line scan ablation is used with a 4-$\mu$m laser beam to minimize laser induced U/Pb fractionation. The small volume of material consumed by the 4-$\mu$m line scan is ideally suited for the small, elongate nature of typical baddeleyite crystals. Results are presented for three baddeleyite samples of known age. External precisions for $^{207}$Pb/$^{206}$Pb dates range from < 0.6% for baddeleyites older than 1000 Ma to ~5% for baddeleyites younger than 1000 Ma. The described method can be used to date mafic rocks where high-precision data are not required or as a compliment to TIMS analyses when high-precision data are necessary.

**Keywords.** baddeleyite, U-Pb geochronology, laser ablation, MC-ICPMS.

## 1 Introduction

Baddeleyite ($ZrO_2$) is an ideal geochronometer for dating mafic rocks by the U-Pb method. It is a proven useful mineral for U-Pb dating due to its high U (200 – 1000 ppm) and negligible initial common Pb (Heaman and LeCheminant 1993). Baddeleyite is present in a variety of silica-poor terrestrial rocks such as anorthosites, gabbros, troctolites and carbonitites as well as lunar rocks and Martian meteorites. It has been used in a variety of applications from dating terrestrial magmatic events associated with minerals deposits (e.g. Amelin et al. 1999) to determining the age of Martian crust (e.g. Herd et al. 2007). Baddeleyite can be dated by bulk (TIMS) or microbeam methods (SHRIMP, SIMS, LA-ICPMS) but small grains have proven challenging for laser ablation methods.

Microbeam methods such as laser ablation inductively coupled plasma mass spectrometry (LA-ICPMS) are increasingly used for applications in the Earth Sciences where high precision data are not required. While use of U-Pb zircon geochronology by LA-ICPMS has rapidly increased, U-Pb baddeleyite geochronology by LA-ICPMS has lagged behind. This has been due to many factors including limited well-characterized references materials for U-Pb baddeleyite geochronology, extensive U/Pb fractionation during spot analysis of baddeleyite, and the narrow, elongated shape of many baddeleyite crystals (Fig. 1), which make laser analyses difficult to position.

We present a U-Pb dating method for baddeleyite by laser ablation multi-collector ICP-MS using multiple ion counters for the simultaneous collection of $^{202}$Hg, $^{204}$Pb, $^{206}$Pb, $^{207}$Pb, $^{208}$Pb, $^{235}$U, $^{238}$U isotopes. A slow line scan ablation is used with a 4-$\mu$m laser beam, ideal for smaller baddeleyite grains typically found in mafic rocks (Fig. 2). We then test our method using several baddeleyite reference materials with well characterized crystallization ages determined by TIMS. The smaller volume of material consumed and the shorter ablation time required for the multi-collector U-Pb method is ideal for smaller baddeleyite grains.

## 2 Method

All data were acquired using a Thermo Scientific NEPTUNE multi-collector ICPMS at Memorial University (MUN). The NEPTUNE at MUN is equipped with 9 Faraday cups and 8 ion counter (Channeltron) detectors (Fig. 3). Concurrent, static measurements of $^{202}$Hg, $^{204}$Pb, $^{206}$Pb, $^{207}$Pb, $^{208}$Pb were made in 5 ion counters mounted onto the low mass Faraday cup (L4). $^{235}$U and $^{238}$U were measured in ion counters attached to Faraday cups H3 and H4, respectively.
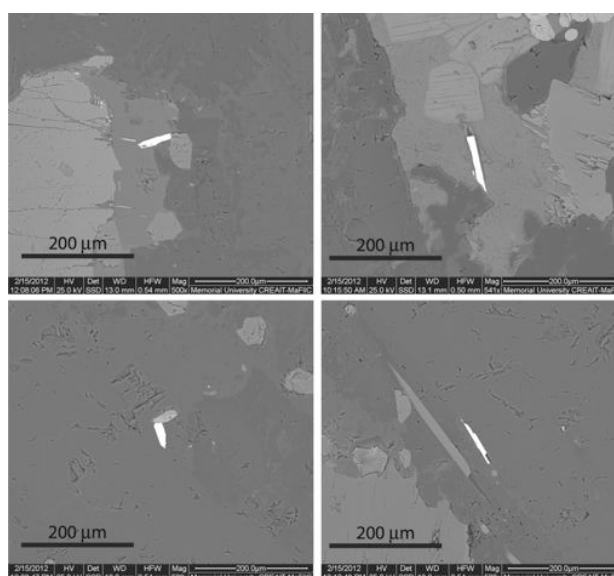


**Figure 1.** Back-scattered electron images of representative baddeleyite grains in thin section. The baddeleyite grains are the bright phases located in the center of each image. The elongate nature is typical of baddeleyite crystals identified in thin section and grain mount. Generally, baddeleyite grains are no more than 30 – 50 μm in the longest dimension and < 20 μm in the smallest dimension (Heaman and LeCheminant 1993).
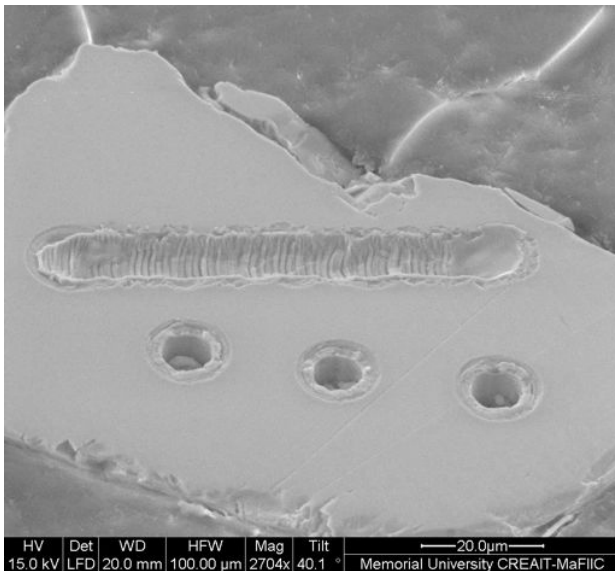
**Figure 2.** Baddeleyite crystal with example of a laser ablation slow line scan (top) and three laser ablation spot analyses (bottom).

Further information regarding the NEPTUNE operating parameters and ion counter set-up and cross-calibration can be found in Souders and Sylvester (2008a,b).

For laser ablation analyses, the NEPTUNE is linked to a Lambda Physik ComPex Pro 110 ArF excimer GeoLas laser ablation system operating at a wavelength of 193 nm and a pulse width of 20 ns. Samples were ablated in helium gas, which reduces sample re-deposition while increasing sensitivity for 193 nm laser ablation. A slow line scan ablation (Fig. 2) is used where a 4-µm laser beam with an energy density of 10 $J/cm^2$ and a repetition rate of 5 Hz scans across the sample surface at a rate of 2 µm/sec. A scanning method is employed to reduce the depth of ablation and supply a more constant mass-load to the ICP, reducing U/Pb fractionation while providing stable signals at high spatial resolution long enough to produce precise and accurate U-Pb ages. The duration of each analysis was ~120 seconds. The first ~30 seconds of the measurement were with the laser off measuring the background count rates followed by 30 seconds of laser ablation, and then ~60 seconds of recorded wash out. The NEPTUNE software was used for both ion counter yield and dark noise corrections prior to downloading the measured mass count rates into 'Baddeleyite-Tool', an in-house macro-based excel spreadsheet modified from 'LAM-Tool', for interval selection and isotope ratio calculations (Kosler et al. 2008). Final ages and Concordia diagrams were produced using Isoplot/Ex 3 macro (Ludwig 2008).

Several techniques have been used to correct for the mass discrimination (bias) of the ICPMS instrument. Two of the available options are to (1) use a well-characterized baddeleyite U-Pb standard for external calibration by standard – sample – standard bracketing, or (2) aspirate an enriched isotope tracer solution (e.g. $^{205}$Tl, $^{209}$Bi, $^{233}$U, $^{237}$Np) during sample analysis. In this study, we have employed standard – sample – standard bracketing to correct for instrumental mass bias due to limitations related to the NEPTUNE cup configuration.

Three standards, followed by three unknowns, followed by three standards are run sequentially using identical ablation conditions for both standards and samples. The calculated U-Pb and Pb-Pb isotopic ratios for every three standards are averaged together and the U-Pb and Pb-Pb isotopic ratios of each sample are determined by linear interpolation of the average ratios of standards run before and after every group of three unknowns.

Baddeleyite grains from sample FC-4b, a gabbroic anorthosite sample of the Duluth gabbro complex sampled at Forest Center, MN (USA), were used as the external standard for instrumental mass bias corrections. Thermal ionization mass spectrometry (TIMS) analyses of FC-4b baddeleyite grains yield a U-Pb age of 1095.42 ± 0.16 Ma.
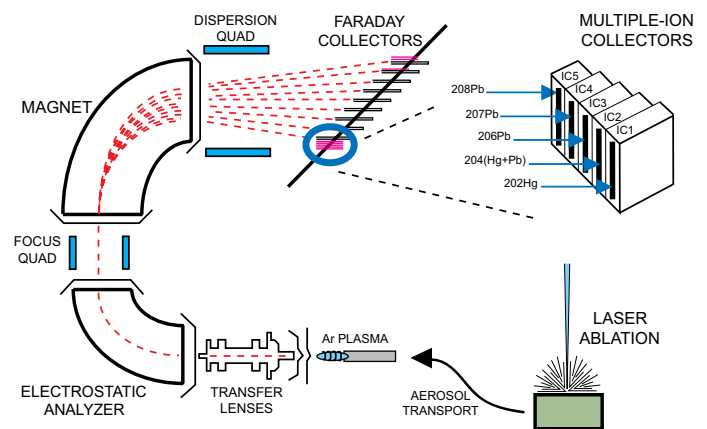


**Figure 3.** Schematic of the NEPTUNE MC-ICPMS and laser ablation system at Memorial University.

## 3 Results

In order to evaluate our U-Pb multi-ion counting method, three well-characterized baddeleyites with known U-Pb crystallization ages were analysed as unknowns using FC-4b baddeleyite as the external standard. Multiple grains of FC-4b baddeleyite, Sorkka baddeleyite (1256.2 ± 1.4 Ma; Söderlund et al. 2004), Kovdor baddeleyite (378.54 ± 0.23 Ma; Amelin and Zaitsev 2002), and Phalaborwa baddeleyite (2059.60 ± 0.35 Ma; Heaman 2009) were mounted in a single 25 mm diameter epoxy resin mount and polished, exposing a cross-section of each grain.

### 3.1 Sorkka baddeleyite

LA-MC-ICPMS analysis of baddeleyite separates from the Sorkka dolerite sill, western Finland yield a Concordia age of 1249 ± 15 Ma (2σ, n = 11) with an external precision of 1.2 % (2RSD) (Fig. 4). This date is within 0.6% of the TIMS age reported by Söderlund et al. (2004). The weighted mean $^{207}$Pb/$^{206}$Pb age for the Sorkka baddeleyite analyzed is 1260 ± 7.0 Ma (2σ, n = 14) with an external precision of 0.6 % (2RSD) (Fig. 4). This date is within 0.3 % of the TIMS value.
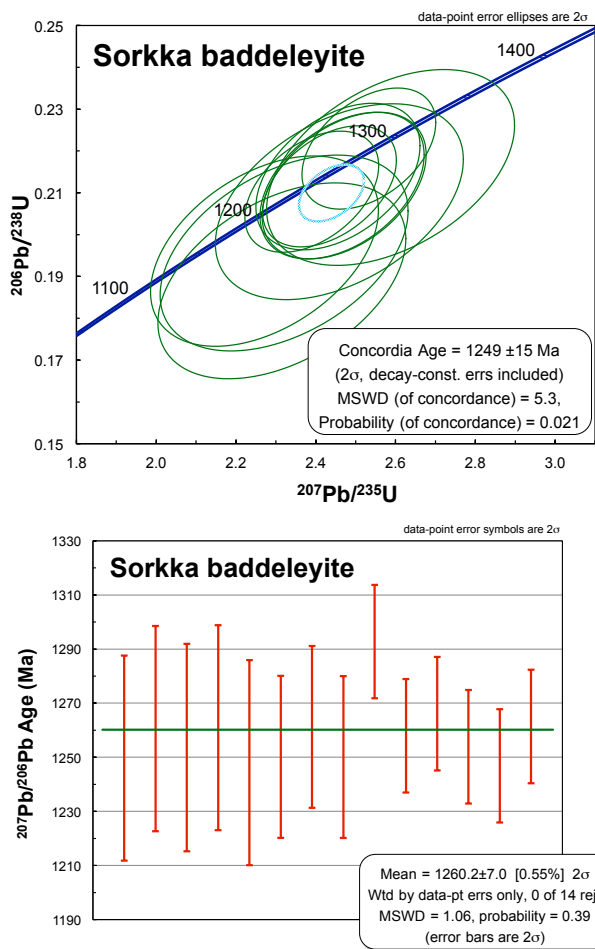
**Figure 4.** Concordia plot of data from 11 analyses of Sorkka baddeleyites and the weighted average for 14 $^{207}$Pb/$^{206}$Pb dates for Sorkka baddeleyite.

### 3.2 Phalaborwa baddeleyite

Nine analyses of baddeleyite separates from the Phalaborwa Complex, South Africa yield a weighted mean $^{207}$Pb/$^{206}$Pb date of 2058.2 ± 9.7 Ma (2σ, n = 9) with an external precision of 0.47 % (2RSD) (Fig. 5). This date is within 0.04 % of the TIMS date reported in Heaman (2009).
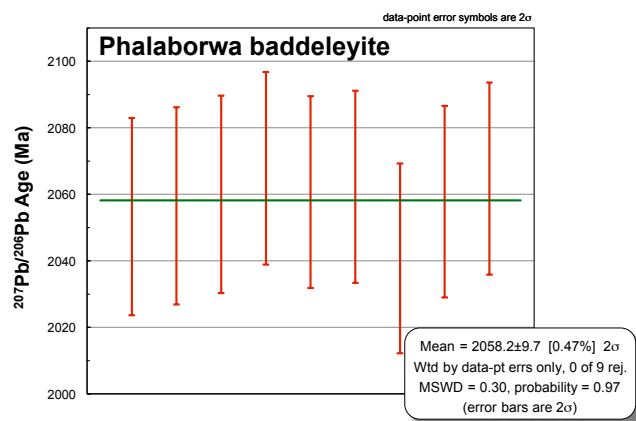


**Figure 5.** Weighted average for 9 $^{207}$Pb/$^{206}$Pb dates for Phalaborwa baddeleyite.

### 3.3 Kovdor baddeleyite

Analyses of baddeleyite grains from the Kovdor ultramafic-alkaline carbonatite massif, Kola Peninsula, Russia yield a Concordia age of 370 ± 24 Ma (2σ, n = 8) and a weighted mean $^{207}$Pb/$^{206}$Pb age of 386 ± 18 Ma (2σ, n = 8) (Fig. 6). These dates are accurate within 2.3% and 2% of the reported TIMS value, respectively (Amelin and Zaitsev 2002). External precisions for both the Concordia age and the weighted mean $^{207}$Pb/$^{206}$Pb age are imprecise (6.5 % (2RSD) and 4.7 % (2RSD), respectively) due to the comparatively young age and low radiogenic $^{207}$Pb of the Kovdor baddeleyite grains.
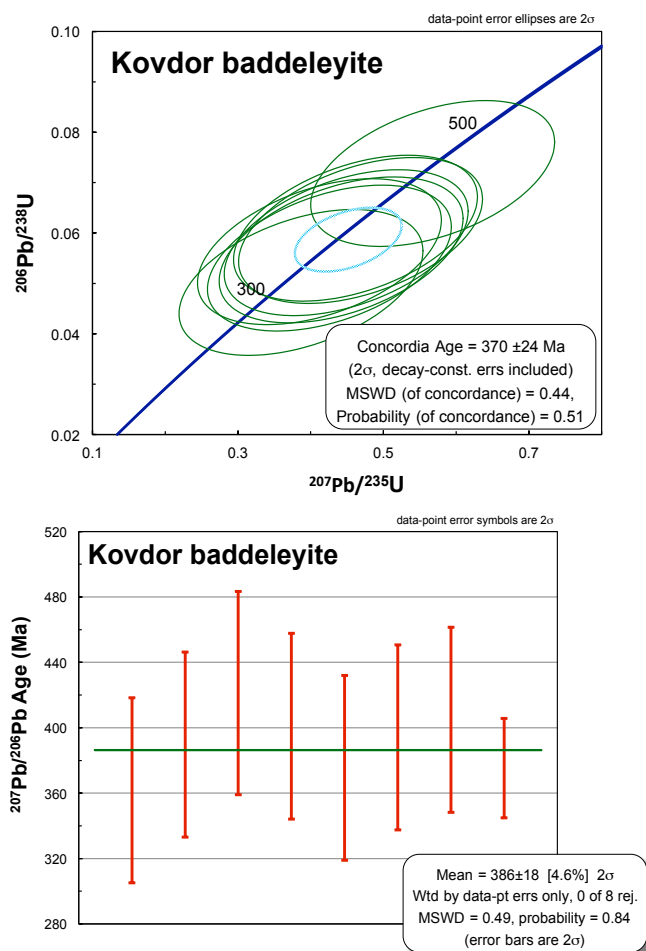




**Figure 6.** Concordia plot of data from 8 analyses of Kovdor baddeleyites and the weighted average for 8 $^{207}$Pb/$^{206}$Pb dates for Kovdor baddeleyite.

## 4 Conclusions

Baddeleyite is an ideal accessory mineral for U-Pb geochronology of mafic rocks. Unlike zircon, many baddeleyites found in thin section form small, elongate grains no more than 30 – 50 μm in the longest dimension and < 20 μm in the smallest dimension. This makes U-Pb analyses of baddeleyite by laser ablation more challenging than zircon because smaller laser spot sizes and shorter ablation times are required. The LA-MC-ICPMS U-Pb dating method presented produces results comparable to U-Pb baddeleyite dating by single-

collector LA-ICPMS using a line scan with a larger laser beam (10 – 20 μm) and requiring baddeleyite grains to be at least 80 μm in length. The smaller volume of material consumed and shorter ablation time required to achieve such precision during multi-collector analysis is more suitable for the typically small and elongated baddeleyite crystals. The method can be applied when less-precise dates (~2 % for grains older than ~1000 Ma) provide geologically useful information, or as a compliment to high-precision TIMS analyses when more precise dates are required.

## Acknowledgements

## References

Amelin Y, Li C, Naldrett AJ (1999) Geochronology of the Voisey's Bay intrusion, Labrador, Canada, by precise U-Pb dating of coexisting baddeleyite, zircon, and apatite. Lithos 47:33-51

Amelin Y, Zaitsev AN (2002) Precise geochronology of phoscorites and carbonatites: the critical role of U-series disequilibrium in age interpretations. Geochim Cosmochim Acta 66:2399-2419

Heaman LM (2009) The application of U-Pb geochronology to mafic, ultramafic and alkaline rocks: An evaluation of three mineral standards. Chem Geol 261:43-52

Heaman LM, LeCheminant AN (1993) Paragenesis and U-Pb systematics of baddeleyite ($ZrO_2$). Chem Geol 110:95-126

Herd CDK, Simonetti A, Peterson ND (2007) In-situ U-Pb geochronology of martian baddeleyite by laser ablation MC-ICP-MS. LPSC XXXVIII #1664

Kosler J (2008) Laser ablation sampling strategies for concentration and isotope ratio analyses by ICPMS. In: Sylvester PJ (ed) Laser Ablation ICPMS in the Earth Sciences: Current Practices and Outstanding Issues. Mineralogical Association of Canada, pp 79-92

Koser J, Forst L, Slama J (2008) LAMDATE and LAMTOOL: Spreadsheet-based data reduction for laser ablation-ICPMS. In: Sylvester PJ (ed) Laser Ablation ICPMS in the Earth Sciences: Current Practices and Outstanding Issues. Mineralogical Association of Canada, pp 315-317

Ludwig K (2008) Iosplot 3, A Geochronological Toolkit for Microsoft Excel. Special Pulbication 1a. Berkeley Geochronology Center

Söderlund U, Patchett PJ, Vervoort JD, Isachsen CE (2004) The [176]Lu decay constant determined by Lu-Hf and U-Pb isotope systematics of Precambrian mafic intrusions. Earth Planet Sci Lett 219:311-324

Souders AK, Sylvester PJ (2008a) Improved in-situ measurements of lead isotopes in silicate glasses by LA-MC-ICPMS using multiple ion counters. J Anal At Spectrom 23:535-543

Souders AK, Sylvester PJ (2008b) The use of multiple Channeltron ion counter for LA-MC-ICPMS analysis of common lead isotopes in silicate glasses. In: Sylvester PJ (ed) Laser Ablation ICPMS in the Earth Sciences: Current Practices and Outstanding Issues. Mineralogical Association of Canada, pp 265-281

# Synchrotron X-ray fluorescence and field emission gun scanning electron microscopy mapping shed light on fluid evolution and origin of IOCG prospects, Gawler Craton, South Australia

Yulia Uvarova, James Cleverley, Rob Hough
*CSIRO Earth and Resource Engineering, ARRC, Kensington, WA 6151 Australia*

**Abstract.** Synchrotron X-ray Fluorescence (SXRF) and Field Emission Gun Scanning Electron Microscopy (FEG SEM) were used for element mapping of subeconomic IOCG mineralisation at Emmie Bluff, Gawler Craton, South Australia. These techniques allowed rare micronscale features to be documented, providing important textural information for understanding the transport of elements such as Cu. Using SXRF and FEG SEM it was possible to document subtle differences in the chemical composition of chlorite. There were at least two stages of chlorite formation. It is therefore, possible to make conclusions about chemistry of the fluids involved. It is shown for the first time for the IOCG prospects in the Olympic Dam district, that Cu mineralisation was affected by a late fluid event. Alteration of Cu mineralisation is associated with the formation of Mn-rich chlorite which is host to a previously undescribed Cu-Cl phase. FEG SEM spectra also showed the presence of Zr, Y and U in the unknown Cu-Cl phase. This shows that there was remobilisation of previously existing Cu mineralisation in the form of chloride complexes in Zr-, Y- and U-bearing fluids.

**Keywords.** Synchrotron X-ray Fluorescence Microprobe, Field Emission Gun Scanning Electron Microscopy, Iron-oxide-Copper-Gold prospects, fluid history

## 1 Introduction

The Gawler Craton, in South Australia, is host to the giant Olympic Dam deposit and a number of economic to subeconomic IOCG prospects including Prominent Hill (Belperio et al. 2007), Oak Dam (Davidson et al. 2007), Wirrda Well (Drexel et al. 1993), Acropolis (Drexel et al. 1993), and Carrapateena (Fairclough 2005). Geologic observations for these IOCG deposits and prospects suggest at least two stages of hydrothermal activity that likely were of regional scale. Several models for ore formation at the Olympic Dam deposit have been proposed (Oresekes and Einaudi, 1990, 1992; Reeve et al., 1990; Haynes et al., 1995), as well as for the subeconomic mineralisation at the Emmie Bluff prospect (Gow et al. 1994). The genetic models are mainly based on the interaction between a high-temperature reduced, magnetite-stable fluid and a low-temperature, oxidized, hematite-stable fluid. Bastrakov et al. (2007) also proposed a model of upgrading of pre-existing Cu-Au mineralisation. In this study we demonstrate the application of Synchrotron X-ray Fluorescence (SXRF) and Field Emission Gun Scanning Electron Microscopy (FEG SEM) element mapping to document fluid evolution in subeconomic IOCG prospects and help to elucidate the origin of the mineralisation.

This study is based on a number of samples from the Emmie Bluff prospect, which is located approximately 70 km south-south-west of Olympic Dam. The iron-oxide zone is 150 m thick and is at ~800 m depth at Emmie Bluff (Gow et al. 1994). Samples studied are from the drill hole SAE4 between 790 and 1160 m.

## 2 Analytical techniques

### 2.1 Petrography and Scanning Electron Microscopy

The samples were initially examined with a Zeiss AxioImager polarisation microscope and Backscatter Electron Microscope (BSEM) with an attached cathodoluminescence (CL) detector on a Phillips XL40 instrument to determine macroscale textural properties and mineral compositions.

### 2.2 Synchrotron X-ray Fluorescence Microprobe

The synchrotron elemental mapping was performed on a polished thin section of a mineralised sample using a Maia 384 detector array (Ryan et al., 2010) at the Australian Synchrotron facility with X-rays focussed into a beam spot of ~1.5 μm with the Kirkpatrick–Baez mirror based lens system on the X-ray Fluorescence Microprobe (XFM) beamline (Paterson et al., 2007). This system enables rapid analysis (8 h) of a large area (~2 cm$^2$) at about 1–2 μm spatial resolution. This method is at least an order of magnitude more efficient compared with conventional X-ray detectors for identifying and mapping trace elements at ppm levels in a sample.

### 2.3 Field Emission Gun Scanning Electron Microscopy

Carbon-coated polished thin-sections were studied using a Zeiss Ultra-Plus FEG SEM coupled with a Bruker X-Flash EDX detector for elemental analyses at the ARRC laboratories (CSIRO, Kensington). An accelerating voltage of 20 kV and a beam current of 3 nA were used.

### 2.4 Electron microprobe analysis

Polished thin sections were carbon-coated and analysed

with a JEOL 8530F electron microprobe operating in wavelength-dispersion mode with an accelerating voltage of 15 kV, a specimen current of 50 nA, beam size of 15 µm and counting times on peak and background of 20 and 10 s, respectively. The following standards were used for Kα and Lα X-ray lines for the elements sought in chlorites and micas: Si, Al: biotite; Fe: anandite; Mg: periclase, Mn: spessartine, Ti: rutile; Cr: chromite, Ni: Ni-olivine, Cu: cuprite, Ca: wollastonite, Sr: SrSO$_4$, Ba: barite, Na, Cl: sodalite, K: orthoclase, F: Durango apatite. Data were reduced using the X-PHI procedure (Merlet 1992).

## 3 Results

Petrographic observations show that in the drill hole SAE4 the mineralisation occurs in an interval from ca. 890 to 910 m, where it is associated with the typical hematite-chlorite-sericite-carbonate alteration over a magnetite-±amphibole±K-feldspar assemblage. Directly above and below the mineralisation zone the rocks display magnetite±chlorite±Ca-silicate alteration, and further from the mineralisation (>30 m above and below the mineralisation) the rocks display mainly potassic alteration and hematite-carbonate-chlorite alteration in breccia and granite at the bottom of the drill hole.

The Cu mineralisation is present dominantly in the form of chalcopyrite within a low-temperature assemblage of hematite+chlorite+pyrite±quartz (Fig. 1). Much of the hematite shows magnetite cores, indicating overprinting of precursor magnetite. Chalcopyrite occurs after pyrite (Fig. 1). Copper mineralisation in the form of chalcopyrite was also altered and most of the chalcopyrite grains have patchy chlorite alteration (Fig. 1).

Detailed element mapping of chlorite in contact with chalcopyrite using FEG SEM resulted in a number of interesting findings. An unknown phase was observed filling voids and pores in chlorite (Fig. 2). This phase is a Cu-Cl-O (possibly OH) mineral (Fig. 3) which has not been previously described for IOCG prospects in the district. The Cu-Cl phase is widespread and disseminated through the sample typically occurring in the chlorite matrix in proximity to chalcopyrite grains (Figs. 3, 4, 5).

There are multiple generations of chlorite in the subeconomic IOCG Emmie Bluff prospect. These generations are quite different in chemical composition. Both SXRF and FEG SEM element mapping showed that early chlorite is Fe-rich (Figs. 1, 3). Later chlorite with which the Cu-Cl phase is associated is Mn- and Al-rich (Figs. 1, 6, 7).

Electron-microprobe analysis showed that the late chlorite associated with chalcopyrite alteration contains up to 1.75 wt.% MnO and 0.21 wt.% Cu$_2$O. Chemical composition of the unknown Cu-Cl phase could not be determined successfully by conventional electron microprobe analysis because of the small size and because the phase was not stable under the beam. However, analysis of the FEG SEM spectra showed that the phase consists of Cu, O, Cl, with minor Zr, Y and U.
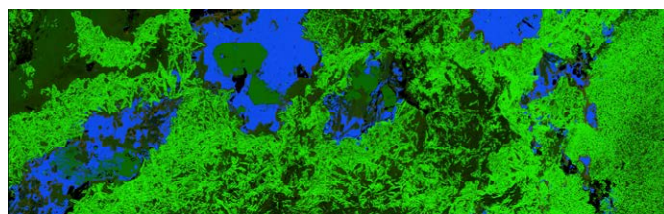


**Figure 1.** Element mapping using SXRF for sample SAE4-900.9 showing Mn (red), Fe (green) and Cu (blue) distribution. In this RGB map, chalcopyrite is blue, pyrite is green within blue, hematite is bright green, and chlorite is dark green; Mn-rich rims of chlorite are reddish in colour.

## 4 Discussion

Mapping of a large area using SXRF and, conversely, small areas using FEG SEM showed that on a sample scale there are different generations of chlorite that are also chemically distinct. Patchy chlorite associated with the late alteration of chalcopyrite is Mn-rich (Fig. 1 and 7). Mn-rich chlorite hosts the previously undescribed in IOCG rocks Cu-Cl phase (Figs. 2, 3, 4, and 5). This Cu-Cl phase is interpreted to be a by-product of late chalcopyrite alteration and also contains minor Zr, Y and U. The observations made possible with the use of cutting-edge SXRF and FEG SEM techniques show for the first time that subeconomic IOCG mineralisation in the Olympic Dam district was affected by a late fluid event, which resulted in partial dissolution of Cu mineralisation and transport of Cu in the form of chloride complexes. The fluids must therefore have been rich in chlorine, and as is also suggested from chemical composition of the unknown Cu-Cl phase, Zr-, Y- and U-bearing. This might be an indication of remobilisation and re-deposition of Cu along with other metals elsewhere in the district.

## 5 Conclusions

1. Combined SXRF and FEG SEM element mapping allows rare micron-scale features in geologic samples to be documented, which provides important textural information for understanding the transport of elements.
2. Mapping large areas using SXRF enables us to establish the distribution of trace elements in heterogeneous samples. This is key to truly understand in which mineral phases elements reside and with which other trace elements they are associated thus constraining the relative timing of multiple fluid events and the composition of the fluids.
3. Using the aforementioned analytical techniques, it was shown for the subeconomic IOCG prospect that Cu mineralisation formed after pyrite and was in its turn altered by late fluids. The by-product of this late chalcopyrite alteration is a Cu-Cl phase with minor Zr, Y and U. This suggests that there was later remobilization and migration of Cu in Zr-, Y- and U-bearing chloride fluids.
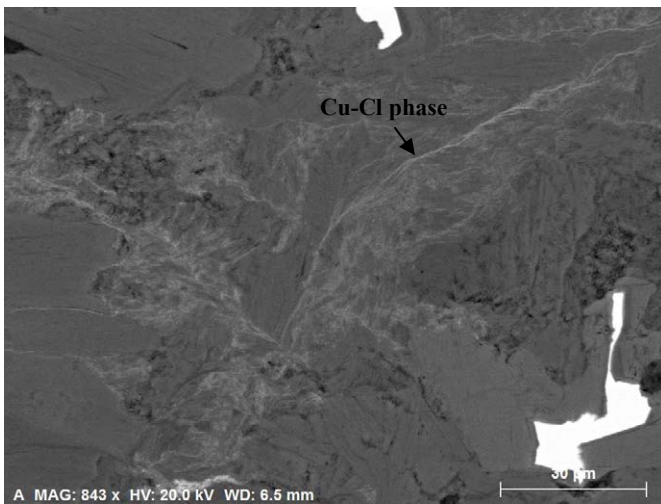
**Figure 2.** BSEM image of sample SAE4-900.9, showing chalcopyrite (white), surrounded by chlorite (dark grey) and Cu-Cl phase filling pore spaces in chlorite (light grey).
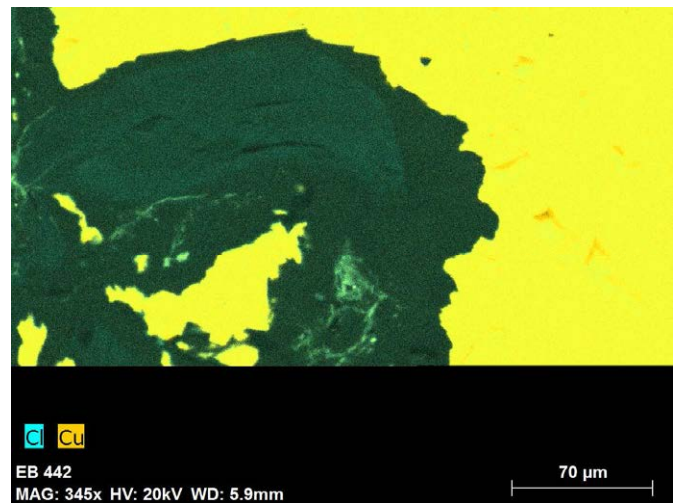


**Figure 5.** Cu-Cl map of the same area as in Fig. 4 showing distribution of the Cu-Cl phase (light blue) filling spacings and pores in chlorite.
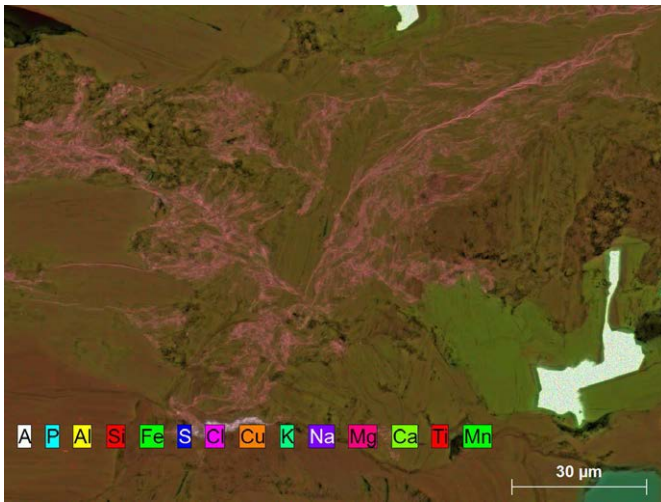


**Figure 3.** Element mapping using FEG SEM of the same area as in Fig. 2, showing Fe-Mn-rich chlorite surrounding chalcopyrite and Cu-Cl phase (pinkish).
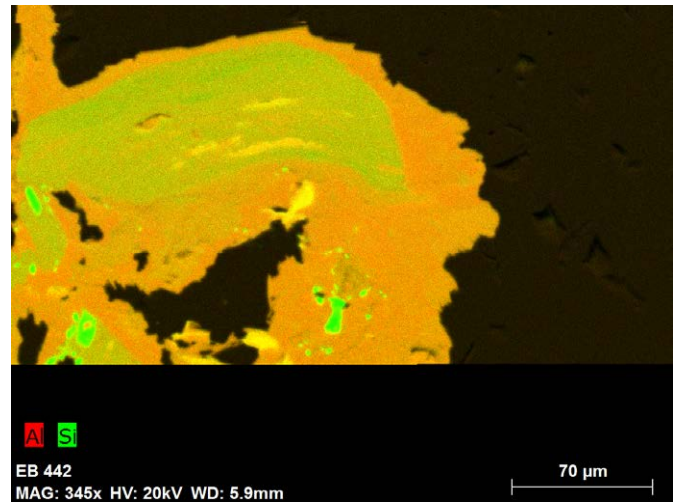


**Figure 6.** Al-Si map of the same area as in Fig. 4 showing differences in chemical composition of chlorites.
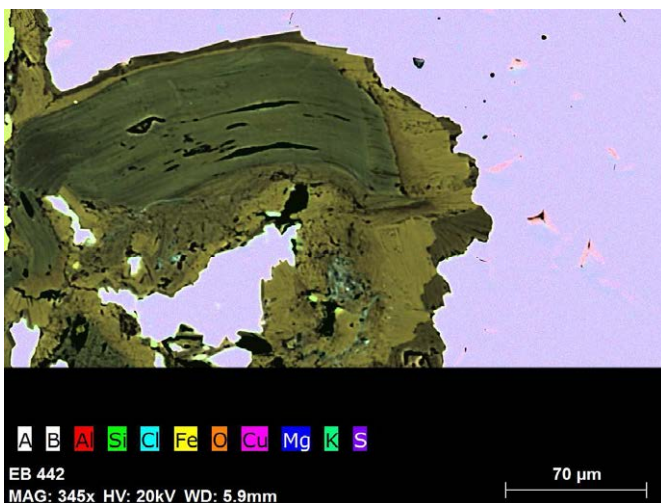


**Figure 4.** Element mapping using FEG SEM of the sample SAE4-900.9 showing chalcopyrite (light purple), different generations of chlorite (different shades of green) and Cu-Cl phase in chlorite (light blue) filling spacings and pores in chlorite.
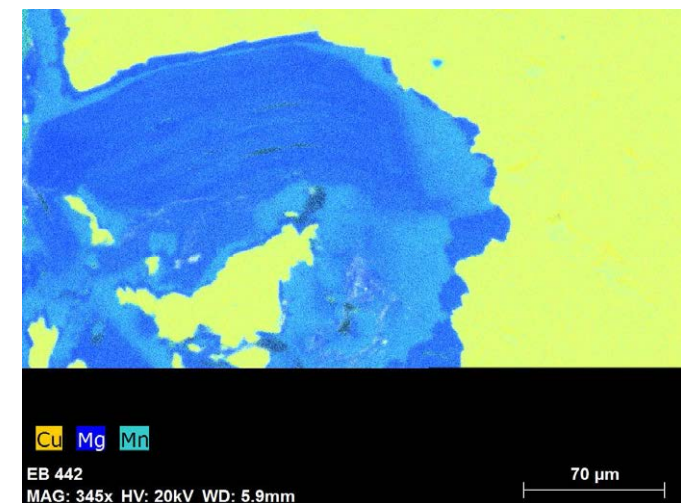


**Figure 7.** Cu-Mg-Mn map of the same area as in Fig. 4 showing differences in chemical composition of chlorites.

## Acknowledgements

## References

Bastrakov EN, Skirrow RG, Davidson GJ (2007) Fluid evolution and origins of iron oxide-Cu-Au prospects in the Olympic Dam District, Gawler Craton, South Australia. Economic Geology 102: 1415-1440.

Belperio A, Flint R, Freeman H (2007) Prominent Hill: a hematite-dominated, iron oxide copper-gold system. Economic Geology 102: 1499-1510.

Davidson GJ, Paterson H, Meffre S, Berry RF (2007) Characteristics and origin of the Oak Dam East breccia-hosted, iron oxide Cu-U-(Au) deposit: Olympic Dam region, Gawler Craton, South Australia. Economic Geology 102: 1471-1498.

Drexel JF, Preiss WV, Parker AJ (1993) The geology of South Australia. Volume 1, The Precambrian: South Australia. Geological Survey Bulletin 54: 242 pp.

Fairclough M (2005) Geological and metallogenic setting of the Carrapateena FeO-Cu-Au prospect – a PACE success story. Mesa Journal 38: 4-7.

Gow PA, Wall VJ, Oliver NHS, Valenta RK (1994) Proterozoic iron oxide (Cu-U-Au-REE) deposits: further evidence of hydrothermal origins. Geology 22: 633-636.

Haynes DW, Cross KC, Bills RT, Reed MH (1995) Olympic Dam ore genesis: a fluid-mixing model. Economic Geology 90: 281-307.

Merlet C (1992) Quantitative electron probe microanalysis: new accurate φ(ρz) description. Mikrochimica Acta 12: 107-115.

Oresekes N, Einaudi MT (1990) Origin of rare earth element-enriched hematite breaccias at the Olympic Dam Cu-U-Au-Ag deposit, Roxby Downs, South Australia. Economic Geology 85: 1-28.

Oresekes N, Einaudi MT (1992) Origin of hydrothermal fluids at Olympic Dam: Preliminary results from fluid inclusions and stable isotopes. Economic Geology 87: 64-90.

Paterson DJ, Boldeman JW, Cohen DD, Ryan CG (2007) Microspectroscopy beamline at the Australian Synchrotron. Australian Institute of Physics Congress Conference Proceedings 879: 864.

Reeve JS, Cross KC, Smith RN, Oresekes N (1990) Olympic Dam copper-uranium-gold-silver deposit. Melbourne, Australasian Institute of Mining and Metallurgy Monograph Series 14: 1009-1035.

Ryan CG, Kirkham R, Siddons, DP, Dunn PA, Laird JS, Kuczewski A, Moorhead G, De Geronimo G, Davey P, Jensen M, Paterson DJ, de Jonge MD, Howard DL, Hough RM (2010) The Maia 384 detector array in a nuclear microprobe: A platform for high definition PIXE elemental imaging. Nuclear Instruments and Methods in Physics Research Section B – Beam Interactions with Materials and Atoms 268(11-12): 1899-1902.

# Sparging Os into plasma source mass spectrometers: preliminary isotopic ratio of chromite

Laurène-Marie Wavrant, Sarah-Jane Barnes, Dany Savard, Philippe Pagé
*Département des Sciences de la Terre, Université du Québec á Chicoutimi (UQAC), Chicoutimi, QC, Canada, G7H 2B1*

André Poirier
*Geotop Research Center, Université du Québec á Montréal (UQAM), C.P. 8888, Succ. Centre-Ville, Montréal, CQ, Canada, H3C 3P8*

**Abstract.** Results of preliminary tests for rapid determination of Os concentrations and Os isotopic ratios using isotope dilution ICP-MS and HR-ICP-MS combined with HPA (High Pressure Asher) digestion are presented. With this method, volatile $OsO_4$ is directly transferred to the ICP-torch via a flux of Ar gas bubbling into the solution (sparging). Three kinds of tubing to introduce Ar into the Os solution were tested: 1) A single 3.2 mm PFA tubes, 2) Four 0.8 mm PFA tubes and 3) A single 3.2 mm PFA tubing with holes and enclosed at the extremity in the sample solution. Sparging Os does not require any chemical separation prior to analysis which is a noticeable advantage. Sparging Os also reduces the washout time to c.a. 15 minutes between samples. Osmium concentrations determined by sparging of two reference materials (ChrPt+: a chromite powder, and WPR-1: a peridotite powder) are comparable with their published values. For the determination of $^{187}Os/^{188}Os$ isotopic ratios, preliminary results are promising. However, some adjustments must be done to improve the precision and accuracy of the analyses which are affected by the signal stability during analysis, such as a digestion of chromite powder for 15h by HPA and the use of freshly digested sample solutions. The sparging method is expected to be a powerful and efficient tool for determining osmium isotopic ratios of chromite concentrate powders from layered intrusions.

**Keywords.** Osmium isotopic ratio, sparging method, isotope dilution, HR-ICP-MS, geochemical reference material

## 1  Introduction

Osmium isotopic ratios are a unique tool in ore deposit research due to the affinity of Re and Os for sulphide minerals. Osmium is present in PGM (Platinum-Group Mineral) such as laurite $((Ru,Os)S_2)$ which may occur as inclusions in chromite. The Re-Os isotopic system is a powerful tool for determining the origin of chromite. The aim of this study is to completely digest chromite powder and to develop a rapid method for determining their Os isotopic ratios.

The use of the Os isotopic system is constrained by the complex and time consuming chemistry required to separate and purify Os (Birck et al. 1997). Another limitation of the classical technique of Os isotopic measurement is the length of time it takes for analysis by negative thermal ionization mass spectrometry (N-TIMS). The development of inductively coupled plasma source in mass spectrometry is an alternative ionization mechanism. The main advantage of the ICP-MS is the theoretically simpler sample preparation and the shorter analysis time than for N-TIMS (i.e. not slow heating-up procedure). Rhenium concentrations and other PGEs can also be determined by ICP-MS (Savard et al., 2010). Classical determination of Re cannot be achieved by N-TIMS easily because of common Re contamination in the source and thus often require the use of another instrument such as ICP-MS. Lichte et al. (1986) and Dickin et al. (1988) have tried using ICP-MS to determine Os isotopic ratios but their methods were hampered by memory effects. One way to solve the memory effect problem is the use of the sparging method in which volatile osmium goes directly in the ICP glass torch (Russ et al. 1987, Hirata et al. 1989, Gregoire. 1990, Hassler et al. 2000, Norman et al. 2002, Nozaki et al. 2012). Because a number of sample preparation steps (such as Os extraction, micro-distillation and filament loading) can be completely omitted and if the presented method proves effective for geological materials, the quantity of samples analysed could be increased by several fold over those that have been analysed by N-TIMS.

High Resolution (HR)-ICP-MS (double-focussing sector field) with high mass resolution has great potential to determine Os isotopic ratios with high precision. Our goals are: 1) to ensure efficient chromite dissolution by HPA and 2) to increase the sample throughput while preserving high precision.

## 2  Methodology and materials

Osmium concentrations and Os isotopic ratios were determined for two rock powder reference materials (ChrPt+ and WPR-1). ChrPt+ is a chromite powder from the Unst ophiolite of Shetland Island (N Scotland) provided by the Centre de Recherches Pétrographiques et Géochimiques, Nancy (France) and its Os concentration is published (e.g. Bedard et al., 2005). The second reference material selected was WPR-1, a peridotite from the Wellgreen Intrusion of British Columbia, provided by CCRMP of Ontario (Canada). Both Os concentration and Os isotopic ratios are published (e.g. Morcelli et al., 2004, Meisel and Moser, 2004, Schaefer et al., 2010).

### 2.1  Equipment

Samples were digested at LabMaTer at the Université du Québec à Chicoutimi (UQAC) by High Pressure Asher (HPA-S; Anton Paar, Graz, Austria). A first set of test runs of the reference materials was performed by ICP-

MS Quadrupole (Agilent Technology 7700x) at LabMaTer, UQAC. Another set of analyses was carried out at GEOTOP, Université du Québec à Montréal (UQAM) on a HR-ICP-MS (Nu Instruments Attom).

## 2.2 Sample Preparation

Between 0.5g and 1g of powders were digested in 50mL quartz vessels by HPA in a mixture of 3mL HCl and 5 mL $HNO_3$. A spiked solution enriched in $^{190}Os$ was added to some of the samples prior to digestion to determine the Os concentration by isotopic dilution (Savard et al., 2010). Digestion at high temperature (300°C) and high pressure (120 bars) was processed carried out for 4 h 30 min or 15 hours. Solutions were then transferred to Savillex PFA beakers with a cap with two holes for PFA tubing (Fig.1) and diluted in deionized water.

## 3 Sparging Os

An essential aspect of the sparging method is that Os must be oxidized to its higher valence state Os (VIII) which is ensured by the use of inverse aqua regia during digestion. Argon gas was then bubbled into the sample solution allowing the osmium tetroxide ($OsO_4$) to be extracted by the Ar flux into the ICP-torch (Fig. 1). Instrumental sensitivity was optimized by the sparging of an in-house standard solution containing 5 ng $g^{-1}$ of total Os, prepared from Os 1000mg/L standard solution (PlasmaCAL). A few mL of $H_2O_2$ was added to ensure oxidation. An important point to obtain the best signal intensity and stability is the Ar gas flow rate and its constant bubbling. With this intention, 3 different sparging tube configurations were tested (Fig.1).
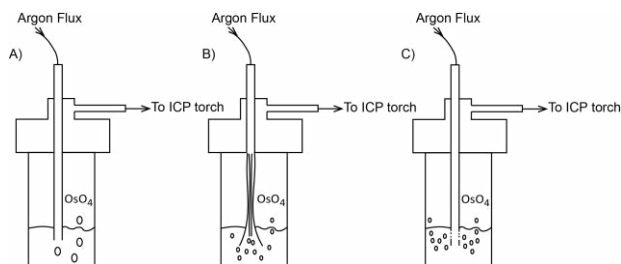


**Figure 1.** Scheme for sparging setup. A) Single 3.2 mm (Inside diameter) PFA tube, B) Four 0.8 mm (Inside diameter) PFA tubes C) Single 3.2 mm (Inside diameter) PFA tube with holes and enclosed at the extremity. A 30 or 60mL Savillex PFA vial can be used with a cap with two holes for PFA tubing.

## 4 Results

During our analysis less than 30 counts per second were obtained on the $^{185}Re$ with ICP-MS and less than 10 counts per second with HR-ICP-MS, which implies negligible of direct interference from $^{187}Re$ on $^{187}Os$ (<0.1%). Between each analysis the apparatus was cleaned by a mixture of HCl and $HNO_3$ diluted in ultrapure water. For each sample analysis blank contribution was less than 1%.

## 4.1 Types of tubing

During the preliminary tests, three different tubing configurations were tested. The signals obtained and the isotopic ratio and uncertainty on measurement (2σ) for analyses of ChrPt+ sample solution from the same digestion with the different tubing are shown in Table 1.

| | $^{192}Os$ CPS | $^{187}Os/^{188}Os$ | 2σ |
|---|---|---|---|
| ICP-MS: 3.2 mm PFA tubing | 88 800 | 0.1278 | 0.0201 |
| ICP-MS: 4x0.8 mm PFA tubing | 400 000 | 0.1303 | 0.0108 |
| HR-ICP-MS : 3.2 mm tubing with holes | 70 000 | 0.1299 | 0.0071 |

**Table 1.** $^{192}Os$ counts per second, $^{187}Os/^{188}Os$ and uncertainties based on measurement of the same ChrPt+ digestion solution obtained with the three kinds of tubing.

First we used a simple 3.2 mm inside diameter tubing as described by Hassler et al. (2000). This set up produced individual, large bubbles that did not "flow" constantly thus leading to large signal instabilities. About 88,800 counts per second were obtained on $^{192}Os$ by ICP-MS. The second tubing tested was four small PFA tubes. With this arrangement the bubbles that formed were smaller and more abundant thus the stability and intensity observed on the $^{192}Os$ signal was significantly better in the ICP-MS. The third setting was tested only with the HR-ICP-MS and consists of a single, 3.2 mm PFA tube sealed by heating at the output, in which four holes at the extremity were drilled with a Dremel. About 70,000 CPS were obtained on the $^{192}Os$ which was lower than for four tubing configuration. However, with this set up the flow of bubbles observed was more regular and gave a much more stable signal and thus a better precision. This single-drilled tubing was not tested on the quadrupole ICP-MS.

## 4.2 Osmium concentration

Osmium concentrations were obtained by ID-ICP-MS or ID-HR-ICP-MS. For WPR-1 we obtained Os values between 14.45-14.75 ppb. The range of published values is from 12.5 to 19.4 ppb (e.g. Morcelli et al., 2004, Meisel and Moser, 2004, Schaefer et al., 2010). Our results are in good agreement with published value. Osmium concentration values obtained for ChrPt+ are between 1731 and 2312 ppb, published concentration varying between 1900 and 2110 ppb (Govindaraju, 1995 and Bédard et al. 2004). Variations observed for our Os concentration are probably due to the digestion time in HPA. Analysis of solution from 4h 30 min digestion times gave lower concentrations than for 15h digestion times, suggesting that for chromite an extended digestion time is necessary.

## 4.3 Osmium isotopic ratio

No Os isotopic ratios have been published for ChrPt+, however, O'Driscoll et al. (2012) has analysed Os isotopic ratios on chromite from the same ophiolitic complex of Unst, which varied between 0.125 and 0.129

(Fig.2). WPR-1 isotopic ratios were published by Ripley (2001) and Schaefer et al. (2010) and ranged between $0.1450 \pm 0.0001$ and $0.1460 \pm 0.0007$.

All our isotopic ratios were corrected for mass fractionation based on the $^{192}Os/^{188}Os$ (3.08271, Nier (1937)). ICP-MS values for $^{187}Os/^{188}Os$ for ChrPt+ ranged from $0.1283 \pm 0.0121$ (2σ) to $0.1320 \pm 0.0194$ (2σ) (average $0.1299 \pm 0.0008$) and are in agreement with O'Driscoll et al. (2012) (Fig. 2). For WPR-1 only our ICP-MS Os isotopic ratios are available at present and ranged from $0.1432 \pm 0.0314$ (2σ) to $0.1487 \pm 0.0477$ (2σ) (average $0.1465 \pm 0.0023$).

Isotopic ratios obtained by HR-ICP-MS gave similar values as the ICP-MS. However precision is much better on the magnetic sector instrument than on the Quadrupole. We can distinguish two data fields: one for ChrPt+ values which are nearly mantle-like and one for WPR-1 which are more radiogenic.
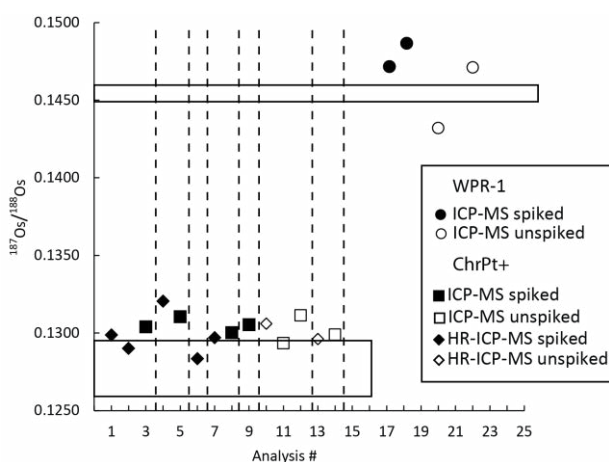


**Figure 2.** Variation of $^{187}Os/^{188}Os$ by ICP-MS and HR-ICP-MS with analysis number for ChrPt+ and WPR-1 reference materials. For better visibility errors bars are not shown here. Analyses from the same digestion solution are shown between two dashed lines. Fields surrounded in black shown the variation of published values.

## 4  Discussion and Conclusion

The aim of this work was to prepare chromite samples to measure their Os isotopic ratios. During these preliminary tests we tried to determine the best conditions for the analyses. We tested two digestion durations (4h30 min and 15h) by HPA, three kinds of sparging systems and compared analysis by ICP-MS and HR-ICP-MS.

Digestion by HPA for 15h is the most efficient way to digest the chromite sample (ChrPt+). Shorter digestion times underestimate the concentration of Os. It is also important to analyse solution freshly digested to have the most oxidizing conditions necessary to obtain the best signal during analysis.

Our preliminary tests show that Os concentrations are in good agreement with published data. In the case of isotopic ratios, results obtained by ICP-MS are too variable and the error is too large. Based on Figure 2 the reproducibility of the HR-ICP-MS data is the same as the one from the ICP Quadrupole. However HR-ICP-MS analyses yields more precise results.

These preliminary analyses for Os isotopic ratios by sparging method are promising. Adjustments will be made to our method such as a digestion time of 15h for all powder digested and the use of freshly digested solution. This will bring a better signal on HR-ICP-MS and so better precision. WPR-1 reference material will be also analysed by HR-ICP-MS. This method will be applied to determine $^{187}Os/^{188}Os$ ratios in chromite concentrate powder from the Stillwater Complex chromite layers (Montana, US).

## References

Bédard LP., Barnes SJ (2004) Improved platinum-group element extraction by NiS fire assay from chromitite ore samples using a flux containing sodium metaphosphate. Geostand. and Geoanal. Res. 28 (2) 311-316

Birck JL, Roy Barman M, Capmas F (1997) Re-Os isotopic measurements at the femtomole level in natural samples. Geostand. Newslett 21 (1):19-27.

Dickin AP, McNutt RH, McAndrew JI (1988) Osmium isotope analyses by inductively coupled plasma-mass spectrometry. J. Anal. At. Spectrom., 3 337-342

Govindaraju K. (1995) 1995 working values with confidence limits for twenty-six CRPG, ANRT and IWG-GIT geostandards. Geostand. Newslett. 19 (special) 1-32

Gregoire DC (1990) Sample introduction techniques for the determination of osmium isotope ratios by inductively coupled plasma mass spectrometry. Anal. Chem. 62 141-146

Hassler DR, Peucker-Ehrenbrink B, Ravizza GE (2000) Rapid determination of Os isotopic composition by sparging OsO(4) into a magnetic-sector ICP-MS. Chem. Geol. 166 (1-2):1-14

Hirata T, Akagi T, Shimizu H, Masuda A (1989) Determination of osmium and osmium isotope ratios by microelectrothermal vaporization inductively coupled plasma mass spectrometry. Anal. Chem. 61 2263-2266

Lichte F E, Wilson S M, Brooks R R, Reeves R D, Holzbecher J, Ryan D E (1986) New method for the measurement of osmium isotopes applied to a New Zealand Cretaceous/Tertiary boundary shale. Nature 322 816-817

Meisel T., Moser J. (2004) Reference materials for geochemical PGE analysis: new analytical data for Ru, Rh, Pd, Os, Ir, Pt and Re by isotope dilution ICP-MS in 11 geological reference materials. Chem. Geol. 208 319-338

Morcelli CPR, Figueiredo AMG., Enzweiler J, Sarkis JES, Jorge AP de S., Kakazu M. (2004) Determination of platinum-group elements in geological reference materials by high resolution-ICP-MS after nickel sulfide fire-assay collection and Te co-precipitation. Geostand. and Geoanal. Res. 28 (2) 305-310

Nier A O, (1937) The isotopic constitution of osmium. Phys. Rev. 52 (8):885-885

Norman M, Bennet V, McCulloch M, Kinsley L (2002) Osmium isotopic compositions by vapour phase sample introduction using a multi-collector ICP-MS J. Anal. At. Spectrom. 17 1394-1397

Nozaki T, Suzuki K, Ravizza G, Kimura J I, Chang Q (2012) A method for rapid determination of Re and Os isotope compositions using ID-MC-ICP-MS combined with the sparging method. Geostand. and Geoanal. Res.36 (2):131-148

O'Dricoll B, Day J MD, Walker R J, Daly J S, McDonough W F, Piccoli P M (2012) Chemical heterogeneity in the upper mantle recorded by peridotites and chromitites from Shetland ophiolite complex, Scotland. Earth Planet. Sci. Lett. 333-334 226-237

Potts PJ, Gowing C JB, Govindaraju K (1992) Preparation, homogeneity evaluation and cooperative study of two new chromitite reference samples ChrPt+ and Chr-Bkg. Geostand. Newslett., 16 (1):81-108

Ripley EM, Park Y-R, Lambert DD, Frick LR (2001) Re-Os isotopic variations in carbonaceous pelites hosting the Duluth Complex:implications for metamorphic and metasomatic processes associated with mafic magma chambers. Geochim. Cosmochim. Acta 65 (17) 2965-2978

Russ G P, Bazan J M, (1987) Osmium isotopic ratio measurement by inductively coupled plasma source mass spectrometry Anal. Chem. 59 984-989

Savard D, Barnes SJ, Meisel T, (2010) Comparison between Nickel-Sulfur Fire Assay Te Co-precipitation and Isotope Dilution with High-Pressure Asher Acid Digestion for the Determination of Platinum-Group Elements, Rhenium and Gold Geostand. and Geoanal. Res., 34 281-291

Schaefer B, Pearson DG, Rogers NW, Barnicoat A.C. (2010) Re-Os isotope and PGE constraints on the timing and origin of gold mineralisation in the Witwatersrand Basin Chem. Geol. 276 88-94

# Perspectives of LA-ICP-MS analysis
# of rutile in mineral deposit research

Thomas Zack, Johan Hogmalm, Robert H. Hellingwerf
*Department of Earth Sciences, University of Gothenburg, Sweden*

**Abstract:** Rutile is becoming an increasingly important tracer mineral that can contain a range of interesting petrogenetic constraints. Noticeable advances have been made with regards to establish rutile as a reliable temperature and geochronometer/ thermochronometer recorder. In this contribution we would like to outline some of the potential rutile might bear in the field of mineral deposit research.

**Keywords:** Rutile, trace elements, U/Pb dating, gold mineralization, Protogine Zone.

## 1  Introduction

Rutile geochemistry and geochronology received considerable attention the last decade in the form of several 100 publications, mostly in the fields of petrology and sedimentary geology. This interest was sparked by 1.) an increased understanding in the geochemical behaviour of rutile and 2.) the development of matrix-matched standards. The most prominent examples are the development of a Zr-in-rutile geothermometer (e.g., Zack et al. 2004), Nb-Cr-in-rutile systematics (e.g., Triebold et al. 2012) and reliable in-situ U/Pb age determination based on a $^{208}$Pb correction (e.g., Zack et al. 2011).

In principle, the field of economic geology is at least equally well suited for rutile-based studies. Rutile is a common mineral in several ore-related deposits, e.g., porphyry copper and hydrothermal gold mineralization.

In this contribution, we would like to illustrate how rutile can help tying mineral deposit models into better time frames. It cannot be stressed strongly enough that perhaps the biggest potential of rutile in mineral deposit studies lies in its ability to host a range of redox-sensitive trace elements (in particular V, Mo, Sn, Sb and W), some of which are additionally considered to be strategic metals.

## 2  Analytical requirements

Spatially controlled in-situ analysis of rutile is principally possible using either SIMS or LA-ICP-MS. While SIMS arguably is able to give the more accurate results (see Schmitt & Zack 2012), LA-ICP-MS is significantly faster. Our current Laser ablation (LA)-Inductively Coupled Plasma (ICP)- Mass Spectrometer(MS) facility at the Department of Earth Sciences of the University of Gothenberg consists of a New Wave NWR213 laser (Nd:YAG laser at 213 nm) coupled to an Agilent 7500a quadrupole ICP-MS.

Our system is designed to achieve maximum signal sensitivity at maximum throughput with no compromise on accuracy. To achieve highest sensitivity with the existing facility, we installed a second vacuum pump for the ICP-MS, used a shield torch and added $N_2$ to the He carrier gas. A high throughput is possible by use of a Two-Volume Cell that allows inserting several samples (thin sections and/or grain mounts) together with standard mounts in a 10 by 10 cm sample cell. After sample spots for laser ablation are set, it is analysed in automized mode.

Routinely, rutile is analysed in two steps: First, trace elements (Fe, V, Zr, Nb, Mo, Sn, Sb, Hf, Ta, W, Pb, Th and U) are measured within an 8 micron laser spot for 15 seconds using the NIST SRM 610 glass as a primary standard and the rutile R10 as a secondary standard. Based on the results of the trace element run, spots are selected for U/Pb dating. Primarily, the U content is the crucial variable. Usually, areas with U content >10 ppm can be dated within 50 micron spots (or smaller), while U contents between 1 and 10 ppm require spot sizes of 80 micron. Below 1 ppm, dating is currently not possible (however, an upgrade is planned that will further push these current limits).

For U/Pb measurements, the following isotopes are analysed: $^{202}$Hg, $^{204}$(Hg+Pb), $^{206}$Pb, $^{207}$Pb, $^{208}$Pb, $^{232}$Th and $^{238}$U. As a primary standard, rutile R10 is used (Luvizotto et al. 2009), while R19 is used as a secondary standard (Zack et al. 2011). Masses 202 and 204 are only measured for long-term monitoring purposes, as common Pb correction is achieved by the $^{208}$Pb correction, as rutile mostly has no Th. Long term reproducibility for U/Pb rutile ages is better than 2%. See Zack et al. (2011) for further details.

## 3  Applications to mineral deposits

### 3.1  Gold mineralization

In Minas Gerais, gold deposits along a >500 km long fault system are often associated with small, but conspicuous amounts of rutile. We successfully dated rutile from the locality Diamantina in a recent study (please note that analysis were performed at the University of Mainz, Germany). At U levels between 6 and 15 ppm, ages with an error of ca 3% were obtained (524±16 Ma; Cabral et al. 2013). Although the error is rather large, it is noteworthy that even at medium to low U concentrations, those ages are concordant ages, where each single analysis is common Pb corrected. This illustrates the advantage of the $^{208}$Pb based correction method.

### 3.2 Kyanite-rutile-quartz mineralization

In a first application to mineral deposits in Sweden, we measured a suite of large rutile crystals from Hålsjöberg. Rutile from this locality occurs within a significant kyanite-rutile-quartz mineralization zone that forms part of a larger fault system loosely associated with the Protogine Zone.

A remarkable, yet currently unexplained feature of those rutiles is a persistently high Sb content of between 600 and 3800 ppm. Unfortunately, U contents are very low (<0.03 ppm to a maximum of 6 ppm). 30% of all analysed grains had U content <0.5 ppm. Without a rapid screening technique, dating efforts would have had a high chance of failure. However, choosing the most-enriched areas, we could successfully date rutile from this locality at 892±21 Ma (figure 1). At such low U contents, a common Pb correction leads to very high propagated errors. Instead, this age is based on a 15-point intercept age, with a MSWD of 0.67 and an upper intercept on a Tera-Wasserburg consistent with crustal common Pb.

This age places kyanite-rutile-quartz mineralization at the end of the Sveconorwegian orogeny. Overlapping Ar-Ar biotite and white mica formation ages (920 to 860 Ma; Viola et al. 2011) associated with the greenschist-facies late orogenic extensional phase indicate that our rutile ages are also formation ages, considering that samples from Viola et al. (2011) are from a more interior position of the orogeny (ca 50 km to the SW). We therefore argue that the kyanite-rutile-quartz mineralization in Hålsjöberg formed at around 890 Ma ago, where significant fluid focussing (and hence element remobilization) must have occurred in an otherwise cooling overthickened mountain belt. This prediction can be tested most easily by dating rutile from surrounding lithologies. If Hålsjöberg rutile indeed records formation ages, surrounding lithologies should record older cooling ages (as old as ca 960 Ma, as indicated by U/Pb titanite ages; Söderlund et al. 1999).

### References

Cabral A, Eugster O, Brauns M, Lehmann B, Rösel D, Zack T, de Abreu F, Pernicka E, Barth M (2013) Direct dating of gold by radiogenic helium: testing the method on gold from Diamantina, Minas Gerais, Brazil. Geology 41:163-166

Luvizotto GL, Zack T, Meyer HP, Ludwig T, Triebold S, Kronz A, Münker C, Stockli DF, Prowatke S, Klemme S, Jacob DE, von Eynatten H (2009) Rutile crystals as potential trace element and isotope mineral standards for microanalysis. Chemical Geology 261:346-369

Söderlund U, Jarl LG, Persson PO, Stephens MB, Wahlgren CAH (1999) Protolith ages and timing of deformation in the eastern, marginal part of the Sveconorwegian orogeny, southwestern Sweden. Precambrian Research 94: 29-48

Triebold S, von Eynatten H, Zack T (2012) A recipe for the use of rutile in sedimentary provenance analysis. Sedimentary Geology 282:268-275

Viola G, Henderson IHC, Bingen B, Hendriks BWH (2011) The Grenvillian-Sveconorwegian orogeny in Fennoscandia: Back-thrusting and extensional shearing along the "Mylonite Zone". Precambrian Research 189: 368-388

Zack T, Moraes R, Kronz A (2004) Temperature dependence of Zr in rutile: empirical calibration of a rutile thermometer. Contribution to Mineralogy and Petrology 148:471-488

Zack T, Stockli DF, Luvizotto GL, Barth MG, Belousova E, Wolfe MR, Hinton RW (2011) In situ U-Pb rutile dating by LA-ICP-MS: Pb-208 correction and prospects for geological applications. Contributions to Mineralogy and Petrology 162:515-530

**Figure 1**: U/Pb rutile ages from a kyanite-rutile-quartz mineralization at Hålsjöberg.

S 2.4:

# Advances in the mineral chemistry of Fe oxides: ore-forming processes and implications for exploration

Convenors:
Georges Beaudoin & Thomas Angerer

# The use of trace elements in Fe-oxides as provenance and petrogenetic indicators in magmatic and hydrothermal environments

**Sarah A.S. Dare, Sarah-Jane Barnes, Julien Méric, Alexandre Néron**
*Université du Québec à Chicoutimi (UQAC), Chicoutimi, Québec, Canada, G7H 2B1*

**Georges Beaudoin, Emilie Boutroy**
*Université Laval, Québec, Québec, Canada, G1V 0A6*

**Abstract.** In order to use trace element composition of magnetite as an indication of its origin it is necessary to understand the processes that control the trace element concentrations in magnetite. We have characterised trace element distribution in magnetite, using laser ablation ICP-MS, from magmatic ore deposits (Fe-Ti-V-P and Ni-Cu-PGE) where the paragenetic sequences are well constrained. Changes in composition of the liquid, driven by crystal fractionation, are recorded by magnetite in both silicate and sulfide melts. The composition of magnetite is sensitive to co-crystallizing phases, with marked depletion in Ti when ilmenite crystallizes before magnetite and in Cu when a sulfide liquid segregates. Multi-element variation diagrams show that magmatic magnetites have chemical signatures distinct from hydrothermal magnetite due to differences in fluid composition and different conditions of formation (e.g., competing phases, redox and temperature). Chemical fingerprinting of magnetite from the magnetite 'lava flows' of El Laco, northern Chile, provides new evidence to support the hydrothermal alteration model rather than a magmatic origin.

**Keywords. Magnetite, trace elements, laser ablation-ICP-MS, provenance, El Laco**

## 1 Introduction

Magnetite forms under a wide variety of conditions, crystallizing at high temperature from silicate, sulfide and carbonatite magmas or it can precipitate at lower temperatures from hydrothermal fluids. These different conditions may lead to distinctive trace element signatures for the magnetite. Recent analytical developments make it possible to determine a much wider range of trace elements than previously. Thus it may become possible to use the trace element signature of magnetite as petrogenetic and provenance indicators.

One problem is how to establish which trace element variations are significant. Modern laser ablation-ICP-MS systems provide results for ~ 20-25 elements. Some studies have been carried out using a statistical approach (e.g., Dupuis and Beaudoin 2011; Nadoll et al. 2012). Other studies have concentrated on petrogenesis (e.g., Reguir et al. 2008; Dare et al. 2012). Our current studies consider well characterized samples from different settings to establish which elements are the most diagnostic and which processes have the most effect. These studies could then be applied to less well understood examples or provenance studies. For example, we show that the difference observed in the behaviour of trace elements between magnetite of magmatic and hydrothermal origin permits a re-evaluation of the nature of the fluid (Fe-rich melt or hydrothermal) involved in forming the enigmatic magnetite 'lava flows' of El Laco, northern Chile (Nyström and Henriquez 1994; Sillitoe and Burrows 2000).

## 2 Methodology

To characterise magnetite formed from high temperature silicate melts we have analysed magnetite in Fe-Ti-V-P deposits from both layered intrusions, such as the Bushveld (South Africa) and Sept-Iles (Quebec, Canada) Complexes, and massif-type anorthosites, such as Lac St. Jean (Quebec, Canada). Magnetite from Sudbury and Voisey's Bay Ni-Cu-Platinum-Group-Element (PGE) sulfide deposits (Canada) represent magnetite formed from sulfide liquids. Samples from hydrothermal and low temperature environments include examples of Fe-oxide-Copper-Gold (IOCG) from Ernest Henry (Australia), porphyry-Cu from Morococha (Peru) and banded iron formation from Thompson Ni Belt (Manitoba, Canada). Samples from the El Laco area represent our test case.

The LA-ICP-MS system used at LabMaTer, UQAC, is a Resonetics M-50 193nm laser coupled with an Agilent ICP-MS. An international reference material (GSE-1g) was used for calibration and Fe used as the internal standard. A beam size of 55 – 80 µm was used so that any fine-grained exsolution lamellae (e.g., ilmenite, spinel) were incorporated into the analysis to better represent the initial composition of the Fe-Ti oxide (Dare et al. 2012). The data are presented in order of increasing compatibility with magnetite and normalized to average crust (Fig. 1). We find that these types of diagrams help to investigate the behaviour of trace elements during crystallization of magnetite from different melt compositions (silicate and sulfide) and anomalies due to the competition for an element among co-crystallizing phases (e.g., magnetite, ilmenite and sulfide) are more readily observed.

## 3 Magnetite records changing melt composition

The concentration of an element in magnetite depends

on: a) the concentration of the element in the liquid from which it crystallizes, b) whether other minerals are crystallizing at the same time and competing for the element and c) the partition coefficient of the element into magnetite. As a high temperature melt cools, crystal fractionation changes the composition of the residual liquid according to the partitioning behaviour of elements into the crystallizing phases. In two relatively simple and well-constrained systems (silicate and sulfide melts) we can demonstrate the effect fractionation of the melt has on the composition of magnetite (Figs. 1-2).

## 3.1 Magnetite from silicate melts

Magmatic Fe-oxide deposits commonly crystallize from an evolved silicate melt (~ intermediate in composition) at the top of layered intrusions. The lowest Fe-oxide layers of the Bushveld (free of apatite) are richest in V (~ 1.5 wt.%) whereas the uppermost Fe-oxide layers (Fe-Ti-P deposit) are poor in V and contain apatite (Barnes et al. 2004). Oxygen fugacity ($fO_2$) controls whether Ti-rich magnetite crystallizes from the magma before (oxidizing conditions) or after (reducing conditions) ilmenite (Toplis and Caroll 1995). In the layered intrusions studied ($fO_2$ ~ FMQ), Ti-rich magnetite (6–12 wt.% Ti) crystallized either before or at the same time as ilmenite. Both magnetite and ilmenite from the first and last Fe-oxide layers (~ 2 km apart for the Bushveld Complex) were analysed to document the change in composition of trace elements during crystal fractionation of silicate magma (Fig. 1).
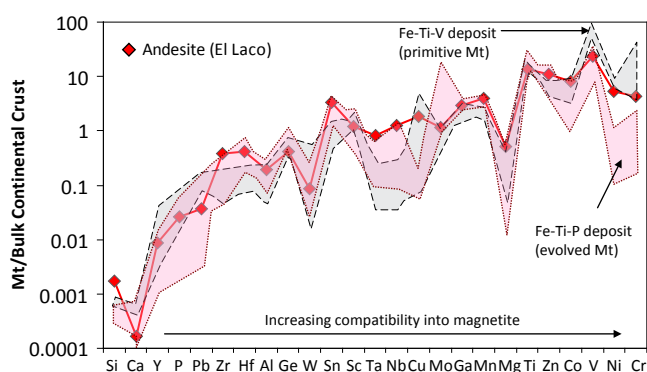


**Figure 1.** Multi-element variation diagram for magnetite (Mt) from magmatic Fe-oxide deposits. Magnetite from Fe-Ti-V deposits (grey field) can be distinguished from those from Fe-Ti-P deposits (pink field) using a few critical elements such as Cr, Ni, V, Mo, Nb and Ta. Order of increasing compatibility of elements into magnetite is taken from Dare et al. (2012). Si and Ca determined by electron microprobe using the trace mode of Dupuis and Beaudoin (2011).

Both magnetite (Fig. 1) and ilmenite record fractionation of the magma. Elements sequestered during crystallization of mafic minerals (e.g., olivine, pyroxene) are highest in concentration in magnetite from the lowest layers (V <1.5 wt. %, Mg <1 wt.%, Cr <6000 ppm and Ni <500 ppm and Co <200 ppm) and decrease up section. Correspondingly, elements that are incompatible during fractionation (Cu, Ga, Ge, Hf, Mn, Mo, Nb, Sc, Sn, Ta, Ti, W, Zn and Zr) increase up section and are concentrated in magnetite from the uppermost layers

(i.e. Fe-Ti-P deposit).

Magnetite composition is also sensitive to specific co-crystallizing phases. The crystallization of ilmenite before magnetite in some anorthosite-hosted Fe-oxide deposits results in magnetite being relatively depleted in elements that preferentially partitioned into early-forming ilmenite, i.e. Ti (3–6 wt.%), Hf, Mg, Mn, Nb, Sc, Ta, W and Zr. Co-crystallization of trace amounts of sulfides, which can segregate towards the end of fractionation (i.e. in Fe-Ti-P deposits), results in depletion of Cu (highly chalcophile) in magnetite relative to other incompatible elements such as Nb and Mo (Fig. 1). However, co-crystallization of apatite will not have any discernable affect on magnetite chemistry because elements that are concentrated into apatite (Ca, P, Y and REE) are highly incompatible in magnetite and generally absent in all magmatic magnetite.

## 3.2 Magnetite from sulfide melts

Ni-Cu-PGE deposits form when immiscible sulfide melt separates from a mafic-ultramafic melt, collecting highly chalcophile elements (i.e. Ni, Cu, PGE) and some mildly chalcophile elements (e.g., Co, Sn, Zn, Mo, Pb) but very little lithophile elements. The main phases to crystallize from a sulfide melt (1180 – 850°C) are first Fe-rich sulfides poor in Pt and Pd, which form pyrrhotite and pentlandite at lower temperatures (< 600°C), followed by Cu-rich sulphides (which form chalcopyrite and cubanite) and typically associated with Pt-Pd-minerals. Primary magnetite (< 15 wt. %) is commonly present in massive sulfide ore where it crystallized from sulfide melt at high temperature (~1000°C). Magnetite from Ni-Cu-PGE deposits can be distinguished from magnetite in hydrothermal ore deposits by their high Ni + Cr content (Dupuis and Beaudoin 2011).

In these deposits, magnetite also records the fractionation history of the sulfide melt (Dare et al. 2012). Yet the composition and behaviour of trace elements in magnetite is different to that in a silicate melt: (a) the composition of sulfide melt (enriched in chalcophile elements) is different to that of silicate melt (enriched in lithophile elements) and (b) crystallizing phases that compete with magnetite are different.
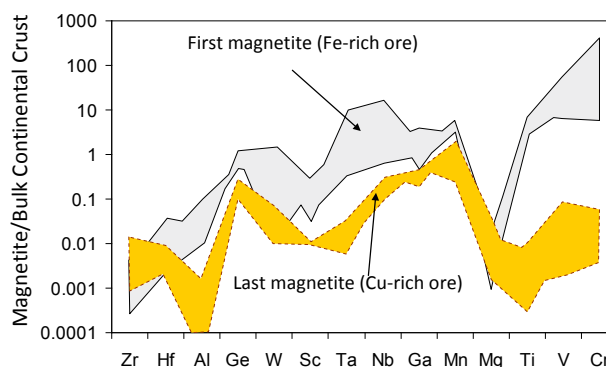


**Figure 2.** Multi-element variation diagram (lithophile elements only) for magnetite (Mt) from Ni-Cu-PGE deposits. Modified from Dare et al. (2012).

As there is no competition with co-crystallizing

silicate minerals, all of the lithophile elements in the sulfide melt are controlled by crystallization of magnetite (Fig. 2). Thus early-forming magnetite in Fe-rich ore is enriched in all of the lithophile elements (< 2 wt.% Ti, V and Cr), which are gradually depleted in the residual melt so that later-forming magnetite in the Cu-Pt-Pd-rich ore contains the lowest concentrations of all these elements (< 50 ppm). Thus the Cr-Ti-V content of magnetite can identify whether the ore is Cu-Pt-Pd rich or Fe-rich and Pt-Pd poor (Dare et al. 2012). Of the chalcophile elements, only Ni, Co, Zn, Sn and Mo are present in magnetite, the concentration of which depends on competition from co-crystallizing sulfides (Fe-rich or Cu-rich).

## 4 Comparison between magmatic and hydrothermal magnetite

Hydrothermal magnetites have distinctly different chemical signatures to magmatic magnetite (Fig. 3). In particular, they have lower concentrations for many of the trace elements that are common in magmatic magnetite (e.g., Ti, Al, Zn and Mo). Magnetite from low temperature hydrothermal environments appears to have the lowest overall abundance of trace elements (Fig. 3b). Elements that are typically absent in magmatic magnetite, i.e. highly incompatible into magnetite (Si, Ca, Y, P and REE), can be enriched in magnetite from some hydrothermal settings (Fig. 3a). The different signature of hydrothermal magnetite must reflect their different liquid composition and conditions of formation (e.g., temperature, redox and competing phases).
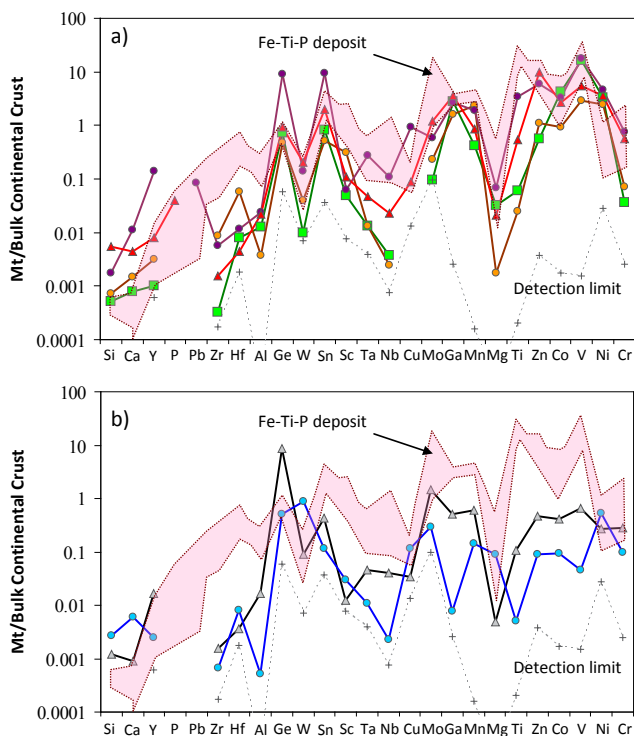


**Figure 3.** Multi-element variation diagrams to compare magnetite (Mt) from magmatic (pink field) and hydrothermal settings: a) High temperature magmatic-hydrothermal deposits such as IOCG (circle), IOA (square) and porphyry (triangle); b) Low temperature hydrothermal settings such as BIF (triangle)

and carbonate veins in serpentinite (circle). In a) samples of IOCG from Ernest Henry (orange: this study) and Bafq, Iran (purple: Bonyadi et al. 2010), IOA from Othrys ophiolite, Greece (Green: Mitsis & Economou-Eliopoulos, 2001) and porphyry from Morococha (this study). All samples in b) are from Thompson Ni Belt (this study).

Another important difference between magmatic and hydrothermal magnetite is the behaviour of Ni and Cr. In magmatic settings their behaviour is coupled, with Ni/Cr ratios $\leq$ 1, as they are both compatible during fractionation of silicate magmas. In contrast, in many high temperature hydrothermal settings, for example skarn, IOCG, Fe-oxide-apatite (IOA) and porphyry, their behaviour is decoupled and Ni/Cr ratio of magnetite is much higher ($\geq$1). This is probably related to a difference in solubility and/or mobility for Ni compared to Cr in many types of hydrothermal fluids.

## 5 Are the magnetite 'lava flows' of El Laco (Chile) magmatic or hydrothermal?

The 2 Ma stratovolcano of El Laco hosts Fe-oxide deposits (500 Mt at 60% Fe) on surface and immediately below (< 300 m depth). The deposits are classified as a 'Kiruna-type' or IOA (Fe-oxide-apatite) subgroup of IOCG deposits and comprises Ti-poor (< 0.1 wt.%) magnetite with minor hematite, apatite and clinopyroxene. The origin of El Laco deposits, and many other Kiruna-type deposits, has been debated for a long time. At El Laco, magnetite ore takes the form of lava flows which led many workers to argue their formation from an Fe-oxide liquid that erupted from the volcano (e.g., Nyström and Henriquez 1994). However, studies on alteration assemblages surrounding the deposits were used to argue that magnetite ore formed by hydrothermal replacement of the andesite lava flows (Rhodes et al. 1999; Sillitoe and Burrows 2000). What can be learned from chemical fingerprinting of the magnetite from both the ore and host rocks?

Our samples of magnetite ore are representative of the magnetite "lava flows" as they have the same compositional range as magnetite concentrates analysed by Nyström and Henriquez (1994) for all of the El Laco deposits. Fresh andesite host rocks at El Laco contain phenocrysts of Ti-rich magnetite, of typical magmatic composition (Fig. 1). However, magnetite from El Laco massive ore has a distinctly different composition to magmatic magnetite in the host andesite (Fig. 4) indicating that the ore magnetite was not in equilibrium with a silicate melt:

1) Magnetite from El laco ore is depleted in many elements but in particular those considered relatively immobile in hydrothermal fluids, e.g., Ti, Al, Cr, Zr, Hf and Sc (Fig. 4a);
2) Magnetite is enriched in elements that are highly incompatible into magnetite (REE, Si, Ca, Y and P) and normally in very low abundance in magmatic magnetite (Fig. 4a) but can be enriched in magmatic-hydrothermal magnetite (Figs. 3a and 4b) from IOCG and IOA (Mitsis and Economou-Eliopoulos 2001; Bonyadi et al. 2010);
3) The behaviour of Ni and Cr is decoupled with ratios

> 1, typical of magnetite from IOCG, IOA and skarns;

4) Oscillatory zoning of Si, Ca, Mg and REE in El Laco magnetite is similar to that found in skarn magnetite (Fig. 5).

Furthermore, magnetite of clear secondary origin in the altered host rock has the same composition (Fig. 4a) and compositional zoning as magnetite from the El Laco massive ore. Thus the chemical fingerprint of magnetite from the El Laco "lava flows" supports the hydrothermal model of alteration of andesite lava flows rather than a magmatic origin.
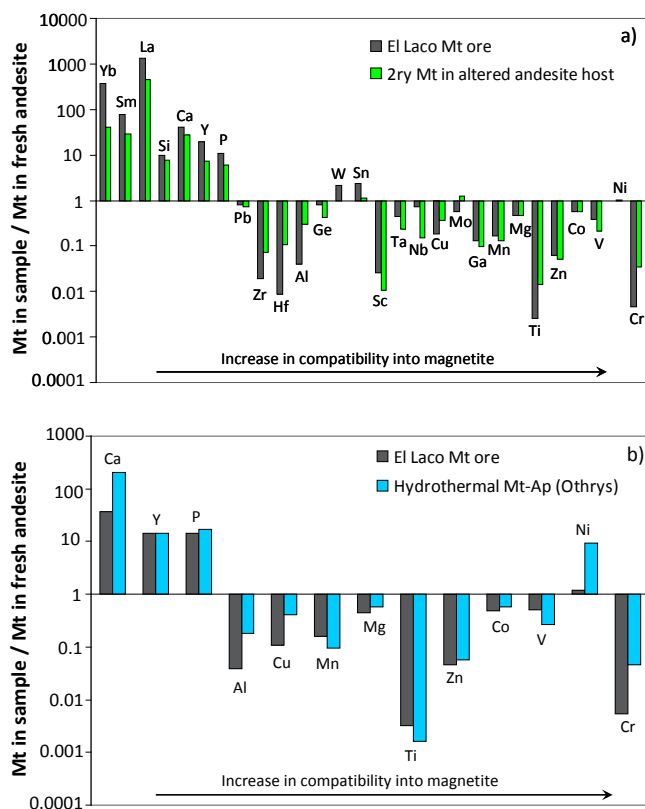


**Figure 4.** Composition of magnetite (Mt) from El Laco ore (black) compared to a) secondary (2ry) magnetite in altered andesite host of El Laco and b) hydrothermal magnetite deposited together with apatite (Ap) in a mantle shear zone of the Othrys ophiolite, Greece (LA-ICP-MS data from Mitsis and Economou-Eliopoulos (2001)). All samples normalized to primary magnetite in the fresh andesite of El Laco.
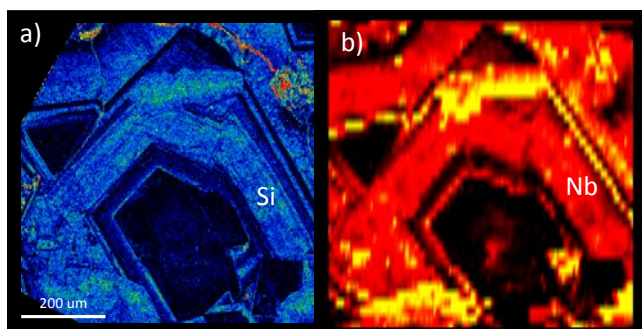


**Figure 5.** Chemical maps of zoned magnetite from El Laco massive ore: a) Si by electron microprobe (beam size 3 μm) and b) Nb by laser ablation ICP-MS (beam size 19 μm). In a) Si-rich zones (blue) contain ~ 1.5 wt.% Si.

# Conclusions

The main processes that control the composition of magnetite in magmatic systems are 1) the partitioning behaviour of an element into magnetite, 2) composition of the liquid, which changes during crystal fractionation, and 3) competition for an element among co-crystallizing phases. Trace element signatures of magnetite from different environments (i.e., magmatic and hydrothermal) are distinct and can be used in provenance studies. As such the chemical signature of magnetite from the El Laco 'lava flows' indicate a hydrothermal rather than a magmatic origin.

# Acknowledgements

# References

Bonyadi Z, Davidson GJ, Mehrabi B, Meffre S, Ghazbam F (2010) Significance of apatite REE depletion and monazite inclusions in the brecciated Se-Chahun iron oxide-apatite deposit, Bafq district, Iran: Insights from paragenesis and geochemistry. Chemical Geology 281:253-269.

Dare SAS, Barnes SJ, Beaudoin G (2012) Variation in trace element content of magnetite crystallized from a fractionating sulfide liquid, Sudbury, Canada: Implications for provenance discrimination. Geochimica et Cosmochimica Acta 88:20-57.

Dupuis C, Beaudoin G (2011) Discriminant diagrams for iron oxide trace element fingerprinting of mineral deposit types. Canada. Mineralium Deposita 46:319-335.

Mitsis I, Economou-Eliopoulos M (2001) Occurrence of apatite associated with magnetite in an ophiolite complex (Othrys), Greece. American Mineralogist 86:1143-1150.

Nadoll P, Mauk J, Hayes TS, Koenig AE, Box SE (2012) Geochemistry of magnetite from hydrothermal ore deposits and host rocks of the Mesoproterozoic Belt Supergroup, United States. Economic Geology 107:1275-1292.

Nyström JO, Henriquez F (1994) Magmatic features of iron ores of the Kiruna Type in Chile and Sweden: Ore textures and magnetite geochemistry. Economic Geology 89:820-839.

Reguir EP, Chakhmouradian AR, Halden NM, Yang P (2008) Early magmatic and reaction-induced trends in magnetite from the carbonatites of Kerimasi, Tanzania. The Canadian Mineralogist 46:879-900.

Rhodes AL, Oreskes N, Sheets S (1999) Geology and rare earth element geochemistry of magnetite deposits at El Laco, Chile. Society of Economic Geologist, Special Publications 7:299-332.

Sillitoe RH, Burrows DR (2000) New field evidence bearing on the origin of the El laco magnetite deposit, northern Chile. Economic Geology 97:1101-1109.

Toplis MJ, Caroll MR (1995) An experimental study of the influence of oxygen fugacity on Fe-Ti oxide stability, phase relations, and mineral-melt equilibria in ferro-basaltic systems. Journal of Petrology 36:1137-1170.

# Trace element geochemistry of magnetite and its relationship to mineralization in the Great Bear magmatic zone, NWT, Canada

**Pedro Acosta-Góngora & Sarah A. Gleeson**
*University of Alberta, Department of Earth and Atmospheric Sciences, Edmonton, Alberta, Canada T6G 2E3*

**Iain M. Samson**
*University of Windsor, Department of Earth and Environmental Sciences, Windsor, Ontario, Canada, N9B 3P4*

**Luke Ootes**
*Northwest Territories Geoscience Office, Yellowknife, Northwest Territories, Canada, NT X1A 2R3*

**Louise Corriveau**
*Geological Survey of Canada, 490 rue de la Couronne, Québec, QC, Canada, G1K 9A9*

**Abstract.** The Paleoproterozoic Great Bear magmatic zone (GBmz) is the focus of ongoing exploration for iron oxide copper-gold (IOCG) mineralization and also hosts numerous iron-oxide-apatite±actinolite (IOA) occurrences. Examples include the Sue-Dianne and NICO deposits and other smaller prospects like DAMP, FAB and Nori/Ra. Furthermore, the past-producing Terra mine (Ag-Ni ±Co,Bi) hosts significant IOCG-like alteration in its vicinity. A petrographic analysis identified the presence of multiple generations of magnetite in NICO, FAB and Nori/Ra and, for the most part, a single generation of magnetite at Sue-Dianne, DAMP and Terra. A laser ablation-inductively coupled plasma mass spectrometric study (LA-ICP-MS), demonstrates important geochemical differences in V, Ni, Cr, Co and Ti. Regionally, the Cr/Co metal ratios proved to be higher for barren magnetite and pre-ore magnetite compared to that of magnetite co-precipitated with ore minerals and/or hosted in veins and breccias. Locally, at the Nori/Ra prospect the V/Ni ratio in magnetite successfully differentiates between pre-ore and syn-ore magnetite and at DAMP and Sue-Dianne the Co/Ni ratio is extremely high, and clearly different from the other magnetites in the Great Bear magmatic zone. These results show that the chemistry of magnetite may be an important tool in the exploration of IOCG-IOA systems.

**Keywords.** Magnetite, IOCG, Great Bear

## 1 Introduction

The Great Bear magmatic zone (GBmz) in the Northwest Territories, Canada, is host to the NICO (Au- Co-Bi±Cu-W) and Sue Dianne (Cu-Au-Ag±U) deposits and other smaller iron-oxide polymetallic systems with comparable alteration and mineralization styles to iron-oxide copper gold (IOCG) deposits in Chile and Australia (e.g. La Candelaria, Raúl-Condestable, Olympic Dam and Lightning Creek). In the GBmz magnetite is common and associated with different styles and types of mineralization and hydrothermal/ alteration (e.g. Corriveau et al., 2010a,b; Corriveau et al., 2011; Montreuil et al. in press a,b), but is also found in least-altered metasedimentary, volcanic and plutonic rocks.

In Northern Canada, large amounts of glacial-derived sediments have covered the bedrock and magnetite is preserved on till and river sediments (e.g.McMartin et al., 2011). Yet, for magnetite to be a useful IOCG indicator mineral, it is necessary to constrain its spatial and temporal association with ore, gangue minerals and barren rocks, and to compare their chemistry and define if significant differences arise.

This work presents a petrographical study of magnetite associated with the ore minerals from the NICO (Au-Co-Bi±Cu-W) and Sue Dianne (Cu-Au-Ag±U) deposits, a magnetite-apatite body adjacent to the past-producing Terra mine (quartz vein-hosted Ag-Ni-Bi-U) as well as the DAMP (Cu-U), FAB (Cu-U) and Nori/Ra (Mo-Cu-U) prospects in the central and southern GBmz. Major and trace element studies were carried out on magnetite phases in host-rocks not associated with mineralization to assess if there are key characteristics of ore stage magnetite. Furthermore, whole-rock geochemistry of the host-rocks is compared to magnetite chemistry in order to test the role of the host-rocks in magnetite crystallization. Based on the petrographic and geochemical analyses we interpret the possible factors affecting the magnetite chemical signature and its utility as an indicator mineral.

## 2 Regional Geology

The multiple iron-oxide dominated polymetallic systems in the study area are hosted by the metasediments of Treasure Lake group (TLG) and volcanic rocks of the GBmz. The TLG (<1885, but >1875 Ma; Gandhi and van Breemen, 2005) hosts the NICO deposit and the Nori/RA prospect. Volcanic feeder dykes and plutons of the GBmz intrude the TLG in the southern portion of the study area and volcanic rocks were deposited unconformably on top. These ca. 1875 to 1865 Ma (Gandhi et al., 2001) volcano-plutonic units host, among others, the Sue-Dianne deposit, the FAB, DAMP and a number of other mineralized prospects.

The TLG is a metamorphosed (up to amphibolite

facies) sequence and four main units have been described by Gandhi and van Breemen (2005) as follows: a lower siltstone; carbonate; quartz-arenite; and upper siltstone. The lower siltstone (T1) is a quartzofeldspathic unit with magnetite-rich, argillaceous beds. Overlying the lower siltstone, the carbonate unit (T2) is dominated by marble, but also includes magnetite-amphibole rich layers. The top of the calc-silicate unit is interfingered with the quartz-arenite. The quartz-arenite (T3) grades into a zone of thin to thickly-bedded siltstone (T4). Within the sequence, numerous zones are highly altered to amphibole-magnetite±K-feldspar metasomatic rocks, albitites or skarns.

The GBmz volcanic rocks concerning to this work mostly consist of dacite, ignimbrite and rhyodacite (e.g. Gandhi et al., 2001).

# 3. Magnetite occurrence and paragenesis

## 3.1 Treasure Lake Group

Magnetite occurs in the TLG in the lower siltstone and the carbonate unit and is not spatially associated with ore minerals. The T1 magnetite (T1mag) commonly occurs as euhedral un-zoned disseminated grains in biotite-rich quartzofeldspathic beds. The T2 magnetite (T2mag) was only recognized in amphibole-altered beds as unzoned euhedral disseminated grains with equally euhedral amphibole grains and is interpreted as metasomatic in origin.

## 3.2 NICO

The NICO deposit hosts economic Au-Co-Bi (±Cu-W) within magnetite-amphibole altered rocks of the Treasure Lake Group (T2 unit). The NICO ore have at least three main generations of magnetite. The earliest generation (NImag1) pre-dates the ore, occurs with amphibole and pervasively replace the host-rocks. In early stages of this generation, well developed atoll textures are preserved as magnetite overgrowing silicate minerals. Another texture commonly observed on NImag1 is the intergrowth of roughly concentric magnetite-rich and magnetite-poor/free silicate inclusion zones. The next phase of magnetite (NImag2) has a coarser grain size with mostly euhedral shapes and no obvious zoning. Ore minerals like arsenopyrite, scheelite, loellingite and cobaltite are co-precipitated in veins, ore 'patches' and disseminated along the bedding with NImag2. The last stage of magnetite (NImag3) is dominantly found in millimeter and micrometer thick veins crosscutting Co-As-S-Fe sulphides. The Nmag3 is mostly co-precipitated with native Bi and bismuthinite.

## 3.3 NORI/RA

The Nori prospect has two different generations of magnetite within the mineralized zones. The earliest magnetite (Nomag1) is an important component (up to 20%) of the biotite-K-feldspar ± muscovite metasiltstone host rocks. Nomag1 is fine grained (30μm), occurs evenly disseminated on the wall-rock and predates the mineralized veins. The later magnetite (Nomag2) phase

is an accessory mineral (<1%) within tourmaline-biotite veins that cut the host metasedimentary rocks. Nomag2 is co-precipitated with pyrite, molybdenite, and uraninite. Commonly, it occurs as euhedral magnetite-pyrite mineral clusters. This magnetite is also found in the potassic feldspar-quartz tension gash-like segregates (NoQKmag; Ootes et al., 2010) in monomineralic mineral clusters and as pyrite-magnetite aggregates.

## 3.4 Terra

At the past-producing Terra mine, a large stock of magnetite-apatite-actinolite±biotite occurs directly adjacent to the Ag-Ni, Co-arsenides, Bi and U-bearing quartz veins. The magnetite is coarse-grained, moderately fractured, with euhedral shapes, and commonly has inclusion-free crystal surfaces. Magnetite and apatite are co-precipitated and are cross-cut by a later generation of actinolite, apatite and quartz veins.

## 3.5 DAMP

The Damp prospect consists of polymetallic (Cu-U-Co-V±Zn-Pb) mineralization hosted by an extensive breccia zone. Magnetite is coarse grained, unzoned and euhedral, moderately to highly fractured and co-precipitated with hematite and pyrite as part of the breccia matrix. Later Cu-Bi-Co sulphides like chalcopyrite, carrolite ($CuCo_2S_4$), bornite, emplectite commonly crosscut pyrite and, to a lesser degree, magnetite.

## 3.6 Sue-Dianne

The Sue-Dianne (Cu-Au-Ag±U) deposit is hosted by a rhyodacite ignimbritic sequence. The mineralization occurs largely within an iron oxide matrix-rich breccia zone. Magnetite is precipitated as euhedral medium-grained crystals forming mineral aggregates precipitated with significant amounts of specular hematite, fluorite and accessory carrolite.

The bulk of the Cu-(±Bi) mineralization largely represented by chalcopyrite and less bornite, carrolite, emplectite and wittichenite ($Cu_3BiS_3$) is post-dating the magnetite deposition as suggested by the abundant infill textures and crosscutting relationships.

## 3.7 FAB

FAB (Cu-U) prospect consists of a Cu-U mineralization within felsic volcanic rocks and hypabyssal porphyries (e.g. Gandhi 1988). Magnetite at FAB occurs as two different generations with different grain sizes. The finest grained and earliest one, Fmag1, has subhedral grains disseminated within the aphanitic matrix of the rhyodacitic host-rock. Inclusions of quartz and feldspars in Fmag1 are most likely remnants from the host-rock matrix. The coarser magnetite phase, Fmag2, consists of inclusion-free euhedral to subhedral grain, distributed along fractures and infill material of a clast-supported breccia co-precipitated with pyrite-K-feldspar and epidote. The main Cu-mineralization is represented by the introduction of chalcopyrite and minor amounts of bornite mostly intergranular to Fmag2 and pyrite located

within micro-veins, breccia matrix or/and pseudomorphing this sulfide.
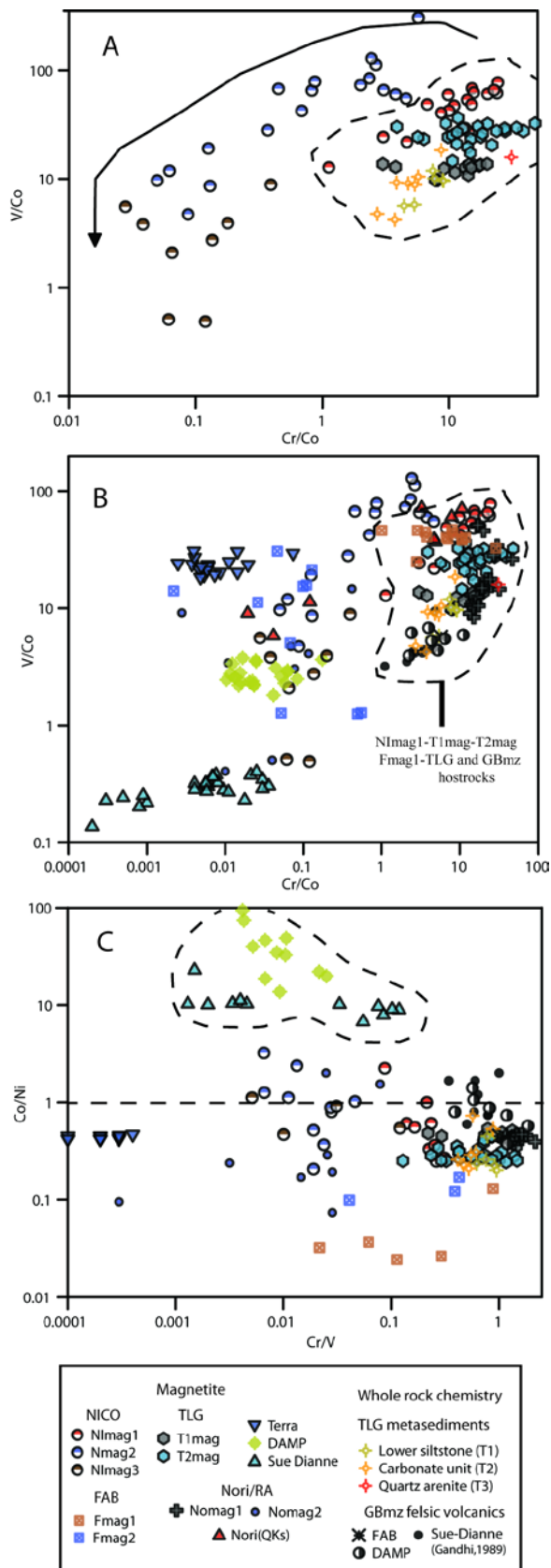


**Figure 1.** Metal ratios of GBmz magnetite. A, progressive decrease of magnetite Cr/Co-V/Co ratios with time (arrow) at NICO. B, Cr/Co and V/Co ratios of barren and pre-ore magnetite (inside dashed field) versus ore-related magnetite. C, Sue-Dianne and DAMP magnetite exhibiting the highest Co/Ni in the GBmz.

## 4. Trace element analysis

In-situ trace elements analysis on magnetite was carried out via laser ablation inductively coupled mass spectrometry (LA-ICP-MS) at the Great Lakes Institute for Environmental research (GLIER), University of Windsor. Whole rock analysis from host rocks was carried out at ActLabs, Ontario.

### 4.1 Cr/Co, V/Co and V/Ni ratios

The Cr/Co-V/Co metal ratios of NICO pre-ore magnetite (NImag1), shown in Figure 1A plot broadly in the same region with the T1mag, Nomag1, T2mag and the TLG host rocks suggesting they might have been equilibrated with the host rocks during its formation. Another interesting feature recognized in NICO magnetite is the evolving V/Co-Cr/Co trend (Fig. 1A) where Cr and V get progressively depleted from NImag1 to NImag3.

At the Nori/RA prospect the V/Ni and Cr/Co metal ratios of Nomag1 are closely grouped together, and they are remarkably similar to those of T1mag which is also not associated with mineralization. The Nomag2 V/Ni and Cr/Co ratios are more variable, but are distinct from Nomag1, consistent with the paragenetic interpretation. The bimodal chemistry of the magnetite in the segregations is more difficult to explain. A bimodal distribution of metal ratios was also identified in the two magnetite generations from FAB; the Cr/Co ratios are distinctively higher in Fmag1 compared to Fmag2 (Fig. 1B). The Fmag1 exhibits Cr/Co ratios that overlap those of its altered host rock values.

Sue-Dianne and DAMP magnetite have similar Cr/Co ratios but distinct V/Co compositions, which are also different from their respective protoliths, the T1mag and T2mag and the TLG rocks (Fig. 1B).

### 4.2 Co/Ni ratio

Our data identify two populations determined by the Co/Ni ratio (Fig. 1C). The first one comprised by Nori/RA, NICO, FAB, Terra and the TLG magnetite correspondingly low Co/Ni<2 values and few outliers slightly below 4. However, the second group represented by Sue-Dianne and DAMP has extraordinarily high Co/Ni ratios (7 to 94) due to a combination of unusual Co enrichment and Ni depletion. Such values are not likely to be achieved by the equilibration of the fluids with their rhyodacitic protoliths as the Co/Ni for these are generally <2 (Fig 1C). Moreover, Co/Ni ratios for mafic, intermediate and felsic magmatic suites and marine sediments average values are < 4.62 (e.g. Niu et al., 1999; Nolte et al. 2012; Li 2000). Metasomatic replacement-type alteration across GBmz IOCG-like systems is extremely pervasive and it has been suggested that the chemical signature of alteration is independent of host rock chemistry (e.g. Corriveau et al., 2010b, 2011; Montreuil et al. in press). Hence, we interpret the high Co/Ni in DAMP and Sue Dianne magnetite as representative of the ore-fluid ratio from which it precipitated.

## 4.3 Exploration implications

The distinct physicochemical controls on magnetite trace element compositions from alteration and mineralization makes this iron oxide a potentially useful indicator mineral for mineral exploration.

The Cr/Co ratio is distinctively higher in pre-ore (>1), and barren magnetite from the TLG compared to those of texturally syn-genetic with ore minerals and/or hosted in iron oxide-rich breccias and veins (<1; Fig 1). Yet, some of NImag2 values have elevated Cr/Co ratios similar to those of non-ore related magnetite. The Terra magnetite-apatite stock is also characterized by magnetite with very low Cr/Co ratios. The V/Ni ratio is less useful at a regional scale, but at the DeVries lake area it proved suitable to distinguish between the metasiltstone hosted (Nomag1) and the vein-hosted magnetite (Nomag2).

The Co/Ni ratios (Fig. 1C) successfully differentiate Sue-Dianne and DAMP from other magnetite (Co/Ni=7-94) and suggests they are characteristic of magnetite associated with Cu-U (±Co-Ag-Au) iron oxide breccia systems in the GBmz.

## Acknowledgements

## References

Corriveau L, Mumin AH, Setterfield T (2010a) IOCG environments in Canada: Characteristics, geological vectors to ore and challenges: In: Porter TM (ed) Hydrothermal iron oxide copper-gold and related deposits: A global perspective, volume 4. PGC Publishing, Adelaide, pp 311–343

Corriveau L, Williams PJ, Mumin H (2010b) Alteration vectors to IOCG mineralization from uncharted terranes to deposits. In: Corriveau L, Mumin AH (eds) Exploring for iron oxide copper-gold deposits: Canada and global analogues. Geol Assoc Can, Short Course Notes 20, pp 89–110

Corriveau L, Mumin H, Montreuil J-F (2011) The Great Bear magmatic zone (Canada): Exposing the IOCG spectrum and related deposit types. SGA2011 - The 11th Biennial SGA Meeting of The Society for Geology Applied to Ore Deposits, Antofagasta, Chile, Transaction volume

Gandhi SS (1988) Volcano-plutonic setting of U-Cu bearing magnetite veins of FAB claims, southern Great Bear magmatic zone, Northwest Territories. Geol Sur of Can 88-1C: 177–187

Gandhi SS, Mortensen JK, Prasad N, van Breemen O (2001) Magmatic evolution of the southern Great Bear continental arc, northwestern Canadian Shield: Geochronological constraints. Can J Earth Sci 38:767–785.

Gandhi SS, van Breemen O (2005) SHRIMP U–Pb geochronology of detrital zircons from the Treasure Lake Group – new evidence for Paleoproterozoic collisional tectonics in the southern Hottah terrane, northwestern Can. Shield. Can. J. Earth Sci 42:833–845

Li YH (2000) A compendium of geochemistry: from solar nebula to the human brain. Princet, NJ

McMartin I, Corriveau L, Beaudoin G (2011) An orientation study of the heavy mineral signature of the NICO Co-Au-Bi deposit, Great Bear magmatic zone, Northwest Territories, Canada. Geochem: Explor Environ Anal 11: 293–307

Montreuil JF, Corriveau L, Grunsky E (in press)a A compositional data analysis of IOCG systems, Great Bear magmatic zone, Canada: To each alteration types its own geochemical signature. Geochem Explor Environ Anal

Montreuil JF, Corriveau L, Potter L (in revision)b Albitite-hosted uranium development within IOCG systems: the Southern Breccia, Great Beat magmatic zone, Northwest Territories, Canada. Miner Depo

Niu Y, Collerson K, Batiza R, Wendt I, Regelous M (1999) Origin of enriched-type mid-ocean ridge basalt at ridges far from mantle plumes, the East Pacific Rise at 11′20 N. J. of Geophys Res 104:7067–7087

Nolte N, Kleinhanns IC, Baero W, Hansen BT (2011) Petrography and whole-rock geochemical characteristics of Västervik granitoids to syenitoids, southeast Sweden: constraints on petrogenesis and tectonic setting at the southern margin of the Svecofennian domain. GFF 133:173–196

Ootes L, Goff S, Jackson V, Gleeson SA, Creaser RA, Samson, IM, Evenson N, Corriveau L, Mumin H (2010) Timing and thermochemical constraint on multi-element mineralization at the Nori/RA Cu-Mo-U prospect, Great Bear magmatic zone, Northwest Territories, Canada. Miner Depos 45:549–566.

# Magnetite chemistry in skarns of the Bohemian Massif: evaluating competing effects of protolith inheritance, crystal chemistry, fluid composition and pressure-temperature conditions

Jan Bubal, David Dolejš
*Institute of Petrology and Structural Geology, Charles University, 12843 Praha 2, Czech Republic*

**Abstract.** Magnetite-rich skarns in the Bohemian Massif (central Europe) frequently occur in supracrustal volcano-sedimentary sequences, metamorphosed up to green-schist, amphibolite or eclogite facies. Their magnetites are very pure (95.5-99.3 mol. % $Fe_3O_4$) and minor and trace element concetrations are very low, defined by hercynite and ulvöspinel substitution trends. These patterns are consistent with derivation of skarns by carbonate or calc-silicate replacement, and exclude their origin in other settings or by involvement exhalative or hydrogeneous components. Significant correlations at trace levels exist between ore-forming element pairs (e.g., Zn-Sn), various divalent pairs (e.g., Zn-Mn) as well as immobile couples (e.g., Al-Ti). Negatively correlated homovalent pairs (e.g., $Mg-Fe^{2+}$, $Mn-Fe^{2+}$, $Al-V^{3+}$) have the largest potential for reflecting the environmental conditions during magnetite crystallization, whereas the positively correlated Al-Ti pair reflects inheritance from the skarn precursor and element partitioning between coexisting phases. The $Al_2O_3/TiO_2$ ratios in magnetites (5.4-11.6 by weight) are substantially lower than those in the bulk magnetite-rich skarns (18.3-22.6), which is due to aluminum partitioning into garnet and/or clinopyroxene. These observations suggest that trace elements in magnetites are subject to redistribution and re-equilibration during superimposed metamorphic or hydrothermal events, in addition to their solubilities in the spinel structure being temperature-dependent as well.

**Keywords.** magnetite, skarn, solubility, partitioning, protolith inheritance, metasomatism

## 1 Introduction

Magnetite, $Fe_3O_4$, is the most common oxide in a number of ore deposit styles, ranging from Ni-PGE, Cu-sulfide or Fe-Ti-V mafic magmatic systems through hydrothermal iron oxide-copper-gold, or skarn deposits. Recent advances in microanalytical techniques prompted systematic studies of minor and trace element variations in magnetites from diverse geological settings (Dupuis and Beaudoin 2011, Dare et al. 2012). Incorporation of additional constituents into magnetite structure is controled by competing effect of protolith bulk composition, fluid composition, crystalochemical constraints, and pressure-temperature conditions. In this contribution we present new analytical data from magnetites in calcic-iron skarns in the Bohemian Massif, central Europe in order to reconcile contributions from these individual factors.

## 2 Geological setting

Calcic and magnesian magnetite-rich skarns are a characteristic minor constituent in numerous volcanosedimentary metamorphic complexes in the Bohemian Massif (Fig. 1). They form lenses or discontinuous horizons up to 200 m thick surrounded by siliciclastic, calc-silicate metasediments, felsic or mafic meta-volcanics, or metagranitic gneisses.
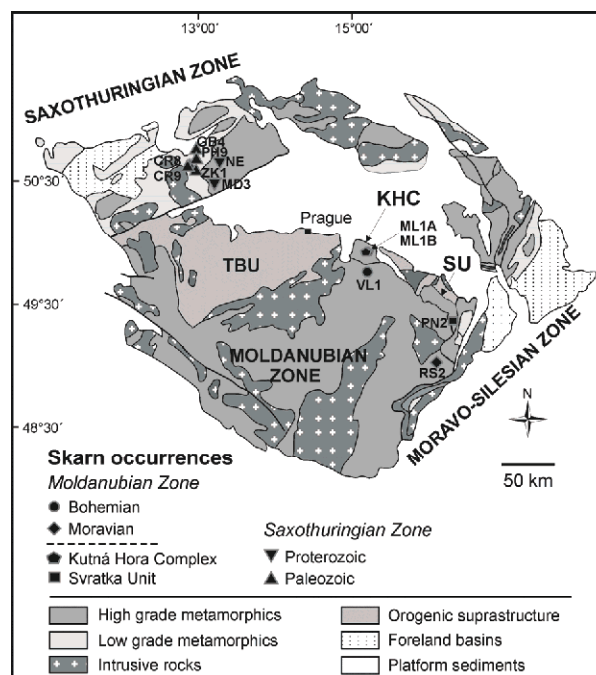


**Figure 1.** Geological map of the Bohemian Massif showing the main geological units and locations of individual magnetite skarn samples: VL1 – Vlastějovice, RS2 – Rešice, PN2 – Pernštejn, ML1A, ML1B – Malešov, MD3 – Měděnec, NE – Niederschmiedeberg, GB4 – Gelbe Birke (Beierfeld), PH9 – Pöhla, CR8, CR9 – St. Christoph (Breitenbrunn), and ZK1 – Zlatý kopec (Boží Dar).

All occurrences underwent regional metamorphism during Variscan orogeny (360-320 Ma) and were overprinted under greenschist, amphibole or eclogite facies conditions. The skarns are homogeneous or modally banded, consisting of clinopyroxene, garnet and magnetite-rich varieties. The magnetite content increases up to 80-90 vol. %, forming characteristic granoblastic texture with clinopyroxene, rare calcic garnet, secondary calcic amphibole, oxide or sulfide ore minerals such as cassiterite, sphalerite or chalcopyrite (Fig. 2a). The skarns were interpreted as products of

metasomatic replacement of carbonate precursors (Němec 1991) or as synsedimentary exhalative deposits (Pertoldová et al. 2009); their origin thus remains unresolved.
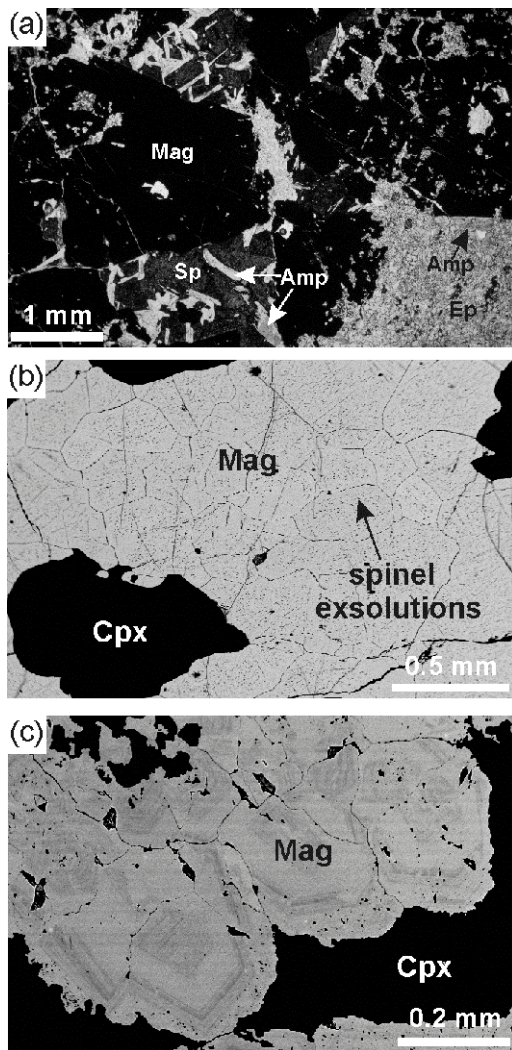
**Figure 2.** Optical and backscattered electron photomicrographs of magnetite-rich skarns: (a) amphibole-magnetite skarn with sphalerite mineralization, CR9; (b) clinopyroxene-magnetite skarn with exsolution lamellae of Mg- and Ti-rich spinel, RS2; (c) clinopyroxene-magnetite skarn showing compositional growth zoning of magnetite, ZK1.

## 3  Methodology

Twelve samples of magnetite-rich skarns were analyzed using the Cameca SX100 electron microprobe at the Institute of Geological Sciences, Masaryk University in Brno. Measurements were conducted with accelerating voltage of 15 kV and a beam diameter of 3.5 μm. The beam current was varied between 40 nA for iron and minor elements (Al, Ca, Cr, Mg, Mn, and Ti) and 100 nA for trace elements (Co, Cu, Ni, Pb, Si, Sn, Ta, V, and Zn). Natural and synthetic solid phases were used for calibration. The detection limits varied between 70-100 ppm (Ti, Si, V), 100-150 ppm (Al, Mg, Ca, Co, Cr, Ni, Sn), and 170-500 ppm (Mn, Cu, Zn, Ta, Pb). We analyzed 18 elements in total and the concentrations of Al, Fe, Mg, Mn, Si, Sn, Ti and Zn commonly exceed the respective detection limits (Fig. 3).
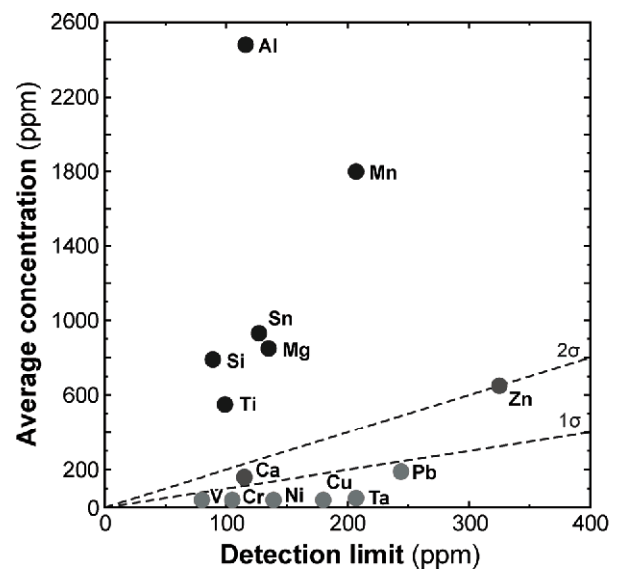
**Figure 3.** Detection limits and average concentrations of minor and trace elements in magnetite.

## 4  Results

Magnetites are compositionally homogeneous, with the exception of the sample ZK1 (Zlatý kopec) where a conspicuous hydrothermal growth zoning is preserved (Fig. 2c). Electron microprobe analyses were recalculated to formula units using 3 cations and 4 oxygen equivalents by adjusting the ferrous and ferric iron proportions (Fig. 4).

All skarn magnetites are nearly pure (95.5-99.3 mol. % $Fe_3O_4$) when compared to those from other hydrothermal or magmatic settings (Dupuis and Beaudoin 2011, Barnes and Roeder 2001). They contain 0.04-0.81 wt. % MnO, 0.01-0.63 wt. % MgO, 0.01-1.50 wt. % $Al_2O_3$, and up to 0.20 wt. % $TiO_2$, and these variations correspond to magnetite-hercynite and magnetite-ulvöspinel substitu-tions as well as homo-valent $M^{2+}$ mixing in the B site.

The data set reveals several regional trends: (i) magnetites from the Moldanubian skarns show the lowest manganese and silicon concentrations (0.06-0.13 wt. % MnO; 0.08-0.12 wt. % $SiO_2$), (ii) magnetites from the Kutná Hora-Svratka skarns are extremely depleted in magnesium (0.003-0.011 wt. % MgO), (iii) the titanium concentrations in magnetites are high in the Moldanubian skarns (0.06-0.21 wt. % $TiO_2$), decrease in the Saxothuringian Neoproterozoic skarns (0.03-0.07 wt. % $TiO_2$), and become irregularly scattered and high in the Saxothuringian Paleozoic occurrences (0.06-0.28 wt. % $TiO_2$), (iv) each locality has a well-defined, narrow range in MgO, MnO and $TiO_2$ concentrations.

Pearson correlation coefficients ($r$) were calculated for all element pairs in the entire data set and they reveal significant positive correlation between $Al_2O_3$ and $TiO_2$ ($r = 0.70$), MnO and ZnO ($r = 0.68$), ZnO and $SnO_2$ ($r = 0.75$), and negative correlation between FeO and MnO ($r = -0.74$). Negative correlations between homovalent elements indicate ionic substitutions, whereas positive correlations appear among both the ore-forming and immobile constituents. For instance, the $ZnO$-$SnO_2$ correlation mainly results from elevated concentrations

in the Saxothuringian Paleozoic skarns that were metasomatized by fluids derived from peraluminous collisional granitic magmas.
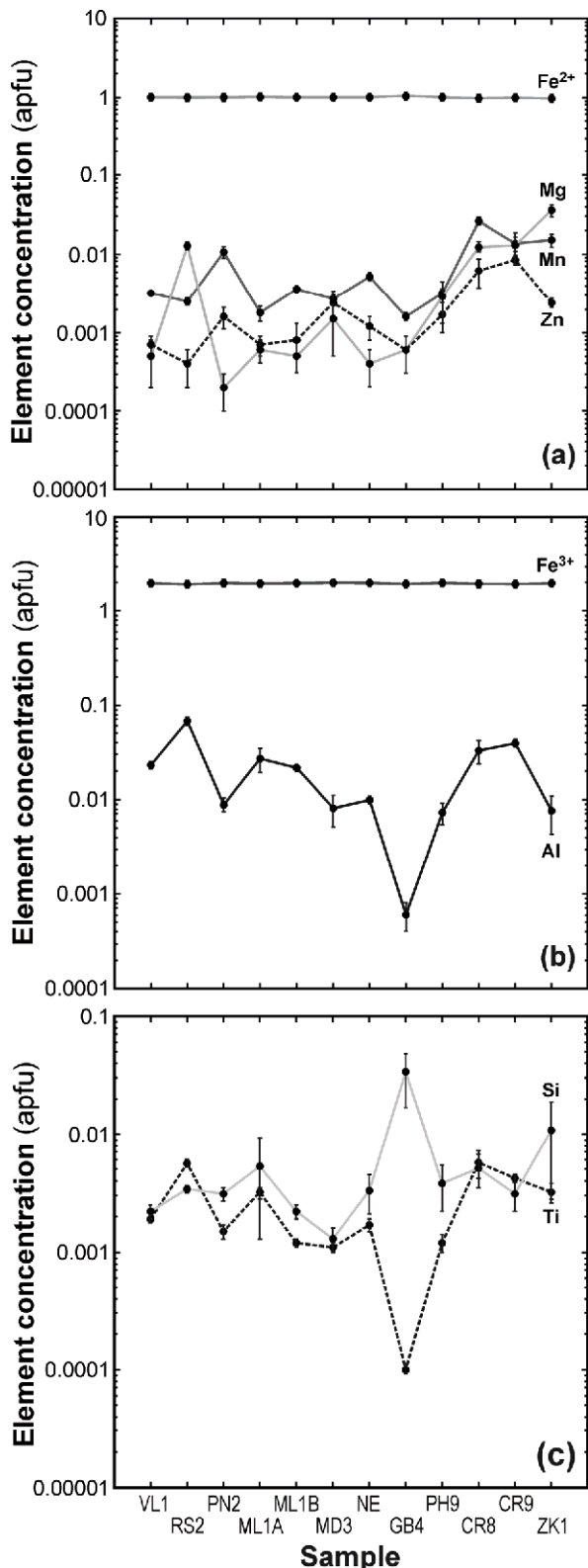


**Figure 4.** Minor and trace element concentrations in magnetites, expressed in atoms per formula unit (apfu).

## 5 Discussion and implications

We interpret our analytical dataset by addressing the following open questions:

(1) Are the observed trace element patterns consistent with skarn origin by epigenetic metasomatic replacement or by involvement of synsedimentary exhalative or hydrogeneous components? The concentrations of $Al_2O_3$, $TiO_2$ and $MnO$ are very low, and $NiO$, $CoO$ and $V_2O_3$ abundances appear to be lower than their detection limits (~ 140 ppm). The depletion in Mn and Ni excludes formation of magnetite by metamorphism of exhalative or hydrogeneous components, and the low Ti and V abundances do not support origin in hydrothermal systems similar to porphyry, iron oxide-copper-gold or Kiruna-type settings (Fig. 5). In addition, the depletion in Ti and V is probably limited by their decreasing solubility in the spinel structure at low hydrothermal temperatures. Subject to this restriction, we suggest that these elements were largely immobile in aqueous fluid during magnetite formation.
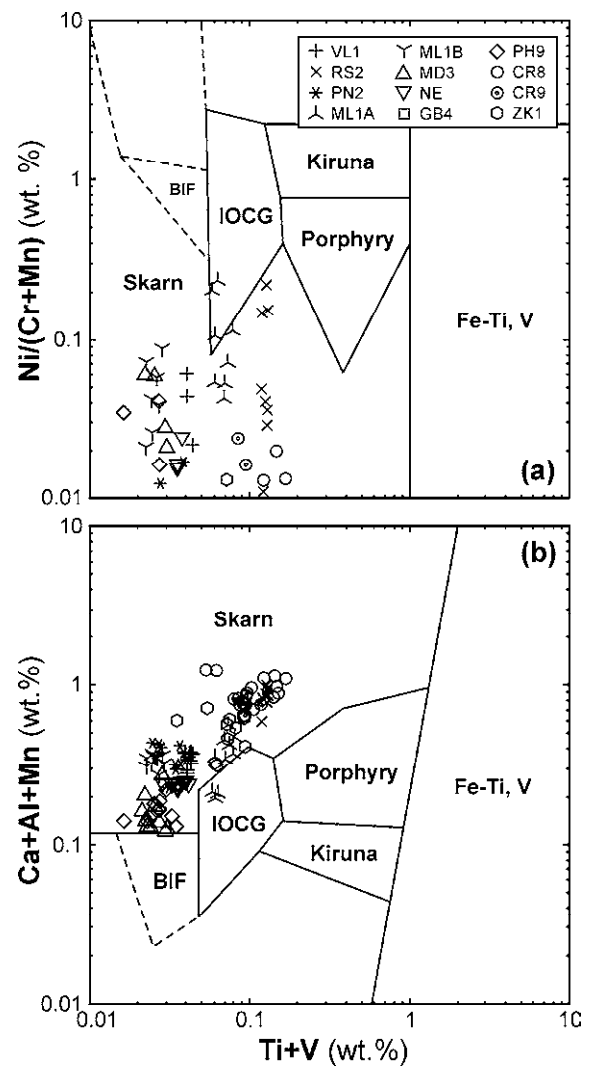


**Figure 5.** Discrimination diagrams for magnetites from various geological settings (Dupuis and Beaudoin 2011).

(2) Are the immobile elements (Al, Ti) in magnetite reflecting inheritance from the skarn precursor? Fig. 5b shows a broad linear trend due to the correlation between Al and Ti ($r = 0.70$). In several occurrences, field and petrographic evidence suggests that skarns formed by replacement of calcitic or dolomitic

precursors as well as their siliciclastic wall rocks (phyllites, mica schists), preserved as incompletely metasomatized relics. The $Al_2O_3/TiO_2$ ratios in magnetites are, however, generally lower than those found in volcanic rocks or average sediments (Fig. 6). Whole rock analyses of magnetite skarns (Vlastějovice, Malešov) reveal the ratio of $Al_2O_3/TiO_2$ = 18.3-22.6, whereas electron microprobe analyses of individual magnetite grains yield $Al_2O_3/TiO_2$ = 5.4-11.6. This departure is related to partitioning of available Al between magnetite, garnet and/or clinopyroxene in the skarns, whereas Ti is almost exclusively hosted by magnetite. Therefore, the Al and Ti enrichments in magnetite seem to generally indicate increasing proportion of detrital component in the skarn precursor but in detail their proportions may be affected by partitioning to other skarn-forming silicates.
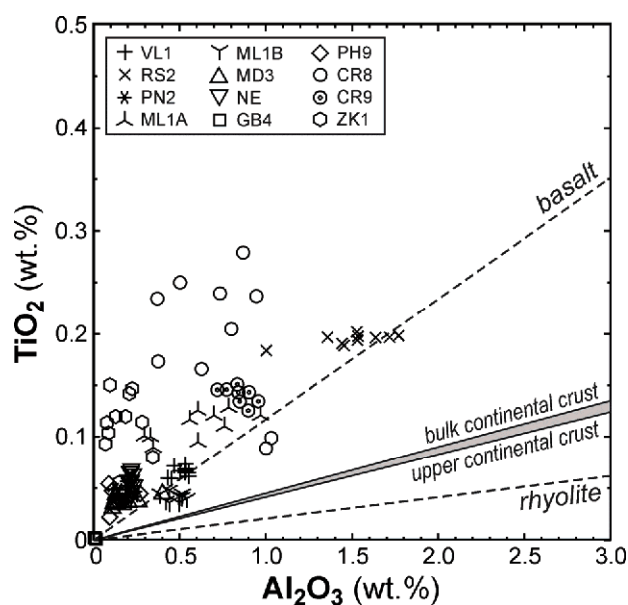


**Figure 6.** $Al_2O_3$ *vs.* $TiO_2$ concentrations in magnetites illustrating the systematic difference from the $Al_2O_3/TiO_2$ ratios in volcanic or sedimentary precursors (represented by the continental crust).

(3) Is the incorporation of Al and Ti in magnetite influenced by subsequent metamorphic events? In general, minor elements such as Ti, Al, Cr and Ni provide useful geochemical discriminators because their incorporation (solubility) in magnetite is expected to be temperature- and pressure-dependent as their ionic radii or partial molar volumes differ. In our data set, the maximum $Al_2O_3$ solubility limit in magnetite has been exceeded in one sample (Rešice, RS2) and this has lead to exsolution of Mg-Ti-rich spinel during post-metamorphic cooling (Fig. 2b). The corresponding $Al_2O_3$ content in magnetite, the largest in the entire data set, is $1.50 \pm 0.15$ wt. %.

The $TiO_2$ concentrations in magnetites increase up to 0.28 wt. % but are generally lower than 0.15 wt. %. Because the Ti incorporation in magnetite is controled by the ulvöspinel substitution and the $Fe^{3+}$ content becomes non-stoichiometric, the activities of FeO and $Fe_2O_3$ in magnetite solid solution provide means for calculating oxygen fugacity during its crystallization. In

our study, the low-Ti magnetites from Měděnec, Niederschmiedeberg and Pöhla formed at more oxidizing conditions than their high-Ti counterparts at St. Christoph near Breitenbrunn or Zlatý kopec.

We conclude that magnetites in calcic and magnesian iron-rich skarns in central Europe are very pure and their Al, Ti, Mn, Mg, V, Zn and Sn concentrations are very low but comparable to replacement skarns worldwide. This behavior results from their low-temperature origin as well as im/mobility of these elements in aqueous fluids. At trace levels, positive correlations between immobile elements, Al and Ti, suggest that they are inherited from impure carbonate protolith but subject to local redistribution and reequilibriation during subsequent metamorphic or hydrothermal events.

## Acknowledgements

## References

Barnes SJ & Roeder PL (2001) The range of spinel compositions in terrestrial mafic and ultramafic rocks. J Petrol 42: 2279-2302

Dare S, Barnes SJ & Beaudoin G (2012) Evolution of trace element concentrations in magnetite from a fractionating magmatic sulfide liquid from the Sudbury (Canada) Ni-Cu-PGE deposits: implications for provenance discrimination. Geochim Cosmochim Acta 88: 27-50

Dupuis C & Beaudoin G (2011) Discriminant diagrams for iron oxide trace element fingerprinting of mineral deposit types. Miner Depos 46: 319-335

Němec D (1991) Regional typization of the iron skarn of the Bohemian-Moravian Heights (Českomoravská vrchovina). Acta Mus Morav Sci Nat 76: 51-82

Pertoldová J, Týcová P, Verner K, Košuličová M, Pertold Z, Košler J, Konopásek J, Pudilová M (2009) Metamorphic history of skarns, origin of their protolith and implications for genetic interpretation; an example from three units of the Bohemian Massif. J Geosci 54: 101-134

# Trace element and oxygen isotope chemistry of iron oxides – a vector for the exploration of concealed BIF-hosted iron ore bodies?

**A.-S. Hensler, S.G. Hagemann, T. Angerer**
*Centre for Exploration Targeting, University of Western Australia, Crawley, WA 6009*

**C.A. Rosière**
*Instituto de Geociências, Universidade Federal de Minas Gerais, Pampulha, 32170-901 Belo Horizonte, Minas Gerais*

**Abstract.** Trace element and oxygen isotope analyses have been applied to different iron oxide species (e.g., martite, granoblastic, platy hematite, specularite from oldest to youngest) from various BIF-hosted high-grade iron ore deposits across the Iron Quadrangle (IQ), Minas Gerais, Brazil. Trace element contents in oxides change through the paragenetic sequence with remarkable Mg-, Mn-, and Al-depletion and Ti-, Cr-, V-enrichment during the recrystallization from martite to granoblastic hematite and a strong depletion in most of these elements during the formation of younger, shear zone-hosted specularite. Hematite from dolomitic BIF-hosted iron ore commonly have higher Mn contents than hematite derived from quartz BIF-hosted ore. Hematite from iron ore bodies that are crosscut by specularite-bearing "jacutinga"-style Au-Pd veins has significant lower abundandes of Mg, Ni, Zn, Pb, Co and Cu. Furthermore, a significant depletion of $^{18}O$ in hematite corresponds to the transition from BIF to high-grade iron ore, which is followed by a slight enrichment in $^{18}O$ from the oldest to youngest iron ore-forming hematite species.

**Keywords. iron oxide, laser ablation ICP-MS, oxygen isotope, Iron Quadrangle, high-grade iron ore**

## 1 Introduction

The Iron Quadrangle (IQ) in Minas Gerais is presently the largest accumulation of single BIF-hosted iron ore bodies worldwide and represents a unique iron ore province (Fig.1). In contrast to other Paleoproterozoic BIF-hosted high-grade iron ore regions worldwide, the IQ was affected during the Paleo- and Neoproterozoic by two distinct orogenies, resulting in a complex framework of folds and thrusts, greenschist- to amphibolite-facies metamorphic rocks, as well as multiple events (e.g., oxidization, gangue leaching, shear-zone related vein emplacement) that formed high-grade (> 63 wt.-%) iron ore bodies. Here we describe new results on oxygen isotope and trace element chemistry on different iron oxide generations forming the high-grade iron ore bodies across the IQ. The goal is to fingerprint chemical characteristics of different ore-forming iron oxides, to understand local and regional controls on iron oxide chemistry, track fluid sources and compare dominant geological signatures from the IQ to other high-grade iron ore districts worldwide.

## 2 Geological Setting and Characteristics of the Iron Quadrangle

The IQ bares many similarities to other iron ore provinces throughout the world (e.g., Hamersley province in Australia or Thabazimbi iron ore deposit in South Africa) in that the host rocks are Lake-Superior type BIFs. However, BIF in the IQ were affected by: 1) the Transamazonian orogeny (2.6 – 2.0 Ga) with the formation of large, regional-scale folds and 2) the Brasiliano orogeny (0.7-0.45 Ga) (Dorr, 1965). The latter event was restricted mainly to the eastern part of the IQ overprinting existing structures and forming a west-verging thrust belt. Rocks in the IQ were metamorphosed to greenschist-facies in the west and to amphibolite-facies in the east.

High-grade iron ore located in the western part of the IQ is massive to banded and consists mainly of martite and granoblastic hematite, with local shear zone-hosted specularite. In the eastern high-strain domain, however, platy hematite/specularite crystals dominate, resulting in schistose ore bodies. Hydrothermal carbonate alteration, which is an important precursor alteration stage for high-grade ore in the Hamersley iron ore province and Thabazimbi deposit, is less evident in most iron ore deposits in the IQ (Taylor et al., 2001, Beukes et al., 2003).
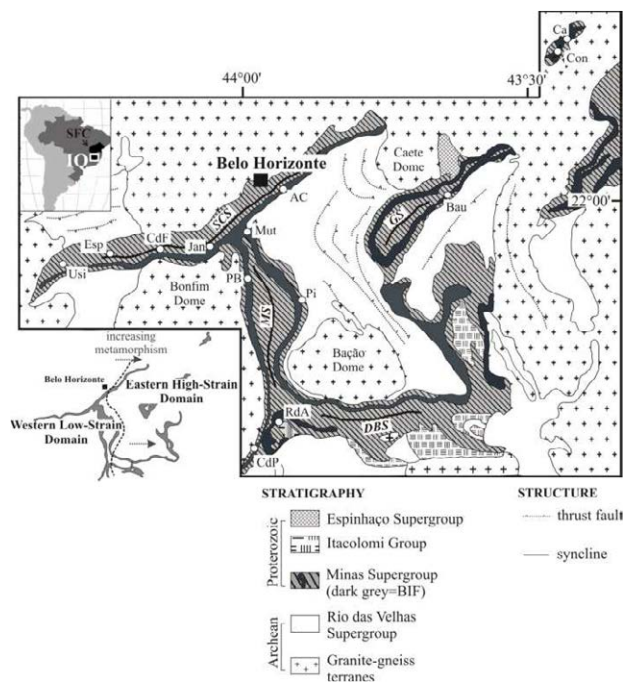


**Figure 1:** Geological map of the Iron Quadrangle, modified after Dorr (1969). High-grade iron ore deposits (subject of this study): AC = Águas Claras, Bau = Baú, CdF = Córrego do Feijão, CdP = Casa de Pedra, Con = Conceição, Esp = Esperança, PB = Pau Branco, Pi = Pico, RdA = Retiro das Almas, Usi = Usiminas Mining District.

Main structures: DBS = Dom Bosco syncline, GS = Gandarela syncline, IS = Itabira synclinorium, MS = Moeda syncline, SCS = Serra do Curral syncline.

# 3 Methodology

For trace element and stable isotope chemistry, samples of mainly high-grade iron ore and minor intermediate-to low-grade ore were selected to represent a wide distribution of different high-grade iron ore deposits across the entire IQ (Fig. 1). The samples vary in their physical textures (massive, brecciated and schistose) and contain different iron oxide generations, from oldest to youngest, including magnetite, martite, granoblastic hematite, platy hematite and specularite.

Element chemistry on iron oxides was analysed using laser ablation ICPMS at the CODES analytical facility, University of Tasmania. Analyses on oxygen isotope chemistry of iron oxides were conducted using laser fluorination method at the Department of Geoscience at the University of Wisconsin-Madison. A detailed description of the methodology is given by Huberty et al. (2010)

# 4 Controls on trace element and oxygen isotope distributions in iron oxides

## 4.1 Iron oxide species and paragenetic sequence

Mineral chemical data were generated for ore forming iron oxide species from twelve different deposits across the entire IQ. Results are compared at a depositional and regional scale.

At the depositional scale, the following trends are significant throughout the paragenetic sequences: The oldest analyzed iron oxide (e.g. at Esperança deposit) is a relict magnetite in a least-altered BIF. It contains considerable contents of Mg (40-910 ppm), Al (250-1200 ppm), Mn (40–60 ppm), Ti (50-400 ppm), Cr (3-12 ppm), V (10–60 ppm) and other transition metals < 7 ppm. Oxidised martite has slightly higher Mn, Al, Ni and Co and lower Cr, W and As contents relative to the paragenetically older relict magnetite. In most iron ore deposits, (e.g., Bau, Pico, Retiro, Usiminas and Aguas Claras), when comparing martite with later recrystallized granoblastic hematite, a remarkable Mg-, Mn- and Al-depletion and Ti-, Cr-, and V-enrichment in granoblastic hematite is documented (Fig. 2). The contents of other trace elements remain the same. A comparison of granoblastic hematite with younger platy hematite, however, shows no major changes in their chemical signature, e.g. enrichment/depletion of certain trace elements. A comparison of shear-zone hosted specularite (the youngest species) with earlier formed iron oxides, such as martite and granoblastic hematite shows that most of the elements (e.g. Mg, Mn, Cr, Pb, Ba, Sr, Y, LREE) are highly depleted in specularite.

Oxygen isotope analyses on BIF-hosted hematite ($\delta^{18}O$ = 7.0‰) obtained by Hoefs et al. (1982) and high-grade iron ore forming martite as subject of this study ($\delta^{18}O$ = -2.5‰, σ = 1.7, n=16) reveal a significant depletion in $^{18}O$ from the BIF-hosted hematite to ore-

hosted martite. Across the paragenetic sequence of the ore-forming hematite species, however, a shift towards higher $\delta^{18}O$ is recorded from the older (martite/granoblastic hematite) to the younger iron oxides (platy hematite/specularite) (Fig.2)
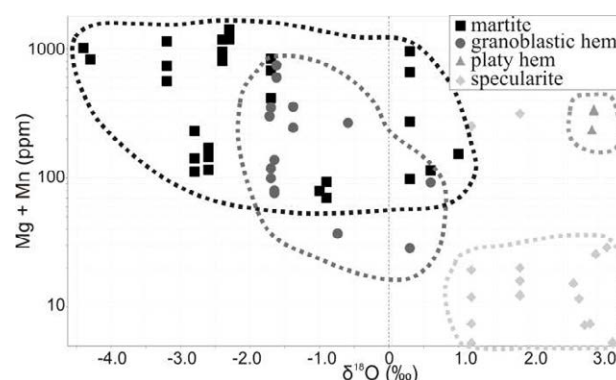


**Figure 2:** (Mg+Mn) vs $\delta^{18}O$ diagram showing trace element distribution through the paragenetic sequence of ore forming iron oxides (earliest to latest: martite to specularite. See the text for interpretation of data).

## 4.2 Host rock lithology

At a regional scale, iron oxide chemical data from the IQ were differentiated by their different host-rock lithology and tectonometamorphic setting with the following results: 1) when comparing one specific iron oxide species (e.g. martite) from different quartz BIF-hosted iron ore deposits (Corrégo de Feijão, Esperança, Jangada, Mutuca and Usiminas) with each other, minor and trace element chemistry are similar except for minor variances (>5 times enrichment/depletion) in Mg, Ni, Co and Cu, 2) the comparison of martite from the Cauê deposit with martite from other quartz-BIF hosted ore deposits, however, documents significant chemical differences, e.g. a strong depletion of Mg, Ni, Zn, Pb, Co, Cu, Sr and LREE, 3) the comparison of martite in dolomitic-BIF, with martite in quartz-BIF-hosted iron ore deposits (e.g. Águas Claras) shows, that the former is highly enriched in Mn, whereas the other trace element contents are similar (Fig. 3). There are no significant differences in oxygen isotope chemistry of the different iron oxides with respect to their host lithologies.
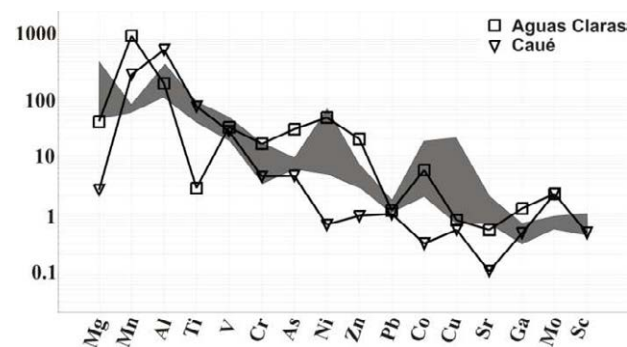


**Figure 3:** Multi-element diagram showing trace element contents of various martites across the IQ. Grey: element distribution in martite from Corrégo de Feijão (n=3), Esperança

(n=4), Jangada (n=6), Mutuca (n=10) and Usiminas (n=12) ore bodies. Rectangle: average element chemistry (n = 6) of martite from the dolomitic BIF-hosted ore of Aguas Claras with remarkable high Mn-contents. Triangle: average element chemistry (n=3) of martite of the Cauê ore deposit with significant differences in the Mg, Mn, Al, Ti, Ni, Pb, Co, Sr contents. The Cauê ore deposit also hosts a specularite-bearing "jacutinga"-style Au-Pd vein.

## 5 Interpretation of Iron Oxide Chemistry and its Implications for Iron Ore Genesis in the IQ

Regional variations in the chemistry of one specific iron oxide generation are mainly influenced by host lithology (e.g. dolomitic vs. quartz BIF), surrounding country rock and geological setting. The remobilization of Mn during decarbonatization of primary, Mn-rich dolomites results in high Mn-contents of the dolomitic BIF-hosted high-grade iron ore deposits. Also, younger jacutinga-style mineralization, for example in the Cauê deposit may lead to a chemical overprint of previous high-grade iron ore and simultaneously the depletion of earlier iron oxides (e.g. martite) in most elements, such as Mg, Ni, Zn, Pb, Co, Cu, Sr and LREE.

During the formation of different iron oxide species, changes in the element chemistry are commonly consistent across the IQ and thus may fingerprint single mineralization events. Remarkable element changes are thereby documented during the oxidization of magnetite to martite and possibly upgrade of BIF to high-grade iron ore (>60% Fe). Oxygen isotope chemistry of hematite shows a strong depletion of $^{18}O$ from precursor BIF to high-grade iron ore, due to the involvement of meteoric water based on $\delta^{18}O$ in equilibrium with martite < 0 per mil @ w/r ratio > 0.1, T=145°C, calculated after Yapp (1990) and Taylor (1997).

Comparing different iron oxide species from granoblastic and platy hematite (different paragenetic stages), a consistent depletion in Mg, Mn and Al and REE, as well as a slight enrichment in Ti, Cr and V are recorded. Specularite is strongly depleted in most elements suggesting that large fluid volumes were involved in its formation. Low oxygen isotope ratios are best explained by meteoric water influx. However, a slight positive shift in $\delta^{18}O$ values from martite/granoblastic hematite to platy hematite/specularite suggests the involvement of modified, slightly heavier meteoric water and/or small volumes of isotopically heavy fluids, such as metamorphic or magmatic fluids.

## 6 Conclusion

Trace element and isotope chemistry of iron oxides from high-grade iron ore deposits across the IQ indicate, that in order to form large BIF-hosted high-grade iron ore deposits in the IQ, the following conditions need to be met: 1) the involvement of large fluid volumes, especially during the oxidization of magnetite to martite and further during the formation of specularite causing a significant change in the iron oxide chemistry, 2) a meteoric fluid source especially during the upgrade of BIF to high-grade iron ore resulting in a depletion of $^{18}O$ in hematite from BIF to high-grade ore. A shift towards higher $\delta^{18}O$ values recorded during the modification of the high-grade iron ore and the formation of platy hematite and specularite may be caused by the 1) involvement of large volumes of modified, slightly heavier meteoric water and/or 2) influence of small volumes of isotopically heavy metamorphic and/or magmatic water. These constraints on trace and isotope chemistry have implications for the exploration of concealed ore bodies by fingerprinting the trace element and oxygen isotope chemistry of different iron oxides and therefore generating "chemical" maps with chemical vectors towards possible high-grade iron ore bodies.

## References

Beukes NJ, Gutzmer J, Mukhopadhyay J (2003) The geology and genesis of high-grade hematite iron ore deposits. Applied Earth Science 112:18-25.

Dorr JVN (1965) Nature and origin of the high- grade hematite ores of Minas Gerais, Brazil. Economic Geology 60:1-46.

Dorr JVN (1969) Physiographic, stratigraphic and structural development of the Quadrilátero Ferrífero, Minas Gerais. U S Geological Survey Professional Paper 641-A:110.

Hoefs J, Müller G, Schuster AK (1982) Polymetamorphic relations in iron ores from the Iron Quadrangle, Brazil: The correlation of oxygen isotope variations with deformation history. Contributions to Mineralogy and Petrology 79:241-251.

Huberty JM, Kita NT, Kozdon R, Heck PR, Fournelle JH, Spicuzza MJ, Xu H, Valley JW (2010) Crystal orientation effects in δ18O for magnetite and hematite by SIMS. Chemical Geology 276:269-283.

Taylor D, Dalstra HJ, Harding AE, Broadbent GC, Barley ME (2001) Genesis of high-grade hematite orebodies of the Hamersley province, Western Australia. Economic Geology and the Bulletin of the Society of Economic Geologists 96:837-873.

Taylor HP (1997) Oxygen and hydrogen isotope relationships

in hydrothermal mineral deposits In: Barnes HL (ed) Geochemistry of Hydrothermal Ore Deposits. John Wiley and Sons, New York, pp 229-302.

Yapp CJ (1990) Oxygen isotopes in iron (III) oxides: 1. Mineral-water fractionation factors. Chemical Geology 85:329-335.

# Oxide mineralogy and magnetite chemistry of the Malmberget apatite iron ore, Northern Norrbotten, Sweden

Cecilia Lund and Olof Martinsson
*Division of Geosciences, Luleå University of Technology, 971 87 Luleå, Sweden*

**Abstract.** The Malmberget deposit has produced more than 600 Mt of ore and comprises several ore bodies that exhibit different mineralogical, chemical and structural features. In the eastern part, the ore bodies occur as massive lenses of magnetite surrounded by ore breccia, while the western part is characterized by hematite dominated ores. In contrast to most other apatite iron ores in Northern Norrbotten, the Malmberget deposit have been strongly affected by deformation, metamorphic recrystallization and felsic intrusions.

Variations in whole rock chemistry of the ores are mainly reflecting primary features with different signatures for massive ore and ore breccia, but also indicating different types of massive ore. Magnetite from ore breccia have low content of trace elements similar to magnetite from IOCG deposits and may have formed by hydrothermal processes while magnetite in massive ore show chemical characteristics typical for apatite iron ores.

The chemistry of magnetite has in various extents been modified due to element redistribution during metamorphic recrystallization and oxidation. Most significant is the preferential partition of Ti and to some extent V into porphyroblasts of hematite. The formation of ilmenite and rutile affects the chemistry of magnetite and gives it a lower content of Ti and V and a signature resembling magnetite from IOCG deposits.

**Keywords.** Apatite iron ore, magnetite, mineral chemistry, Malmberget, Northern Norrbotten

## 1 Introduction

The northern region of the Fennoscandian Shield, involving parts of Finland, Norway and Sweden, is an economically important metallogenic province dominated by Fe-oxide and Cu±Au deposits. Economically most important are the apatite iron ores and Sweden is the most important producer of iron ore in Europe with two large underground mines in Kiruna and Malmberget operated by LKAB. These two deposits have produced over 2000 million tons of crude ore and have a total iron ore reserve of 1010 Mt @ ~ 46 % Fe (LKAB, 2011).

In this study whole rock chemistry of ore, thin section petrography and micro probe analyses of minerals have been used to get a better understanding of the primary character of the ore and the importance of later overprinting events for texture and mineral chemistry of the oxide minerals. This information is of importance for the mineral processing of the ore and the quality of ore concentrates but has also genetic implications.

## 2 The Northern Norrbotten Ore Province

### 2.1 Regional geology

The geology of Northern Norrbotten includes a rift related Palaeoproterozoic Greenstone Belt (~2.3-2.0 Ga) and subduction related igneous and sedimentary rocks of the Svekokarelian Orogen (~1.9-1.8 Ga) deposited on an Archean basement. The most mineralized units are the Kiruna Greenstone Group, the Porphyrite Group and the Kiirunavaara Group with the apatite iron ores occurring in the two latter. The supracrustal rocks are intruded by several suites of mafic to felsic plutons with ages between 1.9 and 1.7 Ga and the bedrock is affected by two major events of deformation and metamorphism at 1.9 and 1.8 Ga, respectively (Bergman et al, 2001, Martinsson, 2004).

### 2.2 Apatite iron ores

Apatite iron ores is a common ore type in the northern part of Sweden (Fig. 1) but quite rare in other parts of the world and they were first described from the Kiruna area (Geijer, 1910). Since then the apatite iron ores have been a focus of genetic discussions with either a magmatic or a hydrothermal origin as the most supported models (Bergman et al., 2001). However, not all features of the apatite iron ores are easily explained with a single genetic model and a magmatic-hydrothermal process has been suggested to have formed these deposits in Northern Norrbotten at 1.88-1.89 Ga (Martinsson, 2004, 2009).

Apatite iron ores occur in intermediate to felsic volcanic rocks, are often tabular and concordant with their host rock and consist mainly of magnetite, hematite, apatite, and actinolite. Two major types of apatite iron ores can be distinguished in the Kiruna area, a breccia type and a stratiform-stratabound (massive) type (Bergman et al., 2001). Ore breccia is an irregular network of ore veins which to a varying extent accompany the massive ore (Geijer, 1910, 1931) but may also be the dominant character of some deposits.

The phosphour content in individual deposits is on average mostly 1-5 wt. % P but could be significantly lower in breccia type of deposits (0.03 to 0.9 wt. % P) and also show large variations in ores of massive character with either very low or high contents (Martinsson, 2003, 2004). Characteristic is the high vanadium content of magnetite while the titanium content is intermediate between that of magmatic and sedimentary iron deposits (Loberg and Horndahl, 1983).
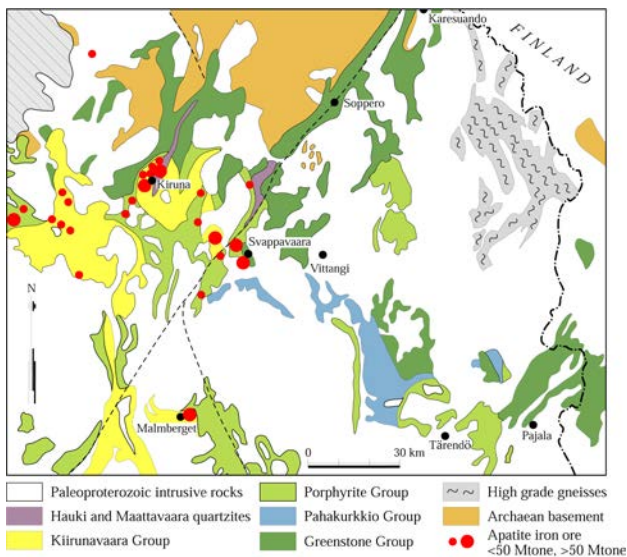
**Figure 1.** Occurrences of Apatite iron ores and simplified geological map of Northern Norrbotten. Modified from Martinsson (1995).



**Figure 2.** Geology of the Malmberget deposit, modified from Geijer (1930).

## 3 The Malmberget deposit

The Malmberget deposit consists of magnetite-hematite ore with 51–61 wt. % Fe and varying contents of phosphorus (Grip and Frietsch, 1973). At the end of 2011, approximately 612 Mt of crude ore have been produced in open pits and underground workings and the reserves were estimated to 279 Mt with 42 wt. % Fe (LKAB Annual report 2011). It is interpreted to have a similar origin as the Kiirunavaara deposit but it is more strongly affected by later metamorphism, deformation and intrusion of granitic rocks (Bergman et al., 2001).

### 3.1 Local geology

The Malmberget deposit includes several ore lenses that occupy a large-scale fold structure (Fig. 2). The ores are hosted by strongly metamorphosed and deformed rocks of felsic to mafic composition that traditionally have been called leptites (Geijer, 1930). A porphyritic texture is locally preserved in the felsic rocks and amygdules are occasionally encountered, suggesting a mainly extrusive origin and a character similar to that of rocks of the less metamorphosed Kiirunavaara Group (Martinsson and Hansson, 2004). Mafic rocks are mainly found adjacent to the ores as conformable to discordant lenses. Some of the mafic rocks are probably dykes, but most of them are suggested to have formed as sills or extrusions (Geijer, 1930).

### 3.2 Ore characteristics

More than 20 different tabular to stock shaped apatite iron ore bodies are known at Malmberget were the individual ore bodies stretches parallel to the fold axis, which plunge 40°-50° towards SSW (Bergman et al., 2001). The ore bodies are recrystallised, coarse grained, and intruded by several generations of felsic and mafic dykes (Martinsson and Virkkunen, 2004). The host rock to the ores is mainly
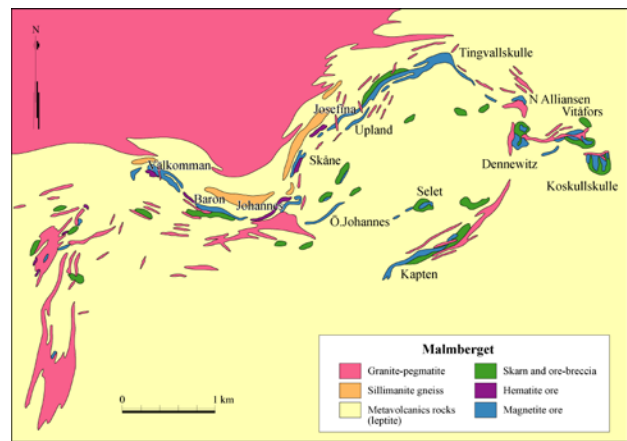
felsic in composition and often rich in albite. The mafic rocks are more common in the eastern part and usually rich in biotite and in some cases, display scapolite alteration.

In the western and northern parts of the deposit, the ores form an almost continuous horizon with a length of about 5 km. Apatite banding is a common feature of these ores, which contain both magnetite and hematite. In the eastern part deposits have a more massive character, consisting of magnetite with low contents of apatite. Locally the ores are strongly banded due to deformation and may contain boudinaged aplite and pegmatite dykes.

Brecciation at different scales is developed in the wall rocks to the ores. Especially ore bodies in the eastern part of the Malmberget area are surrounded by extensive brecciation. Magnetite, apatite, and amphibole are the main constituents of mm- to m wide veins that may develop into networks. Breccias with a high Fe-content are mainly found adjacent to the massive ores, while breccias dominated by amphibole are more distal (Geijer, 1930). In some areas veinlets-schlieren-patches of actinolite-pyroxene occur in a reddish-color feldspar-dominated rock and locally anhydrite is abundant together with various amounts of pyroxene-amphibole, magnetite and minor pyrite-chalcopyrite.

### 3.3 Mineralogy and textures of ore

The mineralogy of the Malmberget deposit exhibit variations both within and between the different ore bodies with different proportions of magnetite, hematite, apatite, amphibole-pyroxene and biotite. Accessory to minor constituents are mainly anhydrite, pyrite, chalcopyrite, and ilmenite.

Magnetite forms the major Fe-oxide mineral in the eastern part of Malmberget but is mostly a minor component in the western part. Magnetite also forms separate lenses close to hematite dominated ore bodies. Magnetite grains are mostly euhedral to subhudral and 0.2-1 mm in size. In massive ore the texture is mostly granoblastic with distinct triple junctions at grain boundaries (Fig. 3). Coarser-grained magnetite occurs as porphyroblasts or in vein like structures. Larger magnetite grains can have an elongated shape following the mineral lineation in the host rock.

In the western part of the Malmberget deposit hematite is the main mineral, occurring as euhedral to anhedral grains 0.2-2mm in size within hematite ore or as larger porphyroblasts (5-20mm) in magnetite ore. Textural relations indicate that several generation of hematite may occur. In the eastern part hematite occur in smaller amounts as single grains or along fractures, octahedral planes and grain surfaces of magnetite.

Ilmenite forms exolution lamella in magnetite but also as single grains (<1 mm) and smaller interstitial grain (0.1-0.2 mm) at grain boundaries of magnetite. Pyrite and chalcopyrite occur locally in small amounts disseminated and as veinlets in massive ore in the eastern part and more abundantly in ore breccia together with anhydrite and pyroxene-amphibole.

Apatite occurs interstitial to magnetite or as elongated grains aligned in the direction of host rock lineation. The apatite grain size is correlated to the grain size of coexisting magnetite and hematite. Amphibole (actinolite and tremolite) and diopside occur partly disseminated in massive ore but more commonly as patches and schlieren. These minerals are most abundant close to wall rock contacts and in ore breccia. Biotite is also most common in massive ore close to wall rock contacts and occur disseminated or in schliren. Anhydrite may occur disseminated or in patches or veins in massive ore but is most common in ore breccia in association with pyroxene-amphibole where it locally is the major constituent.
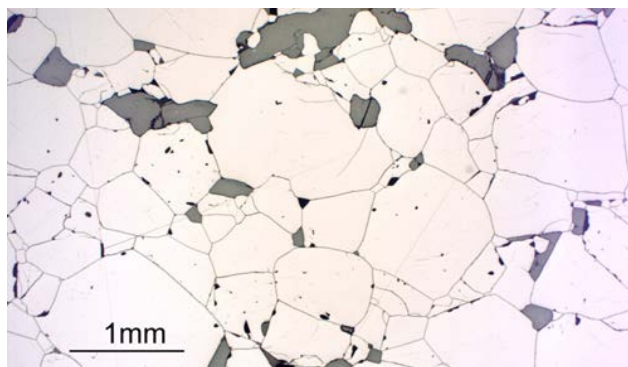


**Figure 3.** Recrystallized granoblastic magnetite ore with triple junctions.

### 3.4 Oxidation textures of ore

Magnetite may be partly to completely altered to hematite within the Malmberget deposit resulting in different kinds of oxidation textures shown by the Fe-Ti oxide minerals. Homogeneous magnetite, magnetite with intergrowths of Fe-Ti oxides (ilmenite, rutile and spinel) and oxidation assemblages of hematite and rutile occur. Magnetite may contain oriented ilmenite lamellas (trellis and sandwich) with a thickness of about 2 μm or exsolved spinel patches 50-200 μm in size. Rutile may be associated to magnetite that has largely been altered to hematite.

Single ilmenite grains occurring interstitial to magnetite contain in their central part exsolved hematite lenses, ranging between 4.5-270 μm in size. Euhedral grains of hematite have inclusions of 20-100 μm thick ilmenite lamellas or they may contain 10-50 μm large rutile needles exsolved at the rim of the grain.

### 3.5 Chemistry of ore

Whole rock chemical data of ore from the Malmberget deposit demonstrates a distinct difference between massive ore and ore breccia but also significant subgroups of massive ore. The main difference between massive ore and ore breccia is the higher content of Fe, P and V and the lower content of Si, Ca, Mg and S in massive ore. The massive ore could be divided into three subgroups based on the content of Fe, P, Ti, V, and Ga with a distinct group having high contents of Ti, V, and Ga and another group with high contents of P. The third group is more heterogeneous in character but show generally low contents of P, Ti, V, and Ga.

Mineral chemistry of magnetite mainly mimics the whole rock chemistry of ore with high content of Ti, V and Mg in magnetite from massive ore and low content of most analysed trace elements in magnetite from ore breccia (Fig. 4). This is also shown in massive ore with higher content of Ti and V in magnetite from ore richer in these elements.

However, the chemistry of magnetite is also controlled by the local oxide mineral assemblages including ilmenite, rutile and hematite. Magnetite in ore containing porphyroblasts of hematite has generally lower content of Ti and V, while the coexisting hematite is very rich in Ti (6-12 % $TiO_2$) and also high in V.
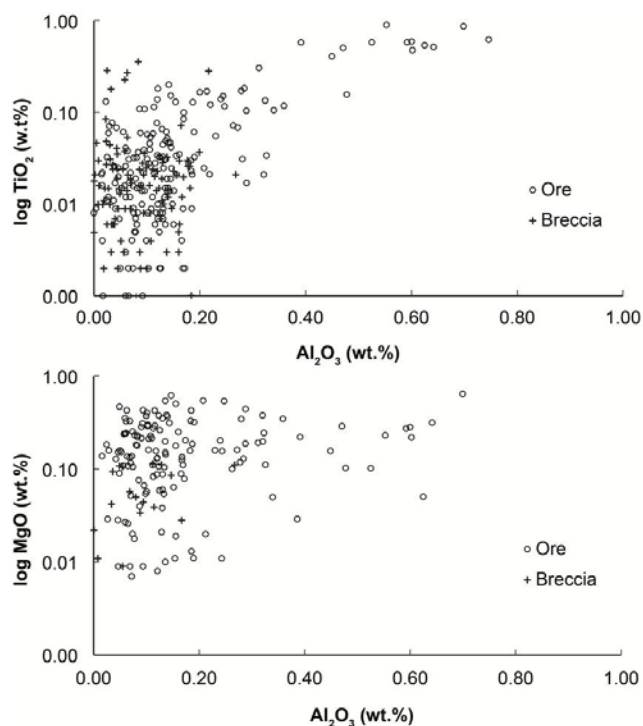


**Figure 4.** Mineral chemistry of magnetite from massive ore and ore breccia at the Fabian ore body.

## 4 Discussion

Magnetite chemistry and whole rock chemistry of ore shows significant differences within and between different ore bodies at Malmberget indicating a multiphase origin which is illustrated by Figure 5. The massive magnetite ore bodies in the eastern part (Viri, Fabian and Printzsköld) plot into the field of Porphyry-Cu or AIO, while the

breccia ore at Fabian and the Hens and Välkomman ore bodies from the western part of Malmberget plot into the the IOCG fields according to the classification by Dupuis and Beaudoin (2011).

The lower trace element composition of magnetite from ore breccia at Fabian compared to massive ore might indicate a formation at lower temperature and possibly a change from magmatic to hydrothermal conditions. A hydrothermal origin of the ore breccia is also supported by the abundance of anhydrite and elevated contents of pyrite and chalcopyrite as well as the textural and structural relation to the wall rocks. This transition from magmatic to hydrothermal ore forming processes has also been suggested for the Kiirunavaara deposit (Martinsson, 2004).

There are several chemically different massive ore types based on both whole rock chemistry and the chemistry of magnetite. At Kiirunavaara the ore is divided into two main types based on phosphorous content and in general they have sharp contacts to each other and are interpreted to have been formed by different injections of iron oxide magma (Grip & Frietsch, 1973; Martinsson, 2004). A similar process might also explain the occurrence of chemically different ore types at Malmberget, although the contacts are less distinct which could be a result of metamorphic recrystallization and deformation.
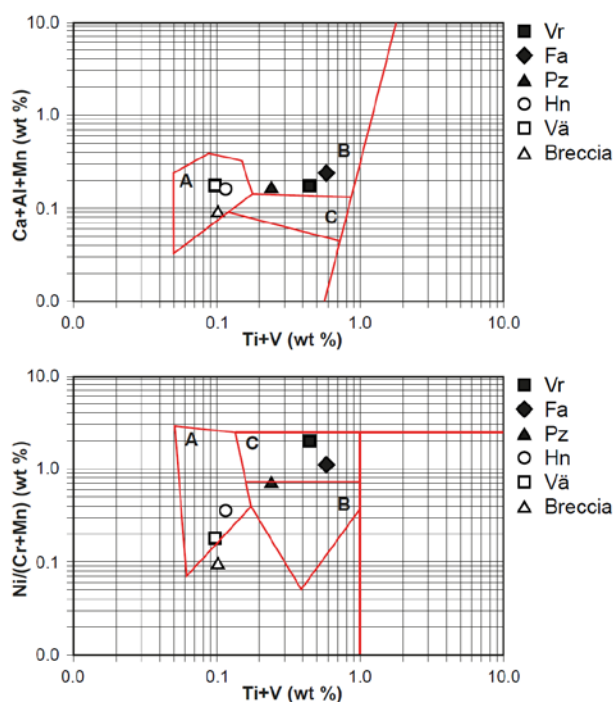


**Figure 5.** Discrimination diagrams for magnetite according to ore type (Dupuis and Beaudoin, 2011). Average composition of magnetite from various ore bodies at Malmberget. A = IOCG, B = porphyry Cu, C = AIO.

The effect of metamorphic overprinting and deformation are expressed by increased grain size of ore and gangue minerals, granoblastic magnetite texture with triple junction grain boundaries, porphyroblastic growth of hematite, mineral lineation, banding and stretching of ore bodies. Oxidation processes related to metamorphic and possibly hydrothermal overprinting related to granite-aplite-pegmatite intrusions have generated several different oxide mineral paragenesis including hematite, ilmenite and rutile.

Element redistribution between magnetite and associated metamorphic-hydrothermal oxide minerals have significantly affected the chemistry of magnetite with in general a loss of Ti and V. This is especially evident for magnetite coexisting with hematite porphyroblasts with a strong partition of Ti and a less pronounced partition of V into hematite. This gives the magnetite a chemical signature different to typical AIO deposits and the lower content of Ti and V generates a signature similar to IOCG deposits.

## Acknowledgements

## References

Bergman S., Kübler L., Martinsson O (2001) Description of regional geological and geophysical maps of northern Norrbotten County (east of the Caledonian orogen). Geol Surv Sweden, Ba 56, 110 p

Dupuis C, Beaudoin G (2011) Discriminant diagrams for iron oxide trace element fingerprinting of mineral deposit types. Min Dep 46:319-335.

Geijer P (1910) Igneous rocks and iron ores of Kiirunavaara, Luossavaara and Tuolluvaara. Ec Geol, 5:697–718.

Geijer P (1930) Geology of the Gällivare ore field. Geol Surv Sweden, Ca 22, 115 p (in Swedish with English summary)

Geijer P (1931) The iron ores of the Kiruna type. Geographical distribution, geological characters, and origin. Geol Surv Sweden, C 367, 39 p

Grip E, Frietsch R (1973) Ore deposits in Sweden 2, northern Sweden, Almqvist & Wiksell, 295 p (in Swedish)

LKAB (2011) Annual report 2011, 118 p

Loberg BEH, Horndahl A-K (1983) Ferride geochemistry of Swedish Precambrian iron ores. Min Dep, 18:487-504.

Martinsson O (1995) Greenstone and porphyry hosted ore deposits in northern Norrbotten. Unpublished report, NUTEK Project nr 92-00752P, Division of Applied Geology, Luleå University of Technology. 58 p

Martinsson O (2003) Characterisation of iron mineralisations of Kiruna type in the Kiruna area, northern Sweden. Proceedings of the Seventh Biennial SGA Conference "Mineral Exploration and Sustainable Development", Athens, Greece, 24-28 August 2003, 1087-1090.

Martinsson O (2004) Geology and metallogeny of the northern Norrbotten Fe-Cu-Au province. In: Allen RL, Martinsson O, Weihed P (eds), Svecofennian ore-forming environments: Volcanic-associated Zn-Cu-Au-Ag, intrusion associated Cu-Au, sediment-hosted Pb-Zn, and magnetite-apatite deposits in northern Sweden. Society of Economic Geologists, Guidebooks Series 33, 131–148

Martinsson O, Virkkunen R (2004) Field trip day six, Apatite iron ores in the Gällivare, Svappavaara and Jukkasjärvi areas. In: Allen RL, Martinsson O, Weihed P (eds), Svecofennian ore-forming environments: Volcanic-associated Zn-Cu-Au-Ag, intrusion associated Cu-Au, sediment-hosted Pb-Zn, and magnetite-apatite deposits in northern Sweden. Society of Economic Geologists, Guidebooks Series 33, 163-167.

Martinsson O (2009) The Narken Iron Oxide-(Cu) Deposits – A Link Between Kiruna-type Iron Ore and IOCG-style Mineralization. The 10th Biennial Meeting of The SGA, Townsville August 17 – 20, 2009, Abstract.

# Fingerprinting volcanogenic massive sulfide deposits using magnetite chemistry: application to till from Izok Lake, Nunavut, Canada

**S. Makvandi, G. Beaudoin, M. Ghasemzadeh-Barvarz**
*Université Laval, Québec, Québec, Canada, G1V 0A6*

**M.B. McClenaghan**
*Geological Survey of Canada, Ottawa, Canada, K1A 0E8*

**Abstract.** Magnetite is a useful indicator mineral for exploration because 1) its chemical composition is determined by the geological environment of formation; 2) It has widespread distribution in a variety of geological settings, and 3) It can be easily recovered from sample media. This study uses the chemistry of detrital magnetite to assess if magnetite can be related to different types of mineralization or hydrothermal alteration. At the Izok Lake District (ILD), magnetite from massive sulfide lenses, alteration zones, host rock, and till, both up- and down-ice flow, was sampled. The chemical composition of magnetite was measured by Electron Probe Micro Analysis (EPMA) and Laser Ablation-Inductively Coupled Plasma- Mass Spectrometry (LA-ICP-MS). Based on the results, the concentration of pathfinder elements (P, Pb, W, Sn, Cu, Mg, Co & Zn) increases in detrital magnetite with proximity to the ore zone, from the farthest till sample sites. Multivariate statistical methods were used to discriminate magnetite derived from different lithologies. Statistical analysis shows that magnetite from massive sulfides, hostrock gahnite-rich dacite, local gabbro, and iron formations can be distinguished using principal component analysis. Magnetite grains from till samples down-ice show similar chemical signature to that in the Izok Lake sulfide lenses and related alteration zones.

**Keywords:** Magnetite, Till Geochemistry, VMS deposit, Izok Lake, Statistics

## 1 Introduction

The cubic spinel structure of magnetite can incorporate a number of cations at minor or trace concentrations. Magnetite chemistry is sensitive to hydrothermal processes and provides a fingerprint of mineral deposit types. Dupuis and Beaudoin (2011) have outlined criteria to discriminate between different types of deposits based on magnetite chemistry. For example, they have offered a Ni+Cr vs. Si+Mg diagram to separate of Ni-Cu-PGE, and Cr deposits from other deposits types. Boutroy et al. (2012) used magnetite chemistry to discriminate between primary and secondary magnetite in Ni-Cu deposits. Magnetite and hematite from Iron Oxide Copper-Gold deposits (IOCG) and those from Iron Oxide-Apatite deposits (IOA) can also be chemically distinguished (Boutroy et al. 2012). Finally, magnetite chemistry has successfully been used to discriminate between different types of hydrothermal deposits (Nadoll et al. 2012). Changes in level of concentration of elements such as

Mg, Al, Ti, V, Co, Mn, Zn, and Ga in magnetite composition enabled Nadoll et al. (2012) to discriminate between Ag-Pb-Zn veins, porphyry Cu-Mo, and skarn deposits.

The present study documents the chemistry of sulfide deposit, country rock, and detrital magnetite from the Izok Lake Zn-Pb-Cu-Ag Volcanogenic Massive Sulfide (VMS) deposits, and investigates whether the composition of detrital magnetite can be used as exploration tool to trace VMS deposits under sediment cover.

## 2 Geological Setting

The Zn-Pb-Cu-Ag Izok Lake deposit (ILD) is an Archean bimodal-mafic volcanogenic massive sulfide deposit located at 65 °39'N, 112°49'W in the northern Slave structural province, Nunavut Territory, Canada. The volcanic and sedimentary rocks in the area have been folded, faulted and metamorphosed to the amphibolite grade.

In this study, magnetite grains recovered from massive sulfide lenses, iron formations, hostrock gahnite-rich dacite, and local gabbro have been analysed chemically to characterize magnetite in the deposit, in hostrocks, and in country rocks as a background. Petrographic studies (Hicken, 2012) demonstrate that the massive sulfides consist of pyrite (40 to 50%) + sphalerite (40%) ± actinolite (10%) + magnetite (5 to 10%) ± muscovite (5%) ± chalcopyrite and galena (tr.). Iron formations are composed of almandine garnet (60%) + biotite (10%) + quartz (10%) + hornblende (10%) + magnetite (10%). Dacite is composed of plagioclase (25%) + gahnite (20%) + sillimanite (15%) + quartz (10%) + magnetite (10%) + pyrite (10%) + biotite (5%) + chalcopyrite (3%) + pyrrhotite (2%). Gahnite rich dacite is located at the margins of, or within, the sulfide stringer zone. Gabbro consists of hornblende (40%) + plagioclase (40%) + biotite (10%) + quartz (5%) + magnetite (5%) + pyrite (tr.). From the 85 till samples collected from the ILD, magnetite grains from 7 samples have been investigated in this study (Figure 1).

## 3 Methodology

**Sample preparation:** massive sulfides, iron formations, hostrock gahnite-rich dacite, and local gabbro bedrock samples were disaggregated using a custom-built CNT

Spark-2 electric pulse disaggregator (EPD). Liberated minerals were placed on a shaking table to separate the heavy and light minerals. Heavy minerals were further concentrated using heavy liquids (specific gravity of 3.2). The ferromagnetic fraction was removed from the heavy minerals concentrates using a hand magnet. Recovery of ferromagnetic fractions from till samples follows the same procedure as rock samples except for the disaggregation stage.
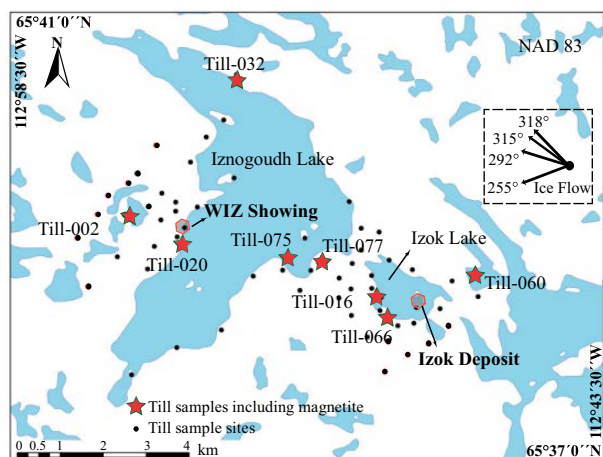


**Figure 1.** The location of till samples at the Izok Lake District (Modified from Hicken 2012). The 4 separate directions of ice-flow in this area are shown by arrows.

**Chemical analytical methods**. A total of 423 magnetite grains from the rocks and till samples were analysed for major, minor, and selected trace elements (including Al, Si, Ti, Mg, Mn, Cr, V, Cu, Zn, Sn) using the EPMA at Université Laval. Eighty-seven of these grains were also analysed by LA-ICP-MS at UQAC the measure trace element concentrations at the tens ppm to ppb level. For analysis by EMPA, grains were analysed in spot mode (10 μm) to avoid zones of alteration, inclusions, and exsolution. Analysis by LA-ICP-MS was performed using a beam size of 20 μm, a laser frequency of 10 Hz and a power of 0.3 mJ/pulse to ablate a line across magnetite grains for 60 s, after a gas blank of 30 s. The line mode was used to analyse magnetite and exsolution products (e.g., ilmenite, ulvöspinel) to obtain the composition of precursor magnetite.

**Multivariate statistical methods.** Analysis by EMPA and LA-ICP-MS produces a large dataset of compositions for of trace elements. In the case of many variables (chemical elements), statistical multivariate tools, mainly Principal Component Analysis (PCA) is used to detect correlations among parameters, and to describe the geological complexity. Using PCA, the maximum variations among different groups are detected and used to discriminate between samples. The relationship between observations is shown graphically as principal components (PC) score plots (e.g. t1, t2), samples with the same chemical features are grouped together. PC loading plots describes the relationship between variables. Principal Component loadings (e.g. PC1, PC2) are correlation coefficients between the PC scores and the original variables. PC scores are the derived composite scores computed for each observation

based on the eigenvectors for each PC. PC loadings introduce the responsible variables for sample classification in score plots. Variables contributing similar information are grouped together graphically in loading plots. Grouped elements are positively correlated, whereas variables on opposite sides of the plot origin, in diagonally opposed quadrants, are negatively correlated. The distance to the origin provides an arbitrary measure of the impact of the variables on samples classification.

## 4  Chemistry of magnetite at Izok Lake

The chemistry of magnetite has been applied to discriminate between different lithologies at the ILD. Figure 2 illustrates the average composition of magnetite grains for each lithology that are normalized to the bulk composition of continental crust (Rudnick et al. 2003). Magnetite from massive sulfides includes high concentrations of P, Pb, Ge, W, Sn, Mn, Mg, Cu, Co and Zn. The Izok Lake MS magnetite is enriched in W whereas the amount of this element in the other lithologies has been beneath the detection limit. Magnetite from dacites is enriched in Ge, Sn, Ga, Mn, Zn and Ni, however, magnetite from gabbro samples is characterized by higher contents of V and Cr. Gabbro is considerably enriched in V, though, in other lithologies magnetite is depleted in this element. Elevated contents of Cu, Mg, and Ti also characterize magnetite from iron formations.
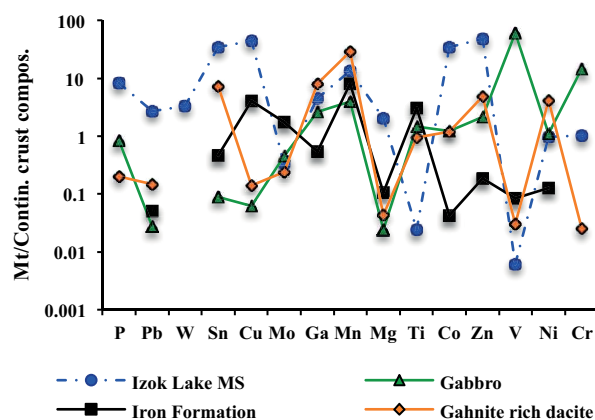


**Figure 2.** A spider diagram showing element concentrations in magnetite from four different lithologies. Magnetite composition measured by LA-ICP-MS and normalized to the bulk composition of continental crust (from Rudnick 2003).

The chemical data shows that till at the ILD has been eroded from different bedrock sources, and at each sample site there are magnetite grains having chemical composition similar to magnetite in the Izok Lake MS or related alteration zones. Some magnetite grains have a chemical signature suggesting they are derived from gabbro or other country rocks in the area, though, there are grains that cannot be categorized chemically with magnetite from the local rocks. Figure 3 shows that a high proportion of magnetite grains from sample Till-002 (7 km down-ice from the deposit) follow the chemical pattern of magnetite in gahnite rich dacite.
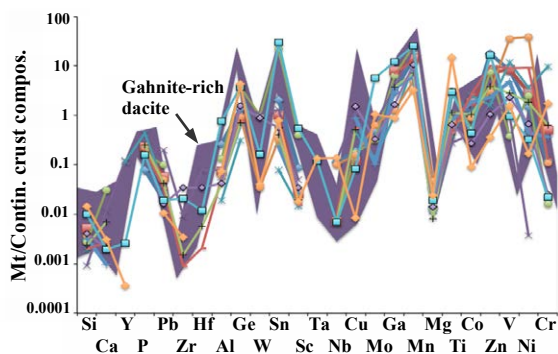
**Figure 3.** A spider diagram showing element concentrations in magnetite normalized to the continental crust composition, from Till-002. Till magnetite follows the chemical pattern of magnetite in gahnite- rich dacite (dark grey background field).

# 5 Statistical analysis of magnetite chemical data

Magnetite chemical data were analysed using PCA to reveal underlying relationship between elements and their impact on discrimination of different populations. Figure 4 shows PC loadings and Figure 5 is the PC score plot showing clusters, patterns and elements of interest within the Izok Lake magnetite dataset. In Figure 5 samples from different lithologies, including massive sulfides, gabbro, dacite and iron formations, form different clusters.

Magnesium, Cu, and V and Cr are coupled in PC loading plot (Fig. 4). A comparison between the loading and score plots (Figs. 4 and 5) shows that Mg and Cu are the principal components that can distinguish between magnetite in massive sulfides and magnetite from the three other bedrock lithologies. The gabbro magnetite forms a distinct population (Fig. 5) due to higher Cr and V concentrations (Fig. 4). Cr and V are positively correlated to each other and negatively correlated to Cu and Mg.
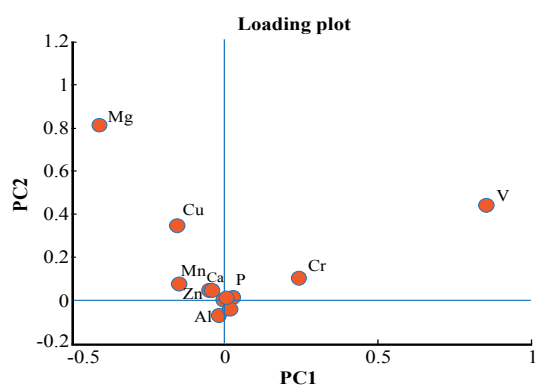


**Figure 4.** The PC loading plot showing Mg, Cu, V, and Cr are the principal components, and have highest impacts on samples classification. The elements situated near the plot origin (e.g. Mn, Al, Zn, Ca & P) have lower impact on this classification.

The statistical results make it possible to geochemically discriminate between at least 2 types of magnetite at the ILD: 1) Mg-Cu rich, and 2) V-Cr rich

magnetite. Vanadium-Cu rich magnetite is a magmatic-generated magnetite that is present in gabbro, whereas, Mg-Cu rich magnetite is a hydrothermally formed magnetite present in massive sulfides. These two types of magnetite are also distinguishable petrographically. In gabbro, magnetite is the most common disseminated opaque mineral and forms euhedral, fine- grained crystals, generally in association with ferromagnesian minerals such as biotite and or hornblende. However, in massive sulfides, magnetite is medium-grained generally in association with sulfide minerals (e.g. sphalerite, pyrite, chalcopyrite). The petrographic evidence shows that magnetite forms as a replacement of pyrrhotite and chalcopyrite. Sulfide and silicate inclusions are often observed in massive sulfide magnetite.

As shown in loading plot (Fig. 4), certain elements such as Mn, Ca, Al, and Zn characterize variance iron formation and dacite samples in score plot (Fig. 5). Figure 5 illustrates how till samples are distributed between rock types and shows that till magnetite retains chemical fingerprintes of magnetite from host lithologies. Detrital magnetite can be grouped with massive sulfides, gahnite rich dacite, and iron formations. There is a gap between till magnetite and magnetite in gabbro. The chemical patterns observed in Figure 5 demonstrate that detrital magnetite at the ILD is mostly derived from the deposit and its country rocks.

# 6 Detrital magnetite chemistry; secondary geochemical dispersion patterns

Resistance to chemical weathering and mechanical abrasion during transport allows magnetite to survive and retain its chemical composition after long distance journey (Anand and Gilkes 1984). Thus, detrital magnetite has the potential to record widespread secondary dispersion haloes around ore deposits. The identification of these dispersion haloes can be used as a vector toward mineralization. Glacial dispersal of magnetite derived from the Izok Lake deposit and related alteration zones has created such a secondary dispersion halo around this deposit. At the ILD, the chemistry of magnetite in till samples changes with proximity to the deposit. The medians for some pathfinder elements such as Cu and Co for each till sample have been calculated (Fig. 6). Figure 6 shows the trend of variations for given elements are ascending with decrease in distance from the deposit location. At a regional scale, till geochemistry revealed that outside of the Izok Lake area, concentrations of pathfinder elements such as Zn and Cu in the till matrix are low, and elevated values are only obtained at the ILD (Hicken 2012).

# 7 Discrimination of different deposit types applying magnetite chemistry

To assess the potential of magnetite chemistry as an exploration tool in discrimination of deposit types, the chemical composition of magnetite from Izok Lake massive sulfides has been compered with that of some other types of deposit (Nadoll et al. 2012). The most important trace elements in hydrothermal magnetite are

Mg, Al, Ti, V, Co, Mn, Zn, and Ga. Figure 7 shows that how it is possible to discriminate between mineral deposits based on the composition of these elements in magnetite. Magnetite from each mineral deposit is enriched in those elements that are characteristics of this type of deposits, as the Izok Lake magnetite, representative of a metamorphosed VMS deposit shows higher in Co and Zn contents. However, the Mg-skarn magnetite contains higher content of Mg. Among elements applied in this diagram, vanadium seems to be the most efficient element in separation of different types of deposits. The Izok Lake magnetite shows a relative depletion in this element that may be related to V depletion in hypogene hydrothermal fluids.
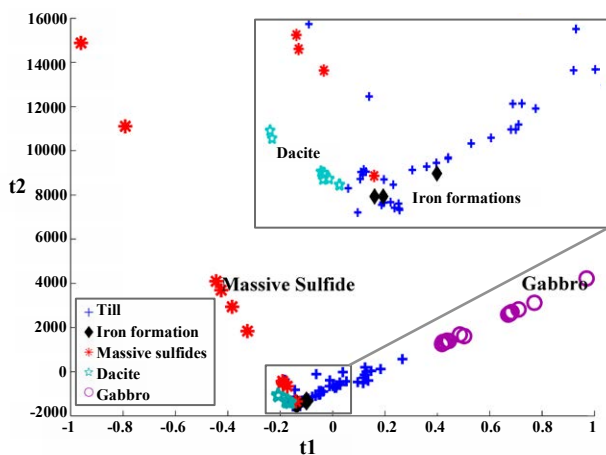


**Figure 5.** The PC score plot allows for classification of the different lithologies based on magnetite chemistry. Till magnetite grains are distributed among rock-derived magnetite grains. The enlargement shows that iron formation and dacite samples form discrete populations.
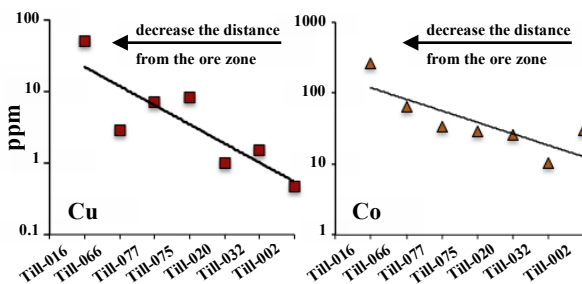


**Figure 6.** The trends of variations in Cu and Co contents in magnetite in different till samples. With proximity to the ore zone, the amounts of these elements increase.

## 8  Concluding Remarks

These results show that magnetite has great potential to be used as a vector toward mineralization because it preserves the chemical fingerprint of a variety of geological settings. Magnetite incorporates pathfinder elements of a deposit during formation, and retains these elements despite secondary transport and deposition. Thus, magnetite can produce widespread secondary dispersion halos around an ore deposit and, if detected, can aid in prospecting. Multivariate statistical methods

facilitate understanding of the relationships between multiple variables from large datasets and suggest which elements may be useful pathfinders for different lithologies, and or mineral deposits. The results of this study of geochemistry of magnetite around a known VMS deposit will aid in the design of VMS exploration programs in glaciated terrain around the world.
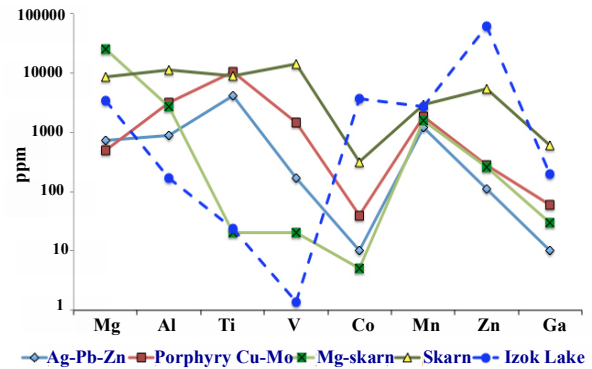


**Figure 7.** A comparison between element concentrations in magnetite from the Izok Lake VMS deposit and four other types of deposits (data from Nadoll et al 2012).

## 9  Acknowledgements

## 10  References

Anand RR, Gilkes RJ (1984) Mineralogical and chemical properties of weathered magnetite grains from lateritic saprolite. Journal of soil science 35: 559-567.

outroy E, Beaudoin G, Barnes SJ, Corriveau L (2012) Minor and trace element composition of iron oxides from IOCG deposits worldwide and its application to mineral exploration, Goldschmidt 2012, Montreal.

Boutroy E, Dare SAS, Beaudoin G, Barnes SJ (2012) Minor and trace element composition of magnetite from Ni-Cu deposits worldwide and its application to mineral exploration. GAC-MAC 2012, St- John's, NL, Canada.

Dupuis C, Beaudoin G (2011) Discriminant diagrams for iron oxide trace element fingerprinting of mineral deposit types. Miner. Deposita 46 (4): 319-335.Hicken AK (2012) Glacial dispersal of indicator minerals from the Izok Lake Zn-Pb-Ag VMS deposit, Nunavut, Canada. MSc thesis, Department of Geological Sciences and Geological Engineering, Queen's University, Canada.

Morrison IR (2004) Geology of the Izok Massive Sulfide Deposit, Nunavut Territory, Canada. Explor Mining Geol 13: 25-36.

Nadoll P, Mauk JL, Hayes TS, Koenig AE, Box SE (2012) Geochemistry of magnetite from hydrothermal ore deposits and host rocks of the Mesoproterozoic Belt Supergroup, United States. Economic Geology 107: 1275-1292.

Nadoll P, Mauk JL, Leveille R, Fisher L, Hough R (2012) Magnetite- An indicator mineral for hydrothermal ore deposits, Goldshmidt. 2012, Montreal, Canada.

Rudnick RL, Gao S, Holland HD, Turekian KK (2003) Composition of the Continental Crust, in Treatise on Geochemistry. Treatise on Geochemistry 3: 1-64.

# Mineral inclusions in magnetite as a guide to exploration – preliminary results

Patrick Nadoll

*CSIRO Earth Science and Resource Engineering, Minerals Down Under Flagship, Perth, Western Australia*

**Abstract.** Mineral inclusions are a common feature in magnetite and can be used to discriminate between barren and mineralized host rocks. Common inclusion types from barren host rocks include silicate phases (e.g. feldspars, mica, sericite, chlorite), apatite, zircon, and rutile reflecting the host rock's mineral assemblage. Magnetite in mineralized rocks often has inclusions of minerals that are directly associated with mineralization such as sulphides or other ore-related mineral phases. Chalcopyrite and pyrite inclusions in magnetite are indicative of porphyry-style sulphide mineralization from porphyry Cu (Mo) and associated skarn deposits in the western United States.

Mineral inclusions in magnetite can be preserved through a range of geologic processes that would otherwise breakdown or alter the included mineral phase. In combination with minor and trace element compositions of the host grains, inclusions can provide useful genetic information and be a powerful asset for exploration using heavy mineral concentrates.

**Keywords. Magnetite, Mineral Inclusions, Indicator Minerals, Exploration**

## 1 Mineral inclusions in magnetite

Mineral inclusions of varying compositions are often observed in oxide minerals such as magnetite. Their mineralogy can give insights into formation-, cooling-, and alteration conditions of the parent mineral and their host rock. Furthermore, mineral inclusions can be preserved within magnetite grains even if the prevailing geochemical environment changes. Mineral and melt inclusions can also help to elucidate complex formation relationships of ore bearing phases and their implications for ore genesis (Godel et al. 2010; Audetat and Pettke 2006; Pollard and Taylor 2002). However, studies that highlight the significance of mineral inclusions and the implications of their mineralogy from an exploration perspective are rather scarce (e.g. Bau and Alexander 2009; Bhattacharya et al. 2007; McLemore et al. 1999; McClenaghan 2005).

A number of elements that commonly occur in solid solution in magnetite such as Ti, V, Mg etc. can also be found in many mineral inclusions at high concentrations (Nadoll and Koenig 2011). Other elements that are more incompatible in magnetite such as Na, Ca, S, Cu, REEs, are typically present in inclusions and can be used to screen data for contaminated analyses (Nadoll et al. 2012). A sound understanding of the mineralogical and petrographic context often allows a first order discrimination among elements that are likely to be incorporated into magnetite and elements that can be attributed to mineral inclusions. For example, inclusions of matrix minerals in magnetite have been described as

a major challenge for magnetite (U-Th)/He dating because U and Th are orders of magnitude more abundant in many common matrix minerals such as apatite and can therefore impede data reliability (Duan et al. 2012). Mineral inclusions in magnetite can also negatively affect electron microprobe and laser ablation ICP-MS-analyses (Nadoll and Koenig 2011).

The main motivation behind this study is to determine if inclusion type and abundance differ systematically between mineralized (hydrothermally altered) and barren host rocks and to assess the suitability of mineral inclusions in magnetite as a first principle tool for exploration. The combination of characteristic minor and trace element signatures of the host grains and their inclusion mineralogy have the potential to discriminate magnetite from different environments and provide vectors towards mineralized areas. As part of this ongoing research we use back-scattered electron/multi-element imaging with a field emission gun scanning electron microscope and laser ablation ICP-MS to illustrate the abundance and variety of mineral inclusions in magnetite from various host rocks and hydrothermal ore deposits (Figure 1).



**Figure 1.** (A) Extent of the metasedimentary Belt Supergroup in the north-western United States. (B) Locations of some important porphyry Cu (Mo) and associated skarn deposits within the Laramide Arc in the south-western United States (modified after Nadoll 2011).

## 2 Inclusions in magnetite from barren and mineralized rocks

The mineralogy of mineral inclusions in magnetite is inevitably a reflection of the surrounding mineral assemblage. For un-mineralized host rocks this includes the whole range of silicates, carbonates, phosphates, oxides, and accessory minerals.

**Table 1.** Petrographic characteristics of hydrothermal magnetite from a number of porphyry Cu (Mo) and associated skarn deposits of the south-western United States (Figure 1B). Visible sulphide inclusions could be observed in all samples. Sulphide inclusion abundance: scarce – only some grains have mineral inclusions (< 10% of the polished grain surface for individual grains), moderate – most grains have inclusions (< 20% of the polished grain surface for individual grains), abundant – all grains have inclusions (>20% of the polished grain surface for individual grains).

| Sample | Deposit | Host Rock | Grain Size | Martite | Habit | Sulfide inclusions* |
|---|---|---|---|---|---|---|
| 1052 | Chino | granodiorite | 200 to 500 μm | abundant | subhedral | scarce to moderate |
| 1060 | Chino | quartzite | 200 to 500 μm | moderate | subhedral | moderate |
| 1003 | Chino | skarn | 200 to 500 μm | none | subhedral | scarce to moderate |
| 1009 | Chino | skarn | < 200 μm | none | anhedral | scarce to moderate |
| 1013 | Chino | skarn | > 500 μm | none | subhedral | scarce to moderate |
| 1019 | Chino | skarn | 200 to 500 μm | moderate | subhedral | moderate |
| 1054 | Chino | skarn | < 200 μm | moderate | subhedral | moderate |
| 1074 | Chino | skarn | 200 to 500 μm | none | subhedral | scarce to moderate |
| 1039 | Cobre | hornfels | 200 to 500 μm | none | subhedral | scarce to moderate |
| 1042 | Cobre | skarn | 200 to 500 μm | none | subhedral | scarce to moderate |
| 1047 | Cobre | skarn | 200 to 500 μm | none | anhedral | moderate |
| 1028 | Copper Flat | skarn | 200 to 500 μm | abundant | subhedral | moderate |
| 10161 | Morenci, Morenci | diabase | 200 to 500 μm | moderate | subhedral | scarce to moderate |
| 10162 | Morenci, Morenci | diabase | 200 to 500 μm | moderate | subhedral | moderate |
| 10166 | Morenci, Producer | diorite | 200 to 500 μm | moderate | subhedral | scarce to moderate |
| 10168 | Morenci, Shannon | skarn | 200 to 500 μm | none | subhedral | moderate |
| 10155 | Morenci, Sun Ridge | granite | < 200 μm | moderate | subhedral | moderate |
| 10159 | Morenci, Sun Ridge | granite | 200 to 500 μm | abundant | anhedral | scarce to moderate |
| 10111 | Safford, Dos Pobres | andesite | < 200 μm | moderate | subhedral | moderate |
| 10106 | Safford, Dos Pobres | andesite | < 200 μm | moderate | subhedral | scarce to moderate |
| 10120 | Safford, Dos Pobres | granodiorite | 200 to 500 μm | none | subhedral | scarce to moderate |
| 1086 | Safford, Lone Star | andesite | 200 to 500 μm | moderate | subhedral | abundant |
| 1091 | Safford, Lone Star | andesite | 200 to 500 μm | abundant | anhedral | scarce to moderate |
| 1096 | Safford, Lone Star | andesite | 200 to 500 μm | abundant | anhedral | moderate |
| 10134 | Safford, San Juan | andesite | 200 to 500 μm | moderate | subhedral | moderate |
| 10135 | Safford, San Juan | andesite | 200 to 500 μm | none | subhedral | scarce to moderate |

\* μm-scale inclusions visible under the microscope
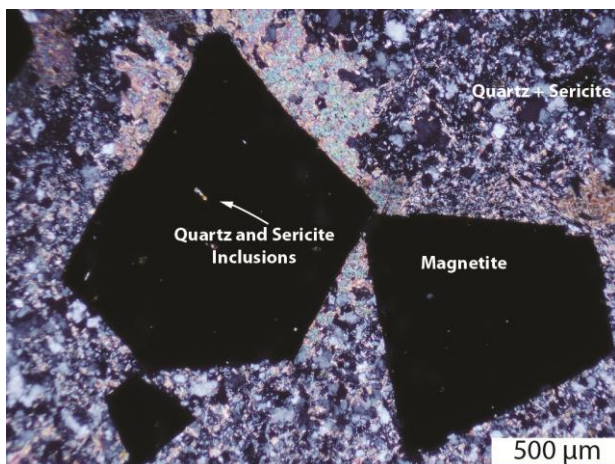


**Figure 2.** Magnetite formed by burial metamorphism in un-mineralized siliciclastic metasediments of the Belt Supergroup (Figure 1A). Silicate inclusions are common features in sub- to euhedral metamorphic magnetite grains.

For example, magnetites from barren metasedimentary host rocks in the Belt Supergroup of the northern United States (Figure 1A) show a range of mineral inclusions that reflect the mineral assemblage of their host rocks, including silicates (e.g. feldspars, mica, sericite, chlorite), apatite, zircon, and rutile (Figure 2). Similar observations have been made for magnetite from various other un-mineralized igneous and metamorphic rocks.

Table 1 lists petrographic characteristics for hydrothermal magnetites from porphyry Cu-(Mo) and skarn deposits of the south-western United States. Irrespective of host rock composition, grain size, degree of martitization, and habit, magnetite associated with these sulphidic hydrothermal ore deposits contains indicative sulphide inclusions that are discernible under the microscope. Additionally, mineral inclusions ranging from 10s of microns to sub-micron size, including silicates, apatite, and zircon, can be found in magnetite from barren and mineralized host rocks.
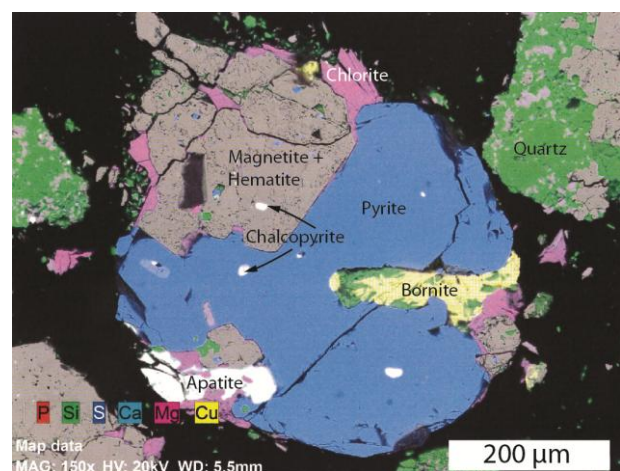


**Figure 3.** False-color field emission gun scanning electron microscope image of hydrothermal magnetite from the Chino (Santa Rita) porphyry Cu deposit in New Mexico, USA. Sulphide inclusions are indicative of the mineralized zone. Gangue minerals such as quartz and apatite are also present as minerals inclusions in magnetite.

A hydrothermal magnetite grain from the Santa Rita (Chino) porphyry Cu deposit in New Mexico is shown in Figure 3. It displays the close spatial association of

Cu-(Fe) sulphides such as chalcopyrite and pyrite and hydrothermal magnetite, which is partly altered to hematite. The composition map in Figure 3 illustrates the complexity of intergrown mineral phases and inclusions that pose a challenge to electron microprobe and laser ablation ICP-MS analysis (Nadoll and Koenig 2011). At the same time, the inclusion mineralogy, including phases such as pyrite and chalcopyrite, is indicative for hydrothermal sulphide mineralization. Inclusions of other matrix minerals such as silicates and apatite are also abundant but not a distinctive feature of mineralized host rocks. Pyrite, chalcopyrite, and other indicative minerals can be preserved as nm to μm-scale inclusions in magnetite through weathering, transport, and re-deposition. As detrital grains or part of in situ regolith magnetites that contain indicative mineral inclusions can point to mineralized host rocks in their source area or zone even if most or all of the contextual petrographic information that normally can be used to characterize mineralization is removed.

## Concluding remarks

Magnetite is an important resistate mineral. Its minor and trace element characteristics have been investigated by a number of workers (e.g. Dupuis and Beaudoin 2011; Nadoll et al. 2012); however, the range of mineral inclusions found in magnetite has not previously been studied in detail from an exploration perspective.

Silicates, apatite, zircon, and rutile are common mineral inclusions in magnetite from barren and mineralized host rocks, whereas sulphide inclusions are restricted to and indicative of mineralized host rocks.

As enclosed relicts, mineral inclusions can be preserved within magnetite grains even if the prevailing $fO_2/fS_2$ or other geochemical conditions change and become unfavourable. Consequently magnetite in regolith or stream sediments has the potential to assist exploration geologists to target prospective areas.

Ongoing research is looking at mineral inclusions in magnetite from a range of hydrothermal ore deposits and their barren host rocks to broaden the database and to confirm that prospective areas show an indicative mineral inclusion assemblage in these indicator minerals. Furthermore, recent analytical advances have led to the onset of microscale X-ray computed tomography of geological samples which give insights into the three-dimensional distribution, texture, size and orientation of mineral inclusions (e.g., Godel et al. 2012).

## Acknowledgements

## References

Audetat A, Pettke T (2006) Evolution of a porphyry-Cu mineralized magma system at Santa Rita, New Mexico (USA). Journal of Petrology 47:2021-2046.

Bau M, Alexander BW (2009) Distribution of high field strength elements (Y, Zr, REE, Hf, Ta, Th, U) in adjacent magnetite and chert bands and in reference standards FeR-3 and FeR-4 from the Temagami iron-formation, Canada, and the redox level of the Neoarchean ocean. Precambrian Research 174:337-346.

Bhattacharya HN, Chakrabortym I, Ghosh KK (2007) Geochemistry of some banded iron-formations of the archean supracrustals, Jharkhand–Orissa region, India. J Earth Syst Sci 116:245–259.

Duan C, Li YH, Yuan SD, Hu MY, Zhao LH, Chen XD, Zhang C, Liu JL (2012) Geochemical characteristics of magnetite from Washan iron deposit in Ningwu ore district and its constraints on ore-forming. Acta Petrologica Sinica 28:243-257.

Dupuis C, Beaudoin G (2011) Discriminant diagrams for iron oxide trace element fingerprinting of mineral deposit types. Mineralium Deposita 46:319-335.

Godel B, Barnes SJ, Barnes S-J, Maier WD (2010) Platinum ore in 3D: Insights from high-resolution X-ray computed tomography. Geology 38:1127-1130.

Godel B, González-Álvarez I, Barnes SJ, Barnes S-J, Parker P, Day J (2012) Sulfides and Sulfarsenides from the Rosie Nickel Prospect, Duketon Greenstone Belt, Western Australia. Economic Geology 107:275-294.

McClenaghan MB (2005) Indicator mineral methods in mineral exploration. Geochemistry: Exploration, Environment, Analysis 5:233-245.

McLemore VT, Munroe EA, Heizler MT, McKee C (1999) Geochemistry of the Copper Flat porphyry and associated deposits in the Hillsboro mining district, Sierra County, New Mexico, USA. Journal of Geochemical Exploration 67:167-189.

Nadoll P (2011) Geochemistry of Magnetite from Hydrothermal Ore Deposits and Host Rocks - Case Studies from the Proterozoic Belt Supergroup, Cu-Mo-porphyry + Skarn and Climax-Mo Deposits in the Western United States School of Environment. University of Auckland, pp 614.

Nadoll P, Koenig AE (2011) LA-ICP-MS of magnetite: methods and reference materials. Journal of Analytical Atomic Spectrometry 26:1872-1877.

Nadoll P, Mauk JL, Hayes TS, Koenig AE, Box SE (2012) Geochemistry of Magnetite from Hydrothermal Ore Deposits and Host Rocks of the Mesoproterozoic Belt Supergroup, United States. Economic Geology 107:1275-1292.

Pollard P, Taylor R (2002) Paragenesis of the Grasberg Cu–Au deposit, Irian Jaya, Indonesia: results from logging section 13. Mineralium Deposita 37:117-136.

# Martitisation: magnetite–hematite transformation and its origin and implications for industrial beneficiation through magnetic separation

**Beate Orberger**
*Université Parus Sud XI-ERAMET RESEARCH, 1 Avenue Albert Einstein, 78190 Trappes, France;*
*beate.orberger@erametgroup.com;*

**Alina Tudryn**
*Université Paris Sud XI, CNRS-UMR IDES 8148, Bât. 504, 91405 Orsay Cedex, France.*

**Christiane Wagner**
*UPMC, Univ Paris 06, ISTeP, CNRS, UMR 7193, 4 Place Jussieu, F-75005, Paris, France*

**Richard Wirth**
*GeoForschungsZentrum Potsdam (GFZ), Department 4, Telegrafenberg, 14482 Potsdam, Germany*

**Jose Domingo Fabris**
*Universidade Federal dos Vales do Jequitinhonha e Mucuri, 39100-00 Diamantina, Minas Gerais, Brazil*

**Jean Marc Greneche**
*LUNAM, Université du Maine, Institut des Molécules et Matériaux du Mans, IMMM UMR CNRS 6283, 72085 Le Mans, France*

**Rachael Morgan**
*Université Paris Sud XI, CNRS-UMR IDES 8148, Bât. 504, 91405 Orsay Cedex, France.*

## Abstract
Understanding of the pseudomorphic hematitisation of euhedral magnetite grains is fundamental as it changes ore quality in iron ore deposits, and impacts exploration, mineralurgical and metallurgical processing (e.g. iron and lateritic REE ores, heavy mineral sands). We tested five mineralogical techniques on two hematite samples from a banded iron formation in Southern India, and a lateritic soil above a hydrothermal vein deposit from the Minas Gerais region in Brazil, both composed of octahedral crystals indicating a magnetite precursor. Scanning electron microscopy detected magnetite patches within the crystals. These magnetite relicts are best analyzed by Curie Balance, magnetic hysteresis, Mössbauer, and Raman spectroscopy. The latter technique detects also maghemite, or a non-stoichiometric phase in the Brazilian martite. 300-K Mössbauer spectroscopy may be useful for the quantification of magnetite on magnetic separations. In the Indian magnetic separate 83 % hematite and 3 % magnetite are present. Magnetite detection on XRD spectra was possible through 3h run over 30-40° 2θ, where a clear distinction of the reflection peak appears at around 2.5 Å, whereas maghemite detection could be indicated by small peaks at 2.78 Å on bulk samples. The presence of maghemite was confirmed by FIB-TEM analyses, along with hematite and magnetite. In the Indian sample, magnetite and maghemite are present in the subhedral nanocrystals; hematite forms the interstitial crystals hosting dislocations and fluid inclusions. In the Brazilian sample, maghemite occurs as non-stoichiometric areas within magnetite or as twin sets in hematite. Nanostructural evidences suggest a fluid and crystallographic deformation induced mechanism for the hematitisation.

**Keywords.** Magnetite, hematite, maghemite, FIB-TEM, banded iron formations, Raman spectroscopy, Curie Balance, Mössbauer spectroscopy, X-ray diffraction, deformation, magnetic susceptibility,

## 1 Introduction
Hematitisation of magnetite can be related to hydrothermal or supergene alteration and is in many cases incomplete. The relict magnetite influences the magnetic properties of the hematite, which control the efficiency of magnetic separation during iron, REE and heavy mineral sand processing. The goal of this paper is to compare five mineralogical techniques on bulk samples and magnetic separates to evaluate the most efficient techniques for magnetite detection. FIB-TEM analyses allowed elucidating the process of hematitisation for a sample from banded iron formations in Southern India and a sample originated from hydrothermal veins in lateritic soils in Brazil.

## 2 Sample materials
The first sample comes from lateritic soils in the Espinhaço Range (Minas Gerais, Brazil: 18°17′31.12″S, 43°38′09.75″W). The octahedral crystals occur in the Middle Proterozoic sedimentary section and belong to hydrothermal veins, which may

be associated with the Brasiliano orogenic and hydrothermal event at ~0.6 Ga. The Brazilian octahedra are essentially composed of sub-to euhedral hematite grains (5-20 µm). Some tabular hematite crystals (~20 µm) occur in linear clusters along planes. Magnetite relics are still present.

The second sample comes from a 500 m thick Archean banded iron formation (BIF) of the Bababudan Group (Western Dharwar Craton, Southern India; N 13°19'539'', E 76°42'300''). The rocks have experienced greenschist-facies metamorphism, a hydrothermal event at about 2.6 Ga and modern weathering (Orberger et al. 2012). The BIF is characterized by alternating millimetric grey Fe-oxide and white quartz layers. The Fe-oxide layers consist of cubic or octahedral crystals (~ 20 µm) of hematite with relics of magnetite. All crystals have a trellis pattern. Scarce goethite particles are present.

## 3 Results

### 3.1 X-ray diffraction (XRD)
For the Brazilian crystals, a well-crystallized hematite with sharp reflection peaks is the major compound. Magnetite may be indexed from the peak 2.96 (I =30, (220)), while maghemite can be indexed by the peaks 2.95 Å (I 34, (220)), 2.78 Å (I = 19, (221)). A long counting run was performed between 51 and 67° 2θ, showing a peak at 1.614 Å, which could correspond to magnetite or maghemite (I 30/33: 1.616 Å, (511 or 333 of magnetite) respectively. The 3h run between 30 and 40° 2θ in the 2.5 Å area, shows a shoulder, at 2.528 Å corresponding to magnetite (I 100; (311)) of the major peak at 2.518 Å of hematite (I 50 (110). Small peaks appear at 2.292 Å and 2.2861 Å, corresponding to maghemite (I 34 (220)) and hematite (I: 2, (006)), respectively. The width and irregular shape of the 2.2923 Å peak may indicate the transformation of magnetite into maghemite or a non-stoichiometric intermediate phase.

For the Indian sample, the XRD spectra of the total sample prior to magnetic separation, shows the presence of quartz, hematite and poorly crystallized goethite. Very small peaks appear at about 2.96 Å, possibly magnetite (I 30, (220), or maghemite (I 34, (220), and at 2.78 Å (I 19, (221)) for maghemite. In the magnetic fraction, the hematite peaks show higher intensities. Higher intensities are also observed for the 2.96 Å and 1.61 Å peaks, which are assigned to magnetite and maghemite, respectively. The peak reflection at I 2.5 is split (2.523 Å (magnetite: (311) and 2.51 Å (maghemite (313)), and may represent maghemite.

### 3.2. Magnetic parameters
The thermomagnetic behavior, based on Curie Balance measurements, of all samples shows a major decrease in magnetization at about 580 °C and a second decrease to zero (UNIT) at 680 °C. It corresponds to that observed for a mixture of magnetite and hematite with Curie temperatures of 580°C and 680°C, respectively. The intensity of the relative magnetization above 580

°C and before 680 °C, related to hematite, varies slightly between the Brazilian and Indian sample, suggesting a higher "content "of hematite compared to magnetite in the Brazilian sample. The magnetic extraction of the Indian sample shows that the magnetic behavior is dominated by magnetite with very low magnetization between 580 °C–680 °C. Indeed, magnetite as a « soft » ferrimagnetic material is easily magnetized and extracted from the total sample compared to 'hard' weak ferromagnetic hematite if grains are physically well separated. In the Brazilian sample, a slight decrease in the magnetization, just below 400 °C indicates the possible presence of maghemite, which inverts to hematite in such a temperature range (e.g. Tarling, 1983, Thompson and Oldfield 1986, De Boer and Dekkers 2001).

Wasp-waisted forms of the magnetic hysteresis loop, widely documented in geological materials, indicate the presence of two different magnetic components with strongly contrasting coercive fields (Day et al. 1977, Roberts et al. 1995, Tauxe et al. 1996). Thus, wasp-waisted magnetic hysteresis loops of all studied Brazilian and Indian samples show a mixture of different components. Low coercivity (Bc) values indicate the presence of a soft material such as magnetite or maghemite. Relatively high remanent coercivity (Bcr) and an open loop at magnetic field values higher than 0.3 T (magnetic field in which magnetization is saturated for soft ferrimagnetic materials, but not for hard materials), indicate the presence of a hard material as hematite or goethite. In the case of such mixed mineral magnetic composition, the content of hard material has to be important to influence the shape of the hysteresis loop. Thus in the studied samples, the amount of hematite is high. Moreover, in the Brazilian sample, a more pronounced constriction in the middle section of the hysteresis loop than in the Indian sample was observed. It indicates a relatively higher amounts of hematite compared to magnetite and/or maghemite in the Brazilian sample, confirming the Curie Balance measurements.

### 3.3 [57]Fe Mössbauer Spectrometry
The 300-K Mössbauer data of the Indian samples, the hyperfine structure exhibits two main components contrarily to that of the Brazilian sample, which consists of a single sextet. In addition, the presence of a small additional line in the magnetic fraction of the Indian sample belongs to one of the two components of magnetite. Thus, the total Indian sample indicates the presence of hematite (86 %) and goethite (14%). The magnetic fraction is mainly composed of hematite (83 %) and minor of magnetite (3%). The 300-K Mössbauer spectrum of Brazilian sample shows only the presence of hematite.

### 3.4 Raman Spectroscopy
In the Brazilian martite, spectra were recorded from the overall bright hematite part (1) and from the scarce small (5-20µm) greyish patches (2) in two different grains. In part (1) the spectra show bands at 222-229, 293-304, 413-419, 505-512, 614-633, 664-679, and

1336-1342 cm$^{-1}$ in grain 1, while in grain 2 a band at 248-250 cm$^{-1}$ is visible and the band at ~300 cm$^{-1}$ may be resolved in two bands (e.g. 291 and 299 cm$^{-1}$). This combination of bands is typical of hematite (e.g. de Faria et al., 1997; Hanesh, 2009). Compared to the expected seven Raman active modes of hematite, some bands require careful examination: the additional band at 668-675 cm$^{-1}$, the position of the $E_{g5}$ mode at 617-631 cm$^{-1}$ instead of 613 cm$^{-1}$, and the position of the magnon band at 1330-1340 cm$^{-1}$ (i.e. a shift up to 20 cm$^{-1}$). The band at 668-675 cm$^{-1}$ may correspond to magnetite (strong $E_g$ mode at 661-680 cm$^{-1}$; de Faria et al., 1997), or reflect the presence of maghemite (even in the lack of the maghemite main peak at 730 cm$^{-1}$, op.cit.). Moreover, the apparent shift of the hematite 1320 cm$^{-1}$ band to a higher wavenumber may also result from a maghemite band at ~ 1330-1360 cm$^{-1}$. Although unusual in hematite, the band at ~ 634 cm$^{-1}$ has also been reported by Gehring et al. (2009) and attributed to non-stoichiometric magnetite undergoing oxidation. Deconvolution reveals hidden peaks at ~ 360 cm$^{-1}$, 565, 612, and ~ 740 cm$^{-1}$, related to the presence of relict magnetite (565 and 669 cm$^{-1}$) and of maghemite (360 and 740 cm$^{-1}$), or a non-stoichiometric magnetite.The maghemite "diagnostic" bands (Hanesh, 2009) are not well defined due to the small size of the maghemite particles. Both magnetite and maghemite contribute to the strong band at ~ 665 cm$^{-1}$.

In the Indian martite, the spectra were acquired in two different massive Fe-oxide layers. Spectra from the bright trellis parallel to [111] directions show typical hematite bands. A band at 660 - 664 cm$^{-1}$ is attributed to magnetite, while the unresolved bands between 800 and 1200 cm$^{-1}$, hidden in the background, might be caused by impurities (Hanesh, 2009). The martite grain contains scarce darker patches of two types: (1) magnetite (bands at 301, 410, 541 and 666 cm$^{-1}$), and (2) goethite (bands at 239-243, 297-299, 383-385, 416-417, 479-480, 548-550,~ 681, cm$^{-1}$).

### 3.5 Focused ion beam-transmission electron microprobe (FIB-TEM)

In the Brazilian sample FIB-TEM cuts were performed in magnetite, and through hematite and magnetite. The FIB-foil 1 in the magnetite part (~150 nm) shows areas rich in dislocations, and non-stoichiometric areas. Selected area electron diffraction patterns of the non-stoichiometric volumes may indicate the presence of maghemite. Diffraction patterns acquired from the thinnest part of the foil, indicate "splitting" of reflections for the higher order intensities, a major pattern with the lattice parameters, providing angles between lattice planes (100) and (111) of 54.7° and an angle between (-111) and (111) = 70.53°, indicating the presence of magnetite. The second crystal seen 'behind' (splitted peak) the first pattern, shows the same cubic system but different lengths of the diffraction vector (111= 0.4461 nm and 0.4756 nm) indicating a shrinking of the crystal lattice and probably the presence of maghemite within the magnetite. The non-stoichiometric zones can be explained by a Fe$^{2+}$ loss, which is combined with the formation of vacancies.

In the foil cut through the hematite-magnetite part, a lamellar area could be observed in a narrow range of tilting angle. These areas also host at least two sets of twins forming an angle of ~60° with a width of ~20 nm. Diffraction patterns performed on the two sets of twins indicate in one of the twin sets a d-spacing of 2.935, which does not fit the d-spacing for hematite (d= 2.69 (104). It is either magnetite (2. 967 (220)) or maghemite (2.951= (202)). The second twin set indicates the presence of maghemite or hematite. As the lamellar part surrounding the twins was clearly identified as hematite and the first twin set is not hematite, it can be deduced that it is maghemite, since twinning cannot occur between the cubic spinel magnetite and the rhombohedral hematite.

The Indian martite was cut through the relict magnetite and hematite. The TEM image indicates the presence of subhedral and interstitial crystals, both containing lamellae. The interstitial crystals are characterized by dislocations with fluid inclusions, high porosity areas and grain boundary migrations. All subhedral crystals have the same orientation. Diffraction patterns of these crystal show splitted peaks, representing magnetite and maghemite. The a$_0$-axes of magnetite were calculated at 0.842 nm and for maghemite 0.828 nm. The diffraction pattern of the interstitial crystal (N° 6) can be indexed as hematite (d: 3.68 (1O-2) and 2.52 (110)).

## 4 Discussion

All methods show hematite as the principal identified mineral. The analytical methods are complementary as they analyze different physical and chemical properties at different scales (microscopic to nanoscopic).

Optical reflected light and scanning electron microscopy show that both samples have cubic shapes, are essentially composed of hematite, but magnetite forms grey patches within the white hematite. The Indian sample shows trellis, subhedral crystals of magnetite and maghemite, and interstitial hematite, while trellis are absent in the Brazilian sample, but sets of nano twins of maghemite within the hematite and maghemite as island structures are common.

Structures are indicative for the processes and/or mechanisms of formation and transformations, such as hydrothermalism, metamorphism, annealing, and weathering, In the Indian sample, the sharp contact of the subhedral and interstitial crystals may represent a process of oxy-exsolution of magnetite to hematite, leading to trellis formation. The Indian sample belongs to a 500 m thick BIF, which chemically precipitated on a shallow platform from a mixture of hydrothermal fluids and seawater. It was affected by greenschist facies metamorphism and later hydrothermal fluids (Orberger et al. 2012). The presence of the two different domains, magnetite+maghemite and interstitial hematite may suggest a low-temperature exsolution process along cleavages planes leaving behind subhedral magnetite crystals with the same crystallographic orientation. The fluid inclusions

within the interstitial crystals (magnetite and maghemite) may reflect the later hydrothermal event related to a granitic intrusion. The grain boundary migrations within the hematite might indicate a dynamic crystallization, related to a syn-precipitational deformation. This would imply that the maghemite in the magnetite is a hydrothermal product.

The Brazilian octahedra have no trellis, but show irregular patches of magnetite within hematite, non-stoichiometric zones, island structures, the presence of maghemite in magnetite, and dislocations, indicating clearly that the transformation comprises a maghemite step. Neoformed euhedral tabular hematite might indicate that the oriented growth of tabular hematite crystals is controlled by the octahedral planes of old magnetite grains. The magnetite veins crosscut the metamorphic fabric, but recorded itself deformation (dislocations). This may have induced the maghemite-hematite transformation along crystal planes. The non-stoichiometric compound can be interpreted as an intermediate transformation product, while the twins observed by FIB-TEM in the hematite may present a transformation product from maghemite to hematite.

**Implications for magnetic separation beneficiation:** Various kinds of magnetic separations (low and high intensity, wet and dry) are applied for various minerals with low and high magnetic susceptibility. It is either used to enrich iron ore, or to clean non-iron ores (e.g. laterites rich in REE, Ni, and Ti or Zr, REE sands). The detection and quantification of magnetite within the martite, which is constituted principally by hematite, is possible with various methods if its content is high enough (Mössbauer spectroscopy, XRD etc). Nevertheless, these methods do not clearly detect magnetite. It is only when magnetite content reach a few %, that the difference between magnetic properties of magnetite and hematite (magnetic susceptibility, remanent magnetizations, Curie temperature etc.) allows clear magnetite identification. Indeed, there is a difference in the magnetic behavior of "hard" (as hematite) and "soft" (as magnetite) magnetic materials. Magnetite is easily magnetized and demagnetized in relatively low magnetic fields compared to hematite. Its remanent magnetization is much higher and its Curie temperature is lower than observed for hematite in the same field. In the Indian and the Brazilian samples, the use of magnetic parameters allowed better identification of the martite composition. At a larger scale, the identification of the nature of various magnetic particles and their contents is useful for optimizing the magnetic field and flow rates to be applied during magnetic separation processes, including high intensity wet magnetic separations (HGMS).

## 5 Conclusions

Magnetic separation is necessary prior to mineralogical analyses to analyze small quantities (~3%) of ferromagnetic compounds in iron oxy-hydroxide rich samples by XRD. The detection of these compounds is crucial to understand the magnetite-hematite transformation process. Raman spectroscopy detects non-stoichiometric phases or maghemite, while FIB-TEM reveals twinning and dislocations. In-field Mössbauer spectrometry needs to be performed in order to quantify precisely the amount of magnetite, hematite and maghemite. The relict amounts of magnetite in hematite of banded iron formations influence the magnetic properties. Its quantification helps to optimize magnetic separation beneficiation. These results can be applied also to magnetic separations in lateritic REE ore, or heavy mineral sands.

## References

Day R, Fuller M.D, Schmidt VA,(1977) Magnetic hysteresis properties of synthetic titanomagnetites, Phys.Earth Planet. Inter. 13: 260-266.

De Boer CB, Dekkers MJ, (2001) Unusual thermomagnetic behaviour of haematites: neoformation of a highly magnetic spinel phase on heating in air. Geophys. J. Int. 144 : 481-494.

De Faria, DL.A., Venancio-Silva S, de Oliveira MT (1997) Raman microspectroscopy of some iron oxides and oxyhydroxides. Journal of Raman spectroscopy, 28: 873-878.

Gehring AU, Fischer H., Louvel M., Kunze K, Weidler PG, (2009) High temperature stability of natural maghemite: a magnetite and spectroscopic study. Geophysical Journal International, 179: 1361-1371.

Hanesh M, (2009) Raman spectroscopy of iron oxides and (oxy)hydroxides at low laser power and possible implications in environmental magnetic studies. Geophysical Journal International, 177: 941-948.

Orberger B, Wagner C, Wirth R, Quirico E, Gallien JP, Derré C, Montagnac G, Noret A, Jayananda M, Massault M, Rouchon V, (2012) Origin of iron oxide spherules in the banded iron formation of the Bababudan Group, Dharwar Craton, Southern India. Journal of Asian Earth Sciences, 52: 31-42.

Roberts AP, Cui Y, Verosub KL, (1995) Wasp-waisted hysteresis loops: mineral magnetic characteristics and discrimination of components in mixed magnetic systems, J. Geophys. Res., 100, B9, 17: 909-17,924.

Shebanova ON, Lazor P (2003) Raman spectroscopic study of magnetite ($FeFe_2O_4$): a new assignment for vibrational spectrum. Journal of Solid State Chemistry, 174: 424-430.

Tarling DH, (1983) Paleomagnetism, Principles and applications in geology, geophysics and archaeology, ed. Chapman & Hall, N. York, 379 pp.

Tauxe L, Mullender TAT, Pick T, (1996) Potbellies, wasp-waisted, and superparamagnetism in magnetic hysteresis, J. Geophys. Res., 101, B1: 571-583.

Thompson R, Oldfield M, (1986) Environmental magnetism, Allen and Unvin eds. London, 227 pp.

Wang A, Kuebler KE, Joliif BL, Haskin LA, (2004) Raman spectroscopy of Fe-Ti-Cr-oxides, case study: Martian

# S 2.5:
# Ore mineralogy and geometallurgy

**SPONSORED BY IMA-COM**

Convenors:
Pertti Lamberg & Federica Zaccarini

# Correlating textures and trace elements in ore minerals

**Nigel J. Cook, Cristiana L. Ciobanu, David Giles**
*Centre for Tectonics, Resources and Exploration (TRaX) and Deep Exploration Technology Cooperative Research Centre (DET CRC), University of Adelaide, Adelaide S.A. 5005, Australia*

**Benjamin P. Wade**
*Adelaide Microscopy, University of Adelaide, North Terrace, SA 5005, Australia*

**Abstract.** The Integrated application of complementary microanalytical techniques (laser ablation ICP-MS spectrometry, electron microprobe, focused ion beam – scanning electron microscopy, transmission electron microscopy) helps resolve key questions concerning which minerals will incorporate which trace elements, and under what circumstances. Mineral characterization at scales from that of the polished section (tens to hundreds of μm) down to the nanoscale can reveal Information on the crystal-structural relationships between host and incorporated element, substitution mechanisms, the range of natural solid solutions and equilibrium partitioning among co-existing minerals. It also assists understanding of physical processes that drive changes in element distributions during superimposed events, notably metamorphism and associated deformation. Collectively, such information contributes to genetic modeling, the development of innovative exploration methods, efficient ore processing and waste monitoring.

**Keywords.** Ore textures, LA-ICP-MS, FIB-SEM, TEM.

## 1 Introduction

The concentrations of minor and trace elements in opaque minerals, and their variations, have long been recognized as rich sources of petrogenetic information. Contemporary microanalytical techniques give unparalleled insights into the scale and nature of trace element incorporation into host sulfides and oxides. Until relatively recently, much of this detail was inaccessible due to high minimum detection limits (e.g. electron probe microanalysis; EPMA) or preparation methods that did not allow site-specific sampling or use of identical sample material for multiple analysis methods.

Problems in bridging scales of observation have been largely overcome by instrumentation such as the Focused Ion Beam - Scanning Electron Microscope (FIB-SEM) which can be readily applied to ore minerals (Ciobanu et al. 2011). Slices extracted *in-situ* from a polished section (Fig. 1) can be used for sub-μm-scale imaging and mapping by High-Angle Annular Dark Field - Scanning Transmission Electron Microscopy (HAADF-STEM; Utsunomiya & Ewing 2003). Furthermore, the slices can

be mapped using synchrotron radiation techniques such as X-Ray Fluorescence Spectroscopy (XFS) to characterize compositional zonation at the sub-μm-scale and, if necessary, μ-X-ray absorption near-edge structure spectroscopy (XANES) to address questions of chemical state (Cook et al. 2012). The same slices can be thinned into foils, <100-60 nm thickness, for high-resolution imaging and electron diffraction by Transmission Electron Microscopy (TEM) (Ciobanu et al. 2011).

The sub-μm- to nanoscale observational techniques can complement spot analysis and element mapping by laser ablation inductively coupled plasma mass spectrometry (LA-ICP-MS). The availability of matrix-matched standards (e.g. Wilson et al. 2002; Danyushevsky et al. 2011) has led to this technique being routinely used to obtain quantitative trace element data. The latest generation of LA-ICP-MS instruments allow sub-ppm level sensitivity, good precision and accuracy, and spatial resolution that meets most requirements, thus enabling compositional zoning and partitioning between coexisting minerals to be characterized. LA-ICP-MS element mapping gives graphic representation of compositional features at the grain-scale (e.g. Large et al. 2009; Cook et al. 2013). The data obtained using the different techniques assist interpretation of trace element distribution patterns. Provided such information is placed into the context of textures. Results can address questions regarding the location of trace elements, whether there are crystal structural controls on the chemical patterning at the nm- to μm-scales and whether element distribution is even throughout a zoning pattern or relates to sub-μm to nm-scale inclusions.

## 2 Sphalerite

Sphalerite incorporates a wide range of trace elements via a complex series of solid solutions. Substituted elements include valuable by-products such as indium or germanium (Cook et al. 2009a, 2011a). Substitution mechanisms can be modeled based on the chemical state
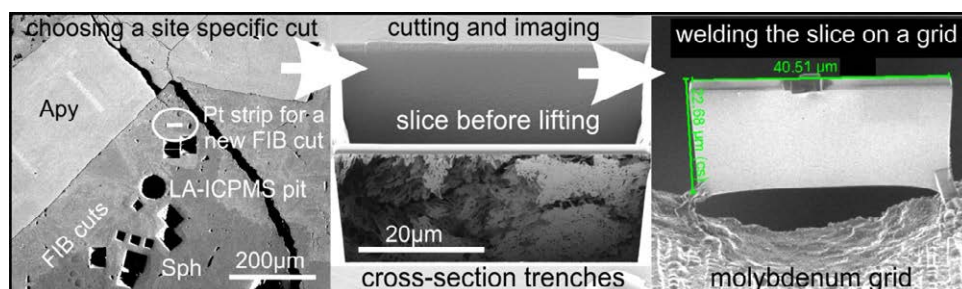
**Figure 1.** Secondary electron images illustrating the conceptual approach for sample characterisation from the LA-ICP-MS to sub-μm-scale by using FIB-SEM to cut and extract a slice from a polished block that has shown enrichment in trace elements in a given area.
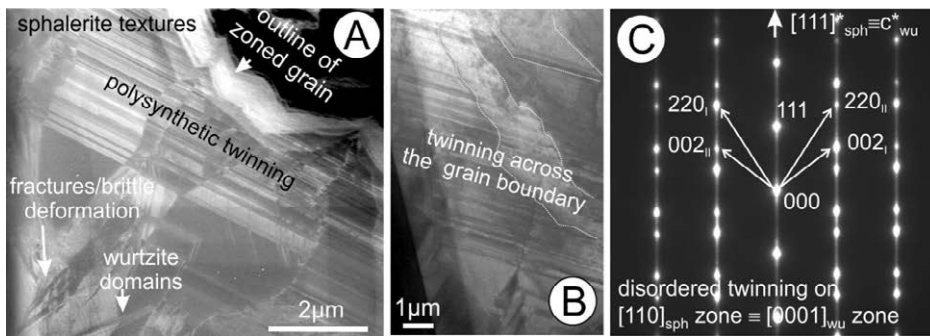
**Figure 2.** Secondary electron image (A) and TEM image (B) of an area in sphalerite showing textures which are relevant for Sn-enrichment superimposed onto Cu-In-zonation. (C) Selected area of electron diffraction on the [110] zone of sphalerite, showing that the polysynthetic twinning is along the [111]* axis, and is disordered.

of contained elements, e.g. μ-XANES evidence for $Cu^+$ in Cu-In-substituted sphalerite (Cook et al. 2012), supporting the coupled substitution $2Zn^{2+} \leftrightarrow Cu^+ + In^{3+}$. Published data indicates that the enrichment of sphalerite in specific elements is influenced by metal source, geological environment and the type and temperature of ore-forming fluids. Murakami & Ishihara (2013) have suggested, for example, that the Ag content of sphalerite may reflect formation depth.

Lattice-scale controls on minor element distributions are identified in sphalerite, notably epitaxial intergrowths of polysynthetically twinned sphalerite and wurtzite polytypes in both Cu-In- and Sn-Ag-substituted sphalerite. However, higher-order wurtzite polytypes (e.g. *6H*) occur together with Ag-Sn-bearing nanoparticles in the latter (Ciobanu et al. 2011). XRF-synchrotron mapping of slices from Sn-rich domains has shown that fine-grained aggregates of sphalerite are richer in Sn relative to coarser grains of Cu-In zoned sphalerite. Imaging of one such slice after thinning reveals that polysynthetic twinning is associated with brittle brecciation of sphalerite, which increases outside the zoned grain (Fig. 2A) but straddles the grain boundary (Fig. 2B). Electron diffractions obtained across both domains indicate disordered [111]* twinning of sphalerite; the same diffraction pattern is equally equivalent to *2H* wurtzite along the ***c**** axis (Fig. 2C). Based on this we infer that mechanical twinning of sphalerite, a prerequisite for the formation of wurtzite polytypes and their intergrowths, is the main control of Sn-enrichment and explains the crystal zoning relative to other textures in the studied sphalerite. Epitaxial relation-ships between (cubic) sphalerite and (hexagonal) wurtzite indicate that metal substitutions are controlled by coupled dissolution and repreciptation reactions.

## 3 Pyrite and arsenopyrite

Trace element microanalysis of pyrite has focused extensively on the distribution of gold, often in order to quantify the role played by "invisible gold". Gold solubility in pyrite is well constrained (Reich et al. 2005), and fine particles (200 nm – 2 μm) and nanoparticles (<200 nm) of gold and other Au-minerals are widely reported (e.g. Palenik et al. 2004, Deditius et al. 2011). We have recently shown nanoparticles of Ag-Au-tellurides in As-free pyrite (Ciobanu et al. 2012) and nanoparticulate gold in arsenopyrite (Cook et al. 2013). Both cases show (a) the presence of sub-μm-sized pores adjacent to gold nanoparticles and (b) a

marked correlation between Au, Bi, Pb and Te. Constraints on the latter signature are modeled for Au-telluride deposits in Cook et al. (2009b).

A further example comes from ongoing research on a roll-front uranium deposit. Data indicates that a range of trace elements, including Tl, Mo and Sb, coupled with in situ S-isotope measurement, may be invaluable for discriminating between distinct pyrite generations and recognizing distinct fluid or metal sources, thus providing evidence for petrogenetic interpretations. Cross-section imaging of pyrite interstitial to U-rich domains in pyrite-cemented sandstone shows films of clay minerals defining sub-μm-scale textures in both coffinite and pyrite. This is an argument favoring (re-)crystallization of pyrite from the same U-rich fluid from which the U-minerals precipitated (Fig. 3A).
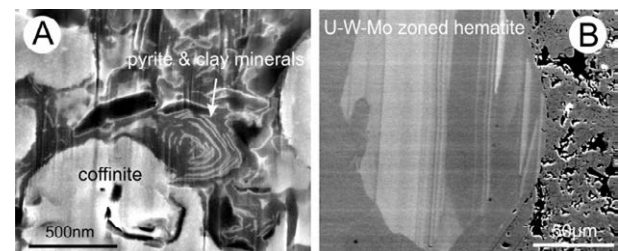


**Figure 3. (A)** SE image obtained by cross-sectioning of U-rich domains in pyrite-cemented sandstone showing sub-μm-scale textures. **(B)** BSE image of oscillatory-zoned hematite, in which the bright zones on the image are U-rich.

## 4 Hematite

Fe-oxides can incorporate a variety of elements and inter-element relationships can be useful for discriminating ore types (e.g. Dupuis & Beaudoin 2011; Nadoll et al. 2012). The suite of elements readily entering hematite also includes U, W, Mo and REE (Ciobanu et al. in review) where such elements can display stunning patterns of oscillatory and sectorial zoning (Figs. 3B & 4). The same elements can be released to form inclusions that vary in size from tens of nm to μm-size.

Accommodation of substituting elements is achieved by superstructuring in the hematite lattice whereas their release is associated with porosity and mechanical twinning of hematite. These findings have potential geochronological applications, have implications for U distributions following the rise of atmospheric $O_2$ in the Paleoproterozoic (2.5–1.6 Ga), and are a basis for exploration models for IOCG deposits.
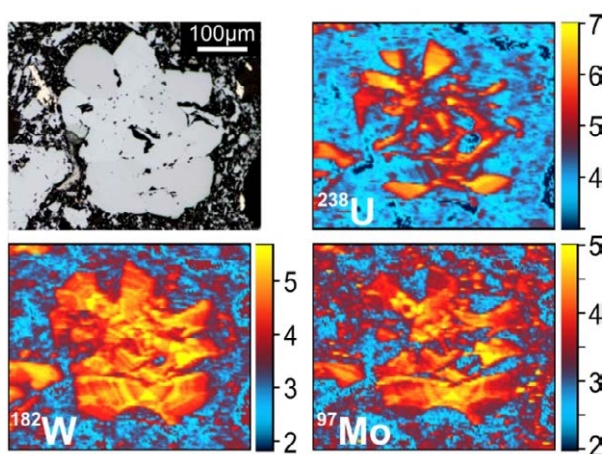
**Figure 4.** LA-ICP-MS element maps of oscillatory and sectorially-zoned aggregate of hematite. $^{206}$Pb (not shown) mimics U. Scales are logarithmic (counts-per-second x10$^3$).

## 5 Other sulfides

Similar approaches can be applied to other mineral systems, including Cu-(Fe)-sulfides, for which data on partitioning of valuable by-product elements is only recently becoming available (Reich et al. 2010; Cook et al. 2011b). Understanding the sequence of superstructure development in associations featuring nanoscale inter-growths between Cu-(Fe)-sulfides can be used to constrain temperatures in a given paragenetic context. Likewise, the relative concentrations of Ag and Bi can discriminate between co-crystallized species (Cook et al. 2011b) and assemblages resulting from replacement.

In some deposit types, notably epithermal systems, all sulfides are likely to display compositional zoning with respect to trace elements, reflecting the evolution of crystal growth. This is illustrated by LA-ICP-MS element maps of compositionally-zoned stibnite (Fig. 5) which contains As-rich and As-poor domains (concentration differences are ca. one order of magnitude). Silver, Cd and Fe are also poorer in the As-poor domains; Pb is markedly enriched in the As-poor domains. Most characteristic, however, are narrow zones of enrichment in Ag, Cu and Pb (and mimicked on maps for Bi, Cd, Hg, In, Mn, Se, Sn, Te, Tl and Zn), separating the As-rich and As-poor domains. The same suite of elements is also enriched at the outer margins of the stibnite lamellae.

## 6 Discussion

The overarching goal of this type of research is to understand the behavior of trace and minor elements, in minerals from different ore types, to identify the mechanisms that allow element for their enrichment, and to understand when and why these enrichment processes take place. The volume of data on natural sulfides (and increasingly oxides) has increased significantly in recent years but there are few reliable experimental data to correlate with empirically-observed partitioning trends (e.g. equilibrium distribution of In between sphalerite and chalcopyrite).

Results can contribute to genetic modeling (e.g. P-T-X environments, metal and fluid sources), development
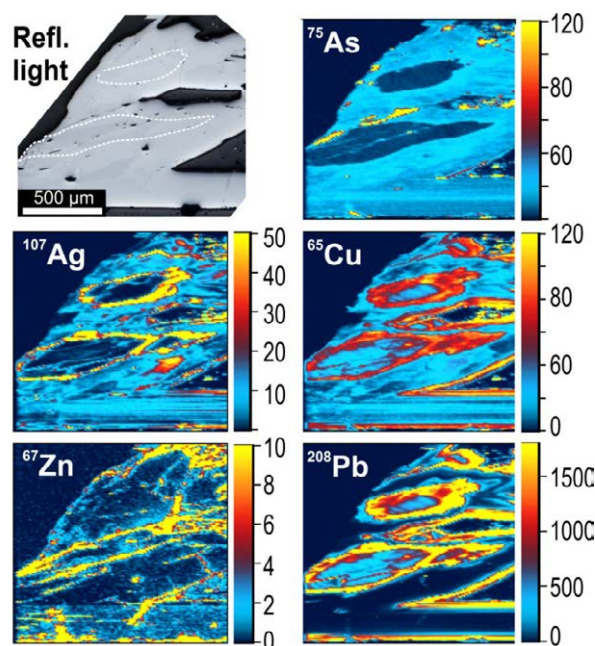


**Figure 5.** LA-ICP-MS element maps of compositionally-zoned stibnite. Scales are linear in counts-per-second (x10$^3$).

of innovative exploration methods (e.g. recognition of minerals where a change in trace element composition can serve as a near-mine vector to ore or define a regional-scale alteration footprint), and to efficient ore processing and waste monitoring (identification of host minerals, trapping/locking mechanisms). Precise compositional data at appropriate scales can also contribute to the growing fields of 'mineral evolution' research (Hazen et al. 2011) and applications of biogeotechnology (Zammit et al. 2012).

The authors are often asked how many data points are sufficient to characterize the trace element signature of a given sulfide. This will vary with the complexity of ore textures, and in particular, any intra-grain compositional zoning or the presence of multiple generations of the same mineral in a given sample or suite of samples. We cannot stress enough the importance of detailed petrological characterization, by optical and scanning electron microscopy, prior to any microanalytical work. This may entail the designation of textural sub-types and should assess any major compositional zoning in the material to be analyzed (i.e. visible optically or in back-scatter electron images). Such variation is likely to be mimicked by other elements present at lower concentrations.

Routine spot analysis by EPMA or LA-ICP-MS at the centers of 'clean-looking' grain is likely to intro-duce a systematic bias into the dataset, with elements that concentrate towards the rim or in specific domains within individual grains being potentially under-estimated. Variation can be expected between samples from different parts of a given ore, and not uncom-monly within a single polished section. Meaningful, quantitative evaluation of the distribution of, e.g. Au in pyrite, may therefore only be attained by determining abundances in a large number of representative samples. Other elements and other minerals, however, often show a more limited inter- and/or intra-sample variation and an accurate appraisal may be possible

with a smaller dataset. Examples include the concentration of Cd, Mn and Hg in sphalerite from metamorphosed ores which often appear quite uniform on the deposit scale, at least in cases when only a single textural type (or generation) of sphalerite is recognized.

The relative ease and speed of data collection using automated LA-ICP-MS instrumentation presents its own potential pitfalls. Interpretation of multi-element datasets is reliant on the choice of statistical methods used (e.g. Winderbaum et al. 2012), and, again, that comprehensive optical characterization of ore textures is essential prior to analysis and data interpretation.

# 7 Concluding remarks

In general, the degree of crystal-scale compositional variation increases with the refractive character of a mineral, analogous to common silicates, where highly refractory minerals like garnet or zircon generally show the greatest degree of compositional zoning. Hence, pyrite or arsenopyrite will often show a greater degree of compositional variation or intra-grain complexity than sphalerite, which in turn shows greater variation than chalcopyrite, galena or pyrrhotite. Despite this, studies on a number of minerals have demonstrated a high degree of trace element heterogeneity in a number of species (e.g. molybdenite; Ciobanu et al. 2013), which lack any indication of compositional heterogeneity under the optical microscope or SEM.

Ore mineralogy remains a vital tool in the ore geologists' arsenal. Given the rapid development of quantitative methods that can generate information down to the nanoscale (Reich et al. 2011), the potential for major breakthroughs in a discipline often deemed old-fashioned is considerable.

## Acknowledgements

## References

Ciobanu CL, Cook NJ, Utsunomiya S, Pring A, Green L (2011) Focussed ion beam-transmission electron microscopy applications in ore mineralogy: Bridging micro- and nanoscale observations. Ore Geol Rev 42: 6-31

Ciobanu CL, Cook NJ, Utsunomiya S, Kogagwa M, Green L, Gilbert S, Wade B (2012) Gold-telluride nanoparticles revealed in arsenic-free pyrite. Amer Mineral 97: 1515-1518

Ciobanu CL, Wade BP, Cook NJ, Giles D, Schmidt-Mumm A, Cleverley J (in review) Uranium-bearing hematite from Iron Oxide - Copper - Gold ores. Amer Mineral (in review)

Ciobanu CL, Cook NJ, Kelson CR, Guerin R, Kalleske N, Danyushvsky LV (2013) Trace element heterogeneity in molybdenite fingerprints stages of mineralization. Chem Geol http://dx.doi.org/10.1016/j.chemgeo.2013.03.011

Cook NJ, Ciobanu CL, Pring A, Skinner W, Danyushevsky L, Shimizu M, Saini-Eidukat B, Melcher F (2009a) Trace and minor elements in sphalerite: a LA-ICP-MS study. Geochim Cosmochim Acta 73: 4761-4791

Cook NJ, Ciobanu CL, Spry PG, Voudouris P & the participants of IGCP-486 (2009b) Understanding gold-(silver)-telluride-(selenide) mineral deposits: Episodes 32: 249-263

Cook NJ, Sundblad K, Valkama M, Nygård R, Ciobanu CL, Danyushevsky L (2011a) Indium mineralisation in A-type granites in southeastern Finland: Insights into mineralogy and partitioning between coexisting minerals. Chem Geol 284: 62-73

Cook NJ, Ciobanu CL, Danyushevsky LV, Gilbert S (2011b) Minor and trace elements in bornite and associated Cu-(Fe) sulfides: A LA-ICP-MS study. Geochim Cosmochim Acta 75: 6473-6496

Cook NJ, Ciobanu CL, Brugger J, Etschmann B, Howard DL, de Jonge MD, Ryan C, Paterson D (2012) Determination of the oxidation state of Cu in substituted Cu-In-Fe-bearing sphalerite via μ-XANES spectroscopy. Amer Mineral 97: 476-479

Cook NJ, Ciobanu CL, Meria D, Silcock D, Wade B (2013) Arsenopyrite-pyrite association in an orogenic gold ore: tracing mineralization history from textures and trace elements. Econ Geol (in press)

Danyushevsky L Robinson P, Gilbert S, Norman M, Large R, McGoldrick P, Shelley M (2011) Routine quantitative multi-element analysis of sulphide minerals by laser ablation ICP-MS: Standard development and consideration of matrix effects. Geochem Explor Environ Anal 11: 51-60

Deditius AP, Utsunomiya S, Reich M, Kesler SE, Ewing RC, Hough R, Walshe J (2011) Trace metal nanoparticles in pyrite. Ore Geol Rev 42: 32-46

Dupuis C, Beaudoin G (2011) Discriminant diagrams for iron oxide trace element fingerprinting of mineral deposit types. Mineral Deposita 46: 319–335

Hazen RM and 12 co-authors (2011) Needs and opportunities in mineral evolution research. Amer Mineral 96: 953–963

Large RR and 11 co-authors (2009) Gold and Trace Element Zonation in Pyrite Using a Laser Imaging Technique: Implications for the Timing of Gold in Orogenic and Carlin-Style Sediment-Hosted Deposits. Econ Geol 104: 635-668

Murakami M, Ishihara S (2013) Trace elements of Indium-bearing sphalerite from tin-polymetallic deposits in Bolivia, China and Japan: A femto-second LA-ICPMS study. Ore Geol Rev. http://dx.doi.org/10.1016/j.oregeorev.2013.01.010

Nadoll P, Mauk JL, Hayes TS, Koenig AE, Box SE (2012) Geochemistry of magnetite from hydrothermal ore deposits and host rocks of the Mesoproterozoic Belt Supergroup, United States. Econ Geol 107: 1275-129

Palenik CS, Utsunomiya S, Reich M, Kesler SE, Ewing RC (2004) Invisible gold revealed: direct imaging of gold nano-particles in a Carlin-type deposit. Amer Mineral 89: 1359–1366

Reich M, Kesler SE, Utsunomiya S, Palenik CS, Chryssoulis SL, Ewing RC (2005) Solubility of gold in arsenian pyrite. Geochim Cosmochim Acta 69: 2781-2796

Reich M, Chryssoulis SL, Deditius A, Palacios C, Zuniga A, Weldt M, Alvear M (2010) "Invisible" silver and gold in supergene digenite. Geochim Cosmochim Acta 74: 6157–6173

Reich M, Hough R, Deditius A, Utsunomiya S, Ciobanu CL, Cook NJ (2011) Nanogeoscience in ore systems research: Principles, methods, and applications: Introduction and preface to the special issue. Ore Geol Rev 42: 1-5

Utsunomiya S, Ewing RC (2003) Application of high-angle annular dark field scanning transmission microscopy, scanning transmission electron microscopy-energy dispersive x-ray spectrometry, and energy-filtered transmission electron microscopy to the characterization of nanoparticles in the environment. Environm Sci Tech 37: 786–791

Wilson SA, Ridley WI, Koenig AE (2002) Development of sulfide calibration standards for the laser ablation inductively-coupled plasma mass spectrometry technique. J Anal Atom Spectr 17: 406-409.

Winderbaum L, Ciobanu CL, Cook NJ, Paul M, Metcalfe A, Gilbert S (2012) Multivariate Analysis of an LA-ICP-MS Trace Element Dataset for Pyrite. Math Geosci 44: 823-842

Zammit CM, Cook NJ, Brugger J, Ciobanu CL, Reith R (2012) The future of biotechnology for gold exploration and processing, Minerals Eng 32: 45-53

# Is ethical gold possible? The example from fluvial gold placer in Lepaguare mining district (Honduras, Central America)

**Simona Alunno, Sabrina Nazzareni, Bartolucci Luca**
*Dipartimento di Scienze della Terra, Università di Perugia, Italy*

**Michele Mattioli, Alberto Renzulli, Marco Menichetti**
*Dipartimento di Scienze della Terra, della Vita e dell'ambiente, Università di Urbino, Italy*

**Abstract.** The mineral assemblage of the gold placer mining of Murcielago in the Lepaguare valley (Central Honduras) has been studied using electron microscopy and single-crystal X-ray diffraction techniques.

In this mine an environmental sustainibile project is developed by Eucantera and a chemical free technologies are used to extract gold from the deposit.

Gold is the principal ore mineral and nuggets are present as rounded grains, wires and sheets. Rare pyrite and cinnabar crystals were found in the concentrated material. Heavy minerals are magnetite and haematite, rutile, ilmenite, zircon. Among gangue minerals quartz is the most abundant phase. However Ca-amphiboles, pyroxenes, epidotes, tourmalines, andradite garnets are also present. Monazite with low to absent thorium concentration and minor xenotime have been recognised. The presence of gold-bearing quartz veins mineralizations (Canaan deposit) located in the Lapaguare mining district is a possible primary source of the gold found in the placer.

**Keywords. Gold, placer deposit, Honduras**

## 1 Introduction

Is a "green" environmental friendly gold extraction possible? A piloting mining project is currently developing in Honduras (central America) by Eucantera company.

Several ore deposits of precious metals are known in Central America (Nelson, 2007). The mining district in the valley of Lepaguare (district of Olancho in central Honduras) is characterized by gold mineralization in quartz vein occurring in low-grade metamorphic rocks, graphitic schists and quartzites of the pre-Mesozoic metamorphic basement (Menichetti et al 2007; Bersani et al 2009)

The current extraction is concentrated in the alluvial gold deposits of the Lepaguare valley (Figure 1 ) where the innovative approach to mining lies in the environmental friendly new technology. The placer is characterised by a sequence of sandstones and conglomerates from fine to coarse grained around 4 meters in thickness.

The processing of gold-bearing sand and gravels does not use cyanide or other harmful chemicals but it is based on piloting gravimetric technology. The material is washed and gravimetric concentrated with a full reprocessing of mining waste (gravel and clay).



**Figure 1.** Location map of the placer gold mine.

Moreover a social program involving the local population is developed.

We studied the gold placer deposit to characterise the mineralogy from chemical and crystallographic viewpoint with the final aim to define the primary source of gold and associated ore minerals.

## 2 Experimental

Materials were sampled from the productive plant at different grain size fractions, from 0.5 mm to 2 mm, including the heavy metal concentrated material containing gold. Neither grinding in a crusher nor diluted HCl acid were performed in order to avoid leaching phosphates and provoking man made changes to the grain surfaces and morphology. A preliminary hand-picking concentration was performed to select different mineral species which were studied by scanning electron microscopy and single-crystal X-ray diffraction. The scanning electron microscope Philips 515 with an energy-dispersive system (SEM-EDAX PW9900) was used for mineral identification and imaging on selected single minerals and concentrated minerals. The Xcalibur single-crystal diffractometer (Agilent technologies) equipped with a CCD camera detector and a Mo kα X-ray source was used to determine the crystal structure of selected minerals.

# 3 Results

Gold nuggets are present in three morphologies rounded grains, sheet and wire with dimensions that vary from few microns to 2 mm. Gold crystals inter-grown with quartz have also been found. The chemistry of the nuggets was analysed by SEM-EDS, the composition varies from pure gold to Au-Ag alloy. Most of the nuggets are electrum and minor zoned grains were found.

Quartz is the most abundant silicate phase present in the sediments. Iron oxides/hydroxides fill cracks or coat irregularly the quartz crystals. Garnets are andradite end-member with lattice parameter $a$ = 12.064(2) Å as obtained by single-crystal X-ray diffraction. Calcic amphiboles and augitic pyroxenes have been recognised by SEM analysis. Epidote with perfect morphologies are found in the smallest fraction sizes. Tourmalines have a dravite-schorl composition with lattice parameters $a$ = 15.973(3) Å, $c$ = 7.158(6)Å and hydiomorphic habitus.

Zircons are present as hydiomorphic crystals of 100-300 microns in size concentrated in the heavy minerals fraction material, crystals of smallest dimension were found associated with quartz during the SEM observations.

Monazite prevails over xenotime. Monazite composition has almost equal amounts of La and Nd (0.2 a.p.f.u), Ce (1.3 a.p.f.u.) and low to absent presence of Th (0 - 0.03 a.p.f.u.).

Magnetite, haematite, ilmenite and rutile are the most common opaque or semi opaque heavy minerals in the placer. Ilmenite crystals have a Mn content between 0.03 to 0.12 a.p.f.u.

Rare hydiomorphic cassiterite, pyrite and cinnabar were found in the concentrated material.

# 4    Conclusions

The primary source of the minerals found in the placer cannot be easily inferred because of the lacking of detailed geological and geochemical studies of the Lepaguare river drainage system. Nevertheless the presence of gold-bearing quartz vein mineralization (Cannan mine) in the Lepaguare mining district has been reported by Menichetti et al (2007), Bersani et al (2009). Further studies (including fluid inclusions study) are in progress to compare the gold placer deposit to the Canaan gold quartz-vein mineralization.

# Acknowledgements

# References

Bersani D, Salvioli-Mariani E, Mattioli M., Menichetti M, Lottici PP (2009) Raman and micro-thermometric investigation of the fluid inclusions in quartz in a gold-rich formation from Lepaguare mining district (Honduras, Central America). Sectroch Acta part A 73:443-449

Menichetti M, Mattioli M, Renzulli A, Salvioli-Marinai E, Martens U (2007) Contesto strutturale, mineralogia e geochimica di giacimenti auriferi in Honduras Centrale. Rend Soc Geol It 4:255-258.

Nelson C, (2007) Metallic mineral resources. Bundschuh J, Alvarado G E Eds Central America: geology, resources and hazard.

# A comparative automated mineralogical analysis of the Nkout (Cameroon) and Putu (Liberia) iron ore deposits

**K.F.E. Anderson, G.K. Rollinson, F. Wall & C. J. Moon**
*Camborne School of Mines*
*College of Engineering, Mathematics and Physical Sciences*
*University of Exeter, Cornwall Campus*
*Penryn, TR10 9EZ*
*United Kingdom*
*Email: kelloandy@yahoo.com*

**Abstract.** The Nkout and Putu iron ore deposits form part of an emerging iron ore region in Central and West Africa. This study aimed to improve the understanding of the mineral deposits in order to predict the metallurgical and environmental responses of the ores. Quantitative mineralogical and geochemical analysis was carried out using automated mineralogy (QEMSCAN®) and the results corroborated with other techniques. The QEMSCAN® species identification protocol developed during the project includes three goethite entries; goethite/limonite, goethite (Al) and goethite (P) and, importantly, a procedure was developed to separate the different Fe-oxides based on their backscattered electron coefficients, thus overcoming one of the main problems in using QEMSCAN® analysis for iron ores. Magnetite was found to be dominant in the weathered profile at Nkout whist hematite is dominant at Putu. Goethite (Al) and chamosite occur as minor minerals at Putu whist goethite (P) occurs in trace quantities. All but goethite (P) occur as major minerals at Nkout. Chamosite is shown to affect the liberation of the iron oxides. The main gangue minerals at Nkout are gibbsite (Al Ox/OH) and quartz whilst quartz is the main gangue at Putu. Apatite is a minor mineral in the magnetite itabirite of both deposits.

**Keywords.** Automated Mineralogy, Iron ores, Fe-oxides, Central / West Africa

## 1 Introduction

The Nkout and Putu iron ore deposits form part of a growing region for the development and production of iron ore deposits in Central and West Africa. The growth of these regions is the result of three main factors; a) they are strategically located to markets in China, Europe and North America compared to either or both of the major suppliers, Brazil and Australia, b) renewed interest in magnetite deposits that can be used for pellet production suitable for blast furnace and c) these regions have been stable for the past decade after years of rebel insurrections making them attractive for investment.

This study aims to improve the mineralogical understanding of these mineral deposits in order to predict the metallurgical and environmental responses of the ores. Quantitative mineralogical analysis of samples from both deposits has been done using automated mineralogy (QEMSCAN®) and the results corroborated with other techniques such as optical microscopy, X-ray diffraction (XRD), X-ray fluorescence (XRF) and electron probe microanalysis (EPMA). A particular aim of the study was to establish a protocol to overcome the difficulty of identifying hematite and magnetite by the QEMSCAN® technique.

## 2 Geology of the Study Areas

### 2.1 Regional Geology

Southern Cameroon is underlain by an Archean to Proterozoic cratonic basement which extends across parts of several West and Central African countries. This basement forms part of the northern extension of the Congo craton and the rocks include quartzites, schists, amphibolites, charnockites, greenstones, granulites and gneiss (Tagne-Kamga 2003). The banded iron formations (BIF) in the region are Archean, hosted by greenstones, and associated with granites and gneiss of similar age.

The Republic of Liberia rests on the Archean West African shield. In Liberia it has been intensely folded and faulted. The dominant rock types in the West African shield are granites, schist and gneiss. The rock types in the northern and western parts of Liberia are mainly gneiss units with siliceous BIFs and schist which are Liberian (2.7 Ga) in age (Tysdal, 1978).

### 2.2 Deposit Geology

According to ground magnetic survey (conducted by one of the authors), Nkout consists of a cap of laterite and saprolite material with a lateral extent of about 9 km E-W, enriched in iron oxide over magnetite rich BIF (itabirite). Itabirite is a term that originated from the province of Itabirito (Pico de itabirito), in the state of Minas Gerais in Brazil which hosts major banded quartz hematite magnetite metamorphosed oxide facies banded iron formations. The BIF at Nkout is hosted by greenstones and has been tilted towards the north. The magnetite itabirite forms the bulk of the deposit.

The Putu deposit is divided into two mountain ranges with different trends; Jideh has a NNW – SSE trend with a lateral extent of about 15 km and Montroh has an E – W trend and a lateral extent of about 4 km. The dominant rock type in the area is the granodiorite gneiss.

Iron minerals within the Putu deposit consist predominantly of magnetite-itabirite. A thick layer of hematite-itabirite lies over the magnetite-itabirite minerals in the Jide mountain range. The itabirites are mainly fine grained and composed or quartz, iron oxides and minor silicates. Magnetite is the main iron-oxide but Jideh in particular is known to have a hematite cap of up to 80m thick with potential to be used as a direct shipping ore (DSO).

## 3 Classification of Material Types

Thirty three drill cores representative of the Nkout deposit based on detailed core logs were selected and sampled. They include saprolites, laterites and fresh BIF. Outcrop and grab samples were also collected during mapping of the area and nine were selected for analysis. Nine coarse rejects samples representative of the Putu deposit were selected by the chief geologist at the time and sent along with eleven representative BIF drill cores for analysis.

Both sets of samples were divided into 4 main groups based on the whole rock Fe content determined by XRF analysis and their degree of weathering. The groups are enriched material (EM), weathered magnetite itabirite (WMI), transitional magnetite itabirite (TMI) and magnetite itabirite (MI). The magnetite itabirite group is divided into 2 groups; high-grade (HMI) and low-grade magnetite itabirite (LMI). The degree of weathering which is an expression of the physical characteristics of the ore grade materials is classified using an intensity of weathering (WI) on a scale of 1 to 6. 1 and 2 represents hard materials such as fresh itabirite or hard massive hematite and BIF outcrops, 3 and 4, medium hard materials and 5 and 6, friable biscuity or lateritic material. Table 1 gives the adopted classification.

**Table 1.** Classification scheme adopted for this research. It is based on the total Fe content and a weathering index of 1 to 6 in which 1 represents fresh itabirite and 6, completely weathered material.

| Code | Material Types | Description |
|------|----------------|-------------|
| EM | Enriched material | $\geq 60$ wt%, WI = 2 to 6 |
| WMI | Weathered magnetite itabirite | 50 wt% $\leq$ Fe < 60 wt%, WI $\geq 4$ |
| TMI | Transitional magnetite itabirite | 15 wt% $\leq$ Fe < 50 wt%, WI = 3 or 4 |
| MI | High-grade magnetite itabirite | Fresh itabirite, 30 wt% $\leq$ Fe < 60 wt%, WI = 1 or 2 |
| MI | Low-grade magnetite itabirite | Fresh itabirite, 15 wt% $\leq$ Fe < 30 wt%, WI = 1 or 2 |

## 4 Methodology

XRF analysis was conducted at Omac Laboratory, Ireland. QEMSCAN® and all other analyses were conducted at Camborne School of Mines, University of Exeter. The original LCU5 SIP file that was provided with the QEMSCAN® was modified based on the geology of the study area and the results of analyses by EPMA, XRD, SEM/EDS and optical microscopy.

The modified SIP includes 3 goethite entries: goethite/limonite, phosphorus bearing and aluminium bearing goethite i.e., goethite (P) and goethite (Al) respectively. This is because EPMA confirmed the presence of Al and P within the goethite in the study areas; a result also confirmed previously for goethite in general (Ramainadu 2008). Goethite (P) contains > 3% P and < 3% Al, Goethite (Al) contains < 3% P and > 3% Al whilst goethite/limonite contains < 3% P and Al. Three percent is the detection limit of the QEMSCAN® settings used in this study. Chamosite, the Fe-rich chlorite was separated from the others i.e. clinochlore (Mg-rich) and pennantite (Mn-rich). Chamosite was found to be present and is intergrown with the Fe-oxides, mainly goethite and hence affected liberation of the Fe-oxides.

One of the main problems in using QEMSCAN® analysis on iron ores is that there is only a 3 wt% difference in the Fe-oxide content of magnetite and hematite and so the 1000 count x-ray spectra used in this technique do not contain enough counts to be able to distinguish the two minerals (e.g. Andersen et al 2009). In order to overcome this, a procedure was developed to separate hematite and magnetite based on their backscattered electron signal (BSE). The BSE range is calibrated to quartz at the lower end (42) and gold at the top end (232). For this research, magnetite is from 89 to 100 and hematite is from 80 to 88. Geothite is less than 80 and includes limonites at the lower range (about 50 or less).The BSE will vary between QEMSCAN® systems (Tonzetic & Dippenaar 2011) and so the signal needs to be carefully set up and calibrated.

The garnet group was divided into two, almandine and andradite because it was noted from EPMA and XRD analysis that almandine was present at Nkout whilst andradite was present at Putu. The issues such as edge effects and variation in BSE signals identified by Rollinson et al. (2011) and Benedictus and Horsch (2008) where considered during the data processing stages.

## 5 Results

### 5.1 Modal Mineralogy

The QEMSCAN® back calculated Fe% in general decreases with decreasing size fraction i.e. decreases from -250/+180 to -125/+90 to -63/+45. Of these three size fractions, the -63/+45 gave back calculated Fe % that is ± 3 % that obtained for the XRF but could be greater when quartz is one of the most abundant minerals in the sample. The other two size fractions gave QEMSCAN® back calculated Fe% higher than the error margin of the -63/+45 fraction. Differences between the XRF and QEMSCAN® are expected due to the differences in techniques and particle sizes. Figure 1 summarises the modal mineralogy, expressed in weight percentages, for the samples from Nkout and Putu. The major difference between the two study areas in terms of the Fe-oxides is the higher concentration of magnetite at

Nkout whereas hematite is higher at Putu in the enriched material to transitional magnetite itabirite. Goethite/limonite is the most abundant goethite at Putu and Nkout. However goethite (Al) and chamosite are limited to the enriched material whist goethite (P) occurs in trace quantities at Putu. Goethite (P) occurs in minor quantities at Nkout but goethite (Al) and chamosite occurs as major minerals in the enriched material to transition magnetite itabirite.

The Al content of the enriched material to the transitional magnetite itabirite at Nkout is higher than that at Putu due to the presence of Al Ox(OH) which is present mainly in the enriched material at Putu. In the magnetite itabirites, the Al is present in the form of the aluminosilicates in both study areas. CaO is higher at Putu mainly due to the higher concentration of Ca Mg Fe silicates (Figure 1). The same trend in which $SiO_2$ increases from the enriched material to the low-grade magnetite is present in both localities and is due to the quartz content. The loss on ignition in general decreases from EM to the magnetite itabirites in both study areas but is higher at Nkout mainly due to its higher goethite concentration.
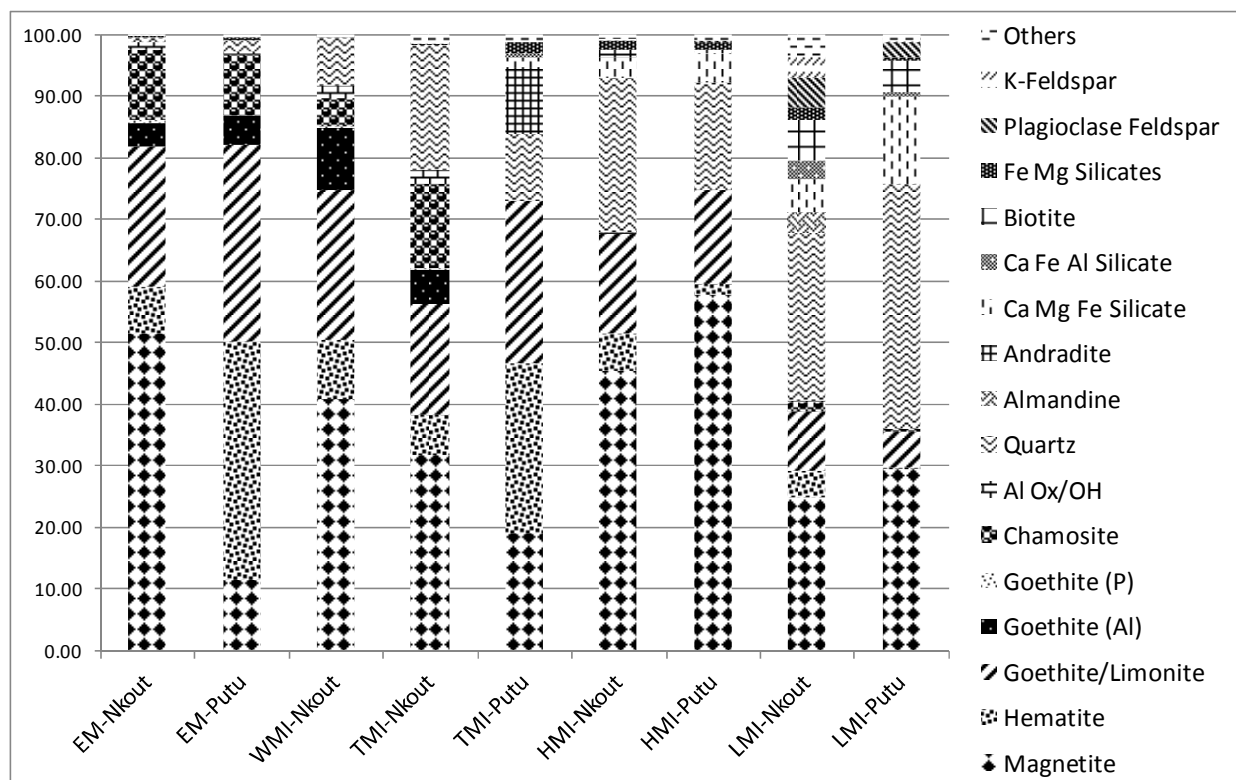


**Figure 1.** Summary of the modal mineralogy (weight %) of the Nkout and Putu deposits. Similar material types are placed side by side for easy comparison. Note that WMI-Putu is absent as none of the samples from Putu fit into this category. See Table 1 for explanations of the material types.

## 5.2 Mineral Association and Liberation

The mineral association is calculated using the QEMSCAN® software to determine which minerals are adjacent for a given particle. The liberation data is classified into 10 % intervals and is based on the weight of a particular mineral in each particle. For this research, a mineral is considered as being liberated if > 90% is free, high grade inter-grown if it is 60-90%, low grade inter-grown if 30-60% and locked if it is < 30%. Both the mineral association and liberation are considered with respect to the modal mineralogy.

The Fe-oxides are closely associated at both localities with magnetite and hematite being about 60% associated. When chamosite is present in both localities, it is mainly associated with Fe-oxides (goethite/limonite in particular) and reduces liberation of the Fe-oxides as illustrated in Table 2 and Figure 2.

**Table 2.** Modal mineralogy weight % data for 4 enriched material samples. The samples with high chamosite have poorer liberation, see Figure 2.

| ID | Mag | Gt/ Lim | Hem | Chm | Qtz |
|---|---|---|---|---|---|
| G02 | 54.34 | 35.07 | 4.68 | 0.09 | 0.03 |
| NCS04 | 35.49 | 16.17 | 3.68 | **31.85** | 1.19 |
| NES04 | 56.81 | 14.74 | 8.51 | **13.67** | 0.18 |
| OUT02 | 59.37 | 24.58 | 13.47 | 0.04 | 2.35 |

In Table 2, the second and third samples have higher chamosite concentration than the first and fourth and this is reflected in the liberation of the Fe-oxides in Figure 2.

Whereas almandine is mainly associated with chamosite at Nkout, andradite at Putu is mainly associated with goethite/limonite. Quartz in both localities is mainly associated with the Fe Mg silicates such as the serpentine group (antigorite).
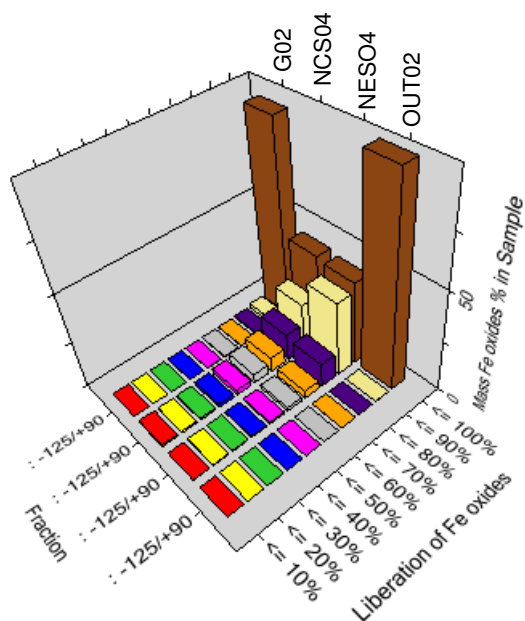
**Figure 2.** Liberation for 4 enriched samples. Note that the 2 samples in the middle have higher chamosite (Table 2) concentration compared to the other 2 on the edges.

For the -125/+90 fraction, as far as the Fe-oxides are concerned, about 36% of magnetite are > 90 % liberated and 57 % are high-grade inter-grown. When magnetite, hematite and the different goethite are combined as Fe-oxides, liberation is > 90 %.

## 6 Conclusions

- The Nkout and Putu deposits consist of iron oxide minerals with no evidence of iron carbonates. Iron sulphides are present mainly in the form of pyrite which is restricted to minor quantities in the magnetite itabirites.

- Hematite is the main Fe-oxide in the enriched material to transitional magnetite itabirite at Putu whereas at Nkout it is magnetite. Magnetite content in the enriched material at Nkout is about 5 times than at Putu whilst for the hematite content the reverse is true with Putu having about 5 times more than Nkout.

- Goethite (Al) and goethite/limonite occur in about equal quantites in the enriched material at Nkout and Putu. Problems with goethite (Al) at Nkout are more noticed in the transitional magnetite itabirite with Nkout having about 105 times than in Putu. Goethite (P) occurs as a trace mineral in the enriched material at Putu but could be significant from a processing point of view at Nkout where it occurs as a minor mineral in the enriched material and weathered magnetite itabirite.

- Chamosite which has been shown to affect liberation of the Fe-oxides is a major mineral at Nkout in all but one of the material types whereas at Putu,it is only a major mineral in the

enriched material. Chamosite occurs in similar proportions in the enriched material but differs significantly in the transitional magnetite itabirite with Nkout having about 156 times more than Putu.

- The main gangue minerals in the enriched material to transitional magnetite itabirite at Nkout are gibbsite (Al Ox/OH) and quartz. Quartz is the main gangue at Putu.

- Apatite is the P-bearing mineral in the magnetite itabirite at both Nkout and Putu and occurs as a minor mineral associated with the silicates. Calcite occurs as a minor mineral in the magnetite itabirite at Putu and occurs in trace quantities at Nkout.

- Magnetite occurs in about equal propotion in the magnetite itabirite at Putu and Nkout. The magnetite itabirite is the main ore material at both Nkout and Putu. The liberation of the Fe-oxides as a group for the -125/+90 µm size fraction is about 90 % making them amenable to inexpensive processing such as crushing, grinding and magnetic separation. The Al Ox(OH) at Nkout could be removed by attrition scrubbing.

## Acknowledgements

## References

Andersen JCØ, Rollinson GK, Snook B, Herrington R, Fairhurst RJ (2009) Use of QEMSCAN for the characterization of Ni-rich and Ni-poor goethite in laterite ores. Minerals Engineering 22 1119-1129. doi:10.1016/j.mineng.2009.03.012

Benedictus A, Horsch H (2008) Enhanced measurement capabilities for iron ore deposits 34th Int. Geol Congr, International Union of Geol Sciences. Brisbane, Australia.

Ramanaidu E, Wells M, Belton D, Verrall M, Ryan C (2008) Mineralogical and Microchemical Methods for the Characterization of High-Grade Banded Iron Formation-Derived Iron Ore. Soc Econ Geol, SEG Reviews 15: 129-156

Rollinson GK, Andersen JCØ, Stickland RJ, Boni M, Fairhurst R (2011) Characterisation of non-sulphide zinc deposits using QEMSCAN. Minerals Engineering 24: 778-787. doi:10.1016/j.mineng.2011.02.004

Tagne-Kamga G (2003) Petrogenesis of the Neoproterozoic Ngondo Plutonic complex (Cameroon, west central Africa): a case of late-collisional ferro-potassic magmatism. Journal of African Earth Sciences 36:149-171. doi:10.1016/S0899-5362(03)00043-5

Tonžetić I, Dippenaar A (2011) An alternative to traditional iron-ore sinter phase classification. Minerals Engineering 24 1258-1263. doi:10.1016/j.mineng.2011.04.012

Tysdal RG (1974) Geology of the Juazohn Quadrangle, Liberia. United States Geological Survey.

# Mineralogical characterization of REE mineralization in Norra Kärr alkaline complex, Sweden

**Petya Atanasova**
*Helmholtz Institute Freiberg for Resource Technology*
*Technical University Bergakademie Freiberg*

**Joachim Krause**
*Helmholtz Institute Freiberg for Resource Technology*

**Jens Gutzmer**
*Helmholtz Institute Freiberg for Resource Technology*
*Technical University Bergakademie Freiberg*

**Abstract.** Alkaline complexes comprise one of the most promising future sources for rare earth element supply. They are particularly enriched in heavy rare earth elements. However, the often complex and highly unusual mineralogy of REE-enriched ores from alkaline complexes pose particular challenges for beneficiation. A geometallurgical approach is required to quantify mineralogical and textural diversity and variability. Based on a geometallurgical model, a suitable approach to beneficiation can be developed. Scanning electron microscope (SEM)-based image analysis can be used to characterize ores as well as beneficiation products. A wide range of tangible mineralogical and textural parameters are constrained for every ore type, including mineral abundance, grain size, and liberation. SEM-based image analysis combined with a quantitative analysis of the chemical composition of the ore minerals is illustrated here for the case of the Norra Kärr alkaline complex, Sweden. Current research focuses on quantitative mineralogical and textural constraints for different lithological domains recognized in the HREE-Zr-mineralized zones of the complex. Based on the results, a geometallurgical model will be developed that will be based on the processing characteristics of the different portions of the mineralized zones.

**Keywords. rare earth elements, alkaline complex, geometallurgy, eudialyte, nepheline-syenite**

## 1 Introduction

The Norra Kärr rare metal deposit in Southern Sweden represents one of the largest resources of rare earth elements (REE) in Europe. The Norra Kärr REE mineralization is notably enriched in the coveted heavy REE (HREE) and has been granted by the Geological Survey of Sweden a "national interest" status. The intrusion was first discovered by the Swedish Geological Survey in the early years of the 20th century and first described by A. E. Törnebohm in 1906. Since its discovery it has been explored – and on a small scale exploited - for nepheline, Zr and Hf. Since August 2009 Tasman Metals pursues an exploration program that focuses on rare metals mineralization, in particular HREE, in the intrusion. Currently, resources in the deposit are 41.6 Mt @ 0.57 % TREO (total rare earth oxide) with 51 % HREO/TREO and 1.7 % $ZrO_2$ (indicated) and 16.5 Mt @ 0.64 % TREO with 49 % HREO/TREO and 1.7 % $ZrO_2$ (inferred).

The mineralization is hosted by aegirine nepheline-syenites that show a considerable textural and compositional diversity. REE-bearing minerals include eudialyte group minerals (EGM) and very minor mosandrite and britholite. Zr is hosted by Zr-silicates catapleiite and EGM.

## 2 Geology

The Norra Kärr deposit is hosted by a metamorphosed and deformed, peralkaline nepheline syenite intrusion, which covers an area of 350 m by 1100 m. This intrusion is situated within a suite of Proterozoic gneisses and granites referred to as the Växjö Granite. The Växjö Granite belongs to the Trans-Scandinavian Igneous belt (1.85-1.65 Ga); the age of the peralkaline intrusion is rather poorly constrained at about 1545 ± 61 Ma (Blaxland 1977, recalculated by Welin 1980). Gross magmatic layering and orientation of early deformation fabrics suggest that the intrusion was emplaced as a sill within the granitic basement (Rankin 2011, unpublished report). The granitoid rocks close to the contact to the peralkaline intrusion exhibit signs of fenitization (Adamson 1944, Eckermann 1968).

The Norra Kärr nepheline syenite and the surrounding basement have been deformed by weak to moderate N-S directed compression under ductile conditions (Rankin 2011). This late-stage fold event has produced rhombic bulging and necking of the intrusion. The body is preserved within an overturned synformal hinge. The intrusion has undergone not only modification of its shape by 3 phases of folding, but also possible transport of the body from its original emplacement locus by both N-S movement and E-vergent movement. In addition, the overprinting of the regional NNE-trending structural corridor by later episodes of extensional faulting also obscures the original geometry.
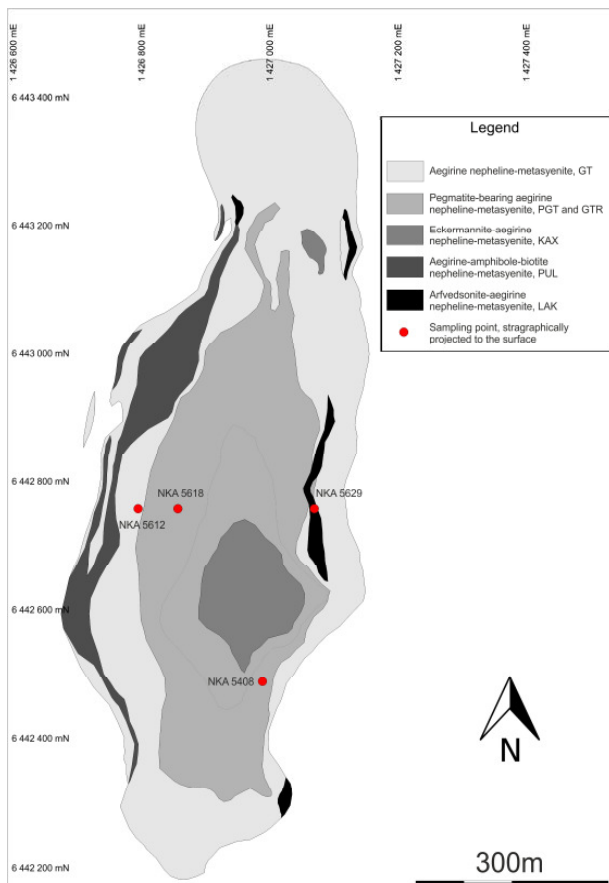
**Figure 1.** Simplified geological map of the Norra Kärr intrusive complex showing main lithologic units and sampling locations (red dots) extrapolated on the surface (after Tasman Metals).

The lithotypes that comprise the intrusion are mostly identified by local names only; they share an agpaitic composition but their spatial and genetic relationship remains unclear at present. The most common lithotype present is best described as a fine to medium grained aegirine-nepheline metasyenite consisting of alkali feldspar, nepheline, aegirine, natrolite, eudialyte and catapleiite (referred to as grennaite by Adamson 1944 and Blaxland 1977). Less common lithotypes include arfvedsonite-aegirine nepheline-metasyenite (lakarpite), eagirine-arfvedsonite-biotite nepheline-metasyenite (pulaskite) and eckermannite-aegirine nepheline-metasyenite (kaxtorpite). Exploration has revealed that much of the rare metal mineralization is associated with pegmatitic intervals within the complexly zoned intrusion, suggesting an important influence of fractional crystallization, recrystallization and (fluid-induced?) re-mobilization on the character and distribution of rare metal mineralization. Mineralogical studies have shown REE bearing minerals to include eudialyte group minerals (EGM) and minor mosandrite and britholite. Beside the EGM, the Zr-silicate catapleiite hosts a large proportion of the zirconium.

## 3 Analytical Methods

Drill core samples were collected from different parts of the Norra Kärr intrusion. Samples were selected to illustrate different degrees of alteration and styles of mineralization (as diagnosed by macroscopic appearance only). Analysed samples represent different eudialyte-bearing aegirine-nepheline metasyenites.

Carbon coated polished thin sections were analysed with a Mineral Liberation Analyser (MLA) and an Electron Microprobe at the Department of Mineralogy of the TU Bergakademie Freiberg. MLA studies were utilised using a FEI MLA Quanta 600F scanning electron microscope equipped with a field emission source and two energy dispersive X-ray spectrometers (Bruker AXS Xflash® 5010) combined with an image analysis software (Fandrich et al. 2007). A working distance of 12 mm and an acceleration voltage of 25 kV were used for all analyses via 'XBSE and GXMAP' measurement modes at a magnification of 175.

Electron microprobe (EMP) measurements were performed with a JEOL JXA 8900RL equipped with five wavelength dispersive spectrometers (WDS). Point analyses were done with an accelerating voltage of 20 kV, a beam current of 20 nA using a defocussed beam of 20 µm diameter. Dwell times varied between 10 and 100 s for both peak and background. Natural and synthetic minerals were used for calibration. X-ray element distribution maps were recorded with an acceleration voltage of 20 kV, a beam current of 105 nA and a beam diameter of 10 µm. The dwell time and stepsize were set to 0.15 s and 10 µm respectively.

## 4 Results and Discussion

### 4.1 Mineral liberation analyses (MLA)

Modern analytical tools, such as SEM-based image analysis, are thus used to quantitatively characterize ores and products of mineral processing. Eudialyte group minerals (EGM) and catapleiite are the most abundant ore minerals in the studied samples. However, minor mosandrite and britholite, which are highly enriched in the LREE, are also detected and quantified in the different lithological units. Preliminary results indicate variable catapleiite contents (0.5 – 3.0 wt.%) within the intrusion. Eudialyte contents range from 2 - 5 wt.% in the aegirine nepheline-metasyenite to 12 – 19 wt.% in the pegmatite-bearing unit. The highest mosandrite contents (up to 0.2 wt.%) are detected within the GT, whereas britholite is more common in the PGT (0.1 wt.%).

MLA classified-color images (e.g. XBSE or GXMAP mode) of eudialyte- and catapleiite-bearing eagirine nepheline-syenites provide information of chemical zonation, crystall intergrowths and overgrowths and allow to resolve complex microstructures (see Fig. 2). The information can be used for more precise elemental analyses (e.g. REE) by WDS electron microprobe or LA-ICP-MS for better characterization of elemental variations.

**Table 1.** Main minerals occurring in different eudialyte-bearing lithotypes from Norra Kärr deposit

| Mineral | Average conc. wt % | Formula |
|---|---|---|
| Albite | 18 | $NaAlSi_3O_8$ |
| Nepheline | 17 | $Na_{0.75}K_{0.25}Al(SiO_4)$ |
| Microcline | 16 | $KAlSi_3O_8$ |
| Leakeite | 15 | $NaNa_2(Mg_2Fe_2Li)Si_8O_{22}(OH)_2$ |
| Zeolite | 11 | $Na_2Al_2Si_3O_{10} \cdot 2H_2O$ |
| Eudialyte | 11 | $Na_4(Ca,Ce)_2(Fe,Mn,Y)ZrSi_8O_{22}(OH,Cl)_2$ |
| Aegirine | 5.7 | $NaFe(Si_2O_6)$ |
| Catapleiite | 1.9 | $(Na,Ca)_2ZrSi_3O_9*2(H_2O)$ |
| Anorthoclase | 0.3 | $(Na,K)AlSi_3O_8$ |
| Britholite | 0.05 | $(Ce,Ca,Th,La,Nd)_5(SiO_4,PO_4)_3(OH,F)$ |
| Mosandrite | 0.03 | $Na(Na,Ca)_2(Ca,Ce,Y)_4(Ti,Nb,Zr)(Si_2O_7)_2(O,F)_2F_3$ |

Furthermore, depending on grind coarse and fine grained complex intergrown eudialyte- and catapleiite-bearing particles are well liberated or still locked (Fig. 3). The data provide information on mineral locking and mineral liberation, which helps sceening mineral processing routes.
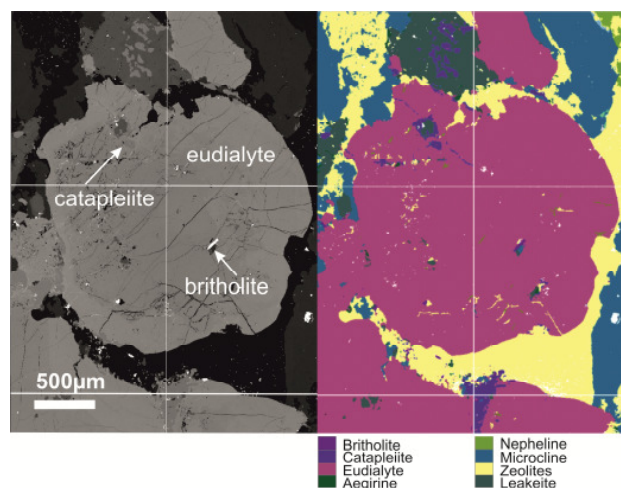


**Figure 2.** Illustrated here are MLA (Mineral Liberation Analyser) images of REE- and Zr-rich pegmatite-bearing aegirine nepheline-syenite (GTR). BSE and EDS-XBSE classified-color images show zoned EGM intergrown by catapleiite and britholite.
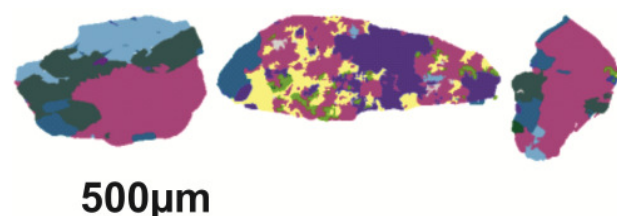


**Figure 3.** Eudialyte- and catapleiite-bearing particles complexly intergrown with other mineral phases. For color coding see Fig. 2.

## 4.2 Microprobe analyses of REE bearing eudialyte group minerals

Eudialyte group minerals from different lithological domains of the Norra Kärr intrusion, including very fine grained aegirine-nepheline metasyenite (GT), medium to coarse grained aegirine-nepheline metasyenite (GTR, GTP respectively) as well as arfvedsonite-aegirine nepheline-metasyenite (LAK) are analysed by electron microprobe. Preliminary results based on four representative samples confirm the enrichment and variability of rare earth elements, yttrium and zirconium within the different lithological domains. Different ore types show diverse geochemical distribution patterns and probably different geometallurgical properties and requirements for beneficiation.

The finer grained ore-bearing unit GT is more enriched in HREE and Y compared to the coarser grained mineralized units GTP and GTR, which show similar REE+Y concentrations (Fig. 4). The less mineralized arfvedsonite-aegirine nepheline-metasyenite LAK contains the smallest proportion of REE and is not of economic interest yet.
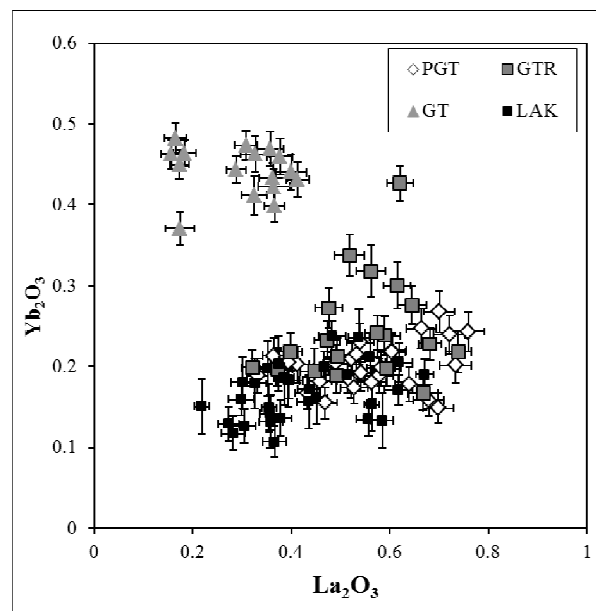


**Figure 4.** Correlation diagram of selected rare earth element oxides (including 2 sigma standard deviation) showing HREE enriched eudialytes from the aegirine nepheline-metasyenite (GT), LREE enriched eudialytes from the pegmatite-bearing aegirine nepheline-metasyenite (GTP, GTR) and eudialytes with lower REE concentrations from the arfvedsonite-albite nepheline-metasyenite (LAK)

In addition, rare earth elements and yttrium show complex distribution patterns within the eudialyte group minerals (Fig. 5). Concentrations of both Ce and Y in large areas of the central part of EGM are low, increasing towards the rim. While Y shows only a narrow, few micrometers wide zone of enrichment at the rim, the zone of enrichment is several 10s micrometers wide for Ce. In contrast other areas of the crystals show elevated contents in both elements with discrete contacts which truncate the above described core-rim zonation. While the increasing Ce and Y concentrations from core to the rim likely reflect the enrichment during

fractionation, the more complex zonation patterns indicate an important influence of recrystallization and/or fluid-induced remobilization on the character and distribution of rare metals mineralization.
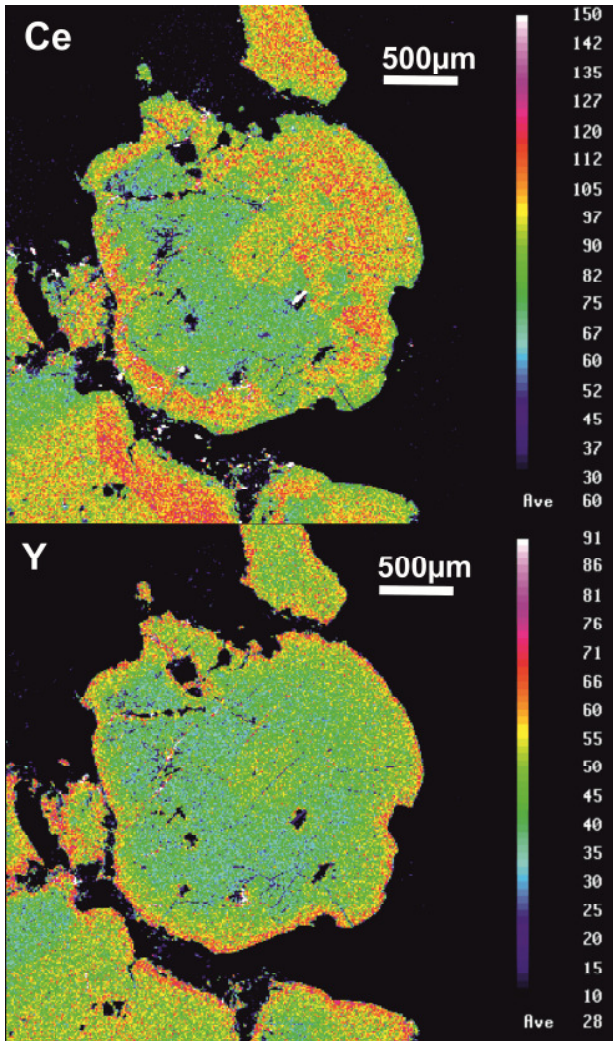


**Figure 5.** WDS electron microprobe elemental mappings illustrating complex elemental distribution of Ce and Y within EGM of the medium grained pegmatite-bearing aegirine nepheline-metasyenite GTR.

## 5 Conclusion

The use of MLA allows detection of HREE- and Zr-bearing minerals including the eudialyte group minerals, catapleiite, britholite and mosandrite. However, complex distribution patters of REE are only detected by microprobe analysis. Results indicate that MLA studies can be improved by integration of quantitative elemental analyses and microprobe element distribution maps.

### Acknowledgements

## References

Adamson OJ (1944) The petrology of the Norra Kärr district, An occurrence of alkaline rocks in Southern Sweden.

Blaxland AB (1977) Agpaitic magmatism at Norra Kärr? Rb-Sr isotopic evidence. Lithos 10/1:1-8

Eckermann H (1968) New contributions to the interpretation of the genesis of the Norra Kärr alkaline body in Southern Sweden. Lithos 1:76-88.

Fandrich R, Gu Y, Burrows D, Moeller K (2007) Modem SEM-based mineral liberation analysis. Int J Miner Process 84:310-320. doi:10.1016/j.minpro.2006.07.018

Törnebohm A E (1906) Katapleiite-syenit, en nyupptäckt varietet af nefelinsyenit i Sverige. SGU Serie C 199:1-54.

Welin E (1980) Tabulation of recalculated radiometric ages published 1960–1979 for rocks and minerals in Sweden. Geologiska Föreningeni Stockholm Förhandlingar 101/4:309-320.

# Textural setting of gold and its implications on mineral processing: preliminary results from three gold deposits in northern Sweden

Glenn Bark & Christina Wanhainen
*Division of Geosciences, Luleå University of Technology, Luleå, Sweden*

Bertil I Pålsson
*Division of Sustainable Process Engineering, Luleå University of Technology, Luleå, Sweden*

**Abstract.** Within the European Union (EU27) the two most important gold producers are Finland and Sweden, covering more than two thirds of the European market. Due to the high gold prize mining companies are looking to extract more of the metal by improving recovery. We have done textural analysis on three gold-bearing deposits to better understand how the gold-textures seen in drill cores might affect the processing of different gold-ore types. In the Nautanen IOCG deposit, gold deportment is different whether gold is associated with pyrite or magnetite, and this must be considered when optimising the future mine and process planning. In the VMS-type Kristineberg deposit, the gold is associated with pyrite, sphalerite, and galena. Low gold recoveries from flotation could be explained by the occurrence of gold-inclusions in the pyrite. In the epigenetic Svartliden lode gold deposit, the gold is rather coarse-grained and associated with arsenopyrite-löllingite, and silicates. The relatively large grain size of gold can result in incomplete breakdown of the largest gold grains in the cyanide leaching process. To properly understand gold deportment in ores and to be able to improve mine planning and predict metal recoveries a comprehensive textural analysis of gold in drill core-samples is essential.

**Keywords.** Gold, ore texture, process mineralogy, in-situ analysis, northern Sweden

## 1   Introduction

Over the past few years the price of gold has been at a record high, which has resulted in an increased interest for gold exploration. The already producing mines are looking to increase their recovery of gold, and thereby maximize the profit of the mines. One important issue when trying to increase the recovery is to properly understand the textural setting and composition of the gold, as well as understanding the distribution of gold between different minerals. Many times the mining companies do not have sufficient knowledge of how the gold actually occurs within the ore.

From a metallurgical perspective, gold ores can be subdivided into free-milling and refractory ore types (Vaughan 2004; Zhou and Cabri 2004). The former type usually gives good gold recoveries (>90 %), whereas the latter, which are regarded as those where the gold is in some way not responding to traditional beneficiation, commonly give gold recoveries as low as 50 %.

The enrichment methods for gold are governed by the mineralogy, thus textural and mineralogical studies can assist and improve the mineral processing of these ores. Wet gravity methods can be used for all ore types, except when the gold is in solid solution, as inclusions, or too fine in size. The gold that occurs as inclusions in, or at grain boundaries between, sulphides cannot be recovered directly. If these gold-containing sulphides in themselves are winnable, like copper or lead minerals, they are won with flotation and the gold is extracted after smelting of the host mineral's concentrate. If the gold is in pyrite or arsenopyrite, the first step is to float a sulphide concentrate and then oxidise it (roasting, autoclave leaching, bacterial leaching) with a following cyanide leaching step on the oxidation residue. Sometimes the gold is merely in the grain borders of pyrite, and then gold may be leached directly, obviating the mineral oxidation step. If the gold is present as fine gold, tellurides or selenides, it is won by direct flotation with frothers only. In all cases, traditional mineral processing unit operations are present in the beneficiation chain, often combined with a hydrometallurgical enrichment step.
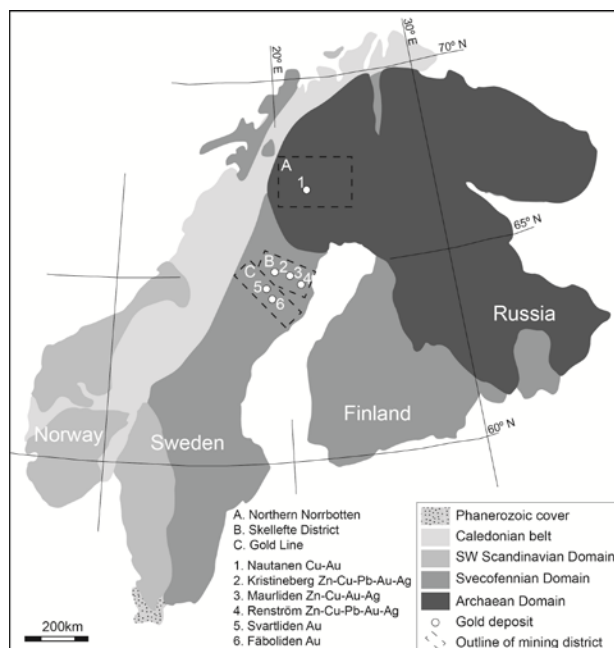


Figure 1. Geological map of the Fennoscandian Shield, modified after Rutland et al. (2001), with the studied mining districts and deposits indicated.

To better understand the influences on mineral processing, and thereby improve recovery of gold, we investigate the textural relationships of gold in six

deposits in northern Sweden (Fig. 1). Detailed elemental identification and quantification of the gold-bearing phases and gold textures are presently work in progress. A regional scale study of gold textures in this region has not been undertaken previously. Here we present preliminary data from three of the deposits (Nautanen, Kristineberg, and Svartliden), one deposit from each mining district.

## 2 District and Deposit Geology

Northern Sweden hosts three important ore districts; 1) Northern Norrbotten, 2) Skellefte District, and 3) Gold Line (Fig. 1). The Northern Norrbotten ore province is important for production of iron, copper and gold in Europe. Economic deposits include apatite iron ores, epigenetic Cu-Au ores, skarn iron ores, and one stratiform Cu deposit (Billström et al. 2010). The district has also been the focus for exploration and research related to Fe-oxide Cu-Au mineralization during the last decades, and the Nautanen deposit has been a target.

The Skellefte District is situated to the south of the Northern Norrbotten ore province (Fig. 1), and hosts more than 85 known massive sulphide deposits, which commonly are Au-rich, and also a few vein-style Au deposits and Cu-Au-Mo porphyry deposits (Rickard and Zweifel 1975; Allen et al. 1996). Since 1924, more than twenty deposits have been mined in the Skellefte District, and besides the large Kristineberg VMS deposit four other deposits are presently in production.

Southwest of the Skellefte District a relatively new gold ore province, the so called Gold Line, is presently being exploited. During the past couple of decades tens of gold occurrences have been discovered in this area. Advanced prospects such as Fäboliden and Stortjärnhobben have been granted mining permits, but presently only one deposit is in production, the Svartliden gold deposit.

*Nautanen Cu-Au deposit*
During the period 1902 to 1907, 72 ktonnes of ore containing 1–1.5 % Cu and some Au were mined in the Nautanen area (Geijer 1918). The economic potential of the Nautanen area has subsequently been investigated by several exploration companies, and in 2009 the property was claimed by Boliden Mineral AB, who also owns the nearby world-class Aitik Cu-Au deposit. The Nautanen deposit has an estimated reserve of ca. 0.6 Mt with 2.4 % Cu, 1.3 ppm Au, 11 ppm Ag (Danielsson 1985), and is considered an iron oxide-copper-gold deposit (Billström et al. 2010). There is generally a positive correlation between Cu and Au, and high gold grades are rarely found without significant Cu mineralization (Martinsson and Wanhainen 2004).

*Kristineberg Zn-Cu-Pb-Au-Ag deposit*
In the western part of the Skellefte District the Kristineberg deposit has been in production since 1941. The annual production is ca. 0.7 Mt of ore, containing 1.9 % Zn, 1.3 % Cu, 0.1 % Pb, 1.2 ppm Au and 24 ppm Ag (New Boliden 2012), which makes it the largest mine in the Skellefte District. The deposit constitutes several massive sulphide lenses. Some of these ore lenses are anomalously gold-rich, with late Au-Cu-rich veins and heavily disseminated sulphides amongst Zn-rich massive sulphide lenses (Årebäck et al. 2005).

*Svartliden Au deposit*
In the Gold Line ore province the Svartliden gold deposit has been in production since 2005. Mining in the open pit has recently been phased out, and the production is presently from underground. By 2011, ca. 2.1 Mt of ore at a grade of 4.5 ppm Au had been produced from the Svartliden deposit (Dragon Mining 2012). The Svartliden gold deposit is considered a structurally controlled epigenetic lode gold deposit (Hart et al. 1999), with many features resembling orogenic gold style mineralization. The mineralization is spatially associated with a banded iron-formation, situated at the contact zone between metasedimentary rocks and amphibolites.

## 3 Sampling and methods

Twenty-four samples were taken from nine different drill cores from the Nautanen, Kristineberg (L-zone) and Svartliden deposits. Based on assay data, gold-anomalous sections in drill cores were studied and samples representing different alteration- and mineralization assemblages within those sections were collected. Polished thin sections were prepared and a detailed examination was performed using conventional optical and scanning electron microscopy for phase identification and textural analysis.

## 4 Gold textures

*Nautanen Cu-Au deposit*
Samples from the Nautanen deposit represent strongly feldspar-mica-chlorite-altered metavolcanic rocks rich in magnetite, pyrite and chalcopyrite. In these samples, gold grains are generally <30 μm and associated with chalcopyrite and Bi-phases. The gold grains are commonly situated within chalcopyrite at the boundary to pyrite, but also as inclusions and fracture fillings within pyrite (Fig. 2A, B). Other sulphides, e.g. galena, are occasionally intergrown with the gold (Fig. 2A). Gold grades of the Nautanen samples range between 0.1 and 1.0 ppm, with a median value of 0.2 ppm.

*Kristineberg Zn-Cu-Pb-Au-Ag deposit*
At the Kristineberg deposit the studied samples represent tremolite-chlorite-altered quartzite from the L-zone, a complex ore lens situated 2 km west of the historic Kristineberg deposit. In these samples, gold grains are generally <20 μm and hosted by pyrite, sphalerite and galena (Fig. 2C, D). Some of the gold grains associated with sphalerite and galena are rich in silver (>50 % Ag). The gold-bearing sulphides are commonly intergrown with chalcopyrite, and *chalcopyrite disease* (replacement patches of chalcopyrite within sphalerite) is observed (Fig. 2C). Gold grades of the Kristineberg samples range between 0.3 and 5.8 ppm, with a median value of 1.8 ppm.
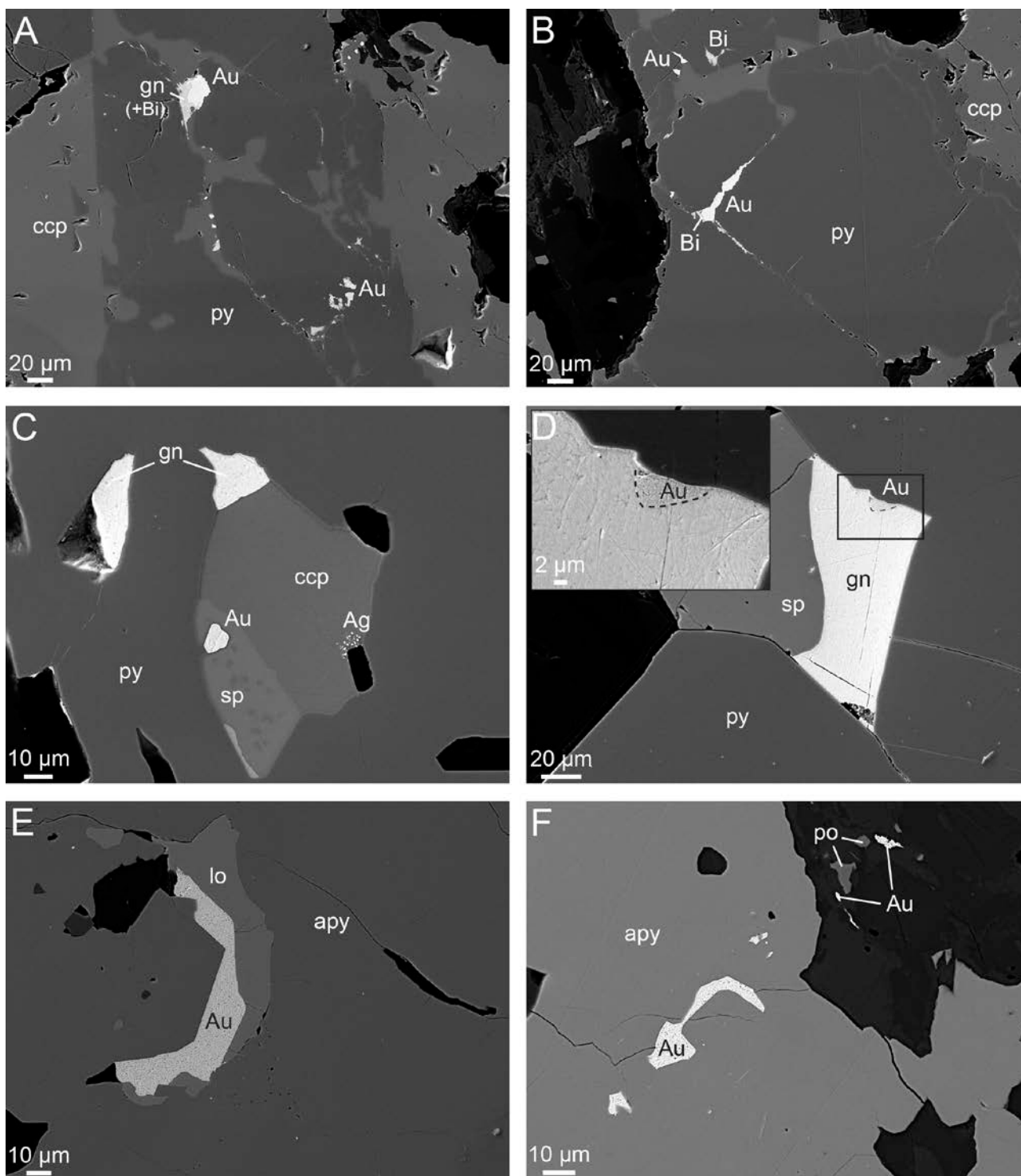
**Figure 2.** Scanning electron microscope images (secondary electrons) of selected samples from the Nautanen-, Kristineberg-, and Svartliden deposits. A) Nautanen; gold in chalcopyrite, intergrown with galena and an unknown Bi-mineral, and as inclusions in pyrite. B) Nautanen; gold, associated with an unknown Bi-mineral, as fracture fillings in pyrite, and associated with chalcopyrite. C) Kristineberg; gold as an inclusion in sphalerite that also hosts minute inclusions of chalcopyrite (e.g. chalcopyrite disease). Native silver occurs within the chalcopyrite. D) Kristineberg; gold associated with galena, at the contact to pyrite. E) Svartliden; gold hosted by a löllingite core within arsenopyrite. F) Svartliden; gold as inclusions in arsenopyrite, but also hosted by silicate minerals (top right). Mineral abbreviations: Ag – silver, apy – arsenopyrite, Au – gold, Bi – Bi-mineral, ccp – chalcopyrite, gn – galena, lo – löllingite, po – pyrrhotite, py – pyrite, sp – sphalerite.

*Svartliden Au deposit*
The Svartliden samples represent hydrothermally altered metasedimentary rocks and amphibolites. In these samples, gold grains are generally <100 µm and occurs within arsenopyrite-hosted löllingite inner cores, commonly at the boundary to arsenopyrite (Fig. 2E), and within arsenopyrite (Fig. 2F). Gold grains are also found among the groundmass silicates, usually in the vicinity of large arsenopyrite crystals (Fig. 2F). Gold grades of the Svartliden samples range between 0.2 and 13.2 ppm, with a median value of 8.4 ppm.

## 5 Discussion

A detailed ore characterization is fundamental for the planning and adjustment of metal extraction processes to improve recoveries and extract new by-products.

In Nautanen there is a strong correlation between gold and chalcopyrite, pyrite, and Bi-phases. Given the rather fine grain size of the Nautanen gold, which makes it less suitable for gravimetric extraction, it is crucial from a mine planning point of view to determine the amount of refractory gold within pyrite. Also the amount of gold associated with magnetite and groundmass minerals should be estimated, since these portions of gold could be lost to the tailings if a general flotation process setup, similar to the one in Aitik, will be applied for the Nautanen ore. A positive correlation between gold and magnetite, and gold and Co-rich pyrite has been observed previously (Hålenius 1983), and since Nautanen is rich in magnetite and pyrite, optional processes such as e.g. magnetic separation and extraction from a pyrite concentrate, may be considered if high concentrations of valuable metals such as Au and Co associated to these minerals are confirmed.

In the Kristineberg deposit, the dominating gold grain size is fine and gold grades vary substantially between ore lenses (Årebäck et al. 2005). Ore with a low gold grade is processed by wet gravity separation and flotation and has a gold recovery of 50–70 %, whereas ore with a high gold grade in addition is processed by leaching and has a gold recovery of ca. 90 %. Gold associated with galena and sphalerite (Fig. 2) is won, but gold hosted by pyrite, commonly occurring at grain boundaries between pyrite grains, is likely lost to the tailings unless leaching is done.

At Kristineberg, silver-rich gold (>50 % Ag) is associated with sphalerite and galena. Due to the greater reactivity of silver these silver-rich gold grains readily tarnish which might have a negative influence on the behaviour of gold during flotation and leaching processes, resulting in an inhibited gold recovery (Harris 1990; Zhou and Cabri 2004; Zhou et al. 2004).

The Svartliden deposit, with a gold recovery of ca. 91 % from a whole-ore Carbon in Leach process (Dragon Mining 2011), has an estimated gold grain size range of 5 to +100 µm, with an average grain size of ca. 45 µm (Eklund 2007; this study). Commonly, large gold grains suffer from incomplete breakdown in a cyanide leaching process, resulting in gold loss. Also, it is well known that pyrrhotite, which is part of the Svartliden ore mineral assemblage, acts as an oxygen consumer in cyanide leaching, and thereby slows down the process (e.g. Coetzee et al. 2011). With a slowed-down cyanidation process dissolution rates of gold decreases and the larger gold grains renders less-affected by the leaching (Harris 1990; Coetzee et al. 2011). To reduce this problem and thereby improve the recovery a pre-leaching wet gravity circuit may be considered for the sulphides. That way the largest gold grains may also be won.

As evident from these preliminary data, textural investigation by optical- and scanning electron microscopy of representative uncrushed ore samples is crucial when planning and optimising the mineral processing of ores.

## References

Allen RL, Weihed P, Svenson S-Å (1996) Setting of Zn-Cu-Au-Ag massive sulfide deposits in the evolution and facies architecture of a 1.9 Ga marine volcanic arc, Skellefte District, Sweden. Econ Geol 91: 1022-1053

Årebäck H, Barrett TJ, Abrahamsson S, Fagerström P (2005) The Palaeoproterozoic Kristineberg VMS deposit, Skellefte district, northern Sweden, part I: geology. Miner Deposita 40: 351-367

Billström K, Broman C, Eilu P, Martinsson O, Niranen T, Ojala J, Wanhainen C, Weihed P (2010) IOCG and related mineral deposits of the Northern Fennoscandian Shield. *In* Porter, T.M. (ed.), 2010 - Hydrothermal Iron Oxide Copper-Gold and Related Deposits: A Global Perspective, volume 4, Advances in the Understanding of IOCG Deposits, PGC Publishing, Adelaide. pp. 381-414

Coetzee LL, Theron SJ, Martin GJ, van der Merwe J-D, Stanek TA (2011) Modern gold deportments and its application to industry. Min Eng 24: 565-575.

Danielsson S (1985) Nautanen, geology and results from diamond drilling 1985: SGAB, Unpublished report, PRAP 85090, 15 p. (in Swedish)

Dragon Mining Annual Report 2011 (2012) Dragon Mining , Perth, 116 p

Eklund D (2007) Mineralogy of the hypozonal Svartliden gold deposit. northern Sweden, with emphasis on the composition and paragenetic relations of electrum. MSc thesis. Department of Earth Sciences. Uppsala University, Sweden

Geijer P (1918) Nautanenområdet, en malmgeologisk undersökning: SGU C283: 104 p

Harris DC (1990) The mineralogy of gold and its relevance to gold recoveries. Miner Deposita 25: S3-S7

Hart I, Marsh S, Laurent I (1999) Svartliden - A new style of mineralisation in the Skellefte District. In: Cook NJ, Sundblad K (Eds). Nordic Mineral Resources Symposium Gold '99 Trondheim. Geol Surv Norway, Trondheim, pp. 175

Hålenius U (1983) An ore mineralogical investigation of the Nautanen Cu-Au mineralization: SGAB, Unpublished report, PRAP 83084, 6 p. (in Swedish)

Martinsson O, Wanhainen C (2004) Character of Cu-Au mineralization and related hydrothermal alterations along the Nautanen deformation zone, Gällivare area, northern Sweden. In: Allen R, Martinsson O, Weihed P (Eds). Svecofennian Ore-Forming Environments Field Trip Volcanic-associated Zn-Cu-Au-Ag and Magnetite-apatite, Sediment-hosted Pb-Zn, and Intrusion-associated Cu-Au Deposits in Northern Sweden. Soc Econ Geol Guidebook Series 33: 149-160

New Boliden Annual Report 2011 (2012) New Boliden, Stockholm, 116 p

Rickard DT, Zweifel H (1975) Genesis of Precambrian ores, Skellefte district, Sweden. Econ Geol 70: 255-274

Rutland RWR, Kero L, Nilsson G, Stoelen LK (2001) Nature of a major tectonic discontinuity in the Svecofennian province of northern Sweden. Prec Res 112: 11-237

Vaughan JP (2004) The process mineralogy of gold: the classification of ore types. JOM 56 (7): 46-48

Zhou JY, Cabri LJ (2004) Gold process mineralogy: objectives, techniques, and applications. JOM 56 (7): 49-52

Zhou JY, Jago B, Martin C (2004) Establishing the process mineralogy of gold ores. In: 36th Annual Meeting of the Canadian Mineral Processors, Ottawa, Ontario, Canada, pp. 200-226

# Tracking ore mineral characteristics from mine to concentrate: the fate of electrum at the Cavanacaw gold deposit, Northern Ireland

**Sandra Birtel**
*Helmholtz Institute Freiberg for Resource Technology, Germany*

**Iris Wunderlich**
*Department of Mineralogy, TU Bergakademie Freiberg, Germany*

**Jens Gutzmer**
*Helmholtz Institute Freiberg for Resource Technology, Germany*
*Department of Mineralogy, TU Bergakademie Freiberg, Germany*

**Abstract.** A systematic geometallurgical assessment was carried out to track changes of mineral composition and microfabric from ore extracted at the Cavanacaw Au Mine through the entire beneficiation process to a polymetallic sulphide concentrate. SEM-based image analysis was the major analytical tool used to carry out this investigation. A cursory assessment of the data quickly reveals that the beneficiation plant suffers only little loss of ore minerals to the tailings. Despite this positive assessment results illustrate that there are some systemic losses: Large electrum grains (>16 µm ecd) that abound in the original ore prior to entering the beneficiation plant only make a very minor contribution to the final concentrate. Due to the ductile behaviour of electrum, fracturing of larger electrum grains into smaller grain sizes appears unlikely – and it is thus concluded that these particles may be trapped in the plant during beneficiation. Furthermore, results reveal that sulphide-rich vein content is typically higher in Au grade than the final sulphide concentrate. This results from processing a mixture of high-grade ore and low-grade wall rock. To reduce processing costs it is thus recommended to introduce optical sorting to separate high-grade from low-grade material very early in the beneficiation process.

**Keywords. gold, MLA, mineral processing, geometallurgy**

## 1    Introduction

Automated SEM-based image analyses is a key method in geometallurgy, because quantitative data is needed with respect to mineralogy and microstructure. Quantitative data on mineralogy and microstructure obtained on the processing intermediates and products, as well as the primary ore, allow identification of possible material loss and illustrate the behaviour of each mineral during beneficiation. Based on such quantitative information the beneficiation process can be optimized.

Information on the mineralogical and fabric relationships in the undisturbed ore is almost totally lost when the material is crushed, milled and beneficiated. The value of studying undisturbed samples has been recently documented by Hoal et al. (2009), Voordouw et al. (2010), Birtel et al. (2011), and Wunderlich (2012).

The present study was carried out at Cavanacaw Mine, exploiting a structurally-controlled hydrothermal gold deposit in Northern Ireland. Cavanacaw is operated by Omagh Minerals Ltd. The gold deposit is hosted by Dalradian metasedimetary rocks (psammites and semipelites). The dominant Au ore mineral is electrum, but minor concentrations of Au are known to also occur in pyrite (up to 0.7-0.8 at. % Au) and galena (up to 1.2 at. % Au) (Parnell et al. 2000). Parnell et al. (2000) describe electrum as small rounded grains within sub- to euhedral pyrite, along the rim of domains or crosscutting veinlets with tetrahedrite, chalcopyrite and pyrite. Birtel et al. (2011) found electrum associated with pyrite, arsenopyrite, galena and quartz.

The study aims to track two mining blocks from the open pit through the processing plant to a high-grade polymetallic sulfide concentrate and corresponding tailings. For each block undisturbed samples of ore and wall rock were taken before extraction of the block and the mined material was followed through the beneficiation plant, where granular samples were collected systematically.

Not only the mineralogy but also fabric relations of the original (uncrushed) material are predestinated to play an important role and therefore must be considered in the geometallurgical assessment. It is thus a particular goal of this study to critically assess the value to study undisturbed ore in conjunction with process samples.

## 2    Methods

For this study two complimentary sample sets were collected from two mining blocks (block I and II). The first sample set that was collected for each block comprises of hand specimen representing the different lithotypes present, including high grade veins, low-grade mineralized wall rock and unmineralized wall rock. For each block 20-25 individual samples were collected. High-grade vein samples (represented ca. 20 Vol % of the each block) are exploited and beneficiated together with wall rocks. These samples of uncrushed ores and wall rocks were prepared and studied as polished thin sections.

The second set of samples was collected from the flotation plant and corresponds to the processed material from the two mined blocks. During sampling it was

assured that the material from the two mining blocks was processed separately – with no other mining blocks contributing to the plant feed at the time of sampling.

Mined material at Cavanacaw first passes a jaw crusher, cone crushers, a ball mill, and a cyclone, prior to entering the flotation plant. As only slimes leave the circuit prior to flotation it was decided to sample only the material within the flotation plant for this study. The material flow is shown in Fig. 1.
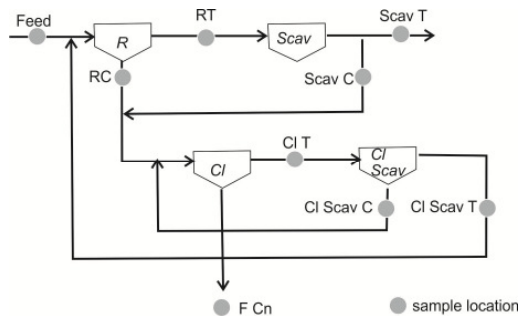


**Figure 1**: Flowsheet for Cavanacaw plant with the 9 sample locations. Abbreviations: R=rougher, Scav=scavenger, Cl=cleaner, F=final, Cn=concentrate, Tn=tailings,

Three survey sample suites were studied for each block (time gap between each suite is ca. 1.5 h). After testing the results obtained by MLA analytics on three individual samples for unsized samples vs. samples sized into different particle size fractions it was decided to limit analysis to unsized grain mounts. Therefore, 27 grain mounts represent the sample set from the flotation plant for each of the two studied mining blocks.

Grain mounts and thin sections were analyzed with a mineral liberation analyzer (MLA) Quanta FEG 600, a FEI field emission scanning electron microscope equipped with two Bruker EDX detectors. The instrument is equipped with MLA software supplied by FEI for automation and data processing (Gu, 2003; Fandrich et al., 2006).

Instrument settings for this study were 25 kV (acceleration voltage) and 190 μA (emission current). In order to detect grains > 4 μm ecd, the XBSE mode was used to map the entire sample at a magnification of 175 times. Measurement time in XBSE mode varied from 2-12 h and 5-12 h for grain mounts and thin sections, respectively. For differentiation of electrum from native gold a grey level trigger in combination with spectrum match was set.

In an effort to validate the results of MLA analysis, modal mineralogical data in combination with mineral chemistry for the ore-forming minerals was used to calculate a modal chemical composition. This was compared with chemical analytical data as supplied by the accredited laboratory OMAC, determined on a representative fraction of each sample.

## 3    Results

Results presented in here focus on the most important ore mineral at Cavanacaw, i.e., electrum. The data is used to track significant and systematic changes of

extensive properties of electrum such as concentration, liberation and grain size. On the other hand, consistency is documented for intensive properties, esp. mineral chemistry from mining blocks to final concentrate.

### 3.1 Modal composition and gold concentration

The mineralogy for both studied mining blocks comprises predominantly of quartz, albite and K-feldspar, muscovite and biotite, chamosite, as well as the sulphides pyrite, arsenopyrite, and galena in very variable amounts. Ankerite and calcite abound in block I, with contents up to 40 wt% but usually not exceeding 10 wt%. Small amounts of barite (2 wt%) occur, as do tetrahedrite, kaersutite, bornite, sphalerite, contribute with <<0.1 wt%. Modal mineralogy confirms the distinction of lithotypes during field mapping as three distinct geometallurgical domains. These are: highly mineralised veins (domain I) dominated by sulphides and quartz, always containing electrum. The actual sulphide mineralogy is very variable in this domain, with arsenopyrite more abundant than pyrite in block I, but pyrite the dominating sulphide in block II. Weakly mineralised wall rock (domain II) is dominated by silicates (in block I also carbonates) with sulphide mineralisation and some electrum. Unmineralized wall rock (domain III) with minor amounts of sulphides and no electrum.

Au occurs nearly exclusively as electrum, very few grains of native Au were found. Electrum is mainly associated with the sulfides pyrite and arsenopyrite and occurs as inclusions in the sulfides which form veinlets in quartz veins (Fig. 2), but also in sulphide patches in more complex microstructures.

Gold grade (calculated assay MLA) for the mineralized vein is 5-153 ppm for block I, most samples exceed 20 ppm. For block II most samples have Au grade > 4 ppm , maximum value is 13,3 ppm, the lower gold grade can be explained by a relative high quartz content compared to the sulfide content in the considered thin sections.
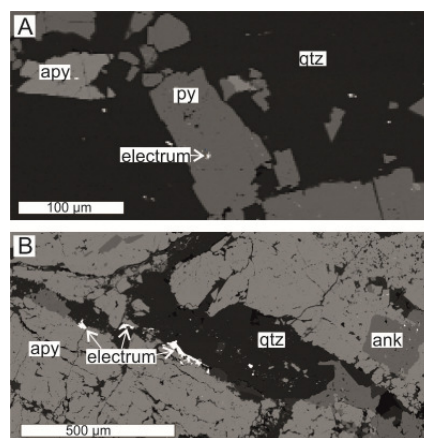


**Figure 2:** BSE images of uncrushed ore sample surfaces (polished thin sections), A: Electrum occurs as inclusions in pyrite. Sulphides occur in cracks of larger qtz veins. B: Large electrum grains (here up to 200 μm long axis) occur in contact with arsenopyrite. Abbreviations: qtz=quartz. apy= arsenopyrite, py=pyrite, ank=ankerite

As the mined block is exploited, the material entering the processing plant is a mixture of all three geometallurgical domains. Considering the proportion of the three geometallurgical domains from the mined block according to detailed grid mapping (Wunderlich, 2012) the composition of an apparent average feed material can be modelled (the first column Fig. 3, 'parent rock'). This modelled protolith is in good agreement with the modal mineralogical composition of the actual feed – sampled as feed to the rougher flotation cell. However, the modelled parent rocks for both blocks overestimates the abundance of sulphides. This is tentatively attributed to the difficulty of mapping the actual vein width in rubble and water-covered mine block surfaces and the required interpolation from a 2 D grid map to 3 D of the actual mining block.

The Au content of the feed is <2 ppm for block I and is –like in all other samples- positively correlated with the total amount of sulfides. This serves to explain that none of the survey samples from block II was found to contain gold in the feed sample (sulfides < 2%).

With further processing, the survey samples from both blocks become more similar to each other with respect to sulfide concentration in the concentrates and separation of silicates and carbonates into the tailings. After passing the cleaner, the R Cn is transferred directly into the final concentrate, F Cn shows Au contents of 40-90 ppm for block I and 28-107 ppm for block II (Fig. 3).
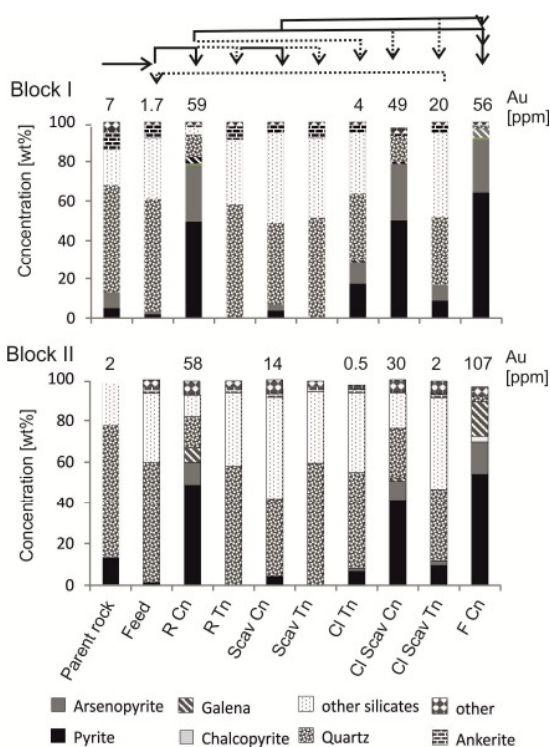


**Figure 3:** Modal mineralogy of processed samples of one survey of block I and block II respectively. Values above the columns indicate Au grade in ppm, (calculated assay from MLA). Arrows on top of figure imply material flow in the plant, straight line goes to concentrate, dotted to tailings. 'Other silicates' include albite and K-feldspar, biotite, muscovite and chamosite. For Abbreviations see Fig. 1

In all surveys Scav Tn (finals tailings) samples gold is below detection limit i.e., negligible gold.

## 3.2 Association and Liberation

80 – 90 % of all electrum grains is associated with pyrite or arsenopyrite for uncrushed samples; 3-17 % are associated with quartz. 80 % of particles entering the flotation circuit are <180 μm (Wunderlich 2012). The association (ratio= length of contact/total length of grain boundary) with other mineral constituents is negligible. For the process samples (expect Cl Tn of Block I and feed) >45 % of the electrum grains are fully liberated (> 90 % liberation by surface). Electrum was identified in the feed sample of only one survey of Block I and liberation is 20 %. For the R Cn values vary between 45 and 70 % depending on the survey, similar value (deviation +/- 5 %) for the Cl Scav Cn for the corresponding survey was identified, except for one survey of Block I, where liberation decreases to 32 % for the Scav Cn. For the F Cn liberation reaches up to 80% for Block I and only increases about 5-10 % compared to the R Cn and Cl Scav Cn concentrate, i.e. reaches a maximum value of 63 % for block II.

The rougher is the first and most efficient step for the concentration of sulfides and electrum. Still process samples collected after the rougher 15-20 % of the electrum remains associated with quartz; 5 % are associated with quartz in the final concentrate. Though galena is also concentrated in the R Cn and F Cn (block II), electrum association with galena is negligible (max. 1 % in the final concentrate).

## 3.3 Grain size distribution

In spite of the fact that electrum, together with sulphides, is effectively concentrated in the flotation circuit, many more electrum grains were identified in a thin section than in concentrate samples (Fig. 4).
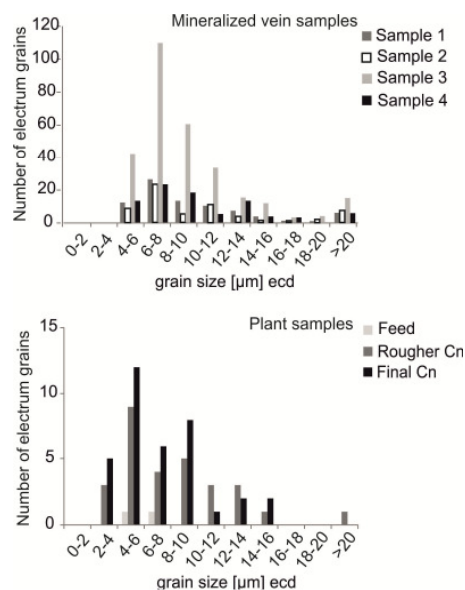


**Figure 4:** Grain size distribution for electrum in vein and process samples of block I. Note the different scale bars. For both sample suites small grain sizes (4-10 μm ecd) dominate, however, for the mineralized vein samples up to 15 grains >20 μm ecd were detected. These are almost absent from the process samples.

This is simply a consequence of the total area analysed for these different sample types. A single polished thin section (ca. 900 mm$^2$) covers a larger area than a grain mount with 30 mm diameter (706 mm$^2$). In addition, the thin section is entirely covered with rock material, whereas the grain mount has a mineral density of no more than 50 % of the surface, to assure that grains are well separated.

Grain size distributions for electrum in the concentrates and thin sections reveal in particular that larger electrum grains ( > 16 µm ecd) are more common in vein samples and contribute very significantly to the total gold content of each sample; e.g., in one of the samples only one single large grain contributes 30 % of the total Au grade. In fact such large grains are absent in the final concentrate and rare in the rougher concentrate.

### 3.4 Validation

The Au content, calculated from MLA data based on the abundance and composition of electrum alone, is consistently lower compared to chemical assay data determined by an accredited laboratory (Fig. 5). This is, most likely due to small amounts of gold substituted into the crystal structure of pyrite and galena. Parnell et al. (2000) determined a Au gold content of up to 0.8 at% in the crystal structure of pyrite and up to 1.2 at% in galena. Adding an average Au content of only 0.0015 at % into the crystal structure of pyrite and galena suffices in our data to minimize the apparent discrepancy between calculated assay and chemical assay data for all analyzed samples (Fig. 5). The value determined by Parnell et al. (2000) seems to be high, though it is a maximum value. Au in solid solution in pyrite is presumably heterogeneously distributed. The Au identified in the pyrite structure by Parnell et al (2000) and the modelled average value of this study illustrate not only the importance of considering the presence of invisible gold during validation of MLA data acquired on gold ores, but also the possibility to validate MLA data acquired for noble metal ores with chemical assay data.
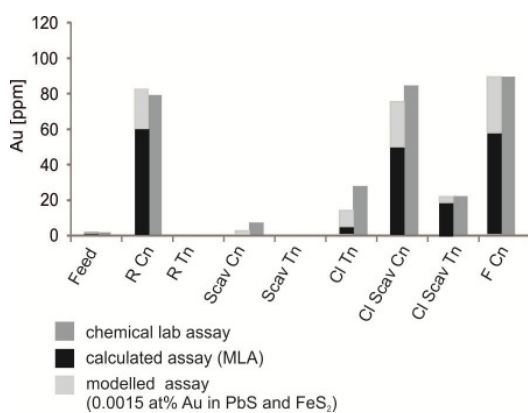


**Figure 5:** Au grade from block I by chemical assay, i.e. fire assay (medium grey) and MLA (black). Taking into account small amounts of Au substituted into pyrite and galena (light grey) yields excellent match between both data sets.

## 4 Implications and conclusions

Most important result of the study is the fact, that tangible characteristics of electrum grains can be tracked from uncrushed ore samples to final concentrate. Extensive characteristics, such as chemical composition of minerals, remain unchanged – a result that surprises little in a beneficiation process that focuses on physical separation processes. Similarly, the study also illustrates that intensive parameters do change systematically and that trends observed are suited to document the effectiveness – or failures – of the technical process route. Furthermore, mineralogical data can be validated with chemical assay data, but only if the partitioning of the elements of interest (here Au) is well understood. These are important results that suggest that observations made on a very heterogeneous ore body using SEM-based image analysis yields reliable quantitative information with regards to mineralogy and microfabric, even if the minerals in question only occur in trace amounts. The study thus affirms the results of Voordouw et al. (2010) and extends them, suggesting that tangible characteristics can be tracked from the mine face to concentrate.

### Acknowledgements

### References

Birtel S., Sandmann D., Gutzmer J. (2011) Geometallurgy: From ore to concentrate – a pilot study on the hydrothermal Au deposit at Cavanacaw, Northern Ireland, 11 biennial meeting SGA in Antofagasta, Chile, September 26-29 2011. Mineralium Deposita

Fandrich R, Gu Y, Burrows D, Moeller K. (2007) Modern SEM-based mineral liberation analysis: Int J Miner Process 84: 310-320.

Hoal K.O., Appleby S.K, Stammer J.G., Palmer, C. (2009) SEM-based quantitative mineralogical analysis of peridotite, kimberlite, and concentrate, Lithos 112S (2009) 41–46

Gu Y. (2003) Automated Scanning Electron Microscope Based Mineral Liberation Analysis. An Introduction to JKMRC/FEI Mineral Liberation Analyser: J Miner Mater Charact Eng 2.1:33-41.

Parnell J, Earls G., Wilkinson JJ, Hutton DHW, Boyce AJ, Fallick AE, Ellam RM, Gleeson SA, Moles NR, Carey PF, Legg I, Carey PF (2000) Regional Fluid Flow and Gold Mineralization in the Dalradian of the Sperrin Mountains, Northern Ireland: Econ Geol 95:1389-1416.

Voordouw R, Gutzmer J, Beukes NJ. (2010) Zoning of platinum group mineral assemblages in the UG2 chromitite determined through in situ SEM-EDS-based image analysis: Mineral Deposita 45:147-159.

Wunderlich, I. (2012) Geometallurgical assessment of polymetallic ores and beneficiation products at the Cavanacaw Au Mine, Northern Ireland, Master thesis TU Bergakademie Freiberg, unpublished, 134 p

# Tellurides, stannides and stannotellurides of Ag and PGE in sulfide droplets from mafic intrusion "Rudniy" in Tsagaan-Shuvuut Range (NW Mongolia)

**Maria Cherdantseva, Andrey Vishnevskiy**
*V S Sobolev Institute of Geology and Mineralogy SB RAS, Novosibirsk, Russia, vishnevsky@igm.nsc.ru*
*Novosibirsk State University, Novosibirsk, Russia*

**Abstract.** The study of the composition of PGE and Ag minerals, found in pentlandite-chalcopyrite-pyrrhotite sulfide droplets from gabbroid body "Rudniy" in NW Mongolia, revealed that most of them belongs to the moncheite group. The PGE and Ag tellurides - hessite, sopcheite and telargpalite, stannides - paolovite and taimyrite are less common, as well as an unnamed new Pt-Pd stannotelluride phase.

**Keywords. PGE, tellurides, stannides, suilfide droplets**

## 1 Introduction

In the Tsagaan-Shuvuut Range, which are located in Northwestern Mongolia, north of Lake Uureg-Nuur, a linear zone of sulfide ores was discovered in one of the numerous Devonian gabbroic intrusions some years ago. Sulfides form small grains between silicate minerals and droplets (globules) of up to 20 mm in size. Based on a study of texture and mineralogy of the ore zone, we identified two horizons in its internal structure. Sulfide droplets have a distinct internal layering. The lower part of the droplet is composed of pyrrhotite, which often forms a monocrystal, and the upper part consists of chalcopyrite-cubanite intergrowth. The central part of the droplets between pyrrhotite and chalcopyrite is composed of granular pentlandite. In the lower horizon sulfide droplets have almost isometric shape and size of 3-10 mm. PGE minerals are tellurides of moncheite-melonite-merenskyite series – ($PtTe_2$-$PdTe_2$-$NiTe_2$) with minor sperrylite ($PtAs_2$). Droplets in the upper horizon are usually flattened and of disc-, or irregular shape. Their size along the long axis is usually less than 20 mm, but sometimes reaches 35-40 mm. A more diverse set of platinum group minerals (PGMs) has been found in this horizon. There are phases containing Sn and Ag, as well as tellurides of silver.

## 2 Sample preparation and techniques

Samples of sulfide droplets from the upper and lower horizons chosen for research, were sawn, mounted in epoxy resin and polished. Total 16 sections of sulfide droplets from the upper horizon have been studied. The study of minerals was carried out using a scanning microscope Tescan Mira 3 with high resolution Oxford X-Max 80 EDS. The accelerating voltage and beam current were 20 kV and 1.6 nA respectively with counting time 15 s. All analyzes were conducted in the scanning mode for the selected rectangular areas to reduce the influence of the microrelief.

## 3 PGE an Ag mineralisation

Most of PGM grains in the droplets of the upper horizon is tellurides of moncheite-melonite-merenskyite group (hereinafter - "moncheite"). Tellurides, arsenides and stannotellurides of Pt, Pd and Ag are less common. They are found in about 30% of the grain and complex intergrowths. The most common of them are hessite ($Ag_2Te$), sopcheite ($Ag_4Pd_3Te_4$), paolovite ($Pd_2Sn$) and stannotelluride Pt and Pd, which further will be referred to as a "phase A". Taimyrite (($Pd,Cu,Pt)_3Sn$) and telargpalite (($Pd, Ag)_3Te$) are much less common in this ore occurrence. They form both single grains and intergrowths with hessite and moncheite.

### 3.1 Hessite

Hessite is found in several different types of grains. First, these are homogeneous grains of different sizes (1-50 microns), which are usually confined to the marginal parts and cracks in the sulfide droplets. Generally, these grains are anhedral and form small clusters (Fig. 2, a). In other cases, hessite forms intergrowths with other tellurides. In nine of the studied grains, hessite was found intergrown with Phase A, which forms a small round or elongated irregular lamellae enclosed in hessite matrix (Fig. 2, b). Hessite - phase A ratio in these grains vary from 2:1 to 3:1, suggesting that Phase A is the result of exsolution of some unknown PGE-Ni-Sn-Te-Bi solid solution. It should be stressed that such intergrowths can be euhedral (Fig. 2, b). Some of hessite - moncheite intergrowths have the similar structure (Fig. 2, c). Besides there are grains of hessite that can be divided
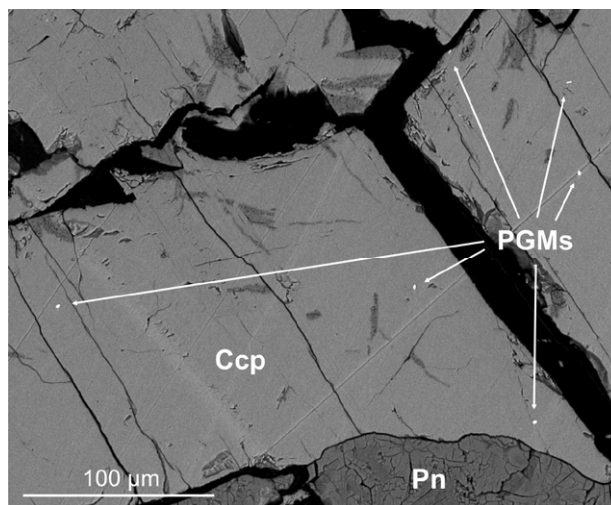


**Figure 1.** PGM grains (white) in chalcopyrite from upper part of sulphide droplets. SEM BSE image.
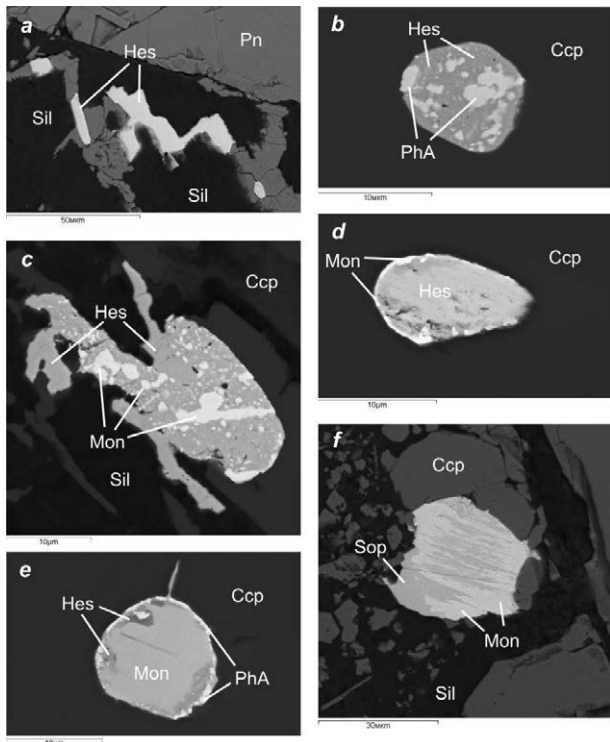
**Figure 2.** Grains of Ag and PGE minerals from sulfide droplets. a – anhedral hessite (Hes) clusters from the edge of the sulfide droplet, b - euhedral hessite with inclusions of unnamed Pt-Pd stannotelluride (PhA), c – intergrowths of hessite and moncheite (Mon), d - moncheite rim around grain of hessite, e - two-phase rim around moncheite core, f – moncheite partly replaced by sopcheite (Sop).

into zones completely devoid of moncheite and zones rich in them. In some cases moncheite forms a thin (0.5-1 mm) rim around of homogeneous hessite grains (Fig. 2, d). In addition, several of studied grains have rims with a more complex structure. The central part of these grains consists of uniform moncheite, while the rim has a two-phase structure. The inner part consists of hessite and the external one is composed of phase A (Fig. 2, e).
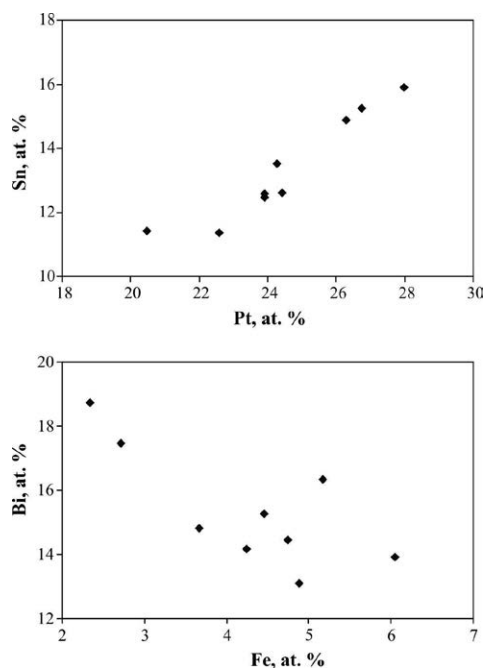


**Figure 3.** Phase A composition patterns

## 3.2    Sopcheite

In comparison to hessite, sopcheite is considerably less common in the upper horizon of sulfide droplets. In most cases, it is found in the marginal parts of moncheite grains and its cracks, forming the replacement structures. Sopcheite formation is always associated here with moncheite grains located in marginal parts and fractured zones of sulfide droplets (Fig. 2, f). Besides, the clusters of anhedral grains of sopcheite were found in fractured zones in association with amphibole and chlorite.

## 3.3    Stannides and telargpalite

Most of the studied grains of paolovite form small monomineral grains of submicron size in chalcopyrite. Sometimes paolovite occurs in association with moncheite and telargpalite. Findings of telargpalite and taimyrite are occasional. They found in association with paolovite, hessite, and phase A.

## 3.4    Pt-Stannotelluride (Phase A)

Stannotelluride of Pt (Phase A) is a new unknown phase. In total, 9 grains of this mineral have been analysed. It is composed of Sn, Te, Bi, Pt, Fe, Cu, Ni occasionally Pd, and, perhaps, Ag. In all cases, analyzed grains have a very small size (0.5-3 μm), and it is clear that in the analysis, silver from the enclosing hessite matrix was superimposed on the resulting spectrum. That has been avoided only in one analysis (in the largest grain). Based on the fact that Sn substitution by other elements, contained in this mineral, is not characteristic of Sn, the composition was recalculated per formula unit of Sn, which resulted in the following formula: $(Pt_{1.94},Pd_{0.36},Cu_{0.24},Ni_{0.19},Fe_{0.18})_{2.91}Sn_{1.00}$ $(Te_{2.53},Bi_{1.48})_{4.01}$. Thus, the general form of the formula of this mineral will appear as $Pt_3SnTe_4$. In addition, several patterns of change in its composition have been identified. There is a clear positive correlation between the concentrations of Sn and Pt (r=0.95), and the inverse correlation between Fe and Bi contents (r=-0.75).

**Table 1.** Phase A compositions (in atomic %). SEM EDS

| № | Fe | Ni | Cu | Ag | Pt | Pd | Sn | Bi | Te |
|---|------|------|------|-------|-------|------|-------|-------|-------|
| 1 | 4.24 | 1.99 | 1.77 | 13.54 | 20.46 | 2.17 | 11.43 | 14.16 | 30.25 |
| 2 | 6.05 | 2.73 | 3.39 | 10.50 | 22.59 |      | 11.37 | 13.91 | 29.45 |
| 3 | 4.75 | 2.62 | 2.69 | 4.58  | 26.30 |      | 14.89 | 14.45 | 29.71 |
| 4 | 4.88 | 1.71 | 3.38 | 2.65  | 27.99 |      | 15.91 | 13.09 | 30.39 |
| 5 | 4.45 | 1.62 | 2.85 | 8.86  | 23.92 |      | 12.57 | 15.27 | 30.45 |
| 6 | 5.17 | 1.94 | 1.91 | 2.68  | 26.75 |      | 15.24 | 16.35 | 29.97 |
| 7 | 2.72 | 2.38 | 2.70 | 4.03  | 23.92 | 3.57 | 12.47 | 17.46 | 30.75 |
| 8 | 2.34 | 2.44 | 3.11 |       | 24.42 | 4.44 | 12.61 | 18.73 | 31.91 |
| 9 | 3.67 | 2.11 | 4.60 | 4.29  | 24.27 | 2.40 | 13.51 | 14.83 | 30.33 |

## Acknowledgements

# Paragenesis of Platinum group minerals in lateritized chromitite of the Niquelândia layered intrusion (Central Goias, Brazil)

**Giorgio Garuti, Federica Zaccarini, Oskar A.R. Thalhammer**
*Department of Applied Geological Sciences and Geophysics, University of Leoben, Austria*

**Joaquin A. Proenza**
*Deparment of Crystallography, Mineralogy and Ore Deposits, University of Barcelona, Spain*

**Abstract.** Peridotites and associated chromitite layers exposed in the highlands of the Niquelândia layered complex have undergone extensive lateritic weathering. The silicate rocks are altered to smectite, kaolinite, garnierite and amorphous silica, while the chromite is transformed into a massive aggregate of a spinel phase having low-Mg and low $Fe^{3+}/Fe^{2+}$ ratio, with accessory ilmenite, rutile, brookite, amorphous Fe-hydroxides, goethite, hematite and magnetite. Three distinct populations of platinum-group minerals (PGM) have been observed included in weathered chromitite. One group corresponds to primary PGM grains which have survived alteration (Ru-Os-Ir sulfides, alloys and sulfarsenides, Pt-Fe alloys with isoferroplatinum-type composition). A second group consists of PGM grains displaying evidence of chemical corrosion and replacement by a secondary phase. A common association consists of laurite showing partial to total alteration into Ru-oxide. A third group of PGM, consists of Pt-Fe-Cu-Ni and Os-Ir alloys characterized by close association with kaolinite and Fe-hydroxides. These PGM are considered to have formed during weathering by precipitation of platinum-group elements dissolved in the surface hydrous solutions. Textural evidence suggests that re-deposition of the secondary PGM was controlled by variation of the redox conditions at a microscopic scale.

**Keywords.** Chromitite; PGM; laterite; weathering; Niquelândia

## 1 Introduction

The Middle Proterozoic (1560-1600 Ma) Niquelândia layered intrusion suffered a long history of high-grade metamorphism (770-795 Ma), tectonic deformation (630 Ma), and surface weathering during the Sul-Americano Cycle (Lower-Tertiary) (Ferreira Filho et al., 2010). The weathering process occurred under tropical climate that caused deep lateritization of the ultramafic units exposed along the Serra da Mantiqueira highlands (Fig. 1). Here, large silicate-Ni deposits of economic relevance (9.50 kt metallic Ni produced in 2011) have formed after thick layers of cumulus harzburgite and dunite (Barros de Oliveira et al., 1992). Chromitite layers alternate with dunite, and were partly to almost totally affected by lateritic alteration as well. The chromitite contains platinum-group element (PGE) mineralization of sub-economic interest (White et al., 1971) expressed by a minute dissemination of PGM grains in the chromite and its silicate matrix (Ferrario and Garuti, 1988). Detailed mineralogical investigation

of the weathered chromitite has revealed that many grains of PGM exposed to the action of weathering solutions have undergone to mineralogical and chemical reworking by re-mobilization of the PGE at low temperature (Garuti et al., 2012).
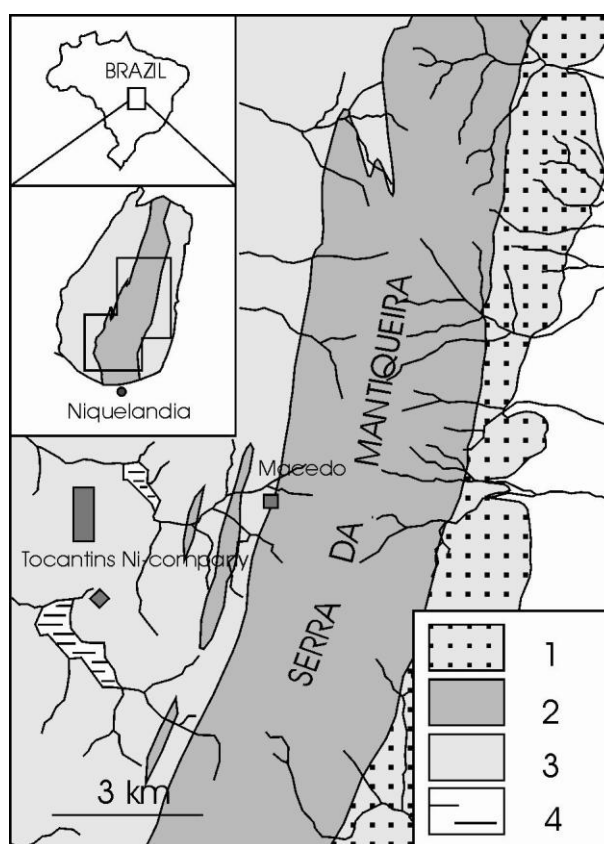


**Figure 1.** Location of the Niquelândia complex and simplified geology of the Serra da Mantiqueira highland. 1) basal gabbro; 2) ultramafic cumulate with chromitite layering; 3) upper layered gabbro; 4) lakes.

## 2 Petrography

At Serra da Mantiqueira, the chromitite layers occur completely embedded in the laterite soil derived from weathering of the original ultramafic country rock. Strongly weathered chromitite consists of a light, black, earthy material characterized by high porosity and bad polishing. Less altered layers consist of a zoned chromite characterized by a low reflective, solid spinel

phase, surrounded by a highly reflective phase intensively pitted with pores (Fig. 2A). The alteration pattern involves depletion of MgO and $Fe_2O_3$ in the pitted chromite and a general increase of $Al_2O_3$ and FeO. This alteration scheme is contrary to that normally resulting from serpentinization which involves systematic increase of the $Fe_2O_3$/FeO ratio in the ferrian-chromite rims, and is ascribed to the different redox condition prevailing during laterite weathering.

A complex assemblage of newly formed silicates and oxides is found in the weathered chromitite. The secondary silicates fill the pores or are aligned along fractures in the weathered chromite. Their assemblage (kaolinite, smectite, serpentine and amorphous silica) reflects the effects of laterite weathering of a primary mafic minerals. Abundant Fe-oxides (goethite, limonite, hematite, magnetite), and Fe-Ti oxides (ilmenite, rutile, brookite, Fig. 2B) occur in weathered chromitite, sometimes aligned along grain-boundaries and cracks. Sulfides are rare, represented by millerite and heazlewoodite occurring as minute inclusions in chromite and silicates.
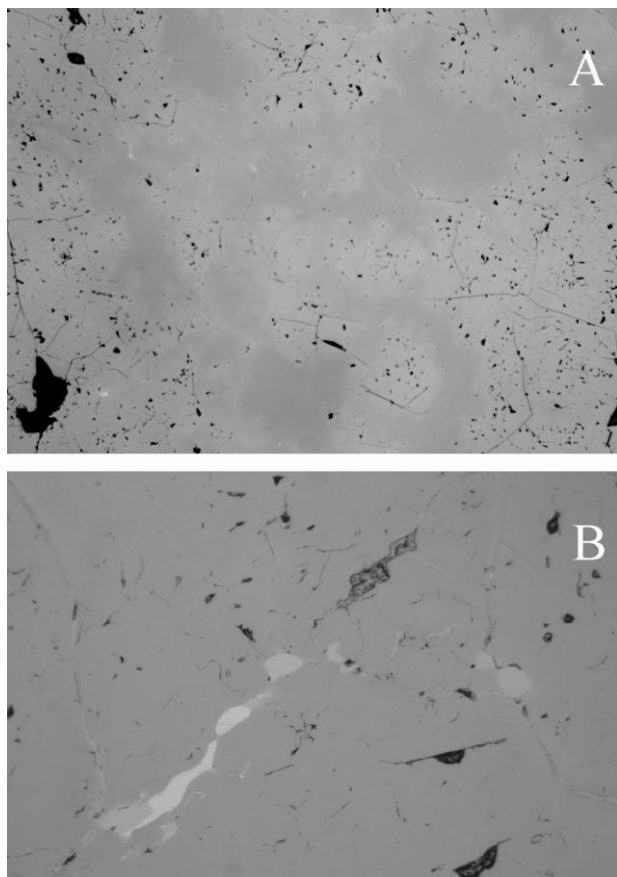


**Figure 2.** Reflected light images of partly weathered chromitite. (A) high reflective pore-pitted chromite with relicts of low reflective solid chromite; (B) ameboid crystals of ilmenite aligned along chromite grain boundaries in pore-pitted chromite.

## 3 The PGM assemblage

Three types of PGM occur in the weathered chromitites

of the Niquelândia igneous complex: type-1: Primary PGM that survived alteration of the enclosing chromite, due to their higher chemical stability compared with the host chromite; type-2: Primary PGM corroded, and chemically modified in situ, by reaction with hydrous solutions at low temperature; type-3: Secondary PGM precipitated from hydrous solutions as a result of PGE mobilization at low temperature. Identification of the different genetic nature of the PGM is based on their mineralogy, morphology, internal texture, and paragenetic association.

Type-1 PGM are mainly Ru-Os-Ir sulfides, sulfarsenides, and alloys, all characterized by euhedral morphology and textures indicative of equilibrium crystallization among different phases (Fig. 3A, B). They occur in both low- and high-reflective chromite, sometimes associated with relict of primary silicates (phlogopite, amphibole). Even some Pt-Fe alloys with isoferroplatinum-type composition and Os-Ir alloys recovered from concentrates produced for mineralogical study (Rudashevsky et al., 2002), may be primary, although their paragenetic relationships could not be observed.

Type-2 PGM are common throughout the weathered chromite showing the effects of in situ alteration. Grains located in fractures may have lost their initial euhedral shape showing corroded boundaries at the contact with altered chromite (Fig. 3C). In other cases, a secondary Ru-oxide is derived from alteration of a laurite precursor whose relicts are still preserved at the core of the secondary grain (Fig. 3D). According to what suggested by Garuti et al. (1997), the alteration of laurite involves total removing of S and Os, and in part of Ir, whereas Ru is oxidized to a phase with stoichiometry between rutile-type ($RuO_2$) and hematite-type ($Ru_2O_3$). The oxide contains small amounts of base metals (Fe, Mn, Ni) and As.
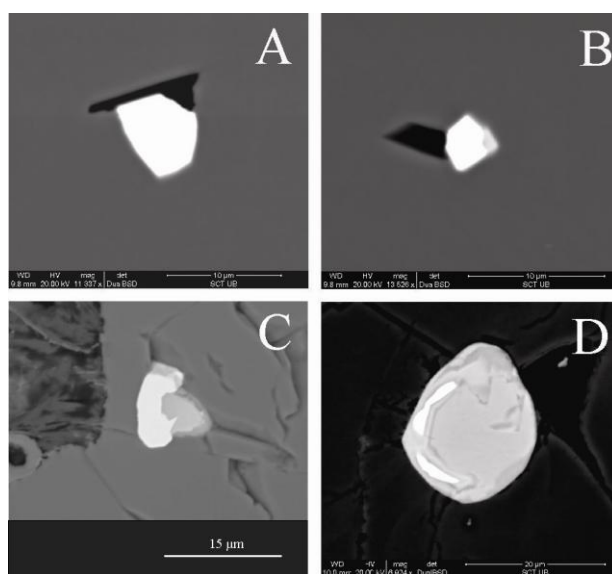


**Figure 3.** BSE images of Ru-Os-Ir sulfide and sulfarsenide in weathered chromitite. Type-1 PGM in low reflective solid chromite: (A) laurite + phlogopite; (B) erlichmanite + NiS + amphibole; Type-2 PGM: (C) corroded grain of laurite + irarsite in fractured chromite, a large kaolinite-Fe-oxide aggregate is visible in the left side; D) grain of Ru-oxide

(middle grey) formed after Os-rich laurite (white patches).

Type-3 PGM are characterized by anhedral shape, and close association with kaolinite, secondary Fe-hydroxides, and ilmenite. Their morphology and paragenetic assemblage are consistent with a deposition at low temperature by precipitation of the PGE from a hydrous solution flushing the laterite. The most common PGM species are alloys in the Os-Ir-Ru and Pt-Fe-Ni-Cu systems.

Large aggregates of Cr-bearing, Fe-hydroxide locally occur at the junction of fractures in the low reflective, solid chromite effected by incipient alteration (Fig. 4A). Alloys composed of Os-Ir with or without Ru may occur in the hydroxide grain, at the contact with chromite (Fig. 4B). In other cases, alloys with a complex Pt-Fe-Ni-Cu composition occur in large kaolinite aggregates at the contact with Fe-hydroxide or chromite (Fig. 4C, D). Composite grains consisting of the two types of alloys Os-Ir and Pt-Fe-Ni-Cu have also been observed at the contact chromite-goethite-kaolinite and chromite-ilmenite-kaolinite. In general, the two types of alloys occur separately, although one composite grain consisting of Os-Ir and Pt-Fe alloys has been reported in one case (Fig. 4E, F).
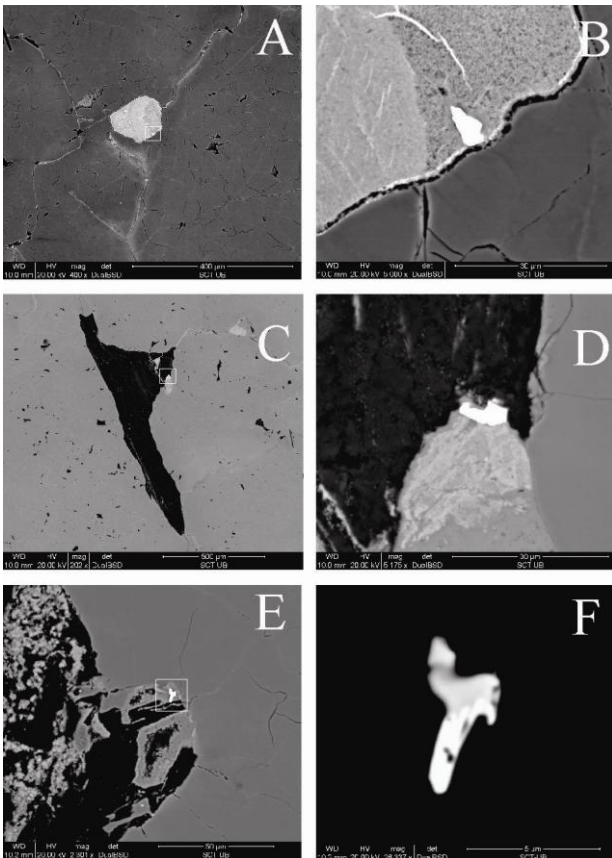


**Figure 4.** BSE images of PGE alloys of type-3: A-B) anhedral grain of Os-Ir in Fe-hydroxide in contact with fresh chromitite. C-D) anhedral grain of Pt-Fe-Ni-Cu alloy at the contact kaolinite- Fe-hydroxide. E-F) composite grain of Os-Ir + Pt-Fe-Ni-Cu alloys in Fe-hydroxide in contact with kaolinite.

Type-3 PGM indicate that Os, Ir, Pt and Ru to some extent are remobilized and carried in solution during the low temperature weathering of the chromitite. Type-1

and -2 PGM must be the source of the dissolved PGE. For example, in situ chemical corrosion of laurite and irarsite can easily provide Os and Ir required for the formation of secondary Os-Ir alloys, while isoferroplatinum-type alloys, with $Pt_3Fe$ stoichiometry, might represent the primary source for Pt remobilization and precipitation of secondary alloys of Pt and base metals.

## 4 Mineral chemistry of PGM

Electron microprobe analysis of PGM from the weathered chromitites of Niquelândia (Table 1) indicates that part of the Ru-Os-Ir minerals (sulfide and alloys) fit the field of similar PGM in unaltered chromitite, possibly representing type-1 PGM (Fig. 5A).
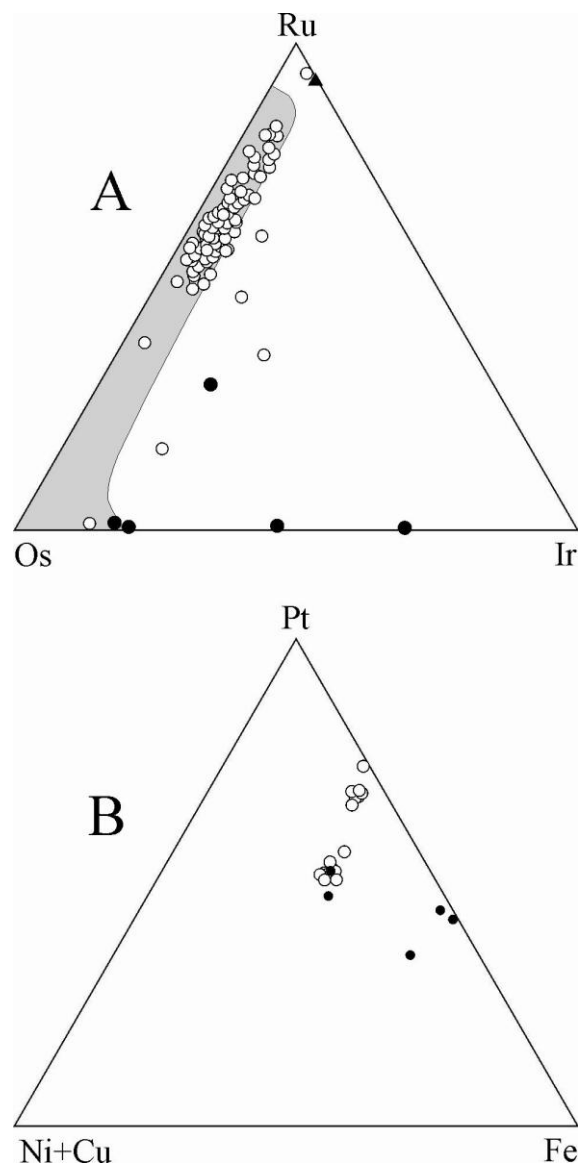


**Figure 5.** Electron microprobe composition of PGM inclusions in weathered chromite: A) Ru-Os-Ir ternary plot (mol. %) for PGM sulfides (open circle), alloys (black spot), and Ru-oxide (black triangle), the field of primary Ru-Os-Ir phases is in gray; B) Pt-Fe-(Ni+Cu) ternary plot for type-3 Pt-Fe alloys (black spot) compared with Pt-Fe alloys from concentrates produced for mineralogical study (open circle).

In contrast, the type-2 laurite-erlichmanite sulfides and type-3 Os-Ir alloys are enriched in Ir and, in one case, in Ru, representing PGM altered in situ or precipitated under low-temperature conditions. Notably, the Ru-oxide is Os free, indicating complete removing of Os during oxidation of laurite.

Type-3 Pt-Fe alloys (i.e. Fig. 3C, D) may fit the field of (Ni+Cu)-rich Pt-Fe alloys from concentrates (Rudashevsky et al., 2002) or they show anomalous enrichment in Fe in most cases (Fig. 5B). Although, we do not have textural evidence for grains in the concentrates, the compositional relationships indicate that (Ni+Cu)-rich and Fe-rich alloys possibly are of type-2 and/or type-3 origin, in contrast with type-1 alloys with $Pt_3Fe$ stoichiometry.

**Table 1. Selected PGM composition.**

|    | 3A | 3B | 3C | 3D | 4B | 4E | 4E | 4D | C-1 |
|----|----|----|----|----|----|----|----|----|-----|
| Os | 31.7 | 29.3 | 0.7 |  | 48.9 | 3.2 | 47.3 |  |  |
| Ir | 3.9 | 5.0 | 61.3 | 7.2 | 43.2 | 17.6 | 42.5 |  |  |
| Ru | 30.5 | 29.6 | 1.2 | 43.6 | 0.3 |  |  | 0.1 |  |
| Rh |  |  | 0.7 | 2.1 |  | 0.2 |  | 0.6 |  |
| Pt |  |  |  |  | 0.6 | 54.1 |  | 78.3 | 89.5 |
| Pd | 1.5 | 1.4 |  |  |  | 0.1 |  |  |  |
| Fe |  | 1.1 | 0.8 | 0.8 | 5.1 | 18.5 | 8.3 | 12.5 | 10.0 |
| Ni | 0.1 | 0.1 | 0.1 | 1.6 | 0.7 | 3.2 | 0.9 | 5.3 | 0.7 |
| Cu | 0.1 | 0.1 |  | 0.1 |  | 1.1 |  | 2.6 | 1.0 |
| S | 30.9 | 31.0 | 9.7 | 0.2 |  |  |  |  |  |
| As |  |  | 24.8 | 3.4 |  |  |  | 0.2 |  |
| O |  |  |  | 33.6 |  |  |  |  |  |
|    | 98.7 | 97.6 | 99.3 | 92.6 | 98.8 | 98.0 | 99.0 | 99.6 | 101.2 |

Labels = figure numbers. C-1 = PtFe alloy from concentrates

## 4 Conclusion

The study of PGM occurring in weathered chromitites of the Niquelândia layered intrusion provides further evidence supporting that PGE may be mobilized under lateritic conditions. Primary magmatic Os, Ir, Pt and Ru species become chemically unstable under the action of highly oxidizing and acid hydrous fluids (Bowles, 1986). Major reactions involve desulfidation and oxidation. Ru is oxidized to a complex phase with stoichiometry intermediate to $RuO_2$ and $Ru_2O_3$ that replaces laurite along rims. Other PGE, mainly Os, Ir, and Pt, are released and taken up into solution probably as complex chloride species. Textural evidence indicates that they are transported through the weathered chromitite ad deposited along cracks as minute particles of complex alloys associated with secondary silicates and oxides. The precipitation consistently occurs at the interface between kaolinite and Fe-hydroxides or ilmenite, possibly representing a local redox micro-boundary necessary to trigger PGE precipitation (Bowles, 1986).

## References

Barros de Oliveira SM, Trescases JJ, Melfi AJ (1992) Lateritic nickel deposits of Brazil. Mineral Deposita 27: 137-146

Bowles JFW (1986) The development of platinum-group minerals in laterites. Econ Geol 81: 1278-1285

Ferrario A, Garuti G (1988) Platinum-Group Minerals in chromite-rich horizons of the Niquelândia Complex (Central Goias, Brazil). In: Prichard HM, Potts PJ, Bowles JFW, Cribb SJ (eds.) Geo-Platinum 87: 261-272, Elsevier Applied Sciences, London New York

Ferreira Filho CF, Pimentel MM, Araujo SM, Laux JH (2010) Layered intrusions and volcanic sequences in Central Brazil: geological and geochronological constraints for Mesoproterozoic (1.25 Ga) and Neoproterozoic (0.79 Ga) igneous associations. Precamb Res 183: 617-634

Garuti G, Zaccarini F, Proenza JA, Thalhammer OAR, Angeli N (2012) Platinum-Group Minerals in chromitites of the Niquelândia layered intrusion (Central Goias, Brazil): their magmatic origin and low-temperature reworking during serpentinization and lateritic weathering. Minerals 2:365-384

Rudashevsky NS, Garuti G, Andersen JCØ, Krester YuL, Rudashevsky VN, Zaccarini F (2002) Separation of accessory minerals from rocks and ores by hydroseparation (HS) technology: method and application to CHR-2 chromitite, Niquelândia intrusion, Brazil. Trans Inst Min Metall 111: B87-94

White RW, Motta J, Arraujo VA (1971) Platiniferous chromitite in the Tocantins complex, Goias, Brazil. In: Geological Survey Research 1971, U.S. Geological Survey Professional Papers 750D: D26-D33

# Chemical variations of Mg in magnetite from the Tapuli skarn iron ore, Northern Sweden

**Jenni Hasa**
*The University of Oulu, Northland Resources AB*

**Åsa Allan**
*Northland Resources AB*

**Eero Hanski**
*The University of Oulu*

**Abstract.** The Tapuli skarn iron ore is located circa 25 km north of Pajala in Northern Sweden. It lays within the Pajala shear zone, and is hosted by Svecofennian supracrustal rocks and Karelian greenstones. Magnetite is the ore mineral. The ore body consist of several lenses which dips 45-60 degrees NE. The hanging wall is consist of Lainio group quartzites, phyllites and mica schists, while the skarn interval itself belongs to Savukoski group metavolcanics. The footwall is Savukoski group's dolomites, graphitic schists and phyllites. Ca-Mg rich skarns (clinopyroxene, actinolite, tremolite) are mainly presented at the hanging wall side and short intervals in the ore, while Mg-rich skarns (serpentine) are the main host of the ore. The surrounding skarn minerals have a significant impact to the magnesia (MgO) amount in the magnetite. Serpentine brings the high MgO values to the magnetite, over 1.2% when pyroxenes and amphiboles are the host rocks the magnesia amount in the magnetite is always < 1%. Micas and dolomitic marbles are magnesia poor. The iron grade in the whole rock analysis did not correlate the magnesia amount in the magnetite.

**Keywords:** Magnetite, skarn, iron ore, Tapuli, Norrbotten.

## 1 Introduction

The Tapuli skarn iron ore is located circa 25 km north of Pajala in Norrbotten, Northern Sweden (Fig. 1). It lays within the Pajala Shear Zone (PSZ) like several other skarn iron ore formations for example Stora Sahavaara and Palotieva.

The Tapuli deposit has long history of exploration starting in 1918 magnetometer measurements followed by diamond drilling in 1960's by SGU (Lindroos et al., 1972). Northland started its first drilling campaigne in the spring of 2007 and has thereafter developed Tapuli into mine, which currently produces a high quality iron concentrate. The SRK's resource estimate of Tapuli is 107.4 Mt of iron with average grade 26.01% Fe and 0.23% S (Baker et al., 2011).

The aim of this study is to investigate the occurrence and behaviour of magnesia (MgO) in magnetite from the Tapuli deposit since a high amount of magnesia in the concentrate effects the quality of the final product.

## 2 Geology

The Tapuli skarn iron formation is mainly hosted by Svecofennian supracrustal rocks (1.96-1.85 Ga) and Karelian greenstones (2.5-2.0 Ga) (Fig 2). There are also intrusive rocks of the Lina (1.8 Ga) and Haparanda groups (1.88-1.86 Ga) in the area. (Eilu et al., 2012, Bergman et al., 2001). The Tapuli skarn iron ore is located within the Pajala Shear Zone, which is a NNE-SSW trending crustal scale shear zone system which outlines the boundary between Norrbotten and Karelian craton. (Baker et al., 2011, Lehtinen et al., 2005).
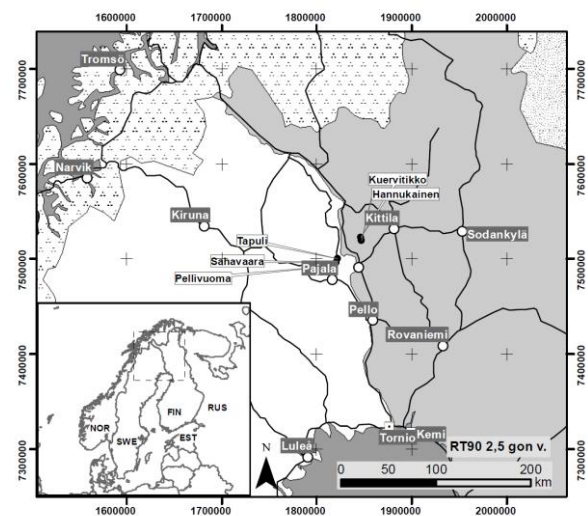


**Figure 1.** Map of northern Fennoscandia showing the location of the Tapuli deposit.

The footwall of the Tapuli deposit is part of the Savukoski group comprising phyllites, graphitic schist and dolomitic marbles (Eilu et al., 2012, Lehtinen et al., 2005). The strict contact between graphitic schist and phyllites is not always clear since the phyllites sometimes are also graphite bearing. The uppermost part of the footwall is dolomitic marbles that have been skarn altered when getting closer to the ore zone.

The hangingwall belongs to Lainio group of metasedimentary rocks (1.96-1.85 Ga) consisting of quartzites, phyllites and mica schists (Eilu et al., 2012, Lehtinen et al., 2005)

The orebody belongs to Savukoski group metavolcanics and consist of skarn and magnetite in

varying proportions. It is steeply dipping and trends in a NE direction, and consist of several lenses dipping 45-60 degrees to the NW (Fig 3.). (Baker et al., 2011). The main host of magnetite ore are mafic Mg-rich skarns consisting of serpentine, phlogopite-biotite and chlorite.Ca-Mg rich (clinopyroxene-actinolite skarn, actinolite skarn, tremolite skarn) are found mainly in the hangingwall, but also as short intervals inside the ore.

Darker green actinolite skarn brecciates pale green clinopyroxene skarn. Tremolite skarn is present together with marbles as short intervals inside the main ore interval. Serpentine skarn has different colours and type of patterns. Mica rich skarns – phlogopite-biotite and chlorite skarns have usually no magnetite.

The skarn contact is rarely clear since the alterations usually continues into metasedimentary rocks of the hanging wall.
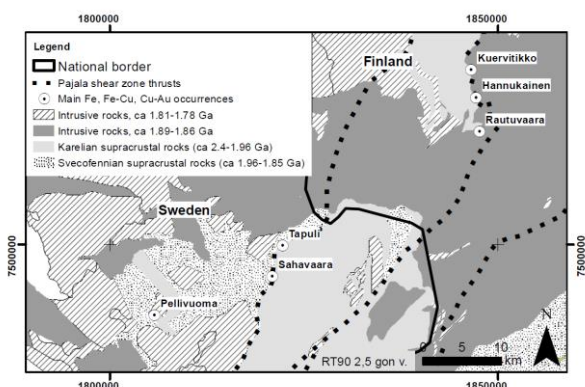


**Figure 2.** Regional geology of the area around the Tapuli deposit.

The ore mineral is magnetite. It is mainly finegrained, but it's texture can vary a lot – disseminated to massive, brecciated to banded. In some parts of the orebody there is coarser grained magnetite grains, that overprint finer grained magnetite (Lindroos et al., 1972). Magnetite can and usually do brecciate skarn minerals. Part of the magnetite is present with Ca-Mg rich skarns (clinopyroxene-actinolite skarn), in the main ore body. Higher magnetite grades goes mostly with serpentine (some cases with dolomitic marbles). Along with magnetite there can be sulphides at footwall side, mainly pyrite and pyrrhotite. The ore is divided into low grade sulphide ore (< 0.5%) and high sulphide ore (> 0.5%) (Baker at al 2011). Short intervals of magnetite is located in dolomitic marbles – usually high grade magnetite without skarn minerals.
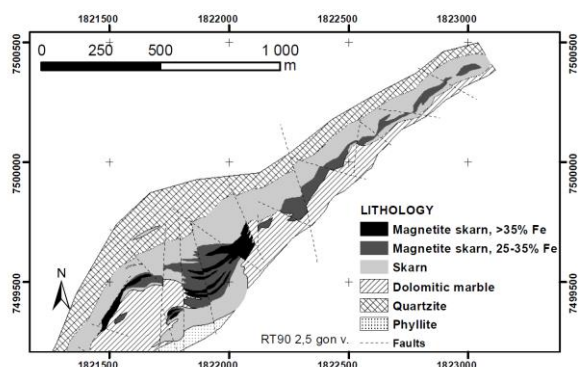


**Figure 3**. Geological map of Tapuli.

# 3 Methods

For this study 20 magnetic fraction buttons out of 65 were selected to be analysed with electron probe microscope in University of Oulu. During 2007 a total amount of 900 m of drillcore from 7 different drillholes were selected to be analysed with Dings Davis Tube tests at Geological Survay of Finland in Outokumpu. The drillcore has been logged, sampled and sent for chemical analysis by Northland. Based on the chemical results circa 5 m long intervals different iron contents were selected for Dings Davis Tube tests (DDT). The samples were divided based on iron and sulphide amount to high grade and low grade ore. These sections thereafter has been combined, homogenized and divided into suitable size of 30 g composite feed samples. Every third sample with a size of 50 g was sent for further mineralogical examination.

The DDT test splitted the samples into magnetic and non-magnetic fractions. After DDT tests every third sample of non- magnetic and magnetic fraction were pressed as a button and analysed with Mineral Liberation Analyser (MLA) in Outokumpu.The mineralogical examination was done for magnetic and non-magnetic fraction with Mineral Liberation Analyser (MLA) to define modal mineralogy, particle size and liberation size of magnetite.

Based on the results of modal mineralogy of the non-magnetic fraction, logging information and results of the chemical analyse samples of the magnetic fraction the buttons were selected to be analysed with electron probe microscope (EPMA) in the Institute of Electron Optics in University of Oulu. 20 magnetite grains were analysed per each button and averages were counted from the analysis. A total amount of 400 analysis were done from 20 buttons were analysed, whereof two buttons were repeat analysis.

# 4 Chemical composition of magnetite

The majority of the samples selected for this study comes from profiles 800 and 700 which represents the central part of the main orebody and can be considered representative for the Tapuli ore body. However the 4 samples come from two other profiles (400 line in the southern part of orebody and 1400 line in the northern part) (Fig 4).

Frietsch described 1985 that average MgO amount in magnetite in Tapuli was 0.3-0.9% (weight percent).
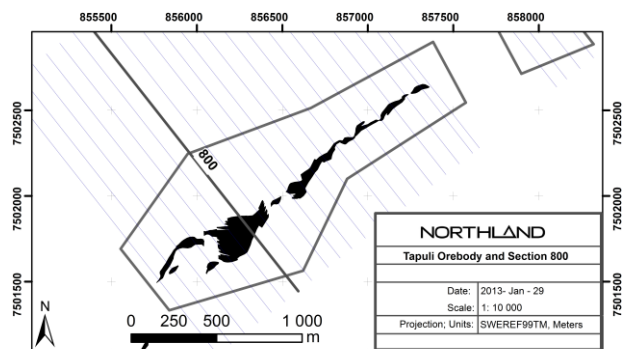


**Figure 4**. Tapuli iron ore with main profile 800.

The selected buttons were divided to 4 different categories: 1) serpentine or magnetite skarn (over 30 % magnetite), 2) pyroxene and amphibole skarn (clinopyroxene skarn, actinolite skarn, tremolite skarn), 3) mica rich skarn (phlogopite-biotite and chlorite skarn) and 4) dolomitic marble. The logging data and results of modal mineralogy of Mineral Liberation Analysis were used selecting the samples. The pyroxene and amphibole skarn are handled together due results are very similar and most of the time they are in same intervals. So called magnetite skarn (> 30% magnetite) is mainly with serpentines and few samples were selected based on high iron content to see does it correlate with magnesia.

In the Mg-rich skarn types the serpentine skarn has highest amount of magnesia in magnetite from 1.2-2.2% (Fig 5.). Mica rich skarns (chlorite, phlogopite-biotite) has usually very low amount of magnetite or no magnetite at all. The MgO amount in magnetite in these mica skarn types are low from 0.06-0.3% (Fig 5).

Ca-Mg rich skarns (clinopyroxene, actinolite and tremolite skarn) have 0.7-0.9% of magnesia in magnetite. Tremolite skarn however is often with dolomitic marble. Magnetite in dolomitic marble has the low amount of magnesia < 0.5%. (Fig 5).

The possible error factors can be the skarn variation in Tapuli, because the skarn type can vary a lot within 5 m interval. Some of the selected intervals were so called mix skarn intervals. When the serpentine amount is higher than 30% it effects the result remarkable. The repeatability of the analysis were tested with two buttons and results were equal.
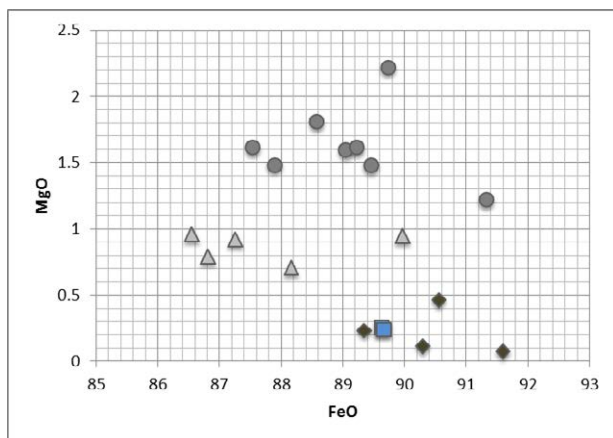


**Figure 5.** MgO amount in magnetite. Circle = serpentine skarn, triangle = clinopyroxene-actinolite skarn, square = mica rich skarns, diamond = dolomitic marble.

## 5 Conclusions

The magnesia amount in magnetite in Tapulivuoma is varying a lot depending of the skarn type, there is good correlation between skarn types and magnesia amount in magnetite. High grade iron ore is mostly with serpentine gangue making the magnesia amount over 1.2%, however the highest values of magnesia in magnetite (> 1.65%) were not following the highest iron grades in whole rock analysis, the magnesia content in the magnetite do not correlate with the iron grade. Mica skarns and dolomitic marble are poor in magnesia (Fig 5). Amphibole skarns and pyroxene skarns have very similar amounts of magnesia in magnetite < 1%.

## References

Baker H, Pattison D, Reardon C (2011) Technical review of the Kaunisvaara iron project, Sweden. June 2011. Cardiff: SRK Consulting (UK) Ltd., 178 p.

Bergman S, Kübler L, Martinsson O (2001) Description of regional geological and geophysical maps of northern Norrbotten County (east of the Caledonian Orogen). 110 p.

Eilu P, Perdahl J-A, Hallberg A, Niiranen T (2012) Mineral deposits and metallogeny of Fennoscandia. Geological Survay of Finland special paper 53, 401 p.

Frietsch R (1985) Formation of Mg-bearing magnetite and serpentine in skarn iron ores in northern Sweden. Geologiska Föreningens i Stockholm Förhandlingar, vol 106. Pt 3, pp. 219-230.

Lehtinen M, Nurmi P.A, Rämö O.T (2005) Precambrian geology of Finland – Key to evolution of the Fennoscandian Shield. Elsevier 736 p.

Lindroos H, Nylund B, Johansson K (1972) Tapuli and Palotieva iron ore occurrence. SGU, unpublished report, series C, Avhandlingar och uppsatser, 695, Årsbok / SGU, 68:2, 45 p.

# High-resolution sulfur isotope and trace element measurements of sphalerites from the Pb-Zn deposits of the Drau Range (Eastern Alps, Austria/Slovenia)

**Elisabeth Henjes-Kunst**
*Resource Mineralogy, Montanuniversitaet Leoben, Peter-Tunner-Str. 5, 8700 Leoben, Austria*

**Adrian J. Boyce**
*Scottish Universities Environmental Research Centre, Rankine Avenue, East Kilbride, Glasgow, G75 0QF, UK*

**Frank Melcher**
*Bundesanstalt für Geowissenschaften und Rohstoffe, Stilleweg 2, 30655 Hannover, Germany*

**Johann G. Raith**
*Resource Mineralogy, Montanuniversitaet Leoben, Peter-Tunner-Str. 5, 8700 Leoben, Austria*

**Abstract.** High-resolution (partly in-situ) sulfur isotope measurements on sulfides in 17 samples from 5 different Pb-Zn deposits of the Drau range have been carried out. High-resolution sulfur isotope investigations provide knowledge on small-scale variations in the sulfur isotopic composition of coexisting sulfides and can help to interpret the mineralization processes. The sulfur isotopic composition provides evidence for different sulfur reservoirs and fluids involved in the mineralization process. Small-scale isotope heterogeneities can be related to textural aspects and this enables to recognize different sulfur reservoirs, one providing bacteriogene reduced sulfur (*BSR*) and another one responsible for thermochemical reduced sulfur (*TSR*). Both reservoirs were involved into ore formation and were able to contribute reduced sulfur during the whole mineralization process.

In addition to isotopic measurements, major, minor and trace element analyses by electron microprobe (*EMP*) have been carried out on sphalerites in order to investigate if any relation between sulfur isotopic and chemical composition exists.

**Keywords:** Sulfur isotopes, carbonate-hosted Pb-Zn deposits, sphalerite, Eastern Alps, genetic models.

## 1 Introduction

Although the carbonate-hosted Pb-Zn deposits of the Drau Range have been studied for decades (see Schroll, 2008) the genesis and the processes leading to ore mineralization are not fully understood yet. Two contrasting hypotheses have been discussed for the so-called *"Alpine type Pb-Zn deposits"*: *(1) syngenetic/synsedimentary* ore-deposition coeval with the sedimentation of the host rocks at about 220 Ma (e.g. Schneider, 1964, Schulz, 1968) vs. *(2) epigenetic* ore formation during (early) diagenetic burial of the host rocks at about 200 Ma (Kuhlemann & Zeeh, 1995, Leach et al., 2003). Preliminary Rb-Sr isotope analyses on sphalerites from Bleiberg confirmed both ages (Melcher et al., 2010).

Various studies (e.g. Herlec et al., 2010, Kuhlemann et al., 2001, Schroll et al., 1983) already reported sulfur isotope data from the Pb-Zn district in the Drau Range. Here we provide information on small-scale spatial variations. High-resolution sulfur isotopic measurements may help to identify different sulfur reservoirs involved in ore-formation. Understanding the processes controlling small-scale isotope variations can contribute some further knowledge to unravel the ore genesis.

## 2 Geological setting/mineralization

The Drau Range (Eastern Alps, Austria/Slovenia) belongs to the Upper Austroalpine unit (Tollmann, 1977), extending over approximately 180 km distance from Austria (W) to Slovenia (E).

The Pb-Zn deposits occurring in the Drau Range are hosted in a Triassic carbonate sequence deposited on a passive continental margin. Pb-Zn mineralization is restricted to three different stratigraphic units of the Triassic: (1) Anisian, the so-called *"Alpiner Muschelkalk"* represents the lowermost ore-bearing horizon; (2) Ladinian, the platform carbonates of the *"Wetterstein Formation"* are by far the most important host rocks; and (3) Carnian; the carbonate interlayers between the *"Raibl/Cardita-shales"* are locally also ore-bearing. Mineralization within all ore-horizons can be concordant (e.g. graded bedding of ore minerals, indicating a sedimentary origin) as well as discordant (e.g. massive breccia ore, or mineralized veins). The ore-gangue assemblage within these deposits is very simple and is principally composed of sphalerite, galena, pyrite/marcasite, carbonates, barite, fluorite, gypsum/anhydrite and quartz, representing a typical low-temperature assemblage. Due to mineralogical, geochemical and isotopic characteristics, these deposits were separated from the large group of carbonate-hosted MVT deposits and were classified as *"Alpine-type Pb-Zn deposits"(APT)* (e.g. Köppel & Schroll, 1988). Bleiberg (Austria) is the type locality for these APT deposits and was mined from 1333 to 1992. During the period of active mining 2.2 Mio. tons of metal (approximately the same amounts of Pb and Zn) were extracted (Schroll, 2008). Mezica (Slovenia) is another large APT deposit in the Drau Range; until its closure in 1994 approximately 1.6 Mio. tons of metal (Pb > Zn) were mined (Herlec et al., 2010).

## 3 Methodology

Sulfur isotope analyses were carried out at the Stable Isotope Laboratory at the Scottish Universities Research Center (SUERC) in Glasgow (Scotland). Sulfur isotope measurements were made using a gas mass spectrometer after combustion of the sulfide samples. Combustion was performed in two different ways: (1) micro-drilled sulfides were fused under vacuum conditions at 1076°C in a $CuO_2$ matrix, and (2) laser-ablation and combustion in an $O_2$-excess environment of ~2 to 14 mm long and ~25 – 50 μm wide trenches using a SPECTRON LASERS 902Q CW Nd-YAG laser (1-W power). The $SO_2$ gas was then cryogenically purified in several heating and freezing steps and afterwards analyzed on VG SIRA II and Thermo Fisher Scientific MAT 253 gas mass-spectrometers. The process for S-isotope analyses is described more detailed in Fallick et al. (1992) and in de Groot (2009). $\delta^{34}S$ values were calculated from the raw $\delta^{66}SO_2$ data (achieved from the gas mass spectrometer) according to the actual standardization of each machine. For the laser-ablated data, also some mineral-depending fractionation factors had to be considered during calculations (Wagner et al., 2002). Sulfur isotope measurements are reported in the standard $\delta^{34}S$ ($^{34}S/^{32}S$) notation in per mill (‰) relative to the Canon Diablo Troilite (CDT). The average uncertainty of the sulfur isotope measurements is 0.053.

Trace element analyses of sphalerites were performed using wavelength dispersive (WDS) electron microprobe techniques *(a)* using a JEOL JXA8200 electron microprobe (EMP) at the chair of Resource Mineralogy (Montanuniversitaet Leoben, Austria) and *(b)* using a CAMECA SX100 EMP at the Federal Institute for Geosciences and Natural Resources (BGR, Hannover, Germany). During EMP sessions the concentrations of As, Fe, Pb, Ge, Cu, Tl, Cd and Zn and S in sphalerites were measured.

## 4 Results

The sulfur isotopic composition of the investigated sulfides (sphalerite, galena, pyrite/marcasite) varies in the -30.4 to +1.8‰ range (Figure 1, Table 1). A strong bias towards light sulfur isotopic composition is evident in the dataset; 52% of the investigated sulfides show $\delta^{34}S$ < -20‰. However, a few sulfides display a heavier sulfur isotopic composition ($\delta^{34}S$ > -5‰). Interestingly, in some samples sulfides (particularly sphalerites) with very light ($\delta^{34}S$ < -20‰) and heavy ($\delta^{34}S$ > -5‰) sulfur isotope composition occur together on a small scale of approximately 1 cm.

No uniform evolution trend of the sulfur isotopic composition of coexisting light and heavy sulfides is evident. An evolution from isotopically light to heavy sphalerite is visible in some samples, others show an opposite trend. Within the same sample the sulfur isotopic composition of coexisting light and heavy sphalerites is related to their Fe- and Cd contents; in these cases isotopically lighter sphalerites are enriched

in Fe (< 0.5 mass%) and depleted in Cd (< 0.1 mass%), whereas heavier ones show the opposite enrichment/depletion pattern. The preferred enrichment of Fe with respect to Cd in isotopically light ZnS is not unequivocally valid, because some rather Cd-rich sphalerites (range 0.2 – 1.1 mass%, average 0.4 mass%) display very low $\delta^{34}S$ values (< -26‰). Furthermore, the heaviest sphalerite values of the sample set ($\delta^{34}S$ +1.8‰, Jauken deposit, Table 1) are Fe-rich (0.2 – 2.2 mass%, average 0.4 mass%) but Cd-poor (< 0.1 mass%). Hence, the observed relation between Fe/Cd and sulfur isotopic composition is only valid for isotopically different sphalerites coexisting within the same sample but not for sphalerites from different ore horizons within an ore deposit or for different ore deposits.

**Table 1:** Ranges of the sulfur isotopic composition of sulfides from different Pb-Zn deposits in the Drau Range.

| Deposit | Sample | $\delta^{34}S$ | | | | |
| | | ZnS | | PbS | | FeS$_2$ |
| | | min | max | min | max | |
|---|---|---|---|---|---|---|
| Bleiberg | R8/2 | -24.5 | -3.7 | | | -24.5 |
| Bleiberg | J10/4 | -28.1 | -24.6 | -25.8 | | |
| Bleiberg | K2/2 | -30.4 | -21.5 | | | |
| Bleiberg | C6.14 | -29.0 | -25.4 | -29.8 | | |
| Bleiberg | E14.6 | -24.4 | -21.2 | -28.8 | | |
| Bleiberg | E14.2-4 | -24.5 | -23.7 | -20.9 | | |
| Bleiberg | EHK02 | -22.6 | -4.6 | -25.5 | -7.7 | -21.8 |
| Bleiberg | WS_Blb07 | | | -8.5 | | |
| Bleiberg | Blb17 | -26.0 | -1.5 | -24.4 | -20.9 | |
| Bleiberg | Blb26 | -21.5 | -19.8 | | | |
| Topla | Tp01 | -23.1 | -20.6 | | | -23.9 |
| Topla | Tp04 | -12.9 | -9.8 | | | -16.5 |
| Mezica | MzH01 | -20.1 | -13.3 | -20.7 | -15.4 | |
| Mezica | Mz08 | -10.8 | -9.1 | | | |
| Mezica | SF03 | -16.0 | -14.0 | -18.7 | -14.4 | |
| Jauken | JK5-9 | -1.6 | +1.8 | | | |
| Töplitsch | Toe01 | -13.2 | -11.5 | | | |

## 5 Dicussion/Conclusion

The wide variation in the sulfur isotope composition of sphalerite (and associated galena plus Fe-sulfides) from the Pb-Zn deposits in the Drau Range indicates, that at least two different sulfur reservoirs were involved in ore-formation; one contributing light, the other heavy sulfur. Since sulfides having small $\delta^{34}S$ values (< -20‰) occur together on a mm-cm scale with those having higher $\delta^{34}S$ values (> -5‰) in samples from different ore horizons, both reservoirs were able to provide reduced sulfur during the whole mineralization process. Since fossil filaments of sulfate-reducing bacteria and ZnS-nanospheres produced by bio-mineralization processes have been described from sphalerite from the main ore horizons of the Bleiberg

deposit (Kucha et al., 2010), it is likely that at least some part of the light sulfide-sulfur derived via bacterial sulfate reduction (BSR) of seawater sulfate. The heavier ($\delta^{34}S$ > -5‰) reservoir probably derived its sulfur signature from thermochemical sulfate reduction (TSR), what may indicate a minor hydrothermal imprint. Since 52% of the investigated sulfides are characterized by $\delta^{34}S$ values < - 20‰, it is very likely that, similar to the Irish Navan deposit (Fallick et al., 2001), BSR played an important role during ore-formation. As sulfides having $\delta^{34}S$-values > -5‰ are very rare, TSR was presumably of minor importance during ore formation. In analogy to the Irish Pb-Zn province only small, uneconomic deposits (e.g. Jauken), exclusively contain TSR-derived sulfur (Fallick et al., 2001).
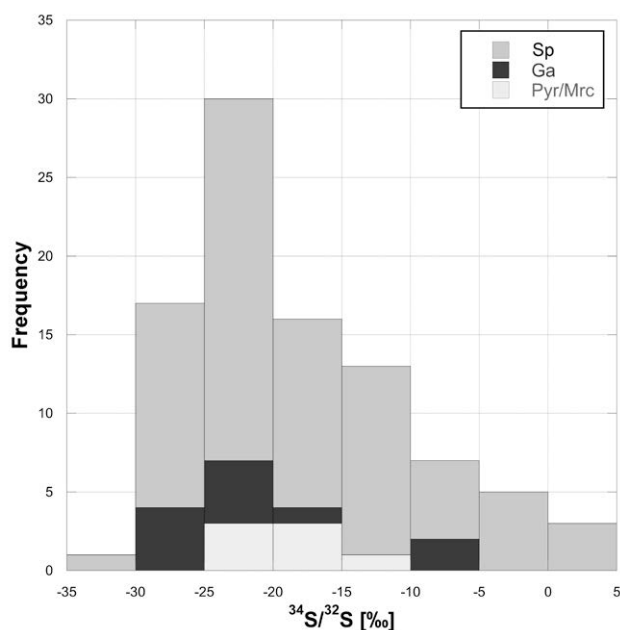


**Figure 1:** Histogram displaying the sulfur isotopic composition of the investigated sulfides. The predominance of rather light sulfur ($\delta^{34}S$ < -20‰) is visible. The samples are from 5 historic Pb-Zn deposits in the Drau Range (see Table 1).

The coexistence of sulfur isotopically light and heavy sulfides leads to some conflicts concerning the temperature of the mineralizing fluids, since bacterial sulfate reduction works less effective at temperatures > 80 – 100°C (Machel et al., 1995). TSR in contrast starts to be effective at temperatures > 80°C. These temperature-dependencies make it plausible that different fluids transported reduced sulfur from the two reservoirs to the depositional side. It can be assumed that at least a part of the ore mineralization occurred in or close to the BSR reservoir, since fossil bacteria filaments and ZnS nanospheres are present in some ore horizons (Kucha et al., 2010). Hydrothermal pulses introducing fluids from the underlying units probably lead to formation of sulfide having a heavy sulfur isotope composition. These hydrothermal pulses occurred sporadically. Intermediate sulfur isotope compositions ranging from -15 to -8‰ can be explained by local mixing of sulfur from the two reservoirs. Since no explicit relation of trace element

and sulfur isotopic composition is evident, it is not very probable that reduced sulfur species and metals were transported by the same fluid. Pb-Zn mineralization in the Drau Range resulted most probably from interaction of two sulfur-bearing and one metal-bearing fluid.

However, a precise genetic model for the Pb-Zn mineralization in the Drau Range requires further analytical information; e.g. high-resolution Pb-isotope data of the ore assemblage can help to determine possible differences in the metal sources. Primary fluid inclusions in sphalerites would contribute further information on fluid composition and formation temperatures. Unfortunately, no primary fluid inclusions in sphalerites have been detected so far. Further on, radiometric Rb-Sr dating of the chemical and sulfur isotopical defined sphalerites should give information on the age of the ore formation. Ore forming processes are best evaluated by using a multi-technical investigation approach.

# References

de Groot PA (2009) Handbook of stable isotope analytical techniques. Amsterdam [u.a.]: Elsevier.

Fallick AE, Ashton JH, Boyce AJ, Ellam RM, Russell MJ (2001) Bacteria were responsible for the magnitude of the worl-class hydrothermal base metal sulfide orebody at Navan, Ireland. Econ Geol 96: 885-890.

Fallick AE, McConville P, Boyce AJ, Burgess R, Kelley SP (1992) Laser microprobe stable isotope measurements on geological materials: Some experimental considerations (with special reference to $\delta^{34}S$ in sulphides). Chem Geol: Isotope Geoscience section 101: 53-61.

Herlec U, Spangenberg J, Lavrič J (2010) Sulfur isotope variations from orebody to hand-specimen scale at the Mežica lead–zinc deposit, Slovenia: a predominantly biogenic pattern. Mineral Deposita 45: 531-547.

Köppel V, Schroll E (1988) Pb-isotope evidence for the origin of lead in strata-bound Pb-Zn deposits in triassic carbonates of the Eastern and Southern Alps. Mineral Deposita 23: 96-103.

Kucha H, Schroll E, Raith JG, Halas S (2010) Microbial sphalerite formation in carbonate-hosted Zn-Pb ores, Bleiberg, Austria; micro- to nanotextural and sulfur isotope evidence. Econ Geol 105: 1005-1023.

Kuhlemann J, Vennemann T, Herlec U, Zeeh S, Bechstaedt T (2001) Variations of sulfur isotopes, trace element compositions, and cathodoluminescence of mississippi valley-type Pb-Zn ores from the Drau Range, Eastern Alps (Slovenia-Austria); implications for ore deposition on a regional versus microscale. Econ Geol 96: 1931-1941.

Kuhlemann J, Zeeh S (1995) Sphalerite stratigraphy and trace element composition of East Alpine Pb-Zn deposits (Drau Range, Austria-Slovenia). Econ Geol 90: 2073-2080.

Leach DL, Bechstadt T, Boni M, Zeeh S (2003) Triassic-hosted MVT Zn-Pb ores of Poland, Austria, Slovenia and Italy. Dublin: IAEG.

Machel HG, Krouse HR, Sassen R (1995) Products and distinguishing criteria of bacterial and thermochemical sulfate reduction. Appl Geochem 10: 373-389.

Melcher F, Henjes-Kunst F, Henjes-Kunst E, Schneider J, Thöni M (2010) Erste Rb-Sr Isotopendatierung an Sphalerit der Zn-Pb Lagerstätte Bleiberg (Kärnten), sowie Sr- und Sm-Nd-Isotopendaten von kogenetischen Karbonat und Fluorit. J Alp Geol 52.

Schneider HJ (1964) Facies Differentiation and Controlling Factors for the Depositional Lead-Zinc Concentration in the Ladinian Geosyncline of the Eastern Alps. In: Amstutz, G. C. (ed.) Dev Sedimentol: Elsevier, 29-45.

Schroll E (2008) Die Blei-Zink Lagerstätte Bleiberg die Geschichte ihrer Erforschung. Klagenfurt: Naturwiss Ver Kärnten.

Schroll E, Schulz O, Pak E (1983) Sulphur isotope distribution in the Pb-Zn-deposit Bleiberg (Carinthia; Austria). Minerali Deposita 18: 17-25.

Schulz O (1968) Die synsedimentaere Mineralparagenese im oberen Wettersteinkalk der Pb-Zn-Lagerstaette Bleiberg-Kreuth (Kaernten). The syngenetic mineral paragenesis in the upper Wetterstein limestone of the Bleiberg-Kreuth lead-zinc deposit, Carinthia. TMPM. Tschermaks Mineral Petrogr Mitt 12: 230-289.

Tollmann A (1977) Die Zentralalpen, Geologie von Österreich mit 25 Tabellen. Wien: Deuticke.

Wagner T, Boyce AJ, Fallick AE (2002) Laser combustion analysis of $\delta^{34}$S of sulfosalt minerals: determination of the fractionation systematics and some crystal-chemical considerations. Geochim Cosmochim Ac 66: 2855-2863.

# Mineral magnetism identifies the presence of pyrrhotite in the Navan Zn-Pb deposit, Ireland: implications for low temperature pyrite to pyrrhotite reduction, timing of mineralization and future exploration strategies

S.C. Johnson[1], T.D. Raub[2] & J.H. Ashton[3]

[1]CODES, ARC Centre of Excellence in Ore Deposits, University of Tasmania, Sandy Bay, Hobart, Tasmania, Australia
[2]Department of Earth and Environmental Sciences, University of St Andrews, North St., St Andrews, Fife, Scotland.
[3]Boliden Tara Mines Limited, Knockumber Rd., Navan, County Meath, Ireland

**Abstract** Presented here are the preliminary results of a pilot study from the Navan Zn-Pb deposit utilising the first example of Superconductive Quantum Interference (SQUID) magnetic microscopy in relation to ore deposits. Using this method of microscale, high-resolution magnetic mapping we have identified the pervasive presence of microscopic ferromagnetic pyrrhotite. A previous palaeomagnetic age based on a limited reference frame from N. America by Symons et al. (2002) suggested an epigenetic origin for Navan. We have compiled a new Apparent Polar Wander (APW) path for Scotland that is better constrained for comparison to Navan, to which the Symons et al. (2002) study does not hold true. The identification of pyrrhotite in the ore assemblage holds promise to aid future investigations into the geochemistry of the Irish ore systematics. In addition, our employment of hand-held magnetic susceptibility tests on drillcore has defined orders of magnitude differences between samples of economic grade and those of little to no mineralization, this can be developed in the near-mine environment as a novel, cost-effective and low impact method of vectoring towards ore.

**Keywords** Irish-type Zn-Pb, Navan, Pyrrhotite, magnetics

## 1 Introduction and rationale

There is a plethora of evidence that metallogenesis in the Irish Midlands took place during the early to mid Lower Carboniferous forming the world class Navan deposit and other Irish-type Zn-Pb deposits. Work also supports that the process involved syndiagenetic replacement and, in places, exhalative deposition (Boyce et al., 1983). Complementary to these results, is the fact that the vast majority of base metal occurrences in the Irish ore-field occur within early to mid Lower Carboniferous strata, a significant framework upon which mineral exploration strategy is built.

Despite this there has been much debate with regard to the age of mineralization in Ireland (i.e. Hitzman, 1999; Wilkinson, et al., 2005 and Blakeman et al., 2002). Textural and isotopic evidence favours early- to mid-Carboniferous age for ore precipitation (Ashton et al., 2003 and references therein); work by Peace & Wallace (2000) suggests an epigenetic, post-Arundian, origin however their focus was on the carbonate phases and host rock, and palaeomagnetism appears to favour late Carboniferous to early Permian age for the various Irish deposits (Symons et al, 2002 & Pannalal et al., 2008).

Extended (tens of millions of years) crustal fluid flow at high geothermal gradient during varying stress regimes of the developing basin, however, is difficult to conceive. Hence workers have favoured one or more discrete, short-lived episodes of mineralization (Ashton et al., 2003 and Blakeman et al., 2002). The main objections to the late, epigenetic age for Navan derived from palaeomagnetism are both external and internal to the method. Proposed ages vary dramatically for the different Iaepetan-suture-proximal Irish Zn-Pb occurrences (Symons et al., 2002 & Pannalal, et al., 2008). In some cases, this age uncertainty reaches ~30 million years between deposits separated only by ~10 km along strike and hosted by units of similar age (Symons et al., 2002), seeming to contradict intuition of reasonable thermal gradients and a common regional history. The late epigenetic age proposed is also in direct conflict with the geology present, namely mineralized clasts present in a submarine flow horizon at Navan, shown to be Chadian in age (345Ma), ~ 10Ma older than the proposed epigenetic age ascertained by palaeomagnetics. Assessing a confident age for mineralization at Navan and the other Irish deposits may aid in defining intelligent exploration strategy and exploitation practice. This can be achieved by assigning enhanced value to, for example, one of the fault generations, or to a particular stratigraphic horizon.

## 2 Age uncertainty

In order to address the variation in ages for Navan and evaluate the epigenetic age proposed by Symons et al. (2002) a comprehensive literature review of published palaeomagnetic data for Scotland, coupled with the most recent radiometric age determinations of the units was undertaken. From this we have compiled a new Apparent Polar Wander path for Scotland during the Carboniferous that we argue is a more apt reference frame than that of N. America used by Symons et al. (2002). When the Symons et al. (2002) published palaeo-pole for Navan is compared to this new reference frame their interpreted position does not correlate well with that of our new APW. We are currently undertaking additional work to increase our sample set and better constrain our new APW path to give an updated age to mineralization at Navan.

## 3 Sample analysis

A series of polished blocks were examined and selections were made based on locations, both proximal and distal to proposed 'feeder' faults, in addition to textures, ore grade and stratigraphic horizon to give a data set that encompassed a range of features and styles of ore, typical within the Southwestern Extension of the deposit (SWEX). From this, 15 samples selected to be analysed for their magnetic properties using a Superconducting Quantum Interference Device (SQUID). The SQUID microscope is the most sensitive magnetometer available for making quantitative measurements of magnetic fields with unprecedented spatial resolutions of micro-scale magnetism within a $1-2cm^2$ sample (Weiss, et al., 2007). Instead of measuring only the net magnetic moment, like other magnetic susceptibility meters, the SQUID microscope measures the vertical component of the magnetic field emitted (Weiss, et al., 2007). To our knowledge this is the first example of such a technique being used on samples form an ore deposit and in the greater context of mineral exploration and ore genesis.

Analysis using thermal demagnetisation experiments has identified the presence of pyrrhotite, combined with the SQUID imaging can allow us to define texture and phase specific occurrences of the pyrrhotite (Fig. 1). Magnetic susceptibility of samples of drill core allowed the collection of whole rock magnetic susceptibility values.

A Barrington MS2 metre was used to collect these readings, unlike the SQUID microscope it measures the, more widely used, net magnetic moment of a sample. Samples analysed where grouped according to ore grade; Group 1- Zn-Pb assay values ranging from +20-5% (5% being ore cut-off grade); Group 2- areas in marginal haloes around ore grade lenses (2-5% Zn-Pb values) and Group 3 was drill core that held little to no mineralization (Zn-Pb values <1%). In addition, a visual estimation, like that practiced by mine geologists, was also used to ensure the samples fell within our defined parameters. What we find is that there are 3 distinct groupings of magnetic susceptibility values, each separated by orders of magnitude difference and correlate well with the three groups defined by varying mineralisation. Samples with high magnetic susceptibilities were also highly mineralized, and those with low values had little in the way of mineralization.

## 4 Implications

The presence of pyrrhotite has implications for the chemistry of the ore forming process as the reduction from pyrite to pyrrhotite is often associated with trace element mobilisation and the release of sulphur into the system, thereby aiding the potential for increased metal sulphide accumulation. This transition is usually considered as occurring at temperatures in excess of 300°C (Craig & Vokes, 1993), though fluid temperature studies at Navan have shown the fluids to be variable, a general consensus is that temperatures were far below 220°C (Wilkinson et al., 2005 and references therein). This is not only evidence in support of the reduction reaction occurring at lower temperatures than previously considered but also sets a framework for future investigation into the thermodynamic constraints and paragenesis of Irish ore minerals. Although the pyrrhotite is often microscopic and sometimes even difficult to image under SEM (micron-scale inclusions) our step demagnetisation results and EPMA analysis show that its signature is present. With this in mind, the large contrast in ferromagnetism between the pyrrhotite present, even as trace, and the other dia- or para-magnetics minerals in the ore assemblage means that it is easily discernable in simple hand-held magnetic susceptibility tests. This can be utilised in the near-mine exploration environment as another potential indicator of ore. With further development and with more in-depth analysis in a future study to fully understand the phases present and the nature of the occurrence of magnetic minerals, we believe that this can add significant understanding of large scale magnetic surveys, giving them better scientific grounding, and be utilised in near mine exploration. Once the character of the magnetic signature of a prospect or deposit is characterised we envisage this would allow for greater a prospecting range in the future at the initial stages of exploration i.e. beyond simple illminite vs. magnetite series granites. In addition, simple hand-held magnetic susceptibility tests on drill-core can be used by mine geologists to aid in the delineation of economic concentrations of ore associated with the magnetic phase
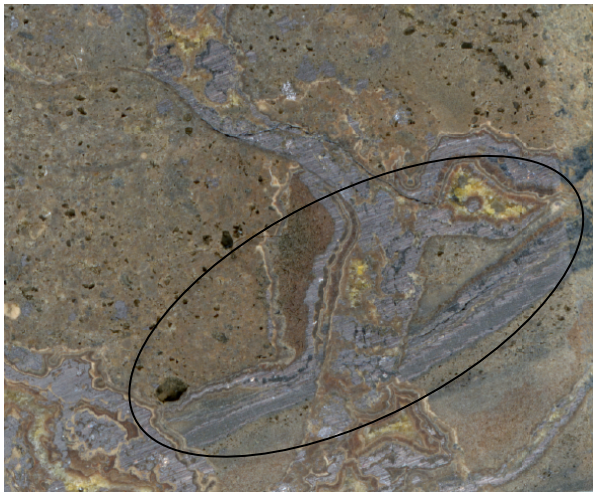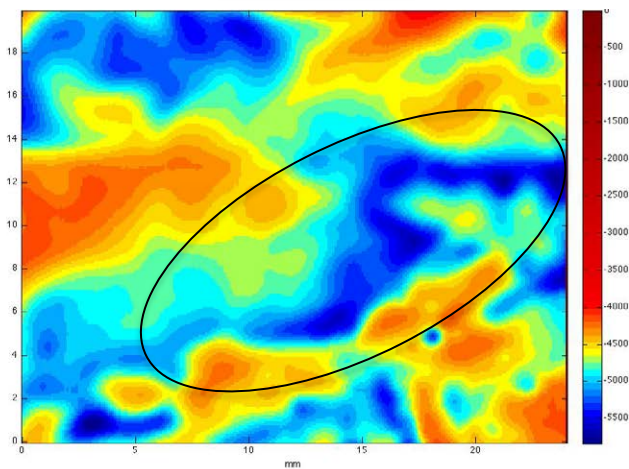
**Figure 1.** Image of polished ore sample (NO1351) containing galena and sphalerite. Below is the SQUID image showing, ferromagnetic signature in blue, red indicates non-magnetic and yellow represents 'return –fields' around the areas of high ferromagnetism. Circled to annotate the association of magnetism with galena phase- where small pyhrrotite inclusions are hosted.

## References

Ashton JH, Holdstock MP, Geraghty JF, O'Keeffe WG, Martinez N, Peace W, Philcox ME (2003) The Navan orebody discovery and geology of the SW extension. In: Proceedings of the IAEG Millenium Conference on Europe's base metal deposits, Galway, May 2000, Irish Association for Economic Geology, Dublin

Blakeman R, Ashton JH, Boyce AJ, Fallick AE, Russell MJ (2002) Timing of Interplay between Hydrothermal and Surface Fluids in the Navan Zn + Pb Orebody,Ireland: Evidence from Metal Distribution Trends, Mineral Textures, and δ34S Analyses. Economic Geology. 97:73-91

Boyce AJ, Coleman ML, and Russell MJ. (1983) Formation of fossil hydrothermal chimneys and mounds from Silvermines, Ireland. Nature, 306: 545–550.

Craig JR. & Vokes FM. (1993) The metamorphism of pyrite and pyritic ore: An overview. Min. Mag., 57:3-18

Hitzman MW (1999) Extensional faults that localize Irish syndiagenetic Zn-Pb deposits and their reactivation during Variscan compression. In: McCaffrey, KJW, Longeran L & Wilkinson JJ (eds) Fractures, Fluid Flow and Mineralization. Geological Society, London, Special Publications, 155: 233-245.

Pannalal SJ, Symons DTA and Sangster DF (2008) Palaeomagnetic evidence of a Variscan age for the epigenetic Galmoy zinc-lead deposit, Ireland. Terra Nova, 20: 385-393

Peace WM, Wallace MW (2000) Timing of mineralization at the Navan Zn-Pb deposit: a post-Arundian age for Irish mineralization. Geology 28:711–714

Symons DTA, Smethurst MT, Ashton JH (2002) Paleomagnetism of the Navan Zn-Pd deposit, Ireland. Economic Geology, 97: 997-1012.

Weiss BP, Lima AE, Fong LE and Baudenbacher FJ (2007), Paleomagnetic analysis using SQUID microscopy. J. Geophys. Res., 112

Wilkinson J.J., Eyre S.L., and Boyce A.J. (2005) Ore forming processes in Irish-type carbonate-hosted Zn- Pb deposits: Evidence from mineralogy, chemistry and isotopic composition of sulfides at the Lisheen Mine: Economic Geology. 100: 63-86

# Composition and phase relations of the complex hydrothermal Fe-Ni-Co arsenide and sulfarsenide minerals from Dobšiná (Slovakia)

Stefan Kiefer* & Juraj Majzlan
*Institute of Geosciences, Friedrich-Schiller-University Jena, Germany (*correspondence: Stefan.Kiefer@uni-jena.de)*

**Abstract.** The Dobšiná ore field has been known since the 13th century and even though there is no longer any industrial mining activity, it is still famous for its remarkable supply of Fe-Ni-Co sulfarsenide and arsenide minerals, representing the most important mineralization type within the deposit. The chemical composition of sulfarsenide and arsenide minerals is rather complex and changes rapidly on a micrometer scale due to extensive substitution on the cation and anion sites as well as broad polymorphism. Although the five-component system Ni-Fe-Co-As-S has been examined in comprehensive studies, the extent of the compositional and stability fields within the system at low temperatures is not yet understood in detail. Within this research, we present extensive optical studies, microprobe analyses and electron backscatter diffraction data and attempt to reach a better understanding of low temperature phase relations, chemical variations and polymorphism in the system.

**Keywords.** Ni-Fe-Co sulfarsenides and arsenides, chemical variations, polymorphism

## 1 Variation(s) in the chemical composition and polymorphism

The Fe-Ni-Co arsenides and sulfarsenides found in nature are a large and variable group of minerals, which – as experimental studies have shown – are more complex than assumed (e.g. Hem and Makovicky 2004a, b).

One fact making the system so complex is the extensive substitution of Fe, Ni, Co on the cationic site and substitution and variations among the covalent bound $(S_2)^{2-}$, $(As_2)^{2-}$, $(AsS)^{2-}$ dimers. The substitution has been examined in various studies at several temperatures (e.g. Yund 1962, Klemm 1965, Maurel and Picot 1974, Kretschmar and Scott 1976, Hem and Makovicky (2004a, 2004b)).

## 2 The samples from the Dobšiná ore field

The samples originate from the Dobšiná ore field (Slovakia). The Fe-Ni-Co ores were deposited during the quartz-sulfide period of the mineralization with formation conditions of 200-300 °C and 3.6-4.4 kbar (Hurai et al. 2002). The exact location of the samples within the ore veins and stockworks is not known because the samples were not taken directly from the mines, but from old dumps.

## 2.1 Optical studies

Optical studies show the presence of many different phases which include gersdorffite, cobaltite, arsenopyrite, loellingite, rammelsbergite, pararammelsbergite, safflorite, and possible triarsenide minerals like skutterudite. Pyrite, chalcopyrite, and fahlore are minor minerals. The microscopic investigations show also mineral zonation and exsolution textures (Fig. 1). The results agree very well with the earlier observations of Halahyjová-Andrusovová (1964).
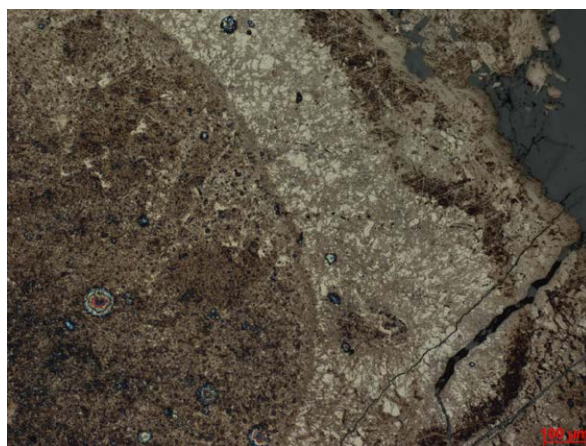


**Figure 1.** A reflected-light microphotograph showing zonation and exsolution textures

## 2.2 Microprobe studies

The composition of the sulfarsenide and arsenide minerals changes rapidly even on micrometer scale documented by back scattered electron images (BSE images) (Fig. 2 and 3).
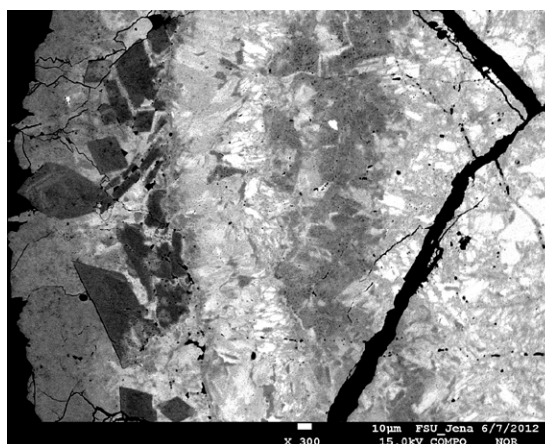


**Figure 2.** BSE image showing occurrence of multiple phases
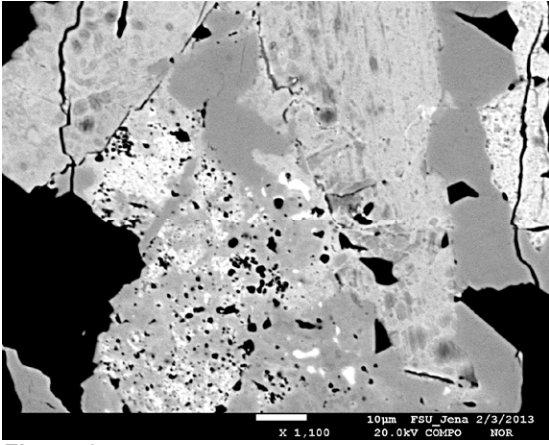
**Figure 3.** BSE image showing occurrence of multiple phases and possible exsolution structures



**Figure 4.** Plot of the composition fields of sulfarsenides in the system FeAsS-NiAsS-CoAsS

The chemical variation within the ore is complex and microprobe analyses show broad variations particularly in the As and S content. Nevertheless, the chemical analyses show that the mineral composition within one phase system (e.g. FeAsS-NiAsS-CoAsS) confirms a chemical trend and shows possible immiscibility fields (Fig. 4).

## 3 Concluding remarks

Earlier studies, investigating this system were narrowed either to fewer components (e.g., Yund 1962) or higher temperatures (e.g., Maurel and Picot 1974) or to a broad temperature field (e.g., Kretschmar and Scott 1976). Temperatures at the high end of these studies are not appropriate to describe natural aggregates. All studies prove that the extent of solid solutions is increasing with the temperature, nevertheless the conclusions regarding the minimal temperature of complete immiscibility or chemical composition of the co-existing phases are not always matching. Although, several deposits of Fe-Ni-Co arsenide and sulfarsenide minerals have been studied in the past (e.g., En Nacri et al. 1995, Hem et al. 2001, Fanlo et al. 2004, 2006, Gervilla et al 2012) the correspondence of these natural assemblages with their estimated temperatures of formation and the experimental studies is satisfactory but not complete. The examination of the samples from the Dobšiná ore field gives us the opportunity to investigate the ore formation at the lower end of the system. With our data we are able to show, that the Fe,Ni,Co sulfarsenides show an extensive immiscibility field at the temperatures and pressures of their formation confirming the experimental studies. Furthermore, it is possible to define the extent of the compositional fields for individual sulfarsenides as well as phase relations which are inaccessible to experimental studies with respect to their formation conditions.
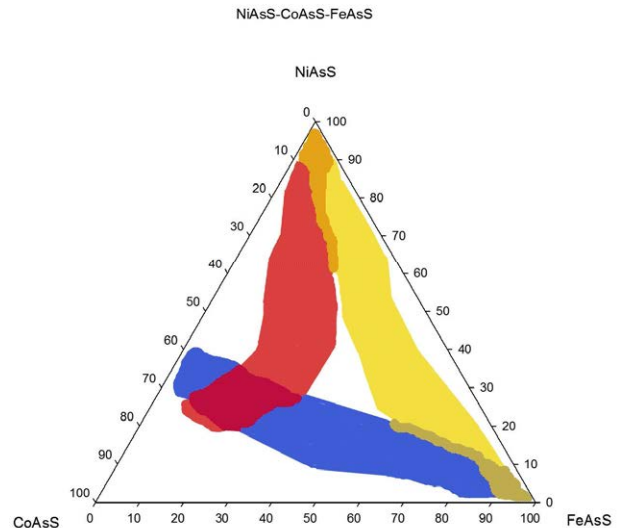
## References

En Nacri, A., Barbanson, L., Touray, J.-C., 1995: Mineralized hydrothermal solution cavities in the Co-As Aït Ahmane mine (Bou Azzer, Morocco). Miner. Deposita 30, 75-77.

Fanlo, I., Subias, I., Gervilla, F., Paniagua, A., Garcia, B., 2004: The composition of Co-Ni-Fe sulfarsenides, diarsenides and triarsenides from the San Juan de Plan deposit, central Pyrenees, Spain. Can. Mineral. 42, 1221-1240.

Fanlo, I., Subias, I., Gervilla, F., Manuel, J., 2006: Textures and compositional variability in gersdorffite from the Crescencia Ni-(Co-U) showing, central Pyrenees, Spain: primary deposition or re-equilibration? Can. Mineral. 44, 1513-1528.

Gervilla, F., Fanlo, I., Colas, V., Subias, I., 2012: Mineral compositions and phase relations of Ni-Co-Fe arsenide ores from the Aghbar mine, Bou Azzer, Morocco. Can. Mineral. 50, 447-470

Halahyjová-Andrusovová, G., 1964: About the genesis of the Dobšiná ore veins. Geol. Pr. Zpr., 33, 53-69. (in Slovak)

Hem, S.R., Makovicky, E., Gervilla, F., 2001: Compositional trends in Fe, Co, and Ni sulfarsenides and their crystal-chemical implications: results from the Arroyo de la Cueva deposits, Ronda peridotite, southern Spain. Can. Mineral. 39, 831-853.

Hem SR, Makovicky E, 2004a: The system Fe-Co-Ni-As-S. I. Phase relations in the (Fe,Co,Ni)As0.5S1.5 section at 650 ° and 500 ºC. Can. Mineral., 42, 43-62.

Hem SR, Makovicky E, 2004b: The system Fe-Co-Ni-As-S. II. Phase relations in the (Fe,Co,Ni)As1.5S0.5 section at 650 ° and 500 ºC. Can. Mineral., 42, 63-86.

Hurai V, Harcová E, Huraiová M, Ozdín, D., Prochaska, W., Wiegerová, V., 2002: Origin of siderite veins in the Western Carpathians I. P-T-X-$\delta^{13}$C-$\delta^{18}$O relations in ore-forming brines of the Rudňany deposits. Ore Geology Reviews 21, 67-101.

Klemm, D.D., 1965: Synthesen und Analysen in den Dreiecksdiagrammen FeAsS-CoAsS-NiAsS und FeS2-CoS2-NiS2. Neues Jahrb. Mineral., Abh. 103, 205-255.

Maurel, C., Picot, P., 1974: Stabilité de l'alloclasite et de la cobaltite dans les systèmes Co-As-S et Co-Ni-As-S. Bull. Soc. Fr. Mineral. Cristallogr. 97, 251-256.

Kretschmar, U., Scott, S.D., 1976: Phase relations involving arsenopyrite in the system Fe-As-S and their application. Can. Mineral., vol. 14, ss. 364-386

Yund, R.A., 1962: The system Ni-As-S: phase relations and mineralogical significance. AJS 260, 761-782.

# Ore dating by Shrimp II proxy analyses; Fe-Ni-Cu-PGE sulphide deposits, Ivrea Verbano Zone, Northern Italy

P. Kollegger, F. Zaccarini, G. Garuti and O.A.R. Thalhammer
*Chair of Resource Mineralogy, Dep. of Appl. Geosc. University of Leoben, Austria*
*(peter.kollegger@unileoben.ac.at)*

Marco L. Fiorentini (second author)
*Centre for Exploration Targeting, ARC Centre of Excellence for Core to Crust Fluid Systems, Univ. of Western Australia*

**Abstract:** In this contribution we present in-situ SHRIMP-II age data gained on zircons which can be taken as proxy for the history of base metal ore formation in the ultramafic pipe of Fei di Doccio hosted by the Ivrea-Verbano-Zone, northern Italy. It's clearly shown that the zircon ages exhibit a direct measure for the ore formation because the zircons are intimately intergrown with the ore minerals wherefore a syngenetic evolution can be stated. The two main phenomena which influence the gained isotopic age data, thermally induced Pb diffusion and fluid related juvenescence are discussed in detail. Based on the calculation of the thermal history of the pipe, a strong thermal influence can be precluded. In contrast to this, mineral characteristics and distinct age distributions within single grains indicate the activity of synmagmatic fluids. These fluids presumably caused a maximum juvenescence of about 20 Ma. Based on our results the maximum emplacement age of the Fei di Doccio pipe as well as the age of the ore formation can be estimated with 277 Ma.

**Keywords:** SHRIMP, zircon, Ivrea-Verbano-Zone, sulphide-ore, juvenescence.

## 1 Introduction

The age and the evolution of the Ivrea-Verbano-Zone which is interpreted as an exhumed segment of the lower continental crust and subcontinental lithospheric mantle (Peressini et al., 2007) is still a matter of discussion. The relationship between the Late Carboniferous underplating event, (Peressini et al., 2007), triggering many magmatic processes and the formation of base metal sulphide deposits is of special interest, because a syngenetic evolution of ore and host is not clearly verified until now. The magmatic sulphide deposits of the IVZ were mined for nickel from 1865 to 1874 and 1939 to 1945 whereupon about 300.000 metric tons of ore were produced (Garuti et al., 1986) (grades Ni 1% and 0.3% (Garuti et al., 1986), and up to 4000 ppb Sum-PGE (Garuti et al., 1990)). These deposits are of economic and strategic relevance because they are the single important Ni deposits of Central Europe. Our study was focused on one of five pipe-like ultramafic pipes occurring in the IVZ, the Fei di Doccio pipe, which is emplaced in the Kinzigite Formation, a sequence of lower crustal rocks. This pipe displays a strong alkaline nature, contains abundant volatile-bearing mineral phases and host widespread Fe-Ni-Cu-Platinum Group Element (PGE) sulphide mineralizations (Fiorentini et al., 2002).
Aside a possible juvenescence driven by thermally induced Pb diffusion especially the occurrence of volatile-bearing mineral phases together with an assumed fluid related juvenescence was taken into consideration.

## 2 Geological and mineralogical background

The IVZ represents an uplifted part of the lower crust and upper mantle transition and comprises three main formations: 1) the Kinzigite Formation, a crustal sequence of high-grade metamorphic rocks; 2) the Mafic Complex, comprising mafic to ultramafic differentiated intrusive rocks, and 3) Mantle peridotite massifs (Quick et al., 1995). The formation has a maximum thickness of about 20 km and is tilted to a subvertical position forming an asymmetrical anticline-structure. The present exposure and orientation are mainly consequences of tilting by about 90 degrees and uplift during Alpine collision (Peressini et al., 2007). The Mafic Complex forms the lower part of the IVZ. Quick et al. (1995) concluded that the gabbroic magmas of the Mafic Complex intruded the paragneiss of the Kinzigite Formation in the intermediate to deep continental crust, and Peressini et al. (2007) interpreted this as an underplating event. During this process, the Kinzigite Formation, structurally located above the Mafic Complex, was metamorphosed to granulite facies conditions (Bea and Montero, 1997). As in detail described by Garuti et al. (2001) overall five ultramafic pipe-like bodies intrude the Mafic Complex as well as in the case of the Fei di Doccio pipe the Kinzigite Formation. These small discordant intrusives consist of mafic and ultramafic rocks, mainly peridotite, pyroxenite and gabbros and display a strong alkaline affinity. The diameter of the Fei di Doccio pipe can be approximated to about 200m. High modal abundance of hydromagmatic phases, together with the occurrence of metasomatic aureoles reflect a strong fluid activity. The pipes host stockwork and disseminated Fe-Ni-Cu-PGE sulfide mineralization, which are frequently accompanied by the occurrence of zircons. The magmatic sulfide assemblage comprises pyrrhotite, pentlandite and chalcopyrite with additional minor pyrite, cubanite and mackinawite. Molybdenite, sphalerite, cobaltite, gersdorffite and graphite occur as accessory phases (Garuti et al., 2001). The pipes do not show any obvious layering or cumulus structures; their contacts to the host rocks are generally sharp and devoid of any chilled margin features.

## 3 Material and methods

The main purpose of the study was to localize zircons in their original petrographic setting, in order to ensure that the age determined by in-situ technique would reflect crystallization of the pipe and do not have a xenocrystic origin. Special care was taken to find zircons which showed an intimate intergrowth with the sulphide mineralizations where a syngenetic evolution can be assumed (Fig. 1). Sample FD4 (cf. Garuti et al.; 2001) was taken approximately 1m next to the contact of the Fei di Doccio ultramafic pipe with the surrounding hostrock of the Kinzigite Formation. The major mineralogical constituents of sample FD4 are hornblende, olivine, clinopyroxene and phlogopite with minor spinel, apatite and carbonates. The ore mineralisation consists of pyrrhotite, pentlandite and chalcopyrite with additional oxides, primarily ilmenite. Seven individual zircons were localized with an adequate shape and size for SHRIMP II analyses at the John De Laeter center, Curtin University, Perth (Western Australia). The analytical conditions were: 20 μm beam diameter; current 1.3 nA; accelerated to 10 keV. In this study the zircons are named as follows: "Zircon A", "Zircon B" and "Zircons C" (a set of 5 minerals).
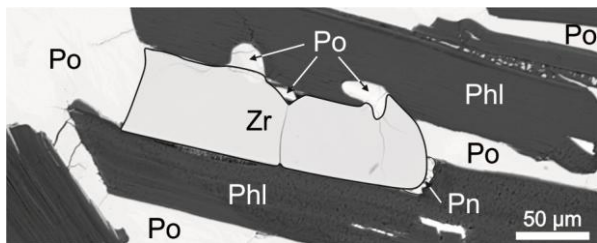


**Figure 1.** Zircon B. Illustration of the intimate intergrowth of the zircons with base metal sulphides.

## 4 Results

The investigated zircons show an intimate intergrowth with base-metal-sulfide minerals, mainly pyrrhotite and pentlandite (Fig. 1). The non-sulfide paragenesis is dominated by hydromagmatic phases, predominantly phlogopite, apatite and amphibole. In general the investigated zircons do not exhibit any strong zonations, detectable using back-scattered-electron (BSE) or cathodo-luminescence (CL) imaging (Fig. 2). Therefore the zircons appear to be largely homogeneous, with no distinct stages of growth or different generations.

Within the eight standard analyses on standard BR 266, the 1 σ external spot-to-spot error of the Pb/U isotopic ratios was 0.52 % which indicates the high quality of the measurement set. Multiple measurement spots were placed on Zircons A and B (Fig. 2). Conversely, the five smaller minerals (Zircon-Set C) were analysed once. (Table 1) Within the age distribution of Zircon A, a pattern can be recognized (Fig. 2). Comparable young age values can be found in the two broken parts in the upper-right corner of the mineral. The age of 252Ma is one of the youngest within the whole measurement set. In general the age values become younger from the core to the margin of the mineral. Due to the shape of Zircon B no core or rim of the mineral could be identified (Fig.

2). No distinct age distribution is visible and the single values vary between 255 and 277 Ma. Because of the limited size of the zircons in set C, only one analysis was attainable for each single mineral. Also these single analyses comprise a similar age distribution between 260 and 271 Ma. Generally it can be noted that the variation of individual mineral ages and the variability between the zircon groups (A-B-C) is almost the same with a range between 251 and 277 Ma.
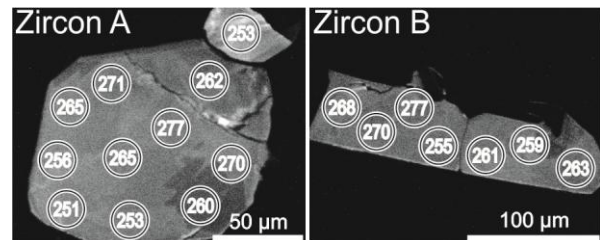


**Figure 2.** Cl-images; Shrimp analysis points (spotsize 20 μm). Numbers denote the mean $^{206}Pb/^{238}U$ Ages in Ma. σ ~ 3 Ma

## 5 Discussion

Age data from in-situ U-Pb measurement of zircons from the Fei di Doccio pipe yield a range between 251 Ma and 277 Ma. The spread of the obtained ages, which occurs both within single zircon minerals and among different grains, is somehow at odds with the observed internal homogeneity of the single crystals, which precludes different stages of growth. Therefore, these results need to be explained otherwise. Two main processes that cause Pb-loss and juvenescence may have occurred during the crystallization of the IVZ pipe which are Pb-diffusion triggered by thermal energy and Pb-loss activated by fluid interaction, respectively.

### 5.1 Temperature related juvenescence

The cooling of the Fei di Doccio ultramafic body was calculated following the "one-dimensional intrusions model" postulated by Stüwe (2007). According to this model the initial conditions as well as the coordinate system were approximated to the assumed genetic conditions as follows. The intrusion temperature Ti was set to 1250 °C for an ultramafic intrusion (in accordance to the assumptions of Henk et al., (1997) and Phipps and Morgan (2001)). The host rock temperature Tb was chosen at 850°C in alignment with the magmatic underplating temperature model of Henk et al. (1997). The thermal diffusivity κ was specified by Stüwe (2007) with a value of $10^{-6}$ $m^2s^{-1}$ in special accordance to the chosen model. The one dimensional extent "l" = 200m corresponds to the diameter of the Fei di Doccio pipe. To understand the process that links the thermal history of the pipe with any age juvenescence, it is necessary to constrain the cooling pattern that affected the Fei di Doccio pipe upon emplacement in the Kinzigite Formation. The pipe is interpreted to be a relatively small intrusion. Therefore the overall thermal budged associated with its emplacement is low. Even though the temperature difference between the intrusion and the host rock is comparatively low (assumed 400°C), the thermal equilibration is almost reached after 10000a as

illustrated by the almost flat isothermal line in Figure 3. As described, Sample FD4 was taken approximately 1 m next to the contact of the pipe to the host rock. This position is chilled initially extremely fast, reaches the 1000°C isotherm after only 600a and the 900°C isotherm after approximately 6000a (Fig. 3). To reach a concordant timespan as observed in our samples (~20Ma) much lower cooling rates would be necessary because the blocking temperature of zircon is determined between 900 and 1100°C (Cherniak and Watson, 2003; Geisler et al., 2003). Therefore the cooling of the pipe itself is much too fast to yield any age interference. Also the regional-scale cooling rates of the underplated mantle in contact with the Kinzigite Formatin (intruded by the Fei di Doccio pipe) were found to be relatively high as calculated by Henk et al. (1997) with ~8 °CMa$^{-1}$. To allow significant age shifts, much lower rates would be necessary to trigger volume diffusion of Pb in zircon as investigated by Ashwal et al. (1999) who assumed cooling rates of 1-2°CMa$^{-1}$ to produce an 80 Ma concordant time span. Beyond high temperature Pb-loss zircons may lose significant amounts of Pb by diffusion when they become metamict (Mezger and Krogstad, 1997) This occurs when they are cooled below their annealing temperature of 600-650°C (Cherniak and Watson, 2003) and heated up again to reach effective diffusivities because the values at 600 °C ($10^{-22}$ m$^2$s$^{-1}$; Cherniak et al., 1991) are far too low for considerable Pb loss. Following Sm-Nd measurement results from the presumably deepest part of the Mafic Complex (Mayer et al., 2000) which precluded a thermal overprint exceeding 650°C after 267±21Ma, also a juvenescence by high diffusion rates of metamict zircons can be neglected. Therefore, it is reasonable to argue that the rapid chilling of the Fei di Doccio pipe and the fast cooling following the underplating event prevents any Pb diffusion. In summary, the hypothesis of temperature related Pb loss and age juvenescence following any anomalous thermal history is can be rejected.
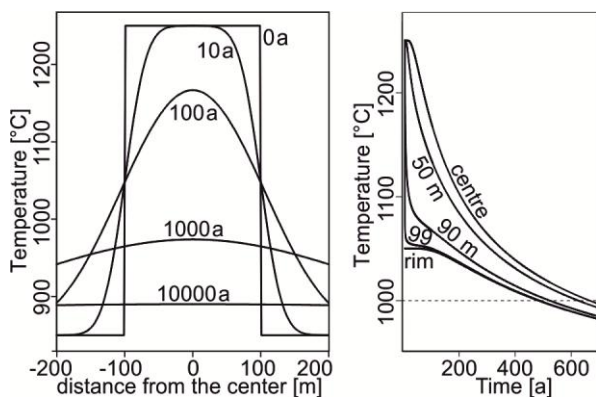


**Figure 3.** Cooling of the pipe. (model by Stüwe, 2007). Left: Isotherms across the pipe with time elapsed from t=0. Right: Temp.-time-diagram by lateral sections from core to rim.

## 5.2 Fluid related juvenescence

An important process causing juvenescence in zircons is caused by an interaction with coexisting fluids. Apart from an isotopic alteration zircon-surface depletion in U and Th is caused (Vavra et al., 1999). The depletion in

Th was stronger, and they called this phenomenon "surface-controlled alteration (SCA)" caused by hydrothermal activity. An analogue process, a dissolution-reprecipitation reaction, in contact with alkaline metamorphic fluids, was described by Rubatto et al. (2008). These assumptions are reinforced by the investigations of Vavra and Schaltegger (1999) on monazite from the Kinzigite Formation where similar phenomena were observed. Taking into account recent monazite closure temperature estimations (e.g. 900°C by Cherniak et al.; 2004) they should have been rejuvenated as early as the zircon.

| No. | U | Th | Age | ±1σ | No. | U | Th | Age | ±1σ |
|---|---|---|---|---|---|---|---|---|---|
| A.1 | 112 | 67 | 256 | 3.4 | B.1 | 110 | 98 | 268 | 5.3 |
| A.2 | 136 | 66 | 253 | 2.9 | B.2 | 84 | 63 | 255 | 6.9 |
| A.3 | 215 | 202 | 260 | 2.6 | B.3 | 115 | 111 | 277 | 5.7 |
| A.4 | 193 | 108 | 251 | 2.5 | B.4 | 98 | 79 | 261 | 6.0 |
| A.5 | 137 | 101 | 271 | 3.0 | B.5 | 75 | 51 | 263 | 10.1 |
| A.6 | 151 | 97 | 265 | 2.7 | B.6 | 104 | 88 | 259 | 5.8 |
| A.7 | 158 | 110 | 265 | 2.3 | B.7 | 113 | 85 | 270 | 4.8 |
| A.8 | 130 | 79 | 277 | 2.8 | C.1 | 86 | 63 | 272 | 7.0 |
| A.9 | 169 | 127 | 270 | 3.7 | C.2 | 97 | 75 | 265 | 4.6 |
| A.10 | 90 | 57 | 253 | 5.0 | C.3 | 104 | 86 | 263 | 5.6 |
| A.11 | 142 | 85 | 262 | 2.5 | C.4 | 109 | 89 | 260 | 7.7 |
| | | | | | C.5 | 98 | 86 | 269 | 11.6 |

**Table 1.** Zircon SHRIMP II analyses. U and Th in ppm. Age: $^{206}$Pb/$^{238}$U Age in Ma. ±1σ standard err. No: Analysis on zircons A, B and zircon set-C

## 5.3 Fei di Doccio zircon ages

The most striking result of the measurement set is the regularity occurring in the age distribution of large zircon A (Fig. 2). Comparably young age values were obtained on positions next to cracks within the mineral as well as next to the rim of the zircon. Together with the stronger Th than U decrease with declining total U+Th contents (Fig. 4) these relationships are a strong evidence for fluid related juvenescence affecting the observed zircons. Thermally induced juvenescence can be neglected based on the observations made on zircon B. This mineral shows a lath shape with a more or less equal thickness. If temperature-induced reactions occurred, it should be rejuvenated equally, which is not the case. The observed differing juvenescence grades again speak in favour of a fluid activity which affected the mineral unequally. The assumed varying fluid interaction is furthermore proved by the similar age ranges of the smaller zircons (Zircon-set C: 260-271 Ma) and the single mineral Zircon A (251 to 277 Ma). It can be suggested that the same processes were influencing Zircon A from the core to the rim as well as the smaller minerals of Zircon set C entirely, whereas fluids could react in this way. Again Pb loss caused by diffusion during slow cooling can be neglected because in this case each mineral would be affected similarly regardless the mineral-size. Based on these observations an interaction of diffusion and recrystallization processes induced by surrounding fluid is presumably responsible for the observed juvenescence patterns. Such patterns were experimentally proved by Geisler et al. (2003). Nonetheless the gained age values are in

agreement with the age determinations of other authors (e.g. Garuti et al. (2001); Fei di Doccio pipe; 288±3 Ma, standard zircon separation technique) as well as within the period of the predicted underplating event 292-250Ma (Peressini et al., 2007).
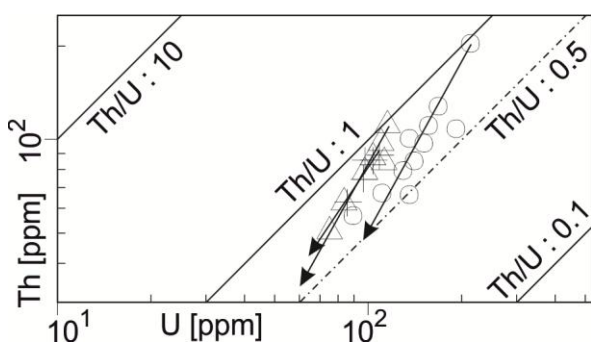


**Figure 4.** Th and U conc. in zircons. Circles: zircon A; triangles: zir. B, crosses: zir.-set C; arrows: depletion trends

## 6 Conclusion

Based on this study the maximum age for the emplacement of the Fei di Doccio pipe can be estimated with 277 Ma. Due to the observed intimate intergrowth of the zircons with the base metal sulfides a direct relationship between the ore formation and the growth of the zircons can be assumed. Therefore the ore formation can be predicted to be isochronous with the general emplacement of the pipe and the same age values can be taken in consideration. This direct interpretation is possible because the zircons were analysed in situ where the genetic characteristic of each zircon was clearly visible. This investigation additionally shows that age values obtained on zircons which are in direct contact with synmagmatic fluids have to be interpreted with special attention. Age values next to the rim of the mineral or values collected on zircons with internal cracks might be comparably low, whereas intact minerals as well as core zones show high age values. This is the case because an assumed interacting fluid affects the zircon from the exterior and additionally yields depletion in U and Th. Thermally induced juvenescence can be precluded because strong diffusion patterns were not observable and the age distributions of the single minerals show no evidence for uniform thermal influence. Furthermore the calculated cooling history of the pipe itself as well as the regional cooling of the underplating event exhibit much too high cooling rates to allow any long lasting thermal high temperature environment which could result in sufficient Pb diffusion yielding juvenescence. In summary it can be stated that the analyzed zircons were influenced by synmagmatic fluids which variably modified the isotopic compositions and caused juvenescence.

## Acknowledgements

## References

Ashwal L D, Tucker R D, Zinner E K (1999) Slow cooling of deep crustal granulites and Pb-loss in zircon. Geochim. Cosmochim Ac 63 (18), 2839-2851.

Bea F, Montero P G, (1997) Rare earth elements, Y, Th, and U in crustal melting; the behavior of accessories during metamorphism and anatexis of metapelites; the Kinzigite Formation (Ivrea-Verbano, N Italy). LPI Contrib. 921, 21

Cherniak D J, Lanford W A, Ryerson F J (1991) Lead diffusion in apatite and zircon using ion implantation and Rutherford Backscattering techniques. Geochim. Cosmochim Ac 55 (6) 1663-1673

Cherniak D J, Watson E B (2003) Diffusion in Zircon. Rev Min Geochem 53 (1) 113-143

Cherniak D J, Watson E B, Grove M, Harrison T M (2004) Pb diffusion in monazite: a combined RBS/SIMS study. Geochim. Cosmochim Ac 68 (4) 829-840

Fiorentini M L, Grieco G, Ferrario, A. Tunesi, A (2002) Petrological and metallogenic outlines of the Valmaggia ultramafic pipe Period di Mineral 71 (3) 219-239

Garuti, G., Fiandri, P., Rossi, A., 1986. Sulfide composition and phase relations in the Fe-Ni-Cu ore deposits of the Ivrea-Verbano basic complex. Miner Deposita 21 (1), 22–34.

Garuti, G., Naldrett, A. J., Ferrario, A., Apr 1990. Platinum-group elements in magmatic sulfides from the Ivrea Zone; their control by sulfide assimilation and silicate fractionation. Econ. Geol. 85 (2), 328–336.

Garuti G, Bea F, Zaccarini F, Montero P, (2001) Age, geochemistry and petrogenesis of the ultramafic pipes in the Ivrea Zone, NW Italy. Journal of Petrology 42 (2) 433-457.

Geisler T, Pidgeon R T, Kurtz R, van Bronswijk W, Schleicher H (2003) Experimental hydrothermal alteration of partially metamict zircon. Am Min 88 (10) 1496-1513

Henk A, Franz L, Teufel S, Oncken O, (1997) Magmatic Underplating, Extension, and Crustal Reequilibration: Insights From A Cross-Section Through the Ivrea Zone and Strona-Ceneri Zone, Northern Italy. J of Geology 105 (3) 367-378.

Mayer A, Mezger K, Sinigoi S, (2000) New Sm-Nd ages for the Ivrea-Verbano Zone, Sesia and Sessera valleys (northern-Italy). Journal of Geodynamics 30 (1-2) 147-166

Mezger K, Krogstad E J, (1997) Interpretation of discordant U-Pb zircon ages: An evaluation J Met Geol 15 (1) 127-140

Peressini G, Quick J E, Sinigoi S, Hofmann A W, Fanning M, (2007) Duration of a large mafic intrusion and heat transfer in the lower crust; a SHRIMP U-Pb zircon study in the Ivrea-Verbano Zone (Western Alps, Italy). J Pe 48 (6) 1185-1218.

Phipps Morgan J (2001) Thermodynamics of pressure release melting of a veined plum pudding mantle. Geochem. Geophys. Geosyst. 2, 39.

Quick J E, Sinigoi S, Mayer A (1995) Emplacement of mantle peridotite in the lower continental crust, Ivrea-Verbano Zone, Northwest Italy. Geology (Boulder) 23 (8) 739-742

Rubatto D, Müntener O, Barnhoorn A, Gregory C (2008) Dissolution-reprecipitation of zircon at low-temperature, high-pressure conditions Am Min 93 (10) 1519-1529

Stüwe K (2007) Energetics: Heat and Temperature. In: Geodynamics of the Lithosphere. Springer pp. 51-137

Vavra G, Schaltegger U (1999) Post-granulite facies monazite growth and rejuvenation during Permian to Lower Jurassic thermal and fluid events in the Ivrea Zone (southern Alps). Contrib Min Pet 134 (4) 405-414.

Vavra G, Schmid R, Gebauer D (1999) Internal morphology, habit and U-Th-Pb microanalysis of amphibolite-to-granulite facies zircons; geochronology of the Ivrea Zone (southern Alps). Contrib Min and Pet 134 (4) 380-404

# Ore minerals distribution in the northern part of Stan Terg deposit, Kosovo: paragenetic relationships and ore textures

**Joanna Kołodziejczyk & Jaroslav Pršek**
*AGH - University of Science and Technology, Faculty of Geology, Geophysics and Environmental Protection, Department of Economic Geology, al. Mickiewicza 30, 30-059 Kraków, Poland*

**Halil Qela, Burim Asllani, Feriz Maliqi & Safet Peci**
*Trepça under AKP Administration, Mitrovicë Industrial Park, Mitrovicë 40000, Republic of Kosovo*

**Abstract.** Mineralogical composition of ore from an external part of the Stan Terg deposit was investigated. Mineralogical composition, textural characteristics and sequence of precipitation were determined. The Stan Terg is a skarn deposit, with economical hydrothermal mineralization. The external ore in the deposit occurs at the northern margin of the deposit, concentrated within 149 ore body in the $X^{th}$ horizon, and 139 ore body in the $IX^{th}$ horizon; those are extracted in present time. Four stages of precipitation of hydrothermal ore have been distinguished. Bournonite, stannite, silver minerals and Pb + Sb sulphosalts are most common in paragenesis. Drusy, vein, corona and replacing textures are recognized.

**Stan Terg deposit, Kosovo, hydrothermal ore mineralization, replacing ore textures, silver minerals**

## 1 Introduction

Pb-Zn deposits related to Miocene volcanic events are of the main potentials in the Middle-Balkan area.

One of the biggest Pb-Zn deposits in Europe is the Stan Terg deposit. It is located in northern Kosovo, near Kosovska Mitrovica. The ore is being extracted here since medieval timed. Currently Stan Terg is owned by Trepça Mining Company and is carrying out an underground extraction of lead and zinc ore. The company is a leading producer of these metallic elements in the Balkan Peninsula.

Stan Terg is described as a classic example of the Pb-Zn-Ag skarn mineralization (e.g. Schumacher 1950, Palinkaš et al. 2013). The majority of ore has hydrothermal origin.

The deposit is well known due to its famous mineralogical specimens. The principal ore minerals are galena, sphalerite, pyrite, pyrrhotite, arsenopyrite, chalcopyrite, and boulangerite. The deposit was studied by several authors – who however were mainly concerned with the metallogenic belt (eg. Smejkal 1960, Jankovic 1978, Jankovic 1995), fluids origin (Palinkaš et al. 2013), or rather general descriptions (Forgan 1950, Hyseni et al. 2010). Thus, there is still lack of information concerning ore composition and its geochemistry. In an earlier project by one of us (Kołodziejczyk 2012), eight minerals, namely freibergite, stephanite, pyrostilpnite, freieslebenite, polybasite, heteromorphite, mackinavite, copiapite have been described for the first time, in this deposit. This situation behoves us to make a detailed mineralogical and geochemical investigation of the deposit.

Below we describe ore composition in the external part of the deposit that seems to comprise the youngest part of ore mineralization characterized with highest variability.

## 2 Samples and investigation methods

The samples have been collected in March and August 2012 from 149, 149e and 149-C2 ore bodies at $X^{th}$ horizon and 139-C1 ore body at $IX^{th}$ horizon. They are located in the northern part of the deposit.

The samples represent only hydrothermal mineralization. 15 polished sections were investigated by the mean of reflected light microscopy. They constitute a variety of ores. Selected silver-bearing minerals were investigated by polarized microscopy in reflected light and by SEM-EDS analyses.

## 3 Geological setting and description of ore minerals

Within Trepça Mineral Belt, different types of Pb-Zn mineralization such as skarn, hydrothermal replacement and vein type of mineralization are known (Jankovic 1995). Apparently the mineralization is controlled by faults or by other tectonic structures.

The Trepça Mineral Belt is a part of the 40 to 60 km width Vardar Zone, a tectonic district strongly marked by NW-SE trending lineaments. The Belt stretches between Kopaonik massif in the north and ends in Kizhnica area in the south. In regional geology it is a part of the Serbo-Kosovo-Macedonian-Rhodope metallogenic belt of Oligocene-Miocene age (Hyseni et al. 2010).

The Stan Terg deposit is located in the northern part of Vardar Zone, in the Kopaonik area build of metamorphosed rocks of Paleozoic and Triassic age underlying an ophiolite complex. Various sedimentary (limestone, chert, sandstone, well-developed turbidite blocks) and magmatic (diabase, gabbro, ultramafites) rocks within a sandy to silty-clay matrix are found within ophiolitic mélange (Palinkaš et al. 2013).

The major mineralized host rock at Stan Terg is recrystallized Upper Triassic limestone with a developed karst system. Limestones are mostly metamorphosed and build a core of an anticline covered by schists. The main structure that caused metasomatic processes in the

deposit is phreatomagmatic breccia pipe that consists of a hydrothermally altered trachyte core (Schumacher 1950, Palinkaš et al. 2013).

A small portion of the ore is metasomatic (skarn mineral paragenesis) while the main part of the ore has been created by precipitation from hydrothermal fluids in wide range of temperatures. According to Palinaš et al. (2013), the deposit was formed by two processes during two distinct mineralization stages: an early prograde closed-system and a later retrograde open-system stage. The basic ore minerals, such us galena, sphalerite, pyrite, chalcopyrite, have precipitated from a moderately saline Ca-Na chloride fluid at around 350°C.

Ore bodies are structurally related to the regional geology of the deposit. The bodies were formed on contact between marbles and schists or marbles and volcanics rocks. They have mostly columnar-like shapes and are lenticularly elongated, parallel to the hinge of anticline; this is the main tectonic structure in the deposit (Forgan 1950, Hyseni et al. 2010). Eleven main ore bodies has been distinguished. Some of them reach surface, others are often split or joined together. The central ore body continues downwards for more than 1500 m. The central ore body has average thickness of 78.5 m. Smaller ore bodies occur at various distances from the volcanic breccias pipe, in both northern and southern part of the deposit. The furthest ore body in the northern part of the mine that is being extracted is named 149 in $X^{th}$ horizon, and 139 in $IX^{th}$ horizon.

The skarn assemblage minerals in the deposit are Ca-Fe-Mn silicates, including pyroxenes, ilvaite, and minor garnets and in lesser amounts Ca-Fe-Mn or Mg carbonates and quartz. Paragenetic studies confirmed that they occurred in several stages, similar to other skarns (Palinkaš et al. 2013). These authors suggested that the hydrothermal ore minerals overprint the skarn and no ore minerals were formed during metasomatic processes.

Younger hydrothermal assemblages are characterized by various ore minerals: pyrrhotite, pyrite, magnetite, galena, sphalerite, chalcopyrite, arsenopyrite, marcasite, lead sulphosalts and many other. Gangue hydrothermal minerals are iron and manganese carbonates and quartz. Gangue carbonates precipitated in several stages (e.g. Schumacher 1950, Dangić 1993).

The oldest ore minerals are magnetite, pyrite and pyrrhotite. They mostly occur in the form of pseudomorphs after hedenbergite. The most abundant ore minerals are black-colored sphalerite and galena. To the younger ore minerals belong mainly chalcopyrite, bournonite, boulangerite and other sulphosalts. Different types of observed textures indicate several stages of precipitation (Kołodziejczyk 2012). Most of the phases have been described in more than one generation. A paragenetic sequence for Stan Terg deposit has been proposed, with metasomatic phase (common for bismuth bearing minerals), hydrothermal phase with "Pb+Zn", "Cu", "Ag" and "Sb" stages and a supergenic phase.

# 4 Mineralogy

## 4.1 Hydrothermal ore minerals in 139 and 149 ore bodies

Galena together with sphalerite, pyrite and pyrrhotite are the most abundant minerals in the ore bodies under study.

The most important Pb mineral is galena, as well as Zn mineral sphalerite; they occur in fine up to coarse grained structures. Common chalcopyrite, pyrite and pyrrhotite inclusions are visible in both galena and sphalerite. Chalcopyrite grains may be intergrown with pyrrhotite. Within chalcopyrite, mackinawite inclusions may be observed (Fig. 1a). Inclusions of pyrrhotite and chalcopyrite are mostly fine, up to 0.05 mm in size (Fig. 1b). In some generations of sphalerite thin chalcopyrite-tetrahedrite veinlets and "chalcopyrite disease" are common (Fig. 1c, d). These are a result of replacing Fe-rich sphalerite with Cu-bearing solutions (distracted blebs) or a result of accumulation on sphalerite grain margins.
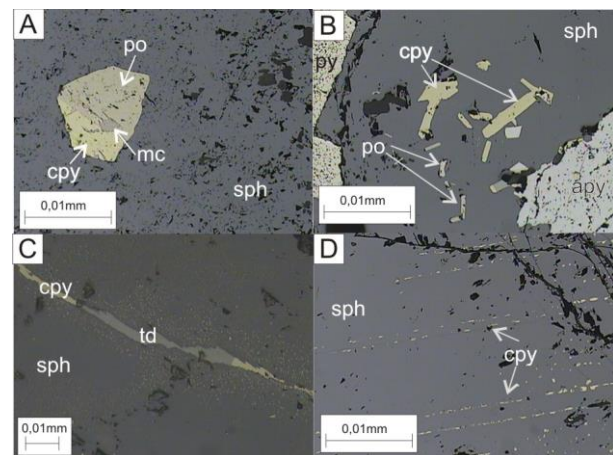


**Figure 1.** a) Chalcopyrite (cpy) bleb intergrowth with pyrrhotite (po). Mackinawite mineral group (mc). Sph = sphalerite; b) Chalcopyrite (cpy), pyrrhotite (po) fine crystals within sphalerite (sph). Py = pyrite, apy = arsenopyrite; c) Chalcopyrite (cpy) with tetrahedrite (td) veinlets in sphalerite. Chalcopyrite emulsion texture surrounds the veinlets; d) Chalcopyrite (cpy) blebs on the sphalerite (sph) growth edges. Reflected light, parallel Nicols.

Chalcopyrite is present in the form of fine to medium-grained aggregates. Often fine sphalerite inclusions within it are observed. Elongated boulangerite inclusions have been found in different generations of sphalerite as well as in galena. Bournonite belongs also to the Cu-bearing minerals in the deposit and occurs together with galena.

Pyrite is present in most of the samples; it occurs in anhedral or euhedral fine to coarse grains. It is often overgrown by euhedral marcasite and arsenopyrite. In addition, euhedral arsenopyrite crystals have been found within sphalerite (Fig. 2a).

The most typical mineral is boulangerite (often called plumosite in the literature). Usually it is the youngest mineral in the deposit. Microscopic observations resulted in finding it within sphalerite (Fig. 2a) and galena. SEM-EDX analyses confirmed the presence of

heteromorphite. Huge amounts of other Pb-Sb sulphosalts (Fig. 2b-f) have been found. All of them occur within carbonates, galena, chalcopyrite and exhibit significant variability.
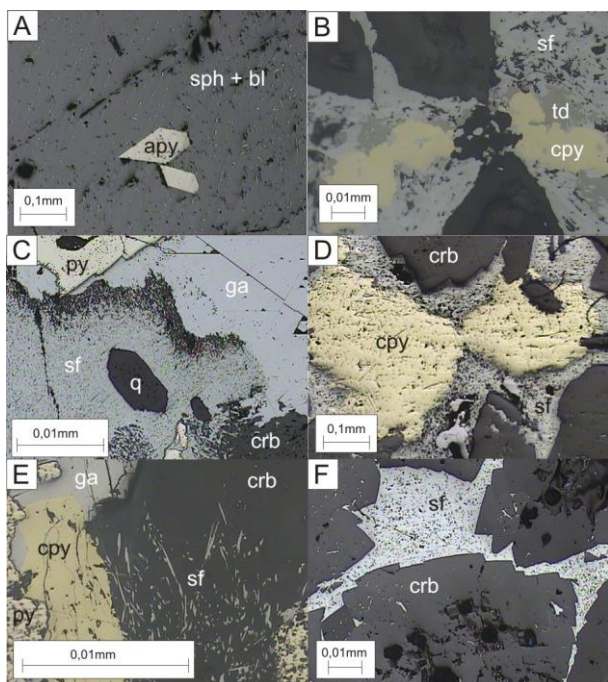


**Figure 2.** a) Boulangerite (bl) inclusions within sphalerite (sph). Apy = arsenopyrite; b) Sulphosalts (sf) replaceing chalcopyrite (cpy) and tetrahedrite (td); c) Sulphosalts (sf) replacing carbonates (crb) and galena (ga). Quartz (q) crystal eroded by sulphosalts. Py = pyrite; d) Sulphosalts (sf) replacing chalcopyrite (cpy). Crb = carbonates; e) Sulphosalts (sf) within carbonates (crb). Cpy = chalcopyrite, ga = galena, py = pyrite; f) Sulphosalts (sf) filling up free spaces within carbonates grains (crb). Reflected light, parallel Nicols

Another important mineral group in ore bodies are silver-bearing minerals. Among them freibergite, stephanite, pyrargyrite, pyrostilpnite, freieslebenite, polybasite and Ag-tetrahedrite have been recognized; see Fig. 3. They occur within galena in anhedral or veinlets forms, often replacing tetrahedrite. This generation of galena is enriched with elongated crystals of boulangerite (macroscopically not observed).
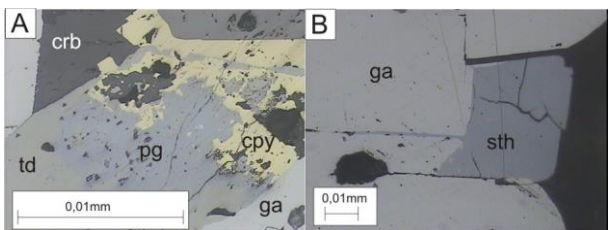


**Figure 3.** a) Crystal of tetrahedrite (td) replaced by pyrargyrite (pg) and chalcopyrite (cpy). Ga = galena, crb = carbonates; b) Crystal and veinlet of stephanite (sth) within galena (ga). Reflected light, parallel Nicols

Stannite group minerals, the only ones containing tin in the deposit, have been found within a young hydrothermal ore (Fig. 4). They occur together with sphalerite as irregular aggregates or together with chalcopyrite, in fine fractures.



**Figure 4.** a) Stannine (st) replacing sphalerite (sph). Cpy – chalcopyrite, ga = galena, crb = carbonates; b) Stannine (st) replacing sphalerite (sph). Chalkopiryte (cpy) is present as chalcopyrite disease within sphalerite; crb = carbonates. Reflected light, parallel Nicols

## 4.2 Textures

The ore in the center of ore bodies is mostly massive, what corresponds to the first Pb + Zn mineralization stage. That ore is mainly composed of galena, sphalerite, pyrrhotite and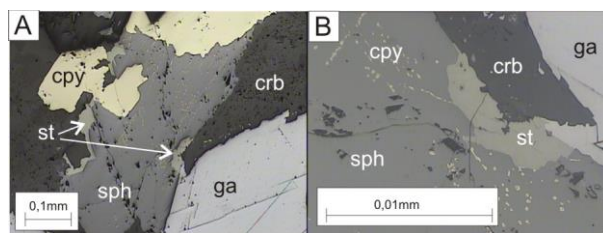 pyrite. These minerals concentrate in the core of ore bodies, but occur also on the outside as younger generations. Final mineralization stages are abundant mostly in veins, veinlets or encrustations or replacement types. Typical here are vein, banded textures with layers of young carbonates (rhodochrosite) and ore minerals.

Within limestones, very large cavities occur as a result of paleocarst processes. Textures related to filling of those cavities are mostly common with the hydrothermal ores. Open druses are usually partially filled up by ore and covered with calcite. Sometimes the youngest minerals in the druses are other carbonates, quartz, late ore minerals. The drusy textures allow crystals to reach very large sizes; e.g. the sphalerite crystals are found up to 7 cm in diameter, quartz up to 20 cm, arsenopyrite up to 3 cm. In some locations breccia-form of ore may be found. In such cases, the pieces of ore are cemented by carbonates (Fig. 5a). Much more common are vein textures, where the crushes within older minerals are filled up by younger ones (Fig. 5b).

Chalcopyrite and tetrahedrite veinlets are especially common (Fig. 1c). Chalcopyrite veinlets occur mostly within sphalerite, whereas tetrahedrite within chalcopyrite (Fig. 5f) or sphalerite. Some galena veinlets have been found within carbonates. Other late-stage minerals fill up fractures, e.g. sphalerite within chalcopyrite (Fig. 5c). The most often replacing minerals are chalcopyrite, that replaces tetrahedrite; silver minerals replaces both of them (Fig. 3a) or sulphosalts, which replace chalcopyrite, tetrahedrite, galena and carbonates (Fig. 2b,c,d,e). Sulphosalts fill up free spaces within carbonate grains (Fig. 2f). Bournonite usually replaces galena, in the form of a rim over it (corona texture) (Fig 5d) or along interfaces of galena with carbonates (Fig. 5e). Stannine replaces sphalerite rich in chalcopyrite blebs (Fig. 4).
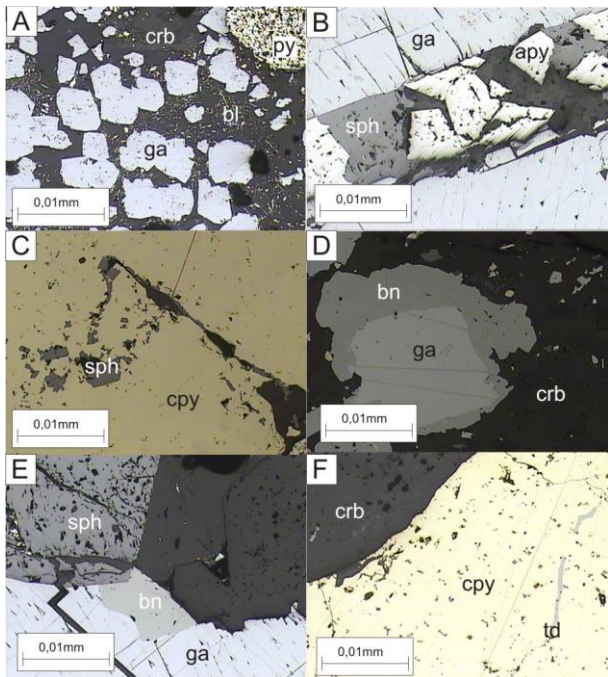
**Figure 5.** a) Rounded galena (ga) grains within carbonate (crb) + boulangerite (bl) matrix. Py = pyrite; b) Fracture within galena (ga) filled up with sphalerite (sph) and arsenopyrite (apy); c) Fine sphalerite (sph) crystals in fractures within chalcopyrite (cpy); d) bournonite (bn) crone texture over galena (ga). Crb = carbonates; e) Bournonitee (bn) grain replacing galena (ga). f) Tetrahedrite (td) veinlet within chalcopyrite (cpy) with sphalerite star-like inclusions. Reflected light, parallel Nicols

### 4.3 Precipitation scheme, ore paragenesis

A general precipitation scheme is suggested in Figure 6.
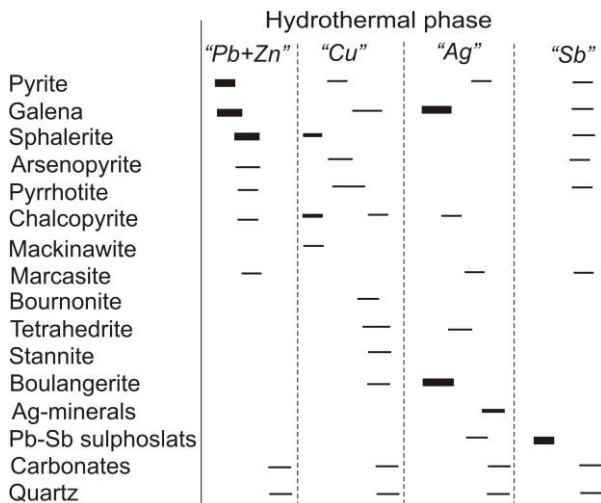


**Figure 6.** Succession scheme for the Stan Terg deposit: hydrothermal assemblage from external northern part

The minerals of hydrothermal origin occurring in 149 and 139 ore bodies may be divided into four mineralization stages. The highest amount of galena, sphalerite and pyrite is typical for "Pb + Zn" stage, sphalerite with "chalcopyrite disease" and chalcopyrite with mackinawite inclusions; bournonite and stannite belongs to "Cu" stage; galena rich in boulangerite inclusions with Ag-minerals and high Ag-content tetrahedrite relates to "Ag" stage, whereas the last "Sb"

stage is characterized by different Pb-Sb sulphosalts that replaced most of previously precipitated minerals.

## 5 Summary
Ore mineralizations within 139 and 149 ore bodies reveal large diversity in comparison to more centrally located ore bodies in the deposit. The mineralizations occur mostly in drusy, vein, corona and replacing textures.

## Acknowledgements

## References

Dangić A (1993) Tetriary lead-zinc ore deposits and calco-alkalice magmatism of the serbo-macedonian province:metallogenic and geochemicak characteristics, hydrothermal systems and their evolution. Ann. Geol. Penins. Balk. 57 1 257-285

Forgan C B (1950) Ore deposits at the Stan Terg lead-zinc mine International Geological Congress. Report of the eighteenth session, London, Great Britain 1948. Part VII. Symposium and proceedings of section F. The Geology. paragenesis and reserves of the ores of lead and zinc, Yugoslavia

Hyseni S, Durmishaj B, Fethaj B, Shala F, Berisha A, Large D (2010) Trepça Ore Belt and Stan Terg mine – Geological overview and interpretation. Kosovo (SE Europe). Geologija 53/1 87-92

Jankovic S (1978) The isotopic composition of lead in some tertiary lead-zinc deposits within the serbo-macedonian metallogenic province (Yugoslavia). Ann. Geol. Penins. Balk. 42 Belgrade 507-525

Jankovic S (1995) The principal metallogenic features of the Kopaonik District. Geology and Metallogeny of the Kopaonik Mt,. BelgradeSymposium 79-101

Kołodziejczyk J (2012) Pb-Zn mineralization in Stan Terg deposit, Kosovo, MS Thesis, College of Geology, Geophysics and Environmental Protection, AGH University of Science and Technology, Cracow

Palinkaš S, Sostarić S, Bermanec V, Palinkaš L, Prochaska W, Furić K, Smajlović J (2013) Metallogenic Model of the Trepcˇa Pb-Zn-Ag Skarn Deposit, Kosovo: Evidence from Fluid Inclusions, Rare Earth Elements, and Stable Isotope Data. Econ Geol 108:135-162

Schumacher F (1950) Die Lagerstätte der Trepca und ihre Umgebung. Izdvacko preduzece Saleta za energetyku i ekstraktivnu industriju vlade fnrj, Belgrade

Smejkal S (1960) Strukture. mineralizacije. mineralne parageneze i geneza olovo cinkovih lezista kopaonicke oblasti. Doktorska disertacija. Rudrsko geoloski fakultet Univerziteta u Beogradu, Belgrade.

# Gold mineralisation in intrusion-related gold systems – an example from the Chillagoe district, Australia

Berit Lehrmann & Thomas G. Blenkinsop
*School of Earth and Environmental Sciences, James Cook University, Townsville, QLD, 4811, Australia*

**Abstract.** Gold mineralisation of three intrusion-related gold deposits of the Chillagoe district (Australia) is associated with four distinct metal assemblages which occur in different paragenetic stages. An early gold event can only be observed at Mungana and is characterised by gold occurring along grain boundaries of Cu-Sb, Cu-As or As-Fe mineral phases, which are hosted in quartz veins cutting rhyolitic porphyry or skarn. Gold grains show elevated concentrations of Cu (up to 4 wt.-%). The second gold event, which is paragenetically very late, can be observed at Redcap and Red Dome. At these deposits gold does not contain any Cu and is associated with Bi-Te-(S) phases, which are hosted in late calcite or quartz-chlorite/sericite veins cutting andradite skarn, porphyry or metasedimentary rocks. It is assumed that gold of the late event was originally incorporated into early sulphide phases, as at Mungana, and was later extracted by Bi-Te-(S) melts and precipitated later together with Bi-Te phases. The petrographically observed metal assemblages are well reflected in the assay data, suggesting that modelling the distribution of gold-associated elements can be used as vectors to locate mineralisation.

**Keywords.** gold, metal associations, genesis, intrusion-related gold systems, Chillagoe district

## 1 Introduction

Intrusion-related gold (IRG) systems are a recently defined class of mineral deposits that occur worldwide, which have been first described in the Tintina Gold Belt of Alaska (McCoy et al. 1997 and references therein). In general, they are characterised by a reduced, sulphur-poor, polymetallic (Bi-Te-W-Mo-As-Sb) metal suite with wide-ranging grades of base metals (Thompson et al. 1999; Lang et al. 2000; Lang and Baker 2001; Hart 2005, 2007). The mineralisation can be hosted in a variety of deposit styles including veins, breccias, skarn and dissemination within intrusive body and country rocks. It can show vertical and/or lateral metal zonation within the deposit and in some places it can be as far as 3 km away from the causative intrusion.

Other characteristics known for IRGs are multiphase, calc-alkaline, compositionally evolved, weakly oxidised to reduced igneous complexes (Thompson et al. 1999; Lang and Baker 2001; Coulson et al. 2001; Hart 2005), and an almost synchronous timing of magmatic and hydrothermal activity (Baker et al. 2005) with very limited isotope data ($\varepsilon_{ND}$) indicating that the magma was derived from continental crust (Lang et al. 2000).

The increasing number of published studies in recent years has helped to improve the definition of IRGs. However, due to a lack of detailed deposit descriptions, nomenclature uncertainties and definition overlap with other magmatic hydrothermal systems like Au-rich copper porphyries, orogenic gold deposits and Au-skarns (Hart 2005), many aspects of IRGs are still not well understood. Some examples are the reasons for the diversity of gold mineralisation styles and their related formation processes, and suitable pathfinder elements to locate the mineralisation.

In this study three polymetallic IRG deposits of the Chillagoe district located in north eastern Queensland were investigated to provide detailed petrographical and chemical information regarding the gold occurrence and style diversity, as well as identify pathfinder elements which will help to increase the discovery rate of IRG systems.

## 2 Geological Setting

The Chillagoe district is located within the Middle Palaeozoic Hodgkinson Province (Fig. 1) which consists of calcareous, siliciclastic and volcanic rocks which were affected by regional low-temperature metamorphism. West of the province, separated by the Palmerville Fault, amphibolites, gneisses, schists and minor migmatites of the Proterozoic Dargalong Metamorphics crop out, which are locally intruded by Silurian Nundah Granodiorite.
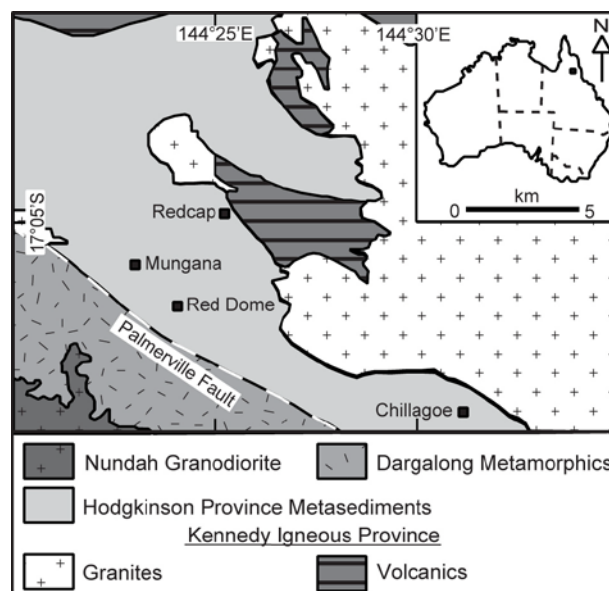


**Figure 1.** Geological map of the Chillagoe district showing the locations of the Redcap, Mungana and Red Dome deposits.

In some places the three stratigraphic units are intruded by Permo-Carboniferous granitic rocks of the Kennedy Igneous Province with granites being subdivided into five geochemically and isotopically distinct supersuites. Only four supersuites are linked to

the formation of base metal and precious mineralisation in the district (Georgees and Nethery 1999).

The investigated Redcap, Mungana and Red Dome deposits are in close proximity (3-5 km) and their formation is related to the emplacement of two intrusions (Lehrmann 2012). Mineralisation related to the primary magmatic event (rhyolitic porphyries) is of typical IRG style and characterised by a sulphur-poor and diverse metallogeny, whereas the emplacement of the second magmatic intrusion (Redcap: granodiorite; Mungana: granite; Red Dome: dacitic porphyry) introduced more Au and Cu at Red Dome, while at Redcap and Mungana existing base metals were remobilised and further metals were introduced. Because of this event the three deposits differ regarding their grades and metal commodities.

## 3 Gold petrography

Gold grains from the three deposits are very small in size (1-15 μm) and differ in their metal association, occurrence and timing. At Mungana gold can be found in the early paragenetic stage within quartz veins cutting skarn and/or porphyry. Gold occurs at the grain boundary of loellingite and arsenopyrite (Fig. 2A), within tetrahedrite or along the grain boundary of tetrahedrite and chalcopyrite (Fig. 2B) and at the grain boundary of tennantite and chalcopyrite together with tellurobismuthite ($Bi_2Te_3$) and arsenopyrite (Fig. 2C).



**Figure 2.** Photomicrographs of representative gold occurrences from Mungana, Redcap and Red Dome; **A**: gold (Au) at the boundary of loellingite (lol) and arsenopyrite (apy) in quartz (qtz); **B**: gold at the boundary of tetrahedrite (td) and chalcopyrite (cp) in quartz; **C**: gold, arsenopyrite and tellurobismuthite (tb) along the grain boundary of cha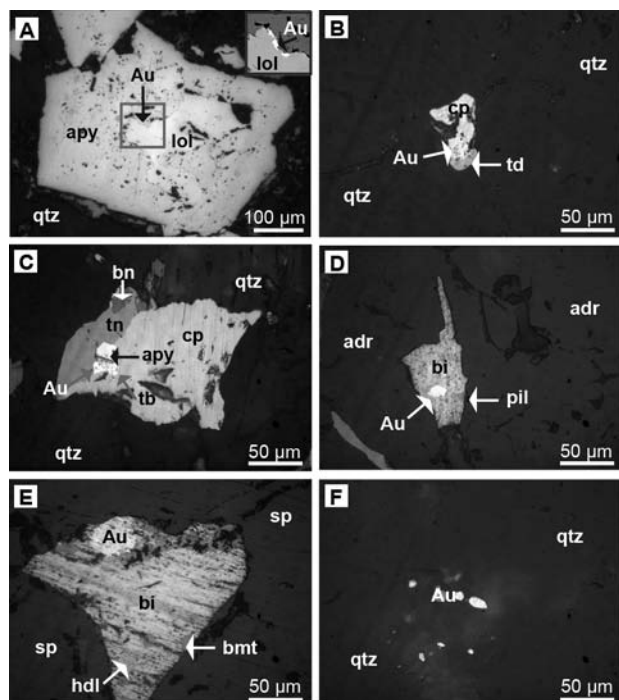lcopyrite (cp), later bornite (bn) and tennantite (tn); **D**: gold associated with native bismuth (bi) and pilsenite (pil) andradite (adr) skarn; **E**: gold, native bismuth (bi), hedleyite (hdl) and bismuthinite (bmt) hosted in sphalerite (sp); **F**: free gold in quartz.

At Redcap and Red Dome gold occurs very late in the paragenesis and can be found within calcite veins cutting andradite skarn or massive sphalerite, or occur together with sericite, or chlorite and calcite in comb-quartz veins cutting porphyry, or metasedimentary rocks. In all cases gold is associated with Bi-Te-(S) phases like pilsenite ($Bi_4Te_3$), hedleyite ($B_7Te_3$), bismuthinite ($Bi_2S_3$) and native bismuth (Fig. 2D & E). In addition, gold from Red Dome occurs also as free grains within quartz veins (Fig. 2F) cutting dacitic porphyry.

## 4 Gold chemistry

The petrographically observed association of gold with either Cu-As-Sb or Bi-Te-(S) mineral phases in the Mungana, Redcap and Red Dome deposit is well reflected in the assay data. Correlation matrixes for Mungana show that copper, arsenic and antimony correlate very well with values ranging between 0.6 and 0.9 and they also show a correlation with gold as observed in thin sections. Gold from Redcap and Red Dome on the other hand shows a strong positive correlation with bismuth and tellurium with correlation coefficient being between 0.6 and 1.0 with Au-Bi correlation coefficient of > 0.6 being typical for IRGs (Baker et al. 2005).

Electron microprobe analyses indicate that gold grains from the three deposits also differ chemically. Gold from Mungana associated with Cu-As-Sb mineral phases is Ag-poor with values ranging between 2 to 4 wt.-% for Cu-As and 9-15 wt.-% for Cu-Sb phases (Fig. 3), whereas gold precipitated along the grain boundaries of loellingite and arsenopyrite is Ag-rich with an average values of 26 wt.-%.
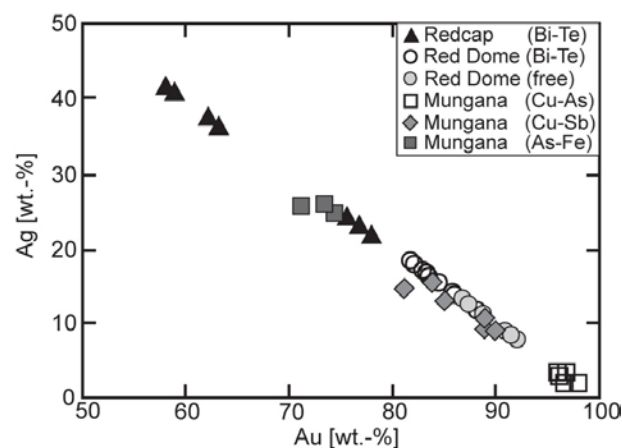


**Figure 3.** Binary plot of Ag vs. Au of gold grains from the Mungana, Redcap and Red Dome deposits illustrating that gold grains from different deposits and metal associations differ regarding their silver content.

Gold from Red Dome is also relatively Ag-poor and associated with Bi-Te mineral phases yielding concentrations of 12-18 wt.-%, whereas the free gold grains hosted in quartz veins cutting the dacitic porphyry (2nd magmatic event) show slightly lower silver content with on average 10 ± 2 wt.-% (n=6). Gold from the Redcap deposit is Ag-rich yielding concentrations between 22 to 42 wt.-% with the gold actually being

electrum.

In addition copper concentrations of the gold were also determined. Gold grains from the Redcap and Red Dome deposit do not show any elevated concentrations of copper (Fig. 4) with values being below the detection limit, whereas gold from Mungana has some copper incorporated with values ranging between 0.15 to 4.26 wt.-%. However, no link between copper concentration and with gold associated metal assemblages can be made.
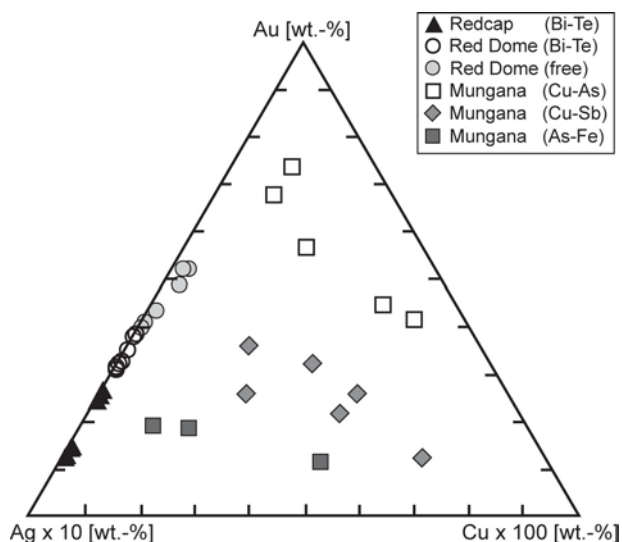


**Figure 4.** Triangular plot showing the compositional differences of gold grains from different metal associations and deposits.

## 5  Implication for the gold genesis

Petrographical and geochemical studies of gold grains from the Mungana, Redcap and Red Dome show that gold from these IRG systems can be associated with four distinct metal assemblages which have different timing within the paragenesis. The early paragenetic gold event can be observed at Mungana and is characterised by gold occurring at the grain boundaries of Cu-As phases (here chalcopyrite and tetrahedrite), Cu-Sb minerals (here chalcopyrite and tennantite) and As-Fe phases (here loellingite and arsenopyrite), with correlation matrixes of assay data assay confirming this link. Overall this gold event only yields low Au grades. Due to the occurrence of gold along grain boundaries it is likely that gold originally was incorporated into the lattice of loellingite and chalcopyrite, as described by Neumayer et al. (1993) and Simon et al. (2000). The gold was exsolved from loellingite during a decrease in the temperature (Tomkins and Mavrogenes 2001) or during progressive sulphidation (Knaak et al. 1995) between 500-600 °C, whereas the decomposition of chalcopyrite to bornite at temperatures of >400 °C, indicated by the simultaneous precipitation of tellurobismuthite (Barton and Skinner 1979) resulted in formation of visible gold grains which contain some wt.-% Cu. This early paragenetic gold event was not observed at Redcap and Red Dome in this study, however, Ewers and Sun (1988) have reported its occurrence at Red Dome.

The late paragenetic gold event can be observed at Redcap and Red Dome and is characterised by Cu-poor gold, which is almost always associated with Bi-Te-(S) assemblages, confirmed by correlation matrixes of assay data, and represents high Au grades. The gold formed at temperatures below 266 °C (Barton and Skinner 1979) with Bi-Te-S melts extracting gold from pre-existing sulphides (Oberthür and Weiser 2008) and acting as a scavenger (Tooth et al. 2011). Evidence for this hypothesis is that at Redcap electrum is hosted by sphalerite with this assemblage indicating remobilisation (Hurley and Crocket 1985).

At the Red Dome deposit more gold was introduced by an Au-bearing copper porphyry during the second magmatic event which occurred ~ 10 Ma after the intrusion-related gold event (Lehrmann 2012) with gold related to this event occurring as free grains and not showing any correlation with other metals.

## 6  Conclusions

Gold mineralisation hosted in IRG systems can be associated with different metal assemblages ranging from the more common Bi-Te-(S) association to the less described Cu-As-Sb assemblages. Little attention has been paid to the original incorporation of gold into the sulphide phases. From the scientific perspective detailed petrographical and geochemical studies seem to be the most appropriate technique to understand the metal precipitation mechanism and reveal the genesis. From the industry perspective correlation matrixes calculated from assay data is the most useful tool as they indicate the metal with which the gold is associated providing information useful for ore processing methods. In addition, modelling of the distribution of gold-associated elements can be used as vectors to locate mineralisation with this information being especially useful in terrains where magmatic sources are buried and deposits are of superimposed nature.

## References

Baker T, Pollard PJ, Mustard R, Mark G, Graham JL (2005) A comparison of granite-related tin, tungsten, and gold-bismuth deposits: implications for exploration. Society of Economic Geology Newsletter 61:5, 10-17

Barton PB, Skinner BJ (1979) Sulfide mineral stabilities. In: Barnes HL (ed) Geochemistry of hydrothermal ore deposits, 2nd edn. Wiley, New York, pp 278-403

Coulson IM, Dipple GM, Raudsepp M (2001) Evolution of HF and HCL activity in magmatic volatiles of the gold-mineralised Emerald Lake pluton, Yukon Territory, Canada. Miner Deposita 36:594-606

Ewers GR, Sun SS (1988) Genesis of the Red Dome deposit, northeast Queensland. Geological Society of Australia abstracts 22:110-115

Georgees C, Nethery JE (1999) The mid Carboniferous tin gold connection, Far North Queensland Conference, Cairns. Australasian Institute of Mining and Metallurgy, Melbourne

Hart CJR (2005) Classifying, distinguishing and exploring for intrusion-related gold systems. The Gangue: Newsletter of the Geological Association of Canada, Mineral Deposits Division 87:1, 4-9

Hart CJR (2007) Reduced intrusion-related gold systems. In: Goodfellow WD (ed) Mineral deposits of Canada: a synthesis of major deposit types, district, metallogeny, the evolution of geological provinces, and exploration method. Geological Association of Canada, Mineral Division, Special Publication 5:95-112

Hurley TD, Crocket JH (1985) A gold-sphalerite association in a volcanogenic base-metalsulfide deposit near Tilt Cove, Newfoundland. Can Mineral 23:423-430

Knaak ML, Dalstra HJ, Ridley JR (1995) Sulpharsenide textures in high-temperature gold deposits: examples from the Southern Cross province, western Australia. In: Pašava J, Křībek B, Žák K (eds) Mineral deposits: from their origin to their environmental impacts. Balkema, Rotterdam, pp 125-128

Lang JR, Baker T (2001) Intrusion-related gold systems: the present level of understanding. Miner Deposita 36:477-489

Lang JR, Baker T, Hart CJR, Mortensen JK (2000) An exploration model for the intrusion-related gold-systems. Society of Economic Geology Newsletter 40:1, 6-15

Lehrmann B (2012) Polymetallic mineralisation in the Chillagoe district of north-east Queensland – insights into base metal rich IRG systems. Ph.D. thesis, James Cook University

McCoy D, Newberry RJ, Layer P, Dimarchi JJ, Bakke A, Masterman JS, Minehane DL (1997) Plutonic-related gold deposits of interior Alaska. In: Goldfarb RJ, Miler LD (eds) Ore Deposits of Alaska. Economic geology publishing company, New Haven, Economic Geology monographs 9, pp 191-241

Neumayer P, Cabri LJ, Groves DI, Mikucki EJ, Jackman LA (1993) The mineralogical distribution of gold and relative timing of gold mineralisation in two Archaean settings of high metamorphic grade in Australia. Can Mineral 31:711-725

Oberthür T, Weiser, TW (2008) Gold-bismuth-telluride-sulphide assemblages at the Viceroy Mine, Harare-Bindura-Shamva greenstone belt, Zimbabwe. Mineral Mag 72:953-970

Simon G, Kesler SE, Essene EJ (2000) Gold in porphyry copper deposits: experimental determination of the distribution of gold in the Cu-Fe-S system at 400° to 700 °C. Econ Geol 95:259-270

Thompson JFH, Sillitoe RH, Baker T, Lang JR, Mortensen JK (1999) Intrusion-related gold deposits associated with tungsten-tin provinces. Miner Deposita 34:323-334

Tomkins AG, Mavrogenes JA (2001) Redistribution of gold within arsenopyrite and löllingite during pro- and retrograde metamorphism: application to timing of mineralisation. Econ Geol 96:525-534

Tooth B, Ciobanu CL, Green L, O'Neill B, Brugger J (2011) Bi-melt formation and gold scavenging from hydrothermal fluids: an experimental study. Geochim Cosmochim Acta 75:5423-5443

# Geological background and qualitative ore characterisation for the geometallurgical project at Rockliden, north-central Sweden

**Friederike Minz, Christina Wanhainen, Pertti Lamberg**
*Luleå University of Technology, Department of Civil, Environmental and Natural Resources Engineering*

**Jonas Lasskogen, Hein Raat**
*Boliden Mines, Exploration Department*

**Abstract.** The Rockliden Zn-Cu massive sulphide mineralisation is located at the stratigraphic top of altered rhyolitic-dacitic volcanic rocks, which in turn are intercalated by meta-sedimentary rocks of the Bothnian Basin, north-central Sweden. After the discovery, in the 1980's, the project was put on hold due to metallurgical and geometallurgical challenges. Exploration drilling restarted in 2007 and resources have increased since then. However, little is known about the mineralogical variability of the ore and how that will affect the processing of the mineralised material. Examples of rock-intrinsic process-relevant parameters are the mineral grain size, the texture of the minerals and the mineral associations, i.e. the mode of occurrence of minerals in the different types of mineralisation, and also the presence and distribution of penalty and bonus elements. Rock-intrinsic parameters and their spatial variability are considered in this study and will form the basis of a 3D-geometallurgical model for the Rockliden mineralisation.

**Keywords.** Massive sulphides, ore characterisation, geometallurgy.

## 1 Introduction

The Rockliden Zn-Cu-Ag volcanic-hosted massive sulphide (VHMS) mineralisation is located approximately 150 km south of the Skellefte district. Similar to the other massive sulphide deposits of the district (cf. Allen et al. 1996), the mineralisation at Rockliden has high concentrations in penalty elements such as As, Sb, and Hg. Flotation tests performed directly after the discovery of Rockliden in the 1980s, showed that the Sb-content lowers the quality and value of the Cu-Pb concentrate which is the feed material to the Cu smelter (Raat and Årebäck 2009).

Studies on the Sb-mineralogy of uncrushed drill core material and flotation samples point towards different controls on the distribution of Sb-bearing minerals during flotation. One control outlined is the interlocking of Sb-minerals with base-metal- and Fe-sulphides composing mineralogical complex particles (Minz et al. in review).

The aim of this study is to characterise the Rockliden mineralisation based on major sulphide minerals (i.e. pyrite, pyrrhotite, chalcopyrite and sphalerite) and to provide a classification which can be used to identify potential process-relevant rock-intrinsic parameters (cf. Walters and Kojovic 2006).

## 2 Geological Background

### 2.1 Geological Setting

The Rockliden project is located within the Bothnian Basin. This basin is limited to the north and south by the Skellefte and Bergslagen Proterozoic volcanic arcs. The sedimentary infill of the basin is represented by the Svecofennian rocks of the Härnö Group. This Group constitutes mainly metamorphosed sedimentary siliciclastic (turbiditic) rocks with minor intercalations of (mostly mafic) volcanic rocks (Kousa and Lundqvist 2000). During the Svecokarelian Orogeny a metamorphic grade of upper amphibolite facies was reached and part of the Bothnian Basin rocks were migmatised (Lundqvist et al 1998).
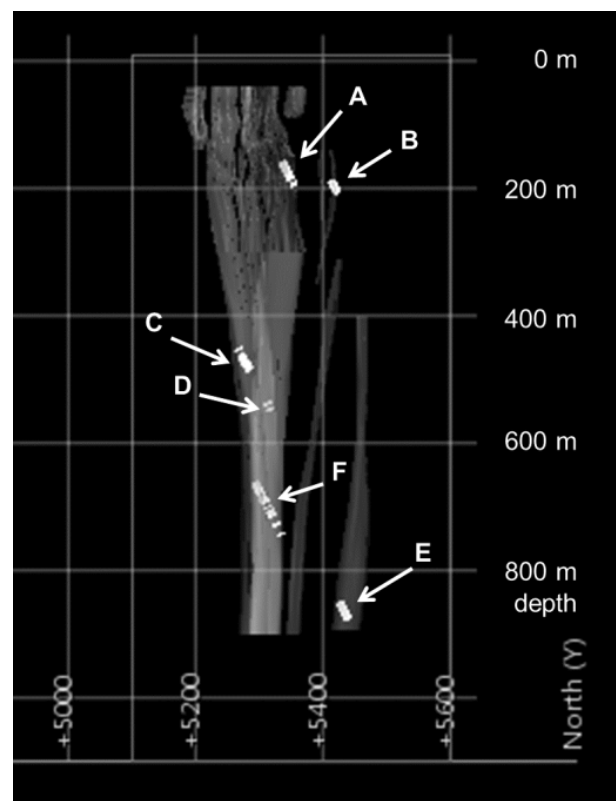


**Figure 1.** View to the west displaying the Rockliden massive sulphide body (translucent shapes) with the location of assayed and sampled drill core intervals (white dashed lines, arrows point to intersections in the selected 6 drill cores).

The Rockliden mineralisation is found mainly at the contact of altered volcanic and turbiditic sedimentary

rocks (Depauw 2009; Mattsson and Heeroma 1985). The meta-volcanic rocks are rhyolitic to dacitic in composition and both volcanoclastic and coherent types occur (Depauw 2009; Evins 2011). The stratigraphy of these volcanic footwall rocks is not well understood, but is likely composed of cryptodomes and lavas, similar to the Skellefte district (cf. Allen et al. 1996). The Rockliden volcanic rocks formed ca. 1875 Ma ago (Welin 1987) and are thought to form an inlier isolated in the Bothnian Basin (Depauw 2009). The siliciclastic hanging wall rocks constitute mainly metamorphosed shales and turbiditic greywackes, locally with Fe-sulphide bearing layers and mafic to ultramafic intrusions, sills and dykes (Raat and Årebäck 2009; Depauw 2009). The host rocks of the Rockliden mineralisation have a relatively low (greenschist facies) metamorphic grade, compared to the regional metamorphic grade (Depauw 2009).

A number of steeply dipping massive sulphide lenses (Fig. 1) can be distinguished from one another, and the complex geometry is a result of folding and faulting (Raat and Årebäck 2009). The main tectonic deformation at Rockliden is related to a N-S compressional deformation event; and the corresponding fold planes are E-W-trending and steeply dipping (Mattsson and Heeroma 1985; Evins 2011). Mobilisation of the sulphide mineralisation occurred concordant to the E-W-trending fold axes (Depauw 2009). Additionally, NE-SW to ENE-WSW trending faults and parallel dolerite dykes transect the Rockliden mineralisation (Depauw 2009; Evins 2011). Remobilisation of Sb during the intrusion of dolerite dykes has been suggested and some of the mafic dykes contain about 1 wt% Sb (Depauw 2009).

### 2.2 Alteration and Mineralisation

According to Depauw (2009) and Raat and Årebäck (2009), sericitisation and silicification commonly occur a few tens of meters to hundreds of meters into the footwall rocks. Carbonate altered zones are found locally in the volcanic rocks. Chlorite and quartz-sericite alteration occur proximal to the mineralisation.

Chemical assays of the Rockliden mineralisation cover the range of base-metal grades plotted for bimodal felsic VHMS type deposits (Barrie and Hannington 1999, Fig. 2). In reference to the classification proposed by Franklin et al. (1981), the assays scatter around the line separating the Cu, Zn-Cu and the Zn-Pb-Cu groups in the Cu-Pb-Zn ternary plot (Fig. 2). Plotting of Cu-Pb-Zn assays from different depth intervals reveals that below ca. 400 m most assayed drill core intervals fall into the field of the Zn-Cu group. Further, interpolation of drill core assays with Leapfrog 3D (geological modelling software) indicate that high Sb-, Ag-, and partly Pb-values cluster in the upper part of the steeply dipping sulphide lenses.
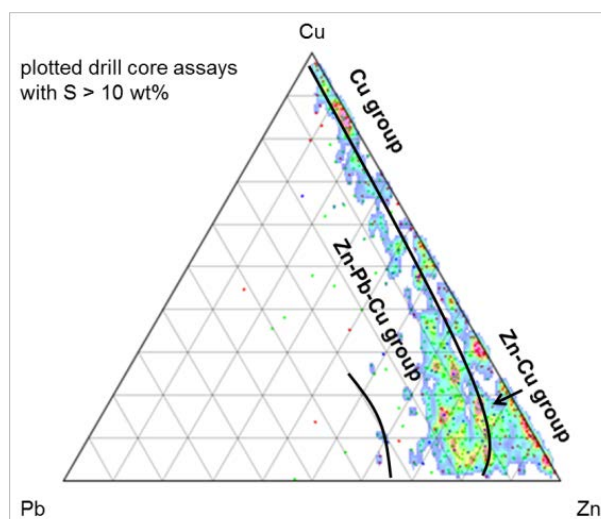


**Figure 2.** Zn-Cu-Pb ternary plot for chemical assays of drill core intervals with S > 10 wt%. The classification lines for different groups are taken from Franklin et al. (1981).

Mattsson and Heeroma (1985) sketched an idealised pre-deformational mineral zoning pattern in a first report on the Rockliden deposit. According to Mattsson and Heeroma (1985), a pyrrhotite-pyrite impregnation is found in the volcanic stratigraphic footwall rocks. It becomes richer in chalcopyrite and arsenopyrite in its central part and is covered by massive non-banded sulphides (Table 1). The latter are followed stratigraphically upward and sideways by massive, banded sulphides, characterised by an alternation of pyrite- and sphalerite-rich bands. The Zn-Ag- and locally Sb-contents of the banded sulphides are higher than of the non-banded massive sulphides. Even slightly higher Zn- and Pb-contents are noted locally in the north-western part of the deposit, for which a different mineralogy was documented (Mattsson and Heeroma 1985, Table 1). The overall mineralogical zoning of the main sulphide phases is a known phenomenon for massive sulphide deposits associated with felsic volcanic rocks (Galley et al. 2007).

**Table 1.** Descriptive classification and sulphide mineralogy at Rockliden (after Mattsson and Heeroma 1985; Raat and Årebäck 2009). Mineral abbreviations: Apy arsenopyrite, Bour bournonite, Ccp chalcopyrite, Gd gudmundite, Gn galena, Po pyrrhotite, Py pyrite, Sp sphalerite, Ttr tetrahedrite.

| Mineralisation types | Major (and minor) sulphide phases |
|---|---|
| Impregnation and semi-massive | Po, Py, Ccp, Apy, +/- Sp |
| Massive non-banded | Py, Po, Ccp, Apy, Sp |
| Massive banded | Py, Sp, Ccp (Gn, Ttr, +/- Gd, Bour); NW deposit part: Py, Po, Sp, Ccp, Gn, Ag-rich Ttr |
| "Remobilised" | Ccp, Po |

However, the above described zoning is not followed strictly in all drill core sections which cut through massive sulphide intervals: obliteration of the zoning, partly related to structural modification and metal mobility during deformation and metamorphism, was suggested as cause for the deviations from the pattern

(Depauw 2009). One class ("remobilised" type, table 1) was added to the previous classification scheme by Mattsson and Heeroma (1985) to account for remobilisation in the ore shoots found along fault planes. The sulphide mineralogy of this class is dominated by chalcopyrite and pyrrhotite (Raat and Åreback 2009).

## 3 Methods

In preparation for sampling, the mineralogy of drill core intervals was recalculated in HSC Geo (Roine 2009) from chemical assays provided by Boliden (S, Cu, Zn, Pb, As, and Sb), assuming a simplified mineralogy (pyrite, chalcopyrite, sphalerite, galena, arsenopyrite and bournonite). Sphalerite and chalcopyrite form the main base-metal minerals and are targets for separation by flotation. Ag and Sb represent bonus and penalty elements. Based on the sphalerite and chalcopyrite content of the plain sulphide fraction (i.e. sulphides recalculated to 100 wt% in the assayed drill core intervals), preliminary classes were defined and further subdivided by their Ag- and Sb-content. Sixty samples were collected from six drill cores to cover most of the preliminary defined classes of the deposit (Fig. 1).

All samples were assayed by the ALS Minerals Division (Piteå, Sweden). Polished thin sections were prepared by Vancouver Petrographics Ltd (Canada) and were studied under the optical microscope to refine the HSC-Geo-based preliminary classification and to provide additional textural information.

The Ag- and Sb-bearing minerals were mainly studied in backscattered electron (BSE) images and by energy-dispersive X-ray spectroscopy (EDS) at the scanning electron microscope (Merlin SEM - Zeiss Gemini, FESEM, Luleå University of Technology, Sweden). The following analytical conditions were used at the SEM: acceleration voltage of 20 keV and emission current of 0.9 to 1.1 nA.

## 4 Results

Based on the total sulphide content (TS) of the drill core samples, the following broad distinction can be made: disseminated (generally < 15 wt% TS), semi-massive (ca. 15 to 50 wt% TS), and massive sulphides (> 50 wt% TS).

Geochemical tools are employed to classify the disseminated to semi-massive sulphides further (cf. Barrett and MacLean 1999). Volcanic rocks and mafic dykes form clusters and can be distinguished in $Zr-TiO_2$ and Y-Zr plots. Regarding the base-metal sulphide minerals, mafic rocks tend to contain more chalcopyrite than the volcanic rocks, which commonly have higher sphalerite content. An indication of differences in the Sb-mineralogy between the altered volcanic rocks and the mafic dykes has also been found (Minz et al., in review). The former locally contains berthierite, jamesonite and other As-Sb-bearing sulphosalts, whereas the latter contains abundant bournonite and varying amounts of boulangerite, meneghinite, tetrahedrite and gudmundite.
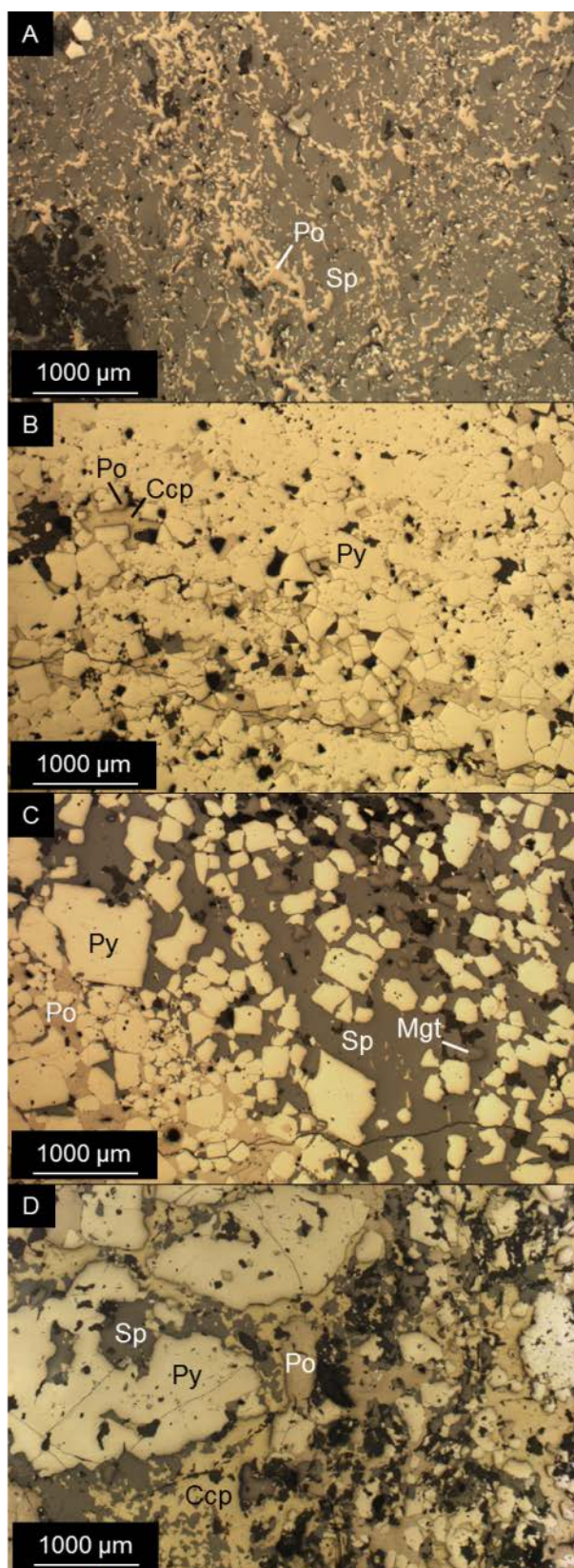


**Figure 3.** Textures in massive sulphide samples. A) Po-Sp-group with diaplectic intergrowth of Po-Sp B) Py-group C) Py-Sp-group (Mgt mangnetite) D) Py-Ccp-Sp group. For abbreviations of mineral names see captions table 1.

The massive sulphides are grouped by their dominating Fe-, Cu- and Zn-sulphide minerals and are listed with their (end member) characteristics in table 2. Textures of the massive sulphide samples are shown in figure 3. It should be noted that samples can show

transitional features between the different groups and there are no strict boundaries. Common Sb-bearing minerals in the massive sulphide samples are tetrahedrite, bournonite and gudmundite. In contrast to massive sulphide samples from the upper part of the Rockliden deposit (i.e. < 400 m below surface), the frequency of Sb-rich massive sulphide samples is lower and gudmundite often forms a dominant Sb-bearing mineral in massive sulphides from the lower part of the deposit (Minz et al., in review).

**Table 2.** Grouping of massive sulphide samples. For abbreviations of mineral names see table 1. Range of base-metal mineral content as calculated by HSC Geo (Roine 2009).

| Group | Characteristics |
|---|---|
| Po-Sp /Ccp | Often with isolated grains of Py; sub-groups: <br> - Ccp + Sp < 15 wt%, <br> - 12–50 wt% Sp (Fig. 3A), locally high Sn values (i.e. > 400 ppm), <br> - ca. 20 wt% Ccp. |
| Py | Banding related to clustering of Py and a variation in grain sizes of Py (Fig. 3B), minor Ccp and Sp (Ccp + Sp < 10 wt%). |
| Py-Sp | Banding partly due to alteration of Sp and Po+/-Ccp in the groundmass surrounding Py grains (Fig. 3C), or due to variation in size and density-packing of Py-grains, Ccp: 0–6 wt%, Sp: 12–25 wt%. |
| Py-Sp /Ccp | Often with metamorphic features such as mineral alignment, intense fracturing and corrosion of Py grains (Fig. 3D), magnetite occasionally arranged in bands; sub-groups: <br> - Ccp: 6–12 wt%, Sp: 7–15 wt%, <br> - Ccp: 6–20 wt%, Sp: 0–7 wt% (often high in As, i.e. > 2 wt% Apy). |

## 5 Summary and Conclusion

The total sulphide content allows for the distinction between disseminated to semi-massive and massive sulphides at the Rockliden deposit. Among the disseminated to semi-massive sulphide samples, acid and mafic rocks can be distinguished based on their geochemical characteristics. Massive sulphide samples were classified based on their pyrrhotite, pyrite, chalcopyrite and sphalerite content. Differences in the Sb-mineralogy were recognised between the mafic and acid rock units and also between disseminated to semi-massive and massive sulphides. Further, indications were found that the Sb-mineralogy of the massive sulphides changes with depth (Minz et al, in review).

The subject of an on-going PhD study is to identify process-relevant rock-intrinsic parameters (cf. Walters and Kojovic 2006), as well as rock-related and deposit-scale variations in the mineralogy, including those which were indicated in early studies at the upper part of the Rockliden mineralisation by Mattsson and Heeroma (1985). For these purposes quantitative, e.g. automated-SEM/EDS, mineralogical data will be acquired. These data are expected to lead to refinement of the proposed qualitative classification of the mineralisation. The data is aimed to be used to form the basis of, the Rockliden 3D-geometallurgical model.

## Acknowledgements

## References

Allen RL, Weihed P, Svenson, S-Å (1996) Setting of Zn-Cu-Au-Ag massive sulfide deposits in the evolution and facies architecture of a 1.9 Ga marine volcanic arc, Skellefte district, Sweden. Econ Geol 91 (6): 1022-1053.

Barrett TJ, MacLean WH (1999) Volcanic sequences, lithogeochemistry, and hydrothermal alteration in some bimodal volcanic-associated massive sulfide systems. Rev in Econ Geol 8: 101-31.

Barrie CT, Hannington MD (1999) Classification of volcanic-associated massive sulfide deposits based on host-rock composition. Rev in Econ Geol 8: 1-11.

Depauw G (2009) Geology of the Rockliden volcanogenic massive sulphide deposit, north central Sweden. Master Thesis, Luleå University of Technology.

Evins P (2011) New map and structural analysis of the Rockliden exposure. Internal Report Boliden Mines, 46346000.

Franklin JM, Lydon JW, Sangster DF (1981) Volcanic-associated massive sulfide deposits. Econ Geol 75: 485-627.

Galley AG, Hannington MD, Jonasson IR (2007) Volcanogenic massive sulphide deposits. Mineral Deposits of Canada: A Synthesis of Major Deposit-Types, District Metallogeny, the Evolution of Geological Provinces, and Exploration Methods: Geological Association of Canada, Mineral Deposits Division, Special Publication (5): 141-161.

Kousa J, Lundqvist T (2000) Svecofennian domain. In Description of the bedrock map of central Fennoscandia (Mid- Norden)., eds. T. Lundqvist, S. Autio. Special Paper 28 ed., 47-74. Espoo, Finland: Geological Survey of Finland.

Lundqvist T, Vaasjoki M, Persson PO (1998) U-Pb ages of plutonic and volcanic rocks in the Svecofennian Bothnian Basin, central Sweden, and their implications for the Palaeoproterozoic evolution of the basin. GFF 120 (4): 357-363.

Mattsson B, Heeroma P (1985) Rockliden prospekteringsresultat 1981-1985. Internal Report Boliden Mines, GP 85 005 2.

Minz F, Bolin N-J, Lamberg P, Wanhainen C (in review) Detailed characterisation of antimony mineralogy in a geometallurgical context at the Rockliden ore deposit, north-central Sweden. Submitted to Minerals Engineering.

Raat H, Årebäck H (2009) Geology, grade and tonnage estimate of the Rockliden VMS deposit, north central Sweden. Internal Report Boliden Mines, 2009-34.

Roine A (2009). HSC Chemistry® 7.0 user's guide - chemical reaction and equilibrium software with extensive thermochemical database and flowsheet simulation. Vol. volume 1/2.

Walters S, Kojovic T (2006). Geometallurgical mapping and mine modeling (GEM3) - the way of the future. Paper presented at International Autogenous and Semi-Autogenous Grinding Technology SAG Conference 2006, Vancouver, Canada.

Welin, E (1987). The depositional evolution of the Svecofennian supracrustal sequence in Finland and Sweden. Precambrian Res (35): 95-113.

# Residence of Au in adularia-sericite epithermal deposits: Implications from the Simberi deposit, Papua New Guinea

**Alicia Newton**
*School of Environment, The University of Auckland, Auckland, New Zealand*

**Jeffrey L. Mauk, Alan E. Koenig, Heather A. Lowers**
*U.S. Geological Survey, MS 973, Denver, Colorado 80225, USA*

**Andrew Menzies**
*Universidad Católica del Norte, Antofagasta, Chile*

**Phil Davies**
*St Barbara Ltd, Eight Mile Plains, Queensland, 4113, Australia*

**Abstract.** The Simberi adularia-sericite epithermal deposit in Papua New Guinea contains oxide and sulphide ore reserves, and is currently mining oxide ore. The sulphide ore is partly refractory. New petrographic, SEM, QEMSCAN, and LA-ICP-MS analyses indicate that the Au in the sulphide ore resides in Au-bearing telluride minerals and also into arsenian pyrite. The telluride minerals most commonly occur as inclusions that are less than 30 microns across in vuggy pyrite. The Au and Ag telluride minerals have excellent liberation properties, in part because of the vuggy nature of the pyrite. Textural and geochemical relations, combined with published literature, lead us to infer that the telluride minerals were deposited by vapour phase transport after deposition of Au-bearing arsenian pyrite.

**Keywords.** Epithermal, arsenian pyrite, refractory Au, geometallurgy

## 1 Introduction

Adularia-sericite epithermal deposits are an important source of Au and Ag (Heald et al. 1987; Simmons et al. 2005). In deposits hosted by calc-alkaline volcanic rocks, Au resides primarily into electrum, but in deposits hosted by alkaline igneous rocks, telluride minerals are quite common. In other Au deposits, such as Carlin-type deposits and some orogenic Au and high-sulfidation epithermal deposits, Au commonly resides in arsenian pyrite (Hofstra and Cline 2000; Reich et al. 2005).

The Simberi deposit, Papua New Guinea (PNG), is an adularia-sericite epithermal deposit hosted in high-K calc-alkaline volcanic rocks with proven and probable reserves of oxide and sulphide ore of 42.5Mt at 1.49g/t Au (Allied Gold Mining plc, Annual Report 2011). The deposit is unusual in two ways: (1) the mineralisation is disseminated, and there are no significant quartz veins in the deposit, and (2) the sulphide mineralization is refractory, with a component of the Au mineralisation in sulphide minerals. In these aspects, and in its geological setting, the deposit is very similar to the Ladolam orebody on Lihir Island, which is the world's largest adularia-sericite epithermal deposit. We describe the Au mineralisation in the sulphide ore at Simberi, and we demonstrate that telluride minerals and arsenian pyrite make important contributions to the Au endowment of the deposit. However, some arsenian pyrite does not contain Au, which may have important implications for other deposits with refractory Au worldwide.

## 2 Regional and local geology

Papua New Guinea consists of a continental craton in the southwest that is part of mainland PNG, a central collisional zone along the north-eastern margin of the New Guinea mainland, and a series of volcanic islands around the Bismarck Sea to the northeast. The Bismarck Archipelago is made up of New Ireland, New Britain, New Hanover, Manus, Bougainville and the Solomon Islands, as well as a number of smaller surrounding islands (McInnes and Cameron 1994). Calc-alkaline volcanism was dominant in the formation of this region, related to the collision of the Pacific and Indo-Australian plates at the Manus-Kilinailau Trench from the Oligocene to the Miocene (McInnes and Cameron 1994). Subduction reversal occurred following the collision of the Ontong-Java Plateau with the Kilinailau Trench, leading to the formation of the New Britain Trench to the south (Müller et al. 2001).

Following cessation of subduction at the Manus-Kilinailau Trench, post-subduction volcanism occurred in the New Ireland Basin, in what used to be the fore-arc region of the Kilinailau Trench (Stracke and Hegner, 1998). This volcanism was controlled by NE trending extensional basement structures (Petersen et al., 2002). The Tabar-Lihir-Tanga-Feni (TLTF) Island Chain, formed by this volcanism, trends approximately NW-SE, parallel to New Ireland. The TLTF chain is dominated by shoshonitic alkali volcanic rocks, and varied plutonic rocks, and volcanism has progressed south-eastwards over time (McInnes and Cameron 1994).

Simberi Island, in the Tabar Island Group, was the first of the TLTF chain to erupt, at approximately 3.6 Ma (Müller et al. 2001). It contains high-K calc-alkaline volcanic rocks, including the most primitive igneous rocks in the TLTF chain. The volcano that makes up most of Simberi Island is eroded to a depth of 2-3 km, and two extinct coral reefs make up the coastal lowlands

and an encircling ring of hills, while a living coral reef encircles the island (McInnes and Cameron 1994).

## 3   Analytical methods

We logged eleven drill holes for a total of 808 m, and collected more than 200 representative samples from those drill holes.  From these, we analysed a subset of approximately seventy samples using XRD, reflected and transmitted light petrography, and whole rock geochemistry.  From these, a further sixteen samples were selected for additional analyses, including electron microprobe analyses of ten samples, quantitative evaluation of minerals by scanning electron microscopy (QEMSCAN) analyses of ten samples, scanning electron microscopy of eight samples, and laser ablation-inductively coupled plasma-mass spectrometry (LA-ICP-MS) analyses of six samples.

Scanning electron microscopy was undertaken at the U.S. Geological Survey in Denver, Colorado, with a FEI Quanta 450 field emission scanning electron microscope operated at 20 kV and approximately 2 nA current. Backscattered electron images of individual grains were acquired with a voltage contrast detector.  Electron microprobe analyses (EMPA) of polished mounts took place at the University of Michigan Cameca SX100 with an accelerating voltage of 20 kV and beam current of 10 nA, using the analytical protocol of Cocker et al. (2013).

Trace element concentrations were determined using LA-ICP-MS analyses using a Photon Machines Analyte G2 LA system (193-nm excimer) equipped with a the 2-volume (HelEx) sample chamber that was coupled to a PerkinElmer DRC-e ICP-MS.  A 12 μm spot size was used for data collection, and signals were calibrated using USGS microanalytical sulphide reference material, MASS-1 (Wilson et al. 2002).  Concentrations were determined using off-line calculations, following the protocol of Longerich et al. (1996).  Iron was used as the internal standard for concentration calculations. Spot analysis locations were selected based on precise location of zones of interest from SEM images and supporting data.  Signals were screened for heterogeneities such as microinclusions or zoning before further data processing (Nadoll and Koenig 2011).  We analysed for the following elements, with their reporting limits in ppm in parentheses: Ag (0.6), As (3.48), Au (0.38), Bi (0.6), Cd (26.9), Co (0.55), Cu (160), Fe (48.47), Hg (10.5), Mn (8), Mo (0.8), Ni (4.51), Pb(2), S (5384), Sb (0.77), Se (56.9), Sn (7.6), Te (12), Tl (0.55), V (9.6), Zn (39.6).

QEMSCAN sample preparation and analytical work was performed at the Centro Mineralogía Antofagasta (CMA) Laboratory of BHPBilliton. Ten samples were pre-crushed to -200 um, and three replicate 30mm epoxy resin blocks per sample analysed. The QEMSCAN modes of measurement used were Bulk Mineralogical Analysis (BMA) for determining bulk mineralogy and Specific Mineral Search (SMS) for identifying the various Au- and Ag-bearing mineral phases, operating at 25 kV and a beam current of 5 nA, with a pixel spacing of 2 um.  The samples were analysed using iMeasure v4.3 and the resultant data processed using iDiscover 5.2.
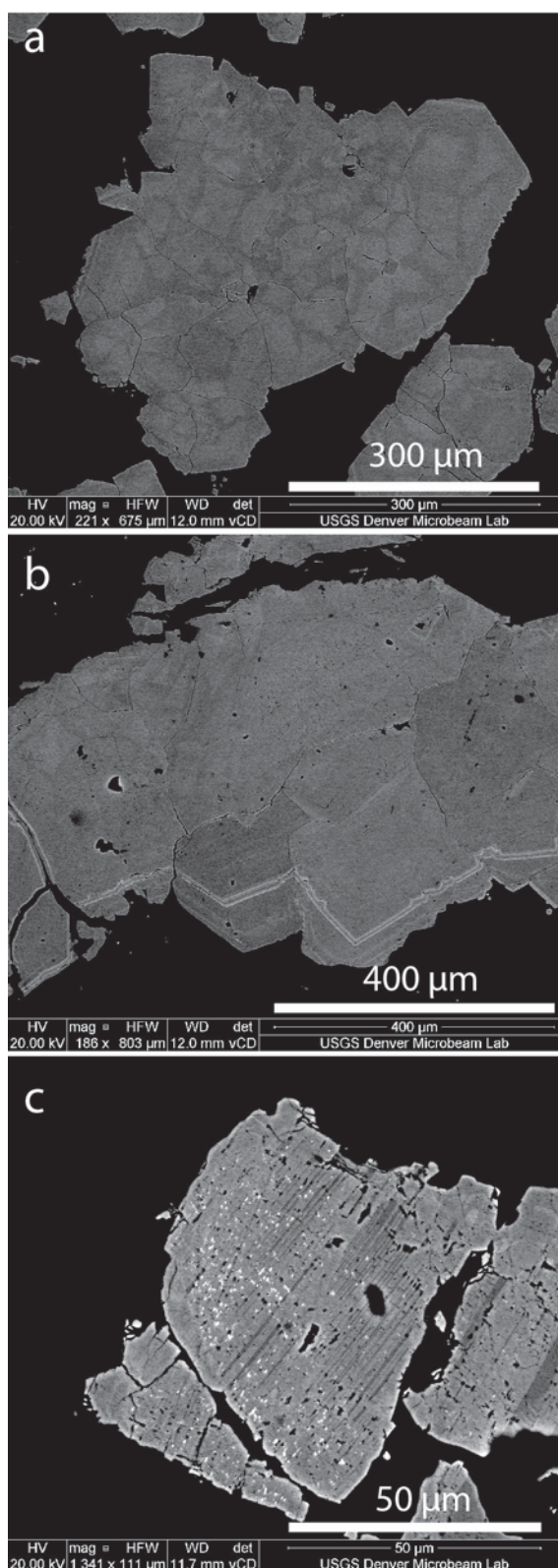


**Figure 1.** Backscattered electron images of pyrite from the Simberi deposit.  **a** Sample AU62655 showing large composite pyrite grain with variable concentrations of As.  **b** Sample AU62655 showing growth zones of arsenian pyrite (light grey bands).  **c** Sample AU62749 showing porous pyrite with abundant inclusions of Au and Ag telluride minerals.

## 4   Results

Petrography, XRD, and whole rock geochemical analyses demonstrate that the rocks at Simberi are

pervasively and intensely altered. The most common and widespread alteration types are potassic, which is characterised by adularia plus illite, and carbonate alteration, where calcite and lesser dolomite are the most common alteration minerals. Rocks typically show intense alteration with more than 90% of the igneous minerals replaced by alteration minerals, but in most places the alteration has not destroyed the original rock textures. Both alteration types contain Au mineralisation, but samples that contain more than 2 ppm Au are more common in carbonate-altered samples.

Sulphide minerals include pyrite, marcasite, arsenopyrite, sphalerite, and galena. Pyrite from Simberi is chemically variable (Fig. 1). Some grains are large, euhedral to subhedral, and show no evidence of chemical zonation with electron microprobe analyses or in backscattered electron (BSE) images. Other grains are composites of smaller grains that show variable As concentrations or growth zones that are defined by arsenian pyrite. Some samples contain pyrite that has abundant pores, and this vuggy pyrite commonly has small inclusions of Au- and Ag-bearing minerals that typically measure less than 5 microns across (Fig. 1c).

More than 350 microprobe analyses of pyrite show that its average composition is stoichiometric $FeS_2$, but this average value masks its heterogeneity. Our LA-ICP-MS analyses focussed on the pyrite, in order to characterise the Au content of the arsenian pyrite, and the significance of inclusions in the pyrite. Arsenic and Sb occur in all analyses of pyrite at levels that exceed their LA-ICP-MS detection limits, with median values of 3805 and 108 ppm, respectively. Thallium, Mn, Pb, and Ag are very commonly detected in pyrite, occurring at levels that exceed their LA-ICP-MS detection limits in 97 to 86% of analyses, with median values of 90, 188, 242, and 43 ppm, respectively. Gold, Mo, Zn, and Co are commonly detected, occurring at levels that exceed their LA-ICP-MS detection limits in 74 to 56% of analyses, with median values of 15, 17, 67, and 2 ppm, respectively. Nickel, V, Cu, Te, Cd, Sn, Bi, and Hg are less commonly detected in pyrite, occurring at levels that exceed their LA-ICP-MS detection limits in 23 to 40% of analyses. As discussed below, many of these elements likely reside in other minerals that are sampled as inclusions by the 12 μm laser beam during analyses.

LA-ICP-MS analyses show variable incorporation of As, Au, and Te in pyrite (Fig. 2). Petrographic, SEM, and QEMSCAN observations indicate that the Te resides in Au and Ag telluride minerals, and that the As resides in arsenian pyrite. Elsewhere, As and Au contents of pyrite define a wedge-shaped zone with an upper limit that defines the solubility of As and Au in pyrite (Fig. 2; Reich et al. 2005). At Simberi, all analyses that exceed this compositional limit contain Te contents that exceed the detection limit, and we infer that at least some of the Au in these analyses is derived from inclusions of telluride minerals (Fig. 2).

Thirty microprobe analyses of sphalerite returned an average composition of $Zn_{1.88}Fe_{0.08}Cu_{0.01}Cd_{0.01}S_2$, twenty microprobe analyses of galena yielded an average composition of $Pb_{1.99}Fe_{0.02}Se_{0.03}S_{1.97}$, and sixteen microprobe analyses of arsenopyrite gave an average composition of $Fe_{0.97}Se_{0.01}As_{0.80}S_{1.19}$. The Cu in

the sphalerite likely reflects chalcopyrite inclusions. Sphalerite also contains As and Se in concentrations that exceed the detection limits in 3 and 10% of the analyses, respectively; all other analysed elements have concentrations that are less than the detection limits of the microprobe. The galena does not contain elements other than Pb, Fe, Se, and S with concentrations that exceed the detection limits of the microprobe; it is not argentiferous. In addition to Fe, Se, As, and S, arsenopyrite contains Ni and Cu at concentrations that exceed their microprobe detection limits in 13 and 19% of analyses, respectively.
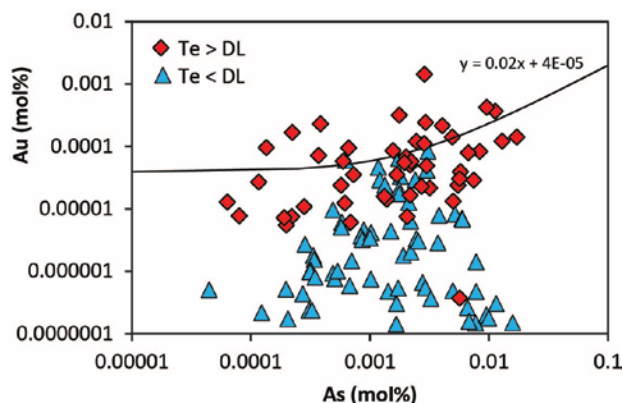


**Figure 2.** As-Au plot of LA-ICP-MS analyses of arsenian pyrite from the Simberi deposit. Points in red contain more than 12 ppm Te, which is the detection limit for these analyses, and likely contain inclusions of telluride minerals. Points in blue have Te contents that are less than the detection limit, and may lack inclusions of telluride minerals. The line, which is from Reich et al. (2005), shows the upper limit of solubility of Au in arsenian pyrite, and samples from Simberi that contain excess Au likely contain inclusions of telluride minerals.

The Au and Ag at Simberi occur in tennantite, calaverite ($AuTe_2$), petzite ($Ag_3AuTe_2$), electrum, hessite ($Ag_2Te$), acanthite ($Ag_2S$), aguilarite ($Ag_4SeS$), and chlorargyrite ($AgCl$). Most Au- and Ag-bearing minerals are less than 20 μm across, but some samples contain grains that range up to 100 μm across. Six microprobe analyses of tennantite show that it is Cu- and Zn-rich, with an average composition of $Cu_{9.51}Zn_{1.70}Fe_{0.22}Ag_{0.15}Cd_{0.01}As_{2.49}Sb_{1.51}S_{12.97}Se_{0.03}$; this indicates that the tennantite is not a major repository of Ag. The other Au- and Ag-bearing minerals were too fine-grained to obtain electron microprobe analyses. QEMSCAN analyses show that the Au- and Ag-bearing minerals were highly liberated (>85%) in samples that were crushed to < 250 microns.

## 5 Discussion and Conclusions

Structurally bound Au in arsenian pyrite has been documented from a variety of types of orebodies, and in some places these deposits also host Au nanoparticles (e.g. Hough et al. 2011; Reich et al. 2005; Large et al. 2009; Deditius et al. 2011). Our LA-ICP-MS analyses confirm that Au in the sulphide ore at Simberi occurs in arsenian pyrite, but there is no evidence for Au nanoparticles, and instead Au- and Ag-bearing telluride minerals locally occur in vuggy pyrite. In this regard,

Simberi shares characteristics with deposits that host Au in arsenian pyrite (Reich et al. 2005; Large et al. 2009), and deposits where telluride minerals, including nanoparticles, provide the host for Au (Ciobanu et al. 2012; Cook et al. 2009).

Correlation coefficients demonstrate that As and Sb correlate strongly, as expected from their common substitution. Silver and Te also correlate strongly, consistent with QEMSCAN and microprobe observations that telluride minerals are the predominant host for Ag. In contrast, Au does not show strong correlations with As or Te, reflecting its incorporation into both arsenian pyrite and telluride minerals (Figs. 1 and 2). The concentrations of Mo, Ni, Bi, and Pb show moderate correlations; we suggest that these elements may also be residing primarily in mineral inclusions, some of which may be nanoparticles (Deditius et al. 2011), that were sampled by LA-ICP-MS analyses.

At Simberi, Te was likely transported in the vapour phase (Cooke and McPhail 2001), and more speculatively, some or all of the Au in the telluride minerals may have been transported in the vapour phase as well (Henley et al. 2012; Larocque et al. 2008). If so, the Simberi deposit provides a key example of liquid and vapour transport of precious metals to form a disseminated adularia-sericite epithermal deposit. Although not common, the enormous endowment of the Ladolam deposit, and the similarity in mineralogy, suggest that these processes may combine to form large resources of Au in the Earth's crust.

## Acknowledgements

## References

Allied Gold Mining plc (2011) Annual Report, 2011

Ciobanu CL, Cook NJ, Utsunomiya S, Kogagwa M, Green L, Gilbert S, Wade B (2012) Gold-telluride nanoparticles revealed in arsenic-free pyrite. Am Mineral 97:1515-1518

Cocker H, Mauk J, Rabone SC (2013) The origin of Ag–Au–S–Se minerals in adularia-sericite epithermal deposits: constraints from the Broken Hills deposit, Hauraki Goldfield, New Zealand. Miner Depos 48:249-266

Cook NJ, Ciobanu CL, Spry PG, Voudouris P (2009) Understanding gold-(silver)-telluride-(selenide) mineral deposits. Episodes 32:249-263

Cooke DR, McPhail DC (2001) Epithermal Au-Ag-Te mineralization, Acupan, Baguio district, Philippines: Numerical simulations of mineral deposition. Econ Geol 96:109-131

Deditius AP, Utsunomiya S, Reich M, Kesler SE, Ewing RC, Hough R, Walshe J (2011) Trace metal nanoparticles in pyrite.

Ore Geol Rev 42:32-46

Heald P, Foley NK, Hayba DO (1987) Comparative anatomy of volcanic-hosted epithermal deposits; acid-sulfate and adularia-sericite types. Econ Geol 82:1-26

Henley RW, Mavrogenes J, Tanner D (2012) Sulfosalt melts and heavy metal (As-Sb-Bi-Sn-Pb-Tl) fractionation during volcanic gas expansion: the El Indio (Chile) paleo-fumarole. Geofluids 12:199-215

Hofstra AH, Cline JS (2000) Characteristics and models for carlin-type gold deposits. Rev in Econ Geol 13:163-220

Hough RM, Noble RRP, Reich M (2011) Natural gold nanoparticles. Ore Geol Rev 42:55-61

Large RR, Danyushevsky L, Hollit C, Maslennikov V, Meffre S, Gilbert S, Bull S, Scott R, Emsbo P, Thomas H, Singh B, Foster J (2009) Gold and trace element zonation in pyrite using a laser imaging technique: Implications for the timing of gold in orogenic and Carlin-style sediment-hosted deposits. Econ Geol 104:635-668

Larocque ACL, Stimac JA, Siebe C, Greengrass K, Chapman R, Mejia SR (2008) Deposition of a high-sulfidation Au assemblage from a magmatic volatile phase, Volcán Popocatépetl, Mexico. J Volcanol Geotherm Res 170:51-60

Longerich HP, Jackson SE, Günther D (1996) Laser ablation-inductively coupled plasma-mass spectrometric transient signal data acquisition and analyte concentration calculation. J Anal Atom Spec 11:899-904

McInnes BIA, Cameron EM (1994) Carbonated, alkaline hybridizing melts from a sub-arc environment: Mantle wedge samples from the Tabar-Lihir-Tanga-Feni arc, Papua New Guinea. Earth Planet Sci Lett 122:125-141

Müller D, Franz L, Herzig PM, Hunt S (2001) Potassic igneous rocks from the vicinity of epithermal gold mineralization, Lihir Island, Papua New Guinea. Lithos 57:163-186

Nadoll P, Koenig AE (2011) LA-ICP-MS of magnetite: methods and reference materials. J Anal Atom Spec 26:1872-1877

Petersen S, Herzig PM, Hannington MD, Jonasson IR, Arribas A (2002) Submarine gold mineralization near Lihir Island, New Ireland fore-arc, Papua New Guinea. Econ Geol 97:1795-1813.

Reich M, Kesler SE, Utsunomiya S, Palenik CS, Chryssoulis SL, Ewing RC (2005) Solubility of gold in arsenian pyrite. Geochim Cosmochim Acta 69:2781-2796

Stracke A, Hegner E (1998) Rifting-related volcanism in an oceanic post-collisional setting: the Tabar–Lihir–Tanga–Feni (TLTF) island chain, Papua New Guinea. Lithos 45:545-560

Simmons SF, White NC, John DA (2005) Geological characteristics of epithermal precious and base metal deposits Econ Geol 100th Anniv Vol. pp 485-522

Wilson SA, Ridley WI, Koenig AE (2002) Development of sulfide calibration standards for the laser ablation inductively-coupled plasma mass spectrometry technique. J Anal Atom Spec 17:406-409

# Siderophore-mediated extraction of platinum and palladium from oxidized PGE ores of the Great Dyke and the Bushveld and indications for beneficiation

**Dennis Mohwinkel & Michael Bau**
*Jacobs University Bremen, School of Engineering and Science, Earth and Space Sciences, 28759 Bremen, Germany*
*d.mohwinkel@jacobs-university.de*

**Thomas Oberthür & Malte Junge**
*Federal Institute for Geosciences and Natural Resources (BGR), Stilleweg 2, 30655 Hannover, Germany*

**Abstract.**
Here we present data on the siderophore-mediated mobilization of platinum-group elements (PGE) platinum and palladium from oxidized PGE ore material originating from the Main Sulphide Zone (MSZ) of the Great Dyke, Zimbabwe as well as from the Platreef and UG2 of the Bushveld complex, South Africa. Processing-Beneficiation of this type of surficial ore is problematic, because currently established metallurgical technologies do not yield high ('economic') recovery rates due to the complex mineralogical composition of the oxidised ores. Hence, oxidised PGE ores are currently not mined, although considerably large resources are available in both the Great Dyke and the Bushveld area.
Siderophores are certain biogenic complexing agents produced by bacteria and plants to cope with iron-deficiency in iron-limited systems. Albeit having high stability constants with Fe, especially high-field strength elements are also strongly complexed and hence mobilized by siderophores. We demonstrate that utilizing siderophore-promoted mobilization of Pt and Pd from oxidised PGE ores from the Great Dyke, Pt extraction efficiencies may be reached that amount to 50-80% when siderophores are used in combination with hydrochloric acid pretreatment. Similar experiments will be conducted for oxidized Platreef and UG2 chromitites from the Bushveld Complex, which are similar to the Great Dyke oxidized PGE ores and also have a high potential for being mined in the future.

Keywords: Platinum-Group Elements, PGE Oxides, Siderophores, Extraction, Beneficiation

## 1 Introduction

Oxidized Platinum-Group Element (PGE) ores from the Great Dyke in Zimbabwe and from the Bushveld Complex in South Africa have high potential for future mining because of relatively high PGE grades on the one hand and big resource estimates on the other (see Prendergast, 1988; Hey, 1999; Oberthür et al., 2012). They are surficial ore deposits ranging to maximum depths of about 15 to 30m, so that relatively low-cost open-pit mining of huge volumes appears to be feasible. For the oxidized PGE ores along the Great Dyke alone, resource estimates range from 160 to 250 Mt of oxidized material (Oberthür et al., 2012) with average grades of 3-5 ppm Pt. The pristine material mined at those sites is treated following conventional metallurgical practice and

recovery grades for Pt of >85% are reached (Rule, 1998). However, all metallurgical tests conducted so far on oxidised ore material both from the Great Dyke as well as the Bushveld suffer from very low Pt recoveries of considerably less than 30% (see Oberthür et al., 2012 and references therein). Relative to the pristine ore, the oxidized PGE ore of the Great Dyke shows higher Pt/Pd ratios (due to depletion of Pd during weathering) and an almost complete removal of sulphur (Locmelis et al., 2010). As reported by Locmelis et al. (2010), PGE in the oxidized Main Sulphide Zone (MSZ), which hosts most of the PGE resources at the Great Dyke, occur as relict primary platinum-group minerals (PGM; sperrylite, cooperite, braggite), in solid solution in relict sulphides as pentlandite, as secondary Pt-Fe alloys, as PGE oxides/hydroxides and as substitutes or adsorbed cations in iron-and manganese (hydr-) oxides. (Pt, Pd)-bismuthotellurides are almost completely destroyed (Oberthür et al., 2012). According to Oberthür & Melcher (2005), about 50% of Pt is hosted by PGM, 45% by hydroxide structures and 5% by relict sulfides. While the major element composition is mostly preserved in oxidized MSZ relative to its pristine counterpart, Oberthür & Melcher (2005) observed significant losses for Na, K, and S, which they assume to be caused by partial destruction of orthopyroxene, feldspar, phlogopite and sulphides – whereas Cu and Au were enriched during weathering due to immobile behaviour. The pronounced gain in LOI (loss on ignition) is according to Oberthür & Melcher (2005) caused by formation of hydrous silicates and formation of FeOOH in the oxidized MSZ. Apparently, the complex and strictly polymodal mineralogical state of the weathered PGE ores is the main cause of the processing issue faced with this ore deposit.

We are using a novel approach for the extraction of PGE from oxidized ore material by combining conventional acid treatment steps with biogenic complexing agents called siderophores. Siderophores are a group of low molecular weight organic molecules synthesized and exuded by various bacteria and plants to cope with iron-deficiency in iron-limited systems (Boukhalfa & Crumbliss, 2002). Whilst $Fe^{2+}$ is highly soluble and hence readily available for organisms and plants, the prevalence of $Fe^{3+}$ in most oxic systems and its tendency to precipitate as insoluble iron-oxyhydroxide leads to deficiencies of bioavailable iron in the environment. To cope with these situations,

siderophores are exuded by plants and organisms. Siderophores facilitate dissolution of iron (hydr-)oxide minerals and preferentially complex and hence mobilize Fe (Kraemer, 2004). However, besides having high stability constants with Fe, most siderophores are also quite effective in binding and solubilizing many high field strength elements such as the rare earth elements, the platinum group elements and some actinides (see e.g. Bouby et al., 1998; Baysse et al., 2000; Yoshida, 2004a,b; Dahlheimer, 2007; Liermann et al., 2007; Bellenger et al., 2008; Duckworth, 2009; Christenson & Schijf, 2011; Desouky et al., 2011; Bau et al., 2013).

## 2 Experimental

All chemical reagents used in this study were of suprapure grade. Purity is cross-checked by measurement of reagent blank samples with ICP-MS. All lab work was conducted in a trace-metal and especially PGE-free environment. Labware used for the leaching experiments as well as for the geochemical analysis was acid-cleaned following standard geochemical lab procedures.

Pt-peak areas as well as composite samples composed of several Pt-peak areas of different drill cores or of a whole core profile were prepared for leaching experiments. The oxidized PGE ores were crushed and milled to grain sizes smaller 64μm and were then thoroughly homogenized. Characterization of the bulk rock compositions of the leaching samples was done by pressure digestion of the sample powders with multiple acids including hydrofluoric acid, hydrochloric acid and nitric acid. Determination of bulk rock composition as well as composition of the leachates was conducted with means of an ICP-MS. For the leaching experiments, the ore samples were treated following the process chart shown in Fig. 1. After crushing and milling, the material was pretreated for 24h with hydrochloric acid. After solid-liquid extraction (retrieval of pregnant solution A), the (dried) solid residue was leached in buffered siderophore solutions for 72h-120h and then again separated from the liquid phase (pregnant solution B). All leaching experiments were carried out in acid-cleaned Nalgene PE bottles on an overhead shaker set at 20 rpm at ambient temperatures. The leachates were digested with a microwave for dissolution of organics and then analyzed with ICP-MS for BMs and Pt and Pd.
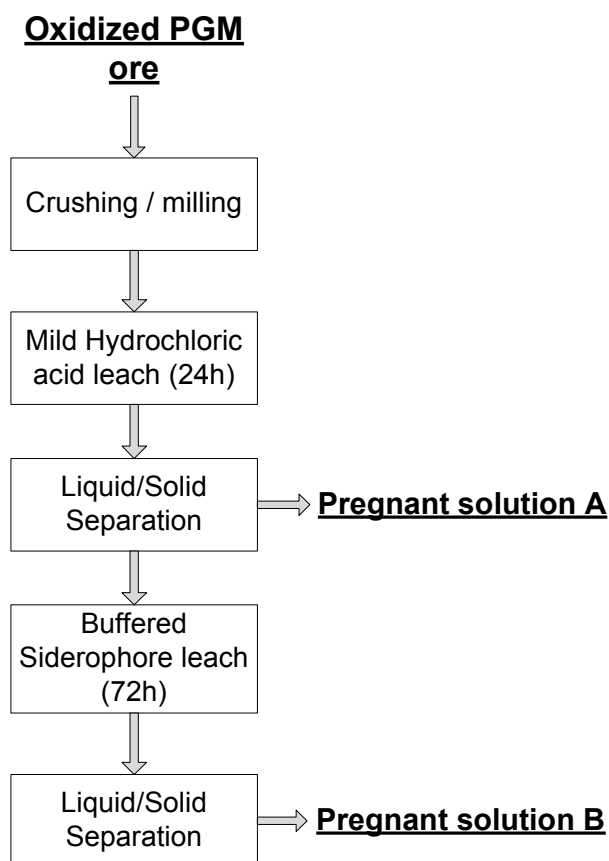


Fig. 1: Process chart of utilized multi-step approach used for siderophore leaching experiments.

## 3 Preliminary Results

Initial siderophore batch leaching experiments on untreated ('fresh') oxidised MSZ ores showed very low Pt recoveries of <<1% into solution, whereas earlier studies (Becker & Wotruba, 2008) claimed that hydrochloric acid leaching is a good approach to mobilize up to 30% of Pt contained in oxidized ores. Additionally, the relatively mild hydrochloric acid leach promotes the dissolution of e.g. FeOOH phases and mobilizes the contained Fe, which would compete with the PGE for complexation with siderophores because of their higher complex-stability constants. Hence, the removal of easy-soluble components and possibly competing cations is a prerequisite for efficient siderophore leaching. After drying of the residue and subsequent leaching with siderophores in pH buffered solutions, we were able to raise the recovery of Pt from <<1% for non-pretreated ores to about 50% for pretreated ores and even reached 78% extracted Pt from bulk rock for a sample set from the Ngezi Open Pit Mine Field in Zimbabwe as shown in Fig. 2. A pH Test (pH 7, 8 and 9) on a composite 'Pt peak' sample from Zimbabwe showed that efficiency of siderophore-promoted mobilization is strongly pH dependent, and that metal selectivity can be directed accordingly by buffering the siderophore solutions to certain pH values.

Pt and Pd mobilization are most efficient at a pH of 9, whereas at pH 7, Pt recoveries are intermediate (15-20% recovered in siderophore leaching step), but Pd extraction is suppressed (~5%).



Fig. 2: Stacked diagram showing the results of the multi-step bulk leaching process for a "Pt peak" section of a drill core from the Great Dyke, Zimbabwe.

## 4 Outlook

With the help of siderophores, we were able to successfully mobilize up to 80% of Pt and up to 30% Pd from oxidised Main Sulphide Zone material from the Great Dyke in Zimbabwe. We showed that sidero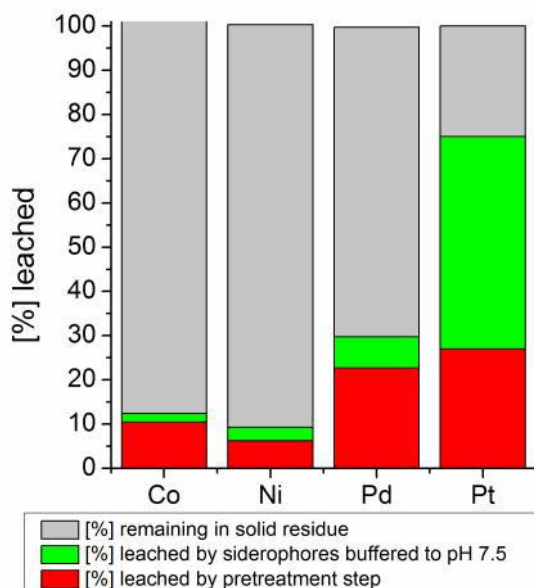phore-mediated extraction of Pt and Pd is very pH dependent and with current knowledge operates best at pH values between 8.2 and 9. Changes in the concentration of siderophores as well as modifications in the pretreatment step do not facilitate or enhance further Pt and Pd mobilization. Mineralogical selectivity of the single leaching steps, especially for the siderophore leach, definitely needs to be investigated for process optimization and enhanced recoveries.

The tested approach is promising, however, PGE recoveries are quite heterogenous from sample set to sample set and range from anywhere between 30 up to 80% Pt extracted. It is not only the polymodal mineralization that is challenging, but also the spatial heterogeneity in PGE mineralogy. Therefore, PGE-mineralogical analyses on oxidized Platreef and the UG2 chromitites of the Bushveld Complex will be done, which will then be compared with results of our established multi-step bulk leaching method to gain more information on the metal and mineral selectivities during the single leaching steps. Therefore, first results of batch leaching experiments on oxidized Platreef and UG2 will be presented.

## References

Bau M, Tepe N, Mohwinkel D (2013) Siderophore-promoted transfer of rare earth elements and iron from volcanic ash into glacial meltwater, river and ocean water. Earth Planet Sc Lett 364: 30-36.

Baysse C, Vos DD (2000) Vanadium interferes with siderophore-mediated iron uptake in Pseudomonas aeruginosa. Microbiology 146: 2425-2434.

Becker KH, Wotruba H (2008) BGR-Hochschulvergabeprojekte Projekt 04/2006: "Aufbereitung PGE-Oxiderze" - Final report.

Bellenger JP, Wichard T, Kustka aB, Kraepiel aML (2008) Uptake of molybdenum and vanadium by a nitrogen-fixing soil bacterium using siderophores. Nat Geosci 1: 243-246.

Bouby M, Billard I, MacCordick J (1998) Complexation of Th (IV) with the siderophore pyoverdine A. J Alloy Compd 273: 206-210.

Boukhalfa H, Crumbliss AL Chemical aspects of siderophore mediated iron transport. Biometals 15: 325-339.

Christenson E, Schijf J (2011) Stability of YREE complexes with the trihydroxamate siderophore desferrioxamine B at seawater ionic strength. Geochim Cosmochim Ac 75: 7047-7062.

Dahlheimer SR, Neal CR, Fein JB (2007) Potential mobilization of platinum-group elements by siderophores in surface environments. Environ Sci Technol 41: 870-875.

Desouky O, El-Mougith A, Hassanien W, Awadalla GS, Hussien SS (2011) Extraction of some strategic elements from thorium–uranium concentrate using bioproducts of Aspergillus ficuum and Pseudomonas aeruginosa. Arabian Journal of Chemistry.

Duckworth OW, Bargar JR, Sposito G (2009) Quantitative structure-activity relationships for aqueous metal-siderophore complexes. Environ Sci Technol 43: 343-349.

Hey PV (1999) The effects of weathering on the UG2 chromitite reef of the Bushveld Complex, with special reference to the platinum-group minerals. S Afr J Geol 102: 251-260.

Kraemer SM (2004) Iron oxide dissolution and solubility in the presence of siderophores. Aquat Sci Research Across Boundaries 66: 3-18.

Liermann LJ, Mathur R, Wasylenki LE, Nuester J, Anbar AD, Brantley SL (2011) Extent and isotopic composition of Fe and Mo release from two Pennsylvania shales in the presence of organic ligands and bacteria. Chem Geol 281: 167-180.

Locmelis M, Melcher F, Oberthür T (2009) Platinum-group element distribution in the oxidized Main Sulfide Zone, Great Dyke, Zimbabwe. Mineral Deposita 45: 93-109.

Oberthür T, Melcher F (2005) Chapter 5: PGE and PGM in the supergene environments: A case study of persistence and redistribution in the main sulfide zone of the Great Dyke, Zimbabwe Mineralogical Association of Canada Short Course 35. Oulu, Finland, pp 97-111.

Oberthür T, Melcher F, Buchholz P, Locmelis M (2012) The Oxidized Ores of the Main Sulphide Zone, Great Dyke, Zimbabwe: Turning Resources into Minable Reserves -

Mineralogy is the Key. The South African Institute of Mining and Metallurgy - Platinum 2012: 647-672.

Prendergast MD (1988) The geology and economic potential of the PGE-rich Main Sulfide Zone of the Great Dyke, Zimbabwe Geo-Platinum '87. Elsevier, Barking, Essex, pp 281-302.

Rule CM (1998) Hartley Platinum Mine - metallurgical processing. In: Prendergast MD (ed) International Platinum Symposium - Guidebook to Pre-Symposium Excursion to the Great Dyke of Zimbabwe.

Yoshida T, Hayashi K, Ohmoto H (2004a) Adsorption of rare earth elements by y-Al2O3 and Pseudomonas fluorescens cells in the presence of desferrioxamine B: implication of siderophores for the Ce anomaly. Chem Geol 212: 239-246.

Yoshida T, Ozaki T, Ohnuki T, Francis A (2004b) Accumulation of heavy element-siderophore complexes by bacteria. jpgu.org: 302.

# Geometallurgical characterization of ore type B2 (high silica ore) at the Kiirunavaara iron ore deposit, northern Sweden

**Kari Niiranen**
*LKAB, R&D, Mineral Processing*
*SE-981 36 Kiruna, Sweden   E-mail: kari.niiranen@lkab.com*

**Andreas Böhm**
*The Institute of Mineral Processing, University of Leoben,*
*Franz-Josef Str. 18, A-8700 Leoben, Austria   E-Mail: andreas.boehm@unileoben.ac.at*

**Abstract.** The iron ore deposit at Kiirunavaara has today a rather low content of silica *in situ*, approximately 2.3 to 3.3 % $SiO_2$. But the information from the exploration drilling and grade control drilling is showing clearly increasing $SiO_2$ grade in the crude ore with the increasing depth because of the increasing amount of the high silica ore (B2). For geometallurgical characterization of this ore type six samples were selected. The test procedure consisted of comminution, screen analysis, Davis magnetic tube tests, optical microscopy, QemScan analysis and chemical assays. The most common silicate minerals in the high silica ore are actinolite, titanite and phlogopite. Besides the mineralogy of the silicates in the crude ore and the silica grade in situ the process mineralogical parameters of the ore such as breakage characteristics, the energy consumption and the liberation of magnetite and silicates are also of great importance for the mineral processing concerning the high silica ore (B2). With these geometallurgical tests and the project 'Silica in the Mine' a lot of new information has been generated regarding the physical, chemical and mineralogical properties of the Kiirunavaara ore, especially of the high silica ore B2.

**Keywords.**
Geometallurgy, iron ore, magnetite, Kiruna, LKAB, mineral processing, magnetic separation, LIMS, Davis magnetic tube, QemScan.

## 1 Introduction

LKAB (Luossavaara-Kiirunavaara AB) is operating an underground iron ore mine, three concentration plants (KA1, KA2 and KA3) and three pelletizing plants (KK2, KK3 and KK4) in Kiruna, Northern Sweden. The methods of separation at LKAB today are low intensity magnetic separation (LIMS) and apatite flotation, where the wet LIMS is regarded as the crucial part of silica separation from the ore (Adolfsson and Fredriksson 2011). The iron ore deposit at Kiirunavaara has today a rather low content of silica in situ, approximately 2.3 to 3.3 % $SiO_2$. But the information from the exploration drilling and grade control drilling is showing clearly increasing $SiO_2$ grade in the crude ore with the increasing depth(Fig 1), especially in the southern and middle part of the orebody (so called Main ore).

The silicate mineralogy in the crude ore and the silica grade in situ have undoubtedly impact  on the silica grade in the final product, i.e. the iron ore pellets or the iron ore fines. But also the process related ore properties

such as breakage characteristics, the specific energy consumption and the liberation of magnetite and silicates seem to be essential for understanding the process at the concentration plants in Kiruna especially concerning the high silica ore (B2).
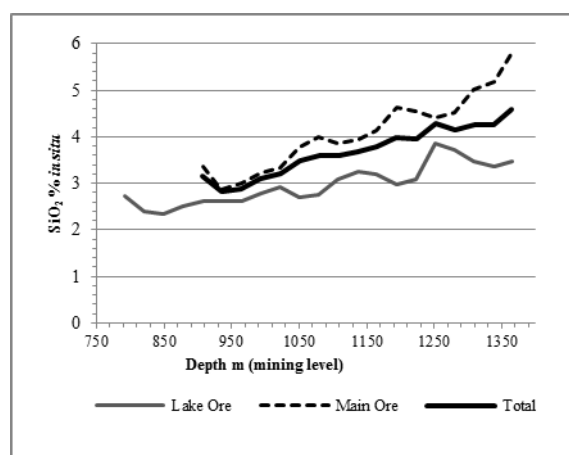


**Figure 1.** $SiO_2$ grade (from the resource block model) in the Kiirunavaara mine (LKAB).

Due to the fact that the silica level is expected to increase in the incoming material to the cobbing plant in Kiruna in the future, this is an important area of development and research at LKAB. In an ongoing R&D program at LKAB the whole chain from the mine to products is studied in several projects. The project 'Silica in the Mine' is an essential part of this program (Adolfsson 2008, Drugge 2009, Niiranen and Fredriksson 2012). This paper is focusing on the geometallurgical characterization the ore type B2 (high silica ore) as part of this project.

## 2 The Kiirunavaara Orebody

### 2.1 Geology and mineralogy

Kiruna is the type area for iron ores of so called Kiruna type (Geijer 1931) and the Kiirunavaara is the largest and the best known example of this type. This high grade magnetite deposit is a sheet like body, north to south striking, approximately 4 km to 4.5 km long and 50 to 100 m thick with the maximum thickness of over 200 m in the northern part. The ore body is well known

about down to the depth of -1365 m level below the surface, but it extends at least down to the depth of -1 800 m level below the surface in the northern part of the deposit. The orebody of Kiirunavaara was probably formed as an intrusive sill (Pehrdal 1994; Martinsson 2004) and the geochronologic data for Kiirunavaara and Luossavaara deposits indicate the emplacement at ca 1.89 Ga (Romer et al 1994).

Few previous studies were carried out to characterize the silicate mineralogy of Kiirunavaara orebody, where the most of the mineralogical investigations are focused on REE and apatite in the last few years (Martinsson et al. 2012, Pålsson and Fredriksson 2012). Recently, even the silicates have been a target of mineralogical investigations because of their importance for the mineral processing (Niiranen 2012 unpubl., Nordstrand 2013). Besides magnetite and apatite, green minerals of the amphibole group, mostly actinolite, are the most common gangue minerals found in the deposit. Hematite, carbonates, biotite / phlogopite, quartz, titanite, talc, albite and sulphide minerals (pyrite, chalcopyrite) are also present, but in lesser quantities (Geijer 1931, Niiranen 2012 unpubl., Nordstrand 2013).

## 2.2 Ore types

The iron ore deposit at Kiirunavaara is divided into two main types (low phosphorous ore and high phosphorous ore) from the practical and also from the traditional point of view (Geijer 1931). The low phosphorous ore is further divided into two subtypes: B1 ore and B2 ore and the high phosphorous ore in three subtypes: D1, D3 and D5. The following limits of the Fe grade and P grade are used for different ore types as outlined in the Table 1.

**Table 1.** Limits (Fe and P grade) for different ore types of the Kiirunavaara orebody used for exploration, the logging of drill cores and the mapping of the geology underground.

| ORE TYPE | Fe % | P % |
|---|---|---|
| **B1** (low P) | > 66 | < 0.1 |
| **B2** (low P, high $SiO_2$) | > 50 | < 0.1 |
| **D1** (high P) | > 50 | 0.1 – 0.8 |
| **D3** (high P) | > 50 | 0.8 – 2.2 |
| **D5** (high P) | > 50 | > 2.2 |

The low phosphorous ore B2 has somewhat lower Fe grade and higher $SiO_2$ grade than the ore type B1. This ore type has earlier used to be called as high alkali ore, but it is recommendable to call this type of ore as high silica ore in the future. Typical for this ore type is the presence of green minerals of actinolite, which sometimes can be quite coarse grained. Until 2009 the different ore types were mined separately, but the different ore types are now mixed together by mining because of the increasing production and only one type of crude ore is hauled. But exploration, the logging of drill cores and the mapping of the geology underground these different ore types are still used.. Until 2009 the material transported by train underground was also sampled at the waggon discharge.

# 3 Geometallurgical Characterization of the High Silica Ore (B2)

## 3.1 Sampling

The process mineralogical tests were carried out at the laboratory of the Institute of Mineral Processing at the University of Leoben, Austria and at the LKAB's metallurgical laboratory in Luleå, Sweden. The chemical assays were carried out at the LKAB's chemical laboratory in Kiruna, Sweden and chemical laboratory of Labtium Oy in Rovaniemi, Finland. The simplified scheme of the used methodology for the systematic characterization of the ore type B2 is presented in Fig 2. As feed material for the tests six samples of ore type B2 (high silica ore) were selected from drill cores originating from the middle and southern part of Kiirunavaara orebody according to the recommendation of the geologist. Essential for selection of the samples were that they were classified by the geologist as ore type B2 (high silica ore) in the drill core with green actinolite in the mineral paragenesis and the relatively high $SiO_2$ grade in the crude ore (3.43-5.98 % $SiO_2$). Also the differences in recovery on silica during the mineral processing tests at LKAB's mineral processing laboratory (communition with laboratory rod mill and ball mill and Davies magnetic tube test) were important.
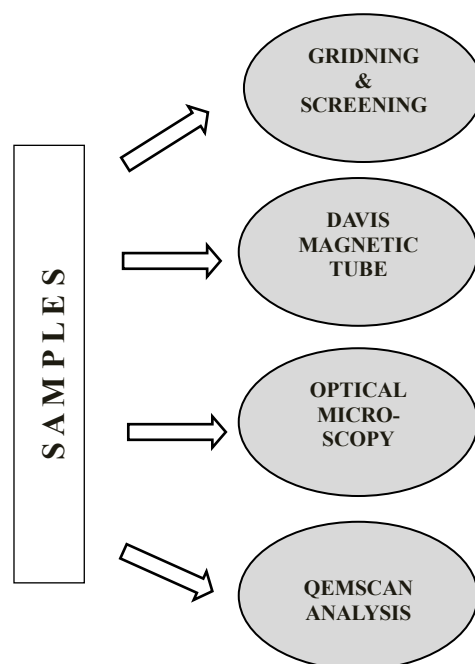


**Figure 2.** Simplified scheme of the used methods for the systematic geometallurgical characterization of the high silica ore B2.

## 3.2 Comminution and Screen Analysis

The first step after crushing down to -3 mm was an open communition circuit in the laboratory rod mill and in the laboratory ball mill. To determine the particle size distribution (screening curves, $P_{80}$ < 45 μm), every communition product was first screened mechanically on laboratory sieve shaker and after that completed

manually. The consumption of energy was calculated for the comminution in the rod mill and measured directly for the comminution in the ball mill. The chemical assays of 11 elements on comminution products were carried out by XRF (X-Ray Fluorescence) at the LKAB's chemical laboratory in Kiruna to study the grade and the content of $SiO_2$ in different particle size classes.

### 3.3 Davis Magnetic Tube Tests

Davis magnetic tube tests were focused on test the degree of liberation of magnetite and silicate minerals. Davis magnetic tube test simulates the (wet low intensity magnetic separation (WLIMS) and is regarded as a most reliable instrument widely used for estimating of amenability of iron ores and for controlling the magnetic separation (Schulz 1963). Also LKAB validates currently the process, with respect to the wet magnetic separation comparing the actual silica levels in the process with the silica levels in the Davis magnetic tube concentrate. This because Davis magnetic tube is regarded to give an optimal result that can be expected from LKAB´s low intensity wet magnetic separators (Adolfsson 2011). For the tests with Davis magnetic tube at the laboratory of the Department of Mineral Processing at the University of Leoben 12 sub-samples were selected representing the finest particle size fractions (80/63 µm, 63/40 µm and < 40 µm) after a grinding time of 35 minutes in the laboratory ball mill. After Davis magnetic tests the chemical assays were carried out on magnetics and non-magnetics by XRF for 27 elements at the laboratory of Labtium Oy in Rovaniemi, Finland. The results were evaluated with the help of so called Henry-Reinhardt charts (Heidenreich 1954, Kogelbauer, A. and Böhm, A., 2009).

### 3.4 Mineralogical Characterization

As the first step for determination and description of the petrology and the mineralogy of these selected samples the studies with an optical microscopy were carried out at LKAB's laboratory of mineral processing in Malmberget. Special interest was paid on the mineralogy of the silicates (Fig 3). The second step of the characterization of the high silica ore type (B2) was the mineralogical studies by QemScan (Quantitative Evaluation of Materials by Scanning Electron Microscope) to get information about the liberation and middlings of magnetite and silicates, quantitative mineralogy and distribution of the silicates and $SiO_2$ in the different particle size classes. For these tests the samples were selected representing the high silica ore after crushing in Malmberget (6 particle size classes) and the comminution products after grinding the ore 10 minutes in the laboratory rod mill followed by 35 minutes in the laboratory ball mill (4 particle size classes). The results of these studies are partly represented in the separate paper (Niiranen and Böhm 2012).
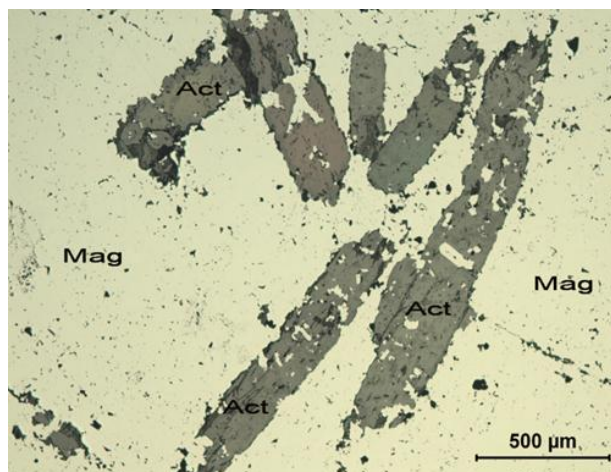


**Figure 3.** Coarse grained actinolite in the fine grained magnetite ore. Sample 6252 (Photo: Kari Niiranen).

## 4 Results and Conclusions

Due to the exploration and grade control drilling, the $SiO_2$ grade (in situ) increases with increasing depth particularly in the southernmost and the middle part of Kiirunavaara orebody. The silica matter (type, amount, liberation size) seems to differ within the three main ore types (B1, B2, D). According to the mineral processing tests with respect to the project 'Silica in the Mine' it is not possible to predict the $SiO_2$ grade in the magnetite concentrate when looking at the $SiO_2$ grade *in situ* in the crude ore. The interaction between mineralogical cause and the technical effect seems to play an important role to predict the $SiO_2$ grade in the magnetite concentrate at the concentration plants in Kiruna.

The results of screen analyses on the material after crushing are plotted as cumulative distribution curves (percentage passing) on GGS grid (Gates Gaudin Schuhmann grid, fully logarithmic) in the Fig 4. The particle size distributions of the samples 6252 and 6387 after crushing differ from the rest of the samples with respect to the overrepresentation of the finest particle size classes (< 0.1 mm).
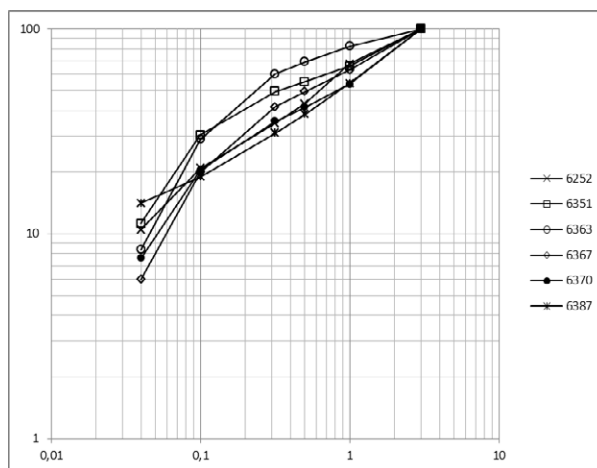


**Figure 4.** Screen curves after crushing -3 mm at the LKAB's Laboratory in Malmberget. Y axis: percentage passing, %; x-axis: Particle size, µm

This can be interpreted that in case of these two samples remarkable amount of fine particles was generated at the early stage of the comminution procedure. It can also be pointed out that the same samples (6252 and 6387) showed poor behavior of silicate minerals and thus elevated $SiO_2$ grades in the magnetic concentrate of the Davis magnetic tube tests performed in Malmberget.

The mineralogy of the silicates and especially their behaviour in the comminution circuit (crushing and grinding) followed by magnetic separation is of the importance for the geometallurgical characterization of the high silica ore B2. According to the mineralogical study the most common silicate minerals are actinolite, phlogopite and titanite. Talc, quartz and chlorite are also quite common, but they are not represented in every sample. phlogopite, actinolite and also talc are clearly enriched in the finest particle size class (< 45 µm) after comminution. Other silicate minerals show more even distribution. However the results of the Davis magnetic tube tests and the QemScan tests clearly show that the degree of liberation of magnetite and silicate minerals is high (in most cases and in most particle size classes over 95 %). In the next step it will be worth to study the behaviour of silicate minerals – especially phlogopite, actinolite and talc – in the chain of the mineral processing consisting the comminution circuit (crushing and grinding of two steps), magnetic separation (WLIMS) and reverse flotation in the concentration plant.

The importance of understanding the iron ore deposit at Kiirunavaara from both mineralogical and geochemical point of view and not least from the mineral processing point of view is increasing as the production in the mine is advancing deeper levels and demand for iron ore is increasing. With these tests and the project 'Silica in the Mine' there has a lot of new information been generated regarding the physical, chemical and mineralogical properties of the Kiirunavaara ore, especially of the high silica ore B2.

## Acknowledgements

## References

Adolfsson, G., 2008: Uppföljning av kisel Gruva – färdig produkt. LKAB Report 08-766, (Internal Report), 21 p.

Adolfsson, G. and Fredriksson A., 2011: Reduction of Silica in LKAB Pellets through Different Mineral Processing Unit Operations. Conference in Minerals Engineering, Luleå University of Technology, Preprints.

Drugge, L., 2009: Validering av metod för simulering av framtida anrikningsresultat. Internal LKAB Report 09-775, 65 pp.

Geijer, P., 1931: The iron ores of Kiruna type: geographical distribution, geological characters, and origin. Sver.Geol. Unders., Ser. C (367) 39 p.

Heidenreich, H. 1954: Die Erfolgsrechnung im Aufbereitungsbetrieb. Verlag Glückauf GmbH, Essen pp.1-37.

Kogelbauer, A and Böhm, A., 2009: Trockene Schwachfeld-Magnetscheidung im Feinkornbereich am Beispiel des Pelletierprojekts am Erzberg, BHM 154. Jahrgang, 164-170.

Martinsson, O., 2004: Geology and Metallogeny of the Northern Norrbotten Fe-Cu-Au Province. Society of Economic Geologists, Guidebook Series, Volume 33, pp. 131-148.

Martinsson, O., Öberg, E. and Fredriksson, A., 2012: Apatite for extraction – Mineralogy of apatite and REE in the Kiirunavaara Fe-deposit. Paper No. 476, International Mineral Processing Congress IMPC 2012, New Delhi India, pp. 3287-3297.

Niiranen, K. and Fredriksson, A., 2012: A Systematic Approach of Geometallurgical Mapping of the Kiirunavaara Iron Ore. Conference in Minerals Engineering, Luleå University of Technology, Preprints, pp. 81-90.

Niiranen, K. and Böhm, A., 2012: A Systematic Characterization of the Ore Body for Minerals processing at Kiirunavaara Iron Ore mine operated by LKAB in Kiruna, Northern Sweden. Paper No. 1039, International Mineral Processing Congress IMPC 2012, New Delhi India, pp.3856-3864.

Nordstrand, J. 2013. Mineral Chemistry of Gangue Mineral in Kiirunavaara Iron Ore. Master thesis, Luleå University of Tchnology, 45 p.

Perdahl, J-A., 1994: Geochemistry of Host Rocks and Ore at the Kiirunavaara Deposit, Subproject, Department of Applied Geology, Luleå University of Technology, 10 p.

Pålsson, B.I. and Fredriksson A. 2012: Benefication of REE containing Minerals. Conference in Minerals Engineering, TU Luleå, Preprints, 98-118.

Romer, R.L, Martinsson, O. and Perdahl, J-A., 1994: Geochronology of the Kiruna iron ores and hydrothermal alterations. Economic Geology Volume 89, pp 1249-1261.

Schulz, N.F., 1963: Determination of the Magnetic Separation Characteristic with the Davis magnetic Tube, The Rocky Mountain Minerals Conference - SME (Society of Mining Engineers), Preprints, 21 p.

# Combining chemical analysis (XRF) and quantitative X-ray diffraction (Rietveld) in modal analysis of iron ores for geometallurgical purposes in Northern Sweden

**Mehdi Parian & Pertti Lamberg**
*Luleå University of Technology, Division of sustainable process engineering, Luleå University of Technology, SE-971 87 Luleå, Sweden*

**Abstract.** Mineralogical information forms an essential basis in geometallurgy. Minimum information required in a mineralogical approach of a geometallurgical program is: modal mineralogy (mineral quantities) and mineral textures. Based on this information it is possible to link geological model with production model. Modal analysis is currently mostly done with Scanning Electron Microscopy (SEM) based image analysis, often called as automated mineralogy. As this method is tedious, slow, and costly, and has some limitation, an alternative technique was developed by combining quantitative X-ray diffraction (XRD) and chemical assays by X-ray fluorescence (XRF). In iron ores in Northern Sweden combined method gives a quantity of about ten minerals with adequate accuracy.

**Keywords.** Geometallurgy, modal mineralogy, X-ray fluorescence, X-ray diffraction, Rietveld

## 1 Introduction

Mineralogical information forms a vital basis for creating a geometallurgical model of an ore. Geometallurgical programs used in production management are based either on small scale metallurgical tests, also called geometallurgical tests, or quantitative mineralogy. In mineralogical approach one needs to collect quantitative mineralogical information through the whole ore body and to link geological information with processing model which needs to be based on minerals, as well. Lamberg (2011) and Lund et al (2013) simplified a geological model for two quantitative information: modal mineralogy and texture.

A state of the art technique in analysing modal composition is scanning electron microscopy (SEM) based image analysis, often called as automated mineralogy (Fandrich et al. 2006, Gottlieb et al. 2000). Other available techniques are quantitative X-ray diffraction end element to mineral conversion. Each of these methods has advantages and disadvantages (Table 1). Automated mineralogy is the most reliable one but it is time consuming and expensive. Quantitative X-ray diffraction can be very fast and inexpensive but it has problems in high detection limit and in reliability if number of phases is high. Element to mineral conversion uses chemical assays and information on chemical composition of minerals and solves mathematically the mineral grades (Whiten 2008; Lamberg et al. 1997). Therefore method is fast and inexpensive and detection limit can be as low as for chemical assays, i.e. ppm level, but method fails in

complex mineralogy. However, in geometallurgy it is often possible to simplify mineralogy for example by combining gangue silicates.

**Table 1.** Methods for determining modal composition in geological and process samples.

| Technique | Advantage | Disadvantage | Hardware / software |
|---|---|---|---|
| Automated mineralogy (1) | Reliable, works with all types of samples | Tedious, requires sizing of samples | MLA, QEMSCAN, IncaMineral |
| Quantitative X-ray diffraction (2) | Fast | High detection limit, does not work non-crystalline phases, requires expertise | PANalytical Empyrean & High Score Plus; Bruker D8 Advance & Topas |
| Element to mineral conversion (3) | Fast, inexpensive, low detection limit | In complicated mineralogy requires additional selective methods | HSC Chemistry, SimFloat, Bilco |

(1) Fandrich et al (2007); (2) Castendyk et al. (2005); Hestenes (2012); Paine (2011); (3) Whiten (2008), Lamberg et al. (1997 and 2009).

Lund et al. (2013) developed a practical way to calculate the mass proportion of nine minerals from routine XRF analysis for Malmberget iron ore in Northern Sweden and process samples. Method uses fixed mineralogy and will give wrong or biased result if samples have some unexpected minerals present like calcite, pyrite, scapolite, garnet and goethite. If semi-quantitative information on existing minerals would be available then the phase list could be selected sample by sample.

For magnetite and hematite ratio two special techniques are routinely used by LKAB: wet chemical titrimetric analysis for the divalent iron and SATMAGAN magnetic balance for magnetic material in a sample. Both methods are tedious and only used when specially needed. The purpose of this study is to find out whether the combination of XRF and XRD could routinely be applied to analyse modal composition for geometallurgical purposes in LKAB's operations.

## 2  Samples and applied methods

A total of 46 samples were selected for the study by T. Lindberg, K. Taavoniku and Didic Mehmedalija of LKAB. Samples come from two different deposits: Gruvberget and Leveäniemi.

Samples were dried, weighed and divided. One subsample was sent to chemical laboratory of LKAB for chemical assays by X-ray fluorescence and titrimetric divalent iron analysis. Another subsample was used at Luleå University of Technology. About 20 g sample was ground for X-ray diffraction analysis by a ring mill to a particle size of 50 microns. X-ray diffraction analysis was made with PANalytical Empyrean equipped with copper tube and Pixel3D detector. 8000-10 000 counts were targeted for the highest peak intensity requiring 1-2.5 hours measurement time. Following analytical conditions: step size 0.02°, the angular range 2θ=5-75° was used to obtain diffraction profiles.

## 3  Rietveld refinement

Rietveld analysis was done with PANalytical HighScore Plus software. A total of 27 different mineral phases were identified in the samples. The most common phases identified in almost all samples were magnetite, hematite, apatite, amphibole (tremolite, actinolite, hornblende), biotite and feldspar (plagioclase, K-feldspar).

The quality of the quantitative XRD analysis can be measured in a number of ways. The Rietveld refinement returns a number of parameters describing the goodness of the fit between the measured and calculated X-ray diffraction pattern, here a so called R-value is used. If R value is below 10 then the analysis is of good quality, if between 10 and 20 then it is moderate and if greater than 20 then the match is not good. In general high grade samples gave low R value. In fifteen samples of 46 (i.e 32%) the R value was below 10, in 60% it was below 15 and in 20% it was above 20. Low grade samples proved out to be the most problematic ones for the Rietveld quantification. This is due to large number of phases present and large number of phases with low crystal symmetry (triclinic).

Another way of estimating the goodness of the analysis is to compare the chemical analysis against chemical composition back calculated from the Rietveld mineralogy. The Rietveld method underestimates the iron and overestimates silica (Fig. 1). R value is low in samples with less than 45% iron and in these samples the difference between the analyzed and calculated contents is the smallest. For divalent iron content Rietveld gives a good estimate if the R value is below 10.

A conclusion from the Rietveld refinement is at as such the quality of the phase quantification is not reliable enough and therefore cannot be used as modal analysis method in iron ore samples. However, for samples with high iron grade (Fe>45%) Rietveld can be used for modal analysis.
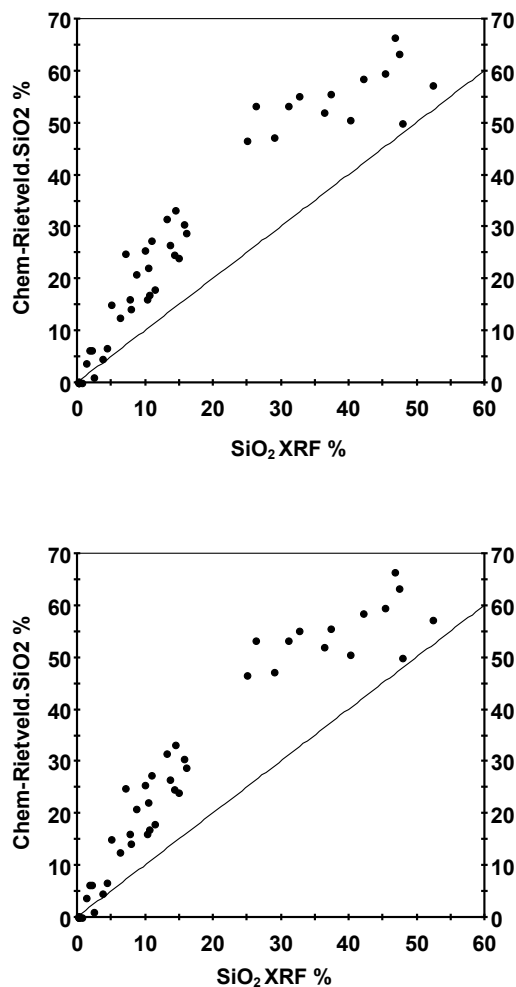




**Figure 1.** Chemical composition of the samples by XRF analysis (x-axis) and back calculated from quantitative XRD by Rietveld (y-axis). R value describes the quality of the Rietveld analysis (see text).

## 4  Modal analysis by combining XRD and XRF

To improve the modal analysis a combined method was developed. It uses both XRD Rietveld and chemical assays by XRF. Three different calculation rules were defined based on mineralogy. The chemical composition of the minerals was taken from Malmberget (Lund et al. 2013).

The calculation rules for Gruvberget, Leveäniemi high grade samples and Leveäniemi low grade samples are given in Tables 2, 3 and 4 respectively. Compared to simple element to mineral conversion or Rietveld analysis alone the combined method uses more information and therefore the result is expected to be better. In calculating the modal composition a weighed non-negative least squares method of HSC Geo was used. It was found that if the calculation is divided into three rounds, as shown in Tables, the residual is minimalized. In weighting the XRF assays were regarded more reliable than Rietveld. Therefore the calculation residue for XRF assays is very low, less than 0.1%.

Divalent iron was not included in the calculation and therefore it can be used to validate the result. Figure 2 shows the divalent iron (Fe II) by wet chemical method against the back calculated one from the developed combined technique. In 95% of the cases the difference is not significant. About half of the minerals in each sample set contain iron and iron assay is used only in the last round. This means that all errors tend to accumulate in that. Therefore having a good match for the divalent iron means that the estimation for mineral quantities is good not only for magnetite and hematite but also for other minerals.

**Table 2.** Element to mineral conversion method developed for the Leveäniemi high grade samples using both X-ray fluorescence and quantitative X-ray diffraction analysis. In finding the solution weighed non-negative least squares technique was used in the HSC Chemistry software.

| Round | Minerals | Elements | Weighing, RSD% |
|---|---|---|---|
| 1 | Albite Apatite | Na XRF | 1 |
| | | P XRF | 1 |
| | | Ap XRD | 10 |
| 2 | Tremolite Biotite Diopside Quartz | Tr XRD | 10 |
| | | Bt XRD | 10 |
| | | Di XRD | 10 |
| | | Qtz XRD | 10 |
| | | Mg XRF | 1 |
| | | K XRF | 1 |
| | | Ca XRF | 1 |
| | | Al XRF | 1 |
| | | Si XRF | 1 |
| 3 | Hematite Magnetite | Fe XRF | 1 |
| | | Mgt XRD | 10 |
| | | Hem XRD | 10 |

**Table 3.** Element to mineral conversion method developed for the Gruvberget data set using both X-ray fluorescence and quantitative X-ray diffraction analysis. In finding the solution weighed non-negative least squares technique was used in the HSC Chemistry software.

| Round | Minerals | Elements | Weighing, RSD% |
|---|---|---|---|
| 1 | Apatite | P XRF | 1 |
| | | Ap XRD | 10 |
| 2 | Garnet Calcite Diopside Quartz | Gar XRD | 10 |
| | | Cal XRD | 10 |
| | | Di XRD | 5 |
| | | Qtz XRD | 10 |
| | | Mg XRF | 1 |
| | | K XRF | 1 |
| | | Ca XRF | 1 |
| | | Al XRF | 1 |
| | | Si XRF | 1 |
| 3 | Hematite Magnetite | Fe XRF | 1 |
| | | Mgt XRD | 10 |
| | | Hem XRD | 10 |

**Table 4.** Element to mineral conversion method developed for the Leveäniemi low grade samples using both X-ray

fluorescence and quantitative X-ray diffraction analysis. In finding the solution weighed non-negative least squares technique was used in the HSC Chemistry software.

| Round | Minerals | Elements | Weighing, RSD% |
|---|---|---|---|
| 1 | Albite Apatite | Na XRF | 1 |
| | | P XRF | 1 |
| | | Ab XRD | 10 |
| | | Ap XRD | 10 |
| 2 | Biotite Orthoclase Tremolite Calcite Diopside Quartz Scapolite | Bt XRD | 10 |
| | | Or XRD | 10 |
| | | Tre XRD | 10 |
| | | Cal XRD | 10 |
| | | Di XRD | 10 |
| | | Qtz XRD | 10 |
| | | Scp XRD | 10 |
| | | Mg XRF | 1 |
| | | K XRF | 1 |
| | | Ca XRF | 1 |
| | | Al XRF | 1 |
| | | Si XRF | 1 |
| 3 | Hematite Magnetite | Fe XRF | 1 |
| | | Mgt XRD | 50 |
| | | Hem XRD | 10 |
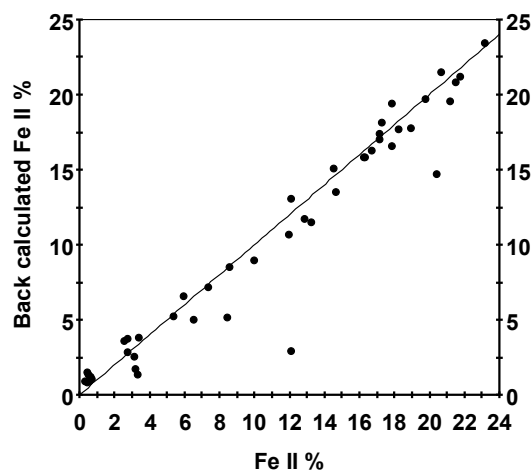


**Figure 2.** Back calculated divalent iron from the combined method plotted against analysed $Fe^{2+}$ by wet chemical method.

## 5 Conclusions

The study shows that quantitative X-ray diffraction with Rietveld method does not give reliable enough the modal mineralogy in LKAB's iron ore samples. However, reliable result can be achieved if both XRD and XRF analysis is used and modal mineralogy is solved with non-negative weighed least squares method using HSC Chemistry. Combined method enables the estimation of modal mineralogy in complex ore deposits where the pure Rietveld or element to mineral conversion would fail.

Method cannot be applied blindly. In each ore deposit one needs enough mineralogical information including

chemical composition of the phases. For geometallurgical purposes in high grade ores the technique is reliable enough and has a potential for routine method and automation.

## Acknowledgements

## References

Castendyk, D.N., Mauk, J.L., & Webster, J.G. 2005. A mineral quantification method for wall rocks at open pit mines, and application to the Martha Au–Ag mine, Waihi, New Zealand. Applied Geochemistry 20 (2005) 135–156.

Fandrich, R., Gu, Y., Burrows, D. and Moeller, K., 2007, Modern SEM-based mineral liberation analysis: International Journal of Mineral Processing, v. 84, p. 310-320.

Gottlieb, P, Wilkie, G., Sutherland, D., Ho-Tun, E., Suthers, S., Perera, K., Jenkins, B., Spencer, S., Butcher, A., and Rayner, R., 2000, Using Quantitative Electron Microscopy for Process Mineralogy Applications, JOM, v. 52, p. 24-25.

Hestnes, K.H. and Sørensen, B.E., 2012, Evaluation of quantitative X-ray diffraction for possible use in the quality control of granitic pegmatite in mineral production: Minerals Engineering, v. 39, p. 239-247.

Lamberg, P. and Tommiska, J., 2009, HSC Chemistry® 7.0 User's Guide. Mass Balancing and Data Reconciliation: http://www.outotec.com/39476.epibrw, Outotec, 1-50 p.

Lamberg, P., 2011, Particles – the bridge between geology and metallurgy: Conference in mineral engineering, Luleå, Sweden, 8-9 February, Proceedings, p. 1-16.

Lamberg, P., Hautala, P., Sotka, S. and Saavalainen, S., 1997, Mineralogical balances by dissolution methodology: Short Course on 'Crystal Growth in Earth Sciences', S. Mamede de Infesta, Portugal, September 8-10, Proceedings, p. 1-29.

Lund, C., Lamberg, P. and Lindberg, T., 2013. Practical way to quantify minerals from chemical assays at Malmberget iron ore operations – an important tool for the geometallurgical program. Minerals Engineering (submitted).

Paine, M., König, U. and Staples, E., 2011, Application of rapid X-ray diffraction (XRD) and cluster analysis to grade control of iron ores: Proceedings, 10th International Congress for Applied Mineralogy (ICAM), Trondheim, Norway, 1-5 August, Proceedings, p. 495-501.

Whiten, B., 2008, Calculation of mineral composition from chemical assays: Mineral Processing and extractive metallurgy review, v. 29, p. 83-97.

# New polymetallic mineral associations in Triassic strata of the Kraków-Silesia Monocline

**Jadwiga Pieczonka**
*AGH-University of Science and Technology, Kraków, Poland, jpieczon@geolog.geol.agh.edu.pl*

**Adam Piestrzynski**
*AGH-University of Science and Technology, Kraków, Poland, piestrz@geol.agh.edu.pl*

**Abstract.** Two new associations of ore minerals have been found in the Lower and Middle Triassic rocks. The first is composed of bornite, chalcopyrite, chalcocite, tetrahedrite, covellite and thiosulphates, which was discovered in the vicinity of the village of Woźniki in the NW part of the Upper Silesian district. The second is represented by Ni-Zn-Pb-Fe thiosulphates found within the typical MVT mineral succession in the Boleslaw Mine.

**Keywords. Thiosulphates, MVT deposits, Poland**

## 1 Introduction

The geology of the Krakow-Silesian Monocline is well known because of numbers of publications e.g. Gruszczyk (1956), Bukowy (1964), Smolarska (1968), Ekiert (1971), Górecka (1993) and several hundred years of mining activity. The stratigraphy was described by Siedlecki (1952), Senkowiczowa and Szyperko-Śliwczyńska (1961), Śliwiński (1961) and Wyczółkowski (1978).

Ore mineralization described in this paper was found in the Middle and Lower Triassic rocks in the vicinity of Woźniki village and at the Boleslaw Mine. These new mineral associations were recognized at the same stratigraphic position as in other parts of the Upper Silesian district (Harańczyk 1962; Ziętek-Kruszewska 1978; Sass-Gustkiewicz (1997) Kozłowski & Górecka (1993), Kucha & Viaene (1993) .

## 2 Methods

Samples for mineralogical studies were collected from the cores of the following drill holes: KW-3, KW-7, KW-9, KW-16, KM-78, KM-81 and LW-9 (Woźniki area). The cores provide data to describe the geology and stratigraphy of the area. Special attention was paid to 20 samples from the Lower Bunter. Microprobe analyses were carried out at the Institute of Non-ferrous Metals in Gliwice using a JEOL Superprobe 753 and at AGH-UST in Kraków using an ARL SEMQ instrument, applying the following conditions, spectral lines and standards: voltage 20 kV; probe current 120 mA; sample current 9 nA; counting time 20 s; SK⇨ and FeK⇨ (FeS$_2$), CuK⇨ (100%), PbM⇨ (PbS), ZnK⇨ (100%), AsL⇨ (100%), SbL⇨ (100%), AgL⇨ (100%). Detection limits were S ↑ 0.05%, Fe ↑ 0.02%, Cu ↑ 0.02%, Pb ↑ 0.05%, Zn ↑ 0.02%, As ↑ 0.02%, Sb ↑ 0.02% and Ag ↑ 0.02%. Analyses of thiosulphates were carried out using an EDS system combined with the electron scanning microscope FEI Quanta-200 FEG (20 kV acceleration voltage) at the Department of Mineralogy, Petrography and Geochemistry in the Faculty of Geology, Geophysics and Environmental Protection (AGH-UST). The stalactites were collected in Bolesław Mine, 6 km North from Olkusz city. Micro chemical analyses were carried out at AGH-UST, FGG&EP laboratories. A basic sample containing typical stalactite is presented on Fig. 2.

## 3 Mineral associations

### 3.1 Woźniki area

Woźniki area is located NW from still operating Zn-Pb mines in the Krakow-Silesian Monocline. In this area a new mineral association composed of chalcopyrite, bornite, tetrahedrite, chalcocite and covellite, accompanied by the typical MVT assemblage and barite and young dolomite was recognized (Pieczonka 2010). The copper sulphides association in this deposits is unusual. The tetrahedrites from this area are characterized with low Cu-contents and significant values of Zn ranging from 7.15 up to 9.08 wt% and As (5.82-13.78 wt%). WDS composition of analysed bornites showed small admixtures of silver (Pieczonka 2010), that are typical in copper deposit in the Fore-Sudetic Monocline (Piestrzynski 2007). Also some sphalerite grains show anomalous Cu content up to 7.34 wt% (Pieczonka 2010). In the studied area a botryoidal grains of Fe sulfides are very common (drill hole KM-78). These minerals were formed at the major ore emplacement stage and reveal a variable concentration of oxygen (3.59-16.26 wt%), iron (37.13-44.20 wt%), sulphur (36.89-51.99 wt%) and Cu (0.87-1.43 wt%), Zn (0,23-0,.65 wt%), Ni (0.00- 3.23 wt%) and As (0.00-2.67 wt%) (Pieczonka 2010). The grains are characterized by the botroidal textures and are composed of fibrous, recrystallized Fe sulphides, thiosulphates and sulphates (Fig. 2). The chemical formula of these compounds corresponds to $(Fe_{0.9191-1.2759}Cu_{0.0057-0.0328}Zn_{0.0056-0.0129}Ni_{0.0050-0.0255})(S_{2.0000}As_{0.0134-0.0579})O_{0.2768-1.6819}$ (Pieczonka 2010).

The reflectivity of these minerals depends on the sulphur valences e.g. presence of sulphates is well visible in the ore microscope light, because of their low reflectivity (Kucha & Viane 1993). Compare also Fig. 1 where the grains with low reflectivity are mixtures of marcasite, pyrite and thiosulphates. The presence of these mineral phases confirms that the Palaeozoic strata can be a metal

source (Górecka 1972; Kozłowski & Górecka 1993) and that these phases can also be precursors for a low temperature mineral associations in this type of deposits.
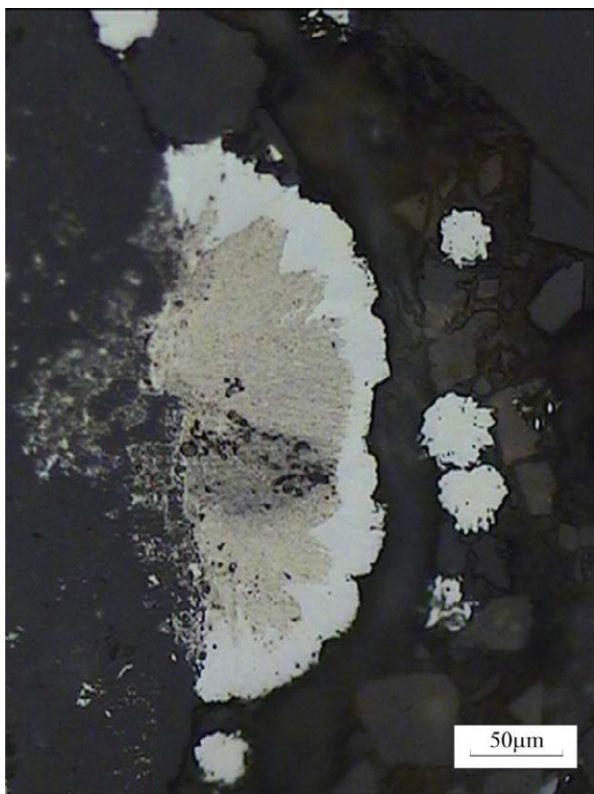


**Figure 1.** A typical replacement textures of marcasite (white) and thiosulphate (cream), dark gray is Fe sulphate. Drill hole KM-78, reflected light.
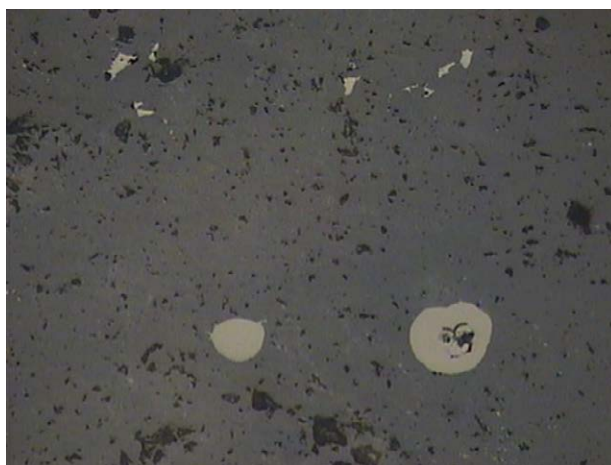
### 3.2 Bolesław Mine

New type of ore minerals containing Ni-bearing oxy-sulphides were detected in the archive samples. Samples were collected in the nest "Joanna" located in the Roetian strata. In this nest collapse breccias type of ore were extracted. This is a rich type of the ore composed of sphalerite, galena and Fe-sulphides (marcasite + pyrite) and minor oxy-sulphides and oxides. In crushed stalactites composed of pyrite and marcasite, and minor sphalerite and galena, inclusions of the new mineral phases have been found in the ZnS matrix (Fig. 2). These inclusions, which are partly replaced by massive sphalerite (see the upper part of Fig.2), were recognized in the reflected light, therefore are characterized with high reflectivity by comparison with the surrounding massive sphalerite (Fig. 2). In general, optical properties of the discussed mineral phases are similar to those described by Kucha & Viaene (1993). Only the zones that did not recrystallise fully show spherulitic anisotropy and relics of thiosulpates (Fig. 3, spot no 3/2 in Table 1). The outer parts are usually isotropic. The major elements of these newly discovered minerals are as follows: S, Fe, Pb and in some points also zinc. Therefore, the mineral phases contain elevated amounts of oxygen, nickel, cadmium and arsenic (Tab. 1). Low content of oxygen present in a majority of the measured points suggests a deep recrystallization of Fe-Zn-Pb-Ni precursors which were only identified as relics in the

micro concretions (Fig. 3, 4).



**Figure 2.** Cross section through the sulphide stalactite from Bolesław Mine with well visible internal channels in fibrous sphalerite and galena. The outer part is composed of banded pyrite and marcasite.



**Figure 3.** Botroidal Fe-Zn-Pb-Ni-oxy-sulfides in sphalerite matrix. Reflected light, sample 3, Boleslaw Mine
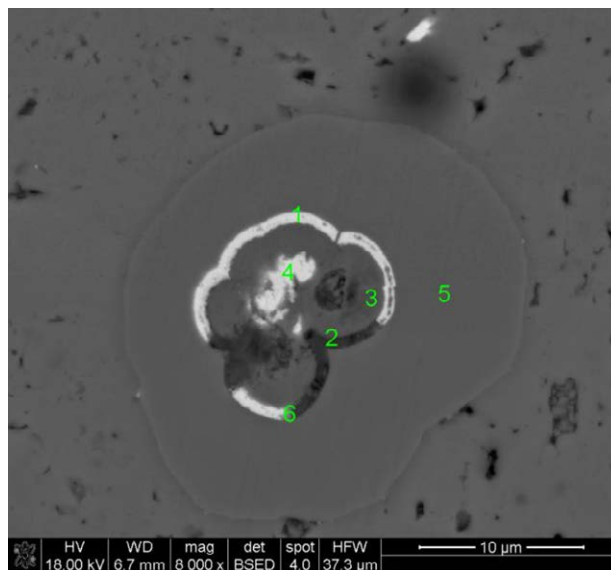


**Figure 4.** BSE image of Fe-Zn-Pb-Ni-oxy-sulphides in sphalerite matrix; 1, 2, 3, 4, 5 positions of micro chemical analyses, sample 3.

In the central part of the micro-concretion (Fig. 4) there are clearly seen dark grey areas characteristic for

compounds with mixed and intermediate sulfur valences (Kucha & Viaene 1993). EDS analyses show a variable chemical composition of all analyzed compounds. More resistant for oxidation is the outer part. It confirms direction of recrystallization, that usually run from outside part of the botroidal structure. Some small in size oxy-sulphide relics (black dots), are also clearly seen in the white-pale ring in central part of micro concretion (Fig. 3). Very interesting in these samples are high concentrations of Ni ranging from 0. 0.77 up to 5.46 wt.% (Tab. 1-2). Such a great concentration of Ni in Zn-Pb ores in the MVT-type deposit is reported for the first time. Some micro concretions show chemical composition close to the pyrite (see Tab. 2), however the As contents are anomalous high e.g. in comparison to data presented in publication by Kucha & Viaene (1993). Concentration of Ni have already been noted in pyrites from Polish MVT deposits (Kucha & Viaene 1993). The presence of Mn, Ca and Sr (Tab. 1) suggests also that ore bearing solutions were aggressive in reactions with host rocks.

**Table 1.** EDS composition of Fe-Zn-Pb-Ni oxy-sulphides from Zn-Pb ores (in wt.%), sample 3

|  | O Kα | S Kα | Fe Kα | Co Kα | Ni Kα | Zn Kα | As Kα | Cd Kα | Pb Mα |
|---|---|---|---|---|---|---|---|---|---|
| 3/1 | 0.87 | 24.45 | 5.30 | 0.53 | 1.04 | 3.69 | 3.30 | 1.11 | 58.0 |
| 3/2 | 29.74 | 19.55 | 19.03 | 0.58 | 1.02 | 22.04 | 0.95 | 0.30 | 4.56 |
| 3/3 | 1.19 | 21.65 | 3.40 | 0.66 | 0.77 | 3.63 | 1.76 | 1.21 | 64.66 |
| 3/4 | 2.01 | 35.37 | 23.08 | 1.17 | 4.43 | 2.69 | 0.31 | 0.40 | 29.86 |
| 3/5 | 2.70 | 29.70 | 14.89 | 0.72 | 2.44 | 3.26 | n.d. | 0.77 | 43.89 |
| 4/1 | 2.77 | 38.09 | 25.25 | 1.14 | 3.77 | 3.64 | 0.49 | 0.68 | 23.03 |

3/2 + Mn= 0.87%, Ca= 1.02%, Sr= 0.32%; 3/4+ Mn= 0.48%, Sr= 0.20%; 3/5 + Mn= 0.52%, Sr= 1.10%; 4/1 + Mn= 0.55%, Sr= 0.60; n.d- not detected

**Table 2.** EDS composition of Fe-Zn-Pb-Ni oxy-sulphides from Zn-Pb ores (in wt.%), sample 1

|  | O Kα | S Kα | Fe Kα | Co Kα | Ni Kα | Zn Kα | As Kα |
|---|---|---|---|---|---|---|---|
| 409A/1/1 | n.d. | 51.14 | 33.40 | 0.80 | 4.20 | 2.00 | 8.46 |
| 409A/1/2 | n.d. | 49.82 | 32.30 | 1.08 | 5.41 | 2.11 | 9.72 |
| 409A/1/3 | n.d. | 49.87 | 31.35 | 1.40 | 5.46 | 3.29 | 8.62 |
| 409A/1/4 | n.d. | 50.83 | 33.80 | 1.25 | 3.40 | 3.29 | 7.43 |
| 409A/1/5 | 3.50 | 47.68 | 31.48 | 1.29 | 5.21 | 2.85 | 7.99 |

n.d.- not detected, Pb sought but not detected

## 4  Discussion

All discussed mineral phases are located in the fibrous type of sphalerite. This type of sphalerite is a major mineral not only in stalactites  but also in typical banded zincblende (botroidal variety of sphalerite). Fibrous sphalerite can be easy recognized under crossed nicols of ore microscope. It is characterized by presence of fibers oriented perpendicularly to botroidal bands with different colour of internal reflection and different chemical composition. It may be concluded, that the presence of fibrous sphalerite and galena (Fig. 4) suggests that these compounds with anomalous chemical composition including a mixed sulphur valences (Kucha & Viaene 1993) were primary minerals to fibrous variety of sphalerite, galena and mielnikovite pyrite. All these

minerals are major mineral phases in this type of deposits. In  addition, fibrous sphalerite is characterized by high porosity clearly visible on a polished surface (Fig. 2-4). A fibrous character reveal also edges of massive galena (Fig. 5).
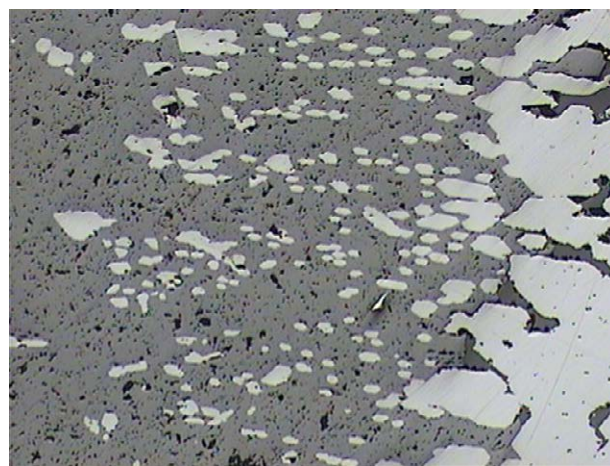


**Figure 5.** Fibrous sphalerite with a skeletal galena. Reflected light, sample 3/1, Boleslaw Mine

It may also be concluded, that the concretions presented in the micro photographs are characterized by concentric micro-bands. They were micro channels distributing the metal bearing solutions responsible for precipitation of the ores. Fibrous sphalerite is a recrystallized phase after the mixed valences and chemically variable compounds. All the mineral phases in the studied stalactites are pseudomorph after unstable compounds like oxy-sulphides. All these compounds are unstable and in supergene conditions are quickly converted to sulphates. Non-stoichiometric composition of studied mineral compounds confirms also such a process of recrystallization.

## Acknowledgements

## References
Bukowy, S. (1964) A new opinions on a geology of the NE border on GZW. Biuletyn Instytutu Geologicznego, 184, pp. 5-20 (in Polish).

Ekiert, F. (1971) Geological structure subpermian basement NE borderland of the Upper Silesian Coal Basin.  Prace Instytutu Geologicznego, 66, pp. 5-77.

Górecka, E. (1993) Geological setting of the Silesian-Cracow Zn-Pb deposits. Kwartalnik Geologiczny, 37, pp. 127-145.

Gruszczyk, H. (1956) Development and genesis of Upper Silesian lead-zinc deposits. Geol. Inst. Pol. Biull, 90, pp. 186.

Harańczyk, C. (1962)  Mineralogy of the ore minerals in the Silesia-Cracow zinc and lead deposits. Prace Geologiczne Komisji Nauk Geologicznych PAN Oddz. w Krakowie, 8, pp. 98 (in Polish).

Kozłowski, A., Górecka, E. (1993) Sphalerite origin in the Olkusz mining  district:  fluid  inclusion  model.  Kwartalnik Geologiczny, 37/2, pp. 291-305.

Kucha, H., Viaene, W. (1993) Compounds with mixed and intermediate sulfur valences as precursors of banded sulfides in carbonate-hosted Zn-Pb deposits in Belgium and Poland. Mineralium Deposita, 28/1, pp. 13-21.

Pieczonka J., (2011) Polymetallic mineralization in Triassic strata

of the NW part of the Krakow-Częstochowa Monocline. Mineralogia 41/1-2: 35-53.

Sass-Gustkiewicz, M. (1996) Internal sediments as a key to understanding the hydrothermal karst origin of the Upper Silesian Zn-Pb ore deposits. In D.F. Sangster (Ed.) Carbonate-Hosted Lead-Zinc Deposits, *SEG Special Publication, 4*, pp. 171-181.

Senkowiczowa, H., Szyperko-Śliwczyńska, A. (1961) Lithology and stratigraphy. In: geological Atlas of Poland, PIG, (pp. 8).

Śliwiński, S. (1961) Olkusz bads. Rudy i Metale Nieżelazne *, 12*, pp. 526-529 (in Polish).

Smolarska, I. (1968) Geological characteristic of Zn-Pb deposits in Trzebiona Mine. Prace Geologiczne Komisji Nauk Geologicznych PAN O. Kraków, 47 pp. 60 (in Polish).

Wyczółkowski, J. (1978) The Lower and Middle Triassic sediments. In J. Pawłowska (Ed.), Prospecting for Zinc and Lead ores in the Silesia-Krakow area. Prace Państwowego Instytutu Geologicznego, 83, pp. 79-104 (in Polish).

# Trace element distribution in sulphides of the epithermal Co-O mine, Mindanao, Philippines

**Iris Sonntag**
*CSIRO Australian Resources Research Centre, 26 Dick Perry Avenue, Kensington WA 6151, Australia*

**Steffen Hagemann**
*Centre for Exploration Targeting, University of Western Australia, M006, 35 Stirling Hwy, Crawley WA 6009, Australia*

**Leonid Danyushevsky**
*CODES, ARC Centre of Excellence in Ore Deposits, University of Tasmania, PB 79, Hobart TAS 7001, Australia*

**Abstract.** The intermediate sulphidation state epithermal Co-O mine in Mindanao comprises several stages of Au-formation related to a complex sulphide paragenesis. In order to confirm and understand these stages in more detail pyrite, chalcopyrite and sphalerite were analysed for their trace element composition using LA-ICP-MS. Gold-rich sulphides are related to stage 2 quartz-carbonate veins, whereas lower grade veins are related to stage 1 and 3 quartz veins or stage 4 calcite veins. Gold is likely related to micro-inclusions within sulphides. Pyrites are partly located in the wallrock, commonly associated with Fe-oxides, and tend to have higher Ni-Co contents, with low Ag-Au values when compared to pyrites from veins. No correlation between Au and As contents is observed in pyrites. Chalcopyrite displays generally low trace element abundance. Sphalerite displays different element trends (e.g., Cu, Sn, In, Te, As and partly Cd) in stage 3 quartz veins when compared to stage 2 quartz-carbonate veins. Preliminary results highlight the complexity of trace element distribution in sulphides and confirm different vein stages related to hydrothermal fluids enriched in different elements linked to various sulphides.

**Keywords trace elements, sulphides, laser ablation ICP-MS, Mindanao, epithermal**

## 1 Introduction

Studies of the distribution of trace elements within sulphides associated with epithermal Au-Ag deposits are rare, even though they may provide insights into important details of ore-forming processes. They assist in determining potential multiple stages of Au-formation or Au-precipitation and provide insights into linked trace element trends for these processes. Pyrite, for example, is often observed across different alteration zones and its composition could be used as a vector to the ore. Furthermore sulphide trace element composition may help to understand the physio-chemical conditions of sulphide precipitation and can be linked to geometallurgy, which can be used to aid the recovery processes.

Laser ablation inductively coupled plasma mass spectrometry (LA-ICP-MS) enables to determine trace element concentrations in various sulphides. In combination with ore petrology and paragenetic studies, this data can be used to unravel the relationships of element distribution and ore forming processes. For this study pyrite, chalcopyrite and sphalerite, related to four defined Au-mineralization stages, from the Co-O mine in southern Mindanao (Phillippines), were analysed for Mn, Fe, Co, Ni, Cu, Zn, As, Se, Mo, Ag, Cd, In, Sn, Sb, Te, W, Au, Tl, Pb, and Bi.

## 2 Geological Setting, Hydrothermal Alteration and Sulphide Paragenesis

Mindanao is located on the south end of the Philippines. The intermediate sulphidation state epithermal Co-O mine is situated in an Oligocene to Miocene magmatic arc segment of Eastern Mindanao (Sonntag et al., 2011)

Gold-bearing quartz-carbonate veins at the Co-O mine are orientated in three different directions (Kolb and Hagemann, 2009). Based on hyperspectral and XRD analyses (Sonntag et al., 2012) the proximal alteration halo, related to Au-mineralization, is defined by illite and quartz, whereas the distal alteration halo displays higher amounts of chlorite with lower amounts of illite and quartz when compared to the proximal zone. Carbonate alteration is dominant in the proximal zone and nearly absent in the distal zone.

Based on vein-type, textures, cross-cutting relationships and paragenesis, four stages are defined (Table 1, based on previous Kolb and Hagemann 2009, Sonntag et al. 2012 and new observations related to this study). Stage 1 veins consist mainly of quartz with minor carbonate, comprising pyrite, locally chalcopyrite and can contain Au. This stage is re-worked in stage 2, and is therefore mainly observed as brecciated fragments with collo-, crusti-form and bladed textures. Gold is mainly observed in stage 2 quartz-carbonate veins with fine brecciated, mosaic and jigsaw textures. The gold in stage 2 veins is 'free' or in textural equilibrium with chalcopyrite, sphalerite, pyrite and locally silver sulphides and galena (Table 1). Stage 2 veins are subdivided into stage 2a and 2b based on texture and the occurrence of sphalerite and chalcopyrite. Stage 3 quartz veins cross-cut the main gold-bearing stage 2 veins, commonly display comb textures with high amounts of sphalerite and galena, locally pyrite and Au. Stage 4 veins are the latest vein stage, consisting mainly of calcite and show banded textures and combs. These veins are frequently associated with barite and contain high amounts of pyrite, which is located along bands, in comb structures, or locally forming small veins within the calcite. This

| stage | vein-type | vein textures | sulphides, gold |
|---|---|---|---|
| 1 | quartz-chalcedony, minor carbonate | colloform, crustiform, quartz after bladed calcite | Py ± Ccp, Au |
| 2 a | quartz-carbonate | brecciated, mosaic to jigsaw | Sp-Py-Au ± Ccp, Gn, Ag$_2$S |
| 2 b | quartz-carbonate | brecciated, mosaic to jigsaw | Ccp-Py-Au ± Sp, Gn, Ag$_2$S |
| 3 | quartz | fine, comb | Sp-Gn-Py-Au |
| 4 | calcite, minor quartz, locally barite | banded, comb | Py, (±Au?) |

**Table 1.** Sulphide paragenesis related to vein stages, vein-type and vein textures modifieded and refined after Kolb and Hagemann (2009) and Sonntag et al. (2012) pyrite (Py), chalcopyrite (Ccp), galena (Gn), sphalerite (Sp), silver sulphide (Ag$_2$S)

stage carries minor Au.

Pyrite is present throughout all vein stages as one of the main sulphides, it is spatially widespread from the proximal into the transition zone of the distal alteration zone. It is also present in the wallrock associated with Fe-rich oxides. Chalcopyrite, sphalerite and galena are only present in the proximal alteration halo, mainly within stage 2 quartz-calcite veins. Chalcopyrite can be observed in stage 1 veins and is rarely located in the wallrock next to stage 2 veins, but much more uncommon when compared to pyrite. Sphalerite appears also as large crystals within comb textures of stage 3 quartz veins, but is absent in the wallrock. Silver sulphides are only observed in high grade ore samples of stage 2 veins together with Au. Galena is related to stages 2 and 3 veins, but dominates in stage 3 veins, also forming larger crystals within quartz combs.

## 3 Vein and Sulphide Textures

Sulphides and Au-mineralization are mainly hosted in quartz-carbonate veins of stage 2 and partly in clear to grey quartz veins of stage 3. Frequently clusters of sulphides are observed within stage 2 veins forming black 'bands' or 'patches'. Stage 2 quartz-carbonate veins, hosting the main Au-mineralization, display two types of textures: a) clear to milky massive quartz with fine carbonate flakes, or b) alternating carbonate-quartz veins.

Gold observed in stage 2a is commonly in textural equilibrium with pyrite, sphalerite and minor galena, silver sulphide and chalcopyrite. Stage 2b displays 'free' gold or gold in textural equilibrium with pyrite, chalcopyrite, galena, minor sphalerite and silver sulphide (Table 1). Commonly chalcopyrite and sphalerite 'substitute' for each other with one of the two sulphides being more abundant. Sphalerite is more prominent in more quartz-rich stage 2a veins, whereas chalcopyrite dominates over sphalerite in carbonate-quartz alternating stage 2b veins.

Based on textural relationships pyrites are subdivided into: type 1 coarse-grained, mostly inclusion-free, and type 2, rare crumbly-poikilitic with zones of dissolution. Both pyrite types are observed in most samples and there appears to be no correlation between their distribution and location in the alteration zones or vein types.

## 4 Sulphide Chemistry

The trace element composition of pyrite, chalcopyrite, and sphalerite was analysed with LA-ICP-MS at CODES, University of Tasmania, using the standard STDGL2b2. For detailed information concerning the method see Danyushevsky et al. (2011).

Elevated Au/Ag-contents in all sulphides are related to relatively sharp positive anomalies of recorded time-resolved element intensities during individual ablation, therefore, likely related to Au micro-inclusions rather than Au in the crystal lattice. For simplification of this summary the Au or Ag contents will be referred to pyrite, chalcopyrite and sphalerite.

Pyrite displays different Ni, Co, Ag and Au trends related to pyrite type, vein type and alteration zone. Types 1 and 2 pyrites in the wallrocks next to stage 2 veins display trends to higher Co-Ni compositions and lower Au-Ag values (Figure 1). Type 1 pyrite tends to show more Ag-rich contents related to higher Au values (Figure 1b). Type 2 pyrites display a trend to lower Ag contents when compared to type 1 pyrites with similar Au contents. In both pyrite types Au values are not correlated to As. One sample of type 1 pyrites, located within the cleavage plains of a stage 4 calcite vein, displays high As contents together with lower Ag and Te concentrations when compared to all other samples (Figure 1b). Carbonate-rich vein samples from stage 2b contain generally higher Ni/Co ratios (Figure 1a). Pyrites (type 1 and 2) located in the wallrocks display a trend to higher Zn contents, whereas Pb values are independent of the pyrite location, Au-values or vein type.

Chalcopyrite only displays detectable Au-Ag values in samples from stage 2 veins. Similar to the pyrites Au and Ag contents are positively correlated. Rare chalcopyrite, from wallrock samples next to stage 2 veins, display generally higher Zn and lower Se concentrations when compared to most stage 2 veins. However, most trace elements are close to the detection limit and no more distinctive trends could be identified.

Sphalerite is mainly observed in stage 2 quartz-carbonate and stage 3 quartz veins. As in all analysed sulphides of stage 2 veins, a trend to higher Ag values is observed related to higher Au. Higher Ag concentrations also correlate with higher Sb values for specific samples, regardless of the vein type. Silver, Sn, Cu and Sn display a higher abundance in stage 2 veins when compared to stage 3 veins. One sample of a stage 3 vein displays high Cd together with low Cu, Pb, Se, Sb and Ag contents. In contrast, all other stage 3 veins show high Ag over Au
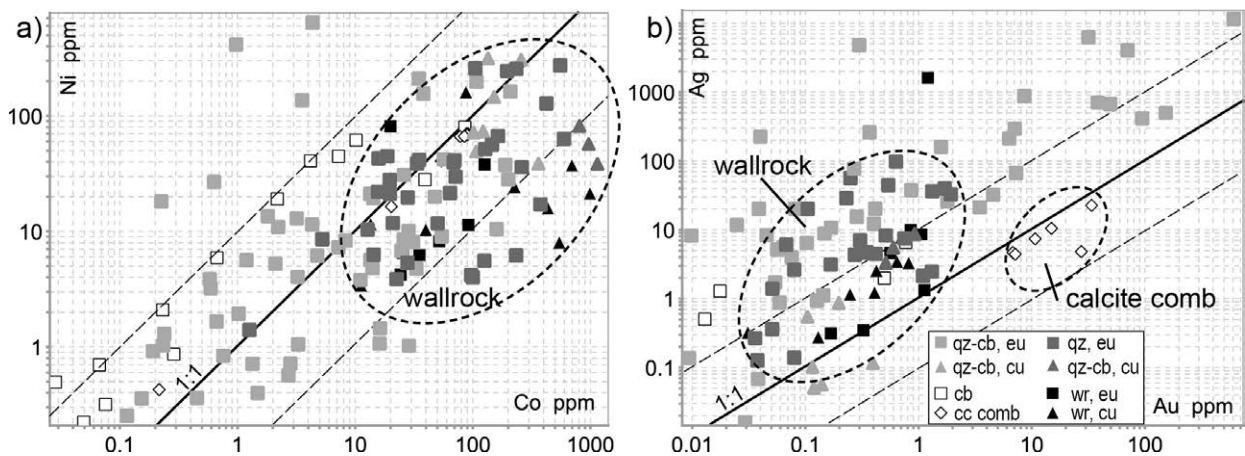
**Figure 1.** Binary plots of pyrite samples showing different trends for wallrock and vein samples with a) Co vs. Ni with a trend to higher Co-Ni contents and ratios (10:1) when compared to vein samples and b) Au vs. Ag with a trend to higher Ag ratios with higher Au contents and one carbonate vein/calcite comb pyrite samples displaying distinctively lower Au-Ag ratios; qz-quartz, cb-carbonate, cc-calcite, eu-euhedral, cu-crumbly, wr-whole rock.

ratios together with positive correlations of Te, Mo, Pb and Sb.

## 5 Discussion and Conclusions

The preceding preliminary results describe trace element trends observed in sulphides from different vein stages and locations (i.e., within and next to the vein). Pyrite can include minor amounts of As, Co, Sb, Au and Ni and trace amounts of Ag, Bi, Cd, Mo, Pb, Pd, Sb, Se, Te, Tl and Zn (Abraitis et al., 2004). However, in sulphides from the Co-O mine only Ni, Co, As, Ag, and Zn show variable trends related to vein types and spatial distribution (vein vs. wallrock). The trend to higher Zn values in the wallrock sulphides is likely related to small sphalerite inclusions in the pyrite. A study by Baker et al. (2006) on the low sulphidation epithermal system of the Pajingo deposit showed various Pb/Mo and Pb/Ag ratios in different alteration zones, which could be used as vector to auriferous veins. Lead and Mo in pyrites of this study display no clear pattern, neither related to alteration, nor pyrite texture or vein type.

Chalcopyrite and sphalerite can substitute major elements for each other replacing 2Cu+2Fe with 4Zn or vice versa. This may also explain their opposite occurrence in stage 2a versus 2b veins in this study. The preliminary results did not reveal any clear trace element trends within chalcopyrite related to vein stage, type, sulphide paragenesis or location.

For sphalerite strong positive correlations of Ag and Sn, as well as Cu and In in ephitermal deposits are described by Cook et al. (2009), but could only be partly confirmed in this study. Most trace elements in sphalerite are relatively close to detection limit in stage 3 quartz veins and spread over a wider range of values for stage 2 quartz-carbonate veins. The relationship between Cd-rich sphalerite in one stage 3 quartz vein sample and the other stage 3 veins is unclear. This could be a local variation within the vein stage or may require a further vein sub-definition in order to identify more Au-rich veins and chemical vectors.

High Ag/Au ratios are also observed in 'free' Au-alloy

grains, which is compatible with the interpreted Au-micro-inclusions in the sulphides. The expected lower Au contents in wallrock pyrites, confirm the local distal alteration halo around the stage 2 veins and suggests that the wallrock acted as buffer related to a chemical change in trace elements in the sulphides. This may also be linked to higher Ni-Co contents of wallrock pyrite. The lower Ag-Au contents in pyrites from stage 3 veins confirm a different vein stage to stage 2, but also a link to different fluid composition and conditions.

The trace element studies of sulphides confirmed that stage 2 quartz-carbonate veins contain sulphides with higher gold contents than early stage 1 quartz, later stage 3 quartz and stage 4 calcite veins, which can be used as vector for mineralization.

In summary, the preliminary trace element results from sulphides from the Co-O mine, are compatible to the different defined vein stages. However, it also shows the complexity of trace element contents of pyrite, especially, and other sulphides. Clearly, more detailed research on the physico-chemical conditions related to the distribution of trace element patterns is necessary in order to link these to sulphide and gold precipitation processes.

## References

Abraitis PK, Pattrick RAD, Vaughan DJ (2004) Variations in the compositional, textural and electrical properties of natural pyrite: a review. Int J Miner Process 74:41-59.

Baker T, Mustard R, Brown V, Pearson N, Stanley CR, Radford NW, Butler I (2006) Textural and chemical zonation of pyrite at Pajingo: a potential vector to epithermal gold veins. Geochem-Explor Env A 6: 283-293.

Cook NJ, Ciobanu CL, Pring A, Skinner W, Shimizu M,

Danyushevsky L, Saini-Eidukat B, Melcher F (2009) Trace and minor elements in sphalerite: A LA-ICPMS study. Geochim Cosmochim Ac 73: 4761-4791.

Danyushevsky L, Robinson P, Gilbert S, Norman M, Large R, McGoldrick P., Shelley M. (2011) Routine quantitative multi-element analysis of sulphide minerals by laser ablation ICP-MS: Standard development and consideration of matrix effects. Geochem-Explor Env A 11: 51-60.

Kolb J, Hagemann SG (2009) Structural control of low-sulfidation epithermal gold mineralization in the Rosario–Bunawan district, East Mindanao Ridge, Philippines. Mineral Deposita 44: 795–815.

Sonntag I, Kerrich R, Hagmeann SG (2011) The geochemistry of host arc volcanic rocks to the Co–O epithermal gold deposit, Eastern Mindanao, Philippines. Lithos 127: 564–580.

Sonntag I, Laukamp C, Hagemann SG (2012) Low potassium hydrothermal alteration in low sulfidation epithermal systems as detected by IRS and XRD: An example from the Co-O mine, Eastern Mindanao, Philippines. Ore Geol Rev 45: 47-60.

# Ingodite from the Jakub Mine, Kasejovice, Czech Republic

**Jan Soumar**
*Department of Mineralogy and Petrology, National Museum, Cirkusová 1740,193 00 Prague 9, Czech Republic*
*Institute of Geochemistry, Mineralogy and Mineral Resources, Faculty of Science, Charles University, Albertov 6, 128 43 Prague 2, Czech Republic*

**Jiří Sejkora, Jiří Litochleb**
*Department of Mineralogy and Petrology, National Museum, Cirkusová 1740,193 00 Prague 9, Czech Republic*

**Abstract.** Research focused on the Bi-Te-S phases present in samples from the Jakub mine, Kasejovice, Czech Republic (49°28'10"N 13°42'54"E), an abandoned mine in an orogenic gold deposit, was performed. Presence of previously reported sulpho-tellurides (Litochleb 1998) was confirmed and zoning was observed in the ingodite grains. No similar zoning in ingodite from the locality has been reported in the literature so far.

**Keywords:** Ingodite, zoning, Kasejovice, orogenic gold deposit, Bohemian Massif

## 1 Introduction

Mineral assemblage of the gold bearing quartz veins from the Kasejovice district belongs among the most interesting ones in the ore area of the Central Bohemian Plutonic Complex. Research of the veins has been performed for a long time and it was this area where tellurides were found and described for the first time in Bohemia (Hofmann 1906). Research on the gold bearing veins continued (Hofmann and Slavík 1913, Sobotka 1959, 1960, 1966, Vymazalová 1997, Litochleb 1998, Zachariáš and Pudilová 2002). New analyses were performed to specify the chemical composition of minerals present at this location and to help to clarify paragenetic relations of the minerals.

## 2 Geological setting and mineral assemblage

### 2.1 Geological setting

The Kasejovice-Bělčice gold-bearing region lies in the exocontact of the south-western part of the Central Bohemian Plutonic Complex 80 km south-east of Prague (Fig. 1) and is formed by the rocks of the Plánice-Kasejovice stripe of the Varied Group (Drosendorf unit) of the Moldanubian zone. All the deposit zone passes between Nekvasovy and Kramolín in the west and Bělčice in the east between the south-west margin of the Chanovice apophysis of the Central Bohemian Pluton and its body (Zachariáš and Pudilová 2002) in an approximate length of 36 km. The gold-mining district is one of many small districts or occurrences found at the NW edge of the Central Bohemian Plutonic Complex in the so-called Central Bohemian Metallogenic Zone (Morávek et al. 1992). Vast majority of them – including

Kasejovice – belong to the orogenic (mesothermal) type. However, mining activity in this area ended decades ago. The deposit – similarly to other gold deposits related with the Central Bohemian Plutonic Complex – formed in a short period of time: 350–340 Ma, which was also the time of the Plutonic Complex intrusion (Zachariáš and Pudilová 2002). The area of interest is divided into two ore districts: Kasejovice in the west and Bělčice in the east. Gold bearing quartz veins of the Kasejovice district containing the Bi-Te-S phases are hosted by the paragneiss and biotite-cordierite migmatites of the Varied Group of the above mentioned Moldanubian zone. The area is surrounded by the Blatná granodiorite of the CBPC in the north, east and south (Zachariáš and Pudilová 2002).

### 2.2 Mineral assemblage

Four mineralisation stages can be distinguished at the locality (Litochleb 1998):

1. Quartz stage (wolframite, scheelite, quartz I, apatite, rutile, tourmaline, arsenopyrite, pyrite I)
2. Gold-bearing stage (quartz II, muscovite, chlorite, pyrite II, pyrrhotite, chalcopyrite I, molybdenite, native bismuth, bismuthinite, Bi-sulpho-tellurides, gold I)
3. Polymetallic stage (Sb-bismuthinite, kobellite, Bi-jamesonite, Bi-berthierite, Bi-andorite, Ag-tetrahedrite, chalcopyrite II, Ag-gold II)
4. Calcite stage (calcite, dolomite, pyrite III).



**Figure 1.** Position of the deposit in the schematic map of the Bohemian massive and the Czech Republic

## 3 Methods

Polished sections made from material collected on the Jakub mine dump were prepared using standard methods for EPMA samples. After examination in reflected light using an ore microscope Nikon Eclipse ME600L (National Museum, Prague, Czech Repulic), Cameca SX100 electron microprobe (National Museum, Prague, Czech Repulic) was used to obtain the back-scattered electron (BSE) images and quantitative chemical compositions of minerals. The instrument operated at the following conditions: wave-length dispersive analysis, 25 kV, 20 nA, electron beam diameter less than 1 μm. The following standards and analytical lines were used: Ag (AgLα), Au (AuMα), Bi (BiMβ), CdTe (CdLα, TeLβ), pyrite (SKα, FeKα), chalcopyrite (CuKα), NiAs (AsLβ), PbS (PbMα), PbSe (SeLβ), $Sb_2S_3$ (SbLα) and HgTe (HgMβ). The concentrations of the above elements, if not included in analytical data tables, were measured but the values were below the respective detection limit (0.01–0.03 wt.% for individual elements). Measured data were corrected using the PAP software (Pouchou and Pichoir 1985).

## 4 Results

A new extensive set of data acquired from Kasejovice with focus on sulpho-tellurides confirmed presence of joséite A, joséite B, tetradymite and ingodite. The minerals form associations mostly consisting of two or three phases with a size of up to several mm. Studying ingodite was of a particular interest because its chemical composition often differs from the ideal formula. Ingodite is the least common sulpho-telluride in the studied association. Small grains of this mineral (up to 300 μm) are often associated with joséite A and B, *horobetsuite (not approved by IMA)*, tetradymite and bismuthinite, sometimes with gold. The grains of ingodite are often intimately intergrown with joséite A and B (Figs. 2 and 3). Significant variation in composition of ingodite ranging from $Bi_{4.57}(S,Te)_{6.30}$ to $Bi_{6.21}(S,Te)_{4.82}$ was observed (Fig. 4). The Se contents are negligible. Pb and Sb contents are also insignificant, whereas ingodite with Pb content of a few wt.% is reported in the literature.

**Table 1.** Average analytical data of the zonal ingodite grain (wt.%)

| | N | Pb | Sb | Bi | Se | Te | S | Total |
|---|---|---|---|---|---|---|---|---|
| Te-rich zone A | 21 | 0.46 | 0.17 | 70.82 | 0.24 | 21.60 | 5.81 | 99.1 |
| Te-med. zone B | 26 | 0.36 | 0.19 | 74.54 | 0.20 | 17.54 | 6.14 | 98.97 |
| Te-poor zone C | 17 | 0.35 | 0.25 | 78.56 | 0.16 | 12.82 | 6.28 | 98.40 |
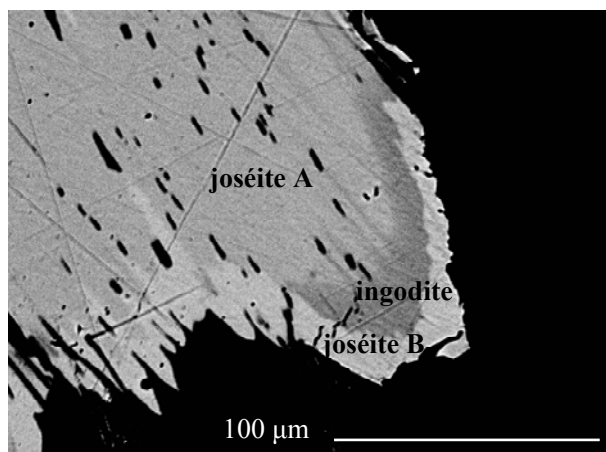


**Figure 2.** An example of the joséite A-joséite B-ingodite intimate association. Jakub mine, Kasejovice, Czech Republic

An irregular grain of ingodite with a size of 150 x 300 μm showing visible zoning in BSE (Fig. 3) intergrown with joséite B and (silverish) gold was discovered in the sample. The zones are characterised by increasing concentration of Te while concentrations of Bi and S are decreasing towards the boundary with joséite B. Te-richest zone (A, 21 point analyses) nearest to the contact with joséite B has the tellurium content 19.9–22.3 wt.%, bismuth 70.2–73.3 wt.% and sulphur 5.7–5.9 wt.%, the medium zone (B, 26 point analyses) 15.4–19.5 wt.% Te, 73–78 wt.% Bi and 6.0–6.2 wt.% S and the most distant zone at the edge of the grain (C, 17 point analyses) 12.5–13.2 wt.% Te, 78.3–78.6 wt.% Bi and 6.2–6.3 wt.% S (Fig. 5). However, boundaries between the zones do not seem sharp.
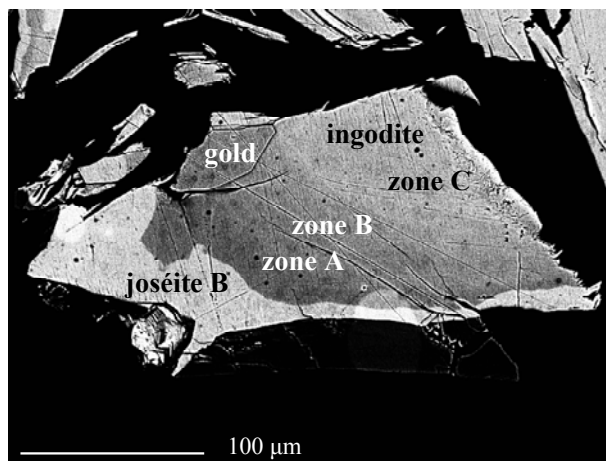


**Figure 3.** BSE image of the ingodite grain with visible zoning (lightest grey: joséite B, darkest grey to light grey – zonal ingodite)
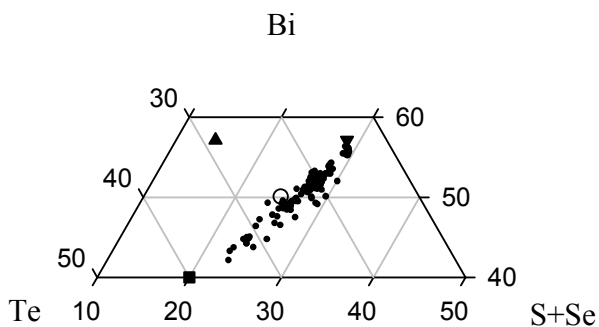
**Figure 4.** Composition of the ingodite from Kasejovice, ternary plot Bi-Te-S+Se. Symbols: full dots – ingodite, triangle up – ideal joséite B, triangle down – ideal joséite A, square – ideal tetradymite, empty circle – ideal ingodite
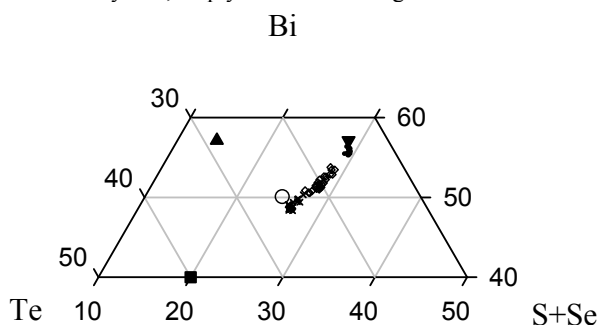


**Figure 5.** Composition of the zonal ingodite from Kasejovice, ternary plot Bi-Te-S+Se. Symbols: full dots – ingodite, zone C, empty diamonds – zone B, crosses – zone A, triangle up – ideal joséite B, triangle down – ideal joséite A, square – ideal tetradymite, empty circle – ideal ingodite
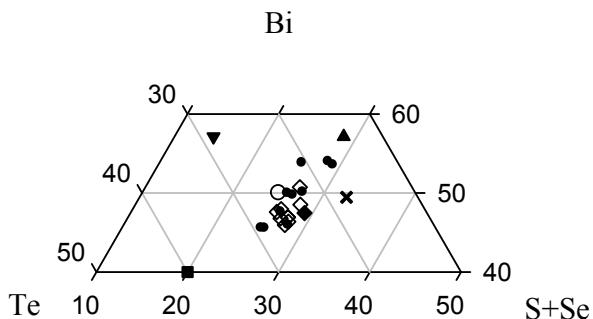


**Figure 6.** Published compositions of ingodite, ternary plot Bi-Te-S+Se. Symbols: full dots – Cook et al. (2007), empty diamonds – Shin et al. (2005), full diamonds – Oberthuer and Weiser (2007), crosses – Ciobanu et al. (2006), triangle up – ideal joséite B, triangle down – ideal joséite A, square – ideal tetradymite, empty circle – ideal ingodite

## 5 Discussion

Cook et al. (2007) report a wide compositional range for ingodite from Carrock Fell, Cumbria, U.K. ranging from approx. $Bi_5(S,Te)_6$ through ideal $Bi(S,Te)$ to approx. $Bi_6(S,Te)_5$. Shin et al., on the other hand, report smaller variation between $Bi_{5.05}(S,Te)_{5.93}$ and $Bi_{5.57}(S,Te)_{5.41}$ (Fig. 6). In case of the ingodites from Kasejovice the values extend from $Bi_{4.57}(S,Te)_{6.39}$ to $Bi_{6.21}(S,Te)_{4.77}$ (Fig. 5) which represents even a wider range than in the Carrock Fell case. Similarly varying population of ingodites is known from Baita Bihor in Romania (Illinca and

Makovicky in Cook et al. 2007).

The composition of zone C is close to the composition of the ideal joséite A. Nevertheless, composition of both joséite A and B is reported to have "discrete nature" without any significant variation (Zav´yalov and Begizov in Cook et al. 2007) so zone C is considered ingodite with a low Te content.

Similar inhomogeneity was observed by Cook et al. (2007) who attribute this fact either to ingodite solid solution or do not exclude the possibility of presence of other structurally distinct phases, e.g. baksanite $(Bi_6Te_2S_3)$.

## References

Cook NJ, Ciobanu CL, Wagner T, Stanley CJ (2007) Minerals of the system Bi-Te-Se-S related to the tetradymite archetype: Review of classification and compositional variation. Can. Mineral, 45, pp 665–708.

Ciobanu CL, Cook NJ, Damian F, Damian G (2006) Gold scavenged by bismuth melts: An example from Alpine shear-remobilizates in the Highis Massif, Romania. Mineralogy and Petrology, 87, pp 351–384.

Hofmann A (1906) Preliminary report about the gold occurrence from Kasejovice. (Vorlaufiger Bericht uber das Goldvorkommen von Kasejovic) Věst. Král. Čes. Společ. Nauk (Prague), Tř. Mat.-přírodověd., 18 (in German).

Hofmann A, Slavík F (1913) About the gold bearing Kasejovice district II. (O zlatonosném obvodu Kasejovickém II). Rozpr. Čes Akad. (Prague), Vědy Slovesn. Umění, Tř. II, 22, pp 1–44 (in Czech).

Ilinca G, Makovicky E (1999) Bismuth sulphotellurides in the Banatitic Province, Romania. International Symposium "Mineralogy in the System of Earth Sciences", Abstract vol., Univ. Bucharest, Romania, pp 40–41.

Litochleb J (1998) Mineralogy of the gold bearing mineralization from the Jakub mine near Kasejovice (SW Bohemia). (Mineralogie zlatonosného zrudnění z dolu Jakub u Kasejovic (JZ. Čechy). Bull. min.-petr. odd. NM v Praze, pp 102–112. (in Czech).

Morávek P et al. (1992) Gold in the Bohemian Massif. Czech Geol. Surv., pp 245 (in Czech).

Oberthuer T, Weiser TW (2008) Gold-bismuth-telluride-sulphide assemblages at the Viceroy Mine, Harare-Bindura-Shamva greenstone belt, Zimbabwe. Mineralogical Magazine, 72(4), pp 953–970.

Pouchou JL, Pichoir F (1985) "PAP" (φ ρZ) procedure for improved quantitative microanalysis. In: Armstrong JT (ed) Microbeam Analysis. San Francisco Press, San Francisco, pp 104–106.

Shin DB, Lee CH, Lee KS (2005) Occurrence and mineral chemistry of bismuth sulphide-telluride-selenide solid solutions (ingodite, joséite, and unnamed phases) in the Nakdong deposit, South Korea. Neues Jahrb. Mineral., Abh. 181, pp 293–302.

Sobotka J (1959) Preliminary report about joséite-B from the gold-bearing veins of the Kasejovice-Bělčice area (Předběžná zpráva o joséitu B na zlatonosných žílách kasejovicko-bělčických). Čas. Mineral. Geol., 4, Prague, pp 476–478 (in Czech).

Sobotka J (1960) Find of native bismuth at the Jakub Mine, Kasejovice (Nález ryzího vizmutu na dole Jakub v Kasejovicích). Čas. Mineral. Geol., 5, 76, Prague (in Czech).

Sobotka J (1966) Kasejovice-Bělčice gold-bearing district and its minerals. (Kasejovicko-bělčická rudní oblast a její nerosty). Lecture Notes, National Museum, Prague, pp 1–23 (in Czech).

Vymazalová A (1997) Tellurides and sulphotellurides from selected gold deposits of the Bohemian Massif (Telluridy a sulfotelluridy vybraných ložisek zlata Českého masívu). M.Sc. Thesis, Faculty of Science, Charles University, Prague, pp 95 (in Czech).

Zachariáš J, Pudilová M (2002) Fluid inclusions and stable isotope study of the Kasejovice gold district, central Bohemia. Bull. Czech Geol. Surv., pp 157–165.

Zav´yalov YN, Begizov VD (1983) New data on the constitution and nomenclature of the sulfotellurides of bismuth of the joseite group. Zap. Vses. Mineral. Obshchest. 112, pp 589–601 (in Russian).

# The formation conditions of sulfide ores of Medek Intrusion, Eastern Sayan, Russia

**Nadezhda D. Tolstykh**
*Institute of Geology and Mineralogy, pr. Ak Koptyga, 3, Novosibirsk, Russia, 630090, tolst@igm.nsc.ru*

**Abstract.** The Medek intrusion, located on the margin of the Siberian Platform (Eastern Sayan, Russia), consists of dunite-peridotite and hosts Cu-Ni sulfide ore with platinum group minerals (PGM). Several ore minerals have been investigated. Cr-spinels have high $Cr\#_{0,92-0,98}$ and low $Mg\#_{0,09-0,13}$ with $TiO_2$ up to 3,26 wt.%. Concentrations of FeO and $TiO_2$ decrease from the core to the rim of the grains. Ilmenite contains MgO up to 10,48 wt.%. Pentlandite is Fe-rich, with Fe varying from 4,60 to 5,33 mol. %. Chalcopyrite contains Ni up to 7,79 wt.%. Minerals of the chalcocite-digenite series are widespread in the investigated samples as well as parkerite. Sperrylite is replaced by orcelite and by $(Fe,Ni)_3Pt$. Sobolevskite contains Cu and Ni (up to 4,80 and 2,67 wt.%, respectively). Stibiopalladinite, Ni-rich mertieite II and three unnamed phases $Pd_5Bi_2$, $Pd_8Bi_3$ and $Pd_2Bi$ were also found. Auricupride usually forms rims on Au-Ag alloys. The compositional zoning of Cr-spinels reflects a magmatic trend. Based on experimental research, we can argue that the studied minerals crystallized at low sulfur fugacity, at temperatures above $600^{\circ}C$ for parkerite, $600-400^{\circ}C$ for pentlandite, $435^{\circ}C$ for chalcocite-digenite series, $400\,^{\circ}C$ for sobolevskite, and below $390^{\circ}C$ for auricupride, under reducing conditions.

**Keywords.** PGE-minerals, Cu-Ni ore, Medek intrusion

## 1 Introduction

The Medek (Ognitsky) dunite-peridotite intrusion is promising from and economic point of view, because it hosts sulfide PGE-Cu-Ni ore. It is located on the margin of the Siberian Platform (Eastern Sayan, Russia) and, according to mineralogical and geochemical data, it shows picritic affinities. The concentration of Ni in sulfide ores dominates over Cu and concentration of Pd over Pt (Mekhonoshin et al. 2013). The following ore minerals have been identified in the Medek deposit: Cr-spinels, ilmenite, pentlandite, mackinawite, heazlewoodite, chalcocite, digenite, chalcopyrite, violarite, parkerite, Au-Ag alloys, auricupride, awaruite, accompanied by several PGM, such as sperrylite, sobolevskote, geversite, stibiopalladinite, mertieite II, Fe-Ni-Pt alloys and three unnamed phases.

## 2 Oxide minerals

Cr-spinels from Medek intrusion have high $Cr\#_{0,92-0,98}$ and $Fe\#_{0,28-0,40}$, whit low $Mg\#_{0,09-0,13}$. According to these parameters, the studied Cr-spinels are different from those of Alpine-type, Ural-Alaskan type and other associations. They are similar to ferrichromite from komatiites and continental mafic intrusions (Barnes and Roeder 2001). Cr-spinels from Medek intrusion are characterized by higher concentrations (wt%) of minor elements : 0,68 – $V_2O_5$; 2,24 – MgO; 0,34 – NiO; 0,36 – ZnO. The $TiO_2$ concentrations vary from 2,09 to 3,26 wt.%. Similar concentrations of titanium were observed in the intrusions of Talnakh, Norilsk1 Jinchuan and Pechenga (Barnes and Kunilov 2000; Barnes et al. 2004). The zoning of the studied Cr-spinels has a magmatic origin. Concentrations of iron and titanium decrease and concentration of chromium increase from the core to the rim of the grains. Ilmenite is enriched in MgO (5,01–10,48 wt.%), reaching the 20 mol.% of geikielite end member ($MgTiO_3$). Ilmenite with similar composition was observed in Norilsk1, Talnakh, Jinchuan intrusions (Cawthorn et al. 1991; Barnes and Kunilov 2000).

## 3 BM-sulfides and arsenides

Pentlandite of Medek intrusion is Fe-rich, and in average corresponds to the formula $Fe_5Ni_4S_8$. The Fe ranged from 4,60 to 5,33 mol. %. According to the structural and chemical classification of minerals (Godovikov 1997), pentlandite is a mineral species, in which a Fe amount is less than 5 atomic units. Therefore, all the compositions in which the Fe amount varies from 5,00 to 5,33 atomic units is conventionally related to mackinawite $(Fe,Ni)_9S_8$.

Pentlandite and mackinawite $(Fe,Ni)_9S_8$ contain minor elements Co (0,51–0,87 wt.%) and Bi (0,15–0,24 wt.%). Heazlewoodite and parkerite occur as intergrowths with pentlandite, often as inclusions in this mineral. Heazlewoodite contains Fe (up to 0,92 wt.%), Cu and Bi (Table 1). Chalcopyrite is a very rare mineral in Medek PGM-bearing ores. It contains Ni (up to 7,79 wt.%) as well as Bi and Pb (Table 1). Some excess of Cu over Fe in chalcopyrite was described in massive ores of Dovyren intrusion (Konnikov et al. 1990).

Minerals of the chalcocite-digenite series are widespread in the studied samples.They contain Fe up to 6,51 wt.%. Chalcocite-digenite are metastable and non-stoichiometric sulfides in which Cu(+Fe)/S ratio ranges from 1,75 to 1,91. The ratio of Cu/S can determine the modification and temperature conditions of formation of these compounds (Vaughan and Craig 1981). The studied compounds are cubic digenite ($Cu_{1,80-1,82}S$) and cubic chalcocite ($Cu_{1,82-1,95}S$). Parkerite $Ni_3Bi_2S_2$ occurs as frequently intergrowth with pentlandite (Fig. 1a). It contains Pb up to 1,5 wt. % and Cu up to 0,30 wt. %. This mineral was described in the Cu-Ni ores of Voisey's Bay, where it also occurs in

**Table 1.** The compositions of sulfide and awaruite of Medek intrusion, wt. %

| № | Ni | Fe | Bi | Pb | S | Cu | Co | Total | Formula of minerals |
|---|----|----|----|----|---|----|----|-------|---------------------|
| 1 | 29.21 | 37.10 | 0.13 | 0.00 | 33.91 | 0.00 | 0.73 | 101.08 | $(Fe_{5.06}Ni_{3.83}Co_{0.09})_{8.98}S_{8.01}$ |
| 2 | 30.18 | 36.26 | 0.11 | 0.04 | 33.04 | 0.00 | 0.76 | 100.39 | $(Fe_{5.03}Ni_{3.99}Co_{0.10})_{9.12}S_{7.87}$ |
| 3 | 29.80 | 36.33 | 0.17 | 0.11 | 32.97 | 0.07 | 0.66 | 100.11 | $(Fe_{5.03}Ni_{3.92}Co_{0.09}Cu_{0.01})_{9.05}(S_{7.96})_{7.96}$ |
| 4 | 30.15 | 36.24 | 0.10 | 0.06 | 33.39 | 0.00 | 0.78 | 100.71 | $(Fe_{4.99}Ni_{3.97}Co_{0.10})_{9.06}S_{7.92}$ |
| 5 | 73.22 | 0.64 | 0.00 | 0.13 | 26.80 | 0.05 | 0.00 | 100.84 | $(Ni_{2.97}Fe_{0.03})_{3.00}S_{1.99}$ |
| 6 | 73.33 | 0.92 | 0.16 | 0.07 | 26.73 | 0.05 | 0.00 | 101.25 | $(Ni_{2.97}Fe_{0.04})_{3.01}S_{1.98}$ |
| 7 | 7.79 | 24.18 | 0.23 | 0.36 | 35.71 | 30.23 | 0.19 | 98.70 | $Cu_{0.88}(Fe_{0.80}Ni_{0.25}Co_{0.01})_{1.06}S_{2.06}$ |
| 8 | 1.81 | 24.86 | 0.00 | 0.09 | 33.19 | 39.55 | 0.32 | 99.81 | $Cu_{1.16}(Fe_{0.83}Ni_{0.06}Co_{0.01})_{0.90}S_{1.94}$ |
| 9 | 0.51 | 25.27 | 0.16 | 0.34 | 32.54 | 39.84 | 0.07 | 98.73 | $Cu_{1.19}(Fe_{0.86}Ni_{0.02})_{0.88}S_{1.93}$ |
| 10 | 0.04 | 0.23 | 0.00 | 0.09 | 22.10 | 76.35 | 0.00 | 98.82 | $(Cu_{1.74}Fe_{0.01})_{1.75}S_{1.00}$ |
| 11 | 0.06 | 0.65 | 0.00 | 0.07 | 20.67 | 78.93 | 0.00 | 100.37 | $(Cu_{1.84}Fe_{0.02})_{1.86}S_{1.00}$ |
| 12 | 0.02 | 0.65 | 0.12 | 0.00 | 21.21 | 78.64 | 0.00 | 100.63 | $(Cu_{1.87}Fe_{0.02})_{1.89}S_{1.00}$ |
| 13 | 0.00 | 0.32 | 0.00 | 0.00 | 20.85 | 78.42 | 0.00 | 99.59 | $(Cu_{1.90}Fe_{0.01})_{1.91}S_{1.00}$ |
| 14 | 25.81 | 0.19 | 60.76 | 1.45 | 9.77 | 0.30 | 0.00 | 98.28 | $(Ni_{2.93}Cu_{0.03}Fe_{0.02})_{2.98}(B_{1.94}Pb_{0.05})_{1.99}S_{2.03}$ |
| 15 | 74.25 | 26.32 | 0.00 | 0.00 | 0.04 | 0.18 | 0.00 | 100.80 | $(Ni_{2.91}Cu_{0.01})_{2.92}Fe_{1.08}$ |

1-4 – pentlandite, 5,6 – heazlewoodite, 7-9 – chalcopyrite, 10-13 – chalcocite-digenite, 14 – parkerite, 15 – awaruite.

association with pentlandite, heazlewoodite and sperrylite (Huminicki et al. 2008).

## 4 Minerals of PGE and Au,Ag

Sperrylite, PtAs$_2$ is the most common PGM in the studied association, and it is often intergrown with pentlandite. Many grains of sperrylite are replacement by orcelite Ni$_{5-x}$As$_2$ (Fig. 1a). Mixed compositions in the diagram lie along the line connecting sperrylite and orcelite (Fig. 2a).
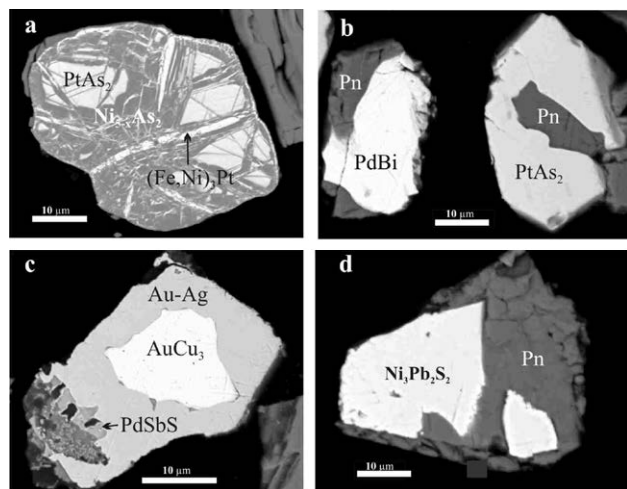


**Figure 1.** Micrographs of SEM. Medek ore occurrence: a – orcelite and (Fe,Ni)$_3$Pt replacing sperrylite; b – sobolevskite and sperrylite grains intergrown with pentlandite; c – the rim of auricupride on the Au-Ag alloy with inclusion of PdSbS; d –parkerite intergrown with pentlandite

Sperrylite contains Rh, Fe, Ni, Sb, S, and Ir (up to 4,93 wt. %), which is typical for the Medek intrusion. Orcelite, in turn, is replaced by Fe-Ni-Pt alloys that form thin veinlets in the orcelite grain. Point of their compositions shows a trend from orcelite to an unnamed phase (Fe,Ni)$_3$Pt (Fig. 2a).

Sobolevskite (PdBi) occurs as intergrowth with pentlandite (Fig. 1b). It contains Sb up to 19 mol. % of sudburyite (PdSb) end member (Fig. 2b). Sobolevskite
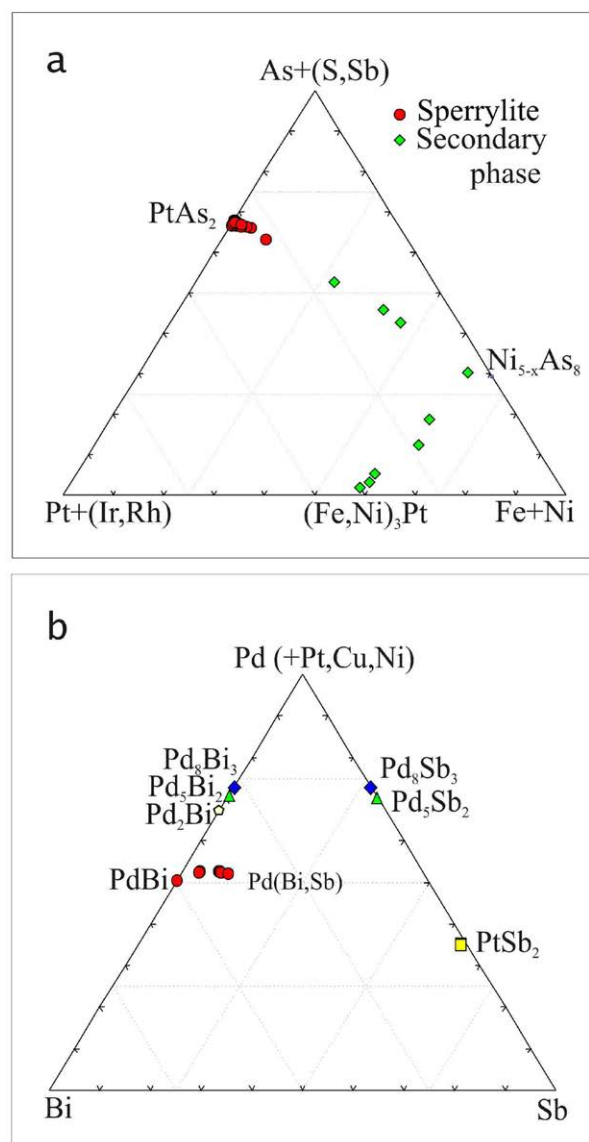


**Figure 2.** Compositions of sperrylite, orcelite, and mixed phases between them (a) and composition of PGM in the system Bi – Pd (+Pt,Cu,Ni,Fe) – Sb from Medek ore (b)

contains significant amounts of Cu and Ni (up to 4,80 and 2,67 wt.%, respectively), which is a common feature of the Medek ore. The following PGM have been also identified: stibiopalladinite $Pd_5Sb_2$, mertieite II $Pd_8Sb_3$ containing Ni (up to 13,86 wt. %) and Cu (up to 9,16 wt.%) (Table 2). The calculated formula of stibiopalladinite, using integer coefficients and is $(Pd_2Ni_2Cu)_5Sb_2$. Three unnamed phases $Pd_5Bi_2$, $Pd_8Bi_3$,

observed in the studied samples.

2. The upper stability limit of parkerite corresponds to 686°C. Heazlewoodite in association with Fe-rich pentlandite crystallized at 600-400°C in a range of sulfur fugacity ($lgfS_2$) from –11 to –16 (Vaughan and Craig 1981). The ratio of Ni/(Ni+Fe) in pentlandite also reflects the conditions of its formation (Kolonin et al. 2000). This parameter applied to the Medek pentlandite

**Table 2.** Compositions of PGM and unnamed phases in the Pd-Bi system of ore deposit of Medek intrusion

| № | Pt | Pd | Sb | Fe | Ni | Cu | Bi | Total | Formula of minerals |
|---|---|---|---|---|---|---|---|---|---|
| 1 | 0.22 | 27.79 | 8.37 | 0.06 | 2.67 | 4.17 | 57.58 | 100.72 | $(Pd_{0.72}Cu_{0.18}Ni_{0.13})_{1.03}(Bi_{0.76}Sb_{0.19}As_{0.02})_{0.97}$ |
| 2 | 0.14 | 27.15 | 2.35 | 0.21 | 1.44 | 4.30 | 63.33 | 98.86 | $(Pd_{0.76}Cu_{0.20}Ni_{0.07}Fe_{0.01})_{1.04}(Bi_{0.90}Sb_{0.06})_{0.96}$ |
| 3 | 0.53 | 26.62 | 0.00 | 0.29 | 0.83 | 4.80 | 68.27 | 100.87 | $(Pd_{0.74}Cu_{0.22}Ni_{0.04}Fe_{0.02}Pt_{0.01})_{1.01}Bi_{0.97}$ |
| 4 | 0.00 | 27.28 | 6.32 | 0.06 | 2.26 | 4.85 | 58.73 | 99.50 | $(Pd_{0.73}Cu_{0.22}Ni_{0.11})_{1.06}(Bi_{0.80}Sb_{0.15})_{0.95}$ |
| 5 | 0.00 | 26.85 | 8.21 | 0.06 | 2.70 | 4.64 | 57.57 | 100.03 | $(Pd_{0.70}Cu_{0.20}Ni_{0.13})_{1.03}(Bi_{0.77}Sb_{0.19})_{0.96}$ |
| 6 | 41.36 | 0.36 | 52.81 | 0.25 | 0.27 | 1.04 | 1.65 | 97.74 | $(Pt_{0.95}Cu_{0.05}Fe_{0.03}Ni_{0.02})_{1.05}(Sb_{1.91}Bi_{0.04})_{1.95}$ |
| 7 | 41.92 | 0.11 | 52.82 | 0.34 | 0.27 | 0.71 | 2.03 | 98.20 | $(Pt_{0.94}Cu_{0.05}Fe_{0.03}Ni_{0.02})_{1.04}(Sb_{1.91}Bi_{0.04})_{1.95}$ |
| 8 | 1.61 | 32.14 | 35.76 | 0.34 | 13.86 | 9.16 | 0.29 | 93.16 | $(Pd_{2.13}Ni_{1.67}Cu_{1.02}Pt_{0.06}Fe_{0.04})_{4.92}(Sb_{2.08})_{2.08}$ |
| 9 | 0.00 | 50.78 | 0.14 | 0.50 | 0.40 | 1.36 | 43.84 | 97.02 | $(Pd_{4.60}Cu_{0.21}Fe_{0.09}Ni_{0.07})_{4.97}(Bi_{2.02}Sb_{0.01})_{2.03}$ |
| 10 | 0.20 | 59.55 | 30.53 | 0.03 | 0.00 | 7.22 | 0.11 | 97.64 | $(Pd_{6.65}Cu_{1.35}Pt_{0.01}Fe_{0.01})_{8.01}(Sb_{2.98}Bi_{0.01})_{2.99}$ |
| 11 | 0.00 | 55.47 | 0.16 | 0.53 | 0.51 | 1.86 | 43.87 | 102.40 | $(Pd_{7.34}Cu_{0.41}Fe_{0.13}Ni_{0.12})_{8.00}(Bi_{2.97}Sb_{0.02})_{2.99}$ |
| 12 | 0.46 | 49.77 | 1.75 | 0.13 | 0.13 | 0.91 | 48.24 | 101.00 | $(Pd_{1.91}Cu_{0.06}Ni_{0.03})_{2.00}(Bi_{0.94}Sb_{0.07})_{1.01}$ |

1-5 – sobolevskite (PdBi) 6,7 – geversite (PtSb$_2$), 8 – stibiopalladinite (Pd$_5$Sb$_2$), 9 – unnamed phase Pd$_5$Bi$_2$,, 10 – mertieite II (Pd$_8$Sb$_3$), 11 – unnamed phase Pd$_8$Bi$_3$, 12 – unnamed phase Pd$_2$Bi.

and $Pd_2Bi$ were found (Table 2, Fig. 2b). These phases have never been reported before (Daltry, Wilson, 1997; Cabri, 2002) and they have no synthetic analogues (except for $Pd_2Bi$).

Awaruite ($FeNi_3$) has been also recognized in the Medek intrusion (Table 1). It formed under reducing conditions at low sulfur activity. Au-Ag alloys represent about the 20% of the discovered grains. Most of them are küstelite, being dominated by Ag over Au. In general, the Au-Ag alloys form a series of solid solutions (Fig. 3), but they contain also minor elements such as Hg and Cu. The auricupride ($Cu_3Au$) is common and usually it forms rims on Au-Ag alloy (Fig. 1c).

## 5. Discussion and conclusions

1. The Cr-spinel of Medek intrusion are similar to other depleted-$Al_2O_3$ and enriched-$TiO_2$ Cr-spinels from continental mafic intrusions (Barnes and Roeder 2001) where they could crystallize from interstitial Ti-rich liquid after high-Mg ilmenite cristallization. Some grains of Cr-spinels from PGM-bearing ore of Medek intrusion are zoned. The compositional zoning shows an increase of $Cr_2O_3$ and a decrease of $TiO_2$ and FeO from the core to the rim. This is an opposite trend if compared to those reported in chromites of the Ural-Alaskan type complexes (Barnes and Roeder 2001) and layered intrusions (Alapieti et al. 2008). The decreasing of the concentration of $TiO_2$ during crystallization of Cr-spinels is due to the subsequent crystallization of Mg-rich ilmenite. We can assume that compositional zoning of Cr- spinels reflects a magmatic trend. The formation of such Cr-spinel is not related to subsolidus transformations that occur during metamorphism (Ewers et al. 1976), which usually lead to the substitution of $Cr^{3+}$ in Fe and formation of magnetite rims that is not

varies from 0,42 to 0,50, indicating a range of $lgfS_2$ from –12 to –10. Experimental studies of the oriented crystallization of the sulfide melt (Sinyakova, Kosyakov 2006) showed that the ratio of Cu/Fe in chalcopyrite depends on the degree of melt crystallization. Cu-rich chalcopyrite of Medek intrusion formed from a Cu-rich residual liquid. The compositions of chalcocite and digenite suggest that they crystallized at temperatures below 495°S (Gablina 2008).
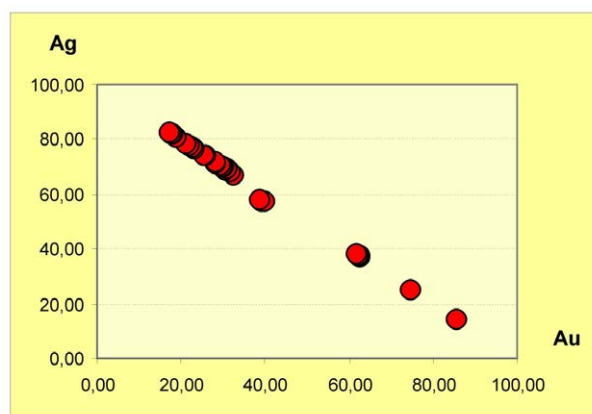


**Fig. 3.** Series of solid solutions of Au-Ag alloys

3. A typical feature of the Medek PGM association is the significant amount of Cu and Ni that occur as minor elements in the Pt-Pd minerals, as well Ir in sperrylite. The native metals and PGE alloys should crystallize at an establishing $lgfS_2$ in association with BM-sulfides (Kolonin et al. 2000), but the prevalence of Pt arsenides and Pd bismuthides in the studied samples indictes the high activity of As and Bi during evolution of sulfide melt. The identified unnamed phase $Pd_8Bi_3$ is similar to

the synthetic phase $Pd_3Bi$ which formed at $400^{\circ}C$ in equilibrium with $PdBi$ (Elliot 1965; Berlincourt et al. 1981). Similar conditions can be applied to the formation of the Pd bismuthides of Medek intrusion. Auricupride can be formed by the ordering of the Au-Cu alloys structure at $390^{\circ}C$, when a Cu-containing fluids is present at low $\lg fS_2$ (Pletnev 2002).

The results of this investigation suggest that most of the studied minerals crystallized at low sulfur fugacity, at temperatures above $600^{\circ}C$ for parkerite, $600–400^{\circ}C$ for pentlandite, $435^{\circ}C$ for chalcocite-digenite series, $400^{\circ}C$ for sobolevskite and below $390^{\circ}C$ for auricupride that formed under reducing conditions.

## Acknowledgements

## References

Alapieti TT, Devaraju TC, Kaukonen RJ (2008) PGE mineralization in the late Archaean iron-rich mafic-ultramafic Hanumalapur Complex, Karnataka, India. Miner Petrol 92:99-128

Barnes SJ, Hill RE, Evans NJ (2004) Komatiites and nickel sulfide ores of the Black Swan area, Yilgarn Craton, Wetern Australia. 3: Komatiite geochemistry, and implications for ore forming processes. Miner Deposita 39: 729-751

Barnes SJ, Kunilov VY (2000) Spinels and Mg ilmenites from the Noril'sk and Talnakh intrusions and other mafic rocks of the Siberian Flood basalt province. Econ Geol 95:1701-1717

Barnes SJ, Roeder PL (2001) The range of spinel compositions in terrestrial mafic and ultramafic rocks. Journal of Petrology 42 (12):2279-2302

Berlincourt LE, Hummel HH, Skinner BJ (1981) Phases and phase relations of the platinum-group elements. In Platinum-Group elements: mineralogy, geology, recovery (ed) by LJ Cabri. Canadian Institute of Mining and Metallurgy, Special 23:19-45

Cabri LJ (2002) The platinum-group minerals. In: Cabri L (ed) The geology, geochemistru, mineralogy and mineral beneficiation of platinum-group elements. Can Inst Min Metall 54:13-129

Cawthorn RG, Mimi de Wet, Hatton C, Cassidy K (1991) Ti-rich chromite from the Mount Ayliff Intrusion, Transkei: Further evidence for high Ti tholeiitic magma. Amer Min 76:561-573

Daltry VDC, Wilson AH (1997) Review of platinum-group mineralogy: compositions and elemental associations of the PG-minerals and unidentified PGE-phases. Miner Petrol 60:185-229

Elliott RP (1965) Constitution of Binary Alloys, ist Supplement, materials science and engineering series, Mcgraw-Hill Book Co, New York

Ewers WE, Graham J, Hudson DR, Rolls JM (1976) Crystallization of chromite from nickel-iron sulphide melts. Contrib Mineral Petrol 54:61-64

Gablina IF (2008) Copper sulfide and copper-iron as indicators of the conditions of formation and transformation of ores. Fedorov Session. IOP Publishing. RMS DPI 2008-2-10-0 (in Russian)

Godovikov AA (1997) Structural and chemical classification of minerals. Moscow (in Russian)

Huminicki MAE, Sylvester PJ, Lastra R, Cabri LJ, Evans-Lamswood D, Wilton DHC (2008) First report of platinum-group minerals from a hornblende gabbro dyke in the vicinity of the Southeast Extension Zone of the Voisey's Bay Ni-Cu-Co deposip, Labrador. Mineral Petrol 92:129-164

Kolonin GR, Orsoev DA, Sinyakova EF, Kislov EB (2000) Using the ratio Ni:Fe in pentlandite to estimate the volatility of sulfur in the formation of PGE-bearing sulfide mineralization Yoko-Dovyren massif. Dokl RAN 370(16):87-91 (in Russian)

Konnikov EG, Kacharovskaya LN, Zaguzin GN Postnikova AA (1990) Features of the main minerals of sulfide ores Baikal copper-nickel deposit. Geol Geophysics 31(2):59-66

Mekhonoshin AS, Tolstykh ND, Podlipsky MYu, Kolotilina TB, Vishnevskiy AB (2013) Platinum-mineralization of dunite-verlite massif of Gutara-Uda watershed (East Sayan). Geology of Ore Deposits 55 (in press in Russian))

Pletnev PA (2002) Genetic mineralogy of copper gold in hydrothermal deposits on the example of the Golden Mount (Urals). Dissertation, Inst of Geol and Geochemistry of Ekaterinburg (in Russian)

Sinyakova EF, Kosyakov VI (2006) Directional cristallization of melt of $CuFeS_2$ composition with monor elements of precious metals. In: Proceedings of the International Mineralogical 4 workshop. Geoprint, Syktyvkar (abstract, in Russian)

Vaughan D, Craig J (1981) Chemistry of sulfide minerals. Mir, Moscow (in Russian)

# Geometallurgical characterisation of Ni-PGE ores through automated mineralogy

K.S. Viljoen, T. Dzvinamurungu, G. Mishra, D. Rose, F. van der Merwe, T. Greeff, M. Knoper, H. Mouri, H. Rajesh
*Department of Geology, University of Johannesburg, P.O. Box 524, Auckland Park, 2006, South Africa*

**Abstract.** The speed and accuracy of automated electron microscope-based instruments such as the Mineral Liberation Analyser (MLA) now allows for the acquisition of fully quantitative and statistically relevant mineralogical data. This contribution serves to document experiences on a field emission MLA at the University of Johannesburg. Three case studies are presented: (1) Through the in-situ study of platinum group minerals (PGM) in thin section, it is demonstrated that bismuthotellurides are significantly more abundant in the Platreef than the Merensky Reef of the Bushveld Complex. This is likely a consequence of footwall assimilation, through introduction of Te and Bi into the magmatic system. (2) Mineralogical evaluation of four ore types of the platinum group elements (PGE) in the Bushveld Complex, and related flotation concentrates, show that a high PGE grade, a low abundance of orthopyroxene, and a high abundance (and good liberation) of base metal sulphides (BMS), represent the most favourable set of characteristics for the efficient recovery of PGE. (3) Mineralogical investigation into Ni recovery through laboratory scale flotation testing of Ni-sulphide ore demonstrate that the relative abundance of pyrrhotite, pentlandite and chalcopyrite, as well as variable quantities of naturally floatable gangue, has a profound influence on the effective recovery of Ni.

**Keywords : platinum group minerals, Bushveld Complex, Mineral Liberation Analyser, sulphide ore, froth flotation**

## 1 Introduction

The application of automated electron microscopy to the mineralogical characterisation of ores and successor products is a rapidly expanding field of scientific research (Boni et al., 2009; Fandrich et al., 2007; Lotter et al., 2011; Rollinson et al., 2011). The increasing availability of modern high speed energy dispersive spectrometers attached to field emission-based electron microscopes, coupled with sophisticated image analysis software, now allow for the rapid acquisition of large, statistically representative mineralogical datasets of use in the geometallurgical characterisation of ores, as well as successor products such as flotation concentrates and tailings (Adams, 2007; Evans et al., 2011; Fandrich et al., 2007; Lotter, 2011). This contribution serves to provide information on methods used with respect to MLA analysis, resulting data and the implications thereof, as applied to the characterisation of minerals in ores and flotation concentrates of mafic magmatic deposits. Three examples of the application of automated mineralogy at the University of Johannesburg are discussed, (1) an investigation into the nature and location of platinum group minerals in-situ in samples of the Merensky Reef as well as the Platreef of the

Bushveld Complex in South Africa, using polished thin sections; (2) the influence of ore mineralogy on milling and flotation performance of three facies types of Merensky Reef, and one sample of UG2, at the Marikana platinum mine on the Bushveld Complex, and (3) an investigation into the influence of ore mineralogy on flotation performance for laboratory scale flotation testing of ore from the Nkomati Ni mine located in a satellite intrusion to the Bushveld Complex.

## 2 Methods

### 2.1 Automated Mineralogy

All analyses were conducted on a FEI 600F field emission MLA, with a Bruker dual detector energy dispersive spectrometry system (two Bruker Xflash 410 silicon drift detectors), using MLA software version 3.1 build 3.1.1.287. Mineral modal abundances, platinum group mineral searches, particle mapping, particle and grains size distributions, and grain liberation measurements were conducted using either of the XMOD, GXMAP, SPL_DD_Lt and the SPL_Lt_MAP procedures (Fandrich et al., 2007).

### 2.2 Laboratory scale flotation testing

Ore samples were crushed to -2mm and then milled to 60% passing 75 micron (flotation of Merensky Reef and UG2) as well as 67% passing 75 micron (flotation of Ni ore). Flotation was conducted in a Denver flotation cell, using standard procedures for a bulk sulphide float.

## 3 Case Studies

### 3.1 Characterisation of platinum group minerals occurring in-situ in samples of the Bushveld Complex

The identification of platinum group minerals in-situ in thin section was traditionally a laborious process involving much manual input from the investigator, as observations were commonly conducted on an optical microscope or an electron microscope, followed by energy dispersive spectrometry to identify each mineral encountered. Once located and identified, the size of each PGM was then also manually recorded. The advent of automated mineralogy now allows for large data sets to be acquired of PGM's in-situ (i.e. in thin section) e.g. data collected here for 1,355 PGM's in Merensky Reef at the Two Rivers platinum mine, 1,206 PGM's in Merensky Reef at the Marikana mine, and 16,726 PGM's at the Akanani prospect in the Platreef of the Bushveld Complex (Table 1; Rose et al., 2011; van der

Merwe et al., 2012; Viljoen et al., 2011). It is demonstrated that PGM's in the Platreef under investigation is dominated by Pt and Pd bismuthotellurides, in contrast to the Merensky Reef where PGE sulphides such as cooperite and braggite predominate. The abundance of PGE tellurides and bismuthotellurides in the Platreef, when compared to the Merensky Reef, is likely a consequence of footwall assimilation, through introduction of Te and Bi, along with other semi-metals, into the magmatic system.

## 3.2 The influence of mineralogy on the milling and flotation behaviour of Merensky Reef and UG2 from the Marikana platinum mine in the Bushveld Complex

The influence of mineralogy on the milling performance and the flotation-based recovery of Au, PGE, Co, Cr, Cu, Ni and S was investigated for three samples of the Merensky Reef (BK, RPM and WP facies types) and one sample of the UG2 at the Marikana mine, using a MLA (Table 2). The samples differ in their milling behaviour in that a range of milling times are required in order to produce a grind of 60% passing 75 micron. This is primarily controlled by the abundance of plagioclase, orthopyroxene and chromite. Upon milling to 60% passing 75 micron, the size distribution of BMS (pyrrhotite, pentlandite and chalcopyrite) is similar for the three samples of Merensky Reef, and is significantly coarser than for BMS in the sample of the UG2. The best BMS liberation is achieved for the BK facies type of Merensky Reef, relative to RPM and WP, while the degree of BMS liberation in the sample of UG2 is lower than that for samples of the Merensky Reef (Fig. 1). Cumulative mass pull during flotation is higher for the sample of the WP facies of Merensky Reef than for the rest of the samples examined. This is due to the higher abundance of orthopyroxene in this sample, which is known to be naturally floating, and which reports to concentrate. A high flotation-based recovery of PGE, Cu and S is observed for all four samples, with the highest recovery associated with the sample of the BK facies type of Merensky Reef. Ni recoveries are generally poor, suggesting that Ni is associated with gangue minerals, in addition to that in pentlandite. Of the three facies types of Merensky Reef examined, the overall characteristics of the BK facies type i.e. a high PGE grade, low abundance of orthopyroxene, a high abundance of BMS, and a higher degree of liberation of the BMS on milling of the ore, represent the most favourable set of characteristics for the efficient recovery of PGE. It is therefore the best quality ore of the three samples of Merensky Reef examined.

## 3.3 The influence of mineralogy on the flotation of ore from the Nkomati Ni mine

The influence of ore mineralogy and ore texture on flotation response was studied for 29 samples from the main mineralized zone at Pit 3 of the Nkomati Ni mine, through laboratory scale flotation testing, laboratory assay, and MLA examination of the ore and the concentrates. The individual sample flotation responses vary widely in terms of concentrate mineralogy, concentrate Ni grade, and cumulative Ni recovery. It is demonstrated that this is a complex function of ore mineralogy and ore texture. Chalcopyrite is the first sulphide to float, followed by pentlandite and finally pyrrhotite, in ore samples with dominant chalcopyrite, or where pentlandite, pyrrhotite and chalcopyrite occur in equal abundance. However in samples with a high ratio of pyrrhotite to pentlandite and chalcopyrite, pyrrhotite floats earlier than expected, reports to concentrate over the entire flotation period, and depress and extend the flotation of pentlandite over the flotation interval with no clear peak of Ni recovery during flotation. Primary silicates (e.g. olivine and pyroxene) and alteration-related minerals (talc, tremolite and chlorite) are naturally floating, and hence affect the flotation of pentlandite in a similar manner to that of pyrrhotite. The most problematic ore at Nkomati in terms of Ni recovery is characterised by fine disseminated and fine bleb- or net-texture sulphides, contain abundant olivine, pyroxene, amphibole, talc and tremolite, and include abundant metamorphism-related country rock xenoliths (with calc-silicate minerals such as diopside and tremolite).

**Table 1.** Modal abundances (in area percent) of PGM's and gold in three areas of the Bushveld Complex of South Africa, obtained through MLA analysis

| Mineral | Two Rivers area% | Marikana area% | Akanani area% |
|---|---|---|---|
| Gold | 2.85 | 3.16 | 4.47 |
| PGE-Antimonides | 0.45 | 0.90 | 3.36 |
| PGE-Sulphides | 34.56 | 53.66 | 5.62 |
| PGE-Arsenides | 2.98 | 6.40 | 12.69 |
| PGE-Bismuthotellurides | 31.70 | 20.29 | 55.53 |
| PGE-Fe Alloys | 26.91 | 12.94 | 14.66 |
| PGE-Other | 0.56 | 2.65 | 3.66 |

**Table 2.** Mineral modal abundances (in weight percent) of samples of Merensky Reef and UG2 from the Marikana mine, obtained through MLA analysis

| Mineral | BK facies | RPM facies | WP facies | UG2 |
|---|---|---|---|---|
| Anorthite | 31.14 | 20.59 | 15.66 | 25.15 |
| Augite | 7.93 | 5.77 | 5.84 | 1.15 |
| Chromite | 0.45 | 1.11 | 0.75 | 49.14 |
| Enstatite | 53.33 | 57.68 | 67.08 | 15.79 |
| Epidote | 0.08 | 0.31 | 0.28 | 0.08 |
| K-Feldspar | 0.11 | 0.18 | 0.27 | 0.20 |

| | | | | |
|---|---|---|---|---|
| Phlogopite | 0.56 | 1.17 | 1.28 | 1.34 |
| Quartz | 0.14 | 0.46 | 0.76 | 0.07 |
| Tremolite | 0.58 | 1.38 | 1.19 | 0.46 |
| Serpentine | 0.33 | 5.35 | 1.43 | 0.27 |
| Chalcopyrite | 0.28 | 0.06 | 0.15 | 0.01 |
| Pentlandite | 0.49 | 0.09 | 0.21 | 0.02 |
| Pyrrhotite | 0.48 | 0.16 | 0.29 | 0.00 |
| Other | 4.09 | 5.68 | 4.82 | 6.32 |
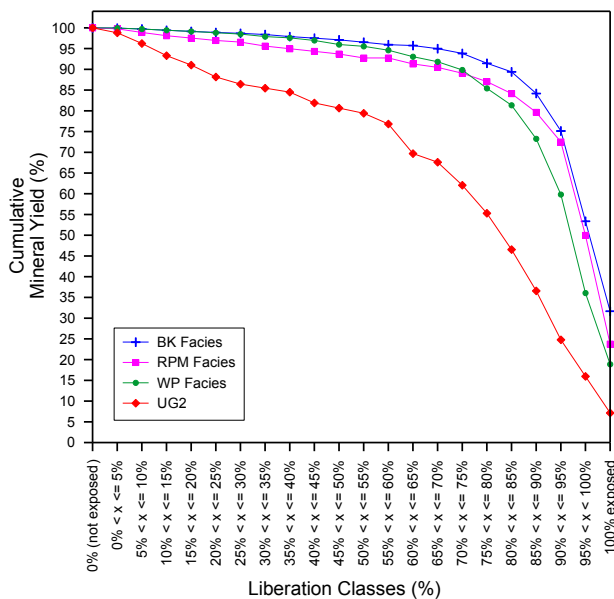


**Figure 1.** Cumulative mineral yield as a function of percent liberation for sulphides in the -75+38 micron fraction of samples from the Marikana mine milled to 60% passing 75 micron. Data obtained through MLA analysis.

## Acknowledgements

## References

Adams MD (2007) Towards a virtual metallurgical plant 2: Application of mineralogical data. Minerals Engineering 20: 472-479.

Boni M, Schmidt PR, De Wet JR, Singleton JD, Ballasone G, Mondillo N (2009) Mineralogical signature of nonsulfide zinc ores at Accha (Peru): A key for recovery. International Journal of Mineral Processing 93: 267-277.

Evans CL, Wightman EM, Manlapig EV, Coulter BL (2011) Application of process mineralogy as a tool in sustainable processing. Minerals Engineering 24: 1242-1248.

Fandrich R, Gu Y, Burrows D, Moeller K (2007) Modern SEM-based mineral liberation analysis. International Journal of Mineral Processing 84: 310-320.

Lotter NO (2011) Modern process mineralogy: An integrated multi-disciplined approach to flowsheeting. Minerals Engineering 24: 1229-1237.

Lotter NO, Kormos LJ, Oliviera J, Fragomeni D, Whiteman E (2011) Modern process mineralogy: Two case studies. Minerals Engineering 24: 638-650.

Rollinson GK, Andersen JCO, Stickland RJ, Boni M, Fairhurst R (2011) Characterisation of non-sulphide zinc deposits using QEMSCAN. Minerals Engineering 24: 778-787.

Rose D, Viljoen F, Knoper M, Rajesh H (2011) Detailed assessment of platinum-group minerals associated with chromitite stringers in the Merensky Reef of the eastern Bushveld Complex, South Africa. The Canadian Mineralogist 49: 1385-1396.

Van der Merwe F, Viljoen F, Knoper M (2012) The mineralogy and mineral associations of platinum group elements and gold in the Platreef at Zwartfontein, Akanani Project, northern Bushveld Complex, South Africa. Mineralogy and Petrology 106: 25-38.

Viljoen F, Knoper H, Greeff T (2011) Application of a field emission mineral liberation analyser to the in-situ study of platinum-group element mineralisation in the Merensky Reef of the Bushveld Complex, South Africa. In: Broekmans MATM (ed) Proceedings, 10th International Congress for Applied Mineralogy, 1-5 August 2011, Trondheim, Norway, ISBN-13: 978-82-7385-139-0, 757-764.

# "Garnierite" ore and Ni-serpentine mineralizations from the Falcondo Ni-laterite deposit (Dominican Republic): an approach from quantitative XR element imaging

Cristina Villanova-de-Benavent, Joaquín A. Proenza, Salvador Galí. Esperança Tauler
*Departament de Cristal·lografia, Mineralogia i Dipòsits Minerals, Facultat de Geologia (Universitat de Barcelona). Martí i Franquès, s/n 08028 Barcelona, Catalonia, Spain.*

Antonio García-Casco
*Department of Mineralogy and Petrology (Universidad de Granada) and Andalusian Institute of Earth Sciences (IACT, UGR-CSIC). Campus Fuentenueva s/n 18071 Granada, Spain.*

John F. Lewis
*Department of Earth and Environmental Sciences, The George Washington University. 20052 Washington D.C., USA.*

Francisco Longo
*Falcondo Xstrata Nickel. Box 1343 Santo Domingo, Dominican Republic.*

**Abstract.** "Garnierites" and Ni-serpentines are the main Ni ores in hydrous silicate-type Ni-laterites. In the Falcondo Ni-laterite, "garnierites" are found within the saprolite horizon mainly as fracture-fillings and thin coatings on joints. Different greenish colours are distinguished, which correspond to different mineral phases, according to XRD: talc-like (10 Å-type), serpentine-like (7 Å-type), a mixture of talc- and serpentine-like, and sepiolite-like. Compositional data suggest continuous solid solution along the joints lizardite-népouite/chrysotile-pecoraite, kerolite-pimelite and sepiolite-falcondoite. In general, talc-like "garnierites" display higher Ni contents than serpentine-like. Deviations from serpentine and talc stoichiometric compositions are due to talc- and serpentine-like mixing at the nanoscale. A detailed textural study by means of quantified X-ray element imaging provides a wealth of new information about the relations between textural position, sequence of crystallization and mineral composition of the studied "garnierite" samples. These results indicate several stages of growth with strongly variable Ni content, pointing to recurrent changes in the physical-chemical conditions of "garnierite" dissolution-precipitation in an aqueous medium.

**Keywords.** "garnierite", Ni-laterite, Dominican Republic, quantitative XR element imaging

## 1 Introduction

Ni-Co laterites are regolith deposits formed by the chemical weathering of ultramafic rocks (e.g. Golightly, 1981). These deposits contain 70% of the world Ni reserves (Gleeson et al., 2003, Kuck, 2011). Also, they are the source of approximately the 40% of world annual Ni production, and there is an increase amount of Ni being extracted from laterite ores (Mudd, 2010). The highest grade Ni-laterites are the hydrous Mg silicate-type, with 1.8-2.5 wt % Ni (Freyssinet et al., 2005). The Falcondo deposit (Dominican Republic) is the main hydrous Mg silicate-type Ni-laterite of the Greater Antilles in terms of Ni content and reserves. The estimated Ni production of this deposit is about 1Mt with grades of 1-2% Ni (Mudd, 2010; Berger et al., 2012).

As in many hydrous Mg silicate-type deposits worldwide, the lower part of the lateritic profile contains most of the main ore minerals: Ni-bearing serpentines and "garnierites" (Freyssinet et al., 2005).

"Garnierites" are green, fine-grained mixtures of Ni-bearing magnesium phyllosilicates, including serpentine, talc, sepiolite, smectite and chlorite (e.g. Brindley and Hang, 1973; Springer, 1974). In addition, an intermediate phase between talc and serpentine was described by Rukavishnikova (1956), karpinskite $(Mg,Ni)_2Si_2O_5(OH)_2$, but it is not yet accepted as a mineral name by the IMA Commission on New Minerals, Nomenclature and Classification. "Garnierites" are supergene minerals precipitated from a Ni-enriched solution during the weathering of the ultramafic protolith. Therefore, they are characterised by having low Fe concentrations (< 1.5% FeO, Manceau & Calas, 1985).

In the case of Falcondo, previous results show that "garnierites" consist mainly of the combination of three solid solutions: lizardite-népouite or chrysotile-pecoraite $[(Mg,Ni)_3Si_2O_5(OH)_4]$, talc-like or kerolite-pimelite $[(Mg,Ni)_3Si_4O_{10}(OH)_2 \cdot n(H_2O)]$ and sepiolite-falcondoite $[(Mg,Ni)_4Si_6O_{15}(OH)_2 \cdot 6(H_2O)]$ (Tauler et al., 2009; Galí et al., 2012). For these minerals, the terminology "serpentine-like" (or 7 Å-type), and "talc-like" (or 10 Å-type) and "sepiolite-like" "garnierites" will be used hereafter (e.g. Brindley & Hang, 1973).

Little work on detailed characterisation of "garnierites", including information of textures and composition has been done, except for sepiolite-falcondoite series (Springer, 1976; Tauler et al., 2009). The aim of this study is to provide new data on textural relations and mineral chemistry of Dominican "garnierites", focusing on the serpentine- and talc-like phases.

## 2 Geological setting and "garnierite" occurrence

Falcondo Ni-laterite soils have been developed on the Loma Caribe peridotite, the main ophiolitic belt outcropping in the Cordillera Central (Dominican Republic). This peridotite massif is mainly composed of lherzolite, clinopyroxene-rich harzburgite, harzburgite and dunite (e.g. Marchesi et al., 2012).

"Garnierite" mineralizations occur mainly as mm-cm vein fillings in fractures, as coatings on joints with random orientations, and in fault planes, often displaying slickensides. They also form boxworks and breccias.

In the field these mineralizations are concentrated in outcrops of tens to a hundred of metres in length, within the lower part of the saprolite horizon. However, they are also located near unweathered serpentinized peridotite rocks, at the base of the lateritic profile, and in the upper saprolite horizon.

## 2 Analytical and computation techniques

Elemental (Si, Ni, Mg and Fe) X-ray images were obtained with a CAMECA SX–50 Electron Microprobe (EMP) at the Centres Científics i Tècnics (Universitat de Barcelona). The instrument operated at 15 keV and 200 nA. The analytical conditions were a focused beam of 5 μm, a step (pixel) size of 3 μm, and counting time of 25-30 ms/pixel. These images were processed with the DWImager software (Torres-Roldán and García-Casco, unpublished) following the quantification procedure described in García-Casco (2007). Analyses of the mineral phases were performed with the same electron microprobe at 15 KeV and 10 nA.

## 3 Results

Eight selected samples from the Falcondo laterite deposit have been studied in detail. These samples contain different greenish coloured "garnierites", showing characteristic X-ray diffractograms and chemical compositions obtained by EMP. X-ray powder diffraction enabled to classify the studied samples into four groups: i) serpentine-like "garnierites" (7 Å-type), ii) talc-like (10 Å-type), iii) mixture of talc- and serpentine-like, and iv) sepiolite-like. In general, talc-like is always wrapping serpentine-like, thus suggesting that talc-like formed later than serpentine-like "garnierites". All "garnierite" types may coexist with late quartz/amorphous silica, filling veinlets and/or remaining porosity.

### 3.1. "Garnierite" composition

The structural formulae of the studied "garnierites" were calculated on the basis of a total cation charge of 7 for serpentine-like phases and mixtures, and of 11 for talc-like phases. For sepiolite-falcondoite, calculations were performed using a total cation charge of 32. In general, oxide totals of "garnierites" are below the ideal for

serpentine-like and talc-like structures. Most of the studied "garnierites" are Al-free; only few analyses show up to 0.11 a.p.f.u. Al. In addition, talc and serpentine fractions were calculated according to the formulae given by Brindley & Hang (1973).

The analyses performed are represented in the ternary Si-Mg-Ni diagram of fig. 1a. The results are also compared to analyses of "garnierites" obtained in other localities by different authors (fig. 1b).
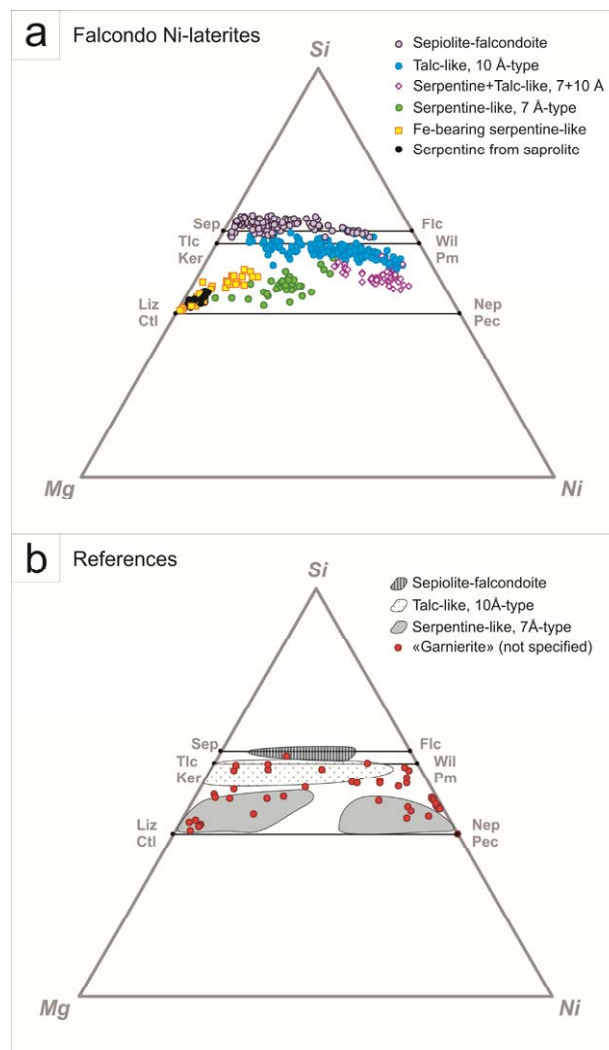


**Figure 1.** Triangular plots showing the "garnierite" compositions from the Falcondo Ni-laterite (a) and from other localities (b). Legend: Sep = sepiolite, Flc = falcondoite, Tlc = talc, Ker = kerolite, Will = willemseite, Pm = pimelite, Liz = lizardite, Ctl = chrysotile, Nep = népouite, Pec = pecoraite. Data from Pecora et al. (1949), Kato (1961), Faust (1966), Naganna & Phene (1968), DeWaal (1970), Brindley & Hang (1973), Maksimovic (1973), Springer (1974), Brindley & Wan (1975), Nickel & Bridge (1975), Springer (1976), Esson & Carlos (1978), Brindley et al. (1979), Poncelet et al. (1979), Gerard & Herbillon (1983), Manceau & Calas (1985), Ducloux et al. (1993), Song et al. (1995), Talovina et al. (2008), Wells et al. (2009).

Serpentine-like "garnierites" are divided into Fe-bearing and Fe-free serpentine-like phases. The Fe-bearing phases show slight deviations of the structural formulae from the ideal serpentine stoichiometry, showing a small excess in the tetrahedral site and a

deficit in the octahedral site. Fe and Ni contents are relatively high (0.07-0.32 a.p.f.u. Fe and 0.03-0.59 a.p.f.u. Ni), similar to those shown by serpentines from the saprolite host (0.05-0.50 a.p.f.u.). On the other hand, the structural formulae of Fe-free serpentine-like "garnierites" are far from the ideal serpentine, with remarkable excess and deficit in the tetrahedral and octahedral sites, respectively. This "garnierite" presents higher Ni (0.30-1.88 a.p.f.u.) and lower Fe (0-0.1 a.p.f.u.) and constitute the only "garnierite" with significant Al (0.01-0.11 a.p.f.u.).

Mixtures of serpentine- and talc-like "garnierites" display similar deviations from the ideal stoichiometry of serpentine, comparable to that of the Fe-free serpentine-like "garnierites". However, the mixtures show higher Ni contents (1.28-2.19 a.p.f.u.) and lower Fe contents (0-0.04 a.p.f.u.). The mean serpentine fraction is 0.53.

Talc-like "garnierite" structural formulae are close to the ideal stoichiometry of talc. These "garnierites" show a wide range of high Ni concentrations (0.89-2.83 a.p.f.u.), as well as the lowest Fe content (0-0.01 a.p.f.u.) of all studied "garnierites".

Sepiolite-like "garnierite" compositions (studied in detail by Tauler et al., 2009) range between 0.34 and 5.24 a.p.f.u. Ni, and low Al and Fe contents (0-0.09 and 0-0.49 a.p.f.u. respectively).

According to fig. 1a, serpentine-like phases with lower Ni and higher Fe concentrations plot near the lizardite-chrysotile end-member. Mixtures of serpentine- and talc-like phases display intermediate compositions between the serpentine and talc solutions and are Ni-dominant. Talc-like and sepiolite-like species show a wide range of continuous compositions along the talc (kerolite)-willemseite (pimelite) and sepiolite-falcondoite solutions, respectively. In addition, the sepiolite-like analyses are slightly shifted towards Si (fig. 1a), as a likely consequence of microscopic intergrowths of quartz within sepiolite (cf. Tauler et al., 2009).

In general, Ni-Mg hydrous silicates from the Falcondo deposit have similar structural and chemical characteristics to "garnierite" minerals examined in other worldwide Ni-lateritic deposits (fig. 1b), except for Ni-dominant serpentine-like phases, which have not been detected in Falcondo.

### 3.2. Quantitative X-ray element maps

A detailed study of quantified X-ray element maps provide the relations between textural position, sequence of crystallization and mineral composition of the studied "garnierite" samples. In order to examine the major element distribution in the different "garnierites", Si, Mg, Ni and Fe were scanned in selected areas containing talc-like "garnierite" (fig. 2a), quartz (fig. 2b) and serpentine-like "garnierite" (fig. 2c).

X-ray maps show that textures and mineral compositions are variable and complex at the μm-scale. The maps show discrete location of Ni distribution, with high contents best developed in talc-like regions that display extreme oscillatory banded botryoidal fabric (fig. 2a). The observed textural-chemical relations indicate

several stages of growth with strongly variable Ni content, pointing to recurrent changes in the physical-chemical conditions of garnierite precipitation-dissolution in an aqueous medium. XR images also stand out the presence of regions with the composition of the intermediate phase Ni-"karpinskite", associated with regions of Ni-serpentine (fig. 2c). This is confirmed by the quantified Si image and EMP point analyses. It is also evident the post-depositional diffusion transport of Fe from relictic serpentinite towards adjacent neoformed talc.
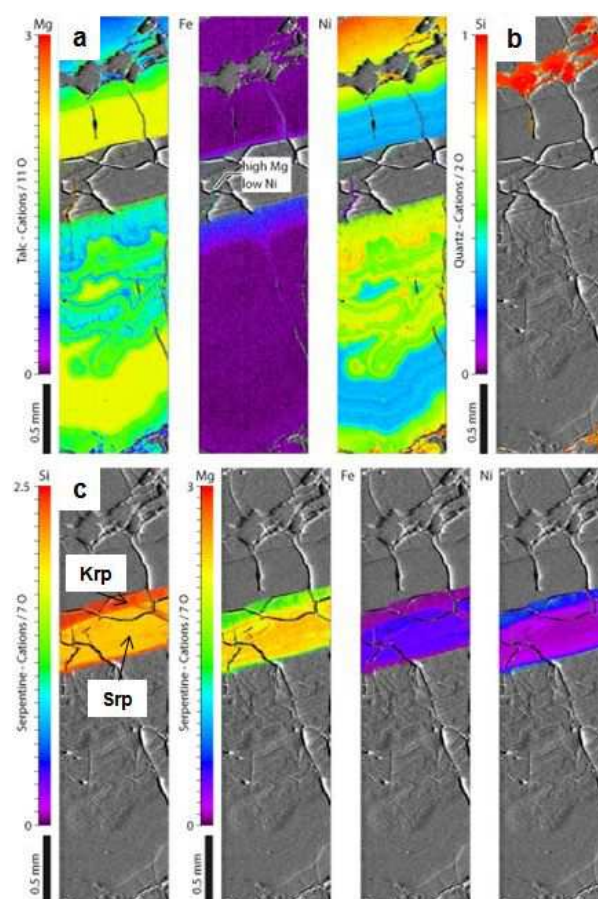


**Figure 2.** Textural and compositional features of (a) talc, (b) quartz, and (c) serpentine and "karpinskite". The scaled (color code) distribution of elements and elemental ratio is expressed in cations per fixed number of oxygens (i.e., charges) in the respective formula units. Mg, Fe and Ni are scaled uniformly in order to better compare mineral compositions.

## 4  Final remarks

Different greenish colourations have been observed in "garnierite" mineralizations from the Falcondo Ni-laterite deposit, identified as serpentine-like, talc-like, and sepiolite-like phases. EMP compositions revealed the presence of an intermediate phase between serpentine and talc. In addition, X-ray quantitative element maps suggest that some of the "garnierites" interpreted as a mixture may correspond to *karpinskite*.

In the case of Falcondo, the dominant "garnierite" is the talc-like phase (10 Å-type), which shows the highest Ni content (up to 2.826 atoms per 11 oxygens). This characteristic contrasts with other deposits, as those of

New Caledonia, where the most abundant phase is a serpentine-like "garnierite". Likely, this difference is the result of the interplay of several physico-chemical factors (hydrogeologic regime, temperature, nature of the protolith) leading to variable chemistry of the solutions and variable reaction-dissolution-precipitation pathways.

Precipitation of Ni ore is a succession of mineral phases progressively enriched in Ni and with higher Si, because silica activity increases with time and through the profile. Thus, the first phases to precipitate are Ni-serpentines (7 Å-type), followed by Ni-kerolite (10 Å-type), while Ni-sepiolite-falcondoite are the last phases to form (Galí et al., 2012). This conclusion is supported by the textures observed in Dominican "garnierites", where talc-like phases always envelop serpentine-like "garnierites", and the remaining porosity is finally filled by quartz and/or silica.

## Acknowledgements

## References

Berger VI, Singer DA, Bliss JD, Moring BC (2011) Ni-Co laterite deposits of the world – Database and grade and tonnage models. USGS Open-File Report 2011-1058.

Brindley GW, Bish DL, Wan HM (1979) Compositions, structures, and properties of nickel-containing minerals in the kerolite-pimelite series: Am. Miner. 64: 615-625.

Brindley GW, Hang PT (1973) The nature of garnierite: I. Structure, chemical compositions and color characteristics: Clay Clay Miner. 21: 27-40.

Brindley GW, Wan H-M (1975) Compositions, structures and thermal behaviour of nickel-containing minerals in the lizardite-népouite series: Am. Miner. 60: 863-871.

DeWaal SA (1970) Nickel minerals from Barberton, South Africa: III. Willemseite, a nickel-rich talc: Am. Miner. 55: 31-42.

Ducloux J, Boukili H, Decarreau A, Petit S, Perruchot A, Pradel P (1993) Un gîte hydrothermal de garniérites: l'exemple de Bou Azzer, Maroc: Eur. J. Mineral. 5: 1205-1215.

Esson J, Carlos L (1978) The occurrence, mineralogy and chemistry of some garnierites from Brazil: Bull. BRGM II-3: 263-274.

Faust GT (1966) The hydrous nickel-magnesium silicates – the garnierite group: Am. Miner. 51: 33-36.

Freyssinet Ph, Butt CRM, Morris RC (2005) Ore-forming processes related to lateritic weathering: Econ. Geol. 100th Anniv. Vol.: 681-722.

Galí S, Soler JM, Proenza JA, Lewis JF, Cama J, Tauler E (2012) Ni-enrichment and stability of Al-free garnierite solid-solutions: a thermodynamic approach: Clay. Clay Miner. 60: 121-135.

García-Casco A (2007) Magmatic paragonite in trondhjemites from the Sierra del Convento mélange, Cuba: Am. Miner. 92: 1232-1237.

Gerard P, Herbillon AJ, (1983) Infrared studies of Ni-bearing clay minerals of the kerolite–pimelite series: Clay Clay Miner. 31:

143-151.

Golightly JP (1981) Nickeliferous laterite deposits. Econ. Geol. 75th Anniv. Vol.: 710-735.

Gleeson SA, Butt CR, Elias M (2003) Nickel laterites: A review: SEG Newsletter 54: 11-18.

Kato T (1961) A study on the so-called garnierite from New-Caledonia: Mineral. J. 3: 107-121.

Kuck PH (2012) Nickel. USGS Mineral Commodity Summaries: 108-109.

Maksimovic Z 1973 Isomorphous series lizardite-nepouite: Zap. Vses. Miner. Obsch. 102(2): 143-149 (in Russian).

Manceau A, Calas G (1985) Heterogeneous distribution of nickel in hydrous silicates from New Caledonia ore deposits: Am. Miner. 70: 549-558.

Marchesi C, Garrido CJ, Proenza JA, Konc Z, Hidas K, Lewis JF, Lidiak E (2012) Mineral and whole rock compositions of peridotites from Loma Caribe (Dominican Republic): insights into the evolution of the oceanic mantle in the Caribbean region. Geophys. Res. Abs. 14: EGU2012-12161.

Milton C, Dwornik EJ, Finkelman RB (1983) Pecoraite, the nickel analogue of chrysotile, $Ni_3Si_2O_5(OH)_4$ from Missouri: Neues Jb. Miner. Monat. 513-523.

Mudd GM (2010) Global trends and environmental issues in nickel mining: sulfides versus laterites: Ore Geol. Rev. 38: 9-26.

Naganna C, Phene SG (1968) Study of the nickel silicates associated with the ultrabasic rocks of Nuggihalli schist belt, Mysore state: Proc. Indian Acad. Sci. B 67: 174-179.

Nickel EH, Bridge PG (1975) A garnierite with a high nickel content from Western Australia: Mineral. Mag. 40: 65-69.

Pecora WT, Hobbs SW, Murata KJ (1949) Variations in garnierite from the nickel deposit near Riddle, Oregon: Econ. Geol. 44: 13-23.

Poncelet G, Jacobs P, Delannay F, Genet M, Gerard P, Herbillon A (1979) Étude preliminaire sûr la localisation du nickel dans une garnierite naturelle: Bull. Miner. 102: 379-385.

Rukavishnikova IA (1957) Some magnesium nickel hydrous silicates of the Nizhne-Tagilsk serpentine massif: Kora Vyvetr. 2: 12-17 (in Russian).

Song Y, Moon H-S, Chon H-T (1995) New occurrence and characterization of Ni-serpentines in the Kwangcheon area, Korea: Clay Miner. 30: 211-224.

Springer G (1974) Compositional and structural variations in garnierites: Can. Miner. 12: 381-388.

Springer G (1976) Falcondoite, Ni analogue of sepiolite: Can. Miner. 14(4): 407-409.

Talovina IV, Lazarenkov GV, Ryzhkova SO, Ugol'kov VL, Vorontsova NI (2008) Garnierite in nickel deposits of the Urals: Lith. Miner. Res. 43: 588-595.

Tauler E, Proenza, JA, Galí S, Lewis JF, Labrador M, García-Romero E, Suárez M, Longo F, Bloise G (2009) Ni-sepiolite-falcondoite in garnierite mineralization from the Falcondo Ni-laterite deposit, Dominican Republic: Clay Miner. 44: 435-454.

Wells MA, Ramanaidou ER, Verrall M, Tessarolo C (2009) Mineralogy and crystal chemistry of "garnierites" in the Goro lateritic nickel deposit, New Caledonia: Eur. J. Miner. 21: 467-483.

# Kotulskite-sobolevskite solid solution, natural occurrence and an experimental investigation

**Anna Vymazalová, Milan Drábek**
*Czech Geological Survey, Geologická 6, 152 00 Prague 5, Czech Republic*

**Federica Zaccarini, Giorgio Garuti**
*University of Leoben, Peter Tunner str. 5, A-8700 Leoben,, Austria*

**Tatiana L. Evstigneeva**
*IGEM RAS, Staromonetnyi per. 35, 119 017 Moscow, Rvussia*

**Abstract.** Kotulskite – sobolevskite solid solution was experimentally investigated at 400, and additionally at 200 and 600 °C. We conducted ten experiments and evaluated them by means of X-ray powder-diffraction analysis, reflected light and electron microscopy. The experiments were performed using the evacuated silica tube method. Experimental results have shown that sobolevskite and kotulskite do not form complete solid solution. The solid solution breaks with the composition of 35 at.% Bi (Bi-rich kotulskite end member) and forms a gap in series solution. Sobolevskite dissolves up to 2 at.% Te. Bi-rich kotulskite, with the same composition as the synthetic end member was observed in the studied natural samples from Noril`sk deposit.

## 1 Introduction

Kotulskite (PdTe) belongs to the most abundant minerals among Pd-tellurides, originally described by Genkin et al. (1963). Its Bi analogue is mineral sobolevskite (Evstigneeva et al. 1975). There are also known numerous natural occurrences of phases falling into the compositional field of kotulskite-sobolevskite series described from Noril`sk (Evstigneeva et al. 1975, Kovalenker et al. 1972, Cook et al. 2002, etc.), Merensky Reef in the western Bushveld (Kingston 1966), Chineyiskyi Massif in Siberia (Tolstykh et al. 1997), Blue Lake, Labrador in Quebec (Beaudoin et al. 1990), the Two Duck Lake intrusion in Coldwell Complex (Watkinson and Ohnenstetter 1992), the Lukkulaisvaara Pluton in northern Karelia (Grokhovskaya et al. 1992), among other deposits. During the reconnaissance of our Noril`sk samples we came across a phase with a chemical composition 36.9 wt.% Pd, 49.6 wt.% Bi, 12.9 wt.% Te, observed as single grains of about 10 to 40 μm in size, in several studied polished sections from the Noril`sk ores. Observed grains were homogenous with a constant chemical composition almost suggesting an occurrence of a new phase. The similar phases belonging to the sobolevskite-kotulskite series from the same locality were also observed by authors given above.

The synthetic system Pd-Bi-Te was so far investigated at the isothermal section in the composition range: Te-$Bi_4Te_3$-$Bi_{60}Pd_{40}$-PdTe at 480ºC by Hoffman and MacLean (1976) and at the isothermal section in the composition range: $Bi_{38}Pd_{62}$-Pd-$Pd_{72}Te_{28}$-$Bi_{19}Pd_{70}Te_{11}$-$Bi_{30}Pd_{63}Te_7$ at 480ºC by El-Boragy and Schubert (1971). None of them cover the PdTe-PdBi region of the phase diagram.

Due to the lack of experimental data explaining the PdBi-PdTe solid solution and controversies within the natural occurrences, the experimental study in the Pd-Bi-Te was carried out.

## 2 Techniques and Methods

The studied natural samples were collected from the Bears brook open pit during the 7th Platinum symposium field trip to the Noril`sk deposit. Minerals of kotulskite-sobolevskite series were investigated in polished sections using reflected light microscopy and electron microprobe. They were quantitatively analyzed for Bi, Te, Sb, Pt and Pd using a JEOL JXA 8200, installed at the Eugen F. Stumpfl Electron Microprobe Laboratory, University of Leoben operated with 20Kv of accelerating voltage and 10nA of beam current. The beam diameter was about 1 micron in size. $L\alpha$ line was used for all the analyzed elements, except for Bi that was analysed using $M\alpha$ line. The following diffracting crystals were used: PETJ for Te and Sb, PETH for Bi and Pd and LIFH for Pt. Te and Bi were calibrated on $Bi_2Te_3$, Pd and Sb on PdSb and Pt on native Pt.

Based on the results from natural samples ten experiments were performed on a line PdTe-PdBi. The experiments were performed in the sealed evacuated silica glass tubes in horizontal furnaces. Charges of 100 – 200 mg in weight were synthesized from pure tellurium, palladium, and bismuth. For the kinetic reasons the experiments started at 1200 °C (for about three days) and, after quenching and re-grinding, under acetone were kept at 400 °C for 70 days, at 600 °C for 60 days and at 200°C for 170 days. After heating, the silica tubes were rapidly quenched in a cold-water bath.

Chemical analyses on synthetic samples were performed by Cameca SX-100 electron microprobe using the wavelength-dispersion mode and a focused beam (size 1-2 μm). The accelerating voltage was set to 15 keV, and the beam current was 10 nA. The samples were analyzed using Pd$L\alpha$, Te$L\alpha$ , and Bi$M\alpha$. Pure metals (Pd, Bi, Te) were used as primary standards. In each sample, compositional data were collected for several grains within the polished section (min *n=5*) and then averaged.

## 3 Results and discussion

The solid solution of sobolevskite (PdBi) – kotulskite (PdTe) was experimentally investigated at 400 °C, ten experiments were performed on a line PdTe-PdBi. Representative runs and their experimental products are given in Table 1 and plotted in Fig.1. Back-scattered electron images representing the natural samples and their synthetic analogues are given in Fig. 2 and 3, respectively.

**Table 1.** A list of representative experimental runs and their products.

| Run No | Starting material | T (°C) | Experimental products |
|---|---|---|---|
| Exp1 | 3Pd+2Bi+Te | 400 | Pd(Te,Bi) |
| | | 200 | Pd(Te,Bi) |
| | | 600 | Pd(Te,Bi) |
| Exp2 | 10Pd+7Bi+3Te | 400 | Pd(Te,Bi) |
| Exp5 | 5Pd+4Bi+Te | 400 | Pd(Te,Bi) + PdBi |
| | | 200 | Pd(Te,Bi) + PdBi |
| | | 600 | Pd(Te,Bi) + PdBi |
| Exp6 | 5Pd+3Bi+2Te | 400 | Pd(Te,Bi) |
| Exp7 | 5Pd+2Bi+3Te | 400 | Pd(Te,Bi) |
| | | 200 | Pd(Te,Bi) |
| | | 600 | Pd(Te,Bi) |
| Exp8 | 5Pd+Bi+4Te | 400 | Pd(Te,Bi) |
| | | 200 | Pd(Te,Bi) |
| | | 600 | $Pd(Te,Bi)+Pd_9(Te,Bi)_4$ |
| Exp10 | 2Pd+2Bi+2Te | 400 | $PdBiTe+PdBi_2+Pd(Te,Bi)$ |

According to the X-ray diffraction data, the studied experimental products show hexagonal symmetry confirming the structure of kotulskite (in Exps 1, 2, 5, 6, 7, 8) and sobolevskite (Exp 5). Chemical analyses of experimental runs on a line PdTe-PdBi are given in Table 2 (average of 5 analyses). The results have shown that sobolevskite and kotulskite do not form a complete solid solution at 400 °C (Fig. 1). The solution breaks with the composition of $Pd_{50}Bi_{35}Te_{15}$, indicating that kotulskite dissolves up to 35 at.% Bi and sobolevskite up to 2 at.% Te. The range of solid solution can be dependent on the temperature therefore we also performed the selected runs at 200 and 600 °C. The results have shown that the solubility of Bi in kotulskite and Te in sobolevskite is not dependant on temperature, see Table 2. The appearance of melt was observed in some experimental products at 600 °C. The phase with the content of Bi 35 at. % seems to be the end member of Bi-rich kotulskite solid solution.
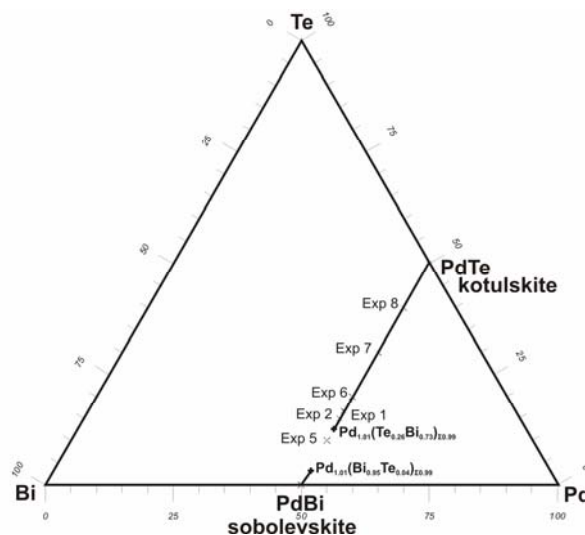


**Figure 1.** Plot of experimental runs in the Pd-Bi-Te diagram showing the assay of sobolevskite-kotulskite solution and its end-members.
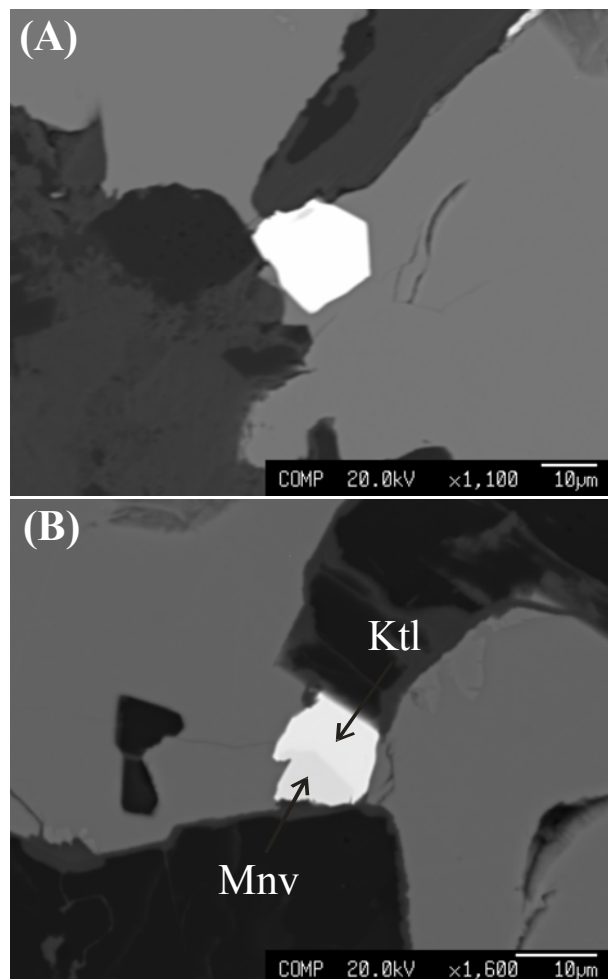


**Figure 2.** Back-scattered electron images of mineral kotulskite with composition of the solid solution end member (A) Bi-rich kotulskite in chalcopyrite. (B) Intergrowth of menshikovite (mnv) and Bi-rich kotulskite (ktl).

The phase with the similar composition, $Pd_{50}Bi_{35}Te_{15}$, has been also observed as several subhedral grains of size up to 40 μm in investigated samples from Noril`sk deposit. As mentioned above mineral kotulskite has a large field of composition in regard to Te-Bi substitution. The most enriched in Bi kotulskite, $Pd(Te_{0.60}Bi_{0.40})$, was found in Talnakh ores (Kovalenker et al. 1972). But in Bi-rich kotulskite always some Pb is found. It is noted that except PdTe, the most frequently reported are minerals with composition close to $\sim Pd(Te_{0.5}Bi_{0.5})$ and $\sim Pd(Te_{0.75}Bi_{0.25})$. It may be due to the formation conditions, such as temperature of crystallization which determine the bismuth content. However the crystallochemical features of the structure also could result in the formation of "stoichiometric" compounds due to the solid solution ordering.

Some further research focused on crystallographic study of natural members in kotulskite – sobolevskite series in needed due to the possible confusion with other PdBi polymorph that is mineral polarite.
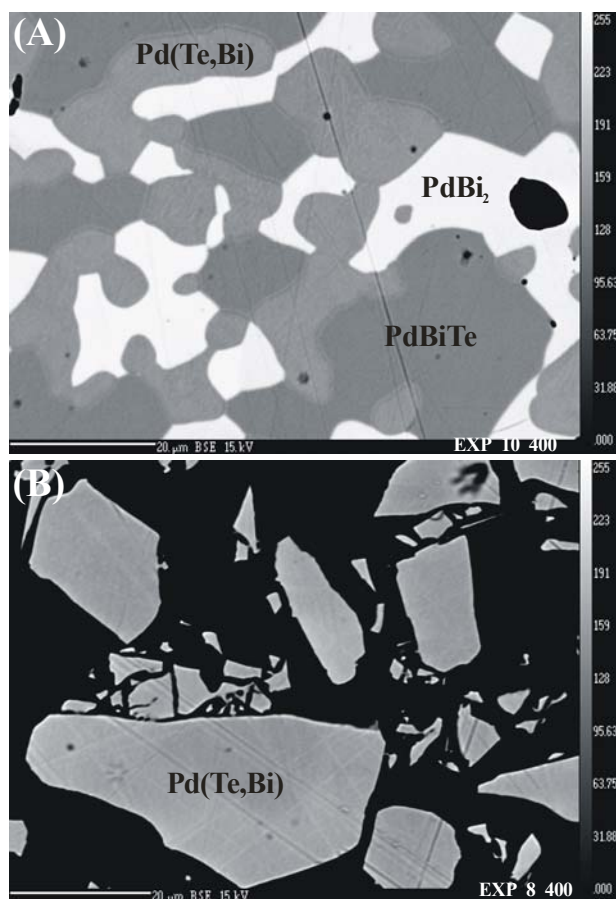
**Figure 3.** Back-scattered electron images of (A) synthetic michenerite (PdBiTe) in association with froodite ($PdBi_2$) and kotulskite solid solution Pd(Te,Bi), Exp_10 at 400°C. (B) kotulskite solid solution Pd(Te,Bi), Exp_8 at 400°C.

**Table 2.** Chemical composition of PdTe-PdBi series.

| Run No | T °C | Pd | Te | Bi | Total | Formula |
|---|---|---|---|---|---|---|
| Exp5 | 200 | 34.8 | 1.0 | 63.4 | 99.2 | $Pd_{1.02}(Bi_{0.95}Te_{0.03})_{\Sigma0.98}$ |
| Exp5 | 200 | 36.8 | 10.6 | 52.6 | 100.0 | $Pd_{1.02}(Te_{0.24}Bi_{0.74})_{\Sigma0.98}$ |
| Exp5 | 400 | 34.7 | 1.6 | 64.0 | 100.3 | $Pd_{1.01}(Bi_{0.95}Te_{0.04})_{\Sigma0.99}$ |
| Exp5 | 400 | 36.8 | 11.4 | 52.5 | 100.7 | $Pd_{1.01}(Te_{0.26}Bi_{0.73})_{\Sigma0.99}$ |
| Exp5 | 600 | 35.0 | 2.0 | 63.4 | 100.5 | $Pd_{1.01}(Bi_{0.94}Te_{0.05})_{\Sigma0.99}$ |
| Exp5 | 600 | 36.9 | 10.6 | 53.5 | 101.0 | $Pd_{1.01}(Te_{0.24}Bi_{0.75})_{\Sigma0.99}$ |
| Exp1 | 200 | 37.4 | 15.3 | 46.5 | 99.1 | $Pd_{1.01}(Te_{0.34}Bi_{0.64})_{\Sigma0.99}$ |
| Exp1 | 400 | 37.3 | 15.7 | 47.1 | 100.1 | $Pd_{1.00}(Te_{0.35}Bi_{0.65})_{\Sigma1.00}$ |
| Exp1 | 600 | 37.2 | 14.2 | 48.5 | 100.0 | $Pd_{1.01}(Te_{0.32}Bi_{0.67})_{\Sigma0.99}$ |
| Exp2 | 400 | 36.9 | 14.3 | 49.3 | 100.5 | $Pd_{1.00}(Te_{0.32}Bi_{0.68})_{\Sigma1.00}$ |
| Exp6 | 400 | 38.1 | 18.2 | 44.4 | 100.7 | $Pd_{1.00}(Te_{0.40}Bi_{0.60})_{\Sigma1.00}$ |
| Exp6 | 600 | 40.0 | 30.5 | 30.1 | 100.6 | $Pd_{0.99}(Te_{0.63}Bi_{0.38})_{\Sigma1.01}$ |
| Exp7 | 200 | 39.7 | 30.2 | 30.0 | 99.8 | $Pd_{0.99}(Te_{0.63}Bi_{0.38})_{\Sigma1.01}$ |
| Exp7 | 400 | 40.0 | 29.7 | 30.4 | 100.2 | $Pd_{1.00}(Te_{0.62}Bi_{0.39})_{\Sigma1.00}$ |
| Exp7 | 600 | 40.0 | 30.5 | 30.1 | 100.6 | $Pd_{0.99}(Te_{0.63}Bi_{0.38})_{\Sigma1.01}$ |
| Exp8 | 200 | 42.5 | 40.9 | 16.7 | 100.1 | $Pd_{1.00}(Te_{0.80}Bi_{0.20})_{\Sigma1.00}$ |
| Exp8 | 600 | 42.7 | 41.5 | 16.6 | 100.9 | $Pd_{1.00}(Te_{0.81}Bi_{0.20})_{\Sigma1.00}$ |
| Exp8 | 400 | 42.5 | 42.0 | 15.9 | 100.3 | $Pd_{0.99}(Te_{0.82}Bi_{0.19})_{\Sigma1.01}$ |

## 4 Conclusions

According to the experiments conducted during this study, sobolevskite with kotulskite seem not to form a complete solid solution at 400°C, there is a gap in the series solution at ~35 at.% Bi ($Pd_{50}Bi_{35}Te_{15}$). The end member of kotulskite solution, Bi-rich kotulskite dissolves up 35 at.% Bi, sobolevskite dissolves up to 2 at.% Te.

## References

Beaudoin G, Laurent R, Ohnenstter D (1990) First report of platinum-group minerals at Blue Lake Labrador Trough, Quebec. Can Mineral 28:409-418

Cook NJ, Ciobanu CL, Merkle RKW, Bernhardt H-J (2002) Sobolevskite, taimyrite, and Pt₂CuFe (tulameenite?) in complex massive talnakhite ore, Talnakh Orefield, Russia. Can Mineral 40:329-340

El-Boragy M, Schubert K (1971) Uber einige Varianten der NiAs-Familie in Mischungen des Palladiums mit B-Elementen. Z Metallkd 62:314-323

Evstigneeva TL, Kovalenker VA (1975) Sobolevskite, a new bismuthide of palladium, and the nomenclature of minerals of the system PdBi-PdTe-PdSb. Int Geol Rev 18:856-866

Genkin AD, Zhuravlev NN, Smirnova EM (1963) Moncheite and kotulskite – new minerals – and composition of michenerite. Zap Vses Mineral Obshchest 92:33-50

Grokhovskaya TI, Distler VV, Klynnin SF, Zakharov AA, Laputina

IP (1992) Low-sulphide platinum group mineralization of the Lukkulaisvaana pluton, northen Karelia. Int Geol Rev 34:503-520

Hoffman E, MacLean WH (1976) Phase realtions of michenerite and merenskyite in the Pd-Bi-Te system. Econ Geol 71:1461-1468

Kingston GA (1966) The occurrence of platinoid bismuthotellurides in the Merensky Reef at Rustenburg platinum mine in the western Bushveld. Miner Mag 35:815-834

Kovalenker VA, Laputina IP, Vyal`sov LN, Genkin AD, Esvtigneeva TL (1972) Tellurium minerals in copper-nickel sulfide ores at Talnakh and Oktyabr` (Noril`sk district). Int Geol Rev 15(11):1284-1294.

Tolstykh ND, Krivenko AP, Pal`chil NA, Izokh AE (1997) New Sb- and Te-containing varieties of sobolevskite PdBi. Dokl Russ Acad Sci, Earth Sci Sect 357:1145-1148

Watkinson DH, Ohnenstetter D (1992) Hydrothermal orogin of platinum-group mineralization in the Two Duck Lake intrusion, Coldwell Complex, nothwestern Ontario. Can Mineral 30:121-136

# Platinum group elements and Re minerals in the magmatic Ni-Fe-Cu sulfide deposits of the Ivrea Verbano Zone (Italy)

Federica Zaccarini, Giorgio Garuti, Peter Kollegger, Oskar A.R. Thalhammer
*Department of Applied Geological Sciences and Geophysics, University of Leoben, Austria*

Marco Fiorentini
*Centre for Exploration Targeting, ARC Centre of Excellence for Core to Crust Fluid System, The University of Western Australia, Australia*

**Abstract.**

The concentration of platinum group elements (PGE), Te, Re and the presence of specific platinum group minerals (PGM) in base metals sulfides from magmatic Ni-Fe-Cu deposits of the Ivrea Verbano Zone, Italy, have been determined by electron microprobe. The PGE were analysed in pyrrhotite, pentlandite and chalcopyrite. Several PGM, generally less than 10 µm in size, have been found included in base metals sulfides. They comprise, in decreasing order of abundance: Pd-rich melonite, merenskyite, moncheite, sperrylite and irarsite. Also a rare sufide of Re, probably rheniite, was found. Our mineralogical observations suggest that the PGE were initially dissolved and collected by an immiscible sulfide liquid probably as small clusters. Subsequently, they were exsolved along with Te and As to crystallize the discrete PGM described in the investigated samples. The precipitation of the rare Re-sulfide, which was found only in one deposit that occurs in contact with metasediments, is most likely related to contamination from the country rocks.

**Keywords. Platinum group minerals, base metals, sulfides, Ivrea Verbano Zone, Italy.**

## 1 Indroduction

The Ivrea Verbano Zone in the Western Alps of Italy represents a 120 km long and 15 km thick section across the deep root of the Adria continental plate. It mainly consists of a series of dismembered mantle lherzolites, contained within and underlying a thick igneous mafic-ultramafic rock sequence (the Basic Complex). These intrude a series of granulitic metasediments and metavolcanics (the Kinzigitic series). Magmatic Ni-Fe-Cu sulfide deposits occur in the Basic Complex associated with: 1) peridotite and pyroxenite layers in the fractionated Cyclic Units, 2) pyroxenite layers at the base of the Main Gabbro unit, 3) a 5 km long, layered Ultramafic Sill emplaced in metasediments, and 4) cross-cutting Ultramafic Pipes characterized by alkaline geochemical signature. These deposits are among the most important in the Ivrea Verbano Zone. They were an economic source of Ni in the past from 1855 to 1948, when the mining activities ceased. It can be estimated that these deposits produced a total of about 300.000 metric tons of ore of which the grade was between 1% and 0.25%. More recently, these Ni-Fe-Cu sulfide deposits have been included in a detailed exploration program for Ni, Cu, Co and PGE in the Ivrea Verbano Zone. The results of this work have been published by Suardi (1983) and by Garuti et al. (1986, 1990). According to these authors, the total PGE concentrations are variable, showing values comprised between 10 and 4500 ppb. Most of the analysed samples show enrichment in PPGE (Rh+Pt+Pd) over IPGE (Os+Ir+Ru). The deposits are believed to have formed by magmatic segregation and accumulation of an immiscible sulfide liquid which crystallized and formed a pyrrhotite-pentlandite-chalcopyrite-pyrite assemblage by on-cooling equilibration of the initial monosulfide-solid-solution ± intermediate-solid-solution (MSS ± ISS). Previous works (Garuti and Rinaldi 1986, Garuti et al. 1986, Garuti et al. 1990) have demonstrated that the immiscible sulfide liquid acted as a collector for the PGE with remarkable prevalence of Pd and Pt, carried in a suite of specific PGM.

This contribution reports the results of a detailed investigation aimed to 1) better define the mineralogical residence of the PGE and Re in the Ivrea Verbano Zone sulfide ores, 2) verify the role of base metal sulfides as carriers of these elements in magmatic systems and 3) determine PGM formation mechanisms in the investigated samples.

## 2 Methodology and analytical uncertainties

The composition of PGM and the concentration of PGE plus Re, Te, Bi, and As in PGM and base metal sulfides have been determined by electron microprobe analyses in pyrrhotite (n. = 320), pentlandite (n. = 244), chalcopyrite (n. = 100) and pyrite (n. = 31). The analysed samples represent massive sulfide with more than 75% of ore.

The quantitative analyses for trace elements in base metal sulfides were obtained using 25 kV of accelerating voltage and 30nA of beam current in 26 selected samples. The counting times were 100 and 50 seconds for the peak and backgrounds, respectively. The beam diameter was set to 1 µm. The selected conditions yielded the following detection limits (ppm): Os(Lα) = 81, Ir(Lα) = 100, Ru(Lα) = 35, Rh(Lα) = 32, Pt(Lα) = 93, Pd(Lα) = 30, Re(Mα) = 78, As(Lα) = 194, Bi(Mα) = 465, and Te(Lα) = 100. The use of the Mα-line was

possible for Re, but not for Os because of the extremely weak and floating signal. As a consequence, the interference of Cu on Os could not be avoided in the analysis of chalcopyrite. A strong, unpredicted interference by Ni on Te was also observed in the analyses of pentlandite. Ru and Bi were always below detection limit, whereas 31.9% of the analyses were found to contain As, 11.5% Os, 31.7% Ir, 20.6% Rh, 27.5% Pt, 38% Pd, 11.4% Re, and 7.9% Te. The PGM were investigated and analysed in about 300 polished sections, about 4 cm$^2$ each, using the procedure described by Zaccarini et al. (2011).

## 3 PGE and Re minerals

More than 250 PGM were found in all the type of ore deposits, except from the Ultramafic Sill. However, in one section from this deposit, two grains composed of Re and S were semi-quantitatively analysed. Probably their composition corresponds to the rare mineral rheniite (ReS$_2$), previously described in fumaroles of Kudryavy volcano (Znamensky et al. 2005), in porphyry-type Pagoni Rachi system (Voudouris et al. 2009) and in sediments from eastern Canada lakes (Chappaz et al. 2008). The Re-sulfide grains are very small in size (less than 3 microns in size) and occur included in pyrrhotite (Fig. 1).
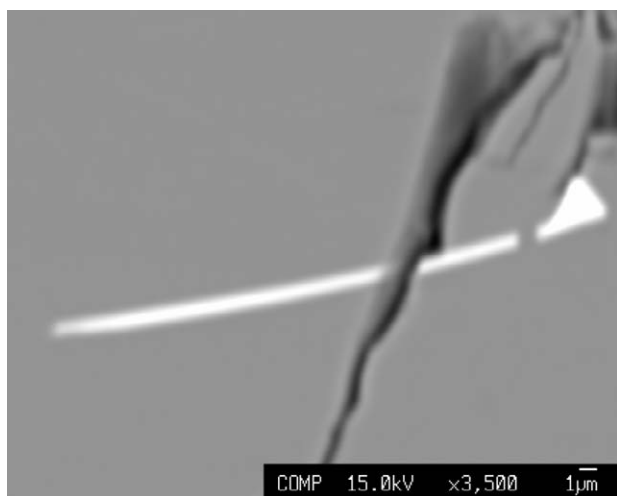


**Figure 1.** BSE image of the Re-sulfide included in pyrrhotite, from the Ultramafic Sill.

Confirming the previous observation of Garuti and Rinaldi (1986), the PGM mineralogy is dominated by the tellurides of the melonite-merenskyite-moncheite serie, accompanied by rare sperrylite and irarsite. The PGM have a size comprised between 3 and 40 microns. They are found included in, or in contact with, the sulfide (no PGM was found as free grains in the silicate gangue), indicating their origin to be related to the crystallization of this phase. (Fig. 2).
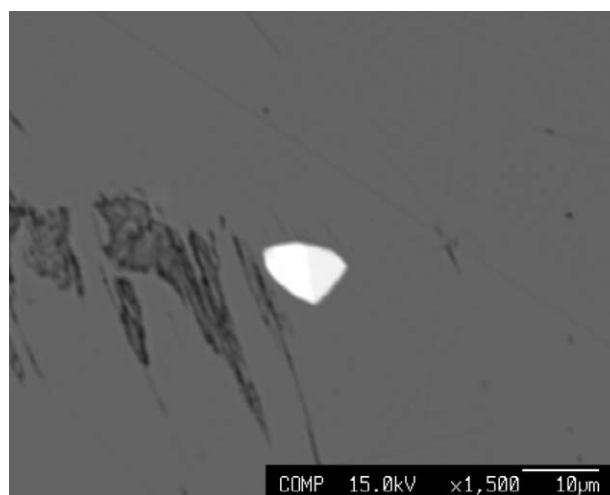


**Figure 2.** BSE image of a PGM composed of merenskyite and moncheite included in pyrrhotite from an Ultramafic Pipe.

In Figure 3, the frequency of PGM occurring as inclusions in each sulfide phase, pyrrhotite, pentlandite, chalcopyrite and pyrite, is compared with the average modal-percentage of these sulfide minerals in the ores. As shown in the graph, chalcopyrite and pyrite are comparatively more common as host-phases of PGM than pyrrhotite and pentlandite.
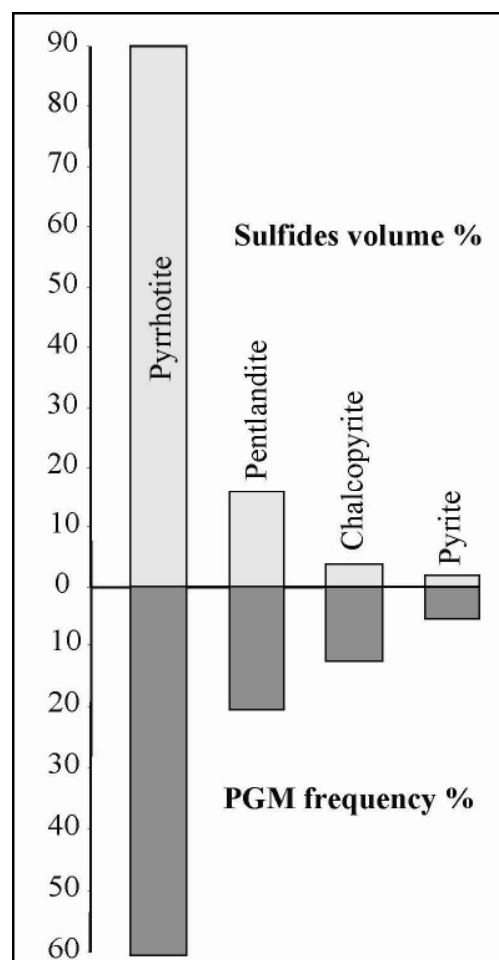


**Figure 3.** Frequency of detected PGM in comparison to the modal abundance of specific sulphide phases in the ore. (Calculation based on 207 grains).

The analysed Ni-Pd-Pt tellurides have been plotted, as atomic %, in the melonite-merenskyite-moncheite ternary diagram (Fig. 4). Their chemical composition indicates the existence of an almost complete solid solution between melonite and merenskyite and a more limited one between merenskyite and moncheite. Moncheite was analysed only in samples from the mine hosted in the Main Gabbro and it shows variable contents of Pd and Ni. In the pipes, melonite is the most common PGE-bearing phase and contains appreciable amounts of Pd and Pt.

# 4 Distribution of PGE, Re and other trace elements in the BMS

The total concentration of PGE is relatively higher in pentlandite (639 ppm) and pyrrhotite (606 ppm), and decreases in pyrite (519 ppm) and chalcopyrite (176 ppm). Distribution of the analysed elements in the four sulfide minerals indicates that Os was detected only in pyrrhotite and pentlandite, with maximum concentration in the deposits of the Cyclic Units. Iridium and Pt are carried in pentlandite, pyrrhotite, and pyrite, but are absent or below detection limit in chalcopyrite. The highest concentrations are found in the Main Gabbro, and the Ultramafic Pipes. Palladium and Rh occur in all the sulfide minerals. However, Pd is mainly hosted by chalcopyrite of the Cyclic Units. The highest Rh concentration is observed in pyrite of the Main Gabbro. Rhenium is particularly abundant in chalcopyrite and pyrite of the Ultramafic Pipes, and it shows a marked positive anomaly in the pyrrhotite of the Cyclic Units.
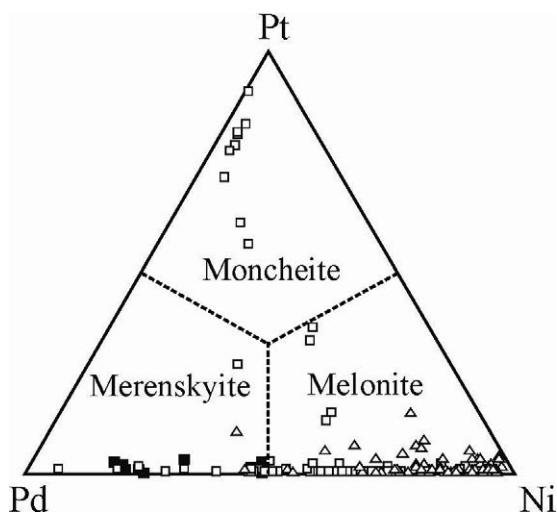


**Figure 4.** Composition (at %) of merenskyite-moncheite-melonite from the Ivrea Verbano Zone sulfide ores. Triangle = Pipes, open square = Main Gabbro, filled square = Cyclic Units

Surprisingly, the lowest Re concentration is observed in pyrrhotite of the Ultramafic Sill, where the Re-sulfide was encountered. The relatively higher abundance of Pd, Re, and Te in chalcopyrite compared with the other sulfide minerals may indicate that these elements possibly concentrated in a late stage of the MSS ± ISS crystallization.
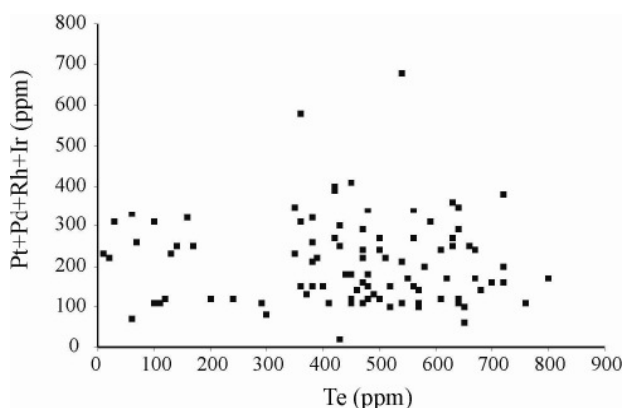
The lack of correlation between the abundance of analysed PGE and Te in the analyses of the major sulfides suggests (Fig. 5) that the spot PGE anomalies are not due to the interception of PGM tellurides under surface, but that PGE occur, probably, as native elements in the sulfide.

# 5 Discussion and conclusion

According to the model proposed by Campbell and Naldrett (1979), the collection of PGE, especially Pt and Pd, by an immiscible sulfide liquid is mainly controlled by the fact that the PGE are highly chalcophile ($D_{PGE}>10^5$). This study has shown that the PGE may occur as traces in solid solution in the BMS and/or form discrete PGM such as tellurides, sulfarsenide and arsenide. These observations suggest that the PGE together with other chalcogens were initially dissolved by an immiscible sulfide liquid at high temperature, and they were subsequently collected as small randomly distributed clusters (Tredoux et al., 1995). This assumption is supported by the heterogeneous distribution of PGE within the same base metal sulfides grains. Therefore, during the magmatic stage, the PGE in the investigated samples behaved as chalcophile elements. Subsequently, they prefer to link with Te and As to crystallize the abundant discrete PGE tellurides such as moncheite, merenskyite and Pd-Pt rich melonite as well as the less abundant arsenides and sulfarsenides (sperrylite and irarsite). However, the crystallization mechanism of PGE tellurides, arsenides and sulfarsenides from an immiscible sulfide liquid is not yet fully understood. On the basis of natural and experimental data, it has been argued that many natural PGE bearing tellurides associated with sulfide may be meta-stable, i.e. modified by low temperature exsolution of a Ni-Te component from the coexisting high-temperature sulfides (Cabri and Laflamme 1976, Helmy et al. 2007, Hutchinson and McDonald 2008). Arsenic also played an important role on PGE collection, since it may form stable high temperature phases such as sperrylite and irarsite.

Our mineralogical results are in agreement with these mechanisms of PGM formation. Therefore, we put forward the hypothesis that arsenides and sulfarsenides precipitate at high temperature, whereas a telluride melt exsolved from the immiscible sulfide liquid scavenging Pt and Pd from the original sulfide melt to crystallize PGE tellurides. The rare Re sulfide was found only in one deposit that occur in contact with metasediments. Therefore, we argue that its precipitation is probably related to contamination from the country rocks during the emplacement of the magma.

Despite of the fact that some samples of the Ni-Fe-Cu sulfide deposits of the Ivrea Verbano Zone are enriched in PGE (up to 4500 ppb), these deposits can be considered only a future potential source for these noble metals. This is due to the fact that the PGE enrichment occurs sporadically and the limited amount of ore reserves.

**Figure 5.** Binary diagram showing the correlation between Te and the analysed PGE.

## References

Cabri JL, LaFlamme JHG (1976) Mineralogy of the platinum group elements from some copper-nickel deposits of the Sudbury area, Ontario. Econ Geol 71:1159-1195.

Campbell IH, Naldrett AJ (1979) The influence of silicate silicate-sulphide ratios on the geochemistry of magmatic sulphides. Econ Geol 74:1503-1505

Chappaz A, Gobeil C, Tessier A 2008 Sequestration mechanism and anthropogenic inputs of rhenium in sediments from Eastern Canada lakes. Geochim. Cosmochim. Acta 72: 6027-6036

Garuti G, Rinaldi R (1986) Melonite-Group and other Tellurides from the IvreaVerbano Basic Complex, Western Italian Alps. Econom Geol 81:1213- 1217

Garuti G, Fiandri P, Rossi A (1986) Sulfide composition and phase relations in the Fe-Ni-Cu ore deposits of the Ivrea Verbano basic complex (Western Alps, Italy). Mineral Deposita 21: 22-34

Garuti G, Naldrett AJ, Ferrario A (1990) Platinum- Group Elements in Magmatic Sulfides from the Ivrea Zone: Their Control by Sulfide Assimilation and Silicate Fractionantion. Econom Geol 85: 328-336

Helmy HM, Ballhaus C, Berndt J, Brockrath C, Wohlgemuth-Ueberwasser C (2007) Formation of Pt, Pd and Ni tellurides: experiments in sulfide-tellurides systems. Contr. Mineral Petrol 153:577-591

Holwell DD, McDonald I (2007) Distribution of platinum-group elements in the Platreef at Overysel, northern Bushveld Complex: a combined PGM and LA-ICP-MS study. Contrib. Mineral Petrol 154:171-190

Suardi M (1983) I risultati della ricerca geomineraria della Zona Ivrea Verbano (Piemonte). Relazione RIMIN, Ind. Miner. 2:1-14

Tredoux M, Lindsay NM, Davies G, McDonald I (1995) The fractionation of platinum-group elements in magmatic system, with the suggestion of a novel causal mechanism. S Afr J Geol 98:157-167

Voudouris PC, Melfos V, Spry PG, Bindi L, Kartal T, Arikas K, Moritz R, Ortell M (2009) Rhenium-rich molybdenite and rheniite in the Pagoni Rachi Mo–Cu–Te–Ag–Au prospect, northern Greece: implications for the Re geochemistry of porphyry-style Cu–Mo and Mo mineralization. Can Mineral 47: 1013-1036

Zaccarini F, Garuti G, Pushkarev E (2011) Unusually PGE-rich chromitite in the Butyrin vein of the Kytlym Uralian-Alaskan-type complex, northern Urals, Russia. Can Min 49:1413-1431

Znamensky VS, Korzhinsky MA, Steinberg GS, Tkachenko SI, Yakushev AI, Laputina IP, Bryzgalov IA, Samotoin ND, Magazina LO, Kuzmina OV, Organova NI, Rassulov VA, Chaplygin IV (2005 Rheniite ReS2, a natural rhenium bisulfide from fumaroles of Kudryavy volcano, Iturup Isl., Kurile Islands. Zap Ross Mineral Obsestva 134:32-40

# Potarite (PdHg) and Pt-Fe-Cu-Ni alloys from chromitites of Eikland Mountain, SW Yukon, Canada

**Federica Zaccarini, Giorgio Garuti**
*Department of Applied Geological Sciences and Geophysics, University of Leoben, Austria*

**Monica Escayola**
*IDEAN-CONICET, University of Buenos Aires, Argentina*

**Thomas Aiglsperger, Joaquin A. Proenza**
*Department of Crystallography, Mineralogy and Ore Deposits, University of Barcelona, Spain*

**Donald C. Murphy**
*Yukon Geological Survey, Whitehorse, Canada*

**Abstract.** Eikland Mountain chromitites, located in SW Yukon, Canada, comprise small layers and schlieren associated with almost fresh mantle peridotites. They have an homogeneous composition (#Cr 0.54 and $TiO_2$ up to 0.62 wt%) and display an enrichment in PGE (2.4 ppm), especially in Rh+Pt+Pd. The following PGM have been found, accounting for these geochemical data: potarite, alloys in system Pt-Fe-Cu-Ni and rare sperrylite and irarsite. The PGM occur solely in the silicate matrix, in contact with the chromite grains, pentlandite and awaruite. These data suggest that the Eikland Mountain chromitites have no affinity with Uralian-Alaskan type complexes and therefore may not be considered the source of PGM nuggets previously reported from Yukon placer deposits. The investigated PGM probably crystallized because of the presence of alkaline-rich magmatic fluids.

**Keywords. Potarite, Pt-Fe-Cu-Ni alloys, chromitites, Yukon, Canada.**

## 1 Indroduction

In recent years, the SW portion of the Yukon (Canada) has attracted the interest of the economic geologists because of occurrences of platinum group minerals (PGM) in placer deposits (Barkov et al. 2008, Fedortchouk and LeBarge 2008, Fedortchouk et al. 2010). Using their mineralogical observations, these authors proposed an Uralian-Alaskan type complex as the possible source for the Yukon PGM nuggets. However, data available on PGM from lode deposits of Yukon are limited (Escayola et al. 2012).

In this contribution we report a detailed mineralogical study on PGM in chromitites recently discovered on Eikland Mountain, SW Yukon, Canada (Escayola et al., 2012). The PGM were investigated in situ on polished sections and on concentrates obtained using hydroseparation technique (Cabri et al. 2006, Aiglsperger et al. 2011, Aiglsperger et al. 2012), and analysed by electron microprobe.

The data are used to verify if Eikland chromitites can be the considered a possible source of the PGM nuggets previously described in the Yukon placer deposits (Barkov et al. 2008, Fedortchouk and LeBarge 2008, Fedortchouk et al. 2010) and to discuss the genesis of

the unusual PGM assemblages presented in this contribution.

## 2 The Eikland Mountain chromitite

The investigated chromitites are hosted in almost fresh mantle peridotite, composed of 60% dunite and 40% harzburgite. They form narrow layers and schlieren of massive ore, with a lateral extension varying from 1 to 5 meters and with a maximum thickness of 15 cm (Fig. 1).
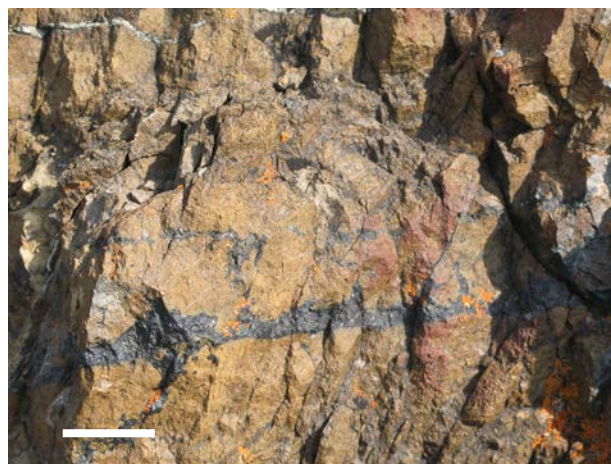


**Figure 1.** Outcrop photograph of the Eikland Mountain chromitites (black veins and schlieren) in sheared dunite. Scale bar = 10 cm.

The chromitites are composed of euhedral to sub euhedral grains of chromite with a size ranging between 0.5 to 5 mm. The chromite crystals are completely fresh and show triple junctions among large grains, thus indicating a magmatic origin.

The matrix is composed mainly of olivine and minor pentlandite with rare awaruite and magnetite. Primary inclusions of calcite, rutile, Na-amphibole and albite have been found.

The composition of chromite is homogenous with a #Cr of about 0.45 and $TiO_2$ between 0.41-0.62 wt%. The total PGE content is relatively high (up to 2.4 ppm) with an enrichment of Rh+Pt+Pd over Os+Ir+Ru (Escayola et al. 2012).

## 3 PGM in the Eikland chromitite

Consistent with the geochemical data, the most abundant PGM discovered in situ and in the concentrates are potarite (ideally PdHg) and alloys in the system Pt-Fe-Cu-Ni with rare sperrylite (ideally PtAs$_2$) and irarsite (ideally IrAsS). The PGM, as shown by the in situ investigation, are never found as inclusions in chromite, but always occur in the matrix, commonly in contact with pentlandite (Fig. 2) and awaruite.
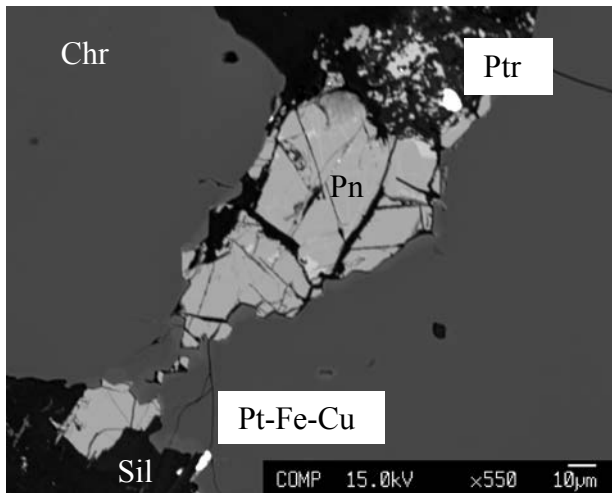


**Figure 2.** Electronic image of potarite (Ptr) and Pt-Fe-Cu alloy Pt-Fe-Cu in contact with pentlandite (Pn), chromite (Chr) and silicates (Sil).

The size of the PGM found in situ varies from 2 to 8 microns, whereas those discovered in the concentrates are bigger (up to 50 microns), as shown in Fig. 3. Therefore, most of the in situ PGM were only qualitatively analysed. The most reliable quantitative analyses were mainly obtained on the bigger PGM from the concentrates.

The compositions of the analysed potarite grains has been plotted in the ternary diagram of Fig. 4 and compared with selected literature data. This diagram shows that the Yukon potarite deviates from ideal stoichiometry, being enriched in Fe. Such a prominent deviation was also reported in potarite from the Butyrin vein of the Kyltym Uralian-Alaskan type complex of the Urals (Zaccarini et al. 2011).

However, the Eikland Mountain chromitite-hosted potarite shows an enrichment in Fe over Cu, whereas the Cu content is higher than that of Fe in the Butyrin vein potarite.

Several alloys containing Pt, Fe and Cu as the major constituent have been also analysed. Their composition has been plotted in Fig. 5, showing that most of the analysed alloys can be classified as tulameenite and isoferroplatinum.
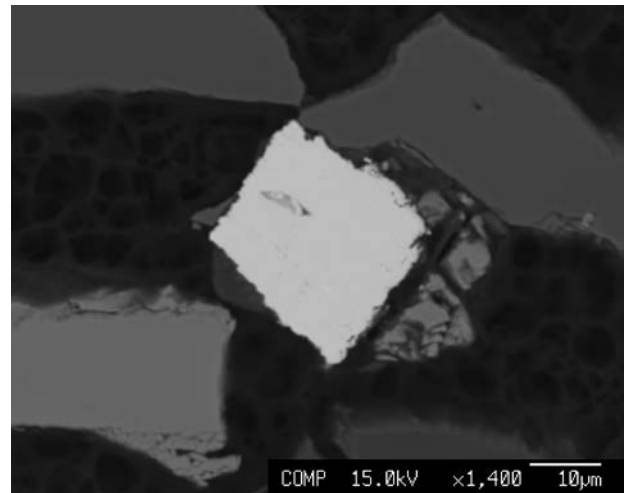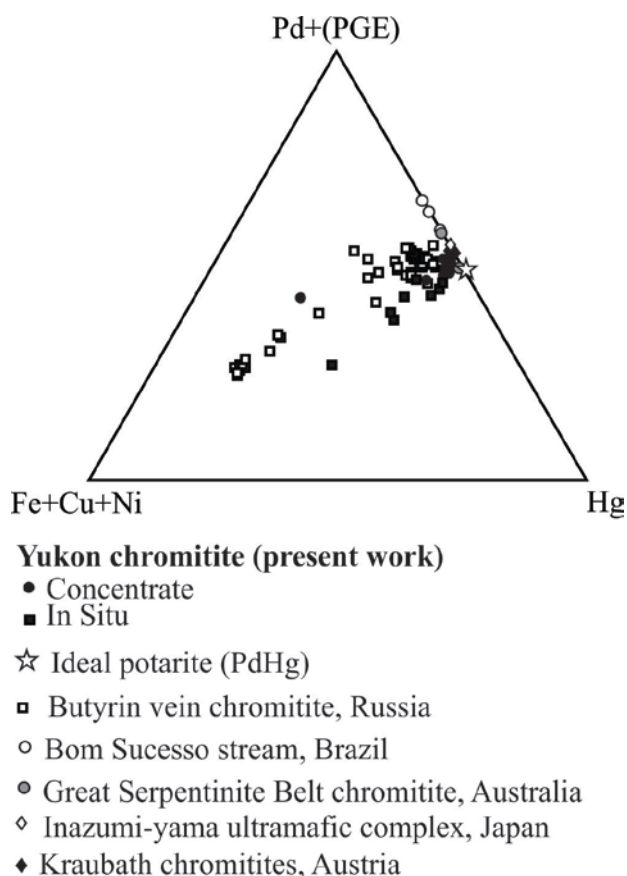


**Figure 3.** Electronic image of Pt-Fe-Cu alloy (white grain) from concentrates.
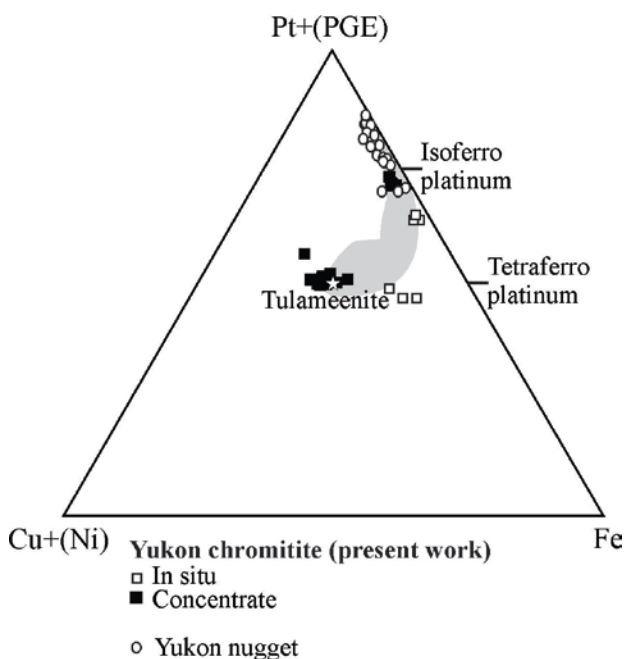
## 4 The Eikland chromitite-hosted PGM versus the Yukon nugget PGM

The mineral assemblage of PGM nuggets, despite of the fact that they can be altered and reworked in the sedimentary environment, can provide useful information concerning their lode deposits. In particular, recent investigations have demonstrated that Ru-Os-Ir minerals are typical for placers formed by the erosion of ultramafic rocks associated with ophiolite complexes. Alloys in the Pt-Fe-Cu-Ni and Os-Ir-Ru systems are the most abundant nuggets related to the presence of Uralian-Alaskan type lode deposits (Fedortchouk et al. 2010 and references therein). PGM nuggets have been reported from four placer deposits in SW Yukon, namely Burwash Creek, Florence Creek, Arch Creek and Canadian Creek (Barkov et al. 2008, Fedortchouk et al. 2010). These authors described abundant Pt-Fe-Cu-Ni alloys, containing a great variety of inclusions of other PGM, such as bowieite, kashinite, miassite, cooperite, vasilite, keithconnite and an unnamed Pd-Te-S phase. On the basis of this PGM association, the authors further suggested a Uralian-Alaskan type complex as their primary source (Barkov et al. 2008, Fedortchouk and LeBarge 2008, Fedortchouk et al. 2010).

In contrast, the PGM found in the Eikland chromitites are characterized by a relatively simple assemblage of potarite, alloys of Pt-Fe-Cu.Ni with rare sperrylite and irariste. Furthermore, the compositions of Pt-Fe-Cu-Ni alloys in the Eikland chromitites are different from those reported for Uralian-Alaskan type chromitites in the Urals as well as from those analysed in the PGM nuggets in Yukon placer deposits by Barkov et al. 2008 and Fedortchouk et al. 2010 (Fig. 5).

Pd+(PGE)

Fe+Cu+Ni

Hg

**Yukon chromitite (present work)**
● Concentrate
■ In Situ

☆ Ideal potarite (PdHg)

□ Butyrin vein chromitite, Russia

○ Bom Sucesso stream, Brazil

◉ Great Serpentinite Belt chromitite, Australia

◇ Inazumi-yama ultramafic complex, Japan

♦ Kraubath chromitites, Austria

**Figure 4.** Compositions of potarite (at.%) in Eikland Mountain chromitites. Compositional data from the literature and ideal composition of potarite are shown for comparison (modified after Zaccarini et al. 2011).



Pt+(PGE)

Isoferro platinum

Tetraferro platinum

Tulameenite

Cu+(Ni)

Fe

**Yukon chromitite (present work)**
□ In situ
■ Concentrate

○ Yukon nugget

**Figure 5.** Compositions of Pt-Fe-Ni-Cu alloys (at.%) in Eikland Mountain chromitites. Compositional data from PGM nuggets from Yukon placer deposits are shown for comparison. Gray field = PGM in Uralian-Alaskan type chromitites of the Urals (data source: Garuti et al. 2002, Barkov et al. 2008, Fedortchouk et al. 2010).

## 5  Concluding remarks

On the basis of the mineralogical data presented in this contribution, the following conclusions can be drawn:

1) by combining a traditional mineralogical investigation of in situ grains with an investigation of grains separated using the hydroseparation technique, a fuller and more comprehensive investigation of heavy minerals, such as PGM in the Eikland chromitites is achieved.

2) The PGM assemblage found in the Eikland Mountain chromitites, as well as their composition and PGE distribution, are not consistent with an Uralian-Alaskan type intrusion.

3) As a consequence, the Eikland chromitites probably cannot be considered the primary source of the PGM nuggets found in Burwash Creek and Florence Creek of Yukon.

4) The PGM assemblage as well as the accessory minerals in the Eikland Mountain chromitites suggest that the chromitites crystallized under the influence of alkaline-rich magmatic fluids.

## Acknowledgements

## References

Aiglsperger T, Proenza JA, Zaccarini F, Labrador M, Navarro-Ciuriana D (2010) Looking for needles in a haystack: how to find PGM in laterites by using hydroseparation technique. Macla 15:23-24

Aiglsperger T, Proenza JA, Escayola M, Zaccarini F, Garuti G, Murphy D, Van Staal C (2012) Chromitites from Eikland Mountain, Yukon: a potential source for platinum placers of SW Canada? Macla 16:200-201

Barkov AY, Martin RF, LaBarge W, Fedortchouk Y (2008) Grains of Pt-Fe alloy and inclusions in a Pt-Fe alloy from Florence Creek, Yukon, Canada: evidence for mobility of Os in a Na-$H_2O$-Cl-rich fluid. Can Min 46:343-360

Cabri LJ, Rudashevsky NS, Rudashevsky VN, Lastra R (2006) Hydroseparation: a new development in process mineralogy of platinum-bearing ores. CIM bull 99:1-7

Escayola M, Murphy DC, Garuti G,  T, Zaccarini F, Proenza JA, Aiglsperger T, Van Staal C (2012) First finding of Pt-Pd-rich chromitite and platinum-group element mineralization in southwest Yukon mantle peridotite complexes. Yukon Geol. Survery open file 12:28p

Fedortchouk Y, LaBarge W (2008) Sources of placer platinum in Yukon: provenance study from detrital minerals. Can J Earth Sci 45:879-896

Fedortchouk Y, LaBarge W, Barkov AY, Fedele L, Bodnar RJ, Martin RF, (2010) Platinum-group minerals from a placer deposit in Burwash Creek, Kluane area, Yukon Territory, Canada. Can Min 48:583-596

Garuti G, Pushkarev E, Zaccarini F (2002) Composition and paragenesis of Pt alloys from chromitites of the Uralian-

Alaskan-type Kytlym and Uktus complexes northern and central Urals, Russia (2002) Can Min 40:357-376

Zaccarini F, Garuti G, Pushkarev E (2011) Unusually PGE-rich chromitite in the Butyrin vein of the Kytlym Uralian-Alaskan-type complex, northern Urals, Russia. Can Min 49:1413-1431

S 2.6
# New advances in geochemical exploration

Convenors:
Pertti Sarala & Robert Hough

# Hydrogeochemistry and other "aqueous phase" media for deep geological sensing in mineral exploration

**David J. Gray, Nathan Reid & Ryan R.P. Noble**
*CSIRO Earth Science and Resource Engineering, Kensington, Western Australia, Australia.*

**Abstract.** Groundwater sampling can represent a cost effective method for regional and prospect scale geochemical exploration. Though sampling methodology is different, as a media it is conceptually similar to partial extractions and biota sampling. Thus, it offers many of the advantages of these methods such as high signal-to-noise, as well as issues such as batch and detection limit concerns. However, groundwaters have demonstrated capacity for deep geological sensing (> 100m) in specific environments, as well as sensitivity to faults and other geological structures. This paper primarily discusses the utility of groundwater for exploration, with some generic ideas for geochemical exploration

**Keywords.**
Geochemical Exploration, groundwater, Aqueous Geochemistry

## 1 "Aqueous Phase" Exploration Methods

Despite some differences, groundwater, biota and selective extraction methods can conceptually be classed together. These techniques all involve dissolution of target elements into an aqueous phase, be they water, a biologically active fluid, or a chemical extractant in the field or laboratory. All these technologies are being actively investigated worldwide, for their potential to add value to "standard" geochemical and geophysical techniques.

This study will concentrate on the utility of groundwater, although many of the issues are common for all these techniques. Understanding robustness and comparative utility is essential, as the usefulness on individual techniques will vary depending on area, lithology and geomorphology.

## 2 Exploration Issues

### 2.1 Not Another Traverse!
Numerous case studies for surface exploration methods show several down to one traverse(s) of a few hundred metres across a mineralised zone, with varying depths of non-mineralised cover. Measures of success could include an apical, "rabbit ear" or other shaped anomaly. The number of acceptable technical successes and potential for various natural (e.g., surface flow) or anthropogenic (e.g., drilling dust) means that "positive" results should be treated with scepticism.

Even if successful, this does not represent a direct exploration technique, as these technologies are more likely to add value for area selection or drilling targeting than for orebody resolution. As such, it is necessary that data values are "stand-alone", requiring good background data for differing rock types and geomorphological environments, and that batch-effects be minor, relative to thresholds. Good meta-data is essential to the success of any exploration method.

### 2.2 Scale
Mineral systems concentrate various elements in particular zones and at various scales. For aqueous phase media, this is further complicated by the differing mobilities of various elements depending on the environment. In acidic groundwater environments, base metals may be highly mobile and give consistent haloes, although there is also a high background concentrations due to acid attack on country rocks. In neutral groundwater environments, base metals commonly have low mobilities and oxy-anions (Mo, W, As) give larger and more consistent haloes.

At close scales (100 m spacing) sulfide ore bodies are clearly delineated by anomalous dissolved sulfate. Commonly this is enrichment due to sulfides fully oxidising, e.g.:

$$2FeS_2 + 3\frac{1}{2}O_2 + 7H_2O \rightarrow 2Fe(OH)_3 + 4SO_4^{2-} + 8H^+$$
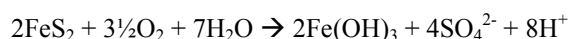
Although in deeper groundwaters and/or eroded terrains (see below), the anomaly could have <u>depleted dissolved</u> sulfate levels, e.g.:

$$5FeS + SO_4^{2-} + 2H_2O + 2H^+ \rightarrow 3FeS_2 + 2Fe(OH)_3$$
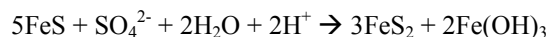
By relating sulfate to conservative elements such as Cl or Br, a sulfate index can be calculated (Figure 1). At <500m scales, sulfate index anomalism can delineate sulfides.
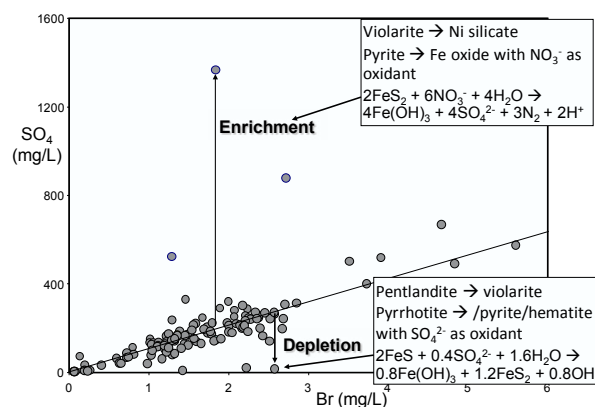


**Figure 1.** Dissolved sulfate vs Br for groundwaters from Ni sulfide ore bodies.

At the regional scale this effect is diluted. However, the similarly calculated S indices will pick up fluid mixing (Figure 2), and particularly the upwelling of deeper groundwater through fault systems.
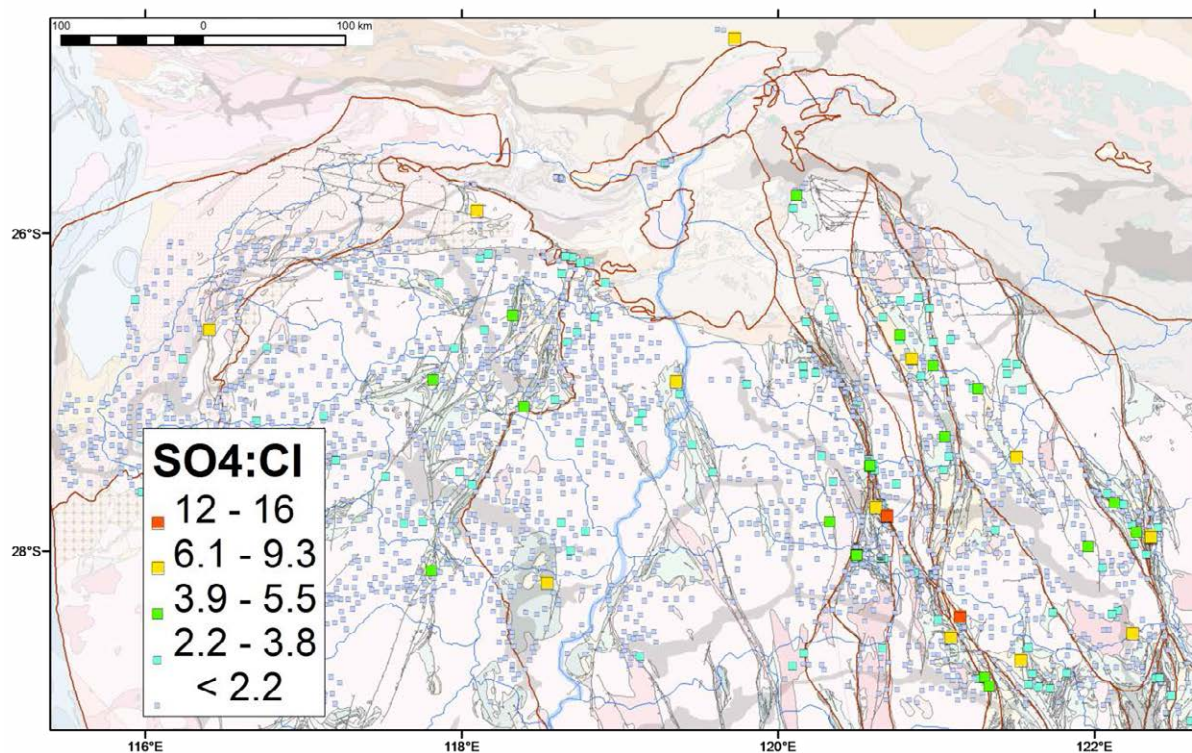
**Figure 2.** Dissolved sulfate enrichment (relative to Cl) for groundwaters from the northern Yilgarn Craton. Brown lines represent major crustal domain boundaries (Cassidy et al., 2006).
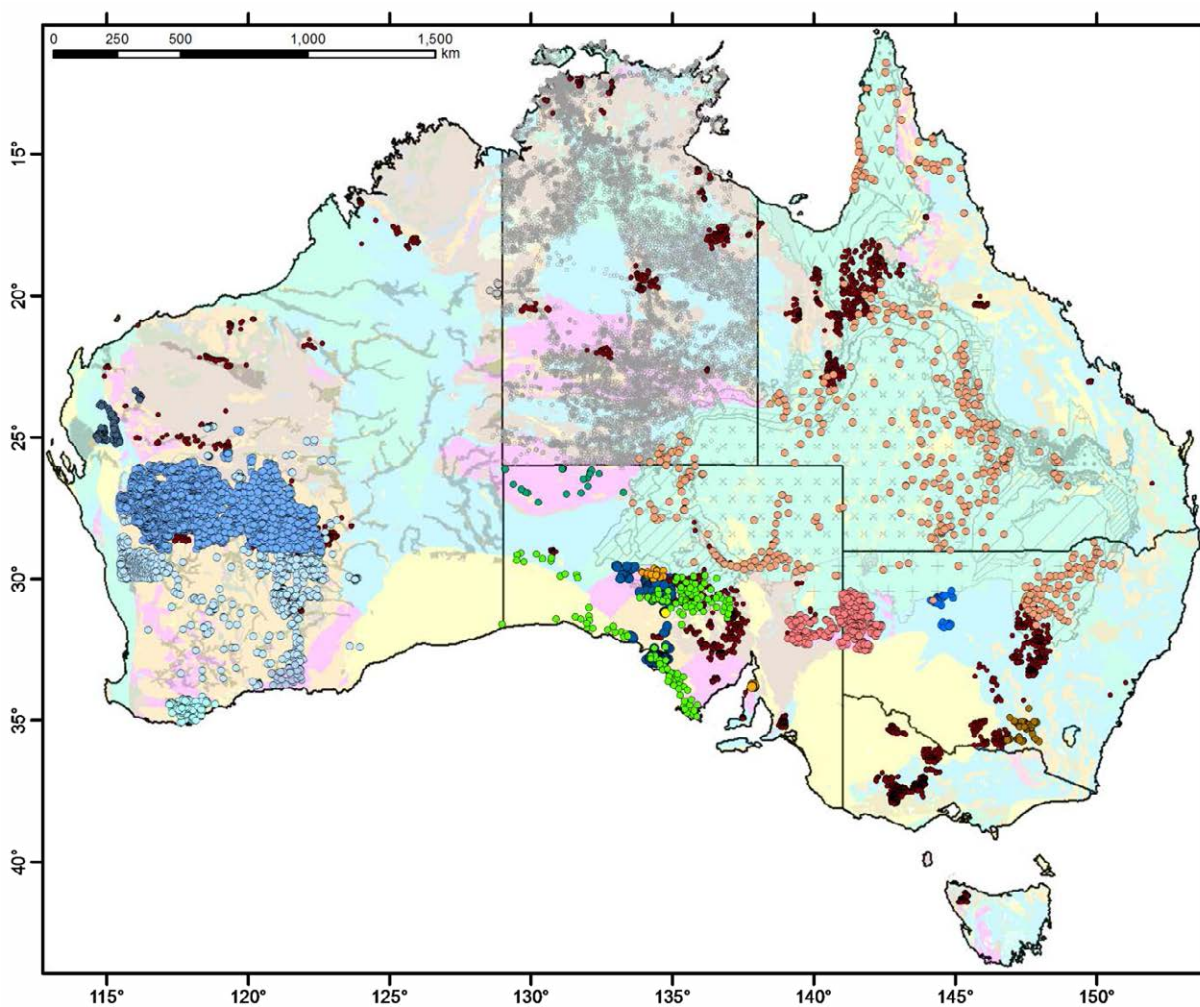


**Figure 3.** Groundwater data partially or wholly processed for incorporation into Continental-scale Hydrogeochemistry database.

## 2.3 Sampling terrain

Despite previous assertions, sample type and geomorphology can have a very strong effect on aqueous phase anomalies. Floodplain soils can give strong soil extraction anomalism, which can mimic buried mineralisation anomalism. Plants show much stronger base metal anomalism in eroded vs covered or deeply weathered terrains. In some terrains, particularly in southern regions of Australia (e.g., the southern half of the Yilgarn Craton), the upper 20 m of the water column can be 3 pH units lower than deeper groundwaters. In such a situation mapping results for both shallow and deeper groundwaters will show highly erroneous spatial patterns.

## 2.4 Contamination

"Aqueous phase" extractions are generally only a small proportion of the various total element concentrations in the original rock. Therefore, they are very sensitive to contamination sources, such as:

- Organic and other contaminants falling into groundwater bores;
- Drilling muds and additives
- Wind-blown soil or, more critically, drilling dust on plant surfaces
- Colluvial and/or alluvial mixing in soils from mineralised areas upgradient
- Drill-spoil contamination of soil

These contamination sources may not be readily observable. Site understanding and/or contamination indices are essential

## 3 Case Studies

### 3.1 Continental-Scale Hydrogeochemistry

Various Craton- or State-based regional groundwater projects and some of the indices developed for interpretation at the Terrain-scale are discussed by Reid et al. (2013) in this compilation. However, interpreting this data at the continental scale (Figure 3) requires resolving issues related to differing analytical quality, and sometimes differing sampling and analytical methods. At this level, this will enable discrimination of utility of these methods for varying terranes, from very acid/saline in the southern periphery of the continent, mostly fresh and neutral in the western 2/3, and sulfate-poor in the artesian dominated system of the NE (Figure 4). In each case, it is likely that totally different element suites and indices will be valuable for exploration.
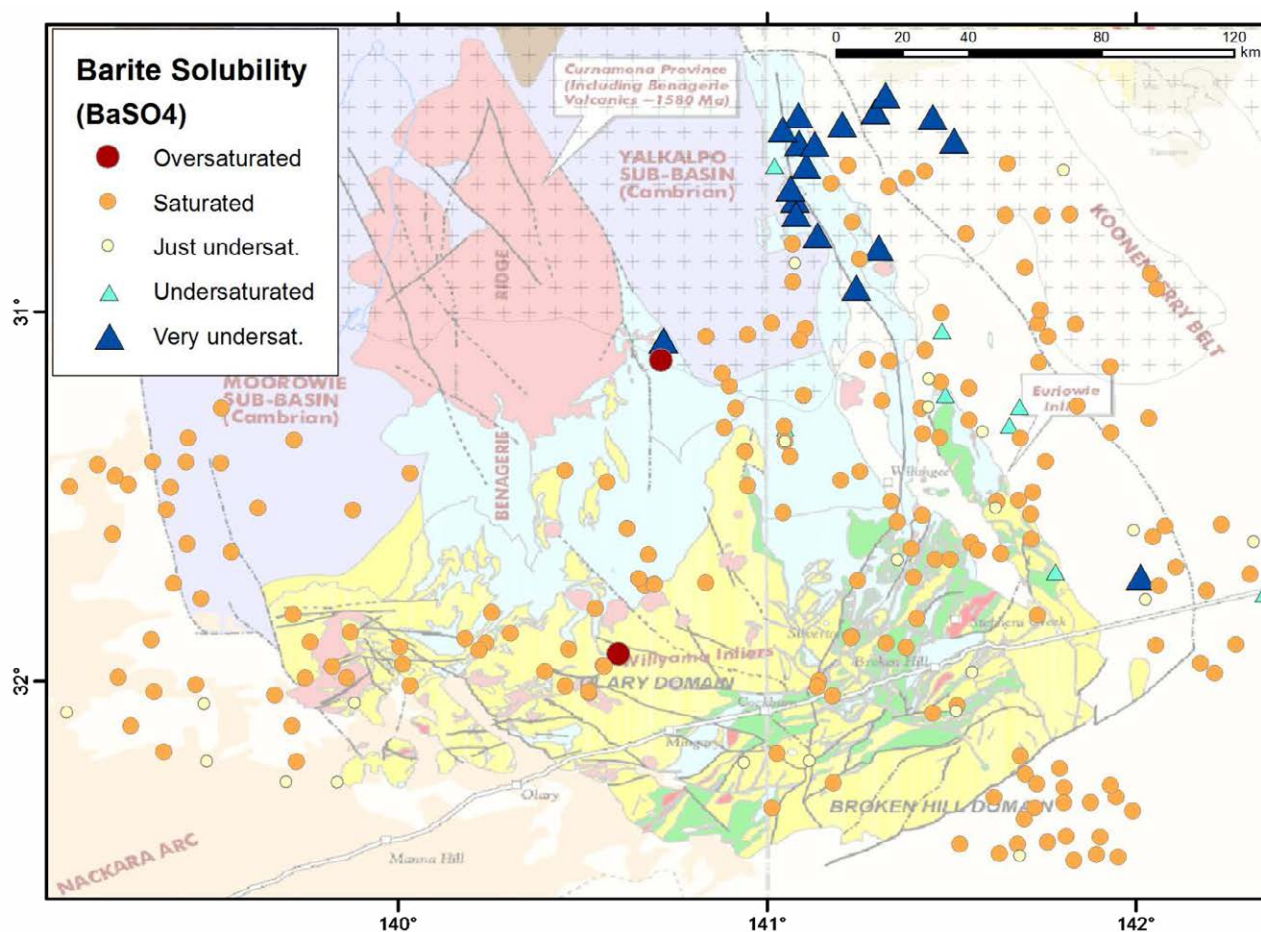


**Figure 4.** Spatial variation in barite solubility, indicating abrupt change from sulfate-poor barite undersaturated groundwaters from the Great Artesian Basin (stippled area), and sulfate-rich barite saturated groundwaters within the Curnamona Domain.

## 3.2 Terrain-Scale Hydrogeochemistry

Various examples of Terrain-scale hydrogeochemistry are given in Reid et al. (2013). At this scale, specific indices have value in delineating large scale lithological discrimination, and major mineral camps. Such a broad-scale approach does obscure camp scale-variation but does delineate major features. At this scale, major hydrothermal systems such as at the Agnew and Granny Smith Gold camps are observed. Other large systems, such as IOCG's or Cu Porphyries may also be observable.

## 3.3 Prospect-Scale Hydrogeochemistry

At this scale, indicator elements (e.g., Au, Ni, Cu, Zn, W, As) as commonly valuable. Geochemical Indices are developed for specific commodities, such as the AuMin (Figure 5) or NiS index (Figure 6). Combined with geophysics (e.g., magnetic, gravity, EM), this may assist in selecting drilling targets.
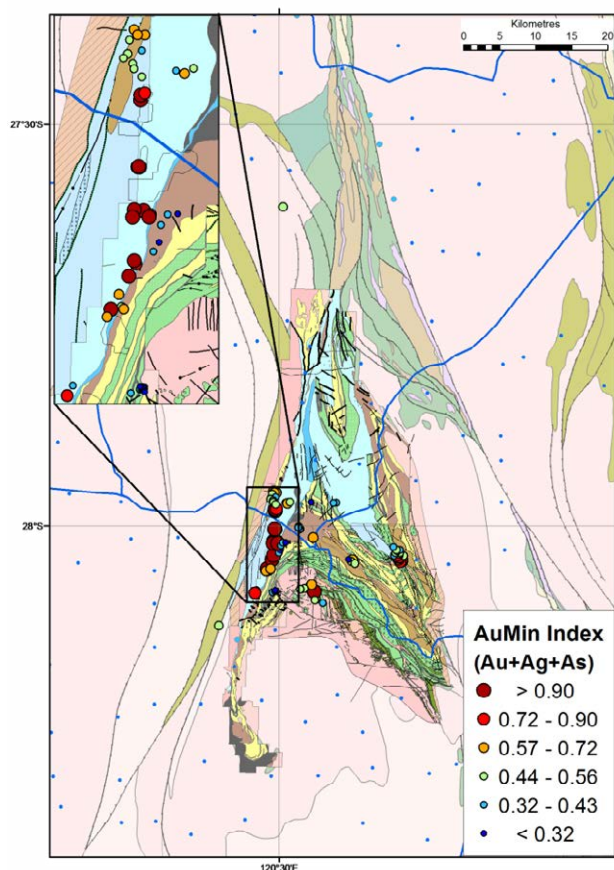


**Figure 5.** Spatial variation in AuMin Index (Au,Ag,As) in the Agnew region. AuMin values above 0.9 represent anomalism greater than for any of the regional samples.
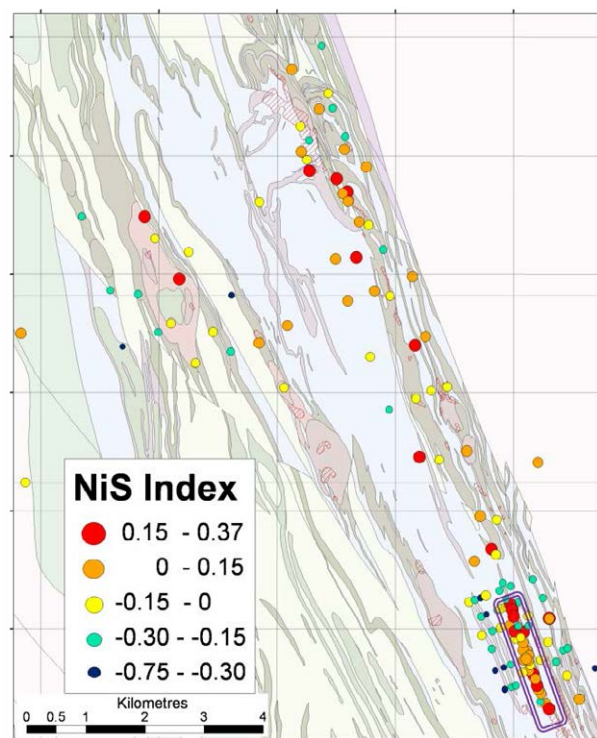


**Figure 6.** Spatial variation in NiS Index in the Harmony region (directly north of Leinster), exactly delineating the Harmony ore body (double purple line), and the line of potential mineralisation to the NNW.

## 4 Conclusion

Aqueous phase methods such as hydrogeochemistry have difficulties and advantages as exploration media. However, if combined with robust understanding of environmental factors, rock weathering and good quality analytical chemistry, these techniques can positively assist exploration at varying scales. This is particularly so when combined with robust geological modelling and geophysics. Continuing research and interaction with explorers should contribute to the next phase of economic mineral deposit discovery.

## Acknowledgements

## References

Cassidy, K.F., Champion, D.C., Krapez, B., Barley, M.E., Brown, S.J.A., Blewett, R.S., Groenewald, P.B. and Tyler, I.M. (2006). A revised geological framework of the Yilgarn Craton, Western Australia. Western Australia Geological Survey Record 2006/8. 8 p.

Reid, N., Gray, D and Noble, R (2013). Regional Hydrogeo-chemistry for Mineral Exploration in Australia. This Volume.

# Re-examination of the Broken Hill gossan: applications to exploration for Broken Hill-type mineralisation

**Ryan Bartlett, Gawen R.T. Jenkin,**
*Department of Geology, University of Leicester, University Road, Leicester, LE1 7RH, UK; grtj1@le.ac.uk, ryan.bartlett.geo@googlemail.com*

**Ian R. Plimer**
*School of Earth and Environmental Sciences, University of Adelaide, South Australia 5005, Australia.*

**Abstract.** The Broken Hill sediment-hosted deposit, New South Wales, Australia, is the type example of middle-lower Proterozoic Broken Hill-type mineralisation (BHT) that remains an important Pb-Zn-Ag exploration target. Remarkably little geochemical characterisation of the gossan at Broken Hill has been carried out since the 1980s, because most of the gossan has been removed by mining or buried. To aid identification of BHT gossan in exploration, we have undertaken a modern study of the mineralogy and geochemistry of the gossan using clasts collected from a lag deposit near to the main line of lode at Broken Hill.

The gossan clasts are typically black and unremarkable, apart from their high density, and dominantly composed of an unusually lead-rich coronadite along with lesser goethite, which is unusually Mn, Pb and Zn rich. These occur with subordinate pyrolusite and hinsdalite-corkite group minerals, minor pyromorphite and other secondary Pb and Zn minerals. Whole rock geochemistry by ICP-MS confirms the Pb and Mn-rich and sulfur–poor nature of the gossan, with some enrichment (>20x) relative to bulk continental crust in Zn and Cu, and greater enrichments (>100x) in Sb, As, Cd and Ag. This distinctive assemblage should provide a marker for exploration for BHT mineralisation elsewhere.

**Keywords.** Broken Hill, gossan, mineralogy, geochemistry, coronadite.

## 1 Introduction

The Broken Hill sediment-hosted Pb-Zn-Ag deposit, New South Wales, Australia, is the world's largest Pb deposit, having yielded 28 Mt of Pb metal from 300 Mt ore (Crawford and Stevens 2006). It is the type example of the middle-lower Proterozoic Broken Hill type of stratiform base metal mineralisation (BHT), which also includes deposits such as Cannington, Zinkgruvan, Aggeneys-Gamsberg and possibly Sullivan. These deposits typically exhibit high tonnages (30 to >250 Mt) of Pb and Zn rich ore (10-20% Pb+Zn) with high Ag credits (>100 ppm) (Walters 1998), and as such this deposit type remains an important target for Pb-Zn-Ag exploration.

Most BHT deposits have been discovered by prospection of spectacular gossan outcrops and it is likely that most deposits exposed at the surface have been found. However, gossan clasts within the regolith may be a much broader target than the deposit itself and

therefore represent an important marker for an unexposed deposit. Gossans form by weathering of various rock types, including ironstones that are fairly abundant in middle-lower Proterozoic sequences; thus it is important to be able to distinguish gossans related to BHT mineralisation from those that are not ("false" gossans). Unfortunately, apart from a number of studies reporting the presence of rare and previously unknown minerals, remarkably little geochemical characterisation of the gossan at Broken Hill has been carried out since early studies (van Moort and Swensson 1982; Plimer 1984). This is because most of the gossan has been removed by extensive mining or buried under waste. To circumvent this we have examined sixty-eight gossan clasts collected from beds in a lag deposit near to the main line of lode at Broken Hill. These are material that was once at the surface of the deposit prior to mining and therefore are representative of what an explorationist would find above and adjacent to an unexploited deposit.

## 2 Petrography

The gossan clasts are typically black and unremarkable apart from their high density and could be easily missed by an inexperienced explorationist. Vein quartz and lithic fragments remain, but the main supergene mineral is coronadite along with lesser goethite (Fig. 1). These occur with subordinate pyrolusite and hinsdalite-corkite group minerals ($Pb[Al,Fe]_3[PO_4,SO_4](OH)_6$) and minor amounts of pyromorphite and other secondary Pb and Zn minerals.
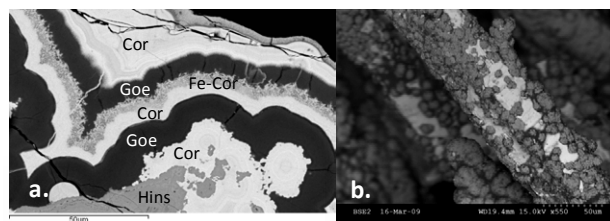


**Figure 1.** SEM back-scattered images: a. alternating phases of coronadite (Cor and Fe-Cor), and goethite (Goe) growing after hinsdalite (Hins), b. disseminations of coronadite on acicular pyromorphite.

## 3 Mineralogy

The coronadite is unusually Pb-rich; average $\sim Pb_{1.8}Mn_{7.3}Fe_{0.4}O_{16}.nH_2O$; $\sim 32\%$ Pb, 35% Mn.

Stoichiometric coronadite should only have one Pb per formula unit: $PbMn_8O_{16}.nH_2O$ whereas Broken Hill coronadite appears to be closer to two Pb per formula unit (Fig. 2). However, our EPMA analyses are consistent with the whole rock Pb/Mn ratios determined in our study and previous work, and it is noted that some equally Pb-rich coronadites exist elsewhere. Thus it seems that coronadite in the lead-rich environment at Broken Hill can contain up to 2 Pb per formula unit.

The goethite contains high (%) levels of Mn, Pb and Zn which is highly unusual apart from in other instances of gossans developed on Pb-Mn-Zn-rich mineralisation (Murciego-Murciego et al. 2012).
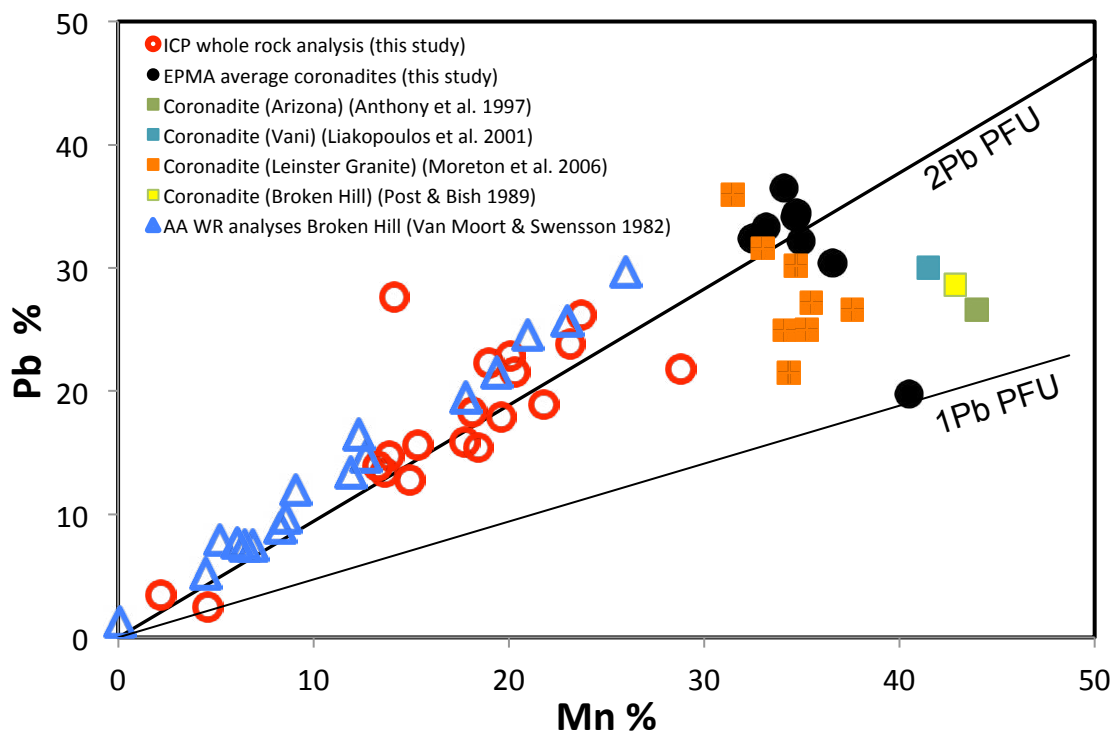


**Figure 2.** Coronadite compositions in Broken Hill gossan measured in this study by EPMA (solid circles) compared to whole rock data (open symbols; ICP - this study; AA - Van Moort & Swensson 1982) and literature coronadite analyses (solid squares). Lines show Pb atoms per formula unit (PFU). The whole rock sample with anomalously high Pb contains pyromorphite; once the Pb in this phase is subtracted this point lies close to the upper line.

## 3 Geochemistry

Whole rock geochemistry by ICP-MS confirms the Pb and Mn-rich and sulphur–poor nature of the gossan (Fig. 3), with some enrichment (>20x) relative to bulk continental crust in Zn and Cu, and greater enrichments (>100x) in Sb, As, Cd and Ag. The gossan contains little Fe and is highly depleted in alkali and alkali earth elements. The Ag in the clasts is notably lower than in samples from the *in situ* gossan (van Moort and Swensson 1982), suggesting that Ag may have been leached from the clasts during transport or by groundwater.

Element concentrations show systematic variations within the Periodic Table (Fig. 4), e.g. Group 1: Na-Cs, or Group 6: Cr-W, which reflect fractionation by processes operating during formation of the primary deposit and in subsequent formation of the gossan.

## 4 Conclusions

The mineralogy and geochemistry of the gossan forms a distinctive assemblage that should provide a marker for exploration for BHT mineralisation elsewhere.

## References

Anthony JW, Bideaux RA, Bladh KW, Nichols MC (1997) Handbook of Mineralogy, Mineralogical Society of America, Mineral Data Publishing.

Crawford AJ, Stevens BPJ (2006) A magmatic-hydrothermal origin for the giant Broken Hill Pb–Zn deposit. Geochim Cosmochim Acta 70, Supplement 1: A115.

Liakopoulos A, Glasby GP, Papavassiliou CT, Boulegue J (2001) Nature and origin of the Vani manganese deposit, Milos, Greece: an overview. Ore Geol Rev 18:181-209.

Moreton S, Green DI, Tindle AG (2006) Manganese oxide minerals from veins in the Leinster granite. Irish J Earth Sci 24:29-36.

Murciego-Murciego A, Álvarez-Ayuso E, et al. (2012) Weathering Products of Pb, Sb, As and Fe-Bearing Sulfides in the Losacio Mining Area (Zamora, Spain). Macla 16:230-231.

Plimer IR (1984) The mineralogical history of the Broken Hill lode, NSW. Aust J Earth Sci 31: 379–402.

Post, JE, Bish DL (1989) Rietveld refinement of the coronadite structure. Am Mineral 74:913-917.

Rudnick RL, Gao S (2003), The Composition of the Continental Crust, pp. 1-64. In: The Crust (ed. R.L. Rudnick) Vol. 3, Treatise on Geochemistry.

van Moort JC, Swensson CG (1982) The oxidised zone of the Broken Hill lode, NSW. In: Ore Genesis, eds. Amstutz. G.C. et al. Springer, Berlin: 251-267.

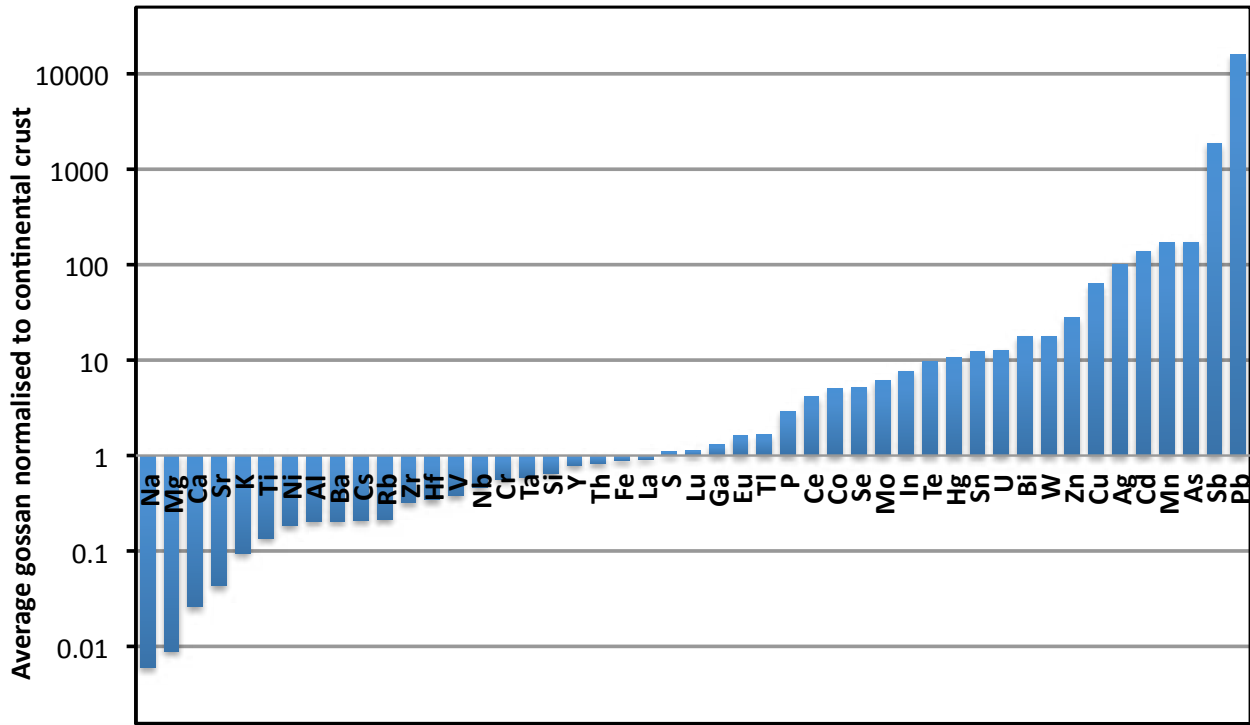Walters SG (1998) Broken Hill-type deposits. AGSO J Aust Geol Geophys 17:229-237.

**Figure 3.** Average Broken Hill gossan compared to continental crust values (Rudnick and Gao 2003) ranked by value.
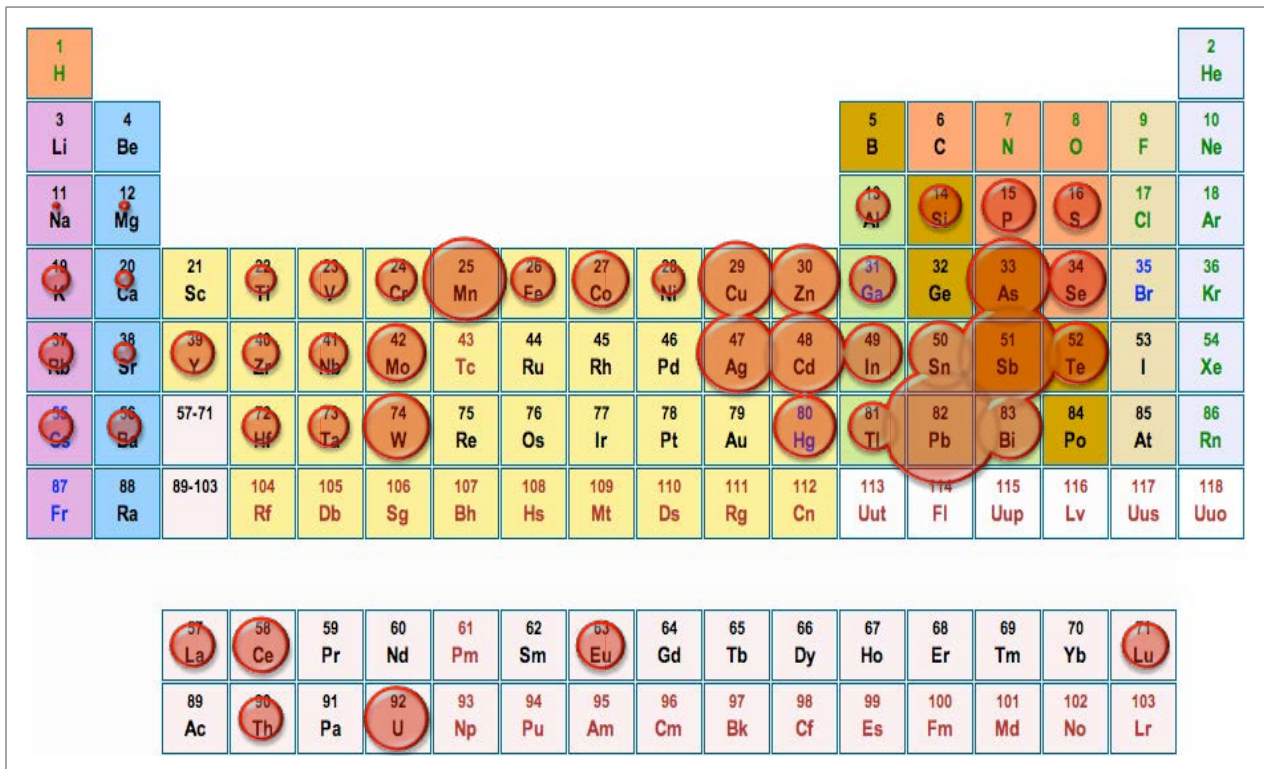


**Figure 4.** Logarithm of data from figure 4 plotted on the Periodic Table. Bubble sizes are relative only – La and S have values equal to continental crust so larger bubbles indicate enrichments, smaller indicate depletions. Note systematic trends within groups.

# Geochemical exploration using palaeo-hydrothermal fluids

Kingsley Burlinson

*Burlinson Geochemical Services P/L, Darwin, Australia. (decrepitation@appliedminex.com)*

**Abstract.** We know a great deal about the characteristics of the hydrothermal fluids which have dissolved, transported and deposited the economic minerals in ore deposits from academic studies of fluid inclusions. Despite the obvious importance of this data we have failed to use this as an exploration technique because data acquisition is wrongly perceived to be too difficult. But there are simple and cheap methods to acquire fluid inclusion data which is highly useful in mineral exploration to provide targeting or discrimination between ore and barren samples. The most diagnostic fluids for exploration are those of very high salinity and those with high gas contents, primarily $CO_2$. Simple microscope observations on crushed samples in oil can quickly detect halite daughter crystals to identify highly saline fluid typical of the core of porphyry Cu deposits. Rapid automated baro-acoustic decrepitation analyses provide information on the gas content of samples which is useful in locating auriferous quartz veins. Both of these techniques easily provide diagnostic information about the fluids which formed the ore deposits and can be used in mineral exploration programs. Fluid inclusion temperatures are far less useful as they are rarely diagnostic, but temperatures from baro-acoustic decrepitation can be useful in more detailed exploration work.

**Keywords.** Baro-acoustic decrepitation, fluid inclusions, $CO_2$ rich fluids, saline fluids, temperature zonation.

## 1 Using the Gas content of inclusions in gold exploration

Numerous studies of fluid inclusions from gold deposits have shown the presence of large quantities of non-condensible gases in the fluids which formed these deposits. The most common gas is $CO_2$, but $CH_4$ is also found. Although neither of these fluids actually complexes with the gold, they provide direct evidence that the fluids are sourced from a region which may have supplied gold, such as green-schist facies metamorphic rocks. $CO_2$ is also able to buffer the pH of fluids such that gold complexes are stable and can be transported to a zone of deposition. (Phillips, Evans, 2004) The presence of $CH_4$ often indicates that the fluids have reacted with carbonaceous rocks, which can destabilize gold–bisulphide complexes and cause gold deposition. To use this important information as an exploration method we need to measure the gas content of a large number of samples and plot the results as profiles or contours to locate the most gas-rich zones for further exploration.

Gas contents can be estimated by microscope observation while breaking open fluid inclusions immersed in oil. The gas content is related to the size of

the bubble formed. (Diamond, Marshall 1990) However this method is rather tedious, quite subjective and rarely used. A far superior technique for exploration use is the baro-acoustic decrepitation method (Burlinson, 2007) which is a rapid, automated and objective method which provides a statistically robust estimate of the total gas content of the samples. Although decrepitation was used in the past to attempt to estimate formation temperatures, it is much better suited to the measurement of gas contents than temperatures, as explained in detail by Burlinson (2011). Gas-rich fluid inclusions decrepitate at unusually low temperatures and are easily recognized on the decrepitation plots. (Fig. 1) This fact is frequently noted in conventional microthermometric studies in which homogenisation temperatures could not be determined because the inclusions decrepitated before they homogenised. This is usually considered to be a problem in academic studies, but is actually a means of identifying gas-rich inclusions which we know are a useful guide in mineral exploration. We should embrace this useful behaviour rather than ignore it as is usually done.

### 1.1 $CO_2$ rich fluids at the Morning Star Au mine, Woods Point, Victoria, Australia

The Woods Point mine is located 120 km NE of Melbourne and has produced some 900,000 oz of gold. It occurs in a dyke swarm hosted within Devonian sandstones and shales. The dyke rocks are of granophyre, peridotite, diorite and gabbro and the gold occurs within quartz and quartz/carbonate veins within the dykes. 34 quartz samples from the Woods Point region were analysed by baro-acoustic decrepitation to determine the relationship between the baro-acoustic decrepitation response and known mineralisation as well as to examine the variability of the results within and between different types of quartz. A prominent feature of most of the sample results is the presence of a decrepitation peak at low temperature, around 250 °C. This peak is caused by the presence of large quantities of non-condensible gases in the fluid inclusions. This is usually caused by the presence of $CO_2$, with $CH_4$ and $N_2$ being less common additional gases. The decrepitation data are plotted together with the gold analyses in Figure 2 and show an interesting correlation between the gold analysis and the height of the low-temperature ($CO_2$ - caused) decrepitation peak. All of the samples (with 1 exception) which contain 10ppm or more of gold show high $CO_2$ peak heights. Many additional samples with low gold contents also show high $CO_2$ peak heights. This is to be expected as the fluid characteristics of a hydrothermal system provide a much

larger anomaly halo around mineralization than does the mineralization itself. This provides a bigger and more homogeneous exploration target than trying to use gold analyses as a geochemical exploration method. The gold analyses are also prone to erratic variations due to inhomogeneous distribution and the nugget effect during sampling and analysis. All of the samples, except for the "cleaning quartz" for which there is no gold analysis, were collected from mineralized quartz occurrences or actual working mines. Unfortunately, there are no confirmed unmineralised samples in the sample suite to provide a comparison between mineralised and barren quartz. It is suspected that distal, barren samples would show low or no $CO_2$ peak as is the case with the cleaning quartz, which is presumed to have no measurable Au content.

The auriferous quartz samples from the Woods Point mineralisation occurrences have significant low temperature decrepitation peaks which are caused by the presence of substantial amounts of $CO_2$ in the fluids which deposited the quartz vein and gold mineralisation. Consequently we can use the presence of $CO_2$ rich fluids as an effective exploration method to discover extensions of the known deposits or to explore for additional new deposits in the region. It is advantageous to use $CO_2$ analyses in exploration because the distribution of $CO_2$ rich fluids is wider and more homogeneous than the distribution of gold itself.

## 2 Using highly saline fluids to target porphyry Cu or intrusion related Au deposits

The association of highly saline fluids with magmatic core zones such as intrusion related gold and porphyry Cu-Au deposits is well documented in the literature. However, this information is almost always buried within large quantities of unnecessarily complicated fluid inclusion data which conceals just how easy it can be to detect these saline fluids and use this information as an exploration tool. It is not necessary to determine precise salinities using thin sections and heating/cooling stage microscopy. For exploration we can rely merely on observations of halite daughter crystals, which indicate salinities greater than saturation, which is about 26 weight % NaCl. This can be done on crushed grains immersed in an oil with the same R.I. as quartz, such as clove oil. We can simply use the presence or absence of halite daughter crystals in the fluid inclusions as an indication of proximity to the core of the magmatic system. This will not be completely precise, but is easy to do and very useful in mineral exploration, particularly on drill-core samples. Basinal brines can also contain halite daughter crystals in fluid inclusions so you do need to be careful of the geological provenance.

## 3 Using baro-acoustic decrepitation temperatures as an exploration method

Studies of hydrothermal fluid systems invariably include vast quantities of formation temperature measurements, determined from the homogenisation temperature of fluid inclusions. However the overwhelming observation from all this data is that temperature measurements are only very poorly diagnostic when trying to explore for mineral deposits. The temperature ranges of deposition are quite broad and both barren and mineralised system form within the same temperature ranges. In an immense study of the Sovetskoye deposit, Siberia, Russia, Tomilenko et. al. (2010) measured 5025 fluid inclusion temperatures on 1425 barren and 3600 gold mineralised quartz samples. The overwhelming majority of the results were within the temperature range of 225 to 425 °C precluding the use of temperature alone to discriminate between barren and potentially auriferous quartz veins. This almost complete temperature overlap between barren and mineralised samples is observed in almost all studies of hydrothermal systems. Because of this, acquisition of fluid temperature data is of very limited use in mineral exploration, at least on a regional or district scale. Temperature information can be useful to exploration, but only in answering well defined questions on a good dataset on a deposit scale and the study must be carefully planned. These conditions cannot usually be met in exploration work so temperature measurements are more appropriate at the deposit appraisal or development stages.

## 3.1 Using decrepitation temperatures to define thermal zonation within a deposit at the Malanjkhand copper deposit, central India

A set of 58 samples were collected from within and near the open pit at the Malanjkhand Cu mine. These were analysed by baro-acoustic decrepitation. None of the samples showed a low temperature peak and it is concluded that the fluids here did not conatain $CO_2$. Each of the decrepigrams was reduced to its component skewed gaussian populations using the fityk deconvolution software. This provided a mathematically precise way to determine the mode temperature of each component population of inclusions in each sample. (Burlinson, 2009). The samples were compared using the fitted mode temperature of the decrepitation peaks in the temperature interval from 450 °C to 510 °C. These temperatures are plotted against sample location and mineralisation type in Figure 3. This shows that there are consistent temperature differences across the pit and between mineralised and barren samples within and near the pit. Baro-acoustic decrepitation provides a means of measuring subtle temperature differences within the mineralising fluid system and could be useful in evaluating nearby mineralisation potential. But the temperature differences are small and cannot easily be used for discrimination between ore and barren regions.

# 4 Conclusions

Mineral deposits are frequently formed from hydrothermal fluid systems. Remnants of these fluids remain trapped as fluid inclusions and provide a means by which we can determine the gas content, salinity and temperature of the palaeo-fluids concerned. This information is extremely useful in genetic studies of ore deposits and yet is completely ignored in field exploration work. This is a serious omission and we can and should use this fluid information in exploration programmes. There are simple methods to acquire this information easily and cheaply on large suites of samples for use in mineral exploration, particularly the baro-acoustic decrepitation method.
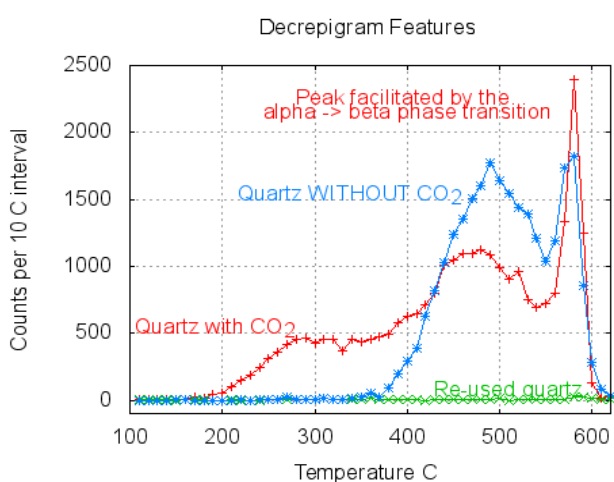


**Figure 1.** Typical decrepitation results comparing quartz containing $CO_2$ rich inclusions (red), which has a low-temperature peak at 300 °C, with quartz lacking $CO_2$ rich inclusions (blue), which does not have any low-temperature decrepitation..
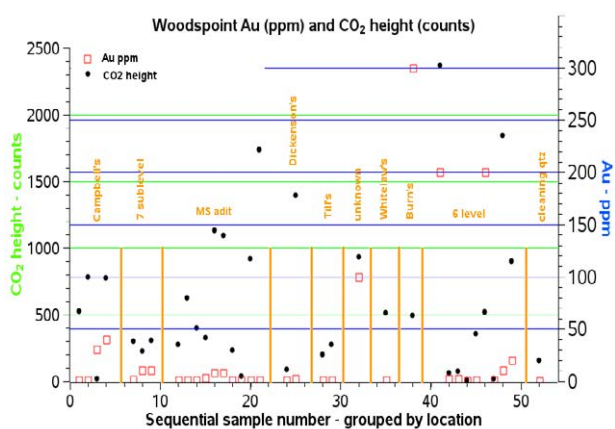


**Figure 2.** Low temperature ($CO_2$-caused) decrepitation height (left y-axis) and gold results (right y-axis) at the Woods Point Au deposits. Note that all except 1 of the samples with >10ppm Au have high decrepitation amounts.
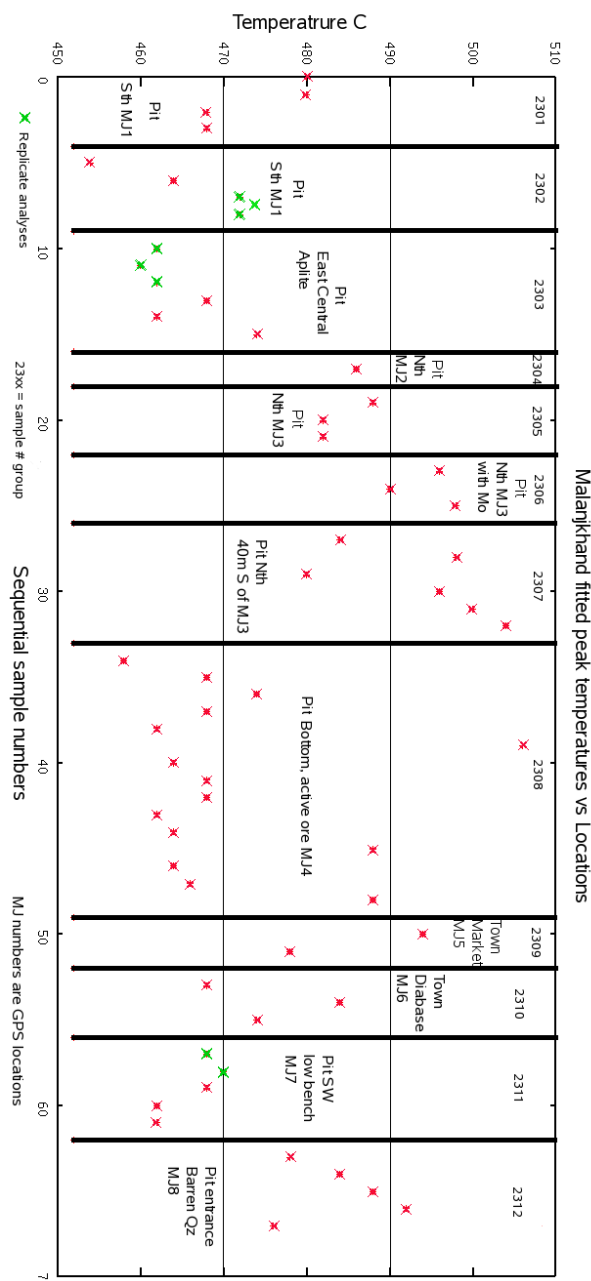


**Figure 3.** Decrepitation temperature variations across the Malanjkhand Cu deposit, India. There are significant temperature differences between different parts of the pit and also the surrounding region samples which could be used to outline potentially economic areas.

# Acknowledgements

## References

Burlinson K (2007) Acoustic Decrepitation as a means of rapidly determining $CO_2$ (and other gas) contents in fluid inclusions and its use in exploration, with examples from gold mines in the Shandong and Hebei provinces, China. Acta Geologica Sinica 23:65-71 .
http://appliedminex.com/decrep/general/burags.htm

Burlinson K (2009) Baro-acoustic decrepitation study of the Malanjkhand Cu mine, central India.
http://appliedminex.com/decrep/india/mj/malanj.htm

Burlinson K (2011) Rapid fluid inclusion data for exploration.
http://appliedminex.com/decrep/decrep.htm

Diamond LW, Marshall DD (1990) Evaluation of the fluid-inclusion crushing-stage as an aid for mesothermal gold-quartz deposits., J Geochem Explor 38:285-297.

Phillips GN, Evans KA (2004) Role of CO2 in the formation of gold deposits. Nature 429:860-863.

Tomilenko A, Gibsher N, Dublyansky Y, Dallai L (2010) Geochemical and isotopic properties of fluids from gold-bearing and barren quartz veins of the Sovetskoye gold deposit (Siberia, Russia) Econ Geol 105:375-394

# Gold-silver ratio as variability factor for epithermal deposits

Irina Chizhova, Alexander Volkov, Konstantin Lobanov
*The Organization of Russian Academy of Sciences Institute of Geology of Ore Deposits, Petrography, Mineralogy, and Geochemistry (IGEM RAS)*

**Abstract.** Comparative studying of regional variations for gold-silver ratio in ores of epithermal deposits is executed. For this purpose the database on 515 deposits of the world have been created. It contains the complete information on their geographical co-ordinates, reserves and contents (gold and silver).

Statistical analysis of distribution for parameters of gold-silver ratio and application of EM-algorithm (*Expectation-Maximization)* for separation of probability distribution mixture has allowed to define the boundaries for definition of gold-silver specialization of deposits: mainly silver (less than 1:250), gold-silver (1:250 - 1:25), mainly gold (more than 1:25). For more detailed classification the last group can be presented as mixture of 4 allocations with boundaries (1:25 - 1:8, 1:8 - 1:3, 1:3 - 1.2:1, more than 1.2).

The executed calculations have allowed to receive the science-based summary about gold-silver specialization of the Central and South Americas and the Northeast of Russia. The North America, Thetis, Northeast of Asia, Oceania and Australia are classified as mainly gold.

**Keywords.** database, epithermal deposit, gold-silver deposit, gold-silver ratio, gold-silver specialization, mixture of probability distributions.

## 1 Introduction

The active implantation of GIS-technologies is one of the tendencies of modern Russian geology development under conditions of personnel deficiency. The various informational-analytical systems are the result of their application, which provide monitoring of bases and banks of geological data. Using the GIS-project for prognostic-metallogenic problem we have executed the comparative studying of regional variations of gold-silver ratio in epithermal ore deposits of the world. In the present theses the main results of this operation are set out.

## 2 About gold-silver ratio in ores

The indicator Ag/Au was entered by V.Lindgren (1953). It was used as one of the main separating tags of epithermal deposits: in limits <10 (Au-Ag deposits) and in limits > 10 (Ag-Au deposits). It is empirically installed, that industrially significant epithermal deposits usually have this indicator less 50:1 (Hedenquist et al. 1988). The indicator Ag/Au can be also used for estimation of regional metallogenic specialization, efficiency of deposits and prediction of conditions for deposit formation.

Previously (Konstantinov 1984) among gold and gold-silver deposits there were selected gold-telluride, gold and gold-silver types (corresponding to them the ranges of gold-silver ratios were: 10:1-1:1; 1:1-1:20; less 1:20). The specified typification was based mainly on materials of the leading foreign deposits.

Among epithermal gold-silver deposits of Chukotka we (Volkov et al. 2006), have selected the following geochemical types: gold (1:1-1:10), gold-silver (1:10-1:100), mainly gold silver (1:100-1:1000). However the most reliable value of this metric can be received from the relation of the common reserves of gold and silver in each studied object (Silver 1989), as the private results of any approbation will give considerable dispersion of the received data owing to zonality and heterogeneity of allocations of concentration of these metals.

Using the author's materials and data, published in scientific geological magazines, reports and systematised by authors, the specialized database has been created for the comparative computer analysis of regional variations of gold-silver ratio in the epithermal ore deposits of different regions of the world. It contains the data about 515 deposits (fig. 1), including geographical co-ordinates, ore reserves, contents of gold and silver, absolute age, type of volcanic belt, type of fundament, ore assemblage, and also quantity of the extracted precious metals in 2011.

Among them are: more than 70 objects – from the Northeast of Russia, about 90 objects – from Oceania, including Australia and New Zealand, about 130 objects – from North and South Americas, about 60 objects – from Central America, about 50 objects – from Thetis; 35 objects – from Japan, about 40 objects – from Mexico.

While statistical data processing it is installed, that the distribution of gold and silver contents submit to log-normal law, and their average values, are, accordingly, 6.33 g/t and 125.81 g/t, medians – 3.45 g/t and 30.00 g/t (i.e. 50 % of sampling less than these values).

The reserves-weighted average is equal to 1.58 g/t for gold and 33.92 g/t for silver.

The distribution of gold and silver reserves submit to log-normal law, and their average values, are, accordingly, 67.95 t and 1463.42 t, medians – 27.90 t and 204.00 t.

It is significant, that about 70 % of the common reserves of gold is concentrated in the largest deposits: Cripple Creek (396), Comstock (392), Round Mountain (403) (USA); Veladero (270), Pascua Lama (275) (Argentina); El Indio (292) (Chile); Yanacocha (313) Pierina (314) (Peru); Kupol (34) (Russia); Hishikari (166) (Japan), etc. In addition about 75 % of the common reserves of silver are concluded in the largest
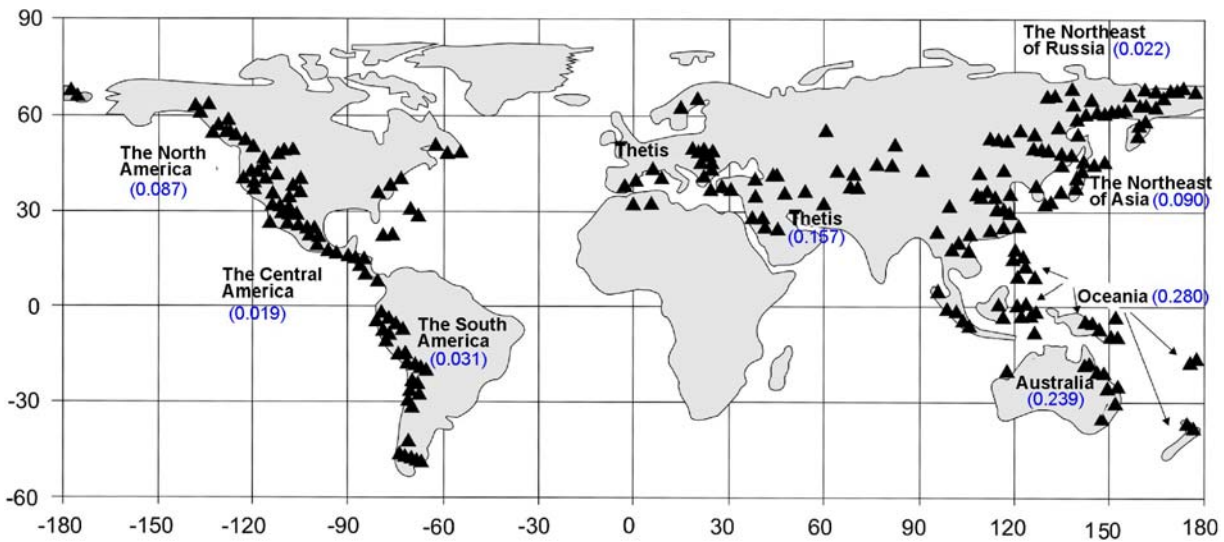
**Figure 1.** The map of distribution of 515 epithermal ore deposit from database. In brackets the Au-Ag ratio is indicated for appropriate continent or region

silver objects, and three of them (Mexico) - Pachuca (354) (40 thousand ton), Guanajuato (353) (34 thousand ton) and Guanacevi (352) (13.9 thousand ton) - contain about 65 % of the common reserves of the American continent. It is necessary to underline, that the high level of the average contents of gold and silver of the region, indicated above, are defined by the high contents of gold and silver of these and other main deposits.

## 3 The comparative analysis of regional variations of gold-silver ratio

Using comparative analysis of materials on 515 epithermal gold-silver deposits of the world (from
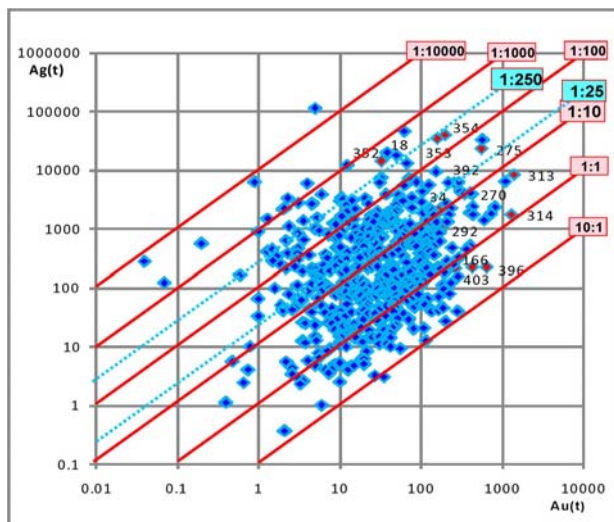


**Figure 2.** The logarithmic diagram of gold-silver reserves. The object's numbers have corresponded to database list. The object's names are indicated in the text. The red lines indicate the deposit position with gold-silver ratio, equal to the value in rectangular box. Blue lines correspond to boundaries for selection of 3 groups of objects: mainly silver, gold-silver and mainly gold.

database) their typification was defined more exactly by the value of gold-silver ratio. Results are set out on fig. 2 and 3.

On fig. 2 the lines spent under the corner 45°, are the lines of equal ratios of gold reserves to silver reserves, these values are inside the frame on the right. Deposit Yanacocha (313) is unique on gold reserves among gold-silver of objects; deposits Pachuca (354) and Guanajuato (353) - are unique on reserves of silver and simultaneously possess of large reserves of gold; deposits Guanacevi (352) and Dukat (18) have unique reserves of silver and averages - gold, and Comstock (392) - large reserves as gold, and silver too.

Using the value of gold-silver ratio in ores the classification of deposits is carried out statistically by determining of component centers within the domain of this parameter. It has been determined (fig. 3, 4), that the sample of this geochemical tag from general totality is submitted to log-normal distribution law.

Checking hypothesis, that there are 3 classes of deposits, which are characterized by various gold-silver ratio, we have simulated the empirical gold-silver ratio
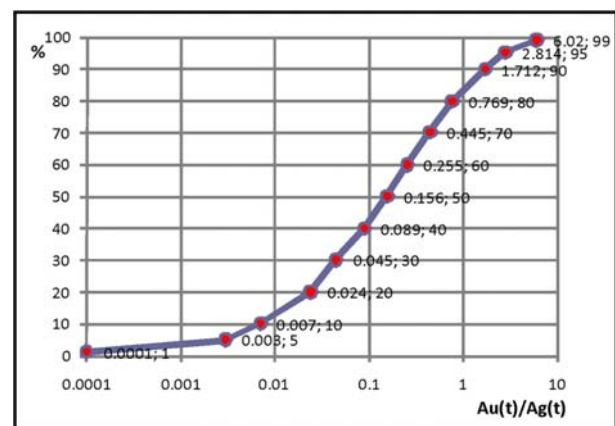


**Figure 3.** The accumulation curve of gold-silver ratio for 515 gold-silver deposits
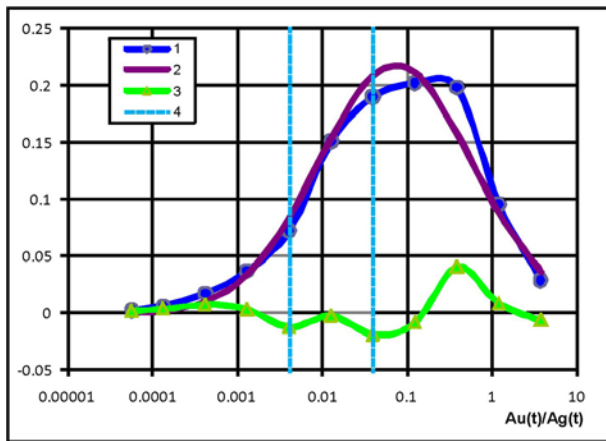
**Figure 4.** The distribution curve of gold-silver ratio for 515 gold-silver deposits (1 – experimental; 2 – theoretical (log-normal) model; 3 – non-log-normal behavior (deviation); 4 – boundary line between mixture components).



**Figure 5.** Gold-silver ratio for various continents and regions. The blue dotted line is the broad for determining of gold-silver specialization.

distribution in the form of distribution mixture, in which separate components are log-normal. The procedure of mixture decomposition was carried out by *EM*-algorithm (*Expectation-Maximization),* which usually used for solving of this problem (Bilmes, 1998).

EM- algorithm is used in mathematical statistic for finding of maximum likelihood estimates for probability model parameters, in a case when the model depends on some latent variables. Each algorithm iteration consists of two steps. On E-step (*Expectation*) expected likelihood function value is calculated. On M-step (*Maximization*) the likelihood estimate maximum is calculated. Thus the expected likelihood, which is calculated on E-step, increases. Then this value is used for E-step on the following iteration. The algorithm is fulfilled until convergence (Boyles, 1983).
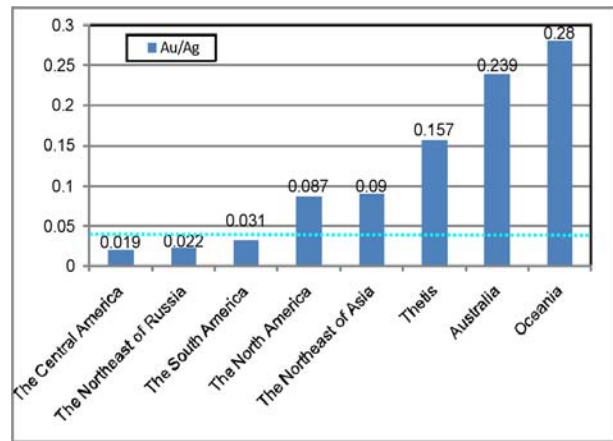
As the result we have received the mixture component centers of these samplings with log-normal distribution. Their parameters are in Table 1.

They are determined by medians accordingly: 0.002, 0.020, 0.328 (ratios of gold to silver – approximately 1:500, 1:50, 1:3).

Statistical analysis of distribution for parameters of gold-silver ratio and application of EM-algorithm for separation of probability distribution mixture have allowed to define the boundaries for definition of gold-silver specialization of deposits (fig.3): mainly silver (less than 1:250), gold-silver (1:250 - 1:25), mainly gold (more than 1:25).

The same boundaries were outlined as 0.01 (1:100) and 0.5 (1:2) by M.M.Konstantinov (1984).

For more detailed classification the last group can be described as mixture of 4 allocations with boundaries (1:25 - 1:8, 1:8 - 1:3, 1:3 - 1.2:1, more than 1.2).

## 4 Results of classification

The criteria for outlining of 3 types of gold-silver deposits has been determined. It was used for classification of regional specialization for gold-silver objects. Eight continents and regions were characterized by gold-silver ratio (fig. 5). The results well illustrate the known regional specialization of gold-silver objects.

The executed calculations have allowed to receive the science-based summary about gold-silver specialization of the Central and South Americas and the Northeast of Russia. The North America, Thetis, Northeast of Asia, Oceania and Australia are classified as mainly gold.

So we have: mainly gold specialization for deposits from Asia, Oceania and the North America (mainly territories of the USA); mainly silver with the subordinate value of gold specialization for deposits from Central America (mainly territory of Mexico); gold- silver specialization for deposits from East of Russia and the South America.

**Table 1.** Statistical parameters of gold-silver ratio distribution

| List of samples | Sample number | Mathematical expectation (mean of distribution) | Standard deviation | MIN | MAX | Median | Au:Ag |
|---|---|---|---|---|---|---|---|
| 1 | 33 | 0.002 | 0.003 | 0.000 | 0.004 | 0.002 | 1:500 |
| 2 | 114 | 0.021 | 0.015 | 0.005 | 0.039 | 0.020 | 1:50 |
| 3 | 368 | 0.081 | 1.652 | 0.040 | 11.667 | 0.328 | 1:3 |
| All sample of data | 515 | 1.493 | 18.107 | 0.000 | 11.667 | 0.156 | 1:6 |

## 5 Discussion

The purpose of carried out research is consisted in studying of Au/Ag variability in various geological situations.

The statistical analysis has shown, that the age of epithermal deposits is in wide limits (from Archaean to Quaternary period).

The epithermal deposits were distributed on subtypes (LS, HS, IS) and their contents (Au,Ag) and ratio (Ag/Au, Au/Ag) were calculated as follows: LS – 2.58, 9.71 and 22, 0.045; HS – 1.21, 24.58 and 20.43, 0.049; IS – 1.95, 42.1 and 26.1, 0.038. So HS-type and LS- type are more gold, than IS.

The common reserves of precious metals in all epithermal deposits from database (taking into account the extraction of the last years) are equal to 35 thousand t of gold and 754 thousand t of silver, the average contents are equal to 1.58 g/t and 33.92 g/t accordingly, and (Ag/Au, Au/Ag) ratio - 21.53, 0.46. The common tonnage of all deposits is 22204 million t.

Let's mark, that in 1985 the common reserves of precious metals in significant epithermal foreign deposits (taking into account the extraction of last years), were only 3332 t of gold and 158.8 thousand t of silver, the common tonnage was equal to 709 million t, and ratio (Ag/Au, Au/Ag) – (47.6, 0.21) (Mosier et al. 1985).

At that time the average contents of metals, weighted by ores, were calculated as 4.7 and 224 g/t. However authors believed (Mosier et al. 1985), that their report covers only 60 % of known deposits in the world.

Therefore, for the last 25 years the total reserves of epithermal deposits have grown in 7 (for gold), and 3 (for silver) times, and the common tonnage – in 31.3 times. In this connection there was a reduction of indicator Ag/Au ratio in 2.1 times.

## 6 Conclusion

Thus, the cited data well illustrate the known regional specialization of gold-silver objects over the world. Using mathematical methods it became possible to outline the exact boundaries of gold-silver ratio for determining of gold-silver specialization of deposits.

## Acknowledgements

## References

Bilmes J. A. (1998) A Gentle Tutorial of the EM Algorithm and its Application to Parameter Estimation for Gaussian Mixture and Hidden Markov Models. Technical report TR-97-021. International Computer Science Institute, Berkeley, CA, (Avaliable at: http://ssli.ee.washington.edu/people/bulyko/papers/em.pdf).

Boyles R. A. (1983) On the convergence of the EM-algorithm // Journal of the Royal Statistical Society. Series B. Vol. 45. P. 47-50.

Hedenquist J.W., Browne P.R., Allis R.G. (1988) Epithermal gold mineralization. Wairakei, New Zeland. 169 p.

Konstantinov M.M. (1984) Gold-Silver Mineralization of volcanogenic world belts. M.: Nedra. 165 p. In Russian.

Lindgren W. (1953) Mineral Deposits. 4th Edition. New York: McGraw-Hill Book Company, 930 p.

Mosier D.L. Menzie W.D., Kleinhamp F.J. (1985) U.S. Geological Survey Bulletin. 1666. P. 1–39.

Silver. (1989) M.: Science. 240 p. In Russian.

Volkov A.V., Goncharov V.I., Sidorov A.A. (2006) Gold and silver deposits of Chukotka. Magadan: SVKNII DVO RAS. 220 p. In Russian.

# In situ Pb and Zn analysis of vein-hosted tourmaline in the Bergslagen ore district, central Sweden, using LA-ICPMS

I.U. Christensson, K.J. Hogmalm, T. Zack, R.H. Hellingwerf
*Department of Earth Sciences, University of Gothenburg*

**Abstract.** Tourmaline is commonly found associated with stratabound zinc-lead deposits. Trace element chemistry of tourmaline has been suggested as a possible indicator for this type of mineralization. In this study we have investigated trace element composition of tourmaline in veins from the Bergslagen ore district, using LA-ICPMS, to test the promising results of previous studies based on the analysis of separates. The advantages of in situ analysis are: 1) it requires less preparation, 2) it avoids inclusions and/or impurities, and 3) it assesses chemical heterogeneities within crystals. Preliminary results show that Pb and Zn concentrations are significantly higher in vein tourmaline collected near stratabound zinc-lead deposits compared to tourmaline from Fe-oxide mineralizations. Analysis of mineral standards indicate that LA-ICPMS analysis of tourmaline is a precise and accurate method for determining Zn and Pb contents of tourmaline, and can be used as an exploration tool.

**Keywords:** LA-ICPMS, Zn-Pb in tourmaline, Bergslagen

## 1 Introduction

Syngenetic sedimentary exhalative zinc-lead deposits are commonly associated with tourmaline, and previous studies have suggested that tourmaline chemistry could be used for mineral exploration (Griffin et al. 1996, Hellingwerf et al. 1994). In general, tourmaline associated with sulphide deposits is characterized by high Mg content, but Mg-rich tourmaline also occurs in certain unmineralized systems and Fe-rich tourmaline has also been reported from some stratabound mineralizations (Slack 1996). High concentrations of Zn, Pb, and Cu in tourmaline is generally more indicative of sulphide mineralizations (Griffin et al. 1996), but this requires analysis of bulk mineral separates or more advanced techniques for *in situ* analysis. Analysis of tourmaline separates is time-consuming, sensitive to mineral inclusions and requires abundant material. Electron microprobe is of limited use since, typically, only concentrations down to 100 ppm can be measured. Laser ablation inductively coupled plasma mass spectrometry (LA-ICPMS) should be the most effective and reliable method for analysis of trace element content in individual tourmaline crystals (cf. Klemme et al. 2011).

The Bergslagen ore district in central Sweden hosts a large number of stratabound Zn-Pb-Ag-(Cu) deposits (Allen et al. 1996; Hellingwerf et al. 1994), and three of these are currently under operation. According to Allen et al. (1996) there are two end-member types of sulphide deposits in this area; 1) stratiform ash-siltstone-hosted sea-floor deposits, similar to the Broken Hill-type deposits 2) and strata-bound volcanic-associated limestone-skarn subsea-floor replacement deposits similar to felsic massive sulfide deposits. Hellingwerf et al. (1994) reported data from tourmaline collected all over the Bergslagen area and demonstrated that the major and trace element composition of tourmaline reflects the size and proximity of the Zn-Pb-Ag deposits. Anomalous trace element chemistry was also found in late quartz vein hosted tourmaline and tourmaline joints in the vicinity of Zn-Pb-Ag deposits. This is of particular interest for exploration since tourmaline in the joint systems could potentially give information about deeper laying sulphide mineralization. However, trace element data are from bulk analyses of tourmaline separates, which means that inclusions of e.g. sulphide minerals in tourmaline could influence the results. The first and foremost objective is to verify previous trace element data with state-of-the art analytical techniques. We therefore analyzed the tourmaline composition *in situ* using LA-ICPMS. Areas free from micro inclusions within the tourmaline crystals were first identified using scanning electron microscopy and then targeted by a relatively small laser spot size. Time resolved signal analysis made it possible to detect inclusions previously not visible on the surface. A secondary objective of this study was to evaluate LA-ICPMS as a method for analysis of Zn and Pb in tourmaline using tourmaline mineral standards.

Tourmaline is a cyclosilicate mineral that can hold a large variety of cations, ranging from one to four in charge (a geochemical trash can). The general formula for tourmaline is $XY_3Z(T_6O_{18})(BO_3)_3V_3W$. The X site is a vacancy site and has the possibility to hold Na, K, Ca, $Pb^{2+}$, and the Y site can incorporate Li, Mg, $Fe^{2+}$, $Mn^{2+}$, $Cu^{2+}$, Al, $V^{3+}$, $Cr^{3+}$, $Fe^{3+}$, $Mn^{3+}$, $Ti^{4+}$. The Z site can incorporate Mg, $Fe^{2+}$, Al, $V^{3+}$, $Cr^{3+}$, $Fe^{3+}$. The tetrahedral T site holds Si, B, Al and the B site holds B. Sites V and W holds OH, O; the W site also holds F. Tourmaline have large number of endmembers, the three most common are the Mg-endmember dravite $(NaMg_3Al_6Si_6O_{18} (Bo_3)_3 (OH)_3(OH)$ and the Fe-endmember schorl $(NaFe^{2+}_3Al_6Si_6O_{18} (Bo_3)_3 (OH)_3(OH)$ and also Li-Al- endmember elbaite $(NaLi_{1.5}Al_{1.5}Al_6Si_6O_{18} (Bo_3)_3 (OH)_3(OH)$ (Hawthorne and Dirlam, 2011).

## 2 Methods

Trace element contents were measured with the LA-ICPMS system at the Department of Earth Science at University of Gothenburg, equipped with a New Wave 213 (Nd:YAG, 213 nm wavelength) laser system coupled to an Agilent 7500a quadrupole inductively coupled plasma mass spectrometer. Data was collected for 49 elements and 55 isotopes with dwell times of 10 ms for each mass, 80 s of ablation, and a beam size of 80 μm. Laser conditions was set to a beam energy density of 8 J/cm$^2$ and a repetition rate of 10 Hz. NIST SRM 610 glass was used for standardization with Si as the normalizing element and the USGS BCR-2G glass was used as a secondary standard.

Tourmaline mineral standards HMM 108796 Dravite, HMM 112566 Schorl, HMM 98144 Elbaite were analyzed and compared to data from solution ICP-MS (Dyar et al. 2001) (Table 1). The data fits best for the Elbaite HMM 98144 which is within 1% for Zn and 10 % for Pb, compared to the literature values. Zn and Pb are ~20-30% lower than solution ICP-MS data for HMM 108796 Dravite and HMM 112566 Schorl.

**Table 1.** Analyses of tourmaline mineral standards and literature values by solution ICP-MS.

| Elbaite HMM 98144 | | | |
|---|---|---|---|
| | Mean | STDEV | Dyar et al. 2001 |
| Zn | 400,0 | 21,8 | 403,0 |
| Pb | 58,3 | 1,6 | 64,0 |

| Dravite HMM 108796 | | | |
|---|---|---|---|
| | Mean | STDEV | Dyar et al. 2001 |
| Zn | 18,8 | 1.05 | 26,0 |
| Pb | 0,6 | 0.03 | 1,0 |

| Schorl 112566 | | | |
|---|---|---|---|
| | Mean | STDEV | Dyar et al. 2001 |
| Zn | 1890,0 | 15,7 | 2387,0 |
| Pb | 3,1 | 0,0 | 4,0 |

## 3 Zn-Pb in tourmaline

The analyzed tourmalines were taken from the original study of Hellingwerf et al. (1994). They were collected from quartz or calcite veins near Nora-Vikern and Pershyttan, which are Fe-oxide deposits characterized by a low Zn-Pb sulphide content, and Evighetsgruvan and Sala which are Zn-Pb-Ag deposits. Results show that Zn content is ~10 times higher and Pb ~3-7 times higher in tourmaline from the Zn-Pb-Ag deposits compared to those from Fe-oxide deposits (Fig. 1). It should be noted that Zn concentration is much lower compared to results from Hellingwerf et al. (1994). This is probably because the new analyses are free from inclusions and other contamination sources.
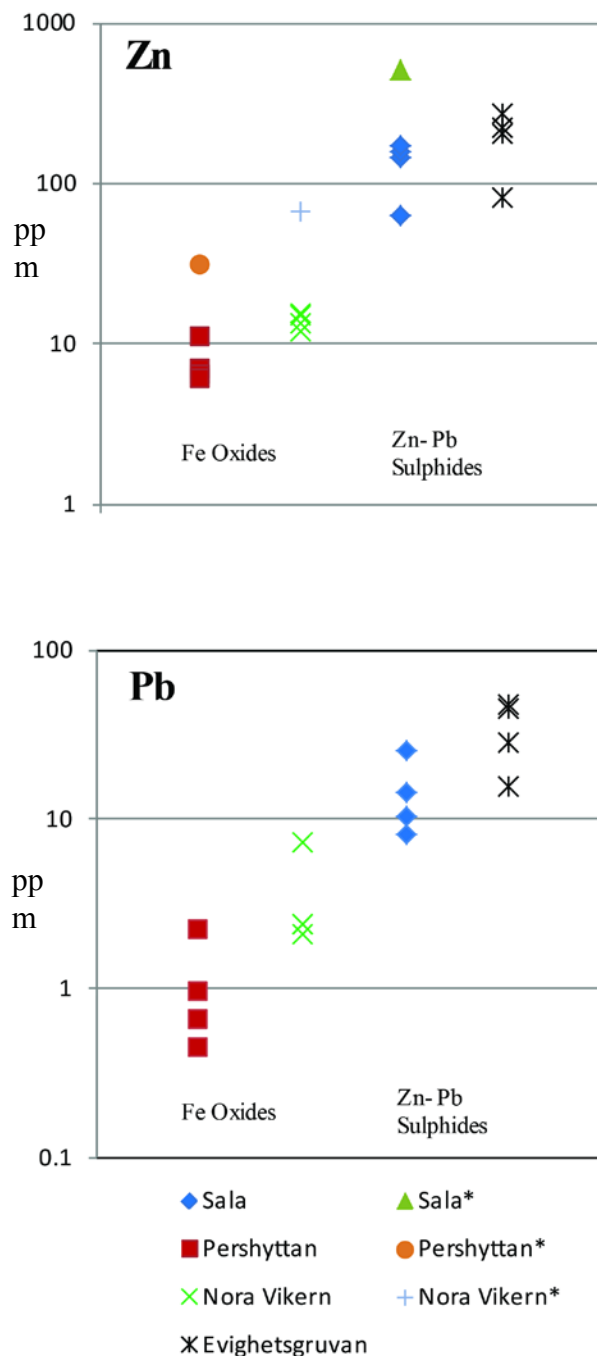


**Fig. 1** Zn and Pb content (ppm) in vein-hosted tourmaline associated with Fe-oxides mineralizations (Pershyttan and Nora Vikern) and Zn-Pb sulphide mineralization (Sala mine and Evighetsgruvan). Tourma-lines in the vicinity of Zn-Pb sulphide mineralizations have significantly higher concentration of Zn and Pb, compared to those associated with Fe-oxides. *: data is an average from Hellingwerf et al. (1994).

## 4    Conclusion

The findings of this preliminary study indicate that LA-ICPMS is a reliable method for quantitative Zn and Pb analysis of tourmaline. Data from vein-hosted tourmalines in Bergslagen show that there are significant differences in Pb and Zn contents between Zn-Pb-Ag deposits and Fe-oxide deposits. These findings justify further work on LA-ICPMS analysis of tourmaline to develop this as a technique for mineral exploration.

## References

Allen RL, Lundström I, Ripa M, Christofersson H (1996) Facies analysis of a 1.9 Ga, continental margin, back-arc, felsic caldera province with diverse Zn-Pb-Ag-(Cu-Au) sulfide and Fe oxide deposits, Bergslagen region, Sweden (*in* A group of papers devoted to the geology of two Paleoproterozoic base metal sulfide and gold mining districts in the Baltic Shield, Sweden) Econ Geol 91(6):979-1008

Dyar M.D., Wiedenbeck M., Robertson D., Cross L.R., Delaney J.S., Ferguson K., Francis C.A., Grew E.S., Guidotti C.V., Hervig R.L., Hughes J.M., Husler J., Leeman W., McGuire A.V, Rhede D., Rothe H., Paul R.L., Richards L., Yates M. (2001) Reference minerals for the microanalysis of light elements. Geostandards Newsletter: The Journal of Geostandards and Geoanalysis 25:441-463

Griffin, W. L.; Slack, J. F.; Ramsden, A. R.; Win, T. T.; Ryan, C. G., (1996).Trace elements in tourmalines from massive sulfide deposits and tourmalinites: Geochemical controls and exploration applications. Economic Geology91:657 – 675

Hawthorne F.C.,  Dirlam D.M. (2011) Tourmaline the Indicator Mineral: From Atomic Arrangement to Viking Navigation. Elements, 7:307-312

Hellingwerf R.H., Gatedal K., Gallagher V., Baker J.H. (1994) Tourmaline in the central Swedish ore district. Mineralium Deposita 29:189-205

Klemmer S, Marschall HR, Jacob DE, Ludwig T, (2011) Trace-element partitioning and boron isotope fractionation between white mica and tourmaline Can Mineral 49:165-176

Slack JF (1996) Tourmaline associations with hydrothermal ore deposits Reviews in Mineralogy and Geochemistry 33:559-643

# The influence of porphyry and epithermal related hydrothermal alteration zones on the geochemical patterns in till, northern Norrbotten, Sweden

**Julio González, Anna Ladenberger, Madelen Andersson & George Morris**
*Geological Survey of Sweden, Uppsala, Sweden*

**Abstract**

A total of 3400 samples of till collected from the C horizon have been analysed within the Geological Survey of Sweden's (SGU) regional survey programme for a current study in Northern Sweden. The geochemical pattern reveals a strong link between the presence of base metal, iron ore and precious metal deposits, and the extensive regional and local metasomatic alteration zones.

The established link between ore mineralisations, metasomatic rocks and their geochemical signatures in till can be used as powerful tool for mineral exploration.

**Keywords.** Till geochemistry, metasomatic (hydrothermal) alteration, metasomatic rocks, mineralisations, Northern Sweden

## 1 Introduction

The main objective of the SGU regional mapping programme is to quantify regional variations in glacial drift geochemical composition in order to provide data for mineral exploration, mining industry, planning purposes, environmental research, agriculture, forestry, veterinary and human medical research (medical geology). The survey area covers approximately 25 500 km$^2$ with one sample collected every six square kilometres (equals 15 samples per 100 square kilometres). The bulk of the collected material is sampled from normal silty or sandy-silty till.

The mapped region is one of the Sweden's major ore districts with the iron ore production at Kiruna and Malmberget, and Cu (+Au, Ag) exploitation at Aitik. Apart from several active mining centres, many historical ore deposits and hundreds of other mineralisations occur in the region (predominately sulphide and iron ores).

The bedrock in the study area is predominantly Archean (>2.5 Ga) and Paleoproterozoic aged rocks (<2.4 Ga old) of the Fennoscandian Shield. The youngest rocks, with ages 1.96 to 1.75 Ga, belong to the Svekokarelian orogeny. The Paleoproterozoic basement hosts a large variety of mineralisations of different origin including: iron ores, base metals and precious metals like Au and Pt. Quaternary geomorphology has a huge impact on the geochemical pattern in the area. The studied region, with the exception of the SE part, is located above the high-coastline. The border of the high-coast line lies at an altitude of ca. 200 metres above sea level (masl) near Svanstein, 180 masl in Lansjärv and 170 masl near Huuki. Glacial drift of different ages covers most of the area. Several generations of ice movement directions have been recognized and two directions dominate: from the southwest and from the northwest. The ice transport distances are generally rather short being approximatly 5 km. The presence of an ice divide in the NE part of the study area complicates the interpretation of the origin of geochemical signatures in till. Complex till stratigraphy provides an additional factor when trying to interpret the influence of local bedrock on the geochemistry of the till cover. Topography, together with a large variety of glaciation-deglaciation related landforms, influences the distribution of many geochemical anomalies. Glaciofluvial systems are responsible for removing, diluting and repositioning the geochemical signal originating from the bedrock. These processes have influenced elemental distribution of K, Na, Au, As, Mo, Sr and other elements.

## 2 Results and discussion

### 2.1 Geochemical characteristics of till

A total of 3400 till samples were collected from hand-dug pits from the C-horizon, usually between 0.7 – 1.0 m depth. After vacuum-drying, the samples were sieved stepwise to <0.063 mm and analysed for major, minor and trace elements by X-ray fluorescence for total contents. Partial leach techniques (Aqua Regia and 7M HNO$_3$) combined with ICP-MS analysis has also been performed (Ladenberger et al. 2012).

The till geochemical pattern in the studied area is dominated by the contrast between mafic-volcanic belts and felsic source lithologies. The main geochemical features of the till in this area are controlled by bedrock geology, with high concentration of elements typically found in mafic rocks (e.g. Co, Cr, Cu, Fe, Mg, Mn, Ni, Ti and V) and low concentration of elements associated with felsic rocks (e.g. As, Bi, Cd, K, Pb, Rb, Si, Sn, Tl, Zr). The distribution pattern of the anomalies coincides with ice movements in the region and is often connected to different glacial epochs. Many of the elemental anomalies show direct correlation to known mineralisations and ore deposits. In the Aitik mining region, PGE anomalies correlate with Cu and Au mineralisations. High gold concentration in till can be found in many places and often correlate well with As, Cu, S, Sb and Bi anomalies and the presence of numerous known gold mineralisations (e.g N, W and SW of Kiruna, SE-NE of Gällivare and in the Svappavaara region). Sulphide mineralisations are outlined by Cu, Co,

Mo and Pb anomalies in till with particularly large Cu anomalies between Kiruna and Vittangi, west of Pajala, and in the Tärendö-Svanstein region. The biggest Cu mine at Aitik however lacks a large Cu anomaly in till, which was probably diluted and transported eastwards by ice. Ag anomalies follow the occurrences of sulphide mineralisations at Lieteksavo, Pårkajaure, Viscaria, and the biggest at Aitik). Mo concentrations have been described from nearly 20 localities in the studied area and Mo anomalies (together with Ni, Co, Cu, Ag, Au) in till are often associated with these sulphide mineralisations. The most prominent feature of the northern part of the region are the numerous Zn anomalies. They correlate well with known Zn mineralisations e.g. Viscaria, west of Kiruna. Ba concentrations in till are higher in the studied region than in the rest of the country. High barium contents may indicate the presence of hydrothermal and metasomatic alterations. A characteristic feature of Norrbotten's till geochemistry is the very high Cl concentrations which spread as a large anomaly diagonally across the studied area. The origin of high Cl contents has been attributed to the widespread scapolitization of mafic rocks and the possible presence of old Paleoproterozoic evaporates which were subsequently eroded and removed only leaving geochemical traces (Fig.1).
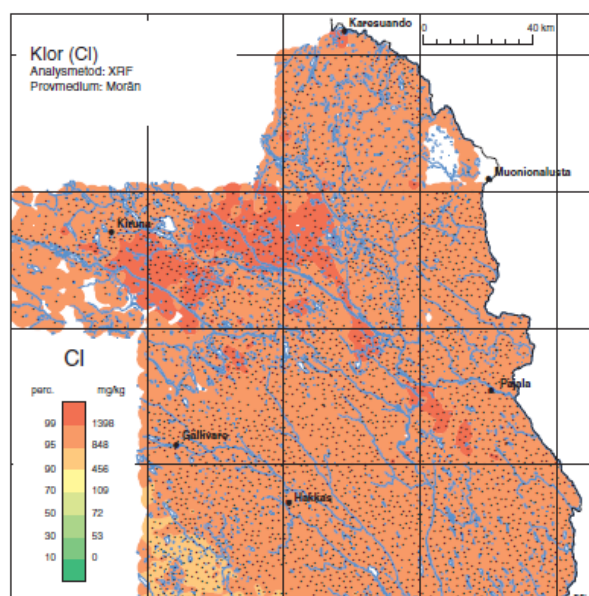


**Figure 1.** Chlorine in till (XRF method). SGU database.

## 2.2 Hydrothermal alteration revealed in till geochemistry

This study has shown that high concentrations of certain elements occurring in areoles surrounding different genetic ore types in Northern Sweden and indicative of hydrothermal alterations may have a major impact on the size of the elemental anomalies in till. Since most of the ore mineralisation in Norrbotten have a spatial connection to hydrothermally altered rocks, this observation might be valuable, and indeed essential, for mineral exploration.

Large parts of the bedrock in the study area have undergone extensive regional metasomatic alteration. The most common type of alteration is sodic (Na metasomatism: spilitization, albitization and scapolitization) mainly occurring in intrusive, volcanic and sedimentary rocks of the Proterozoic greenstone belts (Bergman et al 2001; Melezhik et al 2005).

In several places our investigation has revealed clear geochemical signatures most likely linked with hydrothermally altered rocks formed by acidic leaching. This till type is usually characterized by high levels of Si, Al, K, Ba, Sr, Fe, P, Ti, As, Bi, U, Mo and W. The rocks belonging to the Lower Hauki suite, which have historically been interpreted as hydrothermally altered (Högbom 1910; Geijer 1931; Frietsch 1966) and are represented by phyllic, argillic and possibly also advance argillic alteration types, are a good example. They formed through acid leaching processes connected to volcanic activity and the emplacement of volcanic rocks of the Porphyry Group. Regional metamorphism at greenschist facies changed the original pre-metamorphic argillisites and sericite-rich rocks into (locally) pyrite-chalcopyrite bearing, sericitic- and sericite-chloritic schists and sericitic quartzites. The argillisation and sericitisation led to an increase in Si, Al, K, ferric iron, Ti, P, Ba, Au, Ag, As, Bi, Mo, W, Sb and U, and reduced the amount of calcium, ferrous iron, magnesium and sodium in the rocks. Geochemical maps show relatively high concentrations of a number of elements in the glacial sediments (tills) (e.g. Ba, Al, K, P, As, Rb, Na, Bi, La, Na, Sr, U, W) which have a direct relationship to the Lower Hauki-suite metasomatic rocks (Fig.3). The moraines, in the area where the Lower Hauki-suite metasomatics are widespread, also contain anomalous concentrations of Ag, Ti, Pb, Mo, Sn (7M $HNO_3$ partial leach by ICP MS). The strontium concentration is remarkably high in this area. Enrichment of strontium caused by acid-leaching during wall-rock interaction with highly acidic hydrothermal solutions has been described by Hikov (2004a; 2004b). The negative anomalies of Na, Mg, and Be in till adjacent to the Lower Hauki complex indicate that these elements were mobile and have been removed by the acidic solutions during the hydrothermal process. Both till geochemistry element concentrations and the mineralogical composition of the Lower Hauki suite metasomatic rocks are consistent with gold-bearing epithermal deposits. In general, the elevated concentration of Au, Ag, As, Sb, Bi, Sn and Mo are typical for "high sulphidation epithermal gold deposits", while high concentrations of Au, Ag, As, Sb and K are more common for "low sulphidation epithermal gold deposits" (White and Hedenquist 1995). The till from the area dominated by the Lower Hauki hydrothermally altered rocks contain a mixture of both geochemical signatures.

The studies in the area around the Malmberget apatite-iron ore deposit indicate that it also occurs in close proximity to hydrothermally altered rocks (Högbom 1910; Geijer 1931; Frietsch 1966). This type of hydrothermally altered rocks have however never been reported to have a direct genetic link with the Kiruna-type apatite-iron ores. Modal mineral composition and rock chemistry indicate the presence of

advanced argillic alteration (Pirajno 2009), resulting in the formation of hydrothermal (secondary) quartzites (Fettes and Desmons 2007; Velinov et al. 2007) formed during extensive acid-leaching produced by wall-rock interaction with extremely low pH hydrothermal solutions. During such extreme conditions, only quartz and high alumina minerals such as corundum, andalusite and pyrophyllite are stable. The original protolite were mainly volcanic, intrusive and volcano- sedimentary rocks of acidic to intermediate composition. A spatial correlation seems to occur between the hematite ore and the elongated zones of sillimanite-gneisses striking parallel to the ore bodies. High concentrations of Al, Si, Ba, Bi, Ti, Zr, K, S, Sr, Mn and Fe in till in the Malmberget region are similar to those found in the moraines from the area north of Kiruna where the bedrock is dominated by metasomatic rocks belonging to the Lower Hauki suite. Approximately 2.5 km northeast of the city of Malmberget there are positive strontium anomalies, which are probably connected to the metasomatic process that formed the original hydrothermal quartzites and their current metamorphic equivalent (the corundum, andalusite and sillimanite-bearing gneisses). This geochemical pattern in tills can, to some extent, be linked by analogy to some of the metasomatic rocks associated to the metamorphosed porphyry copper deposit in Aitik, which are chemically of a similar character to those around Malmberget.

Aitik is the largest sulphide mine in Sweden and one of Europe's most important producers of copper and gold. The Aitik Cu-Au is thought to be the metamorphosed equivalent of porphyry copper deposit, which has gone through several phases of ore remobilization (Wanhainen et al. 2012). Mineralisation occurs within biotite- and muscovite schist, and hornblende-bearing gneisses. The most recent investigations showed that Aitik has a magmatic-hydrothermal origin and is genetically related to the quartz monzodioritic intrusions which are located in the structural footwall of the mineralization (Monro 1988, Wanhainen 2012). Extensive hydrothermal activity caused metasomatic alteration of wall-rocks as well as ore mineralisation. The sericitic schist, rich in pyrite, have been proposed to represent a metamorphosed lithocap connected to the porphyry, and is mainly composed of rocks formed by argillic and advance argillic alteration processes. The surrounding hornblende- and epidote-bearing biotite-gneisses are proposed to be the metamorphosed, peripheral, propylitic alteration zones (González in Ladenberger et al. 2012). High K-content in the ore zone is probably connected to biotite-alkalifeldspar metasomatism (potassic alteration), which commonly occurs in the central parts of most porphyry copper deposits (Lowell and Guilbert 1970; Sillitoe 2010).

Aitik's metamorphosed metasomatic rocks have a direct impact on till geochemistry in the area. High concentrations of Si, P, K, Sr, Cu, Ca, Y in till cover are typical for this region. The geochemical characteristics of the moraines resemble those overlying the Lower Hauki complex. Numerous similarities suggest that analogous hydrothermal processes (acid leaching) may have been active in both regions. Till geochemistry maps

reveal high total concentrations (XRF) of Si, K and P, which can be directly linked to the underlying muscovite schist. High K content in the till is however also connected to zones of potassic alteration. The geochemical map of Sr shows a large positive anomaly around the deposit (Fig.2), most likely linked to acid leaching processes connected to hydrothermal alteration. The results correlate well with the observations made by Yngström et al. (1986) and Monro (1988). These metasomatic processes, caused by aggressive solutions with low pH values, appear to be responsible for perceptible strontium accumulation (Hikov 2004 a, b and references therein; Velinov et al. 2007). Likewise, high strontium concentrations are also found in the Lower Hauki complex sericitic-schist and sericitic-quartzites from the Kiruna area and in the hydrothermal (secondary) quartzites from the Malmberget region.
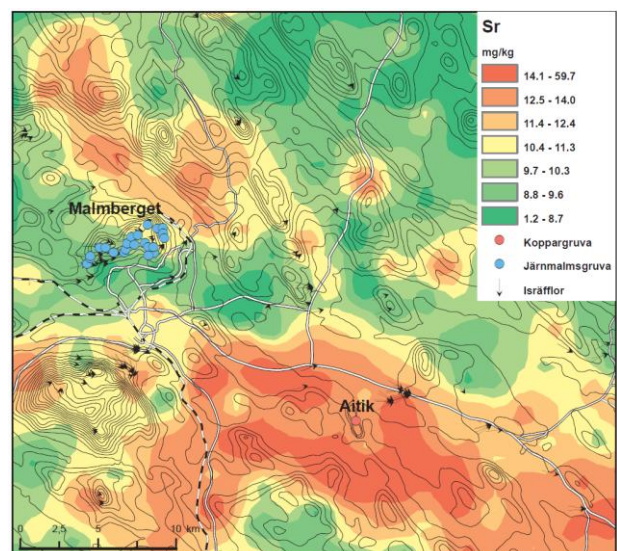


**Figure 2.** Anomalous Sr concentrations in till in the Aitik region (7M HNO$_3$ partial leach - ICP MS method).
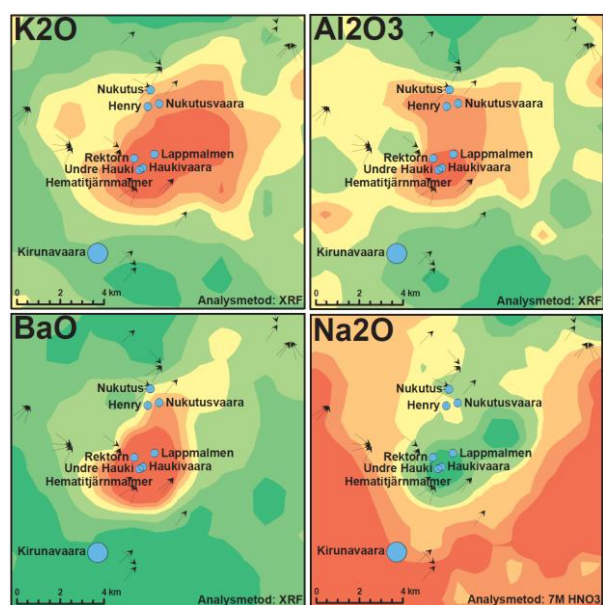


**Figure 3.** Anomalous elemental concentrations in till related to the occurrences of metasomatic rocks of the Lower Hauki complex.
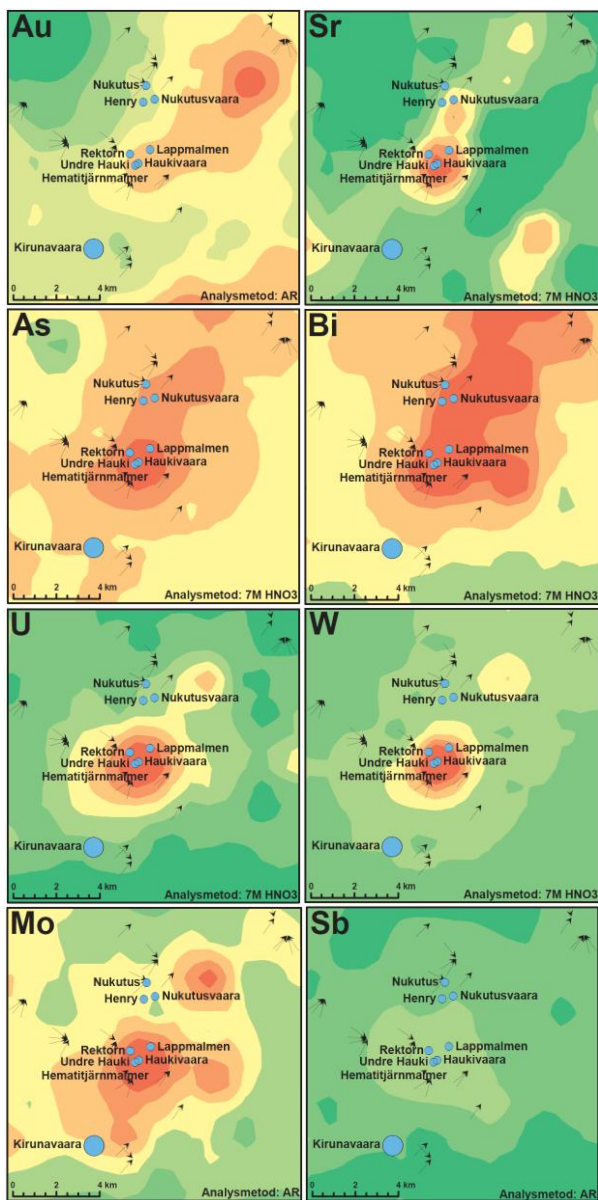
**Figure 3.** Continued.

## 3. Conclusions

Regional geochemical mapping in Northern Sweden reveals large elemental anomalies which can be directly correlated with the presence of hydrothermal alteration zones in the bedrock formed through extensive metasomatic activity and responsible for the creation of numerous mineralisations occurring in the area. Several elements, such as Ba, Si, Al, Sr, K, Au, Ag, Bi, Sb, As etc., form positive anomalies of different magnitude in close proximity to ore deposits of apparently magmatic-hydrothermal and hydrothermal origin.

If a genetic link between the metasomatic rocks and ore mineralisation can be demonstrated, then an extremely powerful tool for exploration geochemistry may be developed.

## Acknowledgements

## References

Bergman S, Kübler L, Martinsson O (2001) Description of regional geological and geophysical maps of northern Norrbotten County (east of the Caledonian orogen). Sveriges geologiska undersökning Ba 56, p 110.

Fettes D, Desmons J (2007) Metamorphic rocks: a classification and glossary of terms. Recommendations of the International Union of Geological Sciences Subcommission on the Systematics of Metamorphic Rocks, p 244.

Frietsch R (1966) Berggrund och malmer i Svappavaarafältet, norra Sverige. Sveriges geologiska undersökning C 604, p 282.

Geijer P (1931) Berggrunden inom malmtrakten Kiruna–Gällivare–Pajala. Sveriges geologiska undersökning C 366, p 225.

Hikov A (2004a) Geochemistry of strontium during advanced argillic alteration associated with some epithermal and porphyry copper deposits in Bulgaria. I A. Chatzipetros & S. Pavlides (red.): Proceedings of 5th Intern. Symp. of Eastern Mediterranean Geology 3:1402–1405.

Hikov A (2004b) Geochemistry of strontium in advance argillic alteration systems-possible guide to exploration. Bulgarian Geological Society. Annual Scientific Conference "Geology 2004", pp 29–31.

Högbom AG (1910) The Gellivare iron mountain. A guide for excursions. Geologiska Föreningens i Stockholm Förhandlingar 32:561–600.

Ladenberger A, Andersson M, González J, Lax K, Carlsson M, Olsson SÅ, Jelinek C (2012) Markgeokemiska kartan. Morängeokemi i norra Norrbotten (eng. Till geochemistry in northern Norrbotten). SGU report K 410, p 112.

Lowell JD, Guilbert JM (1970) Lateral and vertical alteration-mineralization zoning in porphyry ore deposits. Economic Geology 65:373–408.

Melezhik VA, Fallick AE, Rychanchik DV, Kuznetsov AB (2005) Palaeoproterozoic evaporates in Fennoscandia: Implications for seawater sulfate, δ13C excursions and the rise of atmospheric oxygen. Terra Nova 17:141–148.

Monro D (1988) The geology and genesis of the Aitik Cu-Au deposit, Arctic Sweden. Department of Geology, University College, Cardiff, p 386.

Pirajno F (2009) Hydrothermal processes and mineral systems, p 1250.

Sillitoe RH (2010) Porphyry Copper Systems. Economic Geology v. 105, no. 1:3-41.

Velinov I, Kunov A, Velinova N (2007) The metasomatic secondary quartzite formation in Bulgaria, p 199.

Wanhainen C, Broman C, Martinsson O, Magnor B (2012) Modification of a Palaeoproterozoic porphyry-like system: Integration of structural, geochemical, petrographic, and fluid inclusion data from the Aitik Cu–Au–Ag deposit, northern Sweden. Ore Geology Reviews 48:306-331.

White NC, Hedenquist JW (1995) Epithermal gold deposits: styles, characteristics and exploration. SEG Newsletter 23:9–13.
Yngström S, Nord AG, Åberg G (1986) A sulphur and strontium isotope study of the Aitik copper ore, northern Sweden. Geologiska Föreningens i Stockholm Förhandlingar 108:367–372.

# Hydrothermal footprints around magmatic nickel-sulfide deposits: a case study at the Miitel deposit, Yilgarn craton, Western Australia

**Margaux Le Vaillant, Marco L. Fiorentini, John Miller**
*Centre for Exploration Targeting, School of Earth and Environment, ARC Centre of Excellence for Core to Crust Fluid Systems, The University of Western Australia, Perth, Australia.*

**Stephen J. Barnes**
*CSIRO / Earth Science and Resource Engineering, Kensington, Perth, Australia.*

**Peter Muccilli**
*Exploration manager Mincor Resources NL, Perth, Australia.*

**David Paterson**
*Australian Synchrotron, Clayton, Victoria, Australia.*

**Abstract.** Magmatic nickel-sulfide deposits are highly valuable but extremely challenging exploration targets, lacking the distinctive geochemical haloes that allow small targets to be identified from sparse drilling. The remobilization of metals during post-deposition hydrothermal alteration has the potential to result in large haloes, whose recognition could increase exploration success rates. Using the West Australian Miitel komatiite-hosted nickel-sulfide deposit as case study, we investigate the nature and 3D geometry of the footprint created by the remobilization of base metals, gold and platinum group elements into the rocks surrounding the deposit. At Miitel, anomalous metal enrichment in the country rocks surrounding the ore bodies occurs in association with the presence of sulfarsenides, which are formed during the circulation of arsenic-rich hydrothermal fluids. Nickel sulfarsenides, such as gersdorfitte, are concentrated in small sulfide veinlets within the Lunnon basalt footwall, in close proximity to the contact with the overlying komatiite. This NiAs enrichment is associated with elevated concentrations in PGEs, indicating that the nickel sulfides from the Miitel ore bodies are the source of the remobilized Ni. This cryptic NiAs signature, which has been detected using pXRF on drill core up to 200 meters away from the mineralization, could represent a good mineralization vector.

**Keywords.** Targeting, brownfields exploration, metal remobilization, hydrothermal footprint, nickel sulfarsenide

## 1 Introduction

The genesis of magmatic nickel-sulfide deposits has been extensively studied over the years. Knowledge about primary magmatic processes such as crustal contamination (Barnes et al. 1995, 2004) and depletion in chalcophile elements (Duke 1979; Barnes et al. 2013) has been comprehensively applied to exploration targeting. These geochemical tools give information on the NiS potential of mafic-ultramafic bodies but they do not represent geochemical vectors providing information about distance to mineralization.

The study of secondary processes affecting nickel-sulfide deposits, especially post-magmatic circulation of hydrothermal and metamorphic fluids, has received little attention within the research community. By empirically studying the geochemistry of the rocks surrounding the mineralization at the Miitel deposit, the aim of this study is to address the following question: can Ni, Co, PGEs and Au be remobilized by hydrothermal fluids, thus creating a geochemical halo around nickel sulfide ore bodies that can be utilized in exploration targeting?

The Miitel deposit is a "type 1" komatiite-hosted nickel-sulfide deposit (Lesher and Keays 2002) situated on the eastern flank of the Widgiemooltha Dome (Seat et al. 2004), in the southern Kalgoorlie Terrane. The ore is composed of numerous massive nickel-sulfide bodies organized along a single shallow plunging channel, c.150m wide by 3.5 km long. The mineralization is hosted by talc-carbonate altered ultramafic rocks, resting either directly on a tholeiitic unit or on a thin veneer of sulfidic sediments, deposited during a hiatus between tholeiitic volcanism and the emplacement of komatiite flows (Marston 1984). The ore distribution is partly controlled by the presence of embayments in the upper surface of the footwall meta-basalt (Stone 2004).
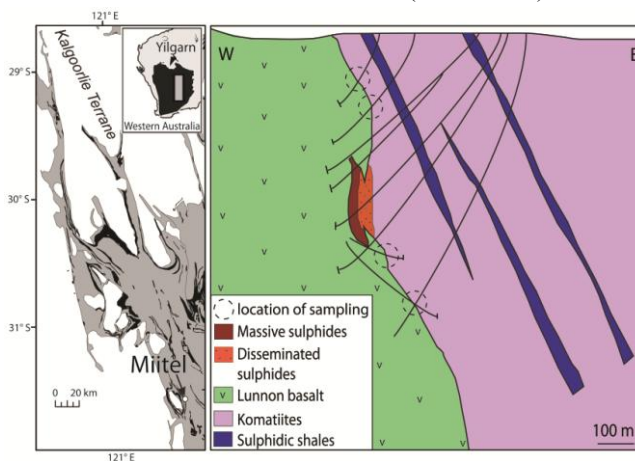


**Figure 1.** Location map and cross section through the Miitel system showing location of samples.

The structural evolution of the system, as outlined by Archibald et al. (1978), can be summarized by 4 main events: (D1) an early repetition of the stratigraphy by sub parallel thrusting, (D2) a folding event due to E-W compression explaining the sub vertical orientation of the stratigraphy, (D3 and D4) and sinistral shearing and late brittle faulting associated with areas of arsenic enrichment.

For the purposes of this study, the sampling focused

on the footwall contact between the komatiitic host rock and the underlying Lunnon basalt, identified as a potential pathway for hydrothermal fluids. 63 samples were collected, located gradually away from the ore bodies both below and above the main mineralized channel (figure 1). These samples were analyzed with various techniques in order to identify and characterize samples showing signs of hydrothermal remobilization. Firstly, the samples collected were analyzed using a portable XRF. Results provided an understanding of the spatial variation of Ni, S, Fe, Cu, Zn, As, Cr, Ti and Zr along each contact and in relation to the ore body. Samples showing anomalous values in Ni and As, representing a possible signature of hydrothermal remobilization, were studied in more detail by optical, electron microscopy, and x-ray fluorescence microscopy. Finally, all these observations were combined with the 3D model of the deposit in order to define the structural association and the geometry of the hydrothermal footprint surrounding the mineralization.

## 2 Material and methods

Portable XRF (pXRF) is a powerful and non destructive instrument allowing the rapid and reliable determination of a range of major and trace elements at a relatively low cost. Analyzes were performed on coarsely polished drill core surfaces at CSIRO using an Olympus-InnovX X500 desktop XRF analyser, which has a 10 W, 50 kV tantalum X-ray tube with a high precision, large-area silicon drift detector (SDD). It has recently been demonstrated, that providing standardization and calibration protocols are followed, pXRF analyses of Ni, S, Fe, Ti, Cr, Cu, Zn, As, and Zr, in mafic ultramafic fine-grained rocks can be used to produce meaningful datasets (Le Vaillant et al. in press). This recommended protocol was followed for 350 analyses of Miitel contact samples, representing an average of 6 analyses per sample. The elements determined and used for this study are Ni, S, Cu, Fe, Zn, As, Cr, Ti and Zr. Their calculated detection limits with pXRF varies between 2ppm for Zn and 0.15% for S, and the instrumental precision determined (calculated as being two times the Relative Standard Deviation of repeated analyses) varies between 1.2% for Fe and 7.5% for Zn.

Once pXRF analyses had been collected, 32 of the contact samples from the Miitel deposit were separated in two by lithology (basalt or komatiite) and sent to the Ultra Trace Laboratories, Perth, for detailed PGE analyses. The main oxide concentrations are obtained by X-Ray Fluorescence (XRF) Spectrometry on samples cast using 12:22 flux to form a glass bead. The samples were then digested and refluxed with a mixture of acids including hydrofluoric, nitric, hydrochloric and perochloric Acids. This extended digest approaches a total digest for many elements: a few refractory minerals such as zircon and chromite are still not completely attacked, although recoveries of better than 90% are indicated for most samples (Barnes et al. 2004). The samples obtained were then analyzed by both Inductively Coupled Plasma (ICP) Mass Spectrometry and ICP Optical Spectrometry (ICP-OES) to obtain trace

elements concentrations. Finally, a lead fire assay process gave a total separation of gold, Platinum and Palladium, which are then determined by ICP-MS.

Some of the samples showing anomalous Ni and As concentrations with pXRF analyses were selected for high-resolution element mapping at the Australian Synchrotron in Melbourne. The data were collected using the Maia detector on the X-ray Fluorescence Microscopy beam line, which generates elemental maps with a precision of up to 2μm pixels, and ppm detection limits.

Two of the anomalous basalt samples were also selected for spot mineral analysis by Laser Ablation Inductively Coupled Plasma Mass Spectrometry (LA-ICP-MS) at the University of Quebec in Chicoutimi (UQAC, Canada). Nickel sulfarsenides were analyzed in order to determine their PGE compositions.

## 3 Results

The results of the pXRF analyses on the contact samples from Miitel show values of Ni significantly higher than expected in some of the basaltic samples close to the contact. The Ni/Ti vs Ni/Cr plot is an effective way of separating the two different lithologies analysed, as komatiites and basalts show different concentrations in Ti and Cr. This plot also highlights enrichment in nickel contents, illustrated by the Ni-addition vector on Figure 2. Samples analysed by laboratory XRF (Ultra Trace labs, Perth) are represented on the ratio/ratio plot by points and characterize "background" samples that have been collected away from the mineralisation and the footwall contact.
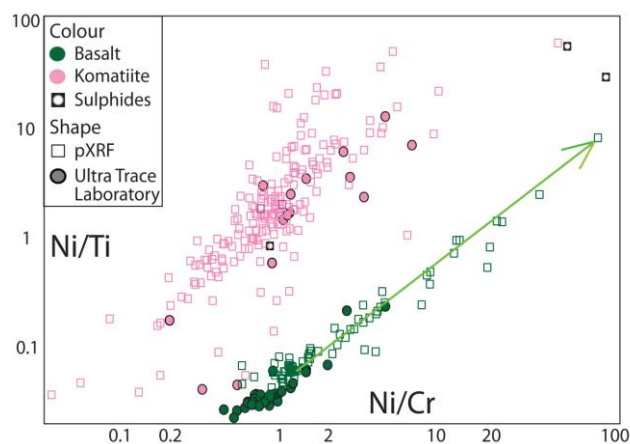


**Figure 2.** Ni/Ti vs Ni/Cr plot of pXRF and laboratory analyses on Miitel contact samples. The contours represent 50th percentiles.

Optical petrographic study, combined with mineral identification using SEM coupled with EDS quantitative analysis, shows that the nickel is either present as pentlandite exsolutions in pyrrhotite or combined with arsenic as gersdorffite or nickeline. The nickel sulfarsenides are mostly situated within small carbonate and quartz veins or in their selvedge area.

Two of the basaltic samples showing anomalous Ni concentrations with pXRF were analyzed at the Australian Synchrotron (AS). The elemental maps produced confirmed the strong association between Ni

and As (Figure 3), as well as their concentration in small secondary carbonate-quartz veins and their selvedge.

Multiple nickel sulfarsenides contained in these small veins located in the footwall basalt close to the contact with the komatiites were analyzed by LA-ICP-MS. The results show that their composition is fairly homogeneous with approximately 50% As, 20% Ni, 15% S, 9% Fe, 3% Co, 19ppm Pd and 4ppm Pt.

Finally, the detailed PGE analyses of 32 of the contact samples highlight anomalously high PGE concentrations (20-200 ppb Pt, 30-150 ppb Pd) in some of the basaltic samples. The PGE enriched samples coincide with samples which presented high Ni and As values with pXRF analyses.

## 4 3D geometry of the footprint

The remobilization of nickel and PGEs observed in some of the basaltic samples collected at the footwall contact seems to be associated with the circulation of arsenic rich fluids. McCuaig interpreted the distribution of high arsenic values at Miitel as being epigenetic, overprinting the Ni-sulfide mineralization during deformation (unpublished SRK report, 2002). This enrichment in As is thought to have been introduced into the system by West dipping shear zones and associated shallower S-SSW shallow dipping splay-structures. The arsenic concentrations are especially elevated at the intersection of these structures with the ore, since the massive sulfides play the role of source of S, Ni and Fe to form

As- bearing minerals, arsenopyrite (FeAsS), gersdorffite (NiAsS) and nickeline (NiAs). In order to determine the 3D geometry of the remobilization of Ni and PGEs around the Miitel deposit, we modeled the distribution of the arsenic in the system using the Leapfrog 3D modeling software and the assay database provided by Mincor Resources NL.

When comparing the distribution of the basalt samples containing high Ni, As and PGEs, with the distribution of the As concentrations within the Miitel system, we observe a close spatial correlation. The anomalous basalt samples are located close to the contact with the komatiites, in arsenic enriched areas and in the prolongation of ore bodies (Figure 4). This NiAs enrichment is interpreted as the signature of the remobilization of nickel and PGEs from the Miitel mineralization by hydrothermal fluids rich in arsenic.

This enrichment seems to be restricted to zones where As-rich fluids circulated and close to basal contacts located in the continuation of mineralization. The maximum extent of this geochemical halo is yet to be determined, but is at least 200m away from the nickel sulfides.

## 5 Conclusion

In this study, pXRF analyses allowed us to detect a subtle and irregular enrichment in Ni and As in the footwall basalt, close to the contact with the komatiite at various distances from the mineralization. The detailed



| Quantification with microprobe ● | | | | | | Quantification with LA-ICP-MS. | | | | | | | |
|---|---|---|---|---|---|---|---|---|---|---|---|---|---|
| S - pct | Fe - pct | Co - pct | Ni - pct | As - pct | Cu - pct | Au - ppm | Ir - ppm | Os - ppm | Pd - ppm | Pt - ppm | Rh - ppm | Ru - ppm | S - pct |
| 16.41 | 8.98 | 3.21 | 21.43 | 52.03 | 0.01 | 12.80 | 0.006 | 0.007 | 18.90 | 3.30 | 0.015 | 0.70 | 17.70 |
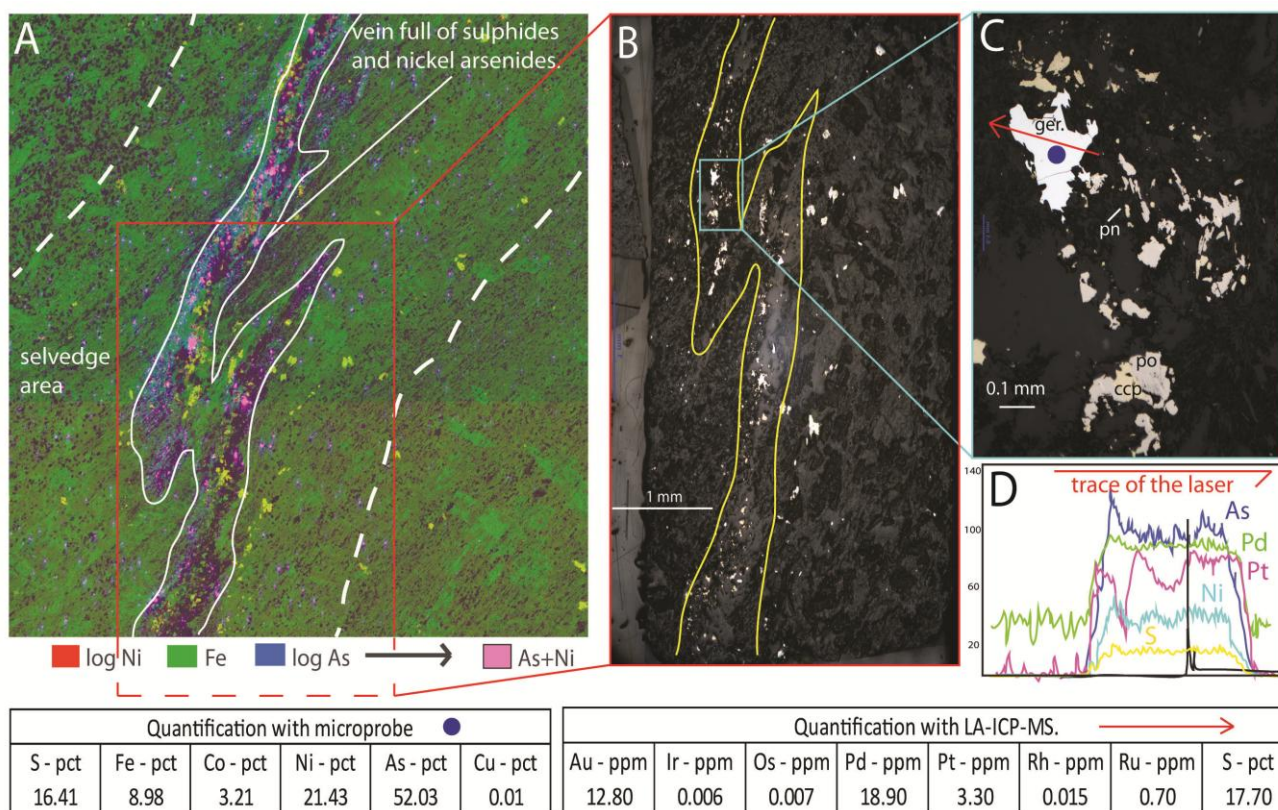
**Figure 3.** (A) Three element RGB map (log of Ni, Fe and log of As) collected at the Australian Synchrotron in Melbourne using the Maia detector on the X-Ray Fluorescence Microscopy beamline. (B) and (C) are microscopic pictures taken under reflective light. ger=gersdorffite, ccp=chalcopyrite, po=pyrrhotite and pn=pentlandite. The red arrow indicates the laser line and the blue spot represents the location of the microprobe analysis. The quantification of the composition with LA-ICP-MS of the gersdorffite was done using Igor Pro™ and Iolite™ softwares, with LAFLAMME as calibrant and Fe as internal standard.
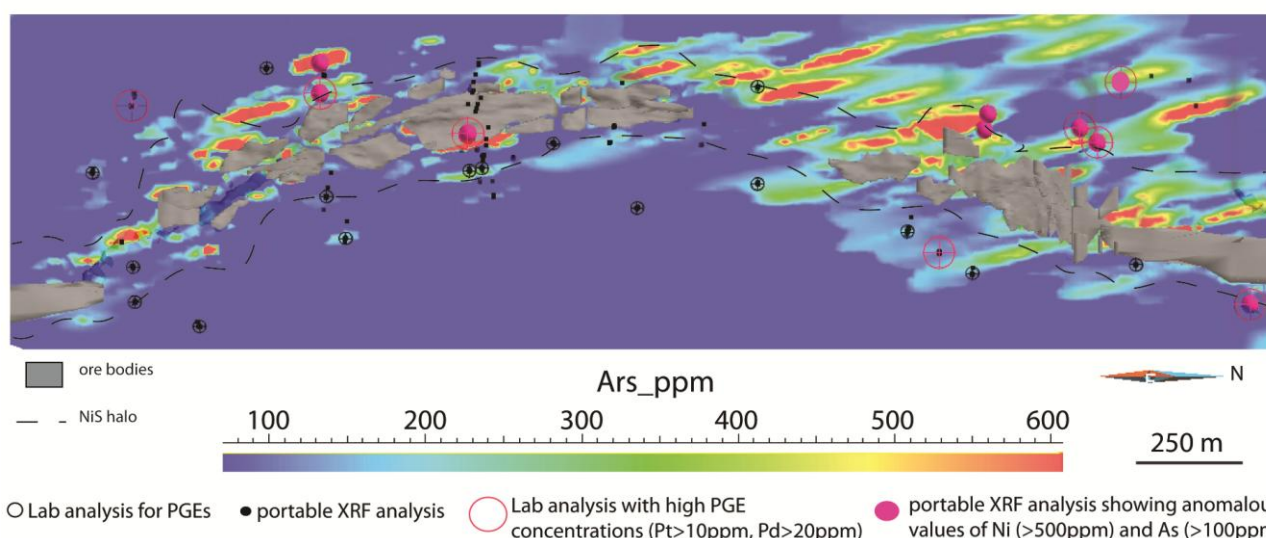
**Figure 4.** Snapshot from gOcad of the 3D model of the Miitel deposit combining the distribution of the arsenic in ppm at the contact between the basalt and the komatiites (model of the distribution effectuated using Leapfrog), and the location of Ni, As and PGEs enriched basaltic samples.

study of some of the samples with Ni-As enriched signatures (petrographic study, SEM-EDS and 3 elemental maps from the Australian synchrotron) allowed us to attribute these Ni-As anomalies to the presence of small veinlets containing nickel sulfarsenides, mainly gersdorffite (NiAsS).

Finally, laboratory analyses of the samples provided more comprehensive information on the geochemistry of this hydrothermal signature, and the presence of PGEs associated with the Ni-As enrichment suggests that the source of the remobilized Ni is composed of sulfides (Miitel Ore bodies) rather than of silicates (Miitel komatiites). The geometry of this hydrothermal footprint depends on the combined distribution of the mineralization and cross cutting fault structures associated with high arsenic concentrations. The signal extends 150 to 200 meters away from the ore bodies along the footwall contact.

## Acknowledgements

## References

Archibald DA, Bettenay LF, Binns RA, Groves DI, Gunthorpe RJ (1978) The evolution of Archaean greenstone terranes, Eastern Goldfields province, Western Australia. Precambrian Research 6:147-163

Barnes SJ (2004) Komatiites and nickel sulfide ores of the Black Swan area, Yilgarn Craton, Western Australia. 4. Platinum group element distribution in the ores, and genetic implications. Mineralium Deposita 39 (7):752-765. doi:10.1007/s00126-004-0440-1

Barnes SJ, Heggie G, Fiorentini ML (2013) Spatial variation in platinum-group element concentrations in ore-bearing komatiite at the Long-Victor deposit, Kambalda Dome, Western Australia: enlarging the footprint of nickel sulfide ore bodies. Economic Geology in press

Barnes SJ, Lesher CM, Keays RR (1995) Geochemistry of mineralised and barren komatiites from the Perseverance nickel deposit, Western Australia. Lithos 34:209-234

Duke JM (1979) Computer simulation of the fractionation of olivine and sulfide from mafic and ultramafic magmas. Canadian Mineralogist 17:507-514

Le Vaillant M, Barnes SJ, Fisher L, Fiorentini ML, Caruso S (2013) Use and calibration of portable X-Ray fluorescence analysers: Applications to lithogeochemical exploration for komatiite-hosted nickel-sulphide deposits. Geochemistry: Exploration, Environment, Analysis Special Volume on pXRF (in press)

Lesher CM, Keays RR (2002) Komatiite-Associated Ni-Cu-(PGE) Deposits: Mineralogy, Geochemistry, and Genesis, in L. J. Cabri (Editor), The Geology, Geochemistry, Mineralogy, and Mineral Benefication of the Platinum-Group Elements. Canadian Institute of Mining, Metallurgy and Petroleum Special Volume 54:579-617

Martson RJ (1984) Nickel mineralisation in Western Australia. GSWA Mineral Resources Bulletin 14:p. 271

Seat Z, Stone WE, Mapleson DB, Daddow BC (2004) Tenor variation within komatiite-associated nickel sulphide deposits: insights from the Wannaway Deposit, Widgiemooltha Dome, Western Australia. Mineralogy and Petrology 82 (3-4):317-339. doi:10.1007/s00710-004-0047-3

Stone WE, Heydari M, Seat Z (2004) Nickel tenor variations between Archaean komatiite-associated nickel sulphide deposits, Kambalda ore field, Western Australia: the metamorphic modification model revisited. Mineralogy and Petrology 82 (3-4):295-316. doi:10.1007/s00710-004-0045-5

# Fe and Zn isotopes in the Navan Zn-Pb deposit, Ireland: implications for mineral exploration

Julian F. Menuge, Gareth J. Barker, Damien Gagnevin*
*School of Geological Sciences, University College Dublin, Belfield, Dublin 4, Ireland*
*\* Present address: Tullow Oil plc, Number 1, Central Park, Leopardstown, Dublin 18, Ireland*

Adrian J. Boyce
*Scottish Universities Environmental Research Centre, East Kilbride, Glasgow G75 0QF, Scotland*

**Abstract.** Fe, Zn and S isotope data are presented for iron and zinc sulphides from the Navan Zn-Pb orebody, Ireland. The samples exhibit large Fe ($\delta^{56}$Fe = -2.2 to -0.3) and Zn ($\delta^{66}$Zn = -0.32 to 0.26) isotope variations. We use the well-understood behaviour of S isotopes in the Navan orebody, combined with experimental and geological studies, to explain Fe and Zn isotope variation. Fe isotopes are strongly fractionated in favour of light isotopes in hydrothermal sulphides relative to sedimentary and diagenetic sulphides. This is inferred to result from incomplete leaching of Fe from source rocks by hydrothermal fluids, allowing hydrothermal Fe to be discriminated from sedimentary and diagenetic Fe. Anticorrelated $\delta^{56}$Fe and $\delta^{34}$S suggest that lesser fractionation of Fe isotopes also occurred during crystallisation of Fe sulphides, during mixing of two fluids of different S isotope composition. Sphalerite Zn isotope variation is consistent with kinetic isotope fractionation during crystallisation, with early-formed sphalerite isotopically lightest. Strongly negative and very variable $\delta^{66}$Zn is likely to correlate with fluid mixing in Irish-type deposits, a feature necessary for the development of large orebodies. Exhaust fluids remaining after Irish-type orebody sulphide crystallisation are predicted to have distinctively heavy Zn isotope signatures.

**Keywords** Fe-Zn-S isotopes, Irish-type, hydrothermal, Zn-Pb ore, Navan.

## 1 Introduction

The increasing demand for many metals, coupled with the exhaustion of many near-surface deposits in much of Europe and elsewhere, requires that new methods be developed to detect more deeply buried orebodies. Many classes of hydrothermal orebody are surrounded by haloes of sub-economic mineralisation and other alteration effects and these may potentially allow remote detection of orebodies (Kelley et al. 2006), if ways can be found to distinguish haloes of substantial orebodies from minor mineralisation.

The past decade or so has seen the development of analytical techniques for precise isotope ratio measurements of Fe and Zn. The redox behaviour and centrality to many biological processes of Fe have seen a large literature develop on its isotope analysis (Dauphas and Rouxel 2006). Both biotic and abiotic reactions have been shown to produce large fractionations of Fe isotopes (e.g. Guilbaud et al. 2011). Several studies have demonstrated substantial Fe isotope

variability in hydrothermal ores and ore-forming environments, notably black smokers (Rouxel et al. 2008) and mineralised skarns (Wang et al. 2011). Kinetic and equilibrium Fe isotope fractionation associated with a number of reactions involving iron minerals have been measured, including pyrite-forming reactions (e.g. Guilbaud et al. 2011). Much less work has been done on Zn isotopes, but major Zn isotope variability has been demonstrated in several classes of ore deposit, including Irish-type (Gagnevin et al. 2012), other sediment-hosted (Kelley et al. 2009) and VMS deposits (Mason et al. 2005).

This study uses the Navan Zn-Pb ore deposit (Fig. 1) to explore the variability of Fe and Zn isotopes in this world-class orebody and to infer the possible uses of these isotope methods in mineral exploration. The origin of the Navan deposit is relatively well understood after ~35 years of mining and research (Ashton et al. 2010). In particular, S isotope data provide a firm foundation for interpretation of Fe and Zn isotope data, allowing the utility of Fe and Zn isotope analyses as tracers of metal origin and fluid evolution to be explored.
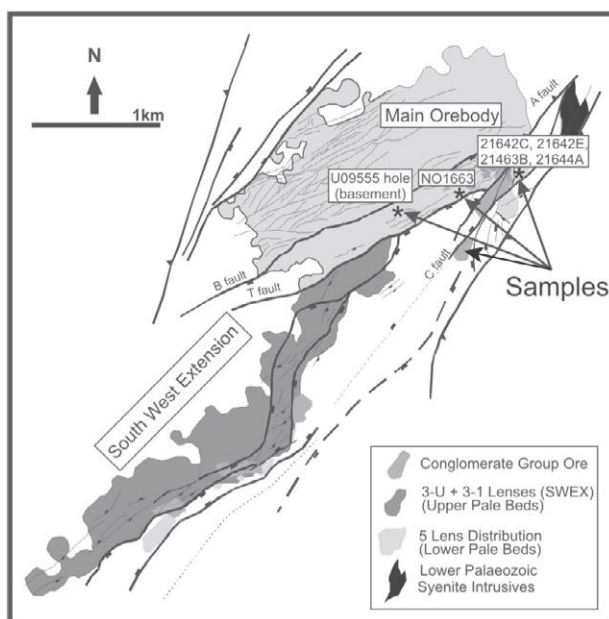


**Figure 1.** Simplified surface projection of the geology of the Navan orebody showing geometry of principal ore lenses and structures, and sampling localities (modified from Tara Mines internal report)

## 2  The Navan Zn-Pb Orebody

The Navan ore deposit, lying 50 km northwest of Dublin, Ireland (Fig. 1), is the largest Irish-type base metal orebody. This deposit class is commonly considered to be part of a larger group of mainly carbonate-hosted base metal deposits that has affinities to both Mississippi Valley-type (MVT) (Leach and Sangster 1993) and SEDEX deposits (Blakeman et al. 2002). Navan reserves and mined ore total 107 million tonnes at an average grade of ~10% zinc and ~2% lead (Ashton pers. comm., 2012). The principal economic sulfides at Navan comprise sphalerite and galena (Ashton et al. 2010), accompanied by gangue barite, calcite, dolomite, pyrite and subordinate marcasite.

The orebody is hosted in Lower Carboniferous sedimentary rocks. The majority (~97%) of ore occurs as a series of mainly replacive stratabound lenses within the Pale Beds, which are Lower Carboniferous shallow-marine carbonates of Courceyan to Chadian age (Ashton et al. 2010). A Chadian unconformity truncates the Courceyan rocks and is considered to be the product of submarine gravitational instability caused by extensional faulting (Boyce et al. 2003). The remaining 3% of ore, termed Conglomerate Group Ore (CGO), is hosted by a sequence of debrite and fault talus, referred to as Boulder Conglomerate (BC), that was deposited in a half graben immediately above the unconformity. CGO mineralization may occur as cement to interclast porosity and stratiform replacement (Ford 1996). CGO differs from the Pale Beds ore in that it contains volumetrically significant Fe disulfides amounting to ~23% of the total ore (Ashton et al. 2010). Mineralization in the CGO is genetically significant, as it may represent the exhalative manifestation of the mainly replacive ore found in the Pale Beds.

The distinctive features of Irish-type deposits, including Navan, include association of mineralisation with active extensional faulting, hosting of mineralisation by the lowermost "clean" carbonate horizons and a bimodal distribution of $\delta^{34}S$ in sulphide minerals with negative values attributed to bacteriogenic reduction of seawater sulfate and positive values attributed to sulphide derived from the Lower Palaeozoic basement (Anderson et al. 1998). Major sulphide precipitation in the orebody was triggered when these two fluids mixed. This last feature implies that metals, including Fe and Zn, are essentially exclusively delivered to the ore from a hydrothermal fluid that has interacted with Lower Palaeozoic supracrustal rocks. Sulphide has a mixed origin, a minor component being basement-derived but most being of bacteriogenic origin (Fallick et al. 2001).

## 3  Sampling and Analytical Methods

Core samples for analysis were collected from 5-lens, the thickest ore horizon, from the central part of the main Pale Beds orebody, and from BC and CGO from south of the C fault (Fig. 1). Textural analysis of samples was done in reflected and transmitted light, and by SEM in some cases. All Pale Beds samples had textures indicative of hydrothermal origin, mostly colloform and other finely banded morphologies. BC and CGO Fe sulphide samples included framboidal pyrite of sedimentary origin, diagenetic plumose marcasite and laminated or concretionary hydrothermal textures that may include pyrite, marcasite or both. CGO sphalerite samples were all of hydrothermal origin.

Following textural analysis, representative samples were selected for S, Fe and Zn isotope analysis. In-situ S isotopic analyses were carried out using a VG SIRA II isotope ratio gas mass spectrometer (Kelley and Fallick 1990).

Sampling of iron sulphides and sphalerite for Zn and Fe isotope analysis was carried out using a New Wave computer-controlled micromill, at a spatial resolution of 100-300 μm. The zone for microdrilling was targeted on the basis of textural features on material matching as closely as possible that sampled for S isotope analysis. Prior to Fe and Zn isotope analysis, sulphide micro-samples were chemically purified on small columns containing 200-400 mesh AG1-X8 anion-exchange resin (Gagnevin et al. 2012). Fe and Zn isotope ratios were then determined using a Thermo-Scientific Neptune MC-ICP-MS instrument, using sample-standard bracketing to correct for instrumental mass bias. Medium resolution was used for Fe isotope analysis to avoid argide interferences. Results are presented in standard delta notation relative to IRMM14 Fe standard and Johnson Matthey Purotronic Zn metal IMC 12053. Further details of analytical techniques are given by Gagnevin et al. (2012), in which the Pale Beds sphalerite, zinc concentrates and basement rock S, Fe and Zn isotope data have also been reported; all other data are previously unreported.

## 4  Iron isotopes

All BC and CGO iron sulphide minerals analysed have negative $\delta^{56}Fe$ and $\delta^{34}S$ values (Fig. 2). They plot into three distinct groups according to their texture and inferred origin.

Framboidal pyrite, of sedimentary origin, exhibits the highest $\delta^{56}Fe$ values, between -0.2 and -0.7‰, and has uniformly low $\delta^{34}S$ values close to -40‰. Diagenetic plumose marcasite has similarly low $\delta^{34}S$, but much lower $\delta^{56}Fe$ around -2‰, whilst hydrothermal textures show a rough anticorrelation of $\delta^{56}Fe$ (-1.5 to -1.0‰) with $\delta^{34}S$ (-15 to -37‰). All types of iron sulphide have lower $\delta^{56}Fe$ than the potential hydrothermal metal source rocks. These varied Lower Palaeozoic sedimentary and volcanic rocks that underlie the Navan orebody have $\delta^{56}Fe$ values of 0.1 to -0.2‰.

Following Anderson et al. (1998), S isotope ratios are taken to indicate the relative contributions of hydrothermal sulphide delivered with the metals from Lower Palaeozoic basement (positive $\delta^{34}S$) and sulphide of bacteriogenic origin delivered from a separate, cooler brine ($\delta^{34}S$ <-10‰). The observed Fe isotope variation is interpreted to result from several causes.
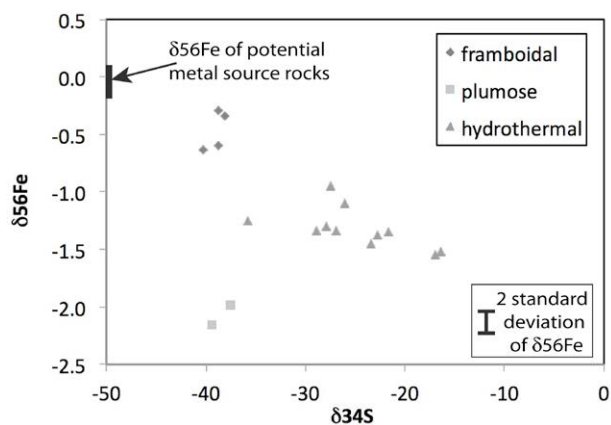
**Figure 2.** Variation in $\delta^{56}Fe$ and $\delta^{34}S$ in framboidal pyrite, plumose marcasite and hydrothermal pyrite / marcasite, all from Boulder Conglomerate and Conglomerate Group Ore. The range of $\delta^{56}Fe$ in potential metal source rocks is also shown. 2SD uncertainty is smaller than the plotted symbols for $\delta^{34}S$.

We propose that the light Fe isotope signature of the syngenetic framboids relative to the average continental weathering flux ($\delta^{56}Fe$ ~0‰ (Beard et al. 2003)) is the result of basinward transport of isotopically light reactive Fe derived from the shelf, as reported in the modern Black Sea (Severmann et al. 2008). We infer that extensive sedimentary Fe redox recycling during early diagenesis generated diagenetic fluids with $\delta^{56}Fe$ averaging ~-0.5‰, which were mobilized in a shelf-to-basin Fe shuttle contemporaneous with syngenetic framboid precipitation. Under the interpreted euxinic conditions the shuttled Fe would be efficiently incorporated into syngenetic framboids leading to quantitative transfer of this light $\delta^{56}Fe$ from solution to pyrite, limiting any fluid-mineral fractionation factors.

The more strongly negative $\delta^{56}Fe$ values (<-1.0‰) of hydrothermal Fe sulphides are interpreted to result primarily from fractionation during incomplete leaching of iron from source rocks. Incomplete leaching is expected due to formation of secondary iron-bearing minerals and has also been implicated in Fe isotope fractionation in sulphide minerals in black smokers (Rouxel et al. 2008) and in a variety of other hydrothermal iron minerals (Markl et al. 2006). The anticorrelation of $\delta^{56}Fe$ with $\delta^{34}S$ suggests a second fractionation effect associated with crystallisation of hydrothermal Fe sulphides; it is proposed that kinetic isotope fractionation was greater for early-formed (high $\delta^{34}S$) sulphides, giving these a more negative $\delta^{56}Fe$ than those that formed later.

The unusually low $\delta^{56}Fe$ values around -2‰, yet with very low $\delta^{34}S$, of the diagenetic plumose marcasite indicates a bacteriogenic sulphide source combined with very isotopically light Fe. Plumose texture suggests rapid crystallisation and it is proposed that its formation was accompanied by extreme kinetic Fe isotope fractionation of the same Fe fluid source as for the sedimentary framboidal Fe sulphide.

## 5 Zinc isotopes

Pale Beds sphalerite (Fig. 3) shows a wide range of both $\delta^{34}S$ (-13 to 15‰) and $\delta^{66}Zn$ (0.23 to -0.32‰) (Gagnevin et al. 2012). All samples with positive $\delta^{34}S$ have $\delta^{66}Zn$ <-0.15‰ and all samples with $\delta^{34}S$ <-8‰ have $\delta^{66}Zn$ >-0.10‰. Samples with $\delta^{34}S$ between 0 and -8‰ show $\delta^{66}Zn$ values spanning almost the entire range of the data. CGO sphalerite is consistent with the trend of Pale Beds sphalerite, extending it to strongly negative $\delta^{34}S$ (-20 to -26‰), with consistently positive $\delta^{66}Zn$ (0.05 to 0.26‰). In contrast to the case of Fe isotopes, potential metal source rocks have $\delta^{66}Zn$ values (-0.02 to 0.23‰) that lie within the range of Pale Beds and CGO sphalerite, being similar to those sphalerites that have $\delta^{34}S$ <-8‰. Zinc concentrates, derived overwhelmingly from Pale Beds sphalerite, have moderately negative $\delta^{34}S$ values and have $\delta^{66}Zn$ values within, or just below, the range of potential metal source rocks (Gagnevin et al. 2012).

By analysis of sequential millimeter-scale bands, Gagnevin et al. (2012) showed that Zn isotopes are fractionated by crystallisation of finely banded sphalerite in the Navan deposit. This is believed to be kinetic fractionation, in line with experimental evidence (Archer et al. 2004) and consistent with inferences from other studies of hydrothermal systems (Wilkinson et al. 2005; Kelley et al. 2009). The range of $\delta^{66}Zn$ values (Fig. 3) is consistent with this model. Sphalerite that crystallised early with mainly hydrothermal sulphide (positive $\delta^{34}S$) exhibits the lowest $\delta^{66}Zn$ values. Where sphalerite crystallised in the presence of mainly bacteriogenic sulphide, $\delta^{66}Zn$ values of these samples are comparable to the values in the proposed source rocks, suggesting less Zn isotope fractionation. The observation that the zinc concentrates, that average large volumes of ore, have a mean $\delta^{66}Zn$ very close to the mean for proposed source rocks suggests that there is negligible Zn isotope fractionation associated with leaching of Zn from its source rocks.
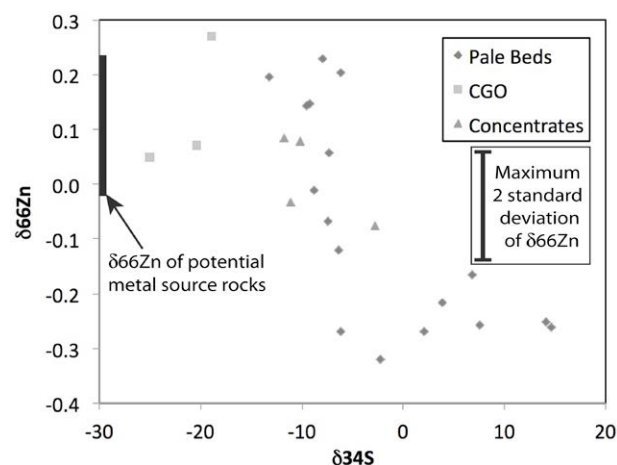


**Figure 3.** Variation in $\delta^{66}Zn$ and $\delta^{34}S$ in sphalerite from the Pale Beds, from Conglomerate Group Ore and from mine Zn concentrates (overwhelmingly Pale Beds in origin). The range of $\delta^{66}Zn$ in potential metal source rocks is also shown. 2SD uncertainty is smaller than the plotted symbols for $\delta^{34}S$.

## 6  Implications for Mineral Exploration

The behaviour of Fe and Zn isotopes at Navan has implications for mineral exploration around the Navan orebody, for other Irish-type orebodies and probably for other classes of hydrothermal base metal deposit.

Since incomplete leaching of Fe from rocks by hydrothermal fluids is likely to be a widespread phenomenon, $\delta^{56}Fe$ values below -1.0‰ are likely to be characteristic of hydrothermal fluids. Conversely, Fe of surficial origin will be only slightly fractionated relative to common crustal rocks and will normally have $\delta^{56}Fe$ >-1.0‰. This may prove useful to discriminate hydrothermal Fe from sedimentary / diagenetic Fe.

Large kinetic Fe and Zn isotope fractionation effects are preserved in rapidly crystallised iron sulphides and sphalerite, respectively; sphalerite may also record large Fe isotope fractionation effects (Gagnevin et al. 2012). Rapid crystallisation of sulphides at Navan and other Irish-type orebodies is a response to mixing of the two fluids required for production of a major orebody. It follows that recognition of widespread very light Fe and Zn in hydrothermal sulphides may indicate the nearby presence of an orebody.

Where a geochemical halo includes rocks that have interacted with the exhaust fluids remaining after orebody sulphide crystallisation, these rocks should be characterised by unusually isotopically heavy Zn and Fe, as pointed out by Gagnevin et al. (2012).

Analyses of whole-rock core samples for Fe and Zn isotope composition could be adequate for mineral exploration purposes where iron or zinc sulfides dominate the iron or zinc budgets, respectively, of rocks. This is likely to be commonplace for Irish-type deposits, where the host rocks are mainly clean carbonate sedimentary rocks.

## Acknowledgements

## References

Anderson IK, Ashton JH, Boyce AJ, Fallick AE, Russell MJ (1998) Ore depositional processes in the Navan Zn-Pb deposit, Ireland. Econ Geol 93: 535-563

Archer C, Vance D, Butler I (2004) Abiotic Zn isotope fractionations associated with ZnS precipitation. Geochim Cosmochim Acta 68: A325

Ashton JH, Blakeman R, Geraghty J, Beach A, Coller D, Philcox M, Boyce A, Wilkinson JJ (2010) The Giant Navan Carbonate-Hosted Zn-Pb Deposit - A Review. IAEG ZINC 2010 Meeting, Cork, Progr Abstracts 33-36

Beard BL, Johnson CM, Skulan JL, Nealson KH, Cox L, Sun H, (2003) Application of Fe isotopes to tracing the geochemical and biological cycling of Fe. Chem Geol 195: 87–117

Blakeman RJ, Ashton JH, Boyce AJ, Fallick AE, Russell MJ (2002) Timing of interplay between hydrothermal and surface fluids in the Navan Zn + Pb orebody, Ireland: Evidence from metal distribution trends, mineral textures, and $\delta^{34}S$ analyses. Econ Geol 97: 73-91

Boyce AJ, Anderton R, Russell MJ (1983) Rapid subsidence and early Carboniferous base-metal mineralization in Ireland. Trans Inst Mining Metall 92: B55–66

Ford CV (1996) The integration of petrologic and isotopic data from the Boulder Conglomerate to determine the age of the Navan orebody, Ireland. PhD thesis, University of Glasgow

Dauphas N, Rouxel O (2006) Mass spectrometry and natural variations of iron isotopes. Mass Spectrom Rev 25: 515–550

Fallick AE, Ashton JH, Boyce AJ, Ellam BM, Russell M.J (2001) Bacteria were responsible for the magnitude of the world-class hydrothermal base metal sulfide orebody at Navan Ireland. Econ Geol 96: 885-890

Gagnevin D, Boyce AJ, Barrie CD, Menuge JF, Blakeman RJ (2012) Zn, Fe and S isotope fractionation in a large hydrothermal system. Geochim Cosmochim Acta 88: 183–198

Guilbaud R, Butler IB, Ellam RM (2011) Abiotic Pyrite Formation Produces a Large Fe Isotope Fractionation. Science 332: 1548–1551

Kelley DL, Kelley KD, Coker WB, Caughlin B, Doherty ME (2006) Beyond the Obvious Limits of Ore Deposits: The Use of Mineralogical, Geochemical, and Biological Features for the Remote Detection of Mineralization. Econ Geol 101: 729–752

Kelley KD, Wilkinson JJ, Chapman JB, Crowther HL, Weiss DJ (2009) Zinc Isotopes in Sphalerite from Base Metal Deposits in the Red Dog District, Northern Alaska. Econ Geol 104: 767–773

Kelley S, Fallick A (1990) High-Precision Spatially Resolved Analysis of Delta-34-S in Sulfides Using a Laser Extraction Technique. Geochim Cosmochim Acta 54: 883–888

Leach DL, Sangster DF (1993) Mississippi Valley-type lead-zinc deposits. In: Kirkham, RV et al. (eds) Mineral Deposit Modeling. Geol Assoc Canada Spec Paper 40: 289-314

Markl G, von Blanckenburg F, Wagner T (2006) Iron isotope fractionation during hydrothermal ore deposition and alteration. Geochim Cosmochim Acta 70: 3011-3030

Mason TFD, Weiss DJ, Chapman JB, Wilkinson JJ, Tessalina SG, Spiro B, Horstwood MSA, Spratt J, Coles BJ (2005) Zn and Cu isotopic variability in the Alexandrinka volcanic-hosted massive sulphide (VHMS) ore deposit, Urals, Russia. Chem Geol 221: 170–187

Rouxel O, Shanks III WC, Bach W, Edwards KJ (2008) Integrated Fe- and S-isotope study of seafloor hydrothermal vents at East Pacific Rise 9–10°N. Chem Geol 252: 214–227

Severmann S, Lyons TW, Anbar A, McManus J, Gordon G (2008) Modern iron isotope perspective on the benthic iron shuttle and the redox evolution of ancient oceans. Geology 36: 487–490

Wang Y, Zhu X, Mao J, Li Z, Cheng Y (2011) Iron isotope fractionation during skarn-type metallogeny: A case study of Xinqiao Cu–S–Fe–Au deposit in the Middle–Lower Yangtze valley. Ore Geol Rev 43: 194–202

Wilkinson JJ, Weiss DJ, Mason TFD, Coles BJ (2005) Zinc isotope variation in hydrothermal systems: Preliminary evidence from the Irish Midlands ore field. Econ Geol 100: 583-590

# Surface media expressions of buried uranium: the Phoenix & Millennium deposits, Athabasca Basin, Saskatchewan, Canada

**Michael J. Power, Keiko Hattori**
*Department of Earth Sciences, University of Ottawa, Ottawa, ON, Canada K1N 6N5*

**Chad Sorba**
*Denison Mines Corp., 200-230 22nd St East, Saskatoon, SK, Canada S7K 0E9*

**Tom Kotzer**
*Cameco Corp., 2121 11th St West, Saskatoon, SK, Canada S7M 1J3*

**Eric G. Potter**
*Geological Survey of Canada, 601 Booth St, Ottawa, ON, Canada K1A 0E9*

**Abstract.** To detect buried uranium deposits using surficial geochemistry, we selected two known deposits: Phoenix and Millennium. The Phoenix has indicated resources of 52.3 million lbs $U_3O_8$ at ~400 m depth, whereas Millennium has indicated resources of 68.2 million lbs $U_3O_8$, at ~750 m depth. Both are located in the southeastern Athabasca Basin, Saskatchewan, Canada. Sampling in 2011 above Phoenix yielded anomalous U, Pb, Ni, Cu, Mo, As and W in humus, B-horizon soil, till and uppermost sandstones above the deposit and WS Shear zone. 2012 sampling reproduced anomalies in soil (2-17 ppm U, 10-27 ppm Cu, 4-7 ppm Ni, 1-1.5 ppm As) in total and partial leaches. Leaching of humus in various acid solutions shows that metals are tightly held in organics. Soil sampling over Millennium in 2012 yielded broad anomalies in U (0.4-0.6 ppm), Pb (15-35 ppm) and Cu (5-15 ppm) in partial leaches of humus and B-horizon soil above the deposit & B1 and Marker faults. Results suggest upward migration of mobile metals from these deposits to surface.

**Keywords.** surficial geochemistry, uranium exploration, glaciated terrain, Athabasca Basin.

## 1 Introduction

In order to evaluate surficial geochemical anomalies over deeply buried uranium deposits, we selected two deposits with no apparent surface expression of mineralization: the Phoenix and Millennium deposits (Fig. 1). The Phoenix deposit, owned by Denison Mines Corporation, occurs along the unconformity between the dominantly siliciclastic Athabasca Group sandstones and the crystalline basement rocks. It has currently defined indicated resources of 52.3 million lbs $U_3O_8$ situated ~400 m below the surface (Roscoe, 2012), whereas Cameco Corporation's basement-hosted Millennium deposit has indicated resources of 46.8 million lbs $U_3O_8$ at a depth of ~750 m (Cloutier et. al, 2009).

Both deposits are located in the southeastern margin of the Athabasca Basin in northern Saskatchewan, a region of sporadic discontinuous permafrost (Burgess et al., 1999). 25-30 m thick glacial tills comprised of moraine plains, streamlined moraines and subordinate eskers cover the area (Schreiner 1984; Campbell 2007).

Whole rock compositions of till samples from both properties suggest that the glacial sediments were sourced from a mixture of granitic basement rocks and Athabasca Group sandstones.
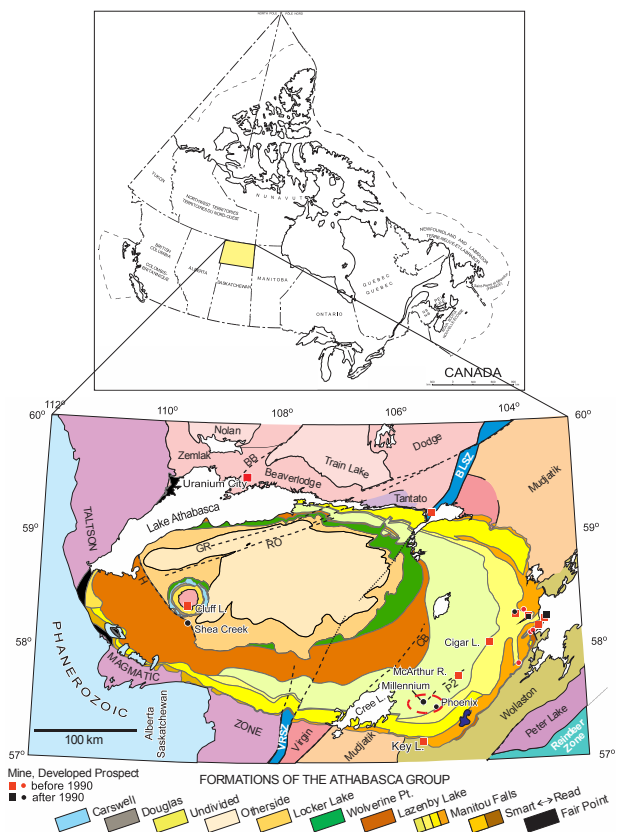


**Figure 1.** Location map of the Athabasca Basin, Saskatchewan, Canada, and the study area (dashed red oval) hosting the Phoenix & Millennium deposits in the southeastern Athabasca Basin. Geology from Jefferson et al. (2007).

At Phoenix, the mineralization is mostly pitchblende, with anomalous amounts of Cu (up to 3,100 ppm Cu) and Pb (up to 9.83 wt % Pb), and minor Ni (up to 461 ppm Ni), Co (up to 119 ppm Co), As (up to 170 ppm As), Zn (up to 1,070 ppm Zn) and Ag (up to 0.1 ppm Ag) (Kerr, 2011; this study).

For both systems, alteration mineralogy in the overlying Athabasca Group is typical of Athabasca

unconformity-related uranium systems with varying silicification and de-silification, tourmaline, chlorite, illite, kaolinite, hematite and drusy quartz. Of note, both properties also occur within the northeast-trending, regional illite and chlorite trend defined by Earle and Sopuck (1989).
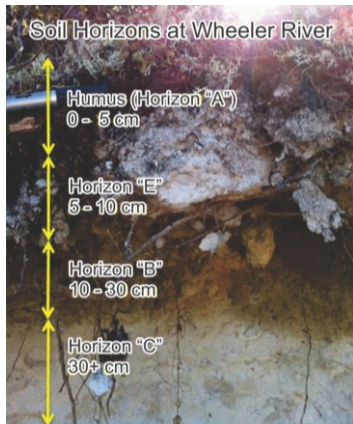


**Figure 2.** Typical soil horizon profile at Phoenix. The humus layer includes charcoal from a previous forest fire event. The photo was taken at 57° 30' 32.285" N, 105° 23' 10.768" W

## 2 Results from the Phoenix Study

2011 field sampling (sampling method, Fig. 2) above the Phoenix deposit yielded anomalous concentrations of U, Pb, Ni, Cu, Mo, As and W in humus, B-horizon soil and C-horizon glacial till in the areas directly above the A and B ore zones and the WS Shear zone (humus, Figs. 3 & 4). 2012 sampling reproduced similar geochemical anomalies in soil samples (2-17 ppm U, 10-27 ppm Cu, 4-7 ppm Ni, 1000-1500 ppb As; Figs. 4 & 5). Furthermore, leaching of humus samples in $H_2O$, HBr, $HNO_3$ and HF-HBr solutions showed that these metals are not simply adsorbed on the surface; instead, they are tightly held in organics (Fig. 6). Finally, analyses of the uppermost Manitou Falls Dunlop Formation sandstones by partial HF-$HNO_3$-HCl digestion above the ore zones contain anomalous U (up to 2 ppm, Fig. 4).
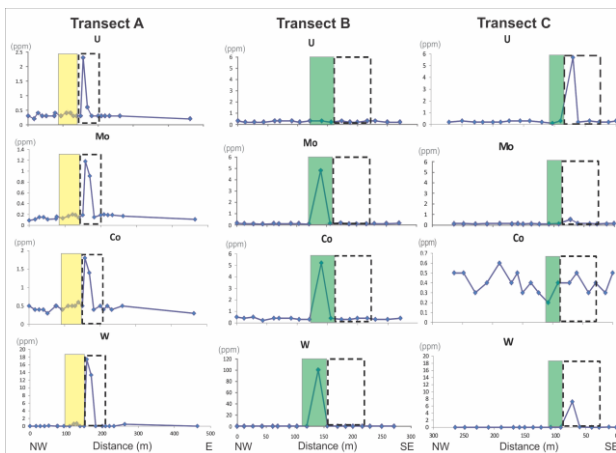


**Figure 3.** Metal abundances along the 2011 transects at Phoenix: U, Mo, Co, W in humus from the 2011 sampling programme after aqua regia digestion. The boxes indicate the areas directly above ore Zones A & B1, and the dotted rectangle encompasses the expression of the WS Hanging Wall shear at the unconformity.

## 3 Results from the Millennium Study

Soil sampling was carried out along transects over the Millennium deposit in the summer of 2012. These samples yielded anomalies in U (0.4-0.6 ppm), Pb (15-35 ppm) and Cu (5-15 ppm) from aqua regia digestions of humus as well as anomalies in ammonium acetate leaches of B horizon soils above the ore zones and surface traces of B1 and Marker faults (Fig. 7). Broad surficial geochemical anomalies in the property likely reflect abundant faults and fault-bound mineralization.
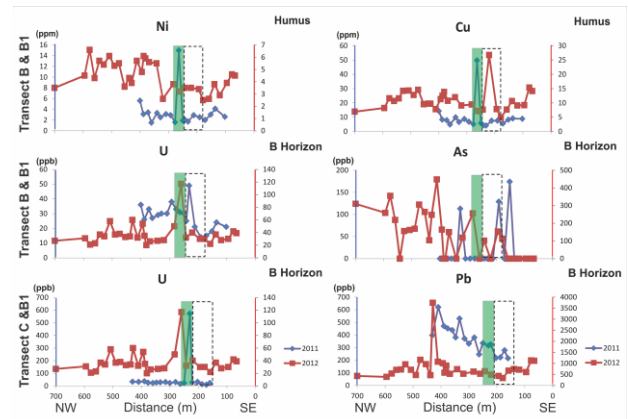


**Figure 4.** Metal abundances along the 2011 B and C transects & 2012 B1 transect at Phoenix: Ni, Cu, U, As and Pb after aqua regia digestion and ammonium acete leach of humus and B horizon. The box indicates the area directly above Zone B1, and the dotted rectangle encompasses the expression of the WS Hanging Wall shear at the unconformity.

## 4 Conclusions

The combined results suggest upward migration of mobile metals from the ore zones to the surface. As such, geochemical analysis of surface media is potentially an efficient and inexpensive too identifying deeply-buried uranium deposits among possible targets.
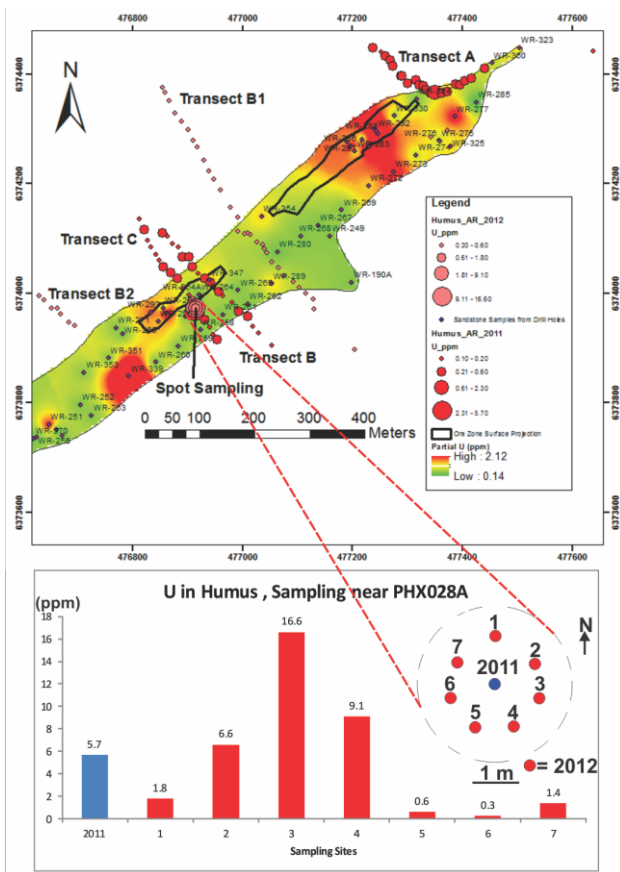
**Figure 5.** Graded geochemical results for U in humus soil samples from Transects A to C (2011), Transects B1-B2 & spot sampling (2012) and uppermost Dunlop Member sandstone (underlying raster). Inset is of dense 2012 humus soil sampling within 1 m from the 2011 site (PHX028) that showed the highest U value. The value on the left is the highest in the 2011 survey, and data in columns 1-7 are from 2012 spot sampling. The results confirm the reproducibility of the anomalous mobile metals trace elements observed in 2011.
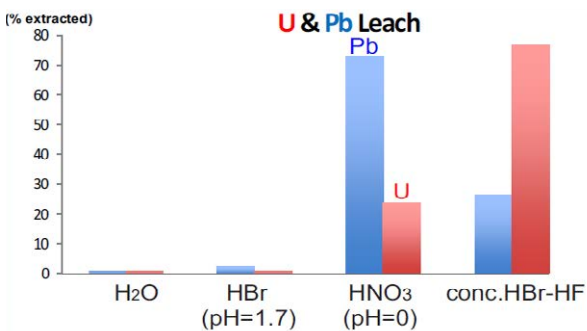


**Figure 6.** Water and a variety of acids were used to extract metals (Cu, Ni, Co, As, U, Pb) from a humus sample. Humus did not release significant amounts of metals in water and weak HBr (pH=1.7). The samples were dried at 60°C, and sieved to -80 mesh (0.177 mm). After adding Milli-Q water, we manually shook the samples several times and let them stand at room temperature for about an hour, after which they were again shaken manually. After removing the solids, then solution was then centrifuged, and analyzed via ICP-MS. Similar procedures were repeated with 0.02 M HBr, 1 N HNO₃ (25°C) and a hot (100°C) concentrated mixture of 3:2 HF-HBr.
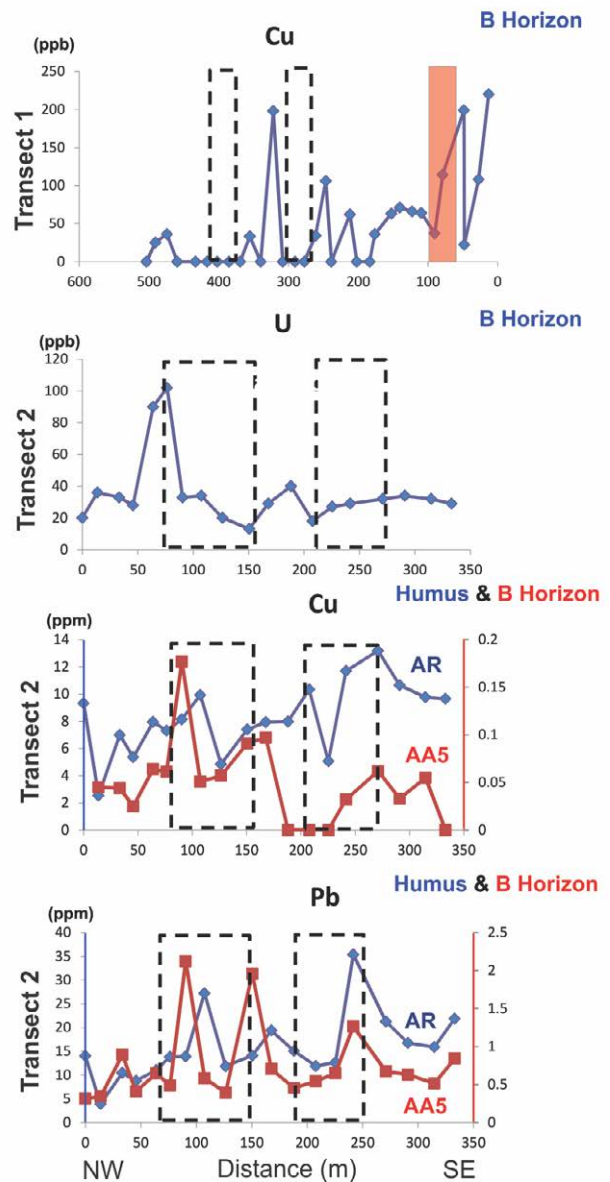


**Figure 7.** Metal abundances along the transects at Millennium: Cu, U and Pb after aqua regia digestion and ammonium acetate weak leach of humus and B horizon soils, respectively. The shaded area indicates the area directly above the ore zone, and dashed lines indicate the likely surface expression of the Marker and B1 faults.

## Acknowledgements

# References

Burgess M., Brown R., Duguay C., Nixon M, Smith S, Wright F (1999) Canadian Contributions to GCOS - Permafrost: a background document to assist in the development of a Canadian initial observing system for the Global Climate Observing System, 23 p.

Campbell JE (2007) Quaternary geology of the eastern Athabasca Basin, Saskatchewan. In C.W. Jefferson, and G. Delaney, (eds.), EXTECH IV: Geology and Uranium Exploration TECHnology of the Proterozoic Athabasca Basin, Saskatchewan and Alberta, Geol Surv Can Bull 588: 211-228

Cloutier J, Kyser K, Olivo G, Alexandre P, Halaburda J (2009) The Millennium uranium deposit, Athabasca Basin, Saskatchewan, Canada: An atypical basement-hosted unconformity-related uranium deposit. Econ Geol 104: 815-840

Earle S, Sopuck V (1989) Regional lithogeochemistry of the eastern part of the Athabasca basin uranium province. IAEA Tec-Doc 500: 263-296.

Jefferson CW, Thomas DJ, Gandhi SS, Ramaekers P, Delaney G, Brisbin D, Cutts C, Quirt D, Portella P, Olson RA (2007) Unconformity associated uranium deposits of the Athabasca Basin, Saskatchewan and Alberta. In Goodfellow WD (ed.), Mineral Deposits of Canada, Geol Assoc Can, Min Dep Div Spec Pub 5: 273-305

Kerr WC (2011) The discovery of the Phoenix deposit: a new high-grade Athabasca Basin unconformity-type uranium deposit, Saskatchewan, Canada. In Goldfarb RJ, Marsh EE and Monecke T (eds.), The Challenge of Finding New Mineral Resources: Global Metallogeny, Innovative Exploration, and New Discoveries, Volume II: Zinc-Lead, Nickel-Copper-PGE and Uranium, Soc Econ Geol, p. 703-725.

Roscoe, WE (2012) Technical Report on a Mineral Resource Estimate Update for the Phoenix Uranium Deposits, Wheeler River Project, Eastern Athabasca Basin, Northern Saskatchewan, Canada. NI 43-101 Technical Report prepared for Denison Mines Corp.

Schreiner BT (1984) Quaternary geology of the Cree Lake area (NTS 74G), Saskatchewan. Sask. Ener. & Mines Op. File Rep. 84: 12, scale 1:250 000

# Regional hydrogeochemistry for mineral exploration in Australia

Nathan Reid, David Gray & Ryan Noble
*Deep Exploration Technologies Cooperative Research Centre, CSIRO Earth Science and Resource Engineering, Kensington, Western Australia, Australia.*

**Abstract.**
Groundwater geochemistry can show broad geological and hydrothermal signatures (e.g. alteration haloes). Unlike other potential media (e.g., drill core) it's readily available on a regional scale due to pre-existing wells and bores. The utility of hydrogeochemistry for prospectivity testing was trialled in the north Yilgarn Craton as a proof of concept, and the successful results of this study led to the expansion of this research into other, more complex areas of Australia.

The results demonstrate the utility of developed indices, as well as providing new pathfinder element suites to improve exploration in the northern Yilgarn Craton. The results from this study have additional value for exploration targeting (near miss detection) and environmental baselines (for water quality, health risks and mine closure).

**Keywords.** Regional exploration, geochemical mapping, groundwater chemistry.

## 1 Regional Hydrogeochemistry

Exploration targets are increasingly difficult to define in large areas of Australia with complex terrains and commonly deep (>30 m) transported cover into basinal terrains. Groundwater interacting with mineralised rocks creates a geochemical signature that may be spatially greater in size than that for sampling the unweathered rocks. Hydrogeochemistry at a regional scale adds value to prospectivity analysis, especially for early stage greenfields exploration. There is the potential for low density (> km scale) sampling, especially in stock grazing areas where bores and wells provide access to groundwater at a relatively regular spacing.

Large scale mineral systems such as hydrothermal gold, IOCGs and porphyry copper have large geochemical footprints (> km), which can be observed in groundwater due to the dissolution and weathering of the host rocks and mineralisation. More localised deposits such as smaller nickel sulphide (NiS) and VHMS deposits may not be consistently observed in regional sampling, although information from hydrogeochemistry may still help in understanding local geology and alteration systems. This technology has been developed for Australian conditions and is easily applied in the field with consistent approaches to sampling, analysis and contamination testing (Noble and Gray 2010).

Some of the general outputs include:
- Lithological indicators separating basic from acid rocks and mapping lithology through cover.
- Recognition of previously unrecognised zones for chemical interpretations differ from previous geological mapping).
- Areas of sulphate enrichment related to varying geological areas and/or fault structures, indicating that these structures still have active input into the surface environment.
- Anion excess and depletion methods have been developed and are a valuable, new application for detecting sulphides. This, coupled with multi-element indices, provides a solid platform for exploration for sulphide systems.
- Various empirical and mineral saturation indices for Au, U, NiS and VHMS exploration

## 2 Methods

Groundwater samples can be collected from a variety of wells and bores originally intended for other uses including domestic water, farm water, mining operations and other industry supply. Electrical conductivity (EC), pH, redox potential (Eh) and temperature are measured in the field. A sample is collected via pumping or, where necessary, bailing. Following this, water is filtered (0.45μm), and various sub-samples collected and treated for later analysis:

1. An unfiltered sample is collected for Alkalinity titration.

2. A filtered sub-sample is used for anion, low level phosphate and organic carbon analysis, using ion chromatography and other techniques.

3. A filtered/acidified sub-sample is analysed for major, minor and trace metal analysis using inductively coupled plasma (ICP) mass spectrometry and ICP-optical emission spectrometry.

4. Gold, Ag and Pt are determined at ng/L levels by first adsorbing these elements from 1L of water onto a small sachet of activated charcoal, and subsequently analysing the charcoal (Gray et al. 2011).

## 3 North Yilgarn, Western Australia

The regional hydrogeochemistry of the north Yilgarn Craton was developed to provide reliable mineral prospectivity maps and indicate different lithology. This proof of concept project showed evidence of large-scale (4-8 km spacing) signatures in groundwater chemistry related to lithology, as well as Au and U mineralisation (Gray et al. 2009).

Over 1700 stock bores, wells and drill holes were included in this study. Results comprised of 62 elements

and parameters. These elements were used to determine mineral saturation indices using Phreeqe software. Normalisation of the data led to the development of elemental indices which could be added together to create exploration indices for improved detection of different styles of mineralisation. For example the lithology index is the sum of normalised V + Cr -2xU.

The lithology index map (Figure 1) highlighted several areas of interest that differed from the mapped geology. These areas are now the subject of further study and exploration.
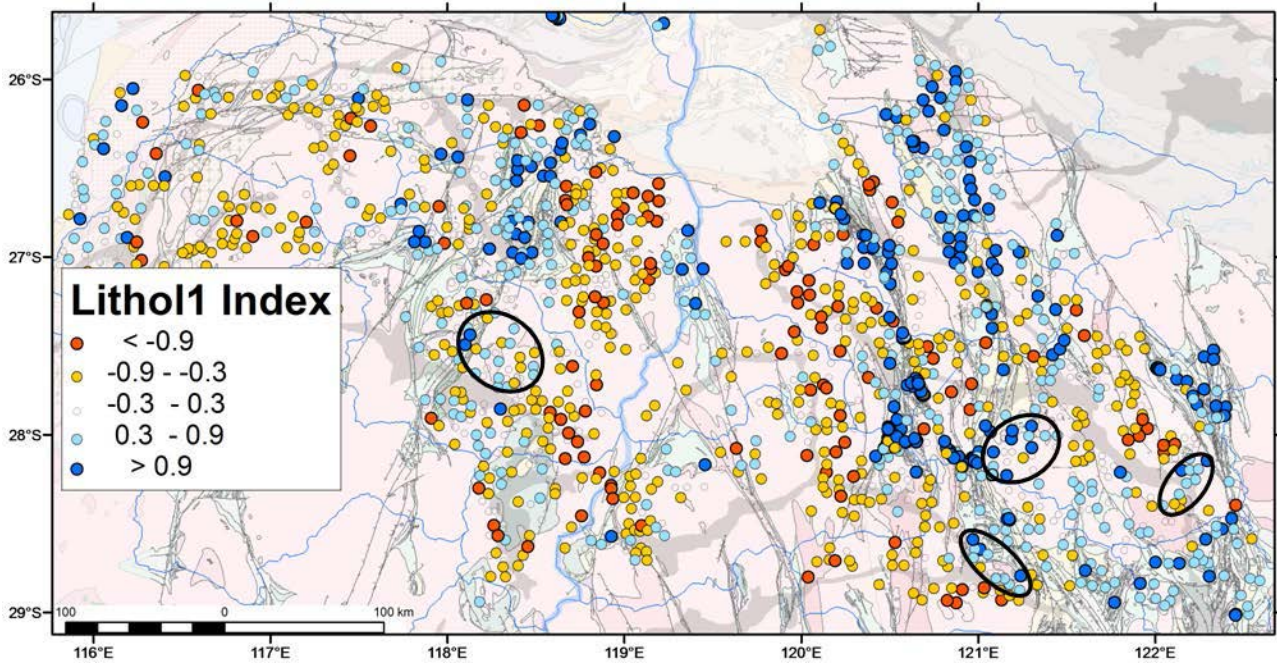


**Figure 1:** Lithol1 Index (V+Cr-2*U) discriminates granites (red dots) and greenstones (blue dots).
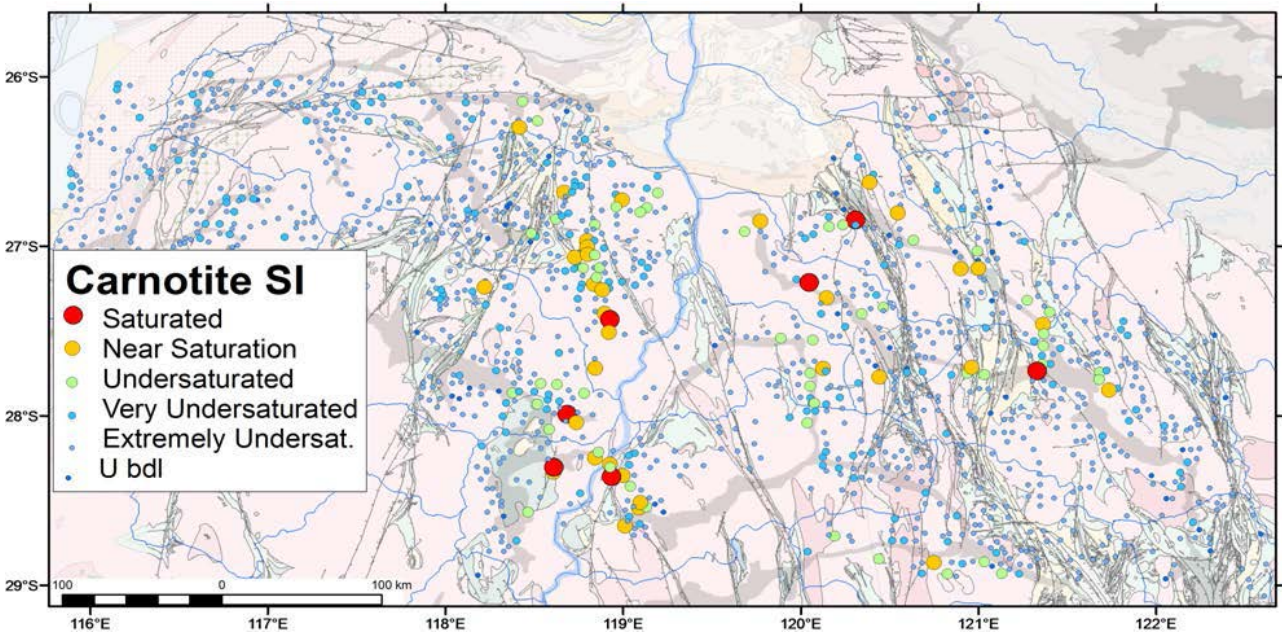


**Figure 2:** Carnotite saturation index for the northern Yilgarn Craton.

Mineral saturation indices were of great value in discriminating alteration haloes. Carnotite saturation in particular highlighted all the secondary U ore bodies in that region (Figure 2).

As a result of these successes, pilot studies in South Australia and New South Wales were initiated, moving into deeper sediments and more complex hydrogeology. This meant that standard methods and sampling protocols needed to be developed so that multiple surveys and companies could integrate their hydrogeochemical results into one database. This resulted in the development of a field guide for hydrogeochemical sampling and a data logging book, which enables consistent sampling and data management.

## 4 New areas in New South Wales and South Australia

A pilot study in the Thomson Orogen in New South Wales (Gray et al. 2012a) and initial work in the Gawler Craton in South Australia (Gray et al. 2012b) are both showing potential areas of interest for various commodities through more complex aquifer systems than the north Yilgarn.

In the Thomson Orogen study the Cuttaburra (W, Zn, Cu, Ag) Prospect was detected with multi-element anomalies through over 100 m of transported cover using groundwaters that generally contained a chemical signature of the Great Artesian basin. In contrast, the Bulla Park (Pb, Zn, Cu, Ag) Prospect is overlain by 50m of transported cover and was not easily detected using the groundwaters that showed a local aquifer signature. These differences may relate to differing pathfinder suites, groundwater host rock type and/or the slightly lesser sampling density at Bulla Park: this indicates that discriminating aquifer sources is of great importance in determining signatures of potential mineralisation.

For the Gawler Craton study, just as in Western Australia, various lithological indicators can be used to map underlying rock through cover. Granitic and felsic lithologies are indicated by greater dissolved F and U, and by a relatively high ratio of dissolved Sr to Ca. Basic lithologies are characterised by high Ca to Sr ratios, and by indicator elements such as V. At this stage, the initial results are a proof of concept for this complex series of terrains. Early interpretation indicates good potential for delineating different aquifer chemistries (essential for recognising anomalism in smaller scale prospecting) and early identification of some areas of interest. More concrete and extensive results will be released as sampling is advanced.
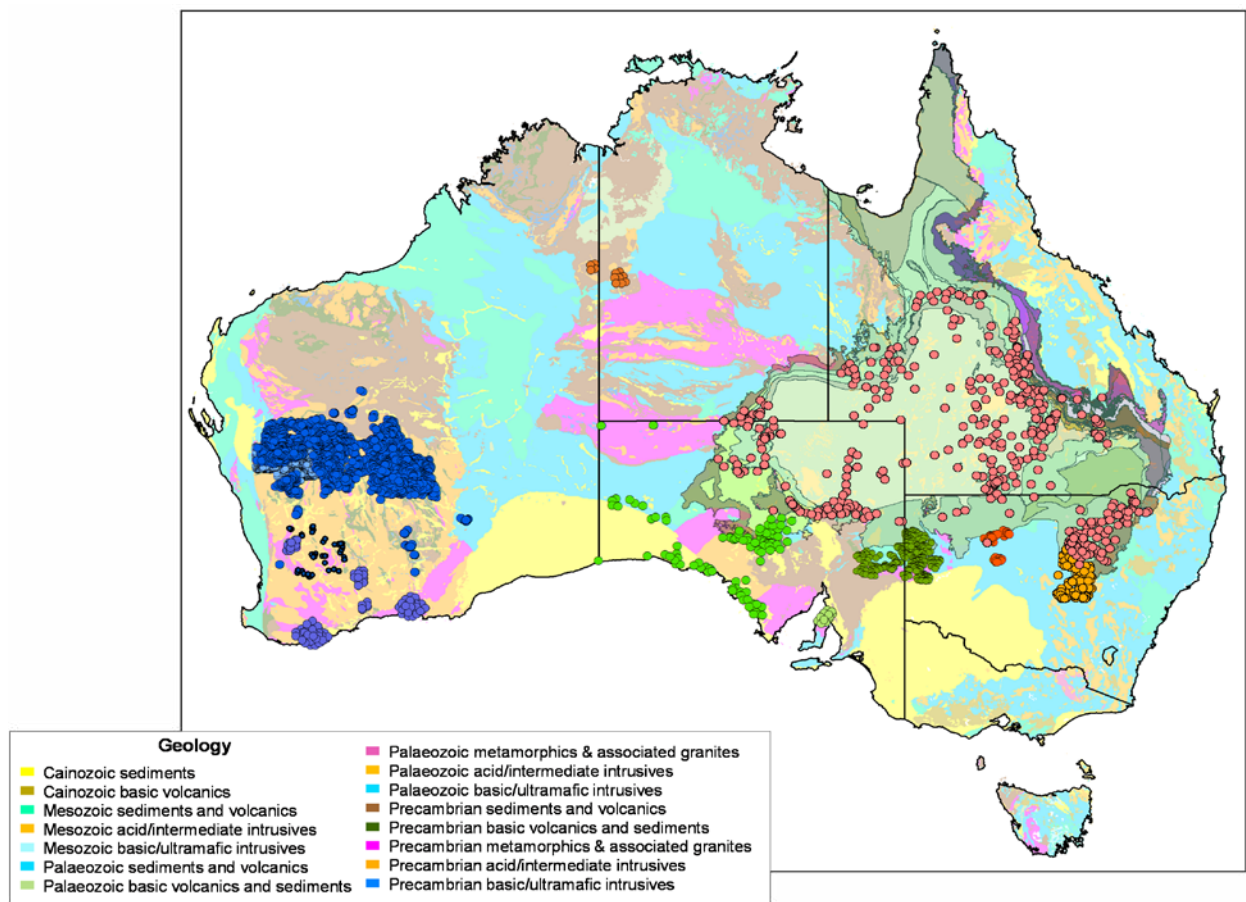
## 5 Conclusions

At this stage the north Yilgarn, Thomson and Gawler data sets have been collated and normalised to start to provide increasing coverage across Australia (over 2000 sample points). This is being integrated with older data sets, from the Great Artesian Basin, Curnamona, Tanami and various south Yilgarn studies (Figure 3), as part of an overarching project within the Deep Exploration Technologies Cooperative Research Centre (DET CRC) which is heading towards state-wide mapping and eventually continent scale hydrogeochemistry.

It is also intended that this database will be used to develop new targets and areas for exploration. This process has been demonstrated in the NE Yilgarn Craton, which was one of the most explored regions on the planet. There are several areas that have unusual water chemistry based on what would be expected from waters over the mapped geology (Figure 1). For example there are samples with high Cr concentration over an area mapped as granites where we would expect Cr to be low. In certain areas, high concentrations of critical indicator elements such as Au, Ag, As (lode gold), anomalous dissolved sulphate (sulphide-rich rocks), Ni, Co, Pt (nickel), U (uranium) or Cu, Zn, Ag (VHMS). On the basis of this information, several new areas have been taken up as tenements by explorers, with promising initial drilling results. In order to repeat this in more complex and varying geology and geomorphology, initial, broader scale delineation of the hydrogeochemistry of the various basins will be required. We are testing the utility of major element ratios (such as Br:Cl, K:Na, Mg:Na, B:Na) elements such as Si (low dissolved Si suggests high residence and/or heating) or other phases (such as organic matter, reduced N and $PO_4$), for delineating basin aquifers. For example, the southern and south-western edge of the Great Artesian Basin sediments are characterised by low salinity and low Ca, Mg, Br, K and B ratios (with respect to Na).

**Figure 3.** Hydrogeochemical sample points from various studies across Australia, overlain on geological age also showing the outline of the Great Artesian basin.

## References

Gray, D.J., Noble, R.R.P. and Reid, N., (2009). Hydrogeochemical Mapping of the Northeast Yilgarn Craton, CSIRO Exploration and Mining Report P2009/1612, Minerals and Energy Research Institute of Western Australia Report No. 280, Geological Survey of Western Australia Record 2009/21, ISBN 978-1-74168-280-9, 73 pages.

Gray, D.J., Noble, R.R.P. and Gill, A.J., (2011). Field guide for mineral exploration using hydrogeochemical analysis. CSIRO Earth Science and Resource Engineering. ISBN 978-0-64310-718-2, 46 pages.

Gray, David J., Reid, Nathan, Dick, Stephen, and Flitcroft, Paul, (2012a). Final Project Report. Project 3.3: Pilot Hydrogeo-chemical investigations in the Thomson Orogen, New South Wales. DET CRC Report 2012/042 / CSIRO Report EP125537 / NSWGS Report GS2012/0972. 25 pages

Gray, D.J., Reid, N., Fidler, R., Fairclough, M. and Wilson, T., (2012b). Hydrogeochemistry: a regional prospecting tool in South Australia? MESA 64, p14-17.

# Regional metamorphism versus hydrothermal alteration/ metasomatism related to sulphide mineralisation in the Bergslagen district, Sweden

Martiya Sadeghi
*Geological Survey of Sweden, Uppsala, SE 751 28, Sweden*

**Abstract.** In the Berglagen district, lithogeochemical data from Geological Survey of Sweden have been investigated using different methods to understanding behaviour of major and trace elements during the hydrothermal processing and metamorphism. This paper present results from comparison of different methodology for detecting altered versus un-altered lithogeochemical samples. In addition principal component analysis has been applied and first score of principal component shows strong relationship with the altered samples related to mineralization.

**Keywords:** Hydrothermal alteration, PCA, lithogeochemistry, Bergslagen, Mineralization

## 1 Introduction

Geographically, Sweden can be divided into seven geological regions, each with a distinct tectonic history and geochemical character (Sadeghi et al. 2012a). Geologically, Swedish bedrock consist of Archean to Neoproterozoic and Phanorezoic rocks, but the majority of Sweden consist of rocks of Svekokarelian orogen, formed during the paleoproterozoic in two distinct phases, one during 2.44- 1.96 Ga and the other 1.96-1.75 Ga. There are two main sulphide mineralization districts in Sweden so called Skellefte in the northern part and Bergslagen in the central part of Sweden. The Skellefte district is a major province of sulphide deposits regarded as a volcanic arc formed in Svecofennian times in a transition zone between an Archeans continent to the north and a Proterozoic sedimentary basin to the South ( Carranza and Sadeghi 2010 and reference there in). Bergslagen district contain base metal sulphide are hosted by the metamorphosed felsic volcanic rocks, intrusive and sedimentary rock (Stephenes et al. 2009).

Detection of regional hydrothermal alteration is a necessary step in mineral exploration and a major focus in modern exploration programs aims to integrate multiple dataset. The ultimate goal of the statistical and spatial analysis of lithogeochemical data for mineral exploration is the detection of zones of elevated concentration such as geochemical anomalies of oxides or trace elements that may reflective of mineral deposits.

The main objective on this paper is to introducing different method to detecting of regional alteration due to mineralization processes, as opposed to regional metamorphic.

## 2 Study area

The study area is situated in the North-Western part of the Bergslagen. Bergslagen region is interpreted as a felsic magmatic region where supracrustal volcanic were deposited on older continental crust in an intra-continental extensional or continental back-arc region tectonic setting about 1.90-1.87 Ga ago. (Weihed et al. 2005). The study area contains a diverse range of ore deposits, including banded iron formation, magnetic skarn, manganiferous skarn and marble hosted iron ore, apatite magnetite iron ore, stariform and stratabound Zn-Pb-Ag (Cu-Au) sulphide ores as well as W skarn (Eilu 2012).
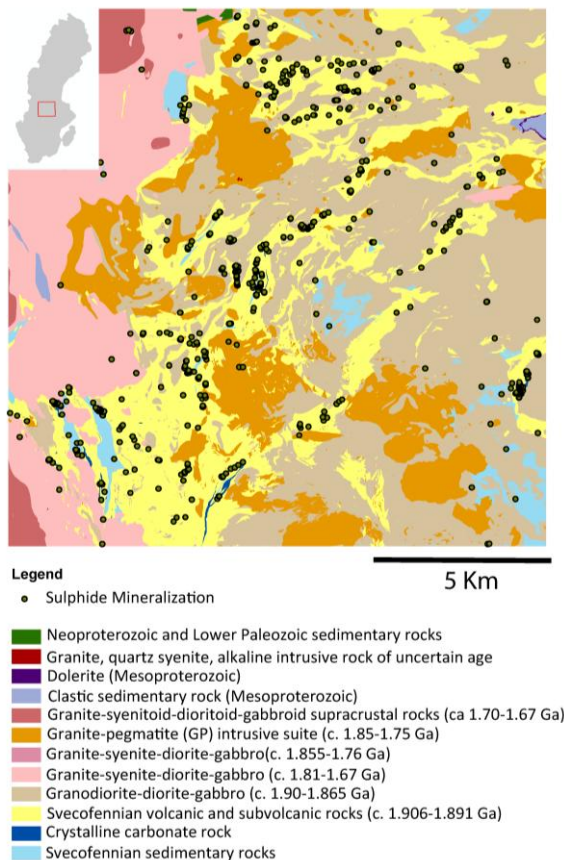
Most of the bedrock of the study area is Paleoproterozoic in age and related to the Svecofennian orogenic event. Only a minor part of the bedrock in the study area formed as post-svecofennian. Summarizing up, the study area consist of Svecofennian volcanic and sedimanry rocks (1.91-1.89 Ga), intrusive rocks (1.90-1.87Ga, intrusive rocks (1.85-1.75Ga) and the younger intrusive rocks (1.70-1.67Ga) and finally crystalline carbonate rocks, clastic sedimentary rocks and mesoproterozoic dolerite. (Figure 1). In this study 57 main sulphide mineralizations have been chosen including active and closed mine to validating the methodology.

## 3 Methodology

### 3.1 Identifying geochemical anomalies (altered Vs un-altered)

There are many methods which can be use for identifying anomalous lithogeochemical samples and by other word altered versus un-altered. Statistical univariate methods (e.g. Probability (QQ) plots) can be use in characterising breakpoints from cumulative probability plots (Harris et al, 1997). Fractal method as well is a powerful method to identifying breakpoints on plots of log concentration versus log area (Cheng et al. 1997).

Alteration indices and ratios of major oxides and trace elements can be used for this purpose. In this case data should be log transformed to correct for major oxides (Carranza 2010). This method is useful for distinguishing regional geochemical background from anomalies. Principal component analysis (PCA) can be use to identifying of residual from linear combination of oxides and trace elements and data should be log transformed to correct for major oxides (Grunsky 2010). There is another method which can be use to identifying geochemical anomalies such as geochemical classification versus map lithology.

components (groups of variables) account for variation in multivariate data (Güller et al. 2002). PC analysis has been applied frequently to process and interpret geochemical and other types of spatial data (e.g., Grunsky 2010; Harris et al. 1997; Carranza 2008; Sadeghi et al. 2012b). The first PC explains most of the variance within the original data, and each subsequent PC explains progressively less of the variance. A multivariate dataset can usually be reduced to two or three PCs that account for the majority of the variance within the dataset.

## 4 Result

Identification of altered samples using different methods have been carried out and the minimum of alteration in bedrock samples have been identified. Reconstructed composition in the samples and mass changes have been calculated. The results of this calculation show that the felsic metavolcanic rocks in the Berglagen show Na, Na+Mg and Mg alterations while the early orogenic granite show depletion of K2O and increasing of Na2O in some area which reflecting the Na alteration. Summary of major oxide element concentration trends of altered and un-altered samples shows in table 1. The altered samples have been flagged according the calculation of alteration in the area. Alteration index shows a range of 0.89 to 98.1 in the Berglagen and the same CCPI shows a range of 0.06 to 99.1.

**Table 1.** Simplified trend of altered versus un-altered oxide element concentration in lithogeochemical samples in the Bergslagen.

| | SiO₂ | Al₂O₃ | CaO | Fe₂O₃ | FeO | MgO | K₂O | TiO₂ | Na₂O |
|---|---|---|---|---|---|---|---|---|---|
| CA = Calc - alkaline andosite | | | ↓ | ↑ | ↓ | ↓ | ↑ | | ↓ |
| CB = Calc - alkaline basalt | ↓ | ↓ | | ↑ | ↓ | ↓ | ↑ | | ↓ |
| CD = Calc - alkaline dacit | ↓ | | ↑ | ↑ | ↓ | ↑ | ↑ | | ↓ |
| CR = Calc - alkaline rhyolite | ↑ | | | ↑ | | ↓ | ↑ | ↑ | ↓ |

There is a strong spatial relationship between high to moderated value of CCPI and the main mineralization in the Berglagen related to sulphide mineralization. The summary of spatial analysis calculation of alteration index and CCPI has been present in Table 2. Principal components from major oxides have been calculated in the study area and there is a strong relationship between fist score of principal component and mineralized samples and specifically sulphide occurrences. (Figure 2).

---



**Figure 1.** Simplified geological map of the study are in the Bergslagen district. The insert map shows the study area in red.

## 3.2 Regional metamorphism versus hydrothermal alteration/metasomatism

The next step after identifying the altered samples is to identify differentiate between altered samples resulting from alteration trends due to metamoprohism and altered samples resulting from local hydrothernmal alteration related to mineralization. Univariate methods include the use of geochemical theresould, and geochemical normalization can be use. Application of calculation of Alteration index and Chrlorite-carbonate-Pyrite-index (CCPI) may be able to highlight the regional alteration depending on mineralization.

## 3.3 Normalization

Principal of normalization of geochemical data is to remove effect of lithlogy in geochemical dataset. In the literatures suggest many different methods (e.g. use of standard deviation, median, mean) (Grunsky 2010; Carranza 2010, Carranza and sadeghi 2010, Sadeghi et al. 2012a).

## 3.4 principal component analysis and cluster analysis

Use Principal Component (PC) analysis has been a conventional multivariate technique that is used for studying geochemical data (Sadeghi et al. 2012a). PC analysis reduces a large number of variables to a smaller number, allowing the user to determine which

**Table 2.** Spatial pattern (p) of alteration features having statistically significant positive spatial association with Sulphide mineralization. Studentized C is calculated using (see Bonham-Carter 1994): N(P), area of a pattern expressed in number of pixels; and N( D∩P), number of pixels in a pattern (P) that contain mineralization (D)

| Spatial Pattern (P) | N(P) | N(D∩P) | Studentized C |
|---|---|---|---|
| *Alteration Area* | | | |
| <10 th percentile | 1670 | 20 | 6.37 |
| <20 th percentile | 4027 | 33 | 6.27 |
| | | | |
| *Alteration index* | | | |
| <10 th percentile | 233 | 8 | 2.78 |
| <20 th percentile | 1093 | 16 | 1.32 |
| <30 th percentile | 3816 | 29 | 2.13 |
| | | | |
| *Chlorite Carbonate Pyrite index (CCPI)* | | | |
| >90th percentile | 2199 | 17 | 4.65 |
| >80 th Percentile | 4401 | 25 | 4.29 |
| >70 th Percentile | 6661 | 36 | 5.02 |
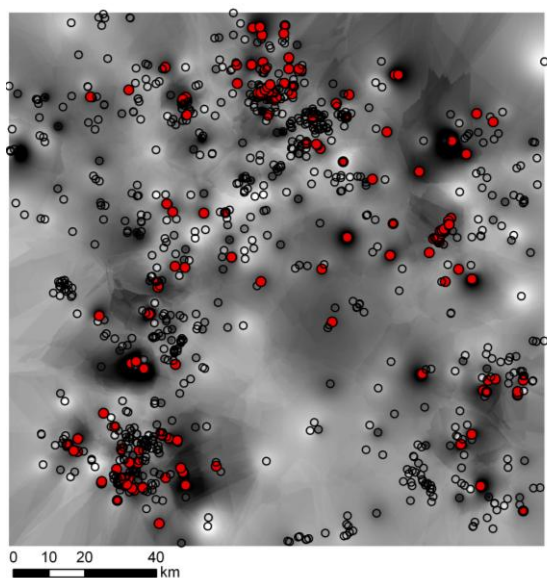


**Figure 2.** Raster map showing the scores of samples on the first principal component (cell size 250× 250 m). Red points are sulphide mineralization.

## 5   Conclusion

Many volcanogenic massive sulphide (VMS) deposits in Bergslagen are associated with K- and Mg-enriched zones. Alteration intensity with respect to $Na_2O$ content of lithogeochemical samples may provide useful information on alteration. Values of alteration index and chlorite-carbonate-pyrite index of weakly to strongly hydrothermally-altered rocks associated with VMS deposits vary from 30 to 100. The results of analyses on lithogeochemical data show that the VMS deposits in the study area have weak positive spatial association with intermediate to high values of AI but have strong positive spatial association with intermediate to high values of CCPI. The results of analyses of geochemical data show the same pattern except for the weak positive spatial association with Al. These results show that CCPI is more useful than AI in detecting regional-scale alteration related to VMS mineralization in the Bergslagen district. Principal component analysis is a powerful method to identifying regional scale alteration related to mineralization even in the metamorphic rocks and show very strong spatial relationship with sulphide mineralization.

## References

Carranza  EJM (2008) Geochemical anomaly and mineral prospectivity mapping in GIS. Handbook of Exploration and Environmental Geochemistry, vol. 11. Elsevier,Amsterdam. 351 pp

Carranza EJM, Sadeghi M (2010) Predictive mapping of prospectivity and quantitative estimation of undiscovered VMS deposits in Skellefte district (Sweden). Ore Geology Reviews, 38: 219-241

Cheng Q, Bonham-Carter GF, Wang W, Zhang S, Li W, Xia Q (2011). A spatially weighted principal component analysis for multi-element geochemical data for mapping locations of felsic intrusions in the Gejiu mineral district of Yunnan, China. Computers & Geosciences 5: 662-669

Eilu P (2011)  Metallic mineral resources of Fennoscandia. Geological Survey of Finland, Special Paper 49, 13–21

Grunsky EC (2010). The interpretation of geochemical survey data. Geochemistry: Exploration, Environment, Analysis 10: 27-74

Güller C, Thyne G, McGray JE, Turner, AK (2002) Evaluation of graphical and multivariate statistical methods for classification of water chemistry data. Hydrogeology Journal 10: 455-474

Harris JR, Grunsky EC, Wilkinson L (1997) Developments in the effective use of lithogeochemistry in regional exploration programs:Application of GIStechnology, in proceeding of Exploration 97, Fourth Decennial international conference on mineral exploration. Edited by A.G.Gubins, pp.285-292

Sadeghi M, Morris GA, Carranza, EJM, Ladenberger A, Andersson M (2012). Rare earth element distribution and mineralization in Sweden: An application of principal component analysis to FOREGS soil geochemistry. Journal of geochemical exploration, In press.

Sadeghi M, Wareing S, Carranza EJM (2012). Detection of regional-scale alteration in the Bergslagen district (Sweden) using lithogeochemical data- IGC 34- 2012-pp 2857.

Stephens M, Ripa M, Lundström I, Persson L, Bergman T, Ahl M, Wahlgren CH, Persson PO, Wickström L (2009) Synthesis of bedrock geology in the Bergslagen region, Fennoscandian shield, south-central Sweden.Geological Survey of Sweden Ba 58: 259PP

Weihed P, Arndt N, Billström K, Duchesne JC, Eilu P, Martinsson O, Papunen H, Lahtinen R (2005). Precambrian geodynamics and ore formation: the Fennoscandian Shield. Ore Geology Reviews 27: 273–322.

# Portable XRF methods in till geochemical exploration – examples from Finland

Pertti Sarala

*Geological Survey of Finland, P.O. Box 77, FI-96101 Rovaniemi, Finland, E-mail pertti.sarala@gtk.fi*

**Abstract.** Bedrock is largely covered by the glaciogenic deposits in glaciated terrains in the Northern Hemisphere. Glaciogenic sediments are always transported from the source(s) with variable distances and include whole range of mineral material from clay to boulders. Conventional till geochemistry is largely used in exploration, but a less time consuming analysis methods have been developed to offer time-consuming and cost-effective way to analyze till samples in mineral exploration.

To find more effective ways to recognize potential source areas for altered or mineralized zones in the bedrock, an application of portable X-Ray Fluorescence (pXRF) analyzers was tested in northern Finland. The focus was in development of the sampling procedure for the pXRF analyzers in exploration when using fresh bedrock, pre-glacial weathered bedrock surface and till samples, and to find out their reliability for determining the content of elements in fresh/natural samples in the field. Samples were collected during different mineral exploration or geochemical mapping projects using percussion drilling, tractor excavations or hand-made test pits. The comparison was done using pXRF analyses for fresh, naturally wet samples vs. dried samples, and comparing the results with the laboratory XRF analyses and the conventional (partial extracted) till geochemistry. Based on the results, modern mobile and portable XRF analyzers seem to provide enough accuracy and the detection limits enough low to determine metals and other indicator elements for example in base metal, gold, PGE and nickel or REE exploration using till.

**Keywords.** till, geochemistry, portable XRF, exploration, Finland

## 1 Introduction

Conventional surficial geological and geochemical methods have been used since the 1950s in mineral exploration in glaciated terrains. Till sampling with variable sampling density and patterns like grids, lines or separate sampling sites have been used.

Numerous till and bedrock or when available, pre-glacial weathered bedrock samples are collected, and after chemical laboratory analyses (commonly using partial leach of the fine till fraction <0.06 mm or total methods like fire assay) the ore potential is estimated. At its best, geochemical anomalies detect directly mineralization in the bedrock or can be used for tracing the source(s).

However, the conventional till sampling with geochemical analyses is time-consuming and expensive part of the exploration process. That is why new technologies are needed for mineral exploration.

## 2 Portable XRF

X-Ray Fluorescence (XRF) method has been used as a standard method in laboratories for decades. The same technology is also used as a solution for the field i.e. portable analyzers although in a light-weight equipment (Fig. 1). The development of portable XRF (pXRF) analyzers progressed during last decade. Detection limits for a large group of elements have reached the level (ppm scale) that is enough for mineral exploration purposes even using till or pre-glacial weathered bedrock as sample media. Many commercial products are nowadays available.



**Figure 1.** Portable XRF analysers can be used in mineral exploration due to its easy and fast usability in the field. Contents of the elements can be quickly analyzed even using natural till samples in fresh walls of the test pits. Photo by P. Sarala.

## 3 Studies in northern Finland

Portable XRF analyzers and methods were tested and compared as a part of mineral exploration and geochemical mineral potential mapping in northern

Finland. The test was carried out in gold, copper and nickel exploration targets mainly in the central Lapland Greenstone Belt. An aim was to test the use of pXRF analyzers and natural till samples in mineral exploration by comparing data with laboratory analyses (ICP-OES after aqua regia digestion, and XRF using briquettes of the <0.06 mm size fraction) and existing till geochemical data. Results are based on both a statistical and visual comparison.

One test area is located in the Central Lapland Greenstone Belt, northern Finland, where the use of the pXRF units (ScanMobile®) and two portable XRF analyzers (Oxford Instruments' X-MET and Innov-X Delta) were tested for 623 basal till samples gathered using percussion drilling. Portable XRF datasets were compared with each other (Table 1) and the Delta XRF records with conventional aqua regia based geochemistry. For example, pXRF records of the natural till for base metals like Cu and Mn are equal to those analysed with aqua regia ICP-OES (Fig. 2). The results also show that the elements' distribution of the pXRF data has good comparison to the underlying bedrock when a short-transported basal till has been used.

**Table 1.** Correlation of the till samples analysed by three different portable XRF methods: Oxford Instruments' X-MET, Innov-X Delta and ScanMobile®. Number of the samples is 623 for Delta and ScanMobile and 350 for X-MET.

|  | X-MET vs. Delta | X-MET vs. MOLS | Delta vs. MOLS |
|---|---|---|---|
| As | *0.66* | - | - |
| Ca | *0.63* | 0.36 | 0.47 |
| Co | 0.44 | 0.50 | *0.74* |
| Cr | 0.50 | - | - |
| Cu | *0.69* | 0.54 | *0.72* |
| Fe | **0.82** | *0.76* | **0.81** |
| Mn | **0.83** | 0.47 | 0.47 |
| Ni | **0.94*** | 0.10* | -0.05* |
| Pb | 0.09* | - | - |
| Rb | - | - | 0.49 |
| Sr | *0.73* | - | - |
| Ti | **0.90** | 0.39 | 0.38 |
| V | - | - | *0.76* |
| Zn | 0.53 | 0.46 | *0.72* |
| Zr | *0.63* | - | - |

\* Number of records i.e. analyses above detection limit is low for Ni and Pb in the pXRF datasets.

Another example comes also from the central Lapland and concerns Ni-Cu-PGE exploration. Till sampling line crosses the Ni-Cu-PGE mineralization. The elements contents range 57-2041 ppm Ni and 91-1759 ppm Cu detected by the Delta pXRF, 155-1051 ppm Ni and 114-1059 ppm Cu detected by the laboratory
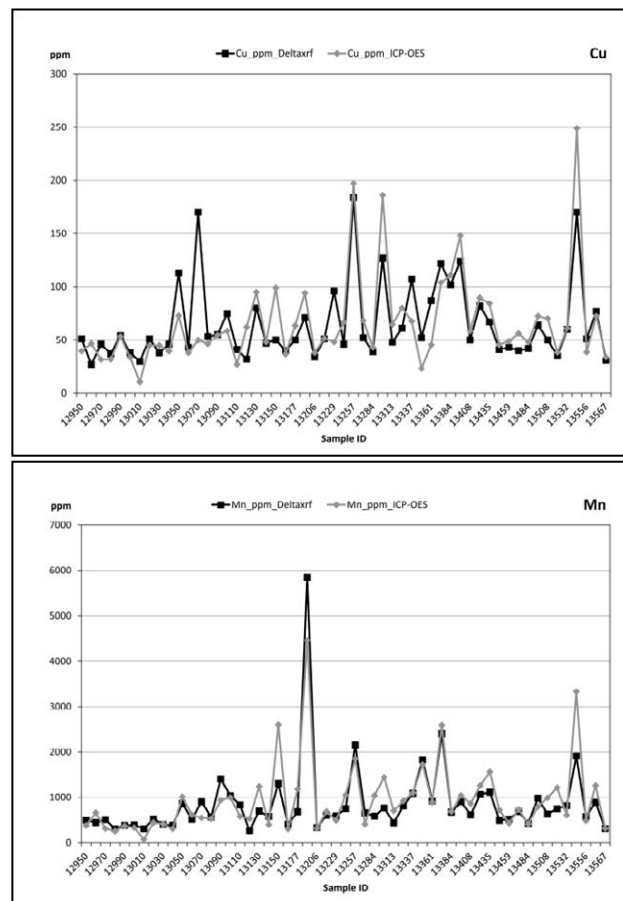


**Figure 2.** Good correlation of the Delta pXRF and the conventional aqua regia ICP-OES records for Cu and Mn in till. Number of the till samples is 59.

XRF and 102-1020 ppm Ni and 105-1080 ppm Cu analyzed by the aqua regia ICP-OES. pXRF records correlate well with the laboratory XRF results (Ni 0.84; Cu 0.65; Fig. 3) and the aqua regia ICP-OES (Ni 0.85; Cu 0.66; Fig. 4). PGE group metals are seldom over the detection limit of XRF methods, so they cannot be used.

## 4  Conclusions

The study proves that the pXRF analyzers are effective methods for analyzing the geochemical characteristics of the till and to trace sources of the mineralized bedrock in glaciated terrain. Portable XRF data correlate well to the conventional aqua regia geochemistry and to the laboratory XRF. Modern pXRF analyzers can reach the ppm level of wide variety of elements (20-30 elements) including main and basic elements as well as some precious metals. A wide range of detectable elements makes them useful in exploration for many types of ore deposits including base metals, Ni-Cu-PGE, Cu-porphyries, REE and Au.
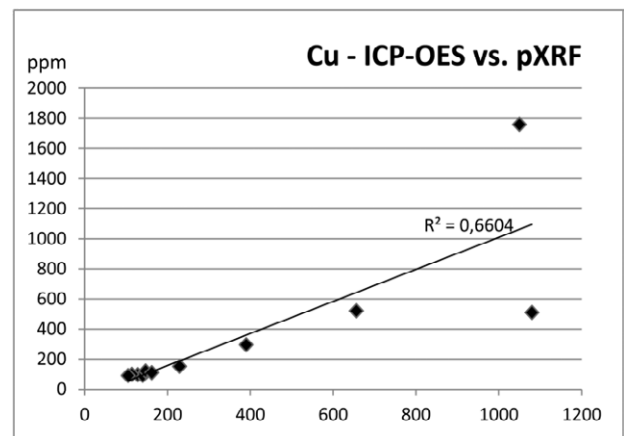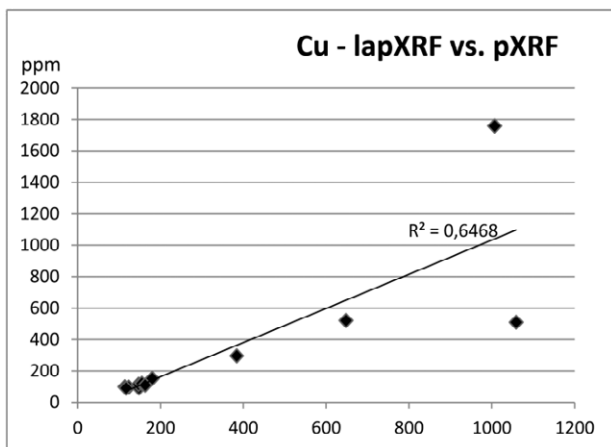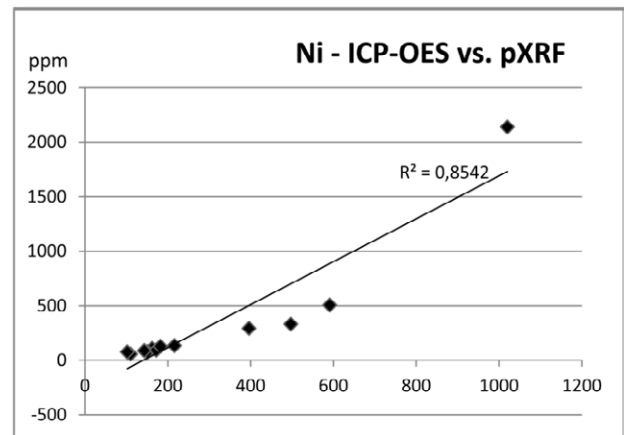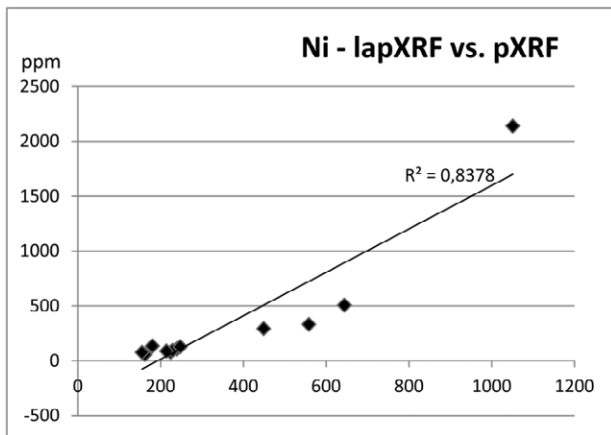
**Figure 3.** Correlation of the pXRF and laboratory XRF records for Ni and Cu in till.



**Figure 4.** Correlation of the pXRF and ICP-OES records for Ni and Cu in till.

## Acknowledgements

# Geochemical sampling of Kangaroo Island, South Australia using a deeply weathered cover sequence and biogeochemistry implications for regional scale geochemical mapping for mineral exploration

**Katherine Stoate**
*Deep Explorations Technologies CRC, Geology and Geophysics, The University of Adelaide, Adelaide, Australia*

**Steven Hill**
*The South Australia Geological Survey, DMITRE, Adelaide, Australia*

**David Giles**
*Deep Explorations Technologies CRC, University of Adelaide, Adelaide, Australia*

**Karin Barovich**
*Geology & Geophysics, University of Adelaide, Adelaide, Australia*

**Abstract:** Geochemical mapping is a fundamental part of the mineral exploration process, and has been carried out on Kangaroo Island, situated off the coast of South Australia.
One aspect of geochemical mapping for exploration is the need to differentiate between what is anomalous and what is a background signature for different types of sampling media. In this study we have looked at sampling using indurated iron oxides (ferricretes) as well as two different species of widely occurring plants (Eucalypts and *Xanthorrhoea*) for biogeochemical analysis.
Kangaroo Island is representative of an exposed deep cover redox system, due to the elevation on the island, which allows for the whole system to be examined.

**Keywords:** geochemistry, mineral exploration, ferricretes, biogeochemistry, South Australia

## 1 Location

Kangaroo Island, a discrete region situated off the coast of South Australia (Fig 1 Inset) provides an ideal place to for geochemical mapping for exploration as it contains areas that are prospective, whilst also a larger part of the island is not prospective, giving insight into the background levels of the same sampling media that are being used in areas of known mineralisation.

The prospective zone is situated to the northern half of the island, where the crystalline basement is the Gawler Craton which is highly prospective for IOCG style deposits(Belperio 1995). This northern area of the island is separated from the southern half of the island by a large-scale fault zone, the Cygnet-Snelling Fault (Fig 1), allowing for the southern area to be used for classifying the 'background' geochemical signatures of the area.

The basement geology is relatively well known, the main units are Cambrian sediments, with a small number of igneous intrusions

## 2 Sampling Media

Sampling strategy was carried out on a grid basis, largely following the road network on the island, and at each sample point, where possible two samples were collected for biogeochemical analysis (*Xanthorrhoea* and *Eucalyptus*) and one ferricrete sample for geochemical analysis (Fig 2). These data points have then been analysed and plotted up into maps such as seen in Figure 3.

### 2.1 Ferricretes

The ferricrete (indurated iron oxide) has been divided into several different classifications (Table 1), based upon the degree of reworking and transportation, modified from Bourman (1989). The affect of this on the usefulness of the different types of ferricretes has been investigated through the analysis of geochemical data.

Geochemical work has been undertaken on surficial ferricretes, to produce the geochemical maps such as that seen in Figure 3. This has then been integrated with data regarding the landscape evolution of the

island, allowing for affects of transportation to be assessed.

This ferricrete surface forms a plateau over much of the central and northern part of the island and is thought to represent a palaeoredox front. The formation and evolution of this plateau is important to determine geochemical and dispersion vectors, as a redox front or ferricrete that has been formed through groundwater and water table movement will contain different information to ferricretes that have formed at the surface.

Correlations within the ferricrete have been seen between the Iron content and Vanadium, which is to be expected (Schwertmann and Pfab 1996; Taylor and Giles 1970).

### 2.2 Biogeochemistry

Biogeochemical analysis has been performed on the two different plant types, *Xanthorrhoea* and Eucalypts (Fig 2 b, c). These are both species prolific on the island and allow for a large regional coverage and geochemical sampling by proxy in areas that do not contain the ferricrete as a portion of the island is dominated by Cenozoic marine sediments.

### 3 Integration of bedrock and weathered cover

There are a significant number of drill holes on the island and these are being targeted for portable XRF data, with the aim to integrate the data collected with that already collected within the previous sampling program.
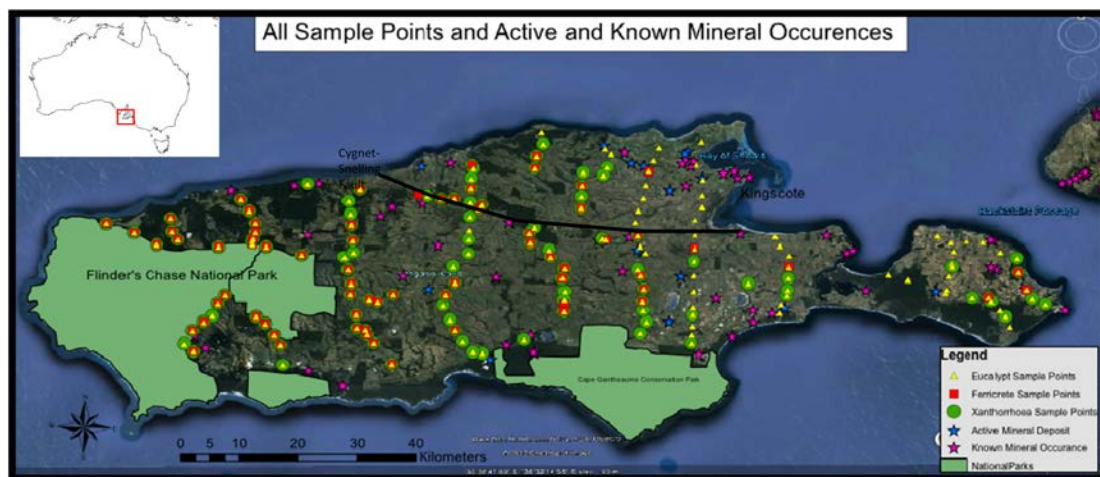


Figure 1: Map of Kangaroo Island showing Sample Points, Active Mineral Deposits, Mineral Occurrences and the National Parks on the Island.
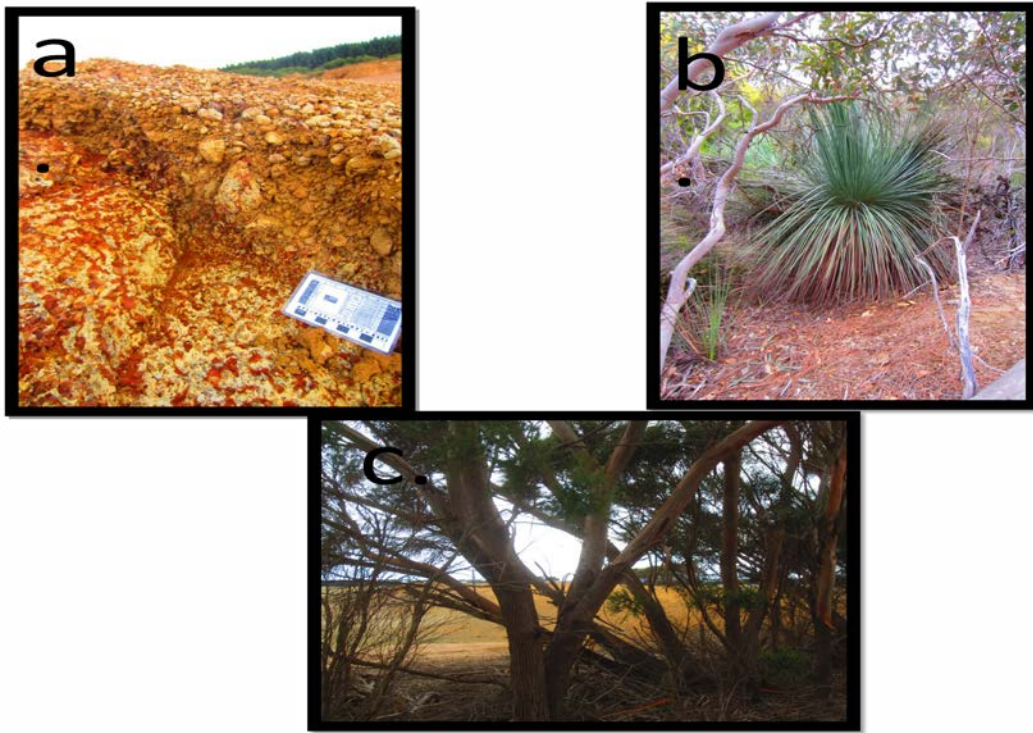*Inset:* Location Map of Kangaroo Island within the Australian continent.

Figure 2: Examples of the sampling media: **a)** Ferricrete;
**b)** *Xanthorrhoea* (Grass tree);     **c.)** Eucalypt (Narrow Leaf Mallee)
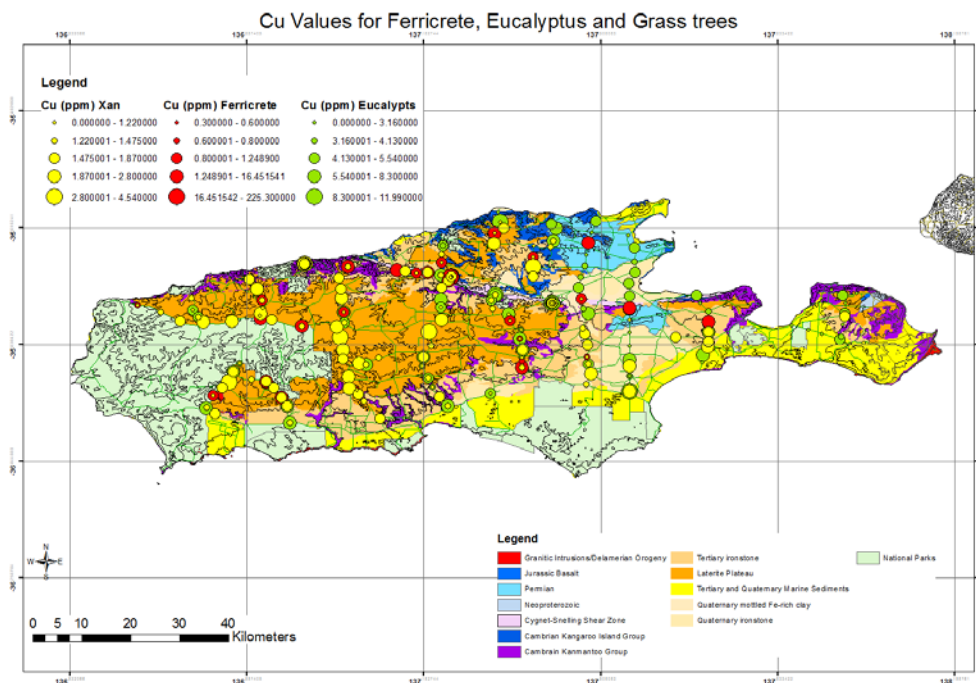


Figure 3: Copper values (ppm) for all three sample media overlain on a simplified geological map of Kangaroo Island.

Table 1: Ferricrete Classifications

| | Classification | Description | Photo |
|---|---|---|---|
| Simple Ferricretes | Ferruginous Saprolite | Weathered bedrock which is iron indurated. Preservation of bedrock features (such as quartz veining ) and textures. |  |
| | Ferruginous Sediments | Iron oxide impregnated and indurated sediments that have an unconformable relationship with the underlying bedrock. |  |
| Complex Ferricretes | Pisolitic Ferricretes | Individual pisolith, which can display multiple rinds and can be cemented together to form a rock-like mass, or remain individually. |  |
| | Nodular Ferricretes | Similar to pisoliths, but without the rinds and the clasts are larger than the pisoliths. |  |

| | Vermiform Ferricretes | Sinuous, worm-like channels often in filled with sands or clays that contrast to the iron rich material. |  |
|---|---|---|---|

Belperio AP (1995) A Guide to the Geology of Kangaroo Island In: Department of Mines and Energy GS (ed). Adelaide.

Bourman RP (1989) Investigations of ferricretes and weathered zones in parts of southern and southeastern Australia : a reassessment of the 'Laterite' concept Department of Soil Science Univeristy of Adelaide, Adelaide, South Australia

Schwertmann U, Pfab G (1996) Structural vanadium and chromium in lateritic iron oxides: Genetic implications. Geochimica et Cosmochimica Acta 60:4279-4283. doi: 10.1016/s0016-7037(96)00259-1.

Taylor RM, Giles JB (1970) THE ASSOCIATION OF VANADIUM AND MOLYBDENUM WITH IRON OXIDES IN SOILS. Journal of Soil Science 21:203-215. doi: 10.1111/j.1365-2389.1970.tb01169.x.

# Regional-scale metasomatism in the Fortescue Group, Hamersley Basin: implications for the scale of hydrothermal ore forming systems

Alistair J R White, Raymond E Smith, Patrick Nadoll, Monica LeGras
*CSIRO Earth Science and Resource Engineering, 26 Dick Perry Avenue, Kensington, WA 6151, Australia*

**Abstract.** Mafic to intermediate volcanic rocks of the Fortescue Group form the lowermost stratigraphic unit of the 100,000 km$^2$ Hamersley Basin on the southern margin of the Archaean Pilbara Craton, Western Australia. A regional burial metamorphic gradient exists across the basin from prehnite-pumpellyite facies in the north to greenschist facies in the south. Superimposed on this metamorphic gradient is a heterogeneous distribution of metasomatized rocks characterized by pumpellyite±epidote+quartz mineral assemblages. Whole-rock geochemistry, XRD and infrared spectroscopic data indicate metasomatism is associated with depletions in Fe, Mn, Mg, alkalis and base metals, with accompanying enrichments in Si and Ca. Such mineralogy and geochemical trends suggest an origin associated with sub-sea floor hydrothermal circulation. The distribution of metasomatized rocks across the entire Hamersley Basin infers fluid flow on the scale of hundreds of kilometres, despite the lack of major cross-cutting structures. Given the size, age and composition of the Fortescue Group is comparable to the highly mineralized greenstones of the Yilgarn Craton, Western Australia, the scale of fluid flow observed here has important implications for the potential size of gold or base metal mineralized systems in the Eastern Goldfields.

**Keywords.** Hydrothermal alteration, metasomatism, mafic, Fortescue Group, Hamersley Basin

## 1   Introduction

The future of greenfields exploration for mineral resources relies on developing tools to detect the signatures of ore deposits at greater and greater distances from the deposit itself. This requires the ability to discriminate between primary geochemical variation in potential host rocks and hydrothermal alteration that may, or may not, be associated with economic mineralization. This is a particular problem in large mafic igneous provinces that can be subjected to hydrothermal alteration in a wide range of settings, including, but not limited to, sea floor alteration (Humphris and Thompson 1978), sub-sea floor circulation (Banerjee et al. 2000), subvolcanic pneumatolytic alteration, cooling-related deuteric alteration (Raam et al. 1969) or metasomatism during metamorphism (Engvik et al. 2011). Each of these processes will impart distinct geochemical signatures on the affected rocks at differing spatial scales. Ultimately, the detection of distal geochemical signatures around mafic-hosted ore deposits requires an understanding of the 'background' geochemical variation that may be expected in a given sequence of rocks.

Low-grade metamorphosed mafic volcanic rocks of the Fortescue Group on the Pilbara Craton, Australia, are comparable in size, age, and composition to the more extensively deformed and metamorphosed, and highly mineralized greenstones of the eastern Yilgarn Craton. As such, the Fortescue Group may be broadly analogous to the pre-mineralization history of the Eastern Goldfields Superterrane (EGS). Therefore, an understanding of the type and scale of geochemical variation in the Fortescue Group may have implications for the expected geochemical heterogeneity in the EGS. In this study, we investigate regional-scale metasomatism observed in the Fortescue Group and discuss the implications it may have for mineral exploration in the Yilgarn Craton.

## 2   Geological setting

The Fortescue Group is a 6.5km thick sequence of mafic to intermediate volcanic rocks in the Pilbara Craton of Western Australia, with an age of approximately 2.7–2.8 Ga (Arndt et al. 1991; Thorne and Trendall 2001; Blake et al. 2004). It forms the lowermost stratigraphic unit in the 100,000 km$^2$ Hamersley Basin. The Fortescue Group is conformably overlain by the banded iron formations of the Hamersley Group, which is itself overlain by dominantly clastic sediment of the Turee Creek

Mafic (basalt to basaltic andesite) sub-aerial flood lavas of the Maddina Formation are widely distributed across the northern side of the Hamersley Basin. Inferred lateral equivalents in the submarine Bunjinah Formation outcrop in the central and southern Hamersley Basin (Thorne and Trendall 2001).

A regional burial metamorphic gradient extends across the Hamersley Basin from prehnite-pumpellyite facies in the north, through to lower greenschist facies in the south and west (Fig. 1; Smith et al. 1982). Reconstructed cross-sections suggest burial depths of 2–3 km in the north to some 10 km in the south (Smith et al. 1982). Four metamorphic zones are defined, based on authigenic mineral growth: Zone 1, prehnite-pumpellyite; Zone 2, prehnite-pumpellyite-epidote; Zone 3, prehnite-pumpellyite-epidote-actinolite; Zone 4, (prehnite)-epidote-actinolite (Smith et al. 1982).

Superimposed on the regional metamorphic gradient is abundant metasomatic alteration, resulting in the heterogeneous appearance, mineral association and chemical composition of the previously homogeneous lavas (Fig. 1; Smith et al. 1982).
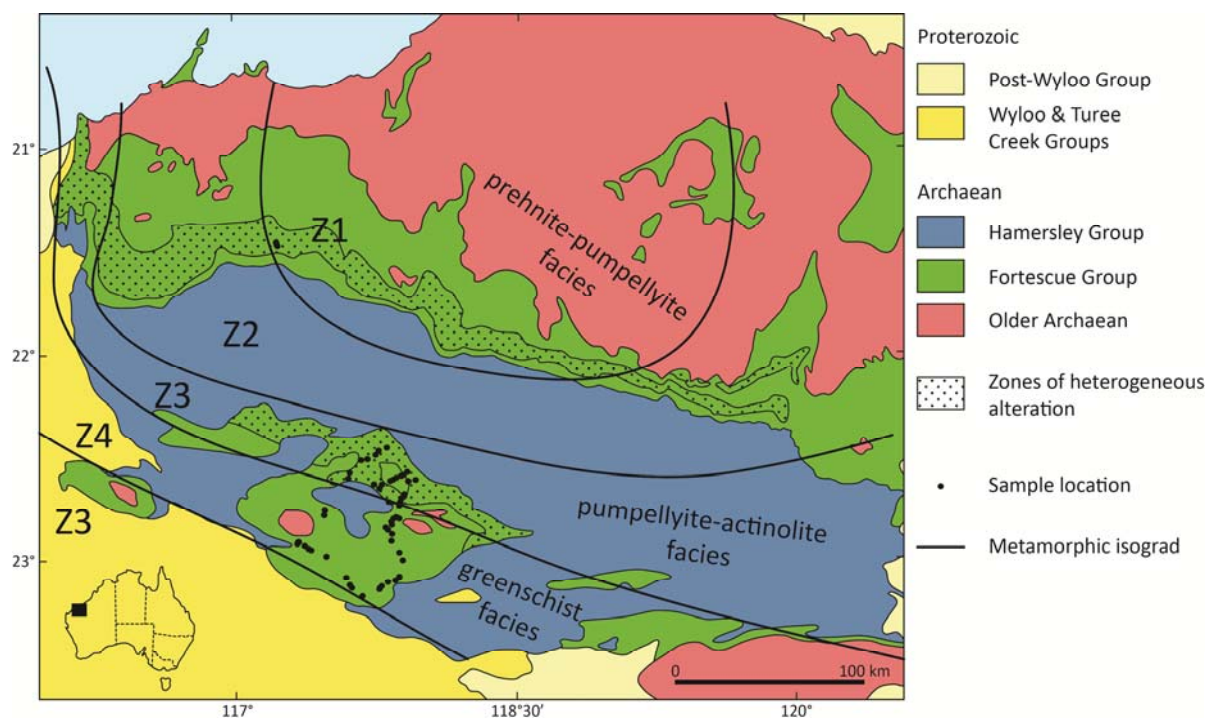
**Figure 1.** Simplified geologic map of the Hamersley Basin, showing the outcrop of Fortescue Group rocks, zones of the regional metamorphic gradient, zones of heterogeneous alteration and metasomatism, and sample locations. After Smith et al (1982).

## 3 Field setting and petrography

Hydrothermal alteration in the Fortescue Group is most extensively developed in the gently dipping lava flows of the Maddina Formation, in the northern Hamersley Basin. The alteration broadly follows volcanic stratigraphy where it is focused along originally vesicular flow tops and flow top breccias. Following the flow tops, metasomatism is essentially continuous over a strike length of 100 km, which is visible with satellite imagery (Smith et al. 1978). Alteration gradually diminishes down through individual lava flows towards a massive 'least altered' base, which has been subjected to a regional metamorphic overprint only.

The 'least altered' domains preserve an igneous texture, although the majority of mineral phases have been partially replaced – albite, prehnite and chlorite replaces plagioclase feldspar, and chlorite replaces pyroxene. In metamorphic zones 3 and 4, the 'least altered' rocks develop a strong actinolite overprint. The increased abundance of metamorphic epidote-clinozoisite in zones 3 and 4, compared to the lack of ferric iron-bearing minerals at lower grades, results in an apparent redox gradient across the basin, which is detectable with infrared spectroscopic techniques.

Hydrothermal alteration is easily recognized in metamorphic zones 1 and 2, and the lower parts of zone 3 due to the formation of pumpellyite±epidote+quartz+sphene rocks that have a distinctive yellow-green colour in outcrop (Fig. 2). These assemblages are completely recrystallised and no traces of the original igneous texture remain. They are qualitatively similar to epidosites described in the Troodos ophiolite, Cyprus, and the Noranda District of Canada (Richardson et al. 1978; Hannington et al.

2003).

In the upper parts of zone 3, and particularly in zone 4, hydrothermal alteration becomes more cryptic in outcrop. In zone 4 it is virtually unrecognizable. This is, in part, due to increased structural complexity, resulting in significantly shorter continuous strike lengths exposed at the surface, but is also related to the complete absence of yellow-green pumpellyite and the dominance of colourless epidote-clinozoisite.
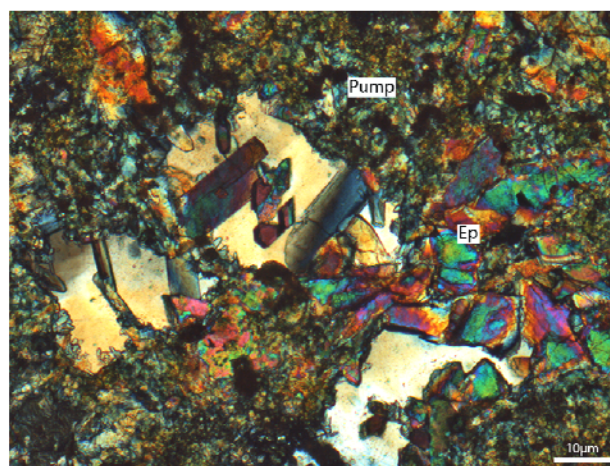


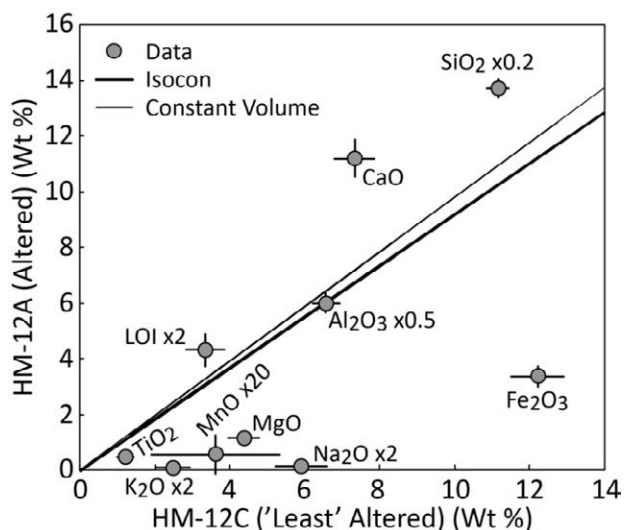**Figure 2.** Photomicrograph (between crossed polars) of a pumpellyite- and epidote-rich metasomatized rock.

## 4 Chemical relationships

Multi-element geochemical data were collected on a subset of samples (n=71) by Genalysis Laboratory

Services, Perth, Australia, using the methods outlined in lithogeochemical package LITH/204X . Additional data were collected on the remaining samples (n=184) using an Olympus InnovX Delta portable XRF instrument at the Australian Resources Research Centre (ARRC), Perth, Australia, following the protocols and procedures of Fisher et al. (in press). All geochemical data were levelled according to primary igneous populations based on immobile trace element ratios (Ti-Zr-Y) to remove geochemical variation related to igneous fractionation. XRD spectra were collected on all samples using a Bruker D4 Endeavour instrument at ARRC and subsequently interpreted with the DIFFRAC.EVA computer program. Infrared spectra in the range 350–2500 nm were collected with an ASD FieldSpec 3 instrument at ARRC and interpreted with The Spectral Geologist.

Metasomatized rocks exhibit marked depletions in Fe, Mn, alkalis, Co and Zn, with significant additions limited to Si and Ca (Figs. 3 and 4). These depletions and enrichments correlate well with an arbitrary visible alteration index and with semi-quantitative XRD data for pumpellyite/epidote+quartz abundance. Total Fe depletion is also recorded in infrared spectral data as a reduction in both ferrous and ferric iron absorption features. These geochemical changes are again similar to epidosites associated with hydrothermal upflow zones in oceanic crust (Richardson et al. 1987; Banerjee et al. 2000; Hannington et al. 2003; Jowitt et al. 2012).

The same geochemical trends are found in all regional metamorphic zones, including zone 4 where there is relatively little mineralogical alteration associated with the metasomatism.

internally consistent data set (Holland and Powell 1998, updated Nov 2003), constrain likely pressure-temperature conditions of equilibration of the alteration assemblages. Zone 1 assemblages are consistent with temperatures in the range 200-250°C, while those in zone 4 likely represent minimum temperatures of 300°C. Pressure conditions are more poorly constrained.

Furthermore, such phase equilibria modelling indicates that in zone 4, even those rocks that are highly metasomatically altered are dominated by assemblages containing actinolite and epidote, i.e., they are similar to zone 4 regional metamorphic assemblages. As such, zones of metasomatic alteration may not be readily identified in the field, based solely on mineralogy (Fig. 4). Consequently, the distribution of metasomatism in the southern Fortescue Group may be significantly broader than previously realised.
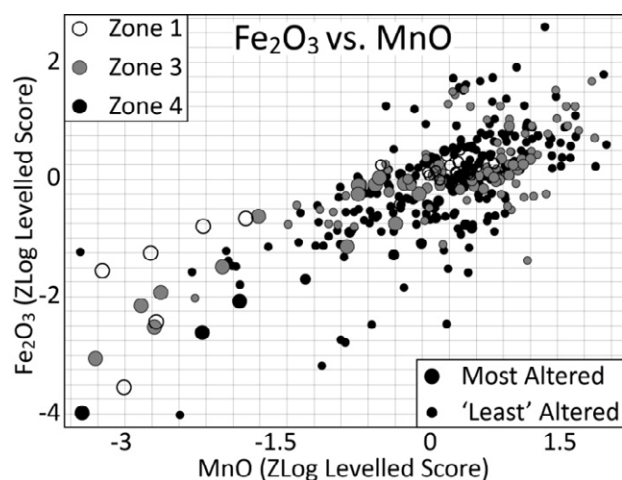


**Figure 4.** Geochemical plot of total Fe as $Fe_2O_3$ versus MnO. Note data are levelled according to primary compositional groupings. Significant depletions in Fe and Mn correlate with a visible alteration index (spot size) based on mineralogy. However, metasomatized rocks from zone 4 (black) rarely show characteristic alteration mineralogy.
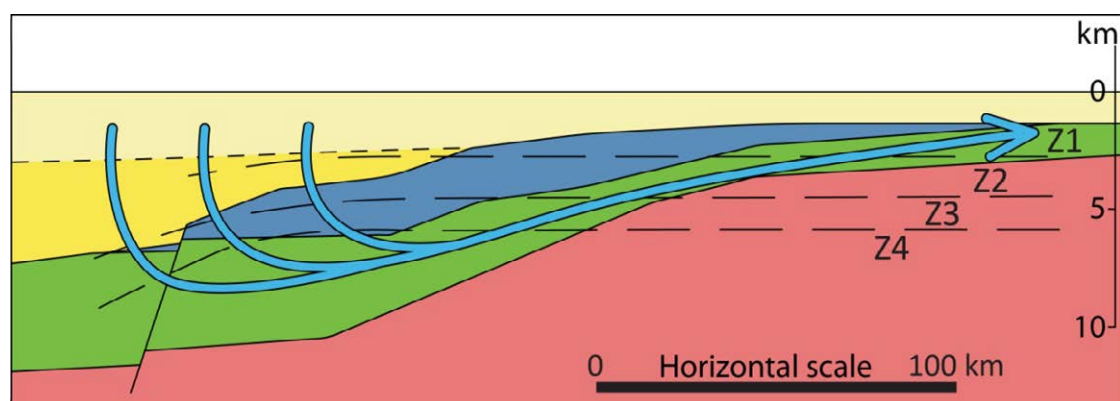
## 6  Discussion and Conclusions

Both the mineralogy and geochemistry of the metasomatized rocks studied here are directly comparable to those associated with hydrothermal upflow zones above volcanic heat sources, often characterized by the formation of epidosites (Richardson et al. 1987; Banerjee et al. 2000; Hannington et al. 2003; Jowitt et al. 2012). Therefore, a similar origin is proposed for the metasomatism in the Fortescue Group.

The stratigraphic control on local-scale occurrence of metasomatism implies a strong lateral component to fluid flow. The vesicular flow tops are interpreted to represent pre-existing paths of enhanced permeability and focussed fluid flow. The dip of lava flow units facilitated the rise of fluids towards the surface without the need for any cross-cutting structures (Fig. 5).

Our analyses of whole-rock geochemistry and petrology indicate consistent alteration trends across the entire Fortescue Group (Fig. 4). Such geochemical



**Figure 3.** Major element isocon plot for metasomatism, assuming constant $Al_2O_3$. Major depletions are in Fe, Mn, Mg and alkalis, with additions in Si and Ca.

## 5  P-T controls on mineral assemblages

Thermodynamic modelling of metasomatically altered rocks with the computer program THERMOCALC (Powell and Holland 1988), and its accompanying

**Figure 5.** Schematic cartoon illustrating interpreted geometry of geology and fluid flow during the metasomatic event. Cross-section after Smith et al. (1982). Legend as per Figure 1.

trends suggest a single alteration event with a common fluid source. This in turns implies fluid flow on the scale of hundreds of kilometres across the Hamersley Basin, aided by primary vesicularity in the lava flow tops.

The scale of fluid flow observed in the Fortescue Group has important implications for the scale of hydrothermal systems in other mafic terranes. Of particular relevance is the potential size of mineralized systems in the Yilgarn Craton, where fluid permeating laterally from major structures could persist for tens to hundreds of kilometres, depending on the primary fluid flux. If such fluid flow could be detected and traced with a range of geochemical techniques, it dramatically enlarges the potential targets for future exploration of mineral resources.

## Acknowledgements

## References

Arndt NT, Nelson DR, Compston W, Trendall AF, Thorne AM (1991) The age of the Fortescue Group, Hamersley Basin, Western Australia, from ion microprobe zircon U-Pb results. Aus J Earth Sci 38:261-281.

Banerjee NR, Gillis KM, Muehlenbachs K (2000) Discovery of epidosites in a modern oceanic setting, the Tonga forearc. Geology 28:151-154.

Blake TS, Buick R, Brown SJA, Barley ME (2004) Geochronology of a late Archaean flood basalt province in the Pilbara Craton, Australia: constraints on basin evolution, volcanic and sedimentary accumulation, and continental drift rates. Precam Res 133:143-173.

Engvik AK, Mezger K, Wortelkamp S, Bast R, Corfu F, Korneliussen A, Ihlen P, Bingen B, Austrheim A (2011) Metasomatism of gabbro – mineral replacement and element mobilization during the Sveconorwegian metamorphic event. J Met Geol 29:399-423.

Fisher L, Gazley MF, Baensch A, Barnes SJ, Cleverley J, Duclaux G (in press) Resolution of geochemical and lithostratigraphic complexity: a work flow for application of portable X-ray fluorescence to mineral exploration. Geochem: Expl, Env, Anal.

Hannington MD, Santaguida F, Kjarsgaard IM, Cathles LM (2003) Regional-scale hydrothermal alteration in the Central Blake River Group, western Abitibi subprovince, Canada: implications for VMS prospectivity. Miner Deposita 38:393-422.

Holland TJB, Powell R (1998) An internally consistent thermodynamic data set for phases of petrological interest. J Met Geol 16:309-343.

Humphris SE, Thompson G (1978) Hydrothermal alteration of oceanic basalts by seawater. Geochim et Cosmochim Acta 42:107-125.

Jowitt SM, Jenkin GRT, Coogan LA, Naden J (2012) Quantifying the release of base metals from source rocks for volcanogenic massive sulphide deposits: Effects of protolith composition and alteration mineralogy. J Geochem Expl 118:47-59.

Powel R, Holland TJB (1988) An internally consistent dataset with uncertainties and correlations: 3. Applications to geobarometry, worked examples and a computer program. J Met Geol 6:173-204.

Raam A, O'Reilly SY, Vernon RH (1969) Pumpellyite of deuteric origin. Am Min 54:320-324.

Richardson CJ, Cann JR, Richards HG, Cowan JG (1987) Metal-depleted root zones of the Troodos ore-forming hydrothermal systems, Cyprus. Earth Planet Sci Let 84:243-253.

Smith RE, Green AA, Roberts G, Honey FR (1978) Use of LANDSAT-1 imagery in exploration for Keweenawan-type copper deposits. Remote Sensing Env 7:12-144.

Smith RE, Perdrix JL, Parks TC (1982) Burial metamorphism in the Hamersley Basin, Western Australia. J Petrol 23:75-102.

Thorne AM, Trendall AF (2001) Geology of the Fortescue Group, Pilbara Craton, Western Australia. Western Australian Geological Survey, Bulletin 144, 249 p.